

Lecture Notes in Mechanical Engineering

Volodymyr Tonkonogyi ·
Vitalii Ivanov · Justyna Trojanowska ·
Gennadii Oborskyi ·
Ivan Pavlenko *Editors*

Advanced Manufacturing Processes III

Selected Papers from the
3rd Grabchenko's International
Conference on Advanced Manufacturing
Processes (InterPartner-2021),
September 7–10, 2021, Odessa, Ukraine

 Springer


Lecture Notes in Mechanical Engineering

Series Editors

Francisco Cavas-Martínez, Departamento de Estructuras, Universidad Politécnica de Cartagena, Cartagena, Murcia, Spain

Fakher Chaari, National School of Engineers, University of Sfax, Sfax, Tunisia

Francesca di Mare, Institute of Energy Technology, Ruhr-Universität Bochum, Bochum, Nordrhein-Westfalen, Germany

Francesco Gherardini , Dipartimento di Ingegneria, Università di Modena e Reggio Emilia, Modena, Italy

Mohamed Haddar, National School of Engineers of Sfax (ENIS), Sfax, Tunisia

Vitalii Ivanov, Department of Manufacturing Engineering, Machines and Tools, Sumy State University, Sumy, Ukraine

Young W. Kwon, Department of Manufacturing Engineering and Aerospace Engineering, Graduate School of Engineering and Applied Science, Monterey, CA, USA

Justyna Trojanowska, Poznan University of Technology, Poznan, Poland

Lecture Notes in Mechanical Engineering (LNME) publishes the latest developments in Mechanical Engineering—quickly, informally and with high quality. Original research reported in proceedings and post-proceedings represents the core of LNME. Volumes published in LNME embrace all aspects, subfields and new challenges of mechanical engineering. Topics in the series include:

- Engineering Design
- Machinery and Machine Elements
- Mechanical Structures and Stress Analysis
- Automotive Engineering
- Engine Technology
- Aerospace Technology and Astronautics
- Nanotechnology and Microengineering
- Control, Robotics, Mechatronics
- MEMS
- Theoretical and Applied Mechanics
- Dynamical Systems, Control
- Fluid Mechanics
- Engineering Thermodynamics, Heat and Mass Transfer
- Manufacturing
- Precision Engineering, Instrumentation, Measurement
- Materials Engineering
- Tribology and Surface Technology

To submit a proposal or request further information, please contact the Springer Editor of your location:

China: Ms. Ella Zhang at ella.zhang@springer.com

India: Priya Vyas at priya.vyas@springer.com

Rest of Asia, Australia, New Zealand: Swati Meherishi at swati.meherishi@springer.com

All other countries: Dr. Leontina Di Cecco at Leontina.dicecco@springer.com

To submit a proposal for a monograph, please check our Springer Tracts in Mechanical Engineering at <http://www.springer.com/series/11693> or contact Leontina.dicecco@springer.com

Indexed by SCOPUS. All books published in the series are submitted for consideration in Web of Science.

More information about this series at <http://www.springer.com/series/11236>

Volodymyr Tonkonogyi ·
Vitalii Ivanov · Justyna Trojanowska ·
Gennadii Oborskyi · Ivan Pavlenko
Editors

Advanced Manufacturing Processes III

Selected Papers from the 3rd Grabchenko's
International Conference on Advanced
Manufacturing Processes (InterPartner-2021),
September 7–10, 2021, Odessa, Ukraine

Editors

Volodymyr Tonkonogyi
Odessa Polytechnic State University
Odessa, Ukraine

Vitalii Ivanov
Sumy State University
Sumy, Ukraine

Justyna Trojanowska
Poznan University of Technology
Poznan, Poland

Gennadii Oborskyi
Odessa Polytechnic State University
Odessa, Ukraine

Ivan Pavlenko
Sumy State University
Sumy, Ukraine

ISSN 2195-4356

ISSN 2195-4364 (electronic)

Lecture Notes in Mechanical Engineering

ISBN 978-3-030-91326-7

ISBN 978-3-030-91327-4 (eBook)

<https://doi.org/10.1007/978-3-030-91327-4>

© The Editor(s) (if applicable) and The Author(s), under exclusive license
to Springer Nature Switzerland AG 2022

This work is subject to copyright. All rights are solely and exclusively licensed by the Publisher, whether the whole or part of the material is concerned, specifically the rights of translation, reprinting, reuse of illustrations, recitation, broadcasting, reproduction on microfilms or in any other physical way, and transmission or information storage and retrieval, electronic adaptation, computer software, or by similar or dissimilar methodology now known or hereafter developed.

The use of general descriptive names, registered names, trademarks, service marks, etc. in this publication does not imply, even in the absence of a specific statement, that such names are exempt from the relevant protective laws and regulations and therefore free for general use.

The publisher, the authors and the editors are safe to assume that the advice and information in this book are believed to be true and accurate at the date of publication. Neither the publisher nor the authors or the editors give a warranty, expressed or implied, with respect to the material contained herein or for any errors or omissions that may have been made. The publisher remains neutral with regard to jurisdictional claims in published maps and institutional affiliations.

This Springer imprint is published by the registered company Springer Nature Switzerland AG
The registered company address is: Gewerbestrasse 11, 6330 Cham, Switzerland

Preface

This volume of Lecture Notes in Mechanical Engineering contains selected papers presented at the 3rd Grabchenko’s International Conference on Advanced Manufacturing Processes (InterPartner-2021), held in Odessa, Ukraine, during September 7–10, 2021. The conference was organized by Odessa Polytechnic State University, National Technical University “Kharkiv Polytechnic Institute,” Sumy State University, and International Association for Technological Development and Innovations in partnership with Poznan University of Technology (Poland).

InterPartner Conference Series promotes research and developmental activities, intensifying scientific information interchange between researchers, developers, and engineers.

InterPartner-2021 received 113 contributions from 22 countries around the world. After a thorough peer-review process, the Program Committee accepted 68 papers written by authors from 19 countries. Thank you very much to the authors for their contribution. These papers are published in the present book, achieving an acceptance rate of about 60%.

We want to take this opportunity to thank members of the Program Committee and invited external reviewers for their efforts and expertise in contributing to reviewing, without which it would be impossible to maintain the high standards of peer-reviewed papers.

Thank you very much to keynote speakers from Poland (Slawomir Luscinski) and Ukraine (Sergiy Kovalevskyy, Ivan Pavlenko, Yuri Petrakov, Yuriy Vnukov).

The book “Advanced Manufacturing Processes III” was organized into eight parts according to the main conference topics: Part 1—Design Engineering, Part 2—Manufacturing Technology, Part 3—Machining Processes, Part 4—Advanced Materials, Part 5—Quality Assurance, Part 6—Mechanical Engineering, Part 7—Process Engineering, and Part 8—Engineering Education.

The first part “Design Engineering” includes recent developments in design technologies and calculations. It presents studies in rational choice of gears, optimization of a swing mechanism, and design elements of hydraulic drives. This part also includes energy management strategy in the synthesis of automated control

systems, methods to research loadings on mechanical structures under moving load distribution.

The second part “Manufacturing Technology” includes ways to implement intelligent solutions within the Industry 4.0 strategy. Recent developments in the application of additive manufacturing and genetic algorithms are also presented in this part. Also, this part includes parameter identification of the vibrational state for machines and shape optimization of designs. Finally, the second part includes studies in ensuring vibration reliability of cutting tools, mathematical modeling of a backlash elimination in a clamping device, and ways for evaluating parameters in precise modeling. Finally, recent developments in the lifecycle management of modular machine tools are also presented in this part.

The third part “Machining Processes” consists of studies concerning measuring grinding temperatures, rational designing of diamond grinding wheels, crankshaft manufacturing, and advanced grinding of gears and hardened steels, including temperature modeling. Notably, simulations of an absorber for vibrations during turning and optimization of electrical discharge grinding are also included in this part. Additionally, the third part deals with improving the MQL efficiency in machining stainless steel by adding nanoparticles to the cutting fluid and the impact of turning operations on forming the rolling bearing’s functional surfaces.

The fourth part “Advanced Materials” is devoted to controlling strength properties for mixtures, probabilistic analysis of corrosion fatigue resistance, and improvement of parameters for designs from hydroxyapatite and beta-tricalcium phosphate. Crack resistance parameters of nano-reinforced products, surface strengthening technologies for improved strength characteristics of steel and hard alloys, i.e., under the laser and ultrasonic treatments, are also presented in this part. This part also aims to improve material properties for manufacturing parts, polymer bulk composites’ application, dispersion hardening methods, and low-plastic materials. It also includes a comparative analysis of tribological and functional properties of multilayer coatings obtained by nitriding and titanizing, improvement characteristics of nanosized oxide coatings, and structure optimization of heat-resistant alloys.

The fifth part “Quality Assurance” presents studies on ensuring the quality of thread profiles and surface layers while grinding hard alloys and porous materials. The general approach in the tolerance control for quality assessment, a qualimetric model for assessing the state of the central nervous system, and ways to improve the quality of environmental protection are also included in this part. The fifth part also describes problems and prospects of cryptocurrency development and improved quality control methods for nuclear power plants.

The sixth part “Mechanical Engineering” is based on recent developments in this field of science. It includes studies in the stress state of a workpiece, designing a hydraulic press, improving the integral characteristics for turbomachine nozzles, contact interaction of elements in a hydrovolumetric transmission, and neutralization of the destabilization effect caused by small damping force in a non-conservative system. Mathematical models of particle movement on internal and external curved surfaces are also presented in this part. Finally, the fifth part

includes an advanced method for diagnostics of the rotor–stator contact by spectral analysis of the vibration state for rotor machines.

The seventh part “Process Engineering” presents research studies devoted to oil filtration through a porous medium, the effectiveness of air cooling systems for marine engines, kinematic analysis of an oscillatory system, cleaning of parts using detonating gas mixtures, and optimal composition of high-octane gasoline with biocomponents. Experiments on gas–liquid layer height in a combined contact device, studies in relaxation shock absorbers with mechanical control circuit, and methods for electro-hydraulic activation of water–lime suspension in sugar production are presented in this part. The seventh part also includes improvements in marine engines’ environmental and energy efficiency and approaches for rational loading combined wastes into a heat recovery cooling system.

The eighth part “Engineering Education” aims at recent developments in implementing digital twins in engineering study programs within the Industry 4.0 strategy and ensuring ecological competencies of agricultural engineering students under professional training. Electronic means for developing professional competencies of engineering students are also presented in this part.

The editors appreciate the outstanding contribution of all the authors. We are deeply convinced that the research papers presented in the book will be helpful to scientists, industrial engineers, and highly qualified practitioners worldwide.

We appreciate a reliable partnership with Springer Nature, StrikePlagiarism, and EasyChair for their support during the preparation of InterPartner 2021.

Thank you very much to InterPartner team. Their involvement, devotion, and hard work were crucial to the success of the conference.

InterPartner’s motto is “Science unites people together”.

September 2021

Volodymyr Tonkonogyi
Vitalii Ivanov
Justyna Trojanowska
Gennadii Oborskyi
Ivan Pavlenko

Organization

Honorary Chair

Anatolii Grabchenko

National Technical University “Kharkiv
Polytechnic Institute,” Ukraine

General Chair

Volodymyr Tonkonogyi

Odessa Polytechnic State University, Ukraine

Co-chair

Vitalii Ivanov

Sumy State University, Ukraine

Steering Committee

Vitalii Ivanov

Sumy State University, Ukraine

Gennadii Oborskyi

Odessa Polytechnic State University, Ukraine

Ievhen Ostroverkh

National Technical University “Kharkiv
Polytechnic Institute,” Ukraine

Ivan Pavlenko

Sumy State University, Ukraine

Volodymyr Tonkonogyi

Odessa Polytechnic State University, Ukraine

Justyna Trojanowska

Poznan University of Technology, Poland

Program Committee

Jean-Francois Antoine

University of Lorraine, France

Katarzyna Antosz

Rzeszow University of Technology, Poland

Michal Balog

Technical University of Kosice, Slovak Republic

Yevheniia Basova

National Technical University “Kharkiv
Polytechnic Institute,” Ukraine

Kristina Berladir	Sumy State University, Ukraine
Cristian Barz	Technical University of Cluj-Napoca, Romania
Ricardo Branco	University of Coimbra, Portugal
Dagmar Caganova	Slovak University of Technology, Slovak Republic
Emilia Campean	Technical University of Cluj-Napoca, Romania
Yelizaveta Chernysh	Sumy State University, Ukraine
Olivian Chiver	Technical University of Cluj-Napoca, Romania
Vasile George Cioata	Polytechnic University of Timisoara, Romania
Olaf Ciszak	Poznan University of Technology, Poland
Nadezda Cubonova	University of Zilina, Slovak Republic
Ivan Cvitic	University of Zagreb, Croatia
Radu Cotetiu	Technical University of Cluj-Napoca, Romania
Predrag Dasic	High Technical Mechanical School of Professional Studies Trstenik, Serbia
Yuliia Denysenko	Sumy State University, Ukraine
Oleksandr Derevianchenko	Odessa Polytechnic State University, Ukraine
Sergey Dobrotvorskiy	National Technical University “Kharkiv Polytechnic Institute,” Ukraine
Kostyantyn Dyadyura	Sumy State University, Ukraine
Mihai Dragomir	Technical University of Cluj-Napoca, Romania
Tygran Dzhuguryan	Maritime University of Szczecin, Poland
Milan Edl	University of West Bohemia, Czech Republic
Sulaymon Eshkabilov	North Dakota State University, USA
Mathieu Gautier	University Lyon, France
Renata Gnatowska	Czestochowa University of Technology, Poland
Marta Grabowska	Poznan University of Technology, Poland
Jakub Grabski	Poznan University of Technology, Poland
Ihor Hrytsay	Lviv Polytechnic National University, Ukraine
Ihor Hurey	Lviv Polytechnic National University, Ukraine
Vitalii Ivanov	Sumy State University, Ukraine
Maryna Ivanova	National Technical University “Kharkiv Polytechnic Institute,” Ukraine
Malgorzata Jasiulewicz-Kaczmarek	Poznan University of Technology, Poland
Lydmila Kalafatova	Donetsk National Technical University, Ukraine
Isak Karabegovic	University of Bihac, Bosnia and Herzegovina
Serhii Khovanskyi	Sumy State University, Ukraine
Lucia Knapcikova	Technical University of Kosice, Slovak Republic
Dmytro Konovalov	Admiral Makarov National University of Shipbuilding, Ukraine
Kateryna Kostyk	National Technical University “Kharkiv Polytechnic Institute,” Ukraine
Jan Krmela	Alexander Dubcek University of Trencin, Slovak Republic

Jaroslav Kusyj	Lviv Polytechnic National University, Ukraine
Maria Lazar	University of Petrosani, Romania
Oleksandr Liaposhchenko	Sumy State University, Ukraine
Vladimir Lebedev	Odessa Polytechnic State University, Ukraine
Slawomir Luszcynski	Kielce University of Technology, Poland
Jose Machado	University of Minho, Portugal
Ildiko Mankova	Technical University of Kosice, Slovak Republic
Angelos Markopoulos	National Technical University of Athens, Greece
Dariusz Mazurkiewicz	Lublin University of Technology, Poland
Mykola Melnychuk	Lutsk National Technical University, Ukraine
Viktor Molnar	University of Miskolc, Hungary
Dmitriy Muzylyov	Kharkiv Petro Vasylenko National Technical University of Agriculture, Ukraine
Arun Nagarajah	University of Duisburg-Essen, Germany
Marek Ochowiak	Poznan University of Technology, Poland
Gennadii Oborskyi	Odessa Polytechnic State University, Ukraine
Daniela Onofrejova	Technical University of Kosice, Slovak Republic
Oleh Onysko	Ivano-Frankivsk National Technical University of Oil and Gas, Ukraine
Vitalii Pasichnyk	National Technical University of Ukraine “Igor Sikorsky Kyiv Polytechnic Institute,” Ukraine
Ivan Pavlenko	Sumy State University, Ukraine
Dragan Perakovic	University of Zagreb, Croatia
Marko Perisa	University of Zagreb, Croatia
Dusan Petkovic	University of Nis, Serbia
Jan Pitel’	Technical University of Kosice, Slovak Republic
Oleksandr Povstyanoy	Lutsk National Technical University, Ukraine
Erwin Rauch	Free University of Bolzano, Italy
Andrii Rogovyi	National Technical University “Kharkiv Polytechnic Institute,” Ukraine
Alessandro Ruggiero	University of Salerno, Italy
Vira Shendryk	Sumy State University, Ukraine
Lesya Shkitsa	Ivano-Frankivsk National Technical University of Oil and Gas, Ukraine
Robert Sika	Poznan University of Technology, Poland
Volodymyr Sokolov	Volodymyr Dahl East Ukrainian National University, Ukraine
Vadym Stupnytskyk	Lviv Polytechnic National University, Ukraine
Marek Szostak	Poznan University of Technology, Poland
Volodymyr Tonkonogyi	Odessa Polytechnic State University, Ukraine
Justyna Trojanowska	Poznan University of Technology, Poland
Nicolae Ungureanu	Technical University of Cluj-Napoca, Romania
Alper Uysal	Yildiz Technical University, Turkey
Iveta Vaskova	Technical University of Kosice, Slovak Republic
Jerzy Winczek	Czestochowa University of Technology, Poland

Oleg Zabolotnyi
Predrag Zivkovic

Lutsk National Technical University, Ukraine
University of Nis, Serbia

Invited External Reviewers

Olena Avdieieva	National Technical University “Kharkiv Polytechnic Institute,” Ukraine
Vladimir Bulej	University of Zilina, Slovak Republic
Nikolaos Karkalos	National Technical University of Athens, Greece
Alexey Kotliar	National Technical University “Kharkiv Polytechnic Institute,” Ukraine
Panagiotis Karmiris Obratanski	National Technical University of Athens, Greece
Vitalii Kolesnyk	Sumy State University, Ukraine
Emmanouil Papazoglou	National Technical University of Athens, Greece
Michal Sajgalik	University of Zilina, Slovak Republic
Serhii Sharapov	Sumy State University, Ukraine
Dimitrios Skondras-Giousios	National Technical University of Athens, Greece
Ioan Radu Sugar	Technical University of Cluj-Napoca, Romania
Valentyna Tkachuk	Lutsk National Technical University, Ukraine
Tatiana Volina	National University of Life and Environmental Sciences of Ukraine, Ukraine
Ihor Yakovenko	National Technical University “Kharkiv Polytechnic Institute,” Ukraine
Dmytro Zhyhylii	Sumy State University, Ukraine

InterPartner Team

Anna Balaniuk	Odessa National Polytechnic University, Ukraine
Kristina Berladir	Sumy State University, Ukraine
Vitalii Ivanov	Sumy State University, Ukraine
Oleksandr Liaposhchenko	Sumy State University, Ukraine
Gennadii Oborskyi	Odessa National Polytechnic University, Ukraine
Ievhen Ostroverkh	National Technical University “Kharkiv Polytechnic Institute,” Ukraine
Ivan Pavlenko	Sumy State University, Ukraine
Andrey Pavlyshko	Odessa National Polytechnic University, Ukraine
Volodymyr Tonkonogyi	Odessa National Polytechnic University, Ukraine

Contents

Design Engineering

Optimal Choice of Worm Gearing Design with Increased Wear Resistance for Machine’s Rotary Table	3
Oleg Krol and Volodymyr Sokolov	
Control Optimization of the Swing Mechanism	13
Elena Naidenko, Oleksandr Bondar, Andrii Boiko, Oleksandr Fomin, and Raul Turmanidze	
Manufacturing Error of the Toothed Profile of Rotors for an Orbital Hydraulic Motor	22
Anatolii Panchenko, Angela Voloshina, Nataliia Boltianska, Viktor Pashchenko, and Sergii Volkov	
Energy Management Strategy in the Synthesis of an Algorithm for Multi-step Conveyor Belt Speed Control	33
Oleh Pihnastyi, Georgii Kozhevnikov, and Maxim Glavchev	
Static Stiffness of the Crane Bridges Under Moving Load Distribution	43
Anatoliy Tkachev, Aleksey Tkachev, Dasic Predrag, Ihor Prokopovych, and Maryna Kostina	
Improvement of the Angular Arrangement of Distribution System Windows When Designing Planetary Hydraulic Machines	53
Angela Voloshina, Anatolii Panchenko, Oleg Boltyansky, Andrii Zasiadko, and Valentyna Verkholantseva	
Manufacturing Technology	
Packing 3D-Models of Products in Build Space of Additive Manufacturing Machine by Genetic Algorithm	67
Yaroslav Garashchenko, Jurii Vitiaziev, and Igor Grimzin	

Identification and Technological Impact of Broadband Vibration on the Object	78
Sergiy Kovalevskyy and Olena Kovalevska	
Shape Optimization of an Object Using the Information Model	88
Oleksii Lopakov, Volodymyr Tigariev, Volodymyr Tonkonogyi, and Volodymyr Kosmachevskiy	
Features of Flexural-Torsional Oscillations of Cantilever Boring Bars for Fine Boring of Deep Holes with Small Diameters	98
Alexandr Orgiyan, Gennadii Oborskyi, Vitalii Ivanov, Volodymyr Tonkonogyi, and Anna Balaniuk	
Mathematical Model of a Backlash Elimination in the New Clamping Mechanism	109
Borys Prydalnyi	
Modeling Parametric Failures of Woodworking Machines According to the Technological Precision Criterion	119
Mariya Pylypchuk, Lidiia Dziuba, Ihor Rebezniuk, Oksana Chmyr, and Mykhailo Burdiak	
Lifecycle Management of Modular Machine Tools	127
Ihor Yakovenko, Alexander Permyakov, Maryna Ivanova, Yevheniia Basova, and Dmitry Shepeliev	
Machining Processes	
Methods for Measuring Grinding Temperatures	141
Ala Bezpalova, Vladimir Lebedev, Tatiana Chumachenko, Olga Frolenkova, and Nataliya Klymenko	
Rational Characteristics of the Diamond Grinding Wheels	151
Vladimir Fedorovich, Ivan Pyzhov, Yevgen Babenko, Yevgeniy Ostroverkh, and Natalia Kozakova	
Model of Milling the Root and Connecting Rod Necks of the Crankshaft for One Manufacturing Process	160
Vitaliy Kalchenko, Volodymyr Kalchenko, Nataliia Sira, Yaroslav Kuzhelnyi, and Vasyl Sklyar	
Gear Grinding Stock Alignment in Advance of Grinding	170
Vasily Larshin, Natalia Lishchenko, Oleksandr Lysyi, and Sergey Uminsky	
Burns of Tempering While Grinding Hardened Steels	180
Vladimir Lebedev, Tatiana Chumachenko, Nataliya Klymenko, and Olga Frolenkova	

Modeling of the Intermittent Grinding Temperature 188
 Natalia Lishchenko, Vasily Larshin, and Sergey Uminsky

Simulation of an Absorber of Vibration in Turning 199
 Yuri Petrakov and Maksim Sikailo

Determination of the Distance Between Grains During Electrical Discharge Grinding with Changing Polarity of Electrodes 209
 Roman Strelchuk and Oleksandr Shelkovyi

Improvement of the MQL Efficiency in Machining Stainless Steel by Adding Nanoparticles to the Cutting Fluid 219
 Youssef Touggui, Alper Uysal, Uğur Emiroglu, Eshreb Dzhemilov, and Salim Belhadi

Impact of Turning Operations on the Formation of Rolling Bearing’s Functional Surfaces 229
 Valentyn Zablotskyi, Anatolii Tkachuk, Anatolii Senyshyn, Ivanna Trokhymchuk, and Kostiantyn Svirzhevskiy

Advanced Materials

Control of the Strength Properties of Mixtures Based on Chromite Sand 241
 Tatyana Berlizeva, Olga Ponomarenko, Nataliia Yevtushenko, Igor Grimzin, and Tatiana Lysenko

Probabilistic Analysis of Corrosion Fatigue Resistance 250
 Svetlana Bershak, Victor Kurgan, Ihor Sydorenko, Oleksandr Levinskyi, and Yuriy Yeputatov

Analysis of Permissible Limits for Leachable of Trace Impurities from Bone Substitutes Containing Hydroxyapatite and Beta-Tricalcium Phosphate 260
 Kostiantyn Dyadyura, Liudmyla Hrebenyk, Tatyana Ivakhniuk, Maria Vyshegorodtseva, and Liudmyla Primova

Crack Resistance Parameters of Nano-reinforced Rubber Products in Mechanical Engineering 272
 Aleksandr Gondlyakh, Aleksandr Kolosov, Valeriy Scherbina, Oleksandr Mamchur, and Yaroslav Shilovich

Surface Strengthening Technology for Hammers of a Four-Die Forging Device 282
 Tetiana Hovorun, Kristina Berladir, and Oleksandr Gusak

Ensuring the High Strength Characteristics of the Surface Layers of Steel Products 292
 Kateryna Kostyk, Viktoriia Kostyk, Oleg Akimov, Kateryna Kamchatna-Stepanova, and Yurii Shyrokyi

Cladded Ferromagnetic Powders for Magnetic Abrasive Working of Hard Alloys	302
Vladimir Lebedev, Svetlana Yakubovskaya, Eshreb Dzhemilov, and Ruslan Dzhemalyadinov	
Comparison of Effects of Laser, Ultrasonic, and Combined Laser-Ultrasonic Hardening Treatments on Surface Properties of AISI 1045 Steel Parts	313
Dmytro Lesyk, Walid Alnusirat, Silvia Martinez, Bohdan Mordyuk, and Vitaliy Dzhemelinskyi	
Improvement of Processes for Obtaining Titanium Alloys for Manufacturing Parts with Design Elements	323
Viktoriya Pasternak, Oleg Zabolotnyi, Nataliia Ilchuk, Dagmar Cagaňová, and Yurii Hulchuk	
Dispersion Hardening of Nano- and Submicrocrystalline Vacuum Cu-Mo Condensates	334
Valentyn Riaboshtan, Anatoly Zubkov, Maria Zhadko, and Tatyana Protasenko	
Polymer Bulk Composites with Strong Noncovalent Interface Interactions	343
Denys Savchenko, Eugen Pashchenko, Svitlana Kukharenko, Oksana Kaidash, and Serhii Riabchenko	
Features of Plasticity Diagram Construction for Low-Plastic Materials	353
Ihor Shepelenko, Yakiv Nemyrovskyi, Yuri Tsekhanov, Volodimir Mirzak, and Sergii Mahopets	
Comparative Analysis of Tribological and Functional Properties of Multilayer Composite Nanostructured Coatings Based on Nitrides of Cr, Mo, Zr, Nb, and Al	363
Alexey Vereschaka and Mars Migranov	
The Structure and Properties of a-C:Ti and a-C:Ti:N Coatings Deposited on a Titanium and Titanium Nitride Sublayer	373
Xiaohong Jiang, Dzmitry Piliptsou, Aliaksandr Rogachev, Ekaterina Kulesh, and Yiming Liu	
Improvement of Operating Properties of Heat-Resistant Alloys by the Structure Optimization	383
Natalia Zaichuk, Sergii Shymchuk, Anatolii Tkachuk, Yurii Shymchuk, and Karim Kashash Badir	

Quality Assurance

Influence of Working Height of a Thread Profile on Quality Indicators of the Drill-String Tool-Joint 395

Volodymyr Kopei, Oleh Onysko, Vitalii Panchuk, Lolita Pituley, and Iryna Schuliar

Impact of the Heterogeneous Structure of Magnetic Hard Alloys on the Quality Characteristics of the Surface Layer During Grinding Processing 405

Maksym Kunitsyn, Anatoly Usov, and Yulia Sikirash

Mathematic Model of the General Approach to Tolerance Control in Quality Assessment 415

Oleksandr Kupriyanov, Roman Trishch, Dimitar Dichev, and Tetiana Bondarenko

Qualimetric Model for Assessing the State of the Central Nervous System of Animals When Studying the Mechanism of Biological Activity for Mineral Waters 424

Alona Kysylevska, Konstantin Babov, Sergey Gushcha, Ihor Prokopovych, and Tatiana Bezverkhniuk

Problems and Prospects of Cryptocurrency Development 435

Alexander Masharsky and Ivan Skvortsov

Improvement of the Quality of the Human Environment by Transporting and Stabilizing Sewage Sludge for Further Processing . . . 445

Vladyslav Vaysman, Natalia Strunnikova, Olena Chukurna, Vitalii Dobrovolskyi, and Oleg Kassien

Influence of the Cutting Temperature on the Surface Layer Quality When Grinding Sintered Porous Materials 455

Oleg Zabolotnyi, Tetiana Bozhko, José Machado, Serhii Yarmoliuk, and Olha Zaleta

Improvement of Quality Control Methods for Filters' Adsorbents in Purification of Gas Emissions of Nuclear Power Plants 466

Sergey Zaitsev, Victor Kishnevsky, Gennadii Oborskyi, Anatoly Tikhomirov, and Valentin Tikhenko

Mechanical Engineering

The Stress State of the Workpiece at the Radius of Matrix Rounding During Drawing, Considering the Bending Moment 479

Roman Arhat, Ruslan Puzyr, Viktor Shchetynin, Roman Levchenko, and Oleksandr Pedun

Hydraulic Press Open Die Forging of 21CrMoV5-7 Steel CCM Roller with Flat Upper and Concave Semi-round Lower Cogging Dies	489
Volodymyr Kukhar, Oleg Vasylevskiy, Olha Khliestova, Ivan Berestovoi, and Elena Balalayeva	
Improved Hybrid Methods for Determining the Integral Characteristics of Turbomachine Nozzle Cascades	499
Alexandr Lapuzin, Valery Subotovich, Yuriy Yudin, and Olena Avdieieva	
Contact Interaction of a Ball Piston and a Running Track in a Hydrovolumetric Transmission with Intermediate Deformable Surface Layers	509
Mykola Tkachuk, Andrey Grabovskiy, Mykola Tkachuk, Iryna Hrechka, and Volodymyr Sierykov	
Diagnostics of the Rotor-Stator Contact by Spectral Analysis of the Vibration State for Rotor Machines	521
Ivan Pavlenko, Ievgen Savchenko, Jan Pitel, Vitalii Ivanov, and Anatolii Ruban	
Movement of a Particle on the Inner Surface with a Preset Meridian	535
Serhii Pylypaka, Tatiana Volina, Olha Zalevska, Svetlana Semirnenko, and Iryna Hryshchenko	
Neutralization of the Destabilization Effect Caused by Small Damping Force in Non-conservative System	546
Volodymyr Puzyrov, Leonardo Acho Zuppa, Gisela Pujol Vazquez, Nina Savchenko, and Nelya Kyrylenko	
Particle Movement on the External Surface of the Cone that Rotates Around the Vertical Axis	557
Tatiana Volina, Serhii Pylypaka, Victor Nesvidomin, Iryna Rybenko, and Larysa Sierykh	
Process Engineering	
Theoretical Substantiation of Mathematical Models of Oil Filtration Through a Porous Medium	571
Iryna Ablieieva, Leonid Plyatsuk, Oksana Burla, Oleh Chekh, and Alex Enrich-Prast	
Analysis of the Effectiveness of the Thermopressor for Charge Air Cooling of Marine Engines	582
Dmytro Konovalov, Mykola Radchenko, Halina Kobalava, Andrii Radchenko, and Oleg Savenkov	
Kinematic Analysis of an Oscillatory System of a Shaking Conveyor-Separator	592
Vitaliy Korendiy, Oleksandr Kachur, and Petro Dmyterko	

Cleaning of Parts with Detonating Gas Mixtures 602
 Alexey Losev, Igor Bychkov, Anna Selezneva, Vira Shendryk,
 and Sergii Shendryk

**Optimization of the Composition of High-Octane Gasoline
 with Bio-Components** 613
 Nina Merezhko, Valentyna Tkachuk, Volodymyr Komakha,
 Oleksandr Povstyanoy, and Taras Karavaiev

**Experimental Investigation of Gas-Liquid Layer Height
 in a Combined Contact Device** 623
 Viktor Moiseev, Oleksandr Liaposhchenko, Michal Hatala,
 Eugenia Manoilo, and Oleg Khukhryanskiy

**Rational Loading on Combined Waste Heat Recovery
 Cooling System** 634
 Andrii Radchenko, Serhiy Forduy, Serhiy Kantor, Oleksii Zelikov,
 and Viktor Khaldobin

**Improvement of Environmental and Energy Efficiency of Marine
 Engines by Utilizing the Ecological Recirculation of Gas Heat
 in an Absorption Chiller** 644
 Roman Radchenko, Maxim Pyrysunko, Victoria Kornienko,
 Andrii Andreev, and Artem Hrych

**Relaxation Shock Absorbers with Additional Mechanical Control
 Circuit** 655
 Ihor Sydorenko, Vladimir Semenyuk, Valeriy Lingur, Liubov Bovnegra,
 and Kateryna Kirkopulo

**Method of Electrohydraulic Activation of Water-Lime Suspension
 in Sugar Production** 664
 Volodymyr Vasyliv, Mikhailo Mushtruk, Marija Zheplinska,
 Roman Mukoid, and Serhii Tkachenko

Engineering Education

**Implementation of Digital Twins for Industry 4.0 in the Engineering
 Study Program** 677
 Peter Arras and Galyna Tabunshchyyk

The Technology of the Learning Outcomes Test Development 687
 Petro Luzan, Oleksandr Koshuk, Olena Titova, and Iryna Mosia

**Administrative Fundamentals of Ecological Competence Forming
 in Agricultural Engineering Students Under Conditions of Their
 Professional Training** 697
 Viktor Nagayev, Iryna Danchenko, Tetiana Mitiashkina,
 and Vecheslav Kyrepin

Electronic Textbooks as Means for Developing Professional Competencies of Engineering Students 707
Vitalii Svyrydiuk, Petro Luzan, Olha Svyrydiuk, Olena Titova,
and Oksana Popova

Author Index 717

Design Engineering



Optimal Choice of Worm Gearing Design with Increased Wear Resistance for Machine's Rotary Table

Oleg Krol^(✉)  and Volodymyr Sokolov 

Volodymyr Dahl East Ukrainian National University, 59-a, Central Ave.,
Severodonetsk 93400, Ukraine
krol.os@snu.edu.ua

Abstract. This work is devoted to the research of circular feed devices for a metal-cutting machine with backlash-free worm gear of increased wear resistance. A spatial model of a rotary table with a gap compensation mechanism as sliding supports in the integrated CAD KOMPAS-3D environment has been developed. A design scheme is proposed, and the efforts required to create a guaranteed hard contact are determined. The effectiveness of the proposed method for compensating the gap due to the worm displacement relative to the wheel is substantiated. The phenomena associated with a decrease in the intensity of wear and arising in the engagement of a worm gear with limitations on rigidity are investigated. A mathematical model of a two-parameter problem of optimizing the wear rate using Lagrange multipliers is formed. The concept of increasing the resource of a mechanical transmission due to the availability of gapless contact between the worm and the wheel is analyzed. The authors conclude that using sliding supports will reduce the time for adjusting machine tools and make the process of manufacturing housing parts more economical. An analytical apparatus for determining the main parameter of the worm gear by the minimum wear criterion is created. The assumption about the rational area of using this design of the backlash-free transmission for the rotary table at low gear ratios and the use of quadric-thread worms is substantiated.

Keywords: Worm engagement · Workpiece-turning mechanism · 3D model · Sliding wear · Contact stress

1 Introduction

For automated manipulation of workpieces of various sizes and shapes in multi-operational CNC machines, rotary and stepping tables of various designs are used [1]. The widespread use of the multi-operational machine is primarily due to the high concentration of processing at one workplace [2, 3]. In the context of a constant change in the configuration [4] of machined parts and the use of machines of various standard sizes, it is promising to design and manufacture a line of rotary tables equipped with hydromechanical drives [5].

The rotary table has a significant effect on the rigidity of the structure and the positioning error of the machine. Calculation of the balance of the relative compliance

of the machine tool carrier system showed that the workpiece and its elastic connections with the rotary table make up 22% of its total compliance. In this case, loading by the forces of the nodes' weight and the forces arising in the processing zone [6]. Simultaneously, the relative compliance of the rotary table reaches 36%. The elastic connections of the rotary table with the cross table of the machine, on which the workpiece is mounted, are up to 10% under the same loading conditions [7].

In turn, the parameters of rigidity and positioning accuracy of the rotary table are formed mainly by the worm gear. As it is known, increased wear and scoring of worm gears are associated with high rubbing speeds and unfavorable sliding direction relative to the contact line. The intensity of wear also depends on the value of contact stresses, which makes the calculation for worm gears contact stresses the main one, and for bending stresses is performed as a checking one.

The positioning accuracy of the table and the inconsistency of the worm wheel movement is associated with the presence of engagement gaps caused by their wear during operation. The misalignment of the rotations of the worm gear elements causes inaccuracy in the positioning of the machine-forming units. Various design solutions related to the development of a backlash-free worm gear are used in the machine tool industry. The direction of research concerns the modernization of the production technology of worm gear elements and the use of special devices to compensate for the gaps in the worm gear. The problems with these two approaches to the complication of both the manufacturing process and the design of the backlash-free worm gear are related. The influence of such design and technological solutions on the wear resistance and performance of the table and workpiece feed mechanisms requires additional research.

2 Literature Review

Several works are devoted to the design and operation of gear mechanisms that implement the table and workpiece feed movement in the process of shaping and positioning on CNC drilling-milling-boring machines.

Work [8] is devoted to using various design options for multi-axis rotary tables with a diameter not exceeding 100 mm. It proposes a design that compensates for the gap in the worm gear ("Anti-Backlash Gears" [9]). Compensation by re-adjusting using adjusting screws to reduce the lateral clearance between the worm and the worm wheel is carried out. The authors of [8] consider an alternative option - a spring-loaded worm gear engagement ("Spring Loaded Gear Mesh"). This option, in particular, in the design of a 5-axis small-sized rotary table in the layout for the vertical machining center of the Haas OM-2 model is used.

The authors of [10] researched the contact surfaces' geometry wheel tooth and proposed a new design solution in the form of a single or double helix to increase the contact length and, consequently, reduce the level of contact stresses.

It should be noted that the contact interaction of the gears and the structural component is also influenced by the technological component associated with the quality of the formation of the gear tooth rear surface. When processing the back surface of the relief tooth by grinding, it is rather complicated to select the cutting

mode. In this regard, the ideas of choosing and optimizing the grinding process presented in [11] are of interest.

The operation of the proposed variant of the gearbox [12] is associated with wear processes [13] and the probability of breakdowns. For analyzing these operational phenomena and prevent possible breakdowns, it is rational to use the method of thermal imaging observation with the Termovision Processing software [14].

In work [15], the problems of CNC machines diagnostics and measurement accuracy using laser interferometric measuring systems are considered. The assessment of various types of errors associated with the main shaping movements is given. A large share of errors associated with the repeatability of dimensions during the operation of machines is shown. The wear degree of the machine tools drive mechanisms is considered one of the error generators [16].

For the dynamic characteristics and their relationship with the wear of the contacting surfaces, the approach proposed in [17] is interesting. The result of wear is uneven engagement (with impacts). For reducing the vibration level during separate and parallel boring and turning tools on a particular processing stand, a mechanism for introducing additional axial vibrations in the feed direction is proposed. In this variant, the possibility of decreasing (with axial vibrations of specific parameters) by 3–4 times the vibrations of the shaping units of the machine is shown experimentally. The consequence of this increases in the resource of the worm gear and the rotary table as a whole.

Questions of geometry, kinematics, and thermal phenomena of worm gears with a cylindrical worm in works [18] The study of contact lines, the curvature of working surfaces, and localization of contact in works were considered [19].

However, these researches related to worm gears with regulated lateral and radial engagement clearances [20]. This article presents the results of a backlash-free worm gear research of increased wear resistance as applied to metal-cutting machines, where synchronization of the worm rotation and the wheel is required, including when reversing.

As [21, 22] stated, one of the leading research goals of mechanical transmissions is developing a three-dimensional working model for studying the geometry for evaluating the ratios of many tooth geometric parameters and visual identification. A method for creating a gearwheel using the composition of the designer's toolkit should include and worm gearing three-dimensional model in the corresponding integrated CAD systems [23]. The performance of the worm gear also depends on the heat dissipation and the removal of wear products from the working area using liquid lubricants. In this regard, an interesting approach is presented in the work [24].

An analysis of the above works showed the directions to improve the performance criteria of the drive mechanisms for the rotary tables of metal cutting machines are associated with creating non-clearance engagement worm transmissions and improving their designs. A large reserve in improvement by searching for the optimal ratio of transmission parameters to maximize the effective operation of machine tools equipment can be achieved.

Based on the analysis of the problem under consideration, to increase the efficiency of machine tools with rotary tables, we formulate the following research goal:

To develop a procedure for finding the optimal design of a worm gear with increased wear resistance for a rotary table of a machine tool by determining the optimal ratio of the engagement parameters of this gear.

For achieving this goal, the following tasks have been proposed:

1. To develop three-dimensional models of the rotary table with the non-clearance engagement of the machine in CAD KOMPAS-3D.
2. Investigate the influence of the input parameters of the worm gear and determine their optimal ratio in terms of the criterion of maximum wear resistance.

3 Research Methodology

Let us consider designing a specialized multioperational CNC machine of the second standard size, milling-drilling-boring type based on the MC200PF4 model. The machine for processing complex housing parts by various cutting methods is intended: milling, drilling, countersinking, and reaming.

The rotary controlled table in the form of an independent unit mounted on the machine table in two positions with horizontal and vertical axes, depending on the surface location is made.

In CAD KOMPAS [7], the 3D model of a rotary table, consisting of more than 300 parts, is built (Fig. 1). When building the model, a specialized application “Shafts and mechanical transmissions-3D” embedded into the system was used [7]. The computer-aided design system with applications allows implementation of collective end-to-end 3D-design of products for various purposes [25]. With its help, the whole range of necessary work is carried out from the initial three-dimensional preparation of the idea of a new design of the rotary table and detailed modeling of the final product to the automatic creation of documentation and drawings.

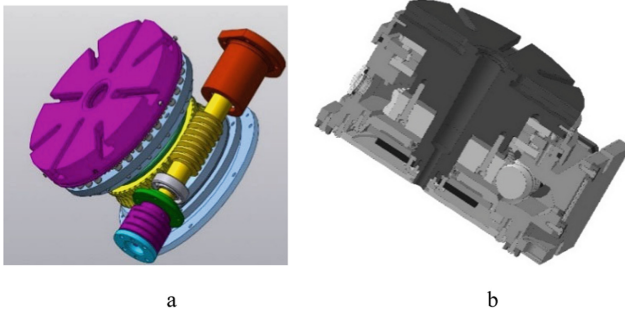


Fig. 1. A three-dimensional model of a rotary table with a faceplate: a – general view without housing; b – the cross-section.

Zeroing of the side clearances in the worm gearing is possible by displacing the worm in a direction parallel to the axis of the worm wheel, Fig. 2a; b.

For realizing this attempt, in the rotary table, on the housing of which there is a faceplate with a worm wheel fixed on it (the teeth of which engagement with the worm threads), the possibility of a downward shift in sliding supports is realized (Fig. 2b).

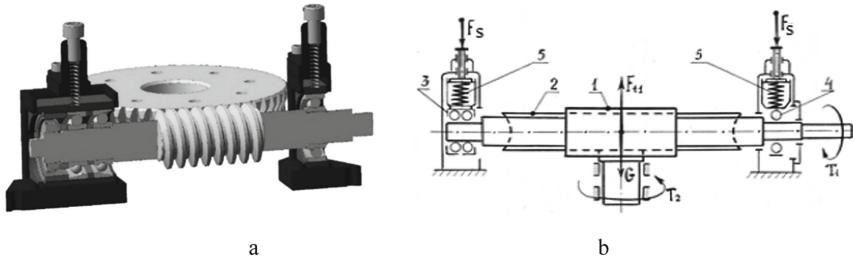


Fig. 2. Antibacklash worm gearing: a – 3D model; b – design scheme.

The shift by the number of clearances in engagement and fixation in this position by springs and clamping screws is carried out. In this case, the engagement of the threads of the worm with the teeth of the worm wheel will be backlash-free for any amount of wear of the threads and teeth, as well as during reverse. In this case, both sides of the worm thread will simultaneously contact the surfaces of two adjacent teeth of the worm wheel.

For determining the forces acting on the worm, the situation is considered when (at a specific direction of the circumferential force on the worm F_{t1} , N), it will tend to return to an unbiased position. The forces of the springs F_s (N) from the equilibrium condition of the system of forces are calculated and shown in Fig. 2b.

By the condition of the balance of forces: $2F_s + G = F_{t1}$:

$$F_s \geq (F_{t1} - G)/2,$$

where G – the weight of the worm shaft assembly, kg.

After transformations, we get the minimum value of the spring force F_s (N) required to create a backlash-free engagement:

$$F_s \geq T_2 \cdot \frac{\operatorname{tg}(\gamma + \varphi')}{d_2} - \frac{G}{2} \quad (1)$$

where $d_2 = m \cdot z_2$ is the pitch diameter of the worm wheel, m; $\gamma = \operatorname{arctg}(z_1/q)$ – pitch angle of the worm threads, degrees;

φ' – the reduced angle of friction in engagement, deg.

q – the coefficient of the worm diameter;

T_2 – torque on the wheel shaft, N m.

It should be noted that when deriving relation (1), an approximate version of calculating the efficiency of a worm pair was used: $\eta \approx \operatorname{tg}\gamma / \operatorname{tg}(\gamma + \varphi')$.

4 Result

The existing standards defining the parameters of the worm gearing for cylindrical worms ZA, Z1, ZN are invariant concerning operating conditions: load mode, and required resource. It means that the choice of the main parameters of the worm gear (WG) is carried out according to uniform recommendations [20].

At the same time, the difference in the service life – long-term or short-term, like the loading T_2 (N·m) $T_2 = const$ or $T_2 = var$ in the requirements for dimensions, and thermal conditions, with the same parameter sets, will lead to different results according to the performance criteria of the worm gear.

Optimization of the worm gear design with a cylindrical worm according to the criterion of wear resistance J is a multivariate task. As the variables to be optimized: the main parameters of the engagement: the number of worms turns z_1 , the number of worm wheel teeth z_2 , and worm diameter factor q (the quotient of reference diameter to the axial module) are considered.

In this article, the criterion is quantitatively assessed not by its absolute value but in a comparative aspect – with various combinations of parameters $[z_1, z_2, q]$. For this reason, a calculation method is adopted here [18], where the wear rate J (N/s) has a linear dependence on the specific load along the contact line of the working surfaces and the speed of their sliding:

$$J = K \cdot p_n \cdot V_S \quad (2)$$

where $K = const$ – coefficient of materials wear;
 p_n – specific load distributed along the contact line, N/mm;
 V_S – the rubbing speed of the worm thread, m/s.

Expanded expressions for the parameters on the right side of Eq. (2):

$$p_n = F_n / l_\Sigma,$$

where $l_\Sigma \approx 1,3 \cdot d_1 / \cos\gamma_w$ – minimum total length of contact lines, mm;
 $F_n = (2 \cdot T_2 / d_2) / (\cos\alpha_n \cdot \cos\gamma_w)$ – normal force in the engagement of the worm threads with the teeth of the worm wheel, N.
 $V_S = \omega_1 \cdot d_1 / (2 \cdot \cos\gamma_w)$ – rubbing speed of the worm threads, m/s.

We introduce new variables: $y = q/z_2$ and $s = q/z_1$, which will allow the three-parameter function $J = J(z_1, z_2, q)$ to be replaced by a two-parameter one $J = J(y, s)$.

After substituting these ratios into Eq. (2) after accounting for $a_w = f(z_2, q, T_2)$, we obtain a calculation formula for the wear rate J , which will be a two-parameter objective function of optimization by the wear resistance criterion:

$$J(y, s) = C \cdot (1 + y) \cdot \sqrt{1 + s^2}/s, \quad (3)$$

here $C = \frac{K_H}{2.6 \cdot \cos \alpha_n} \cdot \frac{T_2 \cdot \omega_1}{a_W} = \text{const}$, since we are considering worm gears of the same dimensions ($a_W = \text{const}$), load level ($T_2 = \text{const}$) and initial kinematics ($\omega_1 = \text{const}$).

Thus, the task is reduced to the fulfillment of the condition: $J(y, s) = \text{min}$.

To minimize a function of two variables $J(y, s)$, we will use the Lagrange multiplier method to optimize two-parameter functions. The equation of connection $g = g(y, s) = 0$ between the optimization parameters y and s based on the following relationships are obtained:

$$s = q/z_1 = (q/z_1) \cdot (z_2/z_2) = (q/z_2) \cdot (z_2/z_1) = y \cdot u. \quad (4)$$

Whence it follows that:

$$g(y, s) = s - y \cdot u = 0. \quad (5)$$

Lagrange function $L = L(s, y)$: $L = J + \lambda \cdot g$,

after substitution in it L and g from formulas (3) and (4), takes the form:

$$L = C \cdot (1 + y) \cdot \sqrt{1 + s^2}/s + \lambda \cdot (s - y \cdot u), \quad (6)$$

here λ – the unknown constant of the Lagrange function.

According to the Lagrange method, we compose a system of three equations:

$$\begin{aligned} \partial L / \partial s &= \partial J / \partial s + \lambda \cdot \partial g / \partial s = 0; \\ \partial L / \partial y &= \partial J / \partial y + \lambda \cdot \partial g / \partial y = 0; \\ \partial L / \partial \lambda &= g(y, s) = 0. \end{aligned} \quad (7)$$

In expanded form, system (6) will be written as follows:

$$\begin{aligned} C \cdot (1 + y) \cdot (2 \cdot s - s^2 - 1) / (s^2 \cdot \sqrt{1 + s^2}) + \lambda &= 0; \\ C \cdot \sqrt{1 + s^2} / s - \lambda \cdot u &= 0; \\ s - y \cdot u &= 0. \end{aligned} \quad (8)$$

As a result of solving the system of Eqs. (7), the optimal value of one of the varied parameters was obtained:

$$y = y(u) = -1/(2 - u) + \sqrt{1/(2 - u)^2 + 1/[u \cdot (2 - u)]}, \quad (9)$$

(the second root for y having a minus sign in front of the root is discarded since, for any gear ratios, it gives deliberately unacceptable values concerning power worm gears).

Another variable parameter – s is obtained using the constraint Eq. (4)

$$s = s(u) = u \cdot y = u \cdot \left\{ -1/(2 - u) + \sqrt{1/(2 - u)^2 + 1/[u \cdot (2 - u)]} \right\}. \quad (10)$$

The objective function $J(s)$ graph and graphical dependence of the variable parameter y on the gear ratio $u: y = y(u)$ – formula (9) is shown in Fig. 3. The function $s = s(u)$ is easy to construct from the obtained values y using the constraint equation $s = u \cdot y$ or directly from the formula (10).

For the convenience of calculating values y at different gear ratios, the graph $y = y(u)$ (Fig. 3) is approximated by a power law: $y(u) \approx 1.05 \cdot u^{-0.69}$, wherein approximation error less than 1%. The numerical values of the parameters according to the criterion of working capacity are systematized in Table 1.

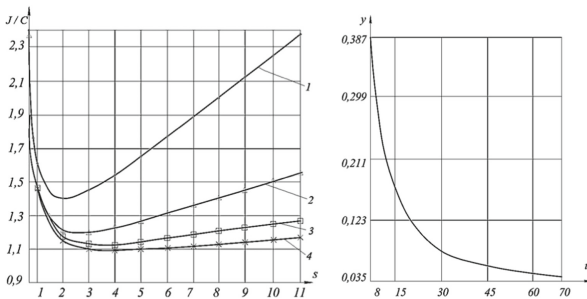


Fig. 3. Objective function: Curve notation.1: $u = 8$; 2: $u = 20$; 3: $u = 40$; 4: $u = 63$.

Table 1. Choice of parameters y, s, q .

u	z_1	y	s	q
8	4	0.25	2	8
10	4	0.18	1.8	7.1
12.5	4	0.13	1.66	6.3
16	4	0.1	1.55	6.3
20	2	0.07	1.46	No
25	2	0.06	1.4	Standard
31.5	2	0.04	1.34	q
40	1	0.03	1.29	No
50	1	0.03	1.25	Standard
63	1	0.02	1.22	q

5 Conclusion

Thus, the modernized design of the rotary table of metal-cutting machine tools of the boring-milling-boring type using a backlash-free worm gear is proposed. A schematic diagram of a worm gear with a gap compensation mechanism when operating in the form of spring-loaded sliding bearings has been developed.

A three-dimensional model of the assembly rotary table structure of the machine was built using the specialized application “Shafts and mechanical transmissions-3D” in CAD KOMPAS-3D. The efforts required to create a guaranteed hard contact have been determined.

The problem is formulated, and a mathematical model for optimizing the design of the worm gear elements by the criterion of wear resistance is built. The efficiency of representing this problem as a two-parameter task is shown by introducing derivatives of variables and solving it using Lagrange multipliers.

The research of the transmission's main parameters influence on the level of wear resistance was carried out. It is shown that the optimal values of the worm diameter coefficient at which the minimum wear rate is ensured. The condition of sufficient rigidity of the worm shaft is considered as a limitation.

The optimal values of the worm diameter coefficient q (and hence associated with it z_1 and z_2), at which the minimum intensity of wear $J = \min$ is ensured, have been determined. The minimum is reached for small gear ratios $u \approx 8 \dots 10$, which corresponds to worms ($z_1 = 4$).

The development of research in optimizing the worm gearing wear rate assumed in the direction of creating such a backlash-free worm engagement, in which the gap compensation will be carried out by compressing the springs and using sliding bearings of a new design.







References

1. Brecher, C., Fey, M., Daniels, M.: Modeling of position-, tool- and workpiece-dependent milling machine dynamics. *High Sped Mach.* **2**, 15–25 (2016)
2. Li, J., Song, Y., Liu, Y.: Development of post-processing system for three types of five-axis machine tools based on solid model. In: Proceedings of the ASME 2017 12th International Manufacturing Science and Engineering Conference collocated with the JSME/ASME 2017 6th International Conference on Materials and Processing, vol. 3: Manufacturing Equipment and Systems, Los Angeles, California, USA , pp. 118–132 (2017). <https://doi.org/10.1115/MSEC2017-2665>
3. Krol, O., Sokolov, V.: Parametric modeling of transverse layout for machine tool gearboxes. In: Gapiński, B., Szostak, M., Ivanov, V. (eds.) MANUFACTURING 2019. LNME, pp. 122–130. Springer, Cham (2019). https://doi.org/10.1007/978-3-030-16943-5_11
4. Kong, J., Cheng, X.: Modal analysis of CNC lathe's spindle based on finite element. *Adv. Eng. Res.* **148**, 318–321 (2017)
5. Rogovyi, A., Korohodskiy, V., Medvediev, Y.: Influence Bingham fluid Viscosity on energy performances of a vortex chamber pump. *Energy* **218**, 119432 (2021). <https://doi.org/10.1016/j.energy.2020.119432>
6. Dassanayake, M., Tsutsumi, M.: High performance rotary table for machine tool applications. *Int. J. Autom. Technol.* **1**, 343–347 (2009)
7. Krol, O., Sokolov, V.: 3D modelling of angular spindle's head for machining centre. *J. Phys. Conf. Ser.* **1278**, 012002 (2019). <https://doi.org/10.1088/1742-6596/1278/1/012002>
8. Bass, D., Riedl, R., Slagle, N.: 4th and 5th Axis Rotary Table. Mechanical Engineering Department. Polytechnic State University, San Luis Obispo, California (2016)
9. Mauro, G.: Anti-Backlash Mechanism for a Rotary Stage. US Patent 6,016,716A (1996).

10. Malashchenko, V., Strilets, O., Strilets, V., Kłysz, S.: Investigation of the energy effectiveness of multistage differential gears when the speed is changed by the carrier. *Diagnostyka* **20**(4), 57–64 (2019). <https://doi.org/10.29354/diag/112397>
11. Syzyi, Y., Ushakov, O., Slipchenko, S., Basova, Y., Ivanova, M.: Simulation of the contact temperature in the cylindrical plunge grinding process. *Diagnostyka* **21**(2), 77–86 (2020)
12. Krivosheya, A.V., Voznyy, V.V., Melnyk, V.E.: Analysis of the gear tooth gearing by the module $m = 2.625$ mm of hydraulic pumps. *J. Eng. Sci.* **4**(1), A11–A15 (2017). [https://doi.org/10.21272/jes.2017.4\(1\).a2](https://doi.org/10.21272/jes.2017.4(1).a2)
13. Babak, V.P., Bilchuk, Y.Y., Shchepetov, V.V.: Increased wear coatings due intrastructural self-correction. *J. Eng. Sci.* **6**(1), C11–C15 (2019). [https://doi.org/10.21272/jes.2019.6\(1\).c3](https://doi.org/10.21272/jes.2019.6(1).c3)
14. Kozłowski, T., Błażej, R., Sawicki, M., Kirjanów, A., Konieczna, M.: Automatic analysis of thermograms as a means for estimating technical of a gear system. *Diagnostyka* **17**(2), 43–48 (2016)
15. Józwick, J., Czarnowski, M.: Angular positioning accuracy of rotary table and repeatability of five-axis machining center DMU 65 monoblock. *Adv. Sci. Technol. Res. J.* **9**(28), 89–95 (2015)
16. Józwick, J., Kuric, I., Łukaszewicz, A.: Analysis of the table motion of a 3-axis CNC milling machine tool at start-up and braking. In: Tonkonogyi, V., et al. (eds.) *InterPartner 2019. LNME*, pp. 108–117. Springer, Cham (2020). https://doi.org/10.1007/978-3-030-40724-7_11
17. Oborskyi, G., Orgiyani, A., Tonkonogyi, V., Aymen, A., Balaniuk, A.: Study of dynamic impacts at combined operations of the thin turning and boring. In: Tonkonogyi, V., et al. (eds.) *InterPartner 2019. LNME*, pp. 226–235. Springer, Cham (2020). https://doi.org/10.1007/978-3-030-40724-7_23
18. Błażej, R., Sawicki, M., Konieczna, M., Kozłowski, T., Kirjanów, A.: Automatic analysis of thermograms as a means for estimating technical of a gear system. *Diagnostyka* **17**(2), 43–48 (2016)
19. Marshek, K.M.: *Design of Machine and structural parts*. Amazon Publishing, Seattle (1987)
20. Litvin, F.L., Qi, F., Fuentes, A.: *Computerized Design, Generation, Simulation of Meshing and Contact of Face-Milled Formate Cut Spiral Bevel Gears*. NASA/CR (2001)
21. Bjonowski, B.: A practical approach for modelling a bevel gear. *Geartechnology March/April*, 68–75 (2015)
22. Pavlenko, I., Neamtu, C., Verbovyi, A., Pitel, J., Ivanov, V., Pop, G.: Using computer modeling and artificial neural networks for ensuring the vibration reliability of rotors. *CEUR Workshop Proc.* **2353**, 702–716 (2019)
23. Ivanov, V., Dehtiarov, I., Pavlenko, I., Liaposhchenko, O., Zaloga, V.: Parametric optimization of fixtures for multiaxis machining of parts. In: Hamrol, A., Kujawińska, A., Barraza, M.F.S. (eds.) *MANUFACTURING 2019. LNME*, pp. 335–347. Springer, Cham (2019). https://doi.org/10.1007/978-3-030-18789-7_28
24. Rogovyi, A., Khovanskyi, S., Hrechka, I., Gaydamaka, A.: Studies of the swirling submerged flow through a confuser. In: Ivanov, V., Pavlenko, I., Liaposhchenko, O., Machado, J., Edl, M. (eds.) *DSMIE 2020. LNME*, pp. 85–94. Springer, Cham (2020). https://doi.org/10.1007/978-3-030-50491-5_9
25. Dervoort, W.H.: *Modern Machine Shop Tools, Their Construction, Operation and Manipulation, Including Both Hand and machine Tools*. Creative Media Partners, London (2018)



Control Optimization of the Swing Mechanism

Elena Naidenko¹  , Oleksandr Bondar¹ , Andrii Boiko¹ ,
Oleksandr Fomin¹ , and Raul Turmanidze² 

¹ Odessa Polytechnic State University, 1, Shevchenko Avenue,
Odessa 65044, Ukraine
avnaidenko@opu.ua

² Georgian Technical University, 77, Kostava Street, 0175 Tbilisi, Georgia

Abstract. Modern production is impossible without developing and improving lifting and transport mechanisms, which is indispensable for various technological processes. The article concerns the optimal control on the swing mechanism regarding speed and simultaneous damping of load oscillations. It is shown that the law of change in the dynamic torque of an electric drive obtained using the Pontryagin maximum principle ensures the damping of the load oscillations by the end of the transient process the turning mechanism and to minimize the duration of these processes. The necessity of joint use of the mechanism for changing the boom outreach as the second control action, which, according to the derived law, changes the radius of rotation of the load suspension point for damping the deflection angle's normal component, has been substantiated. The mathematical model was created for calculating the transient start (braking) process in the Matlab mathematical modeling package for optimal control over the swing mechanism. Analysis of the graph of transient processes allows us to conclude that the proposed method fully satisfies conditions.

Keywords: Suspended load · Damping load fluctuations · Transient process · Performance criterion · Mathematical model

1 Introduction

The performance and quality of various technological processes are largely determined by transport operations, in particular, by the movement of goods using lifting and transport mechanisms of rotary motion, which have found wide application in various technological processes, where performance indicators, reliability, and sometimes accuracy of installation operations are the essential factors for production in general. However, the loads suspended on a flexible thread (rope) in starting and breaking the turning mechanisms are prone to swaying, which can significantly slow down the technological process itself and significantly reduce the quality of operations.

2 Literature Review

Many scientists were engaged in the problem of damping vibrations of a suspended load. In the area of optimal control engineering systems [1], there are many different theoretical solutions made: vertical dynamic loads [2], bistable suspension systems [3], kinematic transmissions [4].

Various researches have been reported in which damping control is proposed using the states of suspended load in transport [5] damping [6] control or cooperative swinging [7]. To increase operator productivity and comfort, to reduce the learning time of novice operators in work [8], automated motions that do not excite dangerous oscillations of the freely-hanging grapple are proposed.

Most publications address comparatively simple models describing only single pendulum load dynamics: swing mechanisms [9], dynamic [10], and harmonic loads [11], in work [12] model for the control to mitigate structural vibrations of mechanism is proposed.

The problems of rotary mechanisms were highlighted in research [13], although this area is still narrowly represented in scientific developments.

In works [14], the transient processes are optimized but regarding mechanisms of translational motion with a suspended load.

In publication [15], a theory for damping the oscillations of the suspended load (pendulum) using the active modification of the length of the suspension string is proposed. In work [16], the numerical optimal control approach is considered. Robust optimization procedure and extended linearization are employed to attenuate oscillations in the crane systems by reconfiguring the position of the payload mass in work [17].

In publication [18], damping control of suspended loads is proposed. The suspended load of a crane is modeled as a double pendulum, and a state feedback control based on the model is used for damping control in consideration of the second bending mode oscillation as well as the first swinging mode oscillation.

3 Research Methodology

Earlier, the law of optimal control of translational movement mechanisms was obtained. Below are the primary dependencies and patterns obtained for these mechanisms in order to subsequently use them for rotation mechanisms in advance.

The mechanism is represented by two lumped masses that move progressively: carts m_1 and loads m_2 , s_1 and s_2 are the paths of their movement, respectively, L is the length of the thread, α is the current value of the angle of deflection of the thread from the vertical.

The time constant T is inverse to the natural frequency of the load:

$$\Omega = \frac{1}{T} = \sqrt{\frac{g(m_1 + m_2)}{Lm_1}} = \Omega_0 \sqrt{\frac{(m_1 + m_2)}{m_1}}, \quad (1)$$

where g – acceleration of gravity and the oscillation frequency of a mathematical pendulum suspended on a structure with infinite mass ($m_1 = \infty$),

$$\Omega_0 = \frac{1}{T_0} = \sqrt{\frac{g}{L}}. \quad (2)$$

Under the principle of the maximum by Pontryagin, to fulfill the condition of the problem posed when optimizing the control of the mechanism of translational motion, namely, to ensure the minimum time of the transient processes of starting and braking at the given restrictions on the location of the load at the end of these processes, a relay law of application of the maximum permissible dynamic force (moment) is required: $M = |M_m|$. In this case, after the completion of the transition process, three conditions should be met:

$$\begin{aligned} V_1 &= V_{1z} \\ \alpha &= 0 \\ \frac{dz}{dt} &= 0. \end{aligned} \quad (3)$$

Based on the fact that these three conditions (3) must be fulfilled by the end of the process, it was concluded that it is appropriate to work in three stages to have two switchings (changes of the M sign). The diagram of the change in the control action – the motor torque M – during acceleration is shown in Fig. 1, where M_m (F_m) – engine torque (the maximum value of the force), admissible under the conditions of its heating.

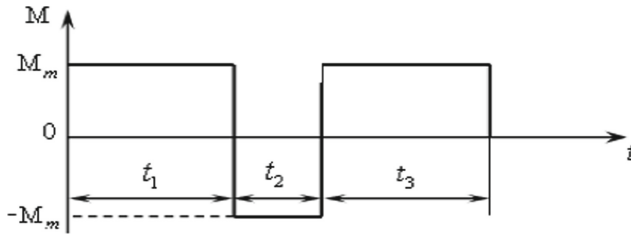


Fig. 1. Diagram of the moment $M(t)$ during acceleration.

Expression for the entire transient time [4]:

$$t_p = t_1 + t_2 + t_3 = T_p + 2t_2, \quad (4)$$

and the time t_2 is found by solving the Eq. [4]:

$$\begin{aligned} \sin\Omega\left(t_2 + \frac{T_p}{2}\right) &= 2\sin\frac{\Omega t_2}{2}, \\ t_1 = t_3 &= \frac{T_p + t_2}{2}, \end{aligned} \quad (5)$$

where the constant value is:

$$T_p = \frac{V_{1z}}{F_m} m, \quad (6)$$

T_p – this is the time of acceleration to a given speed V_1 of the mass $m = m_1 + m_2$ in the absence of swinging of the load and the action of a constant force F_m , this is the minimum time of the transient process, to which the value of T_p can tend under optimal control.

Thus, a basis can be reasonably used to obtain the optimal control law for more complex rotation mechanisms.

4 Results

4.1 Design Model of Swing Mechanism with Suspended Load

The swing mechanism is a rotating platform with a boom, with a suspended load on a rope. Therefore, such a mechanism can also be represented in a two-mass mechanical part (a rotating platform is a load connected by a flexible thread). A motor drives the rotating platform through a gearbox and a pinion-gear transmission – a ring gear with a total gear ratio i .

The design model of such a two-mass mechanical part (the position of the characteristic points of the moving system) at a particular moment and the acting forces and moments are shown in Fig. 2. Here $OA = O'A' = O''A'' = R_1$ – radius of rotation of the load suspension point (boom reach); $O''B = R_1$ – radius of rotation of the load; α is the angle of deflection of the thread with the load from the vertical; $P = m_2g$ – cargo weight; N – the tension force of the thread, and N_τ – its projection onto the horizontal plane. Since the angle α is small ($5 \dots 8^\circ$), we can assume $A'A'' = A'B' = L$, where L is the length of the inextensible thread on which the load is suspended.

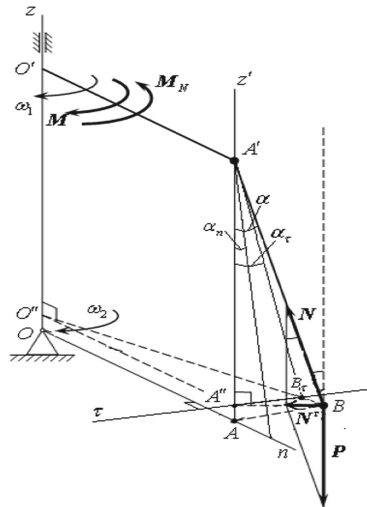


Fig. 2. Design model of a swing mechanism with a suspended load.

The load suspension point A' , located on the boom of the rotating platform with the moment of inertia J_1 , rotates around the fixed axis O_z with the angular velocity ω_1 under the action of the algebraic sum of the driving moment M (the engine torque reduced to the rotating platform with the static moment) and some moment M_N , caused by the force component of the weight P . The load (point B) with the moment of inertia J_2 rotates around the same axis with the angular velocity ω_2 under the action of the moment M_N . Force projections on the horizontal plane are shown in Fig. 3.

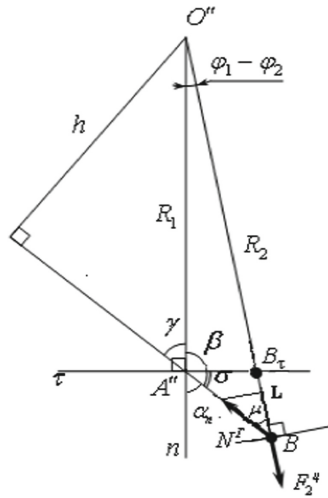


Fig. 3. Force projections on the horizontal plane.

Both formulas (1) and (2) are obtained by the fact that the angles α_τ and α_n are sufficiently small when it is possible to assume that $\text{tg } \alpha \approx \sin \alpha \approx \alpha$.

In contrast to the mechanism of translational motion, it is now necessary to ensure that five conditions are met to damp the oscillations of the load after the completion of the transient start-up process: at the end, for example of acceleration, there should be no tangential deflection angle and the corresponding speed, as well as the normal components of speed and acceleration.

To fulfill these conditions, it is necessary to control in five stages, determining the duration of which is the main difficulty. To accomplish this task, it is necessary to have time dependencies of all quantities.

4.2 The Law of Optimal Control of Swing Mechanisms

The differential equation for radius R_2 is as follows [4]:

$$\frac{d^2 R_2}{dt^2} - \left(\omega_2^2 - \frac{g}{L} \right) R_2 = \frac{g}{L} R_1. \tag{7}$$

Equation (7) includes the speed ω_2 , where the law of change in time is unknown, so it is rather difficult to solve it.

Therefore, to calm the normal component of the angle of deflection of the thread with the load from the vertical, it is proposed to introduce a second control action, namely, to change according to a specific law the radius of the load suspension point R_1 with the help controlling for changing the boom outreach, in this case, the radius R_2 should remain constant. In contrast to the translational displacement mechanism, with the optimal control of the rotation mechanism, after the completion of the transient process, it is necessary to ensure the tangential component of the deflection angle of the thread and the load from the vertical with a constant normal component of the same angle (at start-up) or to ensure the absence of both components after the end of braking (at the stop). To calm down the tangential component, we use (with some assumptions) the law of variation of the moment M_m obtained for translational motion, approximately assuming the moments of inertia of both masses to be constant.

Thus, it becomes clear that determining the optimal control law by using only controlling of rotation mechanism is not easy. The law itself is highly complex.

Considering that at the initial start-up moment $R_1 = R_2 = R_{1_start}$, we finally obtain the law of change in the radius of rotation of the load suspension point, where $R_2 = const$, while $\omega_2 = var$, $cos \alpha = var$ and $cos \Delta\varphi = var$:

$$R_1 = R_{1_start} \left(\frac{1 - \omega_2^2 \frac{L \cdot cos \alpha}{g}}{cos \Delta\varphi} \right). \quad (8)$$

Thus, for optimal control of the swing mechanism, the motor torque should be changed according to the law of Fig. 1. This allows us to compensate for the tangential component of the angle and adjust the radius of the suspension point by relationship (8).

4.3 Model of the Swing Mechanism

Figure 4 shows a block diagram of the swing mechanism.

The start mode simulation of the radius R_1 is shown in Fig. 5. The graphs show that after the transient acceleration, normal and tangential components of the yarn deviation angle from vertical with the load do not exceed 0.001 rad. With the necessary change in the radius R_1 , the radius R_2 does not remain constant. However, the amplitude of its oscillations does not exceed 0.15% of the initial values of the radius. Also, it satisfies the conditions of the posed task.

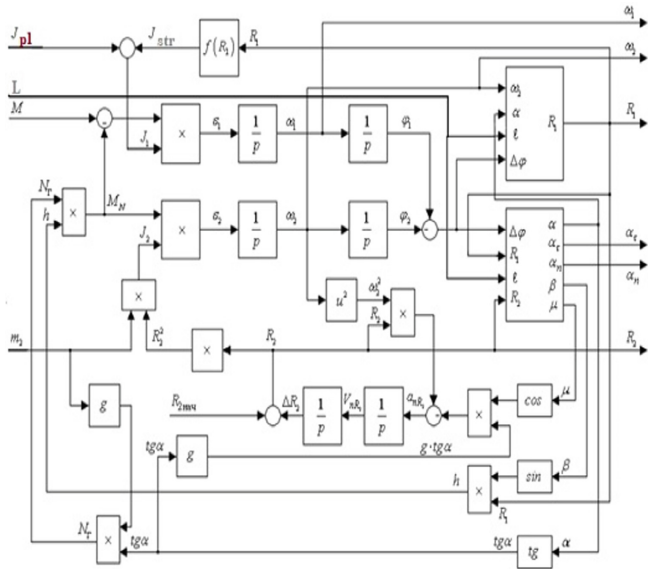


Fig. 4. Block diagram of the model.

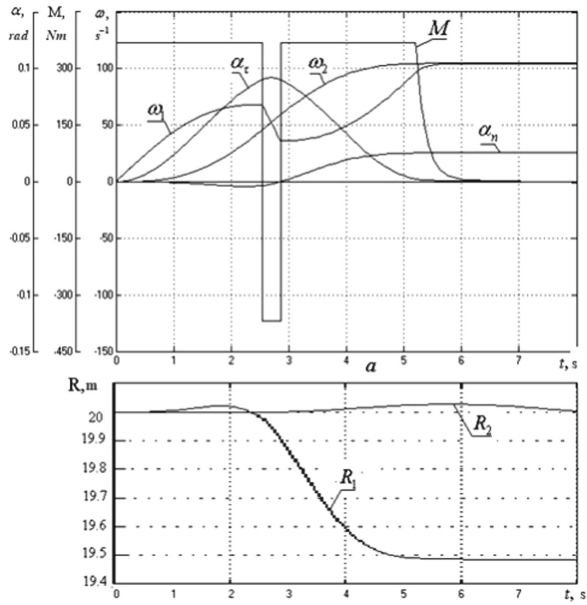


Fig. 5. Transient graphs of starting the swing mechanism.

5 Conclusions

It was shown that it is complicated to determine the law of optimal control if only the drive of the swing mechanism is controlled. Therefore, it is proposed to introduce a second control action to calm the normal component of the angle of deflection of the thread with the load from the vertical, specifically, to change the radius of the load suspension point according to a particular law. At the same time, modeling the transient processes of the turning mechanism convinced that by the end of the transient process, the tangential component of the angle α is equal to zero. The normal component remains small and constant (after the end of acceleration) or tends to zero (after deceleration).

For optimal control of the mechanism that provides fast transient processes and simultaneously damping load oscillations, not smooth, but instantaneous applications of the maximum torque are required (Fig. 1). However, it is known that dynamic moments in transient modes significantly load elastic links – shafts, metal structures of turning mechanisms, and the abrupt application of the moment to transmission links with gaps in the gears leads to the highest dynamic loads in these elements.

In the future, it is planned to investigate the possibility of correcting the recommended control method to limit shock loads in kinematic transmissions.

References

1. Lutsenko, I.: Optimal control of systems engineering: development of a general structure of the technological conversion subsystem (Part 2). *East.-Eur. J. Enterp. Technol.* **1**(2(73)), 43 (2015). <https://doi.org/10.15587/1729-4061.2015.36246>
2. Ślaski, G., Pikośz, H.: The influence of damping changes on vertical dynamic loads of wheel – experimental investigations. *Arch. Transp.* **23**(2), 239–247 (2011). <https://doi.org/10.2478/v10174-011-0016-7>
3. Yang, K., Harne, R.L., Wang, K.W., Huang, H.: Dynamic stabilization of a bistable suspension system attached to a flexible host structure for operational safety enhancement. *J. Sound Vib.* **333**(24), 6651–6661 (2014). <https://doi.org/10.1016/j.jsv.2014.07.033>
4. Naidenko, E.: Dynamic loads in kinematic transmissions with a clearance under optimal control of the turning mechanism. *Electric. Comput. Syst.* **27**(103), 75–81 (2018). [in Russian]
5. Kodani, N., Oushi, S., Takahashi, R., Hirata, H.: Transport control of a jib crane with a rotating cargo. *Trans. Inst. Electric. Eng. Jpn. Ser. C* **136**, 821–831 (2016). <https://doi.org/10.1541/ieejieiss.136.821>
6. Yoshikawa, M., Iwatani, A., Ishikawa, J.: Damping control of suspended load for truck cranes in consideration of control input dimension. In: *Proceeding of the IEEE International Conference on Advanced Engineering Theory and Applications*, pp. 436–446 (2017). https://doi.org/10.1007/978-3-319-69814-4_42
7. Donner, P., Buss, M.: Cooperative swinging of complex pendulum-like objects: experimental evaluation. *IEEE Trans. Rob.* **32**(3), 744–753 (2016)
8. Fodor, S., Freidovich, L., Vazquez, C.: Practical trajectory designs for semi-automation of forestry cranes. In: *Proceedings of ISR 2016: 47th International Symposium on Robotics*, Munich, Germany, pp. 1–8 (2016). <https://doi.org/10.1109/TRO.2016.2560898>

9. Ramli, L., Mohamed, Z., Abdullahi, A., Jaafar, H., Lazim, I.: Control strategies for crane systems: a comprehensive review. *Mech. Syst. Signal Process* **95**, 1–23 (2017). <https://doi.org/10.1016/j.ymssp.2017.03.015>
10. Sun, Z., Bi, Y., Zhao, X., Sun, Z., Ying, C., Tan, S.: Type-2 fuzzy sliding mode anti-swing controller design and optimization for overhead crane. *IEEE Access* **6**, 51931–51938 (2018). <https://doi.org/10.1109/ACCESS.2018.2869217>
11. Sun, N., Wu, Y., Fang, Y., Chen, H.: Nonlinear antiswing control for crane systems with double-pendulum swing effects and uncertain parameters: design and experiments. *IEEE Trans. Autom. Sci. Eng.* **15**(3), 1413–1422 (2018). <https://doi.org/10.1109/TASE.2017.2723539>
12. Golovin, I., Palis, S.: Control-based damping of elastic gantry crane vibrations. In: *Proceedings 22nd International Conference Methods Models Automation Robotics (MMAR)*, pp. 599–604 (2017). <https://doi.org/10.1109/MMAR.2017.8046896>
13. Sawodny, O.: Modeling and control of tower cranes with elastic structure. *IEEE Trans. Control Syst. Technol.* **29**(1), 64–79 (2021). <https://doi.org/10.1109/TCST.2019.2961639>
14. Bai, W.W., Ren, H.: Horizontal positioning and anti-swinging control tower crane using adaptive sliding mode control. In: *2018 Chinese Control and Decision Conference (CCDC)*, Shenyang, pp. 4013–4018 (2018). <https://doi.org/10.1109/CCDC.2018.8407820>
15. Anderle, M., Michiels, W., Čelikovský, S., Vyhlídal, T.: Damping a pendulum's swing by string length adjustment – design and comparison of various control methods. In: *2019 American Control Conference (ACC)*, Philadelphia, PA, USA, pp. 4399–4405 (2019). <https://doi.org/10.23919/ACC.2019.8814293>
16. Vyhlídal, T., Anderle, M., Bušek, J., Niculescu, S.: Time-delay algorithms for damping oscillations of suspended payload by adjusting the cable length. *IEEE/ASME Trans. Mechatron.* **22**(5), 2319–2329 (2017). <https://doi.org/10.1109/TMECH.2017.2736942>
17. Rauh, A., Prabel, R., Aschemann, H.: Oscillation attenuation for crane payloads by controlling the rope length using extended linearization techniques. In: *22nd International Conference on Methods and Models in Automation and Robotics (MMAR)*, pp. 307–312 (2017). <https://doi.org/10.1109/MMAR.2017.8046844>
18. Watanabe, K., Yoshikawa, M., Ishikawa, J.: Damping control of suspended load for truck cranes in consideration of second bending mode oscillation. In: *IECON 2018 - 44th Annual Conference of the IEEE Industrial Electronics Society*, Washington, DC, pp. 4561–4568 (2018). <https://doi.org/10.1109/IECON.2018.8591232>



Manufacturing Error of the Toothed Profile of Rotors for an Orbital Hydraulic Motor

Anatolii Panchenko¹ , Angela Voloshina¹ ,
Nataliia Boltianska¹ , Viktor Pashchenko² , and Sergii Volkov¹ 

¹ Dmytro Motorny Tavsia State Agrotechnological University,
18, B. Khmelnytsky Avenue, Melitopol 72310, Ukraine
tia_tgatu@ukr.net

² National Academy of the National Guard of Ukraine,
3, Zakhysnykiv Ukrainy Square, Kharkiv 61001, Ukraine

Abstract. Like any positive displacement hydraulic machine, an orbital-type hydraulic machine is a rather complex mechanism with parts representing a precision connection. Therefore, control over the manufacturing accuracy of the rotors of these hydraulic machines is relevant. A dimensional chain has been developed that reflects the interaction of the toothed profiles of the rotors of an orbital hydraulic motor, and the controlled parameters that determine the manufacturing error of these rotors have been substantiated. A design scheme has been developed, and the geometric and functional relationship of the location of contact points of the toothed profiles of the rotors of an orbital hydraulic motor has been determined. Methods and devices have been developed to control the shape error of an orbital hydraulic motor's inner and outer rotors. The results of measuring the complex parameters show that the working clearance in the rotors of the orbital hydraulic motor is in the range of 0.02...0.214 mm. The gap between the rotors can serve as a parameter that determines the technical state of the orbital hydraulic motor, and its limiting value can be used as the basis for standardizing the functional parameters that determine the operability of the orbital hydraulic motor.

Keywords: Displacement system · Methods of control · Means of control · Dimensional chain · Form deviations

1 Introduction

Orbital and planetary hydraulic machines are widely used in mechatronic systems of a hydraulic drive of working bodies of mobile equipment. Today we have a fairly large experience in the production of gear [1] and axial piston [2, 3] hydraulic machines, which, unfortunately, cannot be fully used in the production of orbital and planetary hydraulic machines. It is due to the design features of their rotors, the working contour of which is described by cycloidal curves. The systems for displacing the working fluid of hydraulic machines of the orbital (planetary) type and any hydraulic machines of positive displacement are rather complex mechanisms, including precision connections

[4]. The displacement system of the orbital hydraulic motor is represented by an external rotor (Fig. 1a) and an internal rotor (Fig. 1b).

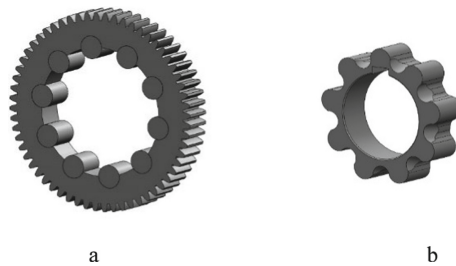


Fig. 1. Elements of the displacement system of the orbital hydraulic motor: a – external rotor with plug-in teeth (rollers); b – inner rotor.

During the orbital hydraulic motor operation, the rotor form a gear pair with an internal hypocycloidal engagement [4]. This geometry of the toothed profile of the rotors was chosen to provide two functions: moving the inner rotor and ensuring the sealing of the pressure zone from the drain zone. Therefore, the accuracy of manufacturing the geometry of the toothed profile [5] of the rotors determines the operability of the orbital hydraulic motor as a whole.

2 Literature Review

An analysis of the results of a complex calculation [6] is proposed, the influence of a multi-component load on thin-walled structures [7] is investigated, the distribution [8] is determined, and the regularities of the distribution [9] of contact pressure, which are important in the implementation of design studies [10, 11], an algorithm for finding rational parameters has been developed that takes into account the features of the shape of the response surface [12, 13]. Issues related to the justification of the controlled parameters were not considered.

A method and a system for active control of dynamic spatial positioning [14] are proposed, conditions for static equilibrium are established [15], algorithms for a control system [16] are developed, a study of dynamic accuracy [17] and dynamic processes [18] of the positioning of spatial drive systems, as well as changes dynamics of the output characteristics of mechatronic systems [19]. A method for designing hydraulic mechatronic systems with elements of multi-criteria optimization has been developed [20]. The influence of the manufacturing accuracy of the elements of mechatronic systems on their functionality has not been studied.

Mathematical modeling of the flow was carried out by solving the Navier-Stokes equations averaged after Reynolds using the SST-model of turbulence [21, 22] and rheological models [23], an engineering techniques to increase the effectiveness [24, 25], and determining the radial compliance [26] was proposed, the effect of the viscosity of Bingham fluids on the energy characteristics of vortex-chamber pumps [23, 27].

Also, much attention is paid to axial piston [2, 3], orbital piston [28], and centrifugal machines [29–31], the design of which differs from orbital and gerotor machines. The change in the output characteristics of the considered hydraulic machines from the accuracy of manufacturing their elements was not considered.

At present, very little research is published on the methodology for the design and manufacture of gerotor pumps, orbital and planetary hydraulic motors [32]. The forces acting in the gearing [33] are considered, and models [34] are prepared, considering the compression state of the working fluid [35] and cavitation phenomena [36–39]. A mathematical model has been developed [40], which describes the change in loads in the gearing, and a program [41], which considers the equations of the hydrodynamics of fluid motion in the working chambers of the gerotor pump. Geometric [42], computational [43, 44], and hydrodynamic [45] models of a gerotor pump are considered, 3D model of an orbital gerotor hydraulic motor is proposed, which takes into account the dynamically changing volume of the working fluid [46], as well as a model that allows you to simulate the processes occurring in planetary hydraulic motors and their elements under operating conditions [47]. Experimental studies have been carried out, confirming the results of modeling the operation of rotors of gerotor [48] and planetary [49] hydraulic machines. In the developed models of the functioning of hydraulic machines, the influence of the accuracy of manufacturing their elements was not still considered [50].

Thus, the determination of the error in the manufacture of the toothed profile of the rotors of an orbital hydraulic motor is an urgent task aimed at improving the output characteristics of an orbital hydraulic motor during its manufacture.

3 Research Methodology

The purpose of these studies is to improve the output characteristics of the orbital hydraulic motor during its manufacture by determining the error in the manufacture of the gear profile of its rotors. To achieve this goal, it is necessary to solve the following tasks:

- develop a dimensional chain that reflects the interaction of the toothed profiles of the rotors of an orbital hydraulic motor and substantiate the controlled parameters that determine the error in the manufacture of these rotors;
- to develop a design scheme and determine the geometric and functional relationship of the location of the contact points of the gear profiles of the outer and inner rotor of an orbital hydraulic motor;
- to develop methods and devices for controlling the shape error of an orbital hydraulic motor's inner and outer rotors, to carry out a production check of the developed control means.

Since an orbital hydraulic motor operates, its rotors do not have a rigid kinematic connection [4]. This dimensional chain determines the error (accuracy) of the manufacture of rotors based on the points of contact of their toothed profiles, ensuring the hydraulic motor's operability. Taking into account the specific operating conditions of the rotors of the orbital hydraulic motor [4], a dimensional chain was developed that

reflects the interaction of the toothed profiles of its outer and inner rotors during operation (Fig. 2). The presented dimensional chain is based on the contact points determined by touching the toothed surfaces of the rotors (a_1, a_2 , and b_1, b_2), which are located diametrically opposite to their centers O_1 and O_2 .

The considered dimensional chain (Fig. 2) consists of a decreasing link A_Δ for the inner rotor and an increasing link B_Δ for the outer rotor. The process (diametrical) gap G which closes the dimensional chain is required to compensate for the thermal expansion of the rotors, $G = B_\Delta - A_\Delta$ [4].

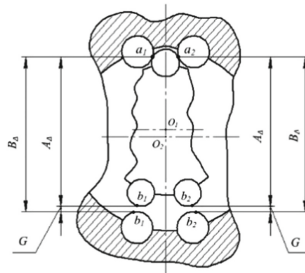


Fig. 2. Dimensional chain of interaction (contact) of the rotors of an orbital hydraulic motor.

To implement the proposed dimensional chain, a design scheme has been developed (Fig. 3), which allows determining the relationship between the location of contact points for the parameters A_Δ and B_Δ .

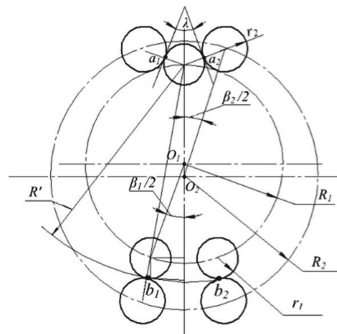


Fig. 3. The design scheme for determining the geometric relationship of the location of contact points formed by the toothed profiles of the outer and inner rotors.

The dimensions A_Δ and B_Δ under consideration are complex and depend on the geometric parameters of the inner rotor (R_1, r_1 , and β_1) and the outer rotor (R_2, r_2 , and β_2), respectively. The location of the points of contact (a_1, a_2) of the teeth of the inner rotor, and two teeth (rollers) of the outer rotor are determined by the radius r_1 of the

tooth of the inner rotor and the angle λ formed by the normals passing through these points of contact (Fig. 3)

$$\lambda = 2 \arccos \frac{R_2 \cdot \sin \frac{\beta_2}{2}}{r_1 + r_2}, \quad (1)$$

R_2 is the radius of the circle of the centers of the teeth of the outer rotor; β_2 is the angle of the center of the teeth of the outer rotor; r_1 and r_2 are the radii of the teeth of the inner and outer rotors, respectively.

The location of the contact points (b_1, b_2) of two pairs of teeth of the inner and outer rotor (Fig. 3) is determined by the radius R' of the contact points described from the center of the opposite tooth of the inner rotor

$$R' = \frac{R_1 \cdot (1 + \cos \frac{\beta_1}{2}) + r_1 \cdot \cos \frac{\beta_1}{4}}{\cos \frac{\beta_1}{4}}, \quad (2)$$

where R_1 is the radius of the circle of the location of the centers of the teeth of the inner rotor; β_1 is the angle of arrangement of the centers of the teeth of the inner rotor.

The deviations of the parameters A_Δ and B_Δ determine the shape error E_1 and E_2 of the inner and outer rotors, respectively [4]: $E_1 = A_{\max} - A_{\min}$, $E_2 = B_{\max} - B_{\min}$.

4 Results

To measure the deviations of the parameters A_Δ and B_Δ , methods and control devices have been developed for their implementation (Fig. 4). A feature of the proposed method for controlling the parameters A_Δ and B_Δ , for both rotors, respectively, is the simultaneous measurement of the controlled parameters on both sides of the line of centers O_1 and O_2 for each rotor. At the same time, the measuring devices are designed in such a way as to provide an imitation of the mating part.

The measuring device for controlling the parameter A_Δ of the inner rotor (Fig. 4a) consists of Table 1, the base surface a of which is made in the form of a prism with an angle λ , to simulate the gearing kinematics. A movable measuring tip 3 is fixed on stand 2 connected to Table 1. Its working surface b is made as a concave segment with a radius R' , which simulates contact points in real engagement. Spring 4 provides constant contact of the measuring tip 3 with the teeth of the controlled rotor 6. Indicator 5, mounted on rack 2, is kinematically connected to the measuring tip 3. Such a basing of the controlled inner rotor provides its self-alignment at the measuring position.

The measuring device (Fig. 4a) is adjusted to the nominal size of the controlled parameter A_Δ of the inner rotor 6 according to the exemplary part. The controlled inner rotor 6 is installed on the base surface a of Table 1 so that the tooth of the controlled rotor 6 contacts the prism at points a_1 and a_2 , and two opposite teeth of the rotor 6 are located on the working surface b of the segment groove of the measuring tip 3, in the points of contact b_1 and b_2 . According to the indications of indicator 5, the deviation from the nominal size is measured.

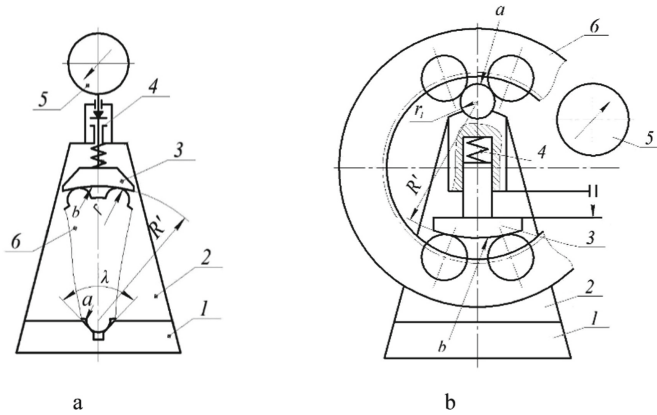


Fig. 4. Measuring devices for monitoring the shape error of the inner (a) and outer (b) rotors of an orbital hydraulic motor: 1 – table; 2 – rack; 3 – measuring tip; 4 – spring; 5 – indicator; 6 – controlled rotor.

The device for measuring the parameter B_{Δ} at the outer rotor assembly with rollers (Fig. 4b) has a similar measuring principle. The measuring device contains Table 1 connected to a post 2, on which there is a base surface made in the form of a roller with a radius r_1 . Movable measuring tip 3, the working surface b of which is made in the form of a convex segment with a radius R' , makes it possible to simulate contact points in real engagement. Spring 4 provides constant compression of the measuring tip 3 with the controlled rotor 6. According to the indications of indicator 5, the deviation of the measured parameter from the nominal value is determined. The measuring tip 3 provides self-alignment of the controlled rotor 6 at the measuring position.

The measuring device (Fig. 4b) is adjusted to the nominal size of the monitored parameter of the external rotor 6 according to the exemplary part. The controlled outer rotor 6 (with rollers) is installed on the measuring device so that its two rollers rest on a base surface made in the form of a roller with a radius r_1 at points a_1 and a_2 . In this case, the movable measuring tip 3, under the action of the spring 4, with its convex segment surface, rests on two opposite rollers of the outer rotor 6 at points b_1 and b_2 . According to the indications of indicator 5, the deviation from the nominal size is measured.

A production check of the developed controls allowed us to identify deviations of the rotor shape error by measuring the proposed complex controlled parameters A_{Δ} and B_{Δ} for the inner and outer rotors, respectively (Fig. 5).

Based on the measurements, the limiting values of the shape error of the inner and outer rotors of the orbital hydraulic motor, due to the existing technology of their manufacture, were determined (Table 1).

The shape error of the inner rotor is $E_1 = 0.052$ mm, and for the outer one – $E_2 = 0.142$ mm. The working clearance in the rotors of the orbital hydraulic motor is in the range $G = 0.02 \dots 0.214$ mm.

A production check has shown that the gap G can serve as a parameter that determines the technical state of an orbital hydraulic motor. Its limiting value can be

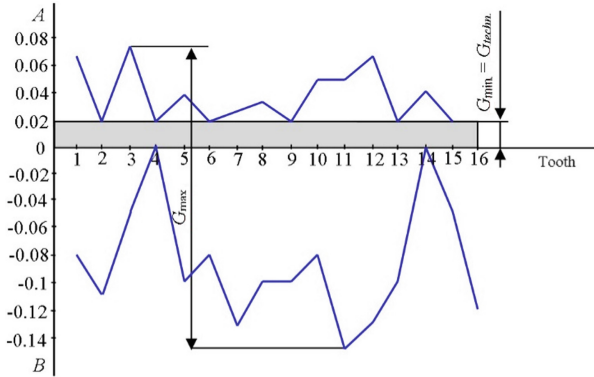


Fig. 5. Deviations of the rotors shape error: 1 – inner rotor; 2 – outer rotor.

Table 1. Limit values of the rotor's shape error.

A	Max	+0,072	E1	0,052	Gmax	0,214
	Min	+0,02				
B	Max	0,00	E2	0,142		
	Min	-0,142				

used as the basis for standardizing the functional parameters that determine the operability of an orbital hydraulic motor.

5 Conclusions

As a result of the research, a dimensional chain has been developed that reflects the interaction of the toothed profiles of the rotors of an orbital hydraulic motor. The controlled parameters that determine the manufacturing error of these rotors have been developed substantiated.

A design scheme has been developed, and the geometric and functional relationship of the location of the contact points of the gear profiles of the outer and inner rotor of the orbital hydraulic motor has been determined.

Methods and devices have been developed to control the shape error of an orbital hydraulic motor's inner and outer rotors. A production check of the developed controls showed that the shape error of the inner rotor is 0.052 mm, and that of the outer rotor is 0.142 mm. The working clearance in the rotors of the orbital hydraulic motor is in the range of 0.02...0.214 mm.

The gap between the rotors can serve as a parameter that determines the technical state of the orbital hydraulic motor, and its limiting value can be used as the basis for standardizing the functional parameters that determine the operability of the orbital hydraulic motor.

References

1. Choi, T., Kim, M., Lee, G., et al.: Design of rotor for internal gear pump using cycloid and circular-arc curves. *J. Mech. Des.* **134**(1), 011005–011012 (2012). <https://doi.org/10.1115/1.4004423>
2. Vacca, A., Klop, R., Ivantysynova, M.: A numerical approach for the evaluation of the effects of air release and vapour cavitation on effective flow rate of axial piston machines. *Int. J. Fluid Power* **1**(11), 33–45 (2010). <https://doi.org/10.1080/14399776.2010.10780996>
3. Elashmawy, M.: Design of swashplate axial piston machines having low piston transverse forces. *Int. J. Mech. Eng. Appl.* **3**(1), 17 (2015). <https://doi.org/10.11648/j.ijmea.s.2015030102.13>
4. Panchenko, A., Voloshina, A., Luzan, P., Panchenko, I., Volkov, S.: Kinematics of motion of rotors of an orbital hydraulic machine. *IOP Conf. Ser. Mater. Sci. Eng.* **1021**, 012045 (2021). <https://doi.org/10.1088/1757-899X/1021/1/012045>
5. Krivosheya, A.V., Voznyy, V.V., Melnyk, V.E.: Analysis of the gear tooth gearing by the module $m = 2.625$ mm of hydraulic pumps. *J. Eng. Sci.* **4**(1), A11–A15 (2017). [https://doi.org/10.21272/jes.2017.4\(1\).a2](https://doi.org/10.21272/jes.2017.4(1).a2)
6. Parsadanov, I., Marchenko, A., Tkachuk, M., Kravchenko, S., et al.: Complex assessment of fuel efficiency and diesel exhaust toxicity. *SAE Technical Paper 2020-01-2182* (2020). <https://doi.org/10.4271/2020-01-2182>
7. Atroshenko, O., Tkachuk, M., Martynenko, O., Tkachuk, M., Saverska, M., Hrechka, I., Khovanskyi, S.: The study of multicomponent loading effect on thinwalled structures with bolted connections. *East.-Eur. J. Enterp. Technol.* **1**(7(97)), 15–25 (2019). <https://doi.org/10.15587/1729-4061.2019.154378>
8. Marchenko, A., Tkachuk, M.A., Kravchenko, S., Tkachuk, M.M., Parsadanov, I.: Experimental tests of discrete strengthened elements of machine-building structures. In: Tonkonogyi, V., et al. (eds.) *InterPartner 2019. LNME*, pp. 559–569. Springer, Cham (2020). https://doi.org/10.1007/978-3-030-40724-7_57
9. Tkachuk, M., Grabovskiy, A., Mykola, T., Hrechka, I., et al.: Investigation of multiple contact interaction of elements of shearing dies. *East.-Eur. J. Enterp. Technol.* **4**(7(100)), 6–15 (2019). <https://doi.org/10.15587/1729-4061.2019.174086>
10. Tkachuk, M., Grabovskiy, A., Tkachuk, M., Saverska, M., Hrechka, I.: A semi-analytical method for analys of contact interaction between structural elements along aligned surfaces. *East.-Eur. J. Enterp. Technol.* **1**(7(103)), 16–25 (2020)
11. Ivanov, V., Pavlenko, I., Liaposhchenko, O., Gusak, O., Pavlenko, V.: Determination of contact points between workpiece and fixture elements as a tool for augmented reality in fixture design. *Wirel. Netw.* **27**(3), 1657–1664 (2019). <https://doi.org/10.1007/s11276-019-02026-2>
12. Bondarenko, M., Tkachuk, M., Grabovskiy, A., Hrechka, I.: Substantiation of thin-walled structures parameters using nonlinear models and method of response surface analysis. *Int. J. Eng.* **44**, 32–43 (2019)
13. Pavlenko, I., et al.: Parameter identification of cutting forces in crankshaft grinding using artificial neural networks. *Materials* **13**(23), 5357 (2020). <https://doi.org/10.3390/ma13235357>
14. Strutinsky, V., Demyanenko, A.: The development of mechatronic active control system of tool spatial position of parallel kinematics machine tool. *J. Theor. Appl. Mech.* **54**(3), 757–768 (2016). <https://doi.org/10.15632/jtam-pl.54.3.757>




15. Strutynsky, V., Hurzhi, A., Kozlov, L.: Determination of static equilibrium conditions of mobile terrestrial complex with lever-type manipulator. *Naukovyi Visnyk Natsionalnoho Hirnychoho Universytetu* **5**, 79–86 (2019). <https://doi.org/10.29202/nvngu/2019-5/7>
16. Strutynskiy, S., Nochnichenko, I.: Design of parallel link mobile robot manipulator mechanisms based on function-oriented element base. *East.-Eur. J. Enterp. Technol.* **4**(7 (100)), 54–64 (2019). <https://doi.org/10.15587/1729-4061.2019.174613>
17. Strutynskiy, S.: Defining the dynamic accuracy of positioning of spatial drive systems through consistent analysis of processes of different range of performance. *Naukovyi Visnyk Natsionalnoho Hirnychoho Universytetu* **3**, 64–73 (2018). <https://doi.org/10.29202/nvngu/2018-3/13>
18. Strutynskiy, S., Nochnichenko, I.: Design of parallel link mobile robot manipulator mechanisms based on function-oriented element base. *East.-Eur. J. Enterp. Technol.* **4**(7 (100)), 54–64 (2018). <https://doi.org/10.15587/1729-4061.2019.174613>
19. Panchenko, A., Voloshina, A., Titova, O., Panchenko, I., Zasiadko, A.: The study of dynamic processes of mechatronic systems with planetary hydraulic motors. In: Tonkonogyi, V., et al. (eds.) *InterPartner 2020. LNME*, pp. 704–713. Springer, Cham (2021). https://doi.org/10.1007/978-3-030-68014-5_68
20. Panchenko, A., Voloshina, A., Titova, O., Panchenko, I., Caldare, A.: Design of hydraulic mechatronic systems with specified output characteristics. In: Ivanov, V., Pavlenko, I., Liaposhchenko, O., Machado, J., Edl, M. (eds.) *DSMIE 2020. LNME*, pp. 42–51. Springer, Cham (2020). https://doi.org/10.1007/978-3-030-50491-5_5
21. Rogovyi, A., Khovansky, S., Grechka, I., Pitel, J.: the wall erosion in a vortex chamber supercharger due to pumping abrasive mediums. In: Ivanov, V., et al. (eds.) *DSMIE 2019. LNME*, pp. 682–691. Springer, Cham (2020). https://doi.org/10.1007/978-3-030-22365-6_68
22. Rogovyi, A., Khovanskyi, S., Hrechka, I., Gaydamaka, A.: Studies of the swirling submerged flow through a confuser. In: Ivanov, V., Pavlenko, I., Liaposhchenko, O., Machado, J., Edl, M. (eds.) *DSMIE 2020. LNME*, pp. 85–94. Springer, Cham (2020). https://doi.org/10.1007/978-3-030-50491-5_9
23. Chernetskaya-Beletskaya, N., Rogovyi, A., Shvornikova, A., Baranov, I., et al.: Study on the coal-water fuel pipeline transportation taking into account the granulometric composition parameters. *Int. J. Eng. Technol.* **7**(4.3), 240–245 (2018)
24. Bun, P., Trojanowska, J., Ivanov, V., Pavlenko, I.: The use of virtual reality training application to increase the effectiveness of workshops in the field of lean manufacturing. In: *4th International Conference of the Virtual and Augmented Reality in Education, VARE 2018*, pp. 65–71 (2018)
25. Ivanov, V., Pavlenko, I., Trojanowska, J., Zuban, Y., Samokhvalov, D., Bun, P.: Using the augmented reality for training engineering students. In: *4th International Conference of the Virtual and Augmented Reality in Education, VARE 2018*, pp. 57–64 (2018)
26. Gaydamaka, A., Kulik, G., Frantsuzov, V., Hrechka, I., et al.: Devising an engineering procedure for calculating the ductility of a roller bearing under a no-central radial load. *East.-Eur. J. Enterp. Technol.* **3**(7(99)), 6–10 (2019). <https://doi.org/10.15587/1729-4061.2019.168145>
27. Rogovyi, A., Korohodskiy, V., Medvediev, Y.: Influence of Bingham fluid viscosity on energy performances of a vortex chamber pump. *Energy* **218**, 119432 (2021). <https://doi.org/10.1016/j.energy.2020.119432>
28. Maiti, R., Nagao, M.: Prediction of starting torque characteristics of epitrochoid generated orbital rotary piston hydraulic motors. *Int. J. Ser. C-Mech. Syst. Mach. Elements Manuf.* **2** (42), 416–426 (1999)

29. González, J., Oro, J., Argüelles-Díaz, K.: Flow analysis for a double suction centrifugal machine in the pump and turbine operation modes. *Int. J. Numer. Meth. Fluids* **2**(61), 220–236 (2009). <https://doi.org/10.1002/fld.1951>
30. Pavlenko, I.: Static and dynamic analysis of the closing rotor balancing device of the multistage centrifugal pump. *Appl. Mech. Mater.* **630**, 248–254 (2014). <https://doi.org/10.4028/www.scientific.net/AMM.630.248>
31. Yao, J., Shi, W., Wu, S., Zhang, D., Wang, H., Hu, Q.: Numerical calculation and experiment on pressure fluctuation in axial flow pump. *Trans. Chin. Soc. Agric. Mach.* **1** (44), 119–124 (2013). <https://doi.org/10.6041/j.issn.1000-1298.2013.S1.022>
32. Gamez-Montero, P., Codina, E., Castilla, R.: A Review of gerotor technology in hydraulic machines. *Energies* **12**, 2423 (2019). <https://doi.org/10.3390/en12122423>
33. Ivanovic, L., Miric, N., Devedzic, G., Ćuković, S.: Analysis of forces and moments in gerotor pumps. *J. Mech. Eng. Sci.* **10**(224), 2257–2269 (2010). <https://doi.org/10.1243/09544062JMES2041>
34. Ivanović, L., Blagojević, M., Devedžić, G.: Assoul analytical and numerical analysis of load gerotor pumps. *Sci. Tech. Rev.* **1**(60), 30–38 (2010)
35. Chang, Y., Kim, J., Jeon, C., Chul, K., Jung, S.: Development of an integrated system for the automated design of a gerotor oil pump. *J. Mech. Des.* **129**(10), 1099–1105 (2006). <https://doi.org/10.1115/1.2757629>
36. Moloshnyi, O.M., Szulc, P., Sotnyk, M.I.: Influence of an inlet rotating axial device on the cavitation processes in a low specific speed centrifugal pump. *J. Eng. Sci.* **6**(1), E25–E32 (2019). [https://doi.org/10.21272/jes.2019.6\(1\).e5](https://doi.org/10.21272/jes.2019.6(1).e5)
37. Fesenko, A., Yevisukova, F., Basova, Y., Ivanova, M., Ivanov, V.: Prospects of using hydrodynamic cavitation for enhancement of efficiency of fluid working medium preparation technologies. *Periodica Polytechnica Mech. Eng.* **62**(4), 269–276 (2018). <https://doi.org/10.3311/PPme.11877>
38. Demianenko, M., Starynskyi, O., Vashyst, B., Pavlenko, I., Liaposhchenko, O., Ivanov, V.: Improvement of hydraulic characteristics for impellers using the finite volume analysis. In: Cagaňová, D., Horňáková, N., Pusca, A., Cunha, P.F. (eds.) *Advances in Industrial Internet of Things, Engineering and Management*. EICC, pp. 161–174. Springer, Cham (2021). https://doi.org/10.1007/978-3-030-69705-1_10
39. Liaposhchenko, O., et al.: Improvement of parameters for the multi-functional oil-gas separator of ‘heater-treater’ type. In: 2019 IEEE 6th International Conference on Industrial Engineering and Applications (ICIEA), Tokyo, Japan, 2019, pp. 66–71 (2019). <https://doi.org/10.1109/IEA.2019.8715203>
40. Stryczek, J., Bednarczyk, S., Biernacki, K.: Strength analysis of the polyoxymethylene cycloidal gears of the gerotor pump. *Arch. Civil Mech. Eng.* **14**(4), 647–660 (2014). <https://doi.org/10.1016/j.acme.2013.12.005>
41. Stryczek, J., Bednarczyk, S., Biernacki, K.: Gerotor pump with POM gears: design, production technology, research. *Arch. Civil Mech. Eng.* **14**(3), 391–397 (2013). <https://doi.org/10.1016/j.acme.2013.12.008>
42. Chiu-Fan, H.: Flow characteristics of gerotor pumps with novel variable clearance designs. *J. Fluids Eng.* **137**(4), FE-14-1137 (2015). <https://doi.org/10.1115/1.4029274>
43. Van de Ven, J. D.: On fluid compressibility in switch-mode hydraulic circuits. – part I: modeling and analysis. *J. Dyn. Syst. Meas. Control* **135**(2), 021013-1–021013-13 (2012). <https://doi.org/10.1115/1.4023062>
44. Van de Ven, J.D.: On fluid compressibility in switch-mode hydraulic circuits. – part II: modeling and analysis. *J. Dyn. Syst. Meas. Control* **135**(2), 021014-1–021014-7 (2012). <https://doi.org/10.1115/1.4023063>

45. Altare, G., Rundo, M. Computational fluid dynamics analysis of gerotor lubricating pumps at high-speed: geometric features influencing the filling capability. *J. Fluids Eng.* **38**(11), FE-15-1757 (2016). <https://doi.org/10.1115/1.4033675>
46. Ding, H., Lu, J.X., Jiang, B.: A CFD model for orbital gerotor motor. *IOP Conf. Ser. Earth Environ. Sci.* **6**(15), 062006 (2012). <https://doi.org/10.1088/1755-1315/15/6/062006>
47. Kiurchev, S., Luzan, P., Zasiadko, A., Radionov, H., Boltianska, N.: Influence of the flow area of distribution systems on changing the operating parameters of planetary hydraulic motors. *IOP Conf. Ser. Mater. Sci. Eng.* **1021**, 012037 (2021). <https://doi.org/10.1088/1757-899X/1021/1/012037>
48. Gamez-Montero, P.J., Garcia-Vilchez, M., Raush, G., Freire, J., Codina, E.: Teeth clearance and relief grooves effects in a trochoidal-gear pump using new modules of GeroLAB. *J. Mech. Des.* **134**(5), 054502–054507 (2012). <https://doi.org/10.1115/1.4006440>
49. Panchenko, A., Voloshina, A., Titova, O., Panchenko, I.: The influence of the design parameters of the rotors of the planetary hydraulic motor on the change in the output characteristics of the mechatronic system. *J. Phys: Conf. Ser.* **1741**, 012027 (2021). <https://doi.org/10.1088/1742-6596/1741/1/012027>
50. Ivanov, V., Dehtiarov, I., Denysenko, Y., Malovana, N., Martynova, N.: Experimental diagnostic research of fixture. *Diagnostyka* **19**(3), 3–9 (2018). <https://doi.org/10.29354/diag/92293>



Energy Management Strategy in the Synthesis of an Algorithm for Multi-step Conveyor Belt Speed Control

Oleh Pihnastyi , Georgii Kozhevnikov^(✉) ,
and Maxim Glavchev 

National Technical University “Kharkiv Polytechnic Institute”,
2, Kyrpychova Street, Kharkiv 61002, Ukraine
Heorhii.Kozhevnikov@khpi.edu.ua

Abstract. The article discusses the synthesis of the optimal algorithm for multistep control of the conveyor belt speed based on Time-Of-Use (TOU) tariffs. The main methods of reducing energy costs for the transport conveyor are discussed. The perspectives of using the energy management strategy to reduce the cost of material transportation are analyzed. Common tariff classes are considered, which can be used for designing the conveyor belt speed control systems. The problem of optimal belt speed control is formulated. The criterion of the quality of the control process is written, the differential connections are determined, and the Hamiltonian function is constructed. An algorithm for multi-step speed control of the conveyor belt is synthesized. For the synthesis of the control algorithm, an analytical model of the conveyor with dimensionless parameters is used, which considers the transport delay. The synthesis of the speed control algorithm considers the limitations on the value of the maximum permissible specific load of the material on the belt.

Keywords: Transport conveyor · Distributed system · Transport delay · TOU-tariff · Uneven distribution

1 Introduction

The use of conveyor transport in the mining industry is due to the low cost of material transportation costs compared to other modes of transport [1]. The cost of transporting material from the source of production to the place of loading the material depends on the length of the conveyor line and the transport system coefficient loading. A typical case is the operation of transport conveyors with a material loading factor of 0.50–0.70 [2]. With a decrease in the loading coefficient of conveyor sections [3], the value of transport costs can grow several times and become the central fact that determines the cost of the extracted material [4]. Even with the standard coefficient of material loading equal to 0.7, the cost of the conveyor transport of the mine is more than 20% of the total extracting material cost [5]. The increase in the length of the conveyor transport route also leads to a non-linear increase in the cost of transport costs. For reducing transport costs, long conveyors are divided into sections [6–8], equipped with an input

accumulator bunker [9]. This allows for optimal control of the flow parameters of the transport system in a separate section [10]. Common methods for reducing energy costs are using systems for belt speed control [11, 12] and systems for material flow intensity control [13, 14] from the bunker.

Along with these methods, many mining companies use the energy management methodology to reduce the cost of extracting material [9]. The main tariffs that can be used in the design of flow parameters control systems: tariff with a fixed price for electricity consumption (FPT); tariff with the price for electricity consumption, depending on the time of day (TOU); tariffs with the price for electricity consumption in real-time (RTT) [15, 16]. An analysis of the factors that determine the choice of tariff is presented in the paper [17]. Tariff coefficients and tariff structure for Great Britain [18], Ukraine [19], South Africa are given in [20]. In South Africa, there are long conveyors, among which it should be noted: Sasol - Shondoni Overland [7] (20.5 km); Western Sahara [21] (128.7 km). The presence of long conveyors in South Africa probably explains the interest in the use of energy management methodology in transport conveyor systems [22]. The structure of Eskom TOU-tariffs (South Africa) is shown in Fig. 1, Fig. 2 [23].

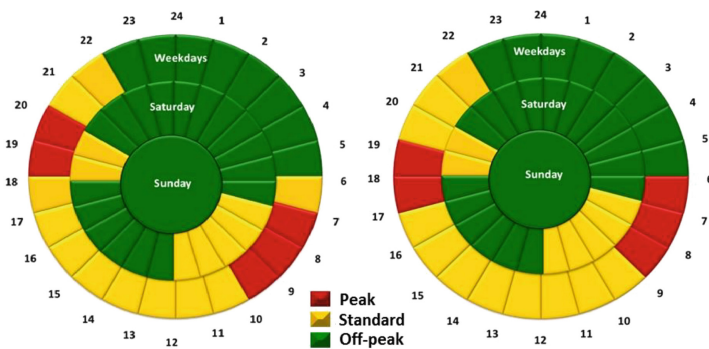


Fig. 1. Periods Eskom–TOU: a – high demand season; b – low demand season (South Africa) [23].

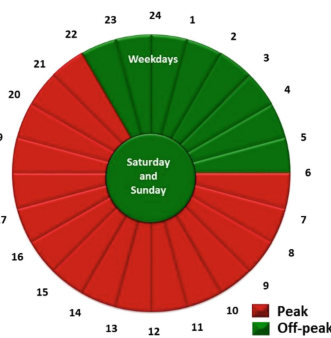


Fig. 2. Nightsave Eskom–TOU periods [23].

The presence of long transport systems and a strong difference in the price of electricity for the peak and off-peak periods determine the interest in using TOU tariffs for belt conveyors. This circumstance requires the development of methods for constructing the speed control system using TOU-tariff.

2 Literature Review

Statistical analysis carried out for 12 thousand enterprises in 44 industries demonstrates that the transition to TOU tariffs for industrial enterprises does not always lead to savings in electricity costs [16]. The use of TOU tariffs in a transport conveyor control is further complicated by the fact that a conveyor is a complex dynamic distributed system, the flow parameters of which contain transport delay. In this regard, the transition of a mining company to TOU tariffs requires developing algorithms for flow parameters optimal control of the transport system [24]. In this paper, let us consider the synthesis of an algorithm for optimal control of the flow parameters of a transport system with multi-step regulation of the belt speed. Multi-step speed control is of interest as an alternative method for continuous speed control of a transport system [25, 26].

When developing the algorithm, the following assumptions will be used:

- the control quality criterion is formulated for a time interval equal to 24 h;
- under DIN 22101, the primary friction model is used [27];
- instant switching of speed modes does not lead to damage to the belt;
- the total time of the modes of acceleration (deceleration) of the belt, associated with switching the belt, is negligible with the total time of the transportation process.

3 Research Methodology

3.1 Conveyor Model

To synthesize an algorithm for multi-step belt speed control based on the TOU-tariff structure, let's use the PiKh-conveyor model [12]:

$$\frac{\partial[\chi]_0(t, S)}{\partial t} + \frac{\partial[\chi]_1(t, S)}{\partial S} = \delta(S)\lambda_1(t), \quad (1)$$

$$[\chi]_0(0, S) = \Psi(S), \quad [\chi]_1(t, S) = a(t)[\chi]_0(t, S), \quad (2)$$

where $[\chi]_0(t, S) \leq [\chi]_{0\max}$, $[\chi]_1(t, S)$ are material distribution density and material flow for $t \in [0, T_d]$ at a route point $S \in [0, S_d]$; $\Psi(S) \leq [\chi]_{0\max}$ is the material distribution density for $t = 0$ along the route; $[\chi]_{0\max}$ is the maximum allowable material distribution density for the conveyor belt; T_d is the transportation process characteristic time; S is belt speed; $\lambda_1(t)$ is material flow from the bunker to the conveyor section input; $\delta(S)$ is Dirac function; $H(S)$ is Heaviside function.

In accordance with the model of primary resistances, the expression that determines the force for the movement of the belt with the material at the specific mass of the belt $[\chi]_{0C}$ the linear rotating parts load $[\chi]_{0R}$ [27], has the form:

$$T = C f_c g_m \int_0^{S_d} (2([\chi]_{0R} + [\chi]_{0C}) + [\chi]_0(t, S)) dS \quad (3)$$

where f_c is the coefficient of resistance to belt indentation and rolling of driving rollers [27]; $g_m = 9.81(\text{m}/\text{sec}^2)$; C is secondary resistance coefficient [27]; η_C efficiency.

Taking into account dimensionless parameters [13]:

$$\tau = t/T_d, \quad \xi = S/S_d, \quad \delta(\xi) = S_d \delta(S), \quad g(t) = a(t)T_d/S_d, \quad (4)$$

$$\psi(\xi) = \frac{\Psi(S)}{[\chi]_{0\max}}, \quad \gamma_1(\tau) = \lambda_1(t) \frac{T_d}{S_d [\chi]_{0\max}}, \quad \theta_0(\tau, \xi) = \frac{[\chi]_0(t, S)}{[\chi]_{0\max}}, \quad (5)$$

$$\theta_{0R} = \frac{[\chi]_{0R}}{[\chi]_{0\max}}, \quad \theta_{0C} = \frac{[\chi]_{0C}}{[\chi]_{0\max}}, \quad n_e(\tau) = N_E(t) \frac{T_d}{C f_c g_m \eta_c [\chi]_{0\max} S_d^2}, \quad (6)$$

the solution of Eqs. (1), (2) for the values of the output flow parameters $\theta_0(\tau, 1)$, $\theta_1(\tau, 1)$, ($\xi = 1$) can be written as follows:

$$\theta_0(\tau, 1) = \begin{cases} \frac{\gamma_1(\tau - \Delta\tau_1)}{g(\tau - \Delta\tau_1)}, & G(\tau) \geq 1, \tau \geq G^{-1}(1), \\ \psi(1 - G(\tau)), & G(\tau) < 1, \tau < G^{-1}(1), \end{cases} \quad (7)$$

$$\theta_1(\tau, 1) = \theta_0(\tau, 1)g(\tau), \quad \tau_1 = G^{-1}(G(\tau) - 1), \quad G(\tau) = \int_0^\tau g(\alpha) d\alpha \quad (8)$$

where $\Delta\tau_1(\tau)$ is the transport delay in the movement of material between the input and output of the section.

Dimensionless electrical power $n_e(\tau)$ (6), required to move a conveyor belt with a material with a total dimensionless mass $m(\tau)$, is determined from the expression:

$$n_e(\tau) = g(\tau)m(\tau), \quad m(\tau) = \int_0^1 (2\theta_{0R} + 2\theta_{0C} + \theta_0(\tau, \xi)) d\xi \quad (9)$$

The system of Eqs. (7)–(9) is used to design a control algorithm.

3.2 Synthesis of an Optimal Control Program

It is required to determine the modes of switching speeds for $\tau = [0, \tau_{24}]$ with coefficients $z(\tau)$ under the structure of TOU tariffs (Fig. 1, Fig. 2), multi-step belt speed control $g(\tau) = u(\tau) = (u_1, u_2, \dots, u_v)$, $0 < u_1 < u_2 < \dots < u_v < \infty$, $u_j = \text{const}$ with the quality control criterion:

$$\int_0^{\tau_{24}} z(\tau)u(\tau)m(\tau)d\tau \rightarrow \min, \quad z_{\min} \leq z(\tau) \leq z_{\max} \quad (10)$$

with differential connections

$$\frac{dm(\tau)}{d\tau} = \gamma_1(\tau) - \theta_1(1, \tau) = \gamma_1(\tau) - \gamma_1(\tau - \Delta\tau_1) \frac{u(\tau)}{u(\tau - \Delta\tau_1)}, \quad (11)$$

$$m(0) = 2(\theta_{0R} + \theta_{0C}) + \int_0^1 \psi(\xi)d\xi, \quad (12)$$

and limitation on energy consumption for the period $\tau = [0, \tau_{24}]$.

$$\int_0^{\tau_{24}} u(\tau)m(\tau)d\tau = b = \text{const} \quad \text{or} \quad \frac{dx_b}{d\tau} = u(\tau)m(\tau), \quad x_b(0) = 0, \quad \psi_m(\tau_{24}) = 0. \quad (13)$$

The Hamiltonian and the conjugate system of equations for the synthesis of the optimal control algorithm have the form

$$H = (\psi_b - z(\tau))u(\tau)m(\tau) + \psi_m \left(\gamma_1(\tau) - \gamma_1(\tau - \Delta\tau_1) \frac{u(\tau)}{u(\tau - \Delta\tau_1)} \right), \quad (14)$$

$$\frac{d\psi_b}{d\tau} = -\frac{\partial H}{\partial x_b} = 0, \quad \frac{d\psi_m}{d\tau} = (z(\tau) - \psi_b)u(\tau), \quad \psi_m(\tau_{24}) = 0. \quad (15)$$

From the solution of Eq. (18) let's determine $\psi_b = C_b = \text{const}$. The optimal belt speed $u(\tau) = (u_1, u_2, \dots, u_v)$ corresponds to the maximum value of the Hamilton function (14). The switching points of speed modes are determined by solving Eqs. (11)–(15).

3.3 Preparing Data for Calculations

To carry out numerical calculations, let's define $T_d = 1(\text{hour})$, $S_d = 20.5(\text{km})$. The choice of such a scale is convenient for the analysis of the schedule of speed switching modes $\tau \in [9; 24]$. The value S_d corresponds to the length of the Sasol - Shondoni Overland conveyor [7]. The speed control modes.

$$a_j = a_{\min} + j(a_{\max} - a_{\min})/10 \text{ (m/sec)} \quad a_{\min} = 1, a_{\max} = 5, j = 0..10.$$

will correspond to dimensionless values of the belt speed.

$$u_j = 0.176 + 0.07j, \quad u_{\min} = 0.176, \quad u_{\max} = 0.876. \quad (16)$$

Let's accept $(\theta_{0R} + \theta_{0C}) = 0.2$ and $\psi(\xi) = 0.8523$. The value $\psi(\xi)$ corresponds to the initial uniform loading of the belt with the material loading factor above the standard, equal to 0.8523. This defines the range of change $m(\tau)$.

$$m_{\min} = 0.4 \leq m(\tau) \leq 1.4 = m_{\max}, \quad m(\tau) = 2(\theta_{0R} + \theta_{0C}) + \int_0^1 \theta_0(\tau, \xi) d\xi, \quad (17)$$

$$m(0) = 2(\theta_{0R} + \theta_{0C}) + \int_0^1 \psi(\xi) d\xi = 1.2523.$$

Let's use the values u_{\min} , u_{\max} , m_{\min} , m_{\max} to calculate the range of variation $x_b(24) = b$.

$$1.69 = 24u_{\min}m_{\min} = b_1 \leq b \leq b_2 = 24u_{\max}m_{\max} = 29.50.$$

From the limit on the maximum permissible load $\lambda_1(t)/a(t) \leq [\chi]_{0\max}$ under expression (6), it follows

$$\gamma_1(\tau) \leq u(\tau) \leq 0.878. \quad (18)$$

Equation (15) and inequality $z_{\min} \leq z(\tau) \leq z_{\max}$ sets the range $z_{\min} \leq \psi_b \leq z_{\max}$.

4 Results

The schedule of belt speed regulation modes for tariff coefficients Ukraine – TOU periods under Eqs. (10)–(16) is shown in Fig. 3 and Fig. 4. Considered two options for the material flow receipt with intensities:

$$\gamma_1(\tau) = 0.15 + 0.15 \sin(\pi\tau/12), \quad b = 4.35, \quad \gamma_1(\tau) = 0.5 + 0.3 \sin(\pi\tau/12), \quad b = 12.85.$$

The type of function selected for analysis allows the transport system to operate in multi-step modes of belt speed adjustment under inequality (18). An increase in the average value of the input flow $\gamma_1(\tau)$ over a period of time $[0, \tau_{24}]$ leads to an increase in the amount of energy consumed b . The minimum allowable belt speed $u(\tau)$ is limited by the value of the intensity of the incoming flow $\gamma_1(\tau)$. The functions that determine the amount of energy consumption in natural $x_b(\tau)$ and cost $J(\tau)$ terms are shown in Fig. 5. The synthesized control algorithm can be characterized by the value of

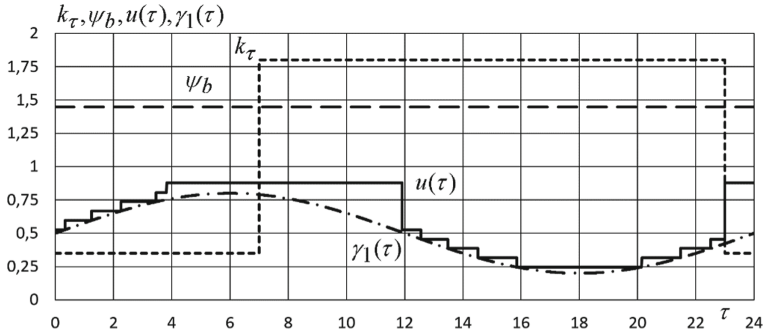


Fig. 3. Modes of belt speed regulation $u(\tau)$ for tariff coefficient $k_\tau(\tau) = (0.35, 1.8)$ at $\psi(\xi) = 0.8523$, $\gamma_1(\tau) = 0.5 + 0.3 \sin(\pi\tau/12)$.

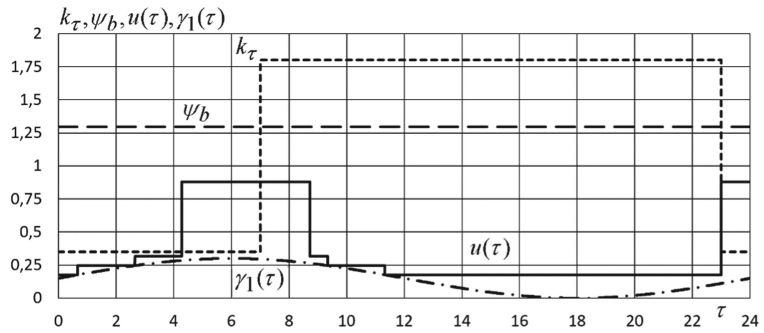


Fig. 4. Modes of belt speed regulation $u(\tau)$ for tariff coefficient values $k_\tau(\tau) = (0.35, 1.8)$ at $\psi(\xi) = 0.8523$, $\gamma_1(\tau) = 0.15 + 0.15 \sin(\pi\tau/12)$.

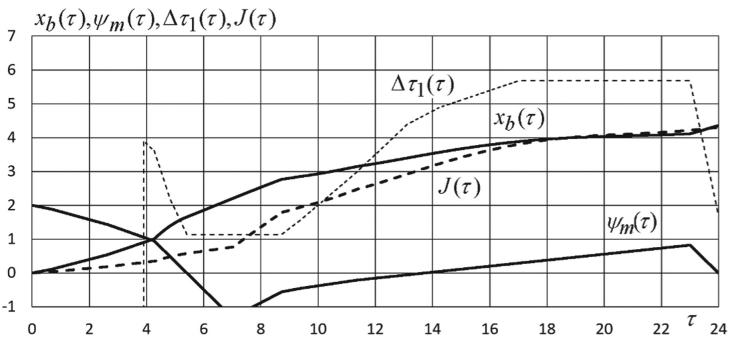


Fig. 5. Energy consumption in natural $x_b(\tau)$ and cost $J(\tau)$ form for tariff coefficient $k_\tau(\tau) = (0.35, 1.8)$ at $\psi(\xi) = 0.8523$, $\gamma_1(\tau) = 0.5 + 0.3 \sin(\pi\tau/12)$

the tariff coefficient $k_{\tau_{24}} = J(\tau_{24})/x_b(\tau_{24}) = 0.98$, averaged over the period $[0, \tau_{24}]$ for the incoming flow with the intensity $\gamma_1(\tau)$. A similar calculation for the intensity of the material flow gives the value $k_{\tau_{24}} = 1.138$. An increase in the intensity of the input flow

of material and its uneven incoming over time lead to an increase in the value of the tariff coefficient k_{r24} . One of the solutions to this problem is the use of input bunkers and material flow control systems from bunkers.

5 Conclusion

The article presents the synthesis of an algorithm for the optimal multi-step control of the belt speed of the transport conveyor section. The synthesis of an algorithm for optimal control of the belt speed is based on the Pontryagin maximum principle. The analytical PiKh-conveyor model is the basis for constructing differential connections. The software is developed and used to synthesize an algorithm for the optimal multi-step control of the belt speed, considering the initial distribution of material along the transport route and the limitation on the maximum load on the material for the conveyor belt. The numerical analysis presented shows negligible savings for a low flow rate input. The control system based on belt speed regulation does not allow efficient use of energy management methodology. This is because there is a problem associated with the fact that the minimum permissible belt speed is limited by the value of the material flow entering the input of the section.

The solution to this problem determines the plans for future research. They can be formulated as follows. Firstly, the synthesis of an algorithm for controlling the flow of material coming from the accumulating bunker to the input of the section. It is assumed that this solution will remove the restriction on the minimum allowable speed of the conveyor belt and, as a result, will reduce energy consumption for material transportation. Secondly, the determination of the minimum capacity of the accumulating bunker for the efficient functioning of the transport system. The risk of overfilling the bunker with material causes the belt speed to be limited. Finally, the determination of the optimal number of sections of the transport system. This approach makes it possible to ensure material movement on different sections of the route at an optimal speed within a separate section.

References






1. Shirong, Z., Wei, M.: Energy efficiency optimization of coal conveying system with consideration of crushers. *Energy Procedia* **105**, 3253–3261 (2017)
2. Jeftenić, B., Ristić, L., Bebić, M., Štatkić, S., Mihailović, I., Jevtić, D.: Optimal utilization of the bulk material transportation system based on speed controlled drives. In: *The XIX International Conference on Electrical Machines*, pp. 1–6. IEEE, Rome (2010)
3. Pihnastyi, O.: Control of the belt speed at unbalanced loading of the conveyor. *Sci. Bull. Natl. Mining Univ.* **6**, 122–129 (2019)
4. Kiria, R., Shyrin, L.: Reducing the energy consumption of the conveyor transport system of mining enterprises. In: *International Conference Essays of Mining Science and Practice, E3S Web of Conferences*, vol. 109, p. 00036 (2019)
5. Razumnyj, J., Ruhlov, A., Kozar, A.: Improving the energy efficiency of conveyor transport of coal mines. *Mining Electromech. Autom.* **76**, 24–28 (2006)

6. Król, R., Kawalec, W., Gładysiewicz, L.: An effective belt conveyor for underground ore transportation systems. *IOP Conf. Ser. Earth Environ. Sci.* **95**(4), 1–9 (2017)
7. Koman, M., Laska, Z.: The constructional solution of conveyor system for reverse and bifurcation of the ore flow. “Rudna” mine KGHM Polska Miedź SA. *CUPRUM* **3**(72), 69–82 (2014)
8. Bajda, M., Błażej, R., Jurdziak, L.: Analysis of changes in the length of belt sections and the number of splices in the belt loops on conveyors in an underground mine. *Eng. Fail. Anal.* **101**, 439–446 (2019)
9. Marais, J., Mathews, E., Pelzer, R.: Analysing DSM opportunities on mine conveyor systems. In: *Industrial and Commercial Use of Energy Conference*, Cape Town, South Africa (2008)
10. Alspauch, M.: The evolution of intermediate driven belt conveyor. *Bulk Solids Handling* **23** (3), 168–173 (2003)
11. Halepoto, I., Shaikh, M., Chowdhry, B.: Design and implementation of intelligent energy efficient conveyor system model based on variable speed drive control and physical modeling. *J. Control Autom.* **9**(6), 379–388 (2016)
12. Pihnastyi, O.M., Khodusov, V.D.: Optimal control problem for a conveyor-type production line. *Cybern. Syst. Anal.* **54**(5), 744–753 (2018). <https://doi.org/10.1007/s10559-018-0076-2>
13. Pihnastyi, O., Khodusov, V.: The optimal control problem for output material flow on conveyor belt with input accumulating bunker. *Bull. South Ural State Univ. Ser. Math. Model. Program. Comput. Softw.* **12**(2), 67–81 (2019)
14. Bardzinski, P., Walker, P., Kawalec, W.: Simulation of random tagged ore flow through the bunker in a belt conveying system. *Int. J. Simul. Model.* **4**, 597–608 (2018)
15. Darby, S., Pisica, I.: Focus on electricity tariffs: experience and exploration of different charging scheme. In: *Proceedings ECEEE Summer Study*, Hyres, France, pp. 2321–2331 (2013)
16. Woo, C., Sreedharan, P., Hargreaves, J., Kahrl, F., Wang, J., Horowitz, I.: A review of electricity product differentiation. *Appl. Energy* **114**, 262–272 (2014)
17. Granell, R., Axon, C., Wallom, D.: Predicting winning and losing businesses when changing electricity tariffs. *Appl. Energy* **133**, 298–307 (2014)
18. National Audit Office. The electricity generating landscape in Great Britain (2010). https://www.nao.org.uk/wp-content/uploads/2010/08/electricity_generating_landscape_gb.pdf, Accessed 10 Oct 2020
19. Iknet. Energy project management, <https://iknet.com.ua/ru/energy-costs-optimization-for-households/>, Accessed 10 Oct 2020
20. A guide to understanding your industrial electricity bill. National Cleaner Production Centre, South Africa. <http://ncpc.co.za/files/Guides/How%20to%20Read%20Your%20Electricity%20guide%20Book.pdf>, Accessed 10 Oct 2020
21. ConveyorBeltGuide. <http://conveyorbeltguide.com>, Accessed 10 Oct 2020
22. Mathaba, T., Xia, X., Zhang, J.: Optimal scheduling of conveyor belt systems under Critical Peak Pricing. In: *10th International Power & Energy Conference (IPEC)*, pp. 315–320. IPEC (2012)
23. Eskom. Megaflex gen# schedule of standard prices for non-local authority supplies – 1 april 2020 to 31 march 2021. <https://www.eskom.co.za/CustomerCare/TariffsAndCharges/Documents/Megaflex%20Gen%20schedule%202020-21.pdf>, Accessed 10 Oct 2020
24. Cousins, T.: Using time of use (TOU) tariffs in industrial, commercial and residential applications effectively. In: *TLC Engineering Solutions*, pp. 1–15 (2010)
25. Reutov, A.: Simulation of load traffic and steeped speed control of conveyor. *IOP Conf. Ser. Earth Environ.* **87**(8), 1–6 (2017)

26. Bebic, M., Ristic, B.: Speed controlled belt conveyors: drives and mechanical considerations. *Adv. Electric. Comput. Eng.* **18**(1), 51–60 (2018)
27. Lauhoff, H.: Speed control on belt conveyors – does it really save energy? *Bulk Solids Handling Publ.* **25**(6), 368–377 (2005)



Static Stiffness of the Crane Bridges Under Moving Load Distribution

Anatoliy Tkachev¹ , Aleksey Tkachev¹ , Dasic Predrag² ,
Ihor Prokopovych¹ , and Maryna Kostina¹ 

¹ Odessa Polytechnic State University, 1, Shevchenko Avenue,
Odessa 65044, Ukraine
tavtkach@ukr.net

² SaTCIP Publisher Ltd., 36210 Vrnjačka Banja, Serbia

Abstract. The paper deals with issues related to the calculation and design of prestressed crane structures of span type. The problem consists of the further application and use of a refined mathematical model of a preformed crane bridge, which allows analytically investigating its deformed behavior according to actual operating conditions. This paper analyzes the mathematical models of the main girders of overhead cranes adapted for use. The most dangerous positions for them with a movable transverse load are considered. The authors provide a refined mathematical model of an overhead crane with prestressed beams based on the general theory of stability of elastic systems. In the design scheme, the resulting vertical movable load was distributed over several transverse movable loads, corresponding to the actual conditions of its loading. In this work, equations for the deflection curve of a span were obtained, which made it possible to additionally investigate its static stiffness, depending on the nature and action of a temporary moving load. The results obtained in this work can be used to modernize cranes to increase their lifting capacity, extend their service life without dismantling, and improve existing structures and engineering calculation methods under actual operating conditions.

Keywords: Overhead crane · Prestress · Main girders · Static rigidity · Flexural stiffness · Deflected mode · Deformed condition

1 Introduction

The subject of consideration is preliminarily stressing the structures: artificial creation of internal forces and stresses to obtain or increase necessary beneficial qualities before operation [1]. The concept of prestressing is based on the property of statically indeterminate mechanical systems to allow internal forces and stresses in their elements in the absence of external force effects [2].

Span cranes with prestressed main girders are widely used in mechanical engineering. Metal bridges of such cranes have a lower moment of inertia of the section. Therefore they are much lighter and cheaper than metal structures of conventional cranes operating under the same operating modes and the same load capacities [3].

At the same time, they are more deformable [4]. Therefore, the criteria for calculating and designing such metal structures are linked inextricably with the causes of their failures [5]. One of the main reasons for malfunctioning a structure is its unacceptably large elastic deformations [6, 7]. So, for example, a significant deflection or bending of span beams can lead to distortions of the end beams, slipping of the running wheels of freight bogies, and unnecessary power consumption for overcoming the slope of the load belt [8, 9].

In this regard, a more accurate determination of the deformation value of the bridge and analysis of its behavior under load will not only improve the operating conditions of the beam and the crane as a whole but also lead to a number of positive measures such as reducing the weight of the crane's metal structure and its cost [10]. Since the crane girder is subjected to longitudinal-transverse bending, the deformed state of the crane bridge must be taken into account using the deflection arrow of the girder itself.

Thus, the purpose of this work is to further study the span beam for static stiffness. And the issues considered in it, in which the nature of the loading of the beam is put forward in the first place with the maximum approximation of the design scheme to the actual constructive form, are relevant [11].

For achieving this goal, it is necessary to solve the following tasks: consider and analyze the already known mathematical models of an overhead crane with prestressed main beams; to develop a mathematical model of an overhead crane with prestressed main beams, which allows you to study its deformed behavior according to the actual conditions of its operation; analyze the results obtained.

2 Literature Review

The analysis of publications on the topic under study shows that the moments unloading a prestressed crane bridge do not depend on the position of the external load and its value [12] (Fig. 1).

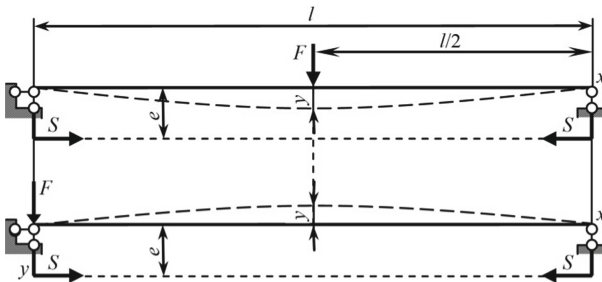


Fig. 1. Prestressed crane bridge.

As a result, one of the disadvantages is the case when a movable cart with a load is located above the support or near it [13]. In this connection, the reverse deflections of the bridge can be commensurate with the working deflections of the beam and even

exceed its permissible deflections. Thus, the calculation of the prestressed main beam for the third limiting state is carried out according to the accepted design scheme for the two most unfavorable loading cases [14, 15]: when the movable vertical load F is in the middle of the span l , that is, the current coordinate of deflection determination $x = 0.5$ or l , where the calculated deflections are checked; when the load F is above the support, where the current coordinate of deflections is $x = 0$ or $x = l$. In this case, the reverse bends of the prestressed bridge are checked.

Analysis of the design scheme for the first case of loading shows that the scheme is significantly simplified and cannot accurately reflect the actual operating conditions of the span beam. This is because the scheme does not consider distributing the concentrated vertical load F between the corresponding n number of crane wheels. The distribution of the force F between the wheels leads to an increase in the lateral forces F_1, F_2, \dots, F_n acting on the beam and complicates the design scheme. But neglect of this factor leads to overestimated values of the calculated deflection of the bridge, and in some cases - to unreasonably overestimated reserves of its static or dynamic stiffness.

The analysis of the second case of loading suggests that the accepted design scheme of the span beam also does not correspond to the maximum approximation of the scheme to the real structural one. So, the design scheme does not consider the permissible minimum distance from the axis of the drive wheels to the axis of the crane rail. Therefore, in a confirmed case of loading, one of the wheels of the cargo carriage at its extreme position will always be at a distance l_b from the end beam, which significantly reduces the value of the calculated bridge deflection (Fig. 2).

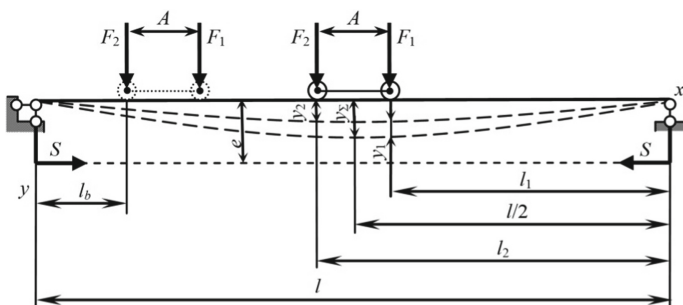


Fig. 2. The design scheme of the crane bridge.

Neglect of this factor, as in the first case of loading, can lead to overestimated reserves of the crane bridge according to the deformation criterion of performance.

3 Research Methodology

When constructing the proposed refined mathematical model, it is assumed that all the crane elements are solid, the beam operates in an elastic stage, rests on ideal hinges, and its bending is carried out in the area of the load suspension. We distribute the transverse working load (from the weight of the bogie with the rated load) between the wheels of the freight bogie and represent it by vertical forces F_1 , F_2 . Then, using the method of superposition of deflections known from the theory of stability of elastic systems (caused separately by each of the transverse forces F_1 and F_2 , acting together with the total longitudinal eccentrically applied force S), we compose the differential equations of the deflection curve for the left section of the prestressed beam

$$EI \cdot \ddot{y}_{1,L} = -\frac{F_1 l_1}{l} x - P(y_{1,L} - e),$$

$$EI \cdot \ddot{y}_{2,L} = -\frac{F_2 l_2}{l} x - P(y_{2,L} - e).$$

Deflection arrow differential equations for right beam segment

$$EI \cdot \ddot{y}_{1,R} = -\frac{F_1(l-l_1)(l-x)}{l} x - P(y_{1,R} - e),$$

$$EI \cdot \ddot{y}_{2,R} = -\frac{F_1(l-l_2)(l-x)}{l} x - P(y_{2,R} - e).$$

where EI is the bending rigidity of the beam in the plane of the load suspension; l is the length of the beam; x is the current coordinate of the location of deflections (bends) y_1 and y_2 , respectively, from the forces F_1 and F_2 ; l_1 , l_2 – distances from the proper support of the beam to the place of action of transverse loads, respectively F_1 and F_2 .

To simplify the subsequent mathematical calculations, we introduce the notation

$$k^2 = \frac{S}{EI}.$$

Then the above differential equations take the form

$$\ddot{y}_{1,L} + k^2 y_{1,L} = -\frac{F_1 l_1}{lEI} x + k^2 e, \quad (1)$$

$$\ddot{y}_{2,L} + k^2 y_{2,L} = -\frac{F_2 l_2}{lEI} x + k^2 e, \quad (2)$$

$$\ddot{y}_{1,R} + k^2 y_{1,R} = -\frac{F_1(l-l_1)(l-x)}{lEI} + k^2 e, \quad (3)$$

$$\ddot{y}_{2,R} + k^2 y_{2,R} = -\frac{F_2(l-l_2)(l-x)}{IEI} + k^2 e. \quad (4)$$

The general solutions of these equations will be, respectively, for the expression (1)

$$y_{1,L} = C_1 \cos(kx) + C_2 \sin(kx) - \frac{F_1 l_1}{Sl} x + e, \quad (5)$$

for the expression (2)

$$y_{2,L} = C_3 \cos(kx) + C_4 \sin(kx) - \frac{F_2 l_2}{Sl} x + e, \quad (6)$$

for the expression (3)

$$y_{1,R} = C_5 \cos(kx) + C_6 \sin(kx) - \frac{F_1(l-l_1)(l-x)}{Sl} + e, \quad (7)$$

for the expression (4)

$$y_{2,R} = C_7 \cos(kx) + C_8 \sin(kx) - \frac{F_2(l-l_2)(l-x)}{Sl} + e. \quad (8)$$

Integration constants C_1, C_3, C_5, C_7 are determined from the conditions at the beam ends, where its deflections are equal to zero.

$$(y_{1,L})_{x=0} = 0, \text{ then } C_1 = -e, \quad (y_{2,L})_{x=0} = 0, \text{ then } C_3 = -e,$$

$$(y_{1,R})_{x=l} = 0, \text{ then } C_5 = -C_6 \operatorname{tg}(kl) - e \sec(kl),$$

$$(y_{2,R})_{x=l} = 0, \text{ then } C_7 = -C_8 \operatorname{tg}(kl) - e \sec(kl).$$

Other integration constants are determined from the conditions that at the point of application of the transverse forces F_1 and F_2 , both sections of the beam deformation curve have the same deflection.

$$(y_{1,L})_{x=l-l_1} = (y_{1,R})_{x=l-l_1}, \quad (y_{2,L})_{x=l-l_2} = (y_{2,R})_{x=l-l_2}$$

and the common tangent.

$$(\dot{y}_{1,R})_{x=l-l_1} = (\dot{y}_{1,L})_{x=l-l_1}, \quad (\dot{y}_{2,L})_{x=l-l_2} = (\dot{y}_{2,R})_{x=l-l_2}.$$

Then, expressions for determining the integration constants C_2, C_4, C_6, C_8 will have the following final form

$$C_2 = \frac{F_1 \sin(kl_1)}{Sk \sin(kl)} - e \operatorname{tg}\left(\frac{kl}{2}\right), \quad C_4 = \frac{F_2 \sin(kl_2)}{Sk \sin(kl)} - e \operatorname{tg}\left(\frac{kl}{2}\right),$$

$$C_6 = -\frac{F_1 \sin(k(l-l_1))}{Sk \sin(kl)} - e \operatorname{tg}\left(\frac{kl}{2}\right), \quad C_8 = -\frac{F_2 \sin(k(l-l_2))}{Sk \sin(kl)} - e \operatorname{tg}\left(\frac{kl}{2}\right),$$

Substitute the obtained expressions for the constants C_1, \dots, C_8 into the corresponding initial Eqs. (5)–(8) and denote, after some transformations, the following expressions for the left and right sections of the deflection curve of the crane bridge

$$y_{1,L} = \frac{F_1}{S} \left(\frac{\sin(kx)\sin(kl_1)}{k \sin(kl)} - \frac{x l_1}{l} \right) - eU, \quad (9)$$

$$y_{2,L} = \frac{F_2}{S} \left(\frac{\sin(kx)\sin(kl_2)}{k \sin(kl)} - \frac{x l_2}{l} \right) - eU, \quad (10)$$

$$y_{1,R} = \frac{F_1}{S} \left(\frac{\sin(k(l-x))\sin(k(l-l_1))}{k \sin(kl)} - \frac{(l-x)(l-l_1)}{l} \right) - eU, \quad (11)$$

$$y_{2,R} = \frac{F_2}{S} \left(\frac{\sin(k(l-x))\sin(k(l-l_2))}{k \sin(kl)} - \frac{(l-x)(l-l_2)}{l} \right) - eU. \quad (12)$$

Applying the method of superposition of deflections, we obtain the total deflection y_{Σ} of the bridge when the forces F_1 and F_2 act simultaneously together with the eccentric longitudinal force S . Adding expressions (9) and (10), we find the equations for the deflection curve for the left section of the beam ($0 \leq x \leq (l-l_2)$)

$$y_{\Sigma,L} = y_{1,L} + y_{2,L}$$

$$= \frac{1}{S} \left(\frac{\sin(kx)}{k \sin(kl)} (F_1 \sin(kl_1) + F_2 \sin(kl_2)) - \frac{x}{l} (F_1 l_1 + F_2 l_2) \right) - 2eU.$$

Adding expressions (11) and (12), we find the equations of the deflection curve for the right section of the beam ($x \geq (l-l_2)$)

$$y_{\Sigma,R} = y_{1,R} + y_{2,R} = \frac{1}{S} \left(\frac{\sin(k(l-x))}{k \sin(kl)} (F_1 \sin(k(l-l_1)) + F_2 \sin(k(l-l_2))) - \frac{(l-x)}{l} \right. \\ \left. \times (F_1(l-l_1) + F_2(l-l_2)) - 2eU. \right.$$

Taking into account the above, we will compose the equation of the deflection curve of the span between the wheels of the cargo trolley in the section between the vertical loads F_1 and F_2

$$y_{\Sigma} = -2eU + \frac{F_1}{S} \left(\frac{\sin(kx)\sin(kl_1)}{k \sin(kl)} - \frac{x l_1}{l} \right) + \frac{F_2}{S} \left(\frac{\sin(k(l-x))\sin(k(l-l_2))}{k \sin(kl)} - \frac{(l-x)(l-l_2)}{l} \right).$$

For studying the span beam's stress state, it is necessary to differentiate twice the total equations of the deflection curves

$$\dot{y}_{\Sigma L} = \frac{\cos(kx)}{S \sin(kl)} (F_1 \sin(kl_1) + F_2 \sin(kl_2)) - \frac{F_1 l_1 + F_2 l_2}{Sl} - 2ek \left(\cos(kx) \operatorname{tg} \left(\frac{kl}{2} \right) - \sin(kx) \right),$$

$$\dot{y}_{\Sigma R} = \frac{\cos k(l-x)}{S \sin kl} (F_1 \sin(k(l-l_1)) + F_2 \sin(k(l-l_2))) - \frac{F_1(l-l_1) + F_2(l-l_2)}{Sl} - 2ek \left(\cos(kx) \operatorname{tg} \left(\frac{kl}{2} \right) - \sin(kx) \right),$$

$$\dot{y}_{\Sigma} = -2ek \left(\cos(kx) \operatorname{tg} \left(\frac{kl}{2} \right) \right) - \sin(kx) + \frac{F_1 \cos(kx) \sin(kl_1)}{S \sin(kl)} - \frac{F_1 l_1 - F_2(l-l_2)}{Sl} - \frac{F_2 \cos(k(l-x)) \sin(k(l-l_2))}{S \sin(kl)}.$$

After the first differentiation, the expressions obtained above represent the small angles of rotation of the ends of the beam, which can be used in the design of a prestressed crane bridge. After the second differentiation, we obtained

$$\ddot{y}_{\Sigma L} = -\frac{k \sin(kx)}{S \sin(kl)} \left(F_1 \sin(kl_1) + F_2 \sin(kl_2) \right) + 2ek^2 \left(\sin(kx) \operatorname{tg} \left(\frac{kl}{2} \right) + \cos(kx) \right),$$

$$\ddot{y}_{\Sigma R} = -\frac{k \sin(k(l-x))}{S \sin(kl)} (F_1 \sin(k(l-l_1)) + F_2 \sin(k(l-l_2))) + 2ek^2 \left(\sin(kx) \operatorname{tg} \left(\frac{kl}{2} \right) + \cos(kx) \right),$$

$$\ddot{y}_{\Sigma} = 2ek^2 \left(\sin(kx) \operatorname{tg} \left(\frac{kl}{2} \right) + \cos(kx) \right) - \frac{F_1 \sin(kx) \sin(kl_1) + F_2 \sin(k(l-x)) \sin(k(l-l_2))}{S \sin(kl)}.$$

In the final form, the equations of bending moments are

$$M_L = -EI(\ddot{y}_{\Sigma L}) = \frac{\sin(kx)}{k \sin(kl)} (F_1 \sin(kl_1) + F_2 \sin(kl_2)) - 2eS \left(\cos(kx) + \sin(kx) \operatorname{tg} \left(\frac{kl}{2} \right) \right),$$

$$M_R = -EI(\ddot{y}_{\Sigma R}) = \frac{\sin(k(l-x))}{k \sin(kl)} (F_1 \sin(k(l-l_1)) + F_2 \sin(k(l-l_2))) - 2eS \left(\cos(kx) + \sin(kx) \operatorname{tg} \left(\frac{kl}{2} \right) \right),$$

$$M = -EI(\ddot{y}_{\Sigma}) = \frac{F_1 \sin(kx) \sin(kl_1) + F_2 \sin(k(l-x)) \sin(k(l-l_2))}{k \sin(kl)} - 2eS \left(\cos(kx) + \sin(kx) \operatorname{tg} \left(\frac{kl}{2} \right) \right).$$

4 Results

Based on the obtained expressions for the deflection curves of the prestressed beam, mathematical studies of its deformed state were carried out. The base is a beam with a span of $L = 10.5$ m. For overhead cranes with a lifting capacity of $F = 1000$ kg, an I-beam No. 24M is recommended [16]. Conveniently, the weight load is distributed between the wheels of the cargo trolley and $F_1 = F_2 = 500$ kg is considered. The distance between the forces F_1 and F_2 is taken as $A = 0.560$ m. It corresponds to the distance between the wheels of the TE1–521 electric hoist. Part of the calculation results in the form of conditional deflections $y/[y]$ of the main beam for a group of operation mode 4K, with an allowable value of conditional deflections $[y/l] = 2 \cdot 10^{-3}$ is presented in Table 1. Graphic interpretation of calculations in the form of deflection curves beams are given for the ratio of transverse and longitudinal forces $F / S = 1.5$ (Fig. 3).

Table 1. Conditional deflections of the main beam.

$\frac{F_1+F_2}{S}$	Position carts	Calculation scheme			
		Acting			The proposed
		$e_1 = e_2$	$e_1 \neq e_2$	$e_1 = e_2 = 0$	
$\frac{F_1+F_2}{1.25}$	Mid-span	0.92	0.96	1.05	0.72
	Near the support	-0.17	-0.12		-0.11
$\frac{F_1+F_2}{1.5}$	Mid-span	0.88	0.94		0.68
	Near the support	-0.20	-0.16		-0.04
$\frac{F_1+F_2}{1.75}$	Mid-span	0.85	0.9		0.63
	Near the support	-0.25	-0.18		-0.06
$\frac{F_1+F_2}{2}$	Mid-span	0.8	0.85		0.51
	Near the support	-0.3	-0.23		-0.1

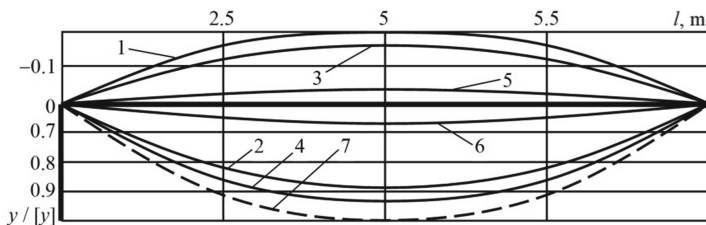


Fig. 3. Deflection curves of a prestressed beam.

Deflection arrows 2, 4, 6, 7 are shown when the crane is operating with a load in the middle of the span. And arrows of bends 1, 3, 5 – when placing one of the cart's wheels near the support at a distance of l_b – the minimum permissible safety zone for overhead cranes. Strain curves 1–4 are obtained by applying an accepted mathematical model for prestressed beams. For deflections 1, 2, the beam was subjected to the action of longitudinal forces applied on one line of action with eccentricity $e_1 = e_2$, and deflections 3 and 4 were obtained in the case of applying compressive forces with different eccentricities $e_1 \neq e_2$. Deflection curve 7 is built for a conventional crane bridge without prestress.

The analysis of the obtained results shows that the deformations of the unloaded beam do not exceed the deflections of a conventional crane bridge. The mathematical models used in the calculation and design of prestressed span beams are significantly simplified and do not always correspond to the actual conditions of its operation, and the deformations of the crane bridge are overestimated significantly. Thus, the deflection arrows 5 and 6, obtained using a new mathematical model proposed by the authors, say that the values of the deflections and deflections of the beam are, on average, 20% and 25% less, respectively, than in the currently used design scheme. The results obtained should be further used to improve existing structures and engineering calculation methods, both at the design stage and in actual operating conditions. At the same time, in the proposed new model, the use of several vertical forces F_1, F_2, \dots, F_n , although it corresponds to the actual loading conditions of the beam, significantly complicates its calculation according to the main criteria of performance.

5 Conclusions

In work, a more accurate mathematical model of a prestressed crane bridge was proposed and investigated. Its use makes it possible to significantly reduce the calculated deformations of the span beams compared to the previously adopted mathematical models of span beams.






The results obtained in this work can be further used for the modernization of cranes to increase their lifting capacity, increase the service life without dismantling, and improve existing structures and engineering calculation methods during design and in actual operation.

References

1. Bonopera, M., Chang, K., Lee, Z.-K.: State-of-the-art review on determining prestress losses in prestressed concrete girders. *Appl. Sci.* **10**, 72–57 (2020)
2. Qu, X., Xu, G., Fan, X., Bi, X.: Intelligent optimization methods for the design of an overhead traveling crane. *Chin. J. Mech. Eng.* **28**(1), 187–196 (2015)
3. Chebrovsky, A., Savva, Y.: Review of the state of prestressed metal beams and the results of the study of operating crane beams when operating on a moving load. *PNU Bull. Khabarovsk* **4**(31), 383–402 (2013)
4. Iodchik, A.: Deflections of a steel beam, prestressed by bending of the I-beam. *Bull. VSSTU* **5**(44), 45–52 (2013)
5. Jianqun, W., Shenghua, T., Zheng, H., Zhou, C., Zhu, M.: Flexural behavior of a 30-meter full-scale simply supported prestressed concrete box girder. *Appl. Sci.* **10**(9), 30–76 (2020)
6. Nie, J., Tao, M., Cai, C., Li, S.: Deformation analysis of prestressed continuous steel-concrete composite beams. *J. Struct. Eng.* **135**(11), 94–102 (2009)
7. Yifei, T., Lijin, L., Guomin, S., Dongbo, L., Xiangdong, L.: Overhead crane camber deformation assessment and energy analysis. *Proc. Inst. Mech. Eng. Part B* **6**, 52–55 (2014)
8. Marefat, M., Ghahremani-Gargary, E., Ataei, S.: Load test of a plain concrete arch railway bridge of 20-m span. *Constr. Build. Mater.* **18**, 661–667 (2011)
9. Oguamanam, D., Hansen, J.: Dynamics of a three-dimensional overhead crane system. *J. Sound Vib.* **242**(3), 411–426 (2012)
10. Liu, J., Wang, T.: Deflection calculation on reinforced concrete beams strengthened by externally prestressing transverse tensioning method. *Adv. Mater. Res.* **71**, 430–436 (2013)
11. Tkachov, A., Tkachov, O., Sydorenko, I.: Improvement of the deformed state of flight beams of bridge cranes. *Fac. Arch. Civil Eng. Appl. Arts* **2**(4), 118–125 (2020)
12. Hongguang, D., Tianxiang, B., Yanzhong, S., Sikun, Y.: The optimum design of single girder bridge-crane based on FEM. *Steel Constr.* **2**, 46–48 (2009)
13. Iodchik, A., Kravchuk, V.: Engineering calculation of steel prestressed beam. *TOGU Gazette* **2**(29), 64–72 (2013)
14. Zhegul'sky, V., Mironov, I., Lukashuk, O.: Design and Calculation of Crane Metal Structures. Ural Publishing House University, Russia (2019)
15. Menzel, U.: Cranes: experience in use and development trends. In: Crane Conference, vol. 14, pp. 77–86 (2006). [in German]
16. Shuishui, L., Yuanxun, F., Tingchun, B.: Introduction for new hoisting mechanism of a crane. *Mach. Des. Manuf.* **5**, 275–276 (2012)



Improvement of the Angular Arrangement of Distribution System Windows When Designing Planetary Hydraulic Machines

Angela Voloshina¹(✉) , Anatolii Panchenko¹ ,
Oleg Boltiansky¹ , Andrii Zasiadko² ,
and Valentyna Verkholantseva¹ 

¹ Dmytro Motornyi Tavria State Agrotechnological University,
18, B. Khmelnytsky Avenue, Melitopol 72310, Ukraine

² Berdyansk College of the Tavria State Agrotechnological University,
23, Eastern Avenue, 71108 Berdyansk, Ukraine

Abstract. The main characteristic of a distribution system is its throughput (flow rate of the working fluid), which is determined by the flow area of this system. An increase in the flow area of the distribution system can be achieved by using the unloading windows of the movable distributor as workers. It was found that the additional use of the unloading windows leads to both an increase in the throughput of the distribution system and a change in the pulsation of the working fluid flow. A diagram of the movement of fluid to the working chambers of the hydraulic motor has been developed, which makes it possible to determine the angular position of the windows of the movable distributor, depending on its kinematic diagram. The maximum number of additional working windows has been substantiated. Practical recommendations have been developed for the angular displacement of the windows of the movable distributor and the determination of the throughput of the distribution system, depending on its kinematic diagram and the number of additional working windows. The developed practical recommendations make it possible to design the distribution systems of planetary hydraulic machines with given output characteristics.

Keywords: Mobile distributor · Stationary distributor · Throughput · Rotating field · Additional channels · Working fluid

1 Introduction

It is known [1] that one of the main units that determine the stability of the planetary hydraulic machine is its distribution system necessary for the formation of a rotating hydraulic field. Such a distribution system usually consists of a movable valve (Fig. 1a), a shaft (Fig. 1b), and a fixed valve (Fig. 1c).

On the end surface of the movable distributor (Fig. 1a), there are working 1 and 2 unloading windows. To increase the throughput of the planetary hydraulic motor [1], unloading windows 2, using the radial channels 3 of the movable distributor, and the commutating grooves 4 on the hydraulic motor shaft are used as additional working

windows (Fig. 1). On the end surface of the stationary distributor (Fig. 1c), there are pressure 5 and drainage windows 6. The contacting of the end surfaces of the movable and stationary distributors forms a zone of formation of a rotating hydraulic field.

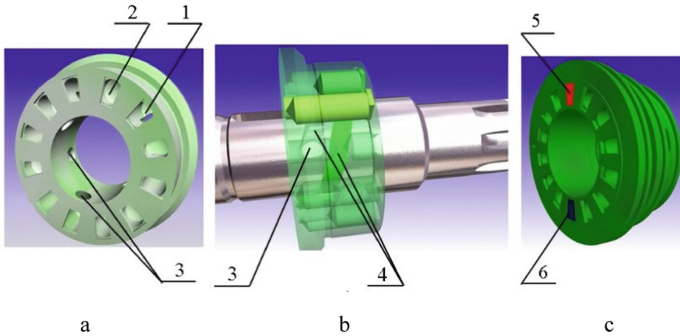


Fig. 1. Elements of the end distribution system: a – movable distributor; b – a hydraulic motor shaft with a movable distributor; c – stationary distributor; 1 – working windows of the movable distributor; 2 – discharge windows of the movable distributor; 3 – radial channels of the movable distributor; 4 – commutation grooves on the shaft of the hydraulic motor; 5 – discharge windows of the stationary distributor; 6 – drain windows of the stationary distributor.

The working fluid enters the annular groove 6 of the stationary distributor 5 (Fig. 2a) and then along the radial 7 and axial 8 channels to the pressure windows 9. From pressure windows 9, the working fluid enters the additional working windows 4.

Then, through the radial channel 3 is connected to the switching groove 12, made on the shaft of the hydraulic motor 11, and enters the working chamber 1 located diametrically opposite.

When the working chambers move relative to the movable distributor 2, the discharge cavity (Fig. 2a) is replaced by the drain cavity (Fig. 2b), and the working fluid is displaced from the working chamber 1. Further, the liquid through channel 3 of the movable distributor 2 enters through the switching groove 12, made on the shaft 11, to the drain window 10 of the fixed distributor 5. Through the end 8 and radial 7 channels of the fixed distributor 5, the working fluid enters the annular groove 6 and enters the drain.

Thus, the use of unloading windows as additional working windows allows increasing the throughput of the distribution system, and their definite angular arrangement makes it possible to ensure the constancy of the output characteristics of the hydraulic motor. Therefore, improving the output characteristics of a planetary hydraulic motor by developing practical recommendations for the angular position of working windows in the design of its distribution systems is an urgent problem.

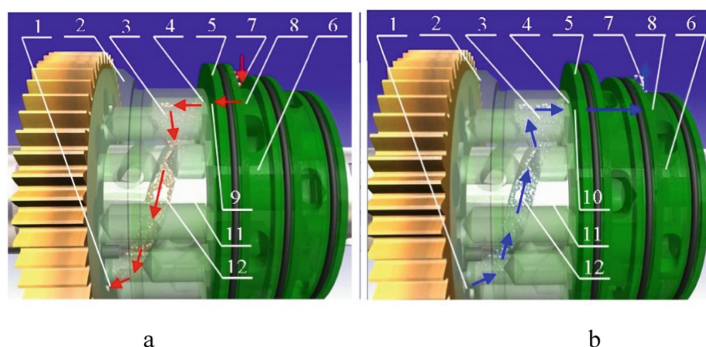


Fig. 2. The movement of the working fluid through additional working windows and the switching groove: a – pressure; b – drain; 1 – working chamber of the hydraulic motor; 2 – movable distributor; 3 – a radial channel of the movable distributor; 4 are additional working window; 5 – stationary distributor; 6 – annular grooves of the stationary distributor; 7 – radial channels; 8 – axial channels; 9 – pressure window; 10 – drain window; 11 – hydraulic motor shaft; 12 – commutation groove.

2 Literature Review

The solution of the Navier-Stokes equations using the SST-model of turbulence [2, 3] is proposed. The RANS approach is applied, which makes it possible to determine the main characteristics of the vortex flow [4, 5]. The effect of Bingham fluids on the energy characteristics of vortex-chamber pumps [6], as well as the impact of the compressibility of the working fluid on the efficiency of hydraulic circuits during transient processes [7, 8], models for modeling aeration of liquid, are described [9]. The study of the accuracy [10, 11] and dynamic processes [12] of the positioning of spatial drive systems, as well as changes in the dynamics of the output characteristics of a mechatronic system with a planetary hydraulic motor [13]. The movement of the working fluid to the working chambers of the hydraulic motor was not considered.

Analysis of literature sources showed that very little research is being published in the calculation, design, and manufacture of orbital and planetary hydraulic machines [14]. A model has been developed that describes the tribological changes in the geometry of the working surfaces of the rotors [15] of an orbital hydraulic machine [16], theoretical studies of the influence of the geometric parameters of the flow parts of a gerotor pumps [17] on their output characteristics have been carried out. The forces and moments that affect the gear pair of a gerotor pump [18, 19] models are proposed that consider the compression state of the working fluid [20], as well as the design of hypocycloidal surfaces [21] and rotors [22] of pumps of this type, are considered. The analysis of the flow rate of the centrifugal machine [23, 24] and the design features of the gerotor pump, affecting the filling ability [25], and the mathematical expressions for assessing the flow rate of the working fluid in the gerotor hydraulic machines [26], the reasons for cavitation phenomena [27, 28] in the distribution have been substantiated [29]. The influence of the design features of the distribution systems of planetary hydraulic machines on their output characteristics has not been studied.

Numerical modeling [30, 31] and experimental analysis [32] of turbine pump instability have been carried out. A three-dimensional transitional model of CFD is described [33], and hydrodynamic calculations using CFD packages [34, 35], particularly for hydraulic machines [36], are considered. Research has been carried out to predict changes in the output parameters of planetary hydraulic motors under operating conditions [37]. Experimental studies of the influence of design features distributors [38, 39] on the functional parameters of a planetary hydraulic motor have been carried out. Despite the proposed novel approaches in engineering design [40–42], there are still no practical guidelines for designing a planetary hydraulic motor exactly.

Thus, the development of practical recommendations for the angular displacement of the windows of the distribution systems of planetary hydraulic machines is an urgent problem, the solution of which improves the output characteristics of the planetary hydraulic motor at the design stage.

3 Research Methodology

To improve the output characteristics of a planetary hydraulic motor, by developing practical recommendations for the angular displacement of the working windows of its distribution systems at the design stage, it is necessary:

- develop schemes for the movement of fluid to the working chambers of the hydraulic motor;
- justify the maximum number of additional working windows;
- to develop practical recommendations for the angular displacement of the windows of the movable distributor;
- develop practical recommendations for determining the throughput of the distribution system.

To determine the angular arrangement of the windows of the movable distributor, schemes of fluid movement (Fig. 3) to the working chambers of the hydraulic motor have been developed, depending on the kinematic scheme (for example, the 7/6 kinematic scheme when using three additional unloading windows) [1].

The angle of arrangement of the working windows of the movable distributor during their displacement is determined from the expressions:

- for kinematic schemes 7/6 and 11/10

$$\alpha'_i = \alpha_i \pm (\gamma_{mean} - \gamma_{lag}), \quad (1)$$

- for kinematic schemes 5/4, 9/8 and 13/12

$$\alpha'_i = \alpha_i \pm (\gamma_{outrun} - \gamma_{mean}), \quad (2)$$

where α_i is the angle of the “current” window of the movable distributor (odd are working windows, even are unloading windows); γ_{mean} is the mean value of the overlap angle, $\gamma_{mean} = (\sum \gamma_{outrun} - \sum \gamma_{lag}) / Z_1$; γ_{outrun} are overlap angle when leading ($\gamma_{outrun} > 0$), $\gamma_{outrun} = \alpha_{closed} - \alpha_{open}$; γ_{lag} are the angle of overlapping windows when lagging ($\gamma_{lag} < 0$), $\gamma_{lag} = \alpha_{closed} - \alpha_{open} < 0$; α_{open} is the opening range of the movable distributor windows, $\alpha_{open} = \beta_i - \alpha_i - \pi / Z_2$; α_{closed} is range of closing windows of the movable distributor, $\alpha_{closed} = \beta_i - \alpha_i + \pi / Z_2$; β_i is the angle of the “current” window of the fixed distributor (odd are pressure windows, even ones are drain); Z_1 and Z_2 is the number of windows of the movable and fixed distributor, respectively.

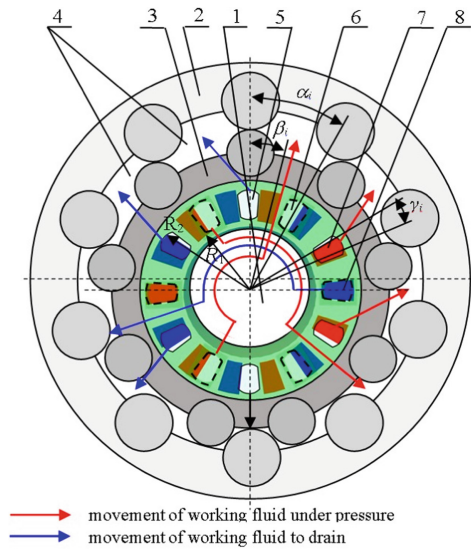


Fig. 3. The scheme of fluid movement to the working chambers of the hydraulic motor: 1 – hydraulic motor shaft; 2, 3 – outer and inner rotors, respectively; 4 – working chambers of the hydraulic motor; 5, 6 – working and unloading windows of the movable distributor, respectively; 7, 8 – windows for pressure and drain of the stationary distributor, respectively.

The throughput of the distribution system (flow area) is determined by the expression [1]:

$$A_i(t) = \sum_{i=1}^{Z_1} \gamma_i \cdot A_{ring}. \quad (3)$$

where γ_i is the angle limiting the overlap of the windows of the movable and fixed distributors, $\gamma_i = \pi/Z_2 - |\beta_i - \alpha_i(t)|$; A_{ring} is the area of the ring on which the distribution windows are located, determined by its inner R_1 and outer R_2 radii, $A_{ring} = (R_2^2 - R_1^2)/2$.

The number of additional working windows involved in the operation of the designed distribution system is determined by the number of commutation grooves (Fig. 4) located on the motor shaft and is limited by the height h of the movable distributor.

The number of commuting grooves is determined from the expression:

$$z = \frac{\pi \cdot D}{(b + b_1)} \cdot \sin \varphi, \tag{4}$$

where φ is the angle of inclination of the commuting groove, $\varphi = \arctg[2 \cdot h / (\pi \cdot D)]$, where h is the height of the movable distributor; D is the diameter of the hydraulic motor shaft; b is the width of the commuting groove; b_1 is the distance between the grooves.

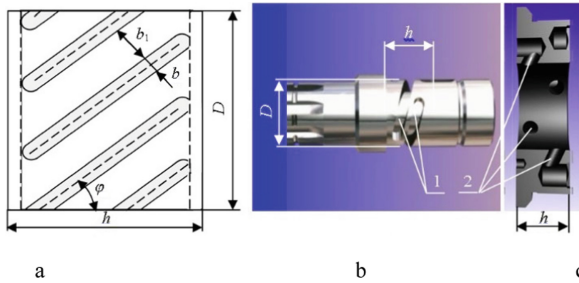


Fig. 4. Implementation of the use of additional working windows: a – design scheme for determining the geometric parameters of the commuting grooves; b – hydraulic motor shaft; c – movable distributor; 1 – commutation shaft grooves; 2 – additional channels of the movable distributor; h – the height of the movable distributor; D – the diameter of the hydraulic motor shaft; b – groove width; b_1 – the distance between grooves.

Practice shows that it is not recommended to place more than four commutation grooves on a given section of the shaft.

4 Results

The research results are developing practical recommendations for designing the distribution systems of planetary hydraulic machines with the given output characteristics.

Table 1. The angular displacement of the windows of the movable distributor, depending on the kinematic diagram and the number of additional working windows.

Distribution window numbers	Kinematic diagram of the distribution system															
	4/3	5/4	6/5	7/6		8/7	9/8		10/9	11/10		12/11	13/12			
	Number of additional working windows															
	2	2	2	2	3	4	2	2	4	2	2	4	2	2	3	4
№ 1			5°08'				-1°24'	-0°30'		2°			1°04'	-0°32'		
№ 2	-6°					0°50'										
№ 3	-12°	-6°	10°17'	-2°08'	2°51'	1°40'	-2°48'	-1°30'	-1°40'	1°20'	-0°36'	-0°58'	0°38'	-0°52'	-0°30'	-0°36'
№ 4		-3°	8°34'		1°25'		-3°30'		-0°50'			-0°14'				
№ 5	12°		6°51'	2°08'		-0°50'	-4°18'	1°30'		3°40'	-1°06'	0°30'	2°32'	0°52'	0°54'	0°36'
№ 6	6°					-1°40'				3°20'			2°22'			
№ 7		-6°	3°26'		2°51'		-0°42'	0°30'	-1°40'	3°	1°06'	-0°30'	2°06'	0°32'	0°24'	
№ 8		-3°	1°43'		1°25'	0°50'			-0°50'						0°12'	
№ 9				-2°08'		1°40'	-2°06'	-0°30'		2°20'	0°36'	-1°28'	1°46'	0°20'		-0°36'
№10												-0°44'				
№11				2°08'	2°51'	-0°50'	2°30'	-1°30'	-1°40'	1°40'			1°20'	-0°20'	-0°30'	-1°12'
№12					1°25'	-1°40'	0°42'		-0°50'							-0°36'
№13								1°30'		1°	-0°36'	-0°58'	0°48'	-0°32'	0°54'	
№14										0°20'		-0°14'				
№15								0°30'	-1°40'		-1°06'	0°30'	0°22'	-0°52'	0°24'	-0°36'
№16									-0°50'				0°12'		0°12'	
№17										2°40'	1°06'	-0°30'		0°52'		0°36'
№18																
№19											0°36'	-1°28'	1°56'	0°32'	-0°30'	
№20												-0°44'				
№21													1°30'	0°20'	0°54'	-0°36'
№22																
№23														-0°20'	0°24'	-1°12'
№24															0°12'	-0°36'

«+» – offset windows clockwise;

«-» – offset windows counterclockwise.

The angular displacement of the windows of the movable distributor (Table 1) is selected depending on the kinematic diagram of the distribution system and the number of additional working windows. According to expression (3), to design a distribution system with a given capacity (flow area), it is necessary to know the total overlap angle γ_i (Table 2) and the area of the A_{ring} ring determined by its geometric parameters.

The developed practical recommendations make it possible to design the distribution systems of planetary hydraulic machines with given output characteristics.

Table 2. Changes in the total angle of overlap γ_i depending on the kinematic diagram and the number of additional working windows.

Kinematic diagram	Number of additional working windows	Distribution system parameters							
		Before shifting windows				After shifting windows			
		Total overlap angle		Amplitude of area fluctuations, %	Amplitude of area fluctuations, %	Total overlap angle		Amplitude of area fluctuations, %	Amplitude of area fluctuations, %
		γ_{max} , rad	γ_{min} , rad			γ_{max} , rad	γ_{min} , rad		
4/3	0	0,39	0,26	44	88	No offset required			
	2	0,77	0,26	99	198	0,54	0,47	13,7	27,4
5/4	0	0,313	0,313	0	0	No offset required			
	2	0,63	0,31	68	136	0,52	0,42	21,3	42,6
	4	0,63	0,63	0	0	No offset required			
6/5	0	0,37	0,31	18,2	36,4	No offset required			
	2	0,63	0,31	68	136	0,49	0,45	8,5	17,02
7/6	0	0,37	0,3	20,9	41,8	No offset required			
	2	0,52	0,37	33,6	67,2	0,45	0,45	0	0
	3	0,52	0,45	15,5	31	0,52	0,49	6,1	12,2
	4	0,67	0,45	39,3	78,6	0,58	0,54	7,1	14,2
8/7	0	0,37	0,34	8,8	17,6	No offset required			
	2	0,56	0,34	48,8	97,6	0,47	0,42	11,1	22,2
9/8	0	0,35	0,35	0	0	No offset required			
	2	0,51	0,36	34	68	0,45	0,43	4,5	9,1
	4	0,52	0,51	1,9	3,8	0,52	0,52	0	0
10/9	0	0,37	0,35	5,5	11	No offset required			
	2	0,52	0,35	39,5	79	0,44	0,42	4,7	9,4
11/10	0	0,37	0,34	8,3	16,6	No offset required			
	2	0,49	0,37	27,9	55,8	0,43	0,43	0	0
	4	0,54	0,4	28	56	0,51	0,49	4	8
12/11	0	0,37	0,36	2,8	5,6	No offset required			
	2	0,5	0,36	32,5	65	0,43	0,42	2,3	4,6
13/12	0	0,36	0,36	0	0	No offset required			
	2	0,48	0,37	26,2	52,4	0,44	0,41	7,1	14,2
	3	0,48	0,44	8,9	17,8	0,46	0,45	2,2	4,4
	4	0,52	0,44	16,6	33,2	0,48	0,48	0	0

5 Conclusions

The developed scheme of fluid movement in the working chambers of the hydraulic motor makes it possible to determine the angular position of the windows of the movable distributor for different kinematic schemes. The maximum possible number of additional working windows has been substantiated.

Practical recommendations have been developed for determining the angular position of the movable distributor windows and the throughput capacity of its distribution system.

The developed recommendations make it possible to design distribution systems of planetary (orbital) hydraulic machines with specified output characteristics.

References

1. Kiurchev, S., Luzan, P., Zasiadko, A., Radionov, H., Boltianska, N.: Influence of the flow area of distribution systems on changing the operating parameters of planetary hydraulic motors. *IOP Conf. Ser. Mater. Sci. Eng.* **1021**, 012037 (2021). <https://doi.org/10.1088/1757-899X/1021/1/012037>
2. Rogovyi, A., Khovanskyi, S., Grechka, I., Pitel, J.: The wall erosion in a vortex chamber supercharger due to pumping abrasive mediums. In: Ivanov, V., et al. (eds.) *DSMIE 2019. LNME*, pp. 682–691. Springer, Cham (2020). https://doi.org/10.1007/978-3-030-22365-6_68
3. Chernetskaya-Beletskaya, N., Rogovyi, A., Shvornikova, A., Baranov, I., et al.: Study on the coal-water fuel pipeline transportation taking into account the granulometric composition parameters. *Int. J. Eng. Technol.* **7**(4.3), 240–245 (2018)
4. Rogovyi, A., Khovanskyi, S., Hrechka, I., Gaydamaka, A.: Studies of the swirling submerged flow through a confuser. In: Ivanov, V., Pavlenko, I., Liaposhchenko, O., Machado, J., Edl, M. (eds.) *DSMIE 2020. LNME*, pp. 85–94. Springer, Cham (2020). https://doi.org/10.1007/978-3-030-50491-5_9
5. Vaneev, S.M., et al.: Investigation of a turbogenerator based on the vortex expansion machine with a peripheral side channel. *J. Eng. Sci.* **8**(1), F11–F18 (2021). [https://doi.org/10.21272/jes.2021.8\(1\).f2](https://doi.org/10.21272/jes.2021.8(1).f2)
6. Rogovyi, A., Korohodskiy, V., Medvediev, Y.: Influence of Bingham fluid viscosity on energy performances of a vortex chamber pump. *Energy* **218**, 119432 (2021). <https://doi.org/10.1016/j.energy.2020.119432>
7. Van de Ven, J.: On fluid compressibility in switch-mode hydraulic circuits—part I: modeling and analysis. *J. Dyn. Syst. Meas. Control* **135**(2), 021013–021010–13 (2012). <https://doi.org/10.1115/1.4023062>
8. Van de Ven, J.D.: On Fluid compressibility in switch-mode hydraulic circuits. – part II: modeling and analysis. *J. Dyn. Syst. Meas. Control* **135**(2), 021014–021014-7 (2012). <https://doi.org/10.1115/1.4023063>
9. Rundo, M.: Models for flow rate simulation in gear pumps: a review. *Energies* **9**(10), 1261 (2017). <https://doi.org/10.3390/en10091261>
10. Strutynskiy, S.: Defining the dynamic accuracy of positioning of spatial drive systems through consistent analysis of processes of different range of performance. *Naukovyi Visnyk NHU* **3**, 64–73 (2018). <https://doi.org/10.29202/nvngu/2018-3/13>
11. Karpus, V.E., Ivanov, V.A.: Locating accuracy of shafts in V-blocks. *Russ. Eng. Res.* **32**(2), 144–150 (2012). <https://doi.org/10.3103/S1068798X1202013X>
12. Strutynskiy, S., Nochnichenko, I.: Design of parallel link mobile robot manipulator mechanisms based on function-oriented element base. *East-Eur. J. Enterp. Technol.* **4** (7100), 54–64 (2018). <https://doi.org/10.15587/1729-4061.2019.174613>
13. Voloshina, A., Panchenko, A., Titova, O., Panchenko, I.: Changes in the dynamics of the output characteristics of mechatronic systems with planetary hydraulic motors. *J. Phys: Conf. Ser.* **1741**, 012045 (2021). <https://doi.org/10.1088/1742-6596/1741/1/012045>
14. Gamez-Montero, P., Codina, E., Castilla, R.: A review of gerotor technology in hydraulic machines. *Energies* **12**, 2423 (2019). <https://doi.org/10.3390/en12122423>
15. Pavlenko, I., Ivanov, V., Kuric, I., Gusak, O., Liaposhchenko, O.: Ensuring vibration reliability of turbopump units using artificial neural networks. In: Trojanowska, J., Ciszak, O., Machado, J.M., Pavlenko, I. (eds.) *MANUFACTURING 2019. LNME*, pp. 165–175. Springer, Cham (2019). https://doi.org/10.1007/978-3-030-18715-6_14




16. Choi, T., Kim, M., Lee, G., et al.: Design of rotor for internal gear pump using cycloid and circular-arc curves. *J. Mech. Des.* **134**(1), 011005–011012 (2012). <https://doi.org/10.1115/1.4004423>
17. Chiu-Fan, H.: Flow characteristics of gerotor pumps with novel variable clearance designs. *J. Fluids Eng.* **137**(4), FE-14–1137 (2015). <https://doi.org/10.1115/1.4029274>
18. Ivanović, L., Blagojević, M., Devedžić, G.: Assoul analytical and numerical analysis of load gerotor pumps. *Sci. Tech. Rev.* **1**(60), 30–38 (2010)
19. Ivanovic, L., Miric, N., Devedzic, G., Ćuković, S.: Analysis of forces and moments in gerotor pumps. *J. Mech. Eng. Sci.* **10**(224), 2257–2269 (2010). <https://doi.org/10.1243/09544062JMES2041>
20. Chang, Y., Kim, J., Jeon, C., Chul, K., Jung, S.: Development of an integrated system for the automated design of a gerotor oil pump. *J. Mech. Des.* **129**(10), 1099–1105 (2006). <https://doi.org/10.1115/1.2757629>
21. Stryczek, J., Bednarczyk, S., Biernacki, K.: Strength analysis of the polyoxymethylene cycloidal gears of the gerotor pump. *Arch. Civil Mech. Eng.* **14**(4), 647–660 (2014). <https://doi.org/10.1016/j.acme.2013.12.005>
22. Stryczek, J., Bednarczyk, S., Biernacki, K.: Gerotor pump with POM gears: design, production technology, research. *Arch. Civil Mech. Eng.* **14**(3), 391–397 (2013). <https://doi.org/10.1016/j.acme.2013.12.008>
23. Pavlenko, I.: Static and dynamic analysis of the closing rotor balancing device of the multistage centrifugal pump. *Appl. Mech. Mater.* **630**, 248–254 (2014). <https://doi.org/10.4028/www.scientific.net/AMM.630.248>
24. González, J., Oro, J.M.F., Argüelles-Díaz, K.M.: Flow analysis for a double suction centrifugal machine in the pump and turbine operation modes. *Int. J. Numer. Meth. Fluids* **2**(61), 220–236 (2009). <https://doi.org/10.1002/fld.1951>
25. Altare, G., Rundo, M.: Computational fluid dynamics analysis of gerotor lubricating pumps at high-speed: geometric features influencing the filling capability. *J. Fluids Eng.* **38**(11), FE-15–1757 (2016). <https://doi.org/10.1115/1.4033675>
26. Yang, D., Yan, J., Tong, S.: Flowrate formulation of deviation function based gerotor pumps. *J. Mech. Des.* **6**(132), 064503–064505 (2010). <https://doi.org/10.1115/1.4001595>
27. Fesenko, A., Yevsiukova, F., Basova, Y., Ivanova, M., Ivanov, V.: Prospects of using hydrodynamic cavitation for enhancement of efficiency of fluid working medium preparation technologies. *Periodica Polytechnica Mech. Eng.* **62**(4), 269–276 (2018). <https://doi.org/10.3311/PPme.11877>
28. Demianenko, M., Starynskyi, O., Vashyst, B., Pavlenko, I., Liaposhchenko, O., Ivanov, V.: Improvement of hydraulic characteristics for impellers using the finite volume analysis. In: Cagaňová, D., Hornáková, N., Pusca, A., Cunha, P.F. (eds.) *Advances in Industrial Internet of Things, Engineering and Management*. EICC, pp. 161–174. Springer, Cham (2021). https://doi.org/10.1007/978-3-030-69705-1_10
29. Velev, E.: Study cavitation gerotor motors, using computer simulation. In: *Renewable Energies and Innovative Technologies: XV International Scientific Conference*, pp. 64–66 (2016)
30. Yao, J., Shi, W., Wu, S., Zhang, D., Wang, H., Hu, Q.: Numerical calculation and experiment on pressure fluctuation in axial flow pump. *Trans. Chin. Soc. Agric. Mach.* **1**(44), 119–124 (2013). <https://doi.org/10.6041/j.issn.1000-1298.2013.S1.022>
31. Liu, C., Jin, Y., Zhou, J., Tang, F., Hao, C., Han, J.: Study of internal flow in cube-type bidirection passages of axial-flow pump system by numerical simulation and experiment. *J. Hydroelectric Eng.* **5**(30), 192–198 (2011)

32. Gentner, C., Sallaberger, M., Widmer, C., Braun, O., Staubli, T.: Numerical and experimental analysis of instability phenomena in pump turbines. *IOP Conf. Ser. Earth Environ. Sci.* **3**(15), 0320422 (2012). <https://doi.org/10.1088/1755-1315/15/3/032042>
33. Ding, H., Lu, J.X., Jiang, B.: A CFD model for orbital gerotor motor. *IOP Conf Ser. Earth Environ. Sci.* **6**(15), 062006 (2012). <https://doi.org/10.1088/1755-1315/15/6/062006>
34. Liaposhchenko, O., et al.: Improvement of parameters for the multi-functional oil-gas separator of 'heater-treater' type. In: 2019 IEEE 6th International Conference on Industrial Engineering and Applications (ICIEA), Tokyo, Japan, 2019, pp. 66–71 (2019). <https://doi.org/10.1109/IEA.2019.8715203>
35. Khovanskyi, S., Pavlenko, I., Pitel, J., Mizakova, J., Ochowiak, M., Grechka, I.: Solving the coupled aerodynamic and thermal problem for modeling the air distribution devices with perforated plates. *Energies* **12**(18), 3488 (2019). <https://doi.org/10.3390/en12183488>
36. Rezvaya, K., Krupa, E., Shudryk, A., Drankovskiy, V., Makarov, V.: Solving the hydrodynamical tasks using CFD programs, vol. 8559548, pp. 205–209 (2018). <https://doi.org/10.1109/IEPS.2018.8559548>
37. Voloshina, A., Panchenko, A., Titova, O., Milaeva, I., Pastushenko, A.: Prediction of changes in the output characteristics of the planetary hydraulic motor. In: Tonkonogyi, V., et al. (eds.) *InterPartner 2020. LNME*, pp. 744–754. Springer, Cham (2021). https://doi.org/10.1007/978-3-030-68014-5_72
38. Moloshnyi, O.M., Szulc, P., Sotnyk, M.I.: Influence of an inlet rotating axial device on the cavitation processes in a low specific speed centrifugal pump. *J. Eng. Sci.* **6**(1), E25–E32 (2019). [https://doi.org/10.21272/jes.2019.6\(1\).e5](https://doi.org/10.21272/jes.2019.6(1).e5)
39. Voloshina, A., Panchenko, A., Titova, O., Pashchenko, V., Zasiadko, A.: Experimental studies of a throughput of the distribution systems of planetary hydraulic motors. *IOP Conf. Ser. Mater. Sci. Eng.* **1021**, 012054 (2021). <https://doi.org/10.1088/1757-899X/1021/1/012054>
40. Ivanov, V., Pavlenko, I., Trojanowska, J., Zuban, Y., Samokhvalov, D., Bun, P.: Using the augmented reality for training engineering students. In: 4th International Conference of the Virtual and Augmented Reality in Education, VARE 2018, pp. 57–64 (2018)
41. Ivanov, V., Pavlenko, I., Liaposhchenko, O., Gusak, O., Pavlenko, V.: Determination of contact points between workpiece and fixture elements as a tool for augmented reality in fixture design. *Wirel. Netw.* **27**(3), 1657–1664 (2019). <https://doi.org/10.1007/s11276-019-02026-2>
42. Bun, P., Trojanowska, J., Ivanov, V., Pavlenko, I.: The use of virtual reality training application to increase the effectiveness of workshops in the field of lean manufacturing. In: 4th International Conference of the Virtual and Augmented Reality in Education, VARE 2018, pp. 65–71 (2018)

Manufacturing Technology



Packing 3D-Models of Products in Build Space of Additive Manufacturing Machine by Genetic Algorithm

Yaroslav Garashchenko¹(✉) , Jurii Vitiaziev¹ ,
and Igor Grimzin² 

¹ National Technical University “Kharkiv Polytechnic Institute”,
2, Kyrpychova Street, 61002 Kharkiv, Ukraine

² Research and Production Center “European Engineering Technologies”,
101, Velyka Panasivska Street, 61002 Kharkiv, Ukraine

Abstract. The study results of the possibilities of fulfilling the optimization task of placing (packing) 3D-models of products in build space using a genetic algorithm are presented. The proposed algorithm for the location of 3D models of products in build space allows to reduce the time of technological preparation and increase the productivity of the process and the efficiency of using the additive machine. The efficiency of use can be ensured by reducing the relative share of the unused volume of the layered build space, which is relevant for SLA, SLM, SLS, and other methods of additive technologies. A step-by-step determination of the free space for placing the next product is proposed, starting from the lower level of the machine platform. An increase in the efficiency of the proposed algorithm was provided by preliminary sorting of 3D models of products according to specified criteria. The rational values of the genetic algorithm parameters have been determined using the example of the placement of a group of industrial products with a rather complex design. Evaluation of the effectiveness of the proposed algorithm for placing 3D models was carried out based on a comparative analysis of the number of layers and the efficiency of filling the build space (relative volume of its use) for the manufacture of a group of 3D models of industrial products. The study was carried out using the developed system “Technological preparation of materialization of complex products by additive technologies”.

Keywords: Additive manufacturing · Technology planning · Triangulated model · Packing · Genetic algorithm

1 Introduction

One of the main tasks of technological preparation for the materialization of industrial products by additive manufacturing (AM) is the rational placement (packing) of the original or pre-oriented 3D models in build space [1]. The solution to this task instead significantly determines the efficiency of using the AM machine [2]. For many AM, it is essential to ensure the conditions for the rational use of the build space. For example,

SLA (laser stereolithography), SLM (selective laser melting), SLS (selective laser sintering), and others are among the most used in the industry [3].

The result of the placing procedure in build space is a 3D model, which includes a geometric description of the products and their position in the AM-machine coordinate system. In this case, several technological requirements must be satisfied. In practice, as a rule, such main requirements are considered to be the correct mutual placement and rational orientation of products, the minimum build height or production time, the quality of the surfaces obtained, and their geometric characteristics.

The purpose of the article is to substantiate the possibility of effectively performing the optimization task of the rational placement of 3D models of complex products in the build space of AM machines using a genetic algorithm.

2 Literature Review

Rational placement of 3D models of products refers to tasks that are called dense packing, 3D packing, loading, or a backpack problem [4]. Such tasks are characterized by a rather significant complexity of the solution due to the low efficiency of existing algorithms.

A distinctive feature of this task is the difficulty of determining the conditions for mutual non-intersection of 3D models of products [5]. The use of the voxel model eliminates this problem, but a drawback appears - it is an increase in the computation time.

The computational complexity of solving this problem in the general formulation makes it necessary to introduce several simplifications [6], but at the same time, it allows finding the optimal placement of 3D models with acceptable time spent on calculations. One of the most common simplifications is fixing the orientation of a 3D model in space or using a set of fixed orientations for each of them [7]. As a rule, before solving the problem of placing products in build space, their rational orientation is usually determined [1].

The task of placing products can be solved for a single-build or multi-build of single- or multi-machine [8].

In known works, the following approaches are used for the rational placement of a group of products in the build space of an additive technology machine: Deepest Bottom-Left technique [9]; Genetic Algorithms [10]; Machine Learning [11]; 2D-method [12]; Placement Heuristic [13]; Genetic Algorithm and Placement Heuristic [9]; Guided Local Search [13]; Mathematical Models [14]; Local Search [15]; Discretisation and Greedy Local Search [16]. In these works, Genetic Algorithms are recognized as the most suitable for solving the 3D packing problem.

As an optimization criterion for solving this problem, the following is mainly chosen: build time [10]; total cost, unprinted parts [14]; profit [17]; nesting rate [18]; a number of product parts during their decomposition [10]. Of the listed criteria, the most important for assessing the effectiveness of the AM-process are selected the build time (determined by the number of layers) and nesting rate.

The main problem is that the current works do not create a methodological basis for a comparative analysis of the effectiveness of algorithms for placing 3D models, taking

into account the geometric features of products. Consideration of the possibilities of the genetic algorithm for placing products of various designs will allow obtaining the necessary fundamental indicators for further studying the influence of the geometry of products on the possibility of increasing the efficiency of using the build space.

3 Research Methodology

The implementation of the optimization problem of placing 3D models of products was carried out within the framework of the system “Technological preparation of materialization of complex products by additive technologies”, developed at NTU “KhPI” Department of Integrated Technologies of Mechanical Engineering named after M. F. Semko. This system makes it possible to assess the design’s manufacturability and the effectiveness of solving the problems of technological preparation based on the statistical analysis of the studied features of the polygonal, voxel, and layered 3D model of products. A subsystem for the rational placement of products in build space has been developed (the screen form is shown in Fig. 1).

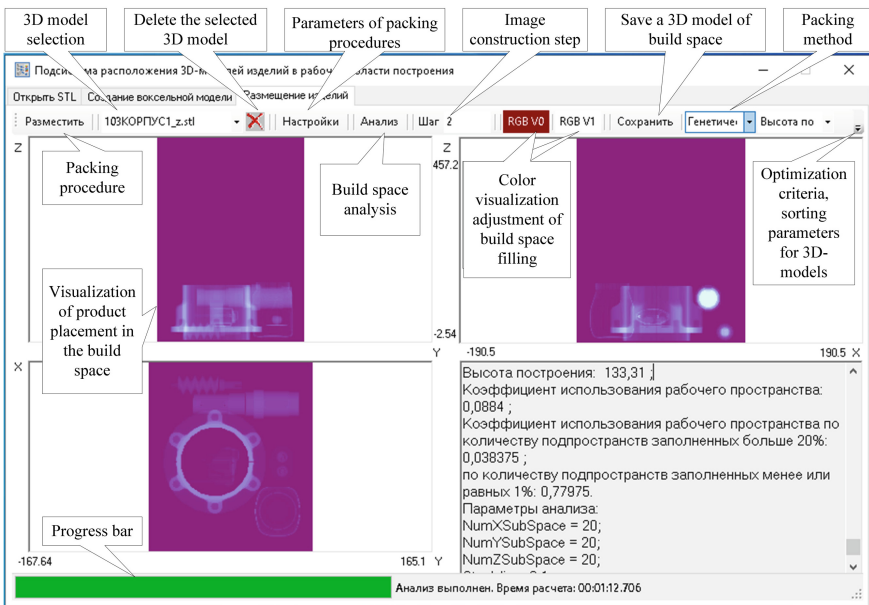


Fig. 1. The subsystem of parts packing in build space.

The developed subsystem provides the user with the following basic capabilities:

- checking the correctness of 3D-models placement in build space;
- creating a set of layers with 2D intersections based on a polygonal 3D model of a product composition (STL file of build space) according to a given building strategy (with a constant or variable step);

- visualization of the placed products behind the projections of build space;
- statistical analysis of product material distribution by subspaces;
- saving the build space with the placed 3D models in an STL file for practical use in CAM software.

The transition from the initial triangulation 3D model to a set of layers was carried out according to the procedure developed, considering the work [19], which implements strategies with a constant and variable building step.

The solution to the optimization problem of product placement is performed using the voxel model [20]. The voxel model consists of an ordered set of voxels, which are presented by volume elements with a given location in space (coordinates $x_{V(i)}$, $y_{V(i)}$, $z_{V(i)}$). Therefore, the voxel model is a set of elementary volumes $V = \{v[0], v[1], \dots, v[n_v]\} = \{v[i]\}$. Unlike triangulated models, voxel models offer a simpler and more efficient way of data processing to packing products in build space.

The creation of a voxel 3D model of a product based on a triangulated model was implemented according to known approaches [21].

In the developed subsystem, the following modes for placing 3D models of packing in the build space of the AM machine are provided: manual; random search (Monte Carlo method); using genetic algorithm.

The proposed placement procedure using a genetic algorithm was developed based on works [8]. After considering existing approaches [6, 10], it is proposed to place 3D models of products in the build space with a step-by-step check of free space.

When placing 3D models in build space, their orientation is fixed [1]. Therefore, the placement task was performed for 3D models with given angles of rotation, determined when solving the problem of the rational orientation of products.

Pre-sorting of 3D models (shown in Fig. 2) was performed with an increase or decrease in the value of the selected criterion according to the following characteristics: model volume; build space utilization coefficient; minimum, maximum overall dimensions or their arithmetic mean.

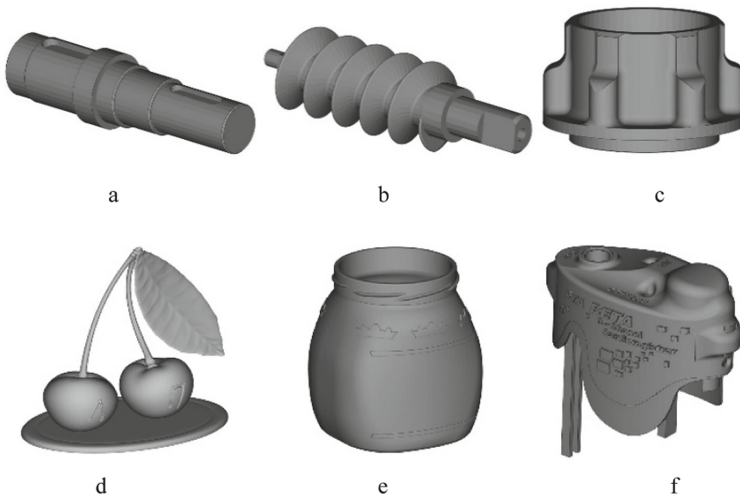


Fig. 2. Test 3D models: a – shaft; b – auger; c – case; d – souvenir; e – container; f – lid.

The following function is taken as an optimization criterion when forming a group of placed 3D models in the build space:

$$f(x) = f(M(p)) \cdot K_f - F_p - F_{cp},$$

where $f(M(P))$ - objective function to determine the building height H_B or relative build space-filling with 3D models K_V ; K_f - the gain coefficient of the objective function allows eliminating the problem of correct placement in build space; F_p - penalty function; F_{cp} - component, which is determined by the sum of the values of genes in the genetic algorithm.

Penalty function introduced to ensure correct placement of 3D models and is determined by the number of “conflicting” voxels, that is, having incorrect placement (the distance between voxels of two checked 3D models is less than the minimum permissible distance):

$$F_p = \sum_{i=1, j=1}^{n \cdot m} n_v, \quad n_v = \begin{cases} 1, & \text{if } (v_i \cdot x - v_j \cdot x)^2 + (v_i \cdot y - v_j \cdot y)^2 + (v_i \cdot z - v_j \cdot z)^2 \leq \Delta_{M \min}^2 \\ 0, & \text{otherwise} \end{cases},$$

where n, m – the number of voxels of two checked 3D models; n_v – number of “conflicting” voxels; $\Delta_{M \min} = 5 \text{ mm}$ – the minimum permissible distance between models.

The F_{cp} function component allows eliminating the problem of the absence of an optimum in the function $f(M(P))$ or the presence of flat areas on the response surface, with which the genetic algorithm “does not work well”. The introduction of this component made it possible to significantly reduce the computation time (by a factor of $5 \div 20$) and to eliminate, in some cases, the impossibility of determining the optimal values. This problem is especially evident for groups of 3D models that need to be obtained in one machine load, with significant differences in overall dimensions. F_{cp} is defined as follows:

$$F_{cp} = \sum_{g=1}^G \text{value}[g],$$

where G – number of genes, $G = 3$; $\text{value}[g]$ – an array of random variables generated during the execution of the genetic algorithm, $\text{value}[g] \in [0, 1]$.

The study of the possibilities of the developed algorithm for placing 3D-models of products was carried out by comparative analysis by the number of layers N_L and the coefficient of the relative use of the build space volume K_V .

4 Results

Checking and researching the efficiency of the developed algorithm was carried out using the example of placing a small group of products. In the beginning, a group of three 3D product models was used (Fig. 2a–c):

- shaft (dimensions $60 \times 216 \times 60 \text{ mm}^3$, the number of faces $N_{tr} = 147\,610$ pcs. The number of voxels $N_{vox} = 47\,172$ pcs. with a voxel size of 2 mm in all coordinate axes);
- auger ($40 \times 144 \times 40 \text{ mm}^3$, $N_{tr} = 10\,366$ pcs., $N_{vox} = 7\,978$ pcs.);
- case ($210 \times 210 \times 125 \text{ mm}^3$, $N_{tr} = 3\,010$ pcs., $N_{vox} = 115\,029$ pcs.).

The algorithm approbation was tested for three variants of preliminary sorting of 3D models. The dimensions of the build space were set using the example of the Vanguard Si2 SLS machine (made by 3D Systems). The number of building layers considered evaluation of manufacturing productivity, and the relative use of build space considered the machine's efficiency. The cutting strategy with a constant building step $h_i = 0.1$ mm, and with a variable step was carried out with the following characteristics: step $h_i \in [0.1; 0.3]$ mm; the maximum permissible deviation from the correct shape is $\Delta S_{max} = 0.1$ mm (description of the cutting method in [25]). Parameters of the genetic algorithm: the probability of crossing $p_c = 80\%$, probability of mutation $p_m = 0.5 \div 3\%$, population size $N_p = 20\text{--}200$ people, limiting the number of generations $N_g = 50 \div 100$, genome size $n_{genom} = 3$, optimization criterion of gain coefficient $K_{op} = \{0.6; 1\}$.

Statistical characteristics (minimum, maximum, and mean value) of the studied features for the obtained set of options for placing 3D-models in build space are given in Table 1.

Table 1. Statistical characteristics of the features under study, obtained by analyzing options for placing 3D models in build space.

Pre-sorting type of 3D models	Statistical characteristics	Number of build layers		Build space utilization factor, K_V
		Constant step	Variable step	
Without sorting	$\{x\}_{min}$,	1250	900	0.054
	$\{x\}_{max}$,	1909	1172	0.086
	\bar{x}	1612	1079	0.067
Sort ascending of volume	$\{x\}_{min}$,	1576	1133	0.036
	$\{x\}_{max}$,	2990	1534	0.066
	\bar{x}	2069	1278	0.054
Sort descending of volume	$\{x\}_{min}$,	1250	855	0.058
	$\{x\}_{max}$,	1658	1074	0.082
	\bar{x}	1367	951	0.074

Analysis of the studied features, given in Table 1, shows the clear advantage of pre-sorting 3D models with volume reduction.

If the population size is set to $N_p = 50$, the lack of sorting is leveled, and sufficiently rational placement options are obtained, all three 3D models are placed directly on the platform (in the minimum permissible position along the Z coordinate axis). The optimal value of the limiting value of generations is $N_g = 50$. According to placement options, an increase in value Ng does not give a noticeable effect (there are insignificant changes in the studied features). In this case, the calculation time increases.

Increasing the mutation probability to $p_m = 2\%$ increases the likelihood of getting more rational options for placing 3D models in build space.

To assess the capabilities of this placement algorithm, an additional build space was created for the machine for the manufacture of 6 items during preliminary sorting of 3D models with a decrease in their volume. The following are added to the three 3D models presented above (Fig. 2d–f):

- souvenir ($73 \times 51,3 \times 70,1 \text{ mm}^3$, $N_{tr} = 8\,090$ pcs., $N_{vox} = 19\,847$ pcs.);
- container ($102 \times 93,6 \times 125,5 \text{ mm}^3$, $N_{tr} = 34\,424$ pcs., $N_{vox} = 68\,613$ pcs.);
- lid ($83,9 \times 101,3 \times 43,2 \text{ mm}^3$, $N_{tr} = 15\,352$ pcs., $N_{vox} = 33\,998$ pcs.).

The studied features, obtained for several calculations with one variant of the parameters, demonstrate the probabilistic nature of their description. Statistical analysis of the values of the studied features for the set of the obtained options for placing 3D models in build space is presented in the form of histograms in Fig. 3.

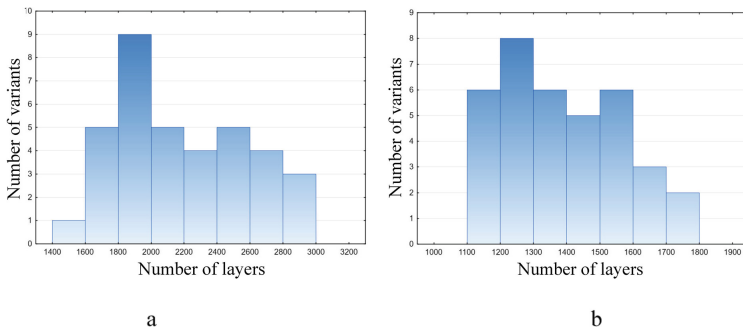


Fig. 3. Distribution of the number of building layers histograms: a – constant build step, b – variable build step.

The studied features (grouped by the genetic algorithm parameters) are presented in the form of histograms in Fig. 4. Some obvious conclusions can be drawn from the histograms (Fig. 4).

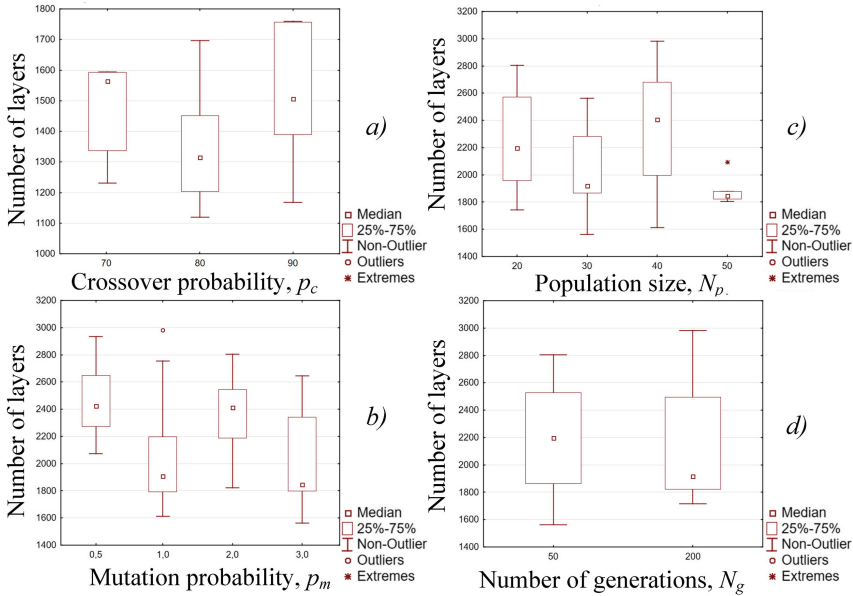


Fig. 4. Comparative analysis of the studied features grouped by the genetic algorithm parameters for the variable build step.

There is a clear improvement in the studied features with an increase in the population size N_p and a decrease in the probability of mutation p_m .

In some cases, the probability of crossing was corrected in the following range $p_c = 70\text{--}90\%$, which ensured obtaining the correct placement.

Based on the results obtained, rational parameters of the proposed placement algorithm are revealed. A small value of the p_m mutation probability leads to a large number of unsuccessful placement options, that is, those that do not ensure the correct placement of 3D models. This is primarily a serious problem with a small population of N_p and a large number of generation N_g . The value $N_g = 50$ is considered rational.

An increase in the population size N_p leads to a significant increase in the computation time, while the expected improvement of the studied features is not demonstrated. The number of generations N_g has an insignificant effect on the resulting features but allows for greater efficiency of the genetic algorithm.

Statistical analysis to identify the optimal value of the crossover probability p_c is shown in Fig. 4a. Of the three considered values, $p_c = 80\%$ provides the smallest height for building a group of products. The analysis by the values of the mutation probability p_m is shown in Fig. 4b. The best values are $p_m = \{1, 3\} \%$. An analysis by population size N_p is shown in Fig. 4c. An increase in the population size makes it possible to increase the efficiency of the genetic algorithm but also significantly increase the time spent on calculations. Therefore, for small groups of products, the rational value $N_p = \{30, 40, 50\}$. For a group of products with complex surface geometry, more than 5 pcs. you should set $N_p = 20$. Analysis by the last parameter - the number of generations N_g is shown in Fig. 4d. Naturally, an increase in the number of

generations N_g allows you to get better results for solving the problem, but the downside is a significant increase in the consumption of time resources. After considering the insignificant change in the studied features, it is necessary to set $N_g = 50$ for large groups of products predominantly (more than 5 pcs). Moreover, perhaps $N_g \geq 200$ is suitable for small groups or the absence of time constraints for technological preparation.

Large values of the coefficient $K_f \in (0; 1]$ allows to obtain the best values of the studied features, but at the same time, the probability of obtaining incorrect placement of 3D models significantly increases. In obtaining a variant with incorrect placement of models, to minimize the cost of time resources, it is not recommended to recalculate but use the manual mode to move or rotate one of the 3D models that fell into the conflict group. At each step of changing the position or orientation of the selected 3D model, the correctness of its placement is checked.

As a result of the study, the following recommendations were obtained regarding the parameters of the genetic algorithm for small groups of complex products:

- crossing probability, $p_c = 80\%$;
- mutation probability, $p_m = 1 \div 3\%$;
- population size, $N_p = 20 \div 50$ ($N_p = 30$ is preferred);
- the number of generations, $N_g = 50$.

Approbation of the algorithm using the example of placing a small group of 3D models of complex products showed some improvement in the features under study (in some cases, it was possible to reduce the number of build layers by $4 \div 6.3\%$) with insignificantly high costs of time compared to the Monte Carlo method (the study results are presented in [23]).

5 Conclusions

Studying the possibilities of the genetic algorithm for efficiently solving the problem of placing a small group of 3D models of products in build space showed an improvement in the studied features with an insignificantly large amount of time compared to the Monte Carlo method.

Based on the analysis of the studied features of the placed 3D models in build space, rational values of the genetic algorithm parameters were revealed. It was revealed that a small value of the mutation probability leads to a large number of unsuccessful placement options, that is, to those that do not provide the correct placement of 3D models. This is primarily a serious problem with a small population and a large number of generations. An increase in population size significantly increases the calculation time, but the expected improvement in indicators is usually not demonstrated. Also, the number of generations makes it possible to influence the efficiency of the genetic algorithm slightly.

The obtained results allow us to formulate the basis for further consideration of placing a large group of complex products in build space using a genetic algorithm to expand the possibilities of technological preparation of additive manufacturing.


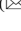

References

1. Zhang, Y., Bernard, A.: AM feature and knowledge based process planning for additive manufacturing in multiple parts production context. In: Proceedings of 25th Annual International Solid Freeform Fabrication Symposium, pp. 1259–1276 (2014)
2. Araújo, L.J.P., Özcan, E., Atkin, J.A.D., Baumann, M.: Analysis of irregular three-dimensional packing problems in additive manufacturing: a new taxonomy and dataset. *Int. J. Prod. Res.* 1–15 (2018)
3. Wohlers Report 2016: 3D Printing and additive manufacturing state of the industry. Annual worldwide progress report. <https://wohlersassociates.com>. Accessed 19 Feb 2021
4. Psiola, V.V.: Approximate solution of a 3-dimensional packaging problem based on heuristics. *Intel. Syst.* **1**, 83–100 (2011)
5. Bezdek, K.: *Classical Topics in Discrete Geometry*. Springer, New York (2010)
6. Stoyan, Y., Gil, N., Scheithauer, G.: Packing of convex polytopes into a parallelepiped. *Optimization* **54**(2), 215–235 (2005)
7. Verkhoturov, M.A., Verkhoturova, G.N., Yagudin, R.R.: On a solution to the problem of dense packing of convex polyhedrons based on the hodograph of the dense placement function. *Inf. Syst. Technol. Orel.* **4**, 31–39 (2012)
8. Oh, Y., Witherell, P., Lu, Y., Sprock, T.: Nesting and scheduling problems for additive manufacturing: a taxonomy and review. *Add. Manuf.* 101492 (2020)
9. Hur, S.-M., Choi, K.-H., Lee, S.-H., Chang, P.-K.: Determination of fabricating orientation and packing in SLS process. *J. Mater. Process. Technol.* **112**(2–3), 236–243 (2001)
10. Oh, Y., Zhou, C., Behdad, S.: Part decomposition and 2D batch placement in single-machine additive manufacturing systems. *J. Manuf. Syst.* **48**, 131–139 (2018)
11. Baumung, W., Fomin, V.V.: Predicting production times through machine learning for scheduling additive manufacturing orders in a PPC system. In: 2019 IEEE International Conference of Intelligent Applied Systems on Engineering (ICIASE), pp. 47–50 (2019)
12. Zhang, Y., Gupta, R.K., Bernard, A.: Two-dimensional placement optimization for multi-parts production in additive manufacturing. *Robot. Comput. Integr. Manuf.* **38**, 102–117 (2016)
13. Egeblad, J., Nielsen, B.K., Brazil, M.: Translational packing of arbitrary polytopes. *Comput. Geom.* **42**(4), 269–288 (2009)
14. Ransikarbum, K., Ha, S., Ma, J., Kim, N.: Multi-objective optimization analysis for part-to-printer assignment in a network of 3D fused deposition modeling. *J. Manuf. Syst.* **43**, 35–46 (2017)
15. Xiao, L., Jia-min, L., An-xi, C., et al.: HAPE3D—a new constructive algorithm for the 3D irregular packing problem. *Front. Inf. Technol. Electron. Eng.* **16**(5), 380–390 (2015)
16. Verkhoturov, M., Petunin, A., Verkhoturova, G., Danilov, K., Kurennov, D.: The 3D object packing problem into a parallelepiped container based on discrete-logical representation. *IFAC-PapersOnLine* **49**(12), 1–5 (2016)
17. Li, Q., Zhang, D., Wang, S., Kucukkoc, I.: A dynamic order acceptance and scheduling approach for additive manufacturing on-demand production. *Int. J. Adv. Manuf. Technol.* **105**(9), 3711–3729 (2019). <https://doi.org/10.1007/s00170-019-03796-x>
18. Wang, Y., Zheng, P., Xu, X., Yang, H., Zou, J.: Production planning for cloud-based additive manufacturing – a computer vision-based approach. *Robot. Comput. Integr. Manuf.* **58**, 145–157 (2019)
19. Pandey, P.M., Reddy, N.V., Dhande, S.G.: Slicing procedures in layered manufacturing: a review. *Rapid Prototyping J.* **9**(5), 274–288 (2003)

20. Bacciaglia, A., Ceruti, A., Liverani, A.: A systematic review of voxelization method in additive manufacturing. *Mech. Ind.* **20**(6), 630 (2019)
21. Gao, W., et al.: The status, challenges, and future of additive manufacturing in engineering. *Comput. Aided Des.* **69**, 65–89 (2015)
22. Garashchenko, Y., Zubkova, N.: Adaptive slicing in the additive manufacturing process using the statistical layered analysis. In: Ivanov, V., Trojanowska, J., Pavlenko, I., Zajac, J., Peraković, D. (eds.) *DSMIE 2020. LNME*, pp. 253–263. Springer, Cham (2020). https://doi.org/10.1007/978-3-030-50794-7_25
23. Garashchenko, Y., Zubkova, N.V.: Packing 3D models of products in the workspace of layered building installation by the Monte-Carlo method. *ZhSTU Bull. Appl. Mech.* **1**(85), 46–52 (2020)



Identification and Technological Impact of Broadband Vibration on the Object

Sergiy Kovalevskyy  and Olena Kovalevska  

Donbas State Engineering Academy, 72, Akademichna Street,
Kramatorsk 84300, Ukraine

Abstract. The research presents the approach consisting of resonant excitation of objects – elements of technological systems, including the machine tool, fixture, cutting tool, and part. Resonant Nano amplitude vibrations of the object under the action of broadband perturbation, which has a spectrum characteristic of “white noise”, are sources of information about the geometric characteristics of objects and indicators of their physical and mechanical properties. The latter is important for the materials of the workpieces. When a constant uniform field of magnetic or thermal nature is applied to an object, the introduction of Nano amplitude vibrations acquires the properties of technological influence, as a result of which the properties of the material from which the object is made may change. Experimental studies of resonant excitation of an object placed in a strong constant, uniform magnetic field on the physical and mechanical properties of materials of objects, particularly on increasing their hardness, are presented. The universality of this approach is shown under the condition of application of neural network models, which allows establishing the relationship between the parameters of the frequency spectra of resonant oscillations of objects and their geometric and physic-mechanical properties. Based on the presented materials, fundamentally new innovative technological processes can be developed, which have the prospect of wide application in the conditions of resource-saving highly automated production of products of various industries.

Keywords: Innovative technology · Resonant vibration · Broadband influence · Technological system · Diagnostics · Neural network

1 Introduction

Object identification is a problem, the solution of which is actualized in the systems of optimal management of these objects. Therefore, the requirements for such models are regulated by their compliance with the criteria of reliability and accuracy for the purposes of application [1]. Based on such models, reference models can be created, used by automated control systems for corrective action on the control object [2].

The creation of identification models is based on the choice and justification of the information source with the subsequent formation of an array of precedents. The reliability of the identification model of the object depends on their volume and quality. One of the features of such identification of objects is the statement about the dependence of the object’s reaction on the complexity of the disturbing effect on this

object [3]. The essence of this statement is that the amount of information about the individual properties of the object is proportional to the complexity of the perturbing function and can be identified as a response to this effect [4]. In the research studies [5, 6], it has been proved that the design of technological equipment should be based on parameter identification for ensuring the reliability of manufacturing processes.

It is known from the theory of automatic control that step effects as an analog of single ones allow revealing the transfer characteristics of the links of dynamic models of objects. This example suggests that the natural oscillations of the object and its elements contain information about the defining set of its properties and characteristics.

2 Literature Review

A promising direction in increasing production productivity due to the flexibility of production is to equip it with equipment with mechanisms of parallel structure [7]. The capabilities of such equipment are based on the modularity of such structures, on the multiplicity and scaling of their configuration, on mechatronic nodes, and on adaptive control algorithms. However, the mechanical part and drive system of actuators of such equipment with mechanisms of a parallel structure requires systematic improvement of the principles of design, control, and monitoring of objects due to the complex relationship of the trajectory of actuators with mechanisms of parallel structure and dynamic processes accompanying work processes [8]. The conclusions of domestic and foreign researchers in improving the accuracy of positioning, kinematics, and dynamics of objects based on the mechanisms of parallel structure confirm the thesis of the complex nature of control of the mechanism. However, the constant development of production and technological systems continues to pose new challenges. Purely systemic approaches based on the principles of synergy are inherent only in complex systems' integrity properties [9]. Therefore, further improvement of equipment systems with parallel structure mechanisms can be achieved by developing and implementing structural and parametric optimization of equipment with parallel structure mechanisms. The control of this equipment is based on dynamic identification mathematical models of positioning the executive unit of such equipment [10]. Principles of harmonization of levels of improvement of structural components of equipment systems with mechanisms of the parallel structure require the creation of appropriate means of providing technological processes of manufacturing machine-building products with technological tools with increased operational properties, corresponding principles of complex active control of dimensional and separate physical and mechanical characteristics of products mechanical assembly production [11].

The prospect of creating competitive technological equipment must be accompanied by structural optimization to ensure structural and technological flexibility of technological equipment [12]; creation of a system of normalized actuators based on the minimum number of energy conversions to expand technological work areas; creation of a system of normalized mechanisms for rapid change of technological tools to increase technological flexibility [13]; creation of technological equipment for the organization of the working space of technological operations based on equipment with parallel kinematics [14]; creation of the reconfigured sites of machine-building

production which are quickly adjusted, from the normalized knots of the equipment with application of mechanisms of parallel structure [15]. According to the research study [16], the design of the manufacturing system should be realized based on “The Ontology on Flexibility”.

This development of technological equipment and systems based on it allows to dramatically increasing the efficiency of multi-item production, including repair production for various areas of economic activity. However, using such equipment and its systems cannot but require intervention in the reliability of the technological processing and diagnostic tools. Therefore, it is justified to use special processes to improve the machining properties of metal-cutting and other technological tools, based on various effects of power, electrical, magnetic, wave, pulse, chemical, nanoscale, and their combinations.

3 Research Methodology

Based on such conclusions, we have developed and tested promising design solutions according to the Research Program of the Problem Laboratory of Mobile Intelligent Technological Machines of the Institute of Artificial Intelligence of the Academy of Sciences of Ukraine and Donbas State Machine-Building Academy of the Ministry of Education and Science of Ukraine.

The problem of dynamic identification of objects is to develop a mathematical modeling apparatus that would have the capabilities to provide the necessary characteristics of the accuracy of $d(t)$ and the adequacy of $A(t)$ of the dynamic model. The authors [17] proposed methods for determining all sample sizes by an acoustic signal, which is an amplitude-frequency characteristic of their own oscillations (frequency spectrum or signature). The accuracy of such dimensional diagnostics reaches 0.1 mm. The same estimates of the coordinates of the configuration of objects with mechanisms of parallel structure [18]. To implement this approach, the following is adopted: $W(f)$ – excitation signal of the object “white noise”; $R[W(f)]$ – the object’s response to excitation by “white noise”; $X_k, X_1, \dots, X_r, \dots$ – properties and parameters of the object (configuration, speed, deformation, force, stress, velocity, acceleration, temperature, etc.) $R[W(f)] = F\{X_k, X_1, X_r, \dots\}$.

The task of diagnostics and creation of a reference model of the object is to determine the properties and parameters of the object $X_k, X_1, \dots, X_r, \dots$ by reaction $R[W(f)]$. Information model for determining the properties and parameters of the object Eq. (1):

$$W(f) - \text{Object} - R[W(f)] - F_y[A_i(f_i)] - X_k, X_1, \dots, X_r \quad (1)$$

The emitter and receiver of the diagnostic device are reversible piezoelectric elements, which are fed (emitter) and from which are removed (sensor) signals. Since the diagnostics of the object is performed relative to the reference signal “white noise”, this approach allows you to normalize the output diagnostic signals relative to the reference signal. Transformation solution $X_k, X_1, \dots, X_r, \dots = F\{X_k, X_1, \dots, X_r, \dots\}$ is recommended to perform using neural network modeling. The solution is proposed based on the

entropy index of the histogram that corresponds to the samples of Table 1 according to Eqs. (2) and (3):

$$H_a(x) = - \sum_{i=1}^n p_i(x) \bullet \log_a p_i(x) \quad (2)$$

$$H_{ai}(x) = \frac{H_a(x)}{n} \quad (3)$$

Where, $H_a(x)$ – the index of entropy of the distribution of pixels of images of samples on brightness;

$p_i(x)$ – probability of the i-th degree of the histogram of the distribution of pixels of images of samples on brightness; n – the number of degrees of the histogram of the pixel distribution of the images of the samples by brightness.

The construction of the model on a neural network basis was performed in NeuroPro-0.25 using Microsoft Access to generate input and output data in *.dbf format. When training and testing the model according to the structure of the metal at different heating temperatures, the same exposure time, and cooling conditions of the samples, it was found that a significant part of the signature is the seventh interval $\times 7$ (150 to 175 on the pixel brightness scale) for each image histogram. The verbal description of the model is given as follows: Solving the inverse problem of the ability to determine the structure (ferrite and perlite) from the values of the interval $\times 7$ of the signature images of micro sections allows obtaining an expert assessment of the elementary heat treatment of samples. The paper formulates the hypothesis that the normalized gradual effect on the controlled part is accompanied by its response, which has specific characteristics. A combination can diagnose the size and accuracy of the size of parts and other characteristics of their quality (Fig. 1).

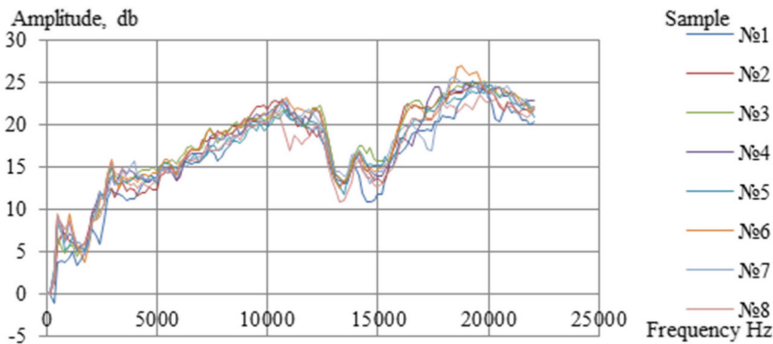


Fig. 1. Frequency spectra of samples.

Studies have shown that the smallest number of synapses is characteristic of a single-layer network. The authors propose a method for assessing the quality of objects based on the spectrum of the acoustic signal given in the cutting tool due to the

response to forced oscillations in the form of “white noise”. The authors performed research, the objectives of which were working out of a technique of definition of the spectral characteristic of own acoustic fluctuations of the cutting tool; assessment of the quality of batches of cutting tools by the degree of similarity of their properties; the formation of similar acoustic spectrum groups of cutting platinum, in a multi-blade prefabricated tool. The method of determining the spectral characteristics of the acoustic oscillations of the cutting tool is developed on the example of non-grinding cutting plates, Pramet acoustic response signal, software package “spectrum analyzer”. The normalized acoustic signal has an amplitude-frequency characteristic of the constant amplitude of the signal in the frequency range 10–20000 Hz (Fig. 2).

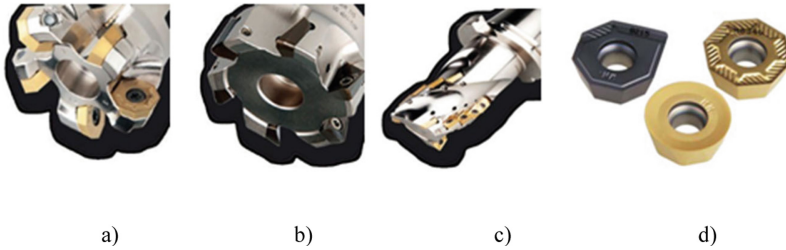


Fig. 2. Samples of prefabricated cutters (a, b, c) and cutting inserts for their assembly (d) Pramet.

For example, the results of processing the digitized spectra of a batch of cutting inserts (30 pieces) in increments of 172.3 Hz, frequencies range 10–20000 Hz. using the Detector Studio Academic package. Figure 3 shows the results of grouping the cutting inserts into three groups formed on Kohonen maps.

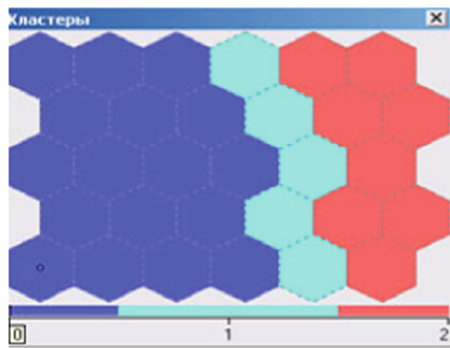


Fig. 3. Grouping of non-grinding cutting inserts in the similarity of the spectra of acoustic signals of the “white noise” response.

The presented example illustrates the uneven distribution of the properties of the cutting inserts of one batch. The plates in the batch are distributed according to the numbers presented in Table 1.

Table 1. The results of grouping cutting inserts on Kohonen maps.

Clusters of cutting inserts for complete sets of prefabricated cutters, identical in a similarity of spectra of acoustic signals, the response of “white noise”		
1 group	2 group	3 group
2,3,4,6,7,9,11,14,16,17,18,19,21,22,25,26,28,30	5,10,13,20,23	1,8,12,15,24,27,29

Tests of stability of the final mills completed with plates from the 1st and 3rd groups showed an increase in stability of combined mills by 31–35%. Plates of the 2nd group were not used.

In the study [19], the possibility of using a broadband vibration flux to influence the volume of the material of the magnetic field formed by powerful permanent magnets is shown. The process of influencing the material volume of the experimental samples was that the effect of a uniform magnetic flux permeating the sample was initiated by resonant oscillations of the sample caused by a broadband effect of equal amplitude using a white noise generator and a peso emitter [20]. The possibility of obtaining a positive effect of a positive change in the physical and mechanical properties of the material of the experimental samples is based on the following provisions [21].

It is well-known [22] that the modulus of elasticity E and the density of the material of the sample ρ are associated with the resonant frequency f_0 of the sample by the following dependence Eq. (4):

$$f_0 = K_f \cdot \sqrt{\frac{E}{\rho}} \quad (4)$$

Where, K_f - coefficient depending on the size of the sample.

Here it is necessary to consider the three-dimensional nature of vibrations (deformations) in the resonance of each element of the volume of the material. To do this, we use the dependence Eq. (5):

$$E = 1,64 \cdot m \cdot L^3 \cdot f^2 / d^4 \quad (5)$$

Where: m is the mass of the sample, L is the length of the sample, d is the diameter of the sample.

Based on these initial conditions, the determination of the resonant frequency of the experimental sample placed in a uniform magnetic field and subjected to resonant vibrations using a piezoelectric emitter and a piezoelectric sensor is made based on the frequency spectrum of the sample in the magnetic field according to Eq. (6):

$$f_0 = \frac{\sum_{i=1}^n f_i \cdot A_{1i}(f_i)}{\sum_{i=1}^n A_i(f_{1i})} \quad (6)$$

where: $A_{1i} = A_i - A_{0i}$; A_{0i} – amplitude i —the degree of the frequency spectrum of the hardware of the experimental stand in the absence of the excitation signal of the generator “white noise”; A_i - amplitudes of the i -th degree of the frequency spectrum of the sample, installed in the zone of the uniform magnetic field of the experimental stand and excited by the signal of the generator “white noise” using a piezoelectric element that is part of the experimental stand; A_{1i} - natural amplitudes of the i -th degree of the frequency spectrum of the sample placed in a uniform magnetic field.

4 Results

Testing of duralumin sample: before vibration treatment in a uniform magnetic field, the hardness of the sample with a diameter of 15 mm and a height of 8 mm is $60 \div 80$ HB; after vibration treatment for 20 min, the hardness of the sample was $208 \div 212$ HB: an increase in the sum of the individual sites of amplitudes indicates that the sample becomes changing the viscosity of the material. The increase in the resonant frequency, which indicates a change in the physical and mechanical properties, is $\Delta f_0 = 225$ HB.

Copper sample test: before vibration treatment in a constant magnetic field, the hardness of the sample with a diameter of 20 mm and a height of 5 mm is $60 \div 100$ HB: after vibration treatment for 20 min, the hardness of the sample was $220 \div 222$ HB. A change in the resonant frequency of the sample may indicate a change in the density of the material, leading to an increase in hardness. The change in the resonant frequency of the samples is $\Delta f_0 = 150$ Hz, which indicates a change in the physical and mechanical properties.

Testing of a non-grinding plate of a cutting tool made of hard alloy HS123: increasing the resonant frequency of the sample ($\Delta f_0 = 120$ Hz) may indicate an increase in the material’s modulus of elasticity while increasing its viscosity. It is typical for polycarbonates, polyamides, composite materials.

Tests of plates at turning a batch of parts $\varnothing 95,5$ mm from steel 42Cr4 at giving of 0,5 mm/rev and cutting speed of 150 m/min dimensional wear of plates HS123 decreased by 40–42%. It is an argument in favor of vibration resonant processing of cutting inserts in a uniform magnetic field.

Non-grinding test of the cutting tool plate made of hard alloy HG30: increasing the resonant frequency of the sample ($\Delta f_0 = 70$ Hz) may indicate an increase in the material’s modulus of elasticity while increasing its viscosity.

Testing of gray cast iron with cutters made of hard alloy HG30 with a hardness of 200–220 HB when turning the sample with a cutting depth of 1.8 mm with a feed rate of 0.2 mm/rev and a cutting speed of 114 m/min wear of plates with HG30 decreased by 32–37% It is shown that with increasing duration of such processing the increase in its efficiency decreases. In addition, the process of changing the properties of the materials continues after vibration resonance treatment in a uniform magnetic field for

the next 3–5 days. The change of these properties is subject to exponential nature and for different materials has a different time constant. Then the indicators $\sum_{i=1}^n A_i(f_{1i})$ and f_0 are stabilized, which indicates the termination of the process of changing the properties of the material of the samples.

Magnetic resonance treatment in a magnetic field of non-grinding cutting plates, CNMA120408E-KD5ACK15A; WNMG080408E-MC3AP301M; WNMG080412E-PD3AC250P, and SNGX1206ANN-MM3AP351U were accompanied by observations of the dynamics of changes in the indicators $\sum_{i=1}^n A_i(f_{1i})$ and f_0 . It is emphasized that the increase in hardness is inversely proportional to the decrease in the resonant frequency of the cutting plate. For different types of cutting inserts, the correspondence of hardness to resonant frequencies is different and depends on the design features. Therefore, on average, the change in resonant frequency is determined by the formula: $\Delta HB = -(0, 65 \dots 0, 75) \cdot \Delta f_0$.

For plates of group SNGX 1206ANN-MM3 AP351U) the result is described by formulas:

$$f_0 = -1, 27 \cdot HB + 11802;$$

$$HB = -0, 79 \cdot f_0 + 9317.$$

The generalized result can be described by the dependence:

$$f_0 = -1, 53 \cdot HB + 11981;$$

$$HB = -0, 66 \cdot f_0 + 7856.$$

5 Conclusions

Making samples of materials placed in a uniform magnetic field, resonant poly frequency vibrations with Nano-dimensional amplitude in the range of 20–80 nm allow changing the viscosity of the material, the modulus of elasticity of the material, and the hardness of the material samples. Thus, nanoscale amplitudes of natural oscillations of objects of complex shape in energy fields, which include uniform magnetic fields, can correct the physical and mechanical properties of materials of such objects to achieve their identity or add strictly defined properties. The study of this effect can be extended to many materials, their atomic-crystalline structures, ranges of magnetic fluxes, frequency ranges, and estimates of the materials' obtained physical and mechanical properties thus treated. It has been confirmed that image pixel signatures allow communication with previous technological transformations. It allows you to examine the technology by which the samples were machined or speed up the receipt of metallographic research data, and speed up the analysis of the material on the composition of structures.

The proposed approach, which consists of the resonant excitation of objects, allows abandoning the traditional schemes of equipping technological systems with many sensors that read information about objects. The frequency spectra of objects can perform this role. It is shown that the frequency spectra of resonantly excited objects are sources of information about the macro geometric characteristics of objects and indicators of their physical and mechanical properties. Experimental confirmation of the influence of the resonant excitation of an object placed in a strong constant, uniform

magnetic field on the physical and mechanical properties of the materials of objects, in particular, on the increase of their hardness, is presented. The universality of the approach to the resonant excitation of the object is shown, illustrated by pixel signatures of images of micro sections of material structures. A special role in the information support of the processes of diagnostics of objects and changes in their physical and mechanical properties is given to intelligent computing and neural network models. The materials of the article have the prospect of wide application in the conditions of resource-saving highly automated production of products of various branches.





References

1. Dumin, O., Prishchenko, O., Pochanin, G.: Subsurface object identification by artificial neural networks and impulse radiolocation. In: 2018 IEEE Second International Conference on Data Stream Mining and Processing (DSMP), pp. 434–437. Lviv (2018)
2. Sonoda, J., Kimoto, T.: Object Identification from GPR images by deep learning 2018. In: Asia-Pacific Microwave Conference (APMC), pp. 1298–1300. Kyoto, Japan (2018)
3. Mohamad, G., Drroubia, N., Faisala, N.: Acoustic emission method for defect detection and identification in carbon steel welded. *J. Constr. Steel Res.* **13**(7), 28–37 (2017)
4. Kishawy, H.A., Hegab, H., Umer, U., Mohany, A.: Application of acoustic emissions in machining processes: analysis and critical review. *Int. J. Adv. Manuf. Technol.* **98**(5–8), 1391–1407 (2018). <https://doi.org/10.1007/s00170-018-2341-y>
5. Pavlenko, I., Trojanowska, J., Ivanov, V., Liaposhchenko, O.: Parameter identification of hydro-mechanical processes using artificial intelligence systems. *Int. J. Mechatron. Appl. Mech.* **2019**(5), 19–26 (2019)
6. Pavlenko, I., Ivanov, V., Gusak, O., Liaposhchenko, O., Sklabinskyi, V.: Parameter identification of technological equipment for ensuring the reliability of the vibration separation process. In: Knapcikova, L., Balog, M., Perakovic, D., Perisa, M. (eds.) 4th EAI International Conference on Management of Manufacturing Systems. EICC, pp. 261–272. Springer, Cham (2020). https://doi.org/10.1007/978-3-030-34272-2_24
7. Chunikhin, A.Y., Glazunov, V.A.: Developing the mechanisms of parallel structure with five degrees of freedom designed for technological robots. *J. Mach. Manuf. Reliab.* **46**(4), 313–321 (2017). <https://doi.org/10.3103/S1052618817040057>
8. Laryushkin, P.A., Rashoyan, G.V., Erastova, K.G.: On the features of applying the theory of screws to the evaluation of proximity to specific positions of the mechanisms of parallel structure. *J. Mach. Manuf. Reliab.* **46**(4), 349–355 (2017). <https://doi.org/10.3103/S1052618817040100>
9. Shalyukhin, K.A., Rashoyan, G.V., Aleshin, A.K., Skvortsov, S.A., Levin, S.V., Antonov, A.V.: Problems of kinematic analysis and special positions of mechanisms of robots with parallel structure. *J. Mach. Manuf. Reliab.* **47**(4), 310–316 (2018). <https://doi.org/10.3103/S1052618818040143>
10. Kovalevskyy, S., Kovalevska, O., Koshevoy, A.: Analysis of accuracy and adequacy of dynamic models of objects. In: Karabegović, I. (ed.) NT 2020. LNNS, vol. 128, pp. 75–80. Springer, Cham (2020). https://doi.org/10.1007/978-3-030-46817-0_8
11. Wahyono, A., Filonenko, K.: Unattended object identification for intelligent surveillance systems using sequence of dual background difference. *Trans. Ind. Inform.* **12**(6), 2247–2255 (2016)

12. Pasquale, G., Ciliberto, C., Rosasco L.: Object identification from few examples by improving the invariance of a deep convolutional neural network. In: 2016 IEEE/RSJ International Conference on Intelligent Robots and Systems (IROS), pp. 4904–4911. Daejeon, Korea (South) (2016)
13. Antonov, A.V., Glazunov, V.A., Aleshin, A.K., Rashoyan, G.V., Laktionova, M.M.: Kinematic analysis of a parallel structure mechanism for work in extreme environments. *J. Mach. Manuf. Reliab.* **47**(2), 121–127 (2018). <https://doi.org/10.3103/S1052618818020036>
14. Xiucheng, L., Ruihuan, Z., Bin, W., Cunfu, H.: Quantitative prediction of surface hardness in 12CrMoV steel plate based on magnetic Barkhausen noise and tangential magnetic field measurements. *J. Nondestr. Eval.* **37**(2), 1–8 (2018). <https://doi.org/10.1007/s10921-018-0486-0>
15. Ravska, N., Klymenko, G., Tkachenko, M.: Cutting tool wear heavy lathe. Energy and environmental aspects of tribology. In: AGH University of Science and Technology, pp. 137–147 (2010)
16. Luscinski, S., Ivanov, V.: A simulation study of industry 4.0 factories based on the ontology on flexibility with using FlexSim® software. *Manag. Prod. Eng. Rev.* **11**(3), 74–83 (2020). <https://doi.org/10.24425/mper.2020.134934>
17. Yu, J., Liang, S., Tang, D., Liu, H.: A weighted hidden Markov model approach for continuous-state tool wear monitoring and tool life prediction. *Int. J. Adv. Manuf. Technol.* **91**(1–4), 201–211 (2016). <https://doi.org/10.1007/s00170-016-9711-0>
18. Rodrigo, H., Márcio, B.: A probabilistic neural network applied in monitoring tool wear in the end milling operation via acoustic emission and cutting power signals. *Mach. Sci. Technol.* **20**(3), 386–405 (2018)
19. Wu, J., Zou, Y., Sugiyama, H.: Study on finishing characteristics of magnetic abrasive finishing process using low-frequency alternating magnetic field. *Int. J. Adv. Manuf. Technol.* **85**(1–4), 585–594 (2015). <https://doi.org/10.1007/s00170-015-7962-9>
20. Alireza, D., Khalaj, A., Fadaei, T.: Effects of magnetic assistance on improving tool wear resistance and cutting mechanisms during steel turning. *Mohammadi Wear* **384–385**(15), 1–7 (2017)
21. Yip, W.: Reduction of material swelling and recovery of titanium alloys in diamond cutting by magnetic field assistance. *J. Alloy. Compd.* **722**(25), 525–531 (2017)
22. Kovalevskyy, S., Turmanidze, R., Kovalevska, O.: Principles of systemization as a basis for designing of combination technological systems. In: Karabegović, I. (ed.) NT 2019. LNNS, vol. 76, pp. 256–264. Springer, Cham (2020). https://doi.org/10.1007/978-3-030-18072-0_30



Shape Optimization of an Object Using the Information Model

Oleksii Lopakov , Volodymyr Tigariev^(✉) ,
Volodymyr Tonkonogyi , and Volodymyr Kosmachevskiy 

Odessa National Polytechnic University,
1, Shevchenko Avenue, Odessa 65044, Ukraine
volodymyr_t@ukr.net

Abstract. The article discusses in detail the concepts of optimizing the shape of objects. A general approach to the creation, analysis, and use of an information model (IM) to optimize the shape of an object was studied. The paper proposes the use of an information model to optimize the object's shape to accelerate the design within the framework of theoretical research and practical use. All stages and elements of the information model in the process of optimizing the object's shape are considered in detail. The study was carried out to optimize the shape for a bracket-type part to test the proposed information model. Optimization was carried out in the "Shape Generator" module in CAD Autodesk Inventor. All sets of necessary requirements and restrictions for the 3D model of the detail were specified in the "Shape Generator" module. After optimization in the "Shape Generator" module, a mesh model of the part was obtained in the form of a conceptual model shape. Using the conceptual model shape, a new optimized solid 3D model of the object was created. To verify the correctness of the object shape optimization, simulations of the load actions on the original and optimized model were carried out in the Stress Analysis Simulation CAD module Autodesk Inventor. The weight of the optimized detail is 59% less than the original. The conducted research has proved the expediency of using the information model to optimize the object's shape.

Keywords: Information model · Shape optimization · Mesh-model · Generative design

1 Introduction

The information model (IM) includes all the information for each stage of creating and optimizing the object's shape [1]. In the modern world of technological progress, situations constantly arise in which optimization of the object's shape is the only way to solve complex problems. The concept of optimizing the object's shape can be used in mechanical engineering [2, 3] (creation of a specific part), medicine [4, 5] (creation of skeletal bones, surgical templates), in architecture [6] (building elements and decoration), engine parts design [7], computer-aided fixture design [8], etc. In mechanical engineering, optimization is often done through generative design. Simultaneously, digital versions of the object model are generated in the process of searching for the

shape of completely new products, during the development, modernization, and repair of equipment, as well as in cases when the necessary part is impossible or very difficult to obtain. Optimizing the object shape according to the specified criteria is a very urgent task. There are various methods to optimize the part shape. One method is to use an information model to optimize the object shape. The purpose of this work is to consider such a method for optimizing the object shape. After optimizing the shape, it is necessary to analyze the compliance of the created part with the specified design requirements. Generative design software is not a CAD system but an add-on to it. The generative design method makes it possible to obtain computer 3D models, according to which a new part is quickly created using additive technologies [9–11].

2 Literature Review

Four groups of optimization methods are currently used depending on the method of changing the object shape under study.

The first group of methods is based on the “manual” analysis of the results of modeling the stress-strain state of the part and the corresponding change in its design [2, 3]. This approach is very flexible. It is extremely difficult to create an algorithm that analyzes information in the same way as the human brain does. “Manual” analysis of information and making changes to the design takes much time. Therefore, only a small number of design options can be explored this way.

The second group of methods is based on parametric optimization [9–13]. The object model which needs to be optimized is parameterized. That is, variable values are assigned to some of its characteristic dimensions. By changing the values of these variables, you can change the object’s shape. The combination of parameter values is determined to provide the best solution to the optimization problem. Parametric optimization allows you to explore a fairly large number of design options. However, the shape of the resulting object will not radically differ from the original model because a different set of dimensions describes geometry with a great number of differences.

The third group of optimization methods is topological optimization methods that involve finding the optimal object shape in a certain permissible area [14–16]. As a result of such optimization, an object of an absolutely unpredictable shape can be obtained, which on the one hand, is an advantage since it allows you to find a new, non-obvious solution. However, the resulting form may not be technologically advanced and therefore requires additional analysis.

The fourth group of optimization techniques is generative design techniques. The limiting conditions and the model’s description are set, and the process of “generation” is carried out. As a result, we get several solutions. Based on the given conditions, artificial intelligence chooses what it considers optimal. Studying a large set of parameters, the software tries to identify what a person may miss when developing. It remains for the engineer to choose which of the computer designs is the most optimal. To control the correctness of choice, it is possible to conduct studies of the loads effect on the optimized object [17, 18].

The study aims to develop an IM and its use in the process of optimizing the objects shape, which significantly reduces the time for design, testing, and analysis of the

model for the required loads [19]. Building an IM involves presenting information describing the essential parameters and changes in the object, the relationship between them, and allowing to simulate possible changes in the object's state [20, 21]. Overall, it can be reasonable to create a virtual prototype of a real object and design using up-to-date technologies [22, 23].

3 Research Methodology

The optimization process can be represented as follows: for the optimized model, the stress-strain state is set under the action of workloads. Based on the analysis results, the finite element model of the object is modified by excluding a part of the structure. For the new design obtained, the stress-strain state simulation is repeated, which makes it possible to determine the workability of the object and the need for further optimization. The target optimization function is the mass of the part. Therefore, the material of the original model can be removed as long as the part remains functional. Those areas that ensure the setting of boundary conditions and the interaction of the investigated and associated parts remain unchanged. The optimization process can be iterative so that material removal or addition cycles are repeated until the desired result is obtained. When using generative design technology based on artificial intelligence, the system allows you to create several options for optimizing the shape of a part. The designer will have to choose the most suitable one, taking into account the manufacturing technology.

Creating an IM requires the presentation of information describing the essential parameters and changes in the object, the relationship between them and allows to simulate possible changes in the state of the object [1, 2]. In this work, an IM of the process of optimizing the object shape is proposed, which will later be used to develop adaptive-parametric models. Studies of many works aim to develop the IM of an object, but they lack accurate analytical solutions to problems to reduce the time spent on design, testing, and load analysis. As a result of studying this problem, an IM was developed and proposed (see Fig. 1) for optimizing the object shape, not only within the framework of theoretical research but also for practical use.

The proposed IM can be used to optimize the shape in various modern CAD systems, such as Autodesk Inventor Professional, Siemens Solid Edge, NX, Autodesk Fusion 360, ANSYS Mechanical, Altair OptiStruct, Autodesk Within, Project Dreamcatcher, or when creating separate specialized optimization modules. Let us consider in more detail the structure of the proposed IM optimization of the object shape.

The proposed MI consists of 5 stages of shape optimization and control of the parameters of the optimized object.

Stage 1. Creation of a 3D solid model of a part using standard CAD tools. At this stage, using standard creation and editing tools, a 3D solid model of the part is formed, the shape of which must be optimized.

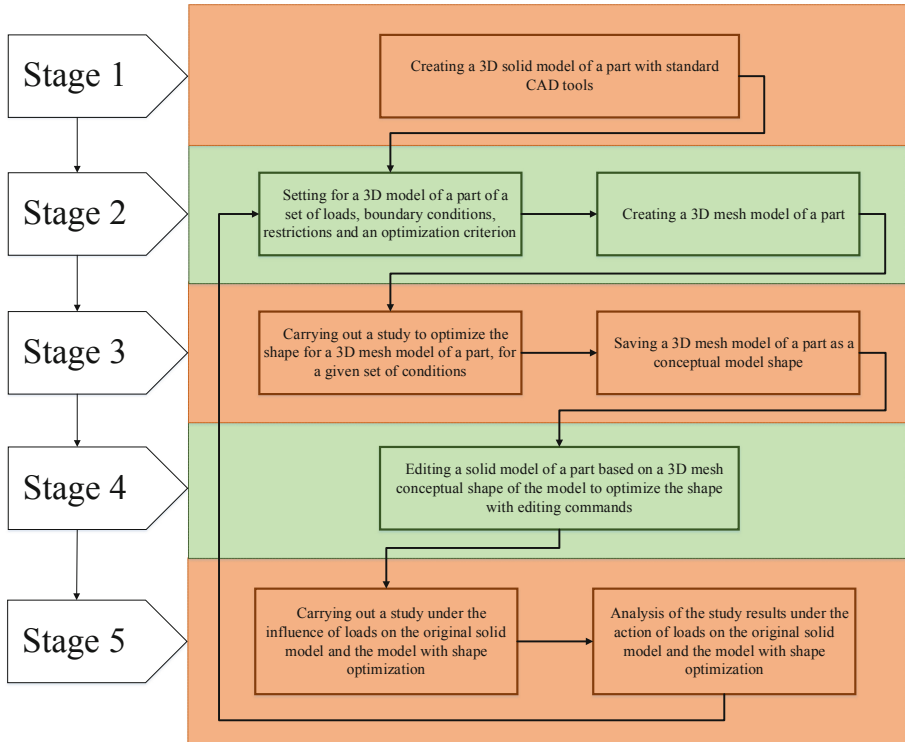


Fig. 1. Information model of object shape optimization.

Stage 2. Setting necessary requirements and constraints for a 3D model of an object and then creating an object's mesh model. At this stage, you need to perform two consecutive steps. First, for the 3D model of the object, the material for analysis, immutable regions in the object's geometry, loads' sets, boundary conditions, and constraints are set. At the next step, optimization criteria are set, for example, weight reduction, parameters of the mesh object being created. Then a mesh object based on a solid model is created.

Stage 3. Conducting a shape optimization study and creating a 3D mesh optimized object model. At this stage, two consecutive steps need to be performed. First, studies are carried out to optimize the object shape based on a 3D mesh model of the part, considering all the requirements and restrictions. Then the 3D mesh of the part as a conceptual shape is saved. The concept shape can be added to the current part as a link or saved to a new file.

Stage 4. Optimizing the shape of a solid model of a part. The saved conceptual shape is overlaid on the 3D solid model. Using the boundaries of the conceptual shape with the help of solid editing commands, an optimized 3D model of the object is generated.

Stage 5. Research and analysis of the results under the load actions on the original solid model and the model with shape optimization. At this stage, two consecutive

steps need to be performed. First, studies are carried out under the influence of loads on the original solid model, and the result is saved as a stress analysis report. Then studies are carried out under the action of the same loads on the solid model with an optimized shape, and then the result is saved as a stress analysis report. The results of studies are analyzed under the load actions on the original solid model and the model with shape optimization at the second step. If the results meet the requirements of the object under study, then it is approved as a ready-made optimized model of the object. If the result does not meet the requirements of the investigated part, then the value of the optimization criterion changes, and stages 2–5 of the information model are repeated.

4 Results

Consider using the created IM to optimize the shape of a bracket-type part. Optimization will be done in the Shape Generator module in Autodesk Inventor Professional. In this case, the levels of IM (see Fig. 1) will be adapted to the specifics of the development and optimization process for CAD Autodesk Inventor Professional.

The Shapes Generator module in Autodesk Inventor Professional belongs to the class of the simplest topology optimization tools. It is one of the world's first part topology optimization tools, directly integrated by the manufacturer into its CAD system. Inventor Shape Generator is the easiest solution in Autodesk's line of generative design tools that reduces the mass of existing parts with minimum expenses without losing their strength under specified conditions.

At the stage of creating a 3D solid model of an object, we will use standard Autodesk Inventor Professional CAD tools such as 2D Sketch, Extrude, Hole, etc. A solid model of the bracket is shown in Fig. 2.

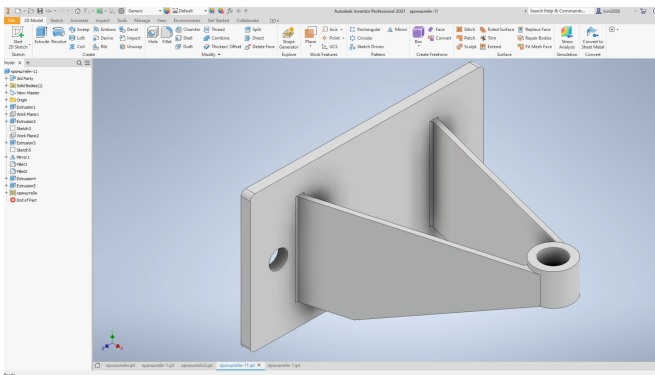


Fig. 2. Solid bracket model.

At the next stage of the IM, we set a set of requirements and restrictions for the 3D model of the part, such as: assigning the model of material properties (Aluminum 6061 – AHC), Fixed Constraint, Pressure (10 MPa), Gravity (9810 mm/s²), Preserve Region

(setting location and size of the area). We adjust the optimization criterion – weight reduction by 60% (Fig. 3). A solid model with tuned requirements and constraints looks like Fig. 4.

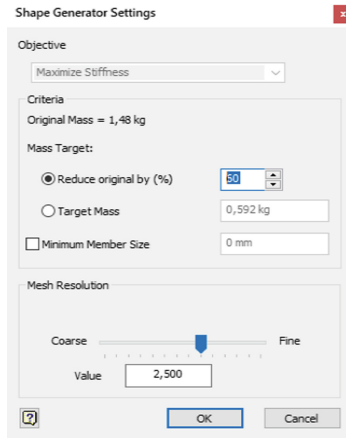


Fig. 3. Settings of Shape Generator.

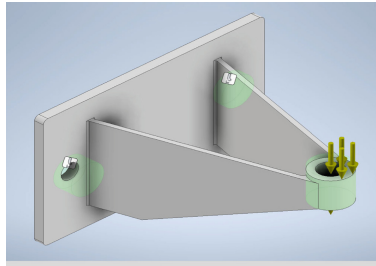


Fig. 4. A solid model with customized requirements and constraints.

Then Mesh Settings are set up and a mesh model of the object is created (Fig. 5).

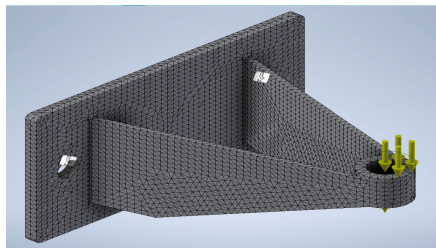


Fig. 5. Mesh model of the object.

At the stage of research on shape optimization, we run Generate Shape. The program calculates and creates a 3D mesh model of the object with an optimized shape (Fig. 6). The 3D mesh of the object as a conceptual model shape is saved. The conceptual form of the model can be saved in the current part file or as a separate STL file. The conceptual form of the model in the current object file is saved. The Visual Style - Wireframe is set up (Fig. 7). Setting the visual style will make it easier to edit the original object model.

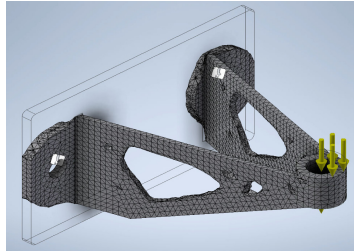


Fig. 6. Mesh model of the object with an optimized shape.

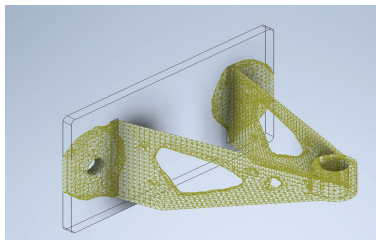


Fig. 7. Conceptual form of the optimized model.

The next step is to edit the original solid model of the bracket part. Based on the 3D mesh conceptual form of the model, editing with the CAD commands Autodesk Inventor Professional is carried out. Part editing is carried out in several steps. The results of editing and creating the optimal shape of the bracket part are shown in Figs. 8, 9.

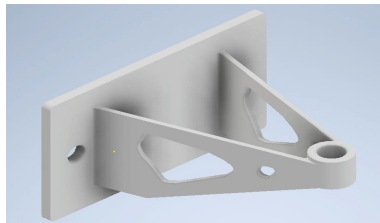


Fig. 8. Model editing stage.

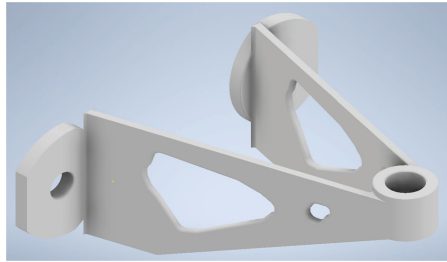


Fig. 9. Optimized object model.

The created model of the optimized object shape is saved as a new file. It will allow load studies to be carried out separately from the original model.

We proceed to the final stage of IM - conducting research and analyzing the results under the influence of loads on the original solid model and the model with shape optimization. To do this, in the file with the original model of the bracket, go to the Stress Analysis Simulation CAD module Autodesk Inventor Professional. All the requirements and restrictions are adjusted in preparation for optimizing the form. A study of the model is conducted. The study for a part with an optimized shape is repeated. The main results of both studies are presented in Figs. 10 and 11. The mass of the part is reduced by 59%, which is close to the original requirements. The offset difference is 1.1 mm, which is satisfactory for the task. Other physical and static test results are also within acceptable ranges.

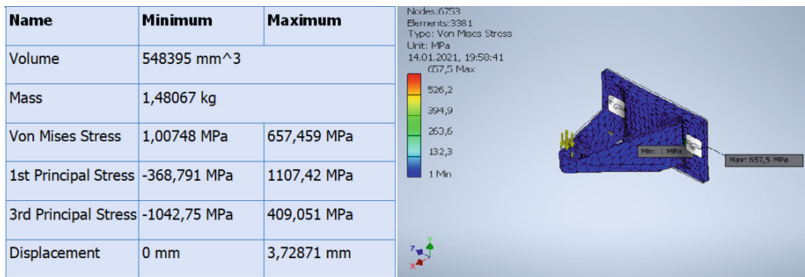


Fig. 10. Original model.

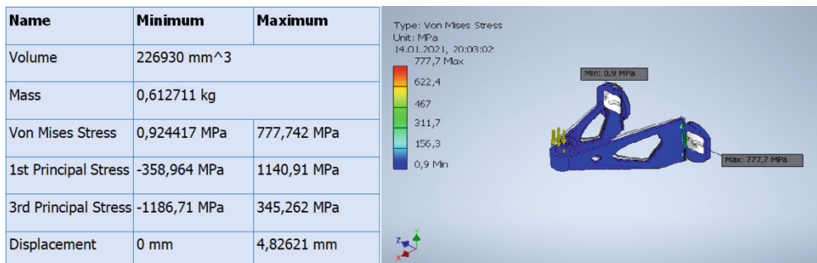


Fig. 11. Optimized model.

5 Conclusions

The paper discusses in detail the concepts of optimizing the object's shape. A general approach was proposed for the creation, analysis, and use of an information model to optimize the shape of an object. IM includes all information for each stage of object shape optimization using generative design technology. The technology of optimizing the shape for the solid model of the bracket part is described in detail. Optimization was carried out to reduce the mass of the object. The weight of the optimized object is reduced by 59%, which is close to the specified requirements. The original and optimized objects were subjected to the same loads of 10 MPa. The difference in offset is 1.1 mm, which is satisfactory for the task. Other physical and static test results are also within acceptable ranges. The studies carried out proved the expediency of using the information model to optimize the object shape.

Using the created and validated information model, you can propose its use in other areas of design. For example, it can be used in the development and optimization of an implant for femoral reinforcement. In this case, the information model will be transformed to solve a specific problem. After all, it is necessary to create a virtual prototype of a real object and design the anatomical shape of the implant, which will fit snugly against the complex surface of the bone. When simulating loads, the possible directions of the force application (horizontal, vertical, and rotational) must be taken into account. The use of an implant with an optimal shape significantly reduces the values of bone overload, taking maximum stress on itself.

IM significantly reduces the time spent on designing, testing, and analyzing the model for the required loads, not only within the framework of theoretical research but also for practical use.

The development of the proposed IM will be used when creating objects of optimal shape for various fields of application.






References

1. Wagner, G.: Information and process modeling for simulation. *J. Simul. Eng.* **1**(1), 1–25 (2018)
2. Larsson, R.: *Methodology for Topology and Shape Optimization: Application to a Rear Lower Control Arm*. Chalmers University of Technology, Goteborg, Sweden (2016)
3. Rohit, B.B., Niloy, K.N., Shailesh, S.P.: Design and analysis of connecting rod with abaqus. *Int. J. Recent Innov. Trends Comput. Commun.* **4**(4), 906–912 (2016)
4. Sergeev, A.N.: 3D printers in medicine - a field of application and prospects for the development of printing. <https://www.sciencedebatecom/3d-printery-v-meditsine-oblast-primeneniya-i-perspektivy-razvitiya-pechati/>. Accessed 25 Apr 2017
5. Kamonichkin, D.T.: 3D printing of surgical templates. Site of the center for additive manufacturing. <https://studia3d.com/hirurgshablon>. Accessed 15 Mar 2018
6. Dapogny, C., Faure, A., Michailidis, G., Allaire, G., Couvelas, A., Estevez, R.: Geometric Constraints for shape and topology optimization in architectural design. *Comput. Mech.* **59**, 933–965 (2017)

7. Pavlenko, I., et al.: Parameter identification of cutting forces in crankshaft grinding using artificial neural networks. *Materials* **13**(23), 5357 (2020). <https://doi.org/10.3390/ma13235357>
8. Ivanov, V., Pavlenko, I., Liaposhchenko, O., Gusak, O., Pavlenko, V.: Determination of contact points between workpiece and fixture elements as a tool for augmented reality in fixture design. *Wireless Netw.* **27**(3), 1657–1664 (2019). <https://doi.org/10.1007/s11276-019-02026-2>
9. Kumar, M.D., Teja, P.S., Krishna, R., Sreenivasan, M.: Design optimization and simulation analysis of Formula SAE frame using chromoly steel. *J. Eng. Sci.* **6**(2), D9–D13 (2019). [https://doi.org/10.21272/jes.2019.6\(2\).d2](https://doi.org/10.21272/jes.2019.6(2).d2)
10. Zhou, Y., Kalogerakis, E., Wang, R., Grosse, I.R.: Direct shape optimization for strengthening 3D printable objects. *Pac. Graph.* **35**(7), 333–342 (2016)
11. Knyazev, E.Y.: Design and topological optimization of parts for additive manufacturing. Computer modeling of 3D printing processes based on solutions of the MSC corporation Software. www.mssoftware.com. Accessed 8 Dec 2020
12. Vlah, D., Žavbi, R., Vukašinić, N.: Evaluation of topology optimization and generative design tools as support for conceptual design. In: *International Design Conference 2020*, pp. 451–460. Cambridge University Press (2020)
13. Limarenko, A.M., Romanov, A.A., Alekseenko, M.A.: Optimization of the connecting rod of a car engine by the finite element method. *Proc. Odessa Polytech. Univ.* **2**(39), 98–100 (2012)
14. Moezi, S.A., Zakeri, E., Bazargan-Lari, Y., Zare, A.: 2&3-dimensional optimization of connecting rod with genetic and modified cuckoo optimization algorithms. *IJST, Trans. Mech. Eng.* **39**(M1), 39–49 (2015)
15. Muhammad, A., Shanono, I.: Static analysis and optimization of a connecting rod. *Int. J. Eng. Technol. Sci.* **6**(1), 24–40 (2019)
16. Janigová, S., Schürger, B.: Design optimization of the modified planetary carrier. *J. Eng. Sci.* **8**(1), E17–E22 (2021). [https://doi.org/10.21272/jes.2021.8\(1\).e3](https://doi.org/10.21272/jes.2021.8(1).e3)
17. Leen, R., Antlej, K., Usma, C., Collins, P.: Shape optimization of a snowboard binding highback. A case study of generative design process comparison collins y Deakin University. In: *International Conference on Design and Technology*, pp. 73–83. KEG (2017)
18. <https://www.thefabricator.com/additivereport/article/additive/generative-design-software-a-different-approach-to-designing>. Accessed 11 Apr 2020
19. <https://www.assemblymag.com/articles/94984-generative-design-software-is-transforming-the-design-process>. Accessed 12 Aug 2019
20. Tigariev, V., Salii, V., Babych, Y., Kitsenko, K.: Development of the information model support for children of patients with calculations. *Inf. Math. Methods Model.* **9**(1–2), 96–105 (2019)
21. Tigariev, V., Salii, V., Lopakov, A., Goncharenko, A.: Designing of engineering objects using the information model. *Proc. Odessa Polytech. Univ.* **2**(58), 91–96 (2019)
22. Bun, P., Trojanowska, J., Ivanov, V., Pavlenko, I.: The use of virtual reality training application to increase the effectiveness of workshops in the field of lean manufacturing. In: *4th International Conference of the Virtual and Augmented Reality in Education, VARE 2018*, pp. 65–71 (2018)
23. Ivanov, V., Pavlenko, I., Trojanowska, J., Zuban, Y., Samokhvalov, D., Bun, P.: Using the augmented reality for training engineering students. In: *4th International Conference of the Virtual and Augmented Reality in Education, VARE 2018*, pp. 57–64 (2018)



Features of Flexural-Torsional Oscillations of Cantilever Boring Bars for Fine Boring of Deep Holes with Small Diameters

Alexandr Orgiyan¹ , Gennadii Oborskyi¹ , Vitalii Ivanov² ,
Volodymyr Tonkonogyi¹ , and Anna Balaniuk¹ 

¹ Odessa Polytechnic State University,

1, Shevchenko Avenue, Odesa 65044, Ukraine

² Sumy State University, 2, Rymyskogo-Korsakova Street, Sumy 40007, Ukraine

Abstract. Coupled bending-torsional vibrations of boring cantilever bars were studied in this work concerning the fine boring of small diameter deep holes. For determining the influence of the torsional shape on the excitation of the rising level oscillations, a number of experimental and theoretical studies were carried out. As a result, the amplitudes and frequencies of flexural and torsional oscillations were determined when changing the cantilever span and length, the ratio of the amplitudes of the components of flexural and torsional oscillations. A computational analysis of the dynamic system features has been carried out in work, making it possible to assess the vibration resistance of the boring process. A dynamic model has been developed, and motion equations have been composed for stability study, which determines the processing system's performance. The calculations used the algebraic Routh – Hurwitz stability criterion. Experiments were performed using vibration cutting to reduce the oscillation level when boring small diameter deep holes.

Keywords: Vibration · Vibration stability · Boring bar · Dynamic model · Vibration cutting · Compliance

1 Introduction

Contemporary manufacturing engineering is characterized by a continuous increase in the accuracy of products with a simultaneous increase in productive efficiency. New technological research requires the solution of many issues related to studying dynamic phenomena occurring in machining. Such tasks should include, for example, the influence of dynamic interactions in the technological system on the accuracy of machining or the influence of different modes of vibration in the cutting zone on the vibration resistance of the machine. Fine boring is an advanced process method for machining precise holes with an edge tool.

Cantilever boring bars are mounted on high-precision spindle heads, ensuring the alignment of their longitudinal axis with the spindle axis. There is no “drill run-off” when boring, and the straightness of the bore axis is ensured. The basic geometric

parameters of the boring bars are cantilever part length (l) and diameter (d). The boring cutters are fitted with either carbide inserts or industrial diamonds.

Features of boring bars vibrations:

1. flexural and torsional oscillations develop during cutting;
2. when a radial force is applied to the cutter, the form of static bending coincides with the spatial form of flexural oscillations of rotating boring bars;
3. the use of boring cantilever bars is limited by low radial stiffness; for selected cutting conditions and the material being processed, the ultimate compliance at the cutter is determined, ensuring vibration resistance and tooling workability.

2 Literature Review

In this work, the review part includes the study results of cantilever boring bars oscillations, in particular, boring small diameter ($d = 10\text{--}20$ mm; $l/d > 3\text{--}8$) deep holes. The experiments aimed to study the features of joint flexural-torsional oscillations, the possibility of exciting an increasing level oscillation are presented; the relationship between the components of the amplitudes and the frequency characteristics of flexural and torsional oscillations are discussed.

It should be noted that the low process rigidity of boring cantilever bars does not allow high-quality boring of deep holes with $l/d > 4$. Using such machining, a loss of vibration resistance occurs, the cutter is damaged, and oscillations increase, while the damping factors of oscillations decrease [1]. Therefore, many studies are associated with the study of cantilever boring bar oscillations [2–4]. The number of publications based on these works' results occupies one of the top places in the dynamics of machine tools [5, 6].

To increase the boring bars' bending stiffness, they can be made of hard alloy, but the cost of the tool increases dramatically [7, 8]. Vibration dampers are another effective way to suppress oscillations of cantilever tools [9, 10]. Vibration dampers are often used when a high-quality finishing operation of fine turning shall be performed, let alone boring [11]. Vibration dampers are used significantly often when finishing fine boring. Damping vibrations when using dynamic dampers leads to a decrease in static and dynamic errors, a decrease in cutter wear, and a decrease in the roughness of the machined surface. The use of vibration dampers is especially promising under difficult machining conditions, particularly when boring deep holes of small diameter. In these cases, the use of vibration dampers during cutting makes it possible to expand the technological capabilities of the fine boring operation. At the same time, it is known that the higher the added mass, the higher the efficiency of oscillation damping. However, its value is limited by the dimensions of the boring bar structure [12].

In [13], the effective reduction of vibration was studied when using particular boring bars with built-in cores made of carbon fiber, and the boring bars are characterized by a ratio $l/d > 5 \div 10$. In [14], the study of the flexural stiffness of a rotating composite cantilever boring bar was carried out. The change in amplitudes, frequencies, and damping are provided for different technologies of composite fabrication.

The work [15] shows a vibration-resistant design of a boring unit for deep hole machining. For the efficient use of such a unit, a monitoring system (sensors), a drive system, and a control logic have been developed. Optimal actuators have been developed that damp vibration in two respects: radially when changing the cutting depth and speed direction.

In [16], theoretical and experimental studies of a boring unit designed for deep holes were carried out. The tooling model was developed for deep hole machining. Modal studies of the model and the real object were carried out in static and dynamic loading conditions [17]. Natural frequencies of oscillations, damping coefficients [18], and amplitudes in conditions of pulsed excitation, as well as dynamic stiffness, were determined [19].

A review of literary sources allows us to conclude that the results of studies of oscillations of boring cantilever rods have been widely published. However, in the technical literature, the results of studies of coupled bending-torsional vibrations of boring rods when machining deep holes of small diameter are insufficiently presented. Also, the influence of connectivity on vibration resistance is not reflected, and the characteristic frequencies and ratios of vibration levels have not been studied.

3 Research Methodology

A number of experiments were carried out to study joint bending-torsional vibrations. Samples were processed from steel 45 and cast iron SCH-18. Boring bars with diameters of 10, 12, 16, 20, 25 mm were tested with the ratio $l/d = 3, 4, 6, 8$. The recommended geometry of the cutters was adopted. Cutting modes: when boring steel - $v = 120\text{--}150$ m/min, $S = 0.04$ mm/rev, $t = 0.05\text{--}0.1$ mm; when boring cast iron SCH18 - $v = 100$ m/min, $S = 0.04$ mm/rev, $t = 0.05\text{--}0.1$ mm. Cutting edge material: T30K6 - for steel, VKZ - for cast iron. In each experiment, boring was carried out with a set of 3 cutters with the same geometry. The criterion for regrinding with a cutter is the relative radial wear and roughness of the machined surface.

In the experiments, the amplitudes of the vibrational displacements of the cutters were measured. These displacements are caused by bending in the normal (A_y) and tangential (A_z) directions to the bored holes, as well as caused by the torsion of the boring bar (A_{tors}).

Generalization of experimental studies results led to the following ratios of the components of flexural-and-torsional oscillations: $A_z = (1.1 - 1.6)A_y$, $A_{\text{tors.}} = (0.2 - 0.5)A_y$. The natural frequencies of torsional oscillations are 2–8 times higher than the flexural ones, which are in the range of 0.4–2 kHz for boring bars with a diameter of less than 20 mm. Torsional oscillations are characterized by small amplitude, and their influence on flexural vibrations is manifested at small values of the boring bar diameter (less than 12 mm).

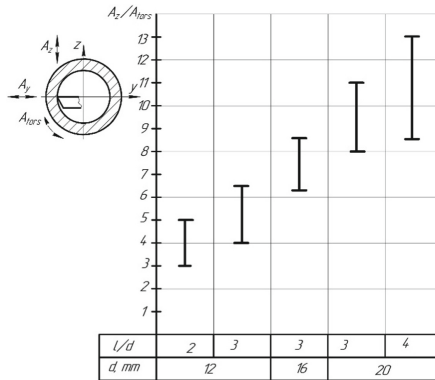


Fig. 1. The ratio of the components of bending and torsional vibrations A_z/A_{tors} and the direction of the components of vibrations.

Since A_{tors} characterizes the movement of the cutter in tangential tearing to the surface of the hole being machined during torsion of the boring bar, to compare the vibration intensity, we will also consider the tangential component A_z , that is, characterize these changes by the ratio A_z/A_{tors} (Fig. 1). Summarizing the results of the experiments, we can conclude that with a decrease in the size of boring bars at $l/d = const$, the increase in A_z occurs less intensively than the increase in A_{tors} . With a decrease in d , the boring bars of the bending and torsional vibration amplitudes increase, and the A_z/A_{tors} ratio decreases and is in the range of 4–6 when boring steel and with $d = 25$ mm - 8–12.

Figure 2 shows typical oscillograms of flexural and torsional oscillations.

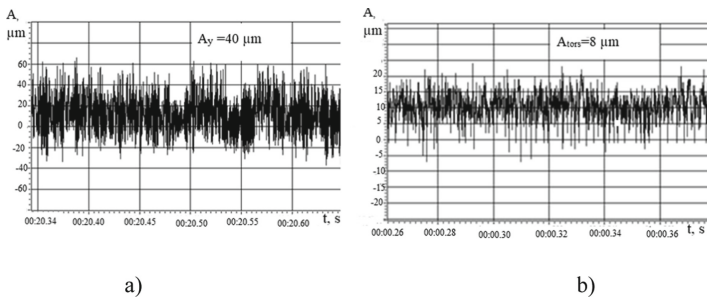


Fig. 2. Oscillograms of flexural and torsional oscillations: $v = 125$ m/min, $d = 12$ mm, $l/d = 8$, $t = 0.15$ mm, $s = 0.03$ mm/rev, steel 45 a) flexural vibrations (A_y) – natural frequency $F_{ben} = 700$ Hz; b) torsional vibrations (A_{tors}) – natural frequency $F_{tor} = 2200$ Hz.

For calculating the amplitudes of flexural-torsional oscillations, a design scheme was developed, and equations of motion were composed, which were studied for stability.

The oscillating system diagram is provided in Fig. 3.

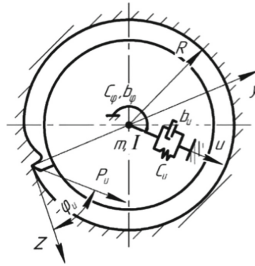


Fig. 3. Flexural-bending oscillations at boring.

The oscillation system has two degrees of freedom: displacement along the u -axis and rotation about the boring bar axis. The direction of the u -axis coincides with the direction of the cutting force. The cutting force P_u is considered constant in the direction and forms an angle φ_u with the z -axis, directed tangentially to the machined surface at the cutter tip. The mass of the system is normalized to the location of the cutter and is secured by springs. One of the springs with stiffness C_u acts along the u -axis, and the other with stiffness C_φ prevents turning. The damping coefficient of the spring with C_u stiffness will be designated as b_u , and the spring with the stiffness C_φ will be designated as b_φ .

Design analysis of the dynamic system features reflecting the interaction of joint flexural and torsional oscillations makes it possible to evaluate the vibration resistance of the boring process. A system of corresponding motion equations describes the design model provided in Fig. 2:

$$\begin{aligned} m\ddot{u} + b_u\dot{u} + c_u u &= (\cos \varphi_u + \mu \sin \varphi_u) \cdot P_z, \\ I\ddot{\varphi} + b_\varphi\dot{\varphi} + c_\varphi \varphi &= RP_z, \\ T_P\dot{P}_z + P_z &= (-k_P \sin \varphi_u)u + k_S\dot{u} + k_S R\dot{\varphi}, \end{aligned} \tag{1}$$

where m, I are the reduced mass and moment of inertia, R is the radius of the hole being features, μ is the coefficient of the chips friction on the cutter front plane, u is the movement in the direction of the vibrations developing in the system, φ is the movement in the direction of torsional oscillations, P_z is the main component of the cutting force.

The angle φ_u projects the direction of the oscillations to the direction of the main movement. With V speed, T_P is the time constant of chip formation, characterizing the inertia of the cutting process, k_S is the speed coefficient [7]. Further, we will pass to variables:

$$W = c_u \cdot u / (\cos \varphi_u + \mu \sin \varphi_u), \quad \tau = \omega_u \cdot t, \quad \alpha = c_\varphi \cdot \varphi / R, \quad \text{and to dimensionless parameters } \gamma_1 = k_P (\cos \varphi_u + \mu \sin \varphi_u) / c_u, \quad \Omega = \frac{\omega_u}{\omega_\varphi},$$

$$\beta_1 = k_S \omega_u \cos \varphi_u (\cos \varphi_u + \mu \sin \varphi_u) / c_u, \quad \beta_2 = k_S R^2 \omega_u / c_\varphi,$$

$$k_1 = b_u (m c_u)^{-\frac{1}{2}}, \quad k_2 = b_\varphi (I c_\varphi)^{-\frac{1}{2}}.$$

Considering new variables and dimensionless parameters, the equations system (1) will take the form

$$\begin{aligned} \ddot{W} + k_1 \dot{W} + W &= P_z, \\ \Omega^2 \ddot{\alpha} + \Omega \cdot k_2 \dot{\alpha} + \alpha &= P_z, \\ \theta \dot{P}_z + P_z &= -\gamma_1 W + \beta_1 \dot{W} + \beta_2 \dot{\alpha}. \end{aligned} \quad (2)$$

The system (2) solution shall be found as (p, c_i – some constants):

$$\begin{aligned} W &= c_1 e^{p\tau}, & \alpha &= c_2 e^{p\tau}, & P_z &= c_3 e^{p\tau}, \\ \dot{W} &= c_1 p e^{p\tau}, & \dot{\alpha} &= c_2 p e^{p\tau}, & \dot{P}_z &= c_3 p e^{p\tau}, \\ \ddot{W} &= c_1 p^2 e^{p\tau}, & \ddot{\alpha} &= c_2 p^2 e^{p\tau}. \end{aligned} \quad (3)$$

Substituting solution (3) in (2) after the transformations, we obtain:

$$\begin{cases} c_1 p^2 + k_1 c_1 p + c_1 = c_3 \\ c_2 (\Omega^2 p^2 + \Omega k_2 p + 1) = c_3 \\ c_3 (\theta p + 1) = c_1 (\beta_1 p - \gamma_1) + c_2 \beta_2 p. \end{cases}$$

Then, we write nonzero solution condition

$$\begin{vmatrix} p^2 + k_1 p + 1 & 0 & -1 \\ 0 & \Omega^2 p^2 + \Omega k_2 p & -1 \\ \gamma_1 - \beta_1 p & -p_2 p & \theta p + 1 \end{vmatrix} = 0 \quad (4)$$

Expanding determinant (4), we obtain the characteristic equation of system (2), from which, following the Routh-Hurwitz criterion, we obtain the values of the coefficients:

$$\begin{aligned} a_0 &= \theta \Omega^2, \\ a_1 &= \theta \Omega k_2 + \Omega^2 (1 + \theta k_1), \\ a_2 &= \theta + \Omega k_2 + (1 + \theta k_1) + \Omega^2 (\theta + k_1) - \beta_2 - \beta_1 \Omega^2, \\ a_3 &= 1 + \theta k_1 + \Omega k_2 (\theta + k_1) + \Omega^2 (1 + \gamma_1) - \beta_2 k_1 - \beta_1 k_2 \Omega, \\ a_4 &= k_1 + \theta + \Omega k_2 (1 + \gamma_1) - \beta_1 - \beta_2, \\ a_5 &= 1 + \gamma_1. \end{aligned} \quad (5)$$

The Routh-Hurwitz stability conditions have the form:

$$\begin{aligned}
 a_0 &> 0, \\
 a_1 &> 0, \\
 a_1 a_2 - a_0 a_3 &> 0, \\
 \bar{a}_1 = a_1(a_2 a_3 - a_1 a_4) - a_0(a_3^2 - a_1 a_5) &> 0, \\
 \bar{a}_2 = a_4 \bar{a}_1 - a_5 \begin{vmatrix} a_1 a_3 a_5 \\ a_0 a_2 a_4 \\ 0 a_0 a_2 \end{vmatrix} &> 0, \\
 a_5 \cdot \bar{a}_2 &> 0.
 \end{aligned} \tag{6}$$

Given the values of the coefficients, we finally obtain:

$$\begin{aligned}
 a_1 a_2 - a_0 a_3 &> 0, \\
 a_1(a_2 a_3 - a_1 a_4) - a_0(a_3^2 - a_1 a_5) &> 0, \\
 a_4 \bar{a}_1 - a_5(a_1(a_2^2 - a_0 a_4) - a_0(a_3 a_2 - a_0 a_5)) &> 0.
 \end{aligned} \tag{7}$$

4 Results

A PC program has been developed to calculate vibration resistance by the Routh-Hurwitz criterion. An example of calculation results using the Routh-Hurwitz criterion is presented in Table 1.

In the program, the search for stable values of the dimensionless seven parameters is based on: 1) the initial values of the parameters; 2) Routh-Hurwitz stability conditions in the form of a system of three algebraic inequalities (7). If, after substituting the initial values of the parameters, all the left-hand sides of the three inequalities are positive, then the boring bar is stable. If at least one of the left-hand sides of the three inequalities is negative, we conclude that there is instability at the initial values of the parameters. Then, a search is carried out for such a value of one of the parameters (for example) with fixed values of other parameters, which corresponds to the stability conditions. Increasing or decreasing the parameter's value is performed with a certain step to determine the sign of the results of calculations of the left sides of the three inequalities.

Table 1 presents the initial design parameters of the boring bars. Lines 1–7 contain the values of the parameters that ensure the position of the setpoint on the stability boundary, and the calculations are presented sequentially, starting with the parameter θ (the first line), then the parameter Ω (the second line), up to the parameter γ (the seventh line).

Table 1. Calculations of vibration resistance for boring bar $d = 12$ mm, $l/d = 3$ ($t = 0.1$ mm, $n = 2.500 \text{ min}^{-1}$, $s = 0.03$ mm/rev, steel 45).

ψ	θ	Ω	k_1	k_2	β_1	β_2	γ	Areas of stable solutions for:	
Source data	0.5	0.125	0.1	0.08	0.05	0.56	0.035	Not stable	
Setpoints numbers	1	1.362	0.125	0.1	0.08	0.05	0.56	0.035	$\theta > 1,362$
	2	1.362	0.126	0.1	0.08	0.05	0.56	0.035	$\Omega < 0,124$
	3	1.362	0.126	0.11	0.08	0.05	0.56	0.035	$k_1 > 0,11$
	4	1.362	0.126	0.11	0.085	0.05	0.56	0.035	$k_2 > 0,8$
	5	1.362	0.126	0.11	0.085	0.051	0.56	0.035	$\beta_1 > 0,051$
	6	1.362	0.126	0.11	0.085	0.051	0.55	0.035	$\beta_2 < 0,56$
	7	1.362	0.126	0.11	0.085	0.051	0.55	0.034	$\gamma < 0,034$

Thus, the first line contains the boundary value θ , ensuring that the setpoint belongs to the stability boundary with constant other parameters. Similarly, in the second line, the boundary value is found Ω ; the last column provides the values of all parameters that ensure the stability region by the Routh-Hurwitz criterion.

The criterion does not allow us to delineate the mutual influence of oscillation modes, although it gives an unambiguous answer concerning the stability of the solutions. After studying the joint flexural-torsional oscillations, it can be concluded that with an increase in the stability and diameter of the boring bars, the connection between these oscillation modes is weak, and the amplitudes of flexural oscillations are much greater than the torsional ones. The A_z/A_{tor} ratio grows with the increase in the boring bar diameter. The results of experiments and calculations indicate that the development of intense oscillation levels in the course of boring does not depend on the coincidence of the natural frequencies of the flexural and torsion forms and their multiplicity. Torsional oscillations on flexural ones occur at small diameters of boring cantilever bars, less than 12 mm. This influence is determined by the fact that with a decrease in the diameter of the boring bar, the coefficients of flexural oscillations coupling with PR (γ) significantly decrease, while the coefficients of torsional oscillations coupling (β_2) with PR increase.

Using the coupling of oscillation modes, the effect of forced oscillations in the axial direction on oscillations normal to the work surface was studied in this work. Methods of vibration cutting have been studied in a number of works based on the possibility of oscillations damping of one form by superimposing oscillating vibrations with specific parameters of another form [6].

To carry out experiments to determine the parameters of forced oscillations and the interaction of oscillation modes, a vibration stand [1] was developed. In the experiments, vibration processing modes were revealed that provide a significant decrease in the amplitudes of flexural oscillations under the action of periodic axial disturbances (Fig. 3), and the oscillation amplitudes decrease by 2–3 times (Fig. 4).

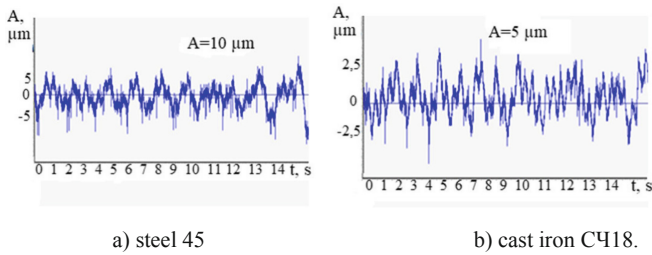


Fig. 4. Flexural oscillations oscillograms for axial vibrations application: $f_{ax} = 22\ \text{Hz}$, $f_{vibm} = 20\ \text{Hz}$, $d = 12\ \text{mm}$, $l/d = 8$, $t = 0.1\ \text{mm}$, $s = 0.03\ \text{mm/rev}$, axial amplitude $A_{ax} = 0.2\ \text{mm}$.

5 Conclusions

In the experiments, the relationships between the components of the vibration amplitudes were established: $A_z = (1.1-1.6)A_y$, $A_{tors} = (0.2-0.5)A_y$, and A_z/A_y changes little, and A_{tors}/A_y decreases noticeably with an increase the diameter of the boring bar. The calculation results show that with a decrease in the diameter of the boring bar, the coefficients of connectivity of bending displacements with the cutting process (γ) become significantly less than their boundary values, and the coefficients of connectivity of angular displacements (β_2) increase, reaching their boundary values.

A dynamic model has been developed that describes coupled flexural-torsional oscillations to calculate oscillations amplitudes. A PC program was developed to solve the equations system, and the vibration resistance of a closed dynamic system was calculated under the Routh-Hurwitz criterion. The results of experiments and calculations indicate that the development of intense oscillation levels does not depend on the coincidence of the natural frequencies of flexural and torsional forms and their multiplicity. The influence of torsional oscillations on flexural ones is manifested for boring bars with a diameter of less than 12 mm. Using the ultimate compliance criterion, vibration resistance during cutting for boring bars with $d > 12\ \text{mm}$ without considering the coupling of flexural and torsional oscillations can be predicted.

An effective reduction in the oscillation level (by 2–3 times) when boring deep holes with $l/d > 3$ was achieved by imposing additional oscillating vibrations with specific parameters on flexural ones.

Further, studies of errors in fine boring will be carried out based on the obtained experimental and theoretical results.

Acknowledgments. The authors appreciate the support of the International Association for Technological Development and Innovations. The research has been carried out to fulfill the objectives of the perspective development plan within the scientific direction “Technical Sciences” at Sumy State University.


References

1. Oborskyi, G., Orgiyan, A., Tonkonogyi, V., Aymen, A., Balaniuk, A.: Study of dynamic impacts at combined operations of the thin turning and boring. In: Tonkonogyi, V., et al. (eds.) *InterPartner 2019*. LNME, pp. 226–235. Springer, Cham (2020). https://doi.org/10.1007/978-3-030-40724-7_23
2. Siddhpura, M., Paurobally, R.: Experimental investigation of chatter vibrations in facing and turning processes. *Int. J. Mech. Aerosp. Ind. Mechatron. Manuf. Eng.* **7**(6), 968–973 (2013)
3. Lebedev, V.A., Solomiichuk, T.G., Novykov, S.V.: Study of a welding pool harmonic oscillations influence on the welded metal hardness and weld bead width. *J. Eng. Sci.* **6**(1), C16–C21 (2019). [https://doi.org/10.21272/jes.2019.6\(1\).c4](https://doi.org/10.21272/jes.2019.6(1).c4)
4. Pavlenko, I., et al.: Parameter identification of cutting forces in crankshaft grinding using artificial neural networks. *Materials* **13**(23), 5357 (2020). <https://doi.org/10.3390/ma13235357>
5. Ostling, D., Tormod, I., Tjomsland, M., Standal, O., Mugaas, N.: Cutting process monitoring with an instrumented boring bar measuring cutting force and vibration. *Procedia GIRP* **77**, 235–238 (2018). <https://doi.org/10.1016/j.procir.2018.09.004>
6. Ivanov, V., Pavlenko, I., Liaposhchenko, O., Gusak, O., Pavlenko, V.: Determination of contact points between workpiece and fixture elements as a tool for augmented reality in fixture design. *Wireless Netw.* **27**(3), 1657–1664 (2019). <https://doi.org/10.1007/s11276-019-02026-2>
7. Mohan, E., Mamundi Azaath, L., Marichamy, S., Dhinakaran, V.: The effect of impact damper on vibration control in internal turning operation. *AIP Conf. Proc.* **2283**, 020061 (2020). <https://doi.org/10.1063/5.0025023>
8. Shvets, S.V., Astakhov, V.P.: Effect of insert angles on cutting tool geometry. *J. Eng. Sci.* **7**(2), A1–A6 (2020). [https://doi.org/10.21272/jes.2020.7\(2\).a1](https://doi.org/10.21272/jes.2020.7(2).a1)
9. Fallah, M., Moetakef-Imani, B.: Investigation on nonlinear dynamics and active control of boring bar chatter. *J. Braz. Soc. Mech. Sci. Eng.* **43**(3), 1–27 (2021). <https://doi.org/10.1007/s40430-021-02808-w>
10. Vishal, K., Saravanamurugan, S., Sanjeev, K., Yedhu, K., Iswar, G., Shanmughasundaram, A.: Vibration control in boring process using a constrained viscoelastic layer damper. *IOP Conf. Ser.: Mater. Sci. Eng.* **1059**, 012031 (2021)
11. Patil, R., Jadhav, S.: Boring parameters optimization for minimum surface roughness using CNC boring machine with passive damping material. In: *2nd International Conference for Convergence in Technology*, pp. 300–303 (2017). <https://doi.org/10.1109/I2CT.2017.8226140>
12. Kobelev, V.: Efficiency of one- and two-element dynamic vibration dampers. In: *Proceedings of the Odessa Polytechnic University*, vol. 2, pp. 7–10 (2008)
13. Thorenz, B., Friedrich, M., Westermann, H.-H., Döpfer, F.: Evaluation of the influence of different inner cores on the dynamic behavior of boring bars. *Procedia CIRP* **81**, 1171–1176 (2019)
14. Ren, Y., Zhao, Q., Liu, Y., Ma, J.: Analysis of bending vibration characteristics of rotating composite boring bar. *J. Phys.: Conf. Ser.* **1303**(1), 012147 (2019)
15. Grossi, N., Croppi, L., Scippa, A., Campatelli, G.: A dedicated design strategy for active boring bar. *Appl. Sci. (Switz.)* **9**(17), 3541 (2019)
16. Kepczak, N., Bechciński, G., Rosik, R.: Experimental verification of the deep hole boring bar model. *Eksplotacja i Niezawodność – Maintenance and Reliability* **23**(1), 55–62 (2021)

17. Ganapathy, R., Saravanamurugan, S.: Regenerative chatter control in turning process using constrained viscoelastic vibration absorber. *IOP Conf. Ser.: Mater. Sci. Eng.* **577**(1), 012152 (2019)
18. Rubio, L., Loya, J., Miguélez, M., Fernández-Sáez, J.: Optimization of passive vibration absorbers to reduce chatter in boring. *Mech. Syst. Signal Process.* **41**(1–2), 691–704 (2013)
19. Saleh, A., Nejatpour, M., Yagci Acar, H., Lazoglu, I.: A new magnetorheological damper for chatter stability of boring tools. *J. Mater. Process. Technol.* **289**, 116931 (2021). <https://doi.org/10.1016/j.jmatprotec.2020.116931>



Mathematical Model of a Backlash Elimination in the New Clamping Mechanism

Borys Prydalnyi^(✉) 

Lutsk National Technical University, 75, Lvivska Street, Lutsk 43018, Ukraine
b.prydalnyi@lutsk-ntu.com.ua

Abstract. A theoretical model of the operation of the electromechanical mechanism for clamping cylindrical workpieces and tools on the spindle of metalworking machines during backlash elimination is considered. The considered design of the clamping mechanism is driven by an electric motor and has many advantages. Based on the model, analytical dependencies are proposed that describe the relationship between the movements of the elements of the mechanism during the first stage of the clamping process. The proposed analytical dependencies allow taking into account stages of the mechanism's functioning when the forces of dissipative characters prevail in its work. The presented dependencies describe the position of the elements of the machine depending on the generalized coordinate, which is the angle of rotation of the electric motor rotor. It allows determining the position of the elements of the mechanism depending on time. The obtained dependencies are a precondition for developing methods for optimizing the design of mechanisms of this type.

Keywords: Clamping mechanism · Kinematic parameters · Model

1 Introduction

As is known, the machining of workpieces requires relative motion between the workpiece and the tool and their force interaction. To transfer the shape-forming movements to workpieces or tools, it is necessary to fix them in a spindle assembly of the machine. Clamping mechanisms (CM) are used for this purpose. The characteristics of CM determine the possibility of using the maximum cutting speed and feed rate and consequently determine productivity and quality of the machining [1]. The magnitude of clamping forces determines the maximum value of the cutting forces that occur during machining. CM of the machines are located on the spindle and are part of the spindle assembly. Hence, requirements for CM are concerning possibilities of creating the required amount of clamping force for a minimum time, ensuring its stability in different modes of operation of the spindle assembly. Therefore, the design features of the CM have a significant impact on the characteristics of the whole spindle assembly as well. That determines the value of resonance (critical) frequency rotation, the possibility of accurate balancing [2] and keeping a balanced state during a given period of operation, etc.

2 Literature Review

There are several types of CM with mechanical and hydraulic converters of supplied energy. All the types have many disadvantages, including those caused by the presence of movable elements or working medium that can move in the radial direction under the action of centrifugal forces. It leads to a deterioration in the performance of the CM and the spindle assembly as a whole. Modern CM are subject to a number of requirements related to the possibility of their operation in the automatic machining cycle on CNC machines, the efficiency of control and regulation of the clamping force in real-time, reliability, energy efficiency, etc. To eliminate the above shortcomings, the design of the electromechanical clamping mechanism with collet chuck has been created (UA Patent No. 95323). The design does not contain elements that are movable in the radial direction. The use of an electric drive expands the possibilities for creating an effective control system of the new CM. Moreover, since it does not require creating special mechanical (hydraulic) subsystems in the machine for powering the new CM, it provides additional opportunities to design machines. It makes it especially easier to implement the new electromechanical CM into structures of new and existing machines.

The characteristics of CM determine the work characteristics of spindle assemblies and consequently productivity and quality of the machining. There are several studies related to the modeling of the processes of spindle assemblies as a whole without separation the dependencies that describe the operation characteristic of the clamping mechanism. There are studies concerning the operation of the clamping chuck [3]. The paper [4] targets a new design of a spindle system with an additional electromagnetic bearing. The paper [5] proposes modeling of spindle-holder assembly and investigates the contact characteristic under clamping and centrifugal forces. Thermal influence on spindle efficiency is considered in [6]. Influences of the axial depth of cut, the machining toolpath, and the initial clamping force on part distortion are shown in [7]. In [8], the method which allows knowing the clamping force from the torque applied by a dynamometric wrench is developed. In the research work [9], the method of cooling can be improved significantly by employing a model-based control strategy on a recirculation cooler unit. The paper [10] points out potential directions to consider when optimizing optimal sustainability performance. In [11], the research of characteristics of the electric motor operates as a part of the clamping mechanism with the corresponding type of load and the locking (stop-braking) mode of operation has been conducted. In the paper [12], a thermal compensation model is developed in a linear regression framework. A mathematical model of the genetic algorithm optimization design of the spindle is established in [13] according to the actual use of the spindle. The influence of the tool's characteristics [14] and the workpiece [15] on the quality of processing is also considered. In the study [16], variations of the mode shapes of the tool-spindle assembly at high spindle speeds are examined using numerical models, and hypotheses are formulated. Identification of interdependences of movement of the elements of the proposed CM is a prerequisite for optimizing its characteristics and consequently for improving the machining.

3 Research Methodology

The operation of the CM is based on the work of an electric motor (see Fig. 1) whose stator is attached to the body of the machine, and the rotor is located on the threaded surface of the spindle. The rotor and spindle form a screw-type transmission, and during the rotor rotation, its axial movement is used to tighten the collet chuck for clamping the workpiece. The rotor (nut) rotation with an angular velocity ω_∂ provides its axial motion with speed V_m transmitted to the tie-rod of the collet.

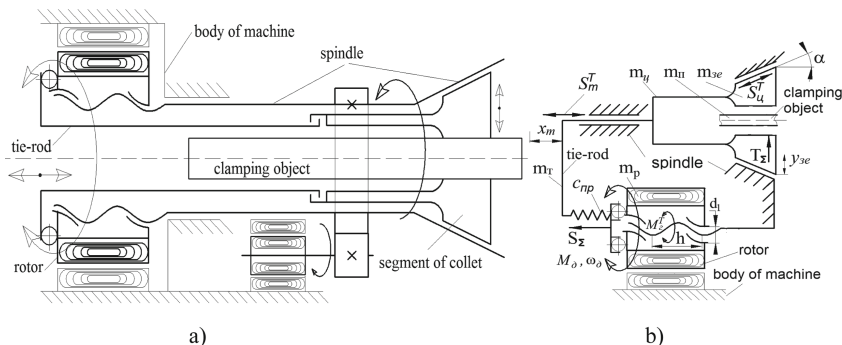


Fig. 1. Constructive scheme of CM (a) and scheme for the calculation of parameters (b).

The clamping process can be conditionally divided into two stages according to the type of forces (dissipative or potential) acting in this CM at a certain stage of the clamping process:

- backlash elimination in the CM – only active dissipative forces act;
- creation of mechanical stress (tension) – the action of potential forces prevails due to significant deformation of an elastic system of the mechanism with insignificant forces of dissipative character.

The relationships among the kinematic parameters of the proposed CM design can be identified based on the equality between the ratio of the angle ϕ_∂ of the engine rotor rotation and the axial movement x_m of the tie-rod connected to the collet.

$$x_m = \frac{\phi_\partial \cdot h}{2\Pi} \tag{1}$$

where h – the pitch of the thread. After differentiation of Eq. (1) regarding time t , we obtain $\frac{\partial x_m}{\partial t} = \frac{\partial \phi_\partial}{\partial t} \cdot \frac{h}{2\Pi}$ and

$$V_m = \omega_\partial \cdot \frac{h}{2\Pi} = 0,5\omega_\partial \frac{h}{\Pi} = \omega_\partial \cdot 0,5d_1 \cdot tg\psi \tag{2}$$

where d_1 – the diameter of the thread, Ψ – the angle of rising of the thread. After representing $0,5d_1 \cdot tg\psi = i_z$ and putting into (2), we get $V_m = \omega_\partial \cdot i_z$ or

$$V_m = \dot{\phi} \cdot i_z. \quad (3)$$

The movement of the collet in the axial direction with speed V_m provides radial movement of its clamping segments with speed V_{3e} . The correlation between V_m and V_{3e} can be found based on the equality between the ratios of the axial displacement x_m of the tie-rod with collet and the radial displacement y_{3e} of the clamping segments $x_m = y_{3e} \cdot ctg\alpha$. From this dependence, it follows that

$$y_{3e} = \frac{x_m}{ctg\alpha}, \quad (4)$$

$\frac{\partial x_m}{\partial t} = \frac{\partial y_{3e}}{\partial t} \cdot ctg\alpha$, $V_m = V_{3e} \cdot ctg\alpha$, α – half the angle of a collet cone, $ctg\alpha = i_u$ then

$$V_{3e} = \frac{V_m}{i_u}. \quad (5)$$

After we put (3) in (5).

$$V_{3e} = \frac{\dot{\phi} \cdot i_z}{i_u} = \dot{\phi} \frac{i_z}{i_u} \quad (6)$$

The frictional torque M_z^T in the screw transmission appears from the tangential component F_t of the friction forces with the arm $0,5d_1$. The force F_t depends on the axial load S_Σ acting from the clamping chuck $F_t = S_\Sigma \cdot tg\phi^T$, where ϕ^T – the angle of friction in the threaded connection.

$$M_z^T = 0,5 \cdot d_1 \cdot S_\Sigma \cdot tg\phi^T \quad (7)$$

The friction force S_u^T in the conical coupling of the collet and the spindle with angle 2α is determined from the expression

$$S_u^T = \frac{z \cdot S_\Sigma}{\cos \alpha + (\sin \alpha)/f_u} \quad (8)$$

where z – the number of collet clamping segments; f_u – coefficient of friction in the conical coupling of the collet and the spindle.

The friction force S_m^T in the coupling of the tie-rod and the spindle is determined from the expression

$$S_m^T = g \cdot m_2 \cdot f_m \quad (9)$$

where g – free-fall acceleration; $m_2 = m_m + m_n$ – mass equal to the sum of the masses of the tie-rod and object of clamping; f_m – coefficient of friction in the coupling of the tie-rod with the spindle.

The considered mechanism has one degree of freedom ϕ_∂ – the angle of rotation of the rotor on which the position of the elements of the CM depends. The angle ϕ_∂ is taken as a generalized coordinate relative to which the differential equation of motion of the system – the Lagrange's equations of the 2nd kind is composed

$$\frac{d}{dt} \left(\frac{\partial E}{\partial \dot{\phi}_\partial} \right) - \frac{\partial E}{\partial \phi_\partial} = M_\Pi \quad (10)$$

E – is the kinetic energy of the mechanism; M_Π – generalized force, which in this case is equal to the main torque of external forces relative to the axis of the rotor rotation; t – time.

At both stages of working the CM, its kinetic energy E does not depend on the angle ϕ_∂ of the rotor rotation, so the partial derivative of the kinetic energy E on the angle ϕ_∂ is

$$\frac{\partial E}{\partial \phi_\partial} = 0. \quad (11)$$

For the conditionally selected first stage of operation of the CM, when at the stage of backlash elimination there are only non-conservative (non-potential) forces, the Lagrange Eq. (10) considering (11) takes the form.

$$\frac{d}{dt} \left(\frac{\partial E}{\partial \dot{\phi}_\partial} \right) = M_\Pi \quad (12)$$

The kinetic energy E of the CM is equal to the sum of the kinetic energies of its elements and is determined by the expression

$$E = J_\partial \frac{\dot{\phi}_\partial^2}{2} + m_1 \frac{V_m^2}{2} + m_{3e} \frac{V_{3e}^2}{2} \quad (13)$$

where $m_1 = m_p + m_m + m_u + m_n$, J_∂ – the moment of the rotor inertia relative to the axis of rotation; ϕ_∂ – the rotation angle of the rotor; V_m, V_{3e} – linear velocity of the tie-rod (and other elements with which it has the possibility of direct force interaction), the movement of the clamping segments in the radial direction; m_p, m_m, m_u, m_n – respectively, the mass of the rotor, tie-rod, collet and clamping object (assumed that the clamping object at the time of the clamping moves with the collet); m_{3e} – the mass of the clamping jaws, which move radially during clamping.

After (3) and (6) put in (13) $E = J_\partial \frac{\dot{\phi}_\partial^2}{2} + m_1 \frac{\dot{\phi}_\partial^2}{2} i_z^2 + m_{3e} \frac{\dot{\phi}_\partial^2}{2} \left(\frac{i_z}{i_u} \right)^2$

$$E = \frac{\dot{\phi}_{\partial}^2}{2} \left[J_{\partial} + m_1 i_z^2 + m_{3e} \left(\frac{i_z}{i_u} \right)^2 \right] = \frac{\dot{\phi}_{\partial}^2}{2} J_{\Pi}. \quad (14)$$

In Eq. (14), the value in square brackets is the moment of inertia J_{Π} of the CM reduced to the motor rotor.

$$J_{\Pi} = \left[J_{\partial} + m_1 i_z^2 + m_{3e} \left(\frac{i_z}{i_u} \right)^2 \right] \quad (15)$$

Therefore (13) takes the form.

$$E = \frac{\dot{\phi}_{\partial}^2}{2} J_{\Pi} \quad (16)$$

The partial derivative of the kinetic energy E (16) expression at the generalized velocity $\dot{\phi}_{\partial}$ has the form $\frac{\partial E}{\partial \dot{\phi}_{\partial}} = \dot{\phi}_{\partial} J_{\Pi}$. Since in the previous expression, when changing the time t changes only the angle ϕ_{∂} , the time derivative of the partial derivative of the previous expression will be equal to

$$\frac{d}{dt} \left(\frac{\partial E}{\partial \dot{\phi}_{\partial}} \right) = \ddot{\phi}_{\partial} J_{\Pi}. \quad (17)$$

According to (17), expression (12) can be written in the following form.

$$\ddot{\phi}_{\partial} J_{\Pi} = M_{\Pi} \quad (18)$$

The generalized force M_{Π} (as the reduced moment) can be determined, taking into account the friction in the CM on the condition of equality of elementary works of forces acting in the mechanism as virtual works of active forces on small displacements

$$M_{\Pi} \delta \phi_{\partial} = M_{\partial} \delta \phi_{\partial} - M_z^T \delta \phi_{\partial} - \delta x_m (S_m^T + S_u^T + S_{nu}) - T_{\Sigma} \frac{1}{3} \delta y_{3e} \quad (19)$$

where M_z^T and S_m^T , S_u^T , S_{nu}^T – the torque of friction forces in the screw transmission and the friction forces in the couplings respectively: the tie-rod with the spindle; the cone of the collet with the cone of the spindle; a clamping object with the feed collet; T_{Σ} – clamping force; $\delta \phi_{\partial}$ and, δx_m , δy_{3e} – the elementary angle of rotation in the direction of action M_z^T and movement in the direction of action, respectively S_m^T, T_{Σ} .

In dependencies (19), to simplify the calculations, the following assumptions are made. Due to the insignificant value of the angle α , the value of the relative displacement of the cone surfaces of the collet and the spindle is equal to the magnitude of

the stroke of the tie-rod δx_m . The part of the radial displacement of the clamping segment, which determines the effective work on the clamping of the workpiece (deformations in contacts of adjoining the surfaces of a clamping segment and an object of clamping) with force T_Σ is less than the total value of the radial displacement y_{3e} of the clamping segment during the clamping process. It depends on conditions of adjoining the surfaces of a clamping segment and an object of clamping. Therefore, in (19), the value of the radial displacement of the clamping segment during the action of force T_Σ and increasing mechanical tension in the coupling of a clamping segment and an object of clamping is conditionally assumed to be equal $0.3y_{3e}$. Some possible exaggeration of the value of work from the action of the force T_Σ , which resulting from this assumption, is partially offset in the overall balance of elementary works (8) by the presence of other elementary works (energy losses) that inevitably exist during the operation of the real CM.

4 Results

The relationship between the elementary angle $\delta\phi_\partial$ of rotation of the rotor and the displacements $\delta x_m = \delta\phi_\partial \frac{h}{2\Pi}$ is represented by analogy with (1) (4) $\delta y_{3e} = \delta\phi_\partial \frac{h}{2\Pi} \cdot tg\alpha$. The forces included in (19) are presented in (7) (8) (9). The force of pushing the workpiece through the feed collet is determined from the expression $S_{nu} = P_{nu}(1 + K\Delta d)$, where P_{nu} – the pushing force of the workpiece with a diameter equal to the diameter of the hole in the feed collet; $K = A/P_{nu}$ – coefficient of proportionality; A – change of force of pushing of a workpiece at the change of its diameter on each 0.2 -mm. After putting (7), (8), and (9) into (19), we get

$$M_\Pi = M_\partial - 0,5d_1S_\Sigma tg\phi^T - \frac{h}{2\Pi} \left(gm_2f_m + \frac{zS_\Sigma}{\cos\alpha + \sin\alpha/f_u} + P_{nu}(1 + K\Delta d) \right) - T_\Sigma \left(\frac{1}{3} \frac{h}{2\Pi} tg\alpha \right) \quad (20)$$

where $S_\Sigma = \frac{2M_\partial}{d_1tg\psi} \cdot \frac{h}{\Pi} = d_1tg\psi$.

Dependence (10) describes the system of non-conservative forces of the CM because of the absence of elastic forces at the stage of backlash elimination, and it makes it possible to make assumptions that before the appearance of tension, the dependence $T_\Sigma = T_\Sigma^0 = k \cdot y_{3e}$ is linear. There is a slight increase of T_Σ^0 with magnification y_{3e} (small angle of the graph of the function), where k – a constant value that reflects the intensity of increasing the clamping force from the radial movement of a clamping segment and can be selected following the operating conditions of the CM.

$$M_\Pi = M_\partial \left(1 - \frac{tg\phi^T}{tg\psi} - \frac{z}{\cos\alpha + \sin\alpha/f_u} \right) - \frac{h}{2\Pi} (gm_2f_m + P_{nu}(1 + K\Delta d)) - T_\Sigma^0 \frac{h}{6\Pi} tg\alpha \quad (21)$$

Considering (4) $T_{\Sigma}^0 = \phi_{\partial} \frac{k \cdot h}{2\Pi} tg\alpha$ and $\frac{h}{\Pi} = d_1 tg\psi$ are put into (21) and two first summands that do not contain variables are denoted by symbols β_1 .

$$\theta_1 = M_{\partial} \left(1 - \frac{tg\phi^T}{tg\psi} - \frac{z}{\cos\alpha + \sin\alpha/f_u} \right) - \frac{h}{2\Pi} (gm_2 f_m + P_{nu}(1 + K\Delta d)) \quad (22)$$

$$\beta_1 = -\frac{k \cdot h^2}{12\pi^2} tg^2\alpha = -\frac{k}{12} d_1^2 tg^2\psi \cdot tg^2\alpha \quad (23)$$

$$M_{\Pi} = \theta_1 + \beta_1 \phi_{\partial} \quad (24)$$

Substituting (24) for (18), we obtain a differential equation of the following form.

$$\ddot{\phi}_{\partial} J_{\Pi} = \theta_1 + \beta_1 \phi_{\partial} \quad (25)$$

Reassignment in (25) $\theta = \frac{\theta_1}{J_{\Pi}}$ and $\beta = \frac{\beta_1}{J_{\Pi}}$.

$$\ddot{\phi}_{\partial} = \theta + \beta \phi_{\partial} \quad (26)$$

When $\frac{d\phi_{\partial}}{dt} = \omega$ then $\frac{d^2\phi_{\partial}}{dt^2} = \frac{d\omega}{dt} = \frac{d\omega}{d\phi_{\partial}} \cdot \frac{d\phi_{\partial}}{dt} = \frac{d\omega}{d\phi_{\partial}} \omega$ and consequently $\frac{d\omega}{d\phi_{\partial}} \omega = \theta + \beta \phi_{\partial}$; $\int \omega d\omega = \int (\theta + \beta \phi_{\partial}) d\phi_{\partial}$; $\frac{\omega^2}{2} = \theta \phi_{\partial} + \beta \frac{\phi_{\partial}^2}{2} + C_1$. The constant of integration C_1 is defined from initial conditions. At the initial moment of time, the speed of the rotor relative to the spindle is equal to zero (but the rotor relative to the stator can rotate with the velocity of the spindle) $\phi_{\partial} = 0$, $\omega = 0$, $C_1 = 0$ consequently $\frac{d\phi_{\partial}}{dt} = \sqrt{\beta \phi_{\partial}^2 + 2\theta \phi_{\partial}}$ or $\int \frac{d\phi_{\partial}}{\sqrt{\beta \phi_{\partial}^2 + 2\theta \phi_{\partial}}} = \int dt + C_2'$ and $\int \frac{d\phi_{\partial}}{\sqrt{\beta \phi_{\partial}^2 + 2\theta \phi_{\partial}}} = \frac{1}{\sqrt{\beta}} \ln \left[2\beta \phi_{\partial} + 2\theta + 2\sqrt{2\theta\beta \phi_{\partial} + \beta^2 \phi_{\partial}^2} \right]$. The solution of the previous equation can be written as follows $\ln \left[2\beta \phi_{\partial} + 2\theta + 2\sqrt{2\theta\beta \phi_{\partial} + \beta^2 \phi_{\partial}^2} \right] = \sqrt{\beta} \cdot t + C_2$. The constant C_2 can be found from the initial condition when $t = 0$, $\phi_{\partial} = 0$. Consequently $\ln 2\theta = C_2$. Substitute in the previous expression $\frac{\beta}{\theta} \phi_{\partial} + \sqrt{2\frac{\beta}{\theta} \phi_{\partial} + \frac{\beta^2}{\theta^2} \phi_{\partial}^2} = e^{\sqrt{\beta} \cdot t} - 1$.

$$\phi_{\partial} = \frac{\left(e^{\sqrt{\beta} \cdot t} - 1 \right)^2}{2\frac{\beta}{\theta} e^{\sqrt{\beta} \cdot t}} \quad (27)$$

The value β is characteristic because its positive values determine the monotonic increase of the function (27) and in the case of negative values – local declines and rises (fluctuations) are possible. Equation (27) describes the dependence of the generalized coordinate ϕ_{∂} on time at the stage of elimination of backlashes (under the action of non-conservative forces) in the CM, which makes it possible to determine

motion characteristics of the CM elements through dependences describing their position depending on ϕ_∂ .

5 Conclusions

The presented researches are a part of researches on a new patented design of the clamping mechanism. The received mathematical dependencies reflect the influence on the operation of the mechanism of forces of friction, mass, and geometrical characteristics of its elements at the stage of backlash elimination. Obtained formula (27) describes the dependence of the generalized coordinate ϕ_∂ on-time t and shows, for example, that the decrease in mass m_2 , friction force f_m , and angle α causes an increase in value θ_1 and, as a result, increase values θ and ϕ_∂ . It means increasing the movement speed of the elements and reducing the time on the backlash elimination process. The mathematical model can be used to calculate parameters of the mechanism's elements to provide performance characteristics and is a prerequisite for the possibility of design optimizing.






References

1. Bouchareb, A., Lagred, A., Amirat, A.: Effect of the interaction between depth of cut and height-to-width ratio of a workpiece on vibration amplitude during face milling of C45 steel. *The Int. J. Adv. Manuf. Technol.* **104**(1–4), 1221–1227 (2019). <https://doi.org/10.1007/s00170-019-03944-3>
2. Zhang, L., Zha, J., Zou, C., Chen, X., Chen, Y.: A new method for field dynamic balancing of rigid motorized spindles based on real-time position data of CNC machine tools. *The Int. J. Adv. Manuf. Technol.* **102**(5–8), 1181–1191 (2018). <https://doi.org/10.1007/s00170-018-2953-2>
3. Thorenz, B., Westermann, H.-H., Kafara, M., Nützel, M., Steinhilper, R.: Evaluation of the influence of different clamping chuck types on energy consumption, tool wear and surface qualities in milling operations. *Procedia Manuf.* **21**, 575–582 (2018)
4. Koriath, H.-J., Glänzel, M., Bogachev, Y., Sakharova, O., Esov, V.: Investigation of adaptive spindle system with active electromagnetic bearing. *Procedia CIRP* **46**, 379–382 (2016)
5. Wan, S., Hong, J., Du, F., Fang, B., Li, X.: Modelling and characteristic investigation of spindle-holder assembly under clamping and centrifugal forces. *J. Mech. Sci. Technol.* **33** (5), 2397–2405 (2019). <https://doi.org/10.1007/s12206-019-0438-3>
6. Liu, T., Gao, W., Zhang, D., Tian, Y.: Analytical modeling for thermal errors of motorized spindle unit. *Int. J. Mach. Tools Manuf.* **112**, 53–70 (2017)
7. Cherif, I., Outeiro, J., Cotton, D., Poulachon, G., Brosse, A.: Effects of toolpath and clamping strategies in machining distortion of stainless-steel parts. *Procedia CIRP* **82**, 427–431 (2019)
8. Estrems, M., Arizmendi, M., Cumbicus, W.E., López, A.: Measurement of clamping forces in a 3 jaw chuck through an instrumented aluminium ring. *Procedia Eng.* **132**, 456–463 (2015)
9. Grama, S.N., Mathur, A., Badhe, A.N.: A model-based cooling strategy for motorized spindle to reduce thermal errors. *Int. J. Mach. Tools Manuf.* **132**, 3–16 (2018)

10. Lu, T., Kudaravalli, R., Georgiou, G.: Cryogenic machining through the spindle and tool for improved machining process performance and sustainability: Pt. II, Sustainability performance study. *Procedia Manuf.* **21**, 273–280 (2018)
11. Prydalnyi, B.: Characteristics of electromechanical clamping mechanism with asynchronous electric motor. In: 2020 International Conference Mechatronic Systems and Materials (MSM), pp. 1–5 (2020). <https://doi.org/10.1109/MSM49833.2020.9202186>
12. Grama, S.N., Mathur, A., Aralaguppi, R., Subramanian, T.: Optimization of high speed machine tool spindle to minimize thermal distortion. *Procedia CIRP* **58**, 457–462 (2017)
13. Xu, Z., Liu, Y., Xie, H., Tian, P.: Application of an improved genetic algorithm in the optimization design of NC machine tool spindle. In: 2018 Chinese Control And Decision Conference (CCDC), pp. 4361–4365. Shenyang (2018)
14. Corne, R., Nath, C., Mansori, M.E., Kurfess, T.: Enhancing spindle power data application with neural network for real-time tool wear/breakage prediction during inconel drilling. *Procedia Manuf.* **5**, 1–14 (2016)
15. Wu, Q., Sun, Y., Chen, W., Chen, G.: Theoretical and experimental investigation of spindle axial drift and its effect on surface topography in ultra-precision diamond turning. *Int. J. Mach. Tools Manuf.* **116**, 107–113 (2017)
16. Özşahin, O., Ritou, M., Budak, E., Rabréau, C., Le Loch, S.: Identification of spindle dynamics by receptance coupling for non-contact excitation system. *Procedia CIRP* **82**, 273–278 (2019)



Modeling Parametric Failures of Woodworking Machines According to the Technological Precision Criterion

Mariya Pylypchuk¹ , Lidiia Dziuba² , Ihor Rebezniuk¹ ,
Oksana Chmyr² , and Mykhailo Burdiak¹ 

¹ Ukrainian National Forestry University, 103, Chuprynky Street, Lviv, Ukraine

² Lviv State University of Life Safety, 35, Kleparivska Street, Lviv, Ukraine

Abstract. A radial model of parametric failure of a woodworking machine according to the precision criterion based on the truncated normal distribution of a machine's disadjustment speed caused by the wear processes in the mating of parts and components of the structure has been developed. It has been found that the density of parametric failures of woodworking machines according to the precision criterion corresponds to alpha distribution. Based on the operational observations, the alpha distribution parameters of operating time to parametric failure for band saw, circular saw, and milling machines have been established. It has been determined that the durations of inter-adjustment periods for band saw, circular saw, and milling machines coincide with the operational data of the duration of these inter-adjustment periods for these machines with an accuracy of seven percent, which proves the adequacy of the mathematical model. The proposed model of parametric failures of woodworking machines based on the processing precision criterion allows determining the durations of inter-adjustment periods of machine operation, during which the precision of processing is ensured in compliance with the current standards.

Keywords: Alpha distribution · Operating time · Machine · Parametric failure · Precision of processing · Inter-adjustment period

1 Introduction

The quality of finished products and the efficiency of using wood depend on the precision of sawing timber in modern woodworking production. In the dynamic system “machine – tool – workpiece” (MTW), the most complex and constant source of processing errors is a machine, the service life of which equals decades.

During the operation of woodworking machines, different types of energy apply: mechanical, thermal, physical, which lead to changing the parameters of individual elements, units, and a machine as a whole. Such processes are reversible or irreversible. Reversible processes, such as elastic and thermal deformations of parts and units, temporarily change the parameters of machine parts and units within certain limits. Irreversible degradation processes, such as aging, corrosion, wear, lead to the significant deterioration of a machine's technical condition over time and significantly affect

the precision of wood cutting. Therefore, the maintenance of a woodworking machine should ensure the reliability and prevention of deviations of its parameters, which lead to the loss of technological precision.

This paper aims to model the parametric failures of woodworking machines based on the criterion of technological precision using α - distribution of operating time, enabling us to determine the duration of inter-adjustment periods of machine operation.

2 Literature Review

The processes of changing parameters in woodworking machines differ in speed [1]. Periodic short-lived processes continue within the machine's operation and wood cutting tool units [2, 3]. These include vibrations of a woodworking machine and tool units; changes of friction forces in kinematic pairs; fluctuations in the workload due to the heterogeneity of the processed wood; parametric oscillations of the wood cutting tool [3], and other processes that affect the mutual placement of the tool and the workpiece at any time, reducing the precision of wood sawing [4].

Slow (degradation) processes occur within the entire period of a machine's operation and are manifested between its regular repairs [5, 6]. Such processes include stress redistribution in parts, material fatigue, corrosion, wear of machine parts, and units in friction pairs [7]. As a result of wear and tear, parametric failures of a woodworking machine periodically occur according to the precision criterion. Partial restoration of the technological precision of a machine is carried out by its regular adjustment and repair [8, 9]. In the works [1], parametric failures are described using a linear model with a scattering of the initial parameter by the normal distribution law. Random processes with a normal distribution law are considered in the works [10, 11]. Published experimental failure distributions of parts and components of structures working to the point of exhaustion are usually asymmetric and modal [2, 8]. The work [12] notes that it is reasonable to use the asymmetric Weibull distribution law to study the reliability indicators and describe the failure models. In work [13], to study the reliability of mechanical equipment, the features of the processing process are used instead of the traditional description of degradation processes. However, these studies do not consider the possibility of estimating the duration of operation between equipment failures, which would allow determining the inter-adjustment periods for equipment. In [14], it is indicated that parametric failures resulting from wear do not correspond to the normal law of failure distribution. Therefore, to describe the operating time until the parametric failure of the woodworking machine, it is reasonable to use an asymmetric α - distribution [14], which allows estimating the duration of operation between failures according to the processing precision criterion.

3 Research Methodology

During machine adjustment, the size adjustment at the time t_1 is set to a particular nominal value X_0 . In the course of further operation of the machine, the value X_0 is randomly changed. Therefore, size X is a polar random function of operating time $X(t)$.

All implementations of random function $X(t)$ pass through one non-random stationary point – pole (X_0, t_1) .

For finding the failure distribution of a woodworking machine by the precision criterion according to the characteristics of the disadjustment process, it is convenient to approximate the random value of X size of the manufactured part by a random radial function [14] as follows:

$$X(t) = X_0 + B \cdot t, \tag{1}$$

where B is the speed of the machine disadjustment process, which is a random variable, and the operating time t is calculated from the moment of arising need for adjustment. To find the numerical characteristics – mathematical expectation m_b and mean-square deviation σ_b , which roughly describe the machine disadjustment process, one should know the X_0 variable and operating time t_0 before pre-adjustment. The speed variable B of changing size X is limited by the lower b_1 and upper b_2 margins. Therefore, according to [14], it is reasonable to consider the truncated normal distribution of the size X change speed, provided that the speed of machine disadjustment is limited, i.e.: $b_1 \leq b \leq b_2$:

$$\bar{f}(b) = cf(b) = \frac{c}{\sigma_b \sqrt{2\pi}} \exp \left[-\frac{(b - m_b)^2}{2\sigma_b^2} \right], \tag{2}$$

where $c = \frac{1}{\Phi(u_2) - \Phi(u_1)}$; $u_1 = \frac{b_1 - m_b}{\sigma_b}$; $u_2 = \frac{b_2 - m_b}{\sigma_b}$; $\Phi(u)$ – Laplace's function. As a result of disadjustment, the X parameter can reach a critical value X_{max} , at which a parametric failure of the woodworking machine occurs according to the precision criterion. Therefore, we further consider B as the absolute value of a woodworking machine's disadjustment speed.

The time $T = \frac{|X_{max} - X_0|}{B}$ to parametric failure according to the precision criterion is a function of a random variable B distributed according to the truncated normal law (2). According to the rule of finding the distribution law of random arguments' functions [14] provided that $\frac{|X - X_0|}{b_2} \leq t \leq \frac{|X - X_0|}{b_1}$ distribution density for T variable has the form of three-parametric α - distribution [14]:

$$f(t) = \frac{\beta \cdot c}{t^2 \sqrt{2\pi}} \exp \left[-\frac{1}{2} \left(\frac{\beta}{t} - \alpha \right)^2 \right], \tag{3}$$

where β , α , c – distribution parameters, $\beta = \frac{|X - X_0|}{\sigma_b}$, $\alpha = \frac{|m_b|}{\sigma_b}$. Parameter β has the dimensionality of failure time (time) and is the relative margin of a machine's durability according to the precision criterion. The parameters α and c are dimensionless values. We consider the value of α parameter to be the average speed of the machine disadjustment, i.e., the relative average speed of a change of the random variable X . As a rule, when the parameter $\alpha = 2$ and may take larger values, the parameter $c = 1$ [14]. Typical density curves of α - distribution for different parameters of the relative

durability of a woodworking machine and the relative average speed of its disadjustment are shown in Fig. 1.

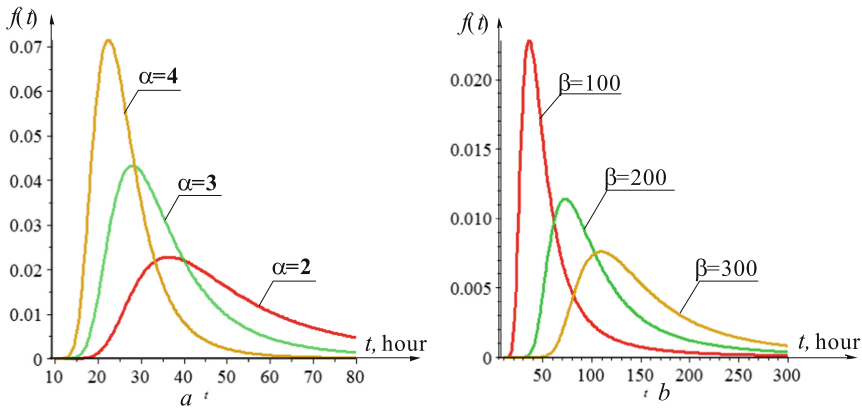


Fig. 1. Charts of α -distribution density functions at different values of parameters: a – for the conditional durability of a machine $\beta = 800$ hours; b – for distribution parameter $\alpha = 2$.

The operating time of a woodworking machine before the beginning of mass failures according to parametric precision is equal to the time when the acceleration of a distribution density change is maximum. The value of this operating time is calculated according to the recommendations [14] as the time when the third derivative of the distribution density function is zero. Then the value of the operating time before the start of mass failures is obtained as the smallest positive root of the equation

$$\frac{\beta}{\sqrt{2\pi}} \frac{d^3}{dt^3} \left(\frac{1}{t^2} \exp \left(-\frac{1}{2} \left(\frac{\beta}{t} - \alpha \right)^2 \right) \right) = 0. \tag{4}$$

Having found the third-density derivative of α -distribution of a random variable X , Eq. (4) is reduced to an algebraic sextic equation:

$$\begin{aligned} & -\frac{1}{t^{11}} \left(10^{-10} \beta \exp \left(\frac{0.5(\alpha t - \beta)^2}{t^2} \right) \right) \cdot (9.6 \cdot 10^{10} t^6 + 1.4 \cdot 10^{11} \alpha \beta t^5 \\ & + t^4 (4.8 \cdot 10^{10} \beta^2 - 1.9 \cdot 10^{11} \beta^2) + (4 \cdot 10^9 \alpha^3 \beta^3 - 10^{11} \alpha \beta^3) t^3 \\ & + (6 \cdot 10^{10} \beta^4 - 1.2 \cdot 10^{10} \alpha^2 \beta^4) t^2 + 1.2 \cdot 10^{10} \alpha \beta^5 t - 4 \cdot 10^9 \beta^6) = 0. \end{aligned} \tag{5}$$

The smallest positive root of the solution (5) is the operating time's value, which equals the duration of the inter-adjustment period for the machine. For example, with the distribution parameters $\alpha = 2$, $\beta = 850$ h, we have six roots: 179.5; 266.2; 482.1; -384.5; -760.7; -2332.5, first of which determines the inter-adjustment period for a wood-working machine according to the precision criterion.

4 Results

The parameters of α -distribution for woodworking machines are calculated according to characteristics of the wear and degradation process:

$$\beta \approx \bar{\beta} = \frac{|X - X_0|}{\sigma_b}, \alpha \approx \bar{\alpha} = \frac{|m_b|}{\sigma_b} = \frac{1}{v_b} \tag{6}$$

where v_b – the variation coefficient of the random disadjustment speed process ranges within 0.25–0.50 for the degradation process of mechanical wear [1]. Variation coefficients obtained from the research results on the technological precision of machines also fall within these limits. Assuming that the disadjustment speed of a woodworking machine is associated with the processes of wear in the mating of components and parts of the construction, according to formulas (6), the α -distribution parameter of the random process of the precision loss will adopt values within $\alpha = 2 - 4$. With mean-square deviations of the random machine disadjustment speed process due to wear $\sigma_b = 0.0008 - 0.002$ mm/h, the value of β -distribution parameter for woodworking machines will vary from 450 h for band saw machines to 9000 h for milling machines. Taking $\sigma_b = 0.002 - 0.004$ mm/h for the band saw machine of the SKTP505–2 brand, we have the value $\beta = 920 - 450$ h; for Barakuda-2 circular saw machine $\sigma_b = 0.0008 - 0.003$ mm/h - $\beta = 2200 - 600$ h; for the jointer-planer AD741 - $\sigma_b = 0.0002 - 0.0004$ mm/h - $\beta = 8200 - 4100$ h; for four-side milling Unimat-17A - $\sigma_b = 0.0005 - 0.0008$ mm/h - $\beta = 4000 - 2000$ h. After considering the dependence (4) and the parametric failure formation, the model of parametric failure of a woodworking machine may be presented in the form of a chart (Fig. 2). In Fig. 2, the following notations are adopted: $T^{(1)}, T^{(2)}$ – durations of the first and second inter-adjustment periods, B_1, B_2 – value of disadjustment speed during the respective period,

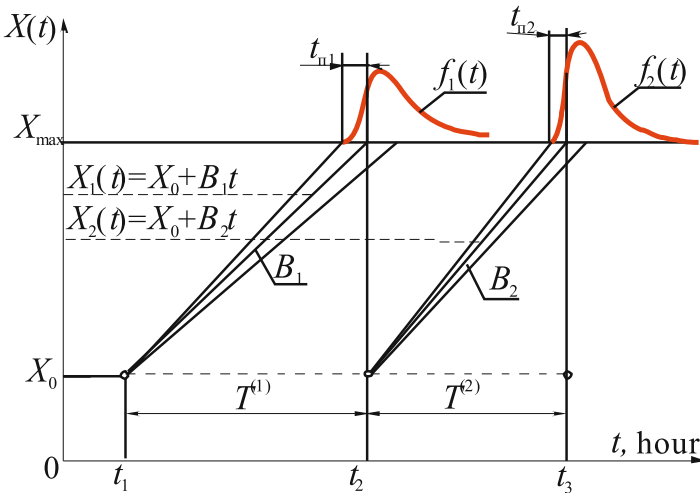


Fig. 2. The scheme of parametric failure formation according to the processing precision criterion in the inter-inspection period of a machine.

$f_1(t), f_2(t)$ – α - distribution density functions in the respective inter-adjustment period, $t_{\Pi 1}, t_{\Pi 2}$ – the smallest positive roots of Eq. (5). X_0 is the determining parameter as the initial error value of processing the nominal size of the part, which is the mode of the Hnidenko-Weibull distribution.

Mathematical modelling of the duration of inter-adjustment periods for woodworking machines has been performed using the scheme shown in Fig. 2. Solving Eq. (5) for specific values of α - distribution parameters, the durations of inter-adjustment periods for SKTP505-2 band saw machine, Barakuda-2 circular saw machine, and milling machines: jointer-planer AD741(Felder) and four-side longitudinal milling machine Unimat-17A, have been obtained. It has been established that the duration of inter-adjustment periods for woodworking machines increases with the increase of conditional durability of a machine β . However, logically, with the increase of relative disadjustment speed, which we consider to be the α -distribution parameter, the duration of inter-adjustment periods decreases. There is a linear relationship between α -distribution parameters and the duration of the inter-adjustment period. For example, for the SKTP505-2 band saw machine, with a reduction of the relative durability of the machine, i.e., β parameter ranging from 850 h up to 450 h (by 47%), the duration of the inter-adjustment period also decreases by 47%. With a decrease in the relative disadjustment speed (α -distribution parameter) by 11.7%, the duration of the inter-adjustment period increases by 17.5%. This increase in the duration of the inter-adjustment period does not depend on β parameter value. Similar linear dependences of the duration of the inter-adjustment period on the distribution parameters apply to Barakuda-2 circular saw machines and Unimat-17A four-side milling machines. The β distribution parameters for the new jointer-planer AD741 and the used four-side milling machine Unimat-17A are significantly different. For the used machine, the relative durability is 40% lower compared to a new machine.

Estimated durations $T^{(1)}, T^{(2)}$ and $T^{(3)}$ of the first three inter-adjustment periods for the following machines: SKTP505-2 band saw machine, Barakuda-2 circular saw machine and milling machines: new jointer-planer AD741 and used four-side milling machine Unimat-17A, are shown in the chart in Fig. 3. Operational values of machines' operating time in the first inter-adjustment period of operation are adopted considering the duration of an interrepair cycle. The standard interrepair cycle for machines of the II category (weighing 1–5 tons) is equal to 11200 h of operation [8]. The structure of the interrepair cycle for category II machines consists of 15 periods (inspections, regular, medium, and capital repairs) lasting 746 h. Taking into account the durability coefficient of a machine, the values of the periods may vary.

For the SKTP505-2 band saw machine, the estimated duration of the first disadjustment period differs from operational duration by 5% with distribution parameters $\alpha = 2$ and $\beta = 850$ h; duration of the second period of disadjustment – by 2.7% with parameters of distribution $\alpha = 3.2$ and $\beta = 850$ h or by 7.4% with distribution parameters $\alpha = 2$ and $\beta = 650$ h, the duration of the third period of disadjustment – by 3.6% with distribution parameters $\alpha = 3.2$ and $\beta = 850$ h.

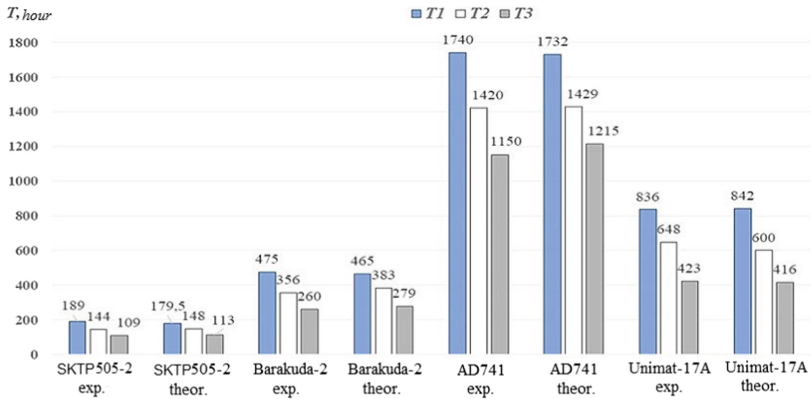


Fig. 3. Diagram for experimental and theoretical results of the duration of inter-adjustment periods of machines' operation.

Thus, in each period of disadjustment, α - distribution parameters take on different values. Each subsequent disadjustment of the machine occurs either at a higher relative speed of disadjustment, or with a lower value of the conditional durability of the machine. The differences between the operational and calculated values of the duration of inter-adjustment periods are the following: for “Barakuda -2” circular saw machine in the first period – 2.1%, in the second period – 7%, in the third period – 6.8%; for the new jointer-planer AD741 in the first period – 0.5%, in the second period – 0.6%, in the third period – 5.6%; and for the used Unimat – 17A in the first period – 0.3%, in the second period – 5.5%, in the third period – 1.4%. Therefore, the proposed model of parametric failures of woodworking machines allows determining the durations of inter-adjustment periods with accuracy sufficient for engineering calculations.

5 Conclusions

According to the precision criterion based on the truncated normal distribution of a machine's disadjustment speed, a radial model of parametric failure of a woodworking machine has been developed. It has been established that the density of parametric failures of woodworking machines according to the precision criterion corresponds to α - distribution. Based on α - distribution of parametric failures, the durations of inter-adjustment periods have been determined for a range of woodworking machines: SKTP505–2 band saw machine, Barakuda-2 circular saw, and AD741 and Unimat-17A milling machines, which coincide with the operational data with an accuracy of 7%.

The proposed model of parametric failures of woodworking machines based on the processing precision criterion, with accuracy sufficient for engineering calculations, allows determining the durations of inter-adjustment periods of machine operation. The precision of processing is ensured in compliance with the current standards.

In further studies, the developed methodology can be used to determine the duration of inter-adjustment periods of other woodworking machines and any







mechanical equipment that has been under operation for a long time and requires developing the optimal structure of repair cycles.

References

1. Pronikov, A.S.: Parametric Reliability of Machines. Publishing House of MSTU named after N.E. Bauman, Moscow (2002)
2. Amalitsky, V.V., Bondar, V.G., Volobaev, A.M., Voiakhin, A.S.: Reliability of Machines and Equipment of the Forestry Complex. Textbook. MSFU, Moscow (2000)
3. Gao, J., Jiang, Z., Zhang, J., Li, H., Shen, D., Zhao, H.: Band saw blade crack before and after comparison and analysis of experiments (2). In: MATEC Web of Conferences, vol. 68, pp. 02003 (2016)
4. Baranov, A.V.: Reliability and diagnostics of technological systems. Textbook. RSATU, Rybinsk (2006)
5. Novoselov, V.G., Pomekhova, T.V.: Theoretical study of the reliability of woodworking technological system according to the “precision” product quality parameter. In: Woodworking: Technologies, Equipment, Management of the XXI Century. Proceedings of the International Eurasian Symposium, pp.108–114, Ekaterinburg (2006).
6. Novoselov, V.G., Glebova, I.T.: A physical method for calculating the reliability of a technological system of woodworking according to the “precision” product quality parameter. In: Reliability and quality: Proceedings of the international symposium, pp. 276–278. Tech. University, Penza (2006)
7. Tsarev, A.M.: Reliability and diagnostics of technological equipment. Textbook. TSU Publishing House, Togliatti (2013)
8. Shostak, V.V.: Installation, maintenance and repair of woodworking equipment. Textbook for higher educational institutions. UkrSFU, Akhil Publishing House, Lviv (2000)
9. Pylypchuk, M.I.: Methods for studying the dynamics of technological accuracy of woodworking machines. In: Proceedings of the IV International Scientific-Practical Conference on T. 1, pp. 70–71. SHEI “Vasyl Stefanyk Precarpathian National University”, Ivano-Frankivsk (2020)
10. Jazwinski, A.H.: Stochastic Processes and Filtering Theory. Dover Publications Inc., Mineola (2007)
11. Knill, O.: Probability and Stochastic Processes with Applications. Overseas Press India Private Limited., New Delhi (2009)
12. Rinne, H.: The Weibull Distribution: A Handbook. Publisher Chapman Hall/CRC (2008)
13. Dai, W., Chi, Y., Zhiyuan, L., Wang, M., Zhao, Y.: Research on reliability assessment of mechanical equipment based on the performance-feature model. Appl. Sci. **8**, 1619 (2018). <https://doi.org/10.3390/app8091619>
14. Druzhynin, G.V.: Reliability of Automated Production Systems. Energoatomizdat, Moscow (1986)



Lifecycle Management of Modular Machine Tools

Ihor Yakovenko , Alexander Permyakov , Maryna Ivanova  ,
Yevheniia Basova , and Dmitry Shepeliev 

National Technical University «Kharkiv Polytechnic Institute»,
2, Kyrpychova Street, Kharkiv 61002, Ukraine

Abstract. The lifecycle management issues of modular equipment, which mainly uses unified units and assemblies, are considered. The study touches upon modern trends in industrial production, which are associated with a reduction in the lifecycle of manufactured products due to the acceleration of its obsolescence and physical depreciation from the point of view of the modern competitive strategy of industrial enterprises. In the research process, the existing practice of design, production, and operation of modular machine tools was used to study the technical re-equipment of industrial enterprises in Ukraine. Based on modern information technology methods and CALS concepts, an enlarged model of the lifecycle of complex, knowledge-intensive technical systems has been developed to manage the lifecycle for such systems to establish the maximum period of use of unified units (modules). A new modular machine tools design model, which allows extending the lifecycle of machines, reducing the cost and timing of equipment design and manufacture, is proposed based on CALS technologies, the modular principle, and equipment certification. The model is based on using the modular principle and certification of equipment elements on the step-by-step information support of the technological system at all stages of the lifecycle. Particular attention is paid to reengineering and related processes during restoration work and machine tools modernization.

Keywords: Lifecycle · CALS technologies · Modular equipment · Power units · Unified elements · Multi-tool machining · Flexible production systems

1 Introduction

According to [1], world production of metal-cutting machine tools amounted to 34.5 million pieces in 2019, which exceeded the value of 2015 by 10.3% (Fig. 1). This indicator grew annually relative to previous years, and the largest increase occurred in 2017 and amounted to 3.0%. In this volume, the portion of special machine tools built according to the modular principle is 4–6% for industrially developed countries. This indicator grew annually relative to previous years, and the largest increase occurred in 2017 and amounted to 3.0%.

For the shutdown of many industries in 2020 due to the coronavirus pandemic and a general failure in the global economy and trade, it is expected that the worldwide

production of metalworking machine tools decreases 15.9% compared to the previous year. The production of machine tools will begin to grow following the recovery of economic activity in subsequent years, and it will reach the pre-crisis level to the 2024 year.

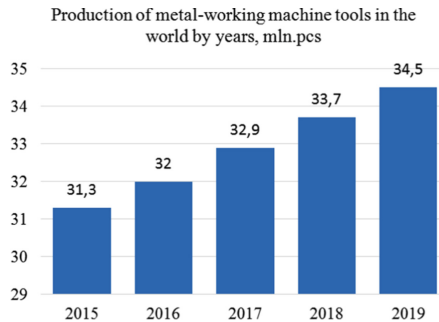


Fig. 1. Production of metalworking machine tools in the world by years, mln. pcs [1].

However, the growth in the production of metal-cutting machine tools must be viewed from the standpoint of the lifecycle of this equipment. Today, machine tools and systems of mechanical engineering manufacturing have a service life of 7–12 years depends on the level of automation and the intensity of technological impact [2]. On the other hand, the main trend of modern machinery production is to reduce the lifecycle of products and increase the requirements for their ergonomic characteristics and quality.

High-performance modular equipment can undoubtedly be attributed to the class of rather expensive, constructively complex knowledge-intensive technical systems. Therefore, consumers strive to extend the life of equipment as long as possible and sometimes go to significant additional costs to upgrade it. The new generation of products that must be manufactured on outdated machine tools may exceed the capabilities of the obsolete machines. In turn, the shortening of the lifecycle of manufactured products increasingly requires flexibility and diversification from the modular equipment.

The paper aims to search possibilities to increase the technical and economic efficiency and increase the lifecycle of special machine tools designed according to the modular principle by optimizing the structure [3] and layout decisions taken when creating a new and modernizing existing engineering manufacturing, based on modern advances in information technology in the field of research and lifecycle management of such equipment.

2 Literature Review

According to [4], shortly, the total costs of the equipment lifecycle will come to the foreground and will be of more and more significant importance. More and more modular machine tools are being created in the world machine tool industry, combining the advantages of fast readjustment of CNC machines and a high concentration of operations typical for modular machines and automatic lines [4, 5].

The work [6] is devoted to the analysis of the modern methodology for lifecycle analysis and design of modular machine tools, based on the clustering method and the similarity matrix. However, the issues related to the possibility of reengineering and reuse of unified units are practically not touched upon.

The design of modern modular machine tools allows multiple uses of unified units (modules) in the production process (Fig. 2).

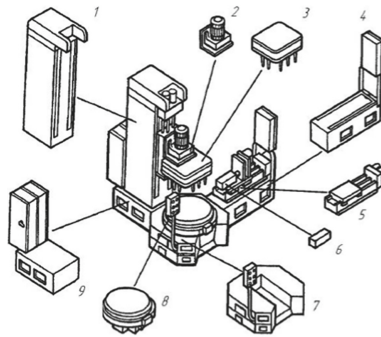


Fig. 2. Elements of modular machine tool [7]: 1 – column base; 2 – power headstock; 3 – multi-spindle head; 4 – wing base; 5 – feed table; 6 – single spindle boring head; 7 – center base; 8 – rotary dividing table; 9 – support base.

The general approach to the design of modular machine tools of varying levels of flexibility is considered in [7, 8]. But in these works, research and optimization of machine tools layouts affected only the design stage and did not consider the rest of the lifecycle of equipment and its elements. Moreover, the design of modern machining centers is formed by a set of specific aggregates as well they could be equipped with additional modular equipment, which is associated with the principle of technological operations concentration at one workplace [9]. In [10], an original approach to the synthesis of layouts of reconfigurable lathe machines was considered, but the issues of multi-tool hole machining were also not considered. A modular approach is used in different areas, particularly in fixture design [11, 12]. The level of flexibility is the main criteria, which allows designing based on modular adjustable units instead of single modular components [13]. The economic efficiency of flexible systems against conventional systems has been proved [14].

The issues of lifecycle stages for mechanical engineering products and the methodology for calculating the “economically justified product service life” are

considered in [15], based on which a design methodology is proposed that takes into account the operational characteristics of the manufactured product and the calculation of the optimal program for its release, however, the studies related only to the lifecycle of the manufactured product, and the production stage with the characteristics of the equipment was not considered in work.

Reconfigurable Machine Systems have found widespread use in machine tool building recently [8, 16]. Authors [17] have developed a machine tool concept featuring a modular machine tool frame using microsystem technology for communication within the frame, which allows for a high level of flexibility. Researchers [18, 19] performed deep analyzes of existing methods for RMS design with further recommendations to design develop modular machine tools. A method [20] for the design of modular, reconfigurable machine tools consists of three steps: module identification, module determination, layout synthesis, and a software package. The authors [21] proposed an improved method to choose the optimal RMS structure based on the preference ranking of key characteristics.

Moreover, a method to control RMS, considering the data obtained by the business processes of production subsystems in different geographic locations when simulating the process, product management, machines, and devices, was proposed [22]. In addition, CALS technologies are widely used to support the lifecycle of products [23]. Based on the computer simulation, the method of selecting the RMS structure that considers changing machine reliability [24–26] to maintain the stability of the production process is developed [27]. A flexible manufacturing system simulation model applying the ontology on flexibility was developed in the research work [28]. Also, novel techniques in lean manufacturing [29], computer-aided fixture design [30], and up-to-date engineering trends [31] are proposed.

Despite the existence of various methods of RMS design, considering many parameters of the processing object and factors affecting the possibility of using such systems, the issues of the possibility of using unified units of already operating equipment from the point of view of further use to ensure the flexibility of production while executing the production program were not considered.

Earlier, a parametric synthesis methodology was proposed for the most rational option of the modular machine tool technological layout, considering structural and parametric characteristics of tool blocks, as well as the possibility of their optimization based on the quantitative relationship between the parameters of the cutting process, the output cycle of the product and the durability of the cutting tool with different methods of replacing the tool [32].

3 Research Methodology

To achieve this purpose, the next tasks were solved:

- to analyze the existing methods of assessment, forecasting, and management of the lifecycle of products in general and metal-cutting machine tools in particular;
- to establish the main features of the lifecycle of special machine tools to other products of engineering manufacturing;

- to develop an enlarged methodology for analyzing the lifecycle and creating new modular machine tools, and reengineering the existing one.

The lifecycle of any mechanical engineering product is largely determined by two main components: obsolescence and physical depreciation.

The lifecycle of any mechanical engineering product is largely determined by two main components: obsolescence and physical depreciation.

Economic depreciation of equipment means the loss of the value of an object during its use. If the cost has decreased due to the aging of the object and the partial loss of its performance, then they speak of physical depreciation. If the cost has decreased because the object has lost its competitiveness in the market in comparison with other similar objects and began to be in less demand, then they talk about obsolescence.

Both types of wear develop independently of each other. It means that a completely new product can lose value before its use due to obsolescence. Even when calculating the full replacement cost by direct comparison with an analog, such adjustments are made to the price of an analog, which in one way or another take into account obsolescence.

Recently, more issues of obsolescence of manufactured products have come to the foreground. Based on these data, after performing marketing research, manufacturers concluded that it is possible to reduce the duration of the predicted operation and, accordingly, to make changes in the technical characteristics of products. To a lesser extent, this applies to metal-cutting machine tools since their rapid depreciation and, therefore, loss of accuracy leads to additional costs for repairs since the requirements for processing accuracy are constantly increasing. The growth of requirements for processing accuracy is explained by the fact that consumers of ultimate products are constantly growing requirements for noiselessness, smoothness, and other quality characteristics of the manufactured products.

Despite the apparent advantages of introducing advanced technologies and inventions, these trends also carry a number of negative factors. So, at a certain stage of reducing the lifecycle of products: general-purpose machine tools will not be able to provide the required volumes of output in a short time, specialized and special machine tools will not have time to pay off, it will be necessary to put into operation new methods of metal processing in conditions of severe time pressure, possibly to the detriment of sufficiently deep research and testing new technology.

The most effective technological equipment used in modern production is universal and multipurpose machine tools operating in automatic mode; the main advantages are a high level of flexibility and full automation of the working cycle. However, such equipment also has a significant drawback - these machine tools are quite expensive. It is necessary to organize parallel production and use many expensive CNC machine tools for large batches and limited production times. It dramatically increases expenses and, accordingly, the technological cost of products.

In the process of creating highly efficient machine tools for specific production conditions, machine tool plants have to solve the difficult problem of resolving the contradiction between the high performance of special multi-position multi-tool equipment and its low readjustment and flexibility, on the one hand, and the relatively

low productivity and quick readjustment of multifunctional machine tools. In designing modular machine tools, it is necessary to consider the lifecycle of processing objects on the one hand and the possibility of readjustment or reuse of normalized units and assemblies conceptually.

Speaking about creating highly efficient production in general, the resolution of the contradictions between flexibility and equipment performance goes in several ways:

- designing of re-adjustable machine tools and automatic lines, based on the existing principles of modular machine tool construction;
- designing of modular systems of traditional layout based on a certain model range of basic components equipped with CNC systems to ensure uniformity of design solutions and quick readjustment for new processing objects;
- reconfiguration of machine tools based on previously used modules (units).

The level of flexibility for the readjustment of such equipment can be quite high. Moreover, the options for this readjustment are quite diverse, from the readjustment of fixtures (replacement of base elements and clamping units) and spindle units (use of spindle equipment with an adjustable spindle position) to their complete replacement.

4 Results

A statistical analysis of the cost of individual modules in the total cost of a medium-sized modular machine tool is shown in Fig. 3. In the general case, the portion of standardized units reaches 80–90% for such equipment. Only the elements directly connected with the part (mounting and clamping device, multi-spindle nozzles, and boxes) are original.

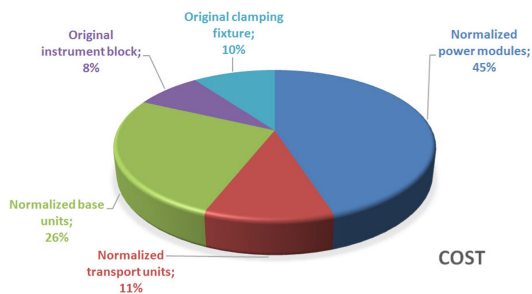


Fig. 3. Portions of the cost of various groups of modules (units and elements) in the total cost of a medium-sized modular machine tool.

Currently, the obsolescence of a manufactured product and its removal from production occurs earlier than the physical depreciation of the machine tools on which this product was produced. Therefore, with tendencies to reduce the lifecycle of the processing object, it is advisable to use the reengineering of the existing modular machine tools and their rearrangement since the operational characteristics of the units

(modules) used have not fully used their resource. The modular principle implies the interchangeability and recoverability of the technical system. Therefore, we offer a model of the lifecycle of modular machine tools with end-to-end support for the information model of the processing object and all elements of the modular machine tool throughout the entire lifecycle.

Usually, when designing equipment, the classic linear lifecycle process is mainly used (Table 1). This process is the most generalized. In reality, a situation may arise when new generations of products, which must be manufactured on old equipment, exceed the capabilities of old machines in the face of increasing competition in the market, and there will be a need to purchase modern, even more, expensive equipment.

At present, most machine tools and technical systems of machinery production have a service life of 7–12 years, although, in reality, the equipment is used much longer, especially in countries with low gross income per capita and low industrial production efficiency. On the other hand, a situation may arise when resolving the technical and technological preparation of production at an enterprise is enough to reengineer the existing modular machines and solve the problem. Such machine tools are the most promising type of metal-cutting equipment in terms of productivity, distinguished by the highest possible level of concentration of technological steps and providing a significant superiority in productivity. However, this equipment has a very low level of flexibility. Therefore, in this case, it is necessary to slightly change the traditional scheme of the lifecycle of modular equipment aimed at the reuse of unified machine units (Fig. 4).

Table 1. Linear lifecycle process.

Lifecycle stage	Tasks to be solved
Research	Market research Patent research Generation of ideas
Machine tool design	Scientific research development Development of design and technological documentation Simulation and testing
Preparation of manufacturing	Design preparation Technological preparation Technical preparation (selection of equipment) Organizational preparation
Production and market entry	Advertising Primary production Auxiliary production
Using	Warranty support Maintenance Repair and restoration work
Recycling	Dismantling equipment Scrapping

As follows from Fig. 4, in contrast to the classical scheme, the modular machine tools do not end their lifecycle at the end of the release of a certain product but are used later to design new machine tools. The basis for such use is the certification of normalized units both at the stage of their initial manufacture and after operation and restoration of technical characteristics. There are two options for the further use of the units (modules).

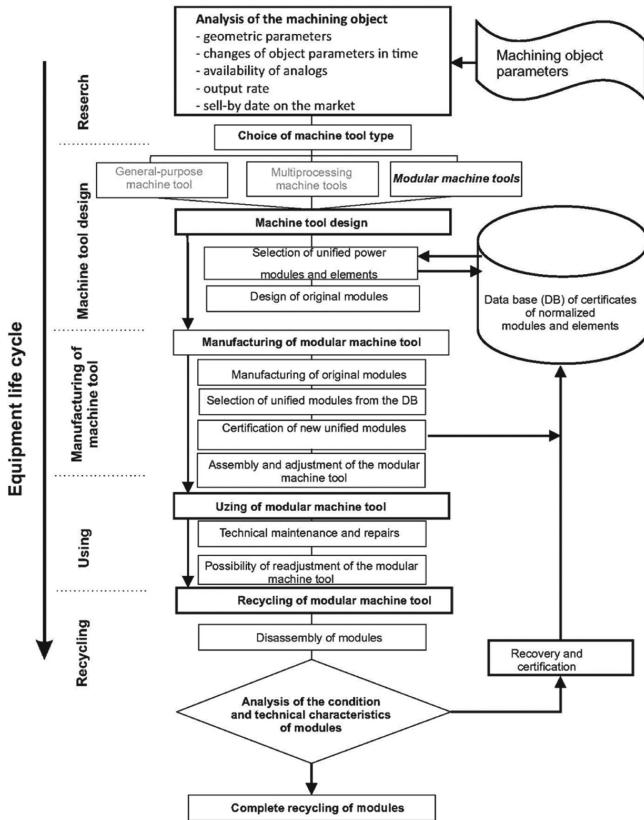


Fig. 4. Lifecycle diagram of the modular machine tool.

The first one is typical for small manufacturing enterprises with a small number of modular machine tools. It is not advisable for these enterprises to independently reengineer the machine tools because there is no experience in operating and designing such equipment. It is advisable to send the restored units (modules) to specialized enterprises that manufacture such equipment.

The second one is typical for large mass-production enterprises with a sufficient number of equipment of this class, a significant base of passports of normalized units (modules), and the technical capabilities of reconfiguring such machine tools.

The industry of Ukraine has a fairly large fleet of aggregate equipment. Therefore, this approach can ensure the effectiveness of the technical preparation of production during its modernization.

5 Conclusions

An analysis of the use, development, and improvement of modular machine tools primarily points to two factors:

- the machine tool industry, based on the application of the modular principle of equipment construction, is still insufficient demand on the market;
- the use of modern approaches in the context of the intensifying competition between manufacturers and the “race” for productivity and a decrease in the cost of goods indicates the need to use CALS technologies and analyze the lifecycle of equipment and products in the modernization of production.

An enlarged model of the lifecycle of complex, science-intensive technical systems has been developed to manage the lifecycle of such systems to establish their maximum duration based on modern information technology methods and CALS concepts. The model is based on the step-by-step information support of the product at all stages of the lifecycle. Particular attention is paid to the issues of reengineering when carrying out modernization and restoration work.

The proposed model for managing the lifecycle of equipment will increase the efficiency of its use in an existing production system, reduce the cost of manufacturing “new” machines built based on the modular principle, and increase the lifecycle of existing modular machine tools, as well as significantly increase flexibility through the use of “replaceable” Certified modules.

References

1. Analysis of the world market for metalworking machines in 2015–2019, assessment of the impact of coronavirus and forecast for 2020–2024. https://businessstat.ru/images/demo/metalworking_machines_world_demo_businessstat.pdf, Accessed 13 May 2021
2. Denkena, B., Harms, A., Jacobsen, J., Möhring, H.C., Lange, D., Noske, H.: Life-cycle oriented development of machine tools. In: Proceedings of the 13th Cooperative Institutional Research Program International Conference on Life Cycle Engineering, pp. 693–698, Leuven, Belgium (2006)
3. Karpus, V.E., Ivanov, V.A.: Choice of the optimal configuration of modular reusable fixtures. *Russ. Eng. Res.* **32**(3), 213–219 (2012). <https://doi.org/10.3103/S1068798X12030124>
4. Mehrabi, M.G., Ulsoy, A.G., Koren, Y.: Reconfigurable manufacturing system and their enabling technologies. *Int. J. Manuf. Technol. Manage.* **1**(1), 114–131 (2000). <https://doi.org/10.1504/IJMTM.2000.001330>
5. Strasser, T., Fessl, K., Hämmerle, A., Ankerl M.: Rapid reconfiguration of machine tools for Holonic manufacturing systems. In: Proceedings of 16th IFAC world congress, p. 1573. IFAC, New York (2005)






6. Wang, P., Liu, Y., Ong, S.K., Nee, A.Y.C.: Modular design of machine tools to facilitate design for disassembly and remanufacturing. *Procedia CIRP* **15**, 443–448 (2014). <https://doi.org/10.1016/j.procir.2014.06.085>
7. Yakovenko, I., Permyakov, A., Prihodko, O., Basova, Y., Ivanova, M.: Structural optimization of technological layout of modular machine tools. In: Tonkonogiy, V., et al. (eds.) *InterPartner 2019. LNME*, pp. 352–363. Springer, Cham (2020). https://doi.org/10.1007/978-3-030-40724-7_36
8. Zhengyi, X., Fengfeng, X., Lilan, L., Li, C.: A method for design of modular recon-figurible machine tools. *Machines* **5**(1), 5 (2017). <https://doi.org/10.3390/machines5010005>
9. Krol, O., Sokolov, V., Tsankov, P.: Modeling of vertical spindle head for machining center. *J. Phys. Conf. Ser.* **1553**, 012012 (2020). <https://doi.org/10.1088/1742-6596/1553/1/012012>
10. Aguilar, A., Huegel, J.C.: A synthesized methodology for machine tool design applied to a reconfigurable lathe-mill. In: 2010 IEEE/ASME International Conference on Advanced Intelligent Mechatronics, pp. 1180–1185 (2010). <https://doi.org/10.1109/AIM.2010.5695858>
11. Karpus', V.E., Ivanov, V.A.: Universal-composite adjustable machine-tool attachments. *Rus. Eng. Res.* **28**(11), 1077–1083 (2008). <https://doi.org/10.3103/S1068798X08110105>
12. Ivanov, V., Dehtiarov, I., Pavlenko, I., Liaposhchenko, O., Zaloga, V.: Parametric Optimization of fixtures for multiaxis machining of parts. In: Hamrol, A., Kujawińska, A., Barraza, M.F.S. (eds.) *MANUFACTURING 2019. LNME*, pp. 335–347. Springer, Cham (2019). https://doi.org/10.1007/978-3-030-18789-7_28
13. Ivanov, V., Vashchenko, S., Rong, Y.: Information support of the computer-aided fixture design system. *CEUR Workshop Proc.* **1614**, 73–86 (2016)
14. Ivanov, V., Liaposhchenko, O., Denysenko, Y., Pavlenko, I.: Ensuring economic efficiency of flexible fixtures in multiproduct manufacturing. *Eng. Manage. Prod. Serv.* **13**(1), 53–62 (2021). <https://doi.org/10.2478/emj-2021-0004>
15. Petrushin, S.I., Gubaidulina, R.: The principles of optimization of the life cycle of mechanical engineering products. *Bull. Tomsk Polytech. Univ.* **321**(6), 96–100 (2012). (In Russian)
16. Koren, Y., Gu, X., Guo, W.: Reconfigurable manufacturing systems: principles, design, and future trends. *Front. Mech. Eng.* **13**(2), 121–136 (2017). <https://doi.org/10.1007/s11465-018-0483-0>
17. Uhlmann, E., et al.: Sustainable solutions for machine tools. In: Stark, R., Seliger, G., Bonvoisin, J. (eds.) *Sustainable Manufacturing. SPLCEM*, pp. 47–69. Springer, Cham (2017). https://doi.org/10.1007/978-3-319-48514-0_4
18. Andersen, A.L., Brunoe, T.D., Nielsen, K., et al.: Towards a generic design method for reconfigurable manufacturing systems: analysis and synthesis of current design methods and evaluation of supportive tools. *J. Manuf. Syst.* **42**(1), 179–195 (2017). <https://doi.org/10.1016/j.jmsy.2016.11.006>
19. Singh, A., Gupta, S., Asjad, M., Gupta, P.: Reconfigurable manufacturing systems: journey and the road ahead. *Int. J. Syst. Assur. Eng. Manage.* **8**(2), 1849–1857 (2017). <https://doi.org/10.1007/s13198-017-0610-z>
20. Xu, Z., Xi, F., Liu, L., Chen, L.: A method for design of modular reconfigurable machine tools. *Machines* **5**(1), 5 (2017). <https://doi.org/10.3390/machines5010005>
21. Wang, G.X., Huang, S.H., Yan, Y., Du, J.J.: Reconfiguration schemes evaluation based on preference ranking of key characteristics of reconfigurable manufacturing systems. *Int. J. Adv. Manuf. Technol.* **89**(5–8), 2231–2249 (2016). <https://doi.org/10.1007/s00170-016-9243-7>
22. Da Silva, R.M., Junqueira, F., Santos Filho, D.J., et al.: Control architecture and design method of reconfigurable manufacturing systems. *Control. Eng. Pract.* **49**, 87–100 (2016). <https://doi.org/10.1016/j.conengprac.2016.01.009>

23. Denysenko, Y., Dynnyk, O., Yashyna, T., Malovana, N., Zaloga, V.: Implementation of CALS-technologies in quality management of product life cycle processes. In: Ivanov, V., et al. (eds.) DSMIE 2018. LNME, pp. 3–12. Springer, Cham (2019). https://doi.org/10.1007/978-3-319-93587-4_1
24. Zimovets, V.I., Shamatin, S.V., Olada, D.E., Kalashnykova, N.I.: Functional diagnostic system for multichannel mine lifting machine working in factor cluster analysis mode. *J. Eng. Sci.* **7**(1), E20–E27 (2020). [https://doi.org/10.21272/jes.2020.7\(1\).e4](https://doi.org/10.21272/jes.2020.7(1).e4)
25. Ivanov, V., Dehtiarov, I., Denysenko, Y., Malovana, N., Martynova, N.: Experimental diagnostic research of fixture. *Diagnostyka* **19**(3), 3–9 (2018). <https://doi.org/10.29354/diag/92293>
26. Altaf, S., Mehmood, M.S., Soomro, M.W.: Advancement of fault diagnosis and detection process in the industrial machine environment. *J. Eng. Sci.* **6**(2), D1–D8 (2019). [https://doi.org/10.21272/jes.2019.6\(2\).d1](https://doi.org/10.21272/jes.2019.6(2).d1)
27. Gola, A.: Reliability analysis of reconfigurable manufacturing system structures using computer simulation methods. *Eksploatacja i Niezawodność – Maintenance Reliab.* **21**(1), 90–102 (2019). <https://doi.org/10.17531/ein.2019.1.11>
28. Luscinski, S., Ivanov, V.: A simulation study of industry 4.0 factories based on the ontology on flexibility with using FlexSim® software. *Manage. Prod. Eng. Rev.* **b**(3), 74–83 (2020). <https://doi.org/10.24425/mper.2020.134934>
29. Bun, P., Trojanowska, J., Ivanov, V., Pavlenko, I.: The use of virtual reality training application to increase the effectiveness of workshops in the field of lean manufacturing. In: 4th International Conference of the Virtual and Augmented Reality in Education, VARE 2018, pp. 65–71 (2018)
30. Ivanov, V., Pavlenko, I., Liaposhchenko, O., Gusak, O., Pavlenko, V.: Determination of contact points between workpiece and fixture elements as a tool for augmented reality in fixture design. *Wireless Netw.* **27**(3), 1657–1664 (2019). <https://doi.org/10.1007/s11276-019-02026-2>
31. Ivanov, V., Pavlenko, I., Trojanowska, J., Zuban, Y., Samokhvalov, D., Bun, P.: Using the augmented reality for training engineering students. In: 4th International Conference of the Virtual and Augmented Reality in Education, VARE 2018, pp. 57–64 (2018)
32. Yakovenko, I., Permyakov, A., Naboka, O., Prihodko, O., Havryliuk, Y.: Parametric optimization of technological layout of modular machine tools. In: Ivanov, V., Trojanowska, J., Pavlenko, I., Zajac, J., Peraković, D. (eds.) DSMIE 2020. LNME, pp. 85–93. Springer, Cham (2020). https://doi.org/10.1007/978-3-030-50794-7_9

Machining Processes



Methods for Measuring Grinding Temperatures

Ala Bezpalo¹ , Vladimir Lebedev² ,
Tatiana Chumachenko² , Olga Frolenkova² ,
and Nataliya Klymenko² 

¹ Odessa State Academy of Civil Engineering and Architecture,
4, Didriksona Street, Odessa 65029, Ukraine

² Odessa National Polytechnic University, 1, Shevchenko Avenue,
Odessa 65044, Ukraine

Abstract. The temperature in the zone of contact between the wheel and the part is an essential characteristic of the grinding process. Under the influence of the grinding temperature, phase and structural transformations occur in the surface layer of the latter, which reduces the reliability and durability of operation by 2–3 times. It should be noted that any temperature value causes the appearance of some residual stresses, then phase and structural transformations occur when the temperature reaches the Ac1 and Ac3 points. This paper describes methods for measuring temperature on samples with micro-thermocouples in the form of wires, the diameter of which is 20–100 μm . Mainly, there is less than the distance between the grains of the grinding wheel, which eliminates cutting the micro-thermocouple with several grains at once, which significantly improves the reliability of the results. In addition, the method of measuring temperatures when grinding non-conductive materials described. The article describes a temperature sensor built into the wheel, which directly measures the grinding temperature at the workplace. In the article, mathematical calculations allow getting the actual values of grinding temperatures depending on thermocouple materials and parts materials.

Keywords: Contact temperature · Instantaneous temperature · Pulse temperature · Micro-thermocouple · Thermal sensor

1 Introduction

The temperature in the contact zone of the wheel with the part is an essential characteristic of the grinding process. Under the influence of the grinding temperature, which can reach the melting temperature of the part's material in the surface layer of the latter, phase and structural transformations occur, which reduce the reliability and durability of operation by 2 to 3 times.

Essentially, the grinding temperature produces additional heat treatment of the surface layer of the part, which is not provided for by the technology of its manufacture. It should be noted that any temperature value causes the appearance of some

residual stresses, then phase and structural transformations occur when the temperature reaches the points Ac1 and Ac3 [1].

Since the temperatures of these points vary depending on the chemical composition of the steel being ground and the processing conditions [2], establishing the laws of a temperature change as a function of the processing conditions and the characteristics of the wheel is of fundamental importance.

Analytical analysis [1, 2] makes it possible to establish general patterns that need experimental verification, which direct measurements of the grinding temperature can do. First, we need to determine what we will measure since the concepts of “temperature grinding method” includes the following components – contact temperature or temperature averaged over the contact spot of a wheel with a part, instantaneous temperature or temperature from a single grain and pulse temperature, which is equal to the sum of the two mentioned [3]. It should be noted that measurements can be carried out on samples and specific details during their processing on the machine.

At present, measuring the temperature of grinding on samples with foil embedded micro-thermocouples is widely used. The thickness of the foil is 20–30 microns. During grinding, when cutting the foil, a micro junction is formed. Such a micro-thermocouple has low inertia and confidently registers the contact temperature and the instantaneous temperature from the grains. However, because the width of the foil micro-thermocouple is several millimeters, it can be simultaneously cut by several grains, as a result of which an incorrect result will be obtained when measuring instantaneous temperature. For avoiding this effect, the width of the thermo-electrode or its diameter should be less than the distance between the cutting grains if a wire is used. In this case, impulses from grains following strictly one after another will be obtained. This will allow to determine the instantaneous temperature correctly and determine the number of really cutting grains, the average thickness of the chips removed by the grain, and, by some calculations, the conditional radius of curvature of the cutting tip of the grain. In addition, the heat flux of the grinding temperature can cause different heating temperatures of the thermal junction and the surface to be ground. An electrical signal from a thermocouple characterizes the thermal junction temperature, which must be brought to surface temperature. There are no such calculations in works devoted to measuring grinding temperatures.

Measuring the grinding temperature of machined parts is carried out by various temperature sensors and infrared radiation detectors, which are built into the wheel or trap infrared radiation through the hole in the circle. This work is devoted to some features of temperature measurement both on samples and on real details.

2 Literature Review

At present, there is extensive literature on measuring the grinding temperature. However, the relationship between the signal and the surface temperature, rather than a thermal junction, has not been sufficiently considered yet. In addition, the issues of measuring the grinding temperature directly during grinding of a particular part are not described fully enough and rely mainly on rather complicated and expensive equipment.

So in [4], temperature measurement was described using foil thermocouples to consider the energy distribution in the workpiece. However, the ratio of the temperature of the thermal junction to the surface temperature has not been considered.

In [5], a technique is described for measuring the grinding temperature with thermocouples. Descriptions of the temperature distribution in the grinding part are presented. The question of possible measurement errors when cutting a foil thermocouple with several grains at the same time was not considered. The relationships between the temperature of the thermal junction and the surface temperature are not considered.

In [6], issues of monitoring the grinding temperature during processing were considered. The dependences of the grinding temperature on the processing parameters are considered. The temperature ratios of the thermal junction and the surface of the part are not considered.

In [7], using foil thermocouples, the distribution of thermal energy between a wheel and a part is studied. It is concluded that the most reliable results were obtained only in the cooling phase. Foil thermocouples were used with the inherent disadvantages indicated above.

In [8], the temperature field was studied during grinding with a small “creeping” feed of the root of a turbine blade. Used digital modeling and experiment showed good convergence of the results was noted. The method is not specified how the power of a heat source is determined theoretically during modeling. There are no correlations between the temperatures of the thermal junction and the measurement surface.

The work [9] describes the operation of an integrated platform for measuring the grinding temperature. Good agreement between the results of theoretical calculations and experimental measurements is shown. The issue of measurement errors is not adequately covered.

In [10], the measurement of the surface grinding temperature by an infrared sensor is described. The method involves measuring only the contact surface temperature and in the phase of the onset of cooling. The measurement scheme is quite complex but can be used when grinding a specific part.

In [11], the process of controlling the grinding temperature by a high-speed airflow, which is fed into the contact zone, is considered. There is a decrease in temperature measured by foil thermocouples, which are characterized by the above disadvantages.

In [14], a method of measuring temperature with an infrared sensor is considered, which does not make it possible to measure the grinding temperature when using a cooling lubricant.

The paper [15] describes a method of measuring the temperature of glass grinding with foil thermocouples. This does not make it possible to separate the temperatures - contact, instant, and pulse, and besides, there is a high probability of cutting foil sheets by several grains at once.

As can be seen in all cases, it is not determined by the ratio between the received signal from the thermocouple and the actual surface temperature.

3 Research Methodology

The purpose of this work is:

- a statement of the method for measuring grinding temperatures by microthermocouples, which excludes the cutting of the thermoelectrode by several grains at the same time, which eliminates the error in measuring the instantaneous temperature and which contains a method for linking the temperature of the thermal junction to the surface temperature;
- a description of the method for measuring temperature by micro-thermocouples when grinding samples from non-conductive materials;
- a statement of the method of measuring surface temperature when grinding a real part using a temperature sensor built into the wheel.

Of the currently developed methods for measuring grinding temperatures, the method of sheared semi-artificial micro-thermocouple, consisting of the metal being processed and the thermoelectrode placed in the ground part, is the most affordable and convenient, giving a visual distribution of the temperature in the cutting zone and allows recording and measuring the cutting temperatures of individual abrasive grains directly in the grinding zone. One of the electrodes of such a micro-thermocouple is the workpiece, and the second thermoelectrode is a constantan wire with a diameter of 20 μm . The wire diameter is much smaller than the distance between the cutting grains of almost any grain size, which excludes cutting it with several grains at once.

After installing the thermoelectrode in the sample (Fig. 1), the end of the latter is displayed on the surface of the sample and polished. During the experiment, contact, instantaneous, and pulsed temperatures are measured simultaneously; therefore, it is necessary to calculate the time and frequency characteristics of the measuring paths (Fig. 3).

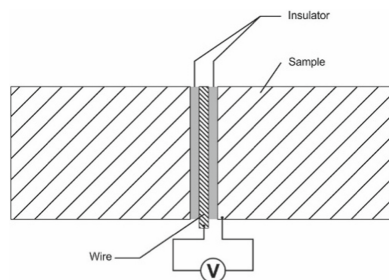


Fig. 1. Sample with thermocouple “thermoelectrode – part”.

The characteristic pulse recorded by the storage oscilloscope has the form Fig. 2.

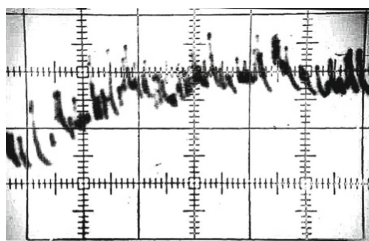


Fig. 2. A typical thermal impulse. Horizontal scale sweep speed 3 ms per 1 cm, vertical scale 250 °C per 1 cm.

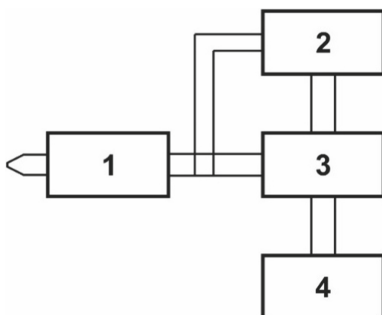


Fig. 3. Block diagram for measuring grinding temperature. 1 – signal amplifier, 2 – sweep trigger amplifier, 3 – amplitude recording oscilloscope, 4 – pulse duration recording oscilloscope.

Since the formation of a thermocouple “thermoelectrode-part” occurs, the signal of such a thermocouple will correspond to the temperature of the thermocouple, while it is necessary to determine the surface temperature of the part. The surface and the end face temperatures of the thermoelectrode can be described by the expression (3):

$$T_s = \frac{1,12Q\sqrt{\tau}}{F \times \varepsilon}; \tag{1}$$

where: Q – the power of a heat source, W;

τ – the duration of the contact, s;

F – is the area of the contact spot of the wheel with the part, m²;

T_s – surface temperature, °C;

ε – is the coefficient of thermal activity J/(m²·K·s^{1/2}); moreover,

$$\varepsilon = \sqrt{\lambda C \rho}$$

where: λ – is the thermal conductivity coefficient J/(m·s·K);
 C – is the specific heat J/(kg·K);
 ρ – is the density kg/m³.

Using the dependences of contact heat transfer [12], we obtain the expression for the surface temperature:

$$T_S = T_{th} \frac{\epsilon_S + \epsilon_{th}}{2\epsilon_S} \tag{2}$$

or

$$T_S = T_{th} \frac{\epsilon_S + \epsilon_{th}}{2\epsilon_S} \times E \times j = k_1 \times k_2 \times E \tag{3}$$

Where

$$k_1 = T_{th} \frac{\epsilon_S + \epsilon_{th}}{2\epsilon_S} \times j, \tag{4}$$

and E – is the value of thermoelectric power, j – is the coupling coefficient between the temperature of the thermal junction and thermo-electromotive force current (thermos-e. f.c), k_2 – is the gain of the circuit, T_s – temperature of the surface being ground, T_{th} – temperature of the micro-thermocouple joint. ϵ_s – the coefficient of thermal activity of the surface being ground, ϵ_{th} – the coefficient of thermal activity of the micro-thermocouple joint.

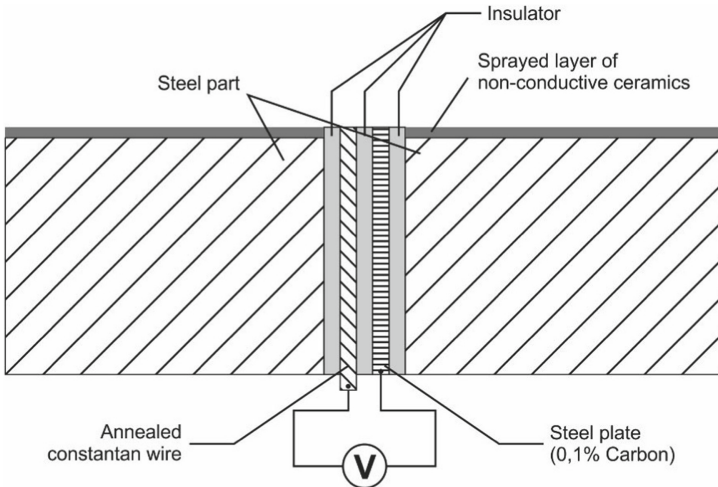


Fig. 4. Sample for measuring the grinding temperature of non-conductive materials.

If it is necessary to measure the temperature during grinding of non-conductive materials, a sample of the following design is proposed for this (see Fig. 4).

The sample shown in Fig. 4 is used to measure the grinding temperature of a non-conductive ceramic layer sprayed onto a steel base. During grinding, a constantan-steel thermocouple is created, which temperature is reduced to the temperature of the ground ceramic according to formula (2).

To measure the temperature during grinding of a particular part, we used a temperature sensor built into the wheel. The sensor meets the following requirements: – high measurement accuracy, low inertia, constancy of properties when editing a wheel, the invariance of the roughness of the ground surface, the ability to work with lubricating-cooling process media (LCPM), low cost (see Fig. 5).

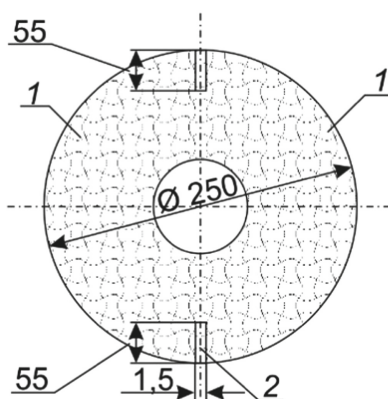


Fig. 5. Wheel sensor. 1 – wheel; 2 – sensor.

The temperature sensor consists of two copper-constantan foil plates between which a gasket of non-conductive material is placed. Foil plates and gasket are glued together with an epoxy adhesive under the press. The shape of the sensor corresponds to the shape of the cross-section of the circle. The total thickness of the sensor is 1.0–1.5 mm. For installing the sensor in an abrasive tool, a groove along the radius is cut in the last:

$$K = \frac{D_{max} - D_{min}}{2} \quad (5)$$

where: K is the length of the groove, mm , D_{max} and D_{min} is the largest and smallest wheel diameter after editing. For ease of measurement, two sensors are installed in a wheel along the radius and are fixed with epoxy glue. Sensors are thus the organic parts of the wheel. When editing, they are easily cut with ruling diamonds. After installing the sensors, the wheel's strength does not decrease, as the verification of the wheel shows at a speed of 1.5 of working (50 m/s). When grinding, the wheel works as follows – the temperature sensors touch the surface to be treated, the foil petals are

closed by this surface, forming a copper-constantan thermocouple whose electrical signal is proportional to the surface temperature, the temperature of which is related to the sensor temperature by the ratio:

$$T_{surf} = T_{sen} \frac{\epsilon_{surf} + \epsilon_{sen}}{\epsilon_{sen}} \tag{6}$$

where: ϵ_{surf} and ϵ_{sen} coefficients of thermal activity of the surface and the sensor. If grinding is carried out using coolant, the latter shunts the temperature sensor signal, introducing a particular error (7). To estimate this error, we consider the equivalent circuit of Fig. 6.

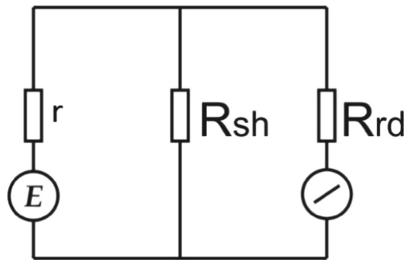


Fig. 6. The equivalent circuit of the electric circuit of a temperature sensor–collector device – coolant: r – is the internal resistance of the temperature sensor, R_{sh} is the shunt resistance of the coolant, R_{rd} is the input resistance of the recording device.

The measurement error will be:

$$\delta = \frac{I_r}{I \left(\frac{R_{rd} \times R_{sh}}{R_{rd} + R_{sh}} + r \right)} \tag{7}$$

Where I -amperage, A.

Considering that the electrical resistance of almost all coolants is greater than 1 kOh-m, it can be argued that the measurement error is negligible. However, the measurement error is not limited to this.

The electrical signal of the sensor is proportional to a specific temperature, the following relation can express the value of which is a general form:

$$U_{sen} = j [T_{surf} - (\Delta T_1 + \Delta T_2 + \Delta T_3 + \Delta T_{fr})], \tag{8}$$

where U_{sen} – sensor voltage V; T_{surf} – surface temperature of the ground metal, °C; ΔT_1 – temperature drop due to the delay of the measurement moment, °C; ΔT_2 – temperature drop due to the short measurement period, °C; ΔT_3 – temperature drop due to thermal resistance, °C; ΔT_{fr} – the friction temperature of the sensor of metal, °C.

Experiments show that the sum of errors 1–3 is always negative, and the error of friction ΔT_{fr} is always positive. These errors are about the same value and therefore cancel each other out. Therefore, the surface temperature through the sensor's temperature is determined by the formula (6).

4 Results

Studies have shown that the use of wire thermoelectrodes with a diameter of 20–100 microns makes it possible to create “semi-artificial” thermoelectrode-part micro-thermocouples when grinding, which have very low inertia, which makes it possible to measure temperatures from a single grain during grinding. These thermocouples make it possible to obtain visual thermal pulses and evaluate the relationships between contact temperature, instantaneous temperature, and pulse grinding temperature. The latter is very important since thermal defects of the polished surface can occur not only under the influence of contact temperatures but also under the influence of pulsed temperatures, the duration of which is several microseconds. The microthermocouple has a low electrical resistance, making it possible to measure the grinding temperature when using coolants.

The electrical insulation between the thermoelectrode and the part should be no thicker than 20 μm to ensure the stable formation of micro-fusion during grinding. The measurement error corresponds to the error of devices providing signal processing and does not exceed 10%.

The temperature sensor built into the wheel makes it possible to measure the contact temperature of grinding directly when grinding a particular part at a particular workplace. The electrical signal from the temperature sensor is a sequence of Π -shaped pulses that can be easily digitalized and can be used to measure the contact temperature of grinding, not only when grinding “dry”, but also when grinding using any coolant. If necessary, the sensor signal can be used for controlling the grinding temperature process.

Thermal sensor plates must be made of carefully annealed copper and constantan foil sheets. The insulating pad can be made of textolite or getinax with a thickness of 0.5–1.0 mm, to ensure a stable closure of the plates by the part's material during grinding.

5 Conclusions

The proposed measurement procedure makes it possible to measure grinding temperatures on samples with high accuracy, eliminating errors in measuring instantaneous temperatures when the foil thermocouple is cut by several grains at once. The proposed methodology makes it possible to determine during grinding the temperature of the thermal junction and the temperatures of the surface being ground, whose thermo-physical characteristics may differ from the thermophysical characteristics of the thermal junction.





The proposed technique makes it possible to measure the grinding temperature of a particular part at the workplace, and, if necessary, adaptive control of the grinding process can be based on it.

References

1. Lebedev, V., Klimenko, N., Chumachenko, T., Uryadnikova, I., Ovcharenko, A.: Definition of the amount of heat released during metal cutting by abrasive grain and the contact temperature of the ground surface. *Eastern-Eur. J. Enterprise Technol* **5**(7 (83)), 43–50 (2016). <https://doi.org/10.15587/1729-4061.2016.81207>
2. Summary planet. Grinding process. Abrasives. <https://www.summaryplanet.com/index.html>. Accessed 13 Feb 2020
3. Usov, A., Oborskij, G.: The effect of thermomechanical phenomena on the stability of cutting process and wear of cutting tools. *Superhard Mater.* **6**, 66–71 (2003)
4. Xu, X., Malkin, S.: Comparison of methods to measure grinding temperatures. *ASME. J. Manuf. Sci. Eng.* May **123**(2), 191–195 (2001)
5. Black, S.C.E., Rowe, W.B., Qi, H.S., Mills, B.: Temperature Measurement in Grinding. In: Kochhar, A.K. (ed.) *Proceedings of the Thirty-First International Matador Conference*, pp. 409–413. Macmillan Education UK, London (1995)
6. Kube, D.A.: Concept development and verification of a test facility for workpiece and tool-side temperature measurement during surface grinding. Student thesis (2003). (in German)
7. Lefebvre, A., Vieville, P., Lipinski, P., Lescalier, C.: Numerical analysis of grinding temperature measurement by the foil/workpiece thermocouple method. *Int. J. Mach. Tools Manuf.* **46**(14), 1716–1726 (2006)
8. Miao, Q., Li, H.N., Ding, W.: On the temperature field in the creep feed grinding of turbine blade root: Simulation and experiments. *Int. J. of Heat Mass Transfer.* **147**, 118957 (2019)
9. Li, R.B., Cui, C.: Optimal design of grinding temperature measurement platform based on improved thermocouple in production. *Appl. Mech. Mater.* **419**, 483–488 (2013)
10. Mallick, S.: Measurement of Grinding Temperature Field Using Infra-Red (IR) Imaging System. *Engineering6* <https://www.slideshare.net/SayanMallick2/measurement-of-grinding-temperature-field-using-infrared-ir-imaging-system>. Accessed 13 Feb 2020
11. Babic, D.M., Murray, D.B., Torrance, A.: Control of grinding temperature by high speed air jets. In: *Thermal Sciences 2004. Proceedings of the ASME - ZSIS International Thermal Science Seminar I*, pp. 399–406 (2004)
12. Laboratory of heat transfer. Experiment Number One. Linear heat conduction, <https://www.slideshare.net/areesalah/linear-heat-conduction>. Accessed 13 Feb 2020
13. Weaver, K.F., Morales, V., Dunn, S.L., Godde, K., Pablo F. Weaver. *An Introduction to Statistical Analysis in Research: With Applications in the Biological and Life Sciences*. Wiley, Hoboken (2018)
14. Brinksmeier, E., Eckebrecht, J., Wilkens, A.: Wheel based temperature measurement in grinding. *Adv. Mater. Res.* **325**, 3–11 (2011)
15. Moussa, T., Garnier, B., Peerhossaini, H.: Temperature measurement of flat glass edge during grinding and effect of wheel and workpiece speeds. *Meas. Sci. Technol.* **28**(6), 065008 (2017)



Rational Characteristics of the Diamond Grinding Wheels

Vladimir Fedorovich , Ivan Pyzhov , Yevgen Babenko,
Yevgeniy Ostroverkh , and Natalia Kozakova 

National Technical University “Kharkiv Polytechnic Institute”,
2, Kyrpychova Street, Kharkiv 61002, Ukraine

Abstract. The article presents theoretical studies using finite element modeling, which made it possible to determine the rational characteristics of diamond grinding wheels based on polymer and ceramic bonds. The effect of the parameters of the diamond-bearing layer on the change in the stress-strain state (SSS) of the diamond-bearing layer in the process of microcutting of hard alloys and superhard materials (SHM) has been studied. A scientific hypothesis was put forward and proved the need for an integrated approach when choosing the concentration and grain size of diamond in the diamond-bearing layer of the grinding wheel. Based on the limiting values of equivalent stress σ_{eq} in the grinding zone, it has been established that the concentration of grains in the working layer of the wheel must be selected, taking into account their grain size, as well as the group of the processed material. The data on the stress-strain state of the diamond-bearing layer during grinding of hard alloys and superhard materials were obtained by the calculation method using the analysis by the finite element method.

Keywords: Diamond grinding · Finite element · Concentration · Grain size · Superhard materials

1 Introduction

Traditional studies of diamond grinding processes are mainly based on costly and time-consuming experiments. Since the quality of the diamond-abrasive tool largely pre-determines the efficiency of the diamond grinding process, then already at the stages of its design and manufacture, it is necessary to theoretically substantiate a rational choice of the structure and physical and mechanical properties of the components of the diamond-bearing layer. Doing this experimentally is very laborious and expensive. At the present stage of the development of computer technology and the appearance of a large number of software products based on the finite element method, it has become possible to increase the efficiency of such studies significantly. The use of computational methods to determine the rational characteristics of diamond wheels at the stage of their design and manufacture will significantly expand the technological capabilities of the diamond grinding process.

2 Literature Review

Along with the choice of the bond grade, grain, and grinding modes, the choice of the relative concentration of diamond grains and their grain size is of great importance [1–3]. A significant number of studies are devoted to studying the effect of concentration on the specific consumption of diamond, grinding performance, and roughness of the processed surface [4–8]. Most of the recommendations for choosing the concentration of diamond grains in polymer and ceramic bonds apply to the processing of carbide materials, high-speed steels, titanium alloys. Model studies carried out by the authors of [9] indicate that a complex choice of grain size and relative concentration of grains can lead to a significant reduction in stresses at the stage of sintering of the diamond layer. By the calculation method, it is possible to determine the stress-strain state of the diamond-bearing layer not only in the manufacture of diamond-abrasive tools but also at the stage of grinding various groups of materials [10].

Modeling the limiting stress values by the computer-aided design and the finite element method [11–13] will allow avoiding expensive experimental studies and, in the future, create a number of recommendations for a wide range of grinded materials.

The diamond content in the amount of 4.4 carats per 1 cm³ of the diamond layer is taken as 100% concentration. The actual amount of diamonds in the diamond-bearing layer N_0 is determined not only by the concentration but also by the grain size [9]. So, for example, at a concentration of 100%, 1 cm³ contains 1522 grains AC6 (State Standard of Ukraine **3292–95**) 63/50, 440 grains AC6 100/80, 68 grains AC6 200/160.

$$N_0 = 0,878K/(100\gamma_a V_z), \quad (1)$$

where: K – relative concentration of the diamonds, %; γ_a – diamond density, g/mm³; V_z – average volume of one grain, mm³.

It can be affirmed that the number of cutting edges that actually take part in the grinding process also changes along with the number of grains. Despite this, the existing recommendations are not differentiated for different grain sizes and are focused on the used bond type and operation. Most often, reference manuals indicate the recommended concentration of 100, 150% both in the processing of hard alloy as well as in the processing of SHM [14, 15].

This choice of concentration is explained by the fact that with an increase in the number of working grains, the heat removal from the grinding zone improves [16]. However, it remains unclear how, in wheels on polymer and ceramic bonds, the picture of heat removal changes with a change in the concentration of grains. Considering the structural features of the diamond-bearing layer of this type of wheel, there is a direct relationship between the volumetric content of diamond grains and a filler. Their ratio is constant, and with a decrease in the content of grains, the volumetric content of the filler in the bond increases [17, 18].

Based on the abovementioned, a hypothesis was put forward that it is possible to calculate the optimal ratio of the volumes of diamond grains and the filler in a polymer and ceramic bond using three-dimensional modeling. The choice of a rational concentration of diamond, depending on the grain size, will significantly reduce the

number of prematurely destroyed grains and increase the durability of the diamond tool during its operation.

3 Research Methodology

The finite element method's modeling of the diamond grinding process was carried out according to the methodology [19, 20] on a specially supplemented three-dimensional model (Fig. 1). The diamond-bearing layer included the elements “grain” and “filler”, and their ratio varied depending on the chosen concentration.

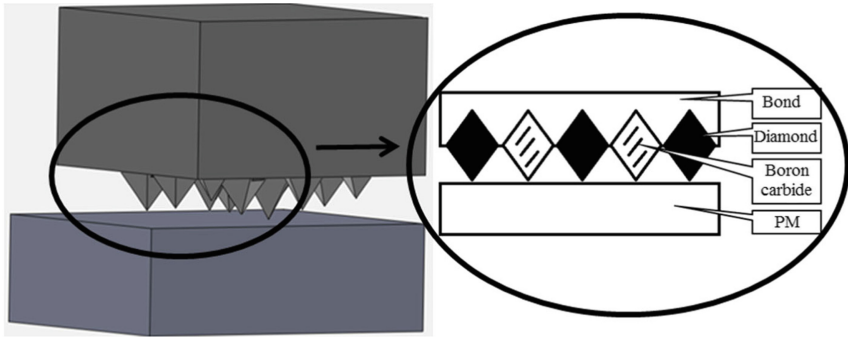


Fig. 1. 3D model of the system “bond–grain–filler–processed material (PM)”, developed to study the effect of grain concentration on the stress-strain state of the system.

As a diamond grain, the “grain” element of AC6 grade 63/50, 100/80, 200/160 was modeled, which contained the inclusion of a Co – Cr-based metal phase. The material to be processed was represented by a hard alloy of the T15K6 grade [11] and a superhard material (synthetic polycrystalline diamond carbonado) of the SPDC grade [6]. Modeling of the grinding process of T15K6 was carried out with the speed of movement of the element “bond–grain” equal to $V_{wh} = 25$ m/s. When processing the SPDC, the movement of the “bond–grain” element was carried out at a speed of $V_{wh} = 30$ m/s. The clamping pressure of the wheel was set by the normal load on the “bond–grain” element. When processing alloy T15K6, the normal pressure was 1 MPa, when processing superhard material SPDC – 2 MPa.

In the model study, the physical properties of the polymer bond corresponded to the B2–01 grade, and the K1–01 bond was considered as a ceramic-based bond. Boron carbide is a filler for such bonds [21]. When modeling the volume of diamond grains, the content of the filler was considered. When the proportion of the components was changed, the physical and mechanical property of a diamond or filler was assigned to a solid body in the form of an octahedron [22].

The physical and mechanical properties of the components of the diamond wheel are given in the table (Table 1).

Table 1. Accepted physical and mechanical properties of the modeled materials [23, 24].

Used properties	Bond					Boron carbide
	B2-01	B1-10	B1-13	K1-01	K2-01	
Mass density of the material ρ , g/cm ³	1.67	2.95	3.24	2.62	3.6	2.48
Hardness, HRB	50	53	54 ± 3	95	110	–
Ultimate compressive strength σ_{comp} , MPa	78 ± 10	136 ± 14	213.0	–	–	1800
Impact strength, kJ/m ²	1.0 ± 0.2	2.5 ± 0.3	2.0 ± 0.2	1.96	1.96	–
Ultimate tensile strength σ_{tens} , MPa	2.60	2.99	2.8	–	–	–
Thermal conductivity, W/m·K	0.55	2.09	2.01	1.4	1.4	11.5
Elastic modulus, GPa	20.3	20.8	16.2	63	63	296
TCLE α , × 10 ⁻⁶ K ⁻¹	5.3	20.6	16.5	3.75	6.41	4.5

The physical characteristics of the filler were also incorporated into the model properties, which made it possible to realistically display the physical properties of the diamond-bearing layer [25].

4 Results

At the first stage of the research, the effect of the relative concentration on the stress-strain state of the “grain” and “bond” element during grinding of the T15K6 hard alloy was studied. The grain concentration in the model varied from 25% to 200%.

As the calculations shown, when modeling grain grade AC6 63/50 in a bond B2-01 (Fig. 2), the limiting value of σ_{eq} in the grain at the selected grinding modes slightly exceeded the permissible stress only in the range from 25 to 50%.

Thus, the stress σ_{eq} at 25 and 50% was 0.7 GPa and exceeded $\sigma_p = 0.67$ GPa only by 20%. With an increase in concentration to 75%, the σ_{eq} value increased to 0.74 GPa, and at the maximum relative concentration, the σ_{eq} value was 1.19 GPa.

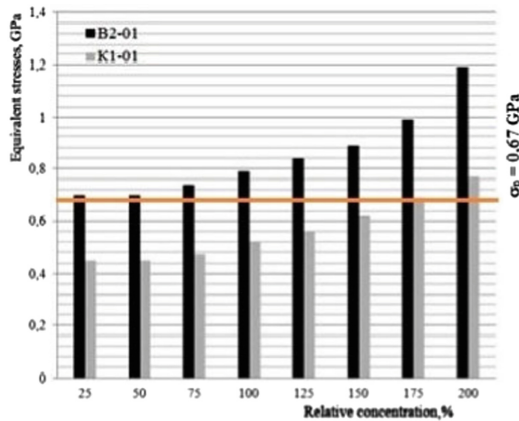


Fig. 2. Calculated limit values of σ_{eq} when grinding hard alloy T15K6. Bond grade – B2-01, K1-01; grain – AC6 63/50. Permissible value $\sigma_p = 0.67$ GPa.

The data are consistent with the theoretical calculation of the stress-strain state of the system when modeling the process of hot pressing of polymer bonds, where the calculated permissible concentration for diamonds of this grain size was also 50%. Considering the small mass of a single grain of this fraction and the average number of grains in 1 cm^3 , the following can be assumed. At a 25–50% concentration in the diamond-bearing layer, there is an optimal ratio of diamond and filler. In this case, the composition's overall thermal conductivity and rigidity lead to minimizing stresses in the diamond. The calculation for the grade of the bond K1–01 and grain AC6 63/50 showed a similar range of the most effective concentration, which should not exceed 50%.

Comparing the values of the obtained stresses, it can be noted that when using a bond based on ceramics, the values of the excited stresses are ~ 1.5 times lower. Presumably, this dependence may be associated with the fact that a wheel on a polymer bond has a relatively low thermal conductivity ($\lambda = 0.55 \text{ W/m}\cdot\text{K}$), but a relatively high value of the thermal expansion coefficient $\alpha = 5.3 \times 10^{-6} \cdot \text{K}^{-1}$. Such a ratio of thermomechanical characteristics can lead to the “clamping” of the diamond grain, which leads to the formation of critical values of σ_{eq} . In addition, the elastic modulus of the ceramic bond is 3 times higher than that of the polymer bond, which is also reflected in the tensile and compressive loads of the diamond composition.

Further studies of the stress fields with a change in the grain concentration in the wheel on the B2–01 and K1–01 bonds showed that for the average fraction AC6 100/80 the range of the smallest values of σ_{eq} is achieved when modeling the relative concentration from 25 to 75% (Fig. 3, a).

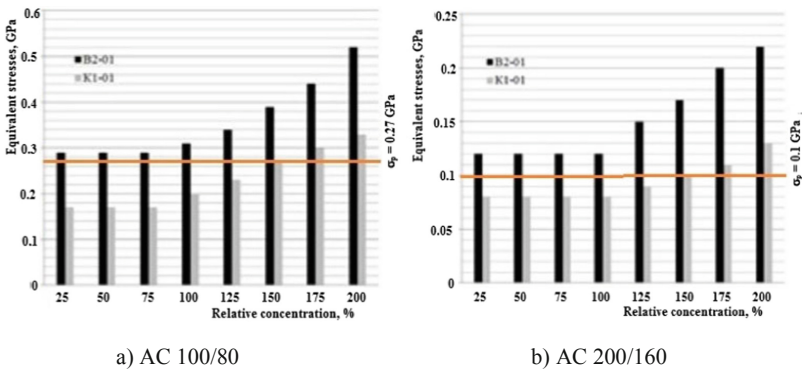


Fig. 3. Calculated limit values of σ_{eq} when grinding hard alloy T15K6. Bond grade – B2–01, K1–01. Permissible value a) $\sigma_p = 0,27 \text{ GPa}$, b) $\sigma_p = 0,1 \text{ GPa}$.

In this concentration range, the given values are minimal and do not exceed the value $\sigma_{\text{eq}} = 0.29 \text{ GPa}$, and with a change in the concentration upward, it only increased. In the case of modeling, the concentration of 200% in the B2–01 bond σ_{eq} reached the value of 0.52 GPa , which is 1,9 times higher than the permissible value $\sigma_p = 0.27 \text{ GPa}$. When grinding with grains of grade AC6 200/160, the range of

permissible concentrations has expanded from 25 to 100%. When using a 125% concentration in the B2–01 bond, breaking stresses σ_{eq} of more than 1.5 GPa arose, and when the maximum concentration value of 200% was selected, σ_{eq} reached 0.22 GPa (Fig. 3, b). For a bond based on ceramics, the permissible concentration was in the range 25–100%, in which the value of σ_{eq} did not exceed 0.08 GPa.

Analysis of stress distribution in the system (Fig. 4) suggests that the probable reason for exceeding the permissible limit σ_p when choosing an increased concentration is a sharp change in the thermal conductivity of the diamond-bearing layer and especially the working surface of the wheel.

In the case of the value of the volumetric content of the filler, corresponding to the range from 43.75 to 25% of the volume of the diamond-bearing layer, the filler serves as a “separator” of diamond grains and prevents the imposition of temperature and contact stresses. With an increase in the concentration, and hence an increase in the volume of diamond grains contained in the wheel, which replace the filler material, an overlap of stress fields appears.

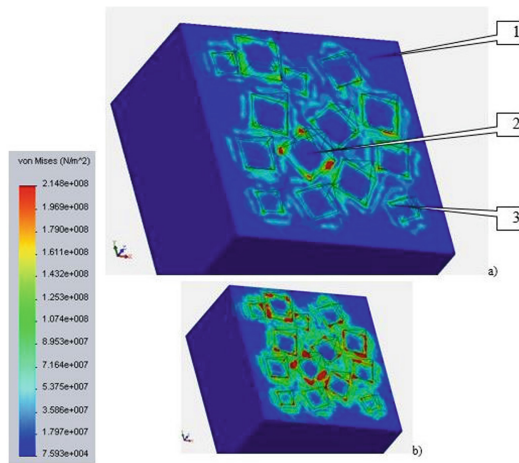


Fig. 4. Stress distribution in the cross-section of the 3D model “bond–grain–filler” when modeling the properties of the concentration: a) 50%; b) 200%; (1 – “bond” element, 2 – “grain” element, 3 – “filler” element); a) $\sigma_{\text{eq}} = 0.12$ GPa, b) $\sigma_{\text{eq}} = 0.22$ GPa; processed material – T15K6; bond – B2–01; grain – AC6 200/160.

At the second stage of the research, the effect of the relative concentration on the stress-strain state of the “grain” and “bond” element when grinding a superhard material of the SPDC grade was studied. Calculations have shown that when grinding superhard materials, a different range of permissible concentrations appears.

Modeling the dimensional and volumetric ratios of the diamond layer for the grain grade AC6 63/50 showed that when using polymer and ceramic bonds, it is possible to use concentrations up to 125%. For example, in wheels on the B2–01 bond, the calculated value of $\sigma_{\text{eq}} = 0.34$ GPa did not change in the range from 25 to 100% concentration. Only

at a concentration of 150–200%, this value increased 1.2 times. A similar dependence was observed for the K1–01 bond based on silicate glass (Fig. 5, a).

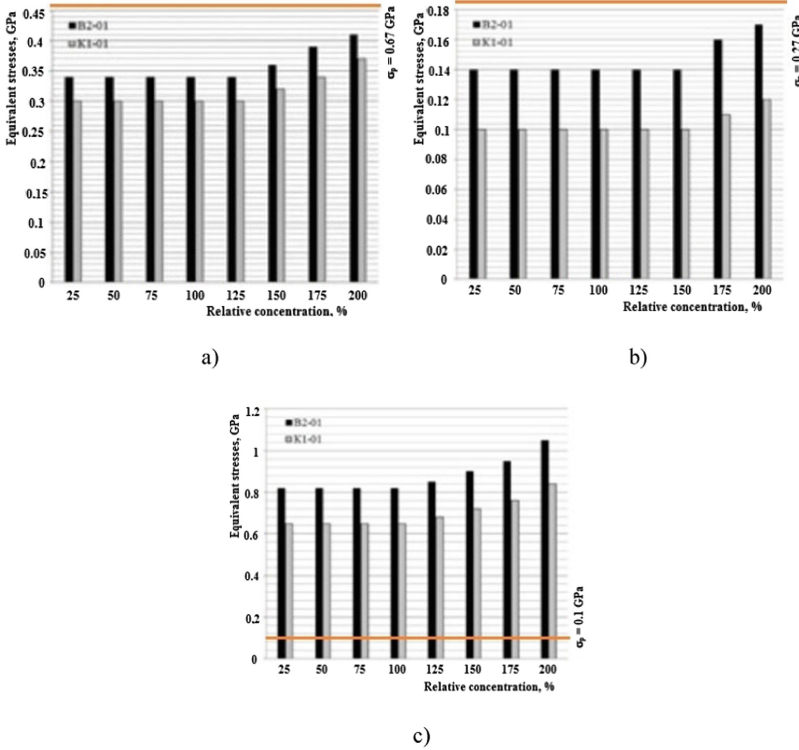


Fig. 5. Calculated limit values of σ_{eq} when grinding SPDC with wheels on polymer and ceramic bond. Permissible values: a) $\sigma_p = 0.67$ GPa; b) $\sigma_p = 0.27$ GPa; c) $\sigma_p = 0.1$ GPa.

In grinding with medium and coarse grains, a more comprehensive range of permissible concentrations was also observed. For AC6 100/80 grain (Fig. 5, b) in B2–01 bond, the limiting value increased only at a concentration of 150%, and in the case of 200% it was $\sigma_{eq} = 0.41$ GPa. Under similar conditions in a ceramic bond, the σ_{eq} value was 0.37 GPa. The use of larger grains allows the use of concentrations up to 150%. So, for the interval 25–150%, the value of σ_{eq} did not change and amounted to 0.14 GPa (for the B2–01 bond). As soon as the diamond content was increased to 175%, the stress in the system increased to 0.17 GPa. This value was critical in the case of the value of the maximum safe load ($p = 0.1$ GPa, which was critical (Fig. 5, c).

The thermal conductivity coefficient of SHM is 10 times higher than the thermal conductivity of the hard alloy, and it can be assumed that a significant part of the heat flux leaves the surface of the processed material. This phenomenon makes it possible to put into operation a more significant number of diamond grains in contact with the SPDC, and the resulting stresses in the grain contact area exceed the permissible values only at a concentration of 150–175%.

5 Conclusions

Thus, it can be argued that the decisive factor in maintaining the integrity of the diamond-bearing layer and the bond as a whole is a comprehensive choice of the concentration and grain size of the diamond grinding wheel. For the first time, the data on the stress-strain state of the diamond-bearing layer during grinding of hard alloys and superhard materials were obtained by the computational method using the analysis by the finite element method. For wheels based on polymer and ceramic bonds, the same tendency of stress changes in the system is observed with varying the relative concentration of diamond grains. Calculations have shown that when processing a hard alloy, the recommended range is a concentration of 25–50% for a grain size of less than 100/80, a concentration of 25–75% for a grain size of 100/80 to 160/125, and a concentration of 25–100% for grains of a coarse fraction 200/160 and more. If these values are exceeded, critical stresses appear in the system, which can prematurely destroy diamond grains. When processing superhard materials, an increased concentration of diamonds is allowed: a concentration of 25–100% for a grain size of less than 100/80, a concentration of 25–125% for a grain size of 100/80 to 160/125, and a concentration of 25–150% for grains of a coarse fraction 200/160 and more.






References

1. Mamalis, A.G., Grabchenko, A.I., Fedorovich, V.A., Kundrák, J.: Methodology of 3D simulation of processes in technology of diamond-composite materials. *Int. J. Adv. Manuf. Technol.* **43**(11–12), 1235–1250 (2009)
2. Zaloga, V., Grabchenko, A., Vnukov Y.: *Integrated cutting processes for materials*. Publishing house “Universitetska kniga”, Sumy (2016) (in Russian)
3. Lishchenko, N.V., Larshin, V.P.: Profile gear grinding temperature reduction and equalization. *J. Eng. Sci.* **5**(1), A1–A7 (2018). [https://doi.org/10.21272/jes.2018.5\(1\).a1](https://doi.org/10.21272/jes.2018.5(1).a1)
4. Pavlenko, I., et al.: Parameter identification of cutting forces in crankshaft grinding using artificial neural networks. *Materials* **13**(23), 5357 (2020). <https://doi.org/10.3390/ma13235357>
5. Klimenko, S.A., Kopeikina, M.Yu., Lavrinenko, V.I., et al: *Finishing of surfaces in the production of parts*. Belarusian Navuka, Minsk (2017). (in Russian)
6. Zubarev, Yu.M., Yur'ev, V.G.: *Instruments from superhard materials and their application*. Publishing house “Lan”, St. Petersburg (2021). (in Russian)
7. Kundrák, J., Fedorovich, V., Markopoulos, A.P., Pyzhov, I., Kryukova, N.: Diamond grinding wheels production study with the use of the finite element method. *J. Adv. Res.* **7** (6), 1057–1064 (2016)
8. Ivanov, V., Dehtiarov, I., Denysenko, Y., Malovana, N., Martynova, N.: Experimental diagnostic research of fixture. *Diagnostyka* **19**(3), 3–9 (2018). <https://doi.org/10.29354/diag/92293>
9. Samuel, R., Asadi, M., Tarda, A., Simbotin, G., Markopoulos, A.P.: Validating dynamic crush response of unidirectional carbon fibre tube via finite element analysis method using LS-DYNA. In: *IOP Conference Series: Materials Science and Engineering*, vol. 1037, no. 1 (2021)
10. Sokhan', S.V., et al.: Diamond grinding the ceramic balls from silicon carbide. *J. Eng. Sci.* **5** (1), A12–A20 (2018). [https://doi.org/10.21272/jes.2018.5\(1\).a3](https://doi.org/10.21272/jes.2018.5(1).a3)

11. Kyratsis, P., Tzotzis, A., Markopoulos, A., Tapoglou, N.: CAD-based 3D-FE modelling of AISI-D3 turning with ceramic tooling. *Machines* **9**(1), 1–14 (2021)
12. Ivanov, V., Vashchenko, S., Rong, Y.: Information support of the computer-aided fixture design system. In: Paper presented at the CEUR Workshop Proceedings, vol. 1614, pp. 73–86 (2016)
13. Kaselouris, E., Kosma, K., Orphanos, Y., Papadogiannis, N.A., Dimitriou, V., et al.: Downscaled finite element modeling of metal targets for surface roughness level under pulsed laser irradiation. *Appl. Sci. (Switzerland)* **11**(3), 1–13 (2021)
14. Shepelev, A.A.: Diamond-abrasive tools in machining technologies. In: Novikov, N.V. (eds.) *Superhard materials. Obtaining and application: in 6 volumes*, vol. 6. Publishing House “ALCON” NASU, Kyiv (2006). (in Russian)
15. Adaskin, A.M.: *Instrumental Materials in Mechanical Engineering*. Forum Publishing House, Moscow (2015). (in Russian)
16. Malkin, S.: Grinding Processes. In: Jane Wang, Q., Chung, Y.-W. (eds.) *Encyclopedia of Tribology*, pp. 1573–1580. Springer, Boston (2013). https://doi.org/10.1007/978-0-387-92897-5_602
17. Kundrák, J., Karpuschewski, B., Pálmai, Z., Makkai, T., Borysenko, D.: The energetic characteristics of milling with changing cross-section in the definition of specific cutting force by FEM method. *CIRP J. Manuf. Sci. Technol.* **32**, 61–69 (2021)
18. Jin, T., Stephenson, D.J.: Three dimensional finite element simulation of transient heat transfer in high efficiency deep grinding. *CIRP Ann. Manuf. Technol.* **53**, 259–262 (2004)
19. Jamal, M., Morgan, M.N.: Characterization of material properties based on inverse finite element modelling. *Inventions* **4**(3), 40 (2019)
20. Mao, C., Zhou, Z.X., Ren, Y.H., Zhang, B.: Analysis and FEM simulation of temperature field in wet surface grinding. *Mater. Manuf. Processes* **25**, 399–406 (2010)
21. Fischer, C.: Runtime and accuracy issues in three dimensional finite element simulation of machining proceedings. In: *The 10th CIRP International Workshop on Modeling of Machining Operations*, pp. 45–50 (2007)
22. Chen, Q., Yu, A., Wu, M., Wu, L., Sun, L., Yuan, J.: Design of assembled substrate of electroplated diamond grinding wheel for disassembly of abrasive layer. *J. Braz. Soc. Mech. Sci. Eng.* **41**(11), 1–8 (2019). <https://doi.org/10.1007/s40430-019-2008-0>
23. Jamal, M., Morgan, M.N.: Materials characterization part II: tip geometry of the vickers indenter for microindentation tests. *Int. J. Adv. Manufact. Technol.* **92**(1–4), 897–908 (2017)
24. Jamal, M., Morgan, M.N.: Materials characterization part I: contact area of the berkovich indenter for nanoindentation tests. *Int. J. Adv. Manufact. Technol.* **92**(1–4), 361–370 (2017). <https://doi.org/10.1007/s00170-017-0115-6>
25. Schieber, C., Hettig, M., Zaeh, M.F., Heinzl, C.: 3D modeling and simulation of thermal effects during profile grinding. *Prod. Eng. Res. Devel.* **14**(5–6), 655–665 (2020). <https://doi.org/10.1007/s11740-020-00983-8>



Model of Milling the Root and Connecting Rod Necks of the Crankshaft for One Manufacturing Process

Vitaliy Kalchenko , Volodymyr Kalchenko , Nataliia Sira ^(✉) ,
Yaroslav Kuzhelnyi , and Vasyl Sklyar 

Chernihiv Polytechnic National University, 95, Shevchenko Street,
Chernihiv 14035, Ukraine

Abstract. During the crankshaft machining process, its axis of rotation does not coincide with the axis of rotation of the connecting rod neck. Therefore, the depth of a cut is always greater than the value of the allowable removed. It leads to uneven removal of allowance, reduces productivity and the quality of machining. The paper proposes a modular spatial model of removing the allowance and shaping of the root and connecting rod necks of the crankshafts during milling with crossed axes of the tool and part for one institution. Based on the developed model, the research of the formation of radical and connecting rod necks of a cranked shaft has been carried out. A method of milling the root and connecting rod necks of the crankshaft with crossed tool axes and parts has been presented, where the angle of rotation of the tool is selected from the condition of ensuring the straightness of the forming neck. In this case, the rough allowance is removed at the end, and the final allowance and calibration - the periphery of the cutter plate, which rotates and simultaneously performs the vertical and transverse movement, and the shaft performs a uniform rotation. The proposed method of milling provides stabilization of the depth of a cut along with the profile of the connecting rod necks, the area of the removed allowance, and the feed rate along the contour of the part.

Keywords: Milling · Crankshaft milling · Crossed axes · Root necks · Modular modeling

1 Introduction

Automotive, tractor, shipbuilding, and other machine-building industries are characterized by extensive use of parts with complex profile surfaces. Such surfaces include, for example, crankshaft necks, camshaft cams, and the like. It is necessary to ensure high productivity of their machining with high manufacturing accuracy in manufacturing such parts.

The necks of the crankshaft are processed at the machine-tool plant “Shlif-verst” on machines of models 3411, 3D4230, 3D4231, 3DB23, LT-235. All root necks of a shaft are ground for one establishment. During the machining of each connecting rod neck to align its axis of rotation with the axis of rotation of the machine spindle, the crankshaft

is reinstalled, which causes an imbalance. It reduces the productivity and accuracy of machining.

For the first time, root and connecting rod necks were machined by Junker (Germany) on a circular grinder in one place. The contact of the neck with the circle is due to the reciprocating motion of the tool, which provides a running-in of the neck for one revolution of the shaft.

One of the productive ways to process complex profile parts is milling. In [1], the influence of high-speed milling on pre-matured tool life is investigated. Paper [2] performs an overview of cutting characteristics of high speed and CNC milling with potentials and applicability for high-performance material. In [3] presents a review of the research work published over the past decade considering five main domains in the free-form surface milling process, which enhance accuracy, machinability, productivity, and machining economy. From the perspective of complex parts robotic milling, this paper [4] focuses on machining process planning and control techniques. Therefore, the development and study of spatial modular models of the removal of allowance and shaping the necks of the crankshafts in milling with crossed axes of the tool and part for one institution is an urgent task. The solution of this task will increase the accuracy of the root and support necks of the crankshafts and the productivity of their machining.

2 Literature Review

Studies of the accuracy of crankshaft machining processes are given in [1, 5–7]. Thus, in [5], an approach to determining the cutting force during machining of crankshafts has been presented, which allows determining the influence of technological parameters on the power characteristics of the cutting process accurately. In [6], researched how to avoid chatter in crankshaft Tangential Point Tracing grinding, Stability lobe diagram has been developed based on the dynamic model to predict chatter. In [7], to improve the crankshaft's accuracy of the crankshaft an automatic alignment approach and apparatus have been proposed and integrated into the non-circular grinder. In [8], the design of a lunette for CNC grinding machines, on which the machining of the crankshaft root and connecting rod necks is carried out, has been proposed. The construction design of the device allows for compensating the influence of the cutting force on the elastic strain of the part, depending on the change in its rigidity. In [9], for the mass production of vehicle-engine crankshafts, a new in-situ roundness measurement strategy has been proposed with high scanning speed. In [10], the process of milling the connecting rod necks of the crankshaft based on the machine's power consumption has been optimized. In [11], a series of experiments were performed to investigate the machinability in crankshaft pin journal path-controlled grinding of 40Cr using vitrified bonded cubic boron nitride (CBN) abrasive. However, the works do not consider methods of single-pass machining of crankshafts.

In [12], the models of milling the support necks and camshaft cams for one institution have been developed. The disadvantage of this method when machining the necks of the crankshaft is the uneven rotation of the part, which will cause the formation error.

In works [13–15] to increase the efficiency of machining and manufacturing crankshafts, their optimization has been carried out. In [13], computer-aided modeling using CATIA and optimization analysis of crankshaft is used to evaluate and compare the fatigue performance of different materials of automotive crankshafts. For the crankshaft system of a four-cylinder in-line gasoline engine, a procedure to build the finite element model is presented [14]. Paper [15] presents the stochastic process for reliability assessment based on the fatigue life data under random loading for structural health monitoring of an automobile crankshaft due to fatigue failure. However, the presented models do not consider the processes of removal of the allowance and the movement of the formation of the crankshafts.

There are no spatial modular models of the processes of removal of allowance and shaping in one-pass milling of the root and connecting rod necks of crankshafts with crossed tool axes and parts in the known works.

3 Research Methodology

The scheme of the process of milling the crankshaft 1 for one institution with crossed axes of it and the cutter 2 is presented in Fig. 1.

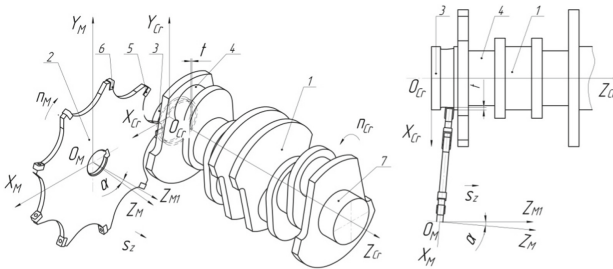


Fig. 1. Crankshaft milling scheme with crossed tool axes and parts.

When machining the root 3 and connecting rod 4 necks of the shaft 1 (Fig. 1), cutter 2 is rotated around the $O_M Y_M$ axis at an angle α , which is selected from the condition of ensuring the required accuracy of the end surfaces of the neck flanges:

$$\alpha = \operatorname{arctg} \frac{2\delta}{-2r_p}, \tag{1}$$

where δ – is the permissible deviation from the perpendicularity of the end surface of the crankshaft neck; H – the difference between the diameters, which determines the height of the flange; r_p – is the radius of curvature of the radius edge of the cutter blade.

Milling of the crankshaft 1 is carried out by a cutter 2, which in the middle of the root neck 3 cuts into the entire depth of cut t (Fig. 1) and moves along the axis $O_Cr Z_Cr$ coordinate system of the part with the supply s_z . Cutting of a mill in the middle of a

neck is carried out to uniform wear of plates of the tool. The rough allowance is removed by the end face of plate 5 (Fig. 1), and the periphery of the plate performs finishing and calibration.

When machining the neck, due to the crossing of the axes $O_M Z_{M1}$ cutter 2 and $O_{Cr} Z_{Cr}$ crankshaft 1 (Fig. 1), there is a deviation from the straightness of the forming neck. The point of intersection D (Fig. 2) of the axes of cutter 2 and part 1 is at a distance $(B-h)$. To ensure the straightness of the forming neck, the axis of rotation of the cutter is shifted in the direction of the axis $O_{Cr} Z_{Cr}$ due to the vertical movement of the tool in the direction opposite to the axis $O_{Cr} X_{Cr}$. In position II (Fig. 2), the distance from the point $D1$ of crossing the axes to the end of the tool decreases and is $(B-h1)$. Consequently, the error of shaping is reduced. Therefore, to ensure the straightness of the generating necks of the crankshaft, the point of intersection of the D axes (Fig. 2) is moved to the extreme position to the end of the tool in the direction of the axis $O_{Cr} Z_{Cr}$.

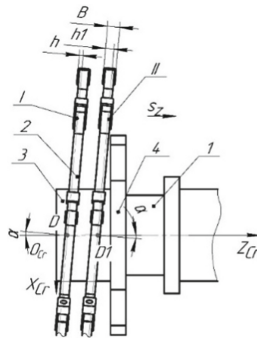


Fig. 2. The scheme of displacement of the cutter to ensure the straightness of the generating neck of the crankshaft.

When machining the root neck 3 of the crankshaft (Fig. 3), cutter 2 is given rotation n_M . To ensure the straightness of the neck profile, the point of intersection of the axes during machining is shifted to the extreme position in the direction of the end face of the flange of the part (Fig. 2).

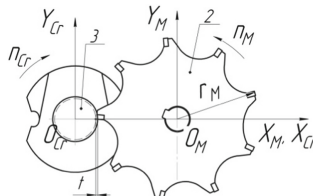


Fig. 3. The scheme of milling of radical necks of a cranked shaft.

When machining the end surface of the neck, the shaft must make at least one turn. After machining the root neck 3, the cutter is moved in the vertical direction of the $O_{Cr}Y_{Cr}$ axis to the height of the location of the connecting rod neck 4 (Fig. 1). In the middle of the connecting rod neck, the cutter cuts into the value of the allowance t , and the process of its machining begins (Fig. 4).

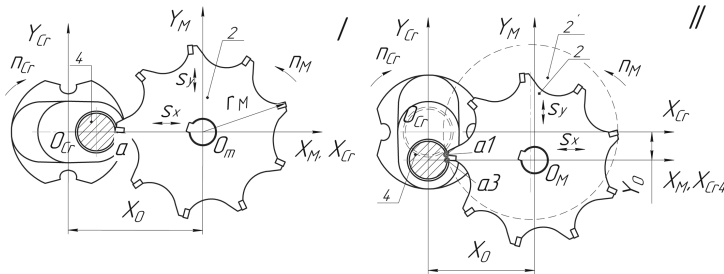


Fig. 4. The scheme of milling of connecting rod necks of a cranked shaft.

Since the axis of rotation of the connecting rod neck 4 and the axis of rotation of the crankshaft 1 (Fig. 1) are in different planes, with uniform rotation of the crankshaft, the point of contact a (Fig. 4, I) of the cutter plate 2 with the part moves relative to the horizontal plane of the connecting rod neck. And due to the transverse movement s_x of the cutter (position 2') occupies the position $a1$ (Fig. 4, II). It ensures the running-in of the neck profile 4.

Synchronous vertical movement s_y of the cutter 2 (Fig. 4, II) ensures the constancy of the location of the contact point $a3$ in the plane passing through the axis of rotation of the connecting rod neck and the cutter. Due to this, the cutting depth t (equal to the value of the allowance), the feed rate along the contour, and the area of the removed allowance remain unchanged during machining.

After machining the connecting rod neck 4 of the crankshaft (Fig. 1), the halves of other root and connecting rod necks are milled according to the described method. After finishing the machining of the half of the root neck 7, the cutter is rotated to the opposite angle $-\alpha$ and the other halves of the root and connecting rod necks of the crankshaft are machined in the feed direction opposite to s_z .

Uniform circular crankshaft feed with simultaneous vertical and transverse tool movements when milling connecting rod necks ensures constant cutting depth and feed rate along the contour. It increases the accuracy of machining of the connecting rod necks of the crankshafts and the possibility of increasing the productivity of their machining by increasing the frequency of rotation of the part.

Set the tool surface with the radius vector \vec{r}_M of the cutter as the product of the matrices M2, M3 (movement along the $O_M Y_M$ and $O_M Z_M$ axes, respectively), and M6 (on the rotation around the $O_M Z_M$ axis (Fig. 1)):

$$\overline{r}_M = M3(Z_M) \cdot M6(\beta) \cdot M2(r_M) \cdot \overline{e}4, \quad (2)$$

where $Z_M = 0 \dots B$ – the linear coordinate of the cutting plate of the cutter, varies from 0 to the width B of the plate; r_M – radius of a mill; $\beta = 0 \dots 360^\circ$ – angular coordinate, which sets the profile of the cutter; $\overline{e}4$ – radius-vector of the beginning of the coordinate system of the cutter.

The nominal surface \overline{r}_{Cr} of the crankshaft is given by the product of the radius vector \overline{r} of the cutter and single-coordinate displacement matrices M1 (movement along the $O_M X_M$ axis), M2, M3, and turns M5 (rotation around the $O_M Y_M$ axis), M6:

$$\overline{r}_{Cr} = M3(Z_{Cr}) \cdot M6(\delta_{Cr}) \cdot M1(X_0) \cdot M5(x) \cdot M2(Y_0) \cdot \overline{r}_M, \quad (3)$$

where X_0, Y_0 – is the wheelbase of the cutter and the part in the horizontal and vertical planes, respectively; δ_{Cr} – angular coordinate, which sets the profile of the shaft; Z_{Cr} – coordinate, which describes the movement of the cutter along the axis $O_{Cr} Z_{Cr}$ relative to the part (feed).

Since the machined surface depends on six parameters (2), we connect the feed Z_{Cr} , wheelbase $X_0(\delta_{Cr}), Y_0(\delta_{Cr})$ cutters, and parts in the horizontal and vertical planes using Eqs. (3)–(6):

$$Z_{Cr} = \delta_{Cr} \cdot \frac{Sz}{2 \cdot \pi}, \quad (4)$$

$$Y_0(\delta_{Cr}) = r_{ec} \cdot \sin \delta_{Cr}, \quad (5)$$

$$X_0(\delta_{Cr}) = r_M + r_{Cr2} + r_{ec} \cdot \cos \delta_{Cr}, \quad (6)$$

$$\overline{V} \cdot \overline{n} = 0, \quad (7)$$

where r_{ec} – eccentricity (distance between the axes of rotation of the connecting rod and the root neck of the crankshaft); r_{Cr2} – the radius of the connecting rod neck of the crankshaft; \overline{n} – is the unit vector of the normal to the tool surface; \overline{V} – is the vector of the speed of relative movement of the tool in the coordinate system of the crankshaft.

The crossing of the axes of the cutter and the crankshaft causes a deviation from the perpendicularity of the end surface of the workpiece. To determine the end profile, find the line of intersection of the part with the coordinate plane $Z_{Cr} O_{Cr} Y_{Cr}$ using the equations:

$$B_{Cr}(x, \delta_{Cr}) =: \text{root}(\text{Det}(\delta_{Cr}, x)_3, \delta_{Cr}), \quad (8)$$

$$\text{Pr}_{Cr}(x) =: \text{Det}(\delta_{Cr}(i, 5 \cdot ^\circ), i). \quad (9)$$

Specific productivity of milling Q , which determines the volume of metal cut by the tooth within the point x :

$$Q(x) = \int_{\beta_1(x)}^{\beta_2(x)} (Vn(\beta, x) - y_v) \cdot r_M(x) \cdot d\beta, \tag{10}$$

where $\beta_1(x), \beta_2(x)$ – the angles of entry and exit of the cutter's tooth from the workpiece on its radius $r_M(x)$; y_v – system flexibility.

4 Results

Calculations and construction of models have been performed using the mathematical package Mathcad.

Using Eqs. (1)–(6), the contact line of the cutter and the neck of the crankshaft have been obtained (Fig. 5). It starts from some point x_{rk} at the end of the plate 5 of the cutter 2 (Fig. 1), passes through the radius of its rounding (coordinate from x_{rk} to x_{r0}), and ends at the periphery at the point of intersection of the axes of the cutter and the neck of the crankshaft.

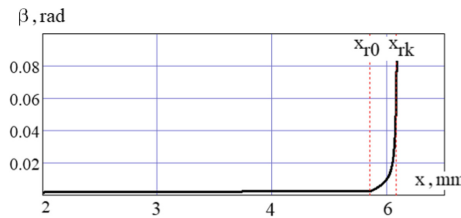


Fig. 5. Contact line of the cutter tooth and parts along with the tool profile.

The contact spot 3 (Fig. 6) of the cutting edge of cutter 2 and the neck of the crankshaft 1 is formed by the intersection of lines 4, 5, 6. Where 4 – is the contact line of the cutting edge of the cutter and the shaft neck (Fig. 5), 5 – is the line of intersection of the tooth cutter and end face of the machined surface, 6 – line of intersection of the outer cylindrical surface of the neck of the shaft and the cutter.

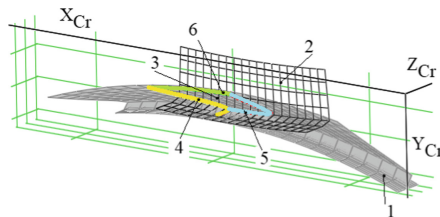


Fig. 6. Contact spot of the cutter tooth and the crankshaft neck.

Using Eqs. (7)–(8), the profile of the treated end surface of the crankshaft collar (Fig. 7) has been obtained.

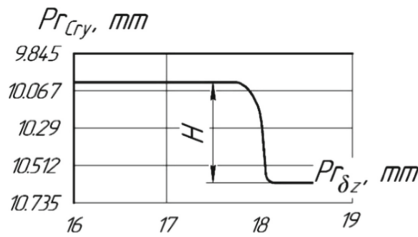


Fig. 7. The profile of the end face of the crankshaft neck.

Synchronous vertical and transverse movement of the cutter, described by Eqs. (5), (6) of the movement of the center of the cutter, ensure the constancy of the point of contact a_3 (Fig. 4) in the plane passing through the axis of rotation of the connecting rod neck and cutter. Due to this, the depth of cut t (equal to the allowance value) (Fig. 8, a), the area of the removed allowance, and the feed rate along the contour of the part remain unchanged during the machining process. And, consequently, the accuracy of shaping the connecting rod necks of the crankshaft increases.

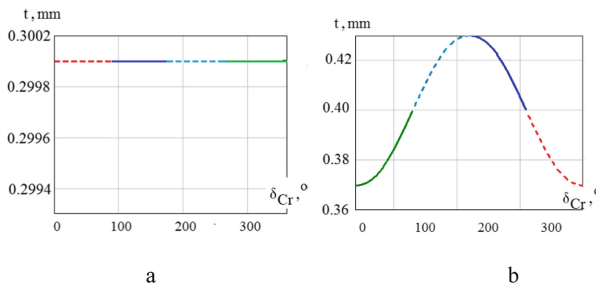


Fig. 8. Graph of distribution of depth of cutting along a contour of a connecting rod neck of a cranked shaft: a – milling with the crossed axes of a mill and details; b – grinding by Junker.

The graph of the distribution of specific productivity Q of machining (Fig. 9) at machining of a cranked shaft with an angle of the crossing of axes of the tool and a detail $\alpha = 1^\circ$, a mill with a diameter of 80 mm and height of a cutting plate of 8,3 mm is received for (9). From the point xr_0 , the graph is developed on the axis coincides with the periphery of a mill's cutting plate.

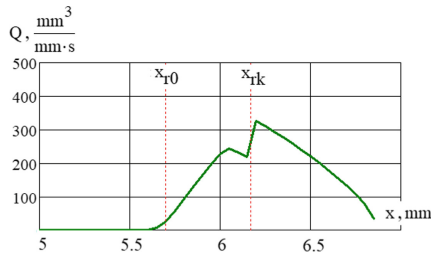


Fig. 9. Distribution of specific productivity Q of milling along with the profile of the cutter tooth.

The largest values of the specific productivity Q of milling (Fig. 9) fall on the area after the coordinate x_{rk} (end of the cutting plate of the cutter), the smallest - the area to the coordinate x_{r0} (periphery of the cutting plate of the cutter) and almost evenly distributed from the coordinate x_{r0} to x_{rk} radial edge of the cutting plate) which is the finishing and calibration area. Removal of the main allowance by an end face of a plate and finishing – by the unloaded periphery of a cutting edge provides an increase of machining accuracy.

For the purpose of uniform wear of quadrilateral plates of a mill at first removal of an allowance from one half of radical and connecting rod necks of a cranked shaft has been carried out, and at the return course of the tool – final machining of necks.

5 Conclusions

Spatial modular models of the tool surface and surface parts have been developed, which give the possibility to analyze the processes of allowance removal and shaping during the milling of a crankshaft root and connecting rod necks.

Based on the developed models, the way of milling of radical and basic necks of crankshafts for one institution where rough milling is carried out by an end face of a quadrilateral plate, and finishing - its unloaded periphery has been offered. The rectilinearity of the shaft necks has been ensured by the displacement of the point of intersection of the tool axes and the part due to the movement of the cutter. The presented method of milling provides stabilization of the depth of cut along with the profile of the connecting rod necks due to synchronous vertical and transverse movement of the cutter with uniform rotation of the crankshaft. The constancy of the depth of cut and reducing the amount of allowance from the end of the plate to its periphery increases the accuracy of shaping the treated surfaces. And milling at the uniform rotation of part gives the chance to increase machining productivity at the expense of increasing the frequency of rotation of a shaft. Milling for the first pass of some halves of necks of a cranked shaft, and for the second – other halves provide uniform wear of plates of the tool.





The proposed method of milling the root and connecting rod necks of the crankshafts can be used to machining various cylindrical surfaces of complex profiles with crossed tool axes and parts on universal sharpening machines with CNC, particular on VZ208F3.

References

1. Zhu, K.: Modeling of the instantaneous milling force per tooth with tool run-out effect in high speed ball-end milling. *Int. J. Mach. Tools Manuf* **118–119**, 37–48 (2017). <https://doi.org/10.1016/j.ijmachtools.2017.04.001>
2. Kar, B.C.: Research trends in high speed milling of metal alloys: a short review. *Mater. Today Proc.* **26(2)**, 2657–2662 (2020). <https://doi.org/10.1016/j.matpr.2020.02.559>
3. Mali, R.A.: A comprehensive review of free-form surface milling – advances over a decade. *J. Manuf. Process.* **62**, 132–167 (2021). <https://doi.org/10.1016/j.jmapro.2020.12.014>
4. Zhu, Z.: High precision and efficiency robotic milling of complex parts: challenges, approaches and trends. *Chinese J. Aeronaut.* 1–25 (2021). <https://doi.org/10.1016/j.cja.2020.12.030>.
5. Pavlenko, I., et al.: Parameter identification of cutting forces in crankshaft grinding using artificial neural networks. *Materials* **13(23)**, 5357 (2020). <https://doi.org/10.3390/ma13235357>
6. Jiang, Z.: Research on stability prediction of the crankshaft CNC tangential point tracing grinding. *Math. Prob. Eng.* **2015**, 1 (2015). <https://doi.org/10.1155/2015/106159>
7. Shen, N., Li, J., Ye, J., Qian, X., Huang, H.: Precise alignment method of the large-scale crankshaft during non-circular grinding. *Int. J. Adv. Manuf. Technol.* **80(5–8)**, 921–930 (2015). <https://doi.org/10.1007/s00170-015-7073-7>
8. Kotliar, A., Gasanov, M., Basova, Y., Panamariova, O., Gubskiy, S.: Ensuring the reliability and performance criterias of crankshafts. *Diagnostyka* **20(1)**, 23–32 (2019). <https://doi.org/10.29354/diag/99605>
9. Yu, H.: In-situ roundness measurement and correction for pin journals in oscillating grinding machines. *Mech. Syst. Sig. Process.* **50–51**, 548–562 (2015). <https://doi.org/10.1016/j.ymsp.2014.05.009>
10. Li, H.L.: Analysis and optimization of milling process for crankshaft pin based on energy consumption. *DEStech Trans. Comput. Sci. Eng.* 355–361 (2019). <https://doi.org/10.12783/dtcse/ica2019/30755>
11. Zhang, M., Yao, Z.: Grinding performance in crankshaft pin journal path-controlled grinding of 40Cr using CBN wheel. *Int. J. Adv. Manuf. Technol.* **82(9–12)**, 1581–1586 (2015). <https://doi.org/10.1007/s00170-015-7473-8>
12. Kalchenko, V.: Development of the single-setup milling process model of the shaft support necks and cams. *Eastern-Eur. J. Enterp. Technol.* **1(106)**, 48–54 (2020). <https://doi.org/10.15587/1729-4061.2020.208579>
13. Rammath, B.V.: Implementation of reverse engineering for crankshaft manufacturing industry. *Mater. Today Proc.* **5(1)**, 994–999 (2018). <https://doi.org/10.1016/j.matpr.2017.11.175>
14. Fan, R.L.: Finite element analysis for engine crankshaft torsional stiffness. *Int. J. Simul. Process Model. (IJSPM)* **14(4)**, 389–396 (2019). <https://doi.org/10.1504/IJSPM.2019.103590>
15. Singh, S.S.K.: Reliability assessment for an automobile crankshaft under random loading. *J. Teknologi (Sciences & Engineering)* **78(6–10)**, 91–96 (2016). <https://doi.org/10.11113/jt.v78.9194>



Gear Grinding Stock Alignment in Advance of Grinding

Vasily Larshin¹ , Natalia Lishchenko² , Oleksandr Lysyi³ ,
and Sergey Uminsky⁴ 

¹ Odessa National Polytechnic University, 1, Shevchenko Avenue,
Odessa 65044, Ukraine

² Odessa National Academy of Food Technologies, 112, Kanatna Street,
Odessa 65039, Ukraine

³ Odessa Military Academy, 10, Fontanskaya doroga Street,
Odessa 65009, Ukraine

⁴ Odessa State Agrarian University, 13, Panteleymonovskaya Street,
Odessa 65012, Ukraine

Abstract. Grinding complex-shaped parts is one of the labor-intensive operations due to the lower stock removal rate and high temperature in the grinding zone at which grinding defects are formed. To reduce the grinding stock unevenness, it is necessary to position the complex-shaped part workpiece on a grinding machine so that the part contour according to the drawing (set by the control program) with the least grinding stock unevenness was inscribed into the contour of this workpiece. The position of the workpiece contour is monitored using an onboard measuring system embedded in a CNC grinding machine. On the example of profile gear grinding, the analysis of three methods of gear positioning is carried out. By the first method, the gear is ground in a single setup on a CNC gear grinding machine, and the gear bore is ground with a preliminary calculation of its axis position based on the results of measuring the toothed surface. By the second method, the bore is ground according to the traditional technology on an internal grinder. An adjustment is made to the gear angular position on a gear grinding CNC machine with an onboard measuring system. A virtual recalculation is performed by the third method for the primary stock measurement data obtained by the second method. The position of the setting tooth space is determined and marked for the gear grinding, which is started from this space on another gear grinding machine, including a machine without both CNC and onboard measuring system.

Keywords: Complex-shaped parts · Profile grinding · Measuring system · Initial space · Setting space · Freeform surface · Digitized surface · Testing gear

1 Introduction

In the last 5–10 years, high productivity profile gear grinding was demonstrated under controlled conditions, i.e., using an onboard or embedded measurement system to determine the grinding stock removed and the grinding machine setting based on the grinding stock measurements results. Onboard grinding stock measurement was

introduced to shorten setup time, in-process and post-process control. In addition and most importantly, onboard measurement is used for the initial grinding machine setup in advance of grinding. Information about the actual location of the grinding stock to be removed on a complex-shaped workpiece allows not only correctly positioning the workpiece relative to the profile grinding wheel but also making a preliminary adjustment to this position. It becomes possible to most successfully position the future part body relative to the actual configuration of the part workpiece using, e.g., a tactile measuring system in advance of grinding.

In general, onboard measurement on CNC gear grinding machines was introduced to shorten grinding machines setting up time (pre-process) and in-process and post-process control based on the CNC intelligent software. Such a grinding machine setting up includes measuring the workpiece's actual grinding stock and orientation in advance of grinding to eliminate uneven stock placement, i.e., such a setup is associated with the automation of locating and clamping the workpiece in advance of grinding.

The task of complex-shaped part location in advance of grinding, e.g., gear grinding, is to a certain extent similar to the task of balancing a manufactured part such as a solid of revolution, for example, balancing a "rotor" type part. The general consists of preliminary measurement of the parameters characterizing each testing part and in the subsequent adjustment of the mass or spatial position of the part, respectively, when balancing and locating the part.

The appearance of practically functioning onboard measuring systems does not mean that their work is effective. Therefore, the development of new methods and algorithms for the effective use of the onboard measuring system is one of the urgent tasks in automated grinding technology. At the same time, this is the aim of this paper. To achieve the aim, the paper discusses three methods of correcting the spatial position of the workpiece (when setting up the machine) based on preliminary measurements: (1) relocating the position of the gear bore datum, (2) correcting the angular position of the gear workpiece relative to the machined bore and (3) calculating and marking the so-called "setting tooth space" position from which gear grinding begins not only on this but also on any other gear grinding machine, including one without both onboard measuring system and CNC.

2 Literature Review

The use of online measurements in mechanical engineering technology is a characteristic trend in its development [1]. Onboard measuring systems built into the process equipment allow considering the individual characteristics of the complex-shaped parts being machined and optimizing their machining [2].

According to the so-called minimax criterion, there is a known method of the preliminary orientation of the complex-shaped part workpiece [3]. If a workpiece of part is installed on a CNC machine tool without aligning its position and without a special fixture, it may turn out that its actual position does not ensure milling contour since the control program corresponds to a position of the part that may extend beyond the workpiece. To allow machining of the part contour specified by the program and fulfill the requirement of preserving the originally designed distribution of milling

stock, it is necessary to set the offset coordinates for the control program along two coordinate axes and the rotation angle. The problem is to find a location of the part in the workpiece with its actual position, where the maximum distance between the contours of the part and workpiece will be minimal. In this case, it is necessary to fulfill the following constraint: the entire part is located in the workpiece and does not go anywhere beyond it.

When machining complex-shaped parts with symmetric shape (gears, impellers, etc.), the task of the initial orientation of these parts is somewhat simplified. For example, grinding a gear in a single setup is proposed: grinding the bore, face, and toothed surface of gear on a single grinding machine [4]. When the stock condition around the circumference and across the gear face is known, grinding strokes can be minimized. There considered not only the radial runout but also the helix distortion and axial runout. During the measurement, the intelligent software finds the best possible alignment between the grinding wheel and teeth to minimize stock removal and ensure that all teeth are completely ground. The software also identifies flanks of tooth spaces that may not be fully ground. It allows the operator to change the grinding parameters before the grinding begins to eliminate grinding strokes with little or no contact. That is why the teeth, bore, and face is to be ground in a single setup. With complete machining of both the bore and teeth on a single machine, the workpiece can be aligned to the unground teeth by the onboard measuring unit and a quick runout alignment device. This technology is the following. Firstly, by aligning the teeth first, the amount of excess stock created by using the conventional method can be removed, resulting in productivity improvements and a shorter carburizing cycle for the same hardness and case hardening depth. Secondly, the bore datum is ground with slightly higher stock removal, still yielding a net benefit. Positive results include: (1) the difference between the maximum and minimum grinding stock is less (more uniform hardening depth); (2) the quality of concentricity of teeth to bore is higher; (3) the quality of the bore is improved, especially if compared to the quality after turning. However, in the considered gear grinding strategy, the following issues are not disclosed: (1) how are related the bore eccentricity and the grinding stock on the tooth flanks; (2) how to grind in a single setup both the bore and the teeth, if a mandrel occupies the bore.

The most common method for aligning the grinding stock in advance of gear grinding is the angular gear adjustment relative to the bore axis, which (axis) is the bore datum [5]. A method of the initial orientation of the workpiece in advance of gear grinding is to align the minimum values of the stock on the left and right flanks of tooth spaces by the following steps. Firstly, one of the gear tooth spaces, moreover random (hereinafter the initial space), is placed in the measurement zone, and the gear is preliminarily fixed on the faceplate. Secondly, the gear is aligned in the radial direction by radial runout decreasing with an unlocked dividing disc. Thirdly, the dividing disc is fixed, the measuring tips are inserted into the tooth space in the measurement zone, and the grinding stock is leveled on both tooth flanks of this gear initial space by turning the faceplate relative to the dividing disc through the faceplate turning mechanism. The setting of the reading device of the measuring system to the zero position had been carried out in advance of measurement according to the reference gear, which is ground to the lower limit size of the tooth thickness. Fourthly, grinding stock is measured on

the left and right flanks of all gear spaces, and the measurement results are recorded, and then a combined diagram of the grinding stock is represented. According to the stock diagram, the difference of the minimum stocks on the left and right flanks of the spaces is determined and the faceplate with the gear under test is rotated relative to the dividing disc in the direction of the flank with the largest minimum stock of the two minimum ones. For example, this difference is equal to 0.09 mm [5]. The correction value to be entered to reposition the gear to be ground equals the half difference of the minimum stocks, i.e., 0.045 mm. The turn value of 0.045 mm is recorded either manually using the reading device of the measuring system or automatically, i.e., in the computer memory through a digital encoder (angle sensor). To make the found correction, the testing gear is additionally rotated in the required direction by the value of 0.045 mm. After correcting the testing gear angular position, the new grinding stock may be remeasured and recorded on both flanks of tooth spaces, and a new combined stock distribution diagram may be plotted or saved in computer memory.

There is a study on adaptive machining or adaptive repairing other complex-shaped symmetrical parts, such as impeller and blisk (a portmanteau of the bladed disk) with construction and investigation of the machining allowance optimization model and model alignment [6] but without expansion on gears.

There are also solutions related to this subject for grinding of biomedical implants [7, 8] and grinding of riblets on compressor blades [9]. Besides, measurement of the position of the workpiece is performed on 3- and 5-axis CNC machines to align the allowance in advance of machining and to detect the current inconsistency by comparing the digitized manufactured surface with the design surface [10, 11]. There is a generalizing study on the so-called cyber-physical systems [12], whereas there is no recommendation for gear grinding.

Of particular interest are new methods for obtaining information on the topography of surfaces of complex-shaped parts: coordinate-measuring machine (CMM) inspection [6], laser scanning [8], and the acoustic emission (AE) signal use [13]. All this is especially important in connection with expanding the profile gear grinding application field [14].

Grinding wheel specification selection [15] and control of grinding accuracy [16] have also to be considered, but this is not directly related to the topic of this paper.

3 Research Methodology

Manufacturing a gear includes many metal cutting operations and abrasive machining (including grinding), between which a chemical-heat treatment is performed, for example, carburizing and hardening. It is known that gear hardening leads to unpredictable deformations and distortions of a complex-shaped gear to be ground. The result is the gear runout and its eccentricity.

According to traditional technology, its bore is ground first on an internal grinding machine after gear hardening. The reference surface for grinding the bore is the toothed surface of the gear or its outer cylindrical surface. Further, the bore datum is used as the processed datum for profile gear grinding. The gear workpiece bore is pushed onto the mandrel with a minimum clearance between the bore and mandrel. After that, the gear

radial runout is eliminated manually by checking mandrel position or gear special reference surface. The grinding stock is measured, e.g., on CNC machine Höfler RAPID 1250 with a Renishaw tactile probe (Fig. 1).

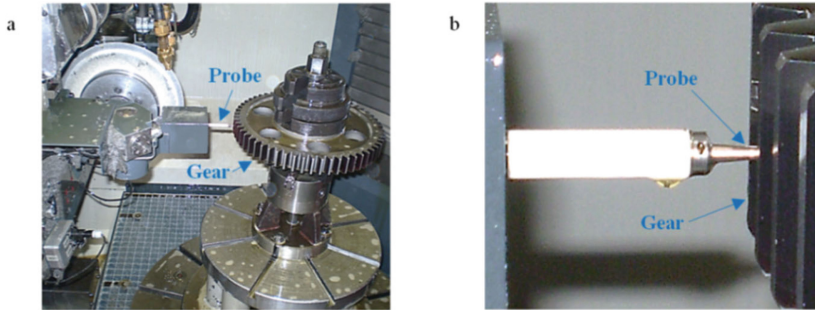


Fig. 1. Tactile measurement made by a special probe (a) and the same after zooming (b).

Instead of a tactile probe, a grinding wheel is often used to measure the topography of the grinding stock when the contact between the grinding wheel and the workpiece is monitored by an AE signal (Fig. 2).

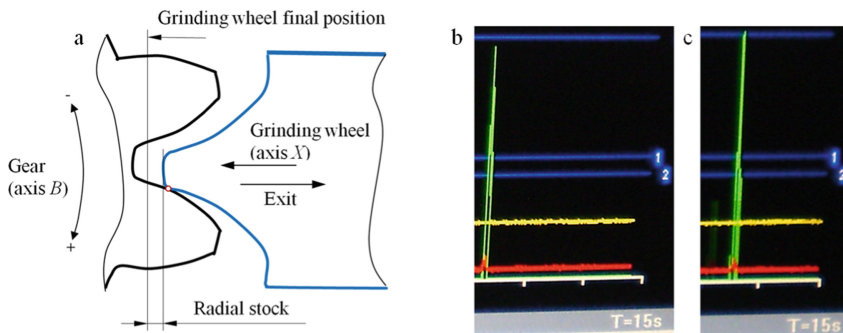


Fig. 2. Centering a grinding wheel to the tooth space (a) and AE signals when one (b) and other (c) flanks of the space are touched with the wheel.

The maximum stock values on the left and right flanks of each tooth space are determined. Further, there are two possible options for using the obtained stock data. According to the first option, the gear angular adjustment’s magnitude and direction are calculated according to the method described above [5] to enter the gear position angular correction value. According to the second option (considered below by an example), a “virtual aligning algorithm” is applied to the obtained data, according to which the obtained “digital topography of the grinding stock” is virtually (i.e., repeatedly, over and over again) recalculated as many times as there are experimental points of the stock measurement except for one – the very first or initial tooth space.

From now on, according to the “virtual aligning algorithm” (or “virtual centering algorithm”), the location of the so-called “setting tooth space” is determined and marked, starting from which this gear can be ground not only on this CNC grinding machine but also on any other gear grinding machine, including an outdated machine, i.e., the machine having neither CNC nor onboard measurement system. This method of redistributing functions between interacting gear grinding machines allows creating a group of gear grinding machines based on one leading (main) gear grinding machine, which has a CNC and an onboard or built-in measuring system, e.g., CNC machine Höfler RAPID 1250, and several driven outdated machines (auxiliary, additional, etc.) that have neither a CNC nor onboard measuring system.

4 Results

To increase the throughput of the group of gear grinding machines mentioned above, a method for centering (aligning, leveling) the grinding stock to be removed without correcting the angular position of the gear to be ground (a patent of Ukraine No. 119835) has been developed.

The method consists of determining the setting tooth space by measuring the gear workpiece’s actual topography around the gear’s circumference, e.g., on a Höfler RAPID 1250 CNC gear grinding machine. The gear grinding machine group, in addition to machine Höfler RAPID 1250, includes domestic gear grinding machines 5A841 and 5843E, which have neither a CNC nor onboard measuring system. The method includes the following sequence of actions to execute the “virtual aligning algorithm” mentioned before.

1. Centering of the measuring instrument (tactile probe or grinding wheel) relative to the random initial space ($i = 1, j = 1$) is performed. Grinding stock readings are formed for all tooth spaces’ left and right flanks except the initial space (Fig. 3).
2. The data obtained is represented in the form of two original row matrices, which are the first main rows of two $N \times N$ matrices for the left and right flanks of the tooth spaces, i.e.

$$Z_{ij}^L = [z_{i1}^L \ z_{i2}^L \ \dots \ z_{ij}^L \ \dots \ z_{in}^L], \quad Z_{ij}^R = [z_{i1}^R \ z_{i2}^R \ \dots \ z_{ij}^R \ \dots \ z_{in}^R], \quad (1)$$

where $1 \leq j \leq n$ is the ordinal number of the tooth space, in which the grinding stock readings are obtained and memorized after centering the measuring tool in the initial ($i = 1$) tooth space; n is the number of tooth spaces (equal to the number of teeth).

3. The “virtual centering” of the measuring instrument is performed in the second ($i = 2$) tooth space by converting the original matrices according to the formulas (1). For this, it is necessary to ensure the fulfillment of the condition $z_{22}^L = z_{22}^R$ by primary recalculation readings, i.e., $z_{22}^L = z_{12}^L \pm \delta_2$ and $z_{22}^R = z_{12}^R \mp \delta_2$, where δ_2 is the correction value that ensures the fulfillment of the condition $z_{22}^L = z_{22}^R$. The rule of signs is as follows: we put a sign “plus” in front of the number δ_2 if the condition

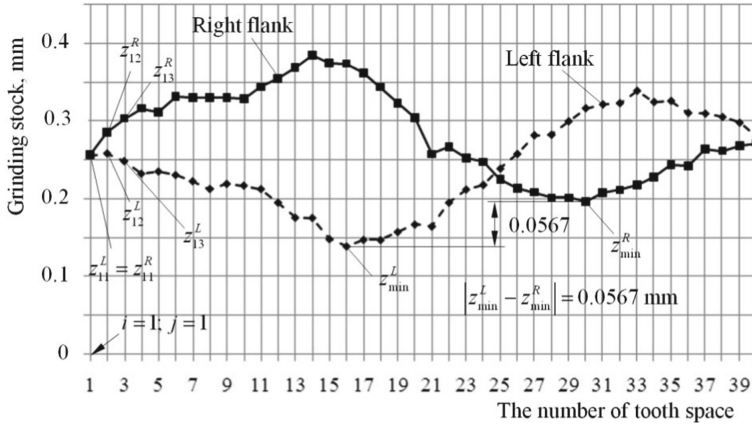


Fig. 3. Grinding stock topography centered on the initial tooth space located in a random place.

$z_{12}^L < z_{12}^R$ is met and $-$ sign “minus” if this condition is violated, and $\delta_2 = (0, 5) \times |z_{12}^L - z_{12}^R|$.

- Row matrices are formed, similar to the previous matrices, but differ in that the centering of the measuring instrument is done in the second tooth space ($i = 2$) by recalculating the readings in the rows of matrices according to formulas (1), changing all the components of these matrices by the same value, taking into account the rule of signs. The following row matrices are obtained for $i = 2$, i.e.

$$\mathbf{Z}_{2j}^L = [z_{11}^L \pm \delta_2 \quad z_{12}^L \pm \delta_2 \quad \dots \quad z_{1j}^L \pm \delta_2 \quad \dots \quad z_{1n}^L \pm \delta_2] = [z_{21}^L \quad z_{22}^L \quad \dots \quad z_{2j}^L \quad \dots \quad z_{2n}^L], \quad (2)$$

$$\mathbf{Z}_{2j}^R = [z_{11}^R \mp \delta_2 \quad z_{12}^R \mp \delta_2 \quad \dots \quad z_{1j}^R \mp \delta_2 \quad \dots \quad z_{1n}^R \mp \delta_2] = [z_{21}^R \quad z_{22}^R \quad \dots \quad z_{2j}^R \quad \dots \quad z_{2n}^R]. \quad (3)$$

- After the “virtual centering” of the measuring instrument in the last n -th tooth space, two square matrices \mathbf{Z}^L and \mathbf{Z}^R are formed for the left and right gear flanks of the tooth spaces, respectively, i.e.

$$\mathbf{Z}^L = \begin{bmatrix} z_{11}^L & z_{12}^L & \dots & z_{1j}^L & \dots & z_{1n}^L \\ z_{21}^L & z_{22}^L & \dots & z_{2j}^L & \dots & z_{2n}^L \\ \dots & \dots & \dots & \dots & \dots & \dots \\ z_{i1}^L & z_{i2}^L & \dots & z_{ij}^L & \dots & z_{in}^L \\ \dots & \dots & \dots & \dots & \dots & \dots \\ z_{n1}^L & z_{n2}^L & \dots & z_{nj}^L & \dots & z_{nn}^L \end{bmatrix}, \quad \mathbf{Z}^R = \begin{bmatrix} z_{11}^R & z_{12}^R & \dots & z_{1j}^R & \dots & z_{1n}^R \\ z_{21}^R & z_{22}^R & \dots & z_{2j}^R & \dots & z_{2n}^R \\ \dots & \dots & \dots & \dots & \dots & \dots \\ z_{i1}^R & z_{i2}^R & \dots & z_{ij}^R & \dots & z_{in}^R \\ \dots & \dots & \dots & \dots & \dots & \dots \\ z_{n1}^R & z_{n2}^R & \dots & z_{nj}^R & \dots & z_{nn}^R \end{bmatrix}. \quad (4)$$

Thus, to obtain all $1 \leq i \leq n$ rows of matrices (4), it is necessary to add to the components of their 1-st main row, if $z_{1i}^L < z_{1i}^R$. Or subtract, if the condition $z_{1i}^L < z_{1i}^R$ is violated, the correction value δ_i , where $\delta_i = 0,5|z_{1i}^L - z_{1i}^R|$. After that, the fixed matrices (4) are subjected to analysis.

6. A database management system is used to find the data row in matrices (4) with the corresponding row number i_s , $1 \leq i_s \leq n$ for which $z_{\min}^L > 0$, $z_{\min}^R > 0$ i $|z_{\min}^L - z_{\min}^R| = \min$. This row is taken as the number of the desired “setting tooth space” which must be marked, and in which a gear grinding machine setting will be made in advance of gear grinding (Fig. 4).

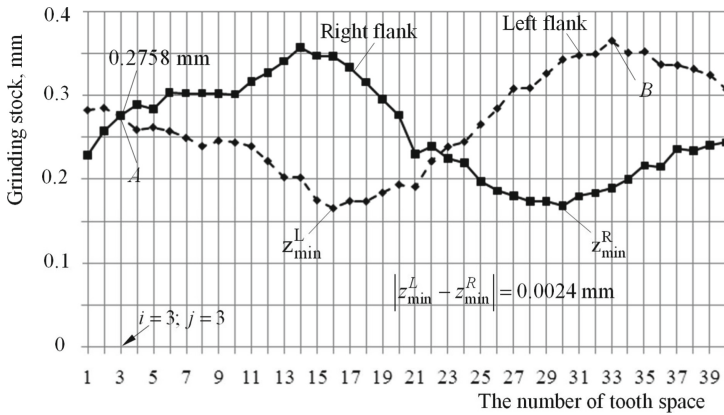


Fig. 4. Grinding stock topography centered on the third tooth space that has been calculated.

For this case, we have $|z_{\min}^L - z_{\min}^R| = 0.0024$ mm (Fig. 4), i.e., the smallest of all possible. Thus, the gear tooth space number three (i.e., $i_s = 3$) has been calculated, which will provide the specified minimum difference of 0.0024 mm if the initial centering of the grinding wheel is performed in this tooth space, i.e., in the third tooth space.

5 Conclusions

With complete machining of both the gear bore and teeth on a single machine, the workpiece can be aligned to the unground teeth by the onboard measuring unit and a quick runout alignment device. However, this requires an algorithm for recalculating the position of the bore center from the results of measuring the teeth. This method is based on the functional relationship between the displacement of the bore datum with a corresponding change in the grinding stock on the flanks of the tooth spaces and the radial runout of the toothed surface relative to the bore.

The method of grinding the gear bore, end face, and toothed surface in a single setup allows reducing both the grinding stock and its unevenness but has the following disadvantages: a complication of the gear grinding machine design which must have an additional grinding head for grinding the gear bore and end face; there are difficulties with the gear installation for grinding the bore which is occupied by the mandrel for the gear locating.

A method for aligning the gear grinding stock has been developed, which consists of finding the “setting tooth space”, into which the grinding wheel is centered at the stage of setting up this or another gear grinding machine, to ensure the alignment of the grinding stock around the circumference of the gear without correcting the angular gear position relative to the gear axis. The method allows replacing the precision angular adjustment of the gear (relative to its axis) by searching for the gear “setting tooth space”. Starting from this “setting tooth space”, it is possible to grind the gear on any other gear grinding machine that does not have an onboard measuring system, and even more, does not have a CNC system.

When the stock location around the circumference and across the gear face is known, as a result of measurement and calculation, grinding passes can be minimized to reduce the grinding time, including eliminating the phenomenon of “air grinding”.

The performed analysis and developed method are shown to profile gear grinding on CNC machines; however, they can be applied to grinding other complex-shaped parts (both symmetrical and non-symmetrical) made of difficult-to-machine materials. For example, these can be gears, lead screws, turbine impellers, cams, biomedical implants (in dentistry and orthopedics), etc.

Acknowledgment. This work was carried out within the State (Ukraine) budget theme of the Odessa National Polytechnic University (2018–2021, registration number: 0118U004400).





References

1. Horst, J., Hedberg, T., Feeney, A.B.: On-machine measurement use cases and information for machining operations. National Institute of Standards and Technology, USA (2019). <https://doi.org/10.6028/NIST.AMS.400-1>
2. Jerard, R.B., Fussell, B.K., T. Ercan, M.T.: Online optimization of cutting conditions for NC machining. In: NSF Design, Manufacturing & Industrial Innovation Research Conference, pp. 1–11. Tampa, Florida (2001)
3. Petrakov, Y., Shuplietsov, D.: Programming of adaptive machining for end milling. *Mech. Adv. Technol.* **1**(79), 34–40 (2017). <https://doi.org/10.20535/2521-1943.2017.79.97342>
4. Undewiss, S., Miller, B.: Grinding large module gears. *Gear solution*, 35–45 (2010)
5. Larshin, V., Lishchenko, N.: Complex-shaped parts grinding technology information ensuring. *Appl. Aspects Inf. Technol.* **3**(4), 246–262 (2020). <https://doi.org/10.15276/aaif.04.2020.3>
6. Zhang, Y., Zhang, D., Wu, B.: An approach for machining allowance optimization of complex parts with integrated structure. *J. Comput. Des. Eng.* **2**(4), 248–252 (2015). <https://doi.org/10.1016/j.jcde.2015.06.007>

7. Denkena, B., de Leon, L., Turger, A., Behrens, L.: Prediction of contact conditions and theoretical roughness in manufacturing of complex implants by toric grinding tools. *Int. J. Mach. Tools Manuf.* **50**, 630–636 (2010). <https://doi.org/10.1016/j.ijmachtools.2010.03.008>
8. Brazel, E., Hanley, R., Cullinane, R., et al.: Position-oriented process monitoring in freeform abrasive machining. *Int. J. Adv. Manuf. Technol.* **69**, 1443–1450 (2013). <https://doi.org/10.1007/s00170-013-5111-x>
9. Denkena, B., Grove, T., Krawczyk, T.: Tools and strategies for grinding of riblets on freeformed compressor blades. *Procedia CIRP* **55**, 182–187 (2016). <https://doi.org/10.1016/j.procir.2016.09.010>
10. Lasemi, A., Xue, D., Gu, P.: Recent development in CNC machining of freeform surfaces: a state-of-the-art review. *Comput. Aided Des.* **42**, 641–654 (2010). <https://doi.org/10.1016/j.cad.2010.04.002>
11. Lasemi, A., Xue, D., Gu, P.: A freeform surface manufacturing approach by integration of inspection and tool path generation. *Int. J. Prod. Res.* **50**(23), 6709–6725 (2012). <https://doi.org/10.1080/00207543.2011.618148>
12. Morgan, J., O'Donnell, G.E.: Cyber physical process monitoring systems. *J. Intell. Manuf.* **29**(6), 1317–1328 (2015). <https://doi.org/10.1007/s10845-015-1180-z>
13. Liu, C.-S., Ou, Y.-J.: Grinding wheel loading evaluation by using acoustic emission signals and digital image processing. *Sensors* **20**(4092), 1–13 (2020). <https://doi.org/10.3390/s20154092>
14. Hayes, M.T.: Winds of change in profile grinding. *Gear Technol.* 47–48 (2004). <http://www.geartechnology.com/issues/0504x/gt0504.pdf>
15. Marchuk, V.I., et al.: On the influence of operating characteristics of grinded wheels on the quality indicators of grinded parts. *Perspect. Technol. Devices* **17**, 86–93 (2020). <https://doi.org/10.36910/6775-2313-5352-2020-17-13>
16. Marchuk, V. et al.: Simulation of dimensional accuracy in an automated grinding system of surfaces of rotation. *Perspect. Technol. Devices* **14**, 82–97 (2019). <https://doi.org/10.36910/6775-2313-5352-2019-14-14>



Burns of Tempering While Grinding Hardened Steels

Vladimir Lebedev^(✉) , Tatiana Chumachenko ,
Nataliya Klymenko , and Olga Frolenkova 

Odessa National Polytechnic University, 1, Shevchenko Avenue,
Odessa 65044, Ukraine
wlebedev29@rambler.ru

Abstract. High heating rates generally characterize the thermal grinding process. Thus, during grinding, secondary surface heat treatment is observed. Notably, that the technology does not provide for this secondary heat treatment, and its modes in most cases are such that they lead to violations of the phase and structural composition of the surface layer or the so-called grinding burns of hardening and tempering. Burns lead to cracks in the surface layer of the part and reduce the reliability and durability by 3–4 times. Tempering burns occur at lower temperatures than hardening burns. Therefore they are more common. It is shown that the temperature of tempering burns is the temperature of the third transformation of tempering, and the value of this temperature depends on the chemical composition of the ground steel and the heating rate. The study made it possible to obtain mathematical dependences for determining the temperature of the tempering burns (the temperature of the third transformation of the tempering). In this work, tables of temperatures of tempering burns have been created for hypoeutectoid, eutectoid, and hypereutectoid steels at different heating rates. It is shown that the grinding modes should provide lower temperatures. The presented material shows that the temperatures of the third transformation of tempering strongly depend on the content of carbide-forming elements, particularly on the concentration of chromium.

Keywords: Burns · Hardening · Tempering · Heating rate · Critical temperature · Martensite · Pearlite · Grinding temperature · Grinding

1 Introduction

The thermal grinding process is generally characterized by high heating rates, short holding times, and high cooling rates. Maximum temperatures can be both above critical points and below critical ones. Thus, during grinding, secondary surface heat treatment is observed.

Remarkably, the technology does not provide for this secondary heat treatment, and its modes in most cases are such that they lead to violations of the phase and structural composition of the surface layer or the so-called grinding burns of hardening and tempering. Tempering burns occur most often since they are formed at relatively low grinding temperatures.

To have the necessary clarity, it is necessary to clearly understand which transformations occur in hardened steel during heating [1, 2].

Martensite of hardening is a non-equilibrium structure that remains due to the low mobility of atoms at room temperature. When this structure is heated (if we are talking about carbon steel), four transformations occur in the metal, the essence of which is briefly reduced to the following [3, 4].

1. In the temperature range 150–200 °C, two-phase or heterogeneous decomposition of martensite occurs. As a result of the first transformation of tempering, tetragonal martensite turns into cubic, which is called as tempered.
2. In the temperature range 200–300 °C, the second transformation occurs, which is characterized by the fact that retained austenite is transformed into tempered martensite.
3. In the temperature range of 300... 400 °C, the third transformation of tempering occurs. As a result of this transformation, a highly dispersed ferrite-cementite mixture is formed, called temper troostite.
4. In the temperature range 400... 600 °C, the fourth transformation occurs, consisting of the growth of carbide particles and their coagulation. The result is a temper sorbit or temper perlite structure.

If the tempering temperature during grinding is considered the temperature at which the martensitic structure of the surface layer completely decomposes, then this will be the temperature of the third tempering transformation. Therefore, in the future, when we study the influence of heating rates and the chemical composition of steel on this temperature, we will mean this temperature.

When studying the tempering process during grinding, it is also necessary to consider the initial structure of the workpiece being ground. In most cases, hardening is accompanied by low tempering, and then the initial structure will be tempered martensite. In some cases, during HFC hardening, tempering is not done, and the surface layer structure is untempered martensite.

2 Literature Review

Numerous works have been devoted to the transformations of tempering during grinding, for example [5–9], which link tempering temperatures with the rates of heating and cooling. However, these works mainly deal with the heating of HFC, the rates of which are several orders of magnitude lower than the heating rates during grinding. In addition, in these works, the effect of the chemical composition of hardened steel on temperature transformations during tempering is not considered, but only the tempering temperature is mentioned, and nowhere is it specified what this means. So in work [10] phase-structural transformations and changes in microhardness of steel 20CrMnTi were studied in detail. The burns of hardening and tempering are shown.

However, grinding temperatures are not given, which reduces the value of the work. In [11], the relationship between steel hardenability and cracking was investigated. However, the heating rates correspond to induction hardening, which is several orders of magnitude lower than during grinding. In work [12], a study was carried out using a statistically planned experiment to link the parameters of the grinding mode with grinding burns. There are no data on heating rates, and changes in the value of the phase transformation temperature depending on the heating rate are not considered.

The work [13] considers the metallurgical reasons for the formation of burns and cracks. However, the dependence of the formation of burns on the heating rates during grinding is not considered.

In [16], the dependence of burns on the state of the wheel is considered – straightening, ligament, graininess. Heating rates are not considered.

In [17], an analysis is presented to predict the distribution of hardness in the surface layer of hardened steel due to tempering and re-hardening associated with high temperatures occurring during grinding. Grinding temperatures are simulated with a triangular heat source in the grinding zone, taking into account the temperature-dependent thermal properties. Heating rates and variations of the chemical compounds were not observed.

3 Research Methodology

Of most significant interest is the study of the third tempering transformation. In particular, the temperature of this transformation depends on the rate of heating, cooling, and the chemical composition of the material.

During the third tempering transformation, carbon leaves the martensite lattice completely. On the one hand, pure ferrite is formed, and on the other, the reaction of the released carbon with ferrite proceeds simultaneously, resulting in cementite. As a result, a ferrite-cementite mixture is formed (see Fig. 1), which is called as pearlite.

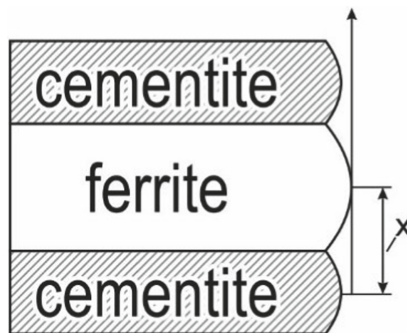


Fig. 1. Scheme of pearlite grain.

The formation of pearlite from martensite can be considered the process of nucleation of pearlite centers with their subsequent growth.

Pearlite grain can be represented as a system consisting of alternating plates of ferrite and cementite (Fig. 1) [4]. It can be assumed that the process begins with the nucleation of a carbide center. As the carbide center grows in the volumes of martensite immediately adjacent to the carbide center, the carbon content decreases, and a ferrite center arises near the carbide center. Further, a new carbide center appears near the ferrite center. Near the carbide center - again ferrite. As the edges of the ferrite and cementite plates grow, they move into the martensite. To determine the transformation's completeness or determine the grain size after a certain time, it is necessary to determine the growth rate of the pearlite grain [13].

Since pearlite formation is accompanied by a change in the carbon concentration in martensite, the change in this concentration can be determined using Fick's second law.

$$\frac{\partial^2 C}{\partial x^2} + \frac{\partial^2 C}{\partial y^2} = \frac{1}{D} \frac{\partial C}{\partial \tau} \quad (1)$$

Under boundary conditions

$$C(x > 0; 0) = 0$$

$$C(0; \tau \geq 0) = C_0 \frac{\partial^2 C}{\partial x^2} + \frac{\partial^2 C}{\partial y^2} + \frac{v \partial C}{D \partial x} = 0 \quad (2)$$

where C is the current concentration;

D – is the diffusion coefficient;

C_0 – is the initial concentration;

τ – current time.

If we denote the speed of advancement of the edges of the pearlite plate into martensite through v and go to a moving coordinate system uniformly moving at a given speed, we can consider the change in the carbon concentration regardless of time.

$$X_l = X - \tau v$$

Then the change in the length of the pearlite plate X can be described as:

$$\frac{\partial^2 C}{\partial x^2} + \frac{\partial^2 C}{\partial y^2} + \frac{v \partial C}{D \partial x} = 0 \quad (3)$$

As a result of solving this equation by the Laplace transform method, we have for the structure tempered martensite

$$T_{\text{tempering}} = \frac{Q}{R \ln \left[\frac{2R_g - v(\tau_3 + \tau_2)}{GA(\tau_3 + \tau_2 - \tau_1)} \right]} \quad (4)$$

And for the structure of untempered martensite

$$T_{\text{tempering}} = \frac{Q}{R \ln \left[\frac{2R_g - v(\tau_3 + \tau_2 - \tau_1)}{GA(\tau_3 + \tau_2 - \tau_1)} \right]} \quad (5)$$

Where,

$$G = \frac{698132(996 - T_h)}{1,4 + \ln \frac{0,015(997 - Q)}{6,67}}$$

R_g – pearlite grain size;

τ_3 – time of contact of a given point of metal with a wheel, s;

τ_2 – cooling time of a given point of the metal, s;

τ_1 – the time required for transformation, s;

A – coefficient characterizing the metal or alloy;

v – is the unsteady growth rate of the pearlite plate, m / s;

R – universal gas constant, J / (mol K);

Q – is the activation energy characteristic of a given metal or alloy J;

T_h – is the temperature of full hardening for hypoeutectoid steels or the temperature of incomplete hardening for hypereutectoid steels, °C;

A_1 – is the temperature of the Ac1 point in the ‘iron-carbon’ diagram [4].

Knowing the tempering temperature, it is possible to determine the specific power spent on transformation when the mass of the material being converted is 1 g:

$$N_{sp} = \frac{c \times m \times \Delta T}{\tau_h} \quad (6)$$

where c – is the specific heat capacity of the metal, J / kg °C;

m – mass, kg;

ΔT – is the difference between the alloy temperature and the ambient temperature;

τ_h – holding time, s.

The tempering temperatures and specific power of transformation for steels DIN C45, C80W1, 100Cr6, 90CrSi, 12Cr2Ni4 were calculated from the given dependences. The steels are selected so that they correspond to hypoeutectoid steels, eutectoid, hypereutectoid, cemented (12Cr2Ni4), and high-carbon alloyed. The tempering temperatures and specific transformation power depending on the speed of part's movement are shown in Table 1.

Table 1. Tempering temperature and specific power transformation.

Speed of a spacement	V_s , m / mm	5	10	15	20	25
	V_s , m / s	0,083	0,166	0,25	0,33	0,416
Holding time	$\tau \cdot 10^{-3}$, s	56,5	24,8	15,65	11,6	9
C45	T_{temp} , °C	$\frac{385}{385}$	$\frac{415}{414}$	$\frac{432}{431}$	$\frac{445}{454}$	$\frac{455}{454}$
	N_{SP} , W	$\frac{4,28}{4,29}$	$\frac{10,51}{10,5}$	$\frac{17,31}{17,3}$	$\frac{24,52}{24,5}$	$\frac{32,1}{32}$
C80W1	T_{temp} , °C	$\frac{418}{417,8}$	$\frac{450}{148}$	$\frac{469}{467}$	$\frac{482}{479}$	$\frac{494}{490}$
	N_{SP} , W	$\frac{4,64}{4,64}$	$\frac{11,4}{11,36}$	$\frac{18,78}{18,69}$	$\frac{26,13}{25,96}$	$\frac{34,28}{34}$
12Cr2Ni4	T_{temp} , °C	$\frac{471}{466}$	$\frac{513}{500}$	$\frac{546}{520}$	$\frac{579}{535}$	$\frac{626}{547}$
	N_{SP} , W	$\frac{5,03}{5}$	$\frac{12,37}{12,1}$	$\frac{20,36}{20,12}$	$\frac{28,36}{27,89}$	$\frac{37,22}{36,12}$
90CrSi	T_{temp} , °C	$\frac{530}{524}$	$\frac{578}{563}$	$\frac{615}{598}$	$\frac{652}{603}$	$\frac{707}{616}$
	N_{SP} , W	$\frac{5,67}{5,63}$	$\frac{13,94}{13,64}$	$\frac{22,94}{22,68}$	$\frac{31,96}{31,43}$	$\frac{41,95}{40,71}$
100Cr6	T_{temp} , °C	$\frac{556}{550}$	$\frac{607}{591}$	$\frac{645}{628}$	$\frac{684}{633}$	$\frac{742}{646}$
	N_{SP} , W	$\frac{5,95}{5,91}$	$\frac{14,6}{14,32}$	$\frac{24}{23,8}$	$\frac{33,5}{33}$	$\frac{44}{42,7}$

Note. In the numerator – the original structure – untempered martensite, in the denominator – the original structure – tempered martensite

Based on the data in Table 1, the dependences (Fig. 2) of the temperature of pearlite formation on the rate of the heat source and the chemical composition are plotted.

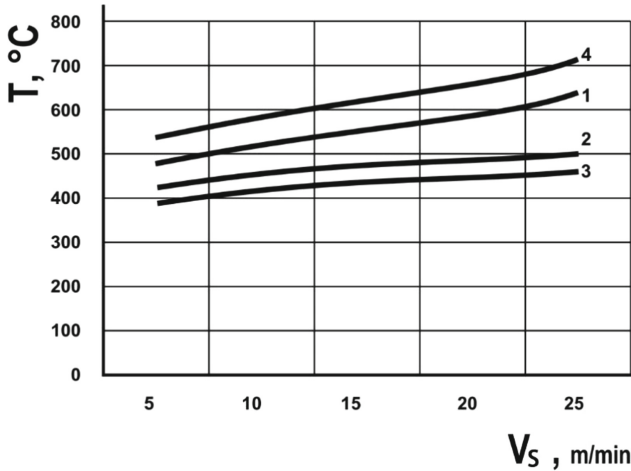


Fig. 2. Dependence of the temperature of pearlite formation on the rate of the heat source and the chemical composition of steel. Steel 45, 2- U8, 3- 12X2H4A, 4- 9XC.

4 Results

The material presented shows that the temperature of the third transformation of tempering depends on the content of carbide-forming elements, particularly on the concentration of chromium. The data in the charts and tables are calculated based on the chromium content indicated in the steel grade. However, this value corresponds mainly to the center of the grouping of the Gaussian curve, for the tolerance for the content of this element, according to which chromium can be distributed in different heats according to the tolerance. The probability of chromium content in the lower and upper tolerance ranges can be within 10%. In this case, higher chromium content is not hazardous because it increases the temperature of the third tempering transformation. The lower chromium content creates a risk of tempering burns when grinding steels of the same grade but different heats since a decrease in the actual content of carbide-forming alloying elements leads to a decrease in the martensite-pearlite transformation temperature.

Even under unstressed processing conditions, grinding temperatures can often exceed the critical temperature - the temperature of the third tempering transformation. Therefore, when designing the grinding operation of a hardened steel part, the data in Table 1 should be used so that the probable grinding temperatures are lower than those given.

The temperature of the third tempering transformation depends on the rate of carbon diffusion. Therefore, steel alloyed with elements that slow down the rate of carbon diffusion, for example, tungsten and molybdenum, have higher temperatures of the third transformation of tempering and can be processed under more stressful conditions without the risk of tempering burns.

5 Conclusions

When grinding parts made of hardened steels, the surface temperature should not exceed the values indicated in Table 1. For obtaining such temperatures, it is necessary to select the appropriate processing modes and select wheels of appropriate characteristics, usually of low hardness or wheels made of synthetic superhard materials.


As a rule, it is necessary to assign low processing modes, which leads to a significant decrease in productivity. For increasing productivity and applying more severe grinding conditions, it is possible to recommend effective cooling systems, for example, the supply of a cooling lubricant under pressure to the contact zone of the wheel with the part.

References

1. Choi, J., Lee, S.: High-frequency heat treatment of AISI 1045 specimens and current calculations of the induction heating coil using metal phase transformation simulations. *Metals* **10**(11), 1484 (2020). <https://doi.org/10.3390/met10111484>
2. Semmler, U., Bräunig, M., Drossel, W.-G., Schmidt, G., Wittstock, V.: Thermal deformations of cutting tools: measurement and numerical simulation. *Prod. Eng. Res. Devel.* **8**(4), 543–550 (2014). <https://doi.org/10.1007/s11740-014-0538-y>
3. Ahlers, M.: The martensitic transformation. *Revista Matéria* **9**(3), 169–183 (2004)
4. Ges, A., Fornaro, O., Palacio, H.A.: *Heat Treatment: Theory, Techniques and Applications*. 2nd ed. Nova Science Publishers (2011)
5. Velling, A.: What Is Heat Treatment? Methods & Benefits. *Fractory*. <https://fractory.com/heat-treatment-methods>. Accessed 13 February 2020
6. Pampania, J.: Heat treatment process for steel. *Engineering*, 19 August 2015
7. Dengel, B.: Heat treating carbon and alloy steels. *Gear Solution*, 15 October 2020
8. Abouelatta, O.B.: Surface roughness prediction based on cutting parameters and tool vibrations in turning operations. *J. Mater. Process. Technol.* **118**, 269 (2001)
9. Usov, A., Oborskij, G.: The effect of thermomechanical phenomena on the stability of cutting process and wear of cutting tools. *Superhard Mater.* **6**, 66–71 (2003)
10. Wang, L., et al.: Mechanism of grinding-induced burns and cracks in 20CrMnTi steel gears. *Mater. Manuf. Process.* **34**(10), 1143–1150 (2019)
11. Li, Z.C., Ferguson, B.L., Nemkov, V., Goldstein, R., Jackowski, J., Fett, G.: Effect of steel hardenability on stress formation in an induction hardened axle shaft. In: *Proceedings of HTS 2013 Conference*. ASM International, ASM HTS 15 Detroit, MI (2013)
12. Del Re, F., Dix, M., Tagliaferri, F.: Grinding burn on hardened steel: characterization of onset mechanisms by design of experiments. *Int. J. Adv. Manuf. Technol.* **101**(9–12), 2889–2905 (2018). <https://doi.org/10.1007/s00170-018-3156-6>
13. MacKenzie, D.S.: Metallurgical reasons for grinding cracks and their detection. *Gear Solution*, 25–27 May 2017
14. Pye, D.: What causes grind burns on carburized gear teeth? *Ind. Heat.*, 2 March 2009
15. Fedoseev, O.: Analysis of tempering and rehardening for grinding of hardened steels. *J. Manuf. Sci. Eng.* **113**(4), 388–394 (2008)
16. de Lima, A., Gâmbaro, L.S., Vieira Junior, M., Baptista, E.A.: The use of cylindrical grinding to produce a martensitic structure on the surface of 4340 Steel. *J. Braz. Soc. Mech. Sci. & Eng.* **33**(1) (2011)
17. Lasaosa, A., Gurruchaga, K., Arizti, F., Martinez-De-Guerenu, A.: Induction hardened layer characterization and grinding burn detection by magnetic barkhausen noise analysis. *J. Nondestr. Eval.* **36**(2), 1–7 (2017). <https://doi.org/10.1007/s10921-016-0388-y>



Modeling of the Intermittent Grinding Temperature

Natalia Lishchenko¹ , Vasily Larshin² ,
and Sergey Uminsky³ 

- ¹ Odessa National Academy of Food Technologies, 112, Kanatna Street,
Odessa 65039, Ukraine
² Odessa National Polytechnic University, 1, Shevchenko Avenue,
Odessa 65044, Ukraine
³ Odessa State Agrarian University, 13, Panteleymonovskaya Street,
Odessa 65012, Ukraine

Abstract. The intermittent grinding technology, which for many years is developing in the scientific school of prof. A.V. Yakimov finds all new and new areas of use when grinding parts made from hard-to-machine materials. Intermittent grinding wheels are currently prefabricated, i.e., they are prefabricated structures. That is why adjusting the number of cutting segments on the grinding wheel and its duty factor (ratio between the length of the cutting segment and the period of repetition of these segments on the wheel) is possible. In this regard, in the paper, the classification of macro- and micro-intermittent grinding wheels has been performed. In the first case (macro-intermittent wheels) these are segmented (prefabricated) abrasive tools, in the second (micro-intermittent) – these are the grinding wheels with high porosity. A new mathematical model for determining the intermittent grinding temperature has been developed. The rationale for this model is made by comparing it with a similar model of H.S. Carslaw and J.C. Jaeger for determining the temperature from the pulsating heat flux. The paper shows that the results of determining the grinding temperature by both these models differ by no more than 5%. With the help of the developed mathematical model, the optimal intervals of changes in the geometric parameters of high porous grinding wheels are determined, at which the grinding temperature is the smallest under otherwise equal conditions.

Keywords: Grinding temperature · Grinding burns · Intermittent wheel · Technological heredity · Heat flux · Pore voids · Duty factor

1 Introduction

The scientific direction associated with the expedient provision of useful properties of the object of labor is called synergetics and is associated with creating synergetic systems. In synergetic systems, it becomes possible to interrupt the inappropriate development of the process to prevent the appearance of the so-called bifurcation point. As applied to grinding, such a bifurcation point is a condition for forming a grinding burn caused by an increase in the maximum temperature in the cutting zone to a critical value of this temperature. The method of intermittent grinding was proposed by

Professor A.V. Yakimov in the seventies of the last century. Being tested many times in practice, this method was not considered from the position of synergetics in theoretical terms. Synergetics is the science of self-organizing systems that arise under certain conditions. The concept of synergetics is also related to the concept of management because the creation of special conditions for the expedient development of the process allows cutting off the appearance of a bifurcation point and thereby ensuring the stability of this process (e.g., grinding).

The grooves on the grinding wheel surface contribute not only to the effective penetration of the grinding fluid into the cutting zone with all the resulting positive consequences which the grinding fluid provides, namely: cooling, lubricating, removing chips, etc. The alternation of cutting segments and no cutting grooves in a short period of time of the grinding cycle makes it possible to interrupt the impractical development of the heat accumulation process by timely removal of this heat together with the chips. Thus, the subsequent cutting segment of the intermittent wheel gives an increment of heat in the cutting zone and removes (together with the chips) the transient process of temperature increase from the previous cutting segment that is “developing” in the material being removed. In other words, the introduction of heat from the subsequent cutting segment is accompanied by the removal of heat from the previous cutting segment. Moreover, the rates of heat introduction and its removal are comparable since the neighboring cutting segments are at a distance of “one order of smallness”. Thus, the bifurcation point associated with the formation of burns is moved back in time, and, with the correct choice of grinding parameters, the temperature in the grinding zone does not exceed the critical level. This synergetic approach applies not only to artificially created cutting segments and grooves on the grinding wheel but also to the so-called “highly porous” grinding wheels. There are special open-pore grinding wheels (high-porous grinding wheel) for working at the machining center where the grinding wheels of different specifications are installed by the tool changer in the same way as if they were milling cutters. At the same time, any reduction in the working surface of the grinding wheel leads to both an increase in the workload on the cutting segments of the wheel and to the appearance of grinding temperature defects (grinding burns and cracks), as well as to the appearance of vibrations that worsen the quality of the surface layer (surface integrity). In other words, the positive qualities of the intermittent grinding wheel can be overcome by its negative qualities, such as violation of technological requirements for surface integrity and surface finish. So, the study of grinding temperature in the grinding with the macro-intermittent wheels or modern high porous micro-intermittent wheels (having pore voids on the working surface) is one of the urgent issues of manufacturing engineering.

A new synergetic approach gives special relevance to such studies, according to which it is established that a preheated section of the ground surface loses part of its preheated mass from the action of the previous cutting segment. This does not allow the temperature field to spread deep into the surface being ground. An additional cooling before the next heating occurs not due to the absence of cutting in the groove area (cavity) of the grinding wheel but due to the removal of the source of the “non-deployed in time” thermal field together with the grinding chips.

2 Literature Review

Modern intermittent grinding is nothing's the same as it used to be. There is much information on the use of grinding wheels with an intermittent working surface. As a rule, literary sources consider certain aspects of intermittent grinding technology, which now is a comprehensive method not only for parts made of metals [1] but also for parts made of non-metallic materials [2], e.g., of natural and artificial stone materials [3, 4]. But nothing is said about the ratio between the diamond segment length and the period of changing heat flux.

It is found that the dynamic number of wheel segments can be used to accurately predict the pulses on the measured temperature curves in the grinding zone [5]. But this conclusion is not specific and requires additional research.

To reduce grinding thermal damage, furthermore a general thermal model is developed [6]. This research aims to choose the slotting or segmental parameters more reasonably and predict grinding temperature. However, these parameters are not connected with the optimal grinding temperature.

It was shown that the machining of the teeth of the broaches with an intermittent grinding wheel provided a higher quality of blade surfaces and increased the process productivity. Besides, the workpiece oscillations amplitude may be chosen as a criterion for determining the period of re-profiling of the grinding wheel [7]. However, the vibration itself may have nothing to do with the geometry of the intermittent grinding wheel.

To reduce thermal damage, the intermittent grinding wheels, which have a cooling effect, have been used [8]. However, it is known that an ordinary intermittent grinding itself does not provide effective cooling of the cutting zone.

There are researches to meet the cooling requirement by using the wheel grinding slots [9, 10], special slotted grinding wheels [11, 12], and the wheel of high porosity for the machining center [13, 14] with VIPER grinding [15, 16] along with making a precision decision [17]. The VIPER stands for vitreous (or very) improved (or impressive) performance extreme removal.

Thus, a comprehensive study of intermittent grinding [1] allowed us to establish that all other things being equal, the maximum values of the pulse temperature are higher than the average values of the same pulse sequence at the same time [18, 19]. Moreover, this average temperature fully corresponds to the equivalent "solid" grinding wheel, i.e., a wheel with a continuous working surface. On the other hand, the long-term practice of intermittent grinding shows that the temperature of intermittent grinding is lower than the temperature of continuous grinding, all other things being equal. In addition, a mechanistic approach is possible to determine the temperature of the intermittent grinding [20].

3 Research Methodology

The literature review shows that intermittent grinding wheels are no longer manufactured as 30–40 years ago, i.e., by cutting the grooves on standard wheels having no these grooves. These are special constructions of two types: either prefabricated wheel

construction made of fixed segments (segmented and slotted wheels) or special grinding wheel with high porosity (porous and high porous wheels) having pore voids on its working surface. The first type of grinding wheel is used in high-speed grinding, i.e., when cutting speeds of about 50–80 m/s. The high porous grinding wheel second type is used, e.g., in the profile gear grinding and VIPER grinding.

A micro-intermittent grinding wheel is the porous or high porous wheel in which the cutting grains areas alternate with pore voids (gaps). Cutting section of length l_1 and non-cutting section of length l_2 were measured experimentally [1]. Thus, the high porous grinding wheel surface geometrical parameters l_1 (cutting segment) and l_2 (not cutting cavity or pore void) are irregular. However, due to the known inertia of the thermal field, the corresponding equivalent of the regular calculation parameters can likely be found for these irregular parameters. To do this, we can use the constancy of the average heat flux for regular and irregular cases. This assumption allows solving the problem of temperature determination for macro- and micro-intermittent grinding from a single point of view.

The complexity of the design and production of intermittent grinding wheels is very high. No less challenging is the selection and optimization of intermittent grinding parameters. For this reason, an integrated system CAD/CAM/CAE [18] is used in mechanical engineering, which allows speeding up the process of creating effective designs of intermittent grinding wheels of both segmented and high porous ones (Fig. 1).

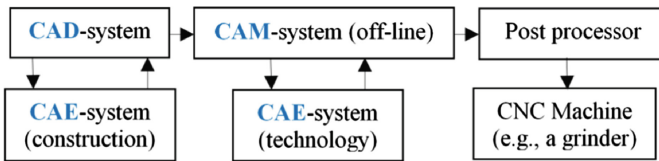


Fig. 1. Integrated system CAD/CAM/CAE in mechanical engineering technology for intermittent grinding wheel design [18].

The modern understanding of CAD/CAM/CAE automation is considered taking into account the product life cycle, which contains a number of time stages, including product design (CAD), process design (CAM), and process systems engineering calculations (CAE) with special computer software packages, as well as the product testing and the process assessing. At the CAM stage of the product life cycle, process design is performed considering the intermittent grinding temperature field. The thermal scheme of intermittent grinding can be represented by a sequence of heat flux pulses $q(\tau)$, which is characterized by a period T , a period duty factor $s = T_1/T$, and the maximum q_{\max} and average q_{ave} values of the heat flux (Fig. 2).

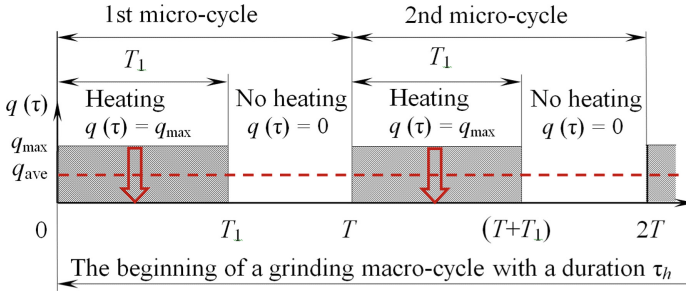


Fig. 2. Pulsating heat flux $q(\tau)$: $0T_1$ and T_1T are time intervals of heating and no heating forming macro- or micro-cycles of intermittent grinding with a cycle period T [1].

Every technological process or operation (as part of the process) is represented by a certain discrete sequence of actions that are carried out on the object of labor that has an initial and final state. Under the laws of mechanical engineering technology, the location of these actions in time and their intensity are determined by certain empirical regulations. For example, to obtain the 6th tolerance grade of the size of a part made using traditional techniques from the stamping of the 16th tolerance grade, at least four technological operations are required. Such operations can be, for example, two turning operations and two grinding operations, each of which, with the existing technology, takes a certain time. This time is a consequence of defect-free machining parameters. Any reduction in this time increases the risk of getting a defective part according to the parameters of dimensional accuracy, surface finish, and surface integrity.

Thus, the reason for the imperative in terms of the number of necessary technological operations and their necessary duration is the minimal risk of obtaining defective parts. Therefore, the only guide to such technological design is empirical information about the manifestation of technological inheritance or technological heredity. Technological inheritance is the phenomenon of transferring the properties of objects from previous technological operations to subsequent ones. These properties can be both useful and harmful. The phenomenon of preserving these properties in objects has been called technological heredity.

To explain the effect of interrupting technological heredity on the accumulation of heat in the cutting zone during grinding, we can use the simplest model of thermal phenomena during grinding. Such a model is called lumped one (i.e., concentrated), in contrast to the distributed model of the thermal field obtained by Carslaw H.S. and Jaeger J.C. for the pulsating heat flux density [1, 19]. Let a hypothetical body simultaneously acquire and lose heat energy. The acquisition of heat occurs due to the heat released during cutting. The loss is due to heat dissipation into the surrounding space (including due to thermal conductivity). For the generality of the problem, let this body have some elevated temperature T_0 at the initial moment of heating (Fig. 3).

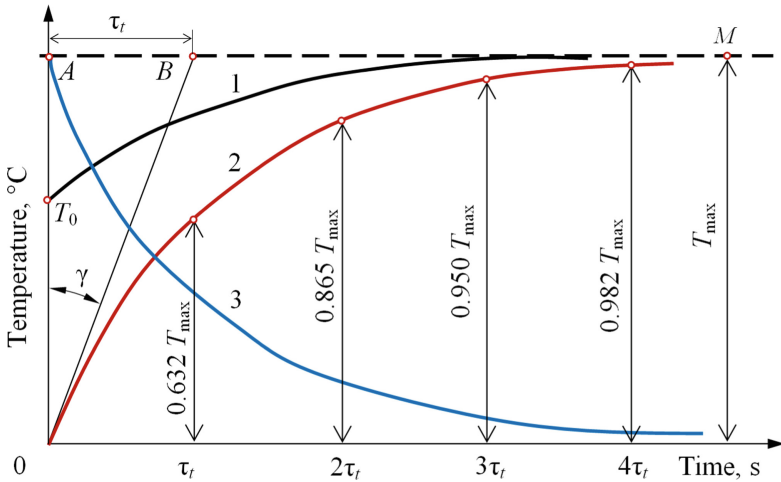


Fig. 3. Characteristics of the lumped (concentrated) model of the thermal field during grinding

It is known (received by L.M. Piotrovsky in 1950) that for such a model of the temperature field, the following equation can be obtained for the current time τ

$$\tau = -\tau_t \ln(T_{\max} - T) + \tau_t \ln(T_{\max} - T_0), \tag{1}$$

where τ_t is the heat time constant of the system, s; T_{\max} is the maximum temperature, °C; T is the current temperature, °C.

Therefore, we have

$$T = T_{\max} \left[1 - \exp\left(-\frac{\tau}{\tau_t}\right) \right] + T_0 \exp\left(-\frac{\tau}{\tau_t}\right) \tag{2}$$

In the special case, when the heating starts from the cold state, i.e. $T_0 = 0$, we have

$$T = T_{\max} \left[1 - \exp\left(-\frac{\tau}{\tau_t}\right) \right] \tag{3}$$

Time constant τ_t may be found as (Fig. 3)

$$\tau_t = T_{\max} \tan \gamma \tag{4}$$

It is known that the heating time constant τ_t can be graphically defined as a segment AB on the line ABM of the final maximum temperature (Fig. 1).

If the body is first heated, e.g., up to the temperature T_{\max} , and then the heat supply is stopped, then the body begins to cool according to the equation

$$T = T_{\max} \exp\left(-\frac{\tau}{\tau_t}\right) \tag{5}$$

Equations (1)–(5) and their graphical interpretation in Fig. 3 allow us to describe the thermal process of heating and cooling during intermittent grinding, considering the influence of transient processes of increasing and simultaneously decreasing temperature in the contact zone. Based on this lumped (concentrated) model, the dependences of the intermittent grinding temperature as a function of time are constructed for the following different cases (Fig. 4): ideal intermittent wheel (heat removal with chips is not taken into account), real solid wheel (i.e., the wheel with the continuous surface), real intermittent wheel (some of the heat is carried away with the chips). Separately, the accumulation of heat (residual heat accumulation) is shown due to incomplete removal of it and the chips.

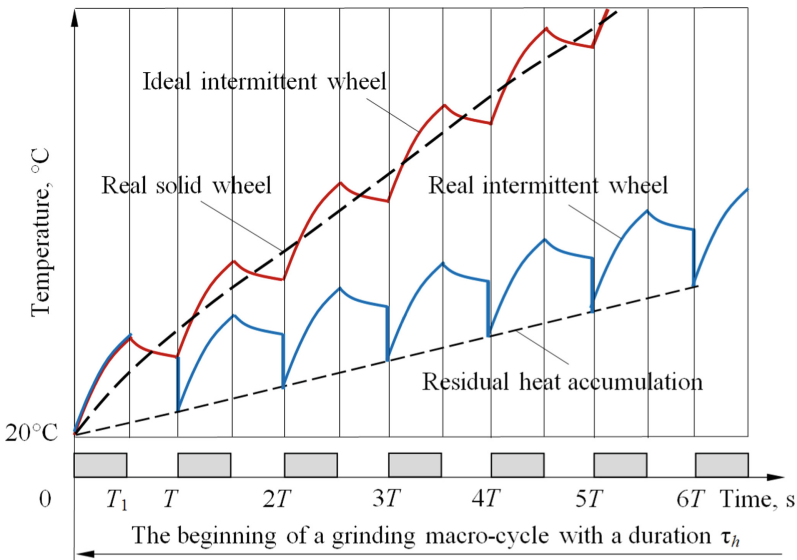


Fig. 4. The initial phase of changing the intermittent grinding temperature

The mathematical model of Carslaw H.S. and Jaeger J.C. for determining the temperature from a pulsating heat flux allows finding the grinding temperature at any time in the time interval of steady-state temperature values [1]. The disadvantage of this model is the uncertainty of this time interval, which occurs after the end of the temperature transition process. It constrains the use of this model for designing intermittent grinding wheel optimal constructions and corresponding formulations (structures) of high porous grinding wheels. That is why a new mathematical model for determining the intermittent grinding temperature is proposed instead of and based on the model of Carslaw H.S. and Jaeger J.C. to wit [1]:

$$\Theta_{sum} = \frac{q_{ave}}{\lambda} \sqrt{\frac{a}{\pi}} \left(2\sqrt{\tau_h} + f(s)\sqrt{T} \right), \tag{6}$$

where $f(s) = A\sqrt{s} + \frac{B}{\sqrt{s}}$ is the function that depends on the duty factor s ; A and B are the dimensionless coefficients which depend on the grinding scheme, for example, for the scheme of surface grinding by the periphery of the wheel, we have found that $A = -1.24$ and $B = 1.62$ (Table 1).

Table 1. The intermittent grinding maximum temperature is calculated by the equations of Carslaw H.S. and Jaeger J.C. [1] and the formula (6).

N	s	$\Theta'_{sum}, \text{ }^\circ\text{C}$	$\Theta_{sum}, \text{ }^\circ\text{C}$	$\delta, \%$
3	0.2	808.088	836.797	3.55
3	0.8	587.59	614.987	4.70
35	0.2	626.336	633.474	1.10
35	0.8	557.753	568.507	1.90

Note: N is the number of cutting segments on the wheel; $\Theta'_{sum}, \Theta_{sum}$ are the estimated temperature by the equations of Carslaw H.S. and Jaeger J.C. [1] and by the formula (6), respectively.

Based on measured the wheel specified geometric parameters l_1 and l_2 for wheels of monocorundum WG946Hs12Vs, sol-gel corundum 3SG46Hs12Vs, and electrocorundum A9946Hs12Vs, the geometrical parameters N (the number of “cutting segments” on the wheel) and s (duty factor) are experimentally found and given in Table 2.

Table 2. Experimentally found parameters N and s for highly porous grinding wheels.

Wheel	N	s
WG946Hs12Vs Monocorundum	313	0.75
3SG46Hs12Vs Sol-gel corundum	292	0.64
A9946Hs12Vs Electrocorundum	288	0.68

Note: $N = 2\pi R / (l_1 + l_2)$; R is the grinding wheel radius, $R = 200$ mm;
 $s = l_1 / (l_1 + l_2)$.

The results of the practical application of the developed software are presented in Table 3, which gives the high porous wheels geometric parameters that provide a minimum grinding temperature, e.g., in the interval of 577–588 °C.

Table 3. The high porous wheels optimum geometric calculated parameters.

Minimum temperature	Duty factor (<i>s</i>)		
	0.2	0.5	0.8
577 °C	$N \geq 311$	$N \geq 40$	$N \geq 7$
582 °C	$N \geq 228$	$N \geq 25$	$N \geq 5$
588 °C	$N \geq 152$	$N \geq 18$	$N \geq 3$

Analysis of the results obtained allowed formulating a scientific hypothesis that explains the decrease in the intermittent grinding temperature by timely removal of the material. The transient temperature distribution process is carried out and does not have time to end.

4 Conclusions

A unified classification of intermittent grinding wheels has been developed based on the frequency of impact of the cutting segments of the wheel on the surface being ground (determined by many cutting sections on the wheel), as well as taking into account the duty factor of the period of heat flux pulses.

A set of the grinding wheel geometric parameters is proposed for designing optimal constructions of intermittent grinding wheels, including segmented, slotted, and high porous wheels, namely: number of cutting sections on the working periphery of the grinding wheel and the duty factor of the period of heat flux pulses. A technique was developed to determine the high porous grinding wheel geometric parameters by the criterion of the ratio of the sizes of the “cutting section” (cutting area, surrounded by pores) and pore.

The temperature field during intermittent grinding results from the cyclic effect of the pulsed heat flux on the surface being ground and is determined by the new mathematical model, which provides a reliable determination of intermittent grinding temperature. The error in determining the intermittent grinding temperature by the formula proposed compared to the more complex solution derived by H.S. Carslaw and J.C. Jaeger does not exceed 5%.

For the first time, a new scientific hypothesis was proposed, which explains the effect of intermittent grinding temperature fall compared to conventional (continuous) grinding under otherwise equal conditions, namely, the effect of grinding heat removing an unfinished transition process of propagation of the thermal field. To judge by the first results obtained, such a hypothesis has the right to exist, and the relevant research should be further conducted.

The developed mathematical model for determining the temperature of the intermittent grinding can be used as the software of the element CAE in the integrated system CAD/CAM/CAE (Computer-Aided Design / Computer-Aided Manufacturing / Computer-Aided Engineering), which can be used at the pre-production (preplanning) stage in the integrated system of design and production.

Acknowledgment. This work was carried out within the State (Ukraine) budget theme of the Odessa National Polytechnic University (2018–2021, registration number: 0118U004400).



References

1. Larshin, V., Lishchenko, N.: Intermittent grinding temperature modeling for grinding system state monitoring. *Appl. Aspects Inf. Technol.* **3**(2), 58–73 (2020). <https://doi.org/10.15276/aaait.02.2020.3>
2. Lee, K., Wong, P., Zhang, J.: Study on the grinding of advanced ceramics with slotted diamond wheels. *J. Mater. Process. Technol.* **100**(1), 230–235 (2000). [https://doi.org/10.1016/S0924-0136\(00\)00403-9](https://doi.org/10.1016/S0924-0136(00)00403-9)
3. Taghi, T., Bahman, A.: Intermittent grinding of advanced ceramic with the T-Tool grinding wheel. *Adv. Mater. Res.* (126-128), 615–620 (2010). <https://doi.org/10.4028/www.scientific.net/AMR.126-128.615>
4. Zeng, W., Xu, X.: Analytical study of temperatures in sawing with segmented blades. *Key Eng. Mater.* (259–260), 490–495 (2004). <https://doi.org/10.4028/www.scientific.net/KEM.259-260.490>
5. Fang, C., Xu, X.: Analysis of temperature distributions in surface grinding with intermittent wheels. *Int. J. Adv. Manuf. Technol.* **71**(1–4), 23–31 (2013). <https://doi.org/10.1007/s00170-013-5472-1>
6. Zheng, H.W., Gao, H.: A general thermal model for grinding with slotted or segmented wheel. *CIRP Ann. Manuf. Technol.* **43**(1), 287–290 (1994). [https://doi.org/10.1016/S0007-8506\(07\)62215-X](https://doi.org/10.1016/S0007-8506(07)62215-X)
7. Bogutsky, V., Novoselov, Y., Shron, L.: Calculating the profile of intermittent grinding wheel for the sharpening teeth of the broach. *MATEC Web Conf.* **224**, 01003 (2018). <https://doi.org/10.1051/mateconf/201822401003>
8. Kwak, J., Ha, M.-K.: Force modeling and machining characteristics of the intermittent grinding wheels. *KSME Int. J.* **15**, 351–356 (2001). <https://doi.org/10.1007/BF03185218>
9. Pérez, J., Hoyas, S., Skuratov, D., Ratis, Y., Selezneva, I., Córdoba, F., Urchueguia, J.: Heat transfer analysis of intermittent grinding processes. *Int. J. Heat Mass Transf.* **51**(15–16), 4132–4138 (2008). <https://doi.org/10.1016/j.ijheatmasstransfer.2007.11.043>
10. Aurich, J., Kirsch, B.: Improved coolant supply through slotted grinding wheel. *CIRP Ann. Manuf. Technol.* **62**(1), 363–366 (2013). <https://doi.org/10.1016/j.cirp.2013.03.071>
11. Jackson, M.: Design of slotted grinding wheels. *Int. J. Nanopart.* **1**(4), 334–352 (2008). <https://doi.org/10.1504/IJNP.2008.026476>
12. Li, Z., Ding, W., Ma, C.-Y., Xu, J.-H.: Grinding temperature and wheel wear of porous metal-bonded cubic boron nitride superabrasive wheels in high-efficiency deep grinding. *J. Eng. Manuf.* **231**(11), 1961–1971 (2015). <https://doi.org/10.1177/0954405415617928>
13. Neslusan, M.: Grinding of NI-based alloys with grinding wheels of high porosity. *Adv. Prod. Eng. Manage.* **4**, 29–36 (2009)
14. Zhenzhen, C., Jiuhua, X., Wenfeng, D., Changyu, M.: Grinding performance evaluation of porous composite-bonded CBN wheels for Inconel 718. *Chin. J. Aeronaut.* **27**(4), 1022–1029 (2014). <https://doi.org/10.1016/j.cja.2014.03.015>
15. Turbine industry – Tyrolit. https://www.tyrolit.at/fileadmin/Documents/Metal_Precision/Folder_Flyer/20041563_GB-0716_Your_Partner_in_the_Turbine_industry_RZ_low.pdf. Accessed 01 May 2021
16. VIPER ULTRA – Tyrolit. https://www.tyrolit.at/fileadmin/products/doc/9b74c2638bd0_20055659-gb-0215_viper_ultra_rz_low.pdf. Accessed 01 May 2021

17. Making a precision decision. <https://www.aero-mag.com/cranden-diamond-milling-grinding-stuart-cleary>. Accessed 01 May 2021
18. Larshin, V.P., Lishchenko, N.V.: Complex-shaped parts grinding technology information ensuring. *Appl. Aspects Inf. Technol.* **3**(4), 246–262 (2020). <https://doi.org/10.15276/aait.04.2020.3>
19. Carslaw, H.S., Jaeger, J.C.: *Conduction of heat in solids*, 2nd edn. Oxford University Press, Oxford (1959)
20. Marchuk, V., et al.: The effect of temperature on the grinding surface quality ring roller. *Perspect. Technol. Devices* **15**, 58–62 (2019). <https://doi.org/10.36910/6775-2313-5352-2019-15-8>



Simulation of an Absorber of Vibration in Turning

Yuri Petrakov^(✉)  and Maksim Sikailo 

National Technical University of Ukraine, Igor Sikorsky
Kyiv Polytechnic Institute, 37, Peremogy Ave., Kyiv 03056, Ukraine

Abstract. This paper presents an interest in simulating a dynamic absorber of vibration for turning. A mathematical model of a turning machining system is presented in the form of a single-mass model with one degree of freedom in the direction of cutting depth and the effect of elastic displacement on the cutting width. The dynamic absorber of vibration is presented as one mass rigidly connected to the tool and linear damper. The mathematical model of the machining system with a dynamic absorber of vibration considers the closed-loop of the cutting process and its delay function. An application soft has been developed for simulating the machining system in time and frequency responses. According to the Nyquist frequency criterion, preconditions are made to assess the machining system's stability with a delay. Simulating allows selecting the dynamic parameters in the design of the absorber of vibration and the vibration-free mode of cutting.

Keywords: Chatter in turning · Absorber of vibration · Closed-loop delay · Simulation in time · Frequency responses

1 Introduction

Any cutting process is accompanied by vibrations, the nature of which is still poorly understood. Depending on the level of vibration amplitude, they can disrupt the processing conditions, deteriorate the surface quality of the part, and lead to premature tool wear. Therefore, the study and solution of vibration during machining operations is extremely important to improve their quality and productivity [1]. Vibration elimination methods are classified as passive chatter control (PCC) and active chatter control (ACC) [2]. The easiest to implement and no less effective are passive methods, which include a dynamic absorber of oscillation, representing an additional mass that is elastically connected with the main, as a rule, the mass of the device instrument. Since the efficiency of vibration damping depends on the accuracy of tuning the dynamic parameters of the additional mass, it is necessary to have a simulating tool that allows you to design a vibration damper for a specific technological machining system [3]. The creation of such tools in the form of special soft using the digital twin of the technological machining system is an urgent scientific and technical task.

2 Literature Review

To form a process control strategy to eliminate vibrations or reduce their amplitude, it is necessary to build a mathematical model reflecting all the dynamic properties that lead to the appearance of vibrations. The identification of the machining system ensures the adequacy of the model as a result of the experimental determination of dynamic parameters, i.e., equivalent stiffness, mass, and damping of the system during operation in a closed-loop configuration [4].

Of great importance for explaining the occurrence of regenerative oscillations in the machining system are lag processes that affect the shape of the allowance and the dynamic change in the cutting thickness [5]. Since the machining system is under the influence of a force disturbance, it is important to consider the dependence of the cutting force on the chip area and the contact of the cutting edge [6]. Such dynamic parameters should be included in the simulation model of the machining system, taking into account its closed-loop and cutting along the already machined surface, i.e., the delay element [7].

Good results for predicting stability are shown by studies of a system in a closed-loop state both in the time and in the frequency domain using numerical analysis methods and focusing on the frequency criteria for the stability of closed-loop systems [8]. When compiling a mathematical model, it is necessary to strive for simplicity of presentation while maintaining maximum adequacy. Second-order dynamic models with the obligatory consideration of the closed-loop of the cutting process and the lagging argument in the feedback fully satisfy such requirements [9]. The solution is often sought by analytical methods, based on the analysis of the roots of the characteristic equation. The results are presented in the form of a stability lobes diagram without using classical stability criteria in the Nyquist diagram [10].

All methods for eliminating vibrations during cutting are conventionally divided into passive chatter control (PCC) and active chatter control (ACC) [2, 11]. The PCC methods include various types of dynamic vibration absorbers, which are structurally performed as additional masses attached to a machine element that directly carries out the cutting process through an elastic connection with damping [12]. Such devices' parameters can sometimes automatically adjust and adapt to the actual cutting conditions (Adaptive Turning Mass Damper - ATMD) [13].

In any case, it is important to determine the optimal parameters of a dynamic absorber to reduce vibrations during turning, especially taking into account the nonlinearities of the cutting process model [14]. It is also important to have a dynamic damper design tool using variable stiffness adjustable dampers (VSTMDs) since these devices are initially used as a conventional passive damper tuned to constant stiffness [15].

Thus, to design a dynamic vibration damper based on the technology of passive vibration control, it is necessary to develop a mathematical model of the processing system, taking into account the closed-loop of the cutting process and machining along surface already machined with a delay argument, to ensure its adequacy, to create a tool in the form of special software that allows simulating a system with damper fluctuations in both the time and frequency responses. Formulate a stability criterion based on the Nyquist frequency diagram for systems with delay and positive feedback.

Such a soft will allow solving the problem of choosing the parameters of an absorber of vibration and designing a cutting mode for performing stable machining with maximum productivity.

3 Research Methodology

Striving for the simplicity of representing the mathematical model while maintaining the necessary adequacy, it is sufficient to describe the processing system as a dynamic model with one mass m and one degree of freedom in the Y-axis direction, normal to the Y-axis surface of the part. According to the chosen paradigm of passive vibration damping, the dynamic vibration damper is presented in the form of a mass m_1 associated with the main mass, which is most close to the cutting zone, with a stiffness k_1 and a viscous friction damper λ_1 (Fig. 1).

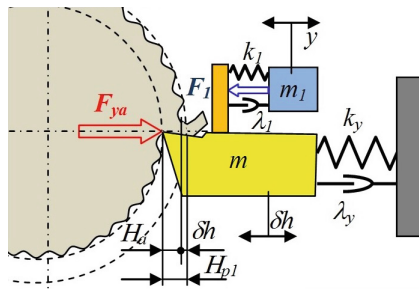


Fig. 1. Scheme of the model.

The main machining system following the diagram in Fig. 1 is represented by an oscillatory link with a transfer function:

$$W_{ms}(s) = \frac{\delta h(s)}{F_{ya}(s)} = \frac{1/k_y}{T^2 s^2 + 2\zeta Ts + 1}, \quad (1)$$

where δh is the elastic displacement of the processing system under the action of the normal component F_{ya} of the cutting force, k_y is the rigidity in the direction of the Y-axis, T is the period of natural oscillations, ζ is the damping coefficient of oscillations, and s is the Laplace operator.

The equation of motion for the additional mass of the vibration damper, which is under the action of kinematic excitation:

$$m_1 \frac{d^2 y}{dt^2} + \lambda_1 \left(\frac{dy}{dt} - \frac{d\delta h}{dt} \right) + k_1 (y - \delta h) = 0, \quad (2)$$

whence the transfer function:

$$W(s) = \frac{y(s)}{\delta h(s)} = \frac{T_2 s + 1}{T_1^2 s^2 + T_2 s + 1}, \tag{3}$$

where are the time constants $T_1 = \sqrt{m_1/k_1}$, $T_2 = \lambda_1/k_1$.

On the other hand, the reaction of the absorber to the bulk is:

$$F_1 = \lambda_1 \left(\frac{d\delta h}{dt} - \frac{dy}{dt} \right) + k_1(\delta h - y), \tag{4}$$

and the transfer function:

$$W_F(s) = \frac{F_1(s)}{\delta h(s) - y(s)} = k_1(T_2 s + 1). \tag{5}$$

Thus, the block diagram of the entire system with a dynamic oscillation compensator can be represented as shown in Fig. 2.

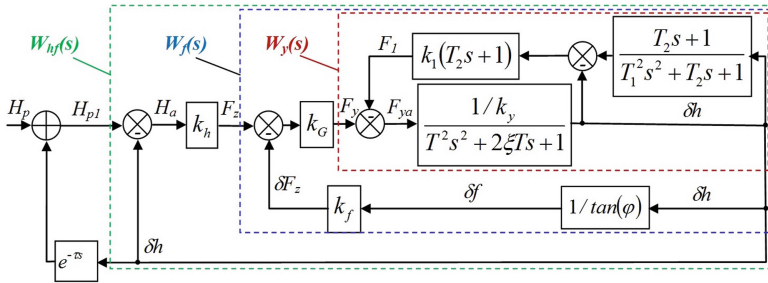


Fig. 2. Block diagram of a machining system with the absorber of vibration.

On the structural diagram, the normal component F_y of the cutting force is related to the tangential component F_z by the coefficient of geometric interaction, where φ is the main angle in the plan of the tool, η is the swarf angle. Taking into account the relatively small values of deformations in comparison with the depth (width) of cutting, the dependence of the cutting force (its component F_z) on the actual depth H_a of cutting and feed f can be represented by linear dependencies [6] with the coefficients:

$$k_h = \left(\frac{\partial F_z}{\partial h} \right)_0, k_f = \left(\frac{\partial F_z}{\partial f} \right)_0 \tag{6}$$

To obtain a mathematical model of a system suitable for modeling, it is necessary to sequentially determine the transfer functions of the link groups, highlighted by a dotted line in the structural diagram of Fig. 2. The transfer function $W_y(s)$ of the main mass of the system and the mass of the vibration damper after the transformations has the form:

$$W_y(s) = \frac{\delta h(s)}{F_y(s)} = \frac{(T_1^2 s^2 + T_2 s + 1)/k_y}{A_0 s^4 + A_1 s^3 + A_2 s^2 + A_3 s + 1}, \quad (7)$$

where $A_0 = T^2 T_1^2$, $A_1 = 2\xi T T_1^2 + T^2 T_2 + T_1^2 T_2 \frac{k_l}{k_y}$, $A_2 = T_1^2 + 2\xi T T_2 + T^2 + T_1^2 \frac{k_l}{k_y}$, $A_3 = 2\xi T + T_2$.

The model considers the effect of deformation of the system in the direction of the Y-axis on the change in the thickness of the cut layer in the direction of feed through geometric interaction on the tool blade. Thus, the model considers two closed contours – in feed rate and the depth of cut.

So, the transfer function $W_f(s)$ of a closed-loop for the feed represents a mathematical model of the processing system according to the scheme in Fig. 2, taking into account the closed-loop of the cutting process along the X coordinate. After transformations, using the rules of transfer functions according to Laplace, you can get:

$$W_f(s) = \frac{\delta h(s)}{F_z(s)} = \frac{B_0 s^2 + B_1 s + B_2}{C_0 s^4 + C_1 s^3 + C_2 s^2 + C_3 s + C_4}, \quad (8)$$

where $B_0 = k_G T_1^2 \tan(\phi)$, $B_1 = k_G T_2 \tan(\phi)$, $B_2 = k_G \tan(\phi)$, $C_0 = A_0 k_y \tan(\phi)$, $C_1 = A_1 k_y \tan(\phi)$, $C_2 = A_2 k_y \tan(\phi) + T_1^2 k_G k_y$, $C_3 = A_3 k_y \tan(\phi) + T_2 k_G k_y$, $C_4 = k_y \tan(\phi) + k_G k_f$.

Now it is possible to obtain the transfer function $W_{hf}(s)$ of the entire system, which displays the dependence of the elastic deformation δh of the machining system in the direction of the Y-axis on the preset cutting depth H_{p1} without taking into account the lag function, which expresses cutting along the already machined surface:

$$W_{hf}(s) = \frac{\delta h(s)}{H_{p1}(s)} = \frac{D_0 s^2 + D_1 s + D_2}{E_0 s^4 + E_1 s^3 + E_2 s^2 + E_3 s + E_4}, \quad (9)$$

where $D_0 = B_0 k_h$, $D_1 = B_1 k_h$, $D_2 = B_2 k_h$, $E_0 = C_0$, $E_1 = C_1$, $E_2 = C_2 + B_0 k_h$, $E_3 = C_3 k_h$, $E_4 = C_4 + B_2 k_h$.

The mathematical model of the entire system should take into account the lag function, which implements cutting along the already machined surface $e^{-\tau s}$, where $\tau = 2\pi/\omega$ is the time of one workpiece revolution, ω – is the spindle rotation velocity. Modeling such a fourth-order system (7), (8), (9) to determine its responses in the time and frequency domains and taking into account the function of the retarded argument is possible only by numerical methods.

4 Results

An application program was created to simulate a machining system with a dynamic absorber of vibration based on the obtained mathematical model. The authors created this original program in the programming language Delphi (Object Pascal). The program performs numerical integration using the standard 4th order Runge-Kutt

procedure and allows obtaining the response of the system in time and the frequency responses in the form of a Nyquist diagram. The program enables simulating the original system without an absorber of vibration and, thus, to determine the stability lobes diagrams for choosing of cutting mode.

The adequacy of the mathematical model is ensured by the dynamic parameters of the processing system during the cutting process, i.e., in a closed form, determined experimentally. Therefore, an approach was used based on the study of vibration chatter of the processing system on the treated surface.

The frequency of the main harmonic of the processing system can be determined from the surface round-diagram (Fig. 3). After several experiments and measurements of the corresponding circular patterns, the frequency of the main harmonic was calculated: $f = n_d/\tau = 350 \text{ Hz}$, $n_d = 21$ is the average number of waves on the surface of the part. This reliable method ensures that the data of the machining system is fully adequate during the cutting process. After measuring the rigidity $k_y \text{ (N/m)}$ of the system in the standard way, loading through a dynamometer and measuring the elastic displacement, the reduced mass can be calculated: $m = k_y/2\pi f = 5950000/2\pi 350 = 1.18 \text{ kg}$.

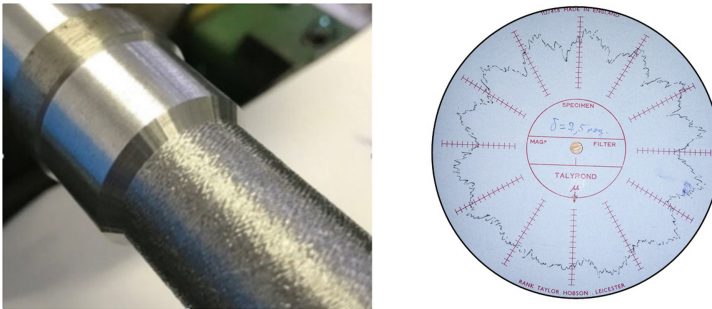
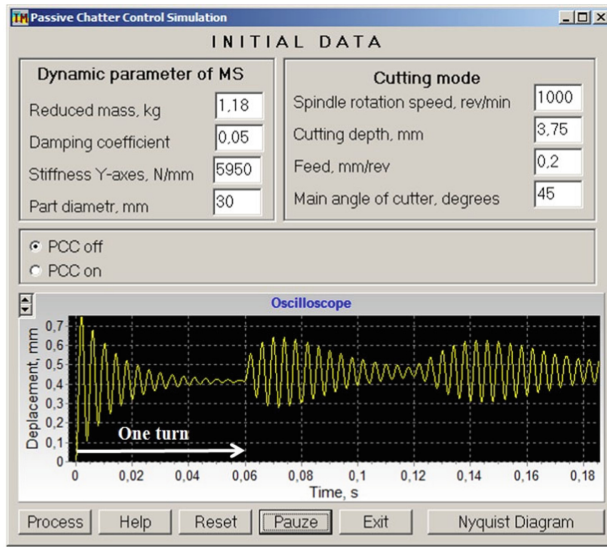
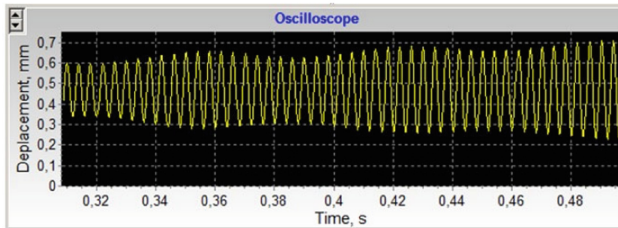


Fig. 3. Machining surface and its round-chart.

The simulation results of the original machining system with the cutting mode specified on the interface on the left are shown in Fig. 4. After the damping of oscillations after one revolution (0.06 s), they resume again, which is the regeneration effect due to cutting on the already machined surface. After 0.4 s, the oscillation amplitude increases. It indicates a possible loss of system stability.



a)



b)

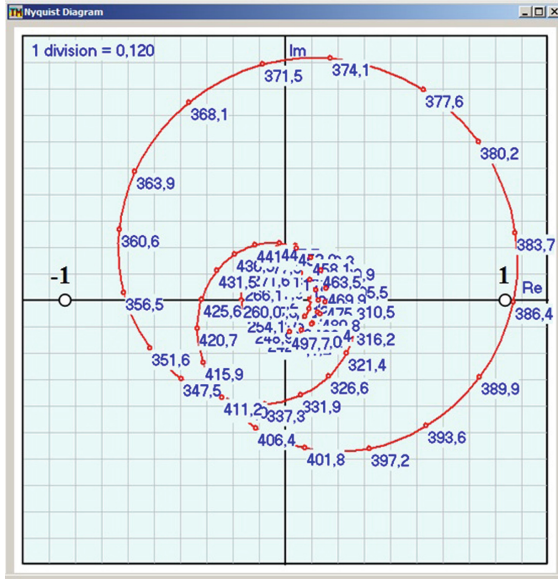
Fig. 4. Simulation results of the original machining system: a) – process start, b) – 0.4 s after the start.

The created soft also allows obtaining the Nyquist diagram of the machining system by the numerical method through the interface, on which the desired frequency values and the calculation step are set (Fig. 5).

The diagram is plotted by a numeric method in the frequency range 100 Hz - 500 Hz with a calculation step of 0.001 rad/s. The original machining system is represented by a second-order system with a delay link in the feedback loop. It is proved that it is convenient to apply the Nyquist stability criterion to analyze the stability of such systems (Ya. Z. Tsytkin – see mathnet.ru). Formulating the Nyquist stability criterion for systems with negative feedback and delay is similar to the formulation for systems without delay.

The delay link introduces an additional phase shift $\varphi = \omega\tau$ without changing the amplitude. From the analysis of the constructed Nyquist diagram for the original system, taking into account the delay, it can be seen that the curve does not cover the

point with coordinates $[-1, 0]$, although the course of the process in time (see Fig. 4) indicates its instability.



At the same time, the plotted curve of the Nyquist diagram for such a processing system with a dynamic vibration damper covers a point with coordinates $[-1,0]$ (Fig. 7).

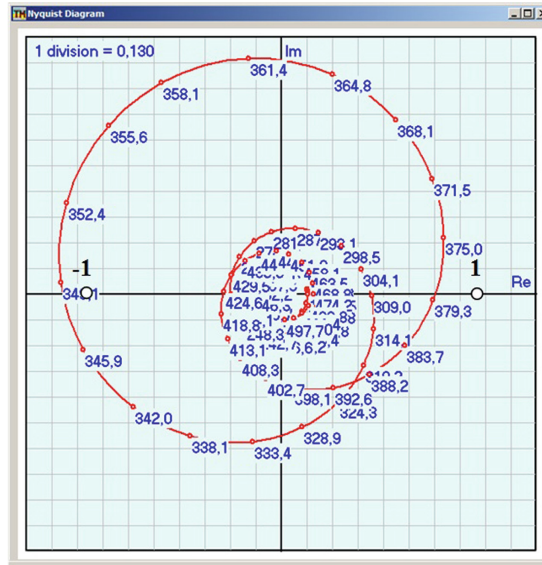


Fig. 7. Nyquist diagram of the machining system with an absorber of vibrations.

It can be assumed that this discrepancy with the formulation of the Nyquist stability criterion for closed-loop systems with negative feedback has changed due to the presence of positive feedback in the retarded link circuit.

5 Conclusion

In the study, the mathematical model of a turning machining system with one degree of freedom in the depth of cutting and taking into account the effect on the width of cutting was created, as well as an application program that allows one to simulate such a machining system with a dynamic absorber of vibration. The necessity of determining the dynamic parameters of the system by measuring chatter on the part surface is shown. The effectiveness of the developed soft for choosing the parameters of a dynamic absorber of vibration has been theoretically proved, which can be used in the design of a real absorber structure.



The created simulation program allows receiving responses in time and frequency responses of the system and thus choosing a vibration-free cutting mode.

References

1. Oborskyi, G., Orgiyan, A., Tonkonogyi, V., Aymen, A., Balaniuk, A.: Study of dynamic impacts at combined operations of the thin turning and boring. In: Tonkonogyi, V., et al. (eds.) *InterPartner 2019. LNME*, pp. 226–235. Springer, Cham (2020). https://doi.org/10.1007/978-3-030-40724-7_23
2. Yue, C., Gao, H., Liu, X., Liang, S., Wang, L.: A review of chatter vibration research in milling. *Chin. J. Aeronaut.* **2**(32), 215–242 (2019)
3. Liu, Y., Liu, Z., Song, Q., Wang, B.: Analysis and implementation of chatter frequency dependent constrained layer damping tool holder for stability improvement in turning process. *J. Mater. Process. Technol.* **266**, 687–695 (2019)
4. Nicolescu, M., Frangoudis, C., Semere, D., Archenti, A., Rashid, A.: New paradigm in control of machining system's dynamics. *J. Mach. Eng.* **15**(3), 117–137 (2015)
5. Budak, E., Ozlu, E.: Analytical modeling of chatter stability in turning and boring operations. *A Multidimension. Approach. Annals of the CIRP* **53**, 401–404 (2007)
6. Lazoglu, I., Atabey, F., Altintas, Y.: Dynamics of boring processes: Part III-time domain modeling. *Int. J. Mach. Tools Manuf.* **42**, 1567–1576 (2002)
7. Atabey, F., Lazoglu, I., Altintas, Y.: Mechanics of boring processes-Part I. *Int. J. Mach. Tools Manuf.* **43**, 463–476 (2003)
8. Petrakov, Y., Danylchenko M., Petryshyn, A.: Prediction of chatter stability in turning. *Eastern-Eur. J. Enterp. Technol.* **5/1**(101), 58–64 (2019)
9. Altintas, Y.: *Manufacturing automation: metal cutting mechanics, machine tool vibrations, and CNC design*. Cambridge University Press, New York (2012)
10. Munoa, J., Beudaert, X., Dombovari, Z., Altintas, Y., Budak, E., Brecher, C.: Chatter suppression techniques in metal cutting. *CIRP Ann. Manuf. Technol.* **65**(2), 785–808 (2016)
11. Mohammadi, Y., Azvar, M., Budak, E.: Suppressing vibration modes of spindle-holder-tool assembly through FRF modification for enhanced chatter stability. *CIRP Ann. Manuf. Technol.* **67**, 397–400 (2018)
12. Habibab, G., Kerschena, G., Stepanb, G.: Chatter mitigation using the nonlinear tuned vibration absorber. *Int. J. Non-Linear Mech.* **91**, 103–112 (2017)
13. Tarnga, Y., Kaob, J., Leea, E.: Chatter suppression in turning operations with a tuned vibration absorber. *J. Mater. Process. Technol.* **105**(1–2), 55–60 (2000)
14. Gourc, E., Seguy, S., Michon, G., Berlioz, A.: Chatter control in turning process with a nonlinear energy sink. *Adv. Mater. Res. Trans. Tech. Publications* **698**, 89–98 (2013)
15. Munoa, J., Dombovari, Z., Iglesias, A., Stepan, G.: Tuneable mass dampers with variable stiffness for chatter suppression. In: *4th International Conference on Virtual Machining Process Technology, CIRP. Vancouver, Canada* (2015)



Determination of the Distance Between Grains During Electrical Discharge Grinding with Changing Polarity of Electrodes

Roman Strelchuk^(✉)  and Oleksandr Shelkovyi 

National Technical University “Kharkiv Polytechnic Institute”,
2, Kyrpychova St., Kharkiv 61002, Ukraine

Abstract. The paper investigates the process of electroerosive diamond grinding by changing the polarity of electrodes in time in the cutting zone for processing various materials, and the distance between the grains is determined. The study aims to determine the effect on the distance between the grains of the electrical modes of electrical discharge grinding (ED grinding) and the characteristics of the wheel using the mathematical method of planning experiments. The planning of the experiment gave the result with the smallest error and made it possible to minimize the number of experiments. As a result of experimental studies, a mathematical model of the distance between grains has been constructed. This model considers the electrical process modes and the wheel characteristics. For various values of electrical modes and the wheel characteristics, using the functional dependence, it is possible to determine the distance between the grains. It was found that the most significant factors that affect the distance between grains are the frequency and relative pulse duration, grain size, and concentration of diamond wheels. The study results obtained allow using the functional dependence to calculate the grinding process's productivity, assess the cutting ability, and simulate the wear of the wheels without lengthy and expensive experimental studies.

Keywords: Functional dependence · Frequency · Relative · Pulse duration · Grit · Concentration · Diamond wheels · Process

1 Introduction

The process of electrical discharge grinding with changing the polarity of electrodes allows obtaining the required qualitative and quantitative indicators with a significant reduction in the specific consumption of the diamond wheel and the consumption of various types of energy [1]. This is because the change in time on the polarity electrodes and the corresponding pulse repetition rate provide stable grinding processes [2]. By changing the frequency of pulses, their relative pulse duration, and power with a corresponding change in the polarity of the electrodes, it is possible to regulate the process itself up to an equilibrium state, providing an equivalent manifestation of electrophysical and electrochemical (even if they are insignificant) processes relative to both electrodes at an optimal working gap [3].

The peculiarity of the process of ED grinding with changing the polarity of the electrodes is that the working gap between the conductive surfaces – the tool and the workpiece – remains practically constant during processing [4]. Therefore, the working surface state of the diamond wheel has not been studied. The wheel's working surface condition is characterized by the distance between the cutting grains [5].

The distance between the cutting grains in ED grinding is determined by the conditions of the processed material interaction with the working surface of the diamond wheel and its state. This state depends on the distance between the cutting grains, their cutting properties, height distribution, and ability to maintain a developed cutting relief [6]. Knowing the distance between the grains allows it to establish the number of active working grains that remove material possible for various process conditions [7].

Thus, for determining the productivity of ED, grinding with the following characteristics are allowable: changing the polarity of electrodes and the wheel wear the calculation of the distance between the grains on the wheel, the establishment of their distribution, the analysis of this distribution during the interaction of the cutting grains with the material, and the probability density of the cut thickness are necessary prerequisites [8].

2 Literature Review

The actual distance between the grains on the working surface of a diamond tool after electrical discharge grinding differs significantly from the non-combined process. This difference is because, in diamond grinding (a non-combined process), not all of the grains in the tool volume are opened to participate in material removal. Only part of the total number of diamond grains is on the wheel's surface [9].

When analyzing the condition of the working surface of a grinding wheel, researchers use different definitions [10]. The publication [11] presents the concept of the roughness of the working surface for the wheel by analogy with the processed surface of a part. In publication [12], the values of height difference and the distance between the grains are considered, putting different meanings into these concepts.

In publication [13], the distance between adjacent height grains, located at 1 cm of the contact length of the grinding wheel with the workpiece, was taken for the height difference. Moreover, in the paper [14], it was suggested that the height difference of grains should be defined as the maximum distance between the most distant grain tops in height located on the periphery of the grinding wheel. The most precise definition of the height difference is given in the publication [15], which considers the difference between the heights of the highest and lowest grain tops in the microscope's field of view.

Since the accompanying processes of metal bond destruction and wear of diamond grains, the intensity of which depends on the tool characteristics and technological processing conditions, take place in the process of electrical discharge grinding, the different distance between grains will be formed on the grinding wheel surface in each case, i.e., different tool working surface topography [16].

The calculation of the distance between the grains is of independent importance since it allows for various grinding conditions and the diamond wheel characteristics to make a qualitative assessment of the conditions for the wheel interaction with the materials being processed [17].

3 Research Methodology

Experimental studies have been carried out on the 3D642E machine, modernized for ED grinding with changing the polarity of electrodes. Additional energy was introduced into the cutting zone from the NO 6506 pulse generator, which converts 380 V alternating current into a monopolar pulse current. The generator controlled the pulse frequency and relative pulse duration. The polarity change was carried out using a device connected from the pulse generator to the machine spindle.

An end-face grinding scheme has been used, which was carried out with conical cup wheels 12A2–45° 150 × 10 × 3 × 32 on a bond M1–01 with diamond grains. Before the experiments, the diamond wheels have been pre-straightened and run-in for 5–10 min. The workpiece material was T15K6 carbide plates with dimensions of 14 × 14 × 5 mm.

The determination of the distance between the grains was carried out based on the analysis of the profilograms of the wheel working surface relief. The profilograms were recorded on a particular setup based on the 201 model profilometer-profilograph. The installation diagram (Fig. 1) is similar to the datasheet debugging of the profilometer-profilograph for measuring waviness, and it is as follows. A probe was mounted on the device sensor, held by a leaf spring. At the end of the sensor, adjusted support, pressed together with the sensor's limit screw by the spring, was fixed. The sensing needle was fixed in the bushing and installed at the end of the probe instead of the pin for registering waviness. With the brought end surface, the sleeve abuts against the diamond needle. Thus, direct contact of the diamond needle with the wheel working surface is excluded.

The sensing needle was made of BK8 hard alloy. Sharpening of the needles was carried out in two technological operations: at the first stage, the needles were grinded on the 3D642E toolroom grinder using a particular device; at the second stage, the needles were refined with diamond paste. In this case, the corner radius of the working edge was 3...4 microns. The radius control was carried out on the MIM-8 microscope.

The profile was recorded as follows. When the device sensor moved relative to the brought surface of the support, the sensing needle, under a slight force, balanced by the leaf spring of the probe, moved along the wheel working surface. The vibrations of the sensing needle were transmitted to the diamond needle of the profilometer-profilograph.

The following technique to isolate the sections of the profilograms occupied by the metal binder and non-conductive diamond grains was used.

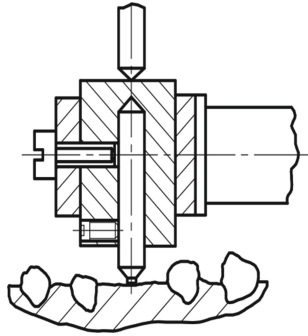


Fig. 1. Installation diagram for recording the relief of the working surface of a diamond wheel.

The essence of the technique is to change the thickness of the profilogram line when the needle, sensing the surface of the grinding wheel, changes from a metal bond to a diamond grain and vice versa. The line thickness is changed by changing the strength of the current passed through the recording needle of the profilometer-profilograph. For this, a device, the diagram of which is shown in Fig. 2, is used. If the sensing needle is located on the surface of the conductive bundle, then at the input of the DD1.1 element and the output of the DD1.2 inverter, a logic level 0 is formed. In this case, VT1 electronic key is closed, and the K1 relay is de-energized. Contacts K1.1 are open, and a normal current of about 2 mA is supplied to the pen arm. The pen arm draws a thin line corresponding to the profile of the metal bond. At the moment of the sensing needle transition to a diamond grain, a logic level 1 appears at the input of the DD1.1 element and the output of the DD1.2 inverter. VT1 electronic key opens, and the K1 relay is activated. In this case, the K1.1 contacts are closed, bypassing the R149 resistor of the device recording unit.

The current supplied to the pen arm increases to 3...4 mA and the profilogram corresponding to the grain surface is drawn with a thickened line. At the same time, HL1 LED lights up, making it possible to record the output of the grain sensing needle visually. The value of the average distance between grains was calculated as:

$$l = \frac{\sum_{i=1}^n l_i}{n}, \quad (1)$$

where l_i – the distance between the vertices of adjacent grains, determined from the profilogram, n – number of measurements.

The mathematical model of the distance between the grains is a function of several variables, making it possible to define the distance with the required accuracy at all points of a specific predetermined area to determine the electrical modes and process conditions. A theoretical solution to the problem of constructing such a model is currently not possible. In this regard, the most expedient is using mathematical methods for planning experiments, making it possible to solve such problems in conditions of incomplete knowledge of the phenomena mechanism.

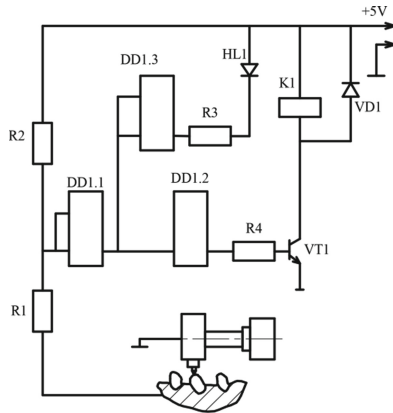


Fig. 2. Diagram of a device for isolating sections of a metal bond and diamond grains on a profilogram.

Experiment planning gives the result with the smallest error and minimizes the number of experiments [18].

Based on a qualitative analysis, it was found that the electrical modes of the ED grinding process and the tool characteristics have the most significant effect on the distance between the grains. As factors in the mathematical model construction, the distance between grains was chosen: f – pulse frequency, KHz; q – relative pulse duration; Z – the grit of diamond wheels, μm ; K – concentration of diamonds in the wheel. The intervals and levels of variation of factors are shown in Table 1.

Table 1. Levels and intervals of factors' variation.

Factor natural designation	f , KHz	q	Z , μm	K
Factor code designation	X_1	X_2	X_3	X_4
Upper level	66	1.5	200	6
Lower level	22	0.5	40	2
Main level	44	1.0	120	4
Variability interval	22	0.5	80	2

The sought functional dependence was represented by a function of the form:

$$y = b_0 + b_1X_1 + b_2X_2 + b_3X_3 + b_4X_4 \tag{2}$$

where $b_0, b_1, b_2, b_3,$ and b_4 – coefficients determined after implementing the planned experiments.

In order to set up the experiment, the full factorial design of type 2^4 was implemented in four randomized series, which made it possible to assess the influence of each factor [19] independently. The planning matrix and the results of the experiments are provided in Table 2.

Table 2. Results of the experiments.

Experiment no.	X ₁	X ₂	X ₃	X ₄	\bar{l} , μm
1	22	0.5	40	2	138
2	66	0.5	40	2	46
3	22	1.5	40	2	54
4	66	1.5	40	2	28
5	22	0.5	200	2	185
6	66	0.5	200	2	91
7	22	1.5	200	2	85
8	66	1.5	200	2	44
9	22	0.5	40	6	28
10	66	0.5	40	6	12
11	22	1.5	40	6	35
12	66	1.5	40	6	20
13	22	0.5	200	6	73
14	66	0.5	200	6	25
15	22	1.5	200	6	32
16	66	1.5	200	6	11

The formulas determined the estimates of the regression coefficients:

$$b_i = \frac{\sum_{i=1}^N x_{iu} \bar{y}}{N}; \tag{3}$$

$$b_u = \frac{\sum_{i=1}^N \bar{y}}{N}; \tag{4}$$

$$b_{ij} = \frac{\sum_{i=1}^N x_{iu} x_{ju} \bar{y}}{N}; \tag{5}$$

where x_{iu} – value of x_i factor in the u -th experiment; x_{ju} – value of x_{ju} actor in the u -th experiment; \bar{y} – optimization parameter value in the same experiment; N – number of experiments. The significance of the coefficients was assessed by comparing the absolute value of the coefficient with the confidence interval value.

The analysis has shown that the $b_0, b_1, b_2, b_3,$ and b_4 coefficients can be considered significant with a 95% confidence level. The regression coefficients for pairwise interactions and higher-order interactions are statistically insignificant. Thus, the regression equation is:

$$y = 173.97 - 1.003X_1 - 36.125X_2 + 0.145X_3 - 13.594X_4 \tag{6}$$

The adequacy of the model, that is, its ability to predict the actual response values with the required accuracy, was tested by Fisher’s test:

$$F = \frac{S_{ad}^2}{S_{\{y\}}^2} \tag{7}$$

where $S_{\{y\}}^2$ – experiment error mean square; S_{ad}^2 – residual variance or variance of adequacy.

The calculated value of Fisher’s criterion has turned out to be less than the tabular value at a 5% significance level, so the resulting model is adequate [20].

4 Results

Figure 3, 4 and 5 shows a graphical interpretation of the obtained mathematical model after experimental research.

Graphical dependence analysis in Fig. 3 shows that the distance between the grains decreases with an increase in the pulse frequency. This can be explained by the fact that an increase in the pulse frequency, other things being equal, decreases the energy of electrical discharges, and there is a decrease in the intensity of the electrical discharge effect on the metal bond of the diamond wheel. An increase in the relative pulse duration leads to a decrease in the discharges’ electric energy action duration. This results in a decrease in the intensity of the electrical discharge action on the metal bond and a decrease in the distance between the grains.

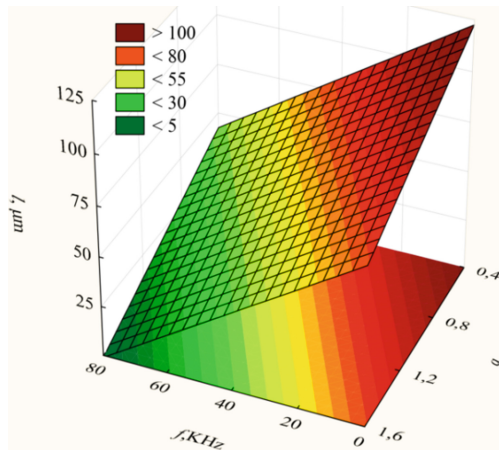


Fig. 3. Response surface $l - (f, q)$. Terms of calculation $Z = 120 \mu\text{m}$, $K = 4$.

An increase in the wheel grit leads to an increase in the distance between grains (Fig. 4). This is due to a decrease in the number of grains per unit volume of the diamondiferous wheel layer.

An increase in the diamonds concentration in the wheel results in a drop in the spacing between grains (Fig. 5). This is due to an increase in the number of grains per

unit volume of the diamondiferous wheel layer. The influence of the diamond concentration in the wheel is opposite to the grit.

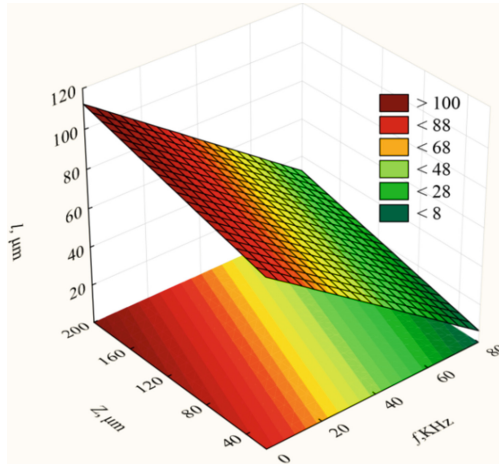


Fig. 4. Response surface $l - (f, Z)$. Terms of calculation $q = 1, K = 4$.

The electrical energy of the discharges characterizes the intensity of the electrical discharge effect on the wheel metal bond and on the surface of the material being processed. The choice of relative pulse duration and the frequency of their repetition, assigned in the complex, should be carried out taking into account the peculiarities of the action of the discharges with various combinations of the wheel characteristics.

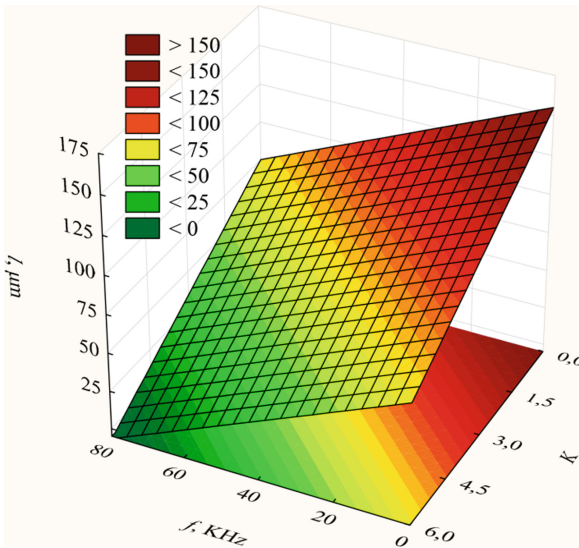


Fig. 5. Response surface $l - (f, K)$. Terms of calculation $Z = 120 \mu\text{m}, q = 1$.

With an increase in the pulse energy, the pre-fracture factor of the bond surface and the metal being processed is more pronounced, and stronger heating of the surface layers occurs, but this increases the possibility of local damage to the bond surface and diamond grains. With short pulses of low energy, the short duration of exposure causes the material's rapid surface evaporation to form an even clean hole, and the wheel bond surface quality becomes higher. The possibility of the formation of microdefects on the treated surface is reduced.

5 Conclusions

The influence of electric modes and wheel characteristics on the value of the distance between grains has been studied experimentally.

It is possible to determine the value of the distance between the grains for various values of electrical modes and the wheel characteristics using the functional dependence. It was found that the most significant factors that influence the distance between grains are frequency and relative pulse duration, grit, and concentration of diamond wheels.

For rough types of grinding of coarse-grained wheels, it is advisable to work with high-energy pulses with a low frequency. This will ensure pre-fracture and heating of the surface layers of the processed material and will facilitate and intensify micro-cutting processes for coarse-grained wheels, where the distance between the grains is greater, and the amount of their embedment in the bundle is greater, the effect of pulses with increased energy values is less dangerous than for fine-grained ones.

For finishing types of grinding performed with fine-grained wheels, it is more expedient to use low-energy pulses at a higher frequency, which provide less damage to the machined surface and less roughness of the bond in the intergranular space of a fine-grained wheel.

In the future, the research task will be to show the real possibility and practical value of forecasting from the obtained functional dependence when analyzing the process of electrical discharge grinding, evaluating the cutting ability and wear of diamond wheels in comparison with partial results obtained, moreover, after unproductive, lengthy, and expensive experiments.






References

1. Strelchuk, R.M., Trokhimchuk, S.M.: Mathematical modeling of the surface roughness of the grinding wheel during straightening. *Nauk. Visnyk Natsionalnoho Hirnychoho Universytetu*, 53–59 (2021)
2. Nadolny, K., Sienicki, W., Wojtewicz, M.: The effect upon the grinding wheel active surface condition when impregnating with non-metallic elements during internal cylindrical grinding of titanium. *Arch. Civ. Mech. Eng.* **15**(1), 71–86 (2014). <https://doi.org/10.1016/j.acme.2014.03.004>
3. Rao, X., Zhang, F., Lu, Y., Luo, X., Chen, F.: Surface and subsurface damage of reaction-bonded silicon carbide induced by electrical discharge diamond grinding. *Int. J. Mach. Tools Manuf.* **154**, 103564 (2020).

4. Strelchuk, R., Trokhymchuk, S., Sofronova, M., Osipova, T.: Revealing patterns in the wear of profile diamond wheels. *Eastern-Eur. J. Enterp. Technol.* **3**, 30–37 (2020)
5. Lin, B., Wang, H., Wei, J., Sui, T.: Diamond wheel grinding characteristics of 3D orthogonal quartz fiber reinforced silica ceramic matrix composite. *Chinese J. Aeronaut.* (2021)
6. Wang, T., Liu, H., Wu, C., Cheng, J., Chen, M.: Three-dimensional modeling and theoretical investigation of grinding marks on the surface in small ball-end diamond wheel grinding. *Int. J. Mech. Sci.* **173** (2020)
7. Chen, J., Fu, Y., Qian, N., Ching, C.Y., Ewing, D., He, Q.: A study on thermal performance of revolving heat pipe grinding wheel. *Appl. Therm. Eng.* **182** (2021)
8. Kahraman, M.F., Öztürk, S.: Experimental study of newly structural design grinding wheel considering response surface optimization and Monte Carlo simulation. *Meas. J. Int. Meas. Confed.* **147** (2019)
9. Javaroni, R.L., et al.: Improvement in the grinding process using the MQL technique with cooled wheel cleaning jet. *Tribol. Int.* **152**, 106512 (2020)
10. Arkhipov, P.V., Lobanov, D.V., Rychkov, D.A., Yanyushkin, A.S.: Determination of high-strength materials diamond grinding rational modes. In: IOP Conference Series: Materials Science and Engineering. Institute of Physics Publishing (2018)
11. Straus, J., Krishnamoorthy, D., Skogestad, S.: On combining self-optimizing control and extremum-seeking control – applied to an ammonia reactor case study. *J. Process Control.* **78**, 78–87 (2019)
12. Luo, B., Yan, Q., Pan, J., Lu, J., Huang, Z.: Influences of processing parameters on metal-bonded diamond wheel wear when grinding a sapphire wafer. *Diam. Relat. Mater.*, 108275 (2021)
13. Shan, Z., Zhou, C., Chen, G., Dai, L.: Experimental study on electro-discharge dressing of super-abrasive grinding wheel using different dielectric. *Jingangshi yu Moliao Moju Gongcheng/Diamond Abrasives Eng.* **40**, 79–84 (2020)
14. Yoshida, T., Karasawa, H., Fukui, R., Fujii, K., Warisawa, S.: Analysis of chip size distribution using image processing technology to estimate wear state of cylindrical grinding wheel. *Tribol. Int.* **153** (2021)
15. Modi, M., Agarwal, G.: Modelling, investigation of process responses, surface assessment and parametric optimization in powder mixed electrical discharge diamond grinding of ti6al4v utilizing grey-based taguchi approach. *Trans. Famena.* **44**, 93–112 (2020)
16. Gupta, A., Kumar, H.: Optimization of EDM process parameters: a review of technique, process, and outcome. In: Singari, R.M., Mathiyazhagan, K., Kumar, H. (eds.) *Advances in Manufacturing and Industrial Engineering*. LNME, pp. 981–996. Springer, Singapore (2021). https://doi.org/10.1007/978-981-15-8542-5_87
17. Krishnamoorthy, D., Pavlov, A., Li, Q.: Robust Extremum Seeking Control with application to Gas Lifted Oil Wells. *IFAC-PapersOnLine.* **49**, 205–210 (2016)
18. Öztürk, S., Kahraman, M.F.: Modeling and optimization of machining parameters during grinding of flat glass using response surface methodology and probabilistic uncertainty analysis based on Monte Carlo simulation. *Measurement* **145**, 274–291 (2019)
19. Zhang, C., Ordóñez, R.: *Extremum-Seeking Control and Applications*. Springer, London, London (2012)
20. Trollberg, O., Jacobsen, E.W.: Greedy extremum seeking control with applications to biochemical processes. *IFAC-PapersOnLine* **49**, 109–114 (2016)



Improvement of the MQL Efficiency in Machining Stainless Steel by Adding Nanoparticles to the Cutting Fluid

Youssef Touggui^{1,2} , Alper Uysal² , Uğur Emiroglu² ,
Eshreb Dzhemilov³ , and Salim Belhadi⁴ 

¹ Structures Research Laboratory (LS), University of Blida1, Blida, Algeria

² Department of Mechanical Engineering, Yildiz Technical University, Beşiktaş, 34349 Istanbul, Turkey
auysal@yildiz.edu.tr

³ Department of Mechanical Engineering,

Crimean Engineering and Pedagogical University, Simferopol, Russia

⁴ Mechanics and Structures Research Laboratory (LMS), May 8th 1945 University of Guelma, Guelma, Algeria

Abstract. In recent years, there has been a significant increase in the demand for environmentally sustainable machining processes to minimize the extravagant use of traditional cutting fluids, thereby reducing their detrimental impact on the environment and the operator's health. This experimental study aims to improve the Minimum Quantity Lubrication (MQL) sustainable approach's efficiency while machining AISI 304 austenitic stainless steel with a carbide insert. Optimum turning parameters were attained through the genetic algorithm (GA) optimization method based on response surface methodology (RSM) models. Present work has claimed the superiority of hybrid nanofluid MQL turning over MQL and nanofluid MQL turning operations. The most prominent achievement of this study is the improvement of surface roughness by 20.29% and 5.17% under hybrid nanofluid MQL compared to MQL and nanofluid MQL conditions, respectively. Similarly, hybrid nanofluid MQL slightly reduced cutting force by 2.36% and 0.83% over MQL and nanofluid MQL conditions, respectively. It is worth mentioning that the adding of nanoparticles in cutting fluid enhances the MQL turning efficiency in the machining of AISI 304 stainless steel.

Keywords: MQL efficiency · Nanofluid · Hybrid nanofluid · AISI 304 · Machining

1 Introduction

Nowadays, the environmentally friendly machining process has greatly increased its significance in metal-cutting industries in order to mitigate the hazardous and unhealthy impacts of metalworking fluids. Minimum Quantity Lubrication (MQL) is considered to be one of the alternative approaches to limiting the many harmful effects induced by the abundant use of conventional cutting fluids. However, mediocre cooling function

because of inability of the lower oil flow rate to fully limit heat generation at cutting region is the main limitation of this alternative [1, 2]. Therefore, the necessity has arisen to improve its efficiency. The focus here is to improve the MQL efficiency by adding MWCNT particles and hybrid (MWCNT + MoS₂) nanoparticles to the vegetable cutting fluid in turning of AISI 304 austenitic stainless steel.

2 Literature Review

In literature, many researchers have commonly used the MQL approach in their experimental works. Li and Lin [3] used the MQL approach in micro-grinding operation, and they concluded that this approach improved surface finish and reduction in cutting forces. Similarly, an enhancement by 15% in terms of surface quality and cutting forces was reported by Singh et al. [4] in their study when they conducted turning experiments of hard-to-cut material under the MQL technique. The machinability characteristics of X210Cr12 steel were investigated experimentally by Nouioua et al. [5] under wet and MQL cooling conditions. In contrast to wet machining, the MQL method produced better results in terms of cutting forces, surface roughness, and tool wear. Elbah et al. [6] implemented MQL in turning of AISI 4140 HSLA steel. Researchers observed that the MQL technique enabled a reduction in resulting cutting force compared to dry and flood machining environments. Bedi et al. [7] studied the effect of cutting speed on Ra and F_c when turning AISI 304 under dry and MQL conditions, and they found that MQL produced better surface finish and lower cutting force than dry turning. Rajaguru and Arunachalam [8] have investigated super duplex stainless steel machining under different coolant environments to improve its machinability. Turning experiments were performed under dry, flood, and MQL conditions to enhance the machinability in terms of cutting force [9] and surface finish. Findings have indicated that the MQL method outperformed other conditions. However, due to the poor thermal properties of the conventional fluids associated with the mediocre cooling function of the MQL process as well as its lubricating feature, there appears to be a need to improve the MQL efficiency. In this way, the applications of nano lubricants assisted MQL [10, 11], and hybrid nanofluid MQL [12] have recently become essential research trends to overcome this issue. Researchers have tried various nanoparticles with lubricating properties such as Al₂O₃ (Aluminum Oxide), MoS₂ (Molybdenum Disulphide), CuO (Copper oxide), Fe₂O₃ (Iron oxide), and MWCNT (Multi-walled Carbon Nanotubes). Das et al. [13] carried out the hard turning experiments of HSLA steel using three different nanofluids (Al₂O₃, CuO, and Fe₂O₃) and compared the results in terms of F_c and Ra . Based on the experimental results, it was concluded that CuO nanofluid performed better than other nanofluids. Öndin et al. [14] evaluated the performance of MWCNT nanoparticles enriched vegetable cutting fluid in turning of PH 13–8 Mo stainless steel and obtained that pure-MQL and MWCNT reinforced nanofluid MQL reduced the Ra by 5% and 12%, respectively, in comparison with the dry condition. Uysal et al. [15] added 1.0% MoS₂ particle to the vegetable cutting fluid in the milling of AISI 304 steel. The authors noticed an amelioration in surface roughness compared to MQL and dry environments. In their opinion, this may be attributed to the lubrication effect of MoS₂ particles. Patole and Kulkarni [16]

analyzed the machinability characteristics, including cutting force and surface roughness of AISI 4340 under MWCNT reinforced nanofluid MQL. They observed that the nanofluid MQL method yielded an improved surface roughness than conventional cooling.

Based on previous studies, it is worth noting that the addition of nanoparticles to cutting fluids to improve MQL efficiency has received so far more attention from researchers. However, less attention has been paid to the addition of MWCNT and its hybrid MWCNT-MoS₂ to the cutting fluid, while the tool-job turning combination consists of AISI 304 as a workpiece, and coated carbide [17, 18] as a cutting tool. Hence, a contribution was made in this research to fill this gap.

3 Research Methodology

Turning experiments on an AISI 304 (ASS) cylindrical workpiece having a diameter of 70 mm and a length of 300 mm were performed on a CNC lathe under MQL, nanofluid MQL, and hybrid nanofluid MQL cooling/lubricating conditions. For nanofluid-MQL, MWCNT particles were added to the vegetable cutting fluid at 0.1%wt. Likewise, in the case of hybrid nanofluid-MQL, MWCNT and nano MoS₂ particles were added to the vegetable cutting fluid at 0.05%wt. and 0.05%wt., respectively. In turning operations, the cutting fluid was pulverized by a nozzle to the rake face at a flow rate of 30 ml/h and pressure of 0.5 MPa through the MQL system. The inserts with the ISO specification of TNMG 160408-MM 2025 were employed in this work. According to Taguchi's L27 (3×3) orthogonal array, twenty-seven experiments were carried out, as is given in Table 1. In this design experiment, the cutting parameters (V_c and f) were defined as continuous variables, the depth of cut was kept constant, and cooling/lubricating conditions were termed as categorical variables. For each set of turning experiments, the cutting time was fixed at 20 s. Measurements of surface roughness values and cutting forces were carried out using Mitutoyo surfstest-210 and Kistler piezoelectric dynamometer (type 9257B). The experimental set-up is shown in Fig. 1.

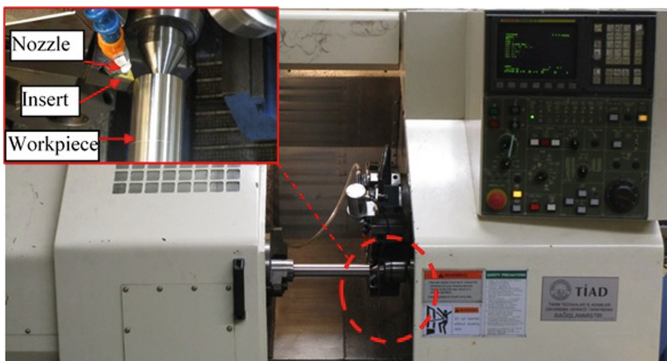


Fig. 1. Experimental set-up.

Table 1. Design of experiments.

Exp. no.	Cooling and lubrication method	Cutting speed, V (m/min)	Feed, f (mm/rev)
1	MQL	160	0.12
2	MQL	190	0.12
3	MQL	220	0.12
4	MQL	160	0.16
5	MQL	190	0.16
6	MQL	220	0.16
7	MQL	160	0.2
8	MQL	190	0.2
9	MQL	220	0.2
10	Nanofluid MQL	160	0.12
11	Nanofluid MQL	190	0.12
12	Nanofluid MQL	220	0.12
13	Nanofluid MQL	160	0.16
14	Nanofluid MQL	190	0.16
15	Nanofluid MQL	220	0.16
16	Nanofluid MQL	160	0.2
17	Nanofluid MQL	190	0.2
18	Nanofluid MQL	220	0.2
19	Hybrid nanofluid MQL	160	0.12
20	Hybrid nanofluid MQL	190	0.12
21	Hybrid nanofluid MQL	220	0.12
21	Hybrid nanofluid MQL	160	0.16
23	Hybrid nanofluid MQL	190	0.16
24	Hybrid nanofluid MQL	220	0.16
25	Hybrid nanofluid MQL	160	0.2
26	Hybrid nanofluid MQL	190	0.2
27	Hybrid nanofluid MQL	220	0.2

4 Results

4.1 The Effect of MQL Turning on Responses (R_a and F_y)

In this experimental work, the lowest R_a and F_y values were obtained by applying hybrid nanofluid based MQL at the combination of the highest cutting speed ($V_c = 220$ m/min) and smallest feed ($f = 0.12$ mm/rev), as shown in Figs. 2 and 3 (Experiment number of 21). Overall, the experimental results showed that the addition of nanoparticles to the vegetable cutting fluid in the MQL system significantly reduced R_a and F_y results compared to pure MQL conditions. This is probably the ability of

nanoparticles to reduce the coefficient of friction because of their structures at the nano-level that help to form a thin layer at the rubbing zone, leading to reducing shear stress and separating the asperities of sliding surfaces effectively [19]. Interestingly, it can be shown that the hybrid nanofluid MQL method gave more enhancement in turning responses (Ra and F_y) than the nanofluid MQL method. The primary reason is that combining the nanoparticles (MWCNT + MoS₂) and increasing their Brownian motion in liquid caused an increase in thermal conductivity of the formulated nanofluid, which resulted in a reduction in heat generated in the cutting area due to its heat dissipation capability [19]. The values for response parameters (Ra and F_y) were presented in Fig. 4. Results demonstrated that hybrid nanofluid MQL outperformed the other lubricating/cooling environments concerning the machinability enhancement of AISI 304 in terms of Ra and F_y . Figure 4 shows that the hybrid nanofluid MQL method exhibits a significant improvement in terms of Ra with 20.29% and 5.17% over pure MQL and nanofluid MQL, respectively. However, slight reductions of 2.36% and 0.83% in cutting forces were observed over pure MQL and nanofluid MQL, respectively. This is because of the better physical synergistic effect of MWCNT and MoS₂ nanoparticles' combination. A similar observation was made in the literature [20].

When the influence of cutting speed and feed on the output parameters are considered, it can be shown that increasing the feed increases Ra , as shown in Fig. 2. The increase in Ra is thought to be due to the generation of helical grooves produced by the relative movement between the workpiece and the insert. In turn, as long as these grooves were deeper and broader, the feed achieved higher values. In addition, the surface roughness tends to be slightly influenced by the cutting speed. Where surface roughness diminished with an increase in cutting speed from the smallest to the highest level, this reduction in surface roughness was because increased cutting speed contributes to generating high temperature in the cutting area. As a result, the workpiece was softened so that the turning operation could be smoothly carried out, thereby surface roughness reduced [14, 21].

Similarly, as can be seen in Fig. 3, the cutting force increased significantly with increasing the feed. The key explanation for this is due to an increase in the chip cross-section, causing an increment in friction force at the tool-chip interface [22]. Furthermore, the cutting speed had substantially less effect on the cutting force than the feed. At lower cutting speeds, higher cutting force values were recorded. This can be explained by an increase in the tool-chip contact [23] length caused by the remaining chip in the tool's rake face over a long time [24]. Decreased cutting force was observed at high cutting speed ($V_c = 220$ m/min). In general, with an increase in cutting speed, the temperature rises at the cutting region, thermal softening occurs, thereby cutting forces are reduced [25].

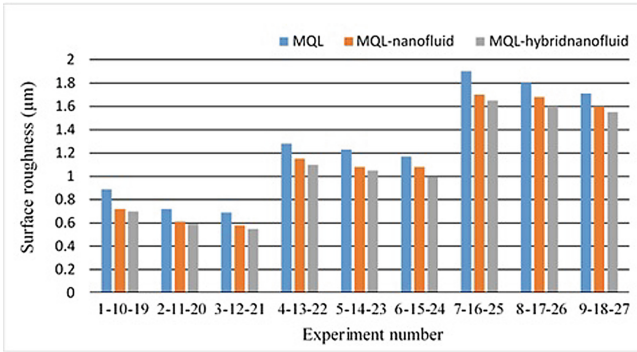


Fig. 2. The surface roughness results.

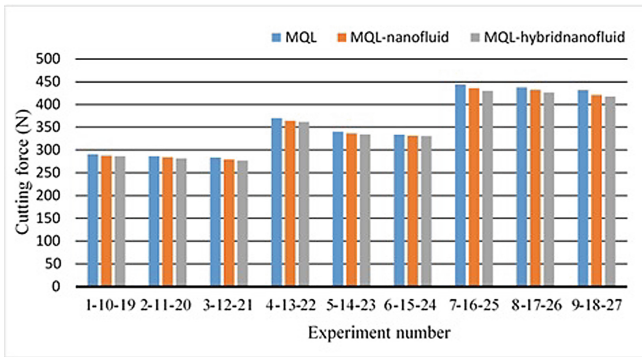


Fig. 3. The cutting force results.

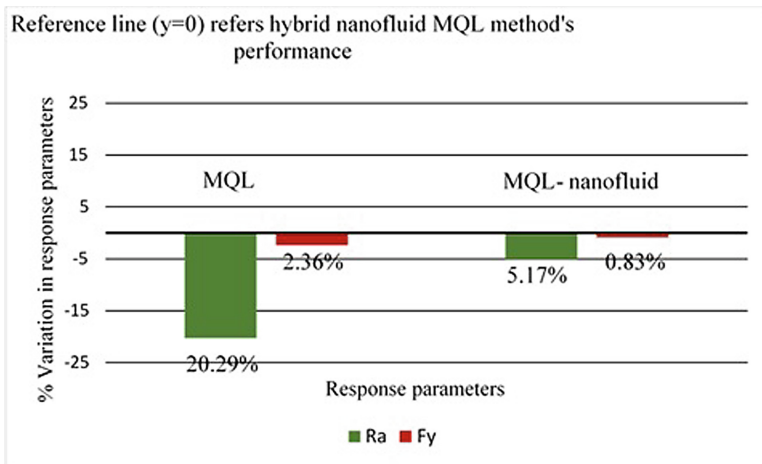


Fig. 4. Effect of hybrid nanofluid MQL on response parameters compared to nanofluid MQL and pure MQL.

4.2 Modeling and Optimization of Turning Parameters

To achieve the optimal configuration of turning parameters while simultaneously decreasing Ra and Fy , a genetic algorithm (GA) optimization approach based on RSM models (Eqs. 1–6) obtained using Design-Expert 10 software was used. The best solutions were found at the cutting speed of 220 m/min and the feed of 0.12 mm/rev with optimal estimated responses of $Ra = 0.83 \mu\text{m}$, $Fy = 278.50 \text{ N}$, $Ra = 0.58 \mu\text{m}$, $Fy = 275.85 \text{ N}$ and $Ra = 0.54 \mu\text{m}$, $Fy = 275 \text{ N}$ under MQL, nanofluid MQL and hybrid nanofluid MQL, respectively. In addition, the optimum results derived by GA were compared with three experiments (3, 12, and 21) as given in Table 2. The obtained percentage deviations are within the acceptable range, i.e., within $<5\%$, except Ra in the MQL case, confirming the validity of the optimal results attained in this study.

$$Fy_{MQL} = 400.54 - 1.51 * Vc - 398.24 * f - 1.07 * Vc * f + 3.60E - 003 * Vc^2 + 7775 * f^2 \quad (R^2 = 0.99\%) \quad (1)$$

$$Fy_{MWCNT} = 405.12 - 1.51 * Vc - 458.57 * f - 1.07 * Vc * f + 3.60E - 003 * Vc^2 + 7775 * f^2 \quad (R^2 = 0.99\%) \quad (2)$$

$$Fy_{MWCNT+MoS2} = 405.58 - 1.49 * Vc - 498.99 * f - 1.07 * Vc * f + 3.60E - 003 * Vc^2 + 7775 * f^2 \quad (R^2 = 0.99\%) \quad (3)$$

$$Ra_{MQL} = 1.40 - 0.01 * Vc + 0.75 * f + 6.94E - 003 * Vc * f + 1.79E - 005 * Vc^2 + 34.03 * f^2 \quad (R^2 = 0.91\%) \quad (4)$$

$$Ra_{MWCNT} = 1.09 - 9.63E - 003 * Vc + 0.58 * f + 6.94E - 003 * Vc * f + 1.79E - 005 * Vc^2 + 34.03 * f^2 \quad (R^2 = 0.91\%) \quad (5)$$

$$Ra_{MWCNT+MoS2} = 1.17 - 9.91E - 003 * Vc + 0.125 * f + 6.94E - 003 * Vc * f + 1.79E - 005 * Vc^2 + 34.03 * f^2 \quad (R^2 = 0.91\%) \quad (6)$$

Table 2. Comparison between optimal solutions derived by GA with experiments.

Cooling/lubricating conditions		Responses	
		<i>Ra</i> , μm	<i>Fy</i> , N
MQL	GA	0.83	278.50
	Experimentally observed value at run 3	0.69	283.49
	<i>Deviation (%)</i>	<i>16.86</i>	<i>1.76</i>
nanofluid MQL	GA	0.58	275.85
	Experimentally observed value at run 12	0.58	279.11
	<i>Deviation (%)</i>	<i>0</i>	<i>1.16</i>
hybrid nanofluid MQL	GA	0.54	275
	Experimentally observed value at run 21	0.55	276.78
	<i>Deviation (%)</i>	<i>1.81</i>	<i>0.64</i>

Italics refer to the deviations that have been obtained

5 Conclusion

In this investigation, an effort was made to improve the MQL efficiency in the machining of AISI 304 (ASS) regarding surface roughness (*Ra*) and cutting force (*Fy*) by adding nanoparticles to the vegetable cutting fluid. The RSM modeling method was applied to develop *Ra* and *Fy* regression models. After that, the optimization by genetic algorithm (GA) of various controlled variables such as cutting speed, feed, and cooling/lubricating conditions for response parameters (*Ra* and *Fy*) was performed. Based on the results, the following noteworthy findings can be drawn:

- The lowest surface roughness (*Ra*) and cutting force (*Fy*) values were found to be 0.69 μm , 0.58 μm , 0.54 μm , and 278.50 N, 276 N, 275 N under pure MQL, nanofluid MQL, and hybrid nanofluid MQL, respectively. Compared to the pure MQL method, a reduction in the *Ra* and *Fy* was noticed when the nanofluid MQL and hybrid nanofluid MQL were applied.
- The results revealed that the hybrid nanofluid MQL caused approximately 20% and 5% improvement in terms of *Ra* and *Fy*, respectively, over the pure MQL method.
- In GA optimization outcomes, it was highlighted that the best combination for simultaneously approaching the smallest *Ra* and *Fy* was cutting speed of 220 m/min, feed of 0.12 mm/rev under hybrid nanofluid MQL condition.
- Overall, combining MWCNT nanoparticles with other lubricant additives such as MoS₂ improves its properties, resulting in a better reduction in *Ra* and *Fy* than MWCNT nanoparticles alone, and thus it could be used as cutting fluid for better MQL turning efficiency.






References

1. Hegab, H., Umer, U., Soliman, M., Kishawy, H.A.: Effects of nano-cutting fluids on tool performance and chip morphology during machining Inconel 718. *Int. J. Adv. Manuf. Technol.* **96**(9–12), 3449–3458 (2018). <https://doi.org/10.1007/s00170-018-1825-0>
2. Gupta, M.K., et al.: Performance evaluation of vegetable oil-based nano-cutting fluids in environmentally friendly machining of Inconel-800 Alloy. *Materials* **12**, 2792 (2019)
3. Li, K.M., Lin, C.P.: Study on minimum quantity lubrication in micro-grinding. *Inter. J. Adv. Manuf. Technol* **62**, 99–105 (2012)
4. Singh, G., et al.: Investigations of machining characteristics in the upgraded MQL-assisted turning of pure titanium alloys using evolutionary algorithms. *Materials* **19**, 999 (2019)
5. Nouioua, M., Yallese, M.A., Khettabi, R., Belhadi, S., Mabrouki, T.: Comparative assessment of cooling conditions, including MQL technology on machining factors in an environmentally friendly approach. *Int. J. Adv. Manuf. Technol.* **91**(9–12), 3079–3094 (2017). <https://doi.org/10.1007/s00170-016-9958-5>
6. Elbah, M., Laouici, H., Benlahmidi, S., Nouioua, M., Yallese, M.A.: Comparative assessment of machining environments (dry, wet and MQL) in hard turning of AISI 4140 steel with CC6050 tools. *Int. J. Adv. Manuf. Technol.* **105**(5–6), 2581–2597 (2019). <https://doi.org/10.1007/s00170-019-04403-9>
7. Bedi, S.S., Behera, G.C., Datta, S.: Effects of cutting speed on MQL machining performance of AISI 304 stainless steel using uncoated carbide insert: application potential of coconut oil and rice bran oil as cutting fluids. *Arab. J. Sci. Eng.* **45**, 8877–8893 (2020)
8. Rajaguru, J., Arunachalam, N.: A comprehensive investigation on the effect of flood and MQL coolant on the machinability and stress corrosion cracking of super duplex stainless steel. *J. Mater. Process. Tech.* **276**, 116417 (2020)
9. Pavlenko, I., et al.: Parameter identification of cutting forces in crankshaft grinding using artificial neural networks. *Materials* **13**(23), 5357 (2020). <https://doi.org/10.3390/ma13235357>
10. Sharma, A.K., Tiwari, A.K., Dixit, A.R.: Effects of minimum quantity lubrication (MQL) in machining processes using conventional and nanofluid based cutting fluids: a review. *J. Clean. Prod* **127**, 1–18 (2016)
11. Sharma, A.K., Singh, R.K., Dixit, A.R., Tiwari, A.K.: Characterization and experimental investigation of Al₂O₃ nanoparticle based cutting fluid in turning of AISI 1040 steel under minimum quantity lubrication (MQL). *Mater. Today Proc* **3**, 1899–1906 (2016)
12. Jamil, M., et al.: Effects of hybrid Al₂O₃-CNT nanofluids and cryogenic cooling on machining of Ti-6Al-4V. *Int. J. Adv. Manuf. Technol* **102**, 3895–3909 (2019)
13. Das, A., Kumar Patel, S., Das, S.R.: Performance comparison of vegetable oil based nanofluids towards machinability improvement in hard turning of HSLA steel using minimum quantity lubrication. *Mech. Ind.* **20**, 506 (2019)
14. Öndin, O., Kırık, T., Sarıkaya, M., Yıldırım, Ç.V.: Investigation of the influence of MWCNTs mixed nanofluid on the machinability characteristics of PH 13–8 Mo stainless steel. *Tribology Int.* **148**, 106323 (2020)
15. Uysal, A., Demiren, F., Altan, E.: Applying minimum quantity lubrication (MQL) method on milling of martensitic stainless steel by using nano MoS₂ reinforced vegetable cutting fluid. In: *Procedia- Social and Behavioral Sciences, Conference 2015*, vol.195, pp. 2742–2747. Elsevier Ltd (2015)
16. Patole, P.B., Kulkarni, V.V.: Optimization of process parameters based on surface roughness and cutting force in MQL turning of AISI 4340 using nano fluid. *Mater. Today Proc* **5**, 104–112 (2018)

17. Ivanov, I.V., Mohylenets, M.V., Dumenko, K.A., Kryvchyk, L., Khokhlova, T.S., Pinchuk, V.L.: Carbonitration of a tool for pressing stainless steel pipes. *J. Eng. Sci.* **7**(2), C17–C21 (2020). [https://doi.org/10.21272/jes.2020.7\(2\).c3](https://doi.org/10.21272/jes.2020.7(2).c3)
18. Sokhan', S.V., et al.: Diamond grinding the ceramic balls from silicon carbide. *J. Eng. Sci.* **5** (1), A12–A20 (2018). [https://doi.org/10.21272/jes.2018.5\(1\).a3](https://doi.org/10.21272/jes.2018.5(1).a3)
19. Singh, R.K., Dixit, A.R., Mandal, A., Sharma, A.K.: Emerging application of nanoparticle-enriched cutting fluid in metal removal processes: a review. *J. Braz. Soc. Mech. Sci. Eng.* **39** (11), 4677–4717 (2017). <https://doi.org/10.1007/s40430-017-0839-0>
20. Gugulothu, S., Pasam, V.K.: Experimental investigation to study the performance of CNT/MoS₂ hybrid nanofluid in turning of AISI 1040 steel. *Aust. J. Mech. Eng.* (2020). <https://doi.org/10.1080/14484846.2020.1756067>
21. Yıldırım, Ç.V., Kivak, T., Sarıkaya, M., Şirin, Ş: Evaluation of tool wear, surface roughness/topography and chip morphology when machining of Ni-based alloy 625 under MQL, cryogenic cooling and cryoMQL. *J. Mater. Res. Technol.* (2020). <https://doi.org/10.1016/J.JMRT.201912.069>
22. Gunichenko, O., Bushlya, V., Zhou, J., Stahl, J.E.: Tool wear and machining dynamics when turning high chromium white cast iron with pcBN tools. *Wear* **309**, 253–269 (2017)
23. Ivanov, V., Pavlenko, I., Liaposhchenko, O., Gusak, O., Pavlenko, V.: Determination of contact points between workpiece and fixture elements as a tool for augmented reality in fixture design. *Wireless Netw.* **27**(3), 1657–1664 (2019). <https://doi.org/10.1007/s11276-019-02026-2>
24. Kulkarni, A.P., Joshi, G.G., Sargade, V.G.: Dry turning of AISI 304 austenitic stainless steel using AlTiCrN coated insert produced by HPPMS technique. In: *Procedia Engineering, Conference 2013*, vol.64, pp. 737–746. Elsevier Ltd (2013)
25. Pramanik, A., Islam, M.N., Basak, A., Littlefair, G.: Machining and tool wear mechanisms during machining titanium alloys. *Adv. Mater. Res.* **651**, 338–343 (2013)



Impact of Turning Operations on the Formation of Rolling Bearing's Functional Surfaces

Valentyn Zablotskyi¹ , Anatolii Tkachuk¹ ,
Anatolii Senyshyn² , Ivanna Trokhymchuk¹ ,
and Kostiantyn Svirzhevskiy¹ 

¹ Lutsk National Technical University, 75, Lvivska St., 43018 Lutsk, Ukraine
a. tkachuk@lntu.edu.ua

² Technical University of Munich, 21, Arcisstraße, 80333 Munich, Germany

Abstract. Under the conditions of operation of high-speed rotor mechanisms, bearing bearings become the primary source of unwanted vibrations, noise, and premature loss of the initial operational properties of the machines. Accordingly, the requirements for the quality of rolling bearings and their performance are constantly growing, and the technological support of the regulated requirements is becoming increasingly problematic. To increase the efficiency of machining operations of bearing parts and ensure the required quality of functional surfaces of rings in automated production, it is necessary to develop new effective methods of design and control of technological processes for the manufacture of individual bearing parts. The article analyzes the principles of technological support of quality parameters of the functional surfaces of the rings to improve and stabilize the performance of roller bearings. The reasons for increasing the vibroactivity of the working surfaces of the rings and the excess of the allowable vibration parameters and bearing noise are investigated. The connections of technological factors of forming operations of turning processing with parameters of microgeometry of the processed surfaces and operational properties of bearings are established. Models of formation of microgeometry of rotation surfaces on turning operations are developed, the reasons and technological features of formation of undulations on the processed surface are revealed.

Keywords: Adaptive control · Formation · Microgeometry · Roller bearing · Vibroactivity

1 Introduction

The quality indicators of an individual unit or machine as a whole are inextricably linked with the quality indicators and performance of each bearing as a separate part of the rotor system, which can potentially be the primary source of undesirable phenomena or characteristics of the whole mechanism, device or machine (Fig. 1a) [1]. Therefore, the requirements for the quality of rolling bearings and their performance are constantly growing, and the technological support of these requirements is becoming more complicated. It is known that the quality of the bearing and its performance

characteristics, such as vibration, noise, accuracy, reliability, durability, and others, depend on the parameters of microgeometry and physical and mechanical properties of the surface layer of functional surfaces [2]. The leading causes of undulations are the dynamic processes of machining parts on metal-cutting machines, associated with the loss of stability of the machine-tool-part system [3]. Vibrations in the cutting process occur due to self-oscillations, forced oscillations, and deformation of the rings. Self-oscillations are the result of the loss of properties of a given motion during cutting. External perturbations cause forced oscillations. The causes of undulation are forced oscillations of the system caused by various periodic perturbations due to the imbalance of the machine-tool-part system (workpiece, machine spindle, shafts, and gears) [4]. Depending on the oscillations frequency ratio and the speed of relative movement of the tool and the part, the surface shape violation nature is changed. The decisive factor affecting the part's shape is the ratio of the frequency of harmonic oscillations for the tool and the workpiece to the rotation speed of the part [5].

Therefore, the technological support of the regulated requirements for the quality of working surfaces and performance characteristics of roller bearings during their manufacture is an urgent problem.

2 Literature Review

Among the scientific works concerning the problem of technological assurance of the quality of shaping and operational properties of rolling bearings, it is possible to distinguish four directions:

- geometrical, based mainly on the dimensional analysis of technological processes and operations in order to achieve the desired level of accuracy of parts, assemblies, and products [6];
- technological, in which the quality of the surface is considered from the standpoint of the relationship with technological factors [7];
- the rigidity characteristics of the technological system's units, and the own deformations of parts and their influence on the quality parameters of the forming surfaces [8];
- complex, considering the whole set of factors that affect the quality of formation [9].

In the works of these areas, various aspects of the technological formation of parameters of geometric structure of surface, physical and mechanical properties of the surface layer of details of bearings and details with contact interaction are investigated, questions of the influence of technological factors of machining on parameters of quality of surfaces and some operational characteristics of surfaces and details [10, 11]. However, technological influence and control of the parameters of the undulation of the working surfaces of roller bearings in the operations of centerless grinding are not correctly reflected [12].

Based on the analysis of literature sources, it is established that the vibroacoustic characteristics of roller bearings and their accuracy and wear resistance are dominated by shape errors, ripples, and roughness of the contact surfaces [13].

Statistical analysis of product defects that occur in the process of manufacturing parts of roller bearings showed that the leading causes of surface layer defects in accuracy and surface ripple are oscillating processes of the dynamic system of forming the working surfaces of roller bearing rings in turning operations, diamond and abrasive operations and finishing operations [14, 15].

3 Research Methodology

Structural vibrations in bearings are due to two main reasons - deformation of the rings under the action of forces from the rolling elements and fluctuations in the stiffness of the bearing during rotation as a result of the radial component of the load F_1 (Fig. 1b). Since the rolling elements move relative to the line of action of the radial load, the stiffness of the bearing changes periodically with frequencies multiples of the frequency of passage of the rolling elements on a fixed ring [16]. In low-precision bearings, structural vibrations are not noticeable, but as the precision of the bearings increases, these vibrations may play a more prominent role. The frequency of structural vibration is equal to or multiple of the value of $f_p = qz f_c$, where z is the number of rolling elements; f_c is the rotational speed of the separator relative to the fixed ring; $q = 1, 2, \dots$ is the coefficient of proportionality.

Vibrations associated with the structural imperfection of the bearing are because, in the design of the bearing and the rolling contacts, there are sliding contact surfaces due to differences in linear and angular velocities of adjacent parts (Fig. 1b) [17].

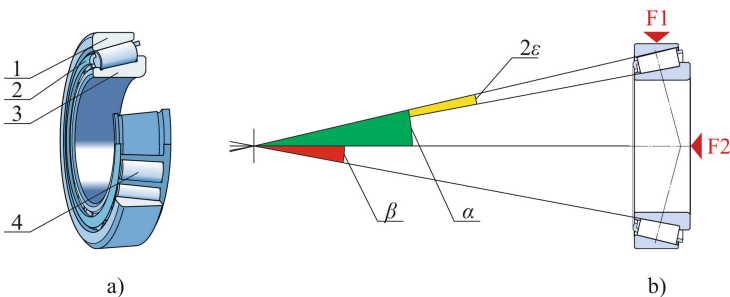


Fig. 1. Construction: 1 – outer ring (fixed); 2 – separator; 3 – inner ring (movable); 4 – rolling elements a) and the scheme of the tapered roller bearing $\beta = \alpha - 2\varepsilon$ b).

The relative speeds between the contacting parts of the tapered roller bearing are determined based on the speed of the inner ring with a fixed outer ring.

$$\text{Separator} \leftrightarrow \text{inner ring} : n_{s/ir} = \frac{\sin \alpha}{\sin \alpha + \sin \beta} n_{ir/or} \quad (1)$$

$$\text{Separator} \leftrightarrow \text{outer ring} : n_{s/or} = \frac{\sin \beta}{\sin \alpha + \sin \beta} n_{ir/or} \quad (2)$$

$$\text{Rolling body} \leftrightarrow \text{separator} : n_{rb/s} = \frac{\sin \beta}{\sin \varepsilon} n_{s/ir} \quad (3)$$

Mismatched frequencies occurring in the bearing are determined from expressions (4–6). Relative frequency of the roller:

$$f_{md} = 2 \cdot n_{rb/s} \quad (4)$$

The relative frequency of the inner ring:

$$f_{ir\ md} = Z \cdot n_{s/ir} \quad (5)$$

Relative frequency of the outer ring:

$$f_{or\ md} = Z \cdot n_{s/or} \quad (6)$$

where Z is the number of rollers (rolling elements) in the bearing; n_{ir} – the number of revolutions of the shaft (inner ring).

For the experimental study of the influence of technological factors on the parameters of the microgeometry of the treated surfaces, an automated research unit based on a lathe and an automated research complex Rank Taylor Hobson Talyskan were used.

4 Results

Vibrations, which are associated with structural imperfections of rolling bearings, are manifested at pronounced frequencies and do not significantly affect the formation of the initial accuracy of bearings and bearing assemblies [18]. The vibrations and the operational characteristics of the roller bearings are influenced to a greater extent by the errors in forming the shape of the working surfaces of the rings, the bodies of rotation, and working environment conditions [19].

Shape errors in the manufacture of bearing parts should be divided into 4 groups:

1. deviations of the first order – errors in the placement of working surfaces (different wall thickness of the rings, radial and axial beating, different sizes of rolling elements, etc.);
2. deviations of the second-order – errors in the shape of working surfaces (ovality, number of faces);
3. deviation of the third-order – undulation;
4. deviations of higher orders – roughness, subroughness.

Depending on the rank, all of the above errors cause low-frequency, medium-frequency, or high-frequency vibrations:

- errors in the shape of the raceways, as well as the size and ovality of the rolling elements – low-frequency vibration (in the frequency range up to $10 \cdot f_0$),

- the undulation of rolling tracks – a vibration of the medium frequency (in the frequency range $10 \dots 60 \cdot f_0$),
- the undulation of rolling elements and roughness of rolling tracks – high-frequency vibrations (in the frequency range over $60 \cdot f_0$).

In the ratio f_0 – the oscillation frequency of the bearing shaft due to the imbalance corresponding to the number of revolutions of the shaft (inner ring) $f_0 = n_{\epsilon} = 1800 \text{ min}^{-1}$.

Given that $f_0 = f_{c/s} + f_{c/o}$, the frequency composition of the spectrum of vibrational oscillations of the bearings due to defects in the rings is determined by the expression:

$$f = |k \cdot f_0 - q \cdot Z \cdot f_{c/o}| \tag{7}$$

where Z is the number of rolling elements in the bearing; k is the order of harmonics of the undulation of the raceway. Figure 2 (side view) shows the relationship of the geometric structure of the roller bearing with the parameters of the undulation of the working surfaces and the number of rolling elements Z .

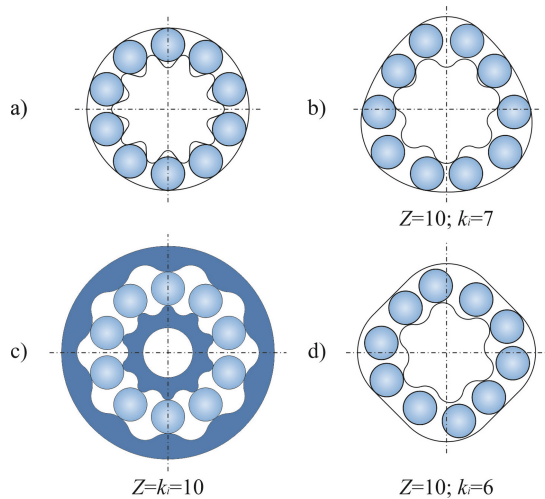


Fig. 2. Influence of the working surfaces’ undulation ratio to the number of rotation bodies on the geometric structure of the bearing.

The equation of radial vibration of the outer ring of the roller bearing has the form:

$$\ddot{\chi} + 2h\dot{\chi} + \omega_p^2\chi = \sum_j F_j \frac{\sin(\omega_j t + \Psi_j)}{M} \tag{8}$$

where χ is the radial vibration displacement of the ring (μm); ω_p – natural frequency; F_j, ω_j, ψ_j, h – amplitude, frequency and phase of the j -th harmonic of vibration disturbances and damping coefficient, respectively.

The solution of Eq. (8) gives the dependencies for vibration displacement χ , vibration velocity $\dot{\chi}$, and vibration acceleration $\ddot{\chi}$.

The modeling of microgeometry parameters is based on surface formation due to the relative movements of a part and a tool [20]. Altitude parameters of the microgeometry such as undulation, surface roughness are determined by the nature and magnitude of the radial movements of the tool relative to the workpiece [21]. The microgeometry step parameters depend on the ratio of the longitudinal feed of the tool and the rotational speed of the workpiece.

For modeling the height parameters of the microgeometry, a mathematical model of the dynamics of forming the working surfaces of the rings on the turning operation are developed. The calculated scheme of the dynamic model of the form's formation process is shown in Fig. 3.

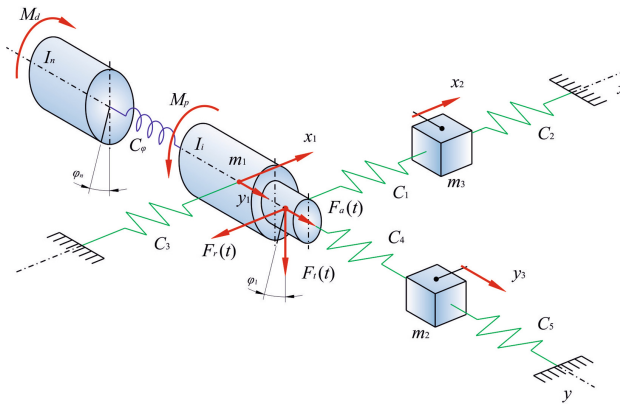


Fig. 3. Calculation scheme of a dynamic system.

The description of the notation of the calculation scheme (Fig. 3) is given in Table 1.

Table 1. Designation of the calculation scheme (Fig. 3).

Denotation	Description
m_1	Spindle weight and part weight
m_2, m_3	Masses of transverse and longitudinal calipers
$C_1 - C_5$	Elastic links
C_φ	Angular stiffness of the drive
M_d, M_p	Moments of cutting
x_1, x_2	Coordinates of displacements of masses m_1 and m_2 along the x -axis
y_1, y_3	Coordinates of displacements of masses m_1 and m_3 along the y -axis
φ_1, φ_n	Coordinates of angular displacements of rotating masses
$F_r(t), F_r'(t), F_a(t)$	Cutting force

For a more accurate representation of the process of surface formation, a detailed scheme of the cutting process is given (Fig. 4).

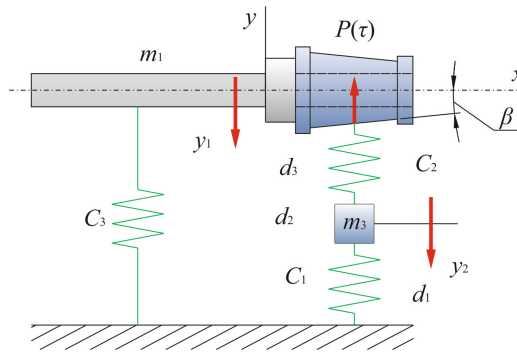


Fig. 4. Scheme of shaping the functional surface of the bearing.

The system of differential equations describing the movement of the tool relative to the workpiece has the form:

$$\begin{cases} m_1 \ddot{y}_1 + d_1 \dot{y}_1 + c_1 y_1 + c_3 (y_1 - y_2) = P(\tau) \\ m_2 \ddot{y}_2 + d_2 \dot{y}_2 + c_2 y_2 + c_3 (y_1 - y_2) = -P(\tau), \end{cases} \quad (9)$$

where m_1 is the mass of the spindle assembly with the part; m_2 – the weight of the caliper with the tool; c_1 – stiffness of the caliper; c_2 – stiffness of supports and spindle assembly; d_1 and d_2 are the damping coefficients of the bonds; $P(\tau)$ – perturbing force.

Application of the complex amplitudes method allows us to obtain the perturbing force as a variable:

$$P(\tau) = P_0 e^{i\omega\tau} \quad (10)$$

where ω is the frequency of the perturbing force; $P_0 = P_y \cdot \cos\beta$ is the amplitude of the force, and P_y is the radial component of the cutting force.

The solution of the system of differential equations yields formulas for determining the amplitudes of the relative oscillations of the part and the tool:

$$u_1 = u_0 \sqrt{\frac{(K_2^2 - \omega^2) + 4\mu_2^2 K_1^2}{F_1^2(\omega) + 2[d\mu_2 K_1^2 + f\mu_1 K_2^2 - F_2(\omega)]\omega^2}} \quad (11)$$

$$u_2 = u_0 \sqrt{\frac{(K_1^2 - \omega^2) + 4\mu_1^2 K_2^2}{F_1^2(\omega) + 2[d\mu_2 K_1^2 + f\mu_1 K_2^2 - F_2(\omega)]\omega^2}} \quad (12)$$

The frequency of natural oscillations is found from the characteristic equation of the system:

$$f = \sqrt{\frac{1}{2} \left(\frac{c_1 + c_3}{m_1} + \frac{c_2 + c_3}{m_3} \right) \pm \sqrt{\left(\frac{c_1 + c_3}{m_1} + \frac{c_2 + c_3}{m_3} \right)^2 - \frac{4(c_1c_2 + c_2c_3 + c_1c_3)}{m_1m_3}}} \text{sec}^{-1} \quad (13)$$

where $x = s\tau/60$ – movement per 1 revolution; $V = \omega (D/2) = (\pi D)/\tau$, $\tau = \pi/\omega$.

In order to increase the accuracy of shaping, the design of a continuous workpiece of two rings of the roller bearing is proposed (Fig. 5).

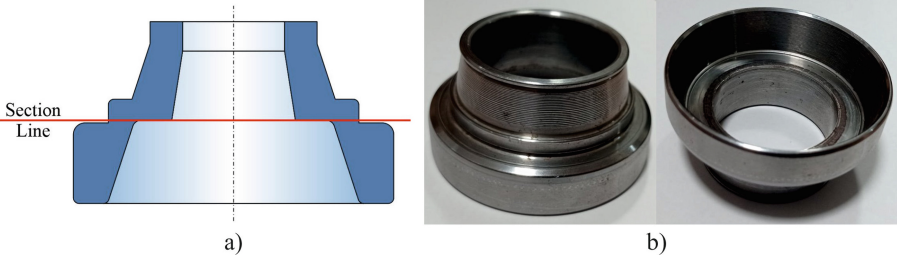


Fig. 5. The continuous design of the workpiece of two rings: a) scheme; b) prototype.

As a result of using this type of workpiece, it was possible to increase the accuracy of forming rings on turning operations, halve the complexity of procurement and forming turning operations, avoid the formation of stresses on functional surfaces that occur during installation in the chuck.

Notably, the vibroactivity of the working surfaces of the rings depends on the parameters of the wavy surfaces. By determining the relationship between the parameters of the undulation of the rolling tracks of the rings and the vibroactivity of the bearing revealed an essential pattern that the worst vibroacoustic characteristics of the bearing occur when the number of waves to the k -th harmonic on the inner and outer rings bearing, or when the number of waves of the k -th harmonic is a multiple of the number of rolling elements, ie $f_k = qz$, where f_k is the number of waves of the main k -th harmonic on the raceway.

The best results were observed when $f_k = qz \pm 1$, $f_k = qz \pm 2$ and so on, $q = 1, 2, 3, \dots$. The proposed method of spectral analysis of vibroactivity of rolling tracks and vibrations of bearings allows diagnosing the causes of the origin of technological defects.

5 Conclusions

The resistance of the dynamic forming system to resonant perturbations is investigated, and the limits of stability in the coordinates stiffness - feed rate are obtained. Theoretical predictions in the process by modeling a dynamic system of formation are confirmed. It is established that for all variants of finishing turning in the feed range 0.05–0.20 mm/rev step of the irregularities S_z to the average value of the height W_z is

less than 40, which indicates the absence of undulation. The maximum deviations of the surface shape ($W_z + R_z$) do not exceed 0.012 mm.

The mechanism of origin of structural and technological defects of roller bearings is investigated. Identification of the relationship between these defects and performance on the example of changes in the bearing's vibroacoustic characteristics formed the basis for developing a strategy for predicting the quality of parts and performance of bearings at the stage of technological design. For diagnosing the causes of vibration, the total spectrum of bearing oscillations should be divided into three bands – low-frequency oscillations (50 Hz–1.5 kHz), medium-frequency (1.5–3.0 kHz), and high-frequency vibrations (1.5–10 kHz). It is established that technological defects cause low-frequency and high-frequency vibrations. The technique on the integrated vibroactivity indicator for rings' working surfaces to define the level of suitability of a ready detail for operation as a part of the bearing and forecasting of vibroacoustic characteristics of rolling bearings are offered.

It is established that the shape errors and waviness of the working surfaces of the rings after the final operations of the superfinishing are transmitted by technological inheritance from the previous shaping operations of turning, roughing, and finishing grinding. In order to prevent such a negative impact of technological heredity, a new method of technological control of the undulation of rolling tracks in turning operations by modeling the dynamics of shaping is being developed. It is established that the reduction of surface waviness in turning operation reduces the oscillations of the components of cutting forces in finishing grinding operations, and hence the geometric ripple, which can account for up to 90% of the error of deviation of shaping accuracy.

In order to increase the accuracy of forming rings on turning operations, as well as to reduce the number of procurement and forming operations, the proposed design of a continuous workpiece set of two roller bearing rings, the introduction of which into production, will reduce the complexity of procurement operations by 35% and reduce cost by 15% of each bearing size.

References






1. Chermensky, O., Fedotov, N.: Rolling bearings. Mechanical Engineering, Moscow (2003)
2. Chernets, M.V.: Prediction of the life of a sliding bearing based on a cumulative wear model taking into account the lobing of the shaft contour. *J. Friction Wear* **36**(2), 163–169 (2015). <https://doi.org/10.3103/S1068366615020038>
3. Ivanov, V., Pavlenko, I., Liaposhchenko, O., Gusak, O., Pavlenko, V.: Determination of contact points between workpiece and fixture elements as a tool for augmented reality in fixture design. *Wireless Netw.* **27**(3), 1657–1664 (2019). <https://doi.org/10.1007/s11276-019-02026-2>
4. Yakimov, A., Novikov, F., Novikov, G., Serov, B., Yakimov, A.: Theoretical foundations of cutting and grinding materials. OGPU, Odessa (1999)
5. Ravska, N.: Fundamentals of kinematic theory of geometrical parameters in the part of the instrument. *Reliab. Tools Optim. Technol. Syst.* **24**, 9–18 (2009). [in Russian]
6. Larshin, V., Lishchenko, N.: Adaptive profile gear grinding boosts productivity of this operation on the CNC machine tools. *Lecture Notes in Mechanical Engineering* **F2**, 79–88 (2019)

7. Tkachuk, A., Zablotskyi, V., Kononenko, A., Moroz, S., Prystupa, S.: Directed formation of quality, as a way of improving the durability of conjugated parts of friction pairs. In: Ivanov, V., et al. (eds.) DSMIE 2019. LNME, pp. 370–377. Springer, Cham (2020). https://doi.org/10.1007/978-3-030-22365-6_37
8. Monkova, K., et al.: Condition monitoring of Kaplan turbine bearings using vibro-diagnostics. *Int. J. Mech. Eng. Robot. Res.* **9**(8), 1182–1188 (2020). <https://doi.org/10.18178/ijmerr.9.8.1182-1188>
9. Saruhan, H., Sandemir, S., Çiçek, A., Uygur, I.: Vibration analysis of rolling element bearings defects. *J. Appl. Res. Technol.* **12**(3), 384–395 (2014). [https://doi.org/10.1016/S1665-6423\(14\)71620-7](https://doi.org/10.1016/S1665-6423(14)71620-7)
10. Teja, P.S., Kumar, M.D., Krishna, R., Sreenivasan, M.: Simulation and optimization studies on the ring rolling process using steel and aluminum alloys. *J. Eng. Sci.* **6**(2), E36–E40 (2019). [https://doi.org/10.21272/jes.2019.6\(2\).e6](https://doi.org/10.21272/jes.2019.6(2).e6)
11. Gold, P., Loos, J.: Wear resistance of PVD-coatings in roller bearings. *Wear* **253**(3–4), 465–472 (2002)
12. Chalyj, V., Moroz, S., Ptachenchuk, V., Zablotskyj, V., Prystupa, S.: Investigation of waveforms of roller bearing's working surfaces on centerless grinding operations. In: Ivanov, V., Trojanowska, J., Pavlenko, I., Zajac, J., Peraković, D. (eds.) DSMIE 2020. LNME, pp. 349–360. Springer, Cham (2020). https://doi.org/10.1007/978-3-030-50794-7_34
13. Iakimov, O.O.: Influence of intermittent grinding wheel design on geometrical parameters of quality of the processed surface. *Cutt. Tool. Technol. Syst.* **85**, 323–330 (2015)
14. Tarelnik, V., et al.: Alternative methods for forming sliding surfaces of face impulse seals. In: 2018 IEEE 8th International Conference Nanomaterials: Application & Properties (NAP), pp. 1–6. IEEE (2018). <https://doi.org/10.1109/NAP.2018.8915077>
15. Lesyk, D.A., et al.: Laser-hardened and ultrasonically peened surface layers on tool steel AISI D2: correlation of the bearing curves' parameters, hardness and wear. *J. Mater. Eng. Perform.* **27**, 764–776 (2018)
16. Dykha, A., Sorokatyi, R., Makovkin, O., Babak, O.: Calculation-experimental modeling of wear of cylindrical sliding bearings. *East-Eur. J. Enterp. Technol.* **5**(1 (89)), 51–59 (2017). <https://doi.org/10.15587/1729-4061.2017.109638>
17. Awrejcewicz, J., Kurpa, L., Shmatko, T.: Investigating geometrically nonlinear vibrations of laminated shallow shells with layers of variable thickness via the R-functions theory. *Compos. Struct.* **125**, 575–585 (2015)
18. Budnik, O.A., Sviderskii, V.A., Budnik, A.F., Berladir, K.V., Rudenko, P.V.: Composite material for chemical and petrochemical equipment friction assemblies. *Chem. Pet. Eng.* **52** (1–2), 63–68 (2016). <https://doi.org/10.1007/s10556-016-0149-x>
19. Berladir, K.V., Sviderskiy, V.A.: Designing and examining polytetrafluoroethylene composites for tribotechnical purposes with activated ingredients. *Eastern-Eur. J. Enterprise Technol.* **6**(84), 14–21 (2016). <https://doi.org/10.15587/1729-4061.2016.85095>
20. Chetverzhuk, T., Zabolotnyi, O., Sychuk, V., Polinkevych, R., Tkachuk, A.: A method of body parts force displacements calculation of metal-cutting machine tools using CAD and CAE technologies. *Ann. Emerg. Technol. Comput. (AETiC)* **3**(4), 37–47 (2019). <https://doi.org/10.33166/AETiC.2019.04.004>
21. Kalchenko, V., Yeroshenko, A., Oyko, S.: Mathematical modeling of abrasive grinding working process. *Sci. Bull. Natl. Min. Univ.* **6**, 76–82 (2017)

Advanced Materials



Control of the Strength Properties of Mixtures Based on Chromite Sand

Tatyana Berlizeva¹ , Olga Ponomarenko¹ ,
Nataliia Yevtushenko¹ , Igor Grimzin² , and Tatiana Lysenko³ 

¹ National Technical University “Kharkiv Polytechnic Institute”,
2, Kyrpychova St., 61002 Kharkiv, Ukraine

² Research and Production Center “European Engineering Technologies”,
101 Velyka Panasivska St., 61017 Kharkiv, Ukraine

³ Odessa Polytechnic State University,
1, Shevchenko Ave., 65044 Odessa, Ukraine

Abstract. The paper presents the results of a study into the processing and physical and mechanical properties of mixtures based on liquid glass (LG) with furfuryl oxypropyl cyclocarbonate (FOPCC) for chromite compounds. The patterns of the interaction between triethanolamine-modified liquid glass with furfuryl oxypropyl cyclocarbonate and chromite sand were established. Parameters such as compressive strength, flexural strength, and tensile strength were studied, which were determined using standard methods. Mathematical models of the properties of mixtures on chromite sand with liquid glass and FOPCC were developed based on the planned experiment. Mathematical models represent a system of equations linking the compressive strength, tensile strength, and flexural strength of the mixture with controlled variables of a technological nature for which the contents of liquid glass, FOPCC, and triethanolamine were chosen. Based on the data obtained, it was found that the flexural strength, tensile strength, and compressive strength increase with an increase in the content of LG and FOPCC. The compositions of cold-hardening mixtures on chromite sand were optimized, allowing obtaining high-quality cores with high strength properties. It has been established that FOPCC is a material that has a double effect; it hardens the mixture during preparation and softens it after pouring metal during decoring. The optimum binder content is 4,5 to 5,5%, and the optimum hardener content is 0,4 to 0,6%. A technological procedure has been developed to prepare chromite sand-based CHM. As a result, the surface quality was improved, and the burn-on on the castings was reduced.

Keywords: Chromite sand · Liquid glass · Triethanolamine · Optimization · Mechanical properties · Strength properties

1 Introduction

The quality of castings is strongly influenced by molding mixtures, the properties of which depend on the starting materials [1]. The preparation of mixtures with the desired properties is a traditional task of the foundry [2]. According to existing data, 40 to 60%

of casting defects are due to the unsatisfactory quality of molding compounds and mixtures [3, 4].

Fillers should have relatively high refractory properties, thermal resistance, inactivity to molten metal, mechanical strength, low coefficient of thermal expansion, uniform grain size distribution, and minimal cost [5]. Quartz sand, chromites, zircon, chrome magnesites are used as refractory fillers [6].

Quartz molding sands are currently most widely used. They account for more than 90% of all sands consumed by foundries. From the point of view of foundry technology, quartz sand has several undoubted advantages: it has a high melting point (1713 °C); high hardness, which contributes to good resistance to abrasion in the processes of preparing mixtures, making molds, and decoring and cleaning castings; chemical inactivity at ordinary temperatures; good mixing properties with various components of mixtures; good wettability with water and with almost all used binders; applicability in the manufacture of castings made of various alloys [7].

Unlike quartz sand, which undergoes allotropic transformations at 575 °C, chromite sand is subject to none of these transformations. It exhibits high thermal shock resistance. With a relatively high melting point of about 1880 °C, chromite sand has a low sintering temperature of 1100 °C. The moisture condensation zone is formed much more deeply in a chromite-based green-sand mold than in quartz sand-based mixtures [8]. The chromite sand is inert to iron oxides at high temperatures in various gas atmospheres. It is also poorly wettable by liquid metal. All these factors improve the conditions for metal solidification and help prevent the formation of the burn-on when manufacturing large steel castings. The high thermal conductivity and thermal storage capacity of chromite sand make it possible to create the directional solidification of casting and prevent solidification irregularities [9].

Therefore, highly refractory and chemically inert Grade AFS45-50 TC U 13.2-35202765-001:2011 chromite sand has become widely used for turbomachinery purposes. The minimum Cr_2O_3 content must be at least 46%. Chromite sand is used as a filler for core and facing mixtures to obtain steel castings. This is particularly advantageous when manufacturing heavy castings where high resistance to ferrostatic pressure is required.

Thus, developing optimal compositions of new chromite sand-based CHM is an urgent task of the foundry.

2 Literature Review

One of the commonly used methods is manufacturing cores and casts on soluble glass (SG), and the technology for their production is used at many enterprises [10]. This is because soluble glass is an affordable, inexpensive and non-toxic binder [11]. The use of SG as a binder for the manufacture of casting and core mixtures allows to obtain more durable casts, reduce the metal consumption of castings by producing thinner products and improve the quality of castings [12, 13].

Depending on the solidifying nature, these mixtures can be divided into mixtures with a solidifier introduced together with a binder during their preparation and mixtures

solidified by blowing with a gaseous solidifier during or after filling equipment by them and their solidification [14, 15].

In the CO₂ process, the binding properties of liquid glass are poorly implemented (up to 20%), which leads to an increase in liquid glass content in the mixture and a decrease in the decorating properties; because of this, liquid hardeners are used for liquid glass-based CHM [16]. The consumption of liquid hardeners is very low, amounting to 10 to 12% of liquid glass mass [17]. Heavy organic ethers or aldehydes have proven to be the most advantageous liquid hardeners [18].

The use of liquid hardeners is one of the most advanced methods for hardening liquid glass-based mixtures, which allows [19]:

- Reducing the consumption of liquid glass to 2,5% to 4%;
- Increased in-mold decorative properties and cores by 1,5 to 2 times;
- Improving the quality of mixtures;
- Abandoning the use of CO₂ and thereby simplifying the technological process;
- Reducing defects and waste castings [20].

The paper proposes to use a universal additive, furfuryl oxypropyl cyclocarbonate (FOPCC), developed at NTU “KhPI” as a promising hardener for the manufacture of liquid glass-based molds and cores [21].

FOPCC is an environmentally friendly material, since when pouring metal into a mold, as a result of thermochemical destruction, FOPCC decomposes and releases CO₂ and water vapor in the volume of the formed composition into the environment.

The paper investigates into the properties of cold-hardening mixtures based on a chromite filler with triethanolamine-modified liquid glass and a universal additive, furfuryl oxypropyl cyclocarbonate.

FOPCC is a material that has a double effect; it hardens the mixture during preparation and softens it after pouring metal during decorating.

The composition (chromite sand – FOPCC – liquid glass) hardens when FOPCC interacts with liquid glass. Any cyclocarbonates (propylene cyclocarbonate, and FOPCC) are unstable in an alkaline medium and decompose with the release of CO₂, which reacts with liquid glass to form polysilicates in the volume of the formed composition. These systems can be referred to nanostructured composite materials, since the interaction processes between FOPCC and LG undergo on the surface of chromite sand in monomolecular layers.

The purpose of the study is to establish the regularities of the interaction between a triethanolamine-modified liquid glass-based binder with furfuryl oxypropyl cyclocarbonate (FOPCC) and chromite sand in the foundry.

3 Research Methodology

FOPCC is a material based on raw materials of plant origin, which was obtained as follows: furfuryl glycidyl ether and a catalyst (2 wt% tetrabutylammonium bromide) were loaded into a three-necked flask equipped with a thermometer, a reflux condenser, and a bubbler. The reaction mixture was heated to 90 °C, and carbon dioxide was introduced through the bubbler. The reaction was carried out for 8 h. The reaction

course was monitored according to variations in the epoxy equivalent and using IR spectroscopy (the appearance of an absorption band at 1790 cm^{-1} , which corresponds to the stretching vibrations of the carbonyl group in the cyclic carbonate ring). After the reaction, the catalyst was removed (washed with water), and the product was vacuum distilled.

The reaction for obtaining FOPCC is shown in Fig. 1.

Furfuryl propyl cyclocarbonate is a transparent liquid of light yellow color, with a boiling point of $t_b = (192\text{ to }194)\text{ }^\circ\text{C}$ at 10 mm Hg, refractive index of $(n_d^{20}) = 1.4920$, density of $1,45\text{ g/cm}^3$ (at $25\text{ }^\circ\text{C}$) [21].

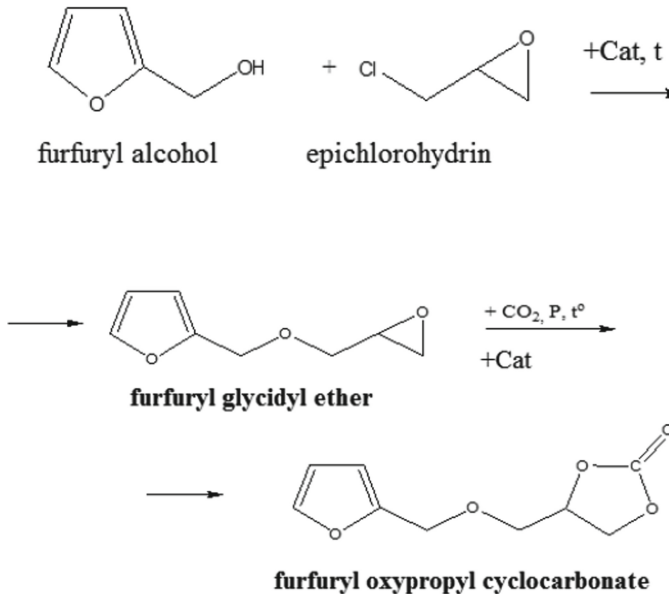


Fig. 1. The reaction for obtaining furfuryl oxypropyl cyclocarbonates.

The mixture was prepared as follows: first, a hardener was added to chromite sand and mixed for 3 min, then liquid glass with triethanolamine was added and mixed for another 2 min. Triethanolamine was introduced into liquid glass. TEA was taken of the total mass of FOPCC. The mixture was molded into a 9-piece mold, which is used to study the properties of CHM. Liquid additive (FOPCC) was added in the content of 0,4 to 0,6 wt%; liquid glass in the content of 4,5 to 5,5 wt%, and TEA in the content of 2 to 10 wt% mass of FOPCC. AFS45-50 quartz sand was used as a filler for molding mixtures.

The mixture was prepared as follows: FOPCC was added per 100 wt% chromite sand and stirred for 3 min, then the triethanolamine-modified liquid glass was introduced into the mixture and stirred for another 2 min.

Testing the compressive strength of the mixtures was carried out under GOST 23409.7 – 78 (strength in the “wet” state) and GOST 23402.9 – 78 (strength in the

“dry” state). For this purpose, a set was used to determine the tensile strength of cast and core mixtures of modules 04116Y with a device for compressing dry samples up to 15 MPa manufactured by UkrNIILitmash by a particular order of National Technical University “Kharkiv Polytechnic Institute”.

4 Results

Recently, a computational and analytical method based on a planned experiment has been widely used to solve the problem of controlling the properties of molding mixtures and their stabilization. This approach opens up new possibilities for controlling the properties of molding mixtures owing to the operational efficiency of process control when modifying the properties of the starting materials.

To establish the regularities of the interaction between a triethanolamine-modified liquid glass-based binder with furfuryl oxypropyl cyclocarbonate (FOPCC) and chromite sand, and the experiment was carried out.

The variation intervals of the factors and their values at the main, upper, and lower levels are shown in Table 1.

Table 1. Experimental conditions for chromite sand-based CHM.

Independent variables	Content of liquid glass, wt%	Content of triethanolamine in liquid glass, wt%	Content of FOPCC, wt%
Factor	x_1	x_2	x_3
Main level	5,0	5	0,5
Variation interval	0,5	2	0,1
Upper level	5,5	7	0,6
Lower level	4,5	3	0,4

The experiment planning matrix 2^{6-3} is shown in Table 2.

Table 2. Experiment planning matrix 2^{6-3} .

Experiment no.	Content of LG (x_1)	Content of FOPCC (x_2)	Content of TEA (x_3)	x_0	x_1	x_2	x_3	x_1x_2	x_1x_3	x_2x_3	Compressive strength, MPa (y_1)	Flexural strength, MPa (y_2)	Tensile strength, MPa (y_3)
1	5,5	0,6	10	+	+	+	+	+	+	+	1,4	7,5	0,5
2	4,5	0,6	10	+	-	+	+	-	-	+	1,3	6,25	0,45
3	5,5	0,4	10	+	+	-	+	-	+	-	1,18	6,5	0,43
4	4,5	0,4	10	+	-	-	+	+	-	-	1,08	5,5	0,4
5	5,5	0,6	2	+	+	+	-	+	-	-	1,05	6	0,4
6	4,5	0,6	2	+	-	+	-	-	+	-	1,2	5,75	0,43
7	5,5	0,4	2	+	+	-	-	-	-	+	1,05	6	0,4
8	4,5	0,4	2	+	-	-	-	+	+	+	0,93	5	0,38

The varying factors were as follows: the content of liquid glass (x_1); the content of triethanolamine in liquid glass (x_2); and the content of FOPCC (x_3). As an optimization

parameter (y), the following indicators of the physical and mechanical properties of the molding mixtures were chosen: compressive strength after 3 h (y_1), flexural strength (y_2), and tensile strength (y_3).

After processing the data obtained, the following equations in a coded scale were obtained:

$$y_1 = 1,15 + 0,02x_1 + 0,09x_2 + 0,09x_3 + 0,03x_{12} + 0,02x_{23} - 0,035x_{13}, \text{ MPa} \quad (1)$$

$$y_2 = 6,06 + 0,44x_1 + 0,38x_2 + 0,31x_3, \text{ MPa} \quad (2)$$

$$y_3 = 0,42 + 0,01x_1 + 0,02x_2 + 0,02x_3 + 0,01x_{12} + 0,01x_{23}, \text{ MPa} \quad (3)$$

When experimenting, account must be taken of the need to determine the experimental error, i.e., the variance of reproducibility. The reproducibility is estimated according to the results of parallel experiments. For this purpose, each experiment is supposed to be carried out three times in the planning matrix. The coefficients of the mathematical models were calculated, and their statistical significance was determined. The significance of the coefficients for each investigated optimization parameter was checked using Student's criterion. The hypothesis about the adequacy of mathematical models was checked using Fisher's criterion.

The effect of the content of LG with TEA and FOPCC on the compressive strength of the mixture is shown in Fig. 2.

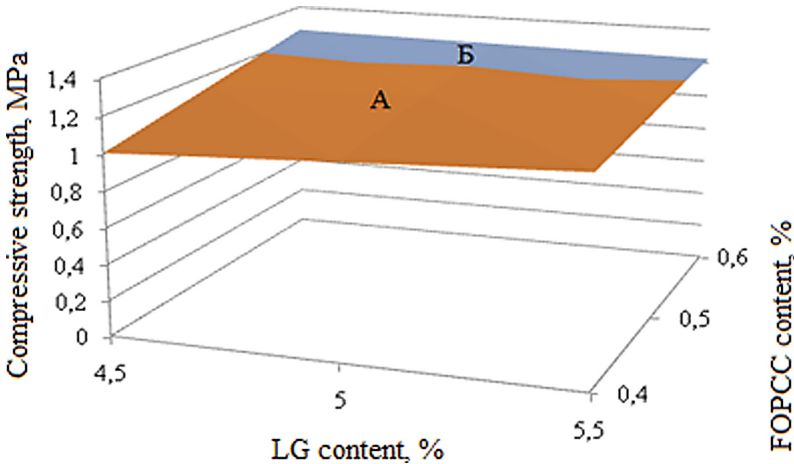


Fig. 2. The effect of the content of LG modified by 6 wt% TEA and FOPCC on the compressive strength of the mixture A: Compressive strength ranging from 1,00 to 1,12 MPa; B: Compressive strength ranging from 1,20 to 1,40 MPa

Figure 3 shows the effect of LG and FOPCC on the flexural strength of the mixture, and Fig. 4 shows the effect of LG and FOPCC on the tensile strength of the mixture.

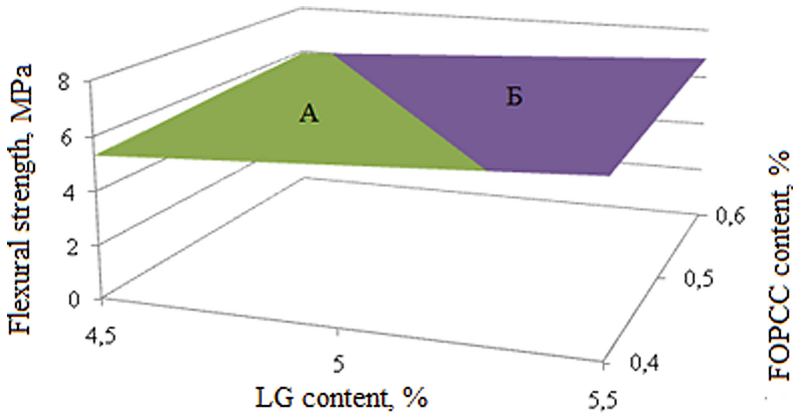


Fig. 3. The effect of the content of LG modified by 6 wt% TEA and FOPCC on the flexural strength of the mixture A: Flexural strength ranging from 4,00 to 6,00 MPa; B: Flexural strength ranging from 6,00 to 8,00 MPa.

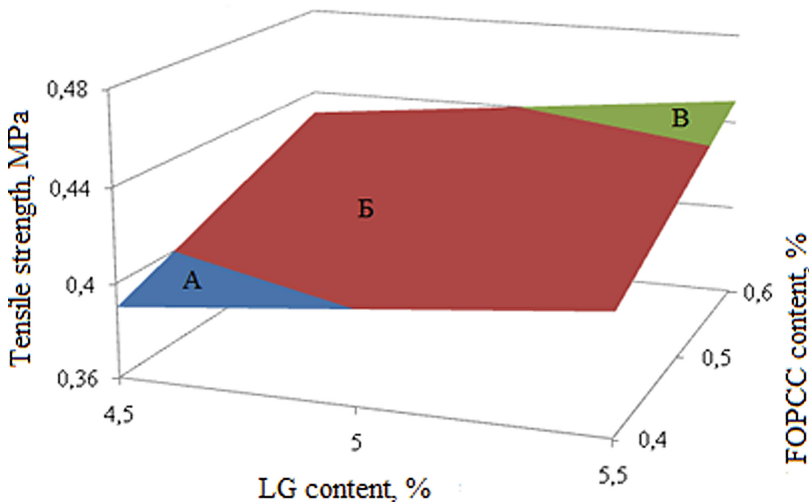


Fig. 4. The effect of the content of LG modified by 6 wt% TEA and FOPCC on the tensile strength of the mixture A: Tensile strength ranging from 0,44 to 0,48 MPa; B: Tensile strength ranging from 0,4 to 0,44 MPa B: Tensile strength ranging from 0,36 to 0,4 MPa.

Based on the analysis of the equations, it was found that the compressive strength, flexural strength, and tensile strength increase with an increase in the content of LG and FOPCC.

According to the process sample, the compressive strength of the mixture is an average of 1,5 MPa after 1 h; 2,5 MPa after 3 h; 3,5 MPa after 24 h. The tensile strength is an average of 0,2 MPa after 1 h, 0,5 MPa after 3 h, 0,8 MPa after 24 h. The flexural strength is an average of 4,5 MPa after 1 h, 7 MPa after 3 h, 9 MPa after 24 h.

The study has found that the developed additive FOPCC had shown the effectiveness of its use in the foundry. FOPCC has a double effect; it hardens the mixture during preparation and softens it after pouring metal during decoring.

5 Conclusions

To create new technological processes for the preparation of chromite mixtures, using triethanolamine-modified liquid glass with furfuryl oxypropyl cyclocarbonates (FOPCC) is a promising area for facing and core mixtures.

According to the process sample, the compressive strength of chromite mixture is an average of 1,5 MPa after 1 h; 2,5 MPa after 3 h; 3,5 MPa after 24 h. The tensile strength is an average of 0,2 MPa after 1 h, 0,5 MPa after 3 h, 0,8 MPa after 24 h. The flexural strength is an average of 4,5 MPa after 1 h, 7 MPa after 3 h, 9 MPa after 24 h.

In developing a technological process for the manufacture of high-quality castings using CHM with chromite sand based on FOPCC, a planned experiment was carried out.

A mathematical model was built for CHM based on chromite filler with FOPCC. This model is a system of equations linking the compressive strength, tensile strength, and flexural strength of the mixture with controlled variables of a technological nature for which it is appropriate to use the content of triethanolamine-modified binder and the content of hardener. It was found that the flexural strength, tensile strength, and compressive strength increase with an increase in the content of LG and FOPCC. The optimum binder content is 4,5 to 5,5%, and the optimum hardener content is 0,4 to 0,6% for the production of steel castings.

The addition of furfuryl oxypropyl cyclocarbonates a double effect; it hardens the mixture during preparation and softens it after pouring metal when decoring.

A technological process for obtaining chromite sand-based CHM was developed. The result was improved surface quality and reduced burn-in on castings.






References

1. Golofaev, A.N., Laguta, V.I., Khinchakov, G.V.: Technology of a Casting Mold. VNU Publishing House, Lugansk (2001)
2. Kukuy, D.M., Skvortso, V.A., Ektova, V.K.: Theory and Technology of Foundry. Design PRO, Minsk (2000)
3. Boldin, A.N., Davydov, N.I., Zhukovsky, S.S.: Foundry molding materials. Molding, core mixtures and coatings. Directory. Mechanical engineering (2006)
4. Lysenko, T.V., Yasyukov, V.V., Prokopovich, I.V.: Casting shaping control concept. Ecology, Odessa (2019)
5. Lyuty, R.V., Houri, I.M.: Molding materials. KPI them. Sikorsky, Kyiv (2020)
6. Maliy, A.V., Karginov, V.P., Leshchenko, A.D., Kuzoviv, A.F.: Improvement of the quality of knockout of mixtures on liquid glass. Casting Ukraine **1**, 24–26 (2008)
7. Dobocz, S.M., Grabarczyk, A., Major-Gabryś, K., Jakubski, J.: Influence of quartz sand quality on bending strength and thermal deformation of moulding sands with synthetic binders. Arch. Foundry Eng. **15**(2), 9–12 (2015)

8. Kukuy, D.M., Melnikov, A.P., Rovin, S.L.: Technology of processes of mixture preparation and manufacturing of sand foundry molds. BNTU, Minsk (2009)
9. Huminski, Y., Rovin, S.L.: Environmentally friendly superfine modified ultrafine liquid glass binder. *Casting Metall.* **3**, 41–45 (2019)
10. Thu, A.H., Zakharov, A.I.: Preparation of inorganic binder for cold-hardening mixtures. *Refract. Ind. Ceram* **59**(3), 313–317 (2018). <https://doi.org/10.1007/s11148-018-0227-z>
11. Al-Sarairah, F.M.: An assessment of the efficiency of utilizing complex modifiers for softening the liquid-glass mixtures to improve iron and steel casting. *ARPN J. Eng. Appl. Sci.* **13**(9) (2018)
12. Al-Sarairah, F.M., Svinoroev, Y.: Assessment of casting binding materials based on modified technical lignosulfonates. *Int. J. Mech. Prod. Eng. Res. Dev. (IJMPERD)* **10**(2), 335–346 (2020)
13. Al-Sarairah, F.M.: An assessment of the efficiency of utilizing complex modifiers for softening the liquid-glass mixtures to improve iron and steel casting. *ARPN J. Eng. Appl. Sci.* **9**(13), 3231–3235 (2018)
14. Al-Sarairah, F.M., Svinoroev, Y.: Production of high quality casting binders from materials containing lignin. *Int. J. Mech. Prod. Eng. Res. Dev. (IJMPERD)* **3**(10), 14575–14584 (2020)
15. Ingebrigtsen, T.S., Dyre, J.C., Schrøder, T.B., Royall, C.P.: Crystallization instability in glass-forming mixtures. *Phys. Rev. X* **9**(3), 031016 (2019)
16. Saikaew, C., Wiengwiset, S.: Optimization of molding sand composition for quality improvement of iron castings. *Appl. Clay Sci.* **67**, 2–31 (2012)
17. Zinchenko, P.S., Aksenenko, M.P., Yovbak, A.V., Orendarchuk, Y.V.: Application of liquid glass mixtures with a low content of liquid glass as a factor in improving the quality of castings for engineering purposes. *Sci. J. Sci. Rise* **5/2**(22), 6–9 (2016)
18. Huminski, Y., Rovin, S.L.: Application of a liquid glass binder modified by ultra-dispersed materials. *Foundry* **11**, 17–20 (2019)
19. Karpenko, V.M., Karpenko, V.M., Marukovich, E.I.: Artistic casting: materials, technologies, equipment. Belarus Science, Minsk (2019)
20. Schetinina, A.A., Ammer, V.A., Turischev, Y.Y.: Advantages and prospects of using cold-hardening mixtures in the manufacture of critical and highly loaded castings for the aviation industry. *Bull. Voronezh State Tech. Univ.* **3**(13), 68–70 (2017)
21. Karateev, A.M., Ponomarenko, O.I., Litvinov, D.A., Kalkamanova, O.S., Berlizeva, T.V.: A method of obtaining cold-hardening mixtures. Patent Ukraine, No. 95138 (2014)



Probabilistic Analysis of Corrosion Fatigue Resistance

Svetlana Bershak¹ , Victor Kurgan² , Ihor Sydorenko² ,
Oleksandr Levinskyi² , and Yuriy Yeputov² 

¹ Odessa National Maritime University,
34, Mechnikova Street, Odessa 65029, Ukraine

² Odessa Polytechnic State University,
1, Shevchenko Avenue, Odessa 65044, Ukraine
kurgan@opu.ua

Abstract. The article defines the existence of correlations between the parameters of the equation describing the dependence of the stress amplitudes arising in part in air and a corrosive environment. The analysis of numerous experimental data on samples and parts of various shapes and sizes, made of carbon and alloy steels, tested in corrosive environments differing in aggressiveness, showed that the relationship between the parameters is linear. Correlation-regression analysis confirmed the existence of a close relationship between the parameters. It was found that the difference in such dependences for different experimental data is statistically insignificant. This made it possible to recommend for practical use a generalized dependence for all investigated corrosive environments. At the same time, when assessing the fatigue resistance of parts that operate in environments of different aggressiveness, it is possible to use individual dependencies between parameters for each tested corrosive environment. Based on the results obtained, it was concluded that the dispersion of the logarithm of durability in the most aggressive of the investigated media (acid solutions) is approximately 20% less than in seawater and in distilled water - 10% more. The results obtained can serve as the basis for creating a method for calculating the strength and durability of parts under aggressive media and assessing the durability of such parts even at the design stage.

Keywords: Aggressive media · Corrosion fatigue · Corrosion fatigue resistance · Durability assessment · Compliance criterion

1 Introduction

A large number of mechanical equipment operates in aggressive environments [1]. Technological tasks performed with the help of such equipment lead to increased requirements for the strength of its components. The most significant number of reasons for the destruction of elements of mechanical equipment operating in an aggressive environment is corrosive fatigue – one of the most common types of metal destruction. Corrosion can be described as the destruction or deterioration of a metal or alloy through a chemical or electrochemical reaction with its environment [2]. Almost

all alloys based on Fe, Al, Mg, Cu, Ni, Ti, and other metals under certain conditions are subject to corrosion fatigue, which occurs when simultaneously exposed to cyclic mechanical loads and an aggressive environment [3]. Extensive experiments and detailed analysis of their results allow you to determine the relationship between various parameters and dependencies. This makes it possible to create methods for calculating the strength and durability of parts that work in various aggressive environments.

2 Literature Review

The impacts of the corrosion, adsorption and hydrogenation factors on the fatigue resistance of structural steels at various loading frequencies are considered in work [4]. The fatigue fractures of steels and parts in working environments are presented in the research [5]. Methods for the operational determination of the fatigue resistance characteristics of steels are considered. Variants of physical models of crack growth during corrosion fatigue destruction of steel are proposed in the paper [6].

The issues of bearing capacity of objects in aggressive media are considered up to the boundary stress, from which the influence of the mechanical factor on the resistance to corrosion-fatigue destruction can be neglected [7]. A method is proposed for constructing an individual corrosion fatigue curve of a new shape by testing under regular loading and up to bases not exceeding those usually used [8]. The main methods for assessing the corrosion resistance of structural steels in aquatic environments and moist atmospheric conditions are presented in work [9].

Methods for planning the main types of mechanical tests and processing their results are given. Recommendations are given for optimizing tests to determine the mechanical properties of materials, bearing capacity, and resource of machine parts with the required accuracy and reliability [10]. A new equivalent model of surface defects is proposed for predicting fatigue life [11]. A novel equivalent surface defect model is proposed to quantitatively describe the corrosion effect for fatigue life [13] prediction using both maximum corrosion and aspect ratios [14]. Another form of degradation is described that links mechanical stress and corrosion fatigue [15]. Questions are considered evaluating material damage and substantiation of life-based on corrosion-fatigue crack development kinetics [16]. Details of various forms of material degradation along with preventive measures have been described in the research [17]. Methods for monitoring corrosion and the cost of corrosion to society were considered in work [18]. The results of probabilistic analysis of metal degradation for a pressure vessel are shown in the paper [19].

3 Research Methodology

The following signs and patterns of corrosion fatigue of destruction of metals are formulated: the absence of a physical limit of corrosion fatigue of metals, that is, a constant decrease in the destructive cyclic-alternating stress with an increase in the number of load cycles; lack of correlation between the mechanical properties of the

metal, determined under static or cyclic loading, and the limit of corrosion fatigue; no correlation between the corrosion resistance of the metal in the unstressed state and the boundary of corrosion fatigue; increased, in comparison with air, metal sensitivity in a corrosive environment to the shape of the cycle and the frequency of loading; inversion of the scale effect, that is, an increase in the corrosion fatigue limit of carbon and low-alloy steels and aluminum-based alloys with an increase in the cross-section of the metal product; a decrease in the sensitivity of corrosion fatigue to the micro-geometry of the surface of a part in comparison with tests in air [4]; the specific multi-plane nature of fracture associated with the development in the initial period of fracture of a large number of cracks, and not one, as in air; non-additivity of influence on corrosion resistance of stress concentration and corrosive environment [7].

Many signs and patterns of corrosion fatigue of destruction of metals determine the research devoted to determining the resistance to corrosion fatigue in the probabilistic aspect as an urgent scientific and applied problem.

The relationship between stress amplitudes in air and a corrosive environment for various durability and aggressive environments is described by a linear relationship [4]

$$\lg \sigma_{\text{hab}} = a + b \lg \sigma_{\text{air}} \quad (1)$$

where σ_{hab} , σ_{air} - stress amplitude according to fatigue curves in medium and air, respectively, for a given number of cycles N (limits of limited endurance); a and b are the parameters of the equation, which depend on the material of the part and the degree of aggressiveness of the corrosive environment.

The research aims to determine the correlations between the parameters of the equations that determine the dependence of the stress amplitudes in air and in a corrosive environment. Analysis of parameters a and b for various construction materials, the aggressiveness of working environments, sizes, and shapes of parts shows that with an increase in parameter a , parameter b decreases. For further processing, a linear relationship of parameters in the form

$$a = \alpha - \beta b, \quad (2)$$

where α and β are constant values for a given environment of a certain aggressiveness.

4 Results

Correlation-regression analysis of expression (2) showed a close relationship between the values of a and b , which is characterized by the correlation coefficient r . This indicates the functional dependence of the parameter a on b , which is presented in Table 1.

As can be seen from the table, the values of the constants α and β of dependence (2) differ insignificantly, which makes it possible to combine $a = f(b)$ into one dependence $a = F(b)$. The same conclusion can be reached when analyzing the graphical representation of this dependence and the nature of the placement of experimental points.

For combining the sample values a and b into a common population, the same for all environments, it is necessary to test two hypotheses: the equality of the variances of a number of populations and the mean values of normally distributed populations.

With an unequal number of observations in individual samples, the homogeneity of variances can be checked using the Bartlett χ^2 test [10]. The calculated value of the χ^2_{α} criterion is compared with the tabular value, which is determined for the selected level of significance and the number of degrees of freedom. When fulfilling the inequality $\chi^2 \leq \chi^2_{\alpha}$, the null hypothesis of the equality of the general variances from which these samples are taken is not excluded.

Table 1. Corrosion fatigue test results of steel parts.

Aggressive environment	α	β	r
Water:			
distilled	2,3983	2,4389	0,97
unleavened	3,0314	2,8785	0,98
Solution:			
NaCl (3%)	3,1392	2,8793	0,98
NaCl (4%)	2,6265	2,6803	0,99
KaCl (10%)	2,6592	2,7799	0,97
KaCl (20%)	2,5384	2,4359	0,98
H ₂ SO ₄ (0,1 Н)	3,0096	2,7085	0,97
HNO ₃ (6,2%)	2,6773	2,5907	0,97
HNO ₃ (4%)	2,4948	2,6257	0,99
KNO ₃ (10%)	3,2538	3,0102	0,99
NaOH (4%)	2,6405	2,8241	0,99

For a sample of nine environments, the value of the criterion $\chi^2 = 2.28$, and its tabular value for the significance level $\alpha = 0.01$ is 2.56, that is, the indicated inequality is satisfied, and the variance can be combined [10]: $S^2 = 0.9584$.

The hypothesis about the equality of the sample mean values is checked using the dispersion ratio - the F criterion [10]. If the calculated dispersion ratio F is less than its table value $F_{1 - \alpha}$ (for a given significance level and the number of degrees of freedom), then the hypothesis is not rejected. For a given sample size, the dependence is $F = 1.92$, and the tabular value $F_{1 - \alpha} = 1.93$. That is, these values satisfy the inequality $F \leq F_{1 - \alpha}$.

So, the difference between the parameters α and β is insignificant (statistically insignificant) for this sample, and the sample between parameters a and b of expression (1) can be combined into one and expression (2) generalized for all studied media can be written in the form

$$a = 2.8064 - 2.775b. \quad (3)$$

The calculated values of the quantity, a , obtained from the individual connections for each medium and the generalized dependence (3) slightly deviate from their experimental values. Moreover, the errors in determining the parameter a by individual connections and generalized dependence are practically equal, although they have some deviations. This allows us to recommend the dependence between the values of a and b as Eq. (3). However, it does not exclude the use of individual dependencies (2) for each of the tested media (Table 1).

Thus, for the practical use of a function (1) when assessing the fatigue resistance of parts operating in media of different aggressiveness, it is necessary to know the law of variation of the parameter b in Eq. (1) depending on the material and type of corrosive medium (Fig. 1).

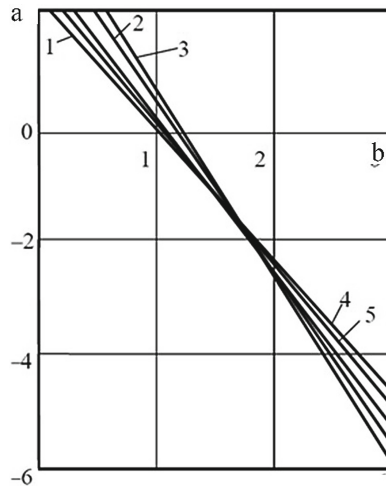


Fig. 1. The relationship of parameters a and b of Eq. (1): 1–10% solution of KNO_3 ; 2–fresh water; 3–10% KCl solution; 4–20% KCl solution; 5 - distilled water.

Based on the results obtained, it is possible to create a substantiated methodology for calculating the strength and durability of parts when exposed to aggressive media and evaluate the durability of such parts already at the design stage.

With the development of calculations of strength and durability, in a probabilistic interpretation, the characteristics of scattering of fatigue properties have become no less important than the average characteristics used in deterministic calculations. Concerning corrosive media, a certain regularity of the scattering of durability in terms of its scattering in the air has become apparent. If the homogeneity of dispersions of the durability logarithm is confirmed in some cases and not confirmed in others, then for objects operating in corrosive environments, the homogeneity of dispersions is beyond

doubt. This was confirmed by the example of a 3% rock salt solution: the load level did not significantly affect the scatter of durability.

Testing samples of steel DIN C45 and X10CrNiTi18–10 confirmed this phenomenon in the investigated liquid media [7]. The tests were carried out in non-movable chambers, which are mounted on a rotating sample. The chambers were carefully sealed. The solution poured into them at the beginning of the tests was stored until the sample broke and was not replaced. Thus, the test conditions brought closer to the real operating conditions of many objects.

Considering that a decrease in the durability with an increase in the load level remains for any medium, the corrosion fatigue curves were constructed both with and without considering the change in the conditional dispersions corresponding to certain load levels (that is, at $\omega_i = 1$). To consider the weight of the changes, we used the function [7].

$$\omega_i(x) = 10^{-2b_1 \lg \sigma_i}$$

At the same time, based on a preliminary analysis, a linear law of change in conditional variances with a change in the stress level was applied according to the expression

$$\lg S_i = a_i \lg \sigma_i + b_i$$

where a_i and b_i are constant coefficients.

The fatigue curves of 45 steel specimens in distilled water, with different fracture probabilities, can be plotted both with and without considering the change in the empirical conditional stress dispersions (Fig. 2).

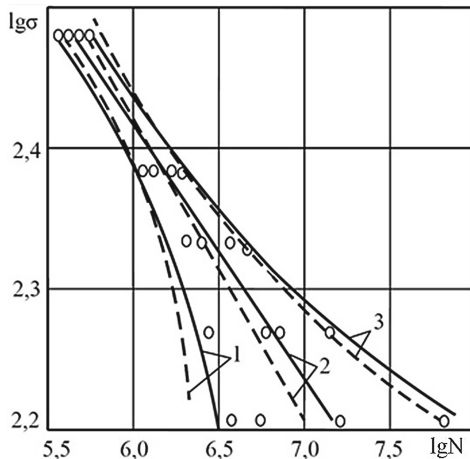


Fig. 2. Fatigue curves plotted considering the variance of longevity (solid lines) and without it (dashed lines) at the probability of failure $P = 5$ (1), 50 (2), and 95 (3)%.

Similar curves were obtained for other corrosive environments with samples from other materials.

As can be seen from the figure, the solid and dashed lines are located close to each other, especially for the average probability curves of corrosion fatigue. This indicates that the variances are statistically independent of the voltage. The Bartlett test did show that the discrepancy between the conditional variances of the logarithm of durability was statistically insignificant at significance levels well above 0.05. Consequently, the intensity of the load has no significant effect on the scattering of life for all investigated liquids.

The dispersion of the logarithm of durability in a specific corrosive environment is practically independent of the object's steel grade and design features. For a 3% solution of rock salt and seawater, the variance of the longevity log rhyme is 0.01. This can be taken (with some excess) for a wide variety of objects. In other words, in the calculations of steel objects intended for operation in seawater, assigning the specified generalized value of the variance of the logarithm of durability or the corresponding standard deviation is possible.

Perhaps this provision should remain valid for any other liquid medium. The lack of published data on the study of fatigue resistance in corrosive environments other than 3% rock salt solution, sufficient for statistical processing, does not allow us to give recommendations on the quantitative values of the variances of the logarithm of durability in them.

It was found that when passing from less aggressive media (distilled water) to more aggressive media (acid solutions), the variance of the logarithm of durability decreases. The homogeneity of a number of dispersions for the studied media can be accepted only at a significance level of 0.001 or less. This means that the hypothesis of homogeneity of the dispersion series for media of different aggressiveness should be rejected. So, the corrosive environment has a significant effect on the dissipation of durability. That is, the dissipation of durability depends significantly on the aggressiveness of the environment.

Based on the data obtained, it can be assumed that the dispersion of the logarithm of durability in the most aggressive of the investigated media (acid solutions) is about 20% less than in seawater and distilled water - 10% more. For other media, which occupy an intermediate position under their specific electrical conductivity, it can be selected by interpolation, taking as the initial value 0.01 for seawater.

The construction of corrosion fatigue curves corresponding to a given probability P of fracture or the probability $1-P$ of non-fracture, provided that the fatigue resistance characteristics are normally distributed, is facilitated by the fact that the stress level does not have a significant effect on the variance of the logarithm of durability, and the variance itself depends on the design features and material of the object.

The generalized variance of the logarithm of durability is in the range from 0.0080 to 0.0098 (on average 0.0093, which is close to 0.01). Based on this value, it is possible to calculate the logarithm of durability for any probability P , for the average probability of its meaning [7]. In this way, a bundle of parallel curves of corrosion fatigue is constructed for any probability P or $1-P$ in the range from 2 to 98%, in which the normal distribution can be confidently used, which is more than sufficient for the vast majority of mechanical engineering problems. So, having built the corrosion fatigue

curve by calculation and knowing the average variance of the logarithms of durability, it is easy to obtain a calculated estimate and the limits of fatigue at given durability.

The limit of limited endurance based on N , corresponding to the probability P , can be represented as

$$\sigma_{RP}^N = \sigma_{RP}^{-N} + U_P S_{\sigma R} = \sigma_{RP}^{-N} (1 + U_P \cdot V_{\sigma R}) \quad (4)$$

where σ_{RP}^{-N} is the average probable value of the endurance limit, determined by the average probable fatigue curve at a given base N ; U_P is the quantile of the normal distribution for the probability P ; $S_{\sigma R}$, $V_{\sigma R}$ is the mean deviation and coefficient of variation of the limited endurance limit.

It is also reasonable to speak about the normal distribution of the logarithm of the limit of limited endurance. The expression for the logarithm of the limited endurance limit is written similarly to expression (4). Under the normal distribution function, to estimate the limit of limited endurance with probability P , the lower value of the confidence interval of the average level of the endurance limit can be used. For example, assuming a log-normal distribution of the fatigue limits, one can write

$$\lg \sigma_{RP}^N = \lg \sigma_{Rmin}^N + U_P S_{max} \quad (5)$$

where σ_{Rmin}^N is the lower value of the confidence interval for the average value of the limited endurance limit at a given confidence level; S_{max} is the upper value of the interval for the standard deviation of the endurance limits and the specified confidence level.

In practical calculations, the coefficient of variation of the endurance limits is a convenient value. This coefficient can be determined using the required base N using a family of corrosion fatigue curves. It is easy to make sure that even in parallel curves of different probabilities, the coefficient of variation of the endurance limits depends on the absolute value of the average endurance limit, that is, the base N and the slope of the curves.

5 Conclusions

Based on the studies carried out, the correlation dependence between the equations of corrosion fatigue of machine parts in environments with different aggressiveness was obtained. In addition, the factors influencing the dispersion of the limited endurance limits of parts in corrosive environments have been determined. The results obtained confirm the existence of correlations between the parameters of the equation describing the dependence of the stress amplitudes arising in part in air and in a corrosive environment and can be used to calculate the fatigue resistance of parts operating in corrosive environments of various intensities.


References

1. Yakovleva, I.L., Tereshchenko, N.A., Smirnov, L.A., Panfilova, L.M.: Stainless high-strength sparingly alloyed steel for operation in aggressive environments. *Met. Sci. Heat Treat.* **59**(1–2), 18–23 (2017). <https://doi.org/10.1007/s11041-017-0095-z>
2. Was, G.S.: Corrosion and stress corrosion cracking fundamentals. In: *Fundamentals of Radiation Materials Science*. Springer, New York, NY (2017). https://doi.org/10.1007/978-1-4939-3438-6_15
3. Baragetti, S., Villa, F.: Corrosion fatigue of high-strength titanium alloys under different stress gradients. *JOM* **67**(5), 1154–1161 (2015). <https://doi.org/10.1007/s11837-015-1360-5>
4. Oleinik, N., Stepurenko, Y., Kurochkin, L.: Fatigue resistance of structural steels in various working environments. *Astroprint* **2**(4), 87–95 (2000)
5. Knysh, V.V., Solovei, S.O., Osadchuk, S.O., Nyrkova, L.I.: Influence of hardening by high-frequency mechanical impacts of butt welded joints made of 15KhSND steel on their atmospheric corrosion and fatigue fracture resistance. *Mater. Sci.* **54**(3), 421–429 (2018). <https://doi.org/10.1007/s11003-018-0201-4>
6. Grin, E.: Analysis of influence of aqueous mediums on cyclic crack resistance of steels. *Inorg Mater* **53**, 1538–1547 (2017). <https://doi.org/10.1134/S0020168517150067>
7. Oleinik, N., Kurochkin, L.: Fatigue resistance of steel structures in seawater. *Astroprint* **1**(1), 25–31 (1999)
8. Knysh, V., Mordyuk, B., Prokopenko, G., Solovey, S.: Increasing corrosion fatigue of welded joints of steel 15KhSND with construction defects by electric discharge surface alloying and high frequency mechanical impact. *Metallofiz. Noveishie Tekhnol.* **41**(12), 1631–1652 (2019). <https://doi.org/10.15407/mfint.41.12.1631>
9. Gladchenkova, J.S.: Methods for determining resistance indices of structural steels under various atmospheric conditions. *Metallurgist* **64**(7–8), 623–632 (2020). <https://doi.org/10.1007/s11015-020-01038-0>
10. Stepnov, M.: Statistical methods for processing the results of mechanical tests. Directory. 2nd edn. *Mechanical engineering* (2005)
11. Jie, C., Bo, D., Jingjing, H., Sen, P., Xuefei, G.: Equivalent surface defect model for fatigue life prediction of steel reinforcing bars with pitting corrosion. *Int. J. Fatigue* **110**, 153–161 (2018). <https://doi.org/10.1016/j.ijfatigue.2018.01.019>
12. Eun, J.: Types and requirements of materials and corrosion. In: *Handbook of Engineering Practice of Materials and Corrosion*. Springer, Cham (2020). https://doi.org/10.1007/978-3-030-36430-4_2
13. Kurgan, V., Sydorenko, I., Prokopovich, I., Bovnegra, L., Lysenko, T.: The study of the elastic characteristics of the coupling with nonlinear feedback when starting the motor. In: Karabegović, I. (ed.) *NT 2020. LNNS*, vol. 128, pp. 122–130. Springer, Cham (2020). https://doi.org/10.1007/978-3-030-46817-0_14
14. Güllich, J.F.: Selection of materials exposed to high flow velocities. In: *Centrifugal Pumps*. Springer, Cham (2020). https://doi.org/10.1007/978-3-030-14788-4_14
15. Pedferri (Deceased), P.: Stress corrosion cracking and corrosion-fatigue. In: *Corrosion Science and Engineering. Engineering Materials*. Springer, Cham (2018). https://doi.org/10.1007/978-3-319-97625-9_13
16. Domozhirov, L.I.: Accumulation of corrosion-fatigue damage by hydro turbine equipment elements. *Power Technol. Eng.* **52**(2), 162–167 (2018). <https://doi.org/10.1007/s10749-018-0926-0>

17. Vachtsevanos, G.: Corrosion modeling. In: Vachtsevanos, G., Natarajan, K.A., Rajamani, R., Sandborn, P. (eds.) *Corrosion Processes*. SI, vol. 13, pp. 163–229. Springer, Cham (2020). https://doi.org/10.1007/978-3-030-32831-3_6
18. Lahiri, A.K.: Material degradation. In: *Applied Metallurgy and Corrosion Control*. Indian Institute of Metals Series. Springer, Singapore (2017). https://doi.org/10.1007/978-981-10-4684-1_8
19. Varde, P.V., Pecht, M.G.: Fatigue and fracture risk assessment: a probabilistic framework. In: *Risk-Based Engineering*. Springer Series in Reliability Engineering. Springer, Singapore (2018). https://doi.org/10.1007/978-981-13-0090-5_8



Analysis of Permissible Limits for Leachable of Trace Impurities from Bone Substitutes Containing Hydroxyapatite and Beta-Tricalcium Phosphate

Kostiantyn Dyadyura^(✉) , Liudmyla Hrebenyk ,
Tatyana Ivakhniuk , Maria Vyshegorodtseva ,
and Liudmyla Primova 

Sumy State University, 2, Rymyskogo-Korsakova Street, Sumy 40007, Ukraine
dyadyura@pmtkm.sumdu.edu.ua

Abstract. A detailed analysis of the regulatory framework for the biological assessment of nanomaterials and medical devices indicates that the main factor of uncertainty in laboratory results of studies on the influence of nanostructures is biological variation due to individual and population characteristics of vital processes in the human body and is characterized by a combination of stability within the average limits of the constancy of the internal environment and dynamic fluctuations around the point of homeostasis. Objectively substantiated recommendations have been developed on the accuracy of laboratory studies when assessing the biological effects of synthetic nanostructures. A basis for assessing the accuracy is the maximum permissible values of analytical errors of quantitative research methods (measurements) of physical quantities (composition and properties of components of biological materials, analytes) in samples of biological materials. The above interpretation of LOD and LOQ is close to the “confidence interval” concept. The statement about detecting the concentration of leachable trace impurities in biofluid is always probabilistic in nature. The revealed patterns indicate that trace impurities elements have different dissolution rates and depend on the ratio of the structural components of the product/material. The study of hydroxyapatite-containing nanomaterials showed that the hydroxyapatite/ β -tricalcium phosphate ratio affects the material’s dissolution rate: the higher the content of β -tricalcium phosphate, the higher the dissolution rate. The results allow providing recommendations for reducing uncertainty in the study of hydroxyapatite and β -tricalcium phosphate bone substitutes, which is associated with individual reactions of the body to various environmental factors and obeys statistical laws.

Keywords: Medical devices · Nano-objects · Safety · Scaffolds · Standardization · Trace impurities

1 Introduction

The search for opportunities to control reparative processes and study the features of newly created bone tissue in conditions of a plastic defect with various materials are important tasks for orthopedic traumatologists and material scientists [1]. Tissue engineering creates 3D systems (bone substitutes – scaffolds), which allow the treatment of bone defects in situ, formed from accidents and diseases. The bone substitutes must fit into the anatomical defect, have the appropriate mechanical properties capable of withstanding the loads in vivo, promote the formation of new blood vessels, and the products of their degradation must not be toxic to the human body [2, 3]. However, natural bone has a unique structure that cannot be reproduced with conventional synthesis methods. In this regard, there are risks of biocompatibility when using scaffolds from different biomaterials for the intended purpose [4, 5]. The biological assessment of any material or medical device intended for human use is a part of the risk management process under ISO 14971 and ISO 10993-1 [6]. It is necessary to consider the risks associated with leachable substances from medical devices that can be hazardous to human health. In the broadest sense, leachable substances can enter the human body in various ways, from skin absorption to ingestion, inhalation, and direct systemic administration. The risk management process [7, 8] is also mandatory for medical devices containing nanomaterials and releasing nano-objects because of degradation, wear, or mechanical processing of medical devices (for example, grinding, in situ polishing). It is expected that the use of the principles and methods of a harmonized regulatory framework will enable timely and integrated identification of potential hazards, risks, and adverse events. Based on the above, the work aims to create an integrated system for assessing the allowable limits for leachable substances from hydroxyapatite and β -tricalcium phosphate bone substitutes after implantation.

2 Literature Review

The selection and assessment of any material or medical device intended for use in medical practice require a systematic approach to assessing the biological effect. The ISO 10993 standards [9] are guidelines for predicting and studying the biological effect of medical devices at the stage of selecting materials intended for the manufacture and research of finished medical devices [10]. Under ISO 10993-9 [11], special methods are used to obtain, identify and/or quantify degradation products. Standards ISO 10993-12 [12], ISO 10993-17 [13], and ISO 10993-18 [14] deal with degradation products resulting from a chemical change in the finished product. The requirements for the biological evaluation of medical devices set out in the ISO 10993 series of standards are also applicable for the biological evaluation of medical devices containing nano-objects that are not released from the device during use since they are an integrated part. With the predicted possibility of the release of nanostructures, it is necessary to conduct a safety analysis of these nano-objects. The components of nanomaterials can also be evaluated separately [4]. It should also be borne in mind that the toxicological risk profile of nanomaterials that have the same chemical composition may differ significantly [5]. It depends on the physicochemical characteristics of the

components of the product and its surface, the conditions, and the time of operation as intended. An important factor of uncertainty in assessing the effects of nano-objects is the change in the characteristics of a product upon contact with the body's biological fluids and tissue structures [6]. It has been established [3] that the nature and intensity of interactions between nanomaterials and biological systems at the initial stages depend on the structural features of the product and its chemical composition. Mutual influence in the "nanomaterial-biological system" system also has certain elements of uncertainty due to the possibility of the influence of the chemical composition of biological body fluids on the dissolution and leaching of the structural components of a medical device. It is known that dissolution in the human body is a complex physicochemical process that includes diffusion, chemical, and electrochemical stages. Risks associated with exposure to hazardous leachable substances can be managed by identifying these substances, setting allowable limits for leachable substances, and limiting exposure to acceptable levels. The ISO 10993-17 standard [13] describes a method by which maximum limits for leachable substances are calculated based on existing data on health hazards. Limits can be based on risks to the entire body and local exposure, immediate or long-term. They can vary in severity (from minor local negative consequences to life-threatening ones). The work aims to analyze permissible limits for leachable trace Impurities from bone substitutes containing hydroxyapatite [15] and beta-tricalcium phosphate [16]. To achieve this aim, the following tasks were set:

- study of the concentration of leachable trace impurities in washout fluid;
- estimation of the measurement error;
- determination of detection limit and quantification limits for test results.

3 Research Methodology

The process of setting limit values for substances leaching from medical devices consists of the following steps:

- assessing the biological risk associated with the leachable substance by: collecting data and identifying health-critical outcomes; determining the tolerant dose (TI) for a specific protocol of substance entry into the human body and the duration of exposure; determining the contact action that is carried by a substance that is washed out as a result of contact with a medical device (PEF), if irritation is an acceptable result;
- determining the effect that is transferred (TE) to the patient from a substance that is washed out by: determining the relevant patient's body weight (mB); modifying the product of consumption and body weight based on the utilization rate (UTF);
- determining the appropriateness and feasibility of use, if necessary.

A review of toxicological data provides the information necessary to establish the "no observable adverse effect level" (NOAEL) [12].

3.1 Establishment of Allowable Limits for Leachable Substance

The formula for calculating TI values in milligrams per kilogram of body weight per day using the modifying factor approach is shown in Eq. (1):

$$TI = \frac{NOAEL}{MF}, \tag{1}$$

where NOAEL is no observable adverse effect level; MF is modifying factor.

The modifying factor is calculated as the product of uncertainty factors

$$MF = UF_1 \cdot UF_2 \cdot UF_3, \tag{2}$$

where UF_1, UF_2, UF_3 are uncertainty factors.

In selecting appropriate uncertainty factors, some aspects (Table 1) include human-to-human variation, species extrapolations, and other uncertainties [13]. The routine uses of a medical device, including its use in systemic therapy, should be determined for a given population. It involves calculating the concomitant impact factor (CEF) and the proportional contact factor (PEF).

Table 1. Factors of uncertainty for the calculation of TI.

Assignment of the uncertainty factor	Range	Standard UF value	Description
UF_1 , individual variability of the human population	From 1 to 10	10	To take into account the variability of the response between the mean of a healthy population and the response of a certain proportion of the sensitive subpopulation
UF_2 , interspecific extrapolation	From 1 to 10	1	To take into account the possibility that humans are more sensitive to the negative effects of the compound than experimental animals
UF_3 , data quality, and relevance research	From 1 to 100	1	To take into account the limitations of available toxicological data for the calculation of TI, including the absence of NOAEL values, the absence of NOAEL long-term studies, and the lack of data on the clinically relevant route of exposure

These factors are multiplied to obtain the utilization factor (UTF), as shown in equation

$$UTF = CEF \cdot PEF \tag{3}$$

Formulas (4) and (5) determine the concomitant influence factor (CEF) (a value between 0.2 and 1.0)

$$CEF = \frac{TI \cdot m_B}{m_{proc}}, \quad (4)$$

where m_B is the body weight in kilograms; m_{proc} is the total mass of the substance that is washed out (released during the procedure, in milligrams per day).

$$CEF = \frac{TI \cdot m_B}{\sum_{25000 \text{ дiб}} \frac{m_{LIFE}}{25000 \text{ диб}}}, \quad (5)$$

where m_{LIFE} is the mass of the substance that is washed out (excreted during life), expressed as the average daily exposure in milligrams.

The utilization rate (UTF) can be adjusted in an upward direction to analyze a situation in which the product/device is not used for the entire duration of the exposure category. For this purpose, the proportional contact factor (PEF) must be calculated. As shown in Eq. (6), PEF is equal to the number of days in the exposure category divided by the number of days the product was used before it was removed

$$PEF = \frac{n_{EXP}}{n_{USE}}, \quad (6)$$

where n_{EXP} is the number of days in the exposure category; n_{USE} is the number of days the product use. If the number of days of product use varies, a reasonable upper bound should be used. If a reasonable upper bound cannot be determined, a PEF of 1 is used. The permissible impact (TE) is determined by the formula

$$TE = TI \cdot m_B \cdot UTF \quad (7)$$

The greater the health benefits expected from the use of the product, the greater the health risk. Only in this case can a factor be introduced to correct the permissible exposure (TE), which considers the health benefits. It should be noted that the toxicity of leachable substances from a medical device is acceptable when compared with the defined health benefits expected from the therapy. In this case, the leachable substances have been reduced to a possible minimum following the protection, maintenance, and improvement of human health in general. Each acceptable AL level is calculated using the following general formula:

$$AL = TE \cdot BF \quad (8)$$

AL is the largest amount of leachable substances recognized as allowable when entering the human body daily through exposure to a medical device (mg/day); BF is a benefit factor.

In cases where leachable substances are toxic compounds, and it is impossible to easily avoid their use by using alternative materials or processing methods, it is

necessary to consider the significance of the benefits of their use. The maximum dose of leachable substances from a long-term medical device is calculated using the formula

$$m_{dev.prol} = AL_{prol} \cdot 30 \quad (9)$$

where $m_{dev.prol}$ is the maximum dose for the patient in milligrams; AL_{prol} is allowable level for the long-term category, in milligrams per day.

3.2 Physical Laws of Mass Transfer

Knowledge of the physical laws of mass transfer is required to study and model mass transfer processes in the human body. The dissolution rate of a substance depends on the total resistance of all successive stages of the process: the diffusion supplies of the solvent substance to the interaction surface, the transition of the substance from the solid-phase to the dissolved state, and the diffusion removal of the dissolved component from the surface into the bulk of the solvent (solution) [17]. The dissolution process is based on the well-known laws of mass transfer processes, namely the conservation law, which underlies the compilation of the material balance. Material balance is the main component of the study of any mass transfer process, in which the determination of material flows of substances. The experimental data will be considered from the standpoint of both the constancy of the volume of the leachable substances and the change in indicators under conditions of variation in the solution's density. The kinetic equation that characterizes the dissolution process can be represented as

$$-\frac{dM}{d\tau} = k \cdot F \cdot (C_s - C) \quad (10)$$

where M is mass of bone substitute components, mg; F is bone substitute surface, mm^2 ; C_s is saturation concentration, mg/m^3 ; C is the concentration of a substance in a biofluid, mg/kg ; τ is time, c; k is coefficient of mass transfer, m/s .

3.3 Test Methodology. Criteria for Analyzing Research Results

The research methodology is based on the principle of modeling the dissolution process of a bone substitute in vitro, which does not consider that the dissolution rate of nanomaterials in vivo has certain differences compared with model systems. The dynamics of the dissolution process and the product's solubility were assessed by measuring the rate of dissolution of the leachable trace impurities and determining the pH value of the washout medium [18]. The studies were carried out using material from samples of three novel synthetic bone substitutes (Fig. 1) containing monophasic hydroxyapatite, monophasic β -tricalcium phosphate, and a two-phase composition of hydroxyapatite/ β -tricalcium phosphate. To measure the dissolution rate of leachable trace impurities, bone substitute samples were placed in three flasks with Tris buffer ($\text{pH } 7.3 \pm 0.1$). The solutions were then incubated at a temperature of 37 ± 1 C under constant stirring conditions at a speed of 200 rpm for 24, 48, and 72 h, respectively. The dissolution rate was measured under conditions of a constant ratio of the starting material's mass to the total volume of the solvent. The ratio of the test material's mass

to the volume of solvent was 3.5 mg/mL. The pH values were measured after 0, 24, 48, and 72 h of immersion in the samples. In the experiment, the pH was monitored, which from the initial value during testing should not change by more than 0.3. Validation studies were performed based on the analysis of a blank sample.

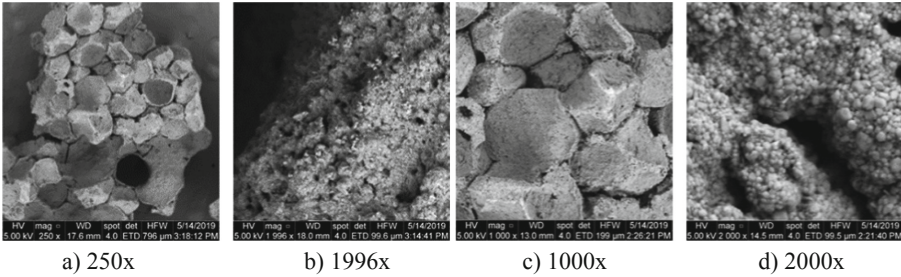


Fig. 1. Structure of bone substitutes based on hydroxyapatite and β -tricalcium phosphate (research method is scanning electron microscopy (SEM)).

The concentration of leachable trace impurities in the solution was determined using X-ray fluorescence analysis (ElvaX-med X-ray fluorescence analyzer, Ukraine). The macropores and micropores’ size was measured on a scanning electron microscope (SEM) SEO-SEM Inspect S50-B. Samples for elemental analysis were prepared according to the standard method. The analytical sensitivity of the research method is the ability to detect the slightest difference between two concentrations of the analyzed component. Terms such as “limit of detection” (LOD) and “limit of quantification” (LOQ) are used [14]. LOD is calculated by the formula [14].

$$LOD \approx 3.3 \cdot s_0 \tag{11}$$

where s_0 is run standard deviation (n) of independent assay blank samples.

LOQ is calculated using the formula

$$LOQ \approx 10 \cdot s_0 \tag{12}$$

The standard deviation s_0 is calculated using the formula

$$s_0 = \sqrt{\frac{1}{n-1} \cdot \sum_{i=1}^n (x_i - \bar{x})^2} \tag{13}$$

where x is parameter value determined during the research; \bar{x} is an arithmetic mean value; n is the number of observations. For a given confidence level $(1-g)$ (95%), the border of the one-sided confidence interval for sw is calculated by the formula

$$\sigma_{1-\gamma} = \sqrt{\frac{v}{\chi_{\gamma,v}^2}} \cdot s_0 \tag{14}$$

where ν is the number of degrees of freedom when assessing the accuracy of the method ($\chi^2_{\gamma,\nu}$ determined from Tables χ^2 is of distribution) and is implicitly determined as a value for which the following conditions are met:

$$\text{prob}[\chi^2 > \chi^2_{\gamma,\nu}] = 1 - \gamma. \quad (16)$$

The convergence limit (r) is calculated by the formula [9]: $r = 2.8 \cdot s_0$.

4 Results

4.1 Calculation of Allowable Limits for Leachable Trace Impurities in Hydroxyapatite and β -Tricalcium Phosphate Bone Substitutes. Results of the Study of the Concentration of Leachable Trace Impurities in Washout Fluid

The results of studies of allowable limits for leachable trace impurities in hydroxyapatite and β -tricalcium phosphate bone substitutes are presented in Table 2.

Table 2. Establishment of limit values for leaching trace impurities.

Element	NOAEL. mg/kg/d	MF	TI. mg/kg/d	CEF	PEF	UTF	TE. mg/d	AL. mg/d	$m_{dev.prol}$ mg
As	0.015	50	0.0003	0.2	1	0.2	0.0042	0.0042	0.126
Cd	0.02	50	0.0004	0.2	1	0.2	0.0056	0.0056	0.168
Hg	0.0003	50	0.00007	0.2	1	0.2	0.00098	0.00098	0.0294
Pb	0.0035	50	0.00007	0.2	1	0.2	0.00098	0.00098	0.0294
Zn	0.3	50	0.006	0.2	1	0.2	0.084	0.084	2.52
Sr	0.02	50	0.0004	0.2	1	0.2	0.0056	0.0056	0.168

The research results correspond to the standard [19], which contains recommendations on allowable limits for leachable trace impurities in hydroxyapatite and β -tricalcium phosphate bone substitutes, the values of which are given in Table 3.

Table 3. The maximum content of trace impurities.

Element	Maximum content, mg / kg	Permissible daily dose for a human mg/kg
As	3,0	0,01–0,015
Cd	5,0	0,01–0,02
Hg	5,0	0,0003
Pb	30,0	0,0035
Zn	50,0	0,3
Sr		0,02–0,07

The study of the dissolution rate of leachable trace impurities of novel synthetic bone substitutes indicates that the medical use of the investigated hydroxyapatite and β -tricalcium phosphate nanomaterial has a low potential for toxicity upon prolonged contact with biological fluids in the human body.

The study of the dissolution process of bone substitutes and the interpretation of research data (C is the concentration of leachable trace impurities in washout fluid) versus the time τ (24, 48, and 72 h) of dissolution in terms of speed n (200 rpm), respectively) are given in Table 4.

Table 4. Experimental study of the dissolution process.

Element	C_{24} . mg/kg	C_{48} . mg/kg	C_{72} . mg/kg
As	0.00006	0.00026	0.001
Cd	0.000001	0.000068	0.00015
Hg	0.00002	0.00009	0.0003
Pb	0.00004	0.00004	0.0003
Zn	0.0005	0.0002	0.005
Sr	0.00001	0.168	0.0007

The results obtained in the study of the dissolution process allow adjusting the allowable limits for leachable trace impurities in novel hydroxyapatite and β -tricalcium phosphate bone substitutes for further research. Moreover, the analysis of the results obtained shows that the hydroxyapatite/ β -tricalcium phosphate ratio affects the material's dissolution rate, namely: the higher the content of β -tricalcium phosphate, the higher the dissolution rate. It is known that the determining factor for the process of implantation of bone substitutes is the porosity of its structure. The study of the synthesized material shows that the macroporosity of the samples is quite large – the size of macropores ranges from 250 to 300 μm . According to the literature [20], a certain macroporosity can provide optimal conditions for bone tissue formation and ensure effective bone ingrowth throughout the entire volume of the implant. The study also evaluated the size of the micropores of synthetic bone substitutes. The size of micropores ranges from 3 to 10 μm . Using nanomaterials for their intended purpose, the investigated range of micropores is decisive for material resorption rate upon contact with a biological medium.

4.2 Estimation of the Measurement Error. Determination of Detection Limit and Quantification Limits for Test Results

Table 5 shows the values of changes in the mass of trace impurities in the washout liquid for various elements.

Table 5. The results of measurements of the increase in the mass of impurities in washout fluid.

Element	Weight gain of micro-impurities in the bioliquid for 24 h, μg						Standard deviation s_0
	Study number						
	1	2	3	4	5	6	
As	0.00002	0.000021	0.000015	0.000018	0.000014	0.000018	1.95448E-05
Cd	0.000004	0.0000011	0.000002	0.000002	0.000006	0.000002	3.61137E-06
Hg	0.00009	0.000022	0.000012	0	0.000012	0.000012	4.24641E-05
Pb	0.00002	0.00006	0.00002	0.00006	0.00008	0.00006	0.00006
Zn	0.00011	0.00011	0.0004	0.00045	0	0.00041	0.000333107
Sr	0.00001	0.000031	0.000014	0.000019	0.000027	0.00003	2.54833E-05

Assuming that three blank samples were used for each batch, using formula (14), we obtain an estimate of the mass measurement uncertainty. It gives the following values for the LOD detection limits and LOQ quantification for the elements (Table 6).

Table 6. The results of determining the limit of detection and the limit of quantification of the mass of micro-impurities in the washing liquid.

Element	S_{95}	LOD	LOQ	r
As	2.54884E-05	8.82944E-05	0.00038374	2.42539E-09
Cd	4.70959E-06	1.63145E-05	5.43817E-05	8.28063E-11
Hg	5.53775E-05	0.000191833	0.000639444	1.14489E-08
Pb	7.82461E-05	0.000271052	0.000903508	2.28571E-08
Zn	7.82461E-05	0.001504824	0.00501608	7.0451E-07
Sr	3.32328E-05	0.000115122	0.00038374	4.12317E-09

The LOD determines the lowest concentration of analyte present in the sample that can be detected using this measurement technique with a given confidence level (95%). The operating range of the measurement is limited from below by the limit of quantification of LOQ.

5 Conclusions

The development of biomaterials, medical device components, finished medical devices, and 3D printed, and regenerative medicines are governed by various international and national standards and guidelines. The regulatory framework regulates the safe use of novel synthesized materials, which are an integral part of medical devices and come into contact with the human body’s biological fluids and tissue structures. Hydroxyapatite and β -tricalcium phosphate bone substitutes are popular in orthopedics and dentistry and deserve special attention in studies related to biodegradation processes. The study of the diffusion rate of molecules with the subsequent prediction of accumulation in tissues should belong to the first stage of assessing the material’s

biological safety. The objectively substantiated recommendations for the accuracy of laboratory studies in determining the concentration of leachable trace impurities in the washout liquid have been developed. A basis for assessing the accuracy is establishing the maximum permissible values of the analytical errors of the quantitative method for studying the composition of the liquid in samples after incubation with hydroxyapatite and β -tricalcium phosphate bone substitutes. The revealed patterns indicate that elements of trace impurities have different dissolution rates. The hydroxyapatite/ β -tricalcium phosphate ratio affects the dissolution rate of the material: the higher the content of β -tricalcium phosphate, the higher the dissolution rate. The research results allow establishing recommendations for reducing the uncertainty in determining the composition of hydroxyapatite and beta-tricalcium phosphate bone substitutes, which is associated with biological variation manifestations, reflecting the body's response to various environmental factors and obeys statistical laws.






References

1. Gubala, V., et al.: Engineered nanomaterials and human health: Part 2. Applications and nanotoxicology (IUPAC Technical Report). *Pure Appl. Chem.* **90**(8), 1325–1356 (2018)
2. Park, J.Y., Park, S.H., Kim, M.G., Park, S.-H., Yoo, T.H., Kim, M.S.: Biomimetic scaffolds for bone tissue engineering. In: Noh, I. (ed.) *Biomimetic Medical Materials*. AEMB, vol. 1064, pp. 109–121. Springer, Singapore (2018). https://doi.org/10.1007/978-981-13-0445-3_7
3. Neacsu, I.A., Serban, A.P., Nicoara, A.I., Roxana Trusca, R., Ene, V.L., Iordache, F.: Biomimetic Composite Scaffold Based on Naturally Derived Biomaterials. *Polymers* **12**, 1161 (2020)
4. Miclăuș, T., et al.: Impact of design on medical device safety. *Therapeutic Innov. Regul. Sci.* **54**(4), 839–849 (2019). <https://doi.org/10.1007/s43441-019-00022-4>
5. Jahan, S., Yusoff, I.B., Alias, Y.B., Bakar, A.F.B.A.: Reviews of the toxicity behavior of five potential engineered nanomaterials (ENMs) into the aquatic ecosystem. *Toxicol Rep.* **4**, 211–220 (2017)
6. Schuh, J.C.L., Funk, K.A.: Compilation of international standards and regulatory guidance documents for evaluation of biomaterials, medical devices, and 3-D printed and regenerative medicine products. *Toxicol. Pathol.* **47**(3), 344–357 (2019)
7. ISO 14971:2019 Medical devices – Application of risk management to medical devices
8. ISO 13022:2012 Medical products containing viable human cells — Application of risk management and requirements for processing practices
9. ISO 10993-1:2018 Biological evaluation of medical devices — Part 1: Evaluation and testing within a risk management process
10. ISO 10993-6:2016 Biological evaluation of medical devices — Part 6: Tests for local effects after implantation
11. ISO 10993-9:2019 Biological evaluation of medical devices — Part 9: Framework for identification and quantification of potential degradation products
12. ISO 10993-12:2012 Biological evaluation of medical devices — Part 12: Sample preparation and reference materials
13. ISO/CD 10993-17.2 Biological evaluation of medical devices — Part 17: Toxicological risk assessment of medical device constituents

14. ISO 10993–18:2020 Biological evaluation of medical devices — Part 18: Chemical characterization of medical device materials within a risk management process
15. Yanovska, G.O., Bolshanina, S.B., Kuznetsov, V.M.: Formation of hydroxyapatite coatings with addition of chitosan from aqueous solutions by thermal substrate method. *J. Eng. Sci.* **4** (2), F1–F4 (2017). [https://doi.org/10.21272/jes.2017.4\(2\).f1](https://doi.org/10.21272/jes.2017.4(2).f1)
16. Chernobrovchenko, V.S., Dyadyura, K.O., Balynskiy, M., Panda, A.: Influence of technological manufacturing conditions on the porosity of calcium-phosphate scaffolds. *J. Eng. Sci.* **8**(1), C18–C28 (2021). [https://doi.org/10.21272/jes.2021.8\(1\).c3](https://doi.org/10.21272/jes.2021.8(1).c3)
17. ISO/CD TR 37137–2
18. ISO/TS 37137–1 Biological evaluation of absorbable medical devices — Part 1: General requirements. Biological evaluation of absorbable medical devices — Part 2: Standard guide for absorbable metals
19. ISO 14155:2020 Clinical investigation of medical devices for human subjects — Good clinical practice
20. Pandova, I., Panda, A., Valicek, J., Harnicarova, M., Kusnerova, M., Palkova, Z.: Use of sorption of copper cations by clinoptilolite for wastewater treatment. *Int. J. Environ. Res. Public Health* **15**(7), 1–12 (2018)



Crack Resistance Parameters of Nano-reinforced Rubber Products in Mechanical Engineering

Aleksandr Gondlyakh^(✉) , Aleksandr Kolosov ,
Valeriy Scherbina , Oleksandr Mamchur ,
and Yaroslav Shilovich 

National Technical University of Ukraine “Igor Sikorsky Kyiv Polytechnic Institute”, 37, Prospect Peremohy, Kyiv 03056, Ukraine

Abstract. This work is devoted to numerical modeling of the destruction and delamination of spatial systems made of nanomodified materials under static loading conditions. Modeling of thin adhesion layers at the microlevel is carried out within the framework of the relations of the refined iterative-analytical theory of deformation of spatial systems. Numerical integration of the resolving equations is performed by the finite element method. Modeling the degradation of the properties of nanocomposites due to the formation in them of various types of nano, micro, and macro damages was carried out based on the method of discrete-virtual propagation of micro and macro defects. The solution of nonlinear boundary value problems is carried out by the finite element method based on the Newton-Kantorovich algorithm, supplemented by a block that implements the iterative-analytical method of variable approximations. A virtual laboratory for determining nanomodified polymer materials’ physical, mechanical and strength characteristics has been developed and implemented. A numerical simulation of the process of pulling out a nanotube from a rubber mass is carried out. The analysis of the accumulation of microdefects and the occurrence of macrodamages of delamination in the contact layer “nanotube - rubber” is carried out. The results of numerical calculations are in good agreement with experimental data. The numerical modeling results of the change in the stress-strain state of nanomodified rubber specimens are given depending on the change in the coefficient of their reinforcement with carbon nanotubes.

Keywords: Fracture · Delamination zone · Numerical simulation · Nanomodification · Rubber · Polymers · Finite element method · Refined iterative-analytical theory

1 Introduction

At present, structural elements made of polymer and rubber materials have been widely introduced in mechanical engineering, aircraft construction, chemical engineering, shipbuilding, and construction. These objects include various types of seals, shock absorbers, facing products, and household appliances. Since such structures, as a rule,

operate in difficult operating conditions under cyclic power and temperature loads, under conditions of aggressive acid and alkaline environments, under conditions of solar and radiation exposure, increased requirements are imposed on the materials from which they are made.

One of the leading directions for improving the properties of rubber and polymeric materials is the procedure for their hardening through nanomodification with carbon nanotubes. Of particular interest in chemical engineering is the problem of nanomodification of tires with carbon nanotubes to improve their physical and mechanical characteristics, strength parameters, reliability, durability, heat resistance, and improve adhesion to the road surface.

However, complete nanomodification of tires leads to an increase in their cost up to 10% of the total cost of a non-nanomodified analog. Therefore, to reduce this indicator, it is necessary to clearly understand all stages of the life cycle of production and operation of tires, formulated within a single physical model that describes the behavior of nanomodified structures and unites the interrelation of the processes of degradation of nanomodified rubber occurring on the macro-, micro- and nanolevels. Therefore, the purpose of this work is to construct and numerically implement a model for physically based prediction of the properties of new nanomodified materials to increase the strength, durability, and endurance parameters of nanomodified objects.

2 Literature Review

Despite a large number of publications devoted to solving the problem of effective dispersion of nanofillers in a rubber matrix, a complete solution to this problem is still far from its logical conclusion.

Mixing carbon nanotubes (CNTs) with a rubber mass is carried out, as a rule, using two leading technologies. The first direction is associated with the mechanical dispersion of CNTs into a polymer or rubber mass. The effects of dispersing CNTs into a polymer matrix by mechanical mixing using a mixer of an open two-roll mill are described in [1]. It was shown in [2] that, due to the high shear stress that occurs during the process of dispersing CNTs into a polymer matrix in high-speed extruders, it is possible to successfully overcome the electrostatic and Van der Waals interactions between nanotubes and efficiently carry out the process of delamination of agglomerates into individual nanotubes.

The authors of [3] have shown that the technique of nanomechanical mapping can be successfully used to effectively determine the characteristics of inhomogeneity and mechanical interfacial regions formed around CNTs [4] when creating nanocomposites from natural rubbers obtained in an open roller mill. The good dispersion of CNTs in the mass of rubber, in this case, is also explained by the high shear stresses arising in this process of mixing CNTs and rubber.

The second direction is associated with the dispersion of CNTs in liquid fillers of a rubber mixture based on ultrasonic cavitation methods [5]. The work [6] investigated the process of mixing rubber (NR) with carbon black (CB) and carbon nanotubes (CNT) based on ultrasonic technology. The results of evaluating the structure and properties of the obtained composites made it possible to conclude that the process of

mixing latex using ultrasound makes it possible to achieve the maximum mechanical properties at a mass ratio of CB (20%), CNT (5%) at NR (100%).

The authors of the article [7] investigated the properties of nanomodified rubber using single-walled carbon nanotubes (SWNTs). After mixing at the latex stage and curing, composite films were obtained with a 56% increased tensile strength [σ_t] at 2.0% SWNT content and a 63% higher elasticity modulus than pure NR. In [8], the WCL method of wet compounding in combination with mixing latex using ultrasound was proposed to obtain nanocomposites such as graphene oxide, carbon black, and natural rubber.

Research has confirmed that graphene and carbon black can be uniformly dispersed in rubber composites, and composites obtained by the WCL method have better mechanical properties than conventional latex mixing [9]. The use of nanomodified rubber in various branches of technology and, particularly, nanomodified automobile tires are given in [10]. Much attention is currently paid to the issues of numerical modeling of deformation processes and determination of the properties of nanomodified polymers and rubbers and structures based on them, under cyclic [11] and static [12] loadings.

In [13], the influence of multilayer carbon nanotubes on the performance characteristics of rubber heat-shielding coatings of elements of aircraft structures based on nitrile butadiene was investigated. The introduction of 0.5–1.0 wt. % CNTs in elastomers of various chemical structures increase their physicomechanical strength characteristics and resistance to wear. In [14], defects in the performance of nanostructures at high loads and temperatures are presented. The mechanical properties of both initial and defect nanostructures are decreased with increasing temperature and defect sizes.

To investigate both linear and nonlinear interactions of a nanotube and a polymer, the authors of most works consider the representative volume element (RVE). The article [15] considers the issues of non-covalent functionalization in various types of interactions between polymers and carbon nanotubes.

A separate area of research into the properties of nanomodified polymers is the development of mathematical models of the interaction of nanotubes with polymer and rubber binders, as well as the numerical simulation of the formation and accumulation of defects, the mechanisms of destruction processes at the interface at the “matrix - nanotube” contact [16]. The analysis of nonlinear deformation of the RVE of the polymer with allowance for damaged nanotubes is considered in [17]. The article [18] investigates the effect of CNT agglomeration on the stiffness modulus of nanomodified composites. Article [19] is devoted to studying the behavior of carbon nanotubes in polymers based on the hybrid method of atomic/continuous mechanics. The RVE model is proposed, consisting of three regions modeled by the potential atomic method, the continuum method, and classical continuum mechanics. In [20], a model of the elementary volume of a polymer surrounding a nanotube with a “CNT – polymer” interface is considered. The nonlinear behavior of nanotubes and specimens of nano-reinforced polymers is investigated.

Modeling the processes of nonlinear deformation of nanotubes in a polymer matrix is very nontrivial and leads to the need to use numerical methods [21], among which the finite element method (FEM) is most widely used [22].

3 Research Methodology

Over the past 30 years, the National Technical University of Ukraine “KPI” at the Department of Chemical, Polymer-Silicate Engineering has been intensively working on the study of the physical and mechanical properties of multilayer composite systems and numerical modeling of the processes taking place in polymer composite structures throughout their entire life cycle. In this work, the modeling of thin adhesive layers at the microlevel is carried out. This modeling has been carried out within the framework of the relations of the refined iterative-analytical theory of deformation of spatial systems. The fundamental equations are given in [23].

For analyzing the mechanisms of formation and propagation of micro- and macro-cracks, a model is used to effectively investigate the strength of spatial systems at the micro-level of the adhesive layer. Methods for predicting the growth of microdefects in adhesive layers of multilayer objects have been developed.

The numerical integration of the resolving equations is carried out by the finite element method for effective modeling of the degradation of the properties of nanocomposites due to the formation of various types of nano, micro, and macro damage in them. For this, the method of discrete-virtual propagation of micro and macro defects is used, based on the representation of the real front of a defect in the form of its discrete finite element analogue (Fig. 1). Along with this, the method introduces the concept of a virtual stratification front, which at the initial stage coincides with the real front (Fig. 1, e). As the virtual crack zone grows, new finite elements are included in the discrete front.

This approach makes it possible to fully consider the entire history of the development of the destruction process, accumulate even the smallest increments of destroyed areas, and adequately correct the corresponding discrete model at each stage of the damage zone advance. Based on this theory, a new refined finite element was developed [22], which makes it possible to simulate the effects of microdamage accumulation depending on macro- and microstress components in individual layers of the composite material (Fig. 1, d).

To make it possible to implement a unified approach to the construction of macro, micro, and nanomodels of nanomodified polymeric and composite systems, the developed FE is currently being adapted, considering the specifics of the known equations of molecular dynamics. The developed FE was tested for solving linear problems of determining the physical and mechanical properties of carbon nanotubes. A large number of control and test problems have been solved to determine the reduced modulus of elasticity CNT of the Armchair and Zigzag types. In [22], the results are compared with solutions known from the literature. The results obtained indicate that the maximum difference with the data does not exceed 5%.

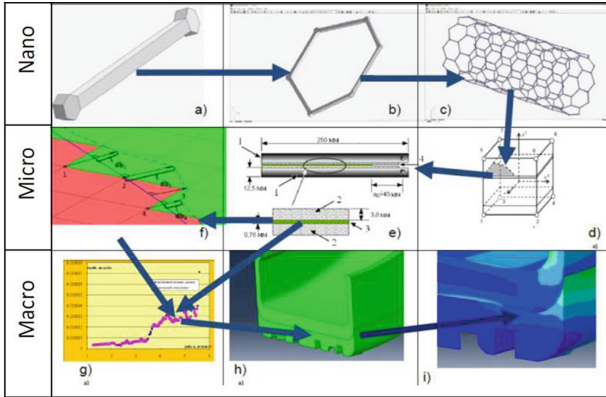


Fig. 1. Nano- (a, b, c), micro- (d, e, f), and nanostructures (g, h, i): a - FE of the relationship between two atoms; b - FE model of a nanocell; c - FE model of the nanotube; d - FE with a microzone of delamination defect; e - full-scale tests of a sample with nanomodified material; f - numerical modeling of material degradation; g - diagram of material degradation during sample testing; h - setting the properties of the nanomodified layer in the design model of the object; i - strength analysis of the nanomodified object.

The modeling of fracture processes in the matrix is interpreted as acquiring specific anisotropic properties by the material in a particular local area of the contact layer. This is due to the influence of the emerging cracks on the stress-strain state of the structure. A characteristic feature of this technique is a physically substantiated correction of the tensor of the physicomechanical constants of the destroyed area based on hypotheses adopted depending on the type of fracture, separation, shear, or crushing. The derivation of an expression for calculating the coefficients of the stiffness matrix of a multilayer eight-node isoparametric FE with cracks is given in [23]. Numerical modeling of the plastic deformation processes of the material and cracking is carried out based on a step-iterative algorithm of sequential loading based on the modified Newton – Kantorovich method. The plastic deformation analysis of the construction material is carried out based on the basic provisions of plastic flow theory with isotropic translational hardening. Redetermination of the approximating functions of the displacement vector over the thickness of the FE layers package considering the formed destruction zones is carried out based on the iterative-analytical method of variable approximations [23].

4 Results

The estimation of the increase in the strength parameters of the nanomodified tire element in this work is carried out by numerically modeling pulling a nanotube from a rubber mass to obtain additional energy required to perform this process. For this, a three-layer model “nanotube - polymer molecule - solid rubber” was used.

In the APROKS system, a parameterized FE model of CNTs with a polymer molecule and covalent bonds was created, which is shown in Fig. 2, a. Armchair nanotubes with a chiral number are considered (15, 5). The finite element model of the sample is shown in Fig. 2a. The nanotube is subject to forced displacements along its axis (Fig. 2b). The rubber layers are fixed at the ends along the direction of the nanotube length, and the outer surface is fixed in the radial direction (Fig. 2c).

Based on this model, calculations were carried out to determine the physical and mechanical properties RVE of nanomodified rubber and the processes of occurrence of microdamages with their subsequent propagation up to the destruction of RVE. Simulation of pulling CNTs from rubber in the APROKS system was carried out based on the step-by-step Newton-Kantorovich method, considering all types of nonlinearities, such as physical and geometric nonlinearities, of accumulation and propagation of damage.

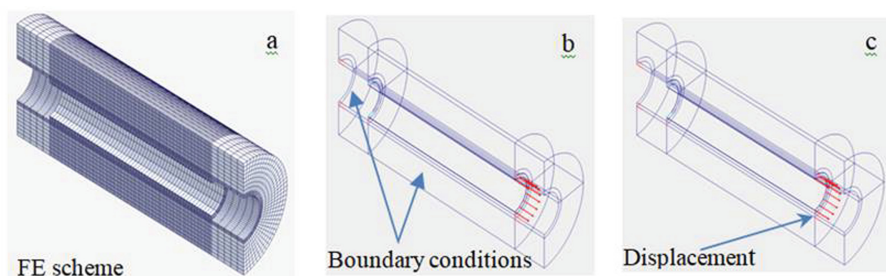


Fig. 2. Design diagram of an elementary sample of a nanomodified rubber element; a - FE model; b - boundary conditions; c - loading conditions.

As a result of numerical modeling of pulling CNTs from rubber, it was found that this process takes place in four stages. At the first stage (Fig. 3a), a local zone of delamination of the nanotube from the rubber mass appears. As a result of the redistribution of stresses after the formation of the delamination zone, a gradual decrease in the covalent interaction occurs (Fig. 3b).

The third stage is the progressive detachment of the nanotube from the rubber (Fig. 3c). Subsequently, at the level of the middle of the nanotube, a rupture of the rubber molecule occurs, and destruction begins at the left end of the nanotube (Fig. 3d).

As a result, the nanotube contact with the rubber mass completely disappears, as evidenced by a sharp drop in the “R” reaction parameter in Fig. 4.

After carrying out a series of numerical experiments for various reinforcement coefficients of the rubber mass, the graphs of the dependence of the total reaction arising at the end of the nanotube to which the forced displacement is applied depending on the level of forced displacements were obtained (Fig. 4a).

Analyzing the maximum values of the graphs “R-U” shown in Fig. 4a, a graph of the dependence of the ultimate strength of the composite “nanotube-rubber” deb). These results showed that the maximum strength of nanomodified rubber is achieved with a reinforcement ratio $V_{nnt}/V = 0.875\%$.

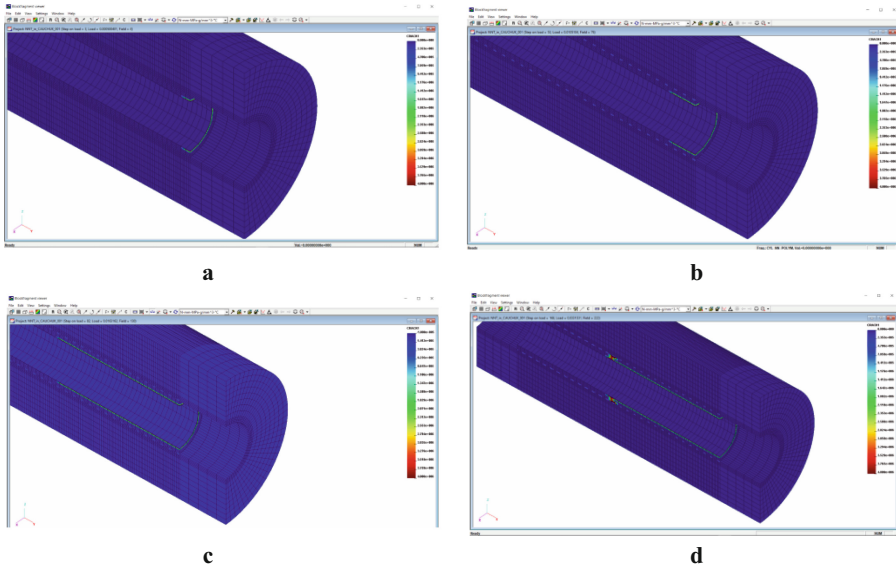


Fig. 3. (a). The appearance of delamination zones. (b). Disruption of covalent bonds. (c). Propagation of the zone of delaminated of the nanotube from the rubber. (d). Complete destruction of the contact layer.

Analysis of this graph shows that for a reinforcement coefficient of 0.875%, the ratio of the tensile strength of nano-reinforced and non-reinforced rubbers is 18%.

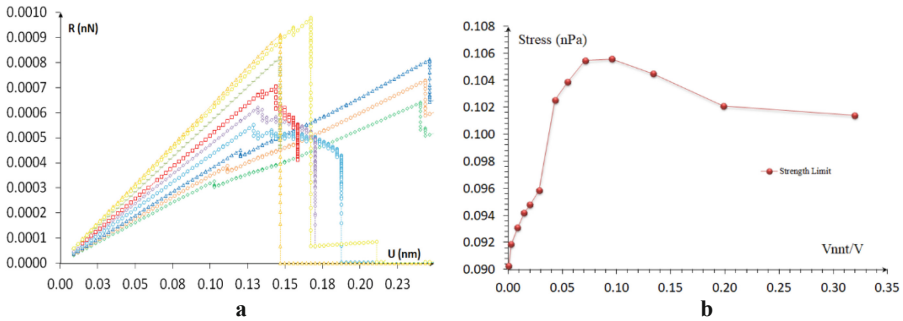


Fig. 4. (a). Graph of the dependence of the total reaction “R” on the forced displacements “U” at various coefficients of reinforcement of the nanopolymer. (b). Dependence of the tensile strength of nano-reinforced rubber on the reinforcement coefficient (V_{nnt} – nanotube volume, V – RVE volume).

Comparison of the numerical simulation results with the results of field experiments given in [13] are shown in Fig. 5 and indicates that the relative error for a reinforcement coefficient of 0.5% is 7.8%, and for a reinforcement coefficient of 1% is 8.7%.

The discrepancy between the results of numerical and field experiments does not exceed 10%. The result allows us to assert that a nanomodification process is a reliable tool for increasing rubber products' strength and crack resistance.

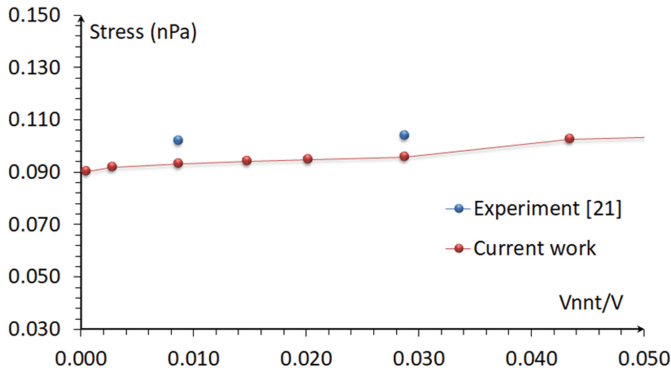


Fig. 5. Comparison of the results of numerical modeling and the results of experiments.

5 Conclusions

To model the processes of deformation of structures from nanomodified rubbers within a single physical model describing the behavior of NM structures and combining the relationship of degradation processes of nanomodified rubber occurring at the macro, micro, and nano levels, developed and numerically implemented a method for determining of the physical and mechanical parameters of the strength of machine-building products from nano-reinforced rubbers.

A model of physically substantiated prediction of the properties of new nanomodified rubbers has been constructed and numerically implemented to increase the strength, durability, and endurance parameters of nanomodified objects. The method is based on the FEM. A particular eight-node isoparametric FE has been developed. It is established that based on the developed FE a detailed study of the processes of nonlinear deformation of nanotubes and nanomodified rubbers is possible.

Numerical modeling of evolutionary processes of accumulation of microdefects in the contact layer “nanotube - rubber” is carried out, and the occurrence of macro-damages of nanotube peeling during its extraction from the rubber array. The numerical simulation results coincide with the data of field experiments with an accuracy of up to 10%.

The developed methods allow to reliably assess the reliability and durability of nanomodified polymeric and rubber elements of mechanical engineering equipment and can be used to develop and implement information support systems for their life cycle.

References

1. Wang, P., Geng, S., Ding, T.: Effects of carboxyl radical on electrical resistance of multi-walled carbon nanotube filled silicone rubber composite under pressure. *Compos. Sci. Technol.* **70**, 1571–1573 (2010)
2. Li, Y., Shimizu, H.: High-shear processing induced homogenous dispersion of pristine multiwalled carbon nanotubes in a thermoplastic elastomer. *Polymer* **48**(8), 2203–2207 (2007)
3. Wang, D., Fujinami, S., Nakajima, K., et al.: Production of a cellular structure in carbon nanotube/natural rubber composites revealed by nanomechanical mapping. *Carbon* **48**, 3708–3714 (2010)
4. Khalid, M., Ismail, A.F., Ratnam, C.T., et al.: Effect of radiation dose on the properties of natural rubber nanocomposite. *Radiat. Phys. Chem.* **79**, 1279–1285 (2010)
5. Tarawneh, M.A., Ahmad, S., EhNoum, S.Y., Lau, K.T.: Sonication effect on the mechanical properties of MWCNTs reinforced natural rubber. *J. Compos. Mater.* **47**(5), 579–585 (2012). <https://doi.org/10.1177/0021998312443394>
6. Zhan, Y.H., Liu, G.Q., Xia, H.S., Yan, N.: Natural rubber/carbon black/carbon nanotubes composites prepared through ultrasonic assisted latex mixing process. *Plast., Rubber Compos.* **40**(1), 32–39 (2011). <https://doi.org/10.1179/174328911X12940139029284>
7. Anoop, A.K., Sunil, J.T., Rosamma, A., Rani, J.: Natural rubber-carbon nanotube composites through latex compounding. *Int. J. Polym. Mater. Polym. Biomater.* **59**, 33–44 (2009). <https://doi.org/10.1080/00914030903172916>
8. Jian, W., Kaiye, Z., Zhengang, C., et al.: Graphene/carbon black/natural rubber composites prepared by a wet compounding and latex mixing process. *Plast., Rubber Compos.* **47**(9), 398–412 (2018). <https://doi.org/10.1080/14658011.2018.1516435>
9. Martin, P.J., Brown, P., Chapman, A.V., Cook, S.: Silica-reinforced epoxidized natural rubber tire treads – performance and durability. *Rubber Chem. Technol.* **88**(3), 390–411 (2015)
10. Foorginejad, A., Taheri, M., Mollayi, N.: Measurement and modelling of the rubber resilience based on ultrasonic non-destructive testing in tires. *AUT J. Model. Simul.* **50**(2), 165–170 (2018). <https://doi.org/10.22060/miscj.2018.14543.5109>
11. Wang, J., Zhang, K., Bu, Q., Lavorgna, M., Xia, H.: Graphene-rubber nanocomposites: preparation, structure, and properties. In: Kaneko, S., et al. (eds.) *Carbon-related Materials— in Recognition of Nobel Lectures by Prof. Akira Suzuki in ICCE*, pp. 175–209. Springer, Cham (2017). https://doi.org/10.1007/978-3-319-61651-3_9
12. Choi, J., Quagliato, L., Lee, S., et al.: Multiaxial fatigue life prediction of polychloroprene rubber (CR) reinforced with tungsten nano-particles based on semi-empirical and machine learning models. *Int. J. Fatigue* **145**, 106136 (2021). <https://doi.org/10.1016/j.ijfatigue.2020.106136>
13. Trachevskiy, V., Kartel, M., Sementsov, Y. et al.: Modification of Specialty Rubbers by Carbon Nanomaterials. *Int. J. Mater. Sci. Appl.* **8**(6), 135–135 (2019). <https://doi.org/10.11648/j.ijmsa.20190806.17>
14. Dehaghani, M.Z., Mashhadzadeh, A.H., Salmankhani, A., et al.: Fracture toughness and crack propagation behavior of nanoscale beryllium oxide graphene-like structures: a molecular dynamics simulation analysis. *Eng. Fract. Mech.*, 107194235 (2020). <https://doi.org/10.1016/j.engfracmech.2020.107194>
15. Bilalis, P., Katsigiannopoulos, D., Avgeropoulos, A., Sakellariou, G.: Non-covalent functionalization of carbon nanotubes with polymers. *RSC Adv.* **4**, 2911 (2014). <https://doi.org/10.1039/c3ra44906h>

16. Qiang, L., Baidurya, B.: Fracture resistance of zigzag single walled carbon nanotubes. *Nanotechnol. Inst. Phys.* **17**, 1323–1332 (2006)
17. HosseinEsbati, A., Saied, I.: Mechanical properties and fracture analysis of functionalized carbon nanotube embedded by polymer matrix. *Aerosp. Sci. Technol.* **55**, 120–130 (2016)
18. Shi, D.-L., Feng, X.-Q., Jiang, H., et al.: Multiscale analysis of fracture of carbon nanotubes embedded in composites. *Int. J. Fract.* **134**, 369–386 (2005)
19. Dong, L.S., Xi, Q.F., Yonggang, Y.H., Keh, C.H.: Critical evaluation of the stiffening effect of carbon nanotubes in composites. *Key Eng. Mater.* 261-263, 1487–1492 (2004). <https://doi.org/10.4028/www.scientific.net/KEM.261-263.1487>
20. Wernik, J., Meguid, S.: Multiscale modeling of the nonlinear response of nano-reinforced polymers. *Acta Mech.* **217**, 1–16 (2011)
21. Shokrieh, M.M., Rafiee, R.: On the tensile behavior of an embedded carbon nanotube in polymer matrix with non-bonded interphase region. *Compos. Struct.* **92**, 647–652 (2010)
22. Gondlyakh, A.V., Sokolskiy, A.L., Kolosov, A.E., Chemeris, A.O., Shcherbina, V.Y., Antonyuk, S.I.: Modeling the mechanisms of fracture formation in nanomodified polymers. In: 2020 IEEE 10th International Conference Nanomaterials: Applications & Properties (NAP), pp. 02TM06–1–02TM06–7. Sumy, Ukraine (2020). <https://doi.org/10.1109/NAP51477.2020.9309637>
23. Sakharov, A.S., Gondlyakh, A.V., Mel'nikov, S.L., Snitko, A.N.: Numerical modeling of processes of failure of multilayered composite shells. *Mech. Compos. Mater.* **25**(3), 337–343 (1989). <https://doi.org/10.1007/BF00614801>



Surface Strengthening Technology for Hammers of a Four-Die Forging Device

Tetiana Hovorun , Kristina Berladir , and Oleksandr Gusak 

Sumy State University, 2, Rymkogo-Korsakova Street, Sumy 40007, Ukraine
kr.berladir@pmtkm.sumdu.edu.ua

Abstract. Strengthening of the hammers of four-die forging devices is considered in this paper. During the manufacture of forgings of future details from high-quality and alloy steels, the hammers of four-die forging devices work in extreme conditions of shock-abrasive wear, which causes them to fail quickly. Various technological methods of their strengthening are applied to prolong the service life of the hammers. One of the promising ways of strengthening the details of forging and pressing equipment is surfacing technology. The existing method of strengthening the hammer's surface of radial forging machine by surfacing with electrodes OZSh-6 and its disadvantages is described. A new method of strengthening the hammer's working surface using a welding machine by flux-cored wire PP-NP-35X6M2 is proposed. It was found that when surfacing AISI L6 tool steel with this flux-cored wire, the hardness of the metal surface after surfacing increases to 53 HRC, and when moving inwards, the hardness decreases to 44 HRC, which indicates a soft and viscous structure that can withstand dynamic loads. There is also an increase in the strength and wear resistance of the detail's surface, which, when surfacing with flux-cored wire PP-NP-35H6M2, is greater than the base metal by 1.5 times. Experimental studies, which have been obtained on the structure, hardness, and wear resistance, confirmed the feasibility of replacing manual arc welding with automatic.

Keywords: Four-die forging device · Hammers · Surfacing · Electrodes · Flux-cored wire · Structure · Hardness · Wear resistance

1 Introduction

Radial forging is when large forces are transmitted through surface contact to alter the diameter of a workpiece through deformation [1, 2]. In radial stamping machines, the workpiece is rotated by an optimized [3], directly controlled, rotating manipulator drive [4].

This process is gaining popularity with the advent of electric vehicles [5]. Radial forging has historically provided perfect surface finishes and lower machining allowances [6].

This type of processing has found its application in various hollow details of complex shapes and its ability to stamp high-alloy steels and superalloys [7]. This process offers several interesting advantages [8] that will become even more important

and widespread due to new requirements for materials, performance, reliability, and material properties, which confirms the relevance of research in this direction [9].

2 Literature Review

The most important part of the technological process of manufacturing and operation of machines and mechanisms is manufacturing details [10], the quality of which is mainly determined by the durability of the hammers of radial forging machines [11]. During the manufacture of forgings of future details from high-quality and alloy steels, the hammers of radial forging machines work in extreme conditions of shock-abrasive wear [12], which causes them to fail quickly [13]. Abrasive wear due to the presence of an abrasive medium in the friction zone [14]: the destruction of friction surfaces occurs due to local plastic deformation [15], micro-scratching, and micro-cutting with abrasive particles [16].

Forging of shaft blanks, for which radial forging machines are used [17], is made of round rolled metal, cut to the required length. Rolled blanks are placed in an induction heater having two inductors and heat both ends of the shaft to 1100 °C. Heating is carried out at a specific rate. Suppose the heating difference is too significant between the more heated (surface) and less heated (inner) metal layers. In that case, stresses can occur, increasing so much that the metal's integrity will be violated, and internal micro- and macrocracks are formed [18]. At a prolonged heating rate, the surface oxidation of the metal increases, and scale is formed. In addition to the irreversible loss of metal with scale, pressing into the metal surface during deformation causes the need to increase the machining allowances. The scale also accelerates the deforming tool's wear because its hardness is much greater than the hardness of the hot metal [19, 20].

Different brands of stamped steels are used to make radial forging machines. Steels used for heat-deforming dies must have high mechanical properties [21] (strength and toughness) at elevated temperatures and high scale resistance and heat resistance, i.e., the ability to withstand repeated heating and cooling without the appearance of hot cracks [22]. Steels must also have high wear resistance and thermal conductivity for industrial heat transfer transmitted by the workpiece [23–25].

To prolong the work of the hammers, use various technological methods to strengthen them [26]. Along with the traditionally existing methods of hardening details by heat and chemical-heat treatment [27], currently, the industry uses a large number of different types of hardening details by surfacing [28]: manual arc surfacing, submerged arc surfacing, vibroarc surfacing, electric arc surfacing, electroslag surfacing, plasma surfacing, and others [29].

Electric arc surfacing is performed by metal fusible single electrodes, electrode beam, plate electrodes, tubular electrodes, flux-cored wire, flux-cored tapes, direct and indirect arc three-phase arc [30]. The surfacing of forging and pressing equipment and wear details of a metallurgical, machine and other types of equipment operating under difficult conditions are surfaced with electrodes OZSh-6 with a diameter of 2.5; 3.0; 4.0. Such electrodes are welded: strikes of radial forging machines; hot and cold stamping stamps; knives or hot cutting of metals; wear details of the metallurgical, engine, and other equipment [31].

3 Research Methodology

The surfacing of forging and stamping equipment of cold and hot deformation works in thermal fatigue conditions (up to 950 °C) and high pressures. The hardness of the weld metal is HRC 52–60. Electrodes OZSh-8 with a 3,0–4,0 mm diameter are applied to the surfacing of forging and stamping equipment of hot deformation of metals working in superheavy conditions of thermal fatigue (to 1100 °C) and even more significant pressures. The hardness, in this case, is HRC 51–57. For massive details that work in abrasive wear conditions in the surfacing process automation, use flux-cored wire brand PP-20H4V10 and PP-AN 135 and flux-coated brands PL-AN150 and PL-U40X38, which provide hardness from 38 to 56 HRC and high wear resistance of the weld metal.

In connection with the small-scale production of radial forging machines and automation of work for surfacing the surface, we choose flux-cored wire PP-NP-35X6M2. The surfacing of large-sized press and hammer dies, and hammers of forging machines using flux-cored wire of this type provide increasing stability more than two times.

Now, the following technology is used in the production of radial forging machines. First, the detail is cast in foundry sand molds made of AISI L6 steel, then after machining, perform surface hardening by manual surfacing electrodes OZSh-6, quenching, and subsequent tempering. During the operation of the hammer, made according to this technology, it quickly loses its efficiency.

This method of strengthening the detail is impractical because it is economically inefficient and has low wear resistance. It negatively affects the mechanical and operational properties of the hammer when working under static and dynamic loads. The detail is subject to high abrasive wear, which leads to its rapid operation and equipment failure.

New technology of strengthening the detail is proposed to eliminate all the negative phenomena in the hammer's manufacture. It consists of using AISI L6 tool steel alloyed with chromium and nickel, and molybdenum, which will significantly increase its hardening.

After producing the hammer from structural carbon high-quality AISI L6 tool steel, it is placed in the furnace for heat treatment – annealing. The material is heated to 600–650 °C, kept at this temperature for 3 h, and cooled together with the furnace. The detail is then removed from the furnace and performs machining and surface hardening by surfacing with flux-cored wire brand PP-NP-35H6M2 using a machine A-874H.

The hammer is tempered with heating to 830–860 °C with exposure at this temperature for about 1.6 h after the surfacing process. For preventing cracks in the hammer and the weld metal, it is cooled in air and then immersed in oil for further rapid cooling. As a result of such heat treatment, a martensitic structure is formed in the base and weld metal, which has high stresses, leading to cracks and premature failure during the hammer's operation. To relieve tension in detail and formation of troostite and sorbitol-troostite structure, we carry out high tempering at a temperature of 500–580 °C.

After the surfacing process, the sample's hardness was measured on a micro-hardness tester PMT-3 and tested for wear resistance on the machine X4B. Hardness

was measured on a fabricated micro grind cut from a sample at the weld metal junction with the base.

Also tested for wear during surfacing of the proposed flux-cored wire PP-Np-35H6M2 and used in industry surfacing electrodes OZSh-6 and flux-cored wire PP-AN-135 compared to AISI L6 steel.

We used the weighing method in determining the abrasive wear of the welded samples. In our studies, the following test parameters were adopted:

- sample size, mm – $7 \times 7 \times 25$;
- the speed of rotation of the rubbing surface, rad/sec – 21.0;
- the speed of rotation of samples, rad/sec – 10.9;
- the pressure of the sample on the abrasive skin, MPa – 0.049;
- wear rate, m/sec – 2.6;
- test time, sec – 120.0;
- wear path, m – 312.0;
- the multiplicity of one experiment – 3.

4 Results

The elements contained in the flux-cored wire provide reliable protection of the molten metal. The chemical composition of AISI L6 steel and metal deposited with flux-cored wires is presented in Table 1.

Table 1. Chemical composition of the base and weld metal, in %

Elements	AISI L6 steel	Powder wire PP-NP-35X6M2	Powder wire PP-AN-135	Surface electrode OZSh-6
C	0.5 – 0.6	0.33 – 0.40	2.8 – 3.0	0.08
Ni	1.4 – 1.8	–	–	10.8
Cr	0.6 – 0.8	5.8 – 6.2	8 – 11	33.0
Mo	0.15 – 0.30	1.15 – 2.30	–	2.5
V	–	0.1 – 0.3	–	–
Si	0.1 – 0.3	0.8 – 1.2	1.5 – 2.5	1.1
S	up to 0.03	up to 0.03	up to 0.04	0.009
P	up to 0.03	up to 0.03	up to 0.06	0.018
Ti	–	–	0.5 – 1.2	–
Nb	–	–	6.0 – 9.0	–
Mn	–	–	–	1.1

During the surfacing of AISI L6 steel, the alloying zone is depleted of carbon and alloying elements. Austenite in this area is unstable, and during deposition, it decays with the formation of martensite. Due to the stresses that occur during surfacing, cracks may form in the transition zone. These defects are widespread in multilayer surfacing. Prevention of cracking is achieved by reducing the depth of penetration of the base metal (surfacing, angle forward, surfacing with several double electrodes and tape) and preheating the workpiece to a temperature of 350–400 °C.

After surfacing, the hardness of the metal surface is increased to 48–53 HRC and improves the wear resistance and strength of the detail's surface. Residual stresses that occur after surfacing are removed by tempering. The tempering of steel softens the action of hardening, reduces or removes residual stresses, increases viscosity, reduces the hardness and brittleness of steel. The tempering is carried out by heating of details to a temperature below critical. Depending on the heating temperature, martensite, troostite, or sorbitol of the tempering structures can be obtained. Cementite on the tempering is granular or point, as in granular perlite. The advantage of the point structure is a more favorable combination of strength and ductility. With the same chemical composition and the same hardness, steel with a point structure has a much higher relative narrowing and toughness, increasing the value of relative elongation and yield strength compared with steel with a lamellar structure.

Carbide-forming elements increase the resistance of austenite as they are dissolved in austenite. If the carbides were out of solution in separated carbides, the austenite, on the contrary, becomes less stable. This is because carbides are the centers of crystallization, and the presence of undissolved carbides leads to the depletion of austenite by the alloying element and carbon. The martensite structure is formed at low content in the steel of chromium, nickel, and molybdenum after hardening.

As a result of high tempering, internal stresses are removed, increasing ductility and viscosity. After heat treatment, the detail has high wear resistance with a hardness of the base metal of about 40 HRC and the weld metal of about 50 HRC. After high tempering in the hammer's base metal, the microstructure is sorbitol with inclusions of troostite (Fig. 1, a), and in the weld metal is sorbitol with inclusions of chromium carbides (Fig. 1, b).

Sorbitol structure with inclusions of chromium carbides, which is formed after high tempering in the weld metal, provides high stability during the radial forging machine's operation in high temperatures and wear conditions. In the application of surfacing, there is a bimetallic connection on the surface of the detail. The deposited layer contains three distinct structural zones of approximately the same thickness.

The most critical problem that arises during the surfacing of steel is that the subsequent long-term heat treatment at the boundary between the base and the weld metal forms a brittle carbon-rich layer, which causes cracks when tested for lateral bending. The microstructure in the area of this transition layer is shown in Fig. 2.

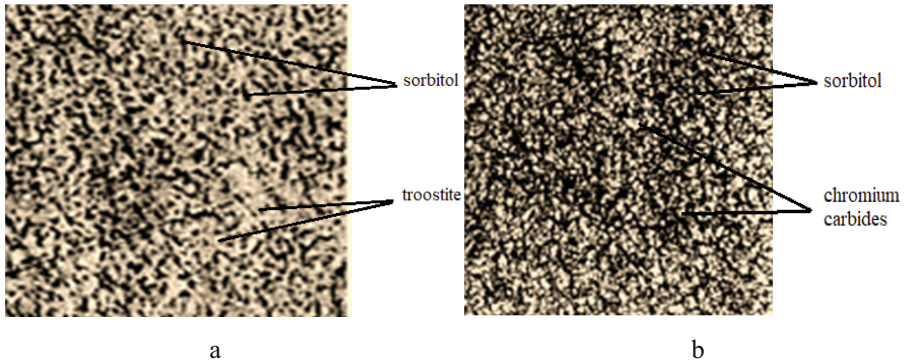


Fig. 1. The microstructure of AISI L6 steel after tempering (a) and weld metal PP-NP-35H6M2 on steel after tempering (b), $\times 200$

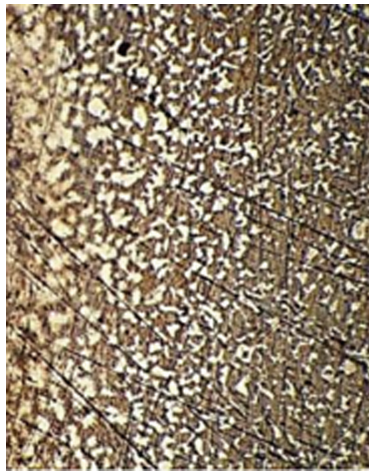


Fig. 2. The microstructure of the transition zone of the weld metal, $\times 200$

It is the boundary layer with a slight decrease in carbon concentration. In the transition zone directly under the deposited layer, there is usually a decarburized layer. Its occurrence is due to the diffusion of carbon from the base metal to the weld metal, which contains elements with a high chemical affinity for carbon. This is because of the burning of carbon during surfacing due to the high temperature of the welding arc and the difference in content in the weld and base metal of carbide-forming elements. The carbon content in the boundary decarburized layer also depends on the heat treatment mode.

The welded surface of the sample has the highest hardness of 53 HRC, and when moving inwards, the hardness decreases to 44 HRC, which indicates a soft and viscous structure that can withstand dynamic loads.

The wear resistance of materials concerning the detail's operating conditions can be obtained only in tests where the actual wear process is ensured. It can be achieved in two cases: accurately copying all the external factors that characterize this detail's operation and modeling the wear process. All tests of materials for wear are reduced to determining the amount of wear. One of the most used methods for determining the wear of small details is to weigh them before and after the test.

Analysis of wear resistance of materials showed that the weld metal flux-cored wire PP-NP-35H6M2 and electrodes OZSh-6 and flux-cored wire PP-AN-135 have significantly higher wear resistance than the base metal AISI L6 steel. It is established that the highest wear resistance has a metal deposited with flux-cored wire PP-NP-35H6M2 and is 1.5 relative to AISI L6 steel (Fig. 3) when using the welded metal with OZSh-6 electrode is by 1.3 times comparable to steel.

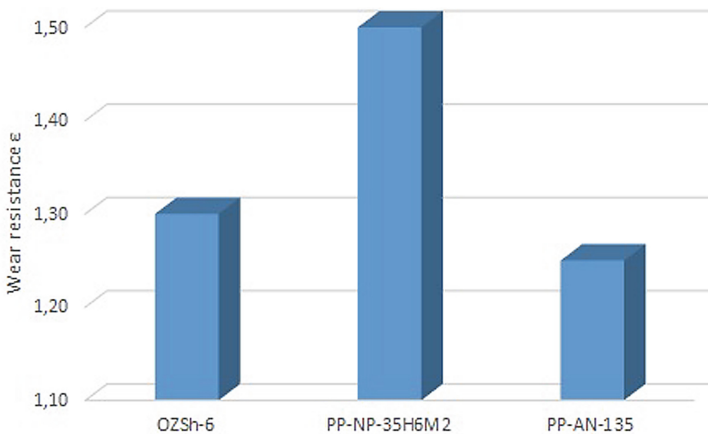


Fig. 3. Diagram of wear resistance (ϵ) of the weld metal relative to AISI L6 tool steel.

The study showed that the hardness and wear resistance of the hammer surface meets the product's technical requirements.

5 Conclusions

Based on the literature review of modern scientific articles on increasing the durability of the hammers of four-die forging devices, it is established that one of the best methods of strengthening is the surfacing of wear-resistant materials.

The choice of materials showed that for the manufacture of the hammers of four-die forging devices, the best material might be AISI L6 tool steel.

It has been established experimentally that the microstructure of the hammer's base metal is sorbitol with inclusions of troostite, and the microstructure of the weld metal consists of sorbitol with inclusions of chromium carbides.

After heat treatment, the hardness of the weld metal is about 53 HRC, and wear resistance when surfacing with flux-cored wire PP-NP-35H6M2 is higher relative to the base metal by 1.5 when using weld metal electrode OZSh-6 is by 1.3 times.

Acknowledgments. The main scientific results have been obtained to fulfill the objectives of the perspective development plan within the scientific direction “Technical Sciences” at Sumy State University within the related research project ordered by the Ministry of Education and Science of Ukraine.

The authors appreciate the International Association for Technological Development and Innovations for the support while conducting this research.

References






1. New Developments in Forging Technology. <https://www.forgingmagazine.com/issues-and-ideas/article/21923033/new-developments-in-forging-technology>. Accessed 20 January 2021
2. Ivanov, V., Pavlenko, I., Liaposhchenko, O., Gusak, O., Pavlenko, V.: Determination of contact points between workpiece and fixture elements as a tool for augmented reality in fixture design. *Wireless Netw.* **27**(3), 1657–1664 (2019). <https://doi.org/10.1007/s11276-019-02026-2>
3. Pavlenko, I., et al.: Parameter identification of cutting forces in crankshaft grinding using artificial neural networks. *Materials* **13**(23), 5357 (2020). <https://doi.org/10.3390/ma13235357>
4. Huang, J., Slater, C.D., Mandral, A., Blackwell, P.: A dynamic model for simulation of hot radial forging process. *Procedia Eng.* **207**, 478–483 (2017). <https://doi.org/10.1016/j.proeng.2017.10.808>
5. Quagliato, L., Kim, D., Lee, W., Berti, G.A., Lee, C., Kim, N.: Radial forging of aluminum to steel preform for the production of light-weighted wheel bearing outer race. *Procedia Eng.* **207**, 1683–1688 (2017). <https://doi.org/10.1016/j.proeng.2017.10.922>
6. Zhang, Y., et al.: Research and application of precision forging forming process for flat thin flash of automobile disc steering knuckle. *Procedia Manuf.* **50**, 32–36 (2020). <https://doi.org/10.1016/j.promfg.2020.08.007>
7. Velychkovych, A., Petryk, I., Ropyak, L.: Analytical study of operational properties of a plate shock absorber of a sucker-rod string. *Shock. Vib.* **2020**, 3292713 (2020)
8. Lazorkin, V., Lazorkin, D., Kuralekh, S.: New four-die forging devices (FDFD) design solutions and open-die forging technologies. *Adv. Mater.* **7**(1), 1–8 (2018). <https://doi.org/10.11648/j.am.20180701.11>
9. Govorun, T.P., Belous, E.A., Lyubich, A.I.: Improvement of properties of high-strength cast irons by surfacing a metal with globular graphite. *Met. Sci. Heat Treat.* **59**(11–12), 675–681 (2018). <https://doi.org/10.1007/s11041-018-0210-9>
10. Zablotskyi, V., Tkachuk, A., Moroz, S., Prystupa, S., Svirzhevskiy, K.: Influence of technological methods of processing on wear resistance of conjugated cylindrical surfaces. In: Tonkonogyi, V., et al. (eds.) *InterPartner 2020. LNME*, pp. 477–487. Springer, Cham (2021). https://doi.org/10.1007/978-3-030-68014-5_47
11. Fan, L., Wang, Z., Wang, H.: 3D finite element modeling and analysis of radial forging processes. *J. Manuf. Process.* **16**(2), 329–334 (2014). <https://doi.org/10.1016/j.jmapro.2014.01.005>

12. Ghaei, A., Movahhedy, M.R.: Die design for the radial forging process using 3D FEM. *J. Mater. Process. Technol.* **182**(1–3), 534–539 (2007). <https://doi.org/10.1016/j.jmatprotec.2006.09.013>
13. Hawryluk, M., Ziemba, J.: Application of the 3D reverse scanning method in the analysis of tool wear and forging defects. *Measurement* **128**, 204–213 (2018). <https://doi.org/10.1016/j.measurement.2018.06.037>
14. Tkachuk, A., Zablotskiy, V., Kononenko, A., Moroz, S., Prystupa, S.: Directed formation of quality, as a way of improving the durability of conjugated parts of friction pairs. In: Ivanov, V., et al. (eds.) *DSMIE 2019. LNME*, pp. 370–377. Springer, Cham (2020). https://doi.org/10.1007/978-3-030-22365-6_37
15. Chotěborský, R., Hrabě, P., Müller, M., Savková, J., Jirka, M., Navrátilová, M.: Effect of abrasive particle size on abrasive wear of hardfacing alloys. *Res. Agr. Eng.* **55**(3), 101–113 (2009). <https://doi.org/10.17221/24/2008-RAE>
16. Hardell, J., Yousfi, A., Lund, M., Pelcastre, L., Prakash, B.: Abrasive wear behaviour of hardened high strength boron steel. *Tribol. – Mater. Surf. Inter.* **8**(2), 90–97 (2014). <https://doi.org/10.1179/1751584X14Y.0000000068>
17. Karpus, V.E., Ivanov, V.A.: Locating accuracy of shafts in V-blocks. *Russ. Eng. Res.* **32**(2), 144–150 (2012). <https://doi.org/10.3103/S1068798X1202013X>
18. Shaimanov, G.S., Simonov, M., Simonov, Y.: Comparative analysis of machine steels structure parameters and dynamic crack resistance after deformation-and-heat treatment. *Mater. Today: Proceed.* **19**(5), 2167–2173 (2019). <https://doi.org/10.1016/j.matpr.2019.07.239>
19. Hawryluk, M., et al.: Analysis of the wear of forging tools surface layer after hybrid surface treatment. *Int. J. Mach. Tools Manuf* **114**, 60–71 (2017). <https://doi.org/10.1016/j.ijmachtools.2016.12.010>
20. Gronostajski, Z., Kaszuba, M., Widomski, P., Smolik, J., Ziemba, J., Hawryluk, M.: Analysis of wear mechanisms of hot forging tools protected with hybrid layers performed by nitriding and PVD coatings deposition. *Wear* **420–421**, 269–280 (2019). <https://doi.org/10.1016/j.wear.2019.01.003>
21. Kulesh, E.A., Piliptsov, D.G., Rogachev, A.V., Hong, J.X., Fedosenko, N.N., Kolesnyk, V.: Boron-carbon coatings: structure, morphology and mechanical properties. *J. Eng. Sci.* **7**(1), C1–C9 (2020). [https://doi.org/10.21272/jes.2020.7\(2\).c1](https://doi.org/10.21272/jes.2020.7(2).c1)
22. Chantzis, D., et al.: Review on additive manufacturing of tooling for hot stamping. *Int. J. Adv. Manuf. Technol.* **109**(1–2), 87–107 (2020). <https://doi.org/10.1007/s00170-020-05622-1>
23. Muro, M., Artola, G., Gorriño, A., Angulo, C.: Wear and friction evaluation of different tool steels for hot stamping. *Adv. Mater. Sci. Eng.* **2018**, 3296398 (2018). <https://doi.org/10.1155/2018/3296398>
24. Karpus, V.E., Ivanov, V.A.: Choice of the optimal configuration of modular reusable fixtures. *Russ. Eng. Res.* **32**(3), 213–219 (2012). <https://doi.org/10.3103/S1068798X12030124>
25. Niederhofer, P., Eger, K., Schwingenschlögl, P., Merklein, M.: Properties of tool steels for application in hot stamping. *Steel Res. Int.* **91**, 1900422 (2020). <https://doi.org/10.1002/srin.201900422>
26. Hawryluk, M.: Review of selected methods of increasing the life of forging tools in hot die forging processes. *Arch. Civ. Mech. Eng.* **16**(4), 845–866 (2016). <https://doi.org/10.1016/j.acme.2016.06.001>
27. Berladir, K., Hovorun, T., Bondarenko, M., Shvetsov, D., Vorobiov, S.: Application of reinforcing thermocycling treatment for materials of stamps hot deformation. *J. Eng. Sci.* **6** (2), C6–C10 (2019). [https://doi.org/10.21272/jes.2019.6\(2\).c2](https://doi.org/10.21272/jes.2019.6(2).c2)

28. Khizhnyakova, L., Ewering, M., Hirt, G., Bobzin, K., Bagcivan, N.: Metal flow and die wear in semi-solid forging of steel using coated dies. *Trans. Nonferrous Metals Soc. China* **20**(3), s954–s960 (2010). [https://doi.org/10.1016/S1003-6326\(10\)60613-9](https://doi.org/10.1016/S1003-6326(10)60613-9)
29. Fernandes, F.A.P., Heck, S.C., Picone, C.A., Casteletti, L.C.: On the wear and corrosion of plasma nitrided AISI H13. *Surf. Coat. Technol.* **381**, 125216 (2020). <https://doi.org/10.1016/j.surfcoat.2019.125216>
30. Govorun, T.P., Lyubich, A.I.: Theoretical substantiation and development of economically alloyed welding materials. *Weld. Int.* **31**(5), 374 (2017). <https://doi.org/10.1080/09507116.2015.1093805>
31. Tarelnyk, V.B., Gaponova, O.P., Konoplianchenko, Y.V. et al.: improvement of quality of the surface electroerosive alloyed layers by the combined coatings and the surface plastic deformation. I. Features of Formation of the Combined Electroerosive Coatings on Special Steels and Alloys. *Metallofiz. Noveishie Tekhnol.* **41**(1), 47–69 (2019)



Ensuring the High Strength Characteristics of the Surface Layers of Steel Products

Kateryna Kostyk¹ , Viktoriia Kostyk² , Oleg Akimov¹ ,
Kateryna Kamchatna-Stepanova¹ , and Yurii Shyrokyi³ 

¹ National Technical University «Kharkiv Polytechnic Institute»,
2, Kyrpychova St., Kharkiv 61002, Ukraine
kateryna.kostyk@khpі.edu.ua

² Donbas State Engineering Academy, 72 Akademichna,
Kramatorsk 84313, Ukraine

³ National Aerospace University named by N.Ye. Zhukovsky «KhAI»,
17, Chkalov St., Kharkiv 61070, Ukraine

Abstract. New technology of nitriding of steel products allows increasing the strength characteristics of the surface layers without reducing the bulk strength of the material. Tool alloyed steels 3Cr3Mo3V, 5CrNiMo, 9CrSi and W6Mo5Cr4V2 were studied, which allowed us to evaluate the effect of alloying elements on the micro-fragility and wear resistance of hardened alloys during nitriding in a powder mixture. Nitriding of the samples was carried out at a temperature of 550 °C for 5 h in a sealed container with a dispersed powder mixture. It is shown that the formation of the diffusion layer does not affect the overall dimensions of the products. It was found that nitriding in a dispersed powder mixture provides a low micro-fineness of the surface layer of steel, which can significantly improve the reliability and durability of products. It is proved experimentally that chemical-thermal hardening allows for an increase in wear resistance of steels twice. Mathematical models of wear resistance of the investigated steels after the proposed hardening technology are obtained.

Keywords: Nitriding · Surface hardening · Micro-coarseness · Wear resistance · Diffusion layer

1 Introduction

Increasing the strength and wear resistance of steel products is becoming increasingly important in connection with the operation of products in conditions of friction, thermal and mechanical loads in an aggressive environment. For its solving, surface hardening processes have been widely used in recent years. Obtaining high strength characteristics of the surface layers of steel products increases their structural strength with economical use of materials and ensures high reliability and durability of tools and machine parts, which is an urgent task in mechanical engineering today [1–3].

To improve the performance of surface layers, various surface hardening methods are used to increase the service life and reduce the cost of repairing worn products [4].

Diffusion saturation of metals with various elements is intended to increase the hardness, wear resistance, anti-friction properties, heat resistance, heat resistance, corrosion resistance, or other operational properties [5, 6].

2 Literature Review

Diffusion coatings are obtained by diffusion into an alloy of atoms of a protective substance in the solid, liquid, or gaseous phase at high temperatures [7]. Thermomechanical coatings are formed because of thermomechanical processing of the shielded and protective alloy by rolling or pulling during its heating [8, 9]. Chemical coatings are prepared by the method of metal ions reduction [10]. Chemical coatings have found their application in the production of printed circuit boards, in the metallization of plastics and inorganic materials, and for applying functional coatings on metals [11]. Vacuum-plasma coatings obtained by the method of vapor deposition (CVD and PVD methods) have wide applications in engineering, medicine, light industry and are used to protect materials and decorative finishes [12]. The functional characteristics of such coatings are divided into classes [13]: resistant; mechanical strength; decorative; heat engineering; lighting; electrical; physico-chemical; shielding; surface-active; transformative; biochemical; special [14]. Diffusion coating on the surface of the product formed because of saturation of the material of the various elements: nonmetals, metals, and the joint saturation of the elements [15]. The nitriding process is carried out in gas, liquid, and powder media [16]. Partially dissociated ammonia, ammonia and nitrogen, ammonia, and carbonaceous gases are used for gas nitriding [17]. For liquid nitriding, melts of cyanide-cyanate and cyanide salts are used, which are very harmful to human health [18].

Therefore, the issue of applying a new technology of nitriding in the powder mixture to obtain high strength characteristics of the surface layers of steel products [19] necessitates research in this direction [20].

Studies were carried out to obtain high strength characteristics of the surface layers of steel products by nitriding [21, 22].

For achieving this goal, it is necessary to solve the following tasks:

- to determine the effect of the developed nitriding technology on the hardening degree for the surface layers and the volume strength of the products;
- to investigate the micro-coarseness of the surface layer of steel after nitriding;
- to investigate the wear resistance of steels after chemical and thermal hardening;
- to obtain a mathematical model of wear resistance of steels after hardening technology.

3 Research Methodology

Investigated alloy tool steels 3Cr3Mo3V, 5CrNiMo, 9CrSi, and W6Mo5Cr4V2, which allowed to assess the effect of alloying elements on microdroplet, change dimensions, the wear resistance of the hardened alloys when nitrided in the powder mixture.

The surface of the samples was mechanically cleaned of scale, rust, oil, and other contaminants. Minor contamination was removed with non-fat gasoline. Then, the surface was polished and polished with 96% alcohol, followed by degreasing [23].

Before nitriding, steel samples were subjected to preliminary heat treatment: quenching followed by high tempering at temperatures depending on the steel grade. The samples had the form of cylinders with a diameter of 12 mm and a height of 20 mm. Nitriding of samples was carried out at a temperature of 550 °C for 5 h in a sealed container with a dispersed powder mixture containing 95–97% melamine $C_3H_6N_6$ and 3–5% sodium fluoride NaF [24].

Studies on the micro-coarseness and wear resistance of the surface layers were carried out after nitriding. The microarray was determined by the type of diamond indenter imprint having the shape of a pyramid with a square base and an angle at the top of 136°. The change in the overall dimensions of the samples after treatment was determined using a micrometer of the MK model 102 type with an accuracy of $\pm 0.004 \mu\text{m}$. The class of accuracy is CL.2 (ISO 3611:2010) on the outer sides of cylindrical samples. The wear resistance of steels was determined by the standard method on the machine for abrasion testing AP 40.613.20 R 43/82 (Germany). Polynomial regression models (PRM) [25] are used to approximate the influence of reinforcing treatments on the change in wear resistance of tool steels [26].

4 Results

4.1 Results of Research of Operational Properties of Steel by Nitriding in Powder Mixture

When saturated with nitrogen at a temperature of 550 °C, a diffusion layer is formed on the surface of alloyed tool steels, which consists of a nitride zone and a sublayer of α -solid solution. The nitride zone consists of ϵ -phase ($Fe_{2-3}N$) and γ' -phase (Fe_4N). The diffusion layer is a multiphase area consisting of nitrides, carbides, iron carbonitrides, and alloying elements, which smoothly passes into the zone of a nitrated solid solution of the base metal.

Since the nitride layers are formed due to the diffusion of nitrogen into the metal, the revealed changes in the overall dimensions of the samples after nitriding by the proposed technology are insignificant. Studies have shown that the greater the degree of alloying of steel (W6Mo5Cr4V2, 3Cr3Mo3V), the smaller the size of the samples and are in the range of 0,001–0,004 mm. In the less alloyed steels (9CrSi, 5CrNiMo) sizes a bit more (0.003–0.009 mm). Therefore, nitriding causes minimal changes in overall dimensions depending on the degree of alloying, which, if necessary, should be taken into account when choosing the material of tools and machine parts depending on their operating conditions.

The brittleness factor was estimated depending on the following factors: the number of prints with cracks, cracks in print, and their character. The assessment of material microfracture was determined by the average score's conventional scale for the fragility from 0 to 5 points, where the nature of the print was considered. The following formula determined the total brittleness score:

$$Z_p = 0 \cdot n_0 + 1 \cdot n_1 + 2 \cdot n_2 + 3 \cdot n_3 + 4 \cdot n_4 + 5 \cdot n_5 \quad (1)$$

$n_0, n_1, n_2, n_3, n_4, n_5$ – the relative number of prints from the total number with the given score of fragility.

The material fragility indicator, reflecting the nature of brittle fracture and its rate of increase with increasing load, was considered the product of the total score of fragility by the value of its derivative of the load

$$\gamma_p = Z_p \left(\frac{\partial Z}{\partial P} \right)_p \quad (2)$$

The average score of fragility from 0 to 5 points and the total score of the fragility of the formulas 1 and 2 was determined. Panorama of indenter prints with a load of 30 g to 200 g when measuring the micro-coarseness of the nitrided layer is shown in Fig. 1. After nitriding of tool steels, the increase in the load from 30 g to 200 g practically does not lead to the formation of micro-cracks in the indenter prints on the surface of the studied samples. The dependence of the total brittleness score of Z_p on the load P after nitriding of steel W6Mo5Cr4V2 is shown in Fig. 2.

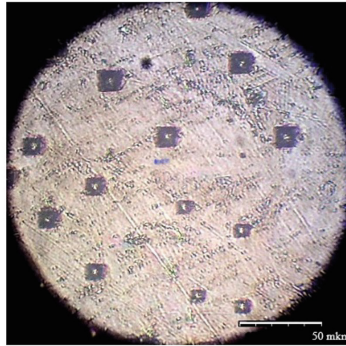


Fig. 1. Panorama of indenter prints with a load of 30 g to 200 g when measuring the micro-fineness of the nitrided layer.

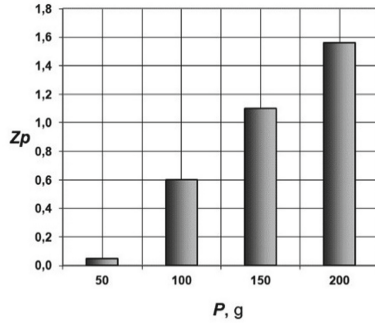


Fig. 2. Dependence of the total score of microdegree Z_p after nitriding of the load P on the indenter.

As shown in Fig. 2, it can be seen that the smallest micro-coarseness ($Z_p = 0-0,05$), where the imprint on the surface of the sample without visible cracks and chips, has a nitrided layer at low loads $P = 30-50$ g of indenter action on the surface layer of steel. The fragility of the nitrided layer increases slightly with increasing load on the indenter from 100 g to 200 g and corresponds to the total score of microfracture from 0.6 to 1.56. Similar low micro-coarseness after nitriding is observed for other investigated steels.

Smooth cylindrical samples were used for testing. The cylindrical sample was pressed against the rotating disk under a static load of 9.55 kgf/cm^2 with a relative load error not exceeding $\pm 1\%$. When the machine was turned on, the holder made a progressive movement along with the rotating disk. The friction velocity of the samples on the abrasive skin was such that the heating of the material during the test did not affect its properties. Calculations of the wear value by weight loss were based on the assumption that the wear occurs uniformly over the friction surface. Also, it is equal to the difference in the mass of the sample before the test and the mass of the sample after the test, washing, and drying. According to weighing the samples before and after the tests, the average weight loss of W samples from the materials under study was determined. In this case, the weight wear W is recalculated to linear wear by the formula

$$I_h = \frac{W}{F \cdot j \cdot L} \quad (3)$$

W – weight wear during the test, g; F – the surface area of friction, cm^2 ; j – the density of the worn material, g/cm^3 ; L – the friction path, m

Evaluation of wear resistance was performed according to the average value of the wear rate of the tested samples according to the formula $I = 1/I_h$.

According to the experimental data, the dependences of wear resistance are constructed (Fig. 3) tool steels from the friction path (with a permissible error limit of 5%) after preliminary heat treatment (hardening followed by high tempering) and after chemical heat treatment by the proposed technology of hardening the surface of alloys in a nitrogen-containing dispersed powder medium.

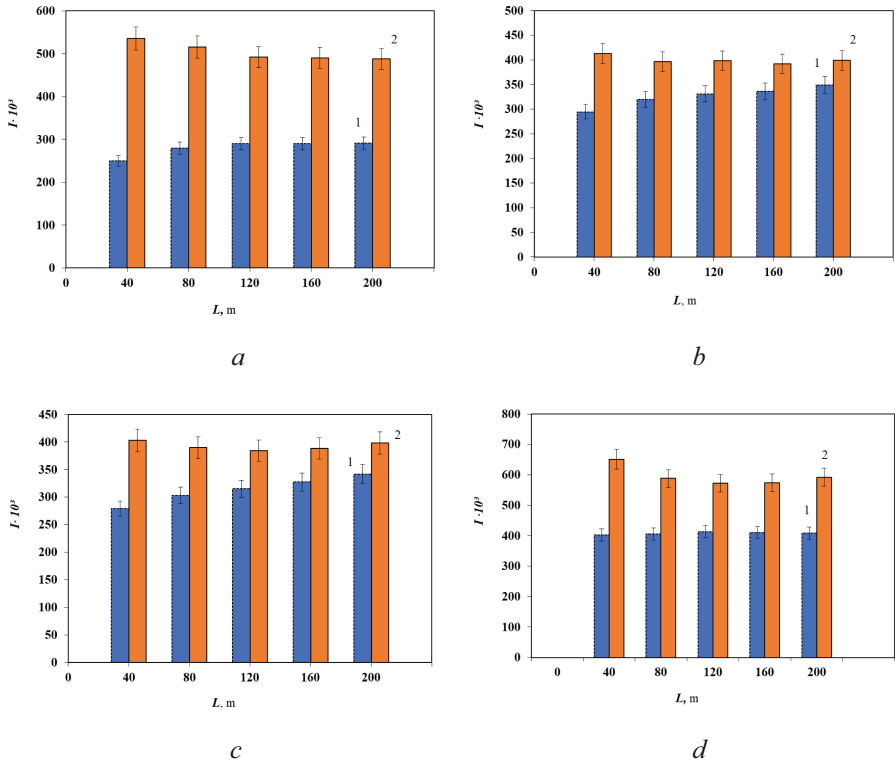


Fig. 3. Wear resistance of specimens from steel 3Cr3Mo3V (a), 5CrNiMo (b), 9CrSi (c) and W6Mo5Cr4V2 (d) after heat treatment (1) and after nitriding (2).

The mathematical models of change of wear resistance of the surface layer of steel after preliminary heat treatment (hardening with subsequent high tempering) and after nitriding, which is presented in the table, are calculated by the methods of approximation of the experimentally obtained Table 1 with the value of the approximation reliability (R^2). The approximation equations are represented by polynomials of the third and fourth degrees in the normalized form.

Table 1. Mathematical models of the influence of reinforcing treatments on the change in wear resistance of tool steels.

Steel grade	Wear resistance after pre-heat treatment	Wear resistance after nitriding
3Cr3Mo3V	$I = 1,78 L^3 - 26,214 L^2 + 127,57 L + 85,418$ $R^2 = 0,9998$	$I = -1,8488 L^4 + 29,726 L^3 - 167,01 L^2 + 369,89 L + 256,04$ $R^2 = 1$
5CrNiMo	$I = 1,7952 L^3 - 23,693 L^2 + 109,92 L + 155,07$ $R^2 = 0,9999$	$I = 2,0406 L^4 - 33,165 L^3 + 195,83 L^2 - 498,64 L + 859,85$ $R^2 = 1$
9CrSi	$I = 4,3694 L^3 - 54,667 L^2 + 228,14 L$ $LR^2 = 0,9267$	$I = -2,3453 L^4 + 37,748 L^3 - 213,63 L^2 + 495,72 L$ $R^2 = 0,8177$
W6Mo5Cr4V2	$I = 6,8845 L^3 - 86,264 L^2 + 338,65 L$ $LR^2 = -9,907$	$I = -4,8348 L^4 + 75,696 L^3 - 410,43 L^2 + 880,23 L$ $R^2 = 0,9211$

From Table 1, it is seen that the wear resistance of alloy tool steels without hardening of chemical-thermal treatment varies according to the law of the polynomial of the third degree, and after chemical-thermal treatment, the wear resistance changes according to the law of the polynomial of the fourth degree depending on the friction path.

4.2 Discussion of the Research Results

After nitriding according to the proposed technology and other traditional nitriding methods, the formation of the diffusion layer adversely affects the change in the overall dimensions of the products. However, it should be noted that according to this nitriding technology, with a short saturation (within 5 h), such deformation of tools and machine parts is insignificant and is within 0.001–0.009 mm. Therefore, in the existing technological version of nitriding in a powder mixture, hardening of complex shape products can be recommended, especially if they are not subjected to further processing after hardening treatment, as the warping and dimensional changes with hardening treatment this method are minimal.

It should be noted that nitriding in the powder mixture provides low micro-coarseness (Z_p is 0–1,56) of the surface layer of steel and allows to increase the wear resistance of steel by 1.3–2.5 times, which in turn contributes to a significant increase in the reliability and durability of products.

The dependence of wear on the friction path for all steels has the same almost linear character. After nitriding, there is much less wear of the samples than after pre-heat treatment. On the friction path up to 200 m, the wear value after nitriding is 1.3–2.5 times less (depending on the steel grade) than the initial state. This is due to the greater hardness of the surface layers after nitriding.

It should also be noted that in contrast to the traditional methods of nitriding, the proposed new method of hardening the surface of steels has a number of advantages:

- minor changes in overall dimensions, no warping of processed products due to low nitriding temperatures (550 °C),
- low micro-coarseness of the surface layer of steel,
- increasing the processing speed by 5–10 times due to the acceleration of diffusion processes and reducing the number of preparatory operations,
- reduction of materials and energy costs,
- non-toxic processes.

That is why the proposed method of obtaining high strength characteristics of the surface layers of steel products should be considered promising and possible for use in enterprises.

5 Conclusions

A new technology of nitriding steel products allows increasing the strength characteristics of the surface layers without reducing the bulk strength of the material.

It was shown that the formation of the diffusion layer does not affect the overall dimensions of the products and is in the range of 0.001–0.009 mm, which is due to the short time of the saturation process (within 5 h). Therefore, in the existing technological version of nitriding in a powder mixture, hardening of complex shape products can be recommended, especially if they are not subjected to further processing after hardening treatment, as the warping and dimensional changes with hardening treatment this method are minimal.

It was found that nitriding in a dispersed powder mixture provides a low micro-fineness of the surface layer of steel and increases the wear resistance of steel by 1.3–2.5 times, which in turn contributes to a significant increase in the reliability and durability of products.

It is proved experimentally that chemical-thermal hardening allows to increase the wear resistance of steels twice. This is due to the greater hardness of the surface layers after nitriding.

Mathematical models of wear resistance of the investigated steels after the proposed hardening technology are obtained.

Acknowledgment. The authors would like to acknowledge financing of National Research Foundation of Ukraine under grant agreement No. 2020.02/0119.

References





1. Lu, K.: Stabilizing nanostructures in metals using grain and twin boundary architectures. *Nat. Rev. Mater.* **1**(5), 16019 (2016)
2. Kulesh, E.A., Piliptsov, D.G., Rogachev, A.V., Hong, J.X., Fedosenko, N.N., Kolesnyk, V.: Boron-carbon coatings: structure, morphology and mechanical properties. *J. Eng. Sci.* **7**(2), C1–C9 (2020). [https://doi.org/10.21272/jes.2020.7\(2\).c1](https://doi.org/10.21272/jes.2020.7(2).c1)

3. Liaposhchenko, O., et al.: Improvement of parameters for the multi-functional oil-gas separator of 'heater-treater' type. In: 2019 IEEE 6th International Conference on Industrial Engineering and Applications (ICIEA), Tokyo, Japan, pp. 66–71 (2019). <https://doi.org/10.1109/IEA.2019.8715203>
4. Boles, M.A., Ling, D., Hyeon, T., Talapin, D.V.: The surface science of nanocrystals. *Nat. Mater.* **15**(2), 141 (2016)
5. Kostyk, K., et al.: Simulation of diffusion processes in chemical and thermal processing of machine parts. *Processes* **9**(4), 698 (2021). <https://doi.org/10.3390/pr9040698>
6. Shekhtman, S.R., Sukhova, N.A.: Synthesis of multilayer vacuum ion-plasma coatings Ti-Tin during the surface modification. In: *Materials Science Forum*, vol. 870, pp. 113–117 (2016)
7. Norhasri, M.M., Hamidah, M.S., Fadzil, A.M.: Applications of using nano material in concrete: a review. *Constr. Build. Mater.* **133**, 91–97 (2017)
8. Xiao, J., Liu, P., Wang, C.X., Yang, G.W.: External field-assisted laser ablation in liquid: an efficient strategy for nanocrystal synthesis and nanostructure assembly. *Prog. Mater. Sci.* **87**, 140–220 (2017)
9. Javanbakht, T., Hadian, H., Wilkinson, K.J.: Comparative study of physicochemical properties and antibiofilm activity of graphene oxide nanoribbons. *J. Eng. Sci.* **7**(1), C1–C8 (2020). [https://doi.org/10.21272/jes.2020.7\(1\).c1](https://doi.org/10.21272/jes.2020.7(1).c1)
10. Sun, C., Xue, Q., Zhang, J., Wan, S., Tieu, A.K., Tran, B.H.: Growth behavior and mechanical properties of Cr-V composite surface layer on AISI D3 steel by thermal reactive deposition. *Vacuum* **148**, 158–167 (2018)
11. Xu, X., et al.: Research on microstructures and properties of Inconel 625 coatings obtained by laser cladding with wire. *J. Alloy. Compd.* **715**, 362–373 (2017)
12. Lazar, A.M., et al.: Corrosion protection of 304L stainless steel by chemical vapor deposited alumina coatings. *Corros. Sci.* **81**, 125–131 (2014)
13. Yang, J., et al.: Thermal cycling behavior of quasi-columnar YSZ coatings deposited by PS-PVD. *J. Therm. Spray Technol.* **26**(1–2), 132–139 (2017). <https://doi.org/10.1007/s11666-016-0491-8>
14. Thanh, D.T.M., et al.: Controlling the electrodeposition, morphology and structure of hydroxyapatite coating on 316L stainless steel. *Mater. Sci. Eng.* **33**(4), 2037–2045 (2013)
15. Belkin, P.N., Kusmanov, S.A.: Plasma electrolytic hardening of steels. *Surf. Eng. Appl. Electrochem.* **52**(6), 531–546 (2016). <https://doi.org/10.3103/S106837551606003X>
16. Sorsa, A., Santa-aho, S., Aylott, C., Shaw, B.A., Vippola, M., Leiviskä, K.: Case depth prediction of nitrided samples with Barkhausen noise measurement. *Metals* **9**(3), 325 (2019)
17. Nam, N.D., Xuan, N.A., Van Bach, N., Nhung, L.T., Chieu, L.T.: Control gas nitriding process: a review. *J. Mech. Eng. Res. Dev. (JMERE)* **42**, 17–25 (2019)
18. Kochmański, P., Nowacki, J.: Activated gas nitriding of 17–4 PH stainless steel. *Surf. Coat. Technol.* **200**(22–23), 6558–6562 (2006)
19. Pavlenko, I., et al.: Parameter identification of cutting forces in crankshaft grinding using artificial neural networks. *Materials* **13**(23), 5357 (2020). <https://doi.org/10.3390/ma13235357>
20. Spies, H.-J., Reinhold, B., Wilsdorf, K.: Gas nitriding–process control and nitriding non-ferrous alloys. *Surf. Eng.* **17**(1), 41–54 (2001)
21. Pavlenko, I., Zajac, J., Kharchenko, N., Duplák, J., Ivanov, V., Kostyk, K.: Estimation of wear resistance for multilayer coatings obtained by nitrogenchroming. *Metals* **11**(8), 1153 (2021). <https://doi.org/10.3390/met11081153>
22. Akhtar, S.S., Arif, A.F.M., Yilbas, B.S.: Evaluation of gas nitriding process with in-process variation of nitriding potential for AISI H13 tool steel. *Int. J. Adv. Manuf. Technol.* **47**(5), 687–698 (2010). <https://doi.org/10.1007/s00170-009-2215-4>

23. Dhafer, W.A.R., Kostyk, V.O., Kostyk, K.O., Glotka, A., Chechel, M.: The choice of the optimal temperature and time parameters of gas nitriding of steel. *East Eur. J. Adv. Technol.* **3**(5), 44–50 (2016)
24. Kostyk, V.O., Kostyk, K.O., Kovalov, V.D., Turmanidze, R., Dašić, P.: Increase of operational properties of tools and machine parts nitriding the powder mixture. In: *IOP Conference Series: Materials Science and Engineering*, vol. 568, no, 1, p. 012118 (2019)
25. Alphonse, M., Bupesh Raja, V.K., Gupta, M., Logesh, K.: Optimization of coated friction drilling tool for a FML composite. *Mater. Manuf. Processes* **36**(3), 351–361 (2021)
26. Özdemir, İB., Lippmann, N.: Modeling and simulation of surface reactions and reactive flow of a nitriding process. *Surf. Coat. Technol.* **219**, 151–162 (2013)



Cladded Ferromagnetic Powders for Magnetic Abrasive Working of Hard Alloys

Vladimir Lebedev¹ , Svetlana Yakubovskaya²,
Eshreb Dzhemilov³  , and Ruslan Dzhemalyadinov³ 

¹ Physical and Technical Institute of the National Academy of Sciences
of Belarus, 10, Kuprevicha Street, 220141 Minsk, Belarus

² Belarusian National Technical University, 65, Independence Avenue,
220013 Minsk, Belarus

³ Crimean Engineering and Pedagogical University named after Fevzi Yakubov,
8, Uchebnyy side Street, Simferopol 29501, Ukraine

Abstract. The influence of the composition and structure of ferromagnetic composite powders on the surface morphology of hard alloys of titanium-cobalt and tungsten-cobalt groups during magnetic-abrasive processing has been investigated. The mechanisms of contact interaction of a ferro-abrasive quasi-plastic medium with the surface of hard alloys are established. Ferromagnetic abrasive powders have been developed for the processing of hard alloys. It is shown that a composite powder clad with silicon carbide and diamond grains has a more intense effect on the surface of hard alloy plates. It increases the intensity of the abrasive component and reduces adhesion during the contact interaction of the powder matrix and the hard alloy. The microhardness of the surface layer of the hard alloy increases by 20–47% relative to the initial one, which is associated with the combined action of the ferromagnetic abrasive powders particles and the magnetic field, which cause deformation of the crystal lattice, an increase in the concentration of dislocations, and refinement of brittle phases.

Keywords: Magnetic abrasive working · Ferro-abrasive powders · Composition · Structure · Surface morphology · Contact interaction · Hard alloy

1 Introduction

In modern mechanical engineering, the technical level of technologies and innovations in the machine building and tool industries is played by the technical level of technologies and innovations. Machining the functional surfaces of parts determines their operational characteristics and the economy of production as a whole.

Modern machining production is aimed at automating processes and uses resource-saving technologies, requiring a reliable cutting tool that excludes equipment failures and an increased risk of rejects. The processes of finishing their functional surfaces, which are more often carried out with abrasive tools. In this case, abrasive processing can be carried out by a rigidly bound, free, and mobile-coordinated medium [1–4]. The latter type is carried out, for example, the most promising from the point of view of productivity and control of processing parameters by the magnetic-abrasive method.

2 Literature Review

Magnetic-abrasive processing is carried out due to the relative movement of the workpiece and abrasive grains, which are coordinated by the magnetic field into the working environment. The magnetic abrasive machining (MAM) method is quite effective when processing flat, shaped, and complex-shaped parts made of various materials. Features of MAM and the ability to control the parameters of the process without interrupting it made it possible to process and assembled parts from dissimilar materials [5–7].

The efficiency of magnetic abrasive machining largely depends on the characteristics of the cutting tool [8]. In MAM, the role of a tool played by magnetic abrasive powders (MAP), bound and coordinated by a magnetic field into the working environment. Magnetic field carries out a controlled interaction of abrasive grains to the surface to be treated, their reorientation during operation to carry out the process of cutting and plastic deformation. Besides MAP, the working environment often contains technological media (pastes, lubricants, etc.) [9–13].

The efficiency of the process is determined by the action of a set of factors: the magnitude and gradient of the magnetic field in the working gap, composition, structure, shape, size, and morphology of MAP particles, distribution of MAP in the working gap [14, 15].

With MAM, the working grains come into contact with the treated surface with abrasive particles and a ferromagnetic base (matrix material). The abrasive component MAP carries out microcutting and dispersion of the surface layer, crushing and smoothing of its microroughness, and the matrix only smoothes the tops of the microprofile and carries out the dispersion products [16, 17].

Despite the low dynamic loads and the size of the removed chips, with MAM, the material is hardened and softened in the surface layer due to the repeated cyclic mechanical action of the medium on the processed material [5, 7, 18]. With MAM, chip formation is significantly different from the cutting process with a fixed abrasive. Up to 50% of the material from the micro-scratch is squeezed into piles, which are removed during subsequent contact with the working medium. It is typical not only for ductile but also for brittle materials. The rheological properties of the working medium play an essential role in this process. They ensure the pressing of MAM grains to the treated surface. The protrusion of the cutting grains from the MAP matrix is not great, and under the action of a strong magnetic field, there is a simultaneous interaction with the processed material of both the cutting tips and the ferromagnetic base.

MAM performance depends on the strength of the magnetic origin and the mechanical component. It occurs due to the compaction of the MAP in the wedge-shaped or crescent-shaped working gap and the collision of the ferromagnetic abrasive powders (FAP) particles with the processed surface. The morphology of particles and their cutting edges, the number of particles simultaneously in contact with the processed surface also affect the productivity and quality parameters of the processed surfaces.

Cutting elements in ferromagnetic abrasive powders are usually grains of aluminum oxide, titanium carbide, tungsten carbide, silicon carbide, and tops and edges of powder from sprayed alloys [17–19]. Such MAPs have a low concentration of cutting elements

on the grain surface. The abrasive ability of such MAPs decreases sharply as the cutting edges become dull.

The cladding method makes it possible to obtain ferroabrasive powders with a surface arrangement of abrasive grains. All other things being equal, it provides a higher concentration of vertices involved in the cutting process. A change in the concentration of abrasive grains involved in the cutting process affects the performance of the magnetic-abrasive processing process and the surface morphology of the processed material. Under these conditions, the scale factor of the ratio of the sizes of the particles of the magnetic base and the abrasive particles is very important.

3 Research Methodology

The object of the study was ferromagnetic composite powders clad with silicon carbide and diamond. FAP with grain size from 630/400 to 200/100 was used as a base. Powders of silicon carbide (SiC) and AC4 diamond with grain sizes of 10/7 and 80/63 were used as abrasive fillers. Solutions of phenol-formaldehyde resin in alcohol-acetone solution (50 to 50 vol. %) were used as a binder. The concentration of phenol-formaldehyde resin in the alcohol-acetone solution was a mass fraction of 10, 20, and 30%. The ratio of the components in the charge ferromagnetic powder-silicon carbide (diamond) phenol-formaldehyde resin mass fraction was 60:30:10%.

Silicon carbide cladding of ferromagnetic abrasive powders was obtained as follows. A phenol-formaldehyde resin solution was added to the FAP, mixed, and then silicon carbide powder was added. The batch mixture was mixed, dried, and heat-treated at 375°K for 1 h. After drying, the agglomerate formed from the loosely bound particles was crushed and then sieved on sieves of 600/400 and 315/250 μm . The resulting powder was heat-treated at 435°K for 20 min. The FAP Ferabraz 310 and Zh15KT clad with silicon carbide was compared with a composite powder, which is a matrix of copper ferrite, in which silicon carbide grains are located.

The concentration of SiC particles in the clad powder and the composite powder mass fraction was 12 wt.% and 25 vol. %. FAP Ferabraz 310 with grain size 315/100 and Zh15KT with grain size 630/400 and 400/100 were clad with diamond AC4 with grain size 40/28 and 10/7. The concentration of diamond grains in the ferroabrasive composite powders mass fraction was 8 and 15%.

Ferroabrasive composite powders were used for magnetic abrasive processing of plates made of MC111, MC131 and MC241 hard alloy and tungsten-free hard alloy TN20, of molds 02114-100608, 03114-150412, 10113-110408 was carried out on an upgraded SFT 2.150 installation. The processing time in the experiments was 2–30 min. The plates were fixed on specially designed mandrels made of steel 10 and non-magnetic alloy AlCuMg1. The cutting speed during processing was 0.5–3 m/s and was regulated by the spindle rotation frequency. The working gap of the electromagnetic system poles was 1–3 mm. The current in the coils varied within 1–25 A, the magnetic field strength in the gap was 0.6–1.5 T. The study of the morphology and microstructure of the surface of ferromagnetic composite powders and treated plates of hard alloys was carried out on scanning electron microscopes VEGA TESCAN, MIRAS TESCAN, and optical microscopes.

4 Results

The study of the morphology of clad ferromagnetic powders showed that on the surface of the particles, there are silicon carbide grains distributed over the surface with their concentration in the depressions and near the protrusions (Fig. 1).

The surface morphology of a composite ferroabrasive particle in the case of using a powder with a grain size of 10/7 is a shell of silicon carbide particles, the spaces between which are filled with phenol-formaldehyde resin (Fig. 1b). When using larger particles of silicon carbide (grain size 80/63) as cutting elements, the surface morphology of the ferroabrasive particle is formed by separately located particles of silicon carbide (Fig. 1c). Thus, a finer-grained abrasive provides a higher concentration of cutting tips on the FAP particles. The filler does not cover the initial microrelief and the working tips of the particles themselves.

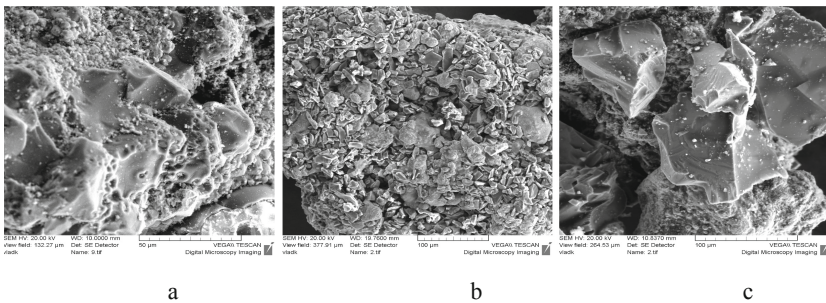


Fig. 1. Surface morphology of clad FAP (The concentration of phenol-formaldehyde resin in the solution is 10 wt. %. Grain size of silicon carbide, microns: a - initial FAP, b - 10/7; c - 80/63).

In the clad FAP, along with the particles of the main fraction (500–315 μm), there are particles of other sizes (Fig. 2a). Particles over 500 μm are agglomerates of fine particles, interlayers of phenol-formaldehyde resin. Smaller particles (315 μm) are agglomerates of silicon carbide and phenol-formaldehyde resin FAP (Fig. 2b).

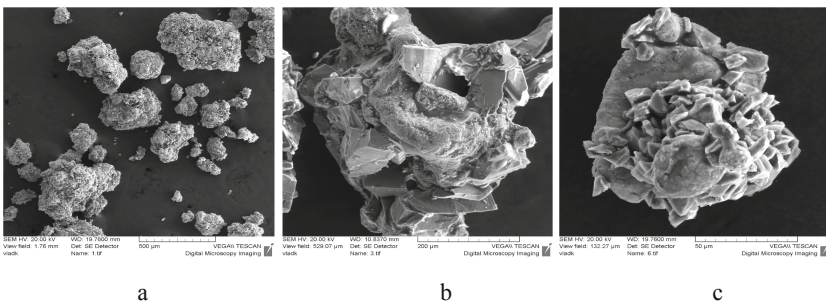


Fig. 2. Surface morphology of agglomerates (Silicon carbide grain size, microns: a - general view of FAP, b - 80/63, c - 10/7).

The use of more concentrated solutions of phenol-formaldehyde resin (20–30 wt. %) for cladding the FAP changes the surface morphology of composite particles. The silicon carbide particles are in the polymer layer on the surface of the ferromagnetic particle, and the cutting edges are poorly expressed. The abrasive ability of such powders is expectedly low.

A phenol-formaldehyde resin film at the interface also provides the adhesion of the SiC grain to the ferromagnetic base. Bond strength can be increased by increasing the thickness of the polymer film by double application of the resin solution (Fig. 3).

After repeated cladding of FAP, drying, and crushing the cake, the content of the powder fraction in the charge is 100 μm to 8 wt. %. Thus, the formation of ferromagnetic-abrasive composite powders by the cladding method makes it possible to increase the content of abrasive particles on the FAP surface, which should increase the productivity of magnetic abrasive processing.

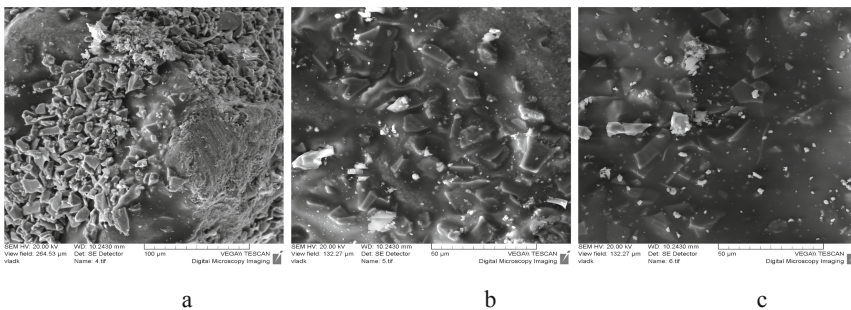


Fig. 3. Surface morphology of a ferroabrasive particle after double cladding with a phenol-formaldehyde resin solution with SiC grain size 10/7 (The concentration of phenol-formaldehyde resin in solution, wt. %: a - 10; b - 20; c - 30).

It is expected that cladding FAP with diamond should increase its abrasive ability due to the high hardness of the diamond and the presence of a large number of sharp peaks on grains of the AC4 grade. The distribution of diamonds over the surface of the FAP particles provides its developed morphology with the presence of groups of diamond filler in the deepening of the FAP particles (Fig. 4c). An increase in the concentration of diamond from 8 to 15 wt. % ensures the presence of sharp elements over almost the entire surface of the FAP.

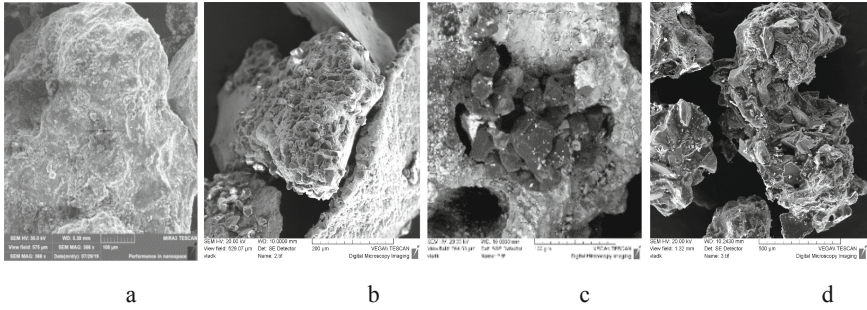


Fig. 4. Surface morphology of FAP Zh15KT 315/250 (a–c) and Ferabraz 310 630/100, clad with a phenol-formaldehyde resin solution with AS4 diamond with a grain size of 10/7 (Diamond concentration, wt. %: a, c - 8, b, d - 15).

The study of the surface morphology of ferromagnetic abrasive powders showed that the cutting elements in the clad FAP are the tops and edges of silicon carbide or diamond grains. In the Ferabraz composite powder, there are rounded tops of particles and developed protrusions on their surface.

Magnetic-abrasive treatment of MC111 hard alloy plates with Ferabraz 310 clad powder leads to forming a characteristic microrelief on the treated surface in the form of a set of ridges with smoothed peaks and valleys between the ridges. The ridges are oriented in the direction of the cutting speed vector during machining. Against the background of ridges and depressions, there are depressions formed by crumbling titanium carbide crystals (Fig. 5). The use of a composite powder based on copper ferrite with a uniform arrangement of silicon carbide grains as a FAP and when using a silicon carbide-clad Ferabraz 310 powder leads to the formation of a similar microrelief on its surface. However, the difference lies in the absence of crumbling carbide crystals in the ridges of the relief.

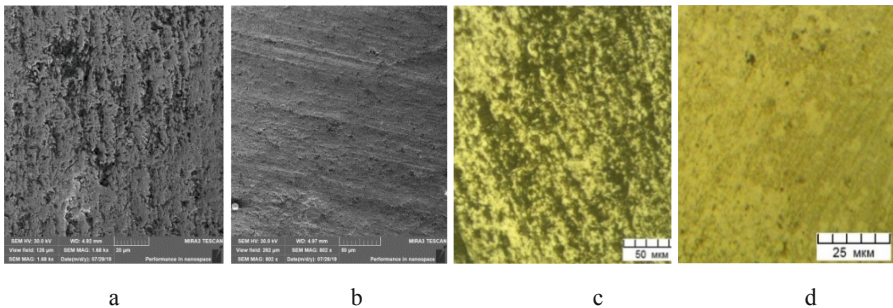


Fig. 5. Surface morphology of a plate of hard alloy MC111 after magnetic-abrasive processing with a clad (Ferabraz 310 630/400-a, composite FAP 400/250 reinforced with SiC 10/7-b, FAP Zh15KT 400/250 clad with AS4 10/7 - c, FAP Ferabraz 310 315/100. Processing time: a – 5 min; b, c – 10 min; d – 15 min).

Analysis of the treated surfaces showed that the diamond-clad FAP Zh15KT exerted the most intense effect on the hard alloy surface. The dynamic effect of FAP manifests itself in varying degrees of destruction of crystals of titanium carbide and tungsten.

After the treatment of MC111 with clad abrasive powders, the titanium carbide grains are partially destroyed, and the cobalt alloy interlayer between them wears out, and the carbide grains protrude above the hard alloy surface. There are no sharp edges on the surface in Ferabraz 310 ferromagnetic powder. The hardness of the alloy and intermetallic particles in it is less than the hardness of silicon carbide grains. As a result, surface treatment of carbide plates does not lead to the destruction of carbide grains; the tops of the grains of titanium and tungsten carbide are rounded. The microrelief is smoother.

The subsequent increase in the duration of the magnetic abrasive processing up to 20 min is accompanied by a change in the microrelief of the surface of the MC111 alloy plates: the initial relief after diamond grinding from the ridges and depressions disappears. The number of depressions from the chipped grains of titanium and tungsten carbides decreases (Fig. 6 c, d).

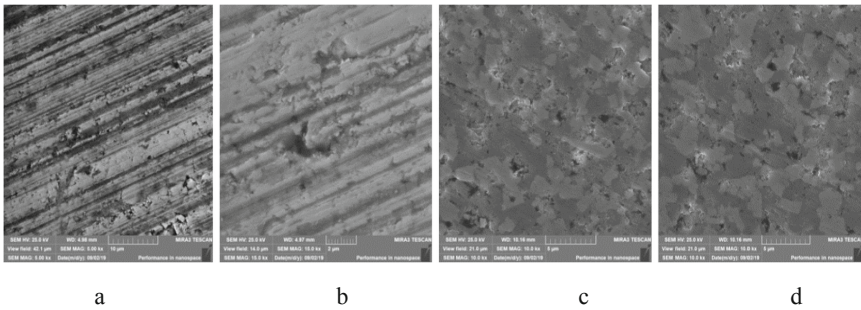


Fig. 6. Morphology of the front surface of the SNMA-150412 MC111 plate after magnetic-abrasive treatment of FAP Zh15KT 400/250 with clad AC4 40/28 - a, AC4 10/7 - b, c, d (Processing time, min: a – 5; b – 10; c – 15; d – 20).

An increase in the concentration of diamond in the clad FAP up to 15 wt. % leads to a faster change in the hard alloy's original texture and surface relief with a processing time of 3–5 min. An increase in the processing time up to 10 min does not lead to a significant change in the surface morphology of the hard alloy plate; the number of depressions from crumbling carbide grains decreases. It may be due to a decrease in the abrasive ability of the FAP due to brittle fracture, chipping, and a decrease in the number of cutting tips of the diamond filler and rounding of the FAP particles themselves.

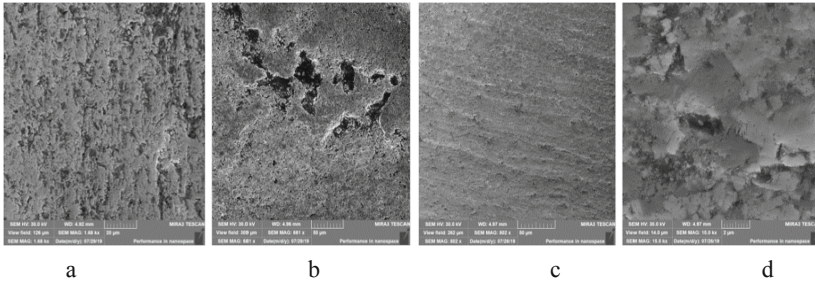


Fig. 7. Morphology of the front surface of the SNMA-150412 MC241 plate after magnetic-abrasive treatment of FAP Zh15KT 400/250 with clad AC4 40/28 - a, AC4 10/7 - b, c, d (Processing time, minutes: 3 a, 10 b, 15 c, 30 g. Diamond concentration 8 wt. %).

When processing the MC241 hard alloy, the microrelief formed on their surface combines protrusions of tungsten carbide particles and depressions – worn-out layers of cobalt binder.

Magnetic abrasive treatment of MC241 FAP hard alloy plates with a diamond grain concentration of 8 wt. % leads to a noticeable change in the initial relief of the surface of the plate after processing for 5 min (Fig. 7 a). After processing for 15 min, the original surface texture is partially retained on the surface of the hard alloy plate in the form of a trace of diamond grinding with single chipped-off grains of tungsten carbide (Fig. 7 b). After 20–30 min of processing, the surface of the plate acquires a chaotically worn relief. In this case, only the macrodepressions present on the surface of an untreated plate of MC241 hard alloy due to sintering defects remain.

After 3–5 min of treatment, magnetic abrasive treatment of the MC241 FAP hard alloy with a diamond grain concentration of 15 wt. % causes the original texture to disappear. After treatment for 15 min, the initial surface relief completely disappears, and a microrelief is formed due to the abrasive action of the FAP on the hard alloy surface. Magnetic abrasive processing of hard alloys and MC111 and MC241, regardless of the concentration of diamond powder in the magnetic abrasive powder, leads, first of all, to wear of the protruding ridges – a trace of diamond grinding. When processing platinum of the hard alloy MC111, a smoothed microrelief is formed on their surface, formed by flat tops of titanium carbide particles and interlayers between them.

Figure 7d shows that the tungsten carbide grains retained their integrity after 10 min of processing. The cobalt interlayers between the grains are not worn out. After the magnetic-abrasive treatment of the plates of the MC241 FAP 400/100 hard alloy, on the surface of the plates against the background of waviness, there is a relief oriented in the direction of the machining marks, the tungsten carbide grains are partially destroyed, and there are microcracks and scratches on individual grains.

The results showed that with a MAP of hard alloys, the FAP performance decreases after 10–15 min of operating time. It is confirmed by studying the morphology of the FAP particles, observations of the kinetics of their composition, shape, and size. Thus, the clad FAP after 15 min of treatment of the MC241 hard alloy begins to lose the

abrasive coating in certain areas of the particle surface (Fig. 8b). Investigation of the surface morphology of magnetic-abrasive particles of 400/100 μm fraction after processing a plate of hard alloy MC241 showed that only individual particles of silicon carbide remained on the surface of the particles (Fig. 8b). The efficiency of diamond powder in the process of magnetic-abrasive processing of hard alloy is higher (Fig. 8c). A more intense abrasive effect on the surface of the FAP hard alloy with a grain size of 400/100 is associated with the participation of large areas of the surface in the contact interaction processes than 630/500 particles. FAP 400/100 contains both magnetic particles clad with silicon carbide and agglomerates of silicon carbide particles with a small magnetic particle. These agglomerates have a different surface morphology than clad particles, which have more protruding sharp edges and tops of silicon carbide or diamond particles. In addition, the size of the agglomerates is smaller than the size of the clad particles of the main fraction 400/250. Therefore, in the process of magnetic abrasive processing, the agglomerates can be more pressed against the hard alloy plate by clad particles. Under these conditions, silicon carbide grains can penetrate the surface of the carbide plate and form tracks characteristic of the abrasive wear mechanism. The intense abrasive effect on the hard alloy surface of 400/100 ferromagnetic composite powders is due to both the fractional composition and the shape of the smaller magnetic particles, which provide a high concentration of silicon carbide particles in the cladding layer.

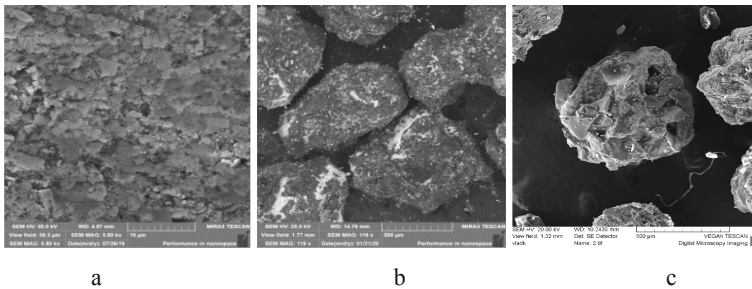


Fig. 8. Surface morphology of MC241 hard alloy after 10 min of magnetic-abrasive processing with clad FAP (a-Zh15KT 630/400, b-FAP 400/100 clad SiC 10/7 after 15 min of operation, c-morphology of FAP 400/100 clad with diamond 40/28 after 10 min of work).

The important positive aspect of magnetic abrasive processing is an increase in the microhardness of the processed material in the surface layer. It was found that under the treatment conditions adopted in the study, the microhardness of the MC241 surface layer increases by 20–47% relative to the initial one. In this case, the phenomena of plastic deformation caused by the combined action of the FAP particles and the magnetic field, which cause twisting of the lattice of the structural components of the hard alloy, an increase in the concentration of dislocations, and refinement of brittle phases, are of great importance. On hard alloy MC241, a sublayer maximum of

microhardness is found due to magnetic abrasive processing. It reaches values of 1800–1940 HV. The depth of the maximum is 10–20 μ and grows to 25–35 μ with an increase in the cutting speed and grain size of the FAP from 200/100 to 400/250. The total thickness of the layer with the changed structure and properties of the hard alloy after magnetic abrasive processing reaches 100–200 μ .

5 Conclusion

It has been established that the morphology of clad ferromagnetic composite powders, the adhesion strength of silicon carbide and diamond particles to the base depends on the concentration of the phenol-formaldehyde resin solution. When the concentration of the binder in the solution is 10 wt. %. The morphology of the FAP surface is a shell of silicon carbide particles, the spaces between which are filled with resin. Application for cladding resin solutions with 20 and 30 wt. % changes the surface morphology of FAP particles, and abrasive grains are in the polymer layer. The adhesion of the abrasive grains to the ferromagnetic base can be increased by increasing the thickness of the polymer film by reapplying the phenol-formaldehyde resin solution.

It is shown that during magnetic-abrasive processing of a hard alloy, fine-grained FAPs (400/100 and less) have a more intense abrasive effect on the plate surface. On the surface of the plates, against the background of the wavy relief, there are tracks oriented in the direction of machining. Tungsten carbide grains are partially destroyed, microcracks and scratches are present on individual grains, cobalt interlayers between grains are not destroyed. Ferromagnetic powders with a wide range of particle sizes are more efficient in processing hard alloys due to the participation of a larger number of silicon carbide and diamond particles in the cladding layer.

In further studies planned to obtain new coated powders containing abrasive particles of synthetic diamond coated with non-metallic refractory elements, applied by chemical deposition with subsequent thermolysis.






References

1. Berdichevsky, E.G.: Energetic activation of the processes of abrasive diamond metal processing. *IOP Conf. Ser. Mater. Sci. Eng.* **656**, 012012 (2019)
2. Singh, S., Gupta, V., Sankar, M.R.: Magnetic abrasive finishing process. In: Das, S., Kibria, G., Doloi, B., Bhattacharyya, B. (eds.) *Advances in Abrasive Based Machining and Finishing Processes*. MFMT, pp. 183–210. Springer, Cham (2020). https://doi.org/10.1007/978-3-030-43312-3_8
3. Maiboroda, V.S., Belajev, O.O., Dzhulii, D., Slobodianiuk, I.V.: AISI 1045 steel flat surfaces machining using the magneto-abrasive method. *J. Eng. Sci.* **7**(1), A1–A7 (2020). [https://doi.org/10.21272/jes.2020.7\(1\).a1](https://doi.org/10.21272/jes.2020.7(1).a1)
4. Zou, Y., Xie, H.: Investigation on the improvement of surface quality by the magnetic plate-assisted magnetic abrasive finishing process. *Mater. Sci. Forum* **1018**, 111–116 (2021)
5. Maiboroda, V.S., Nalimov, Y.S., Solovar, A.N., Bobina, M.N., Teslyuk, N.N.: Effect of complex magnetic-abrasive and chemical/thermal treatment on VT9 alloy fatigue resistance. *Strength Mater.* **48**(5), 704–712 (2016)

6. Maiboroda, V., Tarhan, D., Dzhulii, D., Slobodianiuk, I.: Features of magneto-abrasive machining of taps. *Acta Mech. Autom.* **14**(1), 1–7 (2020)
7. Karpuschewski, B., Byelyayev, O., Maiboroda, V.S.: Magneto-abrasive machining for the mechanical preparation of high-speed steel twist drills. *CIRP Ann. Manuf. Technol.* **58**(1), 295–298 (2009)
8. Shvets, S.V., Astakhov, V.P.: Effect of insert angles on cutting tool geometry. *J. Eng. Sci.* **7**(2), A1–A6 (2020). [https://doi.org/10.21272/jes.2020.7\(2\).a1](https://doi.org/10.21272/jes.2020.7(2).a1)
9. Khattri, K., Choudhary, G., Bhuyan, B.K. and Selokar, A.: A Review on Parametric Analysis of Magnetic Abrasive Machining Process. *IOP Conf. Ser.: Mater. Sci. Eng.* **330**, 012105 (2018).
10. Pavlenko, I., et al.: Parameter identification of cutting forces in crankshaft grinding using artificial neural networks. *Materials* **13**(23), 5357 (2020). <https://doi.org/10.3390/ma13235357>
11. Nahy, A.M., Kadhum, A.H.: Optimizing the micro-hardness of a surface by magnetic abrasive finishing. *IOP Conf. Ser. Mater. Sci. Eng.* **870**, 012018 (2020)
12. Dra umerič, R., Badger, J., Roininen, R., Krajnik, P.: On geometry and kinematics of abrasive processes: the theory of aggressiveness. *Int. J. Mach. Tools Manuf.* **154**, 103567 (2020)
13. Ivanov, V., Pavlenko, I., Liaposhchenko, O., Gusak, O., Pavlenko, V.: Determination of contact points between workpiece and fixture elements as a tool for augmented reality in fixture design. *Wirel. Netw.* **27**(3), 1657–1664 (2019). <https://doi.org/10.1007/s11276-019-02026-2>
14. Farwaha, H.S.: Microstructure and performance investigation of magnetic abrasive particles. *J. Crit. Rev.* **7**(19), 289–295 (2020)
15. Qian, C., Fan, Z., Tian, Y., Liu, Y., Han, J., Wang, J.: A review on magnetic abrasive finishing. *Int. J. Adv. Manuf. Technol.* **112**(3–4), 619–634 (2020). <https://doi.org/10.1007/s00170-020-06363-x>
16. Jackson, M.J.: Recent advances in ultraprecision abrasive machining processes. *SN Appl. Sci.* **2**(7), 1–26 (2020). <https://doi.org/10.1007/s42452-020-2982-y>
17. Baron, Y.M.: Magnetic abrasive deburring technology for blanks. *Int. J. Eng. Res. Afr.* **25**, 1–10 (2016)
18. Zou, Y., Xie, H., Zhang, Y.: Study on surface quality improvement of the plane magnetic abrasive finishing process. *Int. J. Adv. Manuf. Technol.* **109**(7–8), 1825–1839 (2020). <https://doi.org/10.1007/s00170-020-05759-z>
19. Rodichev, Y., Soroka, O., Kovalov, V., Vasilchenko, Y., Maiboroda, V.: Fracture resistance of the edge of cemented carbide cutting tool. In: Tonkonogyi, V., et al. (eds.) *InterPartner 2019. LNME*, pp. 281–288. Springer, Cham (2020). https://doi.org/10.1007/978-3-030-40724-7_29



Comparison of Effects of Laser, Ultrasonic, and Combined Laser-Ultrasonic Hardening Treatments on Surface Properties of AISI 1045 Steel Parts

Dmytro Lesyk¹ , Walid Alnusirat² , Silvia Martinez³ ,
Bohdan Mordyuk⁴ , and Vitaliy Dzhemelinskyi¹ 

¹ Igor Sikorsky Kyiv Polytechnic Institute, National Technical University of Ukraine, 37, Prosp. Peremohy, Kyiv 03056, Ukraine

lesyk_d@ukr.net

² Al-Balqa Applied University, Al-Salt 19117, Jordan

³ University of the Basque Country, 48170 Zamudio, Spain

⁴ G.V. Kurdyumov Institute for Metal Physics, NAS of Ukraine, Kyiv 03680, Ukraine

Abstract. An ultrasonic impact treatment (UIT) in combination with laser heat treatment (LHT) is proposed to improve surface roughness and enhance the subsurface grain refinement and residual stress of hypoeutectoid steel. The LHT treatment was conducted using a fiber laser with 2D scanning optics. The UIT treatment was performed using a multi-pin ultrasonic tool. The surface texture, roughness parameters, and surface hardness of the UIT, LHT, UIT+LHT, and LHT+UIT hardened samples were studied and compared. The surface roughness and hardness were under special attention as possible key factors to additional optimization of the UTI duration. The results indicated that the combined UIT+LHT technique could be applied to get both significant surface hardness and hardening depth in AISI 1045 medium carbon steel. The combined LHT-UIT hardened specimens exhibited the lowest surface roughness and highest surface hardness, which was attributed to the surface attributed to the surface relief and ultrafine-grained martensitic structure in the subsurface formation.

Keywords: AISI 1045 Carbon Steel · Combined LHT+UIT · Combined UIT+LHT · Hardness · Roughness · Topography

1 Introduction

Nowadays, selective surface modification is one of the effective ways to increase the wear and corrosion resistance of carbon steel parts by changing the parameters of the surface relief parameters and structure of the subsurface layer. Given that a large number of metal components work in extreme conditions, conventional surface modification methods often do not allow getting the required surface properties. On the other hand, the use of high-strength materials is often economically unprofitable.

On the one hand, the laser surface hardening process can be applied selectively to increase the wear and corrosion resistance of complexly shaped metal parts, keeping the same chemical composition. On the other hand, the laser surface hardening combined with the surface plastic deformation techniques allows getting a much greater impact in increasing the wear and corrosion resistance of carbon steel parts.

Thereby, the development of combined thermo-mechanical hardening and finishing technologies for surface treatment of carbon steel parts becomes especially relevant.

2 Literature Review

One of the most promising directions is the improvement of technological processes for surface treatment of carbon steel components hardened by the laser beam [1], plasma arc [2], and electron beam [3]. For instance, the plasma surface hardening method can be applied to treat large-scale components, while the electron beam surface hardening method is used for surface modification of small-sized metallic components. However, recently advanced laser hardening systems using a diode laser [4], fiber laser [5], and disk laser [6] can significantly improve the productivity and efficiency of the laser heat treatment (LHT), both small-sized and large-scale carbon steel parts. At the same time, the application of the high-tech 2D scanning optics [7, 8] and 3D scanning optics [6, 9] result in an increase in the laser spot size of more than 50 mm. In most cases, it allows avoiding the overlapping of the laser beam, which caused the heterogeneous hardness in the subsurface layers of AISI S7 tool steel [4], AISI T1 tool steel [10], and AISI 1045 carbon steel [10, 11] via the tempered martensitic structure formation in the overlapping area of the laser beam.

The laser transformation hardening process consists of high-speed local heating of the surface layer by a laser beam above critical temperature points for the austenitic structure formation and subsequent rapid cooling of the treated surface using heat transfer in the inner layers of the material [4, 12]. As a consequence, the fine-grained martensitic structure is formed due to phase transformations, which are characterized by a high wear resistance for AISI 1045 steel [13], R260 grade rail steel [14], and AISI 8620 steel [15], corrosion resistance for AISI 1045 steel [16], and fracture resistance for AISI 1040 steel [17]. It should also be noted that the martensitic-austenitic structure formation depends on the laser surface hardening regimes and the carbon concentration in the alloy. Increasing the concentration of carbon in the carbon steels is accompanied by an increase in the hardening depth through increment in the calcination. Conversely, reducing the hardening depth and increasing the hardening width in the carbon steels occurs with increasing the carbon content due to the reduction of thermal conductivity [18]. The effect of LHT on the hardening depth [19, 20], structure [21, 22], phase transformation [23], grain size [13], hardness distribution [24], and residual stress [25] of hypoeutectoid steels were widely studied.

To significantly increase the fatigue life and wear resistance of hypoeutectoid steels, the combined thermo-mechanical surface hardening and finishing techniques can be applied using the LHT process combined with severe surface plastic deformation methods, such as a laser shock peening [26] or submerged laser shock peening [27], shot peening [28], submerged cavitation peening [29], ultrasonic impact peening [30], etc.

The work aims to study the effects of the UIT, LHT, combined UIT+LHT, and combined LHT+UIT techniques on the surface texture, roughness, and hardness of hypoeutectoid steel.

3 Research Methodology

The flat polished specimens 20 mm thick of AISI 1045 medium-carbon steel, which chemical composition is listed in Table 1, were processed by the ultrasonic impact treatment (UIT), laser heat treatment (LHT), and their combinations (UIT+LHT and LHT+UIT) with the optimized parameters [19].

Table 1. Chemical composition of AISI 1045 carbon steel (wt.%).

Fe	C	Mn	Si	Cr	Ni	Cu	P	S
Bal	0.45–0.5	0.5–0.8	0.17–0.37	≤ 0.25	≤ 0.25	≤ 0.25	≤ 0.035	≤ 0.04

The laser hardening system used was described in more detail elsewhere [13, 16]. The CNC milling center is equipped with a 1 kW fiber laser and galvanometer scanner. In particular, the laser pass of 10 mm wide was scanned with a speed of 1000 mm/s by a high-frequency movement of a laser beam in 1 mm diameter (on the treated part). The LHT parameters of the studied steel are given in Table 2.

Table 2. Laser heat treatment parameters.

Specimen marking	Heating temperature (°C)	Specimen feed rate (mm/min)	Treatment duration (s)	Energy density of laser beam (kJ/cm ²)	Power density of laser beam (W/cm ²)
LHT4	1200	40	1.50	97	5.4·10 ³
LHT5		90	0.66	46	5.5·10 ³
LHT6		140	0.42	31	5.8·10 ³

The heat energy density of laser beam E_{lb} (kJ/cm²) was calculated [16]:

$$E_{lb} = P / (d_{lb} \cdot S), \tag{1}$$

where P is the laser power [W], d_{lb} is the diameter of the laser beam [cm], S is the specimen feed rate of the treated surface [cm/min].

The heat power density of laser beam W_{lb} (W/cm²) was estimated [16]:

$$W_{lb} = AP/h_{lb}l_{lb}, \quad (2)$$

where A is the absorption coefficient of surface [%], P is the laser power [W], h_{lb} and l_{lb} are the width and length of the laser beam, respectively [cm].

The calculated power density of the laser beam (Table 2) varies in the range of $10^3 \dots 10^4$ W/cm² at a treatment duration of 1.5...0.42 s, providing the LHT without surface melting.

The UIT treatment was conducted using an ultrasonic vibration system and ultrasonic generator with a frequency of 21.6 kHz and a power output of 0.3 kW. The ultrasonic system contained a piezoceramic transducer, cylindrical waveguide horn, and a seven-pin impact head with a contact diameter of 3 mm. The ultrasonic vibration system was pressed to the treated surface with a static load of 50 N. A seven-pin impact head was mounted at the horn tip and forcedly rotated by a motor. During the UIT treatment, the ultrasonic horn vibrations induced stochastic impacts of the pins (~ 2 kHz) by the treated surface. The UIT parameters are listed in Table 3.

Table 3. Ultrasonic impact treatment parameters.

Specimen marking	Vibration amplitudes of ultrasonic horn (μm)	Treatment duration (s)	Static loading of ultrasonic vibration system (N)	Rotation speed of impact head (rpm)	Specific mechanical energy of pins (mJ/cm^2)
UIT1	18	60	50	76	26
UIT2		120			53
UIT3		180			77
UIT4		240			105

The mechanical energy W_{UIT} (J/cm^2) to the peened surface of the sample was estimated by the formula [16]:

$$W_{UIT} = I_{UIT} \cdot t_{UIT}, \quad I_{UIT} = 4E_{UIT}/\pi d^2, \quad E_{UIT} = 2m_p \pi^2 f_{UIT}^2 A_{UIT}^2 \quad (3)$$

where I_{UIT} is the impact intensity [J/cm^2], t_{UIT} is the treatment duration by UIT [s], E_{UIT} is the energy of high-frequency impact of horn on the pins [J/cm^2], d is the surface accommodated the impact energy per the surface unit area [cm], m_p is the pin mass [g], v_p is the linear speed of the pin, which is equal to the average vibration speed of the horn tip $v_{\perp} = v_p = 2\pi f_{UIT} A_{UIT}$ (m/s), f_{UIT} is the vibration frequency of the ultrasonic horn [μm], A_{UIT} is the vibration amplitude of the ultrasonic horn [μm].

The calculated values of the impact pulse ultrasonic energy in accordance with the formula (3) were given in Table 3.

The 3D surface texture (3×3 mm² area) and roughness parameters were evaluated using an optical profilometer Leica DCM3D following the ISO 25178 and 4287 standards. The R_a parameter is the arithmetical mean height along the sampling length

for a roughness profile. The Sa parameter is the arithmetical mean height of a line to a 3D surface which describes the difference in the height of each point compared to the arithmetical mean of the surface.

The surface hardness was measured using an FM800 digital tester at a load on an indenter of 10 N. To estimate the stress state, the X-ray diffraction (XRD) analysis of the specimens was performed using a Rigaku Ultima IV diffractometer.

4 Results

4.1 Surface Topography

The surface texture was estimated within a cut-off length of 0.8 mm and traverse the length of 2.5 mm using a non-contact profilometer. Figures 1, 2 and 3 show the resulting surface texture and average surface roughness (parameter Ra) of the laser, laser-ultrasonic, ultrasonic, and ultrasonic-laser hardened hypoeutectoid steel samples. Compared to the LHT-hardened samples, a new surface texture/relief is formed after the combined LHT+UIT technique due to severe plastic deformation (Fig. 1). By increasing the UIT duration, the waviness of the LHT+UIT-processed surface and consequently the high surface texture parameters are increased.

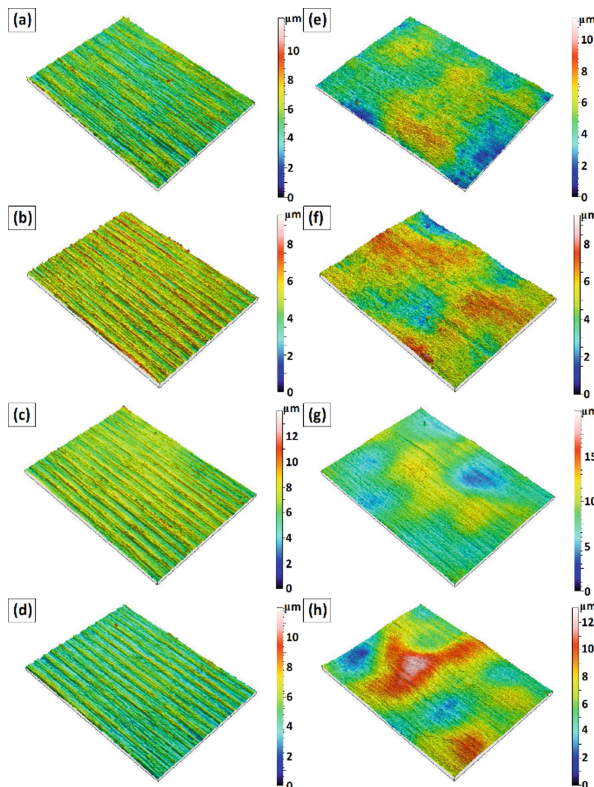


Fig. 1. Surface topography of AISI 1045 carbon steel in the initial state (a) and after LHT4 (b), LHT5 (c), LHT6 (d) and combined LHT5+UIT1 (e), LHT5+UIT2 (f), LHT5+UIT3 (g) and LHT5+UIT4 (h) treatments.

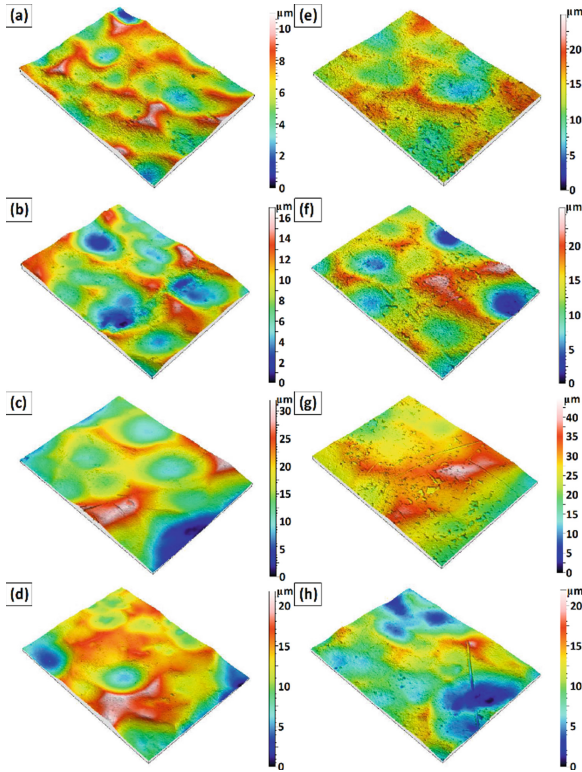


Fig. 2. Surface topography of AISI 1045 carbon steel after UIT1 (a), UIT2 (b), UIT3 (c), UIT4 (d) and combined UIT1+LHT5 (e), UIT2+LHT5 (f), UIT3+LHT5 (g) and UIT4+LHT5 (g) treatments.

Compared to the non-treated and LHT-hardened specimens, the UIT technique or the UIT process followed by the LHT process leads to a significant change of the surface texture, increasing the surface waviness (Fig. 2). Therefore, the increase the cost-effective use lubricants to enhance the wear and friction behaviors can be successfully achieved by the combined UIT+LHT technique.

It should also be noted that the surface roughness of the LHT-hardened specimen is enlarged with specimen feed rate (Fig. 3a). The observed R_a surface roughness parameter (arithmetical mean height of a line) well correlates to the S_a area surface roughness (arithmetical mean height parameter of the surface). Due to the severe surface plastic strain, the UIT treatment-induced average surface roughness values were always let down though in different extents (Fig. 3b). It was observed that for the UIT or combined UIT+LHT treatment case, the R_a parameter was slightly higher than the magnitudes for the combined LHT+UIT treatments case.

The application type of the combined thermo-mechanical surface hardening technique depends on the required surface roughness/waviness parameters.

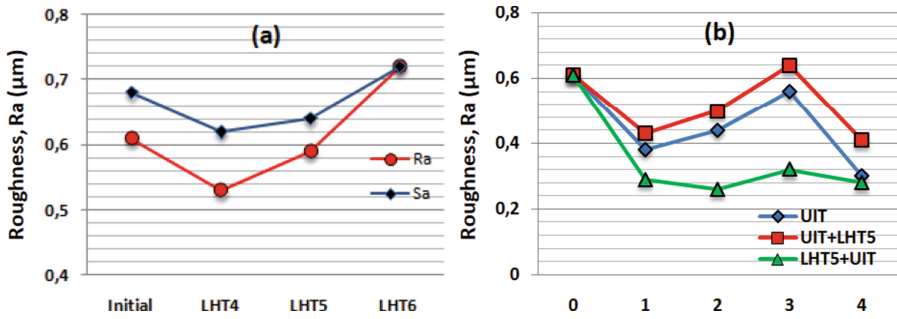


Fig. 3. Surface roughness of AISI 1045 carbon steel of the untreated sample (regime 0) and after LHT4, LHT5, and LHT6 treatments (a), and after UIT1 (regime 1), UIT2 (regime 2), UIT3 (regime 3), UIT4 (regime 4), combined LHT5+UIT1, LHT5+UIT2, LHT5+UIT3, LHT5+UIT4 and combined UIT1+LHT5, UIT2+LHT5, UIT3+LHT5, and UIT4+LHT5 treatments (b).

4.2 Surface Hardness

Figure 4a shows surface macrohardness magnitudes exhibited by the LHT-hardened specimens, varying the feed rate specimen. The average surface hardness for the unprocessed samples was around 18.6 HRC5. It was noted for the lower sample feed rate (40 mm/min) that the average surface hardness was about 52.8 HRC5.

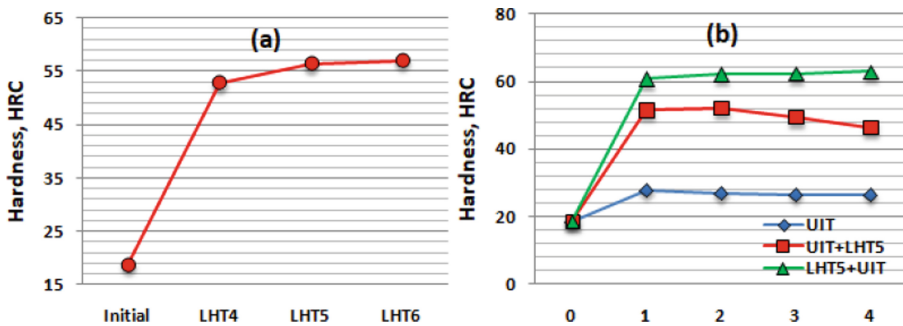


Fig. 4. Surface hardness of AISI 1045 carbon steel of the untreated sample (regime 0) and after LHT4, LHT5, and LHT6 treatments (a), and after UIT1 (regime 1), UIT2 (regime 2), UIT3 (regime 3), UIT4 (regime 4), combined LHT5+UIT1, LHT5+UIT2, LHT5+UIT3, LHT5+UIT4 and combined UIT1+LHT5, UIT2+LHT5, UIT3+LHT5, and UIT4+LHT5 treatments (b).

The surface hardness increased with increasing specimen feed rate, reducing the hardening depth. Despite obtaining the highest surface hardness, the hardening depth was less than 200 μm at the LHT6 regime. To get higher hardening depth and required surface hardness, the LHT treatment must conduct at the heating temperature of 1200 °C and a sample feed rate of ~70 mm/min.

The highest surface hardness was found after the UIT duration of 60 s (Fig. 4b). Further increasing the UIT duration caused a reduction in the average surface

roughness due to the studied steel's surface overstraining. It can be seen that the UIT technique combined with the LHT technique result in a significant enlarge the hardness on the surface regardless of the UIT regime.

Compared to the UIT+LHT technique, the surface hardness magnitudes are slightly higher after the LHT+UIT technique due to the deformation-induced dissolution of retained cementite particles as well as the finer grain structure and white etching layers formation, providing a deeper compressive layer of the residual stress (around – 400 MPa) in the subsurface [13, 16]. Moreover, an oxide film on the surface may be formed after LHT treatment without shielding gas. The main advantage of the combined UIT+LHT technique over the combined LHT+UIT technique is a higher depth of hardening ($\sim 400 \mu\text{m}$) through the laser heating followed by rapid cooling of the preliminary deformed ferrite grains saturated with carbon [13, 19].

Thus, the surface texture/microrelief and structural parameters can significantly impact such important operational properties as the fatigue, wear, and corrosion strength of the hypoeutectoid steels, which largely determine the durability and operational life of the responsible components.

5 Conclusions

The data obtained show that proper selection of the influential LHT and UIT parameters can lead to a good combination of surface integrity and properties.

The UIT duration of 60 s is recommended to select for the combined UIT+LHT method while the UIT duration of 120 s for the combined LHT+UIT method.

The combined UIT+LHT technique can be used to obtain deeper hardening depth than the combined LHT+UIT technique.

To provide the highest surface hardness (compressive residual stress) and the lowest surface roughness/waviness, the combined LHT+UIT technique is recommended for surface finishing and hardening of the AISI 1045 carbon steel.

Acknowledgments. This study is supported financially by the East-West European Network on higher Technical education (EWENT) programme Erasmus Mundus Action 2 Lot 8 and partially supported by the NAS of Ukraine (Project 0119U001167) and the Ministry of Education and Science of Ukraine (the joint Ukrainian-Czech R&D Project for the period of 2021–2022).

References






1. Idan, A.F.I., et al.: The study of the influence of laser hardening conditions on the change in properties of steels. *East. Eur. J. Enterpr. Technol.* **2**, 69–73 (2016)
2. Chabak, Y., et al.: Modification of steel surface by pulsed plasma heating. *Probl. At. Sci. Technol.* **110**, 97–102 (2017)
3. Petrov, P.: Optimization of carbon steel electron-beam hardening. *J. Phys. Conf. Ser.* **223**, 012029 (2010)
4. Santhanakrishnan, S., et al.: An experimentally based thermo-kinetic phase transformation model for multi-pass laser heat treatment by using high power direct diode laser. *Int. J. Adv. Manuf. Technol.* **64**, 219–238 (2013)

5. Sancho, P., et al.: Dynamic control of laser beam shape for heat treatment. *J. Laser Appl.* **30**, 032507 (2018)
6. Hruska, M., et al.: 3D scanning laser hardening. In: *Proceedings of the 23rd International Conference on Metallurgy and Materials*, vol. 2014, pp. 921–926 (2018)
7. Qiu, F., et al.: Surface hardening of AISI 4340 steel by laser linear oscillation scanning. *Surf. Eng.* **28**, 569–575 (2012)
8. Klocke, F., et al.: Optimization of the laser hardening process by adapting the intensity distribution to generate a top-hat temperature distribution using freeform optics. *Coatings* **7**, 1357–1366 (2017)
9. Barka, N., et al.: Effects of laser hardening process parameters on hardness profile of 4340 steel spline—an experimental approach. *Coatings* **10**, 342 (2020)
10. Yao, C., et al.: Study on the softening in overlapping zone by laser-overlapping scanning surface hardening for carbon and alloyed steel. *Opt. Lasers Eng.* **48**, 20–26 (2010)
11. Zhao, Y., et al.: Effects of overlapping distances on steel microstructure and properties after multi-track laser quenching. *J. Mater. Eng. Perform.* **26**, 5973–5982 (2017)
12. Lusquinos, F., et al.: Theoretical and experimental analysis of high power diode laser (HPDL) hardening of AISI 1045 steel. *Appl. Surf. Sci.* **254**, 948–954 (2007)
13. Lesyk, D.A., et al.: Combining laser transformation hardening and ultrasonic impact strain hardening for enhanced wear resistance of AISI 1045 steel. *Wear* **462–463**, 203494 (2020)
14. Yazici, O., et al.: Investigation of effect of various processing temperatures on abrasive wear behaviour of high power diode laser treated R260 grade rail steels. *Tribol. Int.* **119**, 222–229 (2018)
15. Roy, S., et al.: Effect of laser treatment parameters on surface modification and tribological behavior of AISI 8620 steel. *Tribol. Int.* **112**, 94–102 (2017)
16. Lesyk, D.A., et al.: Influence of combined laser heat treatment and ultrasonic impact treatment on microstructure and corrosion behavior of AISI 1045 steel. *Surf. Coat. Technol.* **401**, 126275 (2020)
17. Guarino, S., et al.: High power diode laser (HPDL) for fatigue life improvement of steel: Numerical modelling. *Metals* **7**, 424–438 (2017)
18. Hung, T.P., et al.: Temperature modeling of AISI 1045 steel during surface hardening processes. *Metals* **11**, 1815 (2018)
19. Lesyk, D.A., et al.: Effects of laser heat treatment combined with ultrasonic impact treatment on the surface topography and hardness of carbon steel AISI 1045. *Opt. Laser Technol.* **111**, 424–438 (2019)
20. Ki, H., et al.: Laser transformation hardening of carbon steel sheets using a heat sink. *J. Mater. Proc. Technol.* **214**, 2693–2705 (2014)
21. Ponticelli, G.S., et al.: An optimal genetic algorithm for fatigue life control of medium carbon steel in laser hardening process. *Appl. Sci.* **10**, 1401 (2020)
22. Park, C., et al.: Influence of diode laser heat treatment and wear conditions on the fretting wear behavior of a mold steel. *Wear* **434–435**, 202961 (2019)
23. Orazi, L., Rota, A., Reggiani, B.: Experimental investigation on a novel approach for laser surface hardening modelling. *Int. J. Mech. Mater. Eng.* **16**(1), 2 (2021). <https://doi.org/10.1186/s40712-020-00124-0>
24. Guarino, V., et al.: High Power Diode Laser (HPDL) surface hardening of low carbon steel: Fatigue life improvement analysis. *J. Manuf. Process.* **28**, 266–271 (2017)
25. Kostov, V., et al.: Spatially resolved temporal stress evolution during laser surface spot hardening of steel. *J. Mater. Process. Technol.* **239**, 326–335 (2017)
26. Petana, L., et al.: Influence of laser shock peening pulse density and spot size on the surface integrity of X2NiCoMo18-9-5 maraging steel. *Surf. Coat. Technol.* **307**, 262–270 (2016)

27. Soyama, H., et al.: Comparison between shot peening, cavitation peening, and laser peening by observation of crack Initiation and crack growth in stainless steel. *Metals* **10**, 63 (2020)
28. Mahagaonkar, S.B., et al.: Effect of shot peening parameters on microhardness of AISI 1045 and 316L material: an analysis using design of experiment. *Int. J. Adv. Manuf. Technol.* **238**, 563–574 (2008)
29. Soyama, H., et al.: Effect of compressive residual stress introduced by cavitation peening and shot peening on the improvement of fatigue strength of stainless steel. *J. Mater. Process. Technol.* **288**, 116877 (2021)
30. Fan, Z., et al.: Surface nanocrystallization of 35# type carbon steel induced by ultrasonic impact treatment (UIT). *Int. J. Fatigue.* **27**, 1718–1722 (2012)



Improvement of Processes for Obtaining Titanium Alloys for Manufacturing Parts with Design Elements

Viktoriya Pasternak¹(✉) , Oleg Zabolotnyi¹ , Nataliia Ilchuk¹ ,
Dagmar Cagaňová² , and Yurii Hulchuk¹ 

¹ Lutsk National Technical University, 75, Lvivska Street, Lutsk 43018, Ukraine

² Slovak University of Technology in Bratislava, 5, Vazovova Street,
81243 Bratislava, Slovakia

Abstract. The article presents a systematic block diagram for manufacturing TiAl titanium alloys. Based on the developed block diagram of TiAl components, the main already known stages of powder metallurgy manufacturing technology were improved. Based on the obtained chemical reaction of structurally inhomogeneous materials, the intermetallic phase relationship of titanium aluminides was revealed. It is studied that in the zone of interaction of the composition of titanium and aluminium components, a certain thickness of the transition layer is formed, which practically does not change with increasing exposure time. The crystallization process of inhomogeneous TiAl materials was studied in more detail using the constructed crystal lattice of titanium alloys. As a result, the formation of an atomic grid in space was observed. It should also be noted that the recognition of individual areas in microstructural images was carried out using the Smart-eye software package. The microscopic analysis allowed us to predict the main structural characteristics of TiAl components. In particular, to carry out more detailed control of the particles of TiAl components, their density, porosity, relationships with each other, the shape and size of Ti and Al powders. The structure of the interaction of TiAl materials and the interpolation dependence of the formed intermetallic layer are also presented. Based on the conducted research, the quality indicators of parts with structural elements, particularly gears, have been improved.

Keywords: TiAl components · Physical properties · Microstructure analysis · Morphological parameters · Inhomogeneous materials · Technology

1 Introduction

Titanium intermetallics and alloys based on them are attracting more and more attention in mechanical engineering, aviation, rocket science, and space products. It is essential that due to the unique combination of their physical and operational properties, it is possible to solve a number of modern mechanical engineering problems when designing new parts. It should be noted that an integral part of the development of modern mechanical engineering is the introduction and improvement of new highly efficient heterogeneous materials and technologies for their products based on design. It

is known that titanium and alloys based on it have a unique set of properties. The most important ones include low specific gravity, high corrosion resistance to many reagents, sufficient strength at room temperatures, and elevated temperatures. However, the use of TiAl components is limited due to the high cost compared to other structural materials. Therefore, the main task of modern mechanical engineering technology is to expand the scope of improving the processes of obtaining titanium alloys for parts with structural elements. Also, improving their use by developing new economic technologies reduces the cost of both structurally heterogeneous materials and finished products significantly. It is possible to significantly reduce the cost of titanium alloys and products made from them using classical powder metallurgy methods. The main technological operations of this method include pressing mixtures into the product of the required shape and sintering structurally inhomogeneous materials in a vacuum.

Since titanium alloys are structural materials, they are essential for them to achieve the necessary complex mechanical properties. In alloys manufactured using powder technologies, this is ensured by chemical and microstructural homogeneity, permissible impurity content, and achieving a high relative density close to 99% of the theoretical one. Unfortunately, the specific structure of such composites significantly limits the possibility of using traditional research methods to obtain them. When manufacturing such materials, it is necessary to control the structure parameters during the technology implementation at all its stages. Therefore, progress in creating parts with design elements requires a broader study, research, and prediction of the structural characteristics of these materials. Thus, the urgent task of modern mechanical engineering technology is to investigate the physical and mechanical properties of TiAl materials for manufacturing parts with design elements.

2 Literature Review

Analysis of titanium-aluminium powders is covered in [1]. The biggest problem with studying these materials is their high cost and manufacturing complexity [2]. In addition, the results show that different powder particle sizes and concentrations of hollow material particles lead to high porosity [3]. The disadvantage of these studies is that the authors study powder particles only of a round spherical shape [4]. In [5], various technologies for manufacturing titanium-aluminium powders are investigated and predicted and an increase in their use in the large-scale industry due to the correct percentage of raw materials selected. It was found that Ti-6Al-4V [6] raw materials strongly affect the load mode. In [7], the authors of the paper investigated the edge approach for analyzing inhomogeneous elastic materials. It should be noted that the results obtained are reduced to a system of particular boundary integral equations, which is solved by the numerical method of boundary elements. Research teams [8] investigated the interaction zone between titanium and aluminium in a composite obtained by immersion and exposure of titanium rods in an aluminium melt. It was [9] found that the heat treatment time and cooling conditions affect the thickness and structure of the transition layer formed as a result of the interaction. The results of [10] show the peculiarity of porosity and coordination number calculations. The results obtained make it possible to optimize the version of the charge composition, which

provides an increase in the oil permeability coefficient by 3%, which fully satisfied the technical operating conditions of the bushings. The authors of [11] investigated the production of titanium alloys based on titanium aluminides as a material for gas turbine engine parts. The disadvantages of these methods include high electrical energy costs, which leads to an increase in the cost of titanium alloys and a large chemical heterogeneity of the resulting material [12]. In [13], to establish the possibility of obtaining layered intermetallic composite materials, titanium-based liquid aluminium was aged for different times at different temperatures in the air atmosphere using flux and without it [14].

The authors [15] found that the use of flux based on this powder composition contributes to forming a thicker and denser layer of intermetallides due to high temperature. The peculiarity of works [16] is that this composition of titanium-aluminium powders is limited by their existence's physical and chemical conditions. In many cases, increased requirements are placed on the performance characteristics of parts with design elements that are made based on titanium alloys [17]. The leading quality indicators include physical and mechanical properties of TiAl materials, a wide operating temperature range, the holding time of titanium-based liquid aluminum, which affects the width and density of the intermetallic layer, high stability, and reliability [18]. Therefore, the solution to such a problem requires a more comprehensive approaches such as [19, 20], including new technologies and structures, new ideas, methods, and principles of building methods and technologies [21–23]. Changes in their chemical structure [24], therefore conducting fundamental and applied interdisciplinary research using the latest methods and technologies of production.

3 Researches Methodology

3.1 Titanium Alloy Manufacturing Technology

The study aims to investigate the physical and mechanical properties of TiAl materials for manufacturing parts with design elements, conduct research at the points of the interaction zone of TiAl materials, and construct an interpolation dependence of the intermetallic layer based on the results obtained.

Well-known initial structurally inhomogeneous materials (TiAl components) are commonly used in mass production. At the same time, the manufacturing process takes place with the help of ceramic molds in the form of castings, which will not be able to provide defect-free castings. It should be noted that with the help of developed and optimized technological processes and the technical task set, we produced experimental samples from TiAl components.

The technological scheme for manufacturing TiAl titanium alloys is shown in Fig. 1.

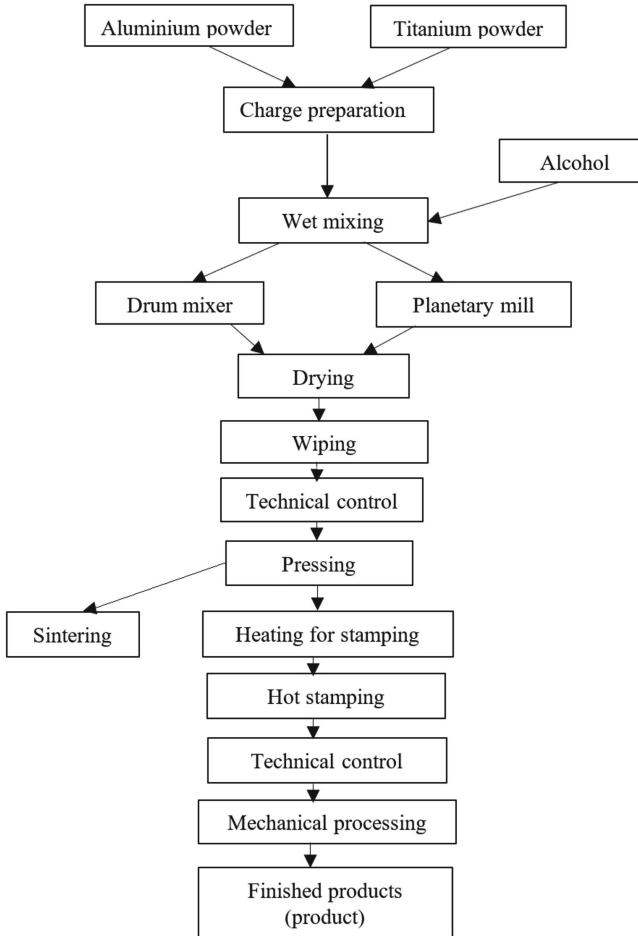


Fig. 1. Technological scheme for manufacturing TiAl alloys.

Before mixing, the powders structurally inhomogeneous materials were dried at a temperature of 70–120 °C for 3 h. Mixing of titanium and aluminium powders was carried out in steel ball mills for 2 h. The ratio of components was selected from stoichiometric calculations to obtain G-TiAl intermetallic phases. The mixed reaction mixture prepared in this way was weighed on an electronic scale of the CAS SW-II model and poured into the reactor. The temperature of the samples TiAl components during the synthesis process was controlled using a W-Mo thermocouple with an accuracy of $\pm 5\text{--}7$ °C. A PSU-125 hydraulic press was used to seal the powder mixture. The samples were formed in a cylindrical shape with a diameter of 25 mm and a height of 30 mm. An important role was played by the density of the samples TiAl components since the thermal auto-ignition mode was observed only for high-density samples at the level of 0,7–0,55 of the density of the starting materials. The porosity of TiAl materials was evaluated by hydrostatic weighing and microstructural analysis using

micrographs of sections and using the Smart-eye program. Hydrostatic weighing was performed for samples TiAl components without surface protection and protection, which made it possible to estimate the proportion of closed and open pores. The weighing was performed in distilled water at a temperature of 25–30 °C with an accuracy of 0,01. The water density was 0,997 kg/m³.

The structure of the TiAl samples was studied using the Smart-eye software package. The principle of operation of Smart-eye software is to connect an optical or electron-raster microscope that displays electrons on samples from TiAl components. Chemical microanalysis of the main structural components of the inhomogeneous material was performed on a raster electron microscope model Sarson MAGNI SCOPE MA-60. It should be noted that the study was carried out at an increased voltage of 19 kV, with a resolution of 1 Nm. It should also be noted that microanalysis was performed on the surface of an etched micro-grinder of structurally inhomogeneous materials and using the scanning method. A characteristic feature of X-ray radiation was studying certain chemical elements at specific points of interaction of raw materials, which was carried out along the studied trajectory.

3.2 Chemical Reaction and Crystallization Process of TiAl Materials

Aluminium and titanium powders with a dispersion of up to 100 μ were used to produce titanium alloys (TiAl). The ratio of components was selected from stoichiometric calculations to obtain the intermetallic phase γ -TiAl, in which the combustion temperature is lower than the melting point, $T_{\text{burning}} < T_{\text{melting}}$. As a result, a compound of titanium alloy TiAl is formed in Table 1.

Table 1. Chemical reaction TiAl.

Reaction $R_1 + R_2 \rightarrow P$	$T_{\text{mel}} (R_1), K$	$T_{\text{mel}} (R_2), K$	$T_{\text{mel}} (P), K$	T_{ad}
$Ti + Al \rightarrow TiAl$	1930	987	1730	1660

In order to study in more detail the crystallization process of structurally inhomogeneous materials, in particular TiAl components, we constructed a pinched hexagonal lattice (GSHG). In this scheme of the crystal lattice of titanium alloys, the atoms are located in the corners and the center of the bases of a hexagonal prism, and the three atoms are located between their bases. The total number of atoms is 17. It is also worth noting that the crystal structure of TiAl materials is characterized by a geometrically correct arrangement of atoms (ions) in space. Metal atoms are located at a certain distance between each other, at which the interaction energy of positively and negatively charged particles is minimal. In the plane, atoms form an atomic grid, and in space – an atomic-crystal lattice (lattice). In addition, the atoms oscillate around the equilibrium point at a high frequency.

The scheme of the crystal lattice of titanium alloys is shown in Fig. 2.

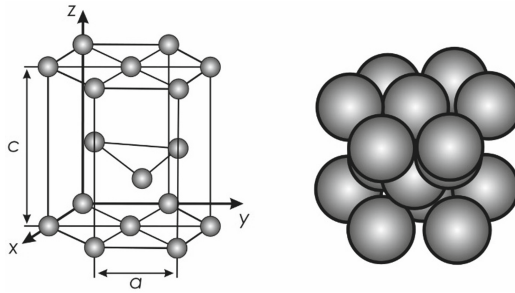


Fig. 2. Diagram of the crystal lattice of titanium alloys TiAl, where: a and c are the lattice period, $c/a = 1,633$.

It should also be noted that the crystallization procedure of TiAl components consists of two main components the formation of embryos, that is, it is the crystallization center. Moreover, the growth of crystals, which occurs in the center of the embryo. Each of these essential components must have individual velocities, which in turn determine the main parameters of the crystallization process as a whole. In particular, the first and main parameter of crystallization is the maximum rate of germ formation (c). The total amount of embryo formation is determined by the total amount of embryo formation, which has a ratio of one volume per unit time and is measured in $1/(\text{cm}^3 \cdot \text{s})$. The second crystallization parameter includes the linear crystal growth rate (a). This parameter is characterized by a rapid change in its linear dimensions (crystals) and is measured in centimeters per second (cm/s).

4 Results

4.1 Investigation of Titanium Alloys Based on Microstructural Analysis

During the manufacture of a blank part with design elements, it is necessary to apply the method of forming teeth by plastic deformation (rolling), which significantly increases mechanical parameters. In order to improve the quality indicators of gears and obtain a qualitative assessment of titanium alloy samples, it is necessary to determine and study the main morphological parameters of their microstructure using TiAl microanalysis. It should be noted that the focus was on the structure of titanium alloys in the solid-state after heat treatment and plastic deformation.

Notably, a sample of a micro-grinder of titanium alloys was examined in the part of the part that, in this case, was of the most significant interest—the destruction of the teeth of the gear wheel. After the technological process of obtaining titanium-aluminium composite materials was carried out, separate zones (red and blue regions) of interaction between structurally inhomogeneous materials during etching, which were close to destruction, were studied. It was found that there is a correlation between the original TiAl components and their properties. This allows us to state that the percentage of raw materials was correctly selected.

Figure 3 shows the structure of TiAl samples at a magnification of 800μ .

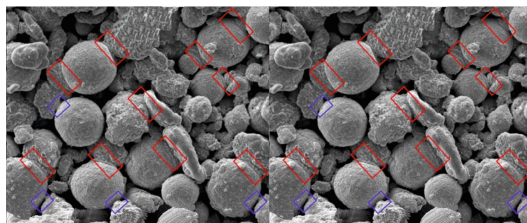


Fig. 3. Microstructure of TiAl titanium alloy samples at magnification $\times 800 \mu$.

Microstructure analysis (Fig. 3) at the selected points (red and blue regions) showed that the interface between titanium and aluminium allows distinguishing a transition layer of the intermetallic phase of titanium aluminides in the interaction zone of the titanium composite aged for different times. They also found that during the interaction between titanium and aluminium, the thickness of the transition layer practically does not change with increasing holding time and averages 6–8 μ (see Fig. 4). At the same time, the porosity was 16%, the total particle area 35478 mcm^2 , and the particle size ranged from 0,45 to 0,54 mcm . The structure of interaction between TiAl materials is shown in Fig. 4.

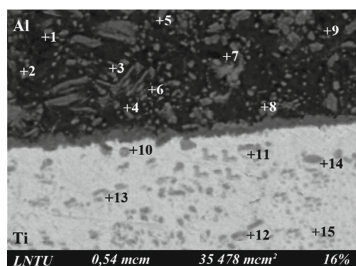


Fig. 4. Structure of interaction of TiAl materials.

From this Fig. 4, the thickness of the transition intermetallic layer, which is formed during the interaction of TiAl titanium alloys, is too small and allows us to obtain reliable results. It is also confirmed that in the considered binary system, both titanium and aluminum powders participate in the diffusion process, regardless of the temperature (above or below the melting point of aluminum).

4.2 Interpolation Dependence of the Intermetallic Layer

Due to significant differences between the molar volumes of titanium and its aluminides, an intermetallic layer was formed (Fig. 4). It is in a stressed state, which leads to its cracking and destruction. As a result, the separated fragments of the layer expose the surface of titanium, where a chemical reaction is restored between it and aluminum.

The consequence of this is the formation of a zone of interaction of the initial components of TiAl materials. Thus, the interpolation dependence is shown in Fig. 5 (Table 2).

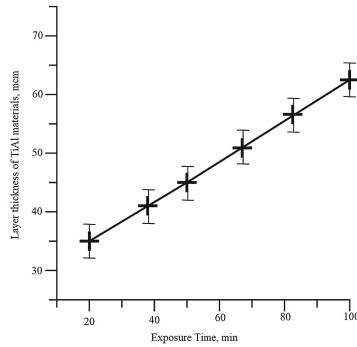


Fig. 5. Interpolation dependence of the intermetallic layer

Table 2. Analysis of the study at the points of the interaction zone of TiAl materials.

Materials	Exposure time, min	Layer thick-ness of TiAl materials, mcm
TiAl	20	35
	40	40
	45	45
	65	50
	80	55
	100	65

The interpolation dependence of an intermetallic layer with a thickness of 6–8 μ with increasing exposure times (20–100 min) shows a clear relationship between the initial components of TiAl materials. This is confirmed by the presence of an intermetallic phase of titanium aluminides in the interaction zone of the titanium composite.

4.3 Experimental and Industrial Justification of the Results Obtained

3D part modeling studies were performed in SolidWorks software. To build a 3D model of a gear wheel, the following main parameters were used: the diameter of the dividing circle d , the diameter of the circle of protrusions of the wheel teeth d_1 , and the circle of depressions d_2 , and the number of teeth z . From the above material and manufacturing technology of TiAl titanium alloys, we can present a complete 3D model of the gear wheel shown in Fig. 6.

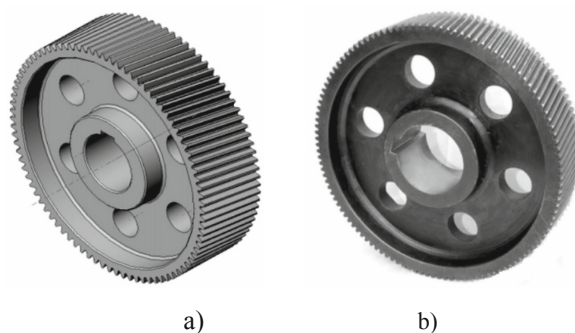


Fig. 6. 3D model of a gear wheel, where: a) in the SolidWorks software window; b) real view of the gear wheel.

Based on the calculations of the efficiency factor (performance factor), an analysis was performed at the points of the TiAl interaction zone of materials. Based on which calculations were made for the strength of a three-dimensional gear model. Using the SolidWorks software, the main recommendations for improving the quality of gears are formulated, which made it possible to optimize and predict the variant of the charge composition of the TiAl component, which provided an increase in the efficiency (performance factor) by 2–3%, which fully satisfied the technical conditions of operation of parts with design elements.

5 Conclusions

Using metallographic analysis, the authors of the article investigated the regularities of forming the TiAl structure of materials and established the dependence of the influence of the structure on mechanical, physical, and mechanical properties.

It was found that during the interaction between titanium and aluminium, the thickness of the transition layer practically does not change with increasing holding time and averages 6–8 μ , which makes it possible to obtain reliable research results.

Experimental and industrial justification of the results obtained showed that the proposed percentage of the TiAl charge composition variant of materials provides good antifriction properties, which is fully satisfied with the technical conditions of operation of structural parts.

References





1. Zhao, B., Yu, T., Ding, W., Li, X.: Effects of pore structure and distribution on strength of porous Cu-Sn-Ti alumina composites. *Chin. J. Aeronaut.* **30**(6), 2004–2015 (2017)
2. Yumak, N., Aslantas, K.: A review on heat treatment efficiency in metastable β titanium alloys: the role of treatment process and parameters. *J. Market. Res.* **9**(6), 15360–15380 (2020)

3. Berto, F., Campagnolo, A., Welo, T.: Local strain energy density to assess the multiaxial fatigue strength of titanium alloys. *Frattura ed Integrità Strutturale* **37**, 69–79 (2017)
4. Berto, F., Campagnolo, A., Welo, T.: Multiaxial fatigue strength of titanium alloys. *Frattura ed Integrità Strutturale* **41**, 79–89 (2017)
5. Smirnov, S., Zamaraev, L.: Comparative study of shot creep of single-phase titanium alloys in air and neutral gas environment on the test temperature in range from 673 to 1323 K. *Frattura ed Integrità Strutturale* **49**, 201–211 (2019)
6. Hu, W.J.: Effects of metal particles on cold spray deposition onto Ti-6Al-4V alloy via Abaqus/explicit. *J. Eng. Sci.* **7**(2), E19–E25 (2020). [https://doi.org/10.21272/jes.2020.7\(2\).e4](https://doi.org/10.21272/jes.2020.7(2).e4)
7. Sulym, H., Pasternak, Ia., Pasternak, V.: Boundary element modeling of pyroelectric solids with shell inclusions. *Mech. Mech. Eng.* **22**(3), 727–737 (2018)
8. Wang, H., et al.: Introducing transformation twins in titanium alloys: an evolution of α -variants during additive manufacturing. *Mater. Res. Lett.* **9**(3), 119–126 (2020)
9. Weston, N., Thomas, B., Jackson, M.: Exploitation of field assisted sintering technology (FAST) for titanium alloys. *MATEC Web Conf.* **321**, 1–17 (2020)
10. Zabolotnyi, O., Pasternak, V., Andrushchak, I., Ilchuk, N., Svirzhevskiy, K.: Numerical simulation of the microstructure of structural-inhomogeneous materials. In: Ivanov, V., Trojanowska, J., Pavlenko, I., Zajac, J., Peraković, D. (eds.) *DSMIE 2020. LNME*, pp. 562–571. Springer, Cham (2020). https://doi.org/10.1007/978-3-030-50794-7_55
11. Varenne, C., Prima, F., Brozek, C., Bourgon, J., Besson, J.: Deformation and fracture behavior of new strain-transformable titanium alloys: a multi-scale investigation. *Web Conf.* **321**, 1–6 (2020)
12. Balachandran, S., Tripathi, A., Banerjee, A., Chinara, M., Teja, R., Suresha, S., Choudhuri, D., Banerjee, R., Banerjee, D.: Transformations, recrystallization, microtexture and plasticity in titanium alloys. *Web Conf.* **321**, 1–13 (2020)
13. Xu, X., Bantounas, I., Dye, D.: Deformation behaviour of beta phase with similar chemical composition in beta and alpha + beta titanium alloys. *Web Conf.* **321**, 1–5 (2020)
14. Venkatesh, V., et al.: Data driven tools and methods for microtexture classification and dwell fatigue life prediction in dual phase titanium alloys. *Web Conf.* **321**, 1–8 (2020)
15. Buzolin, R.H., Ferraz, F.M.B., Lasnik, M., Krumphals, A., Poletti, M.C.: Improved predictability of microstructure evolution during hot deformation of titanium alloys. *Materials* **13**(24), 5678 (2020)
16. Benedicto, E., Rubio, E.M., Carou, D., Santacruz, C.: The role of surfactant structure on the development of a sustainable and effective cutting fluid for machining titanium alloys. *Metals* **10**(10), 1388 (2020)
17. Haar, G., Becker, T., Blaine, D.: Influence of heat treatments on the microstructure and tensile behaviour of selective laser melting-produced Ti-6Al-4V parts. *S. Afr. J. Ind. Eng.* **27**(3), 174–183 (2016)
18. Fathy, N., Ramadan, M., Hafez, K., Alghamdi, A., Halim, A.: Microstructure and induced defects of 6061 Al alloy after short times cyclic semi-solid heat treatment. *MATEC Web Conf.* **67**(5), 1–6 (2016)
19. Mao, W.-M., Zhu, W.-Z.: Tensile properties and microstructure of rheo-diecast 7075 alloy prepared by serpentine channel process. *China Foundry* **16**(3), 161–167 (2019)
20. Ivanov, V., Pavlenko, I., Liaposhchenko, O., Gusak, O., Pavlenko, V.: Determination of contact points between workpiece and fixture elements as a tool for augmented reality in fixture design. *Wirel. Netw.* **27**(3), 1657–1664 (2019). <https://doi.org/10.1007/s11276-019-02026-2>

21. Yan, Q., Qunbo, F., Xin, L., Duoduo, W., Yu, Z.: Crystal plasticity finite element method for slip systems evolution analysis of α/β duplex titanium alloys during quasi-static tensile testing. *Appl. Sci.* **10**, 1–20 (2020)
22. Ivanov, V., Dehtiarov, I., Pavlenko, I., Liaposhchenko, O., Zaloga, V.: Parametric optimization of fixtures for multiaxis machining of parts. In: Hamrol, A., Kujawińska, A., Barraza, M.F.S. (eds.) *MANUFACTURING 2019. LNME*, pp. 335–347. Springer, Cham (2019). https://doi.org/10.1007/978-3-030-18789-7_28
23. Karpus, V.E., Ivanov, V.A.: Choice of the optimal configuration of modular reusable fixtures. *Russ. Eng. Res.* **32**(3), 213–219 (2012). <https://doi.org/10.3103/S1068798X12030124>
24. Nevskii, S., Sarychev, V., Konovalov, S., Granovskii, A., Gromov, V.: Formation mechanism of micro- and nanocrystalline surface layers in titanium and aluminum alloys in electron beam irradiation. *Metals* **10**, 1–14 (2020)



Dispersion Hardening of Nano- and Submicrocrystalline Vacuum Cu-Mo Condensates

Valentyn Riaboshtan ^(✉), Anatoly Zubkov , Maria Zhadko ,
and Tatyana Protasenko 

Kharkiv Polytechnic Institute, National Technical University,
2, Kyrpychova Street, Kharkiv 61002, Ukraine

Abstract. The structure and strength properties of vacuum Cu-Mo condensates, the components of which do not form chemical compounds in equilibrium conditions and have no mutual solubility in liquid and solid states, are studied by transmission electron microscopy and X-ray diffractometry. It is found that in the process of condensation of copper and molybdenum vapor mixtures in a vacuum, anomalous solutions of molybdenum in the FCC copper crystal lattice are formed. The regularities of irreversible decomposition of the indicated solid solutions are studied under isothermal annealing at 620 °C for 3 h. It has been established that as a result of the thermal influence, a peak of precipitation hardening arises, which has a two-stage character. The experimental results are explained by the formation of hardening BCC and FCC molybdenum particles in the volume of the copper matrix and a change in the mechanism of their hardening action with increasing annealing time.

Keywords: Solubility · Grain size · Supersaturated solid solution · Lattice parameter · Electrical resistivity

1 Introduction

The strengthening of metals by dispersed particles is widely used to improve the mechanical properties of metallic materials. Two groups of objects of this class are the most widely known: precipitation-hardening or aging alloys (PHA) and dispersion-strengthened composite materials (DSCM). In the first, strengthening particles are formed during the decomposition of supersaturated solid solutions. In the second group, dispersed particles are introduced artificially into the matrix metal at a certain stage of obtaining the composite. Supersaturated solutions are obtained mainly by quenching from the solid state from temperatures exceeding the line of limited solubility or by high-speed cooling of melts. The use of vacuum technologies for these purposes significantly expands the capabilities of these methods. This fact is because elements and substances can mix in the vapor phase at the atomic and molecular levels in any proportion. Upon condensation of mixtures of such vapors on a cold substrate in a vacuum, metallic materials with a wide range of structural states can be obtained. Examples of such metals are Cu-Mo, Cu-W, Cu-Ta binary systems. Aging alloys in

terms of strength properties, at moderate temperatures, surpass DSCM with an equal volume content of the strengthening phase. This is because controlled decomposition of a supersaturated solid solution, it is possible to realize a better coherent conjugation of the strengthening particles with the matrix metal and their greater dispersion than in DSCM obtained by various technologies. However, in terms of thermal stability and strength at high temperatures, DSCM significantly surpasses precipitation-hardening alloys. In the latter, when exposed to temperature, coagulation and reverse dissolution of the second phase particles occur, leading to a decrease in strength properties. On the contrary, in dispersion-strengthened composites, the described transformations are absent since their components do not have mutual solubility in the solid state, and the strengthening particles have a low coagulation rate.

2 Literature Review

The possibility of obtaining a new class of composite materials combining the advantages of aging alloys and dispersion-strengthened composite materials is due to the ability of metals mutually insoluble in liquid and solid states to form anomalous supersaturated solid solutions during the condensation of mixtures of their vapors in a vacuum. Subsequent heating can lead to their irreversible decomposition with the second phase particles precipitation and an increase in strength properties [1].

However, studies in this direction have not received further development until now. The patterns of these processes have practically not been studied. This also applies to anomalous solutions of molybdenum in copper obtained by mechanical alloying of mixtures of their powders [2]. Moreover, for such a system, various technological factors on the solid solubility and structural state of the materials obtained are studied [3]. The theoretical concepts of the regularities of the formation of such metastable solutions is also developed [4]. High functional properties of these materials is reported [5]. The relevance of this problem is enhanced by the fact that the decomposition of such anomalous supersaturated solutions and the realization of the precipitation hardening peak in metals with a nanoscale structure may differ significantly from conventional metallurgical alloys. This can manifest itself in temperature-time intervals, kinetics, and mechanisms of the mentioned processes [6]. It should also be noted that during the condensation of immiscible metals vapor mixtures, by varying the technological conditions, it is possible to obtain dispersion-strengthened composite materials already during deposition [7]. Most research is devoted to studying the structure and properties of such objects [8].

The next group of publications is devoted to obtaining nanostructured thermally stable metals of the indicated binary systems by vacuum-plasma [9] and powder technologies. In the study [10], criteria were developed to select alloying elements that

form grain boundary segregation in the matrix metal, thereby contributing to the stabilization of the nanostructural state. The diversity of structural-phase states of such grain boundary segregation is also reported [11]. The influence of the physicochemical properties of segregating elements on the state of grain boundaries is considered in [12]. The studies presented in [13] indicate that the state of the internal interfaces in nanostructured metals has a dominant effect on the combination of their strength and plasticity.

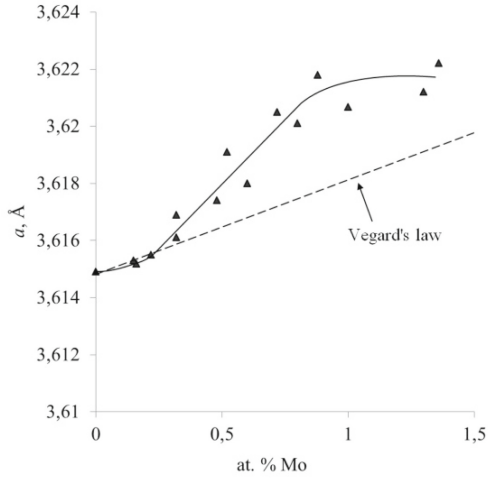
In this regard, the purpose of this work is to study the effect of the molybdenum concentration on the regularities of dispersion hardening of vacuum Cu-Mo condensates during isothermal annealing.

3 Research Methodology

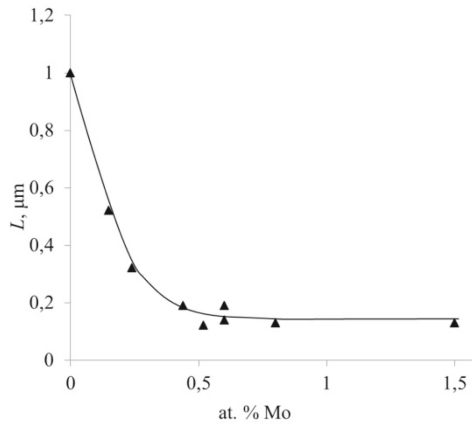
Condensates of the Cu-Mo binary system up to 50 μm thick obtained by separate electron-beam evaporation of the constituent components and subsequent crystallization of their vapor mixtures on a non-orienting substrate in a vacuum pressure $\sim 10^{-3}$ Pa were studied separated from the substrate. The range of Mo concentrations in the investigated condensates was 0.1–2.0% at. The annealing was carried out at a temperature of 620 $^{\circ}\text{C}$, the time of which varied in the range from 15 min to 3 h. The choice of thermal treatment modes was based on the data of [1]. The condensate structure was studied by transmission electron microscopy and X-ray diffractometry. The molybdenum concentration was controlled by X-ray fluorescence analysis. The electrical resistivity of the condensates was measured by a compensation method. The strength properties were controlled by measuring the microhardness. The main analyzed value was the relative microhardness – $H_{\text{an}}/H_{\text{in}}$. Where H_{an} is the microhardness of the annealed samples; H_{in} – microhardness of the same samples in the initial state before annealing. This technique made it possible to exclude the influence of possible heterogeneity of the composition and other poorly controlled factors on the processes under study. The objects were annealed in a vacuum with a residual pressure not exceeding 10^{-2} Pa.

4 Results

Figure 1 shows the dependences of the grain size (L) and the crystal lattice parameter (a) of the copper matrix on the Mo content in the condensates, which have a two-stage nature. Up to a concentration of ~ 0.3 at. %, there is a sharp decrease in the value of L and a slight increase in the crystal lattice parameter.



a



b

Fig. 1. Dependence of the grain size (a) and the crystal lattice parameter (b) on the Mo content.

In the electron microscopic images of these samples, no signs indicate second phase particles' presence (Fig. 2). The experimental results presented and the data obtained on similar objects [10] suggest that the main part of molybdenum atoms in condensates with a concentration corresponding to the descending branch of the $L - f(C)$ dependence is concentrated in grain boundaries in the form of grain boundary segregations.

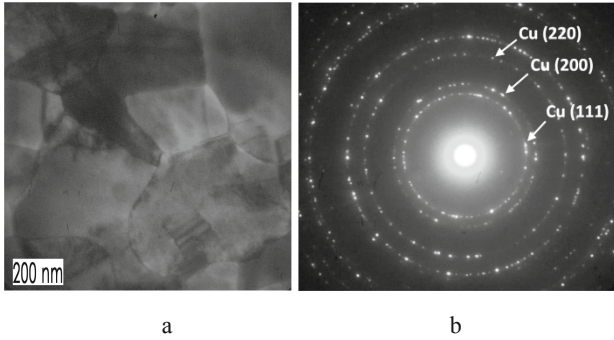


Fig. 2. Electron-microscopic images of the structure of the condensate containing 0.4 at. % Mo: a – bright-field image, b – electron diffraction pattern.

At molybdenum concentrations corresponding to the flat area of the $L - f(C)$ dependence, the structure of the condensates is significantly different. Diffraction reflections of BCC and FCC molybdenum particles, mainly concentrated in the grain boundaries, appear on the electron diffraction patterns (Fig. 3). A significant increase in the crystal lattice parameter in this range of molybdenum concentrations indicates the formation of an anomalous supersaturated solution with Mo atoms in the copper crystal lattice under the used technological conditions for condensate obtaining.

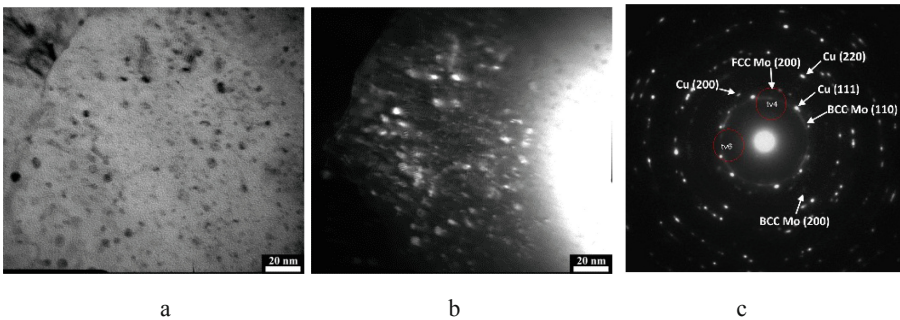


Fig. 3. Electron-microscopic images of the structure of the condensate containing 1.6 at. % Mo: a – bright-field image, b – dark field image, c – electron diffraction pattern.

The high degree of dispersion of the second phase particles, the nanoscale structure of the copper matrix, which is a supersaturated solid solution of molybdenum on its basis, determines the high strength properties of the objects under study and increased electrical resistivity (Fig. 4).

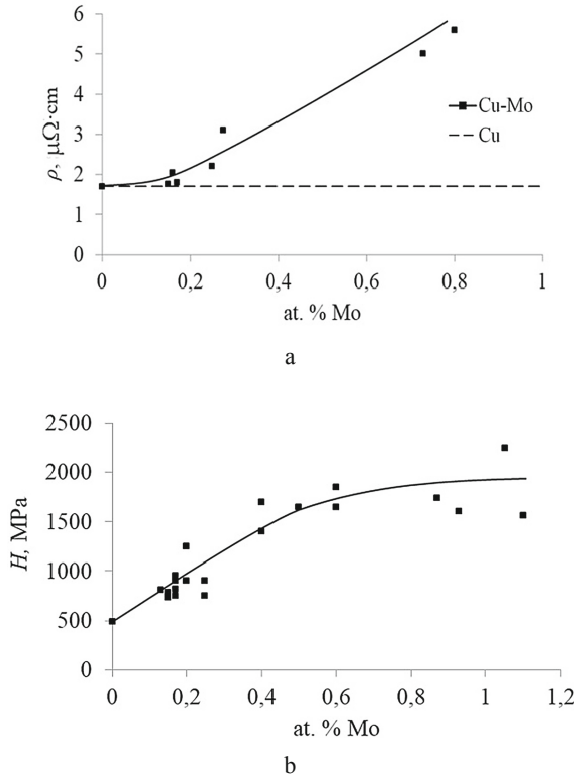


Fig. 4. Dependence of microhardness (a) and electrical resistivity (b) on the Mo content.

Isotherms of relative microhardness ($H_{\text{an}}/H_{\text{in}}$) for condensates annealed at 620 °C with different Mo concentrations are shown in Fig. 5. It is seen that precipitation hardening is not observed for condensates with a Mo content of ~ 0.3 at. % over the entire range of annealing times. An increase in the molybdenum concentration in condensates leads to the appearance of the precipitation hardening effect, the value of which rises with an increase in Mo concentration. This process also manifests itself in two stages as the duration of annealing increases. Figure 6 shows the characteristic isotherms of the crystal lattice parameter of the copper matrix and the electrical resistivity of condensates with a concentration of ~ 1 at. % Mo. It can be seen that within 30 min, the values of a and ρ decrease sharply, followed by reaching a plateau. These data allow us to conclude that the first peak of precipitation hardening, which appears in the region of 30 min of annealing, is caused by the decomposition of a supersaturated solid solution of Mo in the copper crystal lattice. This conclusion is confirmed by the results of electron microscopic studies (Fig. 7), in which second phase particles are observed (both within the grains and at the grain boundaries of the copper matrix).

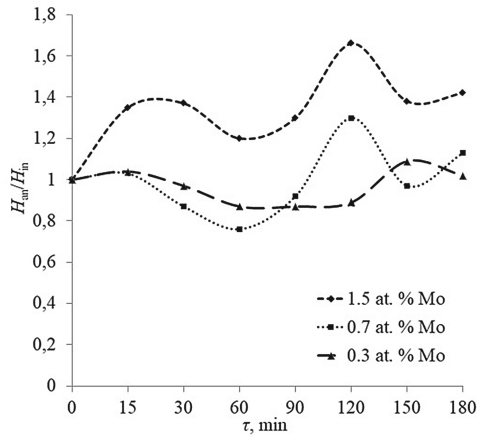


Fig. 5. Influence of annealing time on the relative microhardness of Cu-Mo condensates.

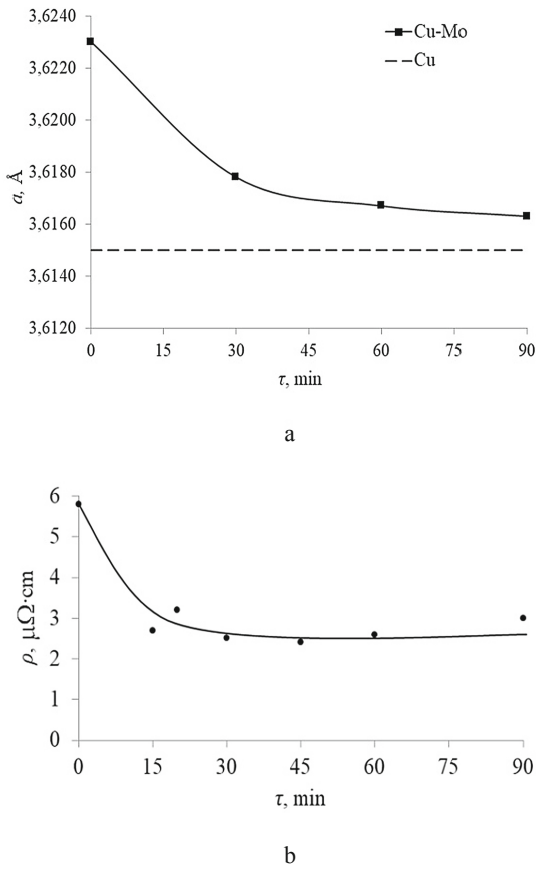


Fig. 6. Dependences of the crystal lattice parameter (a) and electrical resistivity (b) of Cu-Mo condensates on the time of isothermal annealing.

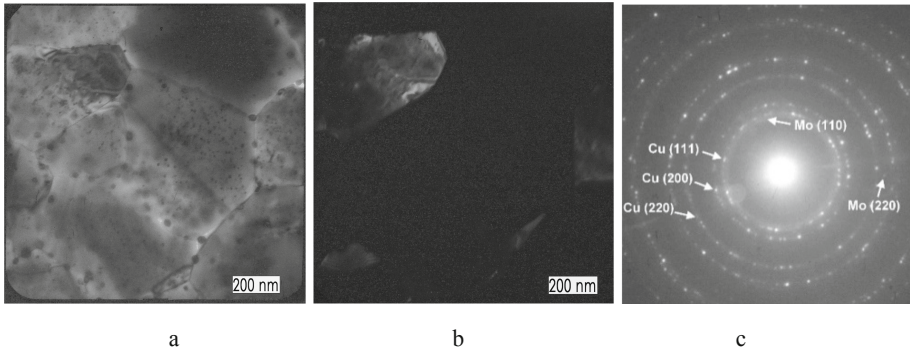


Fig. 7. Electron microscopic images of Cu-Mo condensates annealed at a temperature of 620 °C (a – bright-field image, b – dark-field image, c – electron diffraction pattern).

An analysis of these results suggests that the second peak of precipitation hardening is associated with a change in the mechanism of the hardening action of molybdenum particles and processes occurring in the second dispersed phase, which can be very diverse simultaneously and have different effects on the properties. They may include the following: the emergence and relaxation of stresses around particles, their different growth rates to critical sizes within the grains and in the region of grain boundaries, changes in the structure of adsorption layers of molybdenum atoms at the grain boundaries of the copper matrix. It is essential to note that the initial dimension of the grain structure of the copper matrix remains the same over the entire range of annealing times used.

5 Conclusions

It has been established that anomalous supersaturated solutions of molybdenum in the copper crystal lattice undergo irreversible decomposition at temperatures above 600 °C. The aging process has a two-stage nature. The decomposition of the solid solution causes the first peak of precipitation hardening. It is suggested that the second maximum of microhardness is associated with the processes occurring in the second phase, which induce a change in the mechanisms of their strengthening action. The heights of precipitation hardening peaks increase with increasing supersaturation of the solid solution of molybdenum in the copper crystal lattice. The nano- and submicrocrystalline structure is retained upon annealing above 600 °C for 3 h.






The results of this study indicate the possibility and prospects of obtaining thermally stable nanocrystalline Cu-Mo pseudoalloys with optimal combinations of strength and electrical resistivity.

References

1. Zubkov, A.I., Il'Inskiy, A.I., Podgornaya, O.A., Sevruk, V.I., Sokol-Prusskiy, Y.G.: The possibility of ageing rapidly quenched Cu-Mo alloys. *Phys. Met. Metall.* **70**(4), 189–191 (1990)
2. Patra, A., Karak, S.K., Pal, S.: Effects of mechanical alloying on solid solubility. *Adv. Eng. Forum* **15**, 17–24 (2016)
3. Shang, X., Wang, X., Chen, S.: Effects of ball milling processing conditions and alloy components on the synthesis of Cu-Nb and Cu-Mo alloys. *Materials* **12**(8), 1224 (2019)
4. Martínez, V., Aguilar, C., Marín, J., Ordoñez, S., Castro, F.: Mechanical alloying of Cu-Mo powder mixtures and thermodynamic study of solubility. *Mater. Lett.* **61**, 929–933 (2007)
5. Hernández, O., Aguilar, C., Medina, A.: Effects of Mo concentration on the structural and corrosion properties of Cu-alloy. *Metals* **9**(12), 1307 (2019)
6. Chuistov, K.V., Perekos, A.E., Ruzhitskaya, T.V., Efimova, T.V., Zalutsky, V.P.: Superfine particles of alloys on the basis of copper. 2. Decomposition of supersaturated solid solutions. *Metallofizika I Novejshie Tekhnologii* **23**(7), 949–960 (2001)
7. Grechanyuk, N.I., Minakova, R.V., Vasilyeva, O.P., Kopylova, G.K., Grechanyuk, I.N., Medzinsky, B.: Modern station and promises of application of technology electronbeam evaporation-condensation metals non metals in vacuum for resaving of materials for electrical contacts and electrodes. *IPM, Electrical contacts and electrodes*, pp. 54–67 (2010)
8. Derby, B., Cui, Y., Baldwin, J.K., Misra, A.: Effects of substrate temperature and deposition rate on the phase separated morphology of Co-sputtered Cu-Mo thin films. *Thin Solid Films* **647**, 50–56 (2018)
9. Souli, I., Gruber, G.C., Terziyska, V.L., Zechner, J., Mitterer, C.: Thermal stability of immiscible sputter-deposited Cu-Mo thin films. *J. Alloy. Compd.* **783**, 208–218 (2018)
10. Kalidindi, A.R., Schuh, C.A.: Stability criteria for nanocrystalline alloys. *Acta Mater.* **132**, 128–137 (2017)
11. Meiners, T., Duarte, J.M., Richter, G., Dehm, G., Liebscher, C.H.: Tantalum and zirconium induced structural transitions at complex [111] tilt grain boundaries in copper. *Acta Mater.* **190**, 93–104 (2020)
12. Peter, N.J., Frolov, T., Duarte, M.J., Hadian, R., Ophus, C., Kirchlechner, C., Liebscher, C. H., Dehm, G.: Segregation-induced nanofaceting transition at an asymmetric tilt grain boundary in copper. *Phys. Rev. Lett.* **121**(25), 255502 (2018)
13. Khalajhedayati, A., Pan, Z., Rupert, T.J.: Manipulating the interfacial structure of nanomaterials to achieve a unique combination of strength and ductility. *Nat. Commun.* **7**(1), 10802 (2016)



Polymer Bulk Composites with Strong Noncovalent Interface Interactions

Denys Savchenko^(✉) , Eugen Pashchenko ,
Svitlana Kukhareno , Oksana Kaidash ,
and Serhii Riabchenko 

Bakul Institute for Superhard Materials, 2, Avtozavodska St., Kyiv, Ukraine
lab6_1@ukr.net

Abstract. The paper discusses the possibility of obtaining polymer composite materials with a high content of layered carbon filler (over 50 wt %). The application of the vacuum self-assembly method for this purpose is described. Graphene oxide synthesized by the modified Hammers method was used as a filler. Oligoamidoimide and phenol-formaldehyde oligomer were used as a binder for the preparation of composites. An increase in the ordering of the structure of the polymer layers adjacent to the filler particles is confirmed by the data X-ray diffraction analyses. It is shown that the breaking stress in tension increases by 1.1–1.6 times, and the elongation at the break by 1.2–1.7 times. The optimal concentration of graphene oxide, in this case, is 60–80 wt %. A mechanism is proposed that underlies the increase in mechanical properties based on a change in the nature and spatial density of bonds between functional groups of the polymer and filler.

Keywords: Graphene · Phenolformaldehyde · Oligoamidoimide

1 Introduction

Most often, nanocomposites with a high filler concentration (more than 50%) are obtained by the method of gradual layering: a polymer layer is deposited from the solution onto a substrate, after which a nanofiller layer is applied to it; thus, by gradual layering and alternating layers, bulk nanocomposite materials are obtained. This method's formation of a layered structure is caused by strong aggregation between individual components, which ensures the high strength of the materials [1]. For example, polymer-clay nanocomposites prepared by alternate layering demonstrate an increase in the elastic modulus up to 6 GPa [2]. An alternative is the method of self-assembly of polymer composite materials using a vacuum unit. Vacuum self-assembly is a flexible and relatively simple method for fabricating ordered materials based on a polymer-graphene oxide system with a high filler concentration (>50%). Such composites can be easily obtained by filtering the graphene oxide colloidal solution (pre-dispersed in the polymer solution) through a simple, inexpensive membrane filter. The advantage of the vacuum self-assembly method is its availability, low cost, the ability to choose a wide range of materials, the high growth rate of the material layer, and no need for careful equipment adjustment.

This work aims to create a composite material based on available thermosetting oligomers with a high concentration of graphene oxide (as a filler) by vacuum self-assembly. This approach makes it possible to use the synergism of the interaction of the composite material components, which will make it possible to achieve high properties of composites at the macro-level [3]. For antifriction, abrasive materials, and coatings, the essential properties are mechanical strength, thermal resistance, and thermal stability.

2 Literature Review

The introduction of nanosized fillers, such as nanoribbons and nanotubes, can radically affect composite materials based on polymers: increase thermal conductivity [4] and/or electrical conductivity [5], increase fire resistance [6], or impart antimicrobial resistance [7]. Nanocomposites with a low filler concentration exhibit isotropic properties because the nanofiller particles are randomly oriented. This contrasts with traditional composites containing fillers that are elongated (a significant length to width ratio). When using a high filler concentration (more than 50%), such materials are characterized by the anisotropic orientation of the filler phase [8]. This anisotropic orientation provides a significant improvement in properties in the longitudinal direction of the orientation of the filler. However, in other directions, the effect of the action of the filler is less pronounced or may even lead to deterioration in properties [9]. The solution can be using nanoscale fillers, which will simultaneously increase properties and isotropic structure. However, despite a large array of publications, the effect of high concentrations of nanofiller on the properties of polymer materials has not been studied. This is due to the high cost of such fillers, materials based on them, and the ability of nanofillers to aggregate [10]. However, successes in the synthesis of graphene oxide suggest that the issue can be resolved, making it possible to better study the effect of nanofillers on the structure of polymer composite materials [11].

3 Research Methodology

3.1 Obtaining Materials Based on Graphene Oxide

Source Materials. The starting materials were graphite powders, phenol-formaldehyde, and oligoimidoimide oligomer, N, N-dimethylformamide (DMF). All reagents were purchased from Ukrorgsintez.

Ultrasonic treatment of oxidized graphite to obtain graphene oxide was carried out using an ultrasonic waveguide UZPK-12A (20 kHz) (Ukraine). The vacuum stripping was performed using a Value VE115N vacuum pump (China). An OPn-3M centrifuge (Ukraine) was used for centrifugation.

Synthesis of Materials. Graphite was oxidized to graphene oxide by the Hammers method [12]. The graphite powder (5 g) was pre-oxidized by vigorous stirring for 6 h. The pre-oxidized powder was filtered and washed with water (3 times 50 ml each) and

dried at 50 °C for 12 h. Then this powder was stirred for 48 h at 35 °C in a potassium dichromate solution to increase the amount of oxidized product. This product was purified by five cycles of resuspension in twice-distilled water (30 ml each), followed by centrifugation at 8000 rpm for 30 min to remove residual metal cations [13].

Exfoliation was achieved by sonication of an aqueous suspension of graphite oxide (300 ml, 10 mg/ml) for 1 h in an ultrasonic bath. Non-exfoliated aggregates were removed from the solution by centrifugation at 9000 rpm for 25 min while maintaining the supernatant. Complete exfoliation of graphene oxide nanolayers was confirmed by the absence of a diffraction peak in the diffractogram of a freeze-dried powder prepared from an aqueous dispersion.

Preparation of Constituent Solutions. The constituent solutions of graphene oxide and oligomers were prepared by adding dropwise a dilute aqueous dispersion of graphene oxide (30 ml, 1 mg/ml) to the corresponding oligomer solution in DMFA (10–90 mg in 20 ml of water).

3.2 Instruments and Research Methods

Micrographs of the produced materials (CEM) were obtained on a PEM-106 microscope (Ukraine).

Mechanical properties were measured on a Tiratest-2850 universal testing machine (Germany). Test pieces (2–6 mm wide and 20–40 mm long) were made by pressing. Uniaxial tension was measured in air at room temperature.

X-ray phase analysis was performed on a Rigaku 3000 diffractometer (Rigaku Americas, Inc., The Woodlands, TX) with nickel-filtered $\text{CuK}\alpha$ radiation ($\lambda = 0.15406$ nm), in the range 4°–90°.

Thermogravimetric measurements and differential scanning calorimetry studies were performed on a Perkin-Elmer DSC 6000 scanning calorimeter (Perkin-Elmer, USA) with a heating-cooling apparatus. The sequential heating and cooling rate was 5 °C/min. The temperature range was 25–300 °C, the number of heating-cooling cycles was 5 cycles/sample.

Composite polymer materials were obtained by the thermal pressing of the starting oligomers containing a filler. Samples of the composite material were bars with dimensions of 7 × 7 × 70 mm. Initial pressing parameters: pressure 100 MPa, temperature 180 °C, polymerization time 40 min.

4 Results

For fabricating nanocomposites based on graphene oxide and polymer using the proposed method successfully, initial dispersions containing both graphene oxide nanolayers and a dissolved polymer were prepared (Fig. 1).

For the experiment, we used two types of oligomers: phenol-formaldehyde oligomer and oligoamidoimide.

Since graphene oxide layers have many acidic functional groups on their surface [12], they can be easily dispersed in polar solvents using ultrasonic treatment [13].

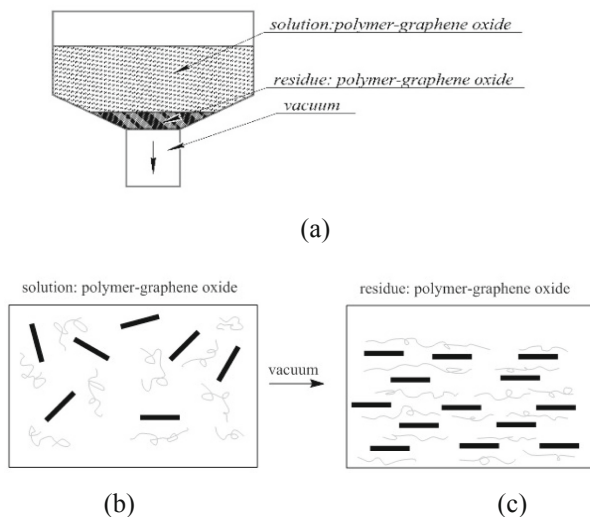


Fig. 1. Schematic representation of the production of nanocomposite films by vacuum self-assembly from a solution containing both graphene oxide nanolayers and a dissolved polymer. The filter membrane immobilizes graphene oxide layers, which, in turn, interacts with the polymer solution flowing through it.

For obtaining hydrophilic polymer nanocomposites based on graphene oxide, the filler is mixed with an aqueous solution of the polymer (oligomer) under the action of ultrasonic treatment. The preparation of hydrophobic compositions requires an additional stage of dissolution of the initial polymer/oligomer in a less polar solvent, for example, in N, N-dimethylformamide (DMFA), which does not cause aggregation of graphene oxide nanoparticles both in the solvent itself and in the oligomer or polymer dissolved in it.

The resulting oligomer solution containing a graphene oxide dispersion is filtered through a membrane under the constant action of ultrasound. Some oligomeric chains begin to pass through it (Fig. 1*b* and *c*); however, this process is inhibited by the deposition of graphene oxide nanoplates on the membrane surface. This graphene oxide film on the filter surface reduces further oligomer losses. Combining the simultaneous action of ultrasound and filtration leads to a uniform deposition of both filler nanolayers and oligomers inside the finished nanocomposite: graphene oxide layers and oligomeric chains are deposited on each other. Although solvent molecules can slowly penetrate the growing structure of the nanocomposite, the oligomer remains intercalated in the interlayer galleries.

As indicated above, since part of the polymer from the initial dispersion passes through the membrane during manufacture, not all of the initially dissolved oligomer remains in the manufactured nanocomposites. However, a significant part of the original oligomer (up to 84%) is retained in the composition. This fact is confirmed by the weight analysis method.

The results of studies of thermogravimetric analysis of materials based on oligoamidoimide (a) and phenol-formaldehyde oligomer (b): 1) graphene oxide 2) without filler and with filler in the amount of wt %: 3) 50; 4) 60; 5) 70; 6) 80.

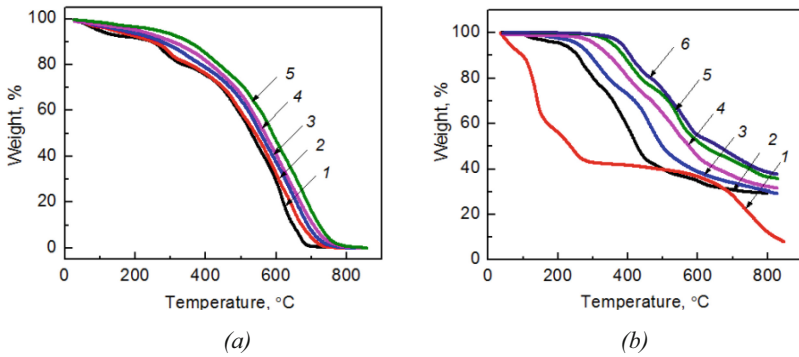


Fig. 2. Thermogravimetric analysis of materials based on oligoamidoimide (a) and phenol-formaldehyde oligomer (b): 1) graphene oxide 2) without filler and with filler in the amount of wt %: 3) 50; 4) 60; 5) 70; 6) 80.

The curve for the phenol-formaldehyde oligomer without filler demonstrates a two-stage process of weight loss: in the range 120–200 °C and lower values between 250 °C and 300 °C, leaving only 6% of the mass of the original sample. The introduction of graphene oxide into the material led to an increase in thermal stability, reflected in a shift in the temperature of the beginning of the mass-loss process up to 420 °C, and the carbon residue was about 43% of the initial mass of the composite. These characteristics were possessed by a composite that contained 70% filler by weight. Comparative analysis of the structures (Fig. 3) indicates a better homogeneity of the structure obtained by vacuum distillation.

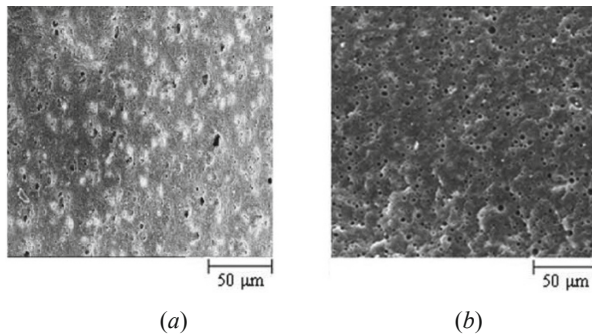


Fig. 3. The structure of the materials after polymerization: (a) without vacuum distillation and (b) by the vacuum distillation method.

It was expected that the polymer interlayers in the composition of the samples would have a high degree of ordering. This assumption was confirmed using the X-ray diffraction method. The diffractograms of the obtained compositions had distinct peaks characterizing broad regions of ordering with long-range order. Diffraction patterns of polymers based on phenol-formaldehyde oligomer (without graphene oxide) had a halo characterizing the short-range order of the structures (Fig. 4 and 5).

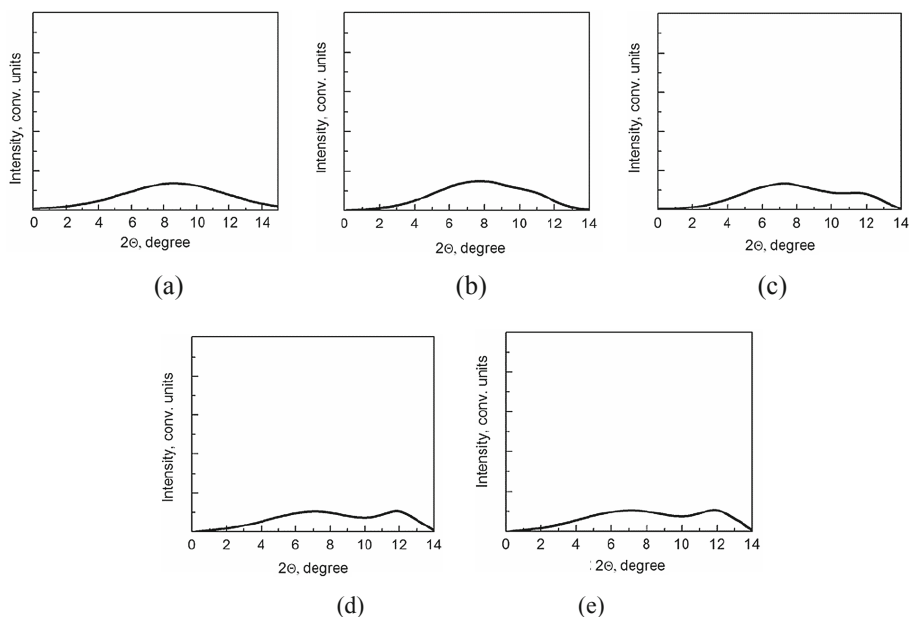


Fig. 4. Diffraction patterns of composite materials: *a*) based on oligoamidoimide oligomer (without filler) and with filler (graphene oxide) in an amount of wt %: *b*) 50; *c*) 60; *d*) 70; *e*) 80.

All fabricated nanocomposites had a high level of mechanical properties (Tables 1 and 2). The mechanical properties for samples with a high filler content were significantly higher than for samples with a low concentration. This is due to the following facts: an increase in the ordering of the polymer in the interplanar space; a decrease in the distance between the planes of graphene oxide; a decrease in possible chain conformations that can be realized in galleries (Table 1 and 2, Fig. 6).

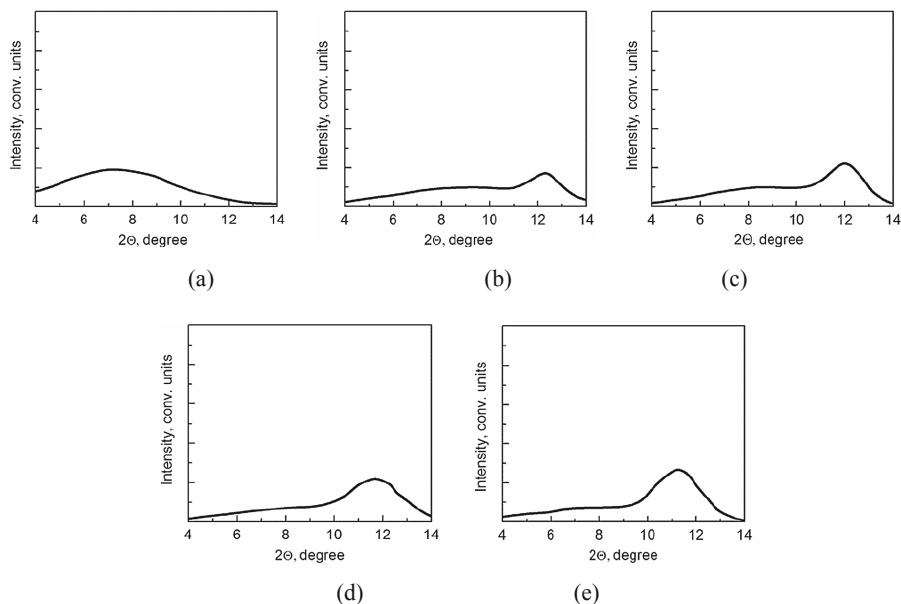


Fig. 5. Diffraction patterns of composite materials: *a*) based on phenol-formaldehyde oligomer (without filler) and with filler (graphene oxide) in an amount of wt %: *b*) 50; *c*) 60; *d*) 70; *e*) 80.

Table 1. Mechanical properties of composite materials based on oligoamidoimide oligomer and filler (graphene oxide).

The amount of graphene oxide in oligoamidoimide %, w/w	Maximum stress at the break, MPa	Maximum deformation, %
0	14.9	1.11
50	15.1	1.21
60	15.6	1.34
80	14.8	1.09
100	13.3	0.97

Table 2. Mechanical properties of composite materials based on phenol-formaldehyde oligomer and filler (graphene oxide).

The amount of graphene oxide in phenol-formaldehyde %, w/w	Maximum stress at the break, MPa	Maximum deformation, %
0	22.6	0.51
50	34.2	0.64
60	36.8	0.71
80	37.1	0.84
100	36.4	0.76

The obtained high indicators of mechanical properties in the first approximation are associated with the active interaction of functional groups of graphene oxide and groups of the phenol-formaldehyde oligomer. Graphene oxide contains on its surface a large number of hydrophilic oxygen-containing functional groups (primarily epoxy and hydroxyl) [14], and the phenol-formaldehyde oligomer has carbonyl, hydroxyl, and methylol groups. These groups can easily interact with each other.

The results of similar polymer composite materials tests, but with a lower content of graphene oxide, showed values of properties lower than those indicated in the article [14]. For example, for systems based on reduced graphene oxide (0.05–0.25 wt %) and phenol-formaldehyde oligomer, 80% of the mass is lost at 400 °C versus 800 °C for the composites we have developed.

Based on the results obtained, it can be assumed that hydrogen bonds play an essential role in increasing the mechanical properties of the developed composite material. An experiment can confirm this under the following conditions: graphene oxide was obtained without polymer, and the obtained samples were pressed without heating in an undried form and with heating at a temperature of 100 °C.

Graphene oxide has hydrophilic properties due to functional groups on the material surface [14]. Samples without drying had a rigid structure (modulus of elasticity ~ 1 – 2 MPa); after drying, the samples were destroyed by their weight [15]. Thus, water should play a crucial role in ensuring interaction between adjacent layers, most likely due to the network of hydrogen bonds (Fig. 6) formed between epoxy and hydroxyl groups on the surfaces of adjacent graphene oxide layers. The network of such bonds can be responsible for the rigidity of specimens in composite materials.

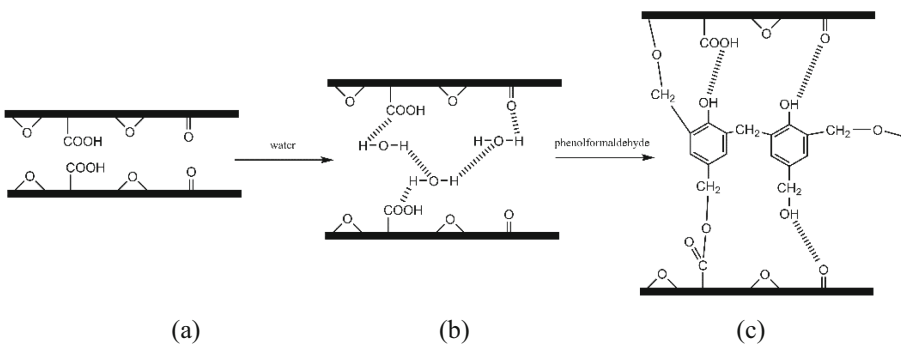


Fig. 6. Schematic diagram showing the ability of intercalated molecules to contribute to the hydrogen bond bridges spanning the gallery.

It is assumed that the presence of water between the graphene oxide nanolayers can significantly increase the degrees of freedom associated with creating a network of hydrogen bonds connecting the layers (Fig. 6b). Such a network would be rare in anhydrous graphene oxide layers (Fig. 6a). The functional groups are too rigid in anhydrous material and spaced far enough apart to create hydrogen bonds. The addition of water molecules with rotational and translational degrees of freedom, which the

functional groups associated with the layers do not have, allows these functional groups to bind to water molecules. The ability of water molecules to serve as both an acceptor and a donor of hydrogen bonds makes them “universal adapters” for forming such a network. When a graphene oxide sample is dried, the absence of water significantly reduces the ability of adjacent layers to interact via hydrogen bonds. For example, if functional groups in adjacent layers cannot form hydrogen bonds, interaction will not occur. Accordingly, the mechanical properties of the material will decrease at the macro level. The second problem is that, in an entirely dehydrated sample based on graphene oxide, the rigidity of the layers significantly limits the degrees of freedom of surface groups, reducing the possibility of hydrogen bonding. Since such bonds appear only at short distances less than 3 \AA [15], their formation requires a particular orientation of the interacting groups.

In graphene oxide-phenolic oligomer nanocomposites, the hydrophilic oligomer chains in the gap between the galleries play the same role as water in creating a large network of hydrogen bonds but significantly improved the strength of covalent bonds between growing polymer chains during polymerization. In other words, an increase in the mechanical properties observed in graphene oxide-phenolic oligomer nanocomposites is due to a combination of hydrogen and covalent bonds, where the side hydroxyl groups of the oligomer chains interact with oxygen-containing groups on the graphene oxide surface via hydrogen bonds.

According to the proposed model of the formation of a network of hydrogen bonds (Fig. 6c), it can be seen that the mechanical properties of nanocomposites based on graphene oxide and phenol-formaldehyde oligomer varied widely depending on the change in the content of graphene oxide. As the amount of filler increased, a significant increase in the density of the hydrogen bond network of the composites was observed. Hydrogen bonds can provide additional self-organization of composite material for tribotechnical or instrumental purposes in the contact zone with the material being processed or a counterbody in a friction pair.

Our proposed model of hydrogen bonds also explains the high tensile strength and deformation upon fracture for nanocomposites with graphene oxide. Once the stress reaches a sufficient level to break the hydrogen bonds between the functional groups of the polymer and the oxygen-containing functional groups on the graphene oxide surface, the layers can accommodate some local slip to reduce defect accumulation. Further research is needed to thoroughly investigate the role of molecular interactions in the operational behavior of the developed composite materials.

5 Conclusion

A technological approach to synthesizing homogeneous composites with graphene oxide content in the range 50–70 wt % is proposed. It is shown that high mechanical properties can be provided due to a large number of hydrogen bonds, which can create the possibility of a self-organization process in the composite in the contact zone.

A promising application of the developed materials will be the instrumental direction, particularly the creation of composites filled with superhard abrasives for grinding and finishing the most critical parts made of metals and non-metallic materials.






One of the ways to improve these composites can be the use of a reducing medium to partially reduce graphene oxide and increase its reactivity. Another promising direction can be the additional chemical functionalization of graphene oxide layers to create possibilities for controlling the dynamics of reversible rearrangement of bonds between the filler and the polymer binder under actual operating conditions.

References

1. Myronyuk, O., Dudko, V., Baklan, D., Melnik, L.: Study of structure influence on wear resistance of hierarchical superhydrophobic coatings. *East.-Eur. J. Enterp. Technol.* **3**(12), 44–49 (2017)
2. Pashchenko, E., Savchenko, D., Kaidash, O., Kukhareno, S., Rumiantseva, Y., Buriachek, O.: Synthesis of hybrid partially oxidized nanodispersed metal particles with simultaneous surface functionalization. In: *Proceedings 2020 IEEE 10th International Conference on Nanomaterials: Applications & Properties, NAP-2020*, pp. 01NSSA04-1–01NSSA04-4 (2020)
3. Liu, S., Chevali, V.S., Xu, Z., Hui, D., Wang, H.: A review of extending performance of epoxy resins using carbon nanomaterials. *Compos. B Eng.* **136**, 197–214 (2018)
4. Duan, G., Wang, Y., Yu, J., Zhu, J., Hu, Z.: Improved thermal conductivity and dielectric properties of flexible PMIA composites with modified micro- and nano-sized hexagonal boron nitride. *Front. Mater. Sci.* **13**(1), 64–76 (2019)
5. Li, Y., et al.: A review of the electrical and mechanical properties of carbon nanofiller-reinforced polymer composites. *J. Mater. Sci.* **54**(2), 1036–1076 (2018)
6. Jamróz, E., et al.: Furcellaran nanocomposite films: the effect of nanofillers on the structural, thermal, mechanical and antimicrobial properties of biopolymer films. *Carbohydr. Polym.* **240**, 116244 (2020)
7. Dang, T.M.L., Kim, C.Y., Zhang, Y., Yang, J.F., Masaki, T., Yoon, D.H.: Enhanced thermal conductivity of polymer composites via hybrid fillers of anisotropic aluminum nitride whiskers and isotropic spheres. *Compos. B Eng.* **114**, 237–246 (2017)
8. Lee, D.J., Song, Y.S.: Thermomechanical anisotropy and flowability of talc and glass fiber reinforced multiphase polymer composites. *Compos. Struct.* **174**, 329–337 (2017)
9. Rodríguez, H.A., Kriven, W.M., Casanova, H.: Development of mechanical properties in dental resin composite: Effect of filler size and filler aggregation state. *Mater. Sci. Eng., C* **101**, 274–282 (2019)
10. Khan, A., et al.: Low-cost carbon fillers to improve mechanical properties and conductivity of epoxy composites. *Polymers* **9**(12), 642 (2017)
11. Qi, W., Zhang, X., Wang, H.: Self-assembled polymer nanocomposites for biomedical application. *Curr. Opin. Colloid Interface Sci.* **35**, 36–41 (2018)
12. Yu, H., Zhang, B., Bulin, C., Li, R., Xing, R.: High-efficient synthesis of graphene oxide based on improved hummers method. *Sci. Rep.* **6**(1), 1–7 (2016)
13. Lin, L., Peng, H., Liu, Z.: Synthesis challenges for graphene industry. *Nat. Mater.* **18**(6), 520–524 (2019)
14. Dimiev, A.M., Eigler, S. (eds.): *Graphene Oxide: Fundamentals and Applications*. Wiley, Hoboken (2016)
15. Xia, X., Weng, G.J., Hou, D., Wen, W.: Tailoring the frequency-dependent electrical conductivity and dielectric permittivity of CNT-polymer nano-composites with nanosized particles. *Int. J. Eng. Sci.* **142**, 1–19 (2019)



Features of Plasticity Diagram Construction for Low-Plastic Materials

Ihor Shepelenko¹ , Yakiv Nemyrovskiy¹ , Yuri Tsekhanov² ,
Volodimir Mirzak¹ , and Sergii Mahopets¹ 

¹ Central Ukrainian National Technical University,
7, Universytetskyi Ave., Kropyvnytskyi 25006, Ukraine
² Voronezh State Technical University,
84, 20 let Oktyabrya St., Voronezh 394026, Russia

Abstract. The presented work aims to construct a plasticity diagram for SCH20 cast iron, which is necessary to predict the ultimate deformation values of this material under deformation conditions with significant negative values of the coefficient of the stress state. A theoretical model of the composite cast iron sample deformation during its joint compression with plastic materials has been developed, influencing hydrostatic pressure values and the stress-deformed state index along with the wall thickness. The calculations performed according to the developed model made it possible to determine the stress-deformed state parameters and create the necessary conditions for determining the deformation accumulated before fracture at various negative values of the coefficient of the stress state. A technique is proposed for experimental studies of the composite sample deformation, including a test program and the development of a device for compressing the studied samples. Experimental studies of a composite sample compression consisting of SCH20 cast iron and L63 brass confirmed theoretical calculations results and made it possible for the first time to obtain significant plastic deformations of cast iron with negative values of the stiffness coefficient of the stress state. The studies carried out made it possible for the first time to construct a cast-iron plasticity diagram, including the area where deformation occurs at significant negative values of the stiffness coefficient of the stress state.

Keywords: Theoretical model · Stress-deformed state · Cast iron · Composite sample · Plasticity · Deformation · Stiffness coefficient · Stress state

1 Introduction

The emerging trends in the production and machines and mechanisms operation are aimed at a significant improvement in their operational properties, primarily by improving the quality of the working surface of parts [1]. The factors influencing the surface quality include the physical and mechanical characteristics of the surface layer properties, which are estimated by the depth of hardening and residual stresses and geometric properties characterizing the microrelief of the processed part [2]. At present,

in addition to the listed indicators, the parameter characterizing the microdefectiveness of the surface layer – the resource of the plasticity used – is increasingly used [3].

The plasticity of a metal depends on several factors. Besides the nature of the material itself, the most important is the thermomechanical parameters of the process itself: the type of stress state, temperature, rate of deformation, and history of deformation [4]. The dependence of plasticity on the type of stress state is characterized by the plasticity diagram, which is a mechanical characteristic of the material [5]. The plasticity diagram is presented in the coordinates: “the stiffness coefficient of the stress state η – the accumulated deformation before fracture e_{ult} ”.

The study of plasticity indicators is significant in processing low-plastic materials by plastic deformation, such as graphite-containing cast iron SCH20, the possibilities of plastic deformation limited by destruction.

In [6], the possibility of cast-iron products’ plastic deformation was proved experimentally, but to quantitatively determine the magnitude of ultimate deformations, select the expansion deformation values, and residual plasticity, it is necessary to construct the plasticity diagram of the studied material. The construction of such a diagram is associated with the performance of studied materials mechanical tests under simple loading and deformation conditions when stresses and deformations vary in proportion to one parameter. Moreover, if plastic materials, tensile, torsion, and compression tests allow achieving significant deformations [7], then for such a low-plastic material as cast iron, traditional research methods do not ensure significant ultimate deformations [8].

Thus, studies aimed at constructing the plasticity diagram of low-plastic materials are becoming relevant.

2 Literature Review

A feature of the plasticity diagram for low-plastic materials, in particular, graphite-containing cast irons, is the need to create a stress state that provides significant negative values of the stiffness coefficient of the stress state η , which will make it possible to achieve significant plastic deformations.

Tensile tests, biaxial tension of cast iron samples showed almost complete absence of plastic deformation (brittle fracture took place). At the same time, during compression tests, where the coefficient of the stress state $\eta = -1$, insignificant plastic deformation of the tested samples was recorded [9]. Plastic deformation (less than 2.5%) is also present during torsion fracture [7].

In works [10] labor-intensive methods of testing materials under conditions of strong hydrostatic compression in high-pressure chambers with complex and expensive equipment are proposed.

Thus, the existing methods for determining the residual deformation for low-plastic materials, which are practically available for technological practice, provide the value of the stiffness coefficient of the stress state only within $\eta = -1$. This does not allow obtaining a continuation of the plasticity diagram into the region of strong hydrostatic compression, where it is possible to achieve large plastic deformations without

destruction, which would make it possible to study the pressure treatment technological processes of such materials.

Consequently, there is a need to develop a technique for determining the plastic deformation before fracture at values $\eta \leq -1$. There are no test data in the literature for such coefficients of the stress state.

In [11], a theoretical model was developed for a cylindrical sample axial compression case, including a cast-iron sample enclosed along the outer surface in a rigid cylindrical cage.

The relationship between stress and deformation tensors is known [12]:

$$\sigma_r = \frac{2 e_r}{3 e_0} \sigma_0(e_0) + \sigma; \quad \sigma_\varphi = \frac{2 e_\varphi}{3 e_0} \sigma_0(e_0) + \sigma; \quad \sigma_z = \frac{2 k}{3 e_0} \sigma_0(e_0) + \sigma \quad (1)$$

where σ_r , σ_φ , σ_z – respectively radial, circumferential and axial stresses; σ – hydrostatic pressure (average stress); $\sigma_0(e_0)$ is the stress intensity, depending for the hardened material on the intensity of the accumulated plastic deformation e_0 ; k – relative axial deformation. This compression model makes it possible to predict large plastic deformations of a cast iron sample. However, its capabilities in terms of practical experimental control of deformation parameters are limited.

In [13], it was shown experimentally that under the joint compression of plastic and low-plastic materials, it becomes possible to influence the parameters of the stress-deformed state (SDS) and the hydrostatic pressure the stiffness coefficient of the stress state. Consequently, there is a need to improve the previously proposed technique [11]. For this, it is necessary to develop a theoretical model for the deformation case of a composite sample in a combination of “cast iron - plastic material”.

The presented work aims to construct a plasticity diagram for graphite-containing cast iron SCH20, which is necessary to predict the ultimate deformation values at significant negative values of the coefficient of the stress state.

For achieving this goal, it is necessary to solve the following tasks:

- to develop a theoretical model of a cast iron sample compression while limiting radial deformation due to the use of a cast iron and plastic material composite sample;
- according to the developed model, determine the SDS parameters of the composite sample;
- to develop a methodology and equipment for conducting experimental studies of a composite sample compression in a combination of cast iron with other materials;
- to determine the SDS parameters for a composite sample under conditions of significant plastic deformation.
- to construct a plasticity diagram for cast iron in the area of high hydrostatic pressure.

3 Research Methodology

The basis for the development of the calculation method is the SDS presentation of a composite pipe workpiece in its uniform settlement with limited radial deformation along the outer surface.

Let us consider the deformation conditions of a composite cast iron sample composed of several cylinders with different materials.

In [11], an equation was obtained to determine the radial stress for the case of a cylindrical sample axial compression enclosed along the outer surface in a rigid cylindrical cage:

$$\sigma_r = \left[\frac{2 e_\varphi}{3 e_0} \sigma_0(e_0) - \frac{2 e_r}{3 e_0} \sigma_0(e_0) \right] \frac{dr}{r}, \tag{2}$$

e_φ, e_r – circumferential and radial deformations at a point with coordinate r . After using the example of a composite sample, the integration of Eq. (2) is carried out sequentially for each layer (Fig. 1) from the inner free surface, on which the normal stress σ_r is equal to zero.

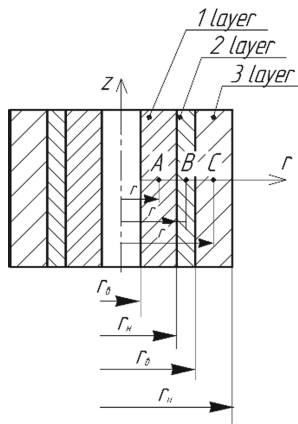


Fig. 1. The calculated scheme for a composite sample.

Then we get that

- for point A:

$$\sigma_r = \int_{r_0}^r \frac{2}{3} \left[\frac{e_\varphi}{e_0} \sigma_{01}(e_0) - \frac{e_r}{e_0} \sigma_{01}(e_0) \right] \frac{dr}{r}; \tag{3}$$

– for point B:

$$\sigma_r = \int_{r_B}^{r_1} \frac{2}{3} \left[\frac{e_\varphi}{e_0} \sigma_{01}(e_0) - \frac{e_r}{e_0} \sigma_{01}(e_0) \right] \frac{dr}{r} + \int_{r_1}^r \frac{2}{3} \left[\frac{e_\varphi}{e_0} \sigma_{02}(e_0) - \frac{e_r}{e_0} \sigma_{02}(e_0) \right] \frac{dr}{r}; \quad (4)$$

– for point C:

$$\begin{aligned} \sigma_r = & \int_{r_B}^{r_1} \frac{2}{3} \left[\frac{e_\varphi}{e_0} \sigma_{01}(e_0) - \frac{e_r}{e_0} \sigma_{01}(e_0) \right] \frac{dr}{r} + \int_{r_1}^{r_2} \frac{2}{3} \left[\frac{e_\varphi}{e_0} \sigma_{02}(e_0) - \frac{e_r}{e_0} \sigma_{02}(e_0) \right] \frac{dr}{r} \\ & + \int_{r_2}^r \frac{2}{3} \left[\frac{e_\varphi}{e_0} \sigma_{03}(e_0) - \frac{e_r}{e_0} \sigma_{03}(e_0) \right] \frac{dr}{r} \end{aligned} \quad (5)$$

where $\sigma_{01}(e_0)$, $\sigma_{02}(e_0)$, $\sigma_{03}(e_0)$ are the approximations of the various materials hardening curves, respectively, of the first, second, and third cylindrical layers of the composite sample.

The hydrostatic pressure σ is determined from (1) taking into account the found σ_r :

$$\sigma = \sigma_z - \frac{2}{3} \frac{e_r}{e_0} \sigma_0(e_0), \quad (6)$$

Substituting values (6) into (1), we find σ_φ , σ_z .

Stiffness coefficient of the stress state

$$\eta = \frac{3\sigma}{\sigma_0(e_0)}, \quad (7)$$

Let us approximate the experimentally obtained curve of SCH20 cast iron hardening by dependence $\sigma_0 = a(e_0)^b$. Parameters a and b were determined by the least-squares method: $\sigma_0 = 952,42 \cdot e_0^{0,167}$. Similarly, we approximate the experimentally obtained dependence under uniaxial compression of L63 brass samples: $\sigma_0 = 820 + 120e_0$.

The calculations were performed with a constant step of axial deformation $k = 0.1$. Figure 2 shows the change in the parameters of the deformation tensor, stresses, hydrostatic pressure, and the stiffness coefficient of the stress state depending on the hole radius in a composite sample of SCH20 cast iron and L63 brass within $1 \leq r \leq 3$, that is, from the inner surface of the hole to the outer surface sample (Fig. 2).

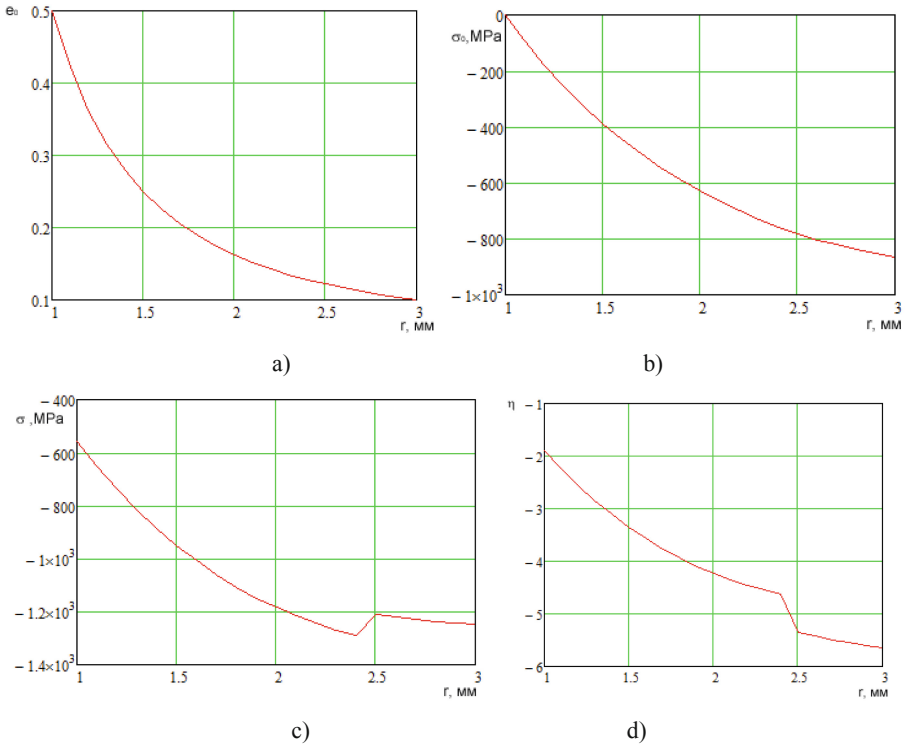


Fig. 2. Changes in the deformation intensity parameters (a), radial stress (b), hydrostatic pressure (c), the stiffness coefficient of the stress state (d) depending on the composite sample radius “cast iron SCH20 - brass L63”.

Calculations performed for the deformation of a cast iron sample in combination with L63 brass (Fig. 2) showed the independence of the deformation values from the material, which is explained by the fact that the deformation values were obtained only from the condition of material incompressibility.

The performed theoretical studies made it possible to establish that when plastic materials are used together with cast iron during combined sample compression under constrained circumferential deformation, it becomes possible to change the hydrostatic pressure σ and the coefficient of the stress state η along with the wall thickness, that is, depending on the range of variation r (Fig. 2).

4 Results

4.1 Experimental Research Technique

The above calculations made it possible to draw up a program for testing composite samples of cast iron and plastic materials at various negative values of the stiffness coefficient of the stress state η .

Compression testing of composite samples was carried out on a UIM-50m universal testing machine with a maximum developed load of 500 kN and operating speeds range of the movable crosshead from 0.001 mm/min to 200 mm/min. For experimental studies, a particular device was developed and manufactured (Fig. 3a and b), consisting of a test composite sample 2, coupled with a clip 1 for compression, as well as two punches 3.

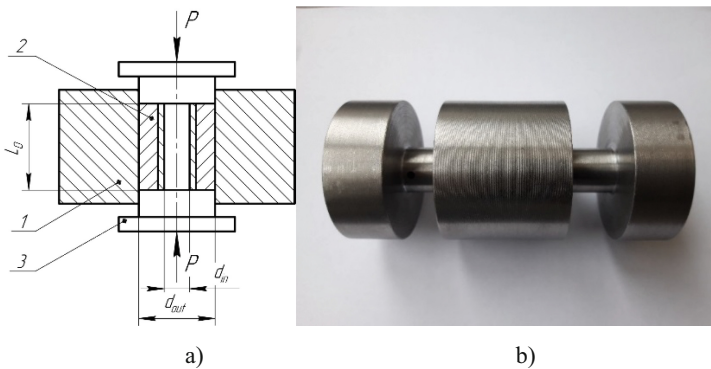


Fig. 3. Device for compressing samples: *a* – device scheme; *b* – general view.

The tested composite sample 2 (Fig. 3a) is two mating cylinders made of SCH20 cast iron and L63 brass. The outer surface of the composite sample mates with the compression holder 1 with an infinite wall thickness does not deform plastically and ensures the absence of plastic deformations on the outer surface of the sample. Axial compression is performed by two punches 3, moving towards each other with an effort P and contacting their end planes with sample 2, and cylindrical surfaces with the inner side surface of the holder 1. Sample 2, when its ends are compressed by punches 3, is deformed in the axial and radial directions.

A composite sample installed in a special device was smoothly loaded with an axially compressive force to determine the ultimate deformation before fracture. The onset of destruction was recorded at the moment of appearance of a characteristic short-term crunching sound using the tracking arrow of the force-measuring device and a force and displacement transducer with a recorder.

For visual control of the cast iron sleeve destruction nature, the composite sample was cut and examined under a microscope.

4.2 Experimental Results

The experimental studies show compression of a composite sample consisting of a cast-iron thin-walled sleeve and L63 brass. It should be noted that brass L63 is a hardenable material that is effectively used as an antifriction coating applied by the method of finishing antifriction non-abrasive treatment on a previously prepared surface of a cast iron product [14].

Figure 4 shows a composite “cast iron – brass” sample in the initial state. It was found that for a given pair of composite samples, the compression process is stable. Axial deformation before fracture is equal to $k = -0.096$. The dimensions of the sample (Fig. 4a) ensured the deformation of the cast iron at $\eta = -1.89$.

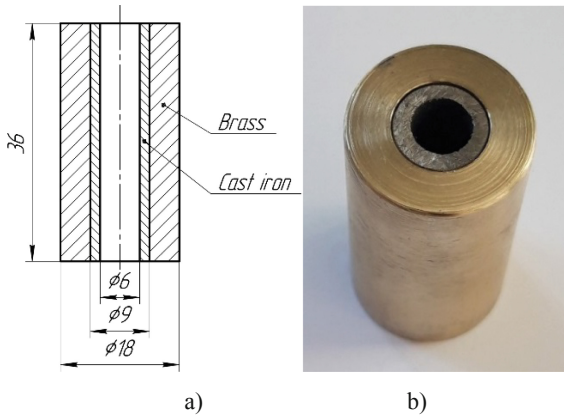


Fig. 4. Composite sample “cast iron SCH20 – brass L63”: *a* – sample dimensions; *b* – general view.

The appearance of the deformed composite sample upon fracture is shown in Fig. 5 (a). A crack on the surface of the cast-iron sleeve is shown in Fig. 5(b).

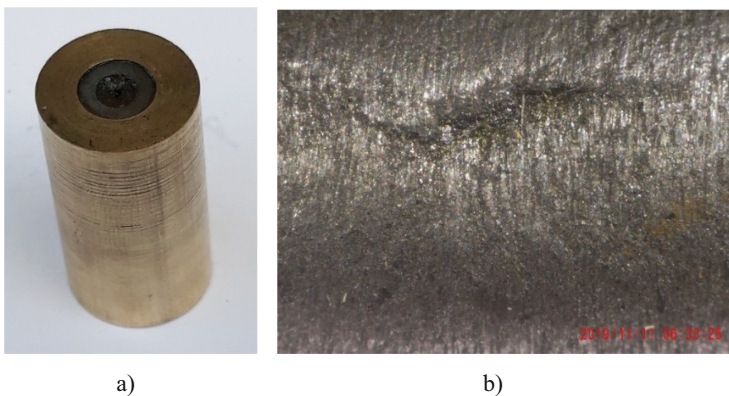


Fig. 5. View of the composite sample “cast iron SCH20 – brass L63” after deformation: *a* – general view of the composite sample; *b* – a crack in a cast iron sample.

As seen from Fig. 5(b) view of cast iron sample destruction is mixed. It should be noted that along with the plastic area's appearance of plasticity resource exhaustion, the crack has areas of brittle fracture.

Thus, the studies carried out made it possible to establish the deformation indices for the composite sample "cast iron – brass": the total deformation of the cast iron sample was $e_0 = 39\%$ with a stiffness coefficient $\eta = -1.89$. This is a very significant plastic deformation for such a semi-brittle material as cast iron SCH20, which was achieved by the proposed theoretical and experimental research programs. Similarly, for the sample "M1 copper – SCH20 cast iron – M1 copper" composed of three sleeves, a large deformation $e_0 = 78\%$ was obtained with a stiffness coefficient $\eta = -3.6$.

The data obtained made it possible for the first time to obtain a cast iron plasticity diagram with significant negative values of the stiffness coefficient of the stress state (Fig. 6).

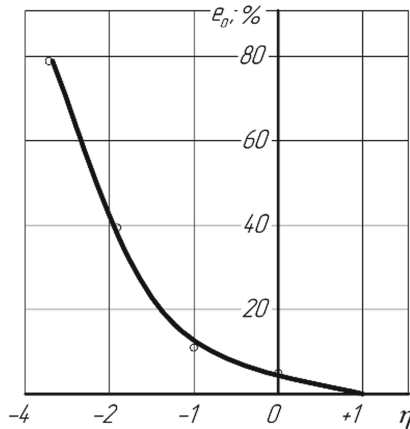


Fig. 6. Plasticity diagram of cast iron SCH20.

5 Conclusions

The studies conducted allowed us to formulate the following conclusions.

A method for obtaining significant plastic deformations of low-plastic cast iron SCH20 has been developed, which consists of developing a model of deformation of a composite cast-iron tubular sample during its joint compression in combination with other materials. This made it possible to influence the values of hydrostatic pressure and SDS indicators over the wall thickness of the studied sample.

It has been proved that semi-brittle cast iron can plastically deform only at negative values of the stiffness coefficient of the stress state, which makes it possible to formulate the following statement: holes processing in cast iron products by plastic deformation is possible only in the absence of plastic deformations near the outer surface. In this case, only the inner wall thickness applied to the hole is plastically deformed.

The experiments planned according to the developed theoretical model of the settlement of the composite sample confirmed the calculation results. They made it possible for the first time to obtain significant plastic deformations of cast iron with negative values of the stiffness coefficient of the stress state.

For the first time, a cast iron SCH20 plasticity diagram was constructed, including a section where deformation occurs at significant negative values of the stiffness coefficient of the stress state.

References

1. Hosseini, A., Kishawy, H.A., Moetakef-Imani, B.: Effects of broaching operations on the integrity of machined surface. *Procedia CIRP* **45**, 163–166 (2016). <https://doi.org/10.1016/j.procir.2016.02.352>
2. Kobets, A., Aulin, V., Derkach, O., Makarenko, D., Hrynkiv, A., Krutous, D., Muranov, E.: Design of mated parts using polymeric materials with enhanced tribotechnical characteristics. *East. Eur. J. Enterp. Technol.* **5**(12)(107), 49–57 (2020). <https://doi.org/10.15587/1729-4061.2020.214547>.
3. Dobrotvorskiy, S., Balog, M., Basova, Y., Dobrovolska, L., Zinchenko, A.: Concept of the software for materials selection using .NET technologies. In: Tonkonogyi, V., et al. (eds.) *Advanced Manufacturing Processes. InterPartner 2019. Lecture Notes in Mechanical Engineering*, pp. 32–43. Springer, Cham (2020). <https://doi.org/10.1007/978-3-030-40724-74>
4. Del, G.D.: Plasticity of deformed metal. *High Press. Phys. Eng.* **11**, 28–32 (1983). (in Russian)
5. Grushko, A.V.: *Maps of materials in cold working by pressure*. Vinnitsa (2015). (in Russian)
6. Rosenberg, O.A.: *Technological mechanics of deforming broaching*. Voronezh (2001). (in Russian)
7. Ogorodnikov, V.A., Kiritsa, I.Y., Muzyichuk, V.I.: Plasticity diagrams and peculiarities of their construction. *Improving pressure treatment processes and equipment in metallurgy and mechanical engineering*, pp. 251–255 (2006). (in Russian)
8. Shekin, S.E., Pogrelyuk, I.M., Sergach, D.A.: Modification of working surface of titanium components of friction units. *J. Superhard Mater.* **37**, 351–356 (2016). <https://doi.org/10.3103/S1063457615050093>
9. Chernyavsky, O.V., Sivak, I.O., Lopatenko, S.G.: Determining the limit of process application of deforming broaching in the processing of cast iron. *Improving the technical level of agricultural production and engineering*, pp. 82–85 (2016). (in Ukrainian)
10. Johnson, G.R.: A constitutive model and data for metal subjected to large strains, high strain and temperatures. In: *Proceedings of 7th Symposium on Ballistics, Hague*, pp. 541–547 (1983)
11. Shepelenko, I., Tsekhanov, Y., Storchak, M., Nemyrovskiy, Y., Cherkun, V.: Mechanics of micro-cutting using FANT. In: Tonkonogyi, V., et al. (eds.) *InterPartner 2020. LNME*, pp. 619–628. Springer, Cham (2021). https://doi.org/10.1007/978-3-030-68014-5_60
12. Khachanov, L.M.: *Fundamentals of Fracture Mechanics*. Moscow (1974). (in Russian)
13. Kukhar, V.V., Grushko, A.V., Vishtak, I.V.: Shape indexes for dieless forming of elongated forgings with sharpened end by tensile drawing with rupture. *SPP* **284**, 408–415 (2018)
14. Ragutkin, A.V., Sidorov, M.I., Stavrovskij, M.E.: Some aspects of antifriction coatings application efficiency by means of finishing nonabrasive antifriction treatment. *J. Min. Inst.* **236**, 239–244 (2019). <https://doi.org/10.31897/PMI.2019.2.239>



Comparative Analysis of Tribological and Functional Properties of Multilayer Composite Nanostructured Coatings Based on Nitrides of Cr, Mo, Zr, Nb, and Al

Alexey Vereschaka¹  and Mars Migranov² 

¹ Institute of Design and Technological Informatics, Russian Academy of Sciences, 18-1a, Vadkovsky Per., Moscow 127994, Russia

² Moscow State Technological University STANKIN, 1, Vadkovsky per., Moscow 127994, Russia

Abstract. The article describes the results of the studies focused on the properties of multilayer composite coatings with nanolayer structures based on nitrides of Cr, Mo, Zr, Nb, and Al. Tests were carried out to study the influence of temperature varying in the range of 600–1000 °C on the value of the adhesion component of the coefficient of friction (COF). The investigation was also focused on the cutting properties of carbide tools with the coating under study during the turning of AISI 321 steel at various cutting speeds. The study revealed the relationship between the value of the adhesion component of the COF and the tool life of coated cutting tools. The tool with the Cr,Mo-(Cr,Mo)N-(Cr,Mo,Al)N coating under study demonstrated good wear resistance on the tool's rake face during the cutting of corrosion and heat-resistant AISI 321 steel. With an increase in the cutting speed, the cutting properties of the tool with the coating under study increase compared to the tools with other coatings or uncoated tools.

Keywords: Physical coatings · Coefficient of friction · Tool life · Thermo stability · Tool wear

1 Introduction

Tribological and frictional properties of coatings are interrelated and significantly influence the performance properties of products on the working efficiency of cutting tools. It should be considered that with an increase in a temperature to 500–1000 °C, which is typical for the cutting zone, the tribological properties of the coatings change significantly. This change relates both to an increase in the material ductility and the formation of tribologically active oxide compounds (Magneli phases) on the surfaces of the coatings. Certain metal oxides are characterized by particularly favorable tribological properties at high temperatures in combination with high thermostability. The inclusion of such metals or their nitrides in the compositions of the coatings for cutting tools contributes to an increase in their working efficiency.

2 Literature Review

At high temperatures, nitrogen is replaced by more active oxygen, and thus, oxides are formed instead of nitrides [1]. Aluminum oxide Al_2O_3 is characterized by favorable properties [2, 3]. During the heating of samples with the Al_2O_3 -based coatings, the COF increases to a certain temperature (about 700 °C) and then the COF decreases significantly [4, 5]. During heating of the coatings based on the nitrides of such metals as Al-doped Ti, Cr [6], V, Nb, Mo, W [7], and Y [8], the oxide phase of Al_2O_3 is being formed, sometimes in the form of a continuous surface film of nanometric thickness [6–8]. Apart from aluminum, molybdenum [9, 10] (which forms MoO_3 oxide [11, 12]) and chromium (which forms Cr_2O_3 oxide) [13] are also able to form strong tribologically active oxide films. Similar films can also be formed at temperatures above 700 °C [12]. However, during heating to temperatures above 900 °C, the coatings with high molybdenum content and chromium begin to lose their performance properties due to the too active oxidation process [14].

Thus, it may be noted that the formation of oxides in the surface layers of the coatings may have both favorable (due to the improvement of tribological parameters and formation of protective films) and unfavorable (due to the total fracture of the surface structure of the coating) influence on the performance properties of the coatings.

The studies focused on the tribological properties find that the coatings with multilayer structures demonstrate better values of the COF, hardness, and adhesion to the substrate compared to the coatings with monolayer structures [15, 16]. However, the COF does not always play a crucial role in the cutting properties of coated tools. In particular, although for the (Ti,Al)N coatings, the value of COF is slightly higher than for the (Cr,Al)N coating, a tool with the (Cr,Al)N coating demonstrated higher wear resistance during turning [17]. The noticeable influence on the cutting process is exercised by forming oxides of Cr_2O_3 and especially MoO_3 , which contribute to a noticeable decrease in the COF at temperatures typical for the cutting zone [18]. With an increase in temperature, the hardness of most coatings decreases, but in some cases, the opposite effect can occur. In particular, as the temperature rises to 800 °C, the coherency strains are being formed in the (Ti,Al,Mo)N coating, and they prevent the sliding of dislocations and thus improve the hardness of the coating [19, 20]. The COF of the coatings first increases as the temperature rises to 500–600 °C and then decreases with further growth of the temperature [21, 22]. The development of coatings with a multi-component composition of a wear-resistant layer (including nitrides of three and more metals) contributed to an additional mechanical and performance properties improvement compared to the coatings with mono- or two-component composition [21, 23]. The main challenge of the article is to study the influence of chromium and molybdenum on the tribological properties of the coatings. The multilayer composite coatings based on nitrides of Cr, Mo, Zr, Nb, and Al were chosen as the main object of the study.

3 Research Methodology

The coatings under study were deposited using the filtered cathodic vacuum arc deposition (FCVAD) technology [16, 24, 25]. The technology was implemented on the VIT-2 unit (developed by VIT-IDTI RAS), which included two evaporators with a pulsating magnetic field and an evaporator with a curved plasma duct longitudinal, continuous, and uniform magnetic field [26, 27].

It is extremely difficult, if possible, to measure the COF directly during the cutting of materials. On the other hand, the standard methods for measuring the COF do not consider the essential features of the cutting process since they do not consider the temperature in the cutting zone and related factors (for example, oxidation and diffusion processes). Thus, it is reasonable to use a measurement method that, on the one hand, simulates the cutting conditions efficiently and, on the other hand, makes it possible to measure the COF adequately and accurately. The current study used the equipment and method described in detail in [21, 22].

In the presented mathematical model, a spherical indenter, which is made of the material identical to the tool material and which simulates a contact patch between a cutting tool and a workpiece being machined, rotates around its own axis, being compressed by two plain parallel inserts made of the material identical to the material being machined [28]. The inserts compress the indenter with certain forces, and a certain temperature in the range from zero to 1000 °C is provided in the entire system. The force F_{exp} required to rotate the indenter compressed by the inserts is measured. The force relates to the shear strength τ_n of adhesive bonds.

The strength τ_{nm} of adhesion bonds on the cut is determined from the relation [29]:

$$\tau_n = \frac{3 F_{exp} R_{exp}}{4 \pi r_{ind}^3} \quad (1)$$

where F_{exp} is the circumferential force on the disk, rotating the indenter; R_{exp} is the radius of the disk in which the indenter is fixed; and r_{ind} is the radius of the indent on the samples.

Normal stresses are defined as follows [29]:

$$p_n = \frac{N}{\pi r_{ind}^2} \quad (2)$$

Thus, the adhesion (molecular) component of the COF is defined as follows [29]:

$$f_M = \frac{\tau_n}{p_n} = \frac{3 F_{exp} R_{exp}}{4 N r_{ind}} \quad (3)$$

where p_n is normal stresses acting on the surface of the sphere.

The hardness (HV) of the coatings was determined by measuring the indentation at low loads according to the method proposed by Oliver and Pharr, which was conducted on a micro-indentometer hardness tester (CSM Instruments) at a fixed load of 10 mN. SNUNISO 1832:2012 carbide (WC+15% TiC+6% Co) inserts were used to study the

cutting properties of coated tools. Indenters of similar compositions (WC+15% TiC +6% Co) were chosen to investigate the tribological properties of the coated samples. An ACU 500 MRD lathe (Sliven) with a ZMMCU500MRD variable-speed drive was involved in the investigation focused on the cutting properties of the tools with the coatings under study. The cutting geometry parameters were: $\gamma = -7^\circ$, $\alpha = 7^\circ$, $\lambda = 0$, $r = 0.4$ mm, at the following cutting conditions: $f = 0.1$ rpm, $a_p = 0.5$ mm, and $v_c = 60, 80, 100, \text{ and } 120$ m/min. The nanostructure of the coating was examined with a JEM 2100 (JEOL, Japan) transmission electron microscope (TEM) using EDX system INCA Energy (OXFORD Instruments) to determine the chemical composition of the coatings.

4 Results

The results of the comparative analysis on the chemical composition of the coatings under study are presented in Table 1. All the coatings are characterized by low content of aluminum (within 6–16 at%). Since there may be a gradient change in the scope of elements in the coating nanolayers, Table 1 also indicates ranges of such change.

Table 1. Chemical composition of the coatings under comparison, at %.

Coating composition	Cr	Mo	Al	Ti	Zr	Nb	Si
Cr,Mo-(Cr,Mo)N-(Cr,Mo,Al)N	67–77	18–25	6–13	–	–	–	–
Ti-TiN-(Ti,Cr,Al,Si)N	32–44	–	6–12	44–53	–	–	2–3
Zr-ZrN-(Zr,Al,Si)N	–	–	6–11	–	87–91	–	2–3
Zr-ZrN-(Nb,Zr,Cr,Al)N	25–33	–	6–12	–	25–35	25–35	–
Zr,Nb-(Zr,Nb)N-(Zr,Nb,Al)N	–	–	7–16	–	39–43	39–45	–
Cr,Mo-(Cr,Mo,Zr,Nb)N-(Cr,Mo,Zr,Nb,Al)N	43–50	16–23	6–8	–	11–14	12–14	–
Ti-TiN-(Ti,Al,Cr)N	29–38	–	8–6	45–55	–	–	–

The nanostructures of the coatings under study are considered (Fig. 1). The presented images depict the nanolayer structures of all the coatings under investigation. The first six coatings have close values of the nanolayer period λ (100–200 nm), and two options – with an extremely large (302 nm) and an extremely small (10 nm) nanolayer period λ – are considered for the Ti-TiN-(Ti,Al,Cr)N coatings. The above methods may be applied to study both the influence of the chemical composition of the coatings and the impact of their nanostructure on the value of the adhesion component

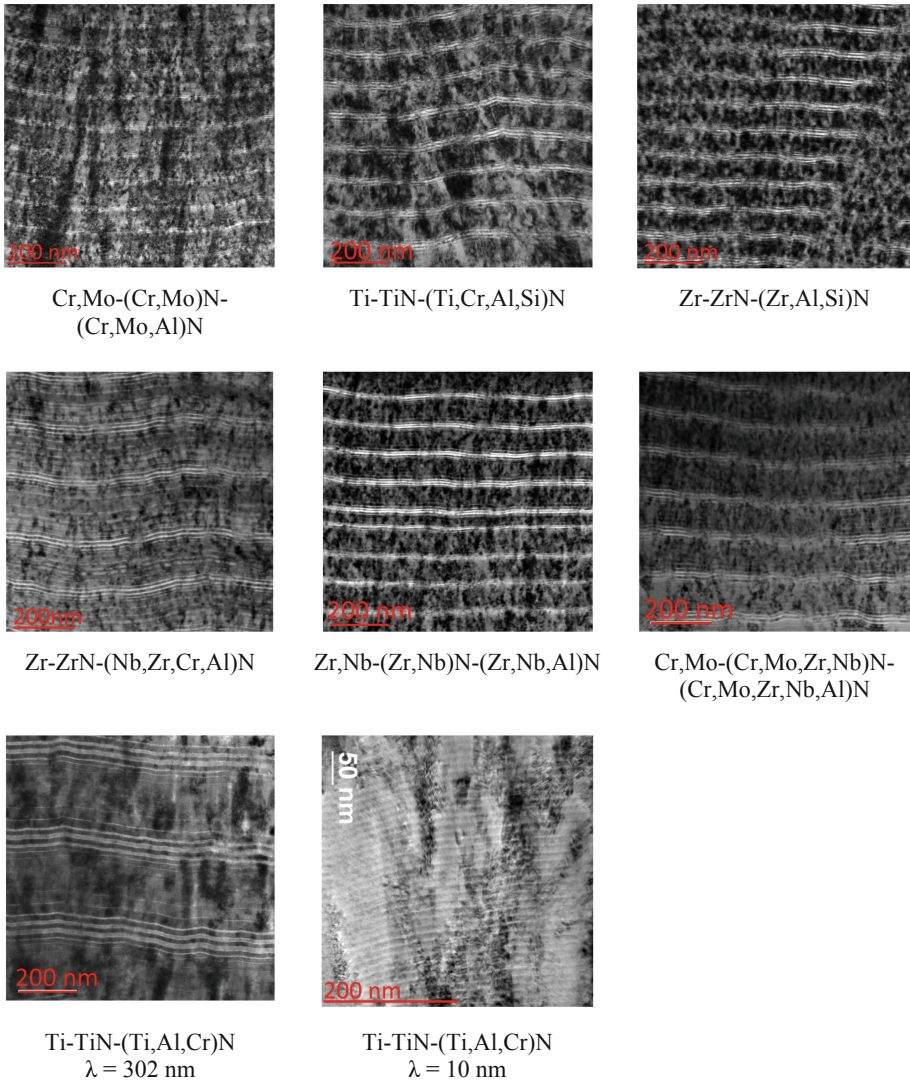


Fig. 1. Nanostructure of the coatings under study.

of the COF. Table 2 gives the results of the measurements of the hardness HV and the nanolayer period λ of the coatings under study. The value of λ has no significant influence on hardness [34, 35]. The tribological properties (the value of f_{adh} , the adhesion component of the COF) of the samples under study are compared (Fig. 2). While at the temperature of 500 °C, the value of f_{adh} for the sample with the Cr,Mo-(Cr,Mo)N-(Cr,Mo,Al)N coatings is slightly higher compared to the values of f_{adh} for the samples with the coatings based on ZrN (Zr-ZrN-(Zr,Al,Si)N and Zr-ZrN-(Nb,Zr,Cr,Al)N) and is close to the values of f_{adh} for the samples with the coatings of

Ti-TiN-(Ti,Cr,Al,Si)N; Zr,Nb-(Zr,Nb)N-(Zr,Nb,Al)N and uncoated samples, then at the temperature of 800 °C, the sample with the Cr,Mo-(Cr,Mo)N-(Cr,Mo,Al)N coating demonstrates the lowest value of f_{adh} among all the samples under study. With a further increase in the temperature to 900 and 1000 °C, the tendency intensifies and the importance of f_{adh} for the sample with the Cr,Mo-(Cr,Mo)N-(Cr,Mo,Al)N coating is noticeably lower than for the other samples under study. At the given temperatures, the values of f_{adh} for all samples with the (Ti,Cr,Al)N-based coatings become even higher than for the uncoated sample.

Thus, the value of f_{adh} increases upon heating from 500 to 800 °C for all the samples under study. During heating to 900 and 1000 °C, the value of f_{adh} begins to decrease for most of the coated samples under study but almost does not change for the uncoated sample and the samples with the coatings containing Nb and not containing Mo: (Zr,Nb-(Zr,Nb)N-(Zr,Nb,Al)N and Zr-ZrN-(Nb,Zr,Cr,Al)N). The Cr,Mo-(Cr,Mo,Zr,Nb)N-(Cr,Mo,Zr,Nb,Al)N coating, containing both Mo and Nb, demonstrates a slight decrease in f_{adh} at the given temperatures. Based on the above, it can be assumed that the presence of Mo in the composition of the coating contributes to a decrease in f_{adh} upon heating to a temperature of 900 °C and above, while the presence of Nb, on the contrary, inhibits such a decrease. This phenomenon can be explained: at high temperatures, the coatings based on the nitrides of Mo, Cr, and Al form solid and dense oxide films of MoO₃, Cr₂O₃, (Cr,Al)₂O₃, and Al₂O₃ [32] that contribute to a decrease in the value of f_{adh} . At the same time, the Nb-containing coatings form soft porous oxides of Nb₂O₅ and CrNbO₄ [33] that inhibit a decrease in f_{adh} . Zirconium oxide ZrO₂ is also a solid and dense compound. It can positively influence the tribological properties of the coatings, which may explain a decrease in f_{adh} for the ZrN-based coatings.

The influence of various coatings on the flank wear rate of carbide cutting tools is considered. Figure 3 depicts the relationship between H_m (the specific value of the flank wear rate per one meter of the cutting path) and the cutting speed during turning with carbide tools with the coatings under study. The lower rake wear rate at all cutting speeds was demonstrated by the tool with the Ti-TiN-(Ti,Al,Cr)N coating ($\lambda = 10$ nm). The tool with the Cr,Mo-(Cr,Mo)N-(Cr,Mo,Al)N coating under study also showed good resistance to wear on the rake face. It should be noted that with an increase in the cutting speed, the difference in the wear rate on the samples with the Ti-TiN-(Ti,Al,Cr)N ($\lambda = 10$ nm) and Cr,Mo-(Cr,Mo)N-(Cr,Mo,Al)N coatings slightly reduces. Such an effect may relate to the fact that the temperature rises with an increase in the cutting speed and, accordingly, it intensifies the formation of the MoO₃ oxide film, which has a positive influence on the cutting conditions. In the course of the earlier tests, the tool with the Cr,Mo-(Cr,Mo,Zr,Nb)N-(Cr,Mo,Zr,Nb,Al)N coating showed the highest wear resistance in turning of AISI 1045 steel. Meanwhile, in the course of a current series of cutting tests, its wear resistance appeared to be lower compared to the tools with the Ti-TiN-(Ti,Al,Cr)N ($\lambda = 10$ nm) and Cr,Mo-(Cr,Mo)N-(Cr,Mo,Al)N coatings. Since corrosion- and heat-resistant AISI 321 steel (HB 179 MPa) is a hard-to-cut material (M20-M25 ISO), the cutting conditions for AISI 321 steel differ significantly from the cutting conditions for AISI 1045 steel [34]. The steel being machined contains Cr (18 at %) and Ni (12 at %), which significantly influences the nature of its machining and wear of the cutting tool.

Table 2. Results of coating hardness measurements (HV, GPa).

Coating	HV, GPa	λ , nm
Cr,Mo-(Cr,Mo)N-(Cr,Mo,Al)N	24.0 ± 1.6	82
Ti-TiN-(Ti,Cr,Al,Si)N	36 ± 1	98
Zr-ZrN-(Zr,Al,Si)N	28 ± 1	110
Zr-ZrN-(Nb,Zr,Cr,Al)N	26 ± 1	205
Zr,Nb-(Zr,Nb)N-(Zr,Nb,Al)N	23.2 ± 3.6	96
Cr,Mo-(Cr,Mo,Zr,Nb)N-(Cr,Mo,Zr,Nb,Al)N	28.2 ± 2.1	138
Ti-TiN-(Ti,Al,Cr)N ($\lambda = 302$ nm)	29.82 ± 1	302
Ti-TiN-(Ti,Al,Cr)N ($\lambda = 10$ nm)	30.64 ± 1	10

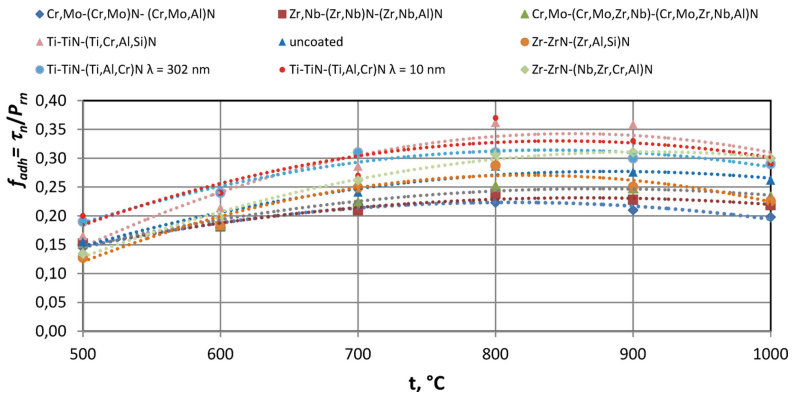


Fig. 2. Comparison of the tribological properties (the value of f_{adh} , the adhesion component of the COF) for the samples under study.

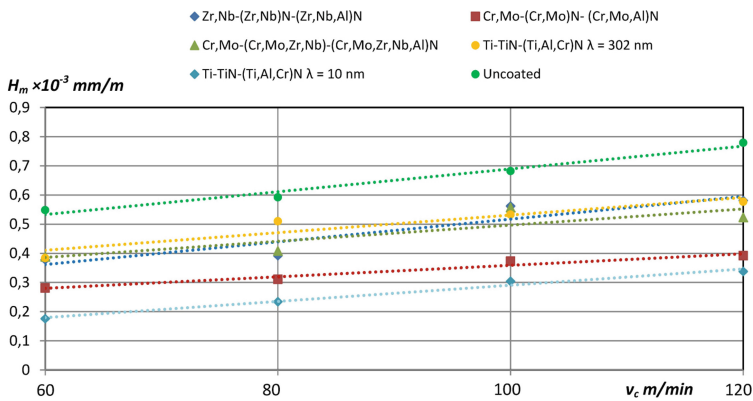


Fig. 3. Relationship between H_m (the specific value of the flank wear rate per one meter of the cutting path) and the cutting speed during turning with carbide tools with the coatings under study.

5 Conclusions

The properties of multilayer composite coatings of various compositions with a nanostructured wear-resistant layer were studied. The conducted studies have found the following.

The Cr,Mo-(Cr,Mo)N-(Cr,Mo,Al)N coating under study demonstrated the lowest value of f_{adh} , the adhesion component of the COF, among all the tested samples, over the entire temperature range of the study.

The presence of Mo in the composition of the coating contributes to a decrease in f_{adh} upon heating to a temperature of 900 °C and above, while the presence of Nb, on the contrary, inhibits such a decrease in f_{adh} .

The tool with the Cr,Mo-(Cr,Mo)N-(Cr,Mo,Al)N coating under study demonstrated good wear resistance on the tool's rake face during the cutting of corrosion and heat-resistant AISI 321 steel. With an increase in the cutting speed, the cutting properties of the tool with the coating under study increase compared to the tools with other coatings or uncoated tools.

Further planned research on this topic is to study the effect of the magnitude of the nanolayer period λ on the properties of various compositions' coatings and the cutting properties of tools with such coatings.

Acknowledgments. This study was supported by a grant of the Russian Science Foundation (Agreement 21-19-00612).

References




1. Deng, W., et al.: Comparative study on wear behavior of plasma sprayed Al_2O_3 coatings sliding against different counterparts. *Ceram. Int.* **43**(9), 6976–6986 (2017)
2. Goel, S., Björklund, S., Curry, N., Wiklund, U., Joshi, S.V.: Axial suspension plasma spraying of Al_2O_3 coatings for superior tribological properties. *Surf. Coat. Technol.* **315**, 80–87 (2017)
3. Schalk, N., Mitterer, C., Czettel, C., Sartory, B., Penoy, M., Michotte, C.: Dry-blasting of α - and κ - Al_2O_3 CVD hard coatings: friction behaviour and thermal stress relaxation. *Tribol. Lett.* **52**(1), 147–154 (2013)
4. Lin, X., Zeng, Y., Ding, C., Zhang, P.: Effects of temperature on tribological properties of nanostructured and conventional Al_2O_3 -3 wt.% TiO_2 coatings. *Wear* **256**(11–12), 1018–1025 (2004)
5. Franz, R., Lechthaler, M., Polzer, C., Mitterer, C.: Oxidation behaviour and tribological properties of arc-evaporated ZrAlN hard coatings. *Surf. Coat. Technol.* **206**(8–9), 2337–2345 (2012)
6. Fox-Rabinovich, G.S., et al.: Design and performance of AlTiN and TiAlCrN PVD coatings for machining of hard to cut materials. *Surf. Coat. Technol.* **204**(4), 489–496 (2009)
7. Biksa, A., et al.: Wear behavior of adaptive nano-multilayered AlTiN/MexN PVD coatings during machining of aerospace alloys. *Tribol. Int.* **43**(8), 1491–1499 (2010)
8. Beake, B.D., Fox-Rabinovich, G.S.: Progress in high temperature nanomechanical testing of coatings for optimising their performance in high speed machining. *Surf. Coat. Technol.* **255**, 102–111 (2014)

9. Kuleshov, A.K., Uglov, V.V., Chayevski, V.V., Anishchik, V.M.: Properties of coatings based on Cr, Ti, and Mo nitrides with embedded metals deposited on cutting tools. *J. Frict. Wear* **32**(3), 192–198 (2011)
10. Cura, M.E., et al.: Friction behavior of alumina/molybdenum composites and formation of MoO_3 -x phase at 400 °C. *Tribol. Int.* **87**, 23–31 (2015)
11. Lyo, I.-W., Ahn, H.-S., Lim, D.-S.: Microstructure and tribological properties of plasma-sprayed chromium oxide - molybdenum oxide composite coatings. *Surf. Coat. Technol.* **163–164**, 413–421 (2003)
12. Lu, Y.-C., Chen, H.-W., Chang, C.-C., Wu, C.-Y., Duh, J.-G.: Tribological properties of nanocomposite Cr-Mo-Si-N coatings at elevated T temperature through silicon content modification. *Surf. Coat. Technol.* **338**, 69–74 (2018)
13. Yuan, G., Lin, Y., Zhikang, M., Chenglei, W.: High-temperature oxidation behavior of (Ti, Cr)N coating deposited on 4Cr13 stainless steel by multi-arc ion plating. *Rare Metal Mater. Eng.* **43**, 1084–1087 (2014)
14. Wang, Y.-X., Lou, B.-Y., Pan, J., Zhang, X.: High temperature oxidation resistance of CrMoAlN gradient coatings prepared by unbalanced magnetron sputtering. *ZhongguoYouse Jinshu Xuebao/Chin. J. Nonferrous Met.* **27**(7), 1403–1410 (2017)
15. Beliardouh, N.E., Bouzid, K., Nouveau, C., Tlili, B., Walock, M.J.: Tribological and electrochemical performances of Cr/CrN and Cr/CrN/CrAlN multilayer coatings deposited by RF magnetron sputtering. *Tribol. Int.* **82**, 443–452 (2015)
16. Vereschaka, A., et al.: Effect of adhesion and the wear-resistant layer thickness ratio on mechanical and performance properties of ZrN - (Zr, Al, Si)N coatings. *Surf. Coat. Technol.* **357**, 218–234 (2019)
17. Tillmann, W., Grisales, D., Stangier, D., Butzke, T.: Tribomechanical behaviour of TiAlN and CrAlN coatings deposited onto AISI H11 with different pre-treatments. *Coatings* **9**(8), 519 (2019)
18. Koshy, R.A., Graham, M.E., Marks, L.D.: Temperature activated self-lubrication inCrN/Mo₂N nanolayer coatings. *Surf. Coat. Technol.* **204**, 1359–1365 (2010)
19. Glatz, S.A., et al.: Effect of Mo on the thermal stability, oxidation resistance, and tribomechanical properties of arc evaporated Ti-Al-N coatings. *J. Vac. Sci. Technol. A* **35**, 061515 (2017).
20. Ju, H., et al.: Crystal structure and tribological properties of Zr-Al-Mo-N composite films deposited by magnetron sputtering. *Mater. Chem. Phys.* **230**, 347–354 (2019)
21. Vereschaka, A., et al.: Effect of adhesion and tribological properties of modified composite nanostructured multilayer nitride coatings on WC-Co tools life. *Tribol. Int.* **128**, 313–327 (2018)
22. Vereschaka, A., Grigoriev, S., Tabakov, V., Migranov, M., Sitnikov, N. Milovich, F., Andreev, N.: Influence of the nanostructure of Ti-TiN-(Ti,Al,Cr)N multilayer composite coating on tribological properties and cutting tool life. *Tribol. Int.* **150**, 106388 (2020)
23. Metel, A.S., Grigoriev, S.N., Melnik, Y., Bolbukov, V.P.: Broad beam sources of fast molecules with segmented cold cathodes and emissive grids. *Instrum. Exp. Tech.* **55**(1), 122–130 (2012)
24. Metel, A., Bolbukov, V., Volosova, M., Grigoriev, S., Melnik, Y.: Source of metal atoms and fast gas molecules for coating deposition on complex shaped dielectric products. *Surf. Coat. Technol.* **225**, 34–39 (2013)
25. Grigoriev, S., Metel, A.: Plasma- and beam- assisted deposition methods. *Nato Sci. Ser. II Math. Phys. Chem.* **155**, 147–154 (2004)
26. Volosova, M.A., Grigor'ev, S.N., Kuzin, V.V.: Effect of Titanium Nitride coating on stress structural inhomogeneity in oxide-carbide ceramic. Part 4. Action of heat flow. *Refract. Ind. Ceram.* **56**, 91–96 (2015)

27. Kuzin, V.V., Grigor'ev, S.N., Volosova, M.A.: Effect of a TiC coating on the stress-strain state of a plate of a high-density nitride ceramic under nonsteady thermoelastic conditions. *Refract. Ind. Ceram.* **54**, 376–380 (2014)
28. Shuster, L.S.: Device for investigating adhesion interaction. Patent of Russia, No 34249 (2003)
29. Shuster, L.S.: Adhesive Interaction of the Cutting Tool with the Material Being Processed. *Mechanical Engineering*, Moscow (1988). (in Russian)
30. Contreras, E., Galindez, Y., Rodas, M.A., Bejarano, G., Gómez, M.A.: CrVN/TiN nanoscale multilayer coatings deposited by DC unbalanced magnetron sputtering. *Surf. Coat. Technol.* **332**, 214–222 (2017)
31. Zhang, Z.G., et al.: Microstructures and tribological properties of CrN/ZrN nanoscale multilayer coatings. *Appl. Surf. Sci.* **255**, 4020–4026 (2009)
32. Wang, Y.-X., Lou, B.-Y., Pan, J., Zhang, X.: High temperature oxidation resistance of CrMoAlN gradient coatings prepared by unbalanced magnetron sputtering. *J. Nonferrous Met.* **27**(7), 1403–1410 (2017)
33. Hu, C., Xu, Y.X., Chen, L., Pei, F., Zhang, L.J., Du, Y.: Structural, mechanical and thermal properties of CrAlNbN coatings. *Surf. Coat. Technol.* **349**, 894–900 (2018)
34. Vereschaka, A., Tabakov, V., Grigoriev, S., Sitnikov, N., Milovich, F., Andreev, N., Sotova, C., Kutina, N.: Investigation of the influence of the thickness of nanolayers in wear-resistant layers of Ti-TiN-(Ti,Cr,Al)N coating on destruction in the cutting and wear of carbide cutting tools. *Surf. Coat. Technol.* **385**, 125402 (2020)
35. Vereschaka, A., et al.: Investigation of the tribological and operational properties of (Mex, Moy,Al1-(x+y))N (Me –Ti, Zr or Cr) coatings. *Tribol. Int.* **165**, 107305 (2022)



The Structure and Properties of a-C:Ti and a-C:Ti:N Coatings Deposited on a Titanium and Titanium Nitride Sublayer

Xiaohong Jiang¹ , Dzmitry Piliptsou^{1,2} ,
Aliaksandr Rogachev^{1,2} , Ekaterina Kulesh^{1,2}, and Yiming Liu^{1,2}

¹ International Chinese-Belarusian Scientific Laboratory by Vacuum-Plasma Technologies, Nanjing University of Science and Technology, 200, Xiaolingwei street, Nanjing 210094, China
jiangxh24@njust.edu.cn

² Francisk Skorina Gomel State University, 104, Sovetskaya St., 246019 Gomel, Belarus

Abstract. This paper presents the deposition of Ti(TiN)/a-C:Ti(TiN) coatings, doped by titanium and nitrogen atoms on steel 316L and Si substrates, to study the microstructures and mechanical properties. The coatings were obtained using titanium cathode DC and graphite target pulse arc sputtering under nitrogen pressure of 10^{-1} Pa. The phase composition in the coatings was studied by XPS and Raman spectroscopy. XPS results showed that Ti-C bonds formed in the Ti/TiN/a-C:Ti coating, while Ti-N, Ti-C, C-N bonds were observed in the Ti/TiN/a-C:Ti:N coatings. Raman spectroscopy exhibited that the doped titanium layers into a-C coatings decrease the size of Csp^2 clusters. An increased disordering was also observed in Csp^2 clusters, which is essential for the mechanical properties. The surface microstructure of the coatings was further characterized by AFM, which indicated strong dependences on the droplet phase, grain size, and nature (such as graphite, titanium carbide, titanium carbonitride) the coating. The microhardness of coatings rose to 12.5 GPa. The doped titanium layers decreased internal stresses in Ti/TiN/a-C:Ti, i.e., 108,1 MPa. The friction coefficient is less than 0.3, dependent on the presence of Ti atoms in a-C coatings. Internal stresses are reduced due to the introduction of doping elements and soft metal layers in the coating structure. The change in the sp^2/sp^3 ratio determines the change in microhardness values and kinetics of friction.

Keywords: Multilayer carbon coatings · Titanium · Nitrides · XPS · Spectroscopy · Structure · Morphology · Friction · Microhardness

1 Introduction

Modern ion-plasma technologies make it possible to deposit protective coatings of various stoichiometric and chemical compositions on the functional surfaces of the cutting tool and various structural elements of machine parts [1, 2]. The thin-film hardening technology consists of the fact that coatings with a thickness of several nanometers to several micrometers are deposited on the working surfaces of assembly parts subjected to increased loads. These coatings provide an increase in the service life. The a-C coatings containing carbon clusters with different hybridization of bonds are characterized by an exceptional combination of physical and mechanical properties. As noted in previous papers on this topic [3, 4, 6, 7], the main variable parameters of multilayer coatings based on solid layers are the thickness values, the nature, and the arrangement of individual layers involved in forming a given structure. A considerable number of papers have been devoted to the peculiarities of the properties of multilayer coatings based on thin layers, and there are theoretical approaches to choosing the optimal geometric parameters of a multilayer structure. However, there are a lot of aspects considering multilayer carbon-containing coatings that remain unclear, including the influence of the nature and parameters of the metal or nitride layer on the structure and properties of the carbon-based upper layer. A structural feature of such coatings is a high proportion of interphase interfaces relative to the total volume of interfaces, which significantly affect the properties of the multilayer coating. The grain boundaries are areas with high compositional heterogeneity. They contain structural defects, which, in particular, are obstacles to the propagation of dislocations and cracks, which implies an increase in the hardness of the coatings and a decrease in internal stresses.

The formation of nanostructured layered coatings with high mechanical properties is possible through a particular selection of conditions and deposition modes, coating design parameters, and the analysis and study of interphase interaction processes. The resulting coatings of the given composition and structure with stable performance properties, resistant to multifactorial operating conditions, are impossible without analyzing the features of the coating structure formation process.

The presence of the metal coating and/or metal nitride in the Me(MeN)/a-C:Me(MeN) structure makes it possible to increase the strength of the adhesive bond between the coating and the substrate, and also to reduce the level of internal stresses due to the plasticity of the metal layers [5, 6]. The application of such coatings is limited by the deposition and growth features, catalytic and chemical processes of interaction between elements in the coating, leading to a change in the structure and, consequently, in mechanical properties.

Mechanical properties (microhardness, internal stresses, friction, and wear resistance) of coatings containing layers of metals or nitrides Me(MeN)/a-C:Me(MeN) depend and are determined by the presence and thickness of titanium (titanium nitride) layers and carbon layers doped with titanium and/or nitrogen [7]. Among the metals used to create composite carbon coatings, titanium is one of the most common elements caused by its ability to interact intensively with carbon to form titanium carbide, which is characterized by high hardness and toughness. The formation of titanium carbide

phases in the volume of the carbon matrix leads to a decrease in the propagation of dislocations in the coating volume, which causes a decrease in the growth of cracks in the contact interaction process, and due to the alternation of the phases “carbon” - “titanium carbide”, the coating retains high hardness at lower values of internal stresses [8].

This paper aims at determining the influence of technological conditions and synthesis modes of multilayer a-C:Ti and a-C:Ti:N coatings, deposited on a titanium and titanium nitride bilayer, on their structure, morphology, and mechanical properties.

2 Research Methodology

The Ti(TiN)/a-C:Ti(TiN) coatings were deposited on monocrystalline silicon wafers (111) and 3261 stainless steel substrates using a combined evaporation method that combines the evaporation of a titanium cathode by a DC arc (discharge current 70 A, titanium VT-100) and a graphite target by a pulsed arc discharge ($f = 15$ Hz, $U_{\text{pulse}} = 350$ V). The nitrogen partial pressure was 10^{-1} Pa. The thickness of the coatings was (450 ± 10) nm. The thickness of TiN layers did not exceed 150 nm. The thickness of Ti layers did not exceed 20 nm. The choice of previously sequentially deposited layers of titanium and titanium nitride as a sublayer makes it possible to ensure high strength of the adhesive bond of the multilayer coating with the substrate and individual layers between themselves [9].

The morphology of the coating surface was studied by atomic force microscopy (AFM) in the modes of topography and phase contrast measurement (scanning area $3 \times 3 \mu\text{m}$) using a Solver-PRO P47 (NT-MDT).

Raman spectra were recorded using a Senterra Raman microscope (Bruker). The spectra were recorded in the spectral range of $600 \div 2500 \text{ cm}^{-1}$. The spectra were excited by radiation with a wavelength of 532 nm and a power of 20 mW.

The chemical composition and structure of carbon bonds were determined by the X-ray photoelectron spectroscopy (XPS) method during the substance excitation by $K\alpha$ -radiation of aluminum with quantum energy of 1486.6 eV and total power of 25 W (PHI Quantera).

The wear tests were carried out according to the “sphere-plane” scheme (UMT 2-EC, Bruker). The Si_3N_4 ball with a diameter of 5/32” was used as a counterbody.

Friction was carried out at a load of 0.5 N and a sliding speed of 0.1 m/s in an air environment at a relative humidity $(42 \div 45)\%$ and a temperature of 22 °C. The contact pressure, Hertz calculated, was equal to 478.6 MPa.

Internal stress (σ) in the coatings was determined using the Stoney formula considering the change in the curvature radius of the silicon substrate before and after the deposition of the coatings (Profiler Dektak XT, Bruker) [10].

The microhardness of the coatings was determined by the Knoop method in 15 different places on the coating surface, and the average value was determined on the basis of the results. The test load and duration were 245 mN and 10 s, respectively. Since the thickness of the coatings did not exceed $1 \mu\text{m}$, the obtained microhardness values were interpreted as the mechanical characteristic of the entire “coating-substrate” system.

3 Results

The concentration of elements in the surface layer of the coating was determined using the XPS (Table 1).

Table 1. The atomic concentration of the elements in the coating

Coating	C, at. %	O, at. %	N, at. %	Ti2p3, at. %
Ti/TiN/a-C	89.6	8.6	1.5	0.3
Ti/TiN/a-C:Ti	86.8	8.8	1.2	3.2
Ti/TiN/a-C:Ti:N	64.5	19.6	9.0	6.9

As can be seen, the coating contains nitrogen, oxygen, titanium, and carbon. Regardless of the deposition method of the upper layer, traces of titanium and nitrogen were found in the coating (presumably the reflexes from the underlying layers). Oxygen in the coating is present as a result of titanium oxidation in the residual atmosphere of the vacuum chamber or as a result of attachment to carbon after depressurization of the vacuum chamber. The presence of titanium and nitrogen is explained by diffusion processes and the coating of sufficiently large titanium particles formed at the deposition stage of Ti or TiN layers.

Figure 1 shows the spectra of C1s states of carbon atoms in the coatings deposited on layers of different nature. The C1s spectrum of the Ti/TiN/a-C coating (Fig. 1a) contains the peaks characteristic of Csp^2 (peak at 284.3 eV), Csp^3 (peak at 285.2 eV), and C–O bonds. Similar peaks (Fig. 1b, c) are also present in the spectra of the Ti/TiN/a-C:Ti and Ti/TiN/a-C:TiN coatings [11]. Some bonds determine the interaction of the Ti–N, Ti–C type in the spectra of Ti/TiN/a-C:Ti and Ti/TiN/a-C:TiN coatings. The presence of these connections is determined by the formation processes of the upper composite layer. The peak characterizing the Ti–C type interaction appears insignificantly in the spectrum of the C1s state of carbon atoms.

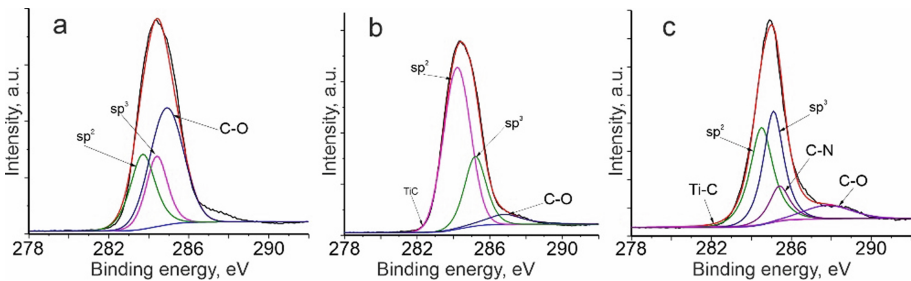


Fig. 1. XPS spectra of C1s peak: a – Ti/TiN/a-C, b – Ti/TiN/a-C:Ti, c – Ti/TiN/a-C:Ti:N

Figure 1(c) shows that doping carbon coatings with titanium and nitrogen leads to an increase in the intensity of the Csp^3 component and a decrease in the Csp^2 intensity,

which is consistent with the data in [12]. Comparing the ratios of the contributions of the integral areas of the Csp^2/Csp^3 components for the coatings of different architectures, it can be concluded that binary doping with titanium and nitrogen causes a decrease in the content of carbon-carbon bonds due to the formation of chemical compounds of a different type, CN for example.

Figure 2(b) shows the spectrum of the $Ti2p3$ state for the Ti/TiN/a-C:Ti:N coating. The $Ti2p3$ spectrum contains peaks characteristic of chemical bonds such as Ti-O, Ti-N, and metallic titanium. The position and shape of the peak located at 457.8 eV characterize the Ti-CN type's bond and are in agreement with the data given in [6]. When the spectrum was decomposed into components, the peak characterizing the bond of the Ti-C type was not detected, which, according to the data given in [7], is associated with a low titanium concentration in the surface layer of the coating.

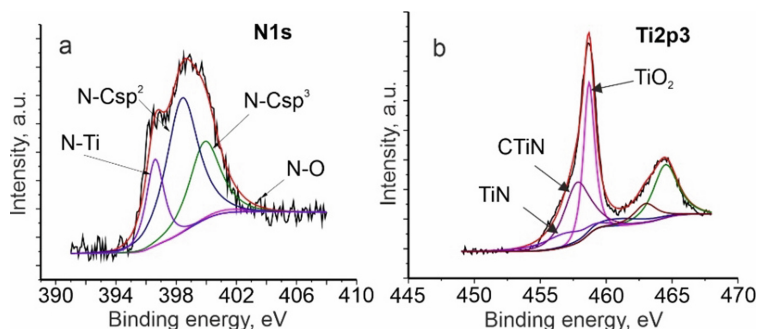


Fig. 2. N1s and $Ti2p3$ XPS spectra of the Ti/TiN/a-C:Ti:N coatings

The low content of titanium in the form of carbide can be explained by the higher chemical activity of titanium and nitrogen than titanium and carbon, as well as by the bombardment of the growing coating with high-energy metal ions, which leads to the destruction of Ti-C bonds [13].

In the spectrum fragment corresponding to the N1s peak (see Fig. 2a), four peaks can be distinguished, localized on the energy scale at (396.0 ± 0.2) eV, $(398.7 \div 399.1)$ eV, $(399, 5 \div 400.2)$ eV and (402.0 ± 0.2) eV. Three dominant peaks located at 396.0, 398.7, and 400.2 eV are attributed to nitrogen chemically bonded to carbon in the states of Csp^2 -, Csp^3 -hybridization, and also characterize the interaction of the N-Ti type. The fourth peak corresponds to the N-O bond or carbon bonds [14].

The Csp^2/Csp^3 ratio is 2.76 for the Ti/TiN/a-C coating, while the value of the Csp^2/Csp^3 ratio decreases to 1.68 for the Ti/TiN/a-C:Ti coating. There is a further decrease in the Csp^2/Csp^3 ratio to values of 1.01 for the Ti/TiN/a-C:Ti:N coatings. Based on these data, the introduction of titanium and nitrogen (along with the presence of nitride sublayers) leads to a decrease in the Csp^2/Csp^3 ratio. Thus, the introduction of Ti and N into the coating structure causes an increase in the number of carbon atoms in the state with sp^3 -hybridization of bonds compared to undoped and doped only with titanium, which is typical for the coating with a high content of the diamond phase. This

behavior of Csp^2/Csp^3 is in close agreement with the data obtained by Raman spectroscopy and is confirmed by the results presented in [15, 16].

It is known [17] that the ratio of integrated intensities I_D/I_G determines the relative abundance of carbon atoms with sp^2 and sp^3 bond hybridization, while the position and width of the G peak determine the change in the size and degree of ordering of carbon Csp^2 clusters. Depending on the deposition mode, the presence of titanium/titanium nitride layers, and titanium or nitrogen atoms in the upper carbon layer, the decomposition parameters of the Raman spectra change (Table 2). When titanium and titanium nitride are introduced into the carbon coating, the I_D/I_G ratio increases, which is caused by an increase in the number of carbon atoms in the state with sp^2 bond hybridization and the formation of CN or CN/CTi/TiN bonds. This, in turn, leads to a decrease in the size of Csp^2 carbon clusters and is characterized by an increase in the G-peak width compared to the Ti/TiN/a-C coating. The change in the degree of disordering of Csp^2 clusters is ambiguous. In Ti/TiN/a-C:Ti coatings, the degree of ordering of carbon clusters increases. The subsequent introduction of nitrogen results in the formation of titanium nitride phases in the coating. This leads to a decrease in the degree of ordering of the carbon matrix, and is confirmed by the shift of the G peak position to the low wavenumbers region. Thus, the introduction of nitrogen or nitrogen/titanium atoms causes an increase in the ordering of carbon clusters compared to the coating containing the a-C layer [18].

As can be seen from the AFM images shown in Fig. 3, there are single drops with a size of at least 500 nm on the coating surface. Dispersion of the surface structure of the composite coatings depends on the nature of doping elements [14].

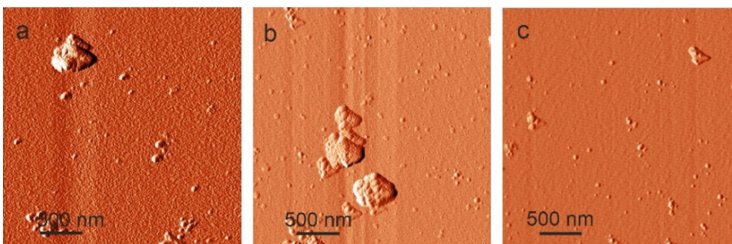


Fig. 3. AFM images of the surface of the coatings: a – Ti/TiN/a-C, b – Ti/TiN/a-C:Ti, c – Ti/TiN/a-C:Ti:N

The results of mathematical processing of the AFM images (see Fig. 3) are shown in Table 2.

Table 2. Statistical processing of AFM results

Coating	Ra, nm	D, nm	I_D/I_G ratio	G peak width, cm^{-1}	G peak position, cm^{-1}
Ti/TiN/a-C:Ti:N	0.6	13.4	1.63	162.4	1567.2
Ti/TiN/a-C:Ti	3.3	18.5	1.64	150.6	1573.1
Ti/TiN/a-C	2.2	19.8	0.66	182.5	1563.5

It has been found that the nature of the doping element affects the coating roughness and grain size. Simultaneous doping with titanium and nitrogen allows a directed change in the grain size and, consequently, control of the parameters of the roughness of the layer [19]. The Ti/TiN/a-C:Ti:N coatings are characterized by the smallest roughness Ra and the smallest grain size D. The Ti/TiN/a-C:Ti coatings are characterized by the highest roughness, and the grain size is comparable to the undoped carbon layer. The surface morphology is determined by the titanium and carbon interaction and the formation of titanium carbide phases and a change in the size of the carbon cluster.

The wear tests showed that the friction kinetics of the Ti/TiN/aC:Ti:N coatings (Fig. 4 and Table 3) differs from the kinetic friction curves, obtained for other coatings by higher values of the friction coefficient and the wear coefficient of the counterbody, as well as by a small running-in area at the initial friction modes (Fig. 4) [20]. The Ti/TiN/a-C:Ti and Ti/TiN/a-C coatings retain their performance during the entire test period and are characterized by lower friction and wear coefficient (Table 3).

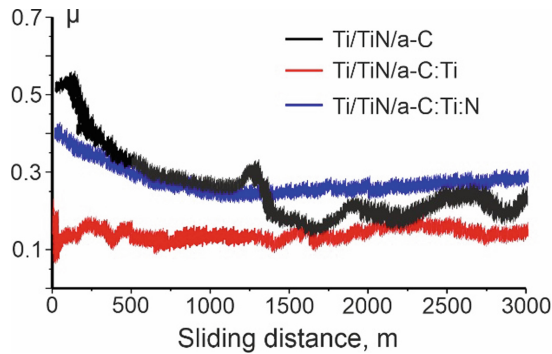


Fig. 4. Kinetic friction curves of the coatings containing titanium and titanium nitride bilayer

The main factors leading to such changes are changes in the strength of the adhesive joint due to the formation of the Ti sublayer. In this case, the formation of Ti or TiN layers leads to the redistribution of residual stresses between layers in the coating. An increase in their plasticity is also due to the formation of the structure containing boundary heterophase layers of a diffusion nature and an increase in the wear resistance of the coating or counterbody due to the presence of the coating graphite component in the coating surface layer [21]. As shown in Table 3, the microhardness of the coatings is determined by the presence of Ti and TiN layers and titanium in the diamond-like carbon layer. When nitrogen is introduced into the a-C:Ti coating structure, the microhardness is increased to 11.3 GPa. According to XPS data, this is determined by the formation of the TiN phase [22].

Table 3. Mechanical properties of the coatings containing layers of nitride nature

Coating	Hk, GPa	σ , MPa	f	$j \times 10^{-11}$, $m^3/(N \times m)$
Ti/TiN/a-C	12.5	167.8	0.29	2.4
Ti/TiN/a-C:Ti:N	11.3	116.3	0.21	10.1
Ti/TiN/a-C:Ti	10.5	108.1	0.14	7.2

It is shown (Table 3) that the formation of the a-C coatings doped with titanium or titanium and nitrogen leads to a decrease in internal stresses. Internal stresses are also reduced due to the content of titanium and titanium nitride layers in the coating structure [23]:

- 1 The Ti/TiN sublayer helps to reduce the effects caused by the difference in the thermal expansion coefficients of the substrate and the coating, which leads to a decrease in stresses in the surface carbon layer.
- 2 The upper layer of the a-C:Ti coating is dominated by bonds characteristic of titanium carbide and titanium metallic phase formation. Inclusions with a crystalline structure are formed in the amorphous carbon matrix, which makes it possible to reduce structural defects due to the alternation of sp^2 and sp^3 regions.

4 Conclusions

The XPS method has shown that the coating contains the Ti-C compounds. They are formed for the coatings with Ti and Ti-N, and Ti-C, CN compounds, which are formed for the coatings with Ti and N. Raman spectroscopy has shown that the introduction of titanium layers into the a-C coating leads to a decrease in the size of Csp^2 clusters and an increase in the coating structure's disorder degree. The change in the sp^2/sp^3 ratio determines the change in microhardness values and kinetics of friction.

AFM has shown the influence of the location of titanium or titanium nitride layers and the type of the alloying element on the surface morphology ($R_a = 0,6$ nm for the Ti/TiN/aC:TiN coating, and for the Ti/TiN/a-C:Ti $R_a = 3,6$ nm).

The carbon component of the coating is characterized by a high concentration of carbon atoms in the state of sp^3 bond hybridization, as well as a low degree of ordering of carbon clusters, which causes an increase in internal stresses due to the formation of the structure with excessive boundary defects [24]. In coatings of the Ti/TiN/aC:Ti:N and Ti/TiN/aC:Ti type, the Csp^3 bonds decrease due to the formation of carbides and carbonitride compounds in the coating structure, which, together with the presence of titanium and titanium nitride sublayers, leads to reduction of internal stresses.

The development of methods for separating plasma flows can be chosen as advanced research directions, i.e., removing microparticles from the plasma flow. Furthermore, the development of deposition technological methods and techniques allowing the formation of carbide/carbon coatings with a minimum content of metal that is chemically unbound with carbon, i.e., the coating consists of two interconnected matrices: carbide and carbon. By varying the ratio of carbide and carbon bonds in the

coating, it is possible to obtain a coating characterized by a polymatrix structure, representing compounds based on carbides/nitrides and diamond-like compounds.

Acknowledgments. Intergovernmental Cooperation Projects supported this work within the National Key Research and Development Plan of the Ministry of Science and Technology of PRC (projects No. 2016YFE0111800, for 2016–2019), and the Ministry of Education of the Republic of Belarus (assignment “Multiphase carbide/carbon coatings for friction units operating under high contact loads”).



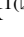



References

1. Xiao, S., et al.: Tin repellence on wave-soldering stainless steel holders coated with Ti/TiC/DLC. *Surf. Coat. Technol.* **320**, 614–618 (2016)
2. Zhou, B., et al.: Structure and optical properties of Cu-DLC composite films deposited by cathode arc with double-excitation source. *Diam. Relat. Mater.* **69**, 191–197 (2016)
3. Dai, M.-J., et al.: A study on metal-doped diamond-like carbon film synthesized by ion source and sputtering technique. *Plasma Process. Polym.* **4**, 215–219 (2007)
4. Martínez-Martínez, D., López-Cartés, C., Gago, R., Fernández, A., Sánchez-López, J.C.: Thermal stability and oxidation resistance of nanocomposite TiC/a-C protective coatings. *Plasma Process. Polym.* **6**, 462–467 (2009)
5. Kolesnyk, V., Peterka, J., Kuruc, M., Šimna, V., Moravčíková, J., Vopát, T., Lisovenko, D.: Experimental study of drilling temperature, geometrical errors and thermal expansion of drill on hole accuracy when drilling CFRP/Ti alloy stacks. *Materials* **13**(14), 32321–323217 (2020)
6. Zhou, B., et al.: Synthesis and characterization of Ti and N binary-doped α -C films deposited by pulse cathode arc with ionic source assistant. *Surf. Interface Anal.* **50**, 506–516 (2018)
7. Ming, M.Y., et al.: Structure, mechanical and tribological properties of Ti-doped amorphous carbon films simultaneously deposited by magnetron sputtering and pulse cathodic arc. *Diam. Relat. Mater.* **77**, 1–9 (2017)
8. Liu, D.G., Tu, J.P., Hong, C.F., Gu, C.D., Mai, Y.J., Chen, R.: Improving mechanical properties of a-CN_x films by Ti–TiN/CN_x gradient multilayer. *Appl. Surf. Sci.* **257**, 487–494 (2010)
9. Castillo, H.A., Restrepo-Parra, E., Arango-Arango, P.J.: Chemical and morphological difference between TiN/DLC and α -C: H/DLC grown by pulsed vacuum arc techniques. *Appl. Surf. Sci.* **257**, 2665–2668 (2011)
10. Stoney, G.G.: The tension of metallic films deposited by electrolysis. *Proc. Roy. Soc. A Math. Phys. Eng. Sci.* **82**(553), 172–175 (1909)
11. Lin, Y., Zia, A.W., Zhou, Z., Shum, P.W., Li, K.Y.: Development of diamond-like carbon (DLC) coatings with alternate soft and hard multilayer architecture for enhancing wear performance at high contact stress. *Surf. Coat. Technol.* **320**, 7–12 (2017)
12. Matsuoka, M., et al.: X-ray photoelectron spectroscopy and Raman spectroscopy studies on thin carbon nitride films deposited by reactive RF magnetron sputtering. *World J. Nano Sci. Eng.* **2**, 92–102 (2012)
13. Ferrari, A.C., Robertson, J.: Interpretation of Raman spectra of disordered and amorphous carbon. *Phys. Rev. B* **61**, 4095–4107 (2000)
14. Igartua, A., et al.: Screening of diamond-like carbon coatings in search of a prospective solid lubricant suitable for both atmosphere and high vacuum applications. *Tribiol. Int.* **114**, 192–200 (2017)

15. Boubiche, N., et al.: Kinetics of graphitization of thin diamond-like carbon (DLC) films catalyzed by transition metal. *Diam. Relat. Mater.* **9**, 190–198 (2019)
16. Huang, L., Yuan, J., Li, C., Hong, D.: Microstructure, tribological and cutting performance of Ti-DLC/ α -C: H multilayer film on cemented carbide. *Surf. Coat. Technol.* **353**, 163–170 (2018)
17. Babak, V.P., Bilchuk, Y.Y., Shchepetov, V.V.: Increased wear coatings due intrastructural self-correction. *J. Eng. Sci.* **6**(1), C11–C15 (2019)
18. Tyagi, A., Walia, R.S., Murtaza, Q., Pandey, S.M., Tyagi, P.K., Bajaj, B.: A critical review of diamond like carbon coating for wear resistance applications. *Int. J. Refract. Metal. Hard Mater.* **78**, 107–122 (2019)
19. Pillari, L.K., Umasankar, V., Sarma, A., Gupta, M.: DLC coating of magnesium nanocomposites using RF sputtering. *Mater. Today Proc.* **4**, 6737–6742 (2017)
20. Zarei Moghadam, R., Ehsani, M.H., Rezagholipour Dizaji, H., Kameli, P., Jannesari, M.: Modification of hydrophobicity properties of diamond like carbon films using glancing angle deposition method. *Mater. Lett.* **220**, 301–304 (2018)
21. Kano, M.: Overview of DLC-coated engine components. In: Cha, S.C., Erdemir, A. (eds.) *Coating Technology for Vehicle Applications*, pp. 37–62. Springer, Cham (2015). https://doi.org/10.1007/978-3-319-14771-0_3
22. Vetter, J.: 60 years of DLC coatings: Historical highlights and technical review of cathodic arc processes to synthesize various DLC types, and their evolution for industrial applications. *Surf. Coat. Technol.* **257**, 213–240 (2014)
23. Bewilogua, K., Hofmann, D.: History of diamond-like carbon films - from first experiments to worldwide applications. *Surf. Coat. Technol.* **242**, 214–225 (2014)
24. Batory, D.A., Stanishevsky, A., Kaczorowski, W.: The effect of deposition parameters on the properties of gradient α -C:H/Ti layers. *J. Achiev. Mater. Manuf. Eng.* **37**, 381–386 (2009)



Improvement of Operating Properties of Heat-Resistant Alloys by the Structure Optimization

Natalia Zaichuk¹ , Sergii Shymchuk¹ , Anatolii Tkachuk¹  ,
Yurii Shymchuk¹ , and Karim Kashash Badir² 

¹ Lutsk National Technical University, 75, Lvivska St., Lutsk 43018, Ukraine
a. tkachuk@lntu.edu.ua

² Advanced Aerospace Industries, Dubai, UAE

Abstract. Fasteners of aircraft gas turbine engines are made of heat-resistant steels and alloys and are operated in intensive conditions under the action of high temperatures. For ensuring reliability, the connecting elements of aircraft engines are made of heat-resistant alloy steels. But under the influence of an aggressive environment, these elements are destroyed, resulting in problems during repairs. The structure of the material of fasteners during the threaded connection by cutting and plastic deformation is considered. The concentration of stresses in the thread plane depends on the density of dislocations, and the depth of corrosion penetration on the outer surfaces of the thread reaches 100 μm . It is proposed to introduce additional heat treatment of parts to improve the physical and mechanical characteristics of the alloy. After additional heat treatment, the σ -phase plates dissolve and prevent the development of micro-cracks. It is proved that the density of material dislocations in the state of delivery reaches critical values, but the introduction of additional heat treatment allows to increase the performance of parts made of alloy HX – Alloy Type 66Ni-17Cr regardless of the method of threading. Prerequisites for the rational selection of heat treatment modes have been developed, which provide the best mechanical and technological characteristics and the necessary structure of the materials used.

Keywords: Alloy · Deformation · Engine · Fractogram · Load · Resource · Wear resistance

1 Introduction

Threaded and riveted connections of parts, assemblies, and units of various types of equipment, including aircrafts [1] and engines [2] are the most common and reliable. Fasteners of gas turbines of aircraft engines work in particularly stressed conditions under static, dynamic, and vibration loads. As a result, these parts are subject to increased reliability requirements [3].

To increase aircraft engines' economic and operational performance, use various technological techniques that reduce the size of the relevant components, such as combustion chambers, but increase the load on the parts and, consequently, reduce their

durability. Gas flows at the entrance to the turbine have a temperature of about 1500°K. Therefore, during operation, the damage of the surface layers from gas corrosion and the action of thermal and mechanical factors increases significantly [4]. Traditionally, the fasteners of gas turbine engines of aircraft are operated for one maintenance period, and to ensure the required resource, they are made of complex alloy heat-resistant steels and alloys such as follows: HD – Alloy Type 28Cr-6Ni; HN – Alloy Type 25Ni-20Cr; HX – Alloy Type 66Ni-17Cr; HW – Alloy Type 60Ni-12Cr; HX – Alloy Type 66Ni-17Cr [1]. The studied steels and alloys belong to the group: Heat Resistant Steel and Alloys ASTM A297 (Specification for Steel Castings; Iron-Chromium and Iron-Chromium-Nickel. For general application/ ANSI/ASTM A297/A297M-97) [5]. However, during the repair, there are some difficulties in disassembling such fasteners because the surface layers of the working surfaces of such parts have various types of damage [6]. Therefore, it is essential to solving the problem of increasing heat resistance and durability, reducing the level of various types of damage to parts made of heat-resistant steels and alloys [7].

2 Literature Review

The yield strength for the test material is 750 MPa. Thus, in the state of supply, the internal stresses exceed the yield strength, which can lead to relaxation processes, during which the deformation of the grains can cause microcracks [8]. After high-temperature heating, the internal stresses are less and do not exceed the yield strength, and the possibility of microcracks disappears or is significantly reduced [9]. In addition, it can be assumed that as a result of additional heat treatment [10], it is possible to eliminate existing microcracks [11].

The microstresses of the second kind, which occur during plastic deformation, are balanced in the volumes of individual crystallites (or blocks), associated with the inhomogeneous elastic deformation of crystallites and an inhomogeneous change interplanar distances [12]. In [13, 14], it was shown that dislocations lead to changes in interplanar distances, while impurity atoms and point defects, due to the relaxation of the lattice around them, do not make a significant contribution to the effect of the expansion of lines on radiographs.

The particles of the secondary phases released from the supersaturated solid solution significantly strengthen the alloy [15]. The increase in the yield strength σ_T depends on the strength, structure, size, shape, distribution method, distance between the released particles, and degree of coherence of the particle lattices and the matrix [16]. All these factors affect the interaction of dislocations with the particles of the secondary phases [17]. In this case, there may be close interaction and long-distance effects associated with stresses caused by particle lattices and matrices [18].

3 Research Methodology

To solve the increasing heat resistance and durability of fasteners of aircraft gas turbine engines, parts (Fig. 1) of the most widely used material HX – Alloy Type 66Ni-17Cr were studied, mechanical properties of which are given in Table 1. As is known, this alloy belongs to heat-resistant [19].

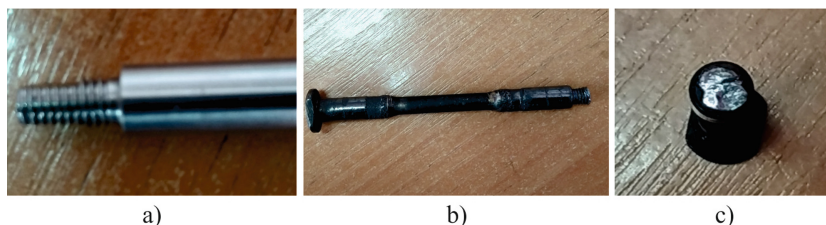


Fig. 1. General view of the surfaces of the fasteners of the aircraft engine: a) the surface of the part that has not been used; b) the surface of detail, after the exploitation with traces of various damages; c) the fracture surface of the threaded connection.

X-ray diffraction analysis of the samples was performed to assess the substructural state of the alloys for different methods of threading and, after the operation, additional heat treatment of parts. The DRON-3M unit was used for such studies. For determining the macro stresses in the test material, the X-ray diffractometric method was chosen, based on the exact determination of the deformation of the crystal lattice, because this express method has the following advantages: it is non-destructive and non-contact [20].

Table 1. Mechanical characteristics of HX – Alloy Type 66Ni-17Cr alloy.

Material	σ_T , MPa	σ_B , MPa	σ_B^{750} , MPa	δ , %	ψ , %
HX – Alloy Type 66Ni-17Cr	72	750	1150	17	19

Fractographic studies were performed using a scanning electron microscope REMMA-102A at a magnification of 120 to 1.2k times, which provides a significant depth of field (about 0.5 mm) and sufficient resolution (about 100...200 Å), which allowed to detect irregularities break and see all the details of the phase composition of the upper layers and identify the inclusion or selection [21]. The samples were cut from the destroyed fasteners taken in the state of delivery, after their operation, and after additional heat treatment, the elements of the destroyed surface were also examined (Fig. 1c).

4 Results

Characterizing the mechanical characteristics of the alloy HX – Alloy Type 66Ni-17Cr, according to Table 1, it is clear that this material has high values of σ_B^{750} , δ , ψ , which is an assessment of its operational reliability. However, under the action of high temperatures, such mechanical properties [22] as elasticity, yield strength, and strength are significantly reduced. Therefore, even at stress values that are less than the yield strength, the phenomenon of creep can occur, which is manifested in a gradual increase in plastic deformation. Since heat-resistant steels and alloys operate in a complex stress state (tension, compression, bending, torsion), combined with alternating vibration loads, these materials must resist fatigue at high temperatures and have high creep characteristics at normal temperature conditions [23].

Fasteners (bolts, studs, spokes) are made by cutting, and therefore the materials must be well subjected to this type of processing. However, it is known that cutting, including threading, heat-resistant steel parts, and alloys, is associated with significant difficulties. This primarily concerns the provision of the necessary roughness and the elimination of various types of damage to work surfaces during cutting in the form of material tears and burrs. Therefore, in this case, the thread on the fasteners is usually applied by rolling [1], which contributes to the appearance of a perfectly smooth surface that has sufficient depth and a strictly periodic step. This design allows you to securely fasten the connected parts and provide the necessary tightening force. However, this technology of cutting causes significant damage to the surface structure of the metal. Plastic deformation in the material when applying the thread promotes periodic zones with tensile and compressive stresses with increased dislocation density ($\approx 1 \cdot 10^{12} \text{ cm}^{-2}$). The possibility of forming and propagating cracks in the cut made by the rolling method is more significant than in the manufacture of threads by cutting [20]. The results of studies of the material HX – Alloy Type 66Ni-17Cr, conducted using an X-ray machine DRON-3M in iron radiation, show that the density of dislocations during rolling is more than twice as high as the density of dislocations during cutting. The concentration of stresses also depends on the density of dislocations, which significantly increases along the entire plane of the thread compared to non-working surfaces. It is known that the stress concentration for plastics materials is harmful under variable loads, elevated temperatures, and vibrations. Peak stresses near the concentrator can exceed the allowable resistance of the material under variable load, which leads to premature failure. The complex operating conditions of the gas turbine engine contribute to the emergence of various diffusion processes that adversely affect the fasteners of the alloy HX – Alloy Type 66Ni-17Cr. In particular, in places of high-stress concentration, microcracks often occur, which penetrate the active components from the environment and can cause a wedging effect (Rebinder effect), the development of corrosion, and other negative processes that significantly affect the durability of such parts and can cause significant difficulties disassembly of the gas turbine engine. This type of brittle fracture occurs under the action of surface-active or corrosive media due to overheating and when exposed to the material of other molten metals.

Appropriate protective coatings are often used to protect against corrosion and various diffusion processes. However, this approach complicates the technological process of manufacturing fasteners and does not always lead to the desired result. In addition, when tightening the fasteners, the protective coatings can be damaged while facilitating the diffusion of active gases from the environment due to the accumulation of dislocations in the places of the cut. The fracture surface of an emergency part is usually contaminated with soot, grease, corrosion products, or oxide film, the formation of which is associated with the action of high temperatures on the part (Fig. 1b). Analysis of the surface layer structure shows that the depth of corrosion penetration on the outer surfaces of the threads operating in the zone of high temperatures reaches 100 μm . In some cases, it was found that the separation of oxide films can occur. Such damage at the mentioned loads is the main reason for the development of fatigue failure. The fractograms of HX – Alloy Type 66Ni-17Cr alloy in the state of delivery and after hardening and aging (Fig. 2) show signs of brittle fracture in the form of a chip near the thread with a gradual transition to intergranular fracture with increasing distance from the thread surface.

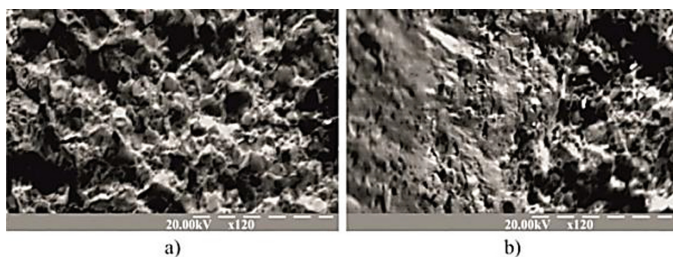


Fig. 2. Fractogram of HX – alloy type 66Ni-17Cr alloy in the state of delivery ($\times 120$): a) in the center of the sample; b) near the cut.

Figure 2 clearly shows the signs of hollow fracture and fracture along the grain boundaries of the alloy HX – Alloy Type 66Ni-17Cr, visible microcracks located at the boundaries of the inclusions.

In the study of these same samples after heat treatment at 900 $^{\circ}\text{C}$ for 20 min, a brittle intergranular fracture is observed (Fig. 3): at the grain boundaries weakened by carbide emissions (Fig. 3a) and at grain boundaries enlarged by coagulated emissions (Fig. 3b).

In the structure (Fig. 3b), microcracks are visible, located along the boundaries of inclusions and microzones with a hollow structure.

As deformation at the drawing of a carving (rolling or cutting) is conducted at low temperatures, in a near-surface layer, the slander is formed. Therefore, a fine-grained structure with thin-plate or fibrous grains is observed (Fig. 4a).

Changes also occur in the near-surface layer after conducting studies of the impact of operation ($\tau = 40 \dots 80$ h). After the long-term operation at elevated temperatures, a fine-grained, partially recrystallized structure is observed (Fig. 4b) with signs of recrystallization texture.

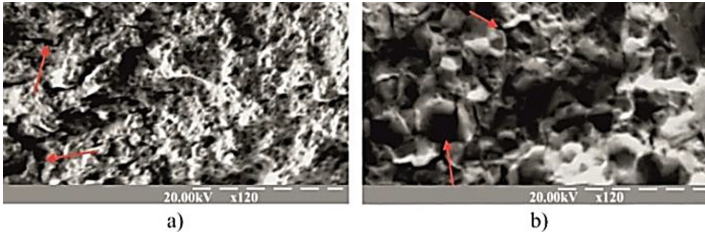


Fig. 3. Fractogram of alloy HX – Alloy Type 66Ni-17Cr after heat treatment at 900 °C (×120): a) near the cut; b) in the sample center.

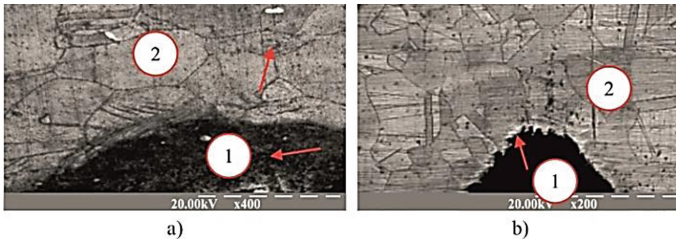


Fig. 4. The structure of the etched surface layer of the alloy HX – Alloy Type 66Ni-17Cr (1 – subsurface layer, 2 – base metal): a) before exploitation (×400); b) after exploitation (×200).

The surface formation of the alloys for an oxide layer is accompanied by a redistribution in the surface layer of the matrix of alloying elements and the formation of an intermediate zone in the form of an oxidized white zone. Alloying elements diffuse into the scale material. The formation of a layer depleted by the alloying element leads to a decrease in hardness, strength, reduction of the crystal lattice period, and the occurrence of stresses. The stresses at any temperature and cause the accumulation of defects and accelerate nucleation and development of cracks. In fasteners made of HX – Alloy Type 66Ni-17Cr alloy, which has worked less than the estimated technical resource, the metallographic analysis revealed σ -phase plates, which may be one of the causes of premature failure of parts (Fig. 5). For addressing this issue, additional heat treatment was performed. After additional heat treatment (1200 °C, 20 min), the σ -phase plates dissolved and, accordingly, the plastic characteristics of the alloy significantly improved.

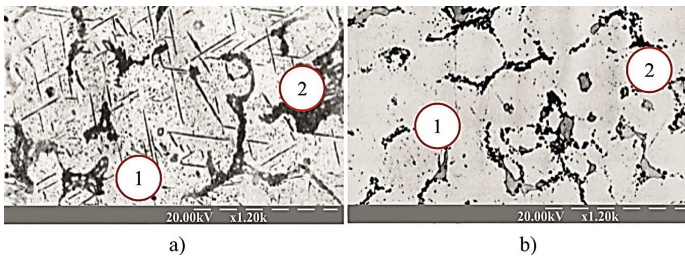


Fig. 5. σ -phase in the alloy HX – Alloy Type 66Ni-17Cr (×1200); (1 – plates of the σ -phase in the main matrix; 2 – the base metal): a) after exploitation; b) after dissolution as a result of additional heat treatment.

Prolonged exposure to high temperatures (500...800 °C) during operation leads to the release of secondary phases – intermetallic compounds at the grain boundaries, making them part of the alloy brittle, significantly reducing their plastic properties and toughness. According to the analysis of the conducted research, σ -phase $(\text{NiCo})_7(\text{WMo})_6$ and μ -phase $(\text{NiCoCr})(\text{WMo})$ are formed in chromium-nickel alloys and steels, due to which this embrittlement process is called “sigmatation”. The intensity of the sigmatation process is determined by the intensity of diffusion processes, and therefore its duration at low temperatures of 500...600 °C is very significant (100...1000 h) and is significantly accelerated at temperatures of the order of 800 °C.

These phases are unstable. The elementary cell of the σ -phase crystal lattice consists of 30 atoms (Fig. 6).

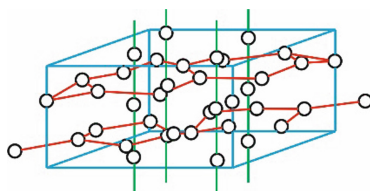


Fig. 6. General view of the σ -phase lattice.

These phases are formed on carbides. As a result of growth, they penetrate all the grain of the metal matrix. The lamellar shape of the phases contributes to the brittle destruction of the alloy. In addition, by extracting refractory metals from the solid solution, these phases weaken it. σ -phases are formed in the form of segregations with chromium carbides in nickel-chromium alloys with a high total content of Al and Ti (more than 10% by weight). The presence of these phases increases the fragility and reduces the ductility, especially under dynamic loads, and reduces the long-term strength at high temperatures, i.e., heat resistance.

Using X-ray diffraction analysis on the DRON-3M device, the details of the HX – Alloy Type 66Ni-17Cr alloy were investigated, and the crystal lattice parameter α , the size of the X-ray scattering blocks D , the relative change of the lattice parameter $\Delta\alpha/\alpha$, the mean square displacement of atoms from the equilibrium position $\sqrt{u^2}$ and density ρ were evaluated. In addition, the main component of the studied steels and alloys (Fe_α and Fe_γ) was evaluated. From the obtained results $\text{Fe}_\alpha \approx 5\%$, $\text{Fe}_\gamma \approx 95\%$. The measurement error in determining D and $\Delta\alpha/\alpha$ was 16...18%, the error in determining the density of dislocations did not exceed 30...40%. The crystal lattice period was calculated with an accuracy of 0.02...0.03% of the specified value. The research results are presented in Table 2.

From the results shown in Table 2, it is seen that the density of dislocations ρ after standard heat treatment, i.e., in the state of delivery, reaches almost a critical value of 10^{12} 1/cm² and depends little on the method of threading (cutting or thread rolling). This density of dislocations causes increased fragility of aircraft engine mounts in the

state of delivery and is one of the reasons for their premature destruction. The dislocation density decreases slightly during operation because the operating temperature (850 °C) is lower than the recrystallization temperature (900 °C). Further evolution of the dislocation structure is associated with the consolidation of dislocations due to the formation of Cottrell atmospheres during operation and the formation, development, and propagation of microcracks under static and alternating loads, which cause fatigue failure of parts.

Table 2. The results of X-ray-structural studies.

Object of research	α , Å	D, sm	$\Delta\alpha/\alpha$	$\sqrt{u^2}$, Å	ρ , sm ⁻²	Remark
HX – Alloy Type 66Ni-17Cr	3.5953	$8.4 \cdot 10^{-6}$	–	0.11	$0.14 \cdot 10^{12}$	In the initial state
HX – Alloy Type 66Ni-17Cr	3.5940	$2.1 \cdot 10^{-5}$	$0.18 \cdot 10^{-2}$	0.08	$6.8 \cdot 10^9$	After additional heat treatment

This high density of dislocations can be explained by phase hardening due to the release of secondary strengthening phases during aging studied the metastable γ' -phase.

Therefore, it is evident that the additional heat treatment can significantly increase the performance of parts made of alloy HX – Alloy Type 66Ni-17Cr, regardless of the threading method.

5 Conclusions

To slow down the fatigue failure of parts and increase their durability, it is necessary to improve the structure of the surface layer of fasteners significantly. The creep of metals causes stress relaxation in pre-loaded parts (tightened fasteners gradually weaken). Therefore, the coarse-grained structure is unacceptable, as it provides increased sensitivity to stress concentrators, which will be the cutting of parts. The manufacture of parts should consider the appearance of zones with tensile and compressive stresses with high dislocation density, which depends on the stress concentration. It is necessary to carefully select the mode of heat treatment, which could provide better mechanical and technological characteristics and the required structure of the materials used. The performed research will be continued and serve to improve the technological process of manufacturing threaded parts from heat-resistant steels and alloys and improve the heat resistance of these materials by optimizing the heat treatment modes.

References






1. Yaroshevich, N., Zabrodets, I., Shymchuk, S., Yaroshevich, T.: Influence of elasticity of unbalance drive in vibration machines on its oscillations. *East. Eur. J. Enterp. Technol.* **5**((7 (95))), 62–69 (2018). <https://doi.org/10.15587/1729-4061.2018.133922>
2. Pavlenko, I., et al.: Parameter identification of cutting forces in crankshaft grinding using artificial neural networks. *Materials* **13**(23), 5357 (2020). <https://doi.org/10.3390/ma13235357>
3. Krmela, J., Hovorun, T., Berladir, K., Artyukhov, A.: Increasing the structural strength of corrosion-resistant steel for elastic components of diaphragm compressor. *Manuf. Technol.* **21**(2), 207–213 (2021). <https://doi.org/10.21062/mft.2021.034>
4. Shatskyi, I.P., Ropyak, L.Y., Makoviichuk, M.V.: Strength optimization of a two-layer coating for the particular local loading conditions. *Strength Mater.* **48**(5), 726–730 (2016). <https://doi.org/10.1007/s11223-016-9817-5>
5. Henderson, M.B., Arrell, D., Larsson, R., Heobel, M., Marchant, G.: Nickel based superalloy welding practices for industrial gas turbine applications. *Sci. Technol. Weld. Joining* **9**(1), 13–21 (2004). <https://doi.org/10.1179/136217104225017099>
6. Maheswari, N., Chowdhury, S.G., Kumar, K.H., Sankaran, S.: Influence of alloying elements on the microstructure evolution and mechanical properties in quenched and partitioned steels. *Mater. Sci. Eng. A* **600**, 12–20 (2014). <https://doi.org/10.1016/j.msea.2014.01.066>
7. Ivanov, I.V., Mohylenets, M.V., Dumenko, K.A., Kryvchyk, L., Khokhlova, T.S., Pinchuk, V.L.: Carbonitration of a tool for pressing stainless steel pipes. *J. Eng. Sci.* **7**(2), C17–C21 (2020). [https://doi.org/10.21272/jes.2020.7\(2\).c3](https://doi.org/10.21272/jes.2020.7(2).c3)
8. Xu, D., Li, J., Meng, Q., Liu, Y., Li, P.: Effect of heating rate on microstructure and mechanical properties of TRIP-aided multiphase steel. *J. Alloy. Compd.* **614**, 94–101 (2014). <https://doi.org/10.1016/j.jallcom.2014.06.075>
9. Bhosle, V.V., Pawar, V.: Texture segmentation: different methods. *Int. J. Soft Comput. Eng. (IJSCE)* **3**(5), 69–74 (2013)
10. Berladir, K., Hovorun, T., Bondarenko, M., Shvetsov, D., Vorobiov, S.: Application of reinforcing thermocycling treatment for materials of stamps hot deformation. *J. Eng. Sci.* **6** (2), C6–C10 (2019). [https://doi.org/10.21272/jes.2019.6\(2\).c2](https://doi.org/10.21272/jes.2019.6(2).c2)
11. Totten, G.E. (ed.): *Heat Treating of Nonferrous Alloys*, vol. 4E (2016). <https://doi.org/10.31399/asm.hb.v04e.9781627081696>
12. Lesch, C., Kwiaton, N., Klose, F.B.: Advanced high strength steels (AHSS) for automotive applications – tailored properties by smart microstructural adjustments. *Steel Res. Int.* **88** (10), 170–210 (2017). <https://doi.org/10.1002/srin.201700210>
13. Haupta, M., Duttta, A., Pongeb, D., Sandlöbesc, S., Nellesenb, M., Hirt, G.: Influence of intercritical annealing on microstructure and mechanical properties of a medium manganese steel. *Procedia Eng.* **207**, 1803–1808 (2017). <https://doi.org/10.1016/j.proeng.2017.10.942>
14. Xiong, X.C., Chen, B., Huang, M.X., Wang, J.F., Wang, L.: The effect of morphology on the stability of retained austenite in a quenched and partitioned steel. *Scripta Mater.* **68**(5), 321–324 (2013). <https://doi.org/10.1016/j.scriptamat.2012.11.003>
15. Speer, J.G., Edmonds, D.V., Rizzo, F.C., Matlock, D.K.: Partitioning of carbon from supersaturated plates of ferrite, with application to steel processing and fundamentals of the Bainite transformation. *Curr. Opin. Solid State Mater. Sci.* **8**(3–4), 219–237 (2004). <https://doi.org/10.1016/j.cossms.2004.09.003>
16. He, B.B., et al.: High dislocation density–induced large ductility in deformed and partitioned steels. *Science* **357**(6355), 1029–1032 (2017). <https://doi.org/10.1126/science.aan0177>

17. Kučerová, L., Jirkova, H., Mašek, B.: The effect of alloying on mechanical properties of advanced high strength steels. *Arch. Metall. Mater.* **59**(3), 1189–1192 (2014). <https://doi.org/10.2478/amm-2014-0206>
18. Schwab, R., Ruff, V.: On the nature of the yield point phenomenon. *Acta Mater.* **61**(5), 1798–1808 (2013). <https://doi.org/10.1016/j.actamat.2012.12.003>
19. Ropyak, L.Y., Pryhorovska, T.O., Levchuk, K.H.: Analysis of materials and modern technologies for PDC drill bit manufacturing. *Prog. Phys. Met.* **21**(2), 274–301 (2020). <https://doi.org/10.15407/ufm.21.02.274>
20. Zurnadzy, V., Zaichuk, N., Sergeev, A., Chabak, Y., Efremenko, V.: Optimal parameters of Q&P heat treatment for high-si steels found by modeling based on “constrained paraequilibrium” concept. In: Ivanov, V., et al. (eds.) *DSMIE 2019. LNME*, pp. 487–496. Springer, Cham (2020). https://doi.org/10.1007/978-3-030-22365-6_49
21. Berladir, K., Gusak, O., Demianenko, M., Zajac, J., Ruban, A.: Functional properties of PTFE-composites produced by mechanical activation. In: Ivanov, V., et al. (eds.) *DSMIE 2019. LNME*, pp. 391–401. Springer, Cham (2020). https://doi.org/10.1007/978-3-030-22365-6_39
22. Demchenko, M.V., Gaponova, O.P., Myslyvchenko, O.M., Antoszewski, B., Bychenko, M. M.: Microstructure and properties of AlCrFeCoNiCux high-entropy alloys. *J. Eng. Sci.* **5**(1), C11–C15 (2018). [https://doi.org/10.21272/jes.2018.5\(1\).c3](https://doi.org/10.21272/jes.2018.5(1).c3)
23. Huang, M.X., He, B.B.: Alloy design by dislocation engineering. *J. Mater. Sci. Technol.* **34**(3), 417–420 (2018). <https://doi.org/10.1016/j.jmst.2017.11.045>

Quality Assurance



Influence of Working Height of a Thread Profile on Quality Indicators of the Drill-String Tool-Joint

Volodymyr Kopei , Oleh Onysko , Vitalii Panchuk ,
Lolita Pituley , and Iryna Schuliar 

Ivano-Frankivsk National Technical University of Oil and Gas,
15, Karpatska St., Ivano-Frankivsk 76019, Ukraine
onysko.oleg@nung.edu.ua

Abstract. Drilling oil and gas wells is always accompanied by the process of screwing and unscrewing the drill-pipe connector. Its effectiveness largely depends on the accuracy and quality of the thread profile, including the profile height's accuracy. Studies show a decrease in the contact pressures and stresses between the threaded surfaces of the box and the pin of the drill string tool-joint as the working height of the profile increases. It is a positive factor influencing the durability and reliability of the drill pipe connector. On the other hand, the same increase of the working height leads to the improvement of the screwing process itself, which is an integral part of lowering and lifting operations during the operation of drill strings. The increased contact area allows the joint to handle high make-up torques without damaging the thread profile. It is also advisable to consider the design of the roots not of around but of an elliptical profile. To ensure leak-tightness and fatigue strength, the operation of joints with a reduced value of h should be avoided.

Keywords: Tapered thread · Screwing-in criterion · Stress distribution · Fatigue · FEM

1 Introduction

The structure of the drill-string includes elements that combine drilling pipes between each other and other objects. These connectors are called tool-joints for drill string elements. They consist of two parts (**Error! Reference source not found.**): a box 1, the female end of the connection, and pin 2, the male end of the connection. One of the quality indicators of the tool-joint is its screwing and unscrewing that is the value that indicates the number of unobstructed screwing and unscrewing processes in it. Such operations always accompany the lowering and lifting process of the drill string. One of the parameters influencing this process is the working height of the thread profile. In its turn, this parameter affects other tool-joint characteristics, including stresses and contact pressures distribution along the thread profile flank side. They occur in a state of complete screwing and affect the reliability and durability of the drill-string connection (Fig. 1).

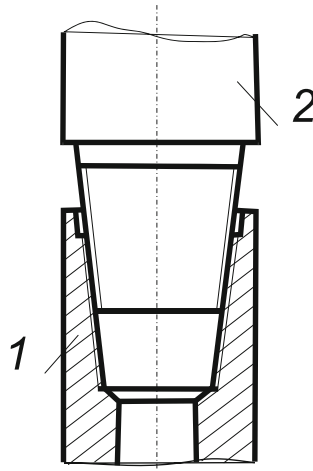


Fig. 1. Scheme of the drill string tool-joint consisting: 1 – box; 2 – pin.

2 Literature Review

There are many studies on the mechanical properties of threaded joints and threaded surfaces.

The scientific approach to the frictional lock of bolted joints to prevent unintentional self-unscrewing is developed [1]. The value of the friction torque that counteracts the self-unscrewing of the collet nut is evaluated. But the distribution of the contact stress along the thread surfaces isn't taken into consideration. A fundamental fretting fatigue test is conducted in [2] to investigate the fretting fatigue mechanism in the threaded connection. The test of the fretting fatigue failure at the middle of the contact surface is achieved only in it. In paper [3], Schneider's method is enhanced to generate an efficient procedure for calculating the fatigue-induced damage at the screws. The failure criterion is the technical relevant incipient crack length in the first load-bearing thread turn of the screw [3]. Using the oil-based fluids in drilling, from the point of view of the fatigue strength of the tool-joints, is preferred [4]. The paper [5] shows the influence of the process parameters on the quality of thread connections, notably, thread formation axial force on the opposite sides of the roots. The articles [3–8] do not demonstrate research of the screwing make-up process.

Several papers demonstrate the technological and design parameters of thread properties improvement.

The experimental researches of comparative wear resistance of the threaded drill-pipe connection Z-117 after their improvement using electromechanical surface hardening are given in [9]. The machining influence on surface roughness obtained during thread grinding is grounded in the article [10]. The machining error influence on the stress state of the conical thread joint is investigated in [11]. The research work of the article [12] is directed on variable pitch thread that enhances the bearing capacity of the casing joint.

The design methods include improving the configuration of drill pipes, and threaded connections are shown in [13, 14]. The contact stresses on the surfaces of the pin and box are determined depending on the size of the technological gap but not on the distribution of the stresses along the thread surfaces [13].

The authors in [15] use ANSYS software to carry out a 3D simulation of the wireline core drill string and joint and determined that the thread root had the highest stress but without considering the distribution of the stresses along the thread surfaces. In [16], a quasi-three-dimensional model for an $\varnothing 89$ mm wireline core string joint under the condition of neglecting the influence of the helix angle. In paper [17], static mechanics analyze the stress state of the negative angle thread of a (74 mm wireline core drill string and calculate the torsional resistance of the thread.

The authors [18] analyzed the stress and strain distribution with the 3D whole structure finite element model's computing results under torque moment, compression force, tension load, and bend moment. But their investigations do not take into consideration the thread parameters, including height of profile. The distributions of von Mises stress and contact pressure in various cases but in the cylindrical thread are studied only [19].

In the [20], the suggested connection design allows the efficient transmission of strain wave energy to a drill bit and the automation of making-up and breaking-out drill pipes but not including the thread profile influence. The general approach for the quality assessment is presented in [21].

The dependences of the contact pressure and the fatigue safety factor on the major diameter of the pin thread were studied in [22]. In [23], the contact pressures at the time of insertion of the pin into the box are investigated based on theoretical assumptions about the effect of the weight of the drill pipe stand. There are no studies of the influence of the working height of the profile h on the strength indicators. In connection with the change of the thread profile, it is also necessary to study the process of connecting the pin into the box because the screwing and unscrewing are very important part-time of the drilling operation of oil and gas wells.

3 Research Methodology

The tool-joint tapered thread parameters are: h_1 is the height of the thread profile (mm), h - the working height of the thread profile (mm), P - the pitch of the thread (mm), a - the width of the thread crest (mm), $\alpha/2$ - the half of the thread profile angle (Fig. 2).

Abaqus/CAE 6.14 and fe-safe 6.5 were used for FEA. The finite element model technique is chosen due to its suitability for use for geometrically complex structures. An axisymmetric model was used to speed up the calculations and increase the accuracy of the calculation in zones of stress concentration. The parametric axisymmetric finite-element model of the drilling tool joint ZN-197 GOST 5286 with Z-152 GOST 28487 thread (6 5/8 REG API Spec. 7 equivalent) has been developed. The material of the parts is SAE-4140 steel with Young's modulus $E = 201$ GPa, a Poisson's ratio $\nu = 0.33$, a yield strength $\sigma_y = 965$ MPa, an ultimate tensile strength $\sigma_t = 1076$ MPa). Material plasticity and friction are simulated. The joint make-up was simulated by axial deformation ("bolt load") $\Delta = 0.25$ mm of the box shoulder. The Brown-Miller strain-life

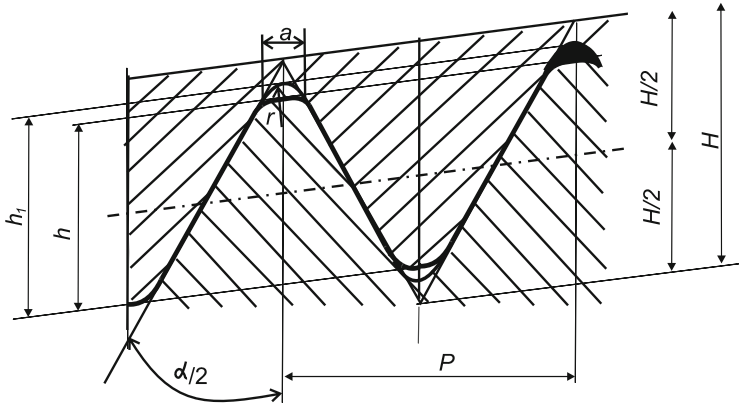


Fig. 2. Scheme of the tool joint tapered thread according to standard API.

dependence was used to calculate the fatigue life N [24]. The calculations were performed using the fe-safe 6.5 software. The fatigue characteristics of SAE-4140 steel (with a material endurance limit of 572 MPa) from the fe-safe material database were used. The Brown-Miller criterion was chosen because it provides an adequate estimation of the fatigue life of the considered material. We considered the fatigue loading cycle with external tensile load $F_{\min} = 0$ MN, $F_{\max} = 4$ MN.

4 Results

4.1 FEA-Results

The influence of the deviations Δh of the h parameter (with a nominal value of 3.293 mm) on the equivalent stresses, the logarithm of the fatigue life $\lg N$, and the contact pressure P_c in the unsafe zones of the joint was investigated. The following connection designs were considered (Fig. 3): $h = 3.293 + 0.6$ mm (a), $h = 3.293 - 0.6$ mm (b), $h = 3.293$ mm (c), $h = 3.293 + 0.6$ mm with additional reduction of the thread root radius to $r = 0.55$ mm (d).

It is noticeable that $\Delta h = +0.6$ mm leads to an increase in stresses (Fig. 3a) and contact pressures P_c (Fig. 4) at the beginning and end of the flank of the thread. In the zone of crest $P_{c\max} = 1908$ MPa. It is significantly higher than the ultimate tensile strength and is due to the interference of the theoretical thread profiles of the pin and box. This phenomenon is less typical for $\Delta h = -0.6$ mm ($P_{c\max} = 897$ MPa) (Fig. 3b) and $\Delta h = 0$ mm ($P_{c\max} = 852$ MPa) (Fig. 3c).

To prevent interference, the radii of the thread roots should be reduced to $r = 0.55$ mm. In this case, the value $\Delta h = +0.6$ mm does not lead to a significant increase in stresses (Fig. 3d) and contact pressures ($P_{c\max} = 733$ MPa) (Fig. 4). In general, the distribution of stresses and contact pressures is somewhat better than for

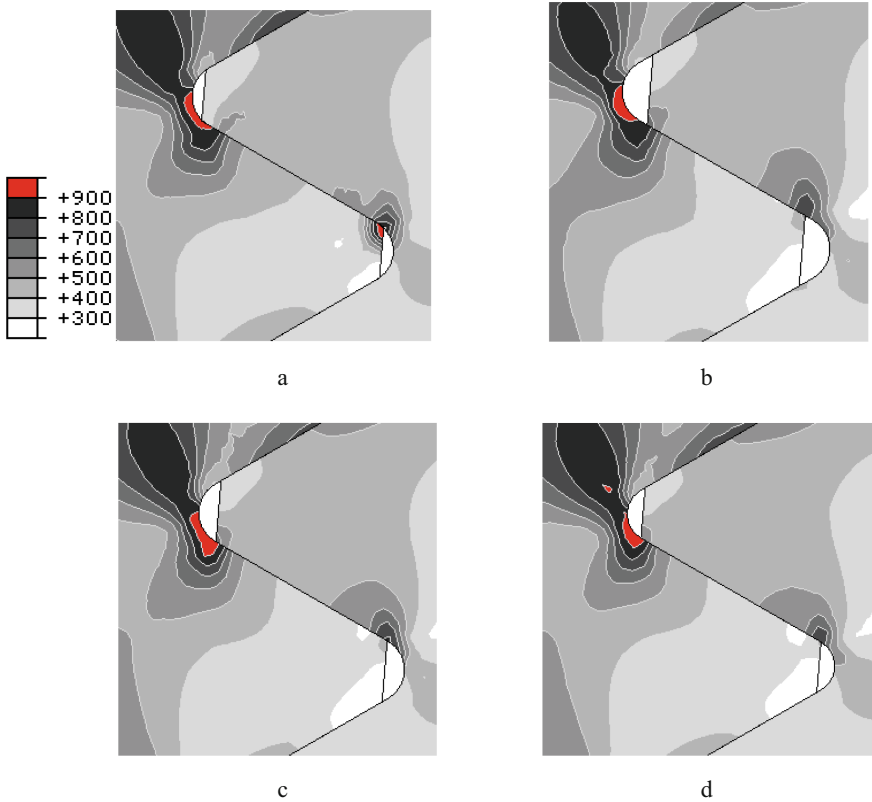


Fig. 3. Distribution of the von Mises stress (MPa) in tool-joints: $\Delta h = +0.6$ mm (a); $\Delta h = -0.6$ mm (b); $\Delta h = 0$ mm (c); $\Delta h = +0.6$ mm, $r = 0.55$ mm (d).

the nominal version $\Delta h = 0$ mm (Fig. 4). This reduces the possibility of operational damage to the thread profile.

The fatigue strength (Fig. 5) of the joint $\Delta h = +0.6$ mm sharply decreases in the zone of the first (*Pin1*) unloaded thread of the pin ($\lg N = 3.18$). This is also typical for $\Delta h = -0.6$ mm ($\lg N = 3.06$). For the variant $\Delta h = +0.6$ mm, $r = 0.55$ mm, the fatigue strength remained almost unchanged ($\lg N = 3.83$) in comparison with the nominal variant $\Delta h = 0$ mm ($\lg N = 3.9$) (Fig. 5). A slight decrease in the value of $\lg N$ is explained by a decrease in the radius r .

The standard provides for the rounding radii of the crest of the turns. They are designed to decrease the P_c values. However, to consider the limiting case, they are not taken into account in the model.

The contact pressure at the shoulder for all considered joints does not change almost and is approximately equal to 80 MPa. Therefore, it is not necessary to correct the Δ value.

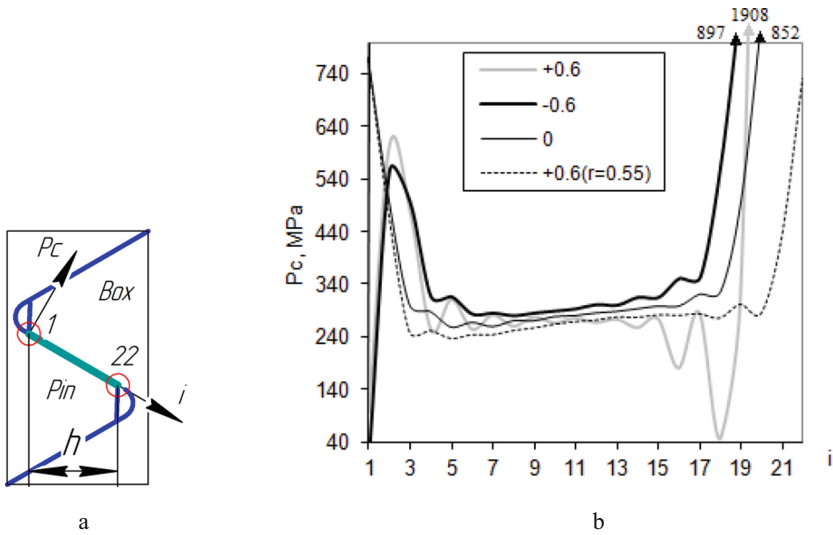


Fig. 4. Scheme of nodes numbering on the loaded flank of the pin thread (a) and values of the contact pressure P_c (MPa) on the first loaded flank of the pin thread in the points i (b).

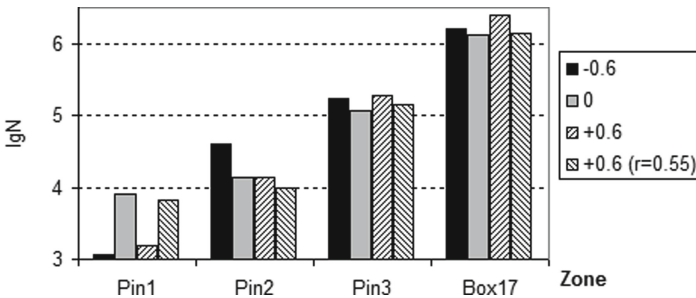


Fig. 5. Values of lgN in thread roots of pin ($Pin1-3$) and box ($Box17$).

4.2 The Determination of the Criteria H and M

The screwing process is determined using special parameters of rejection of the tapered thread tool-joint. It is a very important technique because it provides quality thread screws. The criterion of rejection of the tool joint tapered thread most often in drilling is the value of H (Fig. 6). This value is defined between the pin end and box end when the pin is set into the box before their screwing starts. The box is displayed as a number 1 and pin – number 2. The value of H decreases due to thread flank wearing, and, in theory, the value of H can approach zero. It means that the tool-joint is defective and must be rejected. The criterion of rejection can be achieved by this formula:

$$H = \frac{2h}{K}, \text{ mm} \tag{1}$$

where:

h – the working height of the thread profile (mm).
 K – thread taper.

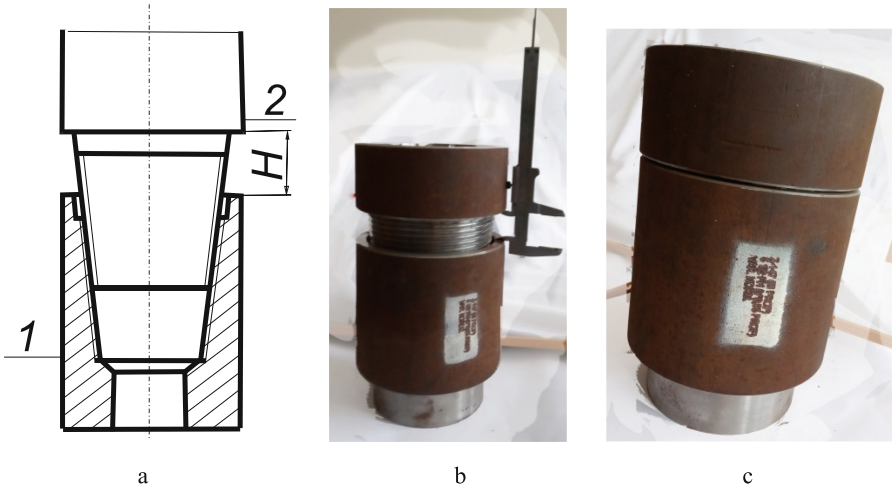


Fig. 6. Scheme for determining the H -criterion (a), before screwing (b), full screwed (make up connector) (c): 1 – box, 2 – pin.

The number of revolutions m that must be carried out for the complete screw-in of elements of the tapered thread tool-joint also depends on the working height of the profile h and the thread taper K :

$$m = \frac{2h}{KP}, \text{ mm} \tag{2}$$

where P – thread pitch.

For tool-joint 6 5/8 REG API Spec. 7 parameters are $h = 3.293$ mm, $P = 6.35$ mm, $K = 0.17$.

4.3 Theoretical Calculations and Practical Results of Measurements of Screwing Criteria

For practical implementation, the tool-joint with a standard value of $h = 3.293$ mm and an increased value of $h_p = h + 0.3$ (mm) were made. The measurements were performed with a caliper on four sides, and the average value was taken (Fig. 6b). Screwing in was made after the measurement, and the rotations were calculated. The results are shown in Table 1.

Table 1. Theoretical calculations and practical results of measurements of screwing criteria.

Parameter	Theoretical calculations		Practical results of measurements	
	H , mm	m	H_p , mm	m_p
For $h = 3.293$ mm	39.51	6.22	34.4	5.75
For $h_p = 3.593$ mm	43.12	6.71	36.9	6.25
Relative increase %	8.4	7.3	6.8	8

The discrepancy between the obtained practical and calculated theoretical results is explained by the fact that formulas 1 and 2 describe only the ideal result. The relative magnification values shown in the last line show the increase in screwing by all criteria. These data indicate that the criterion of rejection H and the amount of rotations of screwing m increases approximately equally – by 7–8% as work height increases by 0.3 mm.

5 Conclusions

An increase in the value of h by 0.6 mm with a mandatory decrease in the radii of the root of the thread to 0.55 mm leads to a decrease in stresses and maximum contact pressures on the flank of the thread by a factor of 1.2 and almost does not decrease the fatigue life of the joint and the values of contact pressure at the shoulder. It reduces the area of the gap and ensures a high leak-tightness of the joint. The increased contact area allows the joint to handle high make-up torques without damaging the thread profile. It is also advisable to consider the design of the roots not of around but an elliptical profile. To ensure leak-tightness and fatigue strength, the operation of joints with a reduced value of h should be avoided.

The criterion of rejection H and the number of rotations of screwing m increases approximately equally – by 7–8% as work height increases by 0.3 mm.

In the forthcoming researches, we plan to carry out comparative tests of the machined thread and theoretical deeper calculations of criteria of screwing instead of only those applied in present practice.

The computer model is further planned to be verified by experimental tests of modified threaded joints for leak-tightness, fatigue strength, and increased torque.

References




1. Shatskyi, I., Ropyak, L., Velychkovych, A.: Model of contact interaction in threaded joint equipped with spring-loaded collet. Eng. Solid Mech. **8**(4), 301–312 (2020)
2. Yosuke, O., et al.: Fretting fatigue on thread root of premium threaded connections. Tribol. Int. **108**, 111–120 (2017)
3. Sorg, A., Utzinger, J., Seufert, B., Oechsner, M.: Fatigue life estimation of screws under multiaxial loading using a local approach. Int. J. Fatigue **104**, 43–51 (2017)

4. Skrynkovskyy, R.M., Yuzevych, V.M., Kataev, A.V., Pawlowski, G., Protsiuk, T.B.: Analysis of the methodology of constructing a production function using quality criteria. *J. Eng. Sci.* **6**(1), B1–B5 (2019). [https://doi.org/10.21272/jes.2019.6\(1\).b1](https://doi.org/10.21272/jes.2019.6(1).b1)
5. Severinchik, N.A., Kopei, B.V.: Inhibitive protection of steel drill pipes from corrosion fatigue. *Sov. Mater. Sci.* **13**(3), 318–319 (1978)
6. Pavlenko, I., et al.: Parameter identification of cutting forces in crankshaft grinding using artificial neural networks. *Materials* **13**(23), 5357 (2020). <https://doi.org/10.3390/ma13235357>
7. Danylova, L., Waiyaki, T.: Effect of kinematics of the process of screwing on a quality of threaded connections. *Mech. Adv. Technol.* **2**(77), 23–27 (2016)
8. Karpus, V.E., Ivanov, V.A.: Locating accuracy of shafts in V-blocks. *Russ. Eng. Res.* **32**(2), 144–150 (2012). <https://doi.org/10.3103/S1068798X1202013X>
9. Fedorova, L., Fedorov, S., Ivanova, Y., Voronina, M.: Increase of wear resistance of the drill pipe thread connection by electromechanical surface hardening. *Int. J. Appl. Eng. Res.* **12**(18), 7485–7489 (2017)
10. Ropyak, L.Y., Vytvytskyi, V.S., Velychkovych, A.S., Pryhorovska, T.O., Shovkoplias, M. V.: Study on grinding mode effect on external conical thread quality. *IOP Conf. Ser. Mater. Sci. Eng.* **1018**, 012014 (2021)
11. Pryhorovska, T., Ropyak, L.: Machining error influence on stress state of conical thread joint details. In: *Proceedings of the International Conference on Advanced Optoelectronics and Lasers*, vol. 9019544, pp. 493–497. IEEE (2019)
12. Dong, L., Wang, J., Zhu, X.: Design and mechanical behavior study of ultrahigh-torque variable pitch casing joint. *Adv. Mech. Eng.* **11**(1), 1–12 (2019). <https://doi.org/10.1177/1687814018814084>
13. Shats'kyi, I.P., Lyskanych, O.M., Kornuta, V.A.: Combined deformation conditions for fatigue damage indicator and well-drilling tool joint. *Strength Mater.* **48**, 469–472 (2016)
14. Zhu, X., Zhang, Z.: Design of an ultra-high torque double shoulder drill-pipe tool joint for extended reach wells. *Nat. Gas Ind. B* **4**(5), 374–381 (2017)
15. Gao, J., Ma, Y., Wang, D., Ji, S.: Fatigue analysis on wireline coring drill pipe joints in torque well-line based on ansys workbench. *Exp. Eng. (Rock Soil Drill. Tunn.)* **44**, 70–78 (2017)
16. Yin, F., Zhang, Y., Xiong, J., Xiong, L.: Simulation analysis on structural mechanism of the thread for wireline drill pipe. *Exp. Eng. (Rock Soil Drill. Tunn.)* **41**, 66–69 (2014)
17. Gao, S., Sun, J., Cai, J., Liu, D.: Calculation analysis on negative angle thread torque of wireline coring drill pipe and test research. *Exp. Eng. (Rock Soil Drill. Tunn.)* **43**, 45–49 (2016)
18. Liangliang, D., Xiaohua, Z., Desheng, Y.: Study on mechanical behaviors of double shoulder drill pipe joint thread. *Petroleum* **5**, 102–112 (2018)
19. Li, Y., Cao, Y., Dou, Y., Yang, Y., Zhang, J., Zhang, L.: FE simulation of sealing ability for premium connection based on ISO 13679 CAL IV tests. *Procedia Struct. Integrity* **22**, 43–50 (2020)
20. Saruev, A.L., Saruev, L.A., Vasenin, S.S.: Drill pipe threaded nipple connection design development. *IOP Conf. Ser. Earth Environ. Sci.* **27**(1), 012056 (2015)
21. Zaloga, V., Yashyna, T., Dynnyk, O.: Analysis of the theories for assessment of the quality management product efficiency. *J. Eng. Sci.* **5**(2), B1–B6 (2018). [https://doi.org/10.21272/jes.2018.5\(2\).b1](https://doi.org/10.21272/jes.2018.5(2).b1)
22. Onysko, O., Kopei, V., Panchuk, V.: Theoretical investigation of the tapered thread joint surface contact pressure in the dependence on the profile and the geometric parameters of the threading turning tool. *IOP Conf. Ser. Mater. Sci. Eng.* **749**, 012007 (2020)

23. Onysko, O., Kopei, V., Medvid, I., Pituley, L., Lukan, T.: Influence of the thread profile accuracy on contact pressure in oil and gas pipes connectors. In: Ivanov, V., Trojanowska, J., Pavlenko, I., Zajac, J., Peraković, D. (eds.) DSMIE 2020. LNME, pp. 432–441. Springer, Cham (2020).https://doi.org/10.1007/978-3-030-50794-7_42
24. Kandil, F.A., Brown, M.W., Miller, K.J.: Biaxial Low Cycle Fatigue Fracture of 316 Stainless Steel at Elevated Temperatures. The Metals Society, London (1982). Book 270



Impact of the Heterogeneous Structure of Magnetic Hard Alloys on the Quality Characteristics of the Surface Layer During Grinding Processing

Maksym Kunitsyn^(✉) , Anatoly Usov , and Yulia Sikirash 

Odessa Polytechnic State University, 1, Shevchenko Ave., Odessa 65044,
Ukraine

m. v. kunitsyn@opu.ua

Abstract. The article deals with fragments of technological heredity, which is the basis of a new scientific and practical direction in mechanical engineering technology aimed at improving machine parts' performance by technological methods in manufacturing parts. The purpose is to study thermomechanical phenomena affecting the quality of the surface layer, taking into account the processing of products and genetic heterogeneities formed in previous technological operations, to establish the influence of these inhomogeneities on crack and burn formation based on quantitative analysis of the thermal and stress state, as well as with taking into account the heterogeneity of the material of the products. The problem of determining the stress-strain state of a piecewise homogeneous product material, the upper layer containing thin inclusions and crack-like defects, and the active layer of which is subject to mechanical processing, is considered. It was found that the presence of various defects in the surface layer of the processed products, introduced at the stage of obtaining the workpiece and subsequent types of processing, requires the formulation of fracture mechanics criteria in the study of the causes of crack formation.

Keywords: Crack · Stress intensity factor · Heat flux · Grinding · Defect · Critical state · Solid

1 Introduction

The linkages between the essential operational properties of details (such as wear resistance, fatigue, and creep strength, contact stiffness, magnetic properties) and technological parameters such as the microrelief of the treated surface, microhardness, presence of microcracks, chipping, the depth distribution of the hardened layer are one of the most critical tasks of engineering technology [1, 2].

The study of the effect of mechanical processing only on the functional properties of products is insufficient, since processing (such as thermal, thermomechanical, chemical-thermal) and especially the methods of obtaining blanks, make a significant contribution to changing the properties of the surface layer, which is subjected subsequently to mechanical processing [3, 4].

The complexity of the processes occurring in the metal of the surface layer subjected to mechanical processing and these parts' operation makes it necessary to consider technological heredity only at the final processing operation [5, 6].

2 Literature Review

The most common final processing method is grinding, ensuring high accuracy and manufacturing parts [7].

However, grinding is associated with the appearance of cauterization, cracks, and tensile stresses in the surface layers of parts, which significantly affects the reliability and durability of these parts during their operation [8].

The following methods currently solve the task of improving the quality of the surface layer of the ground products:

1. Selection of the the rational grinding modes for the material, and the corresponding tool's characteristics.
2. Grinding wheels and belts with an intermittent working surface are used.
3. Automatic control systems of the active cutting power are used.
4. Lubricating and cooling media is recommended, significantly reducing the grinding operation's heat stress and the likelihood of cauterization and cracks.

However, with the existing manufacturing technology, including composite materials, these methods do not entirely exclude the surface layer's defects. It is facilitated by the inevitable fluctuations of the allowance from the errors of previous machining operations; microheterogeneity of the material itself, characterized by the grain size; packaging defects; dislocations and structural transformations; warpage of parts during the heat, and similar treatments [9, 10].

The high thermal intensity of diamond-abrasive processing processes leads to the fact that these processes' thermal physics is often dominant in forming the treated surface's quality characteristics [11]. This position is confirmed by some scientists' research on these processes' specific problems [12, 13].

3 Research Methodology

The purpose is to study thermomechanical phenomena affecting the quality of the surface layer, taking into account the processing of products and genetic heterogeneities formed in previous technological operations, to establish the influence of these inhomogeneities on crack and burn formation based on quantitative analysis of the thermal and stress state, as well as with taking into account the heterogeneity of the material of the products.

Many researchers attribute magnetic alloys' predisposition to cracking when processed by grinding to their magnetic and crystal structure features, designed to obtain high magnetic properties [14, 15]. The presence of stress concentrators in the surface layer of the ground products, which include various kinds of defects introduced in

obtaining the workpiece and subsequent types of processing, fundamentally complicates the study of cracking causes [16, 17]. Therefore, when determining the deformable surface layer's maximum equilibrium state, it is necessary to substitute the stress and strain components' values at the top of the concentrator into the classical strength criteria [18]. This approach is used in fracture mechanics [20], where new strength criteria are formulated, which are certain invariants, both in models of continuum mechanics and models that consider the material's structural features [21].

The stress intensity factors K_I , K_{II} , and K_{III} serve as a measure of the stress singularity near the tip of a crack-like defect. The critical value of the intensity stress K_C is a material's characteristic. When the loading causes the stress intensity to become equal to the critical one, the crack-like defect turns into the main crack. The critical stress is inversely proportional to the square root of the initial length of the crack-like defect [21]:

$$\sigma_C = \frac{K_{IC}}{\sqrt{\pi l}} \quad (1)$$

where $2l$ is the initial length of the crack-like defect, and index 1 is the first type of failure.

Consider the problem of determining the stress-strain state of a piecewise homogeneous product material, the upper layer containing thin inclusions and crack-like defects, and the active layer of which is subject to mechanical processing. The boundary of the treated surface $(-a, a)$ is affected by the heat flow, and on the remaining part, the heat exchange is realized according to Newton's law. Under conditions of uneven heating, stresses arise in the surface layer, which, if there are crack-like defects in the body, can lead to their propagation even in the absence of external mechanical loads. Let the surface layer of the products on the lines $\tilde{x}_1 = 0$, $\tilde{x}_2 = 0, \dots, \tilde{x}_K = 0$ there are defects $|\tilde{y}_1| < l_1$, $|\tilde{y}_2| < l_2, \dots, |\tilde{y}_K| < l_K$ in the transition through which the displacement and stress fields suffer discontinuities. In what follows, we will consider a system of defects consisting of 2 cracks ($k = 1, 2$) located in local coordinates, respectively $\tilde{x}_1 o_1 \tilde{y}_1$ ($k = 1$) and $\tilde{x}_2 o_2 \tilde{y}_2$ ($k = 2$). Figure 1 presents a design scheme for determining the effect of defects on crack formation under thermal load.

Let us introduce the jumps of displacements and stresses on defects:

$$\begin{aligned} \langle \tilde{V}_k(\tilde{y}) \rangle &= \tilde{V}_k(-0, \tilde{y}) - \tilde{V}_k(+0, \tilde{y}); \langle \tilde{\sigma}_x^k(\tilde{y}) \rangle = \tilde{\sigma}_x^k(-0, \tilde{y}) - \tilde{\sigma}_x^k(+0, \tilde{y}); \\ \langle \tilde{U}_k(\tilde{y}) \rangle &= \tilde{U}_k(-0, \tilde{y}) - \tilde{U}_k(+0, \tilde{y}); \langle \tilde{\tau}_{xy}^k(\tilde{y}) \rangle = \tilde{\tau}_{xy}^k(-0, \tilde{y}) - \tilde{\tau}_{xy}^k(+0, \tilde{y}). \end{aligned} \quad (2)$$

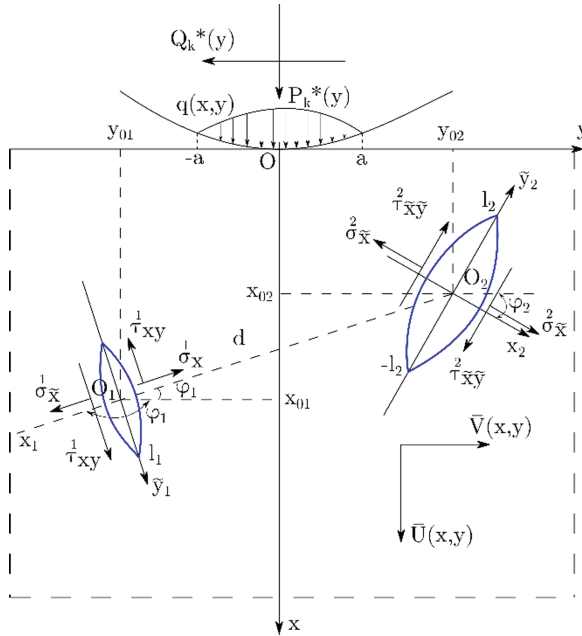


Fig. 1. Calculation scheme for determining the mutual influence of defects on the intensity of the treated surface’s crack formation from the thermomechanical load formed during the product’s machining.

According to conditions (2), the jumps of normal and tangential stresses on defects such as cracks are equal to zero, that is, $\langle \sigma_r^k(y) \rangle \geq 0$, $\langle \tau_{xy}^k(y) \rangle \geq 0$. The displacements $\tilde{U}_K(\tilde{x}, \tilde{y})$, $\tilde{V}_K(\tilde{x}, \tilde{y})$, $\tilde{\theta}_K(\tilde{x}, \tilde{y})$ must satisfy the Lamé equations [22]:

$$\begin{aligned} \frac{\tilde{\theta}'}{1-2\mu} + \Delta \tilde{U}_k &= b^T T'; \quad \frac{\tilde{\theta}'}{1-2\mu} + \Delta \tilde{V}_k = b^T T' \\ \tilde{\theta}_k &= \tilde{U}'_k + \tilde{V}'_k; \quad b^T = \frac{4G(1+\mu)dt}{1-2\mu} \end{aligned} \quad (3)$$

After carrying out the necessary transformations, the final solution of the systems (2) and (3) concerning jumps of displacements and stresses will have the form:

$$\| \langle \tilde{U}' \rangle, \langle \tilde{V}' \rangle, \langle \tilde{\sigma}_x^k \rangle, \langle \tilde{\tau}_{xy}^k \rangle \| = \frac{1}{\sqrt{1-\tau^2}} \left[\Gamma_k + \frac{2}{N} \sum_{m=1}^{N-1} T_m(t) \sum_{v=1}^N g_{kv}^* T_m(\tau_v) \right] \quad (4)$$

where $T(t)$ – Chebyshev polynomials. So, jumps (10) have been found, and the formulas can determine the stress and displacement fields in a heterogeneous material:

$$\begin{aligned}
\|\sigma_x, \tau_{xy}, U', V'\| &= \sum_{i=1}^n \int_{-l_i}^{l_i} \|R_i^{(m)}(x - \zeta, y)\| P^{(i)}(\zeta) d\zeta \\
R_i^m(x, y) &= -(\alpha_i)^m V_i^{(m)} [K_n^{(S_i-m)}], m = 0, 1 \\
K_n^{(1)}(x, y) &= \frac{(-\text{sgny})^n x}{4\pi(x^2 + y^2)} \left[\frac{2y^2}{x^2 + y^2} - (n-1) \right] \\
K_n^{(0)}(x, y) &= \frac{(-\text{sgny})^n |y|}{4\pi(x^2 + y^2)} \left[\frac{x^2 - y^2}{x^2 + y^2} - (n-1) \right], n = 0, 1, 2, \dots \\
(\alpha_i)^m R_i^m(x, y) &= C_i V_i^{(m)} [K_n^{(S_i-m)}] - [C_i + \alpha_i(C_i + d)] V_i^{(m-2)} [K_n^{(S_i-m)}] \\
S_i &= \sin^2 \frac{1}{2k\pi}; C_i = \frac{1 - \mu_i^2}{E_i}; d_i = \frac{\mu_i(1 + \mu_i)}{E_i} \\
P^{(0)}(y) &= \langle \sigma_x(0, y) \rangle, P^{(1)}(y) = \langle \tau_{xy}(0, y) \rangle, -P^{(2)}(y) = \langle \underline{U}'(0, y) \rangle \\
-P^{(3)}(y) &= \langle \underline{V}'(0, y) \rangle, P^{(j)}(x) \equiv 0, |y| > l_k, j = \overline{0, 3}
\end{aligned} \tag{5}$$

Of most significant interest is the behavior of stresses $\sigma_x(o, y) + i\tau_{xy}(o, y)$ at $y \rightarrow lK \pm 0$. These stresses determine the nature of the stress intensity factors SIF ($K_I - K_{II}$).

Let us consider the case of a crack-type defect with a length of $2l$, which is located in a surface layer with a thickness of $2h$ and oriented arbitrarily. The surface layer's stress state is due to the perturbation near the crack of a given temperature field $Tq(x, y, \tau)$. If the $T_0(x, y, \tau) = q(\tau)(y \cos \beta + x \sin \beta)$ function describes the temperature field, then to determine SIF, we have the formula:

$$\begin{aligned}
K_I^\pm - iK_{II}^\pm &= \mp i \frac{\sqrt{\pi l H q l}}{\lambda} \sin(\beta - \phi) \\
&\times \left\{ 1 - \frac{\delta^2}{2} (\alpha_1 - N_{11}) - \frac{\delta^4}{4} [d_2 + \frac{3}{2} d_3 - d_1 N_{11} - N_{11}^2 + N_{31}] + 0(\delta^6) \right\}
\end{aligned} \tag{6}$$

where β is the angle between the direction of the heat flow and the Oy axis; ϕ is the angle between the axis of the defect and the Ox axis; $\delta = \frac{l}{h}$ - the dimensionless bandwidth:

$$\begin{aligned}
d_1 &= -(i \sin 2\phi + e^{-4i\phi}) I_1 - \frac{1}{2} e^{-2i\phi} I_1 - (1 - 2e^{-2i\phi} - e^{-4i\phi}) A_2 - 4e^{-4i\phi} E_4 \\
d_3 &= \frac{1}{6} [(\sin 4\phi - 2e^{-4i\phi} + 2e^{-6i\phi}) I_3 + \frac{1}{2} e^{-4i\phi} I_3 \\
&\quad + (4e^{-2i\phi} - e^{-4i\phi} - 4e^{-4i\phi} - e^{-6i\phi}) A_4 - 4e^{-6i\phi} E_6] \\
d_2 &= \frac{1}{8} [1 - \cos 4\phi + 8\sin^2 \phi + 5i \sin \phi (e^{-5i\phi} - 2e^{-i\phi})] I_1 \\
&\quad + \frac{1}{2} (\cos 4\phi - 5i \sin \phi e^{-5i\phi}) I_3 + I_{3/4} + 2e^{-i\phi} E_6 \\
&\quad + [i \sin \phi (3e^{-i\phi} - 2e^{-i\phi}) - e^{-2i\phi}] \\
&\quad + \frac{1}{2} [2i(3e^{i\phi} - 3e^{-i\phi} - 2e^{-i\phi} + e^{3i\phi}) \sin \phi + e^{2i\phi} - 2e^{-2i\phi} - 16\sin^2 \phi e^{-4i\phi}] E_4 \\
I_n &= 4 \int_0^\infty y^{n+2} sh 2ye(y) dy; I_n = \int_0^\infty y^n [(1 - e^{-2y}) sh 2y - 4y^2] e(y) dy
\end{aligned}$$

$$A_n = \int_0^\infty y^n (ch2y - 1)e(y)dy; E_n = \int_0^\infty y^n e(y)dy; e(y) = \frac{1}{4y^2 - sh^2 2y}$$

$$N_{11} = \frac{\pi^2}{48} (\cos 2\phi \pm 3); N_{31} = \frac{\pi^4}{256} (\cos 4\phi / 15 \pm \cos 2\phi); N_{33} = \frac{N_{31}}{3}$$

The upper sign corresponds to the right end of the defect and the lower one – to the left. In Fig. 2(a) and Fig. 2(b), the dependences of $K_I^* = \lambda K_I / \sqrt{\pi l H q l}$ and $K_{II}^* = \lambda K_{II} / \sqrt{\pi l H q l}$ on the angle of rotation of the crack ϕ are shown at $l/h = \delta = 0.1$. Curve №1 and curve №2 are curves corresponding to the heat conduction problem’s boundary conditions. If the temperature is set at the boundary – curve №1, if the heat flux and heat transfer conditions – curve №2. When the heat flux is perpendicular to OY , solid lines correspond to the right end of the crack, dashed lines – to the left.

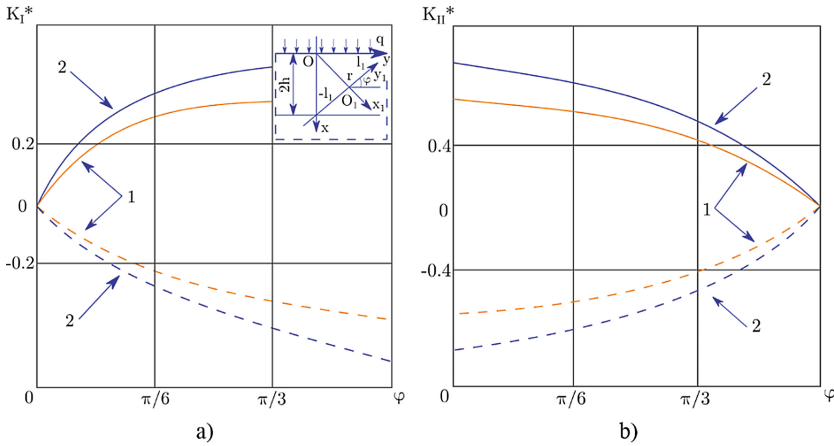


Fig. 2. The dependences of (a) $K_I^* = \lambda K_I / \sqrt{\pi l H q l}$ and (b) $K_{II}^* = \lambda K_{II} / \sqrt{\pi l H q l}$ on the angle of rotation of the crack ϕ at $l/h = \delta = 0.1$.

It follows from the figures that the values of K_I and K_{II} in the absence of heat transfer (curves №2) are more significant in absolute value if the boundary outside the zone of contact of the tool with the machined surface is thermally insulated.

The parameter K_{II} reaches its highest value when the heat flux is perpendicular to the fracture.

Let us investigate the stress intensity at the tops of a crack located at a depth δ^* when the temperature T_0 is maintained on its edges, and a heat flux $q(T, y)$ is specified on the body surface ($x = 0$) directed perpendicularly ($\beta = 0$ is the angle between the direction of the flow and axis Ox) to this surface. The thermoelastic state of the body will be determined only by the perturbed temperature field. Taking into account that on the crack line $T_0 = 2q_0^* \delta^*$ from relations (6), we find:

$$K_I^{*\pm} = \mp q_0^* H l \sqrt{\pi l}; K_{II}^{*\pm} = \pm 2HT_0 \sqrt{\frac{l}{\pi}} \quad (7)$$

If we consider the value of $P\eta = q_0^* H l \delta^*$, where P is the tensile forces formed under the action of temperatures, and η is a parameter, then the following essential characteristics for the behavior of defects can be established. If we know the value of the stress intensity factors, then the angle of the initial crack propagation θ_* , and the limiting value of the heat flux are determined from the following relations [22]:

$$\theta_* = 2\arctan D; D = \frac{K_I - \sqrt{K_I^2 + 8K_{II}^2}}{4K_{II}}; q_{0*} = \frac{\sqrt{3}\lambda K_{IC}}{Hl\sqrt{\pi l}\delta^*} \quad (8)$$

Under the influence of the heat flow, the heat-insulated crack begins to grow from both ends simultaneously. With an increase in the heat flux, the limiting forces decrease; that is, the body's strength decreases with a crack.

Let us consider the mutual influence of defects on the stress intensity by the example of 2 arbitrarily oriented cracks. We select the origin of coordinates on one of the cracks, and the second can be arbitrarily moved relative to the first. From relations (6), (7), and (8) at $l_K = l$, $a_{ij} = a$, $\varphi_1 = 0$, $\varphi_2 = \varphi$, $\delta = l/d$, after calculations with an accuracy of δ^7 , the stress intensity factor expression for the upper crack has the form:

$$K_I^\pm = \frac{1}{\sqrt{\pi l H q l}} [0, 5\delta - 0, 25\delta^3 + 0, 207\delta^5 - 0, 0371\delta^7] \quad (9)$$

$$K_{II}^\pm = \frac{1}{\sqrt{\pi l H q l}} [1 - 0, 25\delta^2 + 0, 195\delta^4 - 0, 1787\delta^8] \quad (10)$$

In Fig. 2(b) for the upper crack, the dependence of the K_S values ($S = I$ – red line, $S = II$ – blue line) on the dimensionless distance between the cracks $\tilde{a} = a/2l$, calculated numerically by formulas (9) and (10), is given. At $\delta < 0.5$, the presence of the second defect has little effect on the value of K_{II} , while the coefficient K_I still significantly depends on the distance between the cracks. Figure 3(a) shows the dependence of SIF on the angle φ (the angle of rotation of the second crack is relative to the first) at $\delta = 1/3$ ($a = 3l$) when $\psi = 0, \pi/6, \pi/3, \pi/2$ (the curves are designated respectively for a moving crack by numbers 1–4, for a stationary crack – 1'–4'; solid lines correspond to SIF at the right tops of the crack (K_j^+), dashed lines – at the left ones (K_j^-). For some locations of the cracks, the coefficient K_I at one of the ends can be negative (this means that in the vicinity of this end of the crack edge, the cracks come into contact). In the case of SIF, in the vicinity of the other end, the macrocracks practically do not change, and they can be used to determine the value of the critical force at which the crack comes to the state of ultimate equilibrium.

It follows from the above figures that at $0 \leq \psi \leq \pi/6$, a stationary crack starts to propagate first, and for all values of φ at vertex I, except for a specific region in the vicinity of $\varphi = \pi/2$. The critical heat flux has the smallest value for $\psi = 0$, $\varphi = 0$, and

$\psi = \pi/6$ at $\varphi = \pi/6$. If $\psi = \pi/3$, then the propagation of cracks starts from the bulkhead's side, and the smallest value of \tilde{q}^* is reached at $\varphi = \pi/4$. When $\pi/2 \leq \varphi \leq 5\pi/6$, the cracks mutually strengthen each other; that is, the strength of the body, in this case, is higher than in the presence of only one crack. At $\psi = \pi/2$ and $\delta = 1/3$, the cracks practically do not interact.

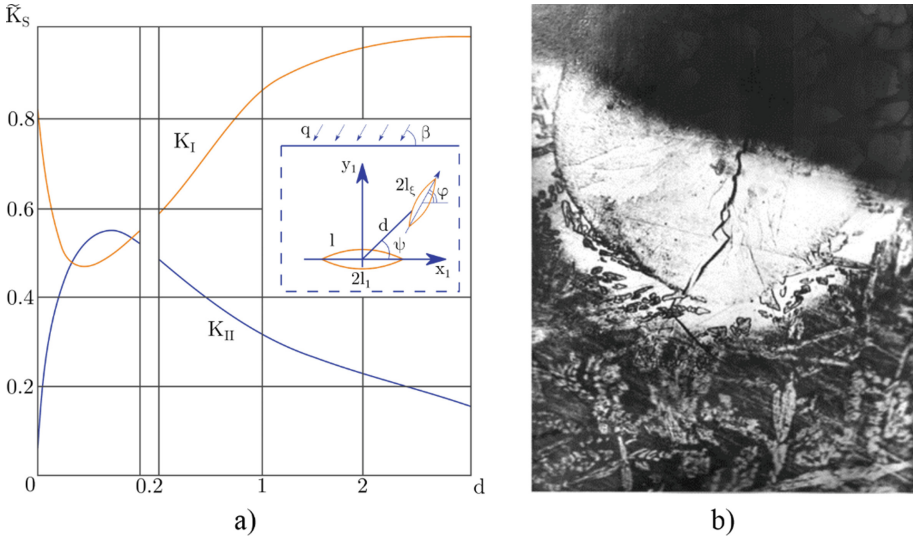


Fig. 3. (a) Dependence of the value of K_S ($S = I$ – red line, $S = II$ – blue line) on the dimensionless distance between cracks $\tilde{a} = a/2l$; (b) Microsection of the surface layer of the alloy Alnico 8HC (R1-1-13) after grinding treatment.

4 Results

In the case of a power load, a rigid inclusion leads to an increase in the value of K_I . In the case of a thermal load, a rigid inclusion leads to a decrease in the value of K_I . Simultaneously, the coefficients of linear thermal expansion of the coating made of composite material have a more significant effect on the character of SIF change. For example, for $\alpha_{r1} < \alpha_{r2}$, $K_I > 0$, and for $\alpha_{r1} > \alpha_{r2}$, $K_I < 0$. The thermal conductivity coefficients λ_1 and λ_2 do not qualitatively affect K_I and K_{II} but change them only quantitatively. Thus, at $\tilde{\lambda} = 4$, the absolute value of SIF is more significant than at $\tilde{\lambda} = 0.5$.

The above examples demonstrate the interaction of cracks and inclusions and the stress state of a material containing the indicated inhomogeneities. It is shown that under certain conditions, more rigid inclusions strengthen the material, while soft structural components make it possible to inhibit microcracks' development into the main ones. By appropriately selecting the inclusions, it is possible to reduce the stress concentration in crack-like defects.

Thus, for defect-free machining of alloys, it is necessary to take into account their structural inhomogeneity. The presence of crack-like defects and inclusions contributes to the fact that one should be guided by the limiting values of the forming heat flux when choosing the tool's processing modes and characteristics.

For example, grinding of hard magnetic alloys Alnico 8HC (R1-1-13) (Al – 7%; Ni – 14%; Co – 38%; Cu – 3%; Ti – 8%; Fe – other) with soft inclusions of the γ -phase and the harder α' -phase of the matrix should be carried out $q_{max} = 107 \text{ W/m}^2$. If we take a grinding circle 25AF4607B, $D_{cr} = 0.26 \text{ m}$ as a tool, and perform processing in the following modes: $V_{cr} = 35 \text{ m/s}$, $V_g = 0.17 \text{ m/s}$, $t = 1.8$ without lubricating-cooling liquid, then the heat flux going into the alloy is 107 W/m^2 . It leads to the fact that the pores present in the alloys turn into microcracks, the trajectory of which passes through ellipsoidal γ -inclusions (Fig. 3(b)).

5 Conclusions

The carried out theoretical studies of the influence of structural heterogeneity of materials on the mechanism of initiation and development of cracks under the action of a thermomechanical load formed during finishing operations allow us to draw the following conclusions.

The presence of various types of defects in the surface layer of the ground products, introduced at the stage of obtaining the workpiece and subsequent types of processing, requires the formulation of fracture mechanics criteria to study the causes of crack formation.

The magnitude of the stress intensity factors for defects (e.g., cracks) is influenced by the following factors: size and orientation of these defects, the depth of their occurrence and relative position, and the magnitude of the heat flux.

For any coefficients of thermal conductivity, linear thermal expansion and shear moduli of the matrix and inclusion of the workpiece, the stress intensity factors $K_I = 0$ and $K_{II} = 0$, if the heat flux is directed perpendicular to the crack in the inclusion, and vice versa, if parallel to the crack, $K_I = 0$ and $K_{II} = 0$.

If the CLTE of the inclusion is less than the CLTE of the matrix, a decrease in the rigidity of the inclusion leads to a decrease in the stress intensity factors K_I ($K_{II} = 0$) for the exact ratios of the thermal conductivity coefficients, that is, there are favorable conditions for the non-propagation of microcracks in the treated surface.


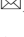



References

1. Soboleva, E.: Microscopy investigation of the surface of some modern magnetic materials. Lappeenranta-Lahti University of Technology LUT, Finland (2021)
2. Yagodkin, Y.D., Lileev, A.S., Menushenkov, V.P., Skakov, Y.A.: Structure of alloys for permanent magnets based on compounds of rare-earth metals. *Met. Sci. Heat Treat.* **42**(8), 314–318 (2000). <https://doi.org/10.1007/BF02471307>
3. Li, Y., Zhang, W., Li, J., Lin, X., Gao, X., Wei, F., Zhang, G., Li, L.: Microstructure and high temperature mechanical properties of advanced W–3Re alloy reinforced with HfC

- particles. *Mater. Sci. Eng. A* **814**, 141198 (2021). <https://doi.org/10.1016/j.msea.2021.141198>
4. Neelima, B., Rao, N.R., Chary, V.R., Pandian, S.: Influence of mechanical milling on structure, particle size, morphology and magnetic properties of rare earth free permanent magnetic Zr₂Co₁₁ alloy. *J. Alloy. Compd.* **661**, 72–76 (2016)
 5. Zhao, Z., Qian, N., Ding, W., Wang, Y., Fu, Y.: Profile grinding of DZ125 nickel-based superalloy: grinding heat, temperature field, and surface quality. *J. Manuf. Process.* **57**, 10–22 (2020)
 6. Pourabbas, M., Abdollah-zadeh, A., Sarvari, M., Pouranvari, M., Miresmaeili, R.: Investigation of structural and mechanical properties of magnetic pulse welded dissimilar aluminum alloys. *J. Manuf. Process.* **37**, 292–304 (2019)
 7. Kansal, H., Singh, A.K., Grover, V.: Magnetorheological nano-finishing of diamagnetic material using permanent magnets tool. *Precis. Eng.* **51**, 30–39 (2018)
 8. Tian, Y., Shi, C., Fan, Z., Zhou, Q.: Experimental investigations on magnetic abrasive finishing of Ti-6Al-4V using a multiple pole-tip finishing tool. *Int. J. Adv. Manuf. Technol.* **106**(7–8), 3071–3080 (2020)
 9. Hayashi, E., Kikuchi, M., Okuno, O., Kimura, K.: Grindability of dental magnetic alloys. *Dent. Mater. J.* **24**(2), 163–171 (2005)
 10. Korneva, A., Korznikova, G., Kashaev, R., Straumal, B.: Microstructure evolution and some properties of hard magnetic FeCr₃₀Co₈ alloy subjected to torsion combined with tension. *Materials* **12**(18), 3019 (2019)
 11. Sun, X.Y., Xu, C.Y., Zhen, L., Gao, R.S., Xu, R.G.: Microstructure and magnetic properties of Fe–25Cr–12Co–1Si alloy thermo-magnetically treated in intense magnetic field. *J. Magn. Magn. Mater.* **283**(2–3), 231–237 (2004)
 12. Stel'mashok, S.I., Milyaev, I.M., Yusupov, V.S., Milyaev, A.I.: Magnetic and mechanical properties of hard magnetic alloys 30Kh21K3M and 30Kh20K2M2V. *Met. Sci. Heat Treat.* **58**(9–10), 622–627 (2017)
 13. Korznikova, G.F.: The structure and mechanical properties of Fe-15% Co-25% Cr hard magnetic alloy subjected to torsion under high pressure. *Rev. Adv. Mater. Sci.* **11**, 109–115 (2006)
 14. Ahmad, Z., Ul Haq, A., Husain, S.W., Abbas, T.: Effect of Mo addition on magnetic properties of Fe–28Cr–15Co hard magnets. *Physica B* **321**(1–4), 96–103 (2002)
 15. Vuong Nguyen, V., Poudyal, N., Liu, X.B., Ping Liu, J., Sun, K., Kramer, M.J., Cui, J.: Novel processing of high-performance MnBi magnets. *Mater. Res. Exp.* **1**(3), 036108 (2014)
 16. Nichterwitz, M., Honnali, S., Kutuzau, M., Guo, S., Zehner, J., Nielsch, K., Leistner, K.: Advances in magneto-ionic materials and perspectives for their application. *APL Mater.* **9**(3), 030903 (2021)
 17. Wohlfarth, E.P.: Hard magnetic materials. *Adv. Phys.* **8**(30), 87–224 (1959)
 18. Oliveira, J.F.G.D., Silva, E.J.D., Guo, C., Hashimoto, F.: Industrial challenges in grinding. *CIRP Ann.* **58**(2), 663–680 (2009)
 19. Wang, Y., et al.: Experimental evaluation on tribological performance of the wheel/workpiece interface in minimum quantity lubrication grinding with different concentrations of Al₂O₃ nanofluids. *J. Clean. Prod.* **142**, 3571–3583 (2017)
 20. Na, S.M., Lambert, P.K., Jones, N.J.: Hard magnetic properties of FeCoNiAlCuXTiX based high entropy alloys. *AIP Adv.* **11**(1), 015210 (2021)
 21. Lawal, L.O., Mahmoud, M., Adebayo, A., Sultan, A.: Brittleness and microcracks: a new approach of brittleness characterization for shale fracking. *J. Nat. Gas Sci. Eng.* **87**, 103793 (2021)
 22. Popov, G.Y.: The Concentration of Elastic Stresses Near the Stamps of Cuts, Thin Inclusions and Reinforcements. Science, Moscow (1982). (in Russian)



Mathematic Model of the General Approach to Tolerance Control in Quality Assessment

Oleksandr Kupriyanov¹  , Roman Trishch¹ ,
Dimitar Dichev² , and Tetiana Bondarenko¹ 

¹ Ukrainian Engineering Pedagogics Academy, 16, Universitetskaya Street,
Kharkiv 61003, Ukraine

a_kupriyanov@uipa.edu.ua

² Technical University of Gabrovo,
4, H. Dimitar Street, Gabrovo 5300, Bulgaria

Abstract. A mathematical model for the numerical determination of the quality indicator value allowing one to obtain non-dimensional values in the range from minus infinity to 1 (the maximum usable value) is proposed. Unlike the traditional system of tolerances, in which the suitability can take two values – 0 or 1, the proposed model allows you to obtain intermediate values of the suitability, depending on the proximity of the actual parameter to the desired value. The model uses the suitability function suggested in the paper, and the shape indicator drives it. The characteristic ranges of the shape indicator of the suitability function have been considered. Those of practical importance has been highlighted. In addition to the general dependence, exceptional cases (linear and parabolic suitability functions, which are mathematically simpler) are also given. It is shown how the use of the proposed model allows sorting parts into quality grades and introducing a technological margin of accuracy. The mathematical model is illustrated by the example of the dimensional suitability of an engineering part. The traditional system of dimensional tolerances is a particular case of the proposed generalized system, which is recommended for high-precision manufacturing.

Keywords: Tolerance · Actual dimension · Quality system · Desirability function · Continuous quality improvement

1 Introduction

The traditional system of tolerances, ubiquitous in mechanical engineering, is quite effective for medium-precision products in mass production. Recently, however, serial production has been declining, and high-precision production, in which the finishing operations are fitting, is becoming more widespread.

Tolerance control of the suitability of dimensions implies that dimensions within certain limits, called tolerances, are considered to be equally fit, and their quality does not differ. First, this does not correspond to the operating conditions under which there is some best design value of the dimension, which we will call the optimal dimension. Secondly, it does not stimulate production in the shop to produce parts with the

narrowest possible range of actual dimensions. In the current tolerance control system, the only way to improve quality is to reduce the dimensional tolerance.

Conversely, the concept of continuous quality improvement is aimed at continuous improvement of design and technology. Therefore, the idea seems to be quite fruitful, in which the quality of dimension, part, and product as a whole is assessed not in a discrete binary system: accepted or rejected, but in a continuous one in which suitability can receive values intermediate between 1 and 0. Such systems are already found in the food (several food quality levels) and electronics industries (sorting structurally identical processors on the models), and they can be helpful in mechanical engineering.

2 Literature Review

For a comparative assessment of the quality of several technologies, the result should be translated into a non-dimensional value. Part dimension standardizing is one mathematical approach for doing this, for which the desirability function can be applied.

Harrington Jr. [1] was one of those who first introduced the desirability function. Using this function, he solved the problem of optimizing a function of several variables and converted the dimensional parameters of products to non-dimensional ones to obtain a generalized quality parameter. G. Derringer and R. Suich [2] set the task of optimizing the parameters of the production conditions to obtain the optimal combination of product properties for the chemical industry. G. Derringer and R. Suich generalized the desirability function for the case when the variables have both upper and lower constraints, and there is also an optimal value.

Kim and Lin [3] proposed a different kind of desirability function, but it lost the ability to influence the shape. Moreover, the proposed functions have not negative values.

If there are several quality parameters of different dimensions, the authors propose calculating the generalized quality indicator as to the geometric mean of the indicators included in it. Safety and quality are “hot topics” in the medical device industry [4]. Regulatory requirements are becoming increasingly stringent throughout the entire product lifecycle, including life cycle and shipping. More and more organizations are expected to demonstrate quality management processes and ensure that they follow best practices for what they do.

The authors slightly modified the functions, but they did not fundamentally remain the same [5]. In mechanical engineering, desirability functions were used to construct quality management systems for enterprises and are intended to summarize quality indicators on a single non-dimensional scale.

Other authors used desirability functions for multicriteria assessment of qualimetry objects of different nature (processes and systems). In these studies, assessment methods were developed considering the nature of the research objects [6]. The method of analysis of hierarchies was used to select the nonlinearity degree of the assessment on a single criterion indicator. Such studies concerned the multicriteria assessment of

the labor safety system in machine-building production and the processes of the quality management system of industrial enterprises.

Quality management consists of four main components: quality planning, quality assurance, quality control, and quality improvement. For many decades, the system of tolerances has been the primary means of quality management.

The development of tolerance has come a significant way from manual methods to modern computer models. Many techniques have emerged over the years. But, the area of constructing geometric tolerances has not received much attention [7].

In addition to the arithmetic interpretation of the tolerance, statistical is quite widely used for dimensional chains. It does not guarantee that all products will be in the required range, but only most of them [8].

Traditional tolerance assumes that all data within tolerance is equally acceptable. Genichi Taguchi was one of the first to propose an alternative approach that agrees that the very best product has exactly as a target. The more the deviation from the target, the more the loss. This is called the quality loss function, and it is the fundamental principle of an alternative system called inertial tolerance [9].

Inertial tolerance is a statistical expression of a tolerance without specifying an interval [10], but it is associated with the influence of the characteristics of parts on the quality of the assembled product.

Taguchi tolerancing method offers many advantages and the increasing of product quality among them. On the other hand, a problem of quality assurance of product for the customer appeared [11].

Using dimension information can significantly increase the dimensional accuracy of joints without increasing the accuracy of manufacturing parts. An approach using marking and a specific selection of parts into kits can be arranged for all dimensions and parts [12]. Thus, the result is a significant increase in dimensional accuracy of joints without changing the manufacturing technology of parts.

Statistical Process Control is widely used to monitor processes now [13]. Although, developments in Industry 4.0 and improvements of machine tools made it traditional [14]. Using Statistical and Engineering Process Control can slightly improve the quality of processes [15]. Nowadays, Automated Process Control became widely popular. It is based on three main innovations: machine learning to control processes more accurately, the simultaneous consideration of all available characteristics in multidimensional processes, and the dissociation between conformity and control for these characteristics [16]. In Automated Process Control production, it is possible to calculate in real-time suitability depending on the proximity of the actual parameter to the desired value.

3 Research Methodology

Proposed in the work terms are illustrated by the example of dimensional suitability. However, they can also be applied to other types of defects and quality parameters, both in manufacturing engineering and other industries.

For quantifying the deviation value of the actual dimension x from the optimal one ko , it is proposed to use the dimensional suitability function $K(x)$, which standardizes the dimensional suitability value along the entire numerical axis.

The function $K(x)$ has the following properties:

1. $K(ko) = 1$.
2. $K(ei) = K(es) = 0$, where ei and es can be the boundaries of the standard tolerance band.
3. Within the permissible values, it changes in the range $[0, 1]$ so that one function value corresponds to two argument values located on opposite sides of ko .
4. Negative, out of permissible values.

An important parameter of this function is the shape index when deviating from the optimal dimension β . Let us consider in more detail the influence of the shape index β on the dimensional suitability function $K(x)$. Figure 1 shows examples of dimensional suitability functions. Dimensions x in mm are plotted along the horizontal axis, non-dimensional values of suitability for dimensions $K(x)$ are plotted along the vertical axis. The shape of the suitability function is established based on the operating conditions of the part. The shape of the suitability function determines how desirable it is to obtain dimensions close to the ko optimal value. The greater its acceleration, the narrower the range of the dimension value should be provided technologically. The suitability function can be asymmetrical if the value of the optimal dimension ko is offset from the center of the permissible values. An asymmetric shape is advisable if structurally required to provide dimensions close to one of the permissible values. From the point of view of operating conditions and manufacturing technology, it is advisable to distinguish the following characteristic values and ranges of β :

1. When $\beta \rightarrow 0$, the function is simplified to the traditional tolerance control (Fig. 1a). The value of the dimensional suitability function is equal to 1 within the tolerance band and tends to $-\infty$ outside it. A jump in the function is observed at the boundaries of the tolerance band $[ei, es]$.
2. At $0 < \beta < 0.5$, the function is characterized by the use of a technological margin of accuracy, in which the range of dimensions with suitability $K(x) \approx 1$ narrows from the permissible values $[ei, es]$ to the desired ones $[ki, ks]$. In this case, the values of the dimensions outside $[ki, ks]$, but within $[ei, es]$ have $0 < K(x) < 1$ (Fig. 1b), when they are permissible but undesirable. Outside the range $[ei, es]$, the suitability function is $K(x) < 0$, which means that the production of parts with such dimensions is penalized.
3. For $0.5 < \beta \leq 1$, only the value of the optimal dimension corresponds to $K(x) = 1$ (Fig. 1c). As the actual dimension moves away from the optimal one, $K(x)$ decreases, at the points of the boundaries of the permissible values $K(x) = 0$, outside them $K(x) < 0$.
4. In the case $\beta = 1$, the left and right halves of the dimensional suitability function are linear (Fig. 1d). This simplifies the mathematical task of determining the suitability value of the actual dimension and constructing the distribution function of the dimensional suitability.

5. For $\beta > 1$, the dimensional suitability function has a downward bulge (Fig. 1e). Such a shape is of limited interest for practice since it is challenging to ensure technologically, the deviation value from the optimal dimension is very high. In the limiting case, when $\beta \rightarrow \infty$, $K(x) = 1$ in the value of the optimal dimension, $K(x) = 0$ within the permissible values and $K(x) = -\infty$ outside them (Fig. 1f).

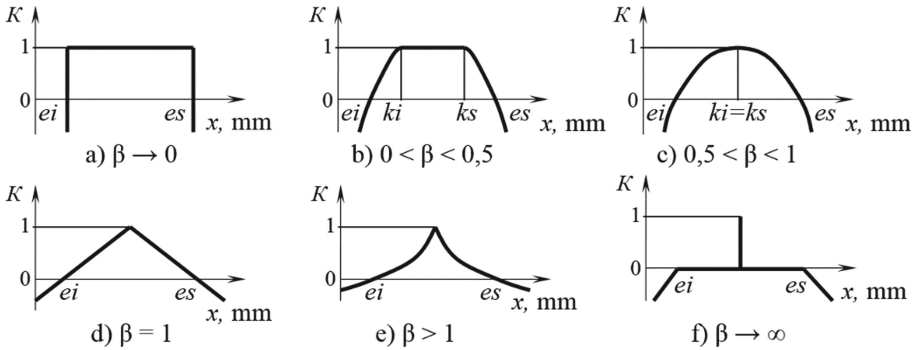


Fig. 1. Family of dimensional suitability functions.

It should be noted that the value of the optimal dimension should be within the range of boundary permissible values, $ei < ko < es$; otherwise, the requirements for the dimensional suitability function $K(x)$ will not be met.

The suitability function can be described by the following proposed by the authors' expression:

$$K(x) = \begin{cases} 1 - \left(\frac{x-ko}{ei-ko}\right)^{\frac{1}{\beta}}, & x \leq ko, \\ 1 - \left(\frac{x-ko}{es-ko}\right)^{\frac{1}{\beta}}, & x \geq ko. \end{cases} \quad (1)$$

The further the actual dimension is from the optimal one, in which the value of $K(x)$ is equal to one, the lower the suitability is. Subtracting the second term (for example, $\left(\frac{x-ko}{ei-ko}\right)^{\frac{1}{\beta}}$ for the left half of the function) from one decreases the value of the function.

There are quality parameters for which the zero levels is the best: shape geometry errors, roughness, and runout. In this case, the optimal level is $ko = 0$, and only the right half of the suitability function has a physical meaning. Accordingly, expression (1) is simplified to the form:

$$K(x) = 1 - \left(\frac{x}{es}\right)^{\frac{1}{\beta}}, \quad (2)$$

where es has the meaning of the quality parameter limit.

A generalized approach to constructing the suitability function described by formulas (1) and (2) is not always justified. You can often use a more mathematically simple formula for functions.

The use of a linear suitability function (Fig. 1d), for which $\beta = 1$, significantly simplifies the mathematical problem of calculating the suitability value of the actual dimension. In this case, the dimension suitability value is determined by the formula:

$$K(x) = \begin{cases} (x - ei)/(ko - ei), & x \leq ko, \\ (x - es)/(ko - es), & x \geq ko. \end{cases} \tag{3}$$

For a given suitability value K , the corresponding suitability values can be determined:

$$x(K) = \begin{cases} ei + K(ko - ei), & x \leq ko, \\ es + K(ko - es), & x \geq ko. \end{cases} \tag{4}$$

In formulas (3) and (4), $ko \neq ei \neq es$.

Using a parabola as the suitability function gives a curve (Fig. 1c), in appearance similar to the normalized curve of the value of obtaining parts with a specific range of dimensions. For this reason, as well as its mathematical simplicity, the parabola as the suitability function will find wide application. The parabola is symmetrical; therefore, the disadvantage of using it as the suitability function will be the impossibility of shifting the value of the optimal dimension relative to the center of the permissible dimensions, i.e., always $ko = (ei + es)/2$. The suitability value of the actual dimension, due to the symmetry of the solution for the left and right halves, can be written in one equation:

$$K(x) = 1 - \left(\frac{2x - es - ei}{es - ei} \right)^2. \tag{5}$$

The following formula determines the value of the two dimensions corresponding to the specified suitability K :

$$x(K) = ko \pm \frac{es - ei}{2} \sqrt{1 - K}. \tag{6}$$

4 Results

We will illustrate the influence of the shape indicator of the suitability of dimensions β on the dimensional suitability function using the example of the dimensions $\varnothing90F8_{+0.036}^{+0.09}$. We have, respectively, $ei = 90.036$, $es = 90.09$. Let the optimal dimension be slightly shifted relative to the middle of the tolerance band and be equal to $ko = 90.055$ mm. The graphs of the suitability function are shown in Fig. 2 for the cases $\beta_1 = 2$, $\beta_2 = 1$, $\beta_3 = 0.5$, and $\beta_4 = 0.05$. Calculating was done in Maple.

For $\beta > 1$, even a small deviation from the optimal dimension significantly decreases the suitability, and the suitability function is concave. For $\beta = 1$, it is linear. For $\beta < 1$, the suitability function is convex. At $\beta \rightarrow 0$, we have a traditional tolerance control, in which within the tolerance band $[ei, es]$, the dimensional suitability $K(x) = 1$ outside of it is negative.

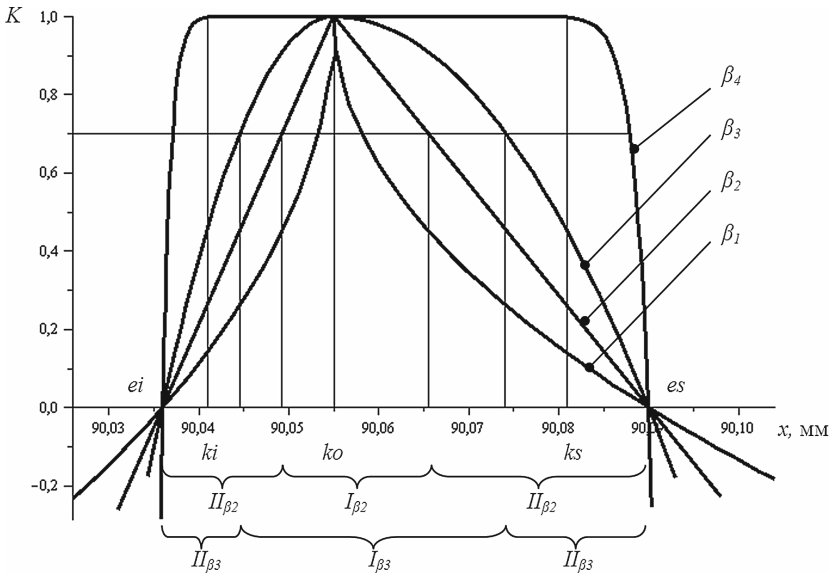


Fig. 2. Suitability function for various parameters of the β shape.

Thus, as β decreases, the deviation from the optimal dimension decreases. The range $0 \leq \beta \leq 1$ is of practical importance. At $0 \leq \beta < 0.25$, the function characterizes a well-known technological method: the use of a technological margin of accuracy, in which the dimension range with the optimality $K(x) = 1$ narrows from the permissible values $[ei, es]$ to the desired values $[ki, ks]$ (Fig. 2).

The dimensional suitability function $K(x)$ allows us to apply the approach of dividing parts into quality grades according to the criterion of the proximity of the actual dimensions to the optimal one. As an example, Fig. 2 shows the division of the part dimensions into two grades of quality for $\beta_2 = 1$. Grade I with a suitability value of $K > 0.7$ includes parts with dimensions in the I_{β_2} range. Grade II with a suitability value of $0 < K < 0.7$ includes parts with other dimensions within the tolerance $[ei, es]$, ranges II_{β_2} . With an increase in the selected limit value of suitability K , the dimension range of quality grade I narrows, correspondingly increasing the dimension ranges of grade II parts. Figure 2 also shows the division into the first I_{β_3} and the second II_{β_3} quality grades for $\beta_3 = 0.5$.

Dimensions can be divided into more grades, but a large number of them are impractical. Apparently, for practical cases, it is sufficient to use 2–3 grades.

With the same suitability value K , the range of dimension values for a particular quality grade decreases with decreasing β . For the above example and $K = 0.7$, the limit values for the dimensions of the first quality grade are given in Table 1.

Table 1. Dimension limits of the first quality grade.

	β	X_{l1} , mm	X_{h1} , mm
1	2	90.053	90.058
2	1	90.049	90.066
3	0.5	90.045	90.074
4	0.05	90.037	90.088

5 Conclusions

A control system in which the quality indicators do not have a discrete value: 0 or 1, but a continuous suitability one, decreasing as they deviate from the optimal value, is proposed. Simultaneously, depending on the indicator values' range, the parts can be divided into grades according to the quality criterion. This criterion has a different value for suitability and a different value for the selling price. When assembling a product from parts of a certain quality, we can say that the product corresponds to this quality.

The dimensional suitability function with the selected β can be used to organize labor remuneration to minimize deviations of the actual dimension from the optimal one. In this case, the actual dimensions are measured, and the worker is entitled to payment for each manufactured part, proportional to the value of the suitability function $K(x)$. This approach can be considered appropriate for high-precision critical parts because with careful adjustment of the equipment, workers, as a rule, can obtain dimensions in a narrowed interval within the tolerance band.

This will stimulate production to continuously improve quality and expand product sales through a differentiated approach to customers with different financial capabilities.

Thus, in the proposed control system, the actual dimensions will have a non-dimensional value of suitability, ranging from 1 for coinciding with the optimal value to negative values outside of the permissible values. The traditional system of dimensional tolerances is a particular case of the proposed generalized system.

In further studies, the authors consider linking the suitability function with technological options.






References

1. Harrington, J.: The desirability function. *Ind. Qual. Control* **21**(10), 494–498 (1965)
2. Derringer, G.C., Suich, D.: Simultaneous optimization of several response variables. *J. Qual. Technol.* **12**(4), 214–219 (1980)

3. Kim, K.-J., Lin, D.: Simultaneous optimization of mechanical properties of steel by maximizing exponential desirability functions. *Appl. Statist.* **48**(3), 311–325 (2000)
4. Pogrebjak, A.D., Krivets, A.S., Dyadyura, K.A., Maksakova, O.V., Shaimardanov, Zh.K., Peplinska, B.: Research of the relief and element composition of the surface coatings based on hydroxyapatite implants from titanium alloys. In: *Nanomaterials: Applications & Properties (NAP-2016)*, vol. 5, no. 2 (2016). <https://doi.org/10.1109/NAP.2016.7757290>
5. Ngoi, B.K.A., Seow, M.S.: Tolerance control for dimensional and geometrical specifications. *Int. J. Adv. Manuf. Technol.* **11**, 34–42 (1996). <https://doi.org/10.1007/BF01177182>
6. Trisch, R., Gorbenko, E., Dotsenko, N., Kim, N., Kiporenko, A.: Development of qualimetric approaches to the processes of quality management system at enterprises according to international standards of the ISO 9000 series. *Eastern-Eur. J. Enterprise Technol.* **4**(3–82), 18–24 (2016). <https://doi.org/10.15587/1729-4061.2016.75503>
7. Wagner, T., Trautmann, H.: Integration of preferences in hypervolume-based multiobjective evolutionary algorithms by means of desirability functions. *IEEE Trans. Evol. Comput.* **14**(5), 688–701 (2010)
8. Leblond, L., Pillet, M.: Conformity and statistical tolerancing. *Int. J. Metrol. Qual. Eng.* **9**(1) (2018)
9. Babu, J.R., Asha, A.: Minimising assembly loss for a complex assembly using Taguchi's concept in selective assembly. *Int. J. Prod. Qual. Manag.* **15**(3), 335–356 (2015)
10. Pillet, M., Maire, J.L.: Inertial tolerancing and acceptance sampling. *Int. J. Eng. Innov. Technol.* **2**(10), 265–271 (2013)
11. Pillet, M., Adragna, P.-A., Germain, F.: Inertial tolerancing: the sorting problem. *J. Mach. Eng.* **6**(1), 95–102 (2006)
12. Kupriyanov, O., Lamnauer, N.: Improvement of the assembling technology for precision joints using the dimensional information. In: Tonkonogiy, V., et al. (eds.) *InterPartner 2020. LNME*, pp. 52–60. Springer, Cham (2021). https://doi.org/10.1007/978-3-030-68014-5_6
13. Tamminen, S., et al.: From measurements to knowledge - online quality monitoring and smart manufacturing. In: Perner, P. (ed.) *ICDM 2018. LNCS (LNAI)*, vol. 10933, pp. 17–28. Springer, Cham (2018). https://doi.org/10.1007/978-3-319-95786-9_2
14. Singer, G., Yuval Cohen, Y.: A framework for smart control using machine-learning modeling for processes with closed-loop control in Industry 4.0. *Eng. Appl. Artif. Intell.* **102** (2021). <https://doi.org/10.1016/j.engappai.2021.104236>
15. Karaoglan, A., Bayhan, G.: A regression control chart for autocorrelated processes. *Int. J. Ind. Syst. Eng.* **16**(2), 238–256 (2014). <https://doi.org/10.1504/IJISE.2014.058838>
16. Muller, T., Pillet, M., Maire, J.L., Pillet, D.: Why and how to move from SPC (statistical process control) to APC (automated process control). In: Aifaoui, N., et al. (eds.) *CMSM 2019. LNME*, pp. 33–40. Springer, Cham (2020). https://doi.org/10.1007/978-3-030-27146-6_4



Qualimetric Model for Assessing the State of the Central Nervous System of Animals When Studying the Mechanism of Biological Activity for Mineral Waters

Alona Kysylevska^{1,2} , Konstantin Babov² ,
Sergey Gushcha² , Ihor Prokopovych¹ ,
and Tatiana Bezverkhniuk² 

¹ Odessa Polytechnic State University,

1, Shevchenko Avenue, Odessa 65044, Ukraine

² State Institute «Ukrainian Scientific-Research Institute of Medical Rehabilitation and Balneology of The Ministry of Health of Ukraine»,
6, Lermontovsky Lane, Odessa 65014, Ukraine

Abstract. The article developed a qualimetric method for assessing the state of the animals' central nervous system when studying the biological activity of mineral waters to identify them as mineral (and their further industrial packaging) or medicinal. The current «open field» method does not cover all behavioral and vegetative reactions of animals; this can lead to an incorrect interpretation of the research results and the studied mineral water classification as biologically active. A qualimetric method is proposed, in which single indicators of the state of the central nervous system of animals are assessed using 17 criteria developed by experts, and a complex indicator is the arithmetic weighted average of single indicators, which allows one to determine the level of biological activity of mineral waters quantitatively. The difference in the interpretation of the results for the study of mineral water's biological activity of well No. 1, located in the village of Dovge, Lviv region, of the existing and developed methods is shown. In the first case, the effect of water was assessed as intensely soothing. In the second case, a moderate change in behavioral responses was observed. In comparison with the current one, the qualimetric method allows a more differentiated approach to the description of changes in the dynamics of animals' behavioral reactions when studying the biological activity of mineral waters and assessing the possibilities of their industrial packaging.

Keywords: Natural mineral waters · Biological activity · Central nervous system · Qualimetric method

1 Introduction

Ukraine is now in the process of reforming the national technical regulation system. Concerning mineral waters, legal and regulatory requirements are harmonized with European [1].

Mineral waters (MW) are used for therapeutic and prophylactic purposes for many diseases – the musculoskeletal system [2], in particular, to improve bone metabolism [3], in diseases of the gastrointestinal tract [4, 5], with functional disorders of the biliary tract [6], with cardiovascular diseases [7, 8] – reduce biomarkers of cardiometabolic risk [9], in metabolic diseases [10, 11] and peripheral nervous system) [12]. Compared to synthetic drugs, MW rarely shows side effects with treatment [13], etc.

In Ukraine, for the practical use of MW following with Order of Ministry of Public Health of Ukraine from 02.06.2003, 243, studies of their physicochemical properties, harmlessness, orientation, and nature of the biological activity (BA) should be preceded, that is, full-fledged preclinical studies in an experiment on animals. According to the Order of Ministry of Public Health of Ukraine from 28.09.2009, № 692, a set of indicators is used that characterize the response to the impact of the morpho-functional structures of organs and tissues, the response from the immune system, and individual links of metabolism. It makes it possible to expand the range of the obtained BA characteristics of new MW sources and to provide a scientific basis for recommendations for their further testing or to justify the absence of BA.

According to Order from 02.06.2003, 243, during physiological studies in the study of the functional state (FS) of the central and autonomic nervous systems, the behavioral responses of animals (white rats) to the effect of MW are assessed by the «open field» method, which is considered a stress stimulus for animals. At the same time, their emotional, motor, and orientation-research activity is assessed. However, when interpreting the data obtained using this method, not all indicators characterizing the features of the functional state of the central nervous system (CNS) and vegetative reactions of animals are taken into account.

2 Literature Review

MW contains a set of cations and anions of different quality and quantities. The intake of these components into the body directly affects the state of biochemical reactions and, indirectly, through the autonomic nervous system's activity, on the of the body's functional systems [2]. It is due to the influence on the hypothalamic-pituitary-adrenal axis, the level of adrenocorticotrophic, cortisol, and adrenaline, which changes the protective and adaptive mechanisms' activity in the body [14, 15].

When using MW, attention is paid to the elemental composition of salts and the small number of microelements that, in combination, can carry BA on the body, since they are in a perfect form for absorption, they do not affect independently, but in combination with a complex of basic MW salts as a single bioactive complex [15, 16].

In the European Union, the assessment of BA of MW is carried out by analogy with its chemical composition and the assessing the implementation of one or more homeostasis indicators [16]. But our long-term experience allows us to believe that the

assessment of BA of any MW should be carried out based on a study of the complex implementation of the main functional systems of the body to identify the features of target organs and mechanisms of BA of MW action [17].

The study of MW concerning their effect on the FS of the CNS and ANS is carried out according to Order from 28.09.2009, 692 in two aspects of MW study: confirmation of its safety during use and to determine the degree of BA, the nature and features of which allow predicting the presence of medicinal properties MW, including for the treatment of neurological pathology. There is evidence that MW can correct (together with other treatment complexes) the state of psychoemotional overstrain and dysadaptation in persons with the consequences of psychological trauma and social disorders. The state of activity of the central nervous system, which is assessed by changes in orienting-exploratory behavior (OEB), motor activity, and the level of the emotional state of animals, is studied using the “open field” method. Features of rats’ behavior in the “open field” is a predictive criterion for the central nervous system’s state [18]. The test is traditionally used to analyze the effects of new compounds on behavioral responses and complexly coordinated motor activity in rodents; it is quite popular because of its simplicity and adequacy [19]. The open field model can be used for understanding the basic neural mechanisms of anxiety responses [20]. Placing animals in a new environment leads to the emergence of research motivation, accompanied by the formation of passive-protective behavior.

A characteristic manifestation of this condition is the vegetative reaction of animals in the form of defecation (bolus) and urination and a change in the level of motor activity. Grooming (cosmetic behavior of animals) is an essential characteristic of rats’ behavior and belongs to the category of comfort. But in the case of short-term grooming and its increased amount, this indicates that the animals are in a state of anxiety [21].

Behavioral indicators are:

- physical activity (number of squares crossed) (according to Order from 28.09.2009, 692 and [22], the norm is (32.1 ± 1.73) crossed squares in 3 min);
- exits to the center;
- vertical stands (norm 18.2 ± 1.1) in 3 min;
- “mink reflex” (norm 13.2 ± 1.0) in 3 min;
- defecation and diuresis;
- duration of grooming and fading, expressed in seconds.

Defecation and running are considered as values associated with the manifestation of emotionality in rodents.

But according to Order from 28.09.2009, 692 and [22], this technique does not describe all behavioral reactions of animals and cardiovascular dysfunction [23]. So it is necessary to develop a complex of behavioral responses that will cover various types of activity and a method for assessing the state of the central nervous system and ANS.

Qualimetry, the science of measuring and quantifying the quality of various objects and processes, can cope with this task in the best way [22, 24]. The purpose of qualimetry is to express the quality of any product with several parameters, with a single digit, which can be used to rank products for a similar purpose [25, 26].

From all the methods for assessing quality (instrumental, calculated, statistical, organoleptic, expert, and sociological) [27, 28], we have chosen the expert method to solve our problem [29].

The individual qualities of an expert depending on his knowledge, experience, intelligence, and other factors. When interviewing experts, certain limitations may arise that will lead to errors in assessing events. The use of statistical methods expands the possibility of using experts' information [30]. The disadvantages of these methods include their inherent subjectivity. When compiling the list of experts, their competence in a particular field should be taken into account.

Assessment of product quality level can be determined by differential, complex and mixed methods [26].

Therefore, the purpose of this work is to develop a qualimetric method for assessing the FS of the central nervous system of animals by the «open field» method when studying BA of MW.

3 Research Methodology

At the first stage of the work, studies of BA of MW were carried out in an experiment using white rats – the FS of the central nervous system of animals was assessed by the «open field» method according to the approved method. We used 40 rats weighing 180–200 g (20 were intact animals, 20 were healthy animals that received a course of MW administration). According to Order from 28.09.2009, 692, MW was injected into the stomach of rats using a probe (1% of the rat body weight) once a day for six days. «Open field» – a rectangular chamber 80 × 80 sm with plastic walls 40 sm high. The floor is a sheet of white plastic, on which a lattice is applied in black paint, dividing the field into 16 equal squares. There are caves in the middle of each square. The rats were placed in a lighted chamber, set in a corner and oriented toward the center, and allowed to move across the field for 6 min. The behavior of the rats was determined by a researcher who was sitting close to the camera. Evaluated: the number of exits to the center, the number, and duration of stops, the number of squares crossed, the number of racks, the number and time of grooming, boluses, and urinations.

Statistical data processing was carried out according to [31]. Significant changes were considered those in which the Student's coefficient was <0.05.

The selection of experts took into account the limited number of experts available in this area. The formation of a group of experts was carried out among specialists with professional knowledge in higher professional education. The group must include at least five and no more than ten people [29] (7 selected). The qualitative composition of the expert group was determined by calculating competence.

Each expert was assigned a specific set of evaluation criteria on a point scale (Table 1). The sum of points for all criteria was calculated for each expert C_i ($i = 1, 2, 3, \dots, N$, N is the number of experts). For each expert, the relative C_i^* value was determined. The range of permissible values of the parameter $q_{min} \leq q \leq Q_{max}$ was set, depending on the order of the estimated numerical characteristic and the absolute acceptable error. According to [30], the following values are proposed for q :

$0.05 \leq 0.30$. Moreover, the smaller q , the more competent the expert is. For each expert, the parameter q was calculated for the membership function:

$$q_i = q_{\max} - \frac{(q_{\max} - q_{\min})}{C_{\max}^*} \cdot C_i^* \tag{1}$$

The quality level was assessed using an integrated method based on comparing complex quality indicators and a baseline indicator:

$$U_{\kappa} = \frac{qk_i - qk_6}{qk_6}, \tag{2}$$

where qki , qkb are single estimates of the i -th indicator of the sample, which is being evaluated, and the base one [26].

4 Results

In the study, we used MW of well No. 1 of the village of Dovege, Lviv region, a medicinal low-mineralized hydrocarbonate-chloride calcium-sodium hydrochloric acid with increased content of organic substances. Table 1 shows the data demonstrating the influence of the MW of well No. 1 of Dovege on animals’ behavioral reactions and emotional state.

Table 1. Influence of MW of well No. 1 of Dovege in the course of ingestion on the FS of the CNS and the emotional state of rats, ($M \pm m$)*

Indicators	Control	Experience (course of the MW)	D**	P***
	($M_1 \pm m_1$)	($M_2 \pm m_2$)		
Number of exits to the center, n	2,50 ± 0,23	1,04 ± 0,07	- 1,46	< 0,001
Stops, n	1,75 ± 0,24	1,66 ± 0,05	- 0,09	> 0,5
Stops, s	74,58 ± 4,54	192,34 ± 2,72	+ 117,76	< 0,001
Number of squares crossed, n	66,41 ± 2,72	35,29 ± 0,69	- 31,12	< 0,001
Number of racks, n	9,36 ± 0,35	6,99 ± 0,38	- 2,37	< 0,001
Number of burrowing visits, n	12,91 ± 0,46	6,16 ± 0,27	- 6,75	< 0,001
Grooming, n	2,31 ± 0,37	1,56 ± 0,04	- 0,75	> 0,05
Grooming, s	28,37 ± 1,64	15,92 ± 1,09	- 12,45	< 0,001
The number of acts of defecation, n	3,80 ± 0,09	2,78 ± 0,10	- 1,02	< 0,001
Number of urination acts, n	5,10 ± 0,40	2,68 ± 0,15	- 2,42	< 0,001

* - ($M_1 \pm m_1$) и ($M_2 \pm m_2$) – arithmetic means with an error of indicators; ** D – the difference in indicators; *** – P – probability of comparison between.

In rats that consumed MW well No. 1 of Dovege, the number of exits to the center decreases, and the duration of stops increases while their number remains unchanged. The number of crossed squares, uprights, and peeking into burrows was significantly reduced, which indicates a weakening of the exploratory behavior. The following changes characterize the state of vigorous activity in rats: the number of grooming acts does not change with a decrease in their total duration. The number of bowel movements and urination decreases. Based on the results obtained, the researchers concluded that the of the MW' influence of well No. 1 of Dovege with ingestion on the FS of the central nervous system could be characterized as a pronounced sedative. This interpretation of the research results contains the subjective assessment of the researcher, who concludes.

The results of assessing the competence of experts are presented in Table 2.

Table 2. Calculation of the competence of experts.

Criterion	Assessment scale	Experts						
		№ 1	№ 2	№ 3	№ 4	№ 5	№ 6	№ 7
The level of education	Doctor of Science – 5 Ph.D. – 4 Researcher – 2 Laboratory assistant – 1	5	4	4	2	2	1	1
Work experience in the field	Up to 10 years – 1 10–20 years – 2 20–30 years – 3 30 years and more – 5	5	5	3	3	2	1	1
Work experience in the field	Participated – 3 Did not participate – 0	3	3	0	3	0	0	0
Calculated part								
C_{\max}	–	13	–	–	–	–		
C_i (sum of points)	–	13	12	7	8	4	2	2
C_i^*	–	1,00	0,92	0,53	0,62	0,31	0,15	0,15
q_i	–	0,05	0,07	0,167	0,145	0,222	0,263	0,263

As can be seen from Table 2, the most competent expert received the value $q = 0.05$, the least competent expert – $q = 0.263$. Considering that the minimum group should consist of at least five, it was decided to exclude the two least competent experts.

For a comprehensive characterization of quality in qualimetry, a multilevel structure of indicators (a hierarchical «quality tree») is used. When constructing it, the complex quality is decomposed into a set of simple, single indicators using a multilevel decomposition of each more complex property into a group of less complex ones [29]. To build a «quality tree», the experts used the «brainstorming» method [29] (Fig. 1).

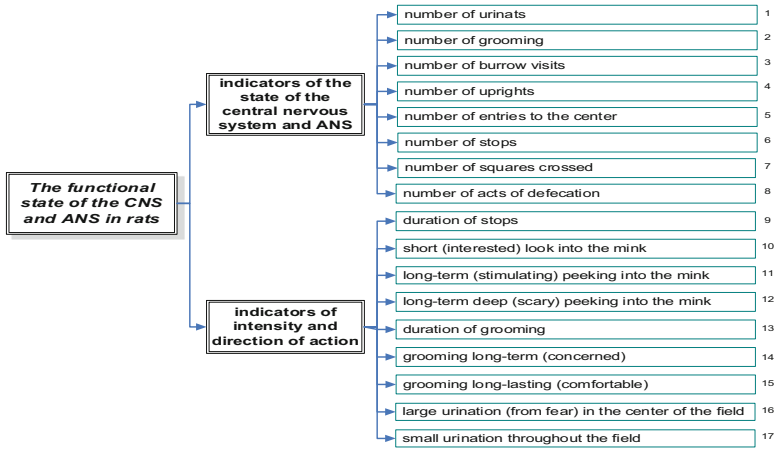


Fig. 1. «Quality tree» for assessing the FS of the CNS and ANS of animals.

According to the assessment of individual indicators, all experts agreed that the ranking method is not suitable for this case. All indicators are weighty; that is, the formula for a complex indicator should be in the form of weighted average arithmetic. The indices of the FS of the central nervous system and the ANS have numerical values, are equally expressed. Indicators of the intensity and direction of changes in the central nervous system and ANS have different expressions of individual indicators (number and duration); therefore, formalization of indicators is necessary.

Considering that when assessing the FS of the CNS and ANS, the changes between the controlled animals' behavioral reactions and the subjects are set, the experts proposed values for each of the 17 obtained indicators, expressed in points from 0 to 3 (Table 3).

Table 3. Scoring of single indices of FS of the central nervous system and ANS of animals.

Nb*	Intervals/Points			Nb*	Intervals/Points		
1	(0 - 2) = 1	(3 - 5) = 2	(6 - 10) = 3	10	(0 - 5) = 1	(6 - 12) = 2	(13 - 20) = 3
2	(0 - 2) = 1	(3 - 5) = 2	(6 - 10) = 3	11	(0 - 5) = 1	(6 - 12) = 2	(13 - 20) = 3
3	(0 - 5) = 1	(6 - 12) = 2	(13 - 20) = 3	12	(0 - 5) = 1	(6 - 12) = 2	(13 - 20) = 3
4	(0 - 5) = 1	(6 - 12) = 2	(13 - 20) = 3	13	(0 - 30) = 1	(31 - 60) = 2	(61 - 100) = 3
5	(0 - 3) = 1	(4 - 7) = 2	(9 - 12) = 3	14	(0 - 2) = 1	(3 - 5) = 2	(6 - 10) = 3
6	(0 - 2) = 1	(3 - 5) = 2	(6 - 10) = 3	15	(0 - 2) = 1	(3 - 5) = 2	(6 - 10) = 3
7	(0 - 30) = 1	(31 - 60) = 2	(61 - 100) = 3	16	(0 - 2) = 1	(3 - 5) = 2	(6 - 10) = 3
8	(0 - 2) = 1	(3 - 5) = 2	(6 - 10) = 3	17	(0 - 2) = 1	(3 - 5) = 2	(6 - 10) = 3
9	(0 - 50) = 1	(51 - 100) = 2	(101 - 200) = 3	-	-	-	-

To formalize the change in the dynamics of the state of animals' behavior, we applied scaling. The Harrington psychophysical desirability scale and its numerical intervals are best suited for our case [32]; therefore, the following criteria are proposed

for making decisions on assessing the functional state (FS) of the central nervous system and ANS of animals: <20% – very poorly expressed a change in behavioral indicators; (20–<37)% – moderately expressed; (37–<63)% – expressed; (63–<80)% – strongly pronounced; (80–100)% – very pronounced.

Estimating the MW of well No. 1 of Dovege using the developed qualimetric method, the following results were obtained (Table 4, Fig. 2).

Table 4. Scoring of single indices of FS of the central nervous system and ANS of animals in the study of the biological action of the MW of well No. 1 of Dovege.

№ *	Scores		№ *	Scores		№ *	Scores	
	Control	Experience		Control	Experience		Control	Experience
1	1	2	7	2	3	13	1	2
2	1	1	8	1	2	14	1	2
3	2	3	9	3	2	15	1	2
4	2	2	10	1	2	16	1	2
5	1	1	11	1	2	17	1	2
6	1	1	12	1	2	Total:	22	33

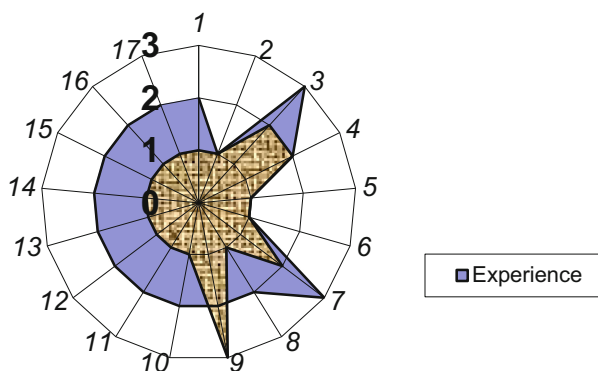


Fig. 2. Cyclogram of assessing the FS of the central nervous system and ANS of animals in studying the biological effect of the MW of well No. 1 of Dovege.

When calculating the percentage of changes in behavioral reactions of animals, 33% were obtained. According to the criteria of the qualimetric method in animals under the influence of MW well. No. 1 of Dovege, moderate changes in behavioral and autonomic reactions occur. This result is somewhat different from the pronounced calming effect obtained when using the current method. It should be noted that these data require additional interpretation by clinicians and rehabilitologists to assess the therapeutic potential of specific MW and its further clinical trials.

5 Conclusions

The work developed a qualimetric method for assessing the functional state of the central nervous system of animals by the «open field» method in the study of the biological action of mineral waters.

Compared with the current method, it allows a more differentiated approach to the description of changes in the dynamics of animals' behavioral reactions when studying the biological action of mineral waters.

Application of this method in a comprehensive preclinical study of mineral waters will make it possible to scientifically substantiate and develop differentiated recommendations for further clinical testing to clarify their effectiveness and harmlessness and assess their industrial packaging possibilities.

References

1. Kysylevska, A., Prokopovich, I., Oborskyi, G., Babov, K., Arabadji, M.: Harmonization of the EU and Ukrainian normative documentation: case study on determination of barium content in mineral waters to develop quality and safety criteria. In: Tonkonogyi, V., et al. (eds.) *InterPartner* 2019. LNME, pp. 157–167. Springer, Cham (2020). https://doi.org/10.1007/978-3-030-40724-7_16
2. Morer, C., Roques, C.-F., Françon, A., Forestier, R., Maraver, F.: The role of mineral elements and other chemical compounds used in balneology: data from double-blind randomized clinical trials. *Int. J. Biometeorol.* **61**(12), 2159–2173 (2017). <https://doi.org/10.1007/s00484-017-1421-2>
3. Wynn, E., Krieg, M.A., Aeschlimann, J.M., Burckhardt, P.: Alkaline mineral water lowers bone resorption even in calcium sufficiency: alkaline mineral water and bone metabolism. *Bone* **44**(1), 120–124 (2009). <https://doi.org/10.1016/j.bone.2008.09.007>
4. Costantino, M., Izzo, V., Conti, V., Manzo, V., Guida, A., Filippelli, A.: Sulphate mineral waters: a medical resource in several disorders. *J. Tradit. Complement. Med.* **10**(4), 320–326 (2020)
5. Quattrini, S., Pampaloni, B., Brandi, M.L.: Natural mineral waters: chemical characteristics and health effects. *Clin. Cases Min. Bone Metab.* **13**(3), 173–180 (2016)
6. Mennuni, G., et al.: The therapeutic activity of sulphate-bicarbonate-calcium-magnesiatic mineral water in the functional disorders of the biliary tract. *Clin Ter.* **165**(5), e346–e352 (2014). <https://doi.org/10.7417/CT.2014.1761>. PMID: 25366951
7. Di Marco, M., De Novellis, A.M.P., Carluccio, V., Bozzelli, R., Orlando, M., Lanuti, P.: Short- and long-term beneficial effects of medicinal mineral water administration. *Environ. Geochem. Health* **42**(2), 353–364 (2019). <https://doi.org/10.1007/s10653-019-00290-x>
8. Bastos, P., Araújo, J.R., Azevedo, I., Martins, M.J., Ribeiro, L.: Effect of a natural mineral-rich water on catechol-O-methyltransferase function. *Magnes Res.* **27**(3), 131–141 (2014). <https://doi.org/10.1684/mrh.2014.0369>. PMID: 25560240
9. Toxqui, L., Vaquero, M.P.: An intervention with mineral water decreases cardiometabolic risk biomarkers. A crossover, randomised, controlled trial with two mineral waters in moderately hypercholesterolaemic adults. *Nutrients* **8**(7), 400 (2016). <https://doi.org/10.3390/nu8070400>. PMID: 27367723; PMCID: PMC4963876

10. Naumann, J., Biehler, D., Lüty, T., Sadaghiani, C.: Prevention and therapy of type 2 diabetes-what is the potential of daily water intake and its mineral nutrients? *Nutrients* **9**(8), 914 (2017). <https://doi.org/10.3390/nu9080914>. PMID:28829398;PMCID:PMC5579707
11. Costa-Vieira, D., Monteiro, R., Martins, M.J.: Metabolic syndrome features: is there a modulation role by mineral water consumption? A review. *Nutrients* **11**(5), 1141 (2019). <https://doi.org/10.3390/nu11051141>
12. Petracchia, L., et al.: Water, mineral waters and health. *Clin. Nutr.* **25**(3), 377–85 (2006)
13. Ziemska, J., Szynal, T., Mazańska, M., Solecka, J.: Natural medicinal resources and their therapeutic applications. *Rocz Panstw Zakl Hig.* **70**(4), 407–413 (2019). <https://doi.org/10.32394/rpzh/2019.0093>. PMID: 31961104
14. Gushcha, S.G., et al.: Comprehensive assessment of functional changes in the organism of healthy rats in external and internal use of silicone malomineralized mineral water. *Eur. J. Clin. Biomed. Sci.* **4**(1), 1–5 (2018)
15. Hall, J.E., Hall, M.E.: *Guyton and Hall Textbook of Medical Physiology*, 14th edn. Elsevier, Amsterdam (2021)
16. Albertini, M., Dacha, M., Teodori, L., Conti, M.: Drinking mineral waters: biochemical effects and health implications – the state-of-the-art. *Int. J. Environ. Health* **1**(1), 153–169 (2007)
17. Kysylevska, A., Babov, K., Gushcha, S., Prokopovich, I., Nasibullin, B.: Using the specific molarity indicator of the chemical parameters of mineral waters in assessing their biological effects. In: Tonkonogyi, V., et al. (eds.) *InterPartner 2020. LNME*, pp. 823–832. Springer, Cham (2021). https://doi.org/10.1007/978-3-030-68014-5_80
18. Prut, L., Belzung, C.: The open field as a paradigm to measure the effects of drugs on anxiety-like behaviors: a review. *Eur. J. Pharmacol.* **463**, 3–33 (2003)
19. Tatem, K.S., Quinn, J.L., Phadke, A., Yu, Q., Gordish-Dressman, H., Nagaraju, K.: Behavioral and locomotor measurements using an open field activity monitoring system for skeletal muscle diseases. *J. Vis. Exp.* (91), 51785 (2014). <https://doi.org/10.3791/51785>
20. Ennaceur, A., Michalikova, S., Chazot, P.L.: Models of anxiety: responses of rats to novelty in an open space and an enclosed space. *Behav Brain Res.* **171**(1), 26–49 (2006). <https://doi.org/10.1016/j.bbr.2006.03.016>. Epub 2006 May 4 PMID: 16678277
21. Salum, C., Morato, S., Roque-da-Silva, A.C.: Anxiety-like behavior in rats: a computational model. *Neural Netw.* **13**(1), 21–29 (2020). [https://doi.org/10.1016/S0893-6080\(99\)00099-4](https://doi.org/10.1016/S0893-6080(99)00099-4)
22. Lobanov, A.S.: The present and future of qualimetry as a scientific discipline. *Sci. Tech. Inf. Process.* **41**(1), 57–65 (2014). <https://doi.org/10.3103/S0147688214010122>
23. Finnell, J.E., et al.: Physical versus psychological social stress in male rats reveals distinct cardiovascular, inflammatory and behavioral consequences. *PLoS ONE* **12**(2), e0172868 (2017). <https://doi.org/10.1371/journal.pone.0172868>
24. Poltavskiy, A.V., et al.: Decision making concept to create complex technical systems. *Reliab. Qual. Complex Syst.* **14**, 74–84 (2016)
25. Azgaldov, G.G., Kostin, A.V.: Applied qualimetry: its origins, errors and misconceptions. *Benchmarking* **18**(3), 428–444 (2011). <https://doi.org/10.1108/14635771111137796>
26. Azgaldov, G.G., Kostin, A.V., Padilla, A.: *The ABC of Qualimetry: Toolkit for measuring the immeasurable*. Ridero (2015)
27. Gossen, E., Kuske, P., Abele, E.: Quantification and assessment method for a company’s product piracy risks. *Procedia CIRP* **28**, 185–190 (2015). <https://doi.org/10.1016/j.procir.2015.04.032>
28. Maletič, D., et al.: The role of maintenance regarding improving product quality and company’s profitability: a case study. *IFAC Proc. Vol.* **4**(31), 7–12 (2012). <https://doi.org/10.3182/20121122-2-es-4026.00040>

29. Razumov-Razdolov, K.L., Protasyev, V.B.: Expert-modeling method for forming scores of activity criteria quality. *Innov. Educ.* **12**(91), 72–78 (2012)
30. European Assessor Training Modulus (Assessed version). EFQM Publication (2003)
31. McDonald, J.H.: *Handbook of Biological Statistics*, 3rd edn. Sparky House Publishing, Baltimore (2014)
32. Trautmann, H., Weihs, C.: On the distribution of the desirability index using Harrington's desirability function. *Metrika* **63**, 207–213 (2006). <https://doi.org/10.1007/s00184-005-0012-0>



Problems and Prospects of Cryptocurrency Development

Alexander Masharsky^(✉)  and Ivan Skvortsov 

Baltic International Academy, 4, Lomonosova Street, Riga 1003, Latvia
info@bsa.edu.lv

Abstract. The article is devoted to the prospects for the integration of cryptocurrencies into the national and world economy. The views of various researchers on the essence of cryptocurrency, its strengths and weaknesses are systematized, the impact of differences in state regulation of cryptocurrency circulation on the nature of its use and the risks of money laundering is assessed, the factors that complicate the implementation of the main functions of money are identified. It has been revealed that in a broad sense, cryptocurrency is a new transaction technology that embodies the properties of money, goods, property, and financial assets but does not fully correspond to any of them. A cross-country analysis of the impact of changes in the economic and political situation on cryptocurrency and financial assets has confirmed a growing interest in investing in cryptocurrency, including institutional investors, which opens up the opportunity to become not just a speculative but also a protective investment asset. Taking into account the identified trends in government regulation of cryptocurrencies creates new opportunities for economic growth.

Keywords: Bitcoin · Blockchain · Electronic money · State regulation · Money laundering · Investment

1 Introduction

The relevance of the research topic is determined by the growing popularity of cryptocurrencies and the ambiguous attitude towards them on the part of investors and the state.

Despite the increasingly broad use of cryptocurrencies to pay for goods and services, as well as an investment assets, the economic essence of this phenomenon remains discussable.

Also, there is no unified approach to defining the role of cryptocurrency in the global financial system and state regulation of cryptocurrency circulations and evaluating the opportunities and threats it creates for the development of the global and national economies and the stability of international financial markets.

The paper aims to define the role, trends, and prospects of the development of cryptocurrency in the global financial system. To achieve it, the following tasks are set:

- To systematize and to precise views on the nature and role of cryptocurrencies.

- To identify the advantages, disadvantages, and risks of using cryptocurrencies for investors and national as well as international financial markets.
- To assess the prospects for using cryptocurrency as a means of payment and as an investment asset.

2 Literature Review

There is a significant difference in the views of different authors on the content and essence of cryptocurrencies. Table 1 reflects the systems of theoretical views of various researchers on the main aspects of the emergence and development of cryptocurrencies.

Table 1. Systems of theoretical views of different authors on the content and essence of cryptocurrencies

Author(s)	Definition	Economic essence
P. Vigna, M. Casey	Currency is a digital unit of value used by people to exchange goods, services, or in exchange for other currencies that tend to fluctuate widely relative to traditional government-issued currencies [1]	Similarity to fiduciary money, based on the concept of Chartalism, according to which the value of money is determined by social agreement, regardless of their material embodiment
L. Leloup	Unlike other currencies, a currency is not the embodiment of a government agency, bank, or company, and each bitcoin is identified in the ledger using the history of all transactions in which it has been involved from the moment of its creation [2]	Not defined
A. Tepper	Open protocol of a decentralized payment system [3]	Currency, and thus money
A. Tapscott, D. Tapscott	An alternative means of payment that does not require the services of third parties to establish trust between the parties of the transaction [4]	An alternative to the traditional banking system

The authors believe that cryptocurrency is a contractual means of payment that has value only to the extent that members of a particular community recognize it. Thus, the main functions of money can be sufficiently manifested in a certain virtual currency only when the scope of participants in this community is wide enough.

Numerous researchers point to two factors that hinder the performance of the main functions of money by cryptocurrency - the uncertainty of the legal status and extremely high volatility. The second factor is largely a consequence of the first one.

The results of a SWOT analysis of the theoretical views of various researchers on the impact of cryptocurrency development on the financial system and the external environment are given in Table 2.

Table 2. The results of a SWOT analysis of the theoretical bases of the development of cryptocurrencies

Strengths	Weaknesses	Opportunities	Threats
1) Low fees for transfers 2) High fault-tolerance 3) Trust, guaranteed by the network protocol	1) High volatility 2) Theoretical probability of attack - 51% 3) Negative reputation 4) Incomplete protection of operators from state restrictions	1) Involvement of people without access to banking services in the global financial system 2) Creation of new working places in the IT sector 3) Use of smart contracts and derivatives thereof for raising investments and activities in other areas	1) Use of cryptocurrencies for illegal activities 2) Job cuts in the financial sector 3) The carbon footprint, created by the infrastructure and, as a result, a contribution to global warming 4) Unproductive use of electricity

It should be noted that the overwhelming majority of researchers also characterize to the advantages of cryptocurrency the decentralized model of its construction and the ability to create a payment system based on blockchain technology, completely independent of state control.

At the same time, they overlook the fact that such a decentralized system is implemented through the global computer network Internet, which is ensured by Internet providers, whose activities are regulated by the state in most countries.

Digital money has numerous advantages, but there is also the possibility of using cryptocurrency for illegal activities. At the same time, this probability is not higher than cash, providing the required level of anonymity.

Practice shows that the situation with money laundering in the country is largely determined not by the rigidity of regulation but by geographical, historical, and institutional factors [5].

3 Research Methodology

The theoretical basis of the study is the following:

- Theories on the nature of money and its payment and savings functions;
- Portfolio theory of investment on asset diversification as a method of risk mitigation;
- Theories of financial markets on the main factors of development - supply and demand for financial services, the composition and level of risks, the level of competition and the development of new technologies, government regulation, economic cycles, and crises.

The methods of logical and statistical analysis, generalization and classification, cross-country comparisons, induction, abstraction, mathematical and expert assessment have been used in the study.

The analysis of the nature and prospects for the development of cryptocurrency is carried out based on:

- Systematization and generalization of theoretical views on the main characteristics of cryptocurrency and its advantages and disadvantages;
- Assessment of the results of opinion polls of the residents of different countries on their attitude to cryptocurrency;
- Statistical data on the trends and factors of dynamics and interrelation of bitcoin market prices with major currencies and classic protective and speculative assets in the conditions of global economic crisis, caused by the COVID-19 pandemic in early 2020;
- Cross-country analysis of the differences in approaches to the regulation of the cryptocurrency market.

4 Results

The analysis of the approaches to state regulation of cryptocurrency circulation, the data from opinion polls of the residents of different countries on their attitude to cryptocurrency, as well as statistical data on the development of the COVID-19 pandemic and the market prices of bitcoin, major currencies and financial assets enabled to reveal the trends and factors and to assess the prospects for the development of cryptocurrency.

4.1 Regulation of Cryptocurrency Turnover

The difference in the approaches to state regulation of cryptocurrencies' circulation is caused by the difference in evaluating the opportunities and threats it creates for developing the global and national economies and the stability of international financial markets.

The analysis of the existing approaches to the regulation of cryptocurrencies' circulation shows that some jurisdictions allow the use of cryptocurrencies as a means of payment (Venezuela, Japan), while in others, they are completely prohibited (Bangladesh, Ecuador) or significantly limited (Lithuania, China, Vietnam, India, Italy, Iran, etc.) [6].

Most countries are still "observing" this phenomenon, determining the balance between the potential for digital technology development and the risks pertaining to the weakening of state control.

There is no clear policy of legal regulation of cryptocurrencies' circulation in the EU. Cryptocurrencies are mentioned mainly in the directives pertaining to money laundering and terrorist financing, which does not stimulate the use of their positive opportunities [7].

In countries with greater opportunities for citizens to influence government decisions and greater availability of electricity, there is greater predictability of financial regulators regarding the free circulation of cryptocurrencies [8].

4.2 Cryptocurrencies in the Global Financial System

The results of sociological surveys conducted in the USA and the EU indicate that the interest of residents of these regions in cryptocurrency is growing [9]. There are also trends in the growth of public confidence in cryptocurrency and the development of interest in it from small and medium-sized businesses [10]. The observed increase in volatility driven by the growth in the number of cryptocurrency acceptance venues is further evidence of its growing acceptance by market participants [11].

The volume of money transfers between cryptocurrency users is also steadily growing. As of May 2020, 19,350 business entities worldwide, including 44 in the territory of Latvia, voluntarily and publicly announced the acceptance of payments in cryptocurrency [12].

In some countries (for example, the USA), cryptocurrency is recognized as an investment product at the level of state regulation. The start of trading futures contracts on Bitcont (CME: BTC, CBOE: XBT) in December 2017 indicates the institutionalization of cryptocurrency on the leading trading platforms Chicago Mercant Exchange (CME) and Chicago Board Option Exchange (CBOE). Cryptocurrency quotes started to be published on the front pages of leading financial portals such as Bloomberg [13] and Yahoo Finance [14].

Thus, in the activities related to cryptocurrencies, development trends are being observed.

The possibilities of using cryptocurrency as an investment asset for the period 2019–2020 were significantly affected by the COVID-19 pandemic. At the beginning of 2020, it moved from a state of moderate growth, close to a recession, to a state of global economic crisis.

Figure 1 shows the dynamics of the development of the pandemic, measured by the number of newly diagnosed cases of COVID-19 disease worldwide, as well as the dynamics of the bitcoin cryptocurrency rate from January 22, 2020, to January 22, 2021.

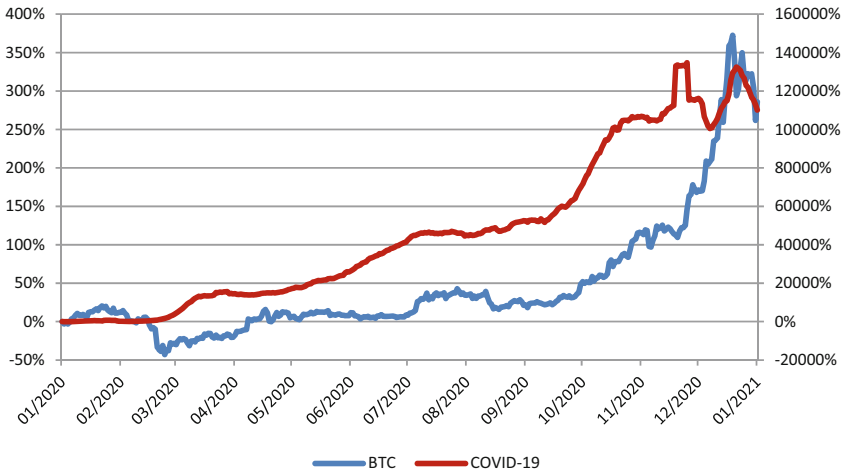


Fig. 1. Dynamics of detected cases of COVID-19 and bitcoin rate, 2020–2021

The left Y-axis of the graph (Fig. 1) reflects the rise in the bitcoin rate, while the right axis increases the incidence of COVID-19. The graph data (Fig. 1) indicate the presence of a positive correlation between the studied data. The authors believe that this may be due to investors’ growing interest in cryptocurrencies as a protective asset amid the economic crisis caused by the COVID-19 pandemic.

The first phase of growth in the bitcoin rate in 2020 (March - June) coincides in time with the first wave of the pandemic. This is followed by a certain period of consolidation (July - September) and the beginning of intensive growth, which coincides in time with the second wave of the pandemic.



Fig. 2. Dynamics of bitcoin, euro, and pound sterling rates, 2019–2020

A comparison of bitcoin and leading world currency rates over a wider time interval to test this assumption is presented in Fig. 2.

The nature of the bitcoin rate dynamics indicates that before the onset of the crisis, it could be used as a defensive asset to hedge the currency risk for the euro and pound. However, with the onset of the pandemic, especially its second wave, the situation changed dramatically.

The results obtained indicate a low correlation between the bitcoin rate and the leading world currencies during the period of moderate growth of the world economy (2019 - early 2020). It can be explained by the difference in factors affecting the dynamics of the exchange rate of traditional national currencies and cryptocurrencies. In the case of traditional national currencies, these are the economic indicators of the issuing country, the actions of national banks and other financial institutions, and geopolitical factors (the latter is especially characteristic of the British pound). In cryptocurrencies, the main factors determining the exchange rate dynamics are the speculative expectations of market participants and the technical aspects of using a particular cryptocurrency.

The dynamics of the bitcoin rate concerning the Japanese yen deserves special attention (Fig. 3).

Figure 3 shows the dynamics of the bitcoin rate to the national currency of Japan, where, unlike most other countries, bitcoin is a legal mode of payment.

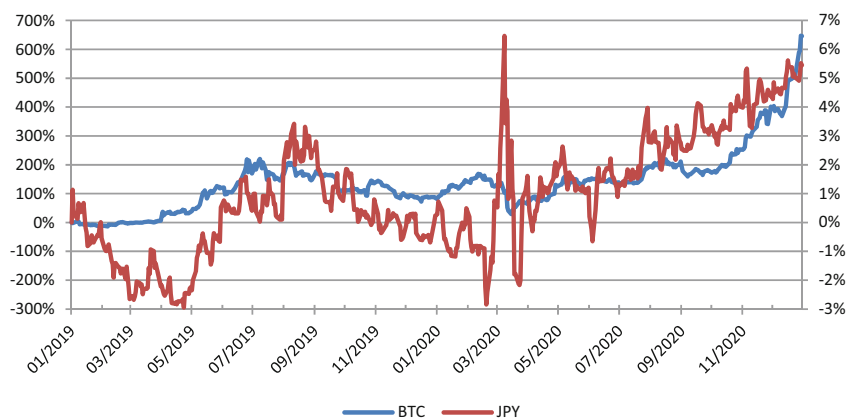


Fig. 3. Dynamics of bitcoin and Japanese yen rates, 2019–2020

The graph data (Fig. 3) indicate a stable positive correlation between the considered financial instruments, which may be because, in Japan, unlike most other countries, bitcoin is recognized as a legal means of payment.

Let us study the dynamics of gold prices, quotations of long-term US Treasury bonds (US 10-years Treasury Bonds), the S&P 500 stock index, and bitcoin cryptocurrency for the period 01.01.2019–31.12.2020 in percent (Fig. 4).

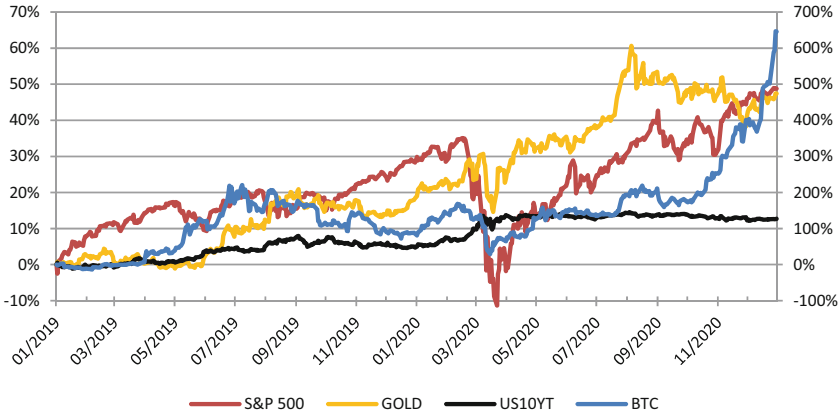


Fig. 4. Dynamics of quotations of separate financial instruments, 2019–2020

Analysis of the graph data (Fig. 4) indicates that in the considered time interval up to September 2020, there is a stable positive correlation between bitcoin quotes and the price of gold. However, in September 2020, the situation changed—this correlation became negative. Bitcoin quotes continued to rise, while gold prices began to decline. This period is characterized by the onset of the second wave of the COVID-19 pandemic and the development of an accompanying economic crisis and political instability in the USA due to the presidential election campaign.

On this background, not only gold prices fell (−4.13% from 08/01/2020 to 12/31/2020), but also the quotations of 10-year US Treasury bonds (−1.47%), traditionally considered a defensive asset, while the S&P index 500, reflecting the state of the US economy as a whole, rose by 5.77%, while bitcoin quotes rose by 154.43%.

This may indicate an increase in interest in cryptocurrency as a protective asset on the part of institutional investors. Thus, the volume of cryptocurrency assets of the US investment fund Grayscale Investments in December 2020 reached 17.5 billion US dollars, while at the beginning of 2020, it was 1.8 billion US dollars [15]. The conclusion of JPMorgan analysts evidences the high prospects for the use of bitcoin that if bitcoin manages to establish itself as an alternative to gold as an investment asset, its value could reach \$146,000 in the foreseeable future [16].

The results of mathematical model analysis of the redistribution of risk between cryptocurrencies and traditional currencies and gold during the COVID-19 pandemic show that in more stable markets, cryptocurrencies can be seen as defensive assets [17].

5 Conclusion

In today’s world, cryptocurrency is used to pay for goods and services but is not as active as financial speculations.

The main functions of money can appear in a particular virtual currency only provided that the number of its users increases significantly.

The limiting factors of the performance of the functions of money by a cryptocurrency are its shortcomings, such as possible use for illegal activities, unproductive use of power energy, high volatility, the uncertainty of legal status, and incomplete protection of operators against state restrictions.

In a broad sense, cryptocurrency is more than money. It is a new technology for accounting of transactions, which has a universal ability to embody the characteristics of money, goods, property, financial asset, and payment systems without fully matching any of them.

There are risks of using cryptocurrency for illegal activities, but their level is generally not higher than cash.

The role of cryptocurrency in the global financial system today is closer to a high-risk speculative digital asset.

Such advantages determine the prospects for using cryptocurrency as its high resiliency, trust guaranteed by the network protocol, low transfer fees, opportunities for high profitability, and diversification to hedge currency risks. These advantages are the drivers of a persistent trend of increasing the interest of individuals and businesses of economically developed countries in investing and money transfer and in paying for goods and services in cryptocurrency.

Certain jurisdictions allow the use of cryptocurrencies as a means of payment and apply favorable tax regulation to transactions in cryptocurrencies, which creates new opportunities for economic growth.






References

1. Vigna, P., Casey, M.J.: *The Age of Cryptocurrency: How Bitcoin and the Block-Chain Are Challenging the Global Economic Order*. St. Martin's Press, New York (2016)
2. Leloup, L.: *Blockchain: La révolution de la confiance*. Groupe Eyrolles, Paris (2017)
3. Tepper, A.: *The People's Money - Bitcoin*. Asia-Australia Technology, Melbourne (2015)
4. Tapscott, A., Tapscott, D.: *Blockchain Revolution: How the Technology Behind Bitcoin Is Changing Money, Business, and the World*. Portfolio, London (2016)
5. Kerimov, A., Azarenkova, G., Masharsky, A., Tomarovich, T.: The methods of managing for risk of combating money laundering (legalization) of proceeds from crime and the financing of terrorism. In: Ismayilov, A., Aliyev, K., Benazic, M. (eds.) *Economic and Social Development (Book of Proceedings Vol. 1/4)*, 55th International Scientific Conference on Economic and Social Development, pp. 846–855. Baku (2020)
6. Kochergin, D.A.: The roles of virtual currencies in the modern payment system. *St Petersburg Univ. J. Econ. Stud.* **33**(1), 119–140 (2017). <https://doi.org/10.21638/11701/spbu05.2017.107>
7. The European Parliament and the Council of the European Union: Directive 2018/843/EU. *Official J. Eur. Union* **61** (2018)
8. Stolbov, M., Shchepeleva, M.: What predicts the legal status of cryptocurrencies? *Econ. Anal. Policy* **67**, 273–291 (2020). <https://doi.org/10.1016/j.eap.2020.07.011>
9. % of Europeans Believe Crypto Will Still Be Around in 10 Years: Survey. *CoinDesk*. <https://www.coindesk.com/66-of-europeans-believe-crypto-around-10-years-survey>. Accessed 29 Jan 2021

10. HSB: Cryptocurrency gaining momentum among small. Hartford Bus. J. <https://www.hartfordbusiness.com/article/hsb-cryptocurrency-gaining-momentum-among-small-mid-sized-biz>. Accessed 29 Jan 2021
11. Sabah, N.: Cryptocurrency accepting venues, investor attention, and volatility. *Financ. Res. Lett.* **36**, 101339 (2020). <https://doi.org/10.1016/j.frl.2019.101339>
12. Crypto ATMs & merchants of the world, Coinmap. <https://coinmap.org/view>. Accessed 29 Jan 2021
13. Bloomberg. <https://bloomberg.com>. Accessed 29 Jan 2021
14. Yahoo Finance - Stock Market Live, Quotes, Business & Finance. <https://finance.yahoo.com>. Accessed 29 Jan 2021
15. Popper, N.: *Digital Gold: Bitcoin and the Inside Story of the Misfits and Millionaires Trying to Reinvent Money*. Harper Paperbacks, New York (2016)
16. Bitcoin tops \$40,000 as investors seek hedge against inflation. *The Guardian*. <https://www.theguardian.com/technology/2021/jan/07/bitcoin-tops-40000-dollars-investors-seek-hedge-against-inflation>. Accessed 29 Jan 2021
17. Hsu, S., Sheu, C., Yoon, J.: Risk spillovers between cryptocurrencies and traditional currencies and gold under different global economic conditions. *North Am. J. Econ. Financ.* **57**, 101443 (2021). <https://doi.org/10.1016/j.najef.2021.101443>



Improvement of the Quality of the Human Environment by Transporting and Stabilizing Sewage Sludge for Further Processing

Vladyslav Vaysman¹ , Natalia Strunnikova² ,
Olena Chukurna³ , Vitalii Dobrovolskyi³ ,
and Oleg Kassien² 

¹ Micron Corporation, 37, Borovskogo Street, Odessa 65031, Ukraine

² Earth Revival Technologies, 57B-23, Stabu Street, Riga, Latvia

oleg.kassien@earth-revival.com

³ Odessa National Polytechnic University,

1, Shevchenko Avenue, Odessa 65044, Ukraine

Abstract. There are many threats to the quality of human life in the environment of the modern world. Among them, one can single out the growing pollution of the environment and water resources, which leads to crop failures, hunger, and disease. Concomitantly, narrowly targeted measures often lead to an aggravation of the situation as a whole. For example, an attempt to solve the problem of yield quality deterioration by increasing the use of synthetic fertilizers leads to accelerated destruction of the fertile layer due to the irreversible loss of organic matter. It is proposed to use complex technology, including standard dewatering of sewage sludge at wastewater treatment plants, transportation, disinfection, and processing into a highly effective organic fertilizer. This paper deals with the problems of transportation of a viscous, epidemically dangerous, biologically aggressive substance for its further processing. To improve the quality of working conditions directly at treatment facilities to protect the environment, human health and counteract the emergence of epidemics, it is necessary to develop sealed systems for safe sludge transportation, maximally isolated from the environment – with taking into account many variables, such as environmental temperature, intern biological processes, various tribometric, rheological and thermophysical properties. Upon the laboratory studies and bench tests, the main affected factors were identified. Fundamental design solutions for transporting substances with rheological characteristics of the sludge below 80% humidity level are proposed. Research has been carried out to decontaminate the substance during its transportation.

Keywords: Quality of the environment · Biological safety · Integrated technology · Transportation · Disinfection processing

1 Introduction

The volume of sewage sludge, requiring deposition and disposal, is growing from year to year. In industrially developed countries, about 1.2 kg of dry substance is collected per inhabitant every day, which is about 6 kg of sediment with a moisture content of 80%. [1]. As a result of the standard dewatering of sewage sludge at city sewage treatment plants, a viscous, epidemically dangerous, biologically aggressive substance that is subject to further disposal is produced daily, which is moved openly on conveyor belts, cars, or manually. To improve the quality of the working conditions directly at the treatment facilities as well as to protect the environment and human health, especially in the context of the problem regarding counteracting the emergence of epidemics, it becomes increasingly important to develop the most isolated from the environment hermetic systems for the safe movement of viscous biopathogenic substances up to the moment of their disinfection and disposal.

Sewage sludge is a natural epidemic focus, making it necessary to comply with hygiene and biological safety standards when interacting with sewage sludge [2]. In connection with the growing volume of transported sewage sludge masses, containing a naturally high concentration of the widest range of human prion, viral, and bacterial pathogens, the complexity of logistic problems also increases. The situation is aggravated by the high concentration of the population and the fact that water treatment plants are located in close proximity to cities, and the personnel of the stations themselves often work in conditions of insufficient security, which creates a risk of infection and further spread of infection [3, 4]. An additional risk factor is that hazardous chemical compounds can enter the municipal sewer system, affecting human health and damaging the environment [5, 6]. It is also important that sewage sludge is unstable and biochemical processes continue in it, leading to the release of bad-smelling substances into the atmosphere. To reduce risks, it is necessary to:

- minimize the contact of a hazardous substance with the environment;
- automate the transportation of such a substance as much as possible;
- reduce the influence of the “human factor” in the course of daily ongoing work;
- reduce the delivery time and distance to the place of disinfection or another method of depositing sewage sludge [7].

The most common methods of transporting dewatered sewage sludge today can be divided into two main groups:

- traditional, known since antiquity - with the only difference that carts were replaced by cars, and belt conveyors are used instead of wheelbarrows;
- modern uses more complex technologies but is expensive to manufacture and operate special equipment for transporting hazardous substances.

The purpose of this study is to determine and improve the conditions for working with urban wastewater sludge, as well as the selection of equipment that ensures the reduction of the risks listed above, as well as the definition of requirements for technology and equipment that meet environmental and biological safety standards.

2 Literature Review

The scientific literature provides data on the texture of sewage sludge. The biochemical composition of WWS [8, 9] and the biological processes occurring in it [10, 11] have been well studied. The high agronomic value of sewage sludge is noted [12, 13]. Much attention in different countries (Italy [14], Oman [15], Sweden [16]) is paid to various methods of utilization and disinfection of sewage sludge in connection with the need to return organic material to agronomic circulation [17, 18]. Practical developments in sludge decontamination, including through heat treatment, are described [19, 20].

The topic of epidemiological safety is especially important in the context of the COVID-19 pandemic. In particular, the detection of SARS-CoV-2 in fecal masses is reported, and a lack of data on the period of inactivation of the virus in sewage is stated. Concerning the sediment formed during the epidemic and undergoing thermal disinfection treatment, the risk of infection with SARS-CoV-2 is considered in the range from low to negligible (“low to negligible”). Nevertheless, it is recommended to strengthen control over the observance of protective measures to be taken by workers of treatment facilities and specialists associated with the work with sewage sludge [21].

The problem of sewage sludge contamination by heavy metals and the methods of sorption of heavy metals are also important and sufficiently represented [22]. In addition to the data on sewage sludge’s mineral and biochemical composition, the granulometric characteristics of the initially stabilized sediment from gravity sedimentation tanks are also given. The sediment obtained from digesters is much finer and more homogeneous [1]. As the humidity decreases, it is noted that the use of various pumping equipment is faced with problems arising from the viscoplastic properties of sewage sludge, which are characteristic of non-Newtonian fluids [23, 24].

3 Research Methodology

Laboratory experiments were carried out in the laboratory of Earth Revival Technologies. The characteristics of the experiments were determined according to the standards accepted in pharmaceuticals [25]. The company’s complex laboratory experiments were carried out to preliminarily determine the principal approaches to the transportation of biologically active substances with a moisture content below 80%. Shear resistance and plastic viscosity of the substance were determined as the key characteristics in the simulation of material movement. When the moisture content of the material is less than 70% in the static state, the material’s texture becomes highly homogeneous; at temperatures below, mesophilic biological processes slowed down or stopped.

However, at room temperature, as a result of continuing exothermic biological processes, accompanied by the decomposition of organic matter, a gradual release of moisture was observed with an active release of heat and strong gas release. During long-term (day or more) observation in the WWS layer with a moisture content of up to ~35%, active exothermic biological processes resembling composting were noted. The decomposition of organic matter in the wastewater sludge proceeded with active

steam and gas separation, with the release of thiols, methane, ammonia, and, in some cases, arenes.

The safety of sewage sludge use is determined by its composition, reflected in the relevant national standards. Chemical analysis of WWS from several treatment plants in the EU, Israel, Ukraine, and comparison of standards by countries showed insignificant discrepancies in terms of the situation with heavy metals pollution. The similarity of these indicators allows us to assume that chemical pollutants can be considered within the framework of a unified approach, both from the point of view of mechanics and in terms of ensuring safety. In the event of a threat, recorded using express tests or regularly scheduled analyses, it is possible to add sorbents to reduce the mobility of heavy metals purposefully.

At the same time, the indicators of ash content differed significantly (approximately: from 30% to 50% of ash impurities), which is probably due to the discrepancy between national standards and practices regarding the separation of the fecal, storm, and industrial effluents, as well as with the state of infrastructure.

There is a significant difference in the part of unseparated garbage: small hygienic garbage, rags of clothing, polyethylene, small wooden, metal, etc., fragments.

Bench tests were carried out at the Earth Revival Technologies testbed, commissioned by Micron Corporations.

The test bench for practical tests and equipment tests is mounted inside a thermoconstant container with an autonomous climate system. The stand consists of the following main units, devices, and assemblies:

- Material feeding device in the form of a feeder.
- High-pressure pipeline system, consisting of several different types of pumps, independently connected to the pipeline.
- Vibration transport system made in the form of a conveyor located in an isolation chamber (Fig. 1).
- Infrared heaters located along the conveyor of the transport system (Fig. 2).
- Intermediate storage hopper (Fig. 3).
- Feeding, distribution, control and measuring devices.

Since the stand design provided for an auxiliary system for thermal disinfection of sewage sludge directly in sediment transfer, the vibration conveyor isolation chamber was equipped with infrared heaters, a thermocouple, and a temperature controller. At the same time, due to the threat of pipeline destruction with significant heating of the transported sediment at the design stage, it was decided to abandon thermal disinfection in the pipeline itself.

Infrared heaters are located along the conveyor belt of the vibratory conveying system. The heating elements are made in the form of quick-mount panels, each of which is a set of ceramic infrared heaters installed in a metal structure made in the form of a reflector. The choice of infrared emitters for disinfection is because the use of inertial thermal elements with low efficiency requires a lot of energy, which leads to high requirements for the energy class of equipment and an increase in production costs.

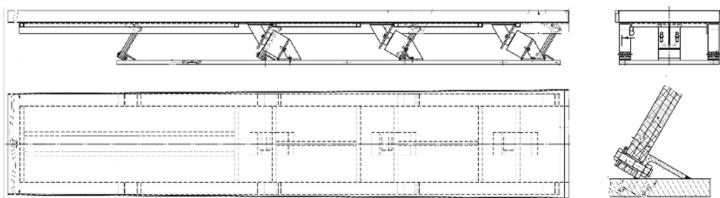


Fig. 1. Vibration transport system in the form of a conveyor, placed in an isolation chamber.

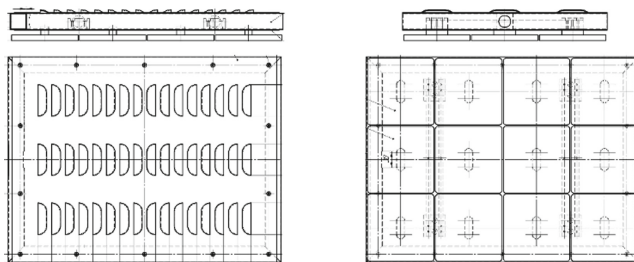


Fig. 2. Infrared heaters located along the conveyor belt of the vibratory transport system.

An intermediate storage hopper, the presence of which is because if the pipeline length needs to be increased, a sequential installation of an additional intermediate pump can be required.

The high-pressure piping system includes piston diaphragm, gerotor and peristaltic pumps selected for simulation and testing. The transported raw materials are picked up by the auger from the closed intermediate storage hopper and fed to the distributor directly to the pumps. The direction of movement of the material is changed to perpendicular. In the process of further movement, the material, with the help of a special mechanical device, can be fed into pipelines of one configuration or another, which makes it possible to study the behavior of the transported material in various environments.

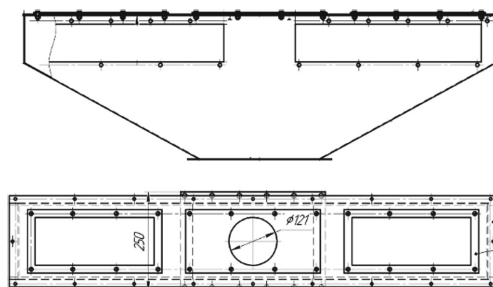


Fig. 3. Intermediate storage hopper.

Then the material is returned to the storage bin, which means the conditional delivery of the material to the endpoint; or, with the help of a special feeder common to all pipeline lines, it is fed to the tray of the vibratory transport system. The vibratory transport system consists of one or several metal vibrating trays located at an inclination of $2.5\text{--}3^\circ$; includes an oscillatory electromagnetic circuit and an elastic mechanical system capable of oscillating in a state of resonance, ensuring the advancement of the material in the direction of inclination. Also, the vibration transport system is equipped with vibration drives with the main power circuit and, in the presence of a forced heating source, can be equipped with an additional forced cooling circuit. Depending on the rheological properties of the transported material, the speed of its passage along the vibrating conveyor can be flexibly regulated by the intensity of vibration and by changing the angles of inclination in a given range. The vibration transport system can consist of several sequentially located similar devices, each lower than the previous one. Thus, if the need to compensate for the height difference arises, the vibration transport system must be operated in conjunction with a pipeline system that allows the transported material to be raised to the desired height.

Using which the material is distributed over the tray of the vibratory transport system, the feeder ensures a uniform supply of the viscous substance over the entire plane of the tray. Layer thickness is determined by the design of the feeder with a given opening height, and the width of the feeder corresponds to the width of the tray. The material enters the tray and then moves in an even layer and at approximately the same speed. In the case of a multisection vibrating conveyor, the material is moved from tray to tray sequentially, under the action of gravity. In the same way, the material is unloaded into the receiving hopper.

After that, the cycle of supply to the pipeline system and, then, to the vibrating conveyor can be resumed, simulating a multi-segment transport system, or the material will be considered delivered to the destination.

Control of the level of raw materials in the storage bin can be carried out tenso-metrically, using ultrasonic sensors and visual control. As it moves along the vibro-conveyor for disinfection, the material is exposed to infrared radiation from heating panels mounted above the trays. Neutralization of biopathogens is ensured by heating to the required temperature for some time sufficient for guaranteed heating and disinfection of the sediment volume throughout the layer thickness. If a disinfection system is used, the speed of the sludge advance must meet the requirements for the intensity and duration of heat treatment required for reliable sludge disinfection. It seems the most rational to heat the material to $90\text{--}95^\circ\text{C}$, which makes it possible to significantly (up to several minutes, according to the formulae of the time-temperature regimes for thermally treated "Class A" sludge with the solid content of the sludge being more than 7% [17]) reduce the time of thermal exposure without switching to a higher class of equipment performance in terms of heat resistance and without reaching the boiling point of water.

At the same time, it should be taken into account that the thermally treated material comes out with a reduced percentage of moisture compared to the initial state. Although a significant drop in humidity in the closed chamber of the vibroconveyor does not occur, a change in the material's rheological properties with strong heating is inevitable, which must be considered when planning a multi-segment combined

pipeline-vibration transport system. It should be especially noted that, despite many advantages (intuitive clarity, the ability to transport dry and viscous materials in a relatively wide range of positive and negative angles), the use of belt conveyor devices does not seem to be a good alternative to the vibrational method of movement. The main reason is that many moving elements impart movement to the conveyor belt, low efficiency, high wear of moving parts of equipment in obviously difficult operating conditions, and aggressive environments, combined with low practical maintainability.

Also, moving with a slope, especially with a slope opposite to the direction of movement, is difficult or inapplicable in the separation of sewage sludge with the release of water. The design of the belt conveyor also makes it difficult to compactly place it in isolation from the external environment, which, combined with the need for frequent manual cleaning of equipment, conflicts to minimize the risk of human illness. In addition, thermal disinfection of the transported material in using a belt conveyor is difficult due to the increased cost of manufacturing and operation under conditions of increased temperature exposure. At the same time, the uneven temperature gradient in the disinfected layer on the conveyor belt does not allow achieving stable disinfection at gentle temperatures in any acceptable period of time.

4 Results

As a result of the bench tests, information was obtained that made it possible to determine the necessary equipment configuration, as well as the features of its operation, in particular:

A piston diaphragm pump does not provide a stable sewage sludge supply with a humidity of 80% and below. A tight plug of the pressed material forms within a few minutes, and further operation becomes impossible.

Peristaltic hose and gerotor pumps of various designs have shown their fundamental suitability for moving sewage sludge with a moisture content of 80% and below.

The duration of operation of gerotor pumps depends on the consistency of the sewage sludge (first of all, from accidental foreign inclusions: pieces of metal, small stones, hard plastic) and varies from tens to hundreds of hours without replacing the stator and from hundreds to thousands of hours without replacing the rotor.

The main problem of wear of the rotor-stator pair is the ingress of solid fractions that grossly damage the stator material directly or indirectly through damage to the working surface of the rotor. Special attention should be focused on the quality of the rotor-stator pair assembly, rotor's quality, stator's material, and quality of the sludge cleaning. The best performance in terms of service life was achieved for stators made of rubber with a high rubber content, which is explained by the diffusion of abrasive particles into the stator body, which increases its resistance to further wear.

The high maintainability of gerotor pumps is an important positive factor. When replacing a worm stator or as the rotor wears out, a new rotor-stator pair is selected. It, however, is fraught with some difficulty: due to the error in the shape of the stator bore and, to a lesser extent, in the shape of the rotor, there is a problem of the inaccuracy of the preload oscillation [26].

A task requiring direct human participation is the need for periodic (once per shift) cleaning of the compression chamber. It is a simple and quick operation but requires adherence to appropriate safety standards.

A possible alternative is to use peristaltic pumps as they do not have any of the above problems since the only part directly exposed to the transported material is an easily replaceable hose made of wear-resistant material, requiring no special adjustment or cleaning.

During the tests, the possibility of air congestion was recorded. It also turned out that it is unacceptable to leave sediment in a multi-segment pipeline of considerable length because the static state of the material promotes delamination, congestion, and build-up on the pipe walls. Sludge fermentation can also lead to the malfunction of all hermetically mated segments of the pipeline system. Thus, the intermediate hopper acts as a safety device and an emergency valve.

Long-term continuous testing of the vibration transport system has fully demonstrated the reliability and high efficiency of sewage sludge transportation using a vibrating conveyor. In the course of the research, several problems were empirically identified, which later found their solution. The following problems may be of greatest interest:

Delamination of the material of the trays under the influence of prolonged vibrations in the event of a hidden defect in the metal sheet.

Less obvious is the solution to another vibration problem: the destruction of the hardware holding the tray assemblies. At the same time, the traditionally used solution - Grover's washers (split lock washers) - has shown its absolute inconsistency. Theoretical confirmation was found on the NASA website [27], but no solution was proposed. The use of various multi-purpose two-component compounds and the use of lock-wedge toothed washers gave only a partial, temporary effect. During the tests, a successful complex multicomponent solution was found, but its description is beyond the scope of this article.

The infrared heating disinfection system has shown consistently successful results. For disinfection of sediment transported along a vibrating conveyor of 150 mm. with a humidity of 80%, it took 15 min, taking into account the heating time of the layer to 95 °C. In this case, the speed of movement of the material was about 1 m per minute.

5 Conclusions

The successful realization of the described method opens the way for its industrial implementation to solve environmental-friendly reloading, transporting, and stabilizing sewage sludge for further processing. A high-pressure pipeline with the right choice of pumping equipment (in the experiment, a gerotor pump), preventing fermentation, solidification, and the formation of air and other congestions, can provide a hermetic movement of dewatered sewage sludge for several tens of meters for each segment. The exact values depend on the homogeneity and moisture content of the material being transported and on many factors determined by local conditions: the material of the pipes and fittings used, the geometry of the pipeline route, and the temperature of the environment. The pipeline can be multi-segment, and the transportation distance will

be solely due to considerations of logistic rationality. In combination with a vibrating conveyor, the high-pressure pipeline is a ready-made line for transporting sewage sludge with its simultaneous disinfection. At short distances (up to 20–30 m, depending on local conditions), the vibroconveyor can be used to transport sewage sludge independently, including with simultaneous disinfection of the sludge.

It seems important to obtain more statistical data for building and adjusting a computer model for flexible adaptation of equipment parameters under changing material parameters and environmental conditions. As part of an integrated approach to improving the quality of the living environment, a rational continuation of the solution to safe transportation of sewage sludge should also be its processing into safe, high-quality organic fertilizer.

Acknowledgment. This research is being conducted based on agreement with SIA “ETKC” (Centre of Competence for Energy and Transportation) within the framework of project Nr.1.2.1.1/18/A/001 co-funded by the European Regional Development Fund.






References

1. Lotosh, V.E.: Utilization of sewage system drainage and its sludge. *Sci. Tech. Aspects Environ. Prot.* **6**, 93–106 (2002). (in Russian)
2. Romdhana, M.H., Lecomte, D., Ladevie, B., Sablayrolles, C.: Monitoring of pathogenic microorganisms contamination during heat drying process of sewage sludge. *Process Saf. Environ. Prot.* **87**, 377–386 (2009)
3. Cieřlik, B.M., Namieřnik, J., Konieczka, P.: Review of sewage sludge management: standards, regulations and analytical methods. *J. Clean. Prod.* **90**, 1–15 (2015)
4. Kelessidis, A., Stasinakis, A.S.: Comparative study of the methods used for treatment and final disposal of sewage sludge in European countries. *J. Waste Manag.* **6**, 1186–1195 (2012). <https://doi.org/10.1016/j.wasman.2012.01.012>
5. Haiba, E., et al.: Sewage sludge composting and fate of pharmaceutical residues – recent studies in Estonia. *Agron. Res.* **14**(5), 1583–1600 (2016)
6. Okareh, O.T., Enesi, O.D.: Removal of heavy metals from sewage sludge using sugarcane waste extract. *J. Sci. Res.* **6**(6), 439–450 (2015)
7. Final Report for the European Commission: Environmental, economic and social impacts of the use of sewage sludge on land. Part III: Project Interim Reports. Milieu Ltd, Brussels (2008)
8. Nascimento, A.L., et al.: Sewage sludge microbial structures and relations to their sources, treatments, and chemical attributes. *Front. Microbiol.* **9**, 1462 (2018)
9. Vucāns, A., Gemste, I., Schōnning, C.: Pathogenic bacteria amount and change in sewage sludge. *LLU Raksti* **17**(312), 1–10 (2006). (in Latvian)
10. Vibornis, V., et al.: Evaluation of sewage sludge for further nutrient conservation. *Key Eng. Mater.* **850**, 166–171 (2020). <https://doi.org/10.4028/www.scientific.net/kem.850.166>
11. Zorza, L., Kalnins, M., Gudra, D., Fridmanis, D., Rapoport, A., Muter, O.: Evaluation of the changes in bacterial community structure and its activity in the presence of *Saccharomyces cerevisiae* and benzalkonium chloride. University of Latvia, Riga (2019)
12. Stentiford, E., Sānchez-Monedero, M.A.: Past, present and future of composting research. *Acta Hort.* **1146**, 1–10 (2016). <https://doi.org/10.17660/ActaHortic2016.1146.1>

13. Kotschi, J.: Adverse impacts of mineral fertilizers in tropical agriculture. AGRECOL, WWF-Study (2015)
14. Lombardi, L., Nocita, C., Bettazzi, E., Fibbi, D., Carnevale, E.: Environmental comparison of alternative treatments for sewage sludge: an Italian case study. *Waste Manage.* **69**, 65–376 (2017). <https://doi.org/10.1016/j.wasman.2017.08.040>
15. Suaad, J.A.K., Mushtaque, A., Malik, A.-W., Ahmed, A.-B., Choudri, B.S.: Wastewater and sludge management and research in Oman: an overview. *J. Air Waste Manag. Assoc.* **67**(3), 267–278 (2017). <https://doi.org/10.1080/10962247.2016.1243595>
16. André, A., et al.: Wastewater treatment in Sweden. Sw.EPA, SwAM & SCB (2016)
17. Carrington, E.G.: Evaluation of sludge treatments for pathogen reduction – final report. CO 5026/1, WRc (2001)
18. Grubel, K., Machnicka, A., Nowicka, E., Waclawek, S.: Mesophilic-thermophilic fermentation process of waste activated sludge after hybrid disintegration. *Ecol. Chem. Eng. S* **21**(1), 125–136 (2014)
19. Davids, M., Gudra, D., Radovica-Spalvina, I., Fridmanis, D., Bartkevics, V., Muter, O.: The effects of ibuprofen on activated sludge: shift in bacterial community structure and resistance to ciprofloxacin. *J. Haz. Mat.* **340**, 291–299 (2017)
20. Dubova, L., Strunnikova, N., Cielava, N., Alsina, I., Kassien, O., Bekker, A.: Thermal decontamination of sewage sludge. *Agron. Res.* **18**(1), 781–787 (2020)
21. The French Agency for Food, Environmental and Occupational Health and Safety: Sewage sludge produced during the COVID-19 epidemic can only be applied to fields after disinfection. Ref. #2020-SA-0043, ANSES, Maisons-Alfort (2020)
22. Zupancic, M., Bukovec, P., Milacic, R., Scancar, J.: Critical evaluation of the use of the hydroxyapatite as a stabilizing agent to reduce the mobility of Zn and Ni in sewage sludge amended soils. *Waste Manage.* **25**(12), 1392–1399 (2006)
23. Trávníček, P., Junga, P.: Thixotropic behaviour of thickened sewage sludge. *J. Environ. Health Sci. Eng.* **12**(1), 72 (2014). <https://doi.org/10.1186/2052-336X-12-72>
24. MoriI, M., Seyssiecq, I., Roche, N.: Rheological measurements of sewage sludge for various solids concentrations and geometry. *Process Biochem.* **41**(7), 1656–1662 (2006). <https://doi.org/10.1016/j.procbio.2006.03.021>
25. Chow, S.-C., Liu, J.-P.: *Statistical Design and Analysis in Pharmaceutical Science: Validation, Process Controls, and Stability* (1st ed. 1995). eBook Publ. (2018). <https://doi.org/10.1201/9781315274294>
26. Goncharov, A.A., Vasiliev, A.S.: Technological Capabilities of a Special Strategy for Processing Cycloidal Helical Surfaces with a Non-Profiled Tool. BMSTU (2021). <https://doi.org/10.21203/rs.3.rs-189911/v1>
27. Barret, R.T.: NASA Ref. Publ. 1228: Fastener Design Manual. Cleveland, Ohio (1990)



Influence of the Cutting Temperature on the Surface Layer Quality When Grinding Sintered Porous Materials

Oleg Zabolotnyi¹ , Tetiana Bozhko¹ , José Machado² ,
Serhii Yarmoliuk¹ , and Olha Zaleta¹ 

¹ Lutsk National Technical University, 75, Lvivska Street, Lutsk 43018, Ukraine

² Department of Mechanical Engineering, University of Minho,
MEtRICs Research Centre, 4804–533 Guimarães, Portugal

Abstract. One of the features of sintered materials is porosity. Depending on the application, this can be both a disadvantage and an advantage. The porosity geometry affects the propagation of heat during the grinding of the sintered material. An experimental study of the temperature in the cutting zone during the grinding of sintered porous materials was carried out. The relationship between the contact temperature in the cutting zone, the parameters of the cutting modes during grinding, and the porosity of the part is revealed. It was found that the use of process coolants is not always possible due to the presence of pores in the material. It is proved that the cutting temperature of porous materials is higher due to the deteriorated heat dissipation properties, but the cutting temperature does not affect the degree of compaction of the surface layers of the powder material. An adequate mathematical model is obtained, which describes the change of cutting temperature depending on the material's cutting depth, grinding speed, and porosity.

Keywords: Abrasive processing · Cutting modes · Grinding wheel · Iron powder · Workpiece

1 Introduction

The main operational properties of machine parts - wear resistance, strength, reliability are largely determined by the condition of the surface layer, which depends on the manufacturing technology. The quality of the polished part is determined by geometric parameters, such as the accuracy of size and shape of the surface and the roughness and properties of the surface layer of the material [1, 2].

In modern production, the technological support of the parameters of the condition of the surfaces of parts, depending on the tool's characteristics, is not sufficiently substantiated, which leads to an overestimation of requirements and higher prices of machines [3, 4]. The roughness of the ground surfaces of sintered powder materials is determined by the characteristics of the grinding wheel, cutting modes, properties of the processed material, and other factors. The problem of the influence of the

characteristics of the grinding wheel on the surface quality of porous bodies is insufficiently covered. Therefore, theoretical and experimental investigations in this direction are relevant.

2 Literature Review

One of the further ways of developing powder metallurgy is the use of parts of complex configuration [5]. However, due to the specifics of the manufacturing technology, this leads to the need to perform additional mechanical processing.

Surface roughness is affected by elastic and plastic deformations in the surface layer, cutting modes, stiffness of the technological system, shape, and condition of the cutting part of the tool [6], as well as the type of material being processed and friction between the treated surface, the fixture [7], and the tool [8, 9].

The quality of the surface of the machined part is determined, in addition to the cutting modes and the initial condition of the working surface of the grinding wheel, the conditions of editing the wheel, and the change of the working surface during operation [10].

The most applicable type of mechanical processing of structural materials is abrasive processing, which provides high accuracy and a class of purity of the processed parts [11]. Thermal phenomena accompanying the grinding process significantly impact the quality of the ground surfaces [12]. High grinding temperatures cause defects in the surface layer of the ground part (e.g., burns, cracks) [13], which reduces the part's quality [14], and therefore the temperature factor becomes one of the main factors of the grinding process [15].

The processing of sintered porous materials differs from compact steels due to porosity and often inhomogeneous microstructure [16]. It's confirmed by research the pore stereology of powder materials [17] using the original computer-informative software for research of the new materials [18].

To improve the processing of sintered materials, mechanical processing additives are used [19], the quality of which can be ensured using the corresponding technological equipment [20]. Increasing the wear resistance of the work surfaces of parts can be achieved through hardening processing methods [21]. It's confirmed by methods of evaluating the wear resistance of the contact surfaces developed in works [22, 23]. To improve the machining of materials can be effective using of machinability enhancer [24]. To reduce the temperature in the cutting zone [25], textured grinding wheels with a discontinuous cutting edge are used [26] and the use of oil or air when processing the detail [27].

Considering the urgency of the problem, the work aims to study the temperature in the cutting zone under various modes and conditions of grinding sintered porous materials.

3 Research Methodology

Sample blanks were made by hydrostatic molding in a hydrostatic installation using oil-resistant rubber elastic shells. The required value of the porosity of the samples was achieved by changing the specific force of formation. The experiments were performed on samples that were made of iron powders. The chemical composition and particle size distribution of the studied iron powder are shown in Table 1 and Table 2.

Table 1. Chemical composition of the iron powder.

Chemical composition (%)						
Fe	C	Si	Mn	S	P	O
98,5	0,02	0,17	0,03	0,01	0,02	0,27

Table 2. Particle size distribution of the iron powder.

The yield of fractions (%) when the particle size (mm)						
Fe	C	Si	Mn	S	P	O
-0400 + 0315	-0315 + 0200	-0200 + 0160	-0160 + 0100	-0100 + 0063	-0063 + 0050	-0050
0,6	8,28	6,82	15,1	34,8	28,6	6,8

The workpiece was made in two stages: pressing and sintering. The iron powder was pressed using a rubber mold in a high-pressure chamber, creating the pressure required to obtain a sample of a given porosity. Grinding of the samples was carried out without cooling on a universal flat-grinding machine of the 3L722B brand. A grinding wheel of the brand 24A20SM2K was used. To determine the temperature in the cutting zone, a chromel-alumel thermocouple was used. The studies were carried out on porous sintered iron with a porosity of 24%, 28%, 32%, which were manufactured by the hydrostatic formation and sintered at a temperature of 1050 °C in a protective environment. The influence of the temperature factor on the surface quality during grinding was determined experimentally by the method of a multifactorial experiment.

The main factors that affect the cutting temperature when grinding a sintered porous materials depend on the cutting depth t , grinding speed V_d , and porosity of the material θ :

$$T = f(t, V_d, \theta) \tag{1}$$

The experiments were carried out using the method of multivariate analysis 2^3 , i.e., simultaneous variation of all variable factors, $x_1(t)$, $x_2(V_d)$, $x_3(\theta)$. Based on the results obtained, using the least-squares method and the properties of the scalar product of the main vectors, a regression dependence is derived. The mathematical model does not describe a whole system but only a separate set of decisive factors in the grinding of porous powder materials.

4 Results

The grinding process of porous sintered materials includes the restriction of the use of a coolant, which, when entering the pores of the workpiece, changes the physical and mechanical characteristics of the surface layer of the material.

It is established that when processing sintered powder materials, the cutting temperature is higher than when processing steel, despite their lower strength, ductility, as well as a lower level of cutting forces. It is due to the lower thermal conductivity (1.5 times...2 times) of sintered powder materials. Depending on the carbon content in the steels, their thermal conductivity varies in the range of 60...80 W/(m · K), and sintered materials of similar composition - in the range of 20...50 W/(m · K), as shown in Fig. 1.

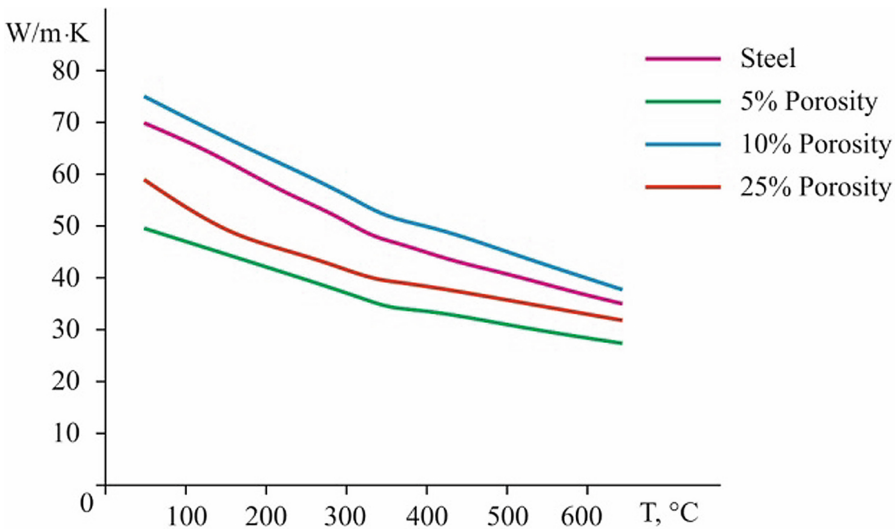


Fig. 1. Dependence of the cutting temperature on the thermal conductivity of the material.

The results of measuring the cutting temperature as a function of the cutting depth are shown in Fig. 2. It was found that with increasing porosity, the cutting temperature increases as the thermal conductivity coefficient decreases and the heat removal conditions deteriorate.

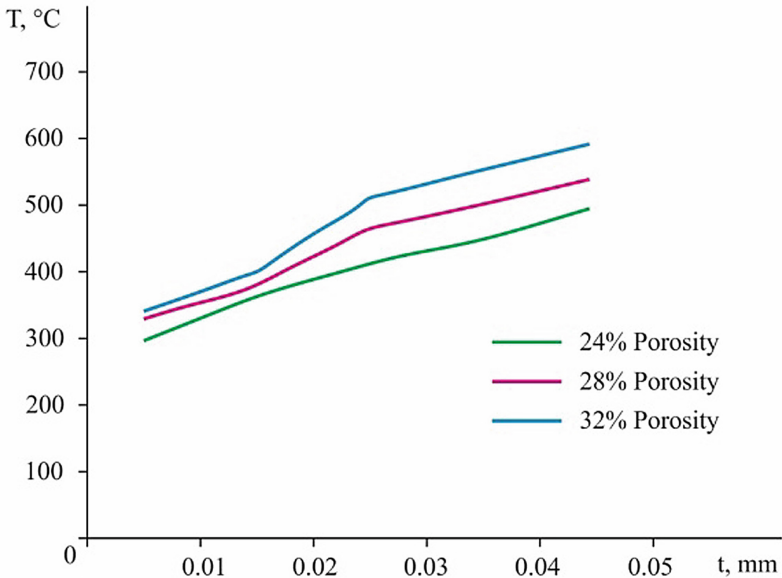


Fig. 2. The dependence of the cutting temperature on the cutting depth at $V_d = 5$ m/min, $V_{kr} = 35$ m/s.

The influence of temperature on the quality of the surface layer of the part when processing porous materials differs from compact materials, and as a result of low thermal conductivity, the influence of temperature extends to the surface layers of the part. Another feature of the grinding process is that the cutting temperature does not affect the degree of compaction of the surface layers of the powder material.

When processing the results obtained by the method of planning a multivariate experiment, a regression dependence was established in the following form:

$$T = 611.8 \cdot t^{0.34} \cdot V_d^{-0.05} \cdot \theta^{0.28} \quad (2)$$

The analysis of the obtained mathematical dependence showed that it adequately describes the temperature change depending on the main factors of the grinding process: cutting depth t , grinding speed V_d , the porosity of the material θ . The greatest influence on the increase in contact temperature has the cutting depth of cut and, to a lesser extent, the porosity of the detail (θ). At the same time, increase speed grinding (V_d) leads to a decrease in temperature effects on the treated surface.

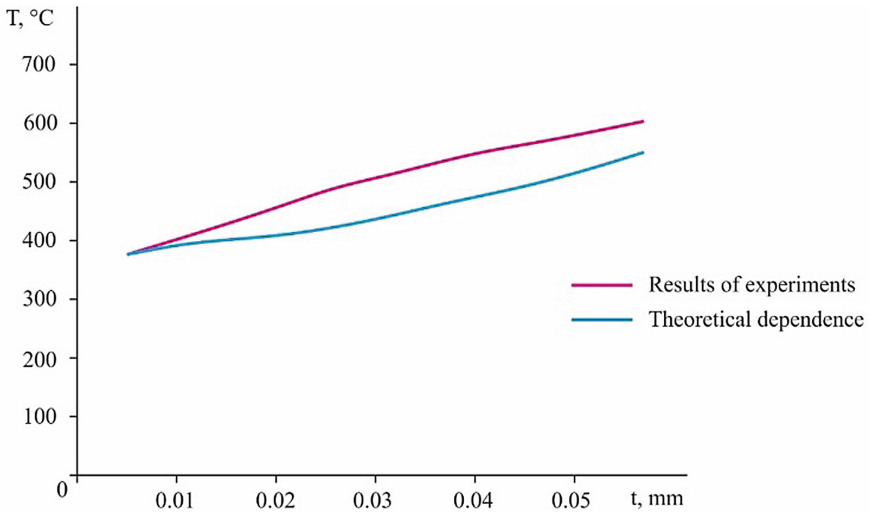


Fig. 3. The effect of the cutting depth on the temperature at $V_d = 5$ m/min, $V_{kr} = 35$ m/s, $\theta = 24\%$

Figure 3 compares the calculated data according to formula (2) and the experimental results depending on the cutting depth.

Figure 4 shows the two-dimensional response surface of the arithmetic mean temperature deviation in the area of the used cutting depth t and grinding speed V_d at $\theta = 28\%$, which is constructed using regression dependence 2.

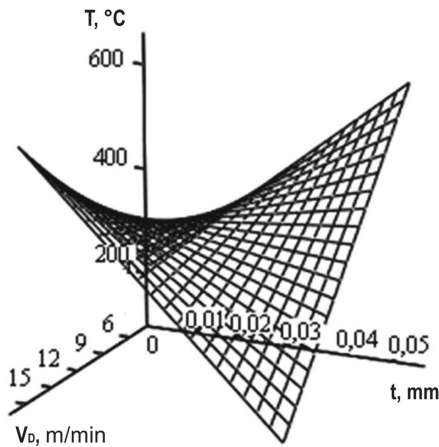


Fig. 4. The response surface of the arithmetic mean deviation of the temperature at $\theta = 28\%$.

High instantaneous temperatures that occur when grinding sintered powder materials lead to structural changes in the surface layer of the material, the appearance of cauterization, and grinding cracks. Thus, when grinding a sample with a porosity of 32%, because of the contact temperature $T = 510\text{ }^{\circ}\text{C}$, cauterization was formed.

The surface of the processed detail is covered with separate cauterization spots (Fig. 5a), which occurred during the following processing modes: $t = 0.05$ (mm) $V_d = 5$ (m/min).

In addition, under these treatment modes, small cauterization caused a decrease in stiffness from HB 80 to HB 66. When grinding a sample with a porosity of 32%, microcracks were formed due to the contact temperature $T = 586\text{ }^{\circ}\text{C}$. The surface of the processed part is covered with individual microcracks (Fig. 5b), which occurred during the following processing modes: $t = 0.05$ (mm) $V_d = 5$ (m/min). Grinding cracks were formed because of high contact pressure, temperatures, and friction forces of abrasive grains on the surface of the ground workpiece.

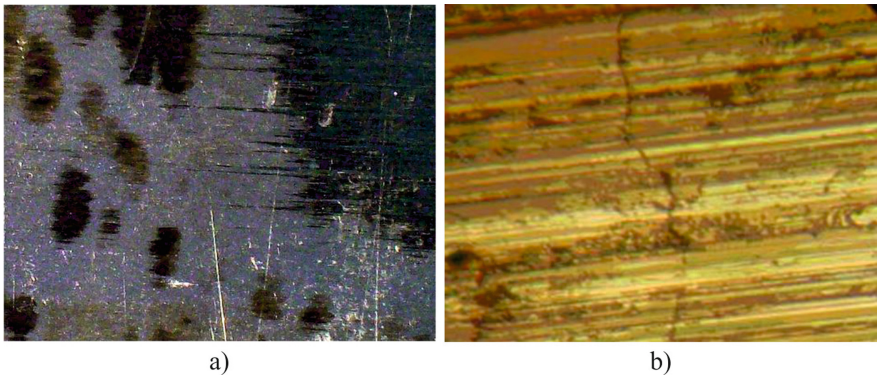


Fig. 5. Cauterization during grinding a); microcracks during grinding b).

No significant defects were found when processing a sample with a porosity of 24% at different cutting modes. Consequently, with an increase in the parameters of the cutting modes and an increase in the porosity of the workpiece, the probability of defects in the form of cauterization and microcracks on the surface of the part increases.

The local change in the structure of the surface layer of the part, which is formed because of high instantaneous temperatures and intense heat release in small areas of the surface layer of the part, causes a decrease in the mechanical properties of the surface layer, mainly a reduction in its hardness and wear resistance.

To reduce the effects of cauterization and the formation of microcracks, oil impregnation of the treated surface was used. In some cases, it is not possible to use impregnations according to the technological conditions on the part. Then we apply intermittent grinding, which was implemented by using circles with an intermittent cutting edge.

As an example, Fig. 6 shows the results of measuring the cutting temperature depending on the depth of cut, which are obtained at the following parameters: $V_d = 9$ m/min, $V_{kr} = 35$ m/s, $S = 0,2$ mm/stroke.

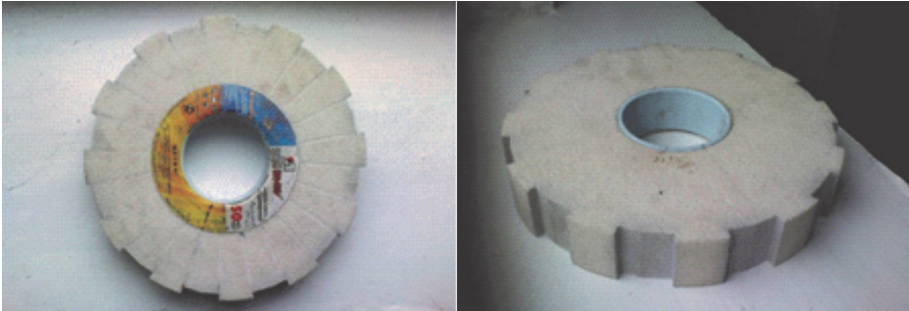


Fig. 6. Intermittent wheel.

These data indicate that grinding with intermittent wheels leads to temperature decrease. The degree of temperature decrease during intermittent grinding compared to grinding with a solid wheel in the range of cutting depth $t = 0.01 \dots 0.05$ mm is 21... 27% (Fig. 7).

There no traces of burns on the treated surfaces were found. Interruption of the cutting process reduces the temperature in the cutting zone by decreasing the duration of heating the elementary area on the part surface, and the temperature does not reach the maximum critical value.

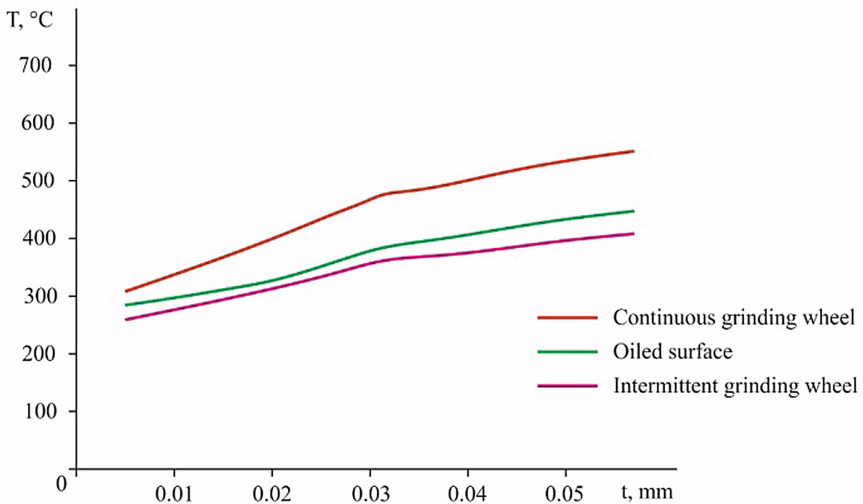


Fig. 7. Dependence of the cutting temperature on the cutting depth under different processing conditions.

Temperature decrease in the cutting zone was observed on average by 20% if the parts are oil-impregnated. The oil in the pores was like a cooling agent. It should be noted that the oil in the pores burns out under high-temperature influence, and it causes environmental pollution. Therefore, grinding of oil-impregnated parts should be implemented on machines equipped with special exhaust equipment.

5 Conclusion

It is experimentally established that when grinding porous sintered materials, possible structural defects of the surface layer of the processed parts, namely, the appearance of cauterization and microcracks. The main factor in the appearance of defects is an increase in the cutting parameters and porosity of the workpiece to be processed.

The intermittent grinding process leads to a temperature decrease in the cutting zone and the avoidance of grinding defects in the form of annealing. The degree of temperature decrease during intermittent grinding compared to grinding with a solid circle in the range of cutting depth $t = 0.01 \dots 0.05$ mm is 21...27%. Lowering the temperature when grinding porous materials by impregnating them with oil is impractical, leading to oil burnout and environmental pollution.

A regression equation is derived to determine the cutting temperature depending on the cutting modes and the porosity of the part. It is established that with the increase of porosity, the cutting temperature on the surface of the part increases due to the decrease of the thermal conductivity coefficient and the deterioration of the heat dissipation conditions.

Experimental studies were conducted based on the limitations of the technological capabilities of the equipment and due to the use of sintered powder materials for structural purposes in mechanical engineering.

Acknowledgment. This research was partially supported by International Association for Technological Development and Innovations.

References






1. Aurich, J.C., Linke, B., Hauschild, M., Carrella, M., Kirsch, B.: Sustainability of abrasive processes. *CIRP Ann.* **62**(2), 653–672 (2013). <https://doi.org/10.1016/j.cirp.2013.05.010>
2. Pavlenko, I., et al.: Parameter identification of cutting forces in crankshaft grinding using artificial neural networks. *Materials* **13**(23), 5357 (2020). <https://doi.org/10.3390/ma13235357>
3. Xia, X., Yub, T., Dinga, W., Xu, J.: Grinding of Ti2AlNb intermetallics using silicon carbide and alumina abrasive wheels: tool surface topology effect on grinding force and ground surface quality. *Precis. Eng.* **53**, 135–145 (2018). <https://doi.org/10.1016/j.precisioneng.2018.03.007>
4. Ivanov, V., Vashchenko, S., Rong, Y.: Information support of the computer-aided fixture design system. *CEUR Workshop Proc.* **1614**, 73–86 (2016)

5. Povstyanoi, O.Y., Rud', V.D., Samchuk, L.M., Zubovets'ka, N.T.: Production of porous materials with the use of energy-saving technologies. *Mater. Sci.* **51**(6), 847–853 (2016). <https://doi.org/10.1007/s11003-016-9912-6>
6. Chalyj, V., Moroz, S., Ptachenchuk, V., Zablotskyj, V., Prystupa, S.: Investigation of waveforms of roller bearing's working surfaces on centerless grinding operations. In: Ivanov, V., Trojanowska, J., Pavlenko, I., Zajac, J., Peraković, D. (eds.) *DSMIE 2020. LNME*, pp. 349–360. Springer, Cham (2020). https://doi.org/10.1007/978-3-030-50794-7_34
7. Karpus, V.E., Ivanov, V.A.: Choice of the optimal configuration of modular reusable fixtures. *Russ. Eng. Res.* **32**(3), 213–219 (2012). <https://doi.org/10.3103/S1068798X12030124>
8. Obikawa, T., Ohno, T., Maetani, T., Ozaki, Y.: Machining of sintered steel under different lubrication conditions. *Mach. Sci. Technol. Int. J.* **22**(2), 338–352 (2018). <https://doi.org/10.1080/10910344.2017.1365893>
9. Shvets, S.V., Astakhov, V.P.: Effect of insert angles on cutting tool geometry. *J. Eng. Sci.* **7**(2), A1–A6 (2020). [https://doi.org/10.21272/jes.2020.7\(2\).a1](https://doi.org/10.21272/jes.2020.7(2).a1)
10. Yin, G., Gong, Y., Li, Y., Wang, F.: Investigation of the grinding temperature and subsurface quality of a novel point grinding wheel. *Int. J. Adv. Manuf. Technol.* **97**, 1565–1581 (2018)
11. Tao, Z., Yaoyao, S., Laakso, S., Jinming, Z.: Investigation of the effect of grinding parameters on surface quality in grinding of TC4 titanium alloy. *Procedia Manuf.* **11**, 2131–2138 (2017). <https://doi.org/10.1016/j.promfg.2017.07.344>
12. Wu, C., Li, B., Yang, J., Liang, S.Y.: Comparison of machining temperature in high speed grinding of metallic materials and brittle materials. *MATEC Web Conf.* **114**, 02006 (2017)
13. Liu, T., Deng, Z., Lv, L., Yi, J., She, S., Wan, L.: Theoretical and experimental study of temperature field in noncircular high-speed grinding. *Int. J. Adv. Manuf. Technol.* **107**(7–8), 3581–3592 (2020). <https://doi.org/10.1007/s00170-020-05295-w>
14. Ivanov, V., Pavlenko, I., Liaposhchenko, O., Gusak, O., Pavlenko, V.: Determination of contact points between workpiece and fixture elements as a tool for augmented reality in fixture design. *Wireless Netw.* **27**(3), 1657–1664 (2019). <https://doi.org/10.1007/s11276-019-02026-2>
15. Cioată, V.G., Kiss, I., Alexa, V., Rațiu, S.A., Racov, M.: Study of the influence of the cutting temperature on the magnitude of the contact forces in the machining fixtures. *IOP Conf. Ser. Mater. Sci. Eng.* **294** (2018). <https://doi.org/10.1088/1757-899x/294/1/012072>
16. Zabolotnyi, O., Pasternak, V., Andrushchak, I., Ilchuk, N., Svirzhevskiy, K.: Numerical simulation of the microstructure of structural-inhomogeneous materials. In: Ivanov, V., Trojanowska, J., Pavlenko, I., Zajac, J., Peraković, D. (eds.) *DSMIE 2020. LNME*, pp. 562–571. Springer, Cham (2020). https://doi.org/10.1007/978-3-030-50794-7_55
17. Mel'nik, V.M., Rud', V.D., Mel'nik, Y.A.: Mathematical formalism of pore stereology of powder materials. *Powder Metall. Met. Ceram.* **53**(1–2), 107–112 (2014). <https://doi.org/10.1007/s11106-014-9592-4>
18. Kuts, Y., Povstyanoy, O.: Computer-informative software for research of the new materials of constructional applications. *Funct. Mater.* **24**(1), 175–178 (2017). <https://doi.org/10.15407/fm24.01.175>
19. Tkachuk, A., Zablotskyi, V., Kononenko, A., Moroz, S., Prystupa, S.: Directed formation of quality, as a way of improving the durability of conjugated parts of friction pairs. In: Ivanov, V., et al. (eds.) *DSMIE 2019. LNME*, pp. 370–377. Springer, Cham (2020). https://doi.org/10.1007/978-3-030-22365-6_37

20. Liaposhchenko, O., et al.: Improvement of parameters for the multi-functional oil-gas separator of 'heater-treater' type. In: 2019 IEEE 6th International Conference on Industrial Engineering and Applications (ICIEA), Tokyo, Japan, pp. 66–71 (2019). <https://doi.org/10.1109/IEA.2019.8715203>
21. Tkachuk, A., Zabolotnyi, O., Chetverzhuk, T., Svirzhevskiy, K., Kononenko, A.: Increasing the wear resistance of the friction surfaces of rotating parts made of bearing steels through hardening processing methods. IOP Conf. Ser. Mater. Sci. Eng. Adv. Mater. Demanding Appl. **1060**, 012025 (2021). (AMDA 2020). <https://doi.org/10.1088/1757-899X/1060/1/012025>
22. Zablotskiy, V., Tkachuk, A., Moroz, S., Prystupa, S., Svirzhevskiy, K.: Influence of technological methods of processing on wear resistance of conjugated cylindrical surfaces. In: Tonkonogyi, V., et al. (eds.) InterPartner 2020. LNME, pp. 477–487. Springer, Cham (2021). https://doi.org/10.1007/978-3-030-68014-5_47
23. Pavlenko, I., Zajac, J., Kharchenko, N., Duplák, J., Ivanov, V., Kostyk, K.: Estimation of wear resistance for multilayer coatings obtained by nitrochroming. Metals **11**(8), 1153 (2021). <https://doi.org/10.3390/met11081153>
24. Hu, B., Warzel, R., Ropar, S., Rodrigues, H., Myers, C.: New machinability enhancer for improved machining of iron-copper-carbon materials. Met. Powder Rep. **71**(3), 12–26 (2015)
25. Bashistakumar, M., Pushkal, B.: Finite element analysis of orthogonal cutting forces in machining AISI 1020 steel by using a carbide tip tool. J. Eng. Sci. **5**(2), A1–A10 (2018). [https://doi.org/10.21272/jes.2018.5\(2\).a1](https://doi.org/10.21272/jes.2018.5(2).a1)
26. Li, H.N., Axinte, D.: Textured grinding wheels: a review. Int. J. Mach. Tools Manuf. **109**, 8–35 (2016). <https://doi.org/10.1016/j.ijmachtools.2016.07.001>
27. Santiuste, C., Diaz-Alvarez, J., Soldani, X., Miguelez, H.: Modeling thermal effects in machining of carbon fiber reinforced polymer composites. J. Reinf. Plast. Compos. **33**(8), 758–766 (2014)



Improvement of Quality Control Methods for Filters' Adsorbents in Purification of Gas Emissions of Nuclear Power Plants

Sergey Zaitsev^(✉) , Victor Kishnevsky , Gennadii Oborskyi ,
Anatoly Tikhomirov , and Valentin Tikhenko 

Odessa National Polytechnic University,
1, Shevchenko Avenue, Odessa 65044, Ukraine
sdjavdet@ukr.net

Abstract. The work aims to increase the reliability of the operation of adsorbents in filters for purifying gaseous emissions of nuclear power plants by monitoring the quality of adsorbents when determining their aerodynamic drag in a flow of dry and humid air and the content of impurities H₂O, N₂, O₂, Ar, CO, CH₄, CO₂, C₂H₄, C₂H₆, C₂H₂, C₃H₆, C₃H₈, C₄H₈, C₄H₁₀, CH₃J, Kr in these streams. Improved: installation for determining in a flow of gaseous air the values of the aerodynamic drag of adsorbents at $T = 293$ K and at linear velocities of air from 0,83 to 310 cm/s at the inlet to the adsorbents at a relative humidity of up to 95% and impurities from $5 \cdot 10^{-4}\%$ by volume and above, as well as to determine the adsorption capacity of adsorbents for impurities; block diagram of a 5-channel gas chromatography. At various constant linear velocities of airflows at the inlet to adsorbents – carbon fiber materials of the UUT-2, ANM, AMT, URAL-T-5 brands, there is no linear relationship between the aerodynamic drag and the number of layers of these materials. Aerodynamic drag depending on the brand of the adsorbent and the number of layers thereof are in the range from 5 Pa to 128,9 kPa. For carbon materials under air humidity $X_1 = 0,16$ g/m³ and $X_2 = 16,7$ g/m³ and its linear velocities $u_1 = 2$ cm/s, $u_2 = 100$ cm/s, $u_3 = 310$ cm/s, the values aerodynamic resistance does not depend on air humidity.

Keywords: Radioactive gas · Adsorption · Aerodynamic drag · Carbon adsorbent · Filter element · Iodomethane · Gas chromatography

1 Introduction

During the operation of NPP equipment, gaseous emissions are formed containing impurities of H₂O, N₂, O₂, Ar, CO, CH₄, CO₂, C₂H₄, C₂H₆, C₂H₂, C₃H₆, C₃H₈, C₄H₈, C₄H₁₀, CH₃J, Kr, Xe, J₂, many of which are radioactive [1]. These emissions must be discharged into the surrounding atmosphere after appropriate purification [2] using various adsorbents (activated carbons, silica gels, alum gels, zeolites) in special filters [3]. Quality control of such adsorbents before loading them into adsorption filters and during their operation is a prerequisite for reliable operation of gas purification systems for NPP emissions [4]. One of the main types of quality control of these

adsorbents is to determine the aerodynamic drag of adsorbents to the flow of gaseous air [5] and the adsorption capacity of adsorbents for vaporous impurities of radioactive iodomethane (CH_3I) [4]. The emergence of various brands of adsorbents and an increase in their quality require improving the schemes and designs of installations for determining the aerodynamic drag and adsorption capacity of adsorbents. The use of vapors of non-radioactive CH_3I for determining the adsorption capacity of adsorbents is promising, which requires improvement of measurement techniques for determining the concentrations of CH_3I vapor in gas streams.

2 Literature Review

The processes of thermal decomposition and oxidation of CH_3I were studied in [1], and it was found that the product of the chemical oxidation of CH_3I is iodine oxide, which can be captured on an inert carrier at a low temperature. Determination of the content of impurities in the analyzed streams is characterized by the complexity of measurement procedures using expensive measuring equipment. In [2], an analysis of data on emissions of inert radioactive gases (IRG) is given. It is shown that the composition of IRG is specific for each NPP (isotopes Ar, Xe determine at least 50% of the emission activity). The paper [3] considers methods for determining the content of the main radionuclides in gaseous emissions from NPP based on the use of techniques for performing measurements of radioactivity. Gas chromatography (GC) methods are not specified. In [4], the methods of performing measurements to determine the adsorption capacity of adsorbents using radioactive CH_3I vapors are considered, and the scheme of the measuring installation is described. In this case, equipment is used to measure the radioactivity of the adsorber sections with the adsorbent. It complicates the measurement procedures, requires expensive equipment, protects the ambient air from the emission of radioactive CH_3I vapors and their disposal. In [5], a study of the performance characteristics (aerodynamic drag; mechanical strength during abrasion; adsorption capacity of adsorbents for radioactive vapors J_2 and CH_3I) of activated carbons for adsorption filters of NPP ventilation systems was carried out. Diagrams of installations for measuring the adsorption capacity of adsorbents of J_2 and CH_3I vapors in the presence of atmospheric air and water vapors are given. However, a diagram of an installation for measuring aerodynamic drag to a gas flow is not provided. In work [6], isotherms and kinetic curves of adsorption of CH_3I , Kr, Xe, J, on NPP at $T = 293 \text{ K}$ are considered. Diagrams of experimental installations and methods of measurements of these substances in gas flows are not given. In [7], the influence of substances impregnating activated carbons (NaOH, KI, and ZnCl_2) on the quality of removal of radioactive CH_3I from the airflow using equipment for measuring the radioactivity of adsorber sections with an adsorbent was investigated. It requires expensive equipment and protects the ambient air from radioactive CH_3I vapors and their disposal. Experimental setup diagrams are not shown. A general approach to developing traps for radioactive organic iodine by creating materials impregnated with organic amines is described in [8]. These materials have a high adsorption capacity of adsorbents for CH_3I at a temperature of $T = 423 \text{ K}$. Techniques for performing measurements when determining the CH_3I concentrations in gas streams and schemes of

experimental installations are not indicated. In [9], a method was proposed for obtaining a sorbent for capturing radioactive iodine from gas streams. Data on the adsorption capacity of adsorbents for CH_3J at different test temperatures are presented. The diagram of the experimental setup is presented. Determination of CH_3J concentrations in gas streams by direct measurements was not performed. The amount of absorbed (decomposed) CH_3J was determined by the gravimetric method using a special absorber. These measurements require periodic weighing, which complicates the measurement procedures. It was shown in [10] that, at temperatures above 473 K, the decomposition of CH_3J to molecular J_2 begins, which can then be absorbed in a layer of metallic Ag. The diagram of the experimental setup is presented. The radioactivity of the sorbent blocks was measured on a gamma-X-ray spectrometer. It complicates the measurement procedures. The paper [11] presents a method for determining the adsorption capacity of adsorbents (carbon materials) using stable iodine isotopes. Diagrams of experimental installations are presented. The radioactivity of individual blocks of the sorbent after testing was measured on a gamma-X-ray spectrometer. A comparison of the methods for determining the adsorption capacity of adsorbents for the SKT-3I adsorbent using ^{131}I and ^{127}I vapors was performed in [12]. In this case, ^{127}I was determined in the carbon matrix by the X-ray radiation of the K-series of iodine atoms, and ^{131}I was determined by recording the induced gamma activity. It makes it possible to use these measurement techniques to assess the cleaning factor of the sorbents of carbon filters in the ventilation systems of nuclear power plants. It requires the use of expensive equipment, protection of ambient air from the release of radioactive vapors ^{131}I and ^{127}I , and their disposal. In [13], methods of performing measurements for the determination of components by GC methods (H_2O , H_2 , N_2 , O_2 , CO , CH_4 , CO_2 , C_2H_4 , C_2H_6 , C_2H_2 «Ionol» additive, water in turbine oil, turbine oil in water) dissolved in mineral turbine oils or water are considered. This work does not propose measurement techniques for determining impurities C_3H_6 , C_3H_8 , C_4H_8 , C_4H_{10} , CH_3J , Ar, Kr in gas flows. The paper [14] considers the measurement techniques for determining CH_3J vapors in the air using measuring equipment with a mass spectral detector. The use of such equipment requires the use of an expensive vacuum system and calibration mixtures. In [15], methods for determining CH_3J in gas flows using photoacoustic spectroscopy or GC are considered. Using the GC method, a capillary chromatographic column and units for expensive automatic control of the separated analyzed gas flows in the chromatography are used. In [16], the adsorption of gaseous ^{131}I at high temperatures by aluminum oxide impregnated with silver is considered. A diagram of the experimental installations is presented. The sorbent activity after testing was measured on a gamma-X-ray spectrometer.

Thus, it is necessary to conduct research aimed at improving the quality control methods of adsorbents for filters for purifying gas emissions from NPP containing vapor and gaseous impurities H_2O , N_2 , O_2 , Ar, CO , CH_4 , CO_2 , C_2H_4 , C_2H_6 , C_2H_2 , C_3H_6 , C_3H_8 , C_4H_8 , C_4H_{10} , CH_3J , Kr (hereinafter referred to as impurities). Implementation of these works will allow: to increase the reliability of operation of adsorbents in filters for purification of gaseous emissions from nuclear power plants; to improve the installations for quality control of adsorbents, and to develop a block diagram of a multichannel gas chromatography to determine the content of impurities in gaseous streams without the use of expensive methods of radiation monitoring and

radioactive control impurities; to determine the adsorption capacity of adsorbents for gas filters at nuclear power plants; to prevent the release of control radioactive gaseous impurities from the adsorbent quality control units into the environment. The work aims to increase the reliability of the operation of adsorbents in filters for purifying gaseous emissions of nuclear power plants by monitoring the quality of adsorbents when determining their aerodynamic drag in a flow of dry and humid air or nitrogen and the content of vaporous or gaseous impurities in these flows.

To achieve this goal, the following tasks were set:

- improvement of the block diagram of the installation to determine: the values of the aerodynamic drag of the adsorbents at various linear velocities (nitrogen) of the air at the entrance to the studied adsorbents; adsorption capacity of adsorbents for impurities in a stream of gaseous nitrogen (air);
- determining the aerodynamic drag values of layers of carbon fibrous materials in various amounts layers and linear air velocities (nitrogen) inlet investigated the carbon fibrous materials;
- development of a structural diagram and selection of the main characteristics of the elements of the measuring channels of a 5-channel gas chromatography for the determination of impurities in gaseous nitrogen (air);
- experimental determination of the metrological characteristics of the results of measurements of the content of impurities in the flow of gaseous nitrogen (air).

3 Research Methodology

3.1 Determination of the Aerodynamic Drag Value of Carbon Fiber Materials Layers

During the research, industrial carbon fiber materials of the UUT-2, ANM, AMT, URAL-T-5 brands were used. The thicknesses of one layer of the investigated carbon fiber materials were as follows: UUT-2 – 0,6 mm; ANM – 2,3 mm; AMT – 1,15 mm; URAL-T-5 – 0,6 mm. The measurements were carried out at a temperature $T_0 = 293$ K. The values of the water vapor content in the air $X_1 = 0,16$ g/m³ (dew point temperature $T_1 = 233$ K) and $X_2 = 16,7$ g/m³ (dew point temperature $T_2 = 293$ K, relative humidity $\varphi = 95\%$). Linear velocity (u) of dry air flow ($X_1 = 0,16$ g/m³) at the entrance to the first layer of carbon fiber material had values in the range $u = 0,83... 310$ cm/s. For all investigated carbon fiber materials at values $X_1 = 0,16$ g/m³ and $X_2 = 16,7$ g/m³, the linear air flow rates were $u_1 = 2$ cm/s, $u_2 = 100$ cm/s, $u_3 = 310$ cm/s.

Figure 1 shows an improved block diagram of the installation for determining the value of the aerodynamic drag ΔP of layers of carbon fibrous materials at various numbers of layers n and linear velocities u of air at the inlet to the filter element, as well as for determining the values of adsorption by adsorbents of impurities from a stream of gaseous N_2 (air).

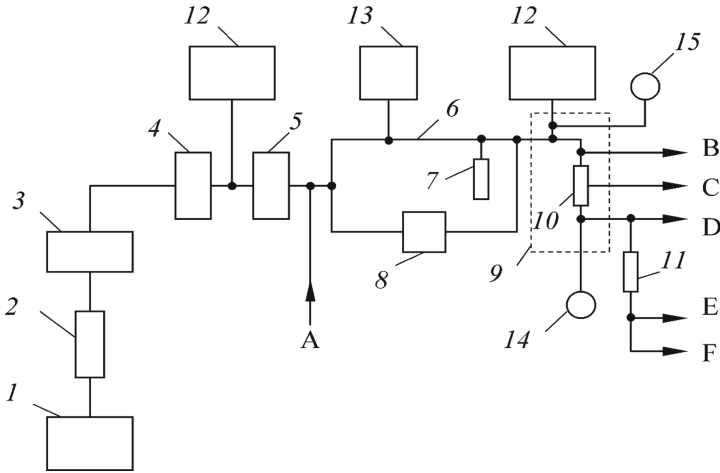


Fig. 1. Block diagram of the installation for determining the value of the aerodynamic resistance of layers of carbon fiber materials and the values of adsorption by adsorbents of impurities H₂O, N₂, O₂, Ar, CO, CH₄, CO₂, C₂H₄, C₂H₆, C₂H₂, C₃H₆, C₃H₈, C₄H₈, C₄H₁₀, CH₃J, Kr from a stream of gaseous N₂ (air): 1 - source of a stream of gaseous N₂ (air); 2 - flow meter; 3 - aerosol filter; 4 - desiccant; 5 - adsorption filter; 6 - introduction of CH₃J vapors into the flow of gaseous N₂ (air); 7 - liquid CH₃J evaporator; 8 - humidifier for the flow of gaseous N₂ (air); 9 - thermostat; 10 - sectioned adsorption column with the investigated adsorbent; 11 - protective column; 12 - regulator of humidity, temperature, absolute pressure and differential pressure; 13 - dispenser of gaseous impurities into the flow of gaseous N₂ (air); 14, 15 - pressure meter; A, B, D, E - lines for periodic supply of N₂ (air) flows to the gas chromatography; C - line for supplying flows of N₂ (air) to the gas chromatography from the sections of the adsorption column (pos. 10); F - purified stream of N₂ (air) to the atmosphere.

The values of aerodynamic drag ΔP of layers of carbon fiber materials of the above grades were experimentally determined for different numbers of layers, n , and linear velocities, u , of gas (air) at the inlet to the filter element.

When determining the aerodynamic drag ΔP by layers of carbon fiber materials, the absolute value of the resulting error does not exceed 2 Pa at a pressure drop of up to 600 Pa and 8 Pa at a pressure drop of up to 2400 Pa.

As an example, Fig. 2 shows the dependence of the aerodynamic drag ΔP for three layers of carbon fiber material of the UUT-2 type on the linear air velocities u .

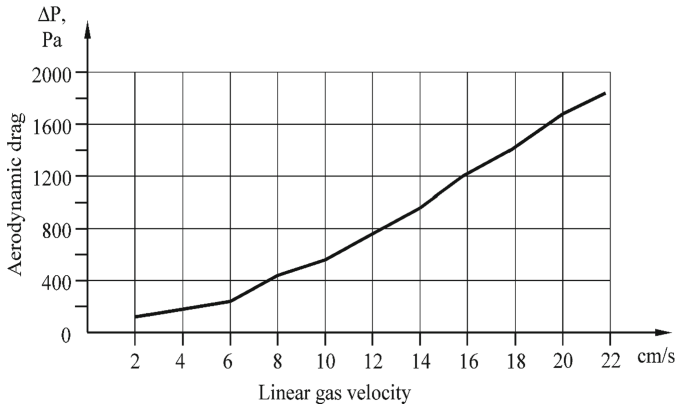


Fig. 2. Dependence of the aerodynamic drag ΔP for three layers of carbon fiber material UUT-2 type on the linear gas velocities u at the entrance to the filter element.

3.2 Development of a Block Diagram of a 5-Channel Gas Chromatography

Figure 3 shows the developed block diagram of a 5-channel gas chromatography for determining impurities in a nitrogen flow.

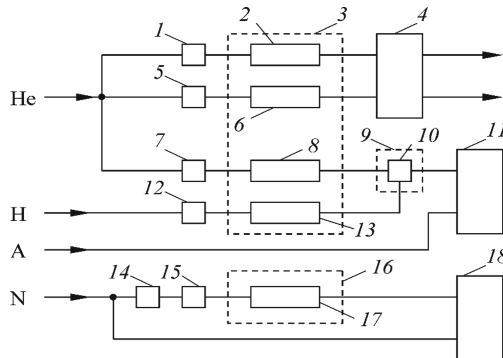


Fig. 3. Block diagram of a 5-channel gas chromatography for determining impurities stream of N_2 (air): 1, 5, 7, 12, 14 - gas metering valves with calibrated metering loops; 2, 6, 8, 13, 17 - chromatographic columns; 3, 9, 16 - thermostats; 4 - thermal conductivity detector (TCD); 11 - flame ionization detector (FID); 15 - evaporator; 18 - electron capture detector (ECD); He, H, A, N - helium, hydrogen, air, nitrogen, respectively.

Table 1 shows the main characteristics of the elements of the measuring channels of a 5-channel gas chromatography to determine impurities.

Table 1. Main characteristics of the elements of the measuring channels of a gas chromatography for the determination of impurities in a flow of gaseous nitrogen.

Channel	Determined components	Characteristics of measuring channel elements
No. 1	Of H ₂ O vapors in nitrogen (air)	Chromatographic column (position 2) – «Polysorb-1» sorbent; gas metering valve (position 1); $t_{cc} = 120$ °C, $t_{tcd} = 150$ °C; working chamber of the TCD (position 4)
No. 2	Of gases Kr, H ₂ , O ₂ , Ar, O ₂ + Ar in nitrogen (air)	Chromatographic column (position 6) – «NaX» sorbent; gas metering valve (position 5); $t_{cc} = 60$ °C, $t_{tcd} = 100... 150$ °C, comparative detector chamber for TCD (position 4)
No. 3	Of gases CO, CH ₄ , CO ₂ , C ₂ H ₄ , C ₂ H ₆ , C ₂ H ₂ in nitrogen (air)	Chromatographic column (position 8) – sorbent «Porapak N80/100»; gas metering valve (position 7); $t_{cc} = 40$ °C, $t_m = 325$ °C, $t_{fid} = 200$ °C, $v = 12$ °C/min from $t_{cc} = 40$ °C to $t_{cc, fin} = 180$ °C, FID (position 11), helium carrier gas line
No. 4	Of gases CH ₄ , C ₃ H ₆ , C ₃ H ₈ , C ₄ H ₁₀ , C ₄ H ₈ in nitrogen (air)	Chromatographic column (position 13) – «Al ₂ O ₃ » sorbent; gas metering valve (position 12); $t_{cc} = 40$ °C, $t_m = 325$ °C, $t_{fid} = 200$ °C, $v = 12$ °C/min from $t_{cc} = 40$ °C to $t_{cc, fin} = 180$ °C, FID (position 11), hydrogen line
No. 5	the content of CH ₃ J vapors in nitrogen (air)	Chromatographic column (position 15) - sorbent «Inerton-super», impregnated with 5% by weight of 1,2,3-tris (2-cyanethoxy) propane; gas metering valve (position 14); $t_{cc} = 40$ °C, $t_{ecd} = 220$ °C, $v = 12$ °C/min from $t_{cc} = 40$ °C to $t_{cc, fin} = 110$ °C, $t_e = 80$ °C, ECD (position 18)

In Table 1: t_{cc} , t_{tcd} , t_{fid} , t_{ecd} , t_m , t_e – temperatures of chromatographic columns (t_{cc} – initial, $t_{cc, fin}$ – final) TCD, FID, ECD, methanator, evaporator, respectively, °C; v is the rate of programming the temperature of the chromatographic columns, °C/min (Table 2).

Table 2. Values of the limits of the permissible relative error δ_i for determining the concentrations of the analyzed impurities C_i in gaseous nitrogen by gas chromatography methods depending on the concentration range.

The range of concentrations of the analyzed impurities, C_i % volumetric				δ_i , %
H ₂ , O ₂ , N ₂ , Ar, vapor H ₂ O	CH ₄ , C ₂ H ₄ , C ₂ H ₆ , C ₃ H ₆ , C ₃ H ₈ , C ₄ H ₈ , C ₄ H ₁₀	C ₂ H ₂	CO, CO ₂	
$<5 \cdot 10^{-3}$	$<10^{-3}$	$<5 \cdot 10^{-4}$	$<5 \cdot 10^{-3}$	≥ 50
$(5...25) \cdot 10^{-3}$	$(1...3) \cdot 10^{-3}$	$(5...15) \cdot 10^{-4}$	$(5...25) \cdot 10^{-3}$	<50
$(25...50) \cdot 10^{-3}$	$(3...50) \cdot 10^{-3}$	$(1,5...25) \cdot 10^{-3}$	$(25...100) \cdot 10^{-3}$	≤ 20
$>5 \cdot 10^{-2}$	$>5 \cdot 10^{-2}$	$>5 \cdot 10^{-2}$	$>0,1$	≤ 10

To determine the thresholds for determining the concentrations of H₂O vapors in gas streams and gadding the chromatography, mixtures of H₂O vapors in gaseous

helium were used. At concentrations of H_2O vapors from $0,16 \text{ g/m}^3$ to 17 g/m^3 ; mixtures of gases H_2 , CH_4 , C_2H_6 , C_2H_4 , C_2H_2 , Ar, CO, CO_2 , O_2 , N_2 , C_3H_6 , C_3H_8 , C_4H_8 , C_4H_{10} in gaseous He (Ar, N_2 , air) were used for impurities in gas streams and for gadding the chromatography, at the concentration of each impurity at the level of 0,5% by volume; For CH_3J vapors in gas streams and for gadding the chromatography, we used calibration solutions with a CH_3J content in heptane at a CH_3J concentration from 0,005 to $0,01 \text{ }\mu\text{g/cm}^3$.

In the improved scheme of the installation to determine the values of adsorption of impurities H_2 , O_2 , Ar, CO, CH_4 , CO_2 , C_2H_4 , C_2H_6 , C_2H_2 , C_3H_6 , C_3H_8 , C_4H_8 , C_4H_{10} , Kr, by adsorbents of the gaseous N_2 stream, a dispenser of these impurities into the gaseous N_2 stream is used. The principle of operation of this dispenser is based on metering these impurities, which are in the form of a gas mixture in gaseous N_2 in a cylinder, through a capillary into a stream of gaseous N_2 (air). Sampling points for gaseous N_2 when testing granular adsorbents should be located after each section of the adsorption column with the adsorbent under study. When examining carbon fibrous materials, sampling points for gaseous N_2 should be placed before and after the adsorption column with the adsorbent under study. In this case, the calculated values of the partial pressure of CH_3J vapors in the flow of gaseous N_2 are in the range of 4 to 375 mm Hg.

4 Results

When determining the value of the aerodynamic drag ΔP of layers of carbon fiber materials with different numbers of layers and linear velocities of air at the entrance to the layer of carbon fiber material, the following was established:

1. At constant values of n numbers for layers of carbon fiber materials (Fig. 2), the relationship between aerodynamic drag ΔP and linear velocities of N_2 (air) flow at the entrance to the layer of carbon fiber material is nonlinear.
2. At constant but different linear velocities of airflows at the entrance to the layer of carbon fiber material, there is no linear relationship between the aerodynamic drag ΔP and the number of layers n for the carbon fiber material. This requires designing adsorption filters using the investigated carbon fiber materials to carry out preliminary experimental studies to select the appropriate material.
3. At a linear airflow velocity at the entrance to the layer of carbon fiber material of 310 cm/s, no mechanical rupture of the investigated carbon fiber materials occurred. It makes it possible to design adsorbents using the investigated carbon fiber materials at a linear airflow velocity of up to 310 cm/s.
4. For all investigated carbon fibrous materials with the values of airflow humidity $X_1 = 0,16 \text{ g/m}^3$ and $X_2 = 16,7 \text{ g/m}^3$ and linear airflow velocities $u_1 = 2 \text{ cm/s}$, $u_2 = 100 \text{ cm/s}$, $u_3 = 310 \text{ cm/s}$, the values of the corresponding aerodynamic resistance ΔP do not depend on the moisture content. It indicates the absence of water vapor condensation in the layers of the investigated carbon fiber materials, which can increase the aerodynamic resistance to the airflow. It makes it possible to determine the values of the aerodynamic drags of adsorbents at a temperature of

$T = 293$ K, the absolute humidity of N_2 or air flows from 0,16 to 16,7 g/m^3 (relative humidity up to 95%), and linear velocities of N_2 (air) flows from 0,83 up to 310 cm/s.

When developing a block diagram of a 5-channel gas chromatography for determining impurities in a nitrogen flow (see Fig. 3), the following was established:

1. The calculated value of the threshold for determining the moisture content N_2 is 0,16 g/m^3 at the volume of the calibrated dose of the gas dispenser $V_d = 1$ cm^3 with the relative error of the measurement result not exceeding 40% at the confidence level $p = 0,95$. The calculated value of the detection threshold is $1,6 \cdot 10^{-7}$ g for H_2O vapor. It corresponds to the data given in [13].
2. The permissible relative total error of determining Kr (Xe) in gaseous N_2 does not exceed 20% at a confidence level of $p = 0,95$.
3. When determining the contents: CO, CH_4 , CO_2 , C_2H_4 , C_2H_6 , C_2H_2 in gaseous N_2 , the sample (or calibration gas mixtures) is introduced into the chromatography using the gas metering valve (pos. 7); CH_4 , C_3H_6 , C_3H_8 , C_4H_{10} , C_4H_8 in gaseous N_2 , a sample (or calibration gas mixtures) is introduced into the chromatography using a gas metering valve (pos. 12); H_2 , O_2 , N_2 , Ar in gaseous N_2 , a sample (or calibration gas mixtures) is introduced into the chromatography using a gas metering valve (pos. 5).

Table 3 shows the values of the limits of the permissible relative error δ_i for determining the concentrations of the analyzed impurities C_i in gaseous nitrogen by gas chromatography methods depending on the concentration range.

The values of the relative standard deviation (RSD, %) of the output signal for the TCD, FID, ECD of the gas chromatography (height, area, retention time of the chromatographic peak), depending on the concentration range of the analyzed impurities C_i % by volume, do not exceed the values, given in Table 3.

Table 3. The values of the relative standard deviation.

C_i , %	less than 0,002	from 0,002 to 0,01	from 0,01 to 0,1	from 0,1 to 1	from 1 to 10
RSD %	more than 10	10	2	2	1

4. When determining the content of non-radioactive CH_3J in the flow of gaseous N_2 : the lower limit of measurement in the chromatographed volume – 0,005 μg ; the lower limit of measurement in the N_2 sample is 0,005 mg/m^3 (sample volume 1 cm^3). The range of measured concentrations of CH_3J in N_2 is from 0,005 to 0,1 mg/m^3 . If the concentration of CH_3J in gaseous N_2 is more than 0,1 mg/m^3 , the analyzed sample must be diluted with pure gaseous N_2 . The calculated value of the permissible relative error of the measurement result does not exceed 10% at a confidence level of $p = 0,95$. Measurement time is approximately 5 min.

5 Conclusions

The block diagram of the installation for determining in laboratory conditions the values of the aerodynamic resistance of adsorbents at various linear velocities of N₂ (air) at the entrance to the adsorbents under study has been improved. The values of aerodynamic resistance of layers of carbon fibrous materials of the UUT-2, ANM, AMT, URAL-T-5 grades were determined at various layers and linear velocities of air at the entrance investigated carbon fibrous materials. It has been found that at different but constant linear velocities of airflows at the entrance to carbon fiber materials, there is no linear relationship between the aerodynamic drag and the number of layers of carbon fiber materials. This requires preliminary experimental studies when selecting carbon fiber material for adsorption filters. At a linear airflow velocity at the entrance to carbon fiber materials of 310 sm/s, no mechanical rupture of the investigated carbon fiber materials occurred. It makes it possible to design absorbers using the investigated carbon fiber materials at a linear airflow velocity at the inlet to carbon fiber materials up to 310 cm/s.

A structural diagram has been developed, and the characteristics of the elements of the measuring channels of 5-channel gas chromatography for the determination of impurities H₂O, N₂, O₂, Ar, CO, CH₄, CO₂, C₂H₄, C₂H₆, C₂H₂, C₃H₆, C₃H₈, C₄H₈, C₄H₁₀, CH₃J, Kr in a stream of gaseous N₂ (air) using TCD, FID, ECD detectors are determined. It allows to determine the specified impurities using one gas chromatography, simplify and reduces the cost of measurement processes.

The metrological characteristics of the results of measurements of the impurity contents of H₂O, N₂, O₂, Ar, CO, CH₄, CO₂, C₂H₄, C₂H₆, C₂H₂, C₃H₆, C₃H₈, C₄H₈, C₄H₁₀, CH₃J in a stream of gaseous N₂ (air) have been determined. When determining the content of non-radioactive CH₃J, the lower limit of measurement is 0,005 mg/m³.

It has been improved block diagram of the installation for determining in laboratory conditions the values of adsorption by porous adsorbents of impurities H₂O, N₂, O₂, Ar, CO, CH₄, CO₂, C₂H₄, C₂H₆, C₂H₂, C₃H₆, C₃H₈, C₄H₈, C₄H₁₀, CH₃J, Kr from a stream of gaseous N₂ (air). It has been established that when determining the adsorption capacity of adsorbents when absorbing vapors of non-radioactive CH₃J, the use of gas chromatography for performing analyzes excludes the use of radioactive liquid CH₃J.

References






1. Pyshkina, M.D.: Determination of the main dose-forming nuclides in emissions from PWR and VVER NPPs. *Biosph. Compat. Hum. Reg. Technol.* **2**(18), 98–107 (2017)
2. Merkushev, A.O., Obruchikov, A.V., Magomedbekov, E.P.: Oxidation of iodomethane vapors in air. *Theor. Found. Chem. Technol.* **53**(4), 440–445 (2019)
3. Ekidin, A.A., Zhukovsky, M.V., Vasyanovich, M.E.: Identification of the main dose-forming radionuclides in NPP emissions. *At. Energ.* **120**(2), 106–108 (2016)
4. Magomedbekov, E.P., Obruchikov, A.V.: A method for properties evaluation of activated charcoal sorbents in iodine capture under dynamic conditions. *Nucl. Eng. Technol.* **51**, 641–645 (2019)

5. Sokolenko, V.I., Khazhmuradov, M.A., Vinokurov, E.I., Grigorova, T.K., Sibileva, R.M., Sharuda, D.V.: Investigation of the complex of properties of adsorbents intended for restoration of filters of ventilation systems of nuclear power plants. *Atomic Sci. Technol. Issues* **2**(90), 85–88 (2014)
6. Tamarkina, Y., Shendrick, T.G.: Lignite adsorbents for capturing ecotoxicants from water and air. *Ecol. Ind.* **4**, 45–48 (2010)
7. Gourani, M., Sadighzadeh, A., Mizani, F.: Effect of impregnating materials in activated carbon on Iodine-131 (¹³¹I) removal efficiency. *Radiat. Prot. Environ.* **37**(3, 4), 179–183 (2014)
8. Li, B., et al.: Capture of organic iodides from nuclear waste by metal-organic framework-based molecular traps. *Nat. Commun.* **8**(485), 1–9 (2017)
9. Grishin, Ya.S., Obruchikov, A.V.: Development of a method for manufacturing a silver-containing iodine adsorbent based on oxide ceramics. In: *Advances in Chemistry and Chemical Technology: Collection of Articles (2020)*. scientific. tr. T. XXXIV, 9(232), 20–22
10. Gasparyan, M.D., et al.: Capture of gaseous methyl iodide on ceramic highly porous block-cellular sorbents in an inert medium. *Chem. Ind. Today* **4**, 34–42 (2015)
11. Levenets, V.V., et al.: Determination of the coefficient of iodine absorption by carbon materials of adsorbents of NPP ventilation systems using stable isotopes. *Atomic Sci. Technol. Issues* **1**(101), 56–60 (2016)
12. Levenets, V.V., Lonin, A., Omelnik, A.P., Sokolenko, V.I., Shchur, A.A.: Comparative assessment of the sorption properties of carbon filters used in the ventilation system of nuclear power plants using ¹³¹I and ¹²⁷I. *Nucl. Phys. Energy* **18**(1), 37–42 (2017)
13. Zaitsev, S., Kyshnevsky, V., Chichenin, V., Tykhomyrov, A.: Development of methods of gas chromatographic analysis of technological media of the main circulation pumps of a nuclear power plant. *Eastern-Eur. J. Enterp. Technol.* **6**(108), 59–70 (2020)
14. Mekić, M., Temime-Roussel, B., Monod, A., Strekowski, R.S.: Quantification of gas phase methyl iodide using H₃O⁺ as the reagent ion in the PTR-MS technique. *Int. J. Mass Spectrometry* **424**, 10–15 (2018)
15. Chebbi, M., Doizi1, D., Manceron, L., Perrin, A., Auwera, J.V., Tchana, F.K.: On line measurement of organic iodine during a severe nuclear accident. *EPJ Web Conf.* **225** (08001), 1–3 (2020)
16. Qing-Hui, C., Li, Z.-J., Chu, T.-W.: Adsorption of gaseous iodine-131 at high temperatures by silver impregnated alumina. *Nuclear Sci. Tech.* **26**, 040303-1–040303-5 (2015)

Mechanical Engineering



The Stress State of the Workpiece at the Radius of Matrix Rounding During Drawing, Considering the Bending Moment

Roman Arhat¹ , Ruslan Puzyr² , Viktor Shchetynin¹ ,
Roman Levchenko² , and Oleksandr Pedun¹ 

¹ Kremenchuk Mykhailo Ostrohradskyi National University,
20, Pershotravneva Street, Kremenchuk 39600, Ukraine

² Kremenchuk Mykhailo Ostrohradskyi National University College,
7, Chumatskyi Shliakh Street, Kremenchuk 39621, Ukraine

Abstract. Most of the research aims to find and introduce production methods of drawing that make it possible to manufacture parts with given mechanical characteristics in local areas, using various technological methods. However, the variety of ways to increase the deformation and wall thickness of the final product is based on a deep theoretical analysis of the process and knowledge of the laws governing the development of plastic flow in the deformation zone. Mathematical modeling of cold plastic metal working processes is an essential and helpful tool for studying the laws governing the transition of workpieces to a plastic state. Such analytical expression is obtained in the paper for calculating the increment of meridional stresses on the drawing edge of the matrix when drawing cylindrical parts. Considering the bending moment acting in the meridional direction in the equilibrium equations is an essential aspect of the formula. An increase in tensile stresses is facilitated by a decrease in the matrix rounding radius and an increase in the thickness of the workpiece. The obtained conclusions allow us to recommend the formula for use in production when designing die tooling, especially when drawing thin-walled parts.

Keywords: Meridional stress · Sheet workpiece · Yield condition

1 Introduction

Drawing as a cold stamping process is used to make cylindrical parts with and without a flange from a sheet workpiece [1]. The complexity of this process of obtaining cylindrical products lies in the following fact. When the workpiece is pulled into the hole of the matrix, stability loss of the flat flange is observed [2]. Wavy folds form on the flange, which interferes with normal process flow [3]. As a result of punch's lowering, the retraction of the flange into the hole of the matrix stops. Therefore, the workpiece is lengthened due to the stretching of the cylindrical walls [4]. These results localize deformations in the walls of the formed cup and at the radius of the punch curvature [5]. In turn, the localization of deformation in these zones contributes to a decrease in the wall thickness of the semi-finished product and its destruction in the form of a crack formation at the transition of the wall to the bottom or on the wall [6].

A flat or tapered ring clamp is used to prevent the formation of folds on the initially flat flange [7]. This somewhat complicates the design of the tooling but eliminates corrugation [8]. Such technological factors as the radius of curvature of the matrix drawing edge, the gap between the wall of the matrix and the workpiece, the punch rounding radius, lubrication of rubbing surfaces, and their cleanliness are of great importance for drawing operation [9]. Considering such a huge number of factors to obtain high-quality parts is impossible without a theoretical analysis of this process [10]. Carrying out such an analysis will allow one, with mathematical accuracy, to determine the most significant combination of the main characteristics of the drawing process that affect the stability of plastic deformation and to identify the most optimal conditions for deformation in terms of quality, energy efficiency, reduction of labor intensity and cost [11].

2 Literature Review

The theoretical study of the drawing process has drawn sufficient attention, starting with papers devoted to the theory of plasticity and research aimed at studying the technological influence on the plastic behavior of the workpiece [12]. These studies continue at the moment, which indicates the scientific and practical interest in this operation of sheet stamping [13]. This is caused by the fact that in the modern production of aircraft, automobiles, apparatuses for the petrochemical industry, electrical engineering, and agricultural machinery, up to 50% of parts are produced by drawing operation [14]. Therefore, most of the work aims to find and introduce production methods of drawing, making it possible, using various technological methods to manufacture parts with given mechanical characteristics in local areas [15]. An extensive review of such drawing methods is given in the paper by Wang [16], describing methods for increasing the thickness of the radial transition between the wall and the bottom of a cylindrical and conical part. In [17], the choice of the geometric shape of the workpiece and the presence of a weld seam are considered. This increases the degree of deformation of the workpiece.

However, the variety of ways to increase the deformation and wall thickness of the final product is based on a deep theoretical analysis of the process [18]. For example, the introduction of plane anisotropy into the mathematical model of the drawing process complicates it for theoretical analysis [19], but the solutions acquire greater accuracy than formulations based on assumptions about an isotropic elastoplastic workpiece material [20]. Supplementing theoretical models, it possible to determine the friction conditions on the flange and the radius of curvature of the drawing edge [21]. Special software systems for finite element modeling of metal forming processes present great opportunities for researchers [1]. In [22], the results of a numerical calculation of the drawing consider the plane anisotropy of the material with kinematic hardening and the elastoviscoplastic material of the workpiece, respectively [23]. In this formulation of the problem, its solution in quadratures is practically impossible [24]. The impact of the gap and the radius of curvature on the stress-strain state of the workpiece is considered in the paper [25]. In turn, analytical solutions are universal for various types of loading and deformation conditions of the workpiece [26]. They give a

reasonably accurate, visual picture of the deformation of the workpiece and make it possible to estimate the regularities of plastic deformation and the influence of technological factors on the course of the drawing process [27].

3 Research Methodology

Since the drawing edge of the matrix is the main structural element of the die tooling, on which the degree of elongation [28], the quality of the surface layer of the part [29], and the loss of stability depend [30], the dependence of the stress distribution on the design and technological factors of the drawing process in this particular area is of great interest [31]. The problem was considered in the following formulation [32]: in the workpiece, a section was separated, which entered the drawing edge of the matrix, by two sections parallel to the circumferential direction (Fig. 1); internal forces simulating the cut-off part of the workpiece were applied to the boundaries of the section; it was assumed that the section of the workpiece that entered the edge of the matrix takes the form of a toroidal surface of revolution (Fig. 2). Therefore, to solve the problem, we used the technical theory of shells [33].

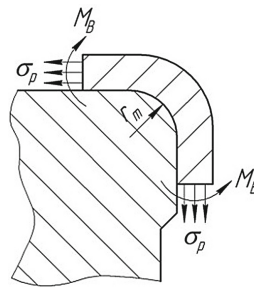


Fig. 1. Workpiece zone in the bending section of the matrix.

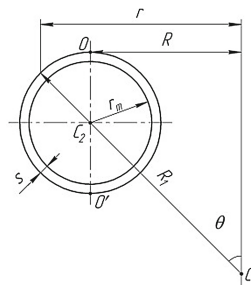


Fig. 2. The toroidal surface of revolution.

Then the equilibrium equations for the section of the workpiece shown in Fig. 1, taking into account the bending moment acting in the meridional direction, and the assumptions given above, take the form [34]

$$\frac{\partial((A_1)N_2)}{\partial\theta} - N_1 \frac{\partial A_1}{\partial\theta} - M_1 \frac{\partial A_1}{R_2 \partial\theta} = 0, \tag{1}$$

where $A_1 = R_1 \sin \theta = \frac{r_m(1+k \sin \theta)}{k \sin \theta}$ – coefficient of the first quadratic form [35]; N_1, N_2 – internal tangential and meridian forces; θ – polar angle in the meridian plane (coordinate axis); $R_2 = r_m$ – principal radius of curvature corresponding to the meridian; M_1 – bending moment acting in the meridian direction; $k = \frac{r_m}{R}$ [36]; $R = R_m + r_m$ – distance from the axis of symmetry to the center of the section; r_m – matrix radius; R_m – matrix entrance hole radius; s – workpiece thickness.

Differentiating Eq. (1), we have the following equality [37]

$$\frac{\partial N_2}{\partial\theta} \frac{1}{k} (1 + k \sin \theta) + (N_2 - N_1) \cos \theta - M_1 \frac{\cos \theta}{r_m^2} = 0. \tag{2}$$

To solve the reduced equilibrium Eq. (2), we use the condition to transition metal to a plastic state according to the hypothesis of maximum tangential stresses [38]. For the case of the opposite stress state circuit, which is observed during drawing, considering $N_2 = s\sigma_\rho$ and $N_1 = s\sigma_\theta$, it will have the form [39]

$$\left. \begin{aligned} M &= \frac{s^2}{4N_s} (N_s^2 - N_2^2) \\ N_2 - N_1 &= N_s \end{aligned} \right\} \tag{3}$$

where N_s – internal force causing plastic deformation [40].

Eliminating N_1 from the equilibrium Eq. (2) by substituting (3), we get

$$\frac{\partial N_2}{\partial\theta} + \frac{ks^2 \cos \theta}{4N_s r_m^2 (1 + k \sin \theta)} N_2^2 = -N_s \frac{k \left(1 - \frac{s^2}{4r_m^2}\right) \cos \theta}{(1 + k \sin \theta)} \tag{4}$$

To solve Eq. (4) in quadratures, the presence of a particular solution for N_2 is a necessary condition [41]. Earlier, an expression was obtained for calculating the internal meridional forces on the drawing edge of the matrix during drawing under the assumption of the momentless stress state [42]

$$N_2 = -N_s \ln(1 + k \sin \theta) + C. \tag{5}$$

We take this solution as a particular one and, carrying out simple transformations, and obtained [43]:

$$\frac{\partial N_2}{\partial\theta} + \frac{ks^2 \cos \theta}{2r_m^2} N_2 = -\frac{ks^2 \cos \theta}{4N_s r_m^2 (1 + k \sin \theta)} N_2^2. \tag{6}$$

Transforming the resulting equation to our conditions and integrating it, we will have

$$N_2 = N_s \frac{2r_m^2 e^{\frac{k^2}{2r_m^2} \sin \theta}}{ks^2 \ln(1 + k \sin \theta)} + C. \tag{7}$$

Expanding functions $e^{\frac{k^2 \sin \theta}{2r_m^2}}$ and $\ln(1 + k \sin \theta)$ into a series [44], we obtain an expression for determining the internal meridional effort

$$N_2 = N_s \left(\frac{2}{k} + \frac{2s^2}{r_m^2} \sin \theta \right) + C. \tag{8}$$

An arbitrary constant is determined from the boundary conditions in the section of flange radius of curvature, where the meridional stresses are of the value $\sigma_\rho = \sigma_s \ln \frac{R_w}{R_m + r_m}$, $\theta = 0$ [45]. Here R_w – the radius of the workpiece, then, passing to stresses, we finally find

$$\sigma_\rho = \sigma_s \left(\ln \left(\frac{R_w}{R_m + r_m} \right) + \frac{2s^2}{r_m^2} \sin \theta \right). \tag{9}$$

The most significant meridional stresses will act when the metal of the workpiece completely covers the edge of the matrix, i.e., at $\theta = \pi/2$ and $\sin \theta = 1$ [46]. Equation (9) take the following form

$$\sigma_\rho = \sigma_s \left(\ln \left(\frac{R_w}{R_m + r_m} \right) + \frac{2s^2}{r_m^2} \right). \tag{10}$$

4 Results

It is of interest to compare the obtained data with the previously conducted research in this direction by Popov [42], who proposed the following formula to take into account the bending and straightening of the metal at the radius of the matrix curvature [47]:

$$\Delta \sigma_\rho = \frac{1}{4} \sigma_s \frac{s}{r_m + \frac{s}{2}}. \tag{11}$$

Below are the graphs for calculating the value of the increment in meridional stresses, calculated in the Mathcad environment, for the following characteristics: $R_w = 100$ mm, $s = 1-3$ mm, $R_d = 60$ mm, $r_m = 2-10$ mm.

As can be concluded from Fig. 3, meridional stresses increase with an increase in the workpiece’s thickness, which corresponds to the concepts of the theory of bending and drawing [40]. However, if Popov’s distribution has a linear dependence of the value of stresses on the thickness of the workpiece, stresses (10) depend on the thickness of the workpiece nonlinearly and approximately resembles a parabola [48].

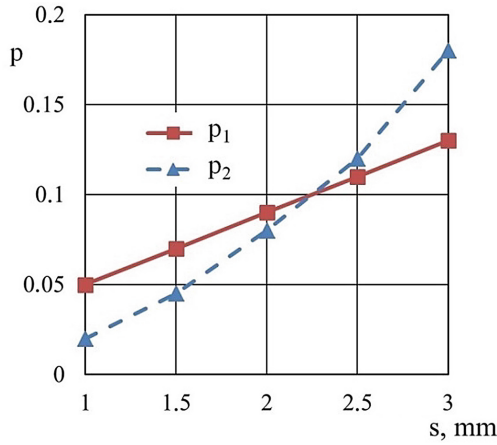


Fig. 3. The increment in meridional stresses at the drawing edge of the matrix depending on the change in the thickness of the workpiece at $r_m = 10$ mm: p_1 – increment of meridional stresses according to Popov’s dependence, ($p_1 = \sigma_p/\sigma_s$); p_2 – increment of meridional stresses by dependence (10), ($p_2 = \sigma_p/\sigma_s$).

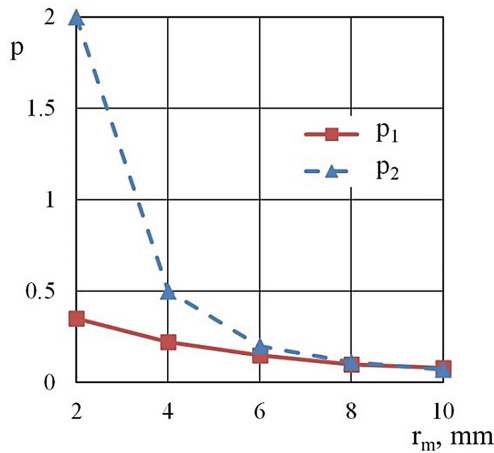


Fig. 4. The increment of the meridional stresses at the drawing edge of the matrix, depending on the change in the value of the radius of its rounding at $s = 2$ mm: p_1 – increment of meridional stresses according to Popov’s dependence, ($p_1 = \sigma_p/\sigma_s$); p_2 – increment of meridional stresses by dependence (10), ($p_2 = \sigma_p/\sigma_s$).

It can be seen in Fig. 4 that in the region of small radii of curvature, the increase in meridional stresses according to dependence (10) is of a sufficiently high value, which almost doubles the meridional stresses that act in the flange. In the range of 6–10 mm, both formulas give almost identical results [49].

5 Conclusions

The theoretical analysis of the drawing process has made it possible to obtain an analytical dependence for determining the meridional stresses on the drawing edge of the matrix, which enables one to more accurately determine the increment of stresses from bending during the transition of the workpiece metal via the rounded edge of the matrix. A decrease in the matrix rounding radius and an increase in the workpiece thickness increases tensile stress. This fact does not contradict the physical aspect of plastic deformation when drawing cylindrical parts.

Comparing the obtained results with those existing earlier and used at present in production for technological calculations revealed that the results practically coincide in some regions of technological parameters. They include the area of $r_m = 6\text{--}10$ mm with $s = 2$ mm and point $s = 2.2$ mm with $r_m = 10$ mm. Therefore, we can conclude that both formulas are equal, but dependence (10) will more accurately describe the stress distribution on the drawing edge of the matrix in the area of its small values of 1–5 mm. This makes it possible to recommend formula (10) for production when designing die tooling, especially when drawing thin-walled parts.

Further research on this topic will be focused on setting up and conducting experiments aimed at confirming the adequacy of the dependence obtained in the area of small workpiece thicknesses.

References

1. Yang, C., Li, P., Fan, L.: Blank shape design for sheet metal forming based on geometrical resemblance. *Procedia Eng.* **81**, 1487–1492 (2014)
2. Kurpe, O., Kukhar, V., Puzyr, R., Burko, V., Balalayeva, E., Klimov, E.: Electric motors power modes at synchronization of roughing rolling stands of hot strip mill. In: Chenchevoy, V. et al. (eds.) CONFERENCE 2020, PAEP, Kremenchuk, Ukraine, pp. 404–412. IEEE (2020). <https://doi.org/10.1109/PAEP49887.2020.9240818>
3. Hattalli, V., Srivatsa, S.: Sheet metal forming processes—recent technological advances. *Mater. Today Proc.* **5**(1), 2564–2574 (2018)
4. Wang, X., Cao, J.: An analytical prediction of flange wrinkling in sheet metal forming. *J. Manuf. Process.* **2**(2), 100–107 (2000)
5. Kukhar, V., Grushko, A., Vishtak, I.: Shape indexes for dieless forming of elongated forgings with sharpened end by tensile drawing with rupture. *Solid State Phenom.* **284**, 408–415 (2018)
6. Weiping, D., Qichao, W., Xiaoming, W., Bin, W.: Stress analysis of cylindrical parts during deep drawing based on Dynaform. In: IOP Conference Series: Materials Science and Engineering, CONFERENCE 2018, ICAMMT, vol. 423, p. 012166 (2018)
7. Haikova, T., Puzyr, R., Savelov, D., Dragobetsky, V., Argat, R., Sivak, R.: The research of the morphology and mechanical characteristics of electric bimetallic contacts. In: Chenchevoy, V., et al. (eds.) CONFERENCE 2020, PAEP, Kremenchuk, Ukraine, pp. 579–582. IEEE (2020). <https://doi.org/10.1109/PAEP49887.2020.9240847>
8. Dewang, Y., Panthi, S., Hora, M.: Some aspects of blank holding force in stretch flanging process. *Mater. Today Proc.* **5**(2), 6789–6798 (2018)

9. Sivak, R.: Evaluation of metal plasticity and research of the mechanics of pressure treatment processes under complex loading. *Eastern-Eur. J. Enterp. Technol.* **6/7(90)**, 34–41 (2017)
10. Lal, R., Choubey, V., Dwivedi, J., Kumar, S.: Study of factors affecting Springback in sheet metal forming and deep drawing process. *Mater. Today Proc.* **5(2)**, 4353–4358 (2018)
11. Chiorescu, D., Chiorescu, E., Olaru, S.: The analysis of the parameters for deep drawing of cylindrical parts. In: MATEC Web of Conferences, CONFERENCE 2018, IManE and E, Chisinau, Moldova, vol. 178, p. 02011 (2018)
12. Holloman, J.: Tensile deformation. *Trans. Am. Inst. Min. Metall. Eng.* **162**, 269–290 (1945)
13. Hill, R.: A theory of the yielding and plastic flow of anisotropic metals. *Proc. Roy. Soc. London* **193**, 281–297 (1948)
14. Kukhar, V., Kurpe, O., Klimov, E., Balalayeva, E., Dragobetskii, V.: Improvement of the Improvement of the method for calculating the metal temperature loss on a Coilbox unit at the rolling on hot strip mills. *Int. J. Eng. Technol. (UAE)* **7(4)**, 35–39 (2018)
15. Ogorodnikov, V.A., Dereven'ko, I.A., Sivak, R.I.: On the influence of curvature of the trajectories of deformation of a volume of the material by pressing on its plasticity under the conditions of complex loading. *Mater. Sci.* **54(3)**, 326–332 (2018). <https://doi.org/10.1007/s11003-018-0188-x>
16. Malinov, L., Malysheva, I., Klimov, E., Kukhar, V., Balalayeva, E.: Effect of particular combinations of quenching, tempering and carburization on abrasive wear of low-carbon manganese steels with metastable austenite. *Mater. Sci. Forum* **945**, 574–578 (2019)
17. Puzyr, R., Shchetynin, V., Arhat, R., Sira, Yu., Muravlov, V., Kravchenko, S.: Numerical modeling of pipe parts of agricultural machinery expansion by stepped punches. In: Dijmărescu, M.-R., et al. (eds.) IOP Conference Series, CONFERENCE 2020, ICAMaT, Bucharest, Romania, vol. 1018, p. 012013 (2021). <https://doi.org/10.1088/1757-899X/1018/1/012013>
18. Felder, C., Levrau, M., Mantel, N.G., Dinh, T.: Identification of the work of plastic deformation and the friction shear stress in wire drawing. *Wear* **286–287**, 27–34 (2012). <https://doi.org/10.1016/j.wear.2011.05.029>
19. Wang, X., Jin, J., Deng, L.: Review: state-of-the-art of stamping-forging process with sheet metal blank. *J. Harbin Inst. Technol. (New Ser.)* **24(3)**, 1–16 (2017)
20. Zhang, R., Shao, Z., Lin, J.: A review on modelling techniques for formability prediction of sheet metal forming. *Int. J. Lightweight Mater. Manuf.* **1(3)**, 115–125 (2018)
21. Leminen, V., Matthews, S., Pesonen, A., Tanninen, P., Varis, J.: Combined effect of blank holding force and forming force on the quality of press-formed paperboard trays. *Procedia Manuf.* **17**, 1120–1127 (2018)
22. Neto, D., Oliveira, M., Alves, J., Menezes, L.: Influence of the plastic anisotropy modelling in the reverse deep drawing process simulation. *Mater. Des.* **60**, 368–379 (2014)
23. Yoon, J., Dick, R., Barlat, F.: A new analytical theory for earing generated from anisotropic plasticity. *Int. J. Plast.* **27(8)**, 1165–1184 (2011)
24. Ozsoy, M., Esener, E., Ercan, S., Firat, M.: Springback predictions of a dual-phase steel considering elasticity evolution in stamping process. *Arab. J. Sci. Eng.* **39(4)**, 3199–3207 (2014)
25. Slater, R.: *Engineering and Plasticity: Theory and Application to Metal Forming Processes*. Macmillan International Higher Education, London (1977)
26. Puzyr, R., Markov, O., Savielov, D., Chernysh, A., Sira, Y.: Finite-element simulation of the process of the tubular workpiece expansion in the manufacture of automotive parts. In: Tonkonogiy, V., et al. (eds.) InterPartner 2020. LNME, pp. 433–442. Springer, Cham (2021). https://doi.org/10.1007/978-3-030-68014-5_43

27. Cao, T.-S., Vachey, C., Montmitonnet, P., Bouchard, P.-O.: Comparison of reduction ability between multi-stage cold drawing and rolling of stainless steel wire – experimental and numerical investigations of damage. *J. Mater. Process. Technol.* **217**, 30–47 (2015)
28. Sosenushkin, E.N., Yanovskaya, E.A., Sosenushkin, A.E., Emel'yanov, V.V.: Mechanics of nonmonotonic plastic deformation. *Russ. Eng. Res.* **35**(12), 902–906 (2015). <https://doi.org/10.3103/S1068798X15120199>
29. Arhat, R., Puzyr, R., Shchetynin, V., Moroz, M.: The manufacture of cylindrical parts by drawing using a telescopic punch. In: Tonkonogyi, V., et al. (eds.) *InterPartner 2020. LNME*, pp. 363–372. Springer, Cham (2021). https://doi.org/10.1007/978-3-030-68014-5_36
30. Wu, T.-Y.: A study of slider motion with servo press. M.Sc. thesis, Department of Power Mechanical Engineering, National Tsing Hua University, Hsinchu (2014)
31. Singh, C.P., Agnihotri, G.: Formability analysis at different friction conditions in axis-symmetric deep drawing process. *Mater Today Proc.* **4**, 2411–2418 (2017)
32. Tang, B., Lu, X., Wang, Z., Zhao, Z.: Springback investigation of anisotropic aluminum alloy sheet with a mixed hardening rule and Barlat yield criteria in sheet metal forming. *Mater. Des.* **31**(4), 2043–2050 (2010)
33. Pipard, J., Balan, T., Abed-Meraim, F., Lemoine, X.: Elasto-visco-plastic modeling of mild steels for sheet forming applications over a large range of strain rates. *Int. J. Solids Struct.* **50**, 2691–2700 (2013)
34. Singh, S., Gupta, A., Mahesh, K.: A study on the extent of ironing of EDD steel at elevated temperature. *CIRP J. Manuf. Sci. Technol.* **3**(1), 73–79 (2010)
35. Hrudkina, N., Aliieva, L., Abhari, P., Markov, O., Sukhovirska, L.: Investigating the process of shrinkage depression formation at the combined radialbackward extrusion of parts with a flange. *Eastern-Eur. J. Enterp. Technol.* **5**(1–101), 49–57 (2019)
36. Markov, O., Gerasimenko, O., Kukhar, V., Abdulov, O., Ragulina, N.: Computational and experimental modeling of new forging ingots with a directional solidification: the relative heights of I.I. *J. Braz. Soc. Mech. Sci. Eng.* **41**(8), 310 (2019)
37. Kapustová, M., Sobota, R.: The design of drawing process of cylindrical cup with oval bottom using computer simulation. In: *MATEC Web of Conferences, CONFERENCE 017, ICMME, Shanghai, China, vol. 95*, p. 10008 (2018)
38. Liu, Y., Li, F., Li, C., Xu, J.: Enhancing formability of spherical bottom cylindrical parts with magnetic medium on deep drawing process. *Int. J. Adv. Manuf. Technol.* **103**(5–8), 1669–1679 (2019). <https://doi.org/10.1007/s00170-019-03505-8>
39. Xu, W., Wu, S., Balamurugan, G.-P.: Evaluating shape memory behavior of polymer under deep-drawing conditions. *Polym. Test* **62**, 295–301 (2017)
40. Taber, L.: On a theory for large elastic deformation of shells of revolution including torsion and thick-shell effects. *Int. J. Solids Struct.* **24**(9), 973–985 (1988)
41. Volmir, A.: *Stability of Deformable Systems*. The Science, Moscow (1967)
42. Ilyushin, A.: *Plastic*. Gostekhizdat, Moscow (1948)
43. Lubliner, J.: *Plasticity Theory*. Dover Publications, New York (2008)
44. Popov, Y.: *Fundamentals of sheet metal stamping theory*. Mechanical engineering, Moscow (1977)
45. Van der Put, M., Singer, M.: *Galois Theory of Linear Differential Equations*. Part of the *Grundlehren der mathematischen Wissenschaften*. Book series GL, vol. 328. Springer, Heidelberg (2003). <https://doi.org/10.1007/978-3-642-55750-7>
46. Barrett, J.: Oscillation theory of ordinary linear differential equations. *Adv. Math.* **3**(4), 415–509 (1969)

47. Džurina, J., Baculíková, B., Jadlovská, I.: Kneser solutions of fourth-order trinomial delay differential equations. *Appl. Math. Lett.* **49**, 67–72 (2015)
48. Krasnov, M., Kiselev, O., Makarenko, H.: *Common differential equations: Tasks and exercises with detailed solutions: Textbook 4th ed., corrected.* Mechanical engineering, Editorial USSR (2002)
49. Yu, H., Chen, S.: *Metal Plastic Processing.* Chuan Hwa Publishing Ltd, Taipei (2015)



Hydraulic Press Open Die Forging of 21CrMoV5-7 Steel CCM Roller with Flat Upper and Concave Semi-round Lower Cogging Dies

Volodymyr Kukhar^{1,3} , Oleg Vasylevskiy¹ ,
Olha Khliestova¹ , Ivan Berestovoi² , and Elena Balalayeva¹ 

¹ Pryazovskyi State Technical University, 7, Universytets'ka Street,
Mariupol 87555, Ukraine

² Azov Maritime Institute of the National University
"Odessa Maritime Academy", Mariupol 87517, Ukraine

³ Technical University "Metinvest Polytechnic" LLC, 71A Sechenov Str.,
Mariupol 87524, Ukraine

Abstract. The cogging schedules were investigated with reduction and rotation joint effect around the workpiece's longitudinal axis, making it possible to improve the shaft forgings quality indices in geometry and distribution of strength properties in cross-sections. The forging for the rollers of continuous casting machine (CCM) of 21XMoV5-7 steel was produced according to the improved process in the forging shop with the hydraulic press combined dies (the upper die is flat, the lower die is semi-round cut-out, U-shaped). The advantage of the developed shaft forging schedules is the significant plastic deformation achievement in the forging cross-section using only one combined dies set. Manufacture of the CCM roller forging according to the new process made it possible to improve by 8.9% in the average yield strength and by 11.9% in the average ultimate tensile strength. It was possible to reduce the forging the data spread for the yield strength from 33% to 17% and the data dispersion for the ultimate tensile strength from 26% to 11%. The minimal ultimate tensile strength was increased by 14.7%.

Keywords: Shafts forging · Cogging · Combined flat-shaped dies · Reduction · Rotation angle · Strength · Grainflow · Grain size

1 Introduction

Several requirements exist for single and multi-diameter shafts forgings, depending upon the parts exploitation conditions to be manufactured. These requirements stipulate the forgings technological groups, the number, and the material mechanical testing [1]. Because of this, it is necessary to obtain of directional orientation grainflow not only in the ingot [2] and in the forging [3], as well as fine-grain micro-structure with maximum uniformity in cross-section is ensuring the best combination of the metal's mechanical properties.

2 Literature Review

Innovative methods of severe plastic deformation are currently being developed [4], mainly based on various types of extrusion [5]. Most of them related to the realization of macroshifts at the cold, severe plastic material deformation in moving dies [6] or at the dieless forming with workpiece local heating [7]. One of the ways to control the formation of the metal's macro- and microstructure (as quality indicators [8]) is to varying the open die forging thermomechanical modes in the cogging operation, which takes up the bulk of the forging time when shafts are manufactured [9]. This solution makes it possible to intensify plastic deformation and obtain the macro-shifts effect at the application of a standard universal tool – flat rhombic and semi-round or combined dies (the upper being flat, the lower of V-shaped or U-shaped configuration) of a forging press [10]. Specific requirements for operating conditions of such shaft forgings like continuous casting machine (CCM) rollers stipulate application of steel, containing chromium, molybdenum, and vanadium, as well as intense forging modes and development of alternative designs of such parts [11]. For the wastes minimization at further forgings machining, it will be necessary to observe the requirements of geometric precision for the round cross-section forgings. Thus, forging schedules development for CCM rollers manufacturing seems to be expedient, with the objective of the geometric precision increasing and improving the indices of shafts forgings mechanical properties, as applied to the forging shop standard conditions, equipped with a hydraulic forging press with universal combined dies (the upper – flat, the lower – semi-round cut-out, U-shaped).

Realization of macro-shifts in material bulk allows refining of ingot cast structure without sufficient alternations in the area of its cross-section. It promotes to close of inner defects [12–18] (like cracks [12], inner voids [13–15], or cast axial non-density [16–18]), even for forging of big ingots with minimal forging ratio. It is convincingly indicated by the results of both modeling [14, 15, 17] and experiments [16, 18]. The macroshift deformations effect is achieved by radial reduction with complicated shape dies [17], the use of a special cast [18], or preformed [19] workpiece. The special four-die devices are applied for these purposes also [20]. Such technological solutions are related to the application of specialized metal-consuming forging devices, their assembling with press, requiring additional labor consumption, and reducing the production range of forgings in weight. In paper [21], theoretically and in work [22], experimentally was proposed to carry out the forging of heavy shafts with shaped dies that allow reducing an ingot into a three-beam or four-beam workpiece. Further cogging from a shaped ingot accompanied by the formation of a round cross-section through macroshift deformations requires the substitution of dies, and it may cause subcooling and the necessity to perform additional heating of ingots. Besides, different assemblies of tools for open die forging are used for obtaining three- and four-beam workpieces. Investigations of forging workpieces with specially shaped dies are described early in [17–19]. As well as the use of dies with a complex curved parting line [23], radial [24], spherical [25] dies, and four-beam workpiece [26] indicates the dimensions controlling possibility and macroshift metal flow initiating.

Material's uniformity improvement and increase at the treatment using increasing or complicating the tools set can be justified economically only for forging ingots made of high alloy steels or rare metals [27]. To equal the mechanical properties over the product cross-section, deformation schedules are combined directly [28] or stepped [29] heat treatment. However, investigations described in [30] deserve attention. According to the results obtained there, macro-shifts achievement revealed at the shafts open die forging with a round or polygonal cross-section combined (flat + shaped) dies using varying cogging modes. In our case, it is necessary to carry out rational forging modes for shafts with the application of combined dies of the type: the upper – flat, the lower – U-shaped [30], i.e., as they are used at the enterprise's shop.

The objective of our research is to develop forging schedules in combined dies (the upper die being flat, the lower – with round cut-out, U-shaped), in the form of rational alternation and determination of optimal reductions strokes, intermittent work feeds, and rotation angles of the ingot around its longitudinal axis, that leads to a satisfactory geometric precision of forged products and closure of core-defects (porosities, blow-holes, etc.) utilizing realization of macroshift-effect in the deformation zone.

3 Research Methodology

The investigation was carried out with due regard to the manufacturing of shafts by forging at a forging shop of one of the industrial enterprises of Mariupol (Ukraine). The computer and physical simulation methods were used to investigate the strain state and shape deformation of workpieces with different reduction, supports, and rotation angles. The computer simulation was carried out in a universal package of the finite-elements analysis (LS-Dyna). The isothermal problem was solved with some assumptions. Other initial parameters were taken according to the processes of shafts forging at the forging shop: the dies were of combined type (the upper die was flat, the lower was U-shaped with the cut-out radius 300 mm, Fig. 1), the ingot's diameter D_0 was 550 mm, ingot's length $L_0 = 1300$ mm, the 21CrMoV5-7 ingot steels was made, the treatment temperature was $t = 1,100$ °C, the upper die stroke velocity – 50 mm/s. The dies were supposed to be absolutely rigid bodies. The deformed workpiece was divided into the finite elements of tetrahedral shape; the length of the middle element's side was equal to 10 mm. To carry out experimental investigations on a 1:10 scale, a laboratory assembly of combined dies were manufactured of C45 (1045) steel. Then they were installed on a hydraulic press with a nominal force of 0.63 MN. Experimental specimens were manufactured of antimony lead of SSu grade (Pb = 99.38... 99.6%, Sb = 0.4...0.6%, Bi ≤ 0.05%).

At computer simulation, the following was specified as varying parameters, Influencing the kinematic characteristics of the process of deformation of the ingot: (i) reduction: $\Delta h_0 = 50$ mm, 66 mm and 100 mm, i.e., relative reduction (reduction ratio) being $\varepsilon_{h\%} = (\Delta h / D_0) \times 100\% = 9.09\%$, 12%, and 18.18%; (ii) die width (the feed value): $B = 180$ mm, 240 mm and 300 mm, i.e., relative feeds (die width to diameter ratio) $B/D_0 = 0.327$, 0.436 and 0.545; (iii) rotation angles: $\varphi = 30^\circ$, 60° and 90° .

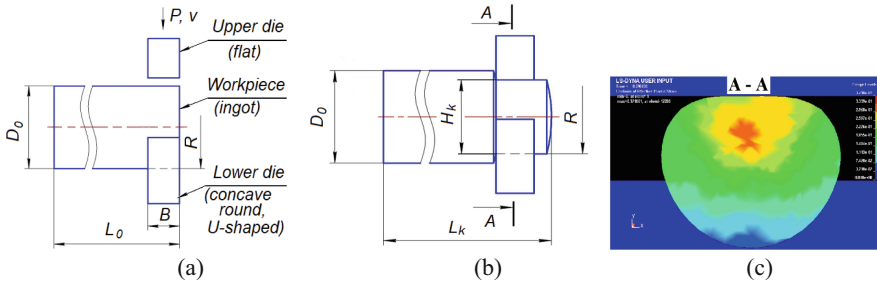


Fig. 1. Position of a workpiece in combined dies before (a), and after (b) reduction and the process simulation by finite elements method (c): B, R – dies geometric parameters; L_0, L_k, D_0, H_k – geometric parameters of the ingot; P, v – kinematic parameters of cogging.

The varied parameters range was enlarged for experimental investigations. The analysis of the received data made it possible to determine that the distribution of the average strain from the workpiece’s center towards the periphery corresponds to a linear equation at all simulated schedules of forging with a correlation coefficient (R) close to 1.0. Thus, the effective strain (e_i) distribution in the cross-section obeys the regularity:

$$e_i = e_{i,max} - a \cdot \rho, \tag{1}$$

where $e_{i,max}$ is the highest effective strain, observed on the axis; a is an angular coefficient of strain reduction towards the periphery; ρ is the radius vector from the center of the workpiece to the investigated point. The determined values of angular coefficients for the relative feed $B/D_0 = 1.0$ are summarized in Table 1.

Table 1. The calculated values of angular coefficients ($B/D_0 = 1.0$).

Reduction, mm × rotation angle (forging schedule)	$e_{i,max}$	a	Correlation (χ^2)
50 × 30°	6.44 ± 0.053	0.01357 ± 0.000505	0.99
50 × 60°	8.04 ± 0.055	0.02099 ± 0.000541	0.99
50 × 90°	7.03 ± 0.073	0.02367 ± 0.000693	0.99
66 × 30°	6.08 ± 0.063	0.01452 ± 0.000599	0.99
66 × 60°	7.10 ± 0.05	0.02083 ± 0.000481	0.99
66 × 90°	7.54 ± 0.05	0.02084 ± 0.000482	0.99
100 × 30°	5.17 ± 0.052	0.01262 ± 0.000495	0.99
100 × 60°	6.46 ± 0.02	0.01967 ± 0.000192	0.99
100 × 90°	6.39 ± 0.12	0.1881 ± 0.0011	0.99

The workpiece cross-section was evaluated to a round shape approximation degree also. The evaluation was made by the relation of the forging perimeter to an equivalent circle perimeter, calculated through the forging cross-section area. Accordingly, the

closer this ratio is to 1.0, the more accurately the geometry requirements for forging are met. The results of the analysis of the obtained theoretical and experimental data allowed us to propose manufacturing forgings of shafts by open die forging in combined dies of the analyzed design. One of the tasks was to reduce the number of processes passes at the application of one dies set and improve workpieces inner metal (closure of internal void defects, refining of grains), which makes it possible to reduce the total energy costs, increase the productivity of open die forging and improve the performance indices of parts. According to this method, a workpiece is forged in combined dies in several passes with rotation and subsequent cogging. Reductions at cogging are made with relative feed $B/D_0 = 0.55 \dots 0.7$ to engineering strain $\varepsilon_h\% = 5 \dots 18\%$ with rotation after each stroke for the angle $\varphi = 60 \dots 90^\circ$, the bigger rotation angle being ensured at smaller strain.

Industrial implementation of the methods was performed for the process of rollers forging for CCM of the oxygen-converter shop. There both rollers, imported from Romania and domestic, manufactured in Ukraine, are employed. The parts chemical composition is summarized in Table 2; their microstructure is shown in Fig. 2(a, b).

Table 2. Chemical composition, hardness of metal of investigated forgings intended for CCM rollers (21CrMoV5-7 steels).

Manufacturer	wt., %								Hardness, HRC
	C	Mn	Si	Cr	Mo	V	S	P	
Romania	0.26	0.57	0.40	1.51	0.61	0.24	0.023	0.036	34
Ukraine	0.24	0.46	0.45	1.72	0.86	0.26	0.019	0.012	31

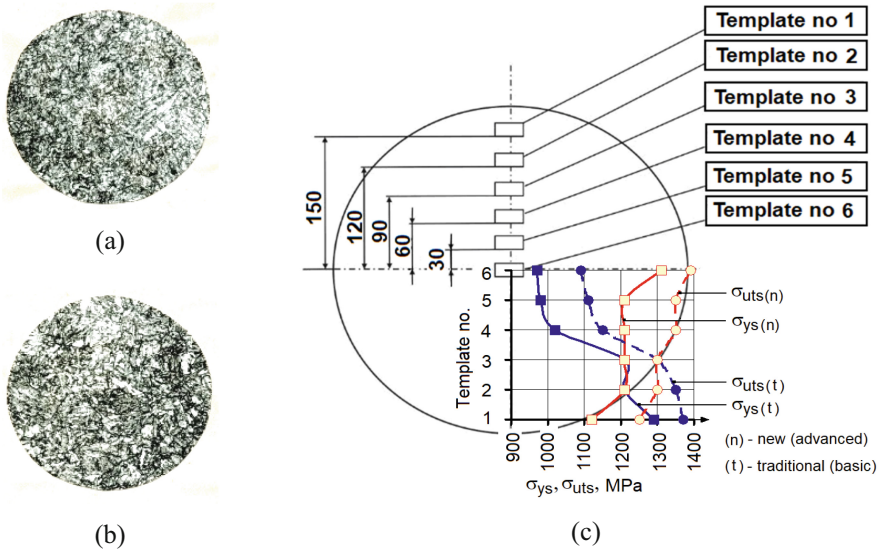


Fig. 2. Microstructure ($\times 500$) of rollers manufactured in Romania (a) and Ukrainian (b); sketch of sampling to determine the metal structure of a workpiece $\varnothing 360$ mm (c).

According to the base process for CCM rollers manufacturing hexahedral forge ingots, 5,000 kg in weight were used as original blanks. Smelting was carried out in electric-arc furnaces. Ingots were cast by the bottom pouring method. Heating was performed in gas chamber ovens with carriage-type bottom and setting up to 30 t in mass. Forging was performed on a hydraulic forging press, 12.5 MN in nominal force, with flat dies, 300 mm wide in “circle-square-circle” schedule with rotate reducing to the round shape of the cross-section at the final pass. The overall forging ratio was 2.7.

4 Results

Templates were chosen following the diagram pictured in Fig. 2c from the forgings cross-section, which eventually underwent subsequent quenching and tempering. After that, the chemical composition, mechanical properties as the yield strength σ_{ys} , ultimate tensile strength σ_{uts} , percent elongation δ_5 , percent reduction in area (necking) ψ and hardness, according to Brinelle (HB) were determined (Table 3 and Table 4). Forging according to the new technology, combined dies with preservation of overall forging ratio, equal to 2.7. Templates were chosen from similar spots in the forgings cross-section to determine properties after additional heat treatment (quenching and tempering) (Table 4).

Table 3. Mechanical properties of templates (basic process).

Template no	σ_{ys} , MPa	σ_{uts} , MPa	δ_5 , %	ψ , %	HB
1	1290	1370	12.5	44.0	415
2	1210	1350	12.5	48.0	415
3	1210	1300	9.0	55.0	415
4	1020	1150	11.5	53.0	302
5	980	1110	10.5	60.0	302
6	970	1090	13.5	62.0	341

Table 4. Mechanical properties of templates (advanced process).

Template no	σ_{ys} , MPa	σ_{uts} , MPa	δ_5 , %	ψ , %	HB
1	1120	1250	11.5	53.0	382
2	1210	1300	11.5	50.0	400
3	1210	1300	9.0	55.0	415
4	1210	1350	12.5	48.0	415
5	1210	1350	12.5	48.0	415
6	1310	1390	12.5	44.0	415

Table 5 summarizes the analysis of maximal, minimal, and average values of yield strength and ultimate tensile strength in forgings cross-section, forged according to the

basic and new (advanced) processes. The data indicated in Tables 3 and 4 were used. The improvement index (I) is evaluated modulo as $I = (|A_t - A_n|/A_t) \times 100\%$, where A_t and A_n are values from Table 5 for the basic and new processes. Improvement in strength indices and their more uniform distribution in cross-section is observed as relative indices become closer to 1.0.

Table 5. Strength characteristics of 21CrMoV5-7 steel.

Forging schedule	$\sigma_{uts,max}$, MPa	$\sigma_{uts,av}$, MPa	$\sigma_{uts,min}$, MPa	$\sigma_{uts,max}^l / \sigma_{uts,min}$	$\sigma_{uts,max}^l / \sigma_{uts,av}$	$\sigma_{uts,min}^l / \sigma_{uts,av}$
Basic (A_t)	1370	1228	1090	1.26	1.12	0.89
Advanced (A_n)	1390	1323	1250	1.11	1.05	0.94
Improvement, %	1.5	7.7	14.7	11.9	6.3	5.6
Forging schedule	$\sigma_{ys,max}$, MPa	$\sigma_{ys,av}$, MPa	$\sigma_{ys,min}$, MPa	$\sigma_{ys,max}^l / \sigma_{ys,min}$	$\sigma_{ys,max}^l / \sigma_{ys,av}$	$\sigma_{ys,min}^l / \sigma_{ys,av}$
Basic (A_t)	1290	1113	970	1.33	1.16	0.87
Advanced (A_n)	1310	1212	1120	1.17	1.08	0.92
Improvement, %	1.6	8.9	15.5	12	6.9	5.7

Macrostructures and microstructure of forgings, forged according to the advanced process, are shown in Fig. 3 and Fig. 4. Table 6 reflects the results of grain size point’s analysis for finished forgings.

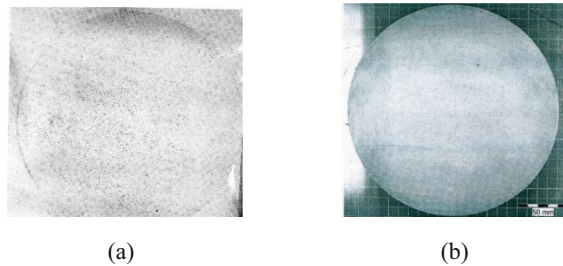


Fig. 3. Sulfur print (a) and macrostructure after pickling (b) of template from 21CrMoV5-7 steel forging.

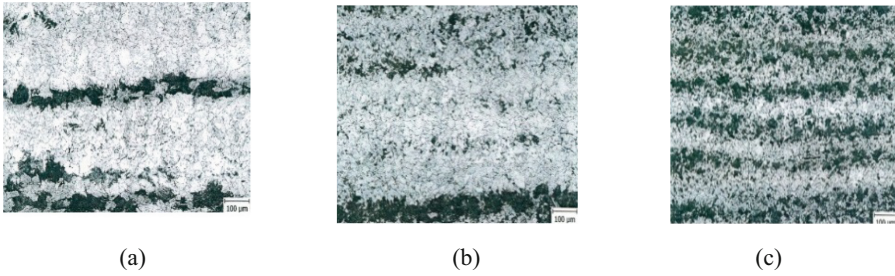


Fig. 4. Microstructure ($\times 100$) of the 21CrMoV5-7 steel forging: (a) near the lateral surface (no 1); (b) at a distance $0.5R$ (no 3); (c) in the axis zone (no 6).

Table 6. Distribution of grain size points in cross-section of 21CrMoV5-7 steel workpiece.

Forging schedule	Grain size, points (GOST 5639)				G_{max}/G_{min}
	G0	G0.5	G0.8	G_{av}	
Basic	5–3	2–3	1–3	2.7	2
Advanced	8–9	8–9	8–7	8.2	1.13

According to the advanced process, manufacturing of forgings resulted in improvement by 8.9% in average yield strength and by 11.9% in average ultimate tensile strength. It was also possible to reduce by 12% (from 33% to 17%) range of yield strength data and by 11.9% (from 26% to 11%) dispersion for ultimate tensile strength data in cross-section, i.e., it was possible to reach more uniform grain structure and distribution of mechanical properties. The value of minimal ultimate tensile strength σ_{uts} , as one of the most limiting index, was increased by 14.7% (Fig. 2c).

5 Conclusions

It is shown that advanced open die forging schedules implementation in combined dies (the upper die is flat, the lower die is U-shaped) is a promising direction for quality improvement for the shafts forgings and the parts operation characteristics improvement. Process methods for the shafts forgings manufacture by cogging with combined dies were developed that allow reaching the severe deformations at the application of just one die tools set, i.e., by selecting rational forging schedules: rotation angles feeds and reduction. At the same time, the ranges of their values for achieving quality indices in terms of the forgings’ mechanical properties and cross-section shape are sufficiently close, which allows optimizing the open die forging schedules for shafts manufacturing. A method of open die forging in combined dies has been developed, according to which reductions at cogging are made with relative feed $B/D_0 = 0.55–0.7$ to engineering strain $\varepsilon_{h\%} = 5–18\%$ with rotation after each stroke to the angle $\varphi = 60–90^\circ$, the bigger rotation angle being ensured at smaller $\varepsilon_{h\%}$ value. It was found out that the regularity of deformations distribution in the cross-section from the center to the

periphery in a shaft forging, forged in combined dies, according to the new schedules, is linear. It was revealed that the proposed process allows increasing by 1.5...15.5% the principal strength properties of forgings, specifically $\sigma_{uts,max}$ from 1370 MPa to 1390 MPa and $\sigma_{ys,min}$ from 970 MPa to 1120 MPa. It has also allowed significantly (from 33% to 17%) reducing the hereditary structural and chemical heterogeneity of forged products.





References

1. Rules for Classification and Construction Materials and Welding. Metallic Materials. Steel and Iron Materials. Germanischer Lloyd Aktiengesellschaft, Hamburg (2009)
2. Markov, O.E., Gerasimenko, O.V., Shapoval, A.A., Abdulov, O.R., Zhytnikov, R.U.: Computerized simulation of shortened ingots with a controlled crystallization for manufacturing of high-quality forgings. *Int. J. Adv. Manuf. Technol.* **103**(5–8), 3057–3065 (2019). <https://doi.org/10.1007/s00170-019-03749-4>
3. Sinczak, J., Majta, J., Glowacki, M., Pietrzyk, M.: Prediction of mechanical properties of heavy forgings. *J. Mater. Process. Technol.* **80–81**, 166–173 (1998)
4. Gronostajski, Z., et al.: Recent development trends in metal forming. *Arch. Civ. Mech. Eng.* **19**(3), 898–941 (2019). <https://doi.org/10.1016/j.acme.2019.04.005>
5. Rosochowski, A.: Severe Plastic Deformation Technology. Whittles Publishing, Dunbeath (2017)
6. Hrudkina, N., Aliieva, L., Abhari, P., Markov, O., Sukhovirska, L.: Investigating the process of shrinkage depression formation at the combined radial-backward extrusion of parts with a flange. *Eastern-Eur. J. Enterp. Technol.* **2**, 5/1(101), 49–57 (2019). <https://doi.org/10.15587/1729-4061.2019.179232>
7. Kukhar, V.V., Grushko, A.V., Vishtak, I.V.: Shape indexes for dieless forming of elongated forgings with sharpened end by tensile drawing with rupture. *Solid State Phenom.* **2**, 408–415 (2018)
8. Liu, G.H., et al.: Influence of the blooming processes of heavy forgings on the forgings quality. *Adv. Mater. Res.* **538–541**, 1067–1071 (2012)
9. Ma, B.C., Tian, X.K.: The application and research on manufacturing technology of the heavy forging. *Adv. Mater. Res.* **941–944**, 1692–1695 (2014)
10. Markov, O.E., Rudenko, N.A., Tarić, A., Šerifi, V.S.: Comparison of Progressive schemes of the forging drawing for shafts manufacturing. *Metalurgia Int.* **XVIII**(9), 48–53 (2013)
11. Shapran, L.A., Hitko, A.Yu., Hrychikov, V.Ye., Ivanova, L.H.: Manufacturing technology of rollers with bimetallic bands for continuous-casting machine. *Metall. Min. Ind.* **3**(4), 151–154 (2011)
12. Wang, M., et al.: Analysis of laminated crack defect in the upsetting process of heavy disk-shaped forgings. *Eng. Fail. Anal.* **59**, 197–210 (2016)
13. Kim, Y., Cho, J., Bae, W.: Efficient forging process to improve the closing effect of inner void on an ultra-large ingot. *J. Mater. Process. Technol.* **211**, 1005–1013 (2011)
14. Lee, Y.S., Lee, S.U., Van Tyne, C.J., Joo, B.D., Moon, Y.H.: Internal void closure during the forging of large cast ingots using a simulation approach. *J. Mater. Process. Technol.* **211**, 1136–1145 (2011)
15. Kukuryk, M.: Experimental and FEM analysis of void closure in the hot cogging process of tool steel. *Metals* **9**(5), 538 (2019)

16. Smyrnov, Y.N., Skliar, V.A., Belevitin, V.A., Shmyglya, R.A., Smyrnov, O.Y.: Defect healing in the axial zone of continuous-cast billet. *Steel Transl.* **46**(5), 325–328 (2016). <https://doi.org/10.3103/S0967091216050132>
17. Christiansen, P., Hattel, J.H., Bay, N., Alves, L.M., Martins, P.A.F.: Open die forging of large shafts with defects – physical and numerical modelling. *Key Eng. Mater.* **554–557**, 2145–2155 (2013)
18. Kim, N., Ko, D.-C., Kang, N., Oh, I.Y., Van Tyne, C.J., Moon, Y.H.: Feasibility of using continuously cast round bloom as a substitute to cast ingot in the manufacture of heavy forgings. *Steel Res. Int.* **91**(9), 202000079 (2020)
19. Markov, O.E., Perig, A.V., Zlygoriev, V.N., Markova, M.A., Kosilov, M.S.: Development of forging processes using intermediate workpiece profiling before drawing: research into strained state. *J. Braz. Soc. Mech. Sci. Eng.* **39**(11), 4649–4665 (2017). <https://doi.org/10.1007/s40430-017-0812-y>
20. Lazorkin, V., Melnykov, Y.: New technologies of forging of ingots and blanks by four dies in open-die forging presses. In: 18th IFM 2011, Pittsburgh, USA, pp. 326–332 (2011)
21. Kargin, S.B.: Development and investigation of resources-saving process of shafts forging. *Metall. Min. Ind.* **7**(1), 33–36 (2015)
22. Kargin, S., Artiukh, V., Mazur, V., Silka, D., Meller, N.: Investigation of degree of internal defects closure in ingots at forging. *Adv. Intell. Syst. Comput.* **982**, 818–824 (2018)
23. Zhibankov, I.G., Perig, A.V.: Intensive shear deformation in billets during forging with specially formed anvils. *Mater. Manuf. Process.* **28**(5), 577–583 (2013)
24. Artiukh, V., Kukhar, V., Balalayeva, E.: Refinement issue of displaced volume at upsetting of cylindrical workpiece by radial dies. *MATEC Web Conf.* **224**, 01036 (2018)
25. Ishchenko, A., Artiukh, V., Mazur, V., Calimgareeva, A., Gusarova, M.: Experimental study of horizontal impact forces acting on equipment of thick sheet rolling stands during rolling. *MATEC Web Conf.* **239**, 01041 (2018)
26. Markov, O.E., Kukhar, V.V., Zlygoriev, V.N., Shapoval, A.A., Khvashchynskyi, A.S., Zhytnikov, R.U.: Improvement of upsetting process of four-beam workpieces based on computerized and physical modeling. *FME Trans.* **48**, 946–953 (2020)
27. Shapoval, A., Drahobetskyi, V., Savchenko, I., Gurenko, A., Markov, O.: Profitability of production of stainless steel + Zirconium metals combination adapters. *Key Eng. Mater.* **864**, 285–291 (2020)
28. Di Schino, A., Gaggiotti, M., Testani, C.: Heat treatment effect on microstructure evolution in a 7% Cr steel for forging. *Metals* **10**(6), 808 (2020)
29. Anishchenko, A.S.: Heat treatment effect on properties of deformed alloy type 36N. *Metallovedenie i Termicheskaya Obrabotka Metallov* **4**, 31–32 (1969)
30. Tajima, J.: Heat forging method for billet. Pat. JP2002102987. Japan, Sumitomo Metal Ind. Ltd. (2002)



Improved Hybrid Methods for Determining the Integral Characteristics of Turbomachine Nozzle Cascades

Alexandr Lapuzin , Valery Subotovich , Yuriy Yudin ,
and Olena Avdieieva 

National Technical University “Kharkiv Polytechnic Institute”,
2, Kyrpychova Street, Kharkiv 61002, Ukraine

Abstract. To determine the integral gas-dynamic characteristics of nozzle cascades of turbomachines, it is necessary to average the parameters of the three-dimensional flow behind the cascade that is non-uniform along with the pitch and along with the height of the cascade. Two types of averaging methods are used. For the first type of methods, the flow parameters at the entrance to the cascade are not taken into account when averaging the parameters of a non-uniform flow behind the cascade. For the second type of methods (hybrid), the pressure behind the cascade is found from the condition of maintaining the enthalpy drop in the initial non-uniform three-dimensional and averaged flows. In a cylindrical flow, the hybrid method is usually used to determine the velocity coefficient. The main disadvantage of this method is the significantly overestimated mass flow mass rate and component onto the axial direction of the angular momentum. To improve the methods of the second type, it is proposed to replace the ratio of the components of the momentum with two parameters, namely: mass flow rate and the component of the moment of momentum on the axial direction. It allows determining the velocity coefficient and two angles for the averaged flow. It is shown that the second kinetic energy of the flow can be replaced by entropy and, thus, the velocity coefficient can be adjusted provided the complex quality criterion is kept constant.

Keywords: Turbomachine · Nozzle cascades · Three-dimensional flow · Non-uniform flow · Loss coefficient · Averaging method

1 Introduction

Turbomachines are widely used in various industries. They have high efficiency and are easily scalable for different power rates. However, in turbomachines, the flow of the working body is accompanied by complex mechanical processes. It is especially characteristic of nozzle grids. When designing turbomachines, it is important to have reliable averaged indicators of the operating parameters of each part of nozzle cascades, which makes the development of averaging methods relevant.

To determine the integral gas-dynamic characteristics of nozzle cascades of turbomachines, it is necessary to average the three-dimensional flow parameters that are non-uniform along with the pitch (in the tangential direction) and along with the height

of the cascade behind it and find the kinetic energy loss coefficient and two averaged flow angles. This averaging can be performed without or using the total parameters in front of the cascade.

2 Literature Review

In the case of averaging without using common parameters before the cascade, the “history” of the flow is not taken into account, and only the parameters of the initial non-uniform flow are averaged in different ways [1–6]. In [2] determines axisymmetric flow, which is averaged through surfaces and meridian streamlines, [3] performs averaging based on mechanical work potential, [4] uses Favre-averaged Fourier-based methods with application to gas turbines, [5, 6] also uses averaging techniques to evaluate turbomachine efficiency. A significant variety of gas flow averaging methods raises the question of their effectiveness and allows you to combine different approaches to improve their performance. In other methods, which can be called hybrid, the concept of an ideal isentropic process is formulated [7], in which the pressure field and the direction of velocities are preserved under the real process in the studied section, which allows us to find the field of theoretical velocities and the average value of the enthalpy drop in the nozzle cascade – specific second kinetic energy of the ideal flow. After calculating the specific second kinetic energy of the initial non-uniform flow, the coefficient of kinetic energy loss in the cascade is found. For a flat flow in hybrid methods [7, 8], the averaged value of the exit angle of the flow $\bar{\alpha}_m$ is found from the average consumption values of the axial and tangential velocity components behind the cascade. The hybrid method [7, 8] is widespread in studying the direct cascade of turbomachines, although it overestimates the entropy, flow mass rate, and angular momentum in the tangential direction. Significantly distort the averaged enthalpy drop in the nozzle cascade (pressure behind the cascade) and non-hybrid averaging methods [9–12]. Papers [13, 14] use original averaging methods, which have some other drawbacks. The similar averaging method uses other fields, such as pumping unit design [15], spraying liquids [16], oxygen-converter production [17], material science [18], separation technologies [19], etc.

3 Research Methodology

3.1 Advanced Method of Averaging the Parameters of a Three-Dimensional Flow of Nozzle Cascade

An advanced hybrid method of averaging the flow parameters behind the nozzle cascade array is proposed. In contrast to the generally accepted hybrid technique [7, 8], in which, when averaging, only the specific kinetic energies of non-uniform planar flows are saved in real and theoretical flow processes, the specific total energy and momentum projections are proposed, in which a mass flow rate and axial component of the momentum of the three-dimensional flow.

The integrated characteristics of the nozzle cascade (loss coefficient and two flow angles) calculated by the proposed method allow one-dimensional thermal calculation of the stage if the total parameters in front of the stage, pressure behind it, rotor speed, and integral characteristics of the rotor cascade (loss coefficient and two flow angles) are known. In a first step, the flow in the test section behind the cascade is divided into a sufficiently large number of annular sections, within each of which the flow parameters along the radius are assumed to be unchanged. In each such section, the gas flow is averaged along with a pitch to a one-dimensional axisymmetric flow. For this purpose, the integral characteristics of the flow are calculated at each section: total energy, kinetic energy, flow mass rate, the axial component of the angular momentum, and the enthalpy differential in the nozzles averaged over the mass flow rate. According to these characteristics, five independent three-dimensional flow parameters are found: total temperature and total pressure, pressure, and two angles that determine the direction of the absolute gas velocity vector.

In a second step, the two-dimensional axisymmetric flow behind the nozzle cascade is reduced to one-dimensional (averaging along the radius). For this, the above-integrated characteristics of all annular sections are summarized, and all parameters of the averaged in two directions three-dimensional flow behind the lattice are determined from them. By the integrated characteristics, you can find the integral efficiency of the stage by the equal

$$\eta_{oi} = \omega(\overline{M}_a + \overline{M}_{a2})/G\overline{H}_p, \quad (1)$$

in which \overline{M}_a and \overline{M}_{a2} are the axial component of the momentum averaged along the step and the radius of the momentum of the gas flow behind the nozzle cascade.

3.2 Averaging Along the Pitch of the Flow Parameters Behind the Annular Nozzle Cascade

Table 1 shows, by way of example, the airflow parameters at one of the radii ($r = 94$ mm) behind the nozzle cascade at seven points in steps located at equal distances in the tangential direction. In front of the grill, the total temperature $T_0^* = 318$ K, excessive total pressure $P_0^* = 2936$ kg/m², barometric pressure $B = 10211$ kg/m². An insignificant radial height of the annular flow stream in Sect. 1 ($\Delta r = 2.4$ mm) allows us to consider the initial non-uniform flow in the cascade as a two-dimensional flow. In Table 1 P and P^* - excess pressure and air total pressure at the measurement points, and - three-dimensional flow angles (Fig. 1). By these parameters and total temperature $T^* = T_0^*$ at each point, the velocity can be found

$$C = \sqrt{2009 \cdot T^* \left[1 - ((P + B)/(P^* + B))^{0.2857} \right]}, \quad (2)$$

temperature $T = T^* - \frac{C^2}{2009}$, density $\rho = (P + B)9,8/(287 \cdot T)$, flow in the vicinity of the point $\Delta g = \rho C \cos \gamma \sin \alpha \cdot \Delta F$, where $\Delta F = F/7 = 0.0002024$ m² ($F = 0.001417$ - end area of the ring).

Table 1. Pitch unevenness of flow parameters behind the cascade.

j	1	2	3	4	5	6	7
P^* , kg/m ²	2929	2931	2892	2530	2610	2913	2930
P , kg/m ²	412	344	290	824	527	245	400
α , degree	19.30	19.30	20.70	19.50	14.90	16.55	17.87
γ , degree	5.6	5.4	4.5	-7.0	2.2	8.0	6
C , m/s	194.1	196.9	197.9	160.3	177.7	200.4	194.6
C_a , m/s	63.8	64.8	69.7	53.1	45.7	56.5	59.3
T , K	299.0	299.0	298.5	305.0	302.0	298.0	299.0
ρ , kg/m ³	1.213	1.205	1.202	1.235	1.213	1.198	1.212
Δg , kg/s	0.01569	0.01580	0.01696	0.01328	0.01121	0.01370	0.01457

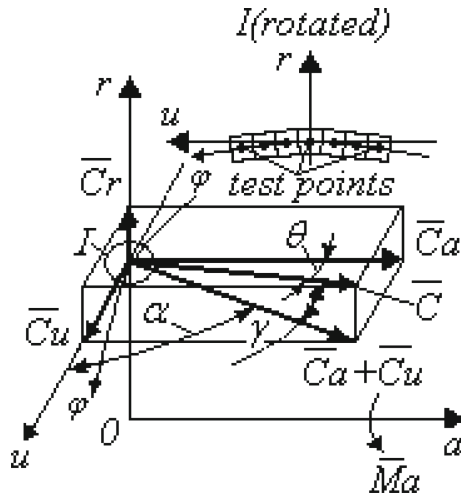


Fig. 1. Cylindrical-coordinate system.

Since there is no large-scale non-uniformity of the flow parameters behind the nozzle, it is conventionally assumed that only seven points are located in the tangential direction and the mass flow rate in the flow stream $g = \sum_{j=1}^m \Delta g_j$. It is convenient to replace the product $\cos \gamma \sin \alpha$ with $\cos \theta$, where θ is the angle between the velocity vector \vec{C} and its axial component \vec{C}_a . General considerations regarding the choice of the averaging method are considered in [1]. It is noted that gas flows with variable cross-sectional parameters in some cases can be considered as one-dimensional. In this case, the problem arises of averaging gas parameters in the cross-section of a non-uniform flow.

The given non-uniform flow is characterized by many total (integral) values: gas flow mass rate, energy, momentum, enthalpy, etc. Replacing this flow with a one-dimensional – average, one should strive to maintain the flow's total characteristics (properties). In the monograph [1], various methods of averaging the non-uniform translational flow are considered, and it is indicated that only three total characteristics of the initial flow can be kept constant. The absence in [1] of recommendations for averaging the three-dimensional flow in the stages of turbomachines was, apparently, one of the reasons for the emergence of not quite justified methods for processing the results of physical experiments [10, 12].

Since the state of the three-dimensional flow in each annular stream is determined by five independent parameters (for example, the total parameters \bar{T}^* , \bar{P}^* , pressure \bar{P} and angles $\bar{\alpha}$ and $\bar{\gamma}$), when averaging over a step, only five total physical characteristics of the initial flow can be kept constant. The flow parameters along the step behind the nozzle cascade and its integral characteristics are marked here and below by a bar above, and index 1 is omitted.

From the equation for the efficiency of a flowing stream (elementary turbine stage)

$$\bar{\eta}_{oi} = \omega \cdot (\bar{M}_a - \bar{M}_{a2}) / (g\bar{H}_p) \quad (3)$$

it follows that for its correct determination, it is necessary to maintain when averaging along with the pitch, \bar{M}_a – the axial component of the angular momentum and the flow mass rate g . In addition to \bar{M}_a and g , it is advisable to preserve, as is customary in the hybrid procedure [1, 7], the specific values of kinetic energies in real ($\frac{\bar{E}_k}{g}$) and theoretical (\bar{h}_c) flows, as well as the total energy (deceleration enthalpy), which allows one to find the integral losses in the cascade.

3.3 Pitch Averaging Method “ $\bar{E}, \bar{E}_k, \bar{h}_c, g, \bar{M}_a$ ”

If the total temperature in front of the cascade T_0^* is constant in cross-section 0, then the total temperature of the grille at all points of the flow is equal to the total temperature T_0^* . Thus, the condition for the conservation of total energy $\bar{E} = C_p \bar{T}^* g = \sum_{j=1}^m C_p T^* \Delta g$ is equivalent to the condition $\bar{T}^* = T_0^*$. After finding the flow in the flow stream

$$g = \bar{\rho} \bar{C} \cos \bar{\gamma} \sin \bar{\alpha} F = \sum_{j=1}^m \rho C \cos \gamma \sin \alpha \Delta F = \sum_{j=1}^m \Delta g \quad (4)$$

from the condition of conservation of the enthalpy drop in the nozzles

$$g \bar{h}_c = g \bar{C}_i^2 / 2 = \sum_{j=1}^m (C_i^2 / 2) \Delta g \quad (5)$$

one can find the averaged theoretical flow mass rate behind the cascade \bar{C}_i . In the last formula, the local theoretical velocity

$$C_t = \sqrt{2009T_0^* \left[1 - ((P+B)/(P_0^*+B))^{0,2857} \right]}. \quad (6)$$

The average pressure behind the cascade $\bar{P}+B = (P_0^*+B)\bar{\pi}_t$, where is the pressure ratio

$$\bar{\pi}_t = \left(1 - 0.1666\bar{\lambda}^2 \right)^{3.5}, \quad (7)$$

determined by the reduced theoretical velocity $\bar{\lambda}_t = \bar{C}_t/18,3\sqrt{T_0^*}$.

From the condition of conservation of kinetic energy $\bar{E}_k = g\bar{C}^2/2 = \sum_{j=1}^m (C^2/2)\Delta g$ the averaged velocity \bar{C} is found, the reduced velocity $\bar{\lambda} = \bar{C}/18,3\sqrt{T_0^*}$, pressure ratio (7), total pressure behind the cascade $\bar{P}^*+B = (\bar{P}+B)/\bar{\pi}$ and gas density

$$\bar{\rho} = (\bar{P}+B) \cdot 9,8/\left(287\left(\bar{T}^* - \bar{C}^2/2009 \right) \right). \quad (8)$$

The last (fifth) integral relation

$$\bar{M}_a = rg\bar{C}_u = \sum_{j=1}^m rC \cos \gamma \cos \alpha \Delta g \quad (9)$$

allows you to find the averaged peripheral velocity component \bar{C}_u and divide the product into factors $\cos \bar{\gamma} \sin \bar{\alpha} = g/\bar{\rho}\bar{C}F$:

$$\bar{\alpha} = \arctg(\cos \bar{\gamma} \sin \bar{\alpha} \cdot \bar{C}/\bar{C}_u), \quad (10)$$

$$\bar{\gamma} = \arccos(\cos \bar{\gamma} \sin \bar{\alpha} / \sin \bar{\alpha}). \quad (11)$$

Loss coefficient in nozzle cascade $\bar{\zeta}_c = 1 - (\bar{C}/\bar{C}_t)^2$.

4 Results

Table 2 presents the results of averaging along the step by different methods of flow parameters from Table 1. The first column refers to the proposed hybrid method “ $\bar{E}, \bar{E}_k, \bar{h}_c, g, \bar{M}_a$ ”, which, according to the authors of the article, is quite reasonable.

In designating the methods in this table, the following integral flow characteristics were used: $\bar{R}_a = g \cdot \bar{C}_a$, $\bar{R}_u = g \cdot \bar{C}_u$, $\bar{R}_r = g \cdot \bar{C}_r$ – component of momentum; $\bar{I}_a = g\bar{C}_a + (\bar{P}+B) \cdot 9,8F$ – axial component of the total momentum; $\bar{R}_r = g\bar{C}_r$ – radial component of the momentum. The condition of conservation of entropy ($\bar{S} = \text{const}$) allows us to find the averaged total pressure by the equal [1]

$$\bar{P}^* + B = \exp g \left(\frac{1}{g} \sum_{j=1}^m [\ln(P^* + B)] \Delta g \right). \tag{12}$$

In the two penultimate columns of Table 2 $P, P^*, \sin \alpha, \cos \gamma$ were averaged over area and flow.

The use of four integral characteristics when averaging the three-dimensional flow in the “ $\bar{E}, \bar{I}_a, \bar{S}, g$ ” method does not allow us to divide the product $\cos \bar{\gamma} \sin \bar{\alpha}$ into factors and, therefore, find the moment \bar{M}_a . In this case [10], the efficiency of the flow stream is found by the equal $\bar{\eta}_{oi} = g C_p (\bar{T}^* - \bar{T}_2) / (g \bar{H}_p)$ which provides acceptable accuracy with a high difference in total temperatures.

Based on the proposed methodology “ $\bar{E}, \bar{E}_k, \bar{h}_c, g, \bar{M}_a$ ”, we will evaluate other methods of averaging the flow parameters (Table 2):

- Averaging over the flow mass rates $P, P^*, \sin \alpha, \cos \gamma$ allows you to reliably determine the pressure behind the nozzles and the loss coefficient. However, it overestimates the mass flow rate by 1.7%, and the moment \bar{M}_a by 2%. If the flow behind the axial stage ($\bar{M}_a = 0$), then such an overestimation will lead to an error in determining the efficiency by 2% relative.
- The simplest averaging over the area leads to somewhat overestimated values of the loss coefficient [20, 21] and pressure \bar{P} .
- To the greatest extent, the pressure \bar{P} , losses are underestimated, and the moment \bar{M}_a is overestimated when using the entropy method “ $\bar{E}, \bar{S}, g, \bar{R}_a, \bar{R}_r$ ”.

Table 2. The results of averaging along the step by various methods.

Parameter	Method						
	$\bar{E}, \bar{E}_k, \bar{h}_c, g, \bar{M}_a$	$\bar{E}, \bar{I}_a, g, \bar{R}_r, \bar{M}_a$ [13]	$\bar{E}, \bar{S}, g, \bar{R}_a, \bar{R}_r$ [12]	$\bar{E}, \bar{I}_a, \bar{S}, g$ [10]	Area Averaging, [20]	Flow averaging	$\bar{E}, \bar{E}_k, \bar{h}_c, \bar{R}_a / \bar{R}_a, \bar{R}_r / \bar{R}$ [7, 8]
\bar{T} , K	318	318	318	318	318	318	318
\bar{P} , kg/m ²	422	438	199	438	434	423	422
\bar{P}^* , kg/m ²	2830	2812	2845	2845	2819	2833	2830
$\bar{\theta}$, degree	71.94	71.85	72.58	71.95	71.75	71.55	71.50
$\bar{\alpha}$, degree	18.25	18.20	17.45	–	18.29	18.49	18.50
$\bar{\gamma}$, degree	7.97	4.1	3.7	–	5.97	5.90	4.10
g , kg/s	0.1012	0.1012	0.1012	0.1012	0.1015	0.1029	0.1036
\bar{E}_k , W	1832	1808	2027	1830	1819	1862	1876
\bar{M}_a	1.702	1.702	1.839	–	1.705	1.736	1.757
$P_0^* - \bar{P}^*$, kg/m ²	106	124	89	89	117	103	106
$\bar{\zeta}_c$	0.036	0.043	0.028	0.032	0.041	0.037	0.036

To calculate the efficiency of an elementary stage of a turbine in different modes, the total parameters in front of it, the pressure behind the stage, the rotation frequency, and the characteristics of the nozzle and rotor cascades averaged over the step should be known. The nozzle cascade characteristics are flow angles $\bar{\alpha}$ and $\bar{\gamma}$, as well as a loss

coefficient $\bar{\zeta}_c$. If these characteristics are determined by the proposed hybrid method $\bar{E}, \bar{E}_k, \bar{h}_c, g, \bar{M}_a$, then this will correctly find the flow parameters behind the nozzle, gas flow mass rate, and axial component of the angular momentum \bar{M}_a . The last column of Table 2 shows the results of averaging by the generally accepted [7, 8] hybrid method “ $\bar{E}, \bar{E}_k, \bar{h}_c, \bar{R}_a/\bar{R}_u$ ” for a flat flow, in which the averaged angle $\bar{\alpha}_{\kappa\delta}$ is determined from the ratio of the axial component of the momentum \bar{R}_a and the tangential component \bar{R}_u

$$\bar{\alpha} = \bar{\alpha}_{\kappa\delta} = \arctg \bar{R}_a/\bar{R}_u = \arctg \left(\frac{\sum_{j=1}^m C \sin \alpha \Delta g}{\sum_{j=1}^m C \cdot \cos \alpha \Delta g} \right). \quad (13)$$

From Table 2, it can be seen that, in comparison with the method $\bar{E}, \bar{E}_k, \bar{h}_c, g, \bar{M}_a$, the method $\bar{E}, \bar{E}_k, \bar{h}_c, \bar{R}_a/\bar{R}_u, \bar{R}_r/\bar{R}$ gives exactly the same averaged values $\bar{P}, \bar{P}^*, \bar{\zeta}_c$ but it overestimates the gas consumption by 2.4%, and the moment \bar{M}_a - by 3.2%.

In [1], it is noted that with any method of averaging the parameters of a non-uniform flow, only a part of its total characteristics is preserved, and some properties of the flow will inevitably be lost. It follows that in each individual case, it is necessary to choose a method of averaging that would most fully reflect the features of the task. Therefore, a slight underestimation of the angle $\bar{\alpha}$ and overestimation of the angle $\bar{\gamma}$ in the proposed method “ $\bar{E}, \bar{E}_k, \bar{h}_c, g, \bar{M}_a$ ” is not a significant drawback, as it provides the ability to correctly find the flow mass rate and moment \bar{M}_a . Apparently, a significant overestimation of entropy is not a drawback either, since it is customary to evaluate the efficiency of the cascade by the magnitude of the loss of specific kinetic energy, and not by the magnitude of the increase in entropy $\Delta S = R \ln((\bar{P}^* + B)/(\bar{P}_0^* + B))$. Unfortunately, when averaging the parameters of a non-uniform flow, it is impossible to preserve both the entropy and kinetic energy without distorting such an important parameter as the pressure behind the nozzle cascade, which is determined from the condition $\bar{h}_c = const$.

According to the proposals [1], in those cases when the meaning of the problem requires evaluating the operability of the initial gas flow, it is advisable to carry out averaging to keep the total value of the entropy of gas constant ($\bar{S} = const$). Such a not quite traditional approach is quite possible if maintained during averaging $\bar{E}, \bar{h}_c, g, \bar{M}_a$. Calculations show that when the kinetic energy is replaced in the “ $\bar{E}, \bar{E}_k, \bar{h}_c, g, \bar{M}_a$ ” method by entropy, the flow parameters \bar{P}, \bar{T}^* and theoretical velocity \bar{C}_t remain the same. An increase in total excess pressure \bar{P}^* from 2830 to 2845 kg/m² increases velocity. Velocity factor $\phi = \bar{C}/\bar{C}_t$ increases from 0.9817 to 0.9841. Since the angle $\bar{\alpha}$ does not practically change. An increase in velocity \bar{C} will occur due to an increase in the radial component of velocity, that is, due to an increase in the angle $\bar{\gamma}$ from 7.97 to 8.89°.

In contrast to the quite acceptable method “ $\bar{E}, \bar{S}, \bar{h}_c, g, \bar{M}_a$ ”, “entropy” methods [10, 12] do not provide conservation of the moment \bar{M}_a and difference of enthalpies \bar{h}_c . Note that the hybrid condition $\bar{h}_c = const$ can be completely replaced by averaging the pressure over the flow mass rate (see Table 2).

It is important to note that in contrast to the velocity coefficient $\bar{\phi}$, $\bar{\gamma}$ which in methods with the same \bar{E} , \bar{h}_c , g , \bar{M}_a increases when replaced \bar{E}_κ by entropy \bar{S} , the product $\bar{\phi} \cos \bar{\gamma}$ remains unchanged (0.9722). Thus, this work is a more universal characteristic of the quality of the cascade. The radial velocity component behind the nozzle cascade ($|\bar{\gamma}| > 0$) is the same drawback as the kinetic energy loss, determined by the velocity coefficient $\bar{\phi}$.

5 Conclusions

The well-known averaging method along the pitch of the parameters of the plane flow behind the nozzle cascade has been improved. It is proposed to replace the value used to find the averaged angle by the mass flow rate through the cascade and the axial direction of the angular momentum (method). The velocity coefficient $\bar{\phi}$ and the flow angles $\bar{\alpha}$, $\bar{\gamma}$ averaged along the pitch behind the cascade can be used as integral characteristics of the nozzle cascade on current surfaces. These characteristics of the nozzle cascade make it possible to correctly perform thermal calculations of the turbomachine stages with the known integrated characteristics of the rotor cascade.

The condition for entropy conservation can replace the condition for the conservation of kinetic energy in the method. At the same time, the product retains its significance despite the increase in the velocity coefficient $\bar{\phi}$ and the flow angle $\bar{\gamma}$. It is proposed to use the product as a universal characteristic of the nozzle cascade on the current surface.






References

1. Abramovich, G.N.: Applied Gas Dynamics. Science, Moscow (1969). (in Russian)
2. Bogdanović-Jovanović, J., Milenković, D., Stamenković, Ž, Spasić, Ž: Determination of averaged axisymmetric flow surfaces and meridian streamlines in the centrifugal pump using numerical simulation results. *Facta Universitatis Ser. Mech. Eng.* **15**(3), 479–493 (2017). <https://doi.org/10.22190/FUME170911026B>
3. Leggett, J., Shabbir, A., Richardson, E., Michelassi, V., Priebe, S., Sandberg, R.: Loss analysis of unsteady turbomachinery flows based on the mechanical work potential. In: Proceedings of the ASME Turbo Expo (Vol. 2A-2019). American Society of Mechanical Engineers (ASME). Phoenix, Arizona, USA (2019). <https://doi.org/10.1115/GT2019-91253>
4. Wang, F., di Mare, L., Adami, P.: Favre-averaged Fourier-based methods for gas turbine flows. In: Proceedings of the ASME Turbo Expo (Vol. 2C-2019). American Society of Mechanical Engineers (ASME). Phoenix, Arizona, USA (2019). <https://doi.org/10.1115/GT2019-91300>
5. Kortikov, N.N.: The method of averaging the gas flow parameters in turbomachines to evaluate their efficiency considering the velocity-field helicity. *Thermophys. Aeromechanics* **26**(2), 215–222 (2019). <https://doi.org/10.1134/S0869864319020057>
6. Avgustinovich, V.G.: Averaging unsteady non-uniform flow in turbomachines for efficiency estimation. *Bulletin PNRPU. Aerospace engineering* 49 (2017)
7. Deutsch, M.E.: Technical Gas Dynamics. Energy, Moscow (1974). (in Russian)

8. Stepanov, G.: Hydrodynamics of Cascade of Turbomachines. Fizmatgiz, Moscow (1962). (in Russian)
9. Merzliakov, I., Pavlenko, I., Chekh, O., Sharapov, S., Ivanov, V.: Mathematical modeling of operating process and technological features for designing the vortex type liquid-vapor jet apparatus. In: Ivanov, V., et al. (eds.) DSMIE 2019. LNME, pp. 613–622. Springer, Cham (2020). https://doi.org/10.1007/978-3-030-22365-6_61
10. Bodrunov, A.P.: Study of the operation of the last stages of powerful turbines in conditions close to natural. Ph.D. thesis, Kharkov Polytechnic Institute, Kharkov, Ukraine (1976)
11. Hu, W.J., Tan, K., Markovych, S., Liu, X.L.: Study of a cold spray nozzle throat on acceleration characteristics via CFD. *J. Eng. Sci.* **8**(1), F19–F24 (2021). [https://doi.org/10.21272/jes.2021.8\(1\).f3](https://doi.org/10.21272/jes.2021.8(1).f3)
12. Dronnik, Y., Vinarsky, B.B., Boguslavskaya, Z.D.: The technique of probe measurements of the spatial flow of steam in the models of nozzle devices of the last stages of turbines. *Power Eng.* **25**, 72–85 (1978)
13. Lim, Ch.S.: A method for the prediction of turbine performance characteristics through the experimental simulation of gas dynamic processes. Ph.D. thesis, NTU “Kharkov Polytechnic Institute”, Kharkov, Ukraine (2012)
14. Lytvynenko, O., Tarasov, O., Mykhailova, I., Avdieieva, O.: Possibility of using liquid-metals for gas turbine cooling system. In: Ivanov, V., Pavlenko, I., Liaposhchenko, O., Machado, J., Edl, M. (eds.) DSMIE 2020. LNME, pp. 312–321. Springer, Cham (2020). https://doi.org/10.1007/978-3-030-50491-5_30
15. Kelin, A., Larin, O., Naryzhna, R., Trubayev, O., Vodka, O., Shapovalova, M.: Mathematical modelling of residual lifetime of pumping units of electric power stations. In: Nechyporuk, M., Pavlikov, V., Kritskiy, D. (eds.) *Integrated Computer Technologies in Mechanical Engineering*. AISC, vol. 1113, pp. 271–288. Springer, Cham (2020). https://doi.org/10.1007/978-3-030-37618-5_24
16. Ochowiak, M., Wlodarczak, S., Pavlenko, I., Janecki, D., Krupinska, A., Markowska, M.: Study on interfacial surface in modified spray tower. *Processes* **7**(8), 532 (2019). <https://doi.org/10.3390/pr7080532>
17. Yushkevich, P.O., Molchanov, L.S.: Report on laboratory research of power-efficient triple-nozzle tuyere oxygen lancing. *J. Eng. Sci.* **4**(1), E1–E7 (2017). [https://doi.org/10.21272/jes.2017.4\(1\).e1](https://doi.org/10.21272/jes.2017.4(1).e1)
18. Vodka, O.: Analysis of quantitative characteristics of microstructures that are generated by the probabilistic cellular automata method. In: 2019 IEEE 2nd Ukraine Conference on Electrical and Computer Engineering (UKRCON), pp. 990–994 (2019). <https://doi.org/10.1109/UKRCON.2019.8879959>
19. Liaposhchenko, O., et al.: Improvement of parameters for the multi-functional oil-gas separator of ‘heater-treater’ type. In: 2019 IEEE 6th International Conference on Industrial Engineering and Applications (ICIEA), Tokyo, Japan, pp. 66–71 (2019). <https://doi.org/10.1109/IEA.2019.8715203>
20. Deich, M.E., Filippov, G.A., Lazarev, L.Ya.: Atlas of axial turbine cascade profiles. Engineering, Moscow (1965). (in Russian)
21. Cumpsty, N.A., Horlock, J.H.: Averaging non-uniform flow for a purpose. *J. Turbomach.* **128**(1), 120–129 (2006). <https://doi.org/10.1115/1.2098807>



Contact Interaction of a Ball Piston and a Running Track in a Hydrovolumetric Transmission with Intermediate Deformable Surface Layers

Mykola Tkachuk^(✉) , Andrey Grabovskiy , Mykola Tkachuk ,
Iryna Hrechka , and Volodymyr Sierykov 

National Technical University «Kharkiv Polytechnic Institute»,
2, Kyrpychova Street, Kharkiv 61002, Ukraine
m. tkachuk@tmm-sapr.org

Abstract. The properties of surface layers need to be accounted for in the analysis of contact interaction of complex-shaped bodies. Surface roughness, films, and coatings provide an additional response to the contact tractions. These microscopic deformations are generally nonlinear. To constitute the relationship between the contact pressure and normal compression of the intermediate layers, an ad hoc model is proposed. It consists of two superimposed layers on one side of the contact. Each layer has a different elasticity modulus and stiffness. As a result, the thicker later gets into contact sooner than the thinner one, which only comes into play after a certain loading level. This approach makes it possible to model an arbitrary bilinear response of the contact interface effectively using the finite element method. This model is applied to the analysis of contact interaction in radial hydrovolumetric drive with spherical pistons. The effect of layer stiffness parameters on the contact pressure distribution and the local stresses in the bodies is studied. The ability of additional compliance to reduce the stresses is found to be useful for further improvement of the strength of the pistons, which is crucial for the design.

Keywords: Hydrovolumetric transmission · Contact interaction · Contact layer · Von mises stress

1 Introduction

Contact interaction of complex-shaped parts can be found in literally any modern mechanism or machine. It is very common to seek the closest geometric form of the contact surfaces, which is possible for any general design. It is done to increase the contact area and reduce the contact pressure, lowering the local stresses around the contact spot. This question has been well studied within the traditional theory of contact mechanics. Practical recommendations have been accordingly developed for numerous applications. However, most of these results are valid for smooth bodies, thus completely disregarding such factors as surface roughness [1], films, and coating [2]. The deformation of these thin media is different from the bulk of the contacting

bodies. The surface layer can be constituted of a single or multiple materials with various physical properties. The microstructure of the surfaces can as well have a considerable effect on their mechanical response. The observed behavior is typically nonlinear to greater or lesser effect. Thus, the effective relationship between the intermediate layer's contact pressure and normal compression deviates from conventional Hooke's law. A new computational model that adequately represents the nonlinear contact layer of a general kind is developed in this paper. The analysis of contact interaction of a spherical piston and a toroidal running track in a hydrovolumetric transmission [3] demonstrates the application of the proposed model.

2 Literature Review

The rational design of modern hydraulic machines and mechanisms requires a thorough analysis of their operation conditions [4]. The output of a planetary hydromotor was studied in [5] concerning the location of the distribution windows and additional discharge windows. Multi-criteria optimization was performed in [6] to improve this hydraulic machine's overall performance.

Contact interaction plays a role that is not much less important than hydrodynamics [7]. The optimal design solutions in terms of performance are often not viable in terms of strength. Naturally, contact causes the concentration of loads [8] which may, in turn, lead to material failure. Various methods have been developed for the analysis of contact interaction of deformable solids [9, 10]. Variational formulations have proved to be beneficial for problem statements and derivation of analytical and numerical solutions. A model for the contact of elastic bodies with intermediate nonlinear Winkler surface layer was developed in [11]. The variational formulation of the problem was derived from a nonquadratic variational inequality and a nonlinear variational equation. The obtained problem is solved numerically using FEM and CFD approaches [12], for which a class of parallel iterative domain decomposition methods was proposed and implemented. Another approach [13] is based on the surface form of the Kalker variational principle that is suitable for applying the boundary element method (BEM). Both approaches display their benefits and weaknesses. In particular, the finite element method can be applied to bodies of arbitrary shape at the cost of a larger size of the discrete model and higher computational volume. Meanwhile, the boundary element method is faster due to the reduction of problem dimensionality while limited by the geometrical form of the bodies and the loading type. This problem can also be solved using artificial neural networks [14] with the consequent application in an engineering environment [15].

The physical behavior of the intermediate surface layers requires an appropriate model [16]. Due to the surface roughness, the real contact is only a partial fraction of the apparent contact spot [17]. Strong adhesion can bring the bodies to a near-complete contact [18, 19]. This discrepancy is manifested through the observed variations in surface conductance [20]. A multiasperity model developed in [21] considers contact distribution between a discrete set of contact spots at microscopic asperities. Importantly, it considers the mutual effect of deformations at each asperity due to the microscopic contact forces in all neighboring points. The effect of roughness on the

contact stiffness of the surface layer is studied in [22]. Depending on the geometrical parameters of the elastic body and the surface roughness, the contact behavior can range from hertzian to fractal [23]. The indenter's geometry has a major effect on the strength of adhesive contacts [24]. A scaling law for interfacial separation and its parameter identification are obtained in [25, 26]. This extends the contact mechanics theory of Persson [25, 27].

It may be concluded that adequate analysis of contact interaction with intermediate layers requires a rigorous combination of micro and macro models. An approach that implements such integration of the two models was proposed in [28]. The application of FEM or BEM governs the macrolevel while the microscopic response is represented as an effective Winkler layer. The nonlinear relation between contact pressure and normal contraction of the layer needs to be properly defined.

3 Research Methodology

A new method to constitute the nonlinear response of the intermediate layer between deformable bodies in contact is the main goal of this research. It is proposed to model it effectively as a combination of superposed layers of various height and material properties. This approach allows for straightforward and efficient implementation in standard finite element analysis software.

The research methodology extends the approach proposed in [28]. It was applied to analyze contact interaction between the spherical piston and toroidal running track on the stator of a hydrovolumetric drive GOP-900 [3]. The design of the entire drive and the arrangement of the pistons pressed to the stator ring in the pump and the motor is displayed in Fig. 1.

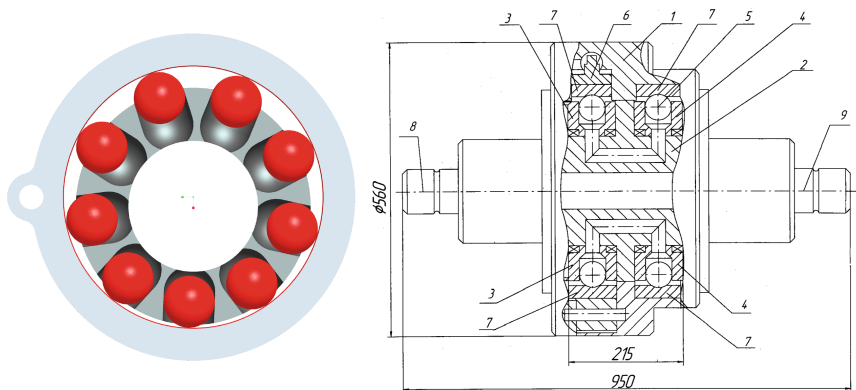


Fig. 1. The hydro volumetric transmission GOP-900 with ball pistons: 1 – housing; 2 – block of pin distributors; 3 – pump cylinder block (rotor); 4 – cylinder block of the hydraulic motor (rotor); 5 – ball-piston; 6 – pump stator; 7 – a running track of the pump and the hydraulic motor; 8 and 9 – input and output shafts of hydraulic transmission [2, 3].

The cross-section of the spherical piston and the stator ring in the plane of motor rotation as well as the lateral profile of the running track have the following geometrical dimensions: $R_p = 31.75$ mm is the radius of the spherical piston, $R_{st} = 160.0$ mm is the radius of the stator ring, $R_t = 38.1$ mm is the curvature radius of the central part of the running track profile, $R_s = 31.65$ mm is the curvature radius of the transition roundings, $\theta = 15^\circ$ is the angle of the central arc.

The compliance of the surface layers between the contacting bodies is sought in a bilinear relation. The contact pressure p depends linearly on layer deformation ε at initial interval 1 bounded by the upper limit ε_1 . A transition to interval 2, the dependence displays a kink. The tangent moduli on this bilinear relation are given accordingly as

$$E'_1 = tg\gamma_1, \quad (1)$$

$$E'_2 = tg\gamma_2. \quad (2)$$

Two overlapping intermediate layers are introduced on one of the contact surfaces to introduce this type of response into a finite element model.

The first layer of thickness $h_1 = 0.1$ mm was assigned the Young's modulus

$$E_1 = E'_1. \quad (3)$$

Such layer responds to the normal pressure nearly identical to the local Winkler foundation. The second layer has a smaller thickness $h_2 = 0.01$ mm, and the elastic modulus

$$E_2 = E'_2 - E'_1, \quad (4)$$

that is positive if the bilinear response displays hardening at the second interval. The thicker layer gets first into contact. The second layer gets only engaged after certain compression when the thickness gap is eliminated.

Such a straightforward approach to modeling the intermediate layer provides great flexibility in representing their physical properties. Particularly, it makes it possible to account for the microstructural characteristics such as surface roughness. The only parameters that need to be specified in the finite element model are the thicknesses of the two layers and their respective elastic moduli.

Once this model is determined, the contact problem is solved on the macroscopic level as a variational inequality [29]. According to the standard formulation of unilateral normal contact, the solution is found as an extremum of energy functional

$$I = \sum_{k=1}^4 I_k(u_k) \rightarrow \min. \quad (5)$$

The total elastic energy is made up by energies I_k of the two elastic bodies ($k = 1, 2$) and the two intermediate layers ($k = 3, 4$), each being a function of the respective displacement u_k :

$$I_1 = \frac{1}{2} \int_{(V_1)} \sigma_{ij}(u_1) \cdot \varepsilon_{ij}(u_1) dv - \int_{(S_u^1)} f_1 \cdot u_1 ds, \quad (6)$$

$$I_2 = \frac{1}{2} \int_{(V_2)} \sigma_{ij}(u_2) \cdot \varepsilon_{ij}(u_2) dv, \quad (7)$$

$$I_3 = \frac{1}{2} \int_{(S_c)} p \cdot (u_3 - u_2) ds, \quad (8)$$

$$I_4 = \frac{1}{2} \int_{(S_c)} p \cdot (u_4 - u_2) ds. \quad (9)$$

Note that the first two terms are defined for the bulk of the material domains V_1 , V_2 of the two bodies (1 – the spherical piston; 2 – the stator ring). The elastic work is thus computed for the components of stresses and deformations σ_{ij} , ε_{ij} . The surface term in the first term also represents the action of the external loading f_1 which is the pressure of the hydraulic fluid on the internal part of the spherical piston surface S_u^1 facing the rotor cylinder. The deformation energies of the intermediate layers are in turn given by reduced surface form as the work of contact tractions p made on the layer compression over the contact area S_c .

The minimum of the functional (5) is sought in the admissible set

$$\kappa = \{u_1, u_3, u_4 : u_v^1 + u_v^3 \leq \Delta; u_v^1 + u_v^4 \leq \Delta + h_1 - h_2\}, \quad (10)$$

of displacements u_v^k that do not violate unilateral contact conditions. The relative normal displacements of the bodies and the layers shall not exceed the initial gap Δ between body 1 and layer 3.

The finite element approximation leads to the discretized version of the functional (5)

$$I = \frac{1}{2} \sum_{m,n} C_{mn} \cdot q_m \cdot q_n - \sum_m F_m \cdot q_m \rightarrow \min, \quad (11)$$

and the minimization problem with the inequality constraints in the form

$$q_e^v + q_r^v \leq \Delta_{er}, \quad (12)$$

Where q_m , q_n are nodal displacements; C_{mn} are the coefficients of the global stiffness matrix; F_m are the nodal forces; q_e^v , q_r^v are the relative normal nodal displacements on the contact surfaces; Δ_{er} are the normal gap values between nodes and segments e and r . The finite element solution provides the stress-strain state of the two bodies as well as the actual contact area S_c' and the contact pressure as a total of the two tractions exerted by the two elastic layers.

As a result, one can establish the parametric relations between the deformations of the contacting bodies and the elastic properties of the intermediate elastic layers E_1' , E_2' (or E_1 , E_2) and their thicknesses

$$\left. \begin{aligned} S'_c &= S'_c(E_1, E_2); p = p(E_1, E_2); u_i^k = u_i^k(E_1, E_2); \\ \sigma_{ij}^k &= \sigma_{ij}^k(E_1, E_2); \varepsilon_{ij}^k = \varepsilon_{ij}^k(E_1, E_2) \end{aligned} \right\}. \tag{13}$$

One can accordingly consider any other parametric dependency of certain characteristics H_g of stress-strain state on the varied parameters π_t

$$H_g = H_g(\pi_t). \tag{14}$$

Maximal contact pressure, maximal von-Mises stress may be chosen as such characteristics H_g . Parameters π_t include the elastic moduli of the elastic E'_1, E'_2 (or E_1, E_2) and their thicknesses h_1, h_2 . These relations can be used to evaluate various design solutions concerning the local strength of the two bodies in contact interaction.

4 Results

The stiffness variation of the intermediate surface layers was considered around their initial reference values

$$E_1^0 = 10^9 \text{Pa}, E_2^0 = 10^{10} \text{Pa}. \tag{15}$$

in terms of the dimensionless parameters

$$\gamma_1 = E_1/E_1^0, \gamma_2 = E_2/E_2^0. \tag{16}$$

that were considered in the range [0.1; 5.0]. The piston loading force was set to be $P = 0 \div 200$ kN with the nominal value $P_0 = 100$ kN. The dimensionless parameter $\gamma_3 = P/P_0$, thus varied from 0 to 2.0.

The controlled quantities for the obtained response were the relative change of the maximal contact pressure level in the two layers

$$\alpha_1(\gamma_1, \gamma_2) = p_{max}^{1(\gamma_1, \gamma_2)} / p_{max}^{1(1, 1)}; \tag{17}$$

$$\alpha_2(\gamma_1, \gamma_2) = p_{max}^{2(\gamma_1, \gamma_2)} / p_{max}^{2(1, 1)}, \tag{18}$$

and the relative variation of the maximal von Mises strength in the spherical piston and the stator ring:

$$\beta_1(\gamma_1, \gamma_2) = \sigma_{max}^{1(\gamma_1, \gamma_2)} / \sigma_{max}^{1(1, 1)}; \tag{19}$$

$$\beta_2(\gamma_1, \gamma_2) = \sigma_{max}^{2(\gamma_1, \gamma_2)} / \sigma_{max}^{2(1, 1)}. \tag{20}$$

Figures 2, 3, 4 and 5 display contact pressure distribution p and the shape of the contact area S'_c for the varied parameters $\gamma_1, \gamma_2, \gamma_3$.

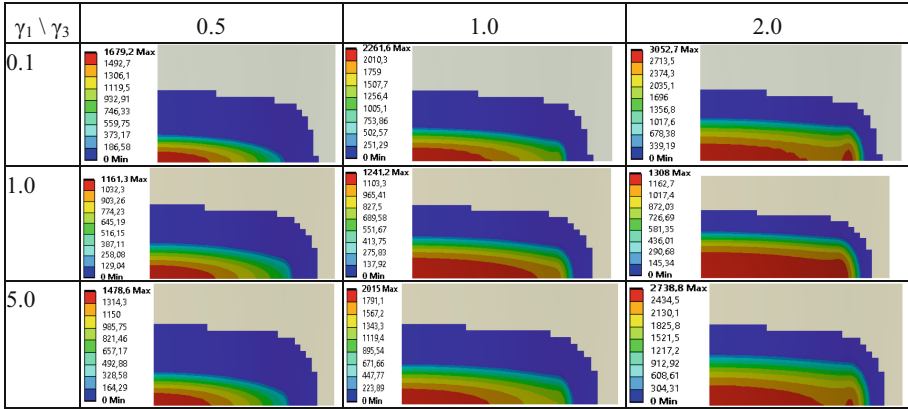


Fig. 2. Contact pressure distribution p (MPa) in layer 1 for variable γ_1 , γ_3 and nominal $\gamma_2 = 1$.

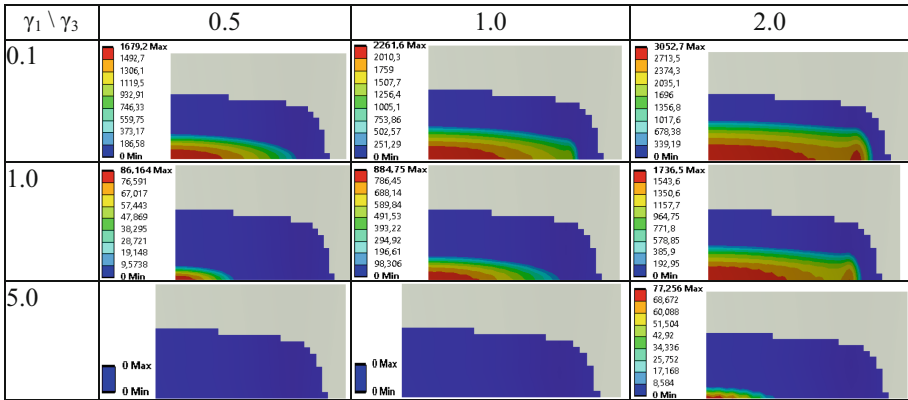


Fig. 3. Contact pressure distribution p (MPa) in layer 2 for variable γ_1 , γ_3 and nominal $\gamma_2 = 1$.

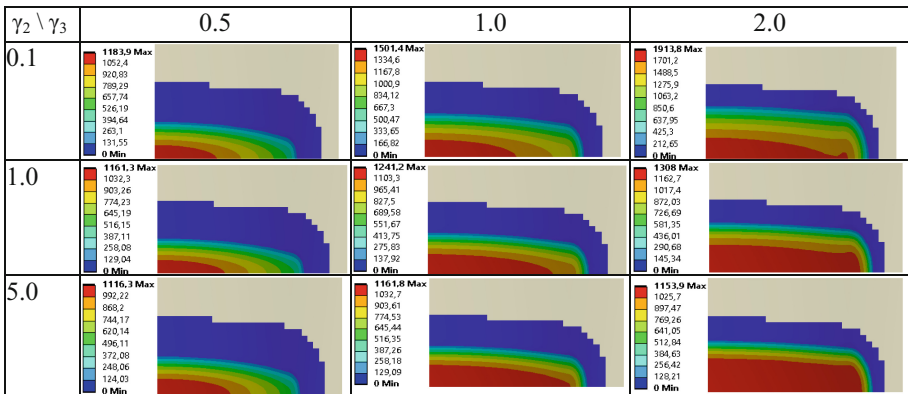


Fig. 4. Contact pressure distribution p (MPa) in layer 1 for variable γ_2 , γ_3 and nominal $\gamma_1 = 1$.

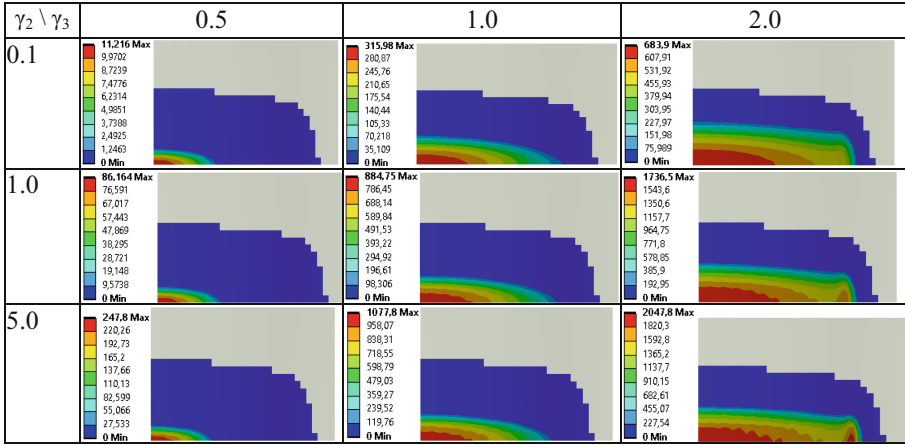


Fig. 5. Contact pressure distribution p (MPa) in layer 2 for variable γ_2, γ_3 , and nominal $\gamma_1 = 1$.

The distribution of von Mises stress in the spherical piston and the stator ring for the nominal parameters $\gamma_1, \gamma_2, \gamma_3$ are shown in Figs. 6, 7. They change according to the contact pressure distribution.

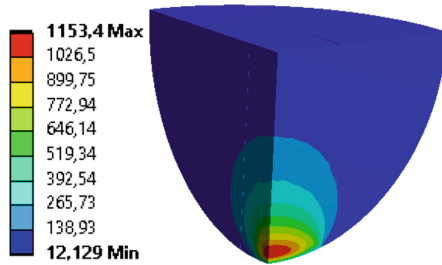


Fig. 6. Von Mises stress distribution in the spherical piston at nominal parameters.

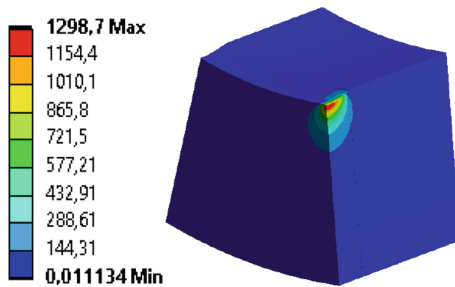


Fig. 7. Von Mises stress distribution in stator ring at nominal parameters.

The relative change of the maximal contact pressure in contact layers $\alpha_1(\gamma_1, \gamma_2, \gamma_3)$ and $\alpha_2(\gamma_1, \gamma_2, \gamma_3)$ are shown in Figs. 8, 9.

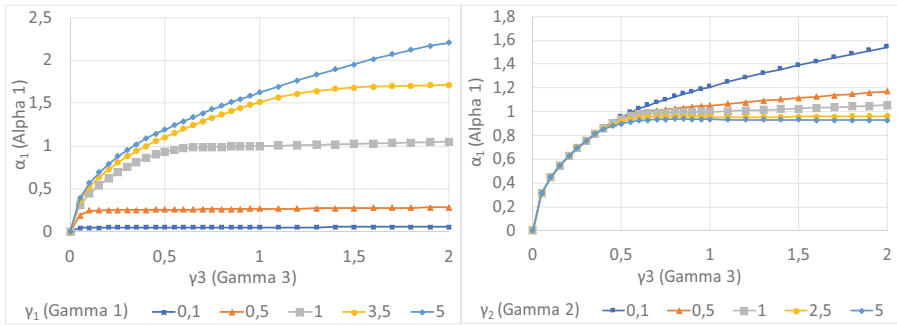


Fig. 8. Variations of relative maximal contact pressure in thicker layer $\alpha_1(\gamma_1, 1, \gamma_3)$ and $\alpha_1(1, \gamma_2, \gamma_3)$.

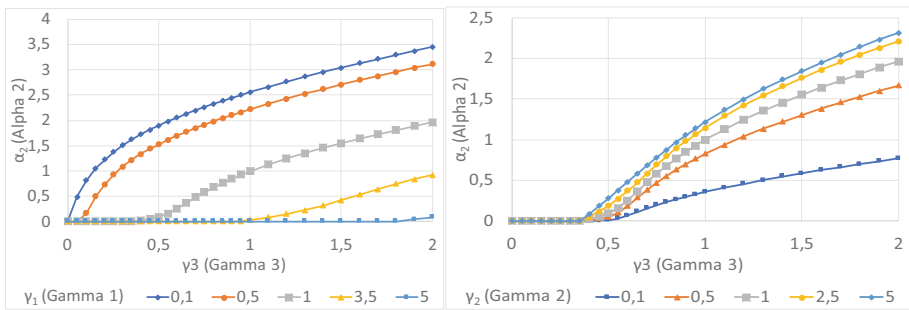


Fig. 9. Variations of relative maximal contact pressure in thinner layer $\alpha_2(\gamma_1, 1, \gamma_3)$ and $\alpha_2(1, \gamma_2, \gamma_3)$.

The relative change of the maximal von Mises stress level in the spherical piston and the stator ring $\beta_1(\gamma_1, \gamma_2, \gamma_3)$ and $\beta_2(\gamma_1, \gamma_2, \gamma_3)$ are shown in Figs. 10, 11.

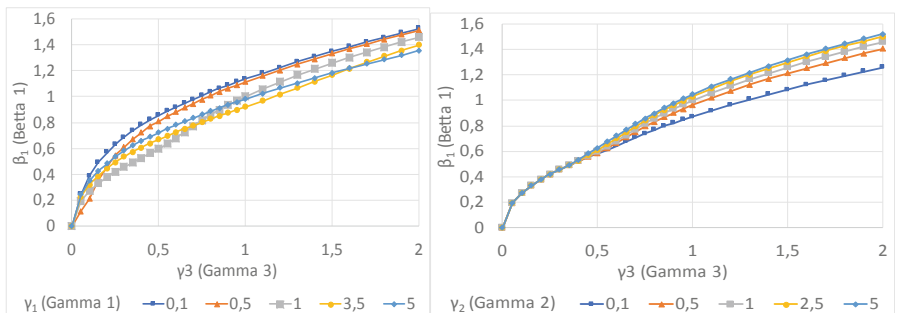


Fig. 10. Variations of relative von Mises stress level in spherical piston $\beta_1(\gamma_1, 1, \gamma_3)$ and $\beta_1(1, \gamma_2, \gamma_3)$.

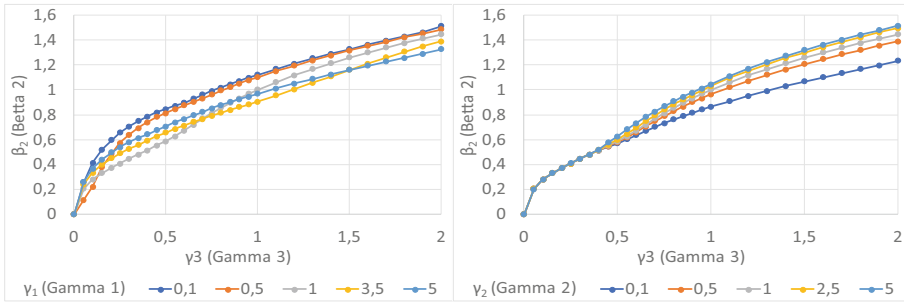


Fig. 11. Variations of relative von Mises stress level in stator ring $\beta_2(\gamma_1, 1, \gamma_3)$ and $\beta_2(1, \gamma_2, \gamma_3)$.

The obtained results prove that the contact pressure p as well as the dimensions and shape of the contact area S'_c at low loadings P are close to the Hertzian solution. The contact area S'_c is close to the oval shape. The maximum contact pressure P_{max} is located in the initial, middle point of contact. Accordingly, it drops steadily at the edge of the contact area.

The contact area S'_c expands with the growth of the loading P . It also changes the shape as it becomes truncated at the rounded transitional part of the running track profile. It transforms first from the oval to the rounded rectangular and further on takes the dumb-bell shape getting thicker at the edge of the central part of the profile. The contact pressure exceedingly grows at this location which ultimately becomes the major stress concentration.

The contact forces are distributed between the two layers non-uniformly. The contact pressure in the thicker first layer first displays steady growth similar to the Hertz theory, but it later saturates and follows nearly linear dependence. The second layer remains inactive until a certain level of the loading P when the gap due to the thickness difference gets closed. Once engaged into contact, the thin layer becomes loaded nearly linear similarly to the first layer. The effect of the resulting hardening shows itself in Fig. 10, 11 as an upturn of the stress levels after reaching a certain threshold of the loading parameter γ_3 .

5 Conclusion

The nonlinear intermediate layer has an essential impact on the contact interaction of the spherical piston with the stator ring. The microscopic deformations in this layer when the contacting bodies are of close conforming shape turn out to be significant. The additional compliance results in regular contact pressure distribution over a larger contact area compared to smooth surfaces with no intermediate layers. Still, the nearly oval shape of the contact spot at low pressing forces and the dumb-bell shape of contact at higher loadings are preserved. But the stress concentration in the middle of the former and at the edges of the latter are far less pronounced.

The bilinear nonlinear characteristics of the layer response manifest in the distinct hardening of the interface. In the finite element model, it occurs when the thinner layer

gets into contact. The increased stiffness of the layer accelerates the upturn of the contact pressure and the local stresses in the bodies with the loading.

The obtained levels of von Mises stress in the spherical piston and the stator ring are crucial for evaluating their strength. Note that their magnitude is generally are twice lower than the total contact pressure at various loads.

The positive effect of the intermediate layer compliance should be utilized in future designs of this class of hydrovolumetric drives. It is possible to choose the surface properties for the pistons and the running track that provide higher strength and durability for any particular geometry of these elements. The synthesis of these design parameters is a subject of further surveys. This approach can also be extended to other machine parts bearing high contact loads: roller and ball bearings, engine pistons, hydraulic pumps, etc.





References

1. Dehtiarov, I.M., Neshta, A.O., Samardak, M.P., Antosz, K., Avramenko, S.E.: Contact of working surfaces for spherical washers and recommendations for determining the gap in the joint. *J. Eng. Sci.* **7**(2), B1–B7 (2020). [https://doi.org/10.21272/jes.2020.7\(2\).b1](https://doi.org/10.21272/jes.2020.7(2).b1)
2. Tkachuk, M.M., Skripchenko, N., Tkachuk, M.A., Grabovskiy, A.: Numerical methods for contact analysis of complex-shaped bodies with account for nonlinear interface layers. *Eastern-Eur. J. Enterp. Technol.* **5**(7(95)), 22–31 (2018)
3. Avrunin, G., Kabanenko, S., Khavil, V.: Volumetric hydraulic transmission with ball pistons GOP-900: characteristics and technical level. *Mech. Mech. Eng.* **1**, 14–21 (2004)
4. Panchenko, A., Voloshina, A., Panchenko, I., Titova, O., Pastushenko, A.: Reliability design of rotors for orbital hydraulic motors. *IOP Conf. Ser. Mater. Sci. Eng.* **708**(1), 012017 (2019)
5. Voloshina, A., Panchenko, A., Panchenko, I., Titova, O., Zasiadko, A.: Improving the output characteristics of planetary hydraulic machines. *IOP Conf. Ser. Mater. Sci. Eng.* **708**(1), 012038 (2019)
6. Panchenko, A., Voloshina, A., Titova, O., Panchenko, I., Caldare, A.: Design of hydraulic mechatronic systems with specified output characteristics. In: Ivanov, V., Pavlenko, I., Liaposhchenko, O., Machado, J., Edl, M. (eds.) *DSMIE 2020. LNME*, pp. 42–51. Springer, Cham (2020). https://doi.org/10.1007/978-3-030-50491-5_5
7. Fesenko, A., Yevsiukova, F., Basova, Y., Ivanova, M., Ivanov, V.: Prospects of using hydrodynamic cavitation for enhancement of efficiency of fluid working medium preparation technologies. *Periodica Polytechnica Mech. Eng.* **62**(4), 269–276 (2018). <https://doi.org/10.3311/PPme.11877>
8. Karpus, V.E., Ivanov, V.A.: Locating accuracy of shafts in V-blocks. *Russ. Eng. Res.* **32**(2), 144–150 (2012). <https://doi.org/10.3103/S1068798X1202013X>
9. Johnson, K.L.: *Contact Mechanics*. Cambridge University Press, Cambridge (1987)
10. Prydalnyi, B.I., Sulym, H.T.: Mathematical model of the tensioning in the collet clamping mechanism with the rotary movable input link on spindle units. *J. Eng. Sci.* **8**(1), E23–E28 (2021). [https://doi.org/10.21272/jes.2021.8\(1\).e4](https://doi.org/10.21272/jes.2021.8(1).e4)
11. Martynyak, R.M., Prokopyshyn, I.A., Prokopyshyn, I.I.: Contact of elastic bodies with nonlinear Winkler surface layers. *J. Math. Sci.* **205**, 535–553 (2015)
12. Khovanskyi, S., Pavlenko, I., Pitel, J., Mizakova, J., Ochowiak, M., Grechka, I.: Solving the coupled aerodynamic and thermal problem for modeling the air distribution devices with perforated plates. *Energies* **12**(18), 3488 (2019). <https://doi.org/10.3390/en12183488>

13. Zhao, J., Vollebregt, E., Oosterlee, C.: Extending the BEM for elastic contact problems beyond the half-space approach. *Math. Model. Anal.* **21**(1), 119–141 (2016)
14. Pavlenko, I., Ivanov, V., Kuric, I., Gusak, O., Liaposhchenko, O.: Ensuring vibration reliability of turbopump units using artificial neural networks. In: Trojanowska, J., Ciszak, O., Machado, J.M., Pavlenko, I. (eds.) *MANUFACTURING 2019*. LNME, pp. 165–175. Springer, Cham (2019). https://doi.org/10.1007/978-3-030-18715-6_14
15. Ivanov, V., Pavlenko, I., Trojanowska, J., Zuban, Y., Samokhvalov, D., Bun, P.: Using the augmented reality for training engineering students. In: *4th International Conference of the Virtual and Augmented Reality in Education, VARE 2018*, pp. 57–64 (2018)
16. Persson, B.N.J., Bucher, F., Chiaia, B.: Elastic contact between randomly rough surfaces: comparison of theory with numerical results. *Phys. Rev. B* **65**(18), 184106 (2002)
17. Paggi, M., Ciavarella, M.: The coefficient of proportionality κ between real contact area and load, with new asperity models. *Wear* **268**(7), 1020–1029 (2010)
18. Ciavarella, M.: Adhesive rough contacts near complete contact. *Int. J. Mech. Sci.* **104**, 104–111 (2015)
19. Ivanov, V., Pavlenko, I., Liaposhchenko, O., Gusak, O., Pavlenko, V.: Determination of contact points between workpiece and fixture elements as a tool for augmented reality in fixture design. *Wireless Netw.* **27**(3), 1657–1664 (2019). <https://doi.org/10.1007/s11276-019-02026-2>
20. Ciavarella, M., Dibello, S., Demelio, G.: Conductance of rough random profiles. *Int. J. Solids Struct.* **45**(3), 879–893 (2008)
21. Papangelo, A., Hoffmann, N., Ciavarella, M.: Load-separation curves for the contact of self-affine rough surfaces. *Sci. Rep.* **7**(1), 6900 (2017)
22. Pohrt, R., Popov, V.L.: Contact stiffness of randomly rough surfaces. *Sci. Rep.* **3**, 3293 (2013)
23. Pohrt, R., Popov, V.L.: Contact mechanics of rough spheres: crossover from fractal to hertzian behavior. *Adv. Tribol.* **2**, 974178 (2013)
24. Pastewka, L., Prodanov, N., Lorenz, B.: Finite-size scaling in the interfacial stiffness of rough elastic contacts. *Phys. Rev. E* **87**, 062809 (2013)
25. Persson, B.N.J.: Relation between interfacial separation and load: a general theory of contact mechanics. *Phys. Rev. Lett.* **99**(12), 125502 (2007)
26. Liaposhchenko, O., et al.: Improvement of parameters for the multi-functional oil-gas separator of ‘heater-treater’ type. In: *2019 IEEE 6th International Conference on Industrial Engineering and Applications (ICIEA)*, Tokyo, Japan, pp. 66–71 (2019). <https://doi.org/10.1109/IEA.2019.8715203>
27. Popov, V.L., Pohrt, R., Li, Q.: Strength of adhesive contacts: influence of contact geometry and material gradients. *Friction* **5**(3), 308–325 (2017). <https://doi.org/10.1007/s40544-017-0177-3>
28. Tkachuk, M.M., Grabovskiy, A., Tkachuk, M.A., Saverska, M., Hrechka, I.: A semianalytical method for analysis of contact interaction between structural elements along aligned surfaces. *Eastern-Eur. J. Enterp. Technol.* **17**(103), 16–25 (2020)
29. Hlavacek, I., Haslinger, J., Necas, J., et al.: *Solution of Variational Inequalities in Mechanics*. Springer-Verlag, New York (1988). <https://doi.org/10.1007/978-1-4612-1048-1>



Diagnostics of the Rotor-Stator Contact by Spectral Analysis of the Vibration State for Rotor Machines

Ivan Pavlenko¹ , Ievgen Savchenko¹ , Jan Pitel² ,
Vitalii Ivanov¹ , and Anatolii Ruban¹

¹ Sumy State University, 2, Rymkogo-Korsakova Street, Sumy 40007, Ukraine
i.pavlenko@omdm.sumdu.edu.ua

² Technical University of Kosice,

1, Bayerova Street, Presov 08001, Slovak Republic

Abstract. The spectral composition of the rotor's vibration characteristic under its contact conditions with the stator was investigated in the article. Based on the clipped sinewave model, it was determined that the signal spectrum contains odd components in addition to the main harmonic. Analytical dependences of amplitudes for spectral composition's components of a signal on the dimensionless radial gap between a rotor and a stator were established. As a result, the main and third harmonics have the highest amplitudes. An analytical dependence determining the dimensionless radial gap by the ratio of the spectral components' amplitudes was obtained. Moreover, theoretically substantiated that the representation of the response for the system "rotor-stator" as a superposition of only the main and third harmonics allows modeling the system's response caused by the influence of contact interaction. This approximation has a maximum relative error of 5% for the dimensionless radial gap in a range of 0.56–1.0.

Keywords: Technical Diagnostics · Contact interaction · Radial gap · Fourier transform

1 Introduction

Rotor machines play an essential role in mechanical and chemical engineering, particularly for the pump and compressor industry [1]. Simultaneously, a constant increase in rotary machines' energy consumption [2] causes adverse events in their functioning, such as radial run-out, friction, wear, and contact interaction of working bodies with the stator [3]. For eliminating these shortcomings, it is necessary to make an appropriate design with a margin of safety by indicators of vibration reliability [4]. Additionally, an essential role is played by detecting defects by the vibration spectrum during the machine's operation. [5].

Self-oscillations also cause increased vibrations and noise in centrifugal machines [6]. Therefore, the determination of frequencies for possible self-oscillations under contact with the stator makes a particular scientific and practical interest for diagnosing

the rotor machine's technical condition. However, in practice, it is not always possible to prevent a reliable margin of safety. Mainly, self-oscillating processes are usually relatively weak due to significant damping. Therefore, they can be undetected without analyzing the spectral composition of the signal [7].

Equipment defects associated with contacts or wearing describe technologically unacceptable processes. Their diagnostic features give practically the same frequency pattern in the spectra of vibration signals [8]. Notably, by the origin, these defects are conventionally divided into two groups: structurally envisaged (e.g., throttling seals in pumps and compressors [9]), and emergency (e.g., wearing of the support bearings [10], changes in technological gaps in seals [11], reshaping of busing parts [12], falling of foreign elements into the working area [13], rotor-stator contact [14]).

Notably, contact between the rotor and the stator leads to modifying the recorded vibration signal's spectrum. The last one includes a wide range of frequencies, multiples of the synchronous component [15].

The power of the vibration signal is also partly due to asynchronous components. They are associated with both nonstationarities of contact interaction [16] and resonant processes' influence in functional elements [17].

Moreover, a characteristic diagnostic indicator of the contact in the system "rotor-stator" is the presence of a temporary clipped sinewave signal. In this case, the spectrum is dominated by components corresponding to the first (asynchronous) and third (multiple) harmonics [8, 15]. The contact interaction clips the sinusoid peaks, and when leaving the contact area, the original sinusoidal waveform is restored. However, despite the number of empirical observations and practical conclusions, the appearance of individual components in the spectrum described above (related to the contact interaction between elements of the rotor system) also requires more thorough theoretical justification.

2 Literature Review

The problem of technical diagnostics of mechanical systems using spectral analysis is urgent in various engineering fields. Notably, Yadav and Prajapati [18] proposed the technology to minimize clipped signals using the tangent rooting companding technique. Esqueda et al. [19] developed an approach for aliasing reduction in clipped signals. Liu et al. [20] studied the methods for signal recovery using the Gaussian mixture GTurbo algorithm. Advancements in fault diagnostics for industrial machines were analyzed by Altaf et al. [21].

Kolomvakis et al. [22] dealt with the reconstruction of clipped signals in quantized uplink massive systems. Finally, Dyer S. and Dyer J. [23] studied the total harmonic distortion in asymmetrically clipped sinewaves.

The essential role of the following researchers in applying Fourier transform in diagnostics of technical systems. Significantly, an approach of fault diagnosis using Hilbert transform and fractional Fourier transform was proposed by Zhou et al. [24]. Additionally, fault detection and diagnosis of rotor machines based on convolutional extended short-term memory algorithm, fast Fourier transform, and continuous wavelet transform were proposed by Jalayer et al. [25]. Finally, Xu et al. [26] developed

approaches based on the inverse short-time Fourier transform and a singular value decomposition for bearing fault diagnosis.

However, the methodologies mentioned above do not analytically study the clipped sinewave signals in terms of spectral components and their impact on the initial signal's total harmonic approximation.

Additionally, Monkova et al. [27] dealt with the condition monitoring of turbines. Finally, the research works [28, 29] aim to ensure vibration reliability of turbopump units and hydromechanical systems using artificial intelligence systems.

Notably, the research's practical significance can be highlighted by a number of research works in the related fields. Remarkably, the papers [30, 31] present the mathematical model and the corresponding design calculation approach for ensuring dynamic characteristics of technological equipment.

Ways for increasing the wear resistance of throttling gaps and bearing supports were developed in the papers [32, 33]. Approaches for calculating the ductility of a roller bearing under an uncentral loading were presented in the article [34]. Additionally, the abrasive medium's influence on the reliability of rotor machines was partially studied in the paper [35].

The discrete Fourier transform theory for solving technical diagnostics problems for mechanical systems was practically implemented in papers [36, 37]. Diagnostics of engines' imbalances using the modulated sliding discrete Fourier transform was applied by Yoon and Brahma [38]. Also, fault diagnostics using fast Fourier transform and artificial neural networks were implemented by Kumar et al. [39].

Ways for parameter identification of technological equipment for ensuring the reliability of multidisciplinary operating processes were proposed in papers [40, 41]. Implementation of data fusion classification technique based on an artificial neural network for rotor machines' fault detection was applied in the article [42]. Additionally, ways for ensuring the reliability criteria were proposed for crankshafts [43] and high-speed machines [44]. The dynamics of a particle on curvilinear and sinewave profiles were stated in the papers [45, 46]. Finally, the dynamic state of machine tools was studied in the papers [47, 48].

Due to the analysis mentioned above, the article aims at identifying and studying individual components of the signal, informing about the dysfunctional vibrational state of a machine caused by contact interaction between the rotor and the stator. For achieving this goal, the following research objectives are formulated:

- –to decompose the clipped sinewave time signal into a trigonometric Fourier series, and to determine analytical expressions for the signal's spectral composition;
- –to carry out a harmonic approximation of the studied signal with an application of the minimum quantity of components of the vibrational spectrum;
- –to evaluate a range of the dimensionless radial gap that provides the specified maximum relative error of the harmonic approximation of the signal;
- –to propose a criterion for estimating the dimensionless radial gap by the vibration signal's spectral composition.

3 Research Methodology

According to the clipped sinewave model, the system “rotor-stator” response resulting from contact interaction of its functional elements is considered (Fig. 1a). This model corresponds to the plain trajectory given in Fig. 1b.

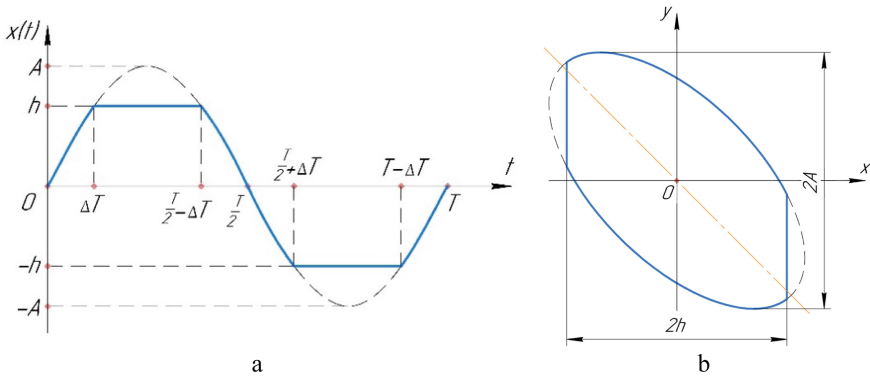


Fig. 1. The clipped sinewave model (a) and the corresponding plain trajectory (b).

According to the previous researches in the field of diagnostics of mechanical systems [8, 15], such a model is inherent in the cases of contact or wearing of the functional elements of the technological equipment (e.g., contact in seals of pumps and compressors, wear of supporting elements, surface reshaping).

The studied model contains the following basic parameters: $T = 2\pi/\omega$ – a period of oscillations [s] associated with frequency ω [rad/s]; A – amplitude of oscillations without contact with the stator [m]; h – the average radial gap between the rotor and the stator [m]. The model can be analytically presented as follows:

$$f(t) = \begin{cases} A\sin(\omega t), & t = [0, \Delta T) \cup [\frac{T}{2} - \Delta T, \frac{T}{2} + \Delta T) \cup [T - \Delta T, T); \\ h \leq A, & t = [\Delta T, \frac{T}{2} - \Delta T); \\ -h \geq -A, & t = [\frac{T}{2} + \Delta T, T - \Delta T), \end{cases} \quad (1)$$

where $\Delta T = \frac{1}{\omega} \arcsin(\eta)$ – time before contact [s], which depends on the dimensionless radial gap $\eta = \frac{h}{A}$.

Given the oddness of the function $f(t)$, that is $f(-t) = -f(t)$, it can be represented as a trigonometric Fourier series [49] with exclusively sinusoidal components:

$$F(t) = \sum_{k=1}^N \beta_k \sin(k\omega t), \quad (2)$$

where N – the number of valuable elements of the frequency spectrum. The following formula determines the coefficients of this series:

$$\beta_k = 2i_k^{<1>} + 2i_k^{<2>} + i_k^{<3>}, \quad (3)$$

which contains auxiliary integrals:

$$\begin{aligned} i_k^{<1>} &= \frac{2}{T} \int_0^{\Delta T} f(t) \sin(k\omega) dt = \frac{2}{T} \int_{T-\Delta T}^T f(t) \sin(k\omega) dt; \\ i_k^{<2>} &= \frac{2}{T} \int_{\frac{T}{2}-\Delta T}^{\frac{T}{2}} f(t) \sin(k\omega) dt = \frac{2}{T} \int_{\frac{T}{2}+\Delta T}^T f(t) \sin(k\omega) dt; \\ i_k^{<3>} &= \frac{2}{T} \int_{\frac{T}{2}-\Delta T}^{\frac{T}{2}+\Delta T} f(t) \sin(k\omega) dt. \end{aligned} \quad (4)$$

After considering function (1) and applying identical transformations, the integrals take the following forms (Fig. 2):

$$\begin{aligned} i_k^{<1>} &= \begin{cases} -\frac{A}{2\pi} \left[\eta \sqrt{1-\eta^2} - \arcsin(\eta) \right], k=1; \\ \frac{A}{\pi(k^2-1)} \left[\sqrt{1-\eta^2} \sin(k\omega\Delta T) - k\eta \cos(k\omega\Delta T) \right], k \geq 2; \end{cases} \\ i_k^{<2>} &= \left[1 - (-1)^k \right] \frac{\eta A}{\pi k} \cos(k\omega\Delta T); \\ i_k^{<3>} &= \begin{cases} -\frac{A}{\pi} \left[\eta \sqrt{1-\eta^2} - \arcsin(\eta) \right], k=1; \\ -(-1)^k \frac{2A}{\pi(k^2-1)} \left[\sqrt{1-\eta^2} \sin(k\omega\Delta T) - k\eta \cos(k\omega\Delta T) \right], k \geq 2, \end{cases} \end{aligned} \quad (5)$$

which allows achieving a general analytical expression for the coefficients of the Fourier series (2):

$$\beta_k = \begin{cases} \frac{2A}{\pi} \left[\eta \sqrt{1-\eta^2} - \arcsin(\eta) \right], k=1; \\ \frac{2A}{\pi} \frac{1-(-1)^k}{k(k^2-1)} \left[k \sqrt{1-\eta^2} \sin(k\omega\Delta T) - \eta \cos(k\omega\Delta T) \right], k \geq 2. \end{cases} \quad (6)$$

4 Results

Absolute values of coefficients β_k ($k = 1, 2, \dots, N$) determine the signal spectrum (Fig. 3). Notably, all even components β_{2k} identically equal to zero due to $i_{2k}^{<2>} = 0$, and $i_{2k}^{<3>} = -2i_{2k}^{<1>}$. Odd components for the most valuable harmonics are determined analytically by the following formulas:

$$\begin{aligned} \beta_1 &= \frac{2A}{\pi} \left[\eta \sqrt{1-\eta^2} + \arcsin(\eta) \right]; \beta_3 = \frac{4A}{3\pi} \eta (1-\eta^2)^{\frac{3}{2}}; \\ \beta_5 &= \frac{4A}{5\pi} \eta (1-\eta^2)^{\frac{3}{2}} \left(1 - \frac{8}{3} \eta^2 \right); \beta_7 = \frac{4A}{7\pi} \eta (1-\eta^2)^{\frac{3}{2}} \left(1 - \frac{20}{3} \eta^2 + 8\eta^4 \right). \end{aligned} \quad (7)$$

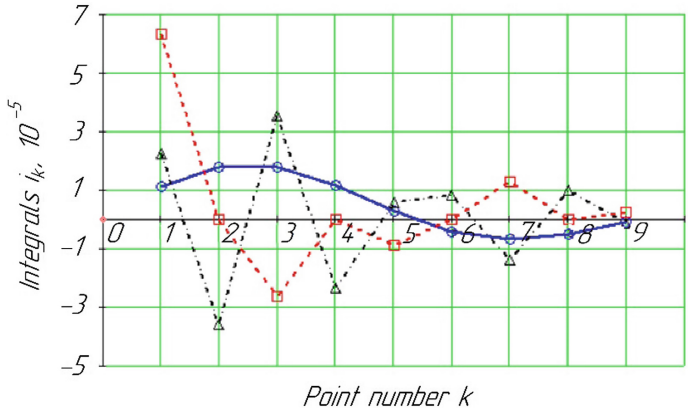


Fig. 2. Values of auxiliary integrals $i_k^{<1>}$ (○), $i_k^{<2>}$ (□), and $i_k^{<3>}$ (△).

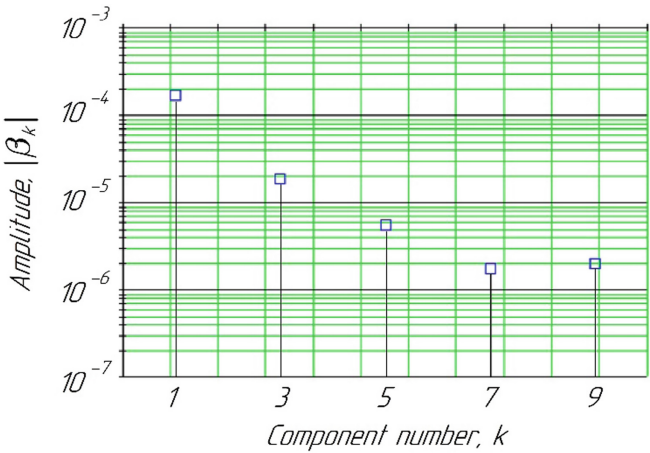


Fig. 3. Signal spectrum.

Considering that the 1st (β_1) and the 3rd (β_3) harmonics are the most valuable, analyzing the signal’s approximation by these two components is necessary. In this case, considering formula (7), expression (2) takes the following form (Fig. 4):

$$\varphi(t) = \frac{2A}{\pi} \left\{ \arcsin(\eta) + \eta \sqrt{1 - \eta^2} \left[3 - 2\eta^2 - \frac{8}{3}(1 - \eta^2)\sin(\omega t) \right] \right\} \sin(\omega t). \quad (8)$$

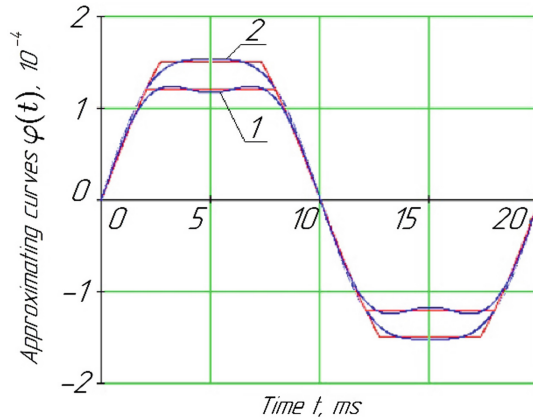


Fig. 4. Approximating curve $\varphi(t)$: 1- $\eta < \eta_0$; 2- $\eta \geq \eta_0$.

Notably, graphical dependencies presented in Figs. 2, 3 and 4 are related to the “rotor-stator” system of the multistage centrifugal pump’s unit [50] with the following parameters: rotor speed $\omega = 314$ rad/s; the average radial gap in a throttling seal $h = 0.15 \cdot 10^{-3}$ m; the theoretical amplitude $A = 0.20 \cdot 10^{-3}$ m.

For determination of the relative error in the approximation of the signal (1) by expression (8)

$$\varepsilon(\eta) = \frac{\max[\varphi(t)] - h}{h} = \frac{\varphi(t_1)}{h} - 1 \quad (9)$$

it is necessary to investigate the function $\varphi(t)$ to the extremum.

Notably, there is a critical value of the dimensionless gap η_0 , which distinguishes two different forms of this approximation curve. For values $\eta \geq \eta_0$, the function has two extremums per period: $t_2 = \frac{T}{4}$; $t_5 = T - t_2$. However, for values $\eta < \eta_0$, it has six extremums: $t_1 < t_2$; $t_2 = \frac{T}{4}$; $t_3 = \frac{T}{2} - t_1$; $t_4 = \frac{T}{2} + t_1$; $t_5 = T - t_2$; $t_6 = T - t_1$. Determining these extremums is reduced to finding time t_1 from the condition of equality to zero for the time derivative of the function $\varphi(t)$. In this case, it can be shown that this condition holds for the following value of the corresponding time:

$$t_1(\eta) = \frac{T}{4\pi} \arccos \left[\frac{\eta \sqrt{1 - \eta^2} (1 - 2\eta^2) - \arcsin(\eta)}{4\eta(1 - \eta^2)^{\frac{3}{2}}} \right]. \quad (10)$$

Additionally, determining the critical value for the dimensionless radial gap is reduced to fulfilling the condition $t_1 = t_2$. It can be shown that the appropriate value corresponds to a single real root $\eta_0 \approx 0.7433$ of the following transcendental equation:

$$\arcsin(\eta_0) = 5\eta_0\sqrt{1-\eta_0^2}\left(1-\frac{6}{5}\eta_0^2\right). \tag{11}$$

Finally, the relative approximation error (9) takes the following form (Fig. 5):

$$\varepsilon(\eta) = \begin{cases} \frac{2}{3\pi\sqrt{2}} \frac{[\arcsin(\eta) + 3\eta\sqrt{1-\eta^2}(1-\frac{2}{3}\eta^2)]^{\frac{3}{2}}}{\eta^{\frac{3}{2}}(1-\eta^2)^{\frac{3}{4}}} - 1, & \eta < \eta_0; \\ \frac{2}{\pi} \left[\frac{\arcsin(\eta)}{\eta} + \frac{1}{3}\sqrt{1-\eta^2}(1+2\eta^2) \right] - 1, & \eta \geq \eta_0. \end{cases} \tag{12}$$

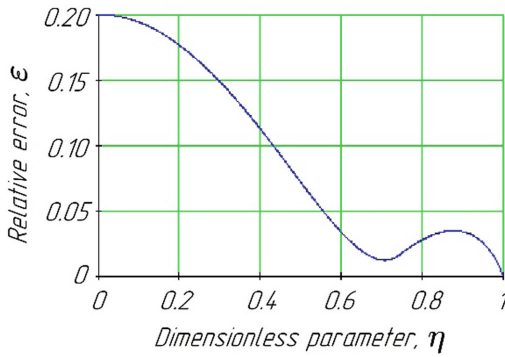


Fig. 5. Relative signal approximation error.

Notably, the relative error for the radial gap’s critical value is $\varepsilon(\eta_0) = 0.017$. Notably, using L’Hôpital’s rule [51], it is possible to prove the existence of the limit

$$\lim_{\eta \rightarrow 0} \varepsilon(\eta) = \left\{ \frac{0}{0} \right\} = \frac{8\sqrt{2}}{3\pi} - 1, \tag{13}$$

which is numerically equal to 0.2.

However, an appropriate application of the series (8) limited to a 5% relative error ($\varepsilon \leq 0.05$) allows evaluating a range of practical applications of the proposed methodology. Mainly, Fig. 5 shows that the corresponding range $0.56 \leq \eta \leq 1.0$ is quite broad. This fact allows applying expression (8) for a wide range of average radial gap: $h = (0.56-1)A$.

Additionally, from a practical point of view, for technical diagnostics of rotary machines, it is crucial to estimate the value of the dimensionless radial gap by the ratio of the amplitudes of the 5th and the 3rd components of the spectrum $\left(\gamma = \frac{\beta_5}{\beta_3}\right)$. After considering the expression (7), it is possible to make the following analytical dependence:

$$\eta = \sqrt{\frac{3}{8} \left(1 - \frac{5}{3}\gamma\right)}. \quad (14)$$

Notably, it is necessary to consider the sign “+” or “-” for the coefficient γ .

The significance of the obtained results is in their advantages compared with previous studies in diagnostics of rotary machines.

Mainly, the estimated components of the spectrum allow us to recognize the appearance of a contact interaction by the odd components of the vibration response from the system “rotor-stator” [52]. Additionally, the obtained results can significantly complement the research methodology for studying the impact of multi-gap seal’s characteristics on rotor dynamics [53].

Moreover, the developed mathematical model allows us to evaluate the vibration state of the multistage centrifugal machines (e.g., pumps [54], compressors [55], and turbines [56]) in terms of a range of the radial throttling gaps [57, 58].

Finally, the presence of multiple harmonics is a theoretical justification for the undesirable use of gears in designing vibration prillers [59]. However, modeling vibration propagation from an actuator to a liquid environment [60] still requires additional research in the future.

5 Conclusions

Thus, odd individual components of the signal spectrum informing about the machine’s unacceptable vibration state caused by the contact between the rotor and the stator have been substantiated theoretically. As a result of the decomposition for the clipped sinewave time signal into a Fourier series, precise analytical expressions for the spectrum’s components were obtained. Remarkably, the 1st and the 3rd components of the spectral composition significantly affect the model’s accuracy for contact interaction between the rotor and the stator.

As a result of harmonic approximation of the studied clipped sinewave signal by superposition of a couple of harmonics, an analytical expression has been obtained, which allows evaluating a range of the dimensionless radial gap with the relative error of not more than 5%.

Additionally, the criterion for estimating the dimensionless radial gap according to the vibration signal’s composition has been proposed, particularly by the ratio of amplitudes for the 5th and the 3rd harmonics.

For proving the developed mathematical model, the obtained results have been applied practically to evaluate the vibration state of the multistage centrifugal pump with the particular parameters of a throttling seal.

Overall, the obtained results are helpful for practical implementation in designing rotor systems (e.g., motors, pumps, compressors, centrifugal granulators, vibration prillers), and ensuring vibration reliability of the corresponding technological equipment.

Further research will be aimed at experimental research of the rotor-stator contact by spectral analysis of the experimentally obtained vibration response.

Acknowledgments. The research has been carried out because of cooperation between Sumy State University (Ukraine) and the Technical University of Košice (Slovak Republic).

The main scientific results have been obtained within the research project “Fulfillment of tasks of the perspective plan of development of a scientific direction “Technical sciences” Sumy State University” ordered by the Ministry of Education and Science of Ukraine (State Reg. No. 0121U112684).

The results have also been partially obtained within the research project “Creation of new granular materials for nuclear fuel and catalysts in the active hydrodynamic environment” ordered by the Ministry of Education and Science of Ukraine (State Reg. No. 0120U102036).

The authors appreciate the International Association for Technological Development and Innovations for the support while conducting this research.

References

- Li, Y., et al.: Numerical and experimental investigation on thermohydrodynamic performance of turbocharger rotor-bearing system. *Appl. Therm. Eng.* **121**, 27–38 (2017). <https://doi.org/10.1016/j.applthermaleng.2017.04.041>
- Heshmat, H., Walton, J. F., II.: On the integration of hot foil bearings into gas turbine engines: theoretical treatment. In: *Proceedings of the ASME Turbo Expo 2019: Turbomachinery Technical Conference and Exposition*. Volume 7B: Structures and Dynamics. Phoenix, Arizona, USA, V07BT34A036 (2019). <https://doi.org/10.1115/GT2019-91710>.
- Nyssen, F., Batailly, A.: Sensitivity analysis of rotor/stator interactions accounting for wear and thermal effects within low-and high-pressure compressor stages. *Coatings* **10**(1), 74 (2020). <https://doi.org/10.3390/coatings10010074>
- Wu, K., Xing, Y., Chu, N., Wu, P., Cao, L., Wu, D.: A carrier wave extraction method for cavitation characterization based on time synchronous average and time-frequency analysis. *J. Sound Vibration* **489**, 115682 (2020). <https://doi.org/10.1016/j.jsv.2020.115682>
- Jayaswal, P., Wadhvani, A.K., Mulchandani, K.B.: Machine fault signature analysis. *International J. Rotating Mach.* **2008**, 583982 (2008). <https://doi.org/10.1155/2008/583982>
- Gadyaka, V., Leikykh, D., Simonovskiy, V.: Phenomena of stability loss of rotor rotation at tilting pad bearings. *Procedia Eng.* **39**, 244–253 (2012). <https://doi.org/10.1016/j.proeng.2012.07.031>
- Bykov, V.G., Tovstik, P.E.: Synchronous whirling and self-oscillations of a statically unbalanced rotor in limited excitation. *Mech. Solids* **53**, 60–70 (2018). <https://doi.org/10.3103/S0025654418050047>
- Rusov, V.A.: *Diagnostics of Defects in Rotating Equipment by Vibration Signals*. Perm, Vibrocenter (2012)
- Butymova, L.N., Modorskii, V.Y.: Development and application of a unified algorithm for solving the interdisciplinary problem of modeling aeroelastic processes in the labyrinth seal of centrifugal compressors. Paper presented at the AIP Conference Proceedings, 1893, 030067 (2017). <https://doi.org/10.1063/1.5007525>
- Gritsenko, V.G., Lazarenko, A.D., Lyubchenko, K.Y., Martsinkovskii, V.S., Tarel'nik, V. B.: Increasing the Life of the slider bearings of the Turbines of high-speed compressors. *Chem. Pet. Eng.* **55**(9–10), 821–828 (2020). <https://doi.org/10.1007/s10556-020-00699-7>
- Kondratiuk, E., Torba, Y., Grebennikov, M., Yemelianova, L., Khavkina, O.: The control of GTE brush seal flow characteristics. In: Tonkonogyi, V., et al. (eds.) *InterPartner 2019. LNME*, pp. 510–519. Springer, Cham (2020). https://doi.org/10.1007/978-3-030-40724-7_52

12. Mammadov, V., Tacon, K., Davies, B., Ahmedov, N.S.: Coatings help to improve centrifugal pump reliability. In: Fluid Machinery Congress, pp. 67–77 (2014). <https://doi.org/10.1016/B978-0-0810-0109-7.50007-8>
13. Davydov, S.Y., Kosarev, N.P., Valiev, N.G., Simisinov, D.I., Kozhushko, G.G., Panov, D. A.: Problems with the use of pneumatic screw pumps to transport bulk cargo. *Refract. Ind. Ceram* **54**(2), 100–105 (2013). <https://doi.org/10.1007/s11148-013-9557-z>
14. Niu, G., Duan, F., Liu, Z., Jiang, J., Fu, X.: A high-accuracy non-contact online measurement method of the rotor-stator axial gap based on the microwave heterodyne structure. *Mech. Syst. Signal Process.* **150**, 107320 (2021). <https://doi.org/10.1016/j.ymsp.2020.107320>
15. Gavrilin, A.N., Moyzes, B.B.: *Diagnostics of Technological Systems: Part 2*. Tomsk Polytechnic Institute (2014)
16. Vedreño-Santos, F., Riera-Guasp, M., Henao, H., Pineda-Sánchez, M., Puche-Panadero, R.: Diagnosis of rotor and stator asymmetries in wound-rotor induction machines under nonstationary operation through the instantaneous frequency. *IEEE Trans. Industrial Electron.* **61**(9), 4947–4959 (2014). <https://doi.org/10.1109/TIE.2013.2288192>
17. Zaccardo, V.M., Buckner, G.D.: Active magnetic dampers for controlling lateral rotor vibration in high-speed rotating shafts. *Mech. Syst. Signal Process.* **152**, 107445 (2021). <https://doi.org/10.1016/j.ymsp.2020.107445>
18. Yadav, A.K., Prajapati, Y.K.: PAPR minimization of clipped OFDM signals using tangent rooting companding technique. *Wireless Pers. Commun.* **105**(4), 1435–1447 (2019). <https://doi.org/10.1007/s11277-019-06151-1>
19. Esqueda, F., Bilbao, S., Välimäki, V.: Aliasing reduction in clipped signals. *IEEE Trans. Signal Process.* **64**(20), 5255–5267 (2016). <https://doi.org/10.1109/TSP.2016.2585091>
20. Liu, T., Jin, S., Wen, C.-K., You, X.: OFDM-clipped signal recovery and learning using gaussian mixture GTurbo approach. *IEEE Wirel. Commun. Lett.* **8**(6), 1533–1536 (2019). <https://doi.org/10.1109/LWC.2019.2926260>
21. Altaf, S., Mehmood, M.S., Soomro, M.W.: Advancement of fault diagnosis and detection process in the industrial machine environment. *J. Eng. Sci.* **6**(2), D1–D8 (2019). [https://doi.org/10.21272/jes.2019.6\(2\).d1](https://doi.org/10.21272/jes.2019.6(2).d1)
22. Kolomvakis, N., Eriksson, T., Coldrey, M., Viberg, M.: Reconstruction of clipped signals in quantized uplink massive MIMO systems. *IEEE Trans. Commun.* **68**(5), 2891–2905 (2020). <https://doi.org/10.1109/TCOMM.2020.2971975>
23. Dyer, S.A., Dyer, J.S.: Distortion: total harmonic distortion in an asymmetrically clipped sinewave. *IEEE Instrum. Meas. Mag.* **14**(2), 48–51 (2011). <https://doi.org/10.1109/MIM.2011.5735256>
24. Zhou, Q., Wu, C., Fan, Q.: Gear fault diagnosis under the run-up condition using fractional fourier transform and hilbert transform. In: Tan, J. (ed.) *ICMD 2019. MMS*, vol. 77, pp. 918–943. Springer, Singapore (2020). https://doi.org/10.1007/978-981-32-9941-2_77
25. Jalayer, M., Orsenigo, C., Vercellis, C.: Fault detection and diagnosis for rotating machinery: a model based on convolutional LSTM, fast fourier and continuous wavelet transforms. *Comput. Ind.* **125**, 103378 (2021). <https://doi.org/10.1016/j.compind.2020.103378>
26. Xu, L., Chatterton, S., Pennacchi, P., Liu, C.: A tacholes order tracking method based on inverse short time fourier transform and singular value decomposition for bearing fault diagnosis. *Sensors (Switzerland)* **20**(23), 1–20 (2020). <https://doi.org/10.3390/s20236924>
27. Monkova, K., et al.: Condition monitoring of Kaplan turbine bearings using vibro-diagnostics. *Int. J. Mech. Eng. Robot. Res.* **9**(8), 1182–1188 (2020). <https://doi.org/10.18178/ijmerr.9.8.1182-1188>







28. Pavlenko, I., Ivanov, V., Kuric, I., Gusak, O., Liaposhchenko, O.: Ensuring vibration reliability of turbopump units using artificial neural networks. In: Trojanowska, J., Ciszak, O., Machado, J.M., Pavlenko, I. (eds.) *MANUFACTURING 2019*. LNME, pp. 165–175. Springer, Cham (2019). https://doi.org/10.1007/978-3-030-18715-6_14
29. Pavlenko, I., Trojanowska, J., Ivanov, V., Liaposhchenko, O.: Parameter identification of hydro-mechanical processes using artificial intelligence systems. *Int. J. Mechatronics Appl. Mech.* **2019**(5), 19–26 (2019)
30. Sokolov, V., Krol, O., Romanchenko, O., Kharlamov, Y., Baturin, Y.: Mathematical model for dynamic characteristics of automatic electrohydraulic drive for technological equipment. *J. Phys. Conf. Series* **1553**(1), 012013 (2020). <https://doi.org/10.1088/1742-6596/1553/1/012013>
31. Sokolov, V., Porkuian, O., Krol, O., Baturin, Y.: Design calculation of electrohydraulic servo drive for technological equipment. In: Ivanov, V., Trojanowska, J., Pavlenko, I., Zajac, J., Peraković, D. (eds.) *DSMIE 2020*. LNME, pp. 75–84. Springer, Cham (2020). https://doi.org/10.1007/978-3-030-50794-7_8
32. Tarelnyk, V., Konoplianchenko, I., Gaponova, O., Sarzhanov, B.: Assessment of hydroabrasive wear resistance of construction materials with functional coatings, which are formed by resource-saving and environmentally friendly technologies. *Key Eng. Mater.* **864**, 265–277 (2020). doi: <https://doi.org/10.4028/www.scientific.net/KEM.864.265>
33. Hovorun, T.P., et al.: Physical-mechanical properties and structural-phase state of nanostructured wear-resistant coatings based on nitrides of refractory metals Ti and Zr. *Funct. Mater.* **26**(3), 548–555 (2019). <https://doi.org/10.15407/fm26.03.548>
34. Gaydamaka, A., et al.: Devising an engineering procedure for calculating the ductility of a roller bearing under a no-central radial load. *Eastern-European J. Enterprise Technol.* **3**(7–99), 6–10 (2019). <https://doi.org/10.15587/1729-4061.2019.168145>
35. Rogovyi, A., Khovanskyi, S., Grechka, I., Pitel, J.: The wall erosion in a vortex chamber supercharger due to pumping abrasive mediums. In: Ivanov, V., et al. (eds.) *DSMIE 2019*. LNME, pp. 682–691. Springer, Cham (2020). https://doi.org/10.1007/978-3-030-22365-6_68
36. Ponomarev, A., Ponomareva, O.: Development of the theory of discrete Fourier transform for solving problems of functional diagnostic of mechanical objects. In: *2020 International Conference on Dynamics and Vibroacoustics of Machines (DVM)*, Samara, pp. 1–7 (2020). <https://doi.org/10.1109/DVM49764.2020.9243916>.
37. Ponomareva, O., Ponomarev, A.: Determining the envelope of real finite discrete signal via parametric discrete Fourier transform. In: *2020 International Conference on Dynamics and Vibroacoustics of Machines (DVM)*, Samara, pp. 1–6 (2020). <https://doi.org/10.1109/DVM49764.2020.9243923>.
38. Yoon, Y., Brahma, A.: Air–fuel ratio imbalance diagnostic of spark-ignited engines with modulated sliding discrete Fourier transform. *J. Dyn. Syst. Measurement Control* **142**(8), 081003 (2020). <https://doi.org/10.1115/1.4046550>
39. Kumar, G.K., Parimalasundar, E., Elangovan, D., Sanjeevikumar, P., Lannuzzo, F., Holm-Nielsen, J.B.: Fault investigation in cascaded H-bridge multilevel inverter through fast fourier transform and artificial neural network approach. *Energies* **13**(6), 1299 (2020). <https://doi.org/10.3390/en13061299>
40. Liaposhchenko, O., Pavlenko, I., Monkova, K., Demianenko, M., Starynskyi, O.: Numerical simulation of aeroelastic interaction between gas-liquid flow and deformable elements in modular separation devices. In: Ivanov, V., et al. (eds.) *DSMIE 2019*. LNME, pp. 765–774. Springer, Cham (2020). https://doi.org/10.1007/978-3-030-22365-6_76
41. Khovanskyi, S., Pavlenko, I., Pitel, J., Mizakova, J., Ochowiak, M., Grechka, I.: Solving the coupled aerodynamic and thermal problem for modeling the air distribution devices with perforated plates. *Energies* **12**(18), 3488 (2019). <https://doi.org/10.3390/en12183488>

42. Altaf, S., Mehmood, M.S., Imran, M.: Implementation of efficient artificial neural network data fusion classification technique for induction motor fault detection. *J. Eng. Sci.* **5**(2), E16–E21 (2018). [https://doi.org/10.21272/jes.2018.5\(2\).e4](https://doi.org/10.21272/jes.2018.5(2).e4)
43. Kotliar, A., Gasanov, M., Basova, Y., Panamariova, O., Gubskiy, S.: Ensuring the reliability and performance criterias of crankshafts. *Diagnostyka* **20**(1), 23–32 (2019). <https://doi.org/10.29354/diag/99605>
44. Dobrotvorskiy, S., Basova, Y., Ivanova, M., Kotliar, A., Dobrovolska, L.: Forecasting of the productivity of parts machining by high-speed milling with the method of half-overlap. *Diagnostyka* **19**(3), 37–42 (2018). <https://doi.org/10.29354/diag/93136>
45. Pylypaka, S., Zaharova, T., Zalevska, O., Kozlov, D., Podliniaieva, O.: Determination of the effort for flexible strip pushing on the surface of a horizontal cylinder. In: Tonkonogyi, V., et al. (eds.) *InterPartner 2019. LNME*, pp. 582–590. Springer, Cham (2020). https://doi.org/10.1007/978-3-030-40724-7_59
46. Pylypaka, S., Volina, T., Mukvich, M., Efremova, G., Kozlova, O.: Gravitational relief with spiral gutters, formed by the screw movement of the sinusoid. In: Ivanov, V., Pavlenko, I., Liaposhchenko, O., Machado, J., Edl, M. (eds.) *DSMIE 2020. LNME*, pp. 63–73. Springer, Cham (2020). https://doi.org/10.1007/978-3-030-50491-5_7
47. Kushnirov, P., Zhyhylii, D., Ivchenko, O., Yevtukhov, A., Dynnyk, O.: Investigation of the dynamic state of adjustable milling heads. In: Ivanov, V., et al. (eds.) *DSMIE 2019. LNME*, pp. 169–179. Springer, Cham (2020). https://doi.org/10.1007/978-3-030-22365-6_17
48. Kolesnyk, V., et al.: Experimental study of drilling temperature, geometrical errors and thermal expansion of drill on hole accuracy when drilling cfrp/ti alloy stacks. *Materials* **13** (14), 3232 (2020). <https://doi.org/10.3390/ma13143232>
49. Liu, Y., Fu, Y., Zhuan, Y., Zhong, K., Guan, B.: High dynamic range real-time 3D measurement based on Fourier transform profilometry. *Optics Laser Technol.* **138**, 106833 (2021). <https://doi.org/10.1016/j.optlastec.2020.106833>
50. Tarasevych, Y., Savchenko, I., Sovenko, N.: Estimation of random flow-rate characteristics of the automatic balancing device influence on centrifugal pump efficiency. In: Ivanov, V., Pavlenko, I., Liaposhchenko, O., Machado, J., Edl, M. (eds.) *DSMIE 2020. LNME*, pp. 105–115. Springer, Cham (2020). https://doi.org/10.1007/978-3-030-50491-5_11
51. Lawlor, G.R.: L'Hôpital's rule for multivariable functions. *Am. Math. Monthly* **127**(8), 717–725 (2020). <https://doi.org/10.1080/00029890.2020.1793635>
52. Li, Q.-F., Huang, S.-R., Huang, H.-J.: Noise and torque characteristics of permanent magnet synchronous motor with unequal pole arc structure. *J. Zhejiang Univ. (Eng. Sci.)* **52**(11), 2210–2217 (2018). <https://doi.org/10.3785/j.issn.1008-973X.2018.11.020>
53. Martsynkovskyy, V.A., Pozovnyi, O.O.: The impact of the multi-gap seals on rotor dynamics. *J. Eng. Sci.* **4**(1), C7–C12 (2017). [https://doi.org/10.21272/jes.2017.4\(1\).c2](https://doi.org/10.21272/jes.2017.4(1).c2)
54. Pozovnyi, O., Zahorulko, A., Krmela, J., Artyukhov, A., Krmelová, V.: Calculation of the characteristics of the multi-gap seal of the centrifugal pump, in dependence on the chambers' sizes. *Manuf. Technol.* **20**(3), 361–367 (2020). <https://doi.org/10.21062/mft.2020.048>
55. Wang, H., Wu, Y., Wang, Y., Deng, S.: Evolution of the flow instabilities in an axial compressor rotor with large tip clearance: an experimental and URANS study. *Aerospace Sci. Technol.* **96**, 105557 (2020). <https://doi.org/10.1016/j.ast.2019.105557>
56. Nemeč, M., Jelinek, T., Uher, J., Milčák, P.: Effect of stage reaction and shaft labyrinth seal in a stage of an axial steam turbine. In: *Proceedings of the ASME Turbo Expo 2020: Turbomachinery Technical Conference and Exposition*, vol. 9: Oil and Gas Applications; Organic Rankine Cycle Power Systems; Steam Turbine. ASME, GT2020–14741 (2020). <https://doi.org/10.1115/GT2020-14741>.

57. Srivastav, O.P., Pandu, K.R., Gupta, K.: Effect of radial gap between impeller and diffuser on vibration and noise in a centrifugal pump. *J. Inst. Eng. (India): Mech. Eng. Division* **84**(1 SEP), 36–39 (2003)
58. Kodnyanko, V., Shatokhin, S., Kurzakov, A., Pikalov, Y.: Theoretical analysis of compliance and dynamics quality of a lightly loaded aerostatic journal bearing with elastic orifices. *Precis. Eng.* **68**, 72–81 (2021). <https://doi.org/10.1016/j.precisioneng.2020.11.012>
59. Neuwirth, J., Antonyuk, S., Heinrich, S., Jacob, M.: CFD-DEM study and direct measurement of the granular flow in a rotor granulator. *Chem. Eng. Sci.* **86**, 151–163 (2013). <https://doi.org/10.1016/j.ces.2012.07.005>
60. Pavlenko, I., et al.: Effect of superimposed vibrations on droplet oscillation modes in prilling process. *Processes* **8**(5), 566 (2020). <https://doi.org/10.3390/PR8050566>



Movement of a Particle on the Inner Surface with a Preset Meridian

Serhii Pylypaka¹ , Tatiana Volina¹  , Olha Zalevska² ,
Svetlana Semirnenko³ , and Iryna Hryshchenko¹ 

¹ National University of Life and Environmental Sciences of Ukraine,
15, Heroyiv Oborony Street, Kyiv 03041, Ukraine
t. n. zaharova@ukr. net

² National Technical University of Ukraine “Igor Sikorsky Kyiv Polytechnic
Institute”, 37, Peremohy Avenue, Kyiv 03056, Ukraine

³ Sumy National Agrarian University,
160 Kondratieva Street, Sumy 40021, Ukraine

Abstract. The particle movement on a surface which rotates around a vertical axis is considered in the article. The surface’s meridian is the parabola’s branch, offset from the axis of symmetry by a given value. When a particle hits the surface in the lower part of the segment, it accelerates with a simultaneous upward movement. Such movement is characterized by a change in relative (sliding) speed and absolute speed. The relative velocity firstly increases and then decreases to zero when the “sticking” of the particle. The absolute velocity of the particle increases all the time and becomes constant after its “sticking”. For the surface of a sieve with parabola meridian, the “sticking” of the particle occurs in a narrow range of changes in the meridian rise angle. As the angular velocity of the sieve rotation increases, this range increases very slowly. Differential equations of relative particle displacement are compiled and solved. Graphs of particle movement trajectories and velocity change are constructed. The regularity of the particle movement during it rises along the surface is found out. The obtained analytical dependencies allow determining the influence of structural and technological parameters on the movement process.

Keywords: Surface of rotation · Angular velocity · Relative motion · Differential equations · Sliding trajectory

1 Introduction

The movement of particles on surfaces that rotate around a vertical axis takes place in centrifugal devices [1]. In particular, this applies to devices for scattering mineral fertilizers, extracting juice from ground vegetables and fruits, cleaning the air from dust particles in cyclones. The kinematic characteristics of the particle movement depend on the form and construction parameters of the operating parts of the device. The research of the laws of particle movement depending on the shape and construction features of the operating parts allows improving the device design. The particle performs a comprehensive motion, which is the sum of two motions: the transportable motion of

the surface and the relative motion (sliding) of the particle. The particle movement on the horizontal plane and on the cone, which rotates around the vertical axis, is thoroughly investigated. The particles' movement on rotating surfaces has features that depend on the meridian's shape.

2 Literature Review

A lot of articles are dedicated to the particle movement along different surfaces. It can be biomass particles [2], particles in the stream [3], particles of liquid [4], gas [5], and so on. The particle movement cannot be equal to body movement [6]. However, undoubtedly, the regularities of the movement of a single particle make it possible to determine dependencies that are applied to a body. It is easier to explore the movement of particles [7] because, in the case of the body moving, the forces of inertia from its rotation should be considered. These forces are often neglected at low angular velocities, for example, during the analysis of material particle movement in the vibratory feeder [8], in a rhomb-shaped apparatus [9], or spray apparatuses [10, 11]. The research of particle movement is a prerequisite for modeling the process of liquid's inertial-filtering separation [12]; for simulation of the interaction between elements of SPR-separator and gas-liquid flow [13]; as well as for the air distribution equipment improvement [14]. Moreover, this methodology can be used for designing gear clutches profiles [15], in complex parts manufacturing [16], or in measuring kinematic properties of granular flows [17]. All these areas demand the analytical dependencies that describe the movement of a particle along the surface. According to it, our research aims to investigate the laws of motion of a material particle on the inner surface, the meridian of which is a branch of the parabola, which is offset from the axis by a given value, and which rotates around a vertical axis with constant angular velocity.

3 Research Methodology

It is common knowledge that particles of material can fall on the surface in different ways: from above, below, or directly on the surface. For example, in centrifugal type juicers, the ground material hits the sieve surface in the form of a cone from below from a horizontal grater, which also rotates. In addition, the sieve can be cylindrical or conical. Figure 1a shows the location of the grater as a horizontal disk (of radius r) and a sieve (in the form of a cone with an angle β of inclination of the generatrices). Thanks to the conical sieve, the pulp can move up its surface to further clean the sieve, which is not possible in cylindrical sieves. However, in cylindrical sieves, the degree of juice squeezing is higher. Our research considers the sieve surface with a variable angle β , which increases as the pulp particles rise (see Fig. 1c). It makes it possible to combine the advantages of both constructions of the sieves.

Additionally, the particle's trajectory of the material from the grater to the sieve has a particular point on the boundary of these surfaces, which consists of an abrupt change in the movement direction. The physical nature of the particle movement provides a trajectory with a smooth change of curvature. As a result, the material sticks and a

surface that provide an acceptable trajectory (see Fig. 1b). To avoid sticking, it is advisable to create a sieve with a variable angle β , which is equal to zero at the lower point (see Fig. 1c). Because of the simplicity of the expression of the surface meridian, let us apply the parabola shifted from the axis of symmetry by the value of r .

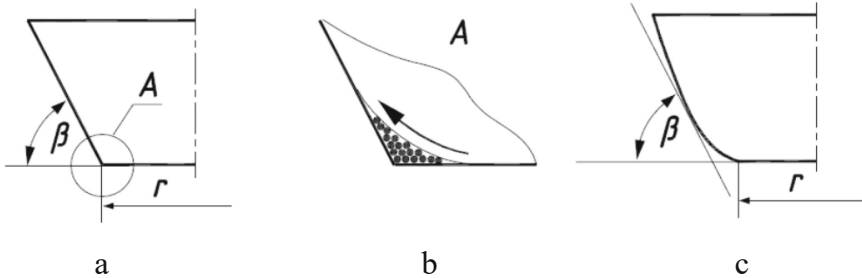


Fig. 1. Scheme of sieve surface variants: a) a conical surface sieve with an angle β of inclination of generatrices; b) an increased fragment of the surfaces of the sieve and grater with a possible new shape due to the sticking of ground material particles; c) a sieve in the form of a surface of rotation with a variable angle β .

In case the parabola $z = b \cdot \rho^2$ (b is a constant value) is applied, the parametrical equations of the surface of rotation with the meridian in the form of the parabola branch, which is shifted from the axis of symmetry by the value of r , can be written:

$$X = (\rho + r) \cos\alpha; \quad Y = (\rho + r) \sin\alpha; \quad Z = b\rho^2, \quad (1)$$

where b is a constant value that affects the shape of the surface;

ρ, α are the independent variables of the surface with a physical meaning: ρ is the distance from the point of the parabola to the axis of its symmetry; α is the angle of rotation of the radius vector $\rho + r$ around the axis OZ from zero to a point on the surface.

The current value of the angle β can be found through the derivative $\dot{z} = \text{tg}\beta$, that is $2b\rho = \text{tg}\beta$. Based on this, one can move from the variable ρ to the variable β in Eqs. (1). As a result, the independent variables of the surface are two angles:

$$X = (2a\text{tg}\beta + r)\cos\alpha; \quad Y = (2a\text{tg}\beta + r)\sin\alpha; \quad Z = a\text{tg}^2\beta, \quad (2)$$

where $a = 1/4b$ is a relationship between constants a and b .

The angle α varies in a range of $\alpha = 0 \dots 2\pi$, the angle β – within limits $\varepsilon = 0 \dots \beta_o < 90^\circ$, where the height of the surface compartment depends on the value of the angle β_o .

The rotation of the surface compartment will be considered concerning the fixed $OXYZ$ and the movable $Oxyz$ coordinate systems, which rotates with the compartment. If the compartment (2) rotates around the OZ axis with an angular velocity ω , it rotates

at the angle $\theta = \omega \cdot t$ during time t . Let us apply the known formulas of rotation of one coordinate system relative to another:

$$\begin{aligned} X &= (2atg\beta + r)\cos\alpha \cos\theta - (2atg\beta + r)\sin\alpha \sin\theta; \\ Y &= (2atg\beta + r)\cos\alpha \sin\theta + (2atg\beta + r)\sin\alpha \cos\theta; \quad Z = atg^2\beta. \end{aligned} \quad (3)$$

After simplifications with $\theta = \omega \cdot t$ in the mind Eqs. (3) take the form:

$$X = (2atg\beta + r)\cos(\alpha + \omega t); \quad Y = (2atg\beta + r)\sin(\alpha + \omega t); \quad Z = atg^2\beta. \quad (4)$$

Even suppose that at the initial moment ($t = 0$), two coordinate systems coincide, the sieve surface and the disk do not rotate and the particle is located on the meridian in the plane OYZ . Figure 2a shows such a position. For clarity, Fig. 2a shows the lower part of the sieve. It should be noted that the following forces are applied to the particle: the force of weight mg (m is a particle mass, $g = 9.81 \text{ m/s}^2$ is the acceleration of gravity), surface reaction N , and friction force $f \cdot N$ (depending on the friction coefficient f), that prevents the particle downflow along with the meridian in the direction of the coordinate system origin. The disk rotates at the angle $\theta = \omega \cdot t$ during time t in case of rotation with a constant angular velocity ω (see Fig. 2b). If the particle does not slide on the disk, it will rotate the disk at an angle θ and take a position on the same meridian. As a result of sliding, the particle will occupy a different position (see Fig. 2b). The particle slides in the opposite direction of rotation of the disk. The relative velocity V_r is directed along the tangent to the particle's trajectory (see Fig. 2b).

The equation of the particle movement can be composed in the form $m\bar{w} = \bar{F}$, where \bar{w} is the acceleration vector \bar{F} is the resulting vector of forces applied to the particle. All vectors should be determined in projections on the axis of the fixed coordinate system. The movement of a single particle with a constant dry friction coefficient f cannot be identified with the movement of a wet groundmass. However, the simplified problem for an individual particle allows identifying the patterns of its relative movement. These patterns partly concern the entire groundmass.

The trajectory of the relative movement of a particle regarding the movable coordinate system $Oxyz$ can be described by the relationship between the curvilinear coordinates (angles) β and α of the surface (2). This dependence can be set in different ways: $\beta = \beta(\alpha)$, $\alpha = \alpha(\beta)$ or through the common variable t : $\beta = \beta(t)$, $\alpha = \alpha(t)$. For our case, the common variable is the time t . Thus, for the accepted relationship $\beta = \beta(t)$ and $\alpha = \alpha(t)$, Eq. (2) specifies the relative trajectory of the particle, and Eq. (4) – the absolute trajectory. These unknown dependencies should be found. It is essential to receive vectors of both relative and absolute velocities. It can be determined by differentiating expressions (2) and (4) by time t . In one case, expressions (2) and (4) are the surface equations (when ε and α are independent variables), and in another – lines on the surface (particle trajectories which should be found). For surfaces, the notation of equations in capital letters is used, and for lines – in lowercase. Besides, the index “r” is used for the relative trajectory, and for the absolute – index “a”.

Therefore, the relative speed of particle movement (sliding) on the sieve surface can be obtained by differentiating Eqs. (2):

$$\begin{aligned} \dot{x}_r &= -\dot{\alpha}(2\alpha \operatorname{tg}\beta + r) \sin\alpha + 2\alpha\dot{\beta} \sec^2\beta \cos\alpha; \\ \dot{y}_r &= \dot{\alpha}(2\alpha \operatorname{tg}\beta + r) \cos\alpha + 2\alpha\dot{\beta} \sec^2\beta \sin\alpha; \\ \dot{z}_r &= 2\alpha\dot{\beta} \sec^2\beta \operatorname{tg}\beta. \end{aligned} \tag{5}$$

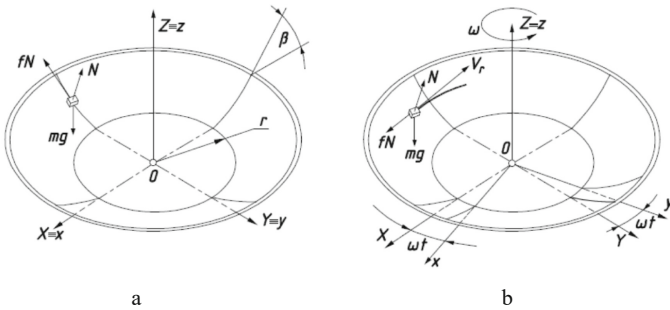


Fig. 2. The location of the particle on the sieve surface and the scheme of forces applied to it: a) fixed and movable coordinate systems coincide at the beginning of the movement; b) the sieve rotates with the movable system, the particle slides on its surface.

The geometric sum of the components (5) gives the value of the sliding speed of the particle on the sieve surface in relative motion:

$$V_r = \sqrt{\dot{x}_r^2 + \dot{y}_r^2 + \dot{z}_r^2} = \sqrt{\dot{\alpha}^2(2\alpha \operatorname{tg}\beta + r)^2 + 4\alpha^2\dot{\beta}^2 \sec^6\beta}. \tag{6}$$

The trajectory unit vector T tangent for the relative motion in the projections on the axis of the system $OXYZ$ is obtained by dividing the projections (5) by the value of the relative velocity (6):

$$\begin{aligned} T_x &= \frac{-\dot{\alpha}(2\alpha \operatorname{tg}\beta + r) \sin\alpha + 2\alpha\dot{\beta} \sec^2\beta \cos\alpha}{\sqrt{\dot{\alpha}^2(2\alpha \operatorname{tg}\beta + r)^2 + 4\alpha^2\dot{\beta}^2 \sec^6\beta}}; \\ T_y &= \frac{\dot{\alpha}(2\alpha \operatorname{tg}\beta + r) \cos\alpha + 2\alpha\dot{\beta} \sec^2\beta \sin\alpha}{\sqrt{\dot{\alpha}^2(2\alpha \operatorname{tg}\beta + r)^2 + 4\alpha^2\dot{\beta}^2 \sec^6\beta}}; \\ T_z &= \frac{2\alpha\dot{\beta} \sec^2\beta \operatorname{tg}\beta}{\sqrt{\dot{\alpha}^2(2\alpha \operatorname{tg}\beta + r)^2 + 4\alpha^2\dot{\beta}^2 \sec^6\beta}}. \end{aligned} \tag{7}$$

Let us find the direction of the surface (2) reaction N . It is directed along with the normal P of the surface. It is determined from the vector product of two vectors tangent to the surface's coordinate lines. The projections of these vectors are partial derivatives of Eqs. (2):

$$\begin{aligned}
\partial X/\partial\beta &= 2a \sec^2\beta \cos\alpha; & \partial X/\partial\alpha &= -(2a \operatorname{tg}\beta + r) \sin\alpha; \\
\partial Y/\partial\beta &= 2a \sec^2\beta \sin\alpha; & \partial Y/\partial\alpha &= (2a \operatorname{tg}\beta + r) \cos\alpha; \\
\partial Z/\partial\beta &= 2a \sec^2\beta \operatorname{tg}\alpha; & \partial Z/\partial\alpha &= 0.
\end{aligned} \tag{8}$$

After vector multiplication of vectors (8) and reduction of the obtained vector to a unit one, projections of the vector P of the normal to the surface can be written:

$$P_x = -\sin\beta \cos\alpha; \quad P_y = -\sin\beta \sin\alpha; \quad P_z = \cos\beta. \tag{9}$$

The absolute velocity of the particle movement regarding a fixed coordinate system can be found by differentiating Eqs. (4):

$$\begin{aligned}
\dot{x}_a &= -(\dot{\alpha} + \omega)(2\alpha \operatorname{tg}\beta + r) \sin(\alpha + \omega t) + 2\alpha\dot{\beta} \sec^2\beta \cos(\alpha + \omega t); \\
\dot{y}_a &= (\dot{\alpha} + \omega)(2\alpha \operatorname{tg}\beta + r) \cos(\alpha + \omega t) + 2\alpha\dot{\beta} \sec^2\beta \sin(\alpha + \omega t); \\
\dot{z}_a &= 2\alpha\dot{\beta} \sec^2\beta \operatorname{tg}\beta.
\end{aligned} \tag{10}$$

Moreover, the projections of the vector of absolute acceleration on the axis of the fixed coordinate system can be compiled by differentiating expressions (10):

$$\begin{aligned}
\ddot{x}_a &= -\left[4\alpha\dot{\beta} \sec^2\beta(\dot{\alpha} + \omega) + \ddot{\alpha}(2\alpha \operatorname{tg}\beta + r)\right] \sin(\alpha + \omega t) + \\
&+ \left[2\alpha(\ddot{\beta} + 2\dot{\beta}^2 \operatorname{tg}\beta) \sec^2\beta - (\dot{\alpha} + \omega)^2(2\alpha \operatorname{tg}\beta + r)\right] \cos(\alpha + \omega t); \\
\ddot{y}_a &= \left[4\alpha\dot{\beta} \sec^2\beta(\dot{\alpha} + \omega) + \ddot{\alpha}(2\alpha \operatorname{tg}\beta + r)\right] \cos(\alpha + \omega t) + \\
&+ \left[2\alpha(\ddot{\beta} + 2\dot{\beta}^2 \operatorname{tg}\beta) \sec^2\beta - (\dot{\alpha} + \omega)^2(2\alpha \operatorname{tg}\beta + r)\right] \sin(\alpha + \omega t); \\
\ddot{z}_a &= 2\alpha \sec^2\beta \left[\dot{\beta}^2 \sec^2\beta + \operatorname{tg}\beta(\ddot{\beta} + 2\dot{\beta}^2 \operatorname{tg}\beta)\right].
\end{aligned} \tag{11}$$

The unit vectors T (7) of the direction of relative velocity V_r and (8) of the normal P to the surface are found for a stationary surface. The surface rotates at an angle $\theta = \omega \cdot t$. Therefore, these vectors must also be rotated at this angle to correspond to the particle's location. The rotation is performed in the same way as the surface rotation according to formulas (3). After rotating, the projections of these vectors are:

- the unit vector of the relative trajectory tangent:

$$\begin{aligned}
 T_x &= \frac{-\dot{\alpha}(2\alpha \operatorname{tg}\beta + r) \sin(\alpha + \omega t) + 2\alpha\dot{\beta} \sec^2\beta \cos(\alpha + \omega t)}{\sqrt{\dot{\alpha}^2(2\alpha \operatorname{tg}\beta + r)^2 + 4\alpha^2\dot{\beta}^2 \sec^6\beta}}; \\
 T_y &= \frac{\dot{\alpha}(2\alpha \operatorname{tg}\beta + r) \cos(\alpha + \omega t) + 2\alpha\dot{\beta} \sec^2\beta \sin(\alpha + \omega t)}{\sqrt{\dot{\alpha}^2(2\alpha \operatorname{tg}\beta + r)^2 + 4\alpha^2\dot{\beta}^2 \sec^6\beta}}; \\
 T_z &= \frac{2\alpha\dot{\beta} \sec^2\beta \operatorname{tg}\beta}{\sqrt{\dot{\alpha}^2(2\alpha \operatorname{tg}\beta + r)^2 + 4\alpha^2\dot{\beta}^2 \sec^6\beta}}.
 \end{aligned} \tag{12}$$

– the unit vector of the normal to the surface:

$$P_X = -\sin\beta \cos(\alpha + \omega t); \quad P_Y = -\sin\beta \sin(\alpha + \omega t); \quad P_Z = \cos\beta. \tag{13}$$

Subsequently, the vector equation $m\bar{w} = \bar{F}$ in the projections on the axis of the fixed coordinate system OXYZ has been derived:

$$m\ddot{x}_a = NP_x - fNT_x; \quad m\ddot{y}_a = NP_y - fNT_y; \quad m\ddot{z}_a = NP_z - fNT_z - mg. \tag{14}$$

The unit directing vectors' projections of the tangent T to the relative trajectory and the normal P to the surface are given in (12) and (13). The expressions of the second derivatives of the absolute trajectory are presented in (11). This system of equations with unknown dependencies ($\alpha = \alpha(t)$, $\beta = \beta(t)$, and $N = N(t)$) can be obtained by substituting these expressions in (14). Let us solve it relatively $\ddot{\alpha}$, $\ddot{\beta}$, N and get:

$$\begin{aligned}
 \ddot{\beta} &= -\frac{\cos^3\beta}{2\alpha} \left[g \sin\beta - (\dot{\alpha} + \omega)^2 (r \cos\beta + 2\alpha \sin\beta) \right] - 3\dot{\beta}^2 - f \frac{\dot{\beta}A}{V_r}; \\
 \ddot{\alpha} &= -\frac{4\alpha\dot{\beta}(\dot{\alpha} + \omega) \sec\beta}{r \cos\beta + 2\alpha \sin\beta} - f \frac{\dot{\alpha}A}{V_r}; \\
 N &= mA,
 \end{aligned} \tag{15}$$

where $A = \sec\beta \left[(\dot{\alpha} + \omega)^2 (r \cos\beta + 2\alpha \sin\beta) \sin\beta + g \cos^2\beta + 2\alpha\dot{\beta}^2 \sec^2\beta \right]$.

The system (15) is a system of the first two equations regarding the unknown dependencies $\alpha = \alpha(t)$ and $\beta = \beta(t)$. The dependence $N = N(t)$ is found after the solving of this system. Numerical methods can solve the obtained system. The found dependencies $\alpha = \alpha(t)$ and $\beta = \beta(t)$ should be substituted into Eq. (2) in order to obtain the relative trajectory of the particle along with the sieve, so the sliding trajectory, and in the Eq. (4) to obtain the absolute trajectory.

4 Results

In Fig. 3a, the relative trajectory of the particle’s movement along with the sieve with the following parameters: $a = 0,01$, $r = 0,05$ m, $\omega = 50$ c^{-1} , $f = 0,3$ were constructed by numerical methods.

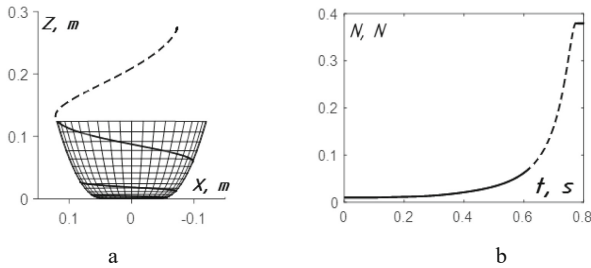


Fig. 3. Characteristics of particle movement along the sieve at $a = 0.01$, $r = 0.05$ m, $\omega = 50$ s^{-1} , $f = 0.3$: a) the relative trajectory on the frontal projection; b) the graph of the reaction of the surface $N = N(t)$ for a particle of mass $m = 0.001$ kg.

Remarkably, the trajectory inside the sieve is shown by a continuous line and by a dashed line outside it. In Fig. 3b, the graph of the surface reaction $N = N(t)$ for a particle with mass $m = 0.001$ kg is constructed by the same lines. This characteristic is important because the value of the reaction characterizes the pressure force of the particles of the groundmass on the sieve surface. The graph shows that the reaction reaches a maximum value at about 0.4 N and becomes constant. It means that the sliding of the particle has stopped and it rotates together with the sieve. This is evidenced by graphs of relative and absolute sliding speeds (see Fig. 4).

In Fig. 3 and Fig. 4, continuous curves referred to the particle's movement within the sieve and dashed – on the sieve in the case if it is extended upwards. Figure 3 shows that the juice will come out of the sieve the most intense before the “sticking” of the particles, so at a sharp deceleration of the sliding speed (see Fig. 4a). It takes place due to the increase of the angle β (see Fig. 1c). In conical sieves, in which the angle β

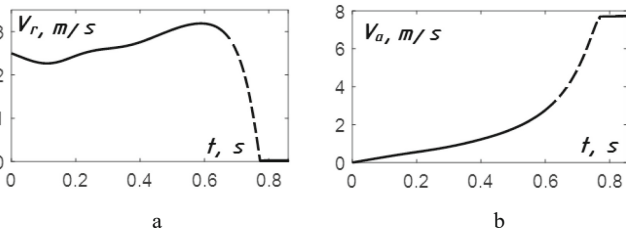


Fig. 4. Graphs of particle velocity changes on the sieve at $a = 0.01$, $r = 0.05$ m, $\omega = 50$ s^{-1} , $f = 0.3$: a) relative velocity; b) absolute speed.

is constant, the deceleration of the sliding speed does not occur. According to it, the degree of juice intake in the conical sieves with the constant angle is much lower than cylindrical sieves, in which the angle $\beta = 90^\circ$.

As the angular velocity ω of the sieve rotation increases, the sliding speed V_r of the particle increases, and its trajectory changes: the spirals of the trajectory are located more densely in the vertical direction (see Fig. 5a). Figure 5b shows the changes in the sliding speed during the particle moves upward, i.e., at a function of the angle β at different values of the angular velocity of rotation of the sieve. A characteristic feature of the graphs (see Fig. 5b) is that the initial sliding speed starts from a specific non-zero value. This effect is explained by the following. At the moment of meeting the particle with the sieve, angular sliding velocity is determined by the difference between the angular velocity of the particle (which does not rotate at the moment of the meeting), and the sieve: $0 - \omega = -\omega$. This value $(-\omega)$ is the initial condition for integrating differential Eqs. (15): $\dot{\alpha}_0 = -\omega$. The second characteristic feature of these graphs is that they seek to zero (before the “sticking” of the particle) at a very narrow range of change of the angle β regardless of the angular velocity ω of rotation of the sieve. According to Fig. 5b this range is $80^\circ \dots 85^\circ$. In this range, the sliding of the particle decreases sharply and it “sticks”. Here is also the most intensive selection of juice from the groundmass. Based on this, the juicer can be provided a cleaning device in this place of the sieve, or it is necessary to reduce its height to prevent clogging of the sieve. The parabola is a meridian, which is not an acceptable curve because at angles $\beta > 80^\circ$, the height of the sieve will be too large regardless of the value of the constant a . In this case, another curve with a more intense increase of the angle β , for example, the ellipse arc, should be taken as the meridian.

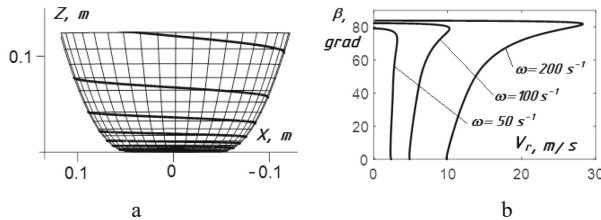


Fig. 5. Characteristics of the relative movement of the particle on the sieve at $a = 0.01$, $r = 0.05$ m, $f = 0.3$: a) the relative trajectory of the motion on the frontal projection at $\omega = 100$ s⁻¹; b) graphs of dependencies $\beta = \beta(V_r)$ for different values of angular velocity ω of rotation of the sieve.

5 Conclusions

The particle’s movement on the rough inner surface of the sieve with a variable angle of the meridian has its features. It relates to the nature of the sliding of the particle on the surface. When a particle hits the surface in the lower part of the segment, it accelerates with a simultaneous upward movement. A change in two speeds characterizes such movement: relative, i.e., sliding speed, and absolute. The relative velocity

firstly increases and then decreases to zero at the “sticking” of the particle. The absolute velocity of the particle increases all the time and becomes constant after its “sticking”. For the surface of a sieve with the parabola’s meridian, particle’s “sticking” occurs in a relatively narrow range of changes in the angle β of the rise of the meridian (about 90°). As the angular velocity of the sieve rotation increases, this range increases very slowly. Doubtless, the received results can be used to design the engineering machines working bodies, for instance, working bodies of devices for scattering mineral fertilizers, extracting juice from ground vegetables and fruits, cleaning the air from dust particles in cyclones. Prospects for further research are experimental verification of the obtained theoretical results and designing improved working bodies of the engineering machines.






References

1. Cunha, J.O.P., Filno, R.S.: Broadcast distribution uniformity of fertilizer with centrifugal spreaders used in variable rate application. *Eng. Agric. Jaboticabal* **36**(5), 928–937 (2016). <https://doi.org/10.1590/1809-4430-Eng.Agric.v36n5p928-937/2016>.
2. Trubetskaya, A., Beckmann, G., Wadenbäck, J., Kai Holm, J., Velaga, S.P., Weber, R.: One way of representing the size and shape of biomass particles in combustion modeling. *Fuel* **206**, 675–683 (2017). <https://doi.org/10.1016/j.fuel.2017.06.052>
3. Reguła, T., Frączek, J., Fitas, J.: A Model of Transport of Particulate Biomass in a Stream of Fluid. *Processes* **9**(1), 5 (2021). <https://doi.org/10.3390/pr9010005>
4. Ostroha, R., Yukhymenko, M., Lytvynenko, A., Bocko, J., Pavlenko, I.: Granulation process of the organic suspension: fluidized bed temperature influence on the kinetics of the granule formation. In: Ivanov, V., et al. (eds.) *DSMIE 2018. LNME*, pp. 463–471. Springer, Cham (2019). https://doi.org/10.1007/978-3-319-93587-4_48
5. Tauroa, F., Piscopiab, R., Grimaldi, S.: PTV-Stream: A simplified particle tracking velocimetry framework for stream surface flow monitoring. *CATENA* **172**, 378–386 (2019). <https://doi.org/10.1016/j.catena.2018.09.009>
6. Agudo, J.R., Luzi, G., Han, J., Hwang, M., Lee, J., Wierschem, A.: Detection of particle motion using image processing with particular emphasis on rolling motion. *Rev. Scientific Instruments* **88**, 051805 (2017). <https://doi.org/10.1063/1.4983054>
7. Pylypaka, S., Klendiy, M., Zaharova, T.: Movement of the particle on the external surface of the cylinder, which makes the translational oscillations in horizontal planes. In: Ivanov, V., et al. (eds.) *DSMIE 2018. LNME*, pp. 336–345. Springer, Cham (2019). https://doi.org/10.1007/978-3-319-93587-4_35
8. Nguyen, V. X., Golikov, N.S.: Analysis of material particle motion and optimizing parameters of vibration of two-mass GZS vibratory feeder. *J. Phys. Conf. Series* **1015**(5), 052020. <https://doi.org/10.1088/1742-6596/1015/5/052020>
9. Lytvynenko, A., et al.: Ensuring the reliability of pneumatic classification process for granular material in a rhomb-shaped apparatus. *Appl. Sci. (Switzerland)* **9**(8), 1604 (2019). <https://doi.org/10.3390/app9081604>
10. Hu, W.J., Tan, K., Markovych, S., Liu, X.L.: Study of a cold spray nozzle throat on acceleration characteristics via CFD. *J. Eng. Sci.* **8**(1), F19–F24 (2021). [https://doi.org/10.21272/jes.2021.8\(1\).f3](https://doi.org/10.21272/jes.2021.8(1).f3)

11. Merzliakov, I., Pavlenko, I., Chekh, O., Sharapov, S., Ivanov, V.: Mathematical modeling of operating process and technological features for designing the vortex type liquid-vapor jet apparatus. In: Ivanov, V., et al. (eds.) DSMIE 2019. LNME, pp. 613–622. Springer, Cham (2020). https://doi.org/10.1007/978-3-030-22365-6_61
12. Liaposhchenko, O., Pavlenko, I., Ivanov, V., Demianenko, M., Starynskiy, O., Kuric, I., Khukhryanskiy, O.: Improvement of parameters for the multi-functional oil-gas separator of ‘HEATER-TREATER’ type. In: 2019 IEEE 6th International Conference on Industrial Engineering and Applications, ICIEA 2019, pp. 66–71 (2019). <https://doi.org/10.1109/IEA.2019.8715203>
13. Liaposhchenko, O., Pavlenko, I., Demianenko, M., Starynskiy, O., Pitel, J.: The methodology of numerical simulations of separation process in SPR-separator. CEUR Workshop Proceedings **2353**, 822–832 (2019)
14. Khovanskyi, S., Pavlenko, I., Pitel, J., Mizakova, J., Ochowiak, M., Grechka, I.: Solving the coupled aerodynamic and thermal problem for modeling the air distribution devices with perforated plates. Energies **12**(18), 3488 (2019). <https://doi.org/10.3390/en12183488>
15. Shevchenko, S., Mukhovaty, A., Krol, O.: Gear clutch with modified tooth profiles. Procedia Eng. **206**, 979–984 (2017). <https://doi.org/10.1016/j.proeng.2017.10.581>
16. Karpus, V., Ivanov, V., Dehtiarov, I., Zajac, J., Kurochkina, V.: Technological assurance of complex parts manufacturing. In: Ivanov, V., et al. (eds.) DSMIE 2018. LNME, pp. 51–61. Springer, Cham (2019). https://doi.org/10.1007/978-3-319-93587-4_6
17. Gollin, D., Bowman, E., Shepley, P. Methods for the physical measurement of collisional particle flows: Earth and Environmental. Science **26**, 012017 (2015). <https://doi.org/10.1088/1755-1315/26/1/012017>



Neutralization of the Destabilization Effect Caused by Small Damping Force in Non-conservative System

Volodymyr Puzyrov^{1,2} , Leonardo Acho Zuppa¹ ,
Gisela Pujol Vazquez¹ , Nina Savchenko³ ,
and Nelya Kyrylenko⁴ 

¹ Universitat Politècnica de Catalunya, Campus Nord, 1, 3, Carrer de Jordi Girona, 08034 Barcelona, Spain

² Nizhyn Gogol State University, 2, Graftska Street, Nizhyn 16600, Ukraine

³ Zhukovsky National Aerospace University “KhAI”, 17, Chkalova Street, Kharkiv 61070, Ukraine
n.savchenko@khai.edu

⁴ Education Municipal Institution of Higher Education, Vinnytsia Humanities and Pedagogical College”, 13, Nagirna Street, Vinnytsia 21000, Ukraine

Abstract. For the first time, the destabilizing effect of small dissipative forces was marked by Thomson and Tait in 1879. They showed that a statically unstable conservative system stabilized by gyroscopic forces could be destabilized again by introducing small damping forces. Later on, in 1924, Kimball noticed the paradoxical effect of damping on dynamic stability for rotor systems that have stable steady motions for a certain range of speed but become unstable when the speed is changed to a value outside the range. Further progress in engineering and technology has witnessed that such phenomenon arises in numerous mechanical applications and may cause equipment malfunction. In the present article, this problem is studied by comparing the stability conditions for undamped and weakly damped systems. The aim is to find the interrelation between the matrix elements characterizing the damping force (assuming that the stiffness matrix is known), which allows to avoid or minimize the negative effect of small damping in the presence of non-conservative positional forces. For the case study of two Degrees-of-Freedom system, a simple analytical technique is suggested for this purpose. This technique is demonstrated on two mechanical systems: a system with friction-induced vibrations and a double pendulum under the action of the follower force.

Keywords: Mechanical system · Friction force · Stability criteria · Following force · Ziegler model

1 Introduction

In 1952, Hans Ziegler published an article [1] which is now considered a classic and widely known in the community of mechanical engineers and specialists in dynamics. Ziegler investigated the flutter problem in aerodynamics and considered the model as a

double pendulum, fixed at one end and loaded with a tangential load at the other end. He discovered a phenomenon with an unexpected property: there was a gap between the regions of stability in the case of vanishingly small damping compared with the case when there is no damping. This effect is a classic example of a Hopf bifurcation in a dynamic system. This problem attracted the attention of scientists in the field of structural mechanics in the second half of the last century, and numerous studies were devoted to the theoretical analysis of flutter resulting from the so-called follower forces that change their direction, following the configuration of the system in which they act.

2 Literature Review

Over the past two decades, the problem of destabilizing the equilibrium of a non-conservative mechanical system under the influence of low friction was reflected in numerous publications. In paper [2], an academic study on the influence of small velocity-dependent forces on the stability of a linear non-conservative 2-DoF system, inspired by Ziegler's results, was presented. Some theorems on the necessary and sufficient conditions for the matrices of velocity-dependent forces to stabilize an unperturbed circulatory system were established. The paper [3] is devoted to a physical explanation of the mechanism behind the destabilizing effect of small internal damping in the dynamic stability of Beck's column. An energy equation is derived from balancing the work done by the non-conservative follower force and the energy dissipated by the internal and external damping forces. Several theorems related to the stability problem of non-conservative linear systems were presented in the paper [4]. While studying the dynamic stability of finite-dimensional autonomous mechanical systems, some paradoxical phenomena were carried out in the paper [5]. The analytically derived stability boundary of the 2-DoF system is analyzed in [6] regarding infinitesimally small, incomplete, and indefinite damping matrices. Systems with two neutrally-stable damping levels, whereby the system initially gains stability but then loses stability as the level of damping is increased, were observed in [7]. In paper [8], Brouwer's problem with a heavy particle in a rotating vessel is considered. This problem highlights some crucial effects that arise in the field of dissipation-induced instabilities. In paper [9], some optimized algorithms were suggested to reduce the computation time and obtain stability conditions in a simpler form. Regarding various mechanical applications, we mention the friction-induced vibrations [10, 11], squeal vibration in drum brakes [12, 13], the Levitron system [14], aeroelastic systems [15], the effect of rocket propulsion as a source of a follower load acting on a beam [16] and others.

3 Research Methodology

Consider a mechanical system with two degrees of freedom. Let q_1, q_2 be the generalized coordinates and $\mathbf{q} = \mathbf{q}_0$ is the equilibrium. After the linearizing in the vicinity of this equilibrium, the equations of motion can be written in the following structural form:

$$M\ddot{q} + \varepsilon D\dot{q} + (K + N)q = 0 \tag{1}$$

(without the loss of generality, we can put $q_0 = 0$). Here symmetrical matrices M, D, K stand for inertia, dissipative, and stiffness matrices, respectively, and the skew-symmetric one N is associated with non-conservative positional (circulatory) force. In the literature, such a system is often referred to as $MDKN$ system. We assume that matrix M is positive definite, D is positive semi-definite, and K can be indefinite, but $tr K = k_{11} + k_{22} > 0$.

We are primarily concerned with the friction-induced instability phenomenon, which is when the stable system in the absence of friction loses stability when a small dissipation of energy appears.

Since the matrix M is positive definite and symmetric, there exists a non-singular transformation which transforms system (1) to $ID\tilde{K}N$ form, where I is an identity matrix. For the sake of simplicity, the over script “ $\tilde{}$ ” is omitted below.

The characteristic polynomial is given by the formula

$$f(\lambda) = a_4\lambda^4 + a_3\lambda^3 + a_2\lambda^2 + a_1\lambda + a_0. \tag{2}$$

Here

$$a_4 = 1, a_3 = \varepsilon tr D, a_2 = tr K + \varepsilon^2 \det D, \\ a_1 = \varepsilon[(tr D)(tr K) - tr(DK)], a_0 = \det(K + N), N = n \begin{pmatrix} 0 & -1 \\ 1 & 0 \end{pmatrix}. \tag{3}$$

For simplicity below, we shall use the following enumeration

$$tr D = d, tr K = k, \det D = \Delta_D, (tr D)(tr K) - tr(DK) = k_d, \det K = \Delta_K. \tag{4}$$

The necessary and sufficient conditions of stability according to the Routh-Hurwitz criterion are

$$a_3 > 0, a_2 > 0, a_0 > 0, \tag{5}$$

$$\Delta_3 = a_1 a_2 a_3 - a_1^2 a_4 - a_0 a_3^2 = d k k_d - d^2 (\Delta_K + n^2) - k_d^2 + \varepsilon^2 d \Delta_D k_d > 0. \tag{6}$$

Taking into account that a_3 is positive, the positiveness of the coefficient a_1 is the necessary condition of stability. If the matrix K is positive definite, this requirement is fulfilled. However, generally speaking, the matrix of positional forces $K + N$ may be indefinite (see Subsect. 4.2), but its determinant should be positive, as well as the expression $d_{11}k_{22} + d_{22}k_{11} - 2d_{12}k_{12}$ (the “covert” requirement).

In the non-dissipative case ($\varepsilon = 0$), the conditions of marginal stability are

$$k > 0, \Delta_K + n^2 > 0, k^2 - 4(\Delta_K + n^2) = (k_{11} - k_{22})^2 + 4(k_{12}^2 - n^2) > 0. \tag{7}$$

In the case of the infinitesimal value of ε two first inequalities of the system (7) and conditions (5) are identical. At the same time, the third inequality of (7) mostly is more “weak” than its counterpart from the condition (6). In literature, this phenomenon is known as the “destabilizing effect” (or “destabilizing paradox”) owing to small damping.

Let us evaluate the discrepancy between the thresholds for parameter n derived from the condition (6) and the third inequality (7). From (6), we have the following restriction on parameter n , which characterizes the influence of circulatory force

$$n^2 < v_1 + \varepsilon^2 d \Delta_D k_d, v_1 = \frac{1}{d^2} (d k k_d - d^2 \Delta_K - k_d^2). \tag{8}$$

The difference between v_1 and $v_2 = k^2/4 - \Delta_K$ is the following expression

$$\begin{aligned} v_1 - v_2 &= \frac{1}{4d^2} (-d^2 k^2 + 4d k k_d - 4k_d^2) + \frac{1}{d} \varepsilon^2 \Delta_D k_d \\ &= -\left(\frac{k}{2} - \frac{k_d}{d}\right)^2 + \frac{1}{d} \varepsilon^2 \Delta_D k_d \end{aligned} \tag{9}$$

As one can see from formula (9), normally, the first term on the right-hand side is negative, thus in a case when n is slightly less, then $\sqrt{v_2}$. The appearance of a small damping force brings instability to a stable undamped system. However, if the equality $k d = 2k_d$ holds, then the system (1) is stable. This condition in explicit form reads

$$(d_{11} - d_{22})(k_{11} - k_{22}) + 4d_{12}k_{12} = 0. \tag{10}$$

The equality (10) can be realized in the case when some of the mechanical parameters of the system (1) are controllable. For instance, the matrix \mathbf{K} and parameter n are given, but the distribution of the elements inside matrix \mathbf{D} can be regulated (e.g., the ratio d_{11}/d_{22} is tunable). This feature will be described in more detailed in the examples below.

Another circumstance that is also important when equality (10) is not fulfilled is the “rate of instability”, i.e., the value of the maximal Lyapunov exponent. So far as we consider the weakly damped system, this value is not large, and the presence of nonlinear terms in motion equations (which are not included in Eqs. (1)) can have a positive effect. That is, the disturbed motion will remain in a sufficiently small neighborhood of the equilibrium position. For this reason, let us now estimate the eigenvalues of the system (1). Substituting the expression

$$\lambda = \lambda_0 + \varepsilon \lambda_1 + \varepsilon^2 \lambda_2 + \dots \tag{11}$$

we find in the chain

$$(\lambda_0)_{1,2} = \pm i \omega_1, (\lambda_0)_{3,4} = \pm i \omega_2,$$

$$\omega_j = \sqrt{k \pm \delta} (j = 1, 2), \delta = \sqrt{k^2 - 4\Delta_K - 4n^2}, \tag{12}$$

$$\lambda_{1j} = \frac{k_d - d\omega_j^2}{2\omega_j^2 - k} = -\frac{1}{4} [d + (-1)^j (dk - 2k_d)/\delta] (j = 1, 2), \tag{13}$$

$$(\lambda_2)_{1,2} = \pm \frac{i}{16\delta^3 \sqrt{2(k + \delta)}} [2k(dk - 2k_d)^2 + \delta(dk - 2k_d)^2 + 4\delta^2(k\Delta_D + dk_d - d^2k_0 + \delta^3(8\Delta_D - 3d^2))]. \tag{14}$$

4 Results

To clarify the proposed approach, let us consider first the following sample (mathematical example).

4.1 Example

Consider the system (1) with matrices.

$$D = \begin{pmatrix} 1+q & -1 \\ -1 & 1 \end{pmatrix}, K = \begin{pmatrix} 3 & 1.5 \\ 1.5 & -1 \end{pmatrix}, N = (2.5 - \varepsilon_1) \begin{pmatrix} 0 & -1 \\ 1 & 0 \end{pmatrix}. \tag{15}$$

Here q is some positive number, which represents the controllable parameter to neglect the possible destabilization effect. The small parameter $\varepsilon_1 > 0$ (independent of parameter ε) characterizes the closeness to the boundary of the stable zone for the undamped system. Taking into account that

$$d = 2 + q, k = 2\Delta_D = q, \Delta_K = -\frac{21}{4}, k_d = 5 - q, kd - 2k_d = 4q - 6,$$

the polynomial (2) and condition (6) now reads

$$f(\lambda) = \lambda^4 + \varepsilon(2+q)\lambda^3 + (2 + \varepsilon^2q)\lambda^2 + \varepsilon(5 - q)\lambda + 1 - 5\varepsilon_1 + \varepsilon_1^2, \tag{16}$$

$$\Delta_3 = -(2q - 3)^2 + \varepsilon_1(5 - \varepsilon_1)(q + 2)^2 + \varepsilon^2q(10 + 3q - q^2) > 0. \tag{17}$$

The relation (10) gives the value $q_0 = 1.5$. Now depending on how two small parameters ε_1 and ε are related to each other. We can choose the range for parameter q in the vicinity of q_0 to avoid dissipation-induced instability. This safe range is presented in Fig. 1a. Note that the domain between the surface and the plane $\varepsilon = 0$ describes the “safe” range for parameter q , i.e., for a given value of ε_1 and appropriate value of q system (1), (15) is asymptotically stable for any infinitely small value of ε . For instance, for $\varepsilon_1 = 10^{-3}$ (Fig. 1b) the appropriate range for q is $\approx (1.38, 1.62)$. Substituting the numerical values $q = 1.4, \varepsilon = 0.002$, we find the roots of the

polynomial (15): $-0.00028596 \pm 1.03476i$, $-0.003114 \pm 0.96399i$. The values for the real parts given by formulas (13) are respectively -0.00028564 and -0.003114 , i.e., give a good enough approximation.

Of course, as ε tends to zero, the maximal Lyapunov exponent also decreasing, but it remains negative $-\max(\text{Re}(\lambda_j)) \approx -0.2856 \cdot 10^{-4}$ for $\varepsilon = 0.0002$, $\max(\text{Re}(\lambda_j)) \approx -0.1428 \cdot 10^{-5}$ for $\varepsilon = 10^{-5}$, etc.

Let us demonstrate the results obtained for two mechanical systems.

4.2 The Friction-Induced Vibrations in 2-DoF Mechanical System

To investigate the flutter instability as a mode-coupling phenomenon, a simple self-excited mechanism was proposed by Hulten [12]. Later on, it was developed and investigated in several papers by Sinou et al. (e.g. [10, 11]).

This model consists of a mass m located on a moving band (Fig. 2); the contact between mass and belt is simulated by two plates supported by two different springs.

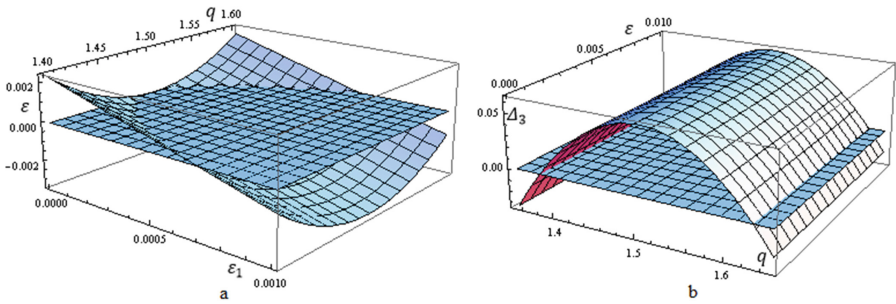


Fig. 1. The “safe” range for parameter q (the domain where the surface is above the plane $\varepsilon = 0$).

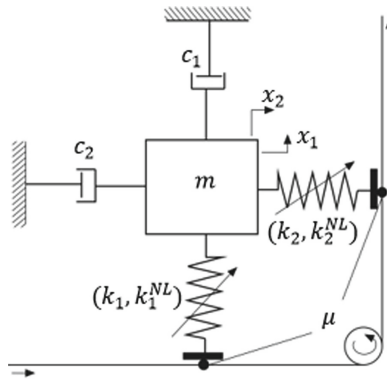


Fig. 2. Mechanical model.

The contact friction coefficient is considered constant, and the band moves at a constant speed. It is supposed that the tangential force FT is proportional to the normal force FN and satisfies Coulomb's law: $FT = \mu FN$. Assuming that the normal force FN is linearly related to the displacement of the mass along the normal to the contact surface, the resulting equations of motion can be expressed in the following form

$$M\ddot{\mathbf{x}} + \varepsilon D\dot{\mathbf{x}} + (\mathbf{K} + \mathbf{N})\mathbf{x} + \mathbf{F}(\mathbf{x}) = 0,$$

where $M = \begin{pmatrix} m & 0 \\ 0 & m \end{pmatrix}, D = \begin{pmatrix} c_1 & 0 \\ 0 & c_2 \end{pmatrix}, \mathbf{K} + \mathbf{N} = \begin{pmatrix} k_1 & -\mu k_2 \\ \mu k_1 & k_2 \end{pmatrix},$

$$\mathbf{F}(\mathbf{x}) = \begin{pmatrix} k_1^{NL}x_1^3 - \mu k_2^{NL}x_2^3 \\ \mu k_1^{NL}x_1^3 + k_2^{NL}x_2^3 \end{pmatrix}.$$

After introducing the dimensionless parameters and time by formulas

$$\varepsilon = c_1/\sqrt{mk_2}, \alpha = c_2\kappa/c_1, \kappa = \sqrt{k_1/k_2}, \tau = \sqrt{k_1/mt},$$

and linearization in the vicinity of origin, we come to the system (1) where

$$D = \begin{pmatrix} \kappa & 0 \\ 0 & \alpha \end{pmatrix}, \mathbf{K} + \mathbf{N} = \begin{pmatrix} \kappa^2 & -\mu \\ \mu\kappa^2 & 1 \end{pmatrix}.$$

Assuming that parameter κ is known, we aim to find the value of damping ratio, which allows neutralizing the possible instability induced by small friction. Applying the results of Sect. 3, we find

$$k = 1 + \kappa^2, \Delta_k = \kappa^2, n = \frac{1}{2}(\mu + \kappa^2), \mu_2 = \frac{(\kappa^2 - 1)^2}{4\kappa^2}, \tag{18}$$

$$d = \alpha + \kappa, k_d = \kappa(1 + \alpha\kappa), v_1 = \frac{\alpha}{(\alpha + \kappa)^2} \left[\frac{(\kappa^2 - 1)^2}{\kappa} + \varepsilon^2(\alpha + \kappa)(1 + \alpha\kappa) \right]. \tag{19}$$

The equality (10) reads $(1 + \kappa^2)(\alpha + \kappa) - 2\kappa(1 + \alpha\kappa) = 0$, which leads to relation $\alpha = \kappa$. Of course, in practice, it is difficult to realize this equality perfectly. Hence, let $\alpha = \kappa + \delta_\alpha$, where δ_α is the discrepancy parameter. The difference between the critical values for the bifurcation parameter μ is equal to $\frac{v_1 - v_2}{\sqrt{v_1} + \sqrt{v_2}}$ and is proportional to the following expression

$$\delta_\mu = 8\kappa^4(\kappa^2 + 1)\varepsilon^2 - (\kappa^2 - 1)^2\delta_\alpha^2 + o_1(\varepsilon^2) + o_2(\delta_\alpha^2).$$

Therefore, as long as $|\delta_\alpha|$ does not exceed the threshold

$$\frac{2\sqrt{2}\kappa^2\sqrt{\kappa^2+1}}{|\kappa^2-1|}\varepsilon \tag{20}$$

the destabilization is prevented. This is illustrated in Fig. 3.

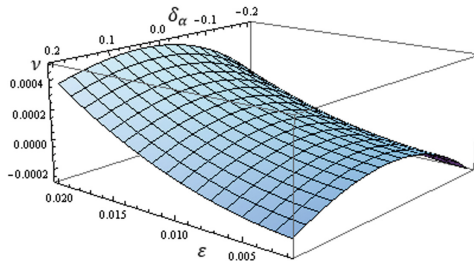


Fig. 3. The surface $v(\varepsilon, \delta_\alpha) = v_1 - v_2$ in case $\kappa = 1.2$.

4.3 The Double Pendulum Under the Action of Follower Force

Consider the double pendulum shown in Fig. 4, consisting of two rigid weightless rods of equal length l , carrying the concentrated masses m_1 and m_2 . A visco-elastic joint connects the rods, and the configuration of the system is determined by the two angles θ_1 and θ_2 formed between the vertical and each of the two rods, respectively. The follower force is applied to the free end. (The case $m_1 = 2m_2, k_1 = k_2$ corresponds to Ziegler’s standard model [1].)

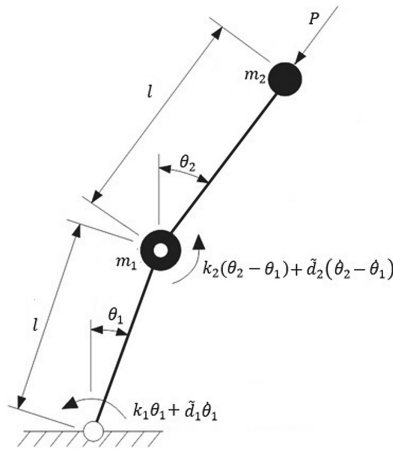


Fig. 4. The double pendulum with follower force.

The kinetic energy and potential energy of the system have the following forms

$$K = \frac{1}{2}l^2 \left[(m_1 + m_2)\dot{\theta}_1^2 + 2m_2\dot{\theta}_1\dot{\theta}_2 \cos(\theta_2 - \theta_1) + m_2\dot{\theta}_2^2 \right],$$

$$\Pi = \frac{1}{2} \left[k_1\theta_1^2 + k_2(\theta_1 - \theta_2)^2 \right]$$

and the non-conservative forces

$$Q_1 = -(\tilde{d}_1 + \tilde{d}_2)\dot{\theta}_1 + \tilde{d}_2\dot{\theta}_2 + Pl \sin(\theta_1 - \theta_2), Q_2 = \tilde{d}_2(\dot{\theta}_1 - \dot{\theta}_2).$$

Lagrange’s equations of motion of the 2nd kind are

$$\frac{d}{dt} \frac{\partial L}{\partial \dot{\theta}_j} - \frac{\partial L}{\partial \theta_j} = Q_j, L = K - \Pi, j = 1, 2.$$

Let’s introduce the dimensionless parameters by the formulas

$$\mu = \frac{m_1}{m_2}, d_j = \frac{\tilde{d}_j}{l} \sqrt{\frac{1}{m_2 k_2}} (j = 1, 2), q = \frac{d_1}{d_2}, \kappa = \frac{k_1}{k_2}, p = \frac{Pl}{k_2}, \tau = \sqrt{\frac{k_2}{m_2 l^2 t}}.$$

Then we have the system (1) with matrices

$$M = \begin{pmatrix} 1 + \mu & 1 \\ 1 & 1 \end{pmatrix}, D = \begin{pmatrix} 1 + q & -1 \\ -1 & 1 \end{pmatrix}, K + N = \begin{pmatrix} 1 + \kappa - p & p - 1 \\ -1 & 1 \end{pmatrix}.$$

The characteristic polynomial has the following form

$$f(\lambda) = \mu\lambda^4 + \varepsilon(4 + \mu + q)\lambda^3 + (4 + \mu + \varepsilon^2 q - 2p + \kappa)\lambda^2 + \varepsilon(\kappa + q)\lambda + \kappa.$$

For the undamped case, two first inequalities (7) are fulfilled, and the third one reads $4p^2 - 4p(4 + \kappa + \mu)(\kappa - \mu)^2 + 8(\kappa + \mu) + 16 > 0$.

For the given values of μ and κ a circulatory Hopf bifurcation occurs when

$$p = p_{crit} = 2 + \frac{1}{2}(\sqrt{\kappa} - \sqrt{\mu})^2. \tag{21}$$

For a weakly damped system, the critical value for parameter p is

$$p_* = \frac{1}{2} \frac{4q^2 + (8\mu - 2\mu\kappa + \kappa^2 + \mu^2 + 16)q + 4\kappa^2}{q^2 + (4 + \kappa + \mu)q + 4\kappa + \mu\kappa} \tag{22}$$

In Fig. 5 the corresponding surfaces $p = p_{crit}(\mu, \kappa), p = p_*(\mu, \kappa)$ are presented.

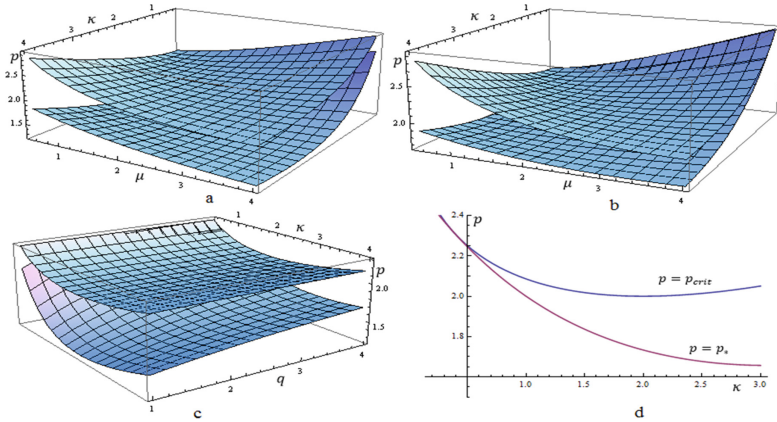


Fig. 5. The discrepancy between the critical load for undamped and weakly damped cases for different values of parameters m, k, q . The surfaces $p = p_{crit}(\mu, \kappa), p = p_*(\mu, \kappa)$ (a. $q = 1$, b. $q = 4$, c. $\mu = 2$, d. $q = 4, \mu = 2$).

5 Conclusions

The article considers the stability problem for a non-conservative mechanical system with weak damping. The possibility of the occurrence of flutter instability is under study, and a way to prevent such a situation is discussed. The “tuning” technique for damping matrix is suggested. Two examples are considered for illustration. In particular, in the case of a double pendulum with a follower force, by varying the damping ratio and reducing the stiffness of the joint at the attachment point, an increase in the threshold for the critical load can be achieved. As one can see from Fig. 5d, for the parameter $k < 1$, there is practically no destabilization, i.e., the stiffness coefficient k_1 should be approximately half that of k_2 . In quantitative terms, this is 8 – 10% better comparatively with Ziegler’s case ($k = 1, p_{crit} \approx 2.058$).






References

1. Ziegler, H.: The stability criteria of elastomechanics. *Engineer Arch.* **20**(1), 49–56 (1952). [in German]
2. Kirillov, O.N., Seyranian, A.P.: Stabilization and destabilization of a circulatory system by small velocity-dependent forces. *J. Sound Vibration* **283**, 781–800 (2005)
3. Sugiyama, Y., Langthjem, M.: Physical mechanism of the destabilizing effect of damping in continuous non-conservative dissipative systems. *Int. J. Non-Linear Mech.* **42**(1), 132–145 (2007)
4. Hagedorn, P., Heffel, E., Lancaster, P., Muller, P.C., Kapuria, S.: Some recent results on MDGKN-systems. *ZAMM* **95**(7), 695–702 (2015)
5. Luongo, A., Ferretti, M., D’Annibale, F.: Paradoxes in dynamic stability of mechanical systems: investigating the causes and detecting the nonlinear behaviors. *SpringerPlus* **5**(1), 1–22 (2016). <https://doi.org/10.1186/s40064-016-1684-9>

6. Jekel, D., Hagedorn, P.: Stability of weakly damped MDGKN-systems: the role of velocity proportional terms. *ZAMM* **97**(9), 1128–1135 (2017)
7. Abdullatif, M., Mukherjee, R., Hellum, A.: Stabilizing and destabilizing effects of damping in non-conservative systems: some new results. *J. Sound Vib.* **413**, 1–14 (2017)
8. Kirillov, O.N., Bigoni, D.: Classical Results and Modern Approaches to Non-conservative Stability. In: Bigoni, D., Kirillov, O. (eds.) *Dynamic Stability and Bifurcation in Non-conservative Mechanics*, pp. 129–190. CISM Int. Centre for Mech. Sci. Springer, Cham (2019). doi: https://doi.org/10.1007/978-3-319-93722-9_4
9. Awrejcewicz, J., Losyeva, N., Puzyrov, V.: Stability and boundedness of the solutions of multi parameter dynamical systems with circulatory forces. *Symmetry* **12**(8), 1210 (2020)
10. Sinou, J.-J., Jézéquel, L.: Mode coupling instability in friction-induced vibrations and its dependency on system parameters including damping. *Eur. J. Mech. A/Solids* **26**, 106–122 (2007)
11. Chomette, B., Sinou, J.-J.: On the use of linear and nonlinear controls for mechanical systems subjected to friction-induced vibration. *Appl. Sci.* **10**(6), 2085 (2020)
12. Hultén, J.: Friction phenomena related to drum brake squeal instabilities. In: *ASME Design Engineering Technical Conferences, CA*, ASME Paper DETC97/VIB-4161, Sacramento (1997)
13. Kang, J., Krousgrill, C., Sadeghi, F.: Dynamic instability of a thin circular plate with friction interface and its application to disc brake squeal. *J. Sound Vib.* **316**(1), 164–179 (2008)
14. Krechetnikov, R., Marsden, J.E.: Dissipation induced instabilities in finite dimensions. *Rev. Mod. Phys.* **79**(2), 519–553 (2007)
15. Selyutskiy, Y.: On dynamics of an aeroelastic system with two degrees of freedom. *Appl. Math. Model.* **67**, 449–455 (2019)
16. Langthjem, M.A., Sugiyama, Y.: Dynamic stability of columns subjected to follower loads: a survey. *J. Sound Vib.* **238**, 809–851 (2000)



Particle Movement on the External Surface of the Cone that Rotates Around the Vertical Axis

Tatiana Volina¹ , Serhii Pylypaka¹ , Victor Nesvidomin¹ ,
Iryna Rybenko² , and Larysa Sierykh³ 

¹ National University of Life and Environmental Sciences of Ukraine,
15, Heroyiv Oborony Street, Kyiv 03041, Ukraine

t.n.zaharova@ukr.net

² Sumy National Agrarian University,

160, Kondratieva Street, Sumy 40021, Ukraine

³ Sumy Regional Institute of Postgraduate Pedagogical Education,
5, Rymaskogo-Korsakova Street, Sumy 40007, Ukraine

Abstract. The relative movement of a particle along the rough outer surface of a cone rotating around a vertical axis with a given angular velocity is considered in the article. Differential equations of the particle movement in projections on the axis of a fixed coordinate system are received and solved by numerical methods. The particle's initial velocity at the moment of contact with the surface of the cone after falling from a certain height is considered. The relative trajectories of particles sliding along the cone's surface and the absolute trajectories of its movement towards the fixed coordinate system are constructed. Visualization of other kinematic characteristics has also been made. The obtained formula allows determining the limiting value of the angular velocity, which depends on the angle of inclination of the generatrices, the coefficient of friction, and the distance from the vertex of the cone to the particle. It is also valid for a flat disk for zero angles of generatrices' inclination.

Keywords: Differential equations · Coordinate system · Sliding · Angular velocity · Absolute trajectory

1 Introduction

It is common knowledge that in many machines, during their work with individual particles of technological material, these particles interact with the rough surfaces of the working bodies. Working bodies can be motionless or perform various movements: rectilinear, translational, rotational, oscillatory. In all cases, the determination of the kinematic characteristics of the particle movement has its peculiarities. These characteristics depend on the shape, design parameters of the working bodies, the nature of the interaction with the technological material, the material's properties, and other factors. It is essential to know the patterns of such interaction since it contributes to improving the machine designs. Undoubtedly, it is complicated to consider the whole complex of factors; thus, simplifications should be used, as in this research, in which a

separate element of a technological material is considered a material particle. The obtained results may not accurately reflect real processes, but they give regularities of process development, which help find the necessary solution.

2 Literature Review

It is a well-known fact that machines interact with particles of technological material in agricultural production. A great deal is being written and said about such interaction. For example, particle motion on the surface of a concave soil-tilling disk is considered in the article [1]. The article [2] presents the analysis of different tillage tools. Interaction of the manure with the scraper units is investigated in [3] and in [4] – the technological process of applying mineral fertilizers by self-loading machine. The article [5] presents the construction of centrifugal working devices for mineral fertilizers spreading and [6] – construction of seed metering mechanisms of the tractor-seeder.

Moreover, separation of material particles occurs on an oscillating surface, for example, in the separation of two-phase multicomponent systems [7], the same as in the process of oil-gas separators [8] and other cleaning equipment [9]. Material particles in contact with the surface can have different origins. Thus, a simplified particle tracking velocimetry framework for stream surface flow monitoring is investigated [10]. The article [11] presents the construction of a spiral-screwing device for the graining of grain material, [12] – the model of crossed movement and gas-liquid flow interaction with captured liquid film in the inertial-filtering separation channels, and [13] – mathematical model of flow in a tube. There are many scientific research works about the movement of particles, which are in contact with the moving spiral working bodies. Instead, modeling the particles' movement in a screw pneumatic separator is done in [14]. Particle movement in the velocity layer on rotating surfaces is analyzed in [15]. Also, particle sliding on the inside of a generic surface of revolution is considered [16]. Accordingly, the results of our research can be applied to the designing of the engineering machines working bodies. Against this background, our research aims to investigate the laws of movement of a particle along the rough outer surface of a cone rotating with a constant angular velocity around its vertical axis.

3 Research Methodology

To begin with, the parametrical equations of a cone with vertex at the origin and straight generatrices directed from the vertex are:

$$\begin{aligned} X &= u \cos \beta \cos \alpha, \\ Y &= u \cos \beta \sin \alpha, \\ Z &= -u \sin \beta. \end{aligned} \tag{1}$$

where β is the angle of inclination of the straight generatrices of the cone to the horizontal plane (constant value), u and α are independent variables of the cone surface, u is the length of the straight generatrix measured from the origin (the vertex of the cone), α is the angle of rotation of the surface point around the axis of the cone.

When the dependence between the variables u and α is established, a line on the cone surface will be described. Let us start by the fact that such dependence is established using the parameter t – the time of the particle sliding along the outer surface of the cone. Hence, the internal equation of the relative particle trajectory will be described by the dependencies $u = u(t)$, $\alpha = \alpha(t)$.

In addition, during rotating around the OZ axis with an angular velocity ω , all points of the cone (1) rotate by an angle $\varphi = \omega t$ with constant z coordinates. So, using the rotation formulas, the parametrical equations of the cone, which describe its position after rotation by an angle φ , can be compiled:

$$\begin{aligned} X &= u \cos\beta \cos\alpha \cos\varphi, \\ Y &= u \cos\beta \sin\alpha \sin\varphi, \\ Z &= -u \sin\beta. \end{aligned} \quad (2)$$

After simplifications, taking into account $\varphi = \omega t$, Eqs. (2) can be written in the following form:

$$\begin{aligned} X &= u \cos\beta \cos(\alpha + \omega t), \\ Y &= u \cos\beta \sin(\alpha + \omega t), \\ Z &= -u \sin\beta. \end{aligned} \quad (3)$$

Indeed, while the cone rotates with an angular velocity ω , a particle slides along its outer surface, the relative trajectory of such a movement is described by the internal dependencies $u = u(t)$, $\alpha = \alpha(t)$. Therefore, if these dependencies are known, after substitution into (1), it will describe the relative trajectory of the particle sliding along the cone's surface regarding the coordinate system rotating together with the cone. Furthermore, if the exact dependencies are substituted into (3), then the absolute trajectory of the particle regarding the fixed coordinate system will be obtained. For the particular case of the particle “sticking”, the relative trajectory is absent (it is a point), and the absolute trajectory is a circle. In both cases, Eqs. (1) and (3) describe not a surface but a line on it. Therefore, in these equations, not uppercase letters “ X ”, “ Y ”, “ Z ”, but lowercase “ x ”, “ y ”, “ z ” will be used. With this in mind, considering the dependencies $u = u(t)$, $\alpha = \alpha(t)$, Eqs. (3) should be sequentially differentiated by time t .

Subsequently, the first derivatives (components of the projection of the particle's absolute velocity) (4) and the second derivatives (components of the projection of the particle's absolute acceleration) (5) on the axis of the stationary coordinate system respectively can be obtained:

$$\begin{aligned} \dot{x} &= [\dot{u}\cos(\alpha + \omega t) - u(\dot{\alpha} + \omega) \sin(\alpha + \omega t)] \cos\beta, \\ \dot{y} &= [\dot{u}\sin(\alpha + \omega t) - u(\dot{\alpha} + \omega) \cos(\alpha + \omega t)] \cos\beta, \\ \dot{z} &= -\dot{u}\sin\beta. \end{aligned} \tag{4}$$

$$\begin{aligned} \ddot{x} &= -\left[(\ddot{u} + 2\dot{u}(\dot{\alpha} + \omega))\sin(\alpha + \omega t) + (-\ddot{u} + u(\dot{\alpha} + \omega)^2)\cos(\alpha + \omega t) \right] \cos\beta, \\ \ddot{y} &= \left[(\ddot{u} + 2\dot{u}(\dot{\alpha} + \omega))\cos(\alpha + \omega t) - (-\ddot{u} + u(\dot{\alpha} + \omega)^2)\sin(\alpha + \omega t) \right] \cos\beta, \\ \ddot{z} &= -\ddot{u}\sin\beta. \end{aligned} \tag{5}$$

Generally, the differential equation of particle movement on the outer surface of the cone is: $m\overline{\omega} = \overline{F}$, where m is the particle mass, $\overline{\omega}\{\ddot{x}; \ddot{y}; \ddot{z}\}$ is an absolute acceleration vector, \overline{F} is the resulting vector of forces applied to the particle. It should be noted that these forces are: the force of the particle weight mg ($g = 9,81 \text{ m/s}^2$), reaction R of the cone surface, and the friction force fR , which resists the particle sliding over the surface of the cone (f is the friction coefficient). Accordingly, a given vector equation should be decomposed in projections on the axis of a fixed coordinate system. As a result, one can obtain a system of three differential equations. Let begin with taking a closer look at applied forces.

The first applied force is the particle weight mg . Since the weight vector is directed downward (Fig. 1a), the projections of the directional unit vector on the coordinate axes are:

$$\{0; 0; -1\}. \tag{6}$$

The second applied force is the reaction R of the cone surface (see Fig. 1a), directed along the normal \overline{N} . The normal direction to the surface is determined from the vector product of two vectors passing through a surface point (in our case, it is a point A) and tangent to the coordinate lines of the surface. These two vectors are partial derivatives of Eqs. (1):

$$\begin{aligned} dX/d\alpha &= -u \cos \beta \sin \alpha, \\ dY/d\alpha &= u \cos\beta \cos\alpha, \\ dZ/d\alpha &= 0, \\ dX/du &= \cos\beta \cos\alpha, \\ dY/du &= \cos\beta \sin\alpha, \\ dZ/du &= -\sin \beta. \end{aligned} \tag{7}$$

By vector multiplication of vectors (7) and reducing it to unit one, the projections of the vector \overline{N} can be found:

$$\overline{N}\{\sin\beta \cos\alpha; \sin\beta \sin\alpha; \cos\beta\}. \tag{8}$$

Finally, the friction force fR is directed opposite the relative velocity v_r of the particle movement (Fig. 1a). Importantly, velocity v_r is the velocity of the particle sliding over the surface without taking into account the rotation of the surface.

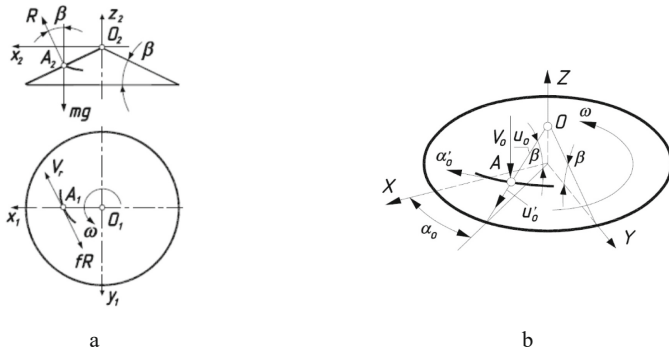


Fig. 1. Graphic illustrations describing the particle position on the surface and the forces applied to it: a) projections of a cone with forces applied to the particle; b) to determine the initial position and velocity of the particle at point A.

Therefore, for determining its projections, it is essential to differentiate Eqs. (1) considering $u = u(t)$, and $\alpha = \alpha(t)$:

$$\begin{aligned} \dot{x} &= \cos\beta(\dot{u} \cos\alpha - \dot{\alpha}u \sin\alpha), \\ \dot{y} &= \cos\beta(\dot{u} \sin\alpha + \dot{\alpha}u \cos\alpha), \\ \dot{z} &= -\dot{u} \sin\beta. \end{aligned} \tag{9}$$

One should not forget that the velocity v_r is defined as the geometric sum of its projections (9):

$$v_r = \sqrt{\dot{x}^2 + \dot{y}^2 + \dot{z}^2} = \sqrt{u^2\dot{\alpha}^2\cos^2\beta + \dot{u}^2}. \tag{10}$$

Mathematically, the projections of the unit vector, along which the particle velocity is directed, are determined by dividing the velocity components (9) by its modulus (10):

$$\left\{ \begin{array}{l} \frac{\cos\beta(\dot{u}\cos\alpha - \dot{\alpha}u\sin\alpha)}{\sqrt{u^2\dot{\alpha}^2\cos^2\beta + \dot{u}^2}}, \\ \frac{\cos\beta(\dot{u}\sin\alpha + \dot{\alpha}u\cos\alpha)}{\sqrt{u^2\dot{\alpha}^2\cos^2\beta + \dot{u}^2}}, \\ \frac{\dot{u}\sin\beta}{\sqrt{u^2\dot{\alpha}^2\cos^2\beta + \dot{u}^2}} \end{array} \right\}. \tag{11}$$

Based on the previous, the values of the applied forces are denoted as mg , R , and fR . Their direction is determined by unit vectors (6), (8), and (11). Since the cone rotates and the projection of the forces is made onto a fixed coordinate system, then the last two vectors must also be rotated by an angle $\varphi = \omega t$ similar to formulas (2). After that, the unit vector that specifies the direction of reaction R of the surface can be derived in projections on the fixed coordinate system axis:

$$\{\sin\beta \cos(\alpha + \omega t); \sin\beta \sin(\alpha + \omega t); \cos\beta\}. \tag{12}$$

In this regard, one also can obtain the projections of the unit vector of the relative velocity by rotating the vector (11) by an angle $\varphi = \omega t$:

$$\left\{ \begin{array}{l} \frac{\cos\beta(\dot{u}\cos(\alpha + \omega t) - \dot{\alpha}u\sin(\alpha + \omega t))}{\sqrt{u^2\dot{\alpha}^2\cos^2\beta + \dot{u}^2}}, \\ \frac{\cos\beta(\dot{u}\sin(\alpha + \omega t) + \dot{\alpha}u\cos(\alpha + \omega t))}{\sqrt{u^2\dot{\alpha}^2\cos^2\beta + \dot{u}^2}}, \\ -\frac{\dot{u}\sin\beta}{\sqrt{u^2\dot{\alpha}^2\cos^2\beta + \dot{u}^2}} \end{array} \right\}. \tag{13}$$

Finally, let compose a system of differential equations of the relative movement of a particle along a rotating cone, taking into account the applied forces and found unit vectors of their action (6), (12), and (13). It is important to emphasize that the friction force fR is directed in the opposite direction of the vector (13):

$$\begin{aligned} m\ddot{x} &= R\sin\beta \cos(\alpha + \omega t) - fR \frac{\cos\beta(\dot{u}\cos(\alpha + \omega t) - \dot{\alpha}u\sin(\alpha + \omega t))}{\sqrt{u^2\dot{\alpha}^2\cos^2\beta + \dot{u}^2}}, \\ m\ddot{y} &= R\sin\beta \sin(\alpha + \omega t) - fR \frac{\cos\beta(\dot{u}\sin(\alpha + \omega t) + \dot{\alpha}u\cos(\alpha + \omega t))}{\sqrt{u^2\dot{\alpha}^2\cos^2\beta + \dot{u}^2}}, \\ m\ddot{z} &= -mg + R\cos\beta + fR \frac{\dot{u}\sin\beta}{\sqrt{u^2\dot{\alpha}^2\cos^2\beta + \dot{u}^2}}. \end{aligned} \tag{14}$$

where the expressions of the absolute acceleration are given in (5).

To summarize, using the solution of the system (14) by the second derivatives of the unknown functions $u = u(t)$ and $\alpha = \alpha(t)$, as well as $R = R(t)$, the following equations were found out:

$$\begin{aligned} \ddot{\alpha} &= -2\frac{\dot{u}}{u}(\dot{\alpha} + \omega) - \frac{f\dot{\alpha}\cos\beta [g - u(\dot{\alpha} + \omega)^2\sin\beta]}{\sqrt{u^2\dot{\alpha}^2\cos^2\beta + \dot{u}^2}}, \\ \ddot{u} &= u(\dot{\alpha} + \omega)^2\cos^2\beta + g\sin\beta - \frac{f\dot{u}\cos\beta [g - u(\dot{\alpha} + \omega)^2\sin\beta]}{\sqrt{u^2\dot{\alpha}^2\cos^2\beta + \dot{u}^2}}, \\ R &= m\cos\beta [g - u(\dot{\alpha} + \omega)^2\sin\beta]. \end{aligned} \tag{15}$$

As a consequence, the first two differential Eqs. (15) compose a system with two unknown functions $u = u(t)$ and $\alpha = \alpha(t)$. At the same time, the surface reaction $R = R(t)$ becomes known after determining these functions. Numerical methods should solve the system, but it has a particular solution. It can be seen that this solution concerns a fixed cone for the case when the particle moves rectilinearly along its generatrix. In this case, $\ddot{\alpha} = \dot{\alpha} = 0$ and $\omega = 0$. Accordingly, the first equation in (15) turns into identity, and the second takes the following form:

$$\ddot{u} = g(\sin\beta - f\cos\beta). \quad (16)$$

The resulting equation is a well-known differential equation of the rectilinear particle movement along the line of the most significant slope of the inclined plane. Such lines for a cone are its rectilinear generatrices. In the case of $f = \operatorname{tg}\beta$, the generatrices of the cone are inclined at the angle of friction, and the acceleration $\ddot{u} = 0$. In this case, the particle can be stationary or move along the cone's generatrix with a constant given speed.

4 Results

The numerical solution of the system of differential Eqs. (15) was carried out using the "Simulink" package of the "MatLab" software product. In this case, the particle falling on the cone from a certain height was taken into account. At the moment of its encounter with the cone's surface, the particle has an initial velocity v_0 (see Fig. 1b), which is directed downward. Consequently, after the encounter, it acquires a component $v_0\sin\beta$, which is directed along the generatrix. For integrating the system (15), it is necessary to set the initial conditions. The first of these conditions is $\dot{u}_0 = v_0\sin\beta$, since the first derivative of the dependence $u = u(t)$ is a component of the movement velocity along the generatrix of the cone. The second component depends on the angular sliding velocity $\dot{\alpha}$ of the particle. At the moment of contact, it has a maximum value equal to the angular velocity ω of cone rotation and is directed in the opposite direction. Thus, $\dot{\alpha}_0 = -\omega$. The particle position on the cone's surface is set by the initial values of the coordinates u_0 and α_0 (Fig. 1a). In Fig. 2a, according to the calculation results, the trajectories of the particle sliding along the cone's surface with the inclination angle of the generatrices $\beta = 20^\circ$ during time $t = 0.1$ s from the moment of the encounter are constructed. Cone rotation speed $\omega = 15 \text{ s}^{-1}$, friction coefficient $f = 0.3$.

Besides, in Fig. 3, the relative and absolute trajectories of a particle falling from different heights, with different initial velocities v_0 at the moment of contact with the cone surface, are shown. Wherein cone rotation speed $\omega = 15 \text{ s}^{-1}$, friction coefficient $f = 0.3$, distance from the vertex $u_0 = 0.03$ m, $\beta = 20^\circ$, observation time $t = 0.15$ s.

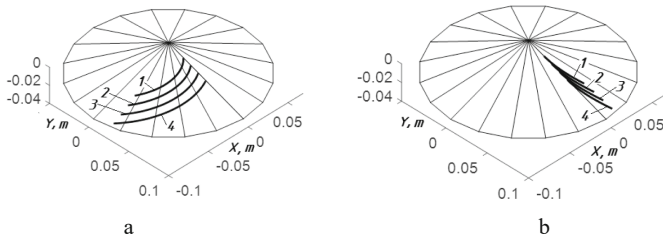


Fig. 2. Relative and absolute trajectories of the particle movement when it encounters with the surface of the cone with an initial velocity $v_0 = 1$ m/s at different distances from its vertex ($1 - u_0 = 0.02$ m, $2 - u_0 = 0.03$ m, $3 - u_0 = 0.04$ m, $4 - u_0 = 0.05$ m): a) relative sliding trajectories; b) absolute trajectories of the movement.

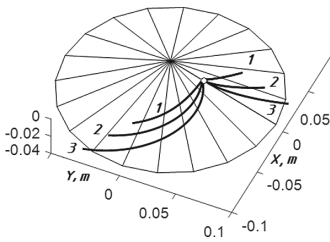


Fig. 3. Relative and absolute trajectories of movement of a particle, which contacts with the cone surface with different values of the initial velocity ($1 - v_0 = 0$ m/s, $2 - v_0 = 0.5$ m/s, $3 - v_0 = 1$ m/s).

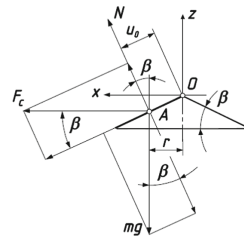


Fig. 4. Scheme of action of forces applied to the particle at point A.

However, if the angle of inclination of the generatrices of the cone is greater than the angle of friction ($\beta > \arctg f$), the particle will start sliding along the cone, even if it does not rotate. At $\beta < \arctg f$, the particle starts sliding at a sufficient value of the angular velocity ω of the cone rotation. Let find this value.

To start sliding, the driving force F_d should be greater than the frictional force F_f . Let project the weight force mg on the generatrix of the cone, along which the particle can start moving: $m \cdot g \cdot \sin \beta$ (see Fig. 4). The second component of the driving force is the component of the centrifugal force F_c ($F_c \cdot \cos \beta$). Thus, $F_d = m \cdot g \cdot \sin \beta + F_c \cdot \cos \beta$. If these forces are projected on the normal N to the surface (see Fig. 5), one can obtain the force of pressure of the particle on the surface. The reaction R of the surface will be directed in the opposite direction: $R = m \cdot g \cdot \cos \beta - F_c \cdot \sin \beta$. The friction force $F_f = f \cdot R$, so, $F_f = f \cdot (m \cdot g \cdot \cos \beta - F_c \cdot \sin \beta)$. The centrifugal force F_c can be found according to the well-known formula: $F_c = m \cdot r \cdot \omega^2$ or $F_c = m \cdot u_0 \cdot \omega^2 \cdot \cos \beta$. After that, the inequality $F_d > F_f$ is composed in the following form:

$$m(g \sin\beta + u_0\omega^2 \cos^2\beta) > mf(g \cos\beta - u_0\omega^2 \sin\beta \cos\beta). \tag{17}$$

An inequality (17) regarding ω , has the following solution:

$$\omega > \sqrt{\frac{g(f - \operatorname{tg}\beta)}{u_0(\cos\beta + f \sin\beta)}}. \tag{18}$$

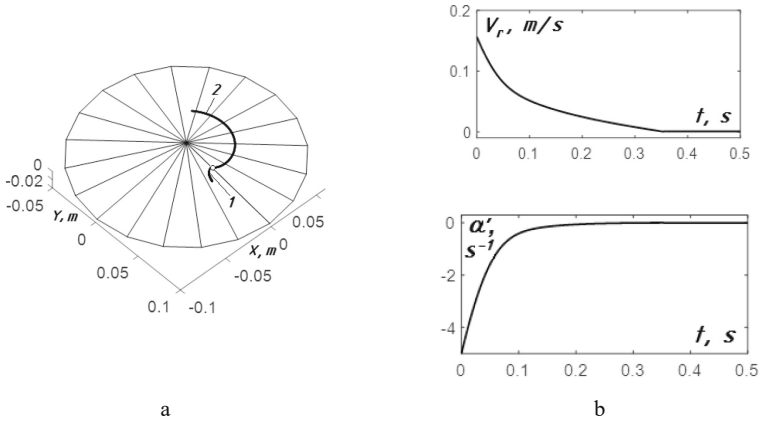


Fig. 5. Graphic illustrations of the particle movement, when it hits the surface of a cone with an initial velocity $v_0 = 0.3$ m/s at the distance $u_0 = 0.03$ m from its vertex ($\omega = 5$ s⁻¹, $\beta = 10^\circ$, $f = 0.3$, $t = 0.5$ s): a) relative – 1 and absolute – 2 trajectories; b) graphs of the relative (at the top) and angular (at the bottom) sliding velocities of the particle

If the angle of inclination of the generatrices of the cone is equal to the angle of friction ($f = \operatorname{tg}\beta$), then the particle sliding begins at any angular velocity of rotation of the cone. For the assumed friction coefficient $f = 0.3$, the friction angle is 16.7° . Let us find the limiting value of the angular velocity of the cone rotation for the angle $\beta = 10^\circ$. If $u_0 = 0.03$ m according to (18) $\omega > 6.25$ s⁻¹. If the angular velocity of the cone rotation is less than the obtained value, then the particle in the state of rest will not start sliding. It is expedient to consider the particle behavior when it falls from a certain height, and at the moment it encounters the surface, it has a velocity $v_0 = 0.3$ m/s. In Fig. 5a, the relative and absolute trajectories of the particle movement at $\omega = 5$ s⁻¹ are constructed. The graphs of the relative and angular velocity of the particle sliding (Fig. 5b) show that it stops after 0.35 s. After that, it becomes motionless in relative movement, and it moves on the circle in absolute movement.

Let us consider the particle movement with the assumed parameters, increasing the angular velocity of rotation of the cone so that it is greater than the limiting one ($\omega = 7$ s⁻¹). Graphical illustrations for this case are presented in Fig. 6.

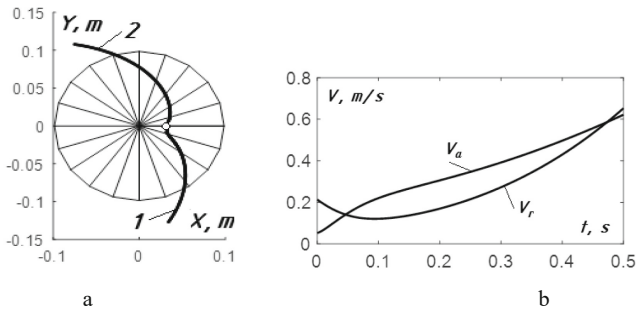


Fig. 6. Graphic illustrations of the particle movement at $\omega = 7 \text{ s}^{-1}$: a) relative – 1 and absolute – 2 trajectories (top view); b) a graph of changes in the relative v_r and absolute v_a speeds.

In this case, the particle accelerates. The absolute speed was obtained by geometric summation of its components (4).

5 Conclusions

For the beginning of the particle sliding, the angle of inclination of the rectilinear generatrices of the cone is essential. If it is greater than the angle of friction, then the particle will begin to slide along the cone surface, regardless of the value of the angular velocity of its rotation. When the angle of inclination is less than the angle of friction, the sliding of the particle is possible with a sufficient value of the angular velocity of cone rotation. The obtained in our research formula allows determining the limiting value of the angular velocity, which depends on the angle of inclination of the generatrices, friction coefficient, and distance from the vertex of the cone to the particle. It is also valid for a flat disk when the angle of inclination of the generatrices is zero. Doubtless, the received results can be used to design the engineering machines working bodies, for instance, working bodies of seeding machines, in which the seeds fall on a rotating cone. Further research is conducted to verify the obtained theoretical results and design improved working bodies of seeders.

References






1. Pylypaka, S., Klendii, M., Klendii, O.: Particle motion on the surface of a concave soil-tilling disk. *Acta Polytechnica* **58**(3), 201–208 (2018). <https://doi.org/10.14311/AP.2018.58.0201>
2. Prem, M., Prem, R., Dabhi, K., Baria, A., Lepcha, P.: Use of different tillage tools for minimizing number of passes in secondary tillage operations. *Int. J. Current Microbiol. Appl. Sci.* **6**(12), 3109–3116 (2017). <https://doi.org/10.20546/ijcmas.2017.612.363>.
3. Golub, G., Lukach, V., Ikalchuk, M., Tesliuk, V., Chuba, V.: Experimental study into energy consumption of the manure removal processes using scraper units. *Eastern-Eur. J Enterprise Technol.* **4**(1), 20–26 (2018)

4. Andreev, K., Terentyev, V., Shemykin, A.: Technological process of application of mineral fertilizers by self-loading machine. In: XII International Scientific Conference on Agricultural Machinery Industry. IOP Conf. Series: Earth and Environmental Science 403 012180, pp. 1–7 (2019). <https://doi.org/10.1088/1755-1315/403/1/012180>.
5. Kobets, A., Ponomarenko, N., Kharytonov, M.: Construction of centrifugal working device for mineral fertilizers spreading. INMATEH – Agricultural Engineering **51**(1), 5–14 (2017)
6. Cortez, J., Anghinoni, M., Arcoverde, S.N.S.: Seed metering mechanisms and tractor-seeder forward speed on corn agronomic components. Engenharia Agrícola **40**(1) (2020). <https://doi.org/10.1590/1809-4430-eng.agric.v40n1p61-68/2020>
7. Ochowiak, M., Włodarczyk, S., Pavlenko, I., Janecki, D., Krupińska, A., Markowska, M.: Study on interfacial surface in modified spray tower. Processes **7**(8), 532 (2019). <https://doi.org/10.3390/pr7080532>
8. Liaposhchenko, O., et al.: Improvement of parameters for the multi-functional oil-gas separator of ‘HEATER-TREATER’ type. In: 2019 IEEE 6th International Conference on Industrial Engineering and Applications, ICIEA 2019, pp. 66–71 (2019). <https://doi.org/10.1109/IEA.2019.8715203>.
9. Plyatsuk, L.D., Ablicieva, I., Vaskin, R.A., Yeskendirov, M., Hurets, L.L.: Mathematical modeling of gas-cleaning equipment with a highly developed phase contact surface. J. Eng. Sci. **5**(2), F19–F24 (2018). [https://doi.org/10.21272/jes.2018.5\(2\).f4](https://doi.org/10.21272/jes.2018.5(2).f4)
10. Tauroa, F., Piscopiab, R., Grimaldi, S.: PTV-Stream: a simplified particle tracking velocimetry framework for stream surface flow monitoring. CATENA **172**, 378–386 (2019). <https://doi.org/10.1016/j.catena.2018.09.009>
11. Isaev, Y., Semashkin, N.M.: Spiral-screwing device for graining of grain material. Int. J. Mech. Eng. Technol. **9**(2), 622–628 (2018)
12. Sklabinskyi, V., Liaposhchenko, O., Pavlenko, I., Lytvynenko, O., Demianenko, M.: Modelling of liquid’s distribution and migration in the fibrous filter layer in the process of inertial-filtering separation. In: Ivanov, V., et al. (eds.) DSMIE 2018. LNME, pp. 489–497. Springer, Cham (2019). https://doi.org/10.1007/978-3-319-93587-4_51
13. Muthu, P., Varunkumar, M.: Mathematical model of flow in a tube with an overlapping constriction and permeability. Procedia Eng. **127**, 1165–1172 (2015). <https://doi.org/10.1016/j.proeng.2015.11.455>
14. Matveev, A.I., Lebedev, I.F., Nikiforova, L.V., Yakovlev, B.V.: Modeling of the particles movement in a screw pneumatic separator. Mining Inf. Analytical Bull. **10**, 172–178 (2014)
15. Pinakov, V., Kulik, K.: Analysis of particle movement in the velocity layer on rotating surfaces. Chin. J. Phys. **60**, 255–261 (2019). <https://doi.org/10.1016/j.cjph.2019.05.007>
16. Carpena, P., Carretero, C., Coronado Jiménez, A.V.: On the circular orbits of a particle sliding on the inside of a generic surface of revolution. Eur. J. Phys. **35**(1), 1 (2014). <https://doi.org/10.1088/0143-0807/35/1/015025>

Process Engineering



Theoretical Substantiation of Mathematical Models of Oil Filtration Through a Porous Medium

Iryna Ablieieva¹(✉) , Leonid Plyatsuk¹ , Oksana Burla¹ ,
Oleh Chekh¹ , and Alex Enrich-Prast² 

¹ Sumy State University, 2, Rymyskogo-Korsakova Street, Sumy 40007, Ukraine
i.ableyeva@ecolog.sumdu.edu.ua

² Linköping University, 581 83 Linköping, Sweden

Abstract. This paper focuses on determining the influence of soil, oil, and environmental factors on the process of oil filtration in a porous medium such as soil. Mathematical modeling of the oil geofiltration process based on classical and modified regularities makes it possible to solve a significant environmental problem associated with predicting the pollution zone due to accidental oil spills. The research methodology is based on the substantiation of theoretical models of oil filtration through porous media, methods for the numerical solution of equations, and computer visualization (ANSYS CFX software). Experimental data supported the verification of the adequacy of the models. Based on obtained results, it was found that all oil flowed into well-permeable sand at a speed of approximately $4 \cdot 10^{-4}$ m/h. The developed model of the stochastic process of petroleum hydrocarbons geofiltration involved obtaining the output as dependent variables, contamination level, contamination depth, and oil spot borders. Numerical solution and visualization using computer simulation showed the distribution of oil hydrocarbons in the soil in vertical and horizontal directions. The mathematical model allowed to predict the formation of the pollution front and assess the contaminated zone's size.

Keywords: Oil pollution · Oil spills · Modelling · Hydrocarbon filtration

1 Introduction

Liquid hydrocarbons that fall on the ground cover due to accidental spills are a serious problem for the environment. Significantly improved efficiency of the process of developing environmental measures allows computer modeling and information technologies. There is a wide range of models of hydrocarbon filtration and software systems that implement these models, but the use of the proposed models for most polluted soils is limited for many reasons: difficulties in later equipping the model with adequate initial data; slow task counting; high cost of software systems. Therefore, creating effective information and computing systems considering the main operating factors, such as the properties of hydrocarbons, soil characteristics, and gravitational-capillary interaction, is highly relevant [1].

As a result of the study, the dynamics of the distribution of spilled hydrocarbons was modeled considering the existing factors to identify areas with a high degree of oil pollution where restoration and cleaning work are necessary. The primary way to solve such problems is numerical methods [1, 2]. Among them, finite difference methods are most often used due to their universality and the presence of a well-developed theory. As a result of the discretization of differential equations using the finite difference method, the continuous distribution of parameters is replaced by a discrete one.

2 Literature Review

It was established [3] that the kinetics of the vertical filtration of oil and oil products on the surface of the soil layer depends on the sorption properties of the soil, which are determined by its fractional composition, namely, the content and ratio of clay and coarse sand fractions. Studies have shown that the greater the silt fraction in the soil and the less coarse sand, the higher the sorption capacity of the soil for oil and oil products and the slower the kinetics of their filtration.

The flows and displacements of different kinds of crude oils with non-Newtonian and yield-stress (plastic fluids) rheology properties have received considerable attention for their various industrial applications [4–8], and some studies reported on the existence of the non-Newtonian behavior of crude oil [9, 10]. Darcy's law for infinitesimal elements of the reservoir does not reflect the microparameters of its pore channels and structural features of their interaction. As a result, they cannot be described by the permeability macroscopic parameter k [11].

Cueto-Felgueroso and Juanes [12] presented a phase-field model of infiltration that explains the formation of gravity fingers during water infiltration in soil. The model is an extension of the traditional Richards equation, and it introduces a new term, a fourth-order derivative in space, but not a new parameter. The transport and retention of a soybean oil-in-water emulsion were evaluated in laboratory columns with a medium packed to fine clayey sand amended with varying amounts of kaolinite. These experiments demonstrated that appropriately prepared soybean oil-in-water emulsions could be distributed in clayey sand at least 80 cm away from the injection point [13].

The generalized Richards' equation provides a good description of the experimentally observed scaling of soil water contents during the horizontal infiltration. In this model, the derivative of water content on time is a fractional one with an order equal to or less than one [14]. Nevertheless, this model is not valid for other liquids such as organic hydrocarbons due to the absence of main physical properties (oil contaminant viscosity, density, temperature, pressure, fractional composition, and the presence of solids).

The study [13] shows that for intermediate wet porous media, pore geometry has a strong influence on interface dynamics, leading to the co-existence of concave and convex interfaces. The mathematical analysis of the Richards equation has almost exclusively dealt with the absorption (moisture movement without gravity) and infiltration problems. Therefore, the analyses of redistribution and drainage processes using the Richards model have almost totally relied upon numerical techniques. Only some of

the more effective approaches will be presented here; however, all are subject to the limitations previously discussed unless stated otherwise [16].

Thus, it is necessary to obtain an adequate mathematical model that describes the petroleum hydrocarbons movement in the soil as pore space, which will predict the oil concentration fields in case of possible accidental spills. This paper focuses on the theoretical description of the oil filtration through the pore space using classic and modified mathematical models with further visualization based on the modern computer modeling software.

For achieving this goal, the following tasks need to be addressed:

- evaluation of the patterns of oil movement in the pore space;
- modeling of the stochastic process of petroleum hydrocarbons geofiltration;
- numerical solution with computer simulation of basic mathematical models that most fully describe the filtration of hydrocarbons through the soil.

3 Research Methodology

3.1 Theoretical Modelling of the Process of Oil Filtration

In modeling the process of oil filtration, the functions of oil conduction, oil capacity, and oil permeability of the soil are used similarly to thermal processes, where heat conduction and heat capacity functions are used, in modeling moisture transfer in porous medium concepts of moisture conductivity and moisture capacity are used. The process of oil geofiltration can be described by two fundamental equations: Darcy's law for fluid flow [17] and the continuity of the moving stream. The Darcy-Buckingham law (1), which is the vadose zone analog of Darcy's law, for unsaturated soil oil flux is given as follows [16]:

$$q = -K(\theta)\nabla\psi(\theta) = -K(\theta)\nabla h, \quad (1)$$

$$h = z + \psi, \quad (2)$$

$$q_x = -K_{xx}(\theta)\frac{\partial\psi}{\partial x}, \quad (3)$$

$$q_y = -K_{yy}(\theta)\frac{\partial\psi}{\partial y}, \quad (4)$$

$$q_z = -K_{zz}(\theta)\frac{\partial\psi}{\partial z} - K_{zz}(\theta), \quad (5)$$

where q is the oil flux (cm/s), θ is the volumetric oil content as a function of location and time t , K is the unsaturated hydraulic conductivity of soil (cm/s) as a function of volumetric oil content, and ψ is soil oil potential or the total soil-oil head (cm) as a function of the volumetric oil content, and z is the vertical coordinate.

If we substitute the equation of the Darcy law in the continuity equation, we get the Richards equation [18]:

$$\frac{\partial \theta}{\partial t} = - \frac{\partial \left[K(h) \left(\frac{\partial h}{\partial z} + 1 \right) \right]}{\partial z} - S(h), \tag{6}$$

or

$$\frac{\partial \theta}{\partial t} = \nabla(K(\theta)\nabla h(\theta)) - \frac{\partial K(\theta)}{\partial z}. \tag{7}$$

A boundary condition (BC) at the oil-supply surface, $z = 0$; either a concentration-type, $\theta = \theta_s(t)$ or $h = H(t)$, or a flux-type, $K - D\partial\theta/\partial z = R(t)$ or $K(1 - \partial h/\partial z = R(t)$.

An initial condition for all z , $\theta(z, t = 0) = \theta_0(z)$ or $h(z, t = 0) = h_0(z)$. Moreover, $R(t)$ is the rate of oil entry at the surface as a function of time.

Soil hydraulic parameters, $K(\theta)$ and $h(\theta)$. The movement of moisture in the unsaturated zone is modeled by the Buckingham-Richards equation [19].

In general form, with z directed upwards, it has the form

$$\frac{\partial \theta}{\partial t} = \nabla_{x,y}(k\nabla_{x,y}(h)) + \frac{\partial}{\partial z} \left(k \left(\frac{\partial h}{\partial z} + 1 \right) \right) + F - Q, \tag{8}$$

where θ is the volumetric oil content as a function of location and time t ; h is potential; F, Q are sources and moisture loss; k is diffusivity coefficient, nonlinearly and ambiguously depending on the potential and its gradient.

In terms of the potential of soil moisture, Eq. (8) takes the form

$$\frac{\partial \theta}{\partial t} = \nabla_{x,y}(k\nabla_{x,y}(h)) + \frac{\partial}{\partial z} \left(k \left(\frac{\partial h}{\partial z} + 1 \right) \right) + \frac{\xi - \eta}{z_0}. \tag{9}$$

In Eqs. (8, 9), x, y are the horizontal coordinates; z is vertical (upward); θ is humidity; h is the potential of soil moisture; $k(h)$ is the coefficient of moisture conductivity (diffusivity); z_0 is the effective thickness of the distribution of sources and losses. Given that

$$\frac{\partial \theta}{\partial t} = \frac{d\theta(h)}{dh} \frac{\partial h}{\partial t} = C(h) \frac{\partial h}{\partial t} \tag{10}$$

Equation (9) can be written as

$$C(h) \frac{\partial h}{\partial t} = \nabla_{x,y}(k(h)\nabla_{x,y}(h)) + \frac{\partial}{\partial z} \left(k(h) \left(\frac{\partial h}{\partial z} + 1 \right) \right) + \frac{\xi - \eta}{z_0}. \tag{11}$$

The moisture conductivity coefficient nonlinearly and ambiguously depends on the potential (or humidity) and its gradient.

The one-dimensional advection-diffusion equation for a dissolved, conservative compound is represented in porous media as [20]

$$\frac{\partial C}{\partial t} = -U \frac{\partial C}{\partial z} + D_{pm} \frac{\partial^2 C}{\partial z^2}, \tag{12}$$

where C is the mass concentration, U is the pore oil velocity, and the dispersion coefficient, D_{pm} , is taken as a linear combination of molecular and hydrodynamic factors through

$$D_{pm} = \frac{D_{mol}}{\tau} + \alpha_L U, \tag{13}$$

where D_{mol} is the molecular diffusivity, τ is the tortuosity correction factor that takes on values near 1.4 for granular porous media, and α_L is the longitudinal dispersivity.

3.2 Modeling of the Stochastic Process of Oil Geofiltration

Nevertheless, a mathematical model of the physical process of oil filtration through porous media cannot be fully described using a consistent pattern of moisture movement in the unsaturated zone or Darcy law. This process can be described by dependence on three groups of factors: oil parameters ($Q_1(t)$), soil parameters ($Q_2(t)$), and environmental parameters ($Q_3(t)$), which represent the input flows (Fig. 1).

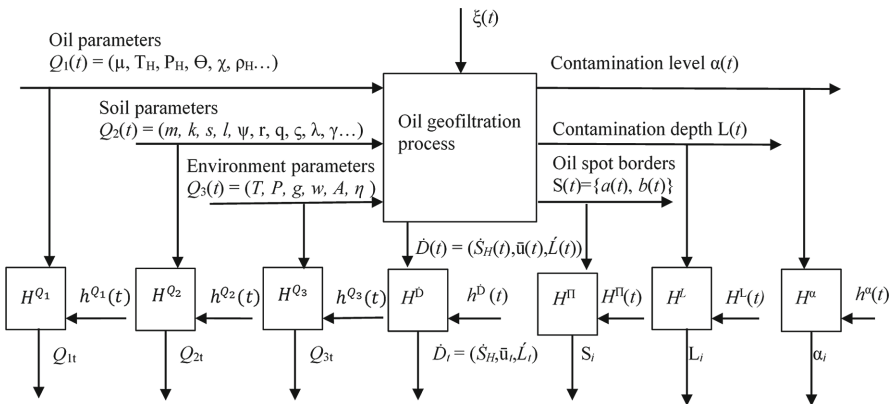


Fig. 1. Scheme of multidimensional stochastic process of oil geofiltration.

Each group of factors forms a vector of influence, including those or other physicochemical parameters characterizing oil, soil, and the environment, respectively. In this case, there is always a vector of random exposure as a set of uncontrolled influences. These parameters are controlled by conducting analytical and instrument measurements with communication channels ($H^{Q_1}, H^{Q_2}, H^{Q_3}$) and the final result at a

particular time point (Q_{1t}, Q_{2t}, Q_{3t}) , taking into account all possible interference $(h^{Q_1}(t), h^{Q_2}(t), h^{Q_3}(t))$.

As shown in Fig. 1, such a model involves obtaining at the output, as dependent variables, contamination level, contamination depth, and oil spot borders. According to the model, the studied parameters form a vector of time-dependent values and discrete values at a given point in time.

4 Results

4.1 Numerical Solution of the Problem of Modeling Oil Geofiltration

The finite difference method includes the following main steps:

- construction of a grid covering the area under consideration;
- construction on the resulting grid of finite-difference approximation equivalent to the original differential equation and additional conditions;
- the formation based on finite-difference approximation of a system of algebraic equations and its solution.

To construct a difference scheme for the original problem, we choose a uniform grid with step h_x in the variable x , step h_y in the variable y , step h_z in the variable z , step τ in the variable t . Get the grid area:

$$W_{h,\tau} = \{x_{i1} = i_1 h_x (0 \leq i_1 \leq n_x), y_{i2} = i_2 h_y (0 \leq i_2 \leq n_y), z_{i3} = i_3 h_z (0 \leq i_3 \leq n_z), t_j = j\phi, 0 \leq j \leq n_t\},$$

where $n_x = L_1/h_x, n_y = L_2/h_y, n_z = L_3/h_z, n_t = T/\tau$.

Replace the derivatives of the internal nodes $W_{h,\tau}$ with finite-difference relations taking into account the representation of the variable coefficient and obtain the explicit difference scheme:

$$\begin{aligned} \frac{S_{i1,i2,i3}^{j+1} - S_{i1,i2,i3}^j}{\tau} = & \frac{1}{h_x} \left[\left(\lambda_{i1+\frac{1}{2},i2,i3}^j \frac{p_{i1+1,i2,i3}^j - p_{i1,i2,i3}^j}{h_x} \right) - \right. \\ & \left. - \left(\lambda_{i1-\frac{1}{2},i2,i3}^j \frac{p_{i1,i2,i3}^j - p_{i1-1,i2,i3}^j}{h_x} \right) \right] \\ + \frac{1}{h_y} \left[\left(\lambda_{i2+\frac{1}{2},i1,i3}^j \frac{p_{i2+1,i1,i3}^j - p_{i2,i1,i3}^j}{h_y} \right) - \right. \\ & \left. - \left(\lambda_{i2-\frac{1}{2},i1,i3}^j \frac{p_{i2,i1,i3}^j - p_{i2-1,i1,i3}^j}{h_y} \right) \right] + \frac{1}{h_z} \left[\left(\lambda_{i3+\frac{1}{2},i1,i2}^j \frac{p_{i3+1,i1,i2}^j - p_{i3,i1,i2}^j}{h_z} \right) - \right. \\ & \left. - \left(\lambda_{i3-\frac{1}{2},i1,i2}^j \frac{p_{i3,i1,i2}^j - p_{i3-1,i1,i2}^j}{h_z} \right) \right] \end{aligned} \tag{14}$$

The system of Eqs. (14) can be solved by the iterative method. As a result of a numerical experiment related to studying the spread of an oil contaminant into the soil under the influence of gravity, considering the influence of pressure, multivariate calculations were performed. The filtration parameters of the model were close to the experimental data and varied within the following limits:

- soil porosity $m = 0.05\text{--}0.55$;
- pollutant density $s_p = 1.15\text{--}1.4 \text{ g/cm}^3$;
- viscosity of the pollutant $m_p = 0.6\text{--}1.0 \text{ mPp}$;
- height of the pollutant filtration area $L = 0.15\text{--}1 \text{ m}$;
- limiting values of saturation $s^* = 0.9$; $s_* = 0.1$;
- saturation at the upper boundary of the region $S_0 = 1.0$;
- acceleration of gravity $g = 9.8 \text{ m/s}^2$.

The developed mathematical model of oil contaminant filtration considers the movement of non-wetting liquid and air in the porous structure. For numerical calculations, a program was implemented using the technology of visual programming Borland C++ and ANSYS.

The vertical flow can serve as a good approximation of the regime of complete penetration of oil, i.e., one of three qualitatively possible regimes of its seepage [21]. This gives an upper bound for the depth of penetration of the petroleum hydrocarbon to the soil. The distribution of oil saturation in-depth at various points in time demonstrates the front moves in the form of a straight line located diagonally relative to the coordinate system. This indicates an increase in frontal saturation. As shown by numerical calculations of the spread of the pollutant under the influence of gravity, the pollution front is first formed, which then moves deeper into the porous soil. The process proceeds rather slowly (in this case, the front advancement speed is approximately $4 \cdot 10^{-4}$ in dimensionless units), which is consistent with experimental data. Phase permeability's are experimentally measured saturation functions. Calculations show that near the source of oil pollution, a pollution zone forms, then the front of oil saturation is formed and advances mainly due to the action of gravitational forces.

4.2 Checking the Adequacy of the Model by Computer Visualization

The reliability of the results of pollution zone determining is confirmed by a satisfactory agreement between theoretical and experimental data. Useful qualitative information on the laws governing the movement of petroleum hydrocarbons in a porous medium can be obtained by analyzing natural conditions and experiments. Laboratory studies of the soil that is classified as a Cambisol, under the Soil Taxonomy with sand texture at room temperature with the volume of oil ($V = 200 \text{ ml}$) showed that the process of oil flow predominantly in the vertical direction, but there is also some spreading to the sides (Fig. 2). The ANSYS CFX software was used to simulate the absorption amount of oil into the ground. The mathematical model uses the standard Navier-Stokes equations and the $k\text{-}\epsilon$ turbulence model.

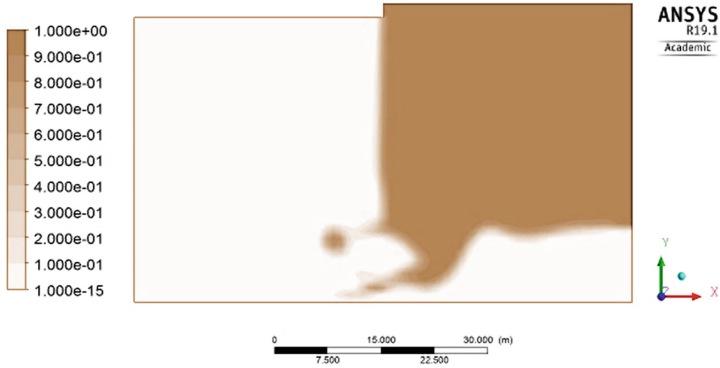


Fig. 2. Computer visualization of vertical and horizontal oil filtration.

The Turbulent Schmidt Number of K Coefficients is 1.0, and Epsilon Coefficients is 1.44 for Ce1 and 1.92 for Ce2 [22]. The user determines the properties of oil and the porous ground to define function. The domain is thin and calculates in a pseudo-2D setting. It has a length of 0.13 m and a height of 0.04 m. An automatically generated mesh using the Sweep Method and has approximately $4 \cdot 10^4$ elements. It was found that all oil flowed into well-permeable sand at a speed of approximately $4 \cdot 10^{-4}$ m/h. This is because the graphitic pressure is stronger than the capillary reaction during the entire observation time. The lower the height of the oil layer, the weaker it is spreading to the sides, so the lateral flows weaken downward. Visualization using computer simulation shows the distribution of oil hydrocarbons in the soil in vertical and horizontal directions. Oil concentration changes are caused by different types of soil, respectively, different physical properties, particularly bulk density and porosity. Figures 3 and 4 show oil concentration and oil velocity after 30 days of oil filtration, respectively.

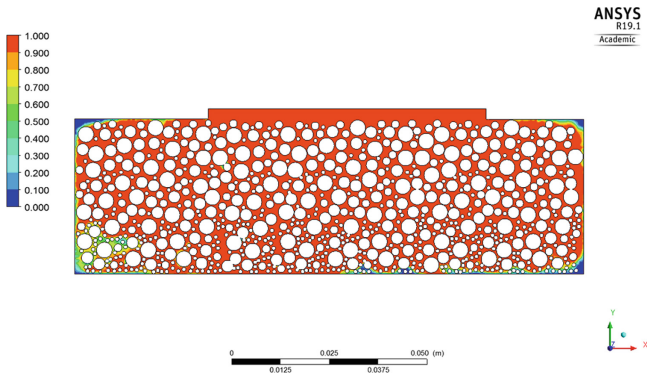


Fig. 3. Visualization of oil concentration for studied soil sample.

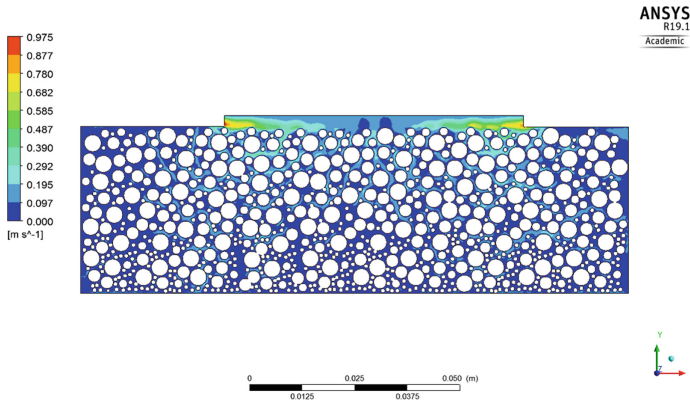


Fig. 4. Visualization of oil velocity for studied soil samples.

The studies showed that the constructed mathematical model allows to predict the formation of the pollution front and assessing the size of the contaminated zone: the depth and width of oil penetration into the soil with the specified properties for a given time, the speed of movement of the hydrocarbon pollutant in the soil, and the filtration coefficient determined by its speed. The developed algorithms and process modeling programs are designed as an information-computing system that allows numerically analyzing the influence of various physical and mechanical parameters on the characteristics of the filtration process.

The growing danger of soil pollution from accidental spills of oil and oil products poses environmental protection. The solution to this problem is complicated because for the assessment of soil pollution, there are still not enough simple models that are widely used for practical calculations. At the same time, studies of the class of geofiltration problems have been carried out for a long time and continue to this day. However, the proposed models are too general; they do not distinguish between significant and non-essential factors. For solving this problem, it is necessary to improve methods for predicting the spread of pollutants, considering the physical and mechanical mechanisms of interaction of pollutants with each other and with a porous medium. The constructed model and studies of the spread of pollutants carried out with its help can be used for practical assessments of the environmental hazard of various economic objects and in planning environmental protection measures.

5 Conclusions

Among mathematical models described the filtration process and fluid flow, such as Darcy law, Darcy-Buckingham law, and Buckingham-Richards law, the last of them is used to model moisture movement in the unsaturated zone. However, volumetric oil content as a function of location and time t is modeled by investigated equations. From this point of view, a system of three vectors of input flows of variables describing the

properties of the oil, soil, and environment was proposed for a complete mathematical description of the process of filtering oil through the soil.

The model of the stochastic process of petroleum hydrocarbons geofiltration involves obtaining at the output, as dependent variables, contamination level, contamination depth, and oil spot borders. According to the model, the studied parameters form a vector of time-dependent values and discrete values at a given point in time.

The ANSYS CFX software was used to simulate the absorption amount of oil into the ground. Numerical solution and visualization using computer simulation showed the distribution of oil hydrocarbons in the soil in vertical and horizontal directions. The mathematical model allows to predict the formation of the pollution front and assess the size of the contaminated zone using the input described in the previous point of these conclusions.

References

1. Bakhvalov, N.S., Kobelkov, G.M., Kuznetsov, Yu.A.: Numerical methods of problems of mathematical physics. Modern problems of computational mathematics and mathematical modeling. Science, Moscow (2005)
2. Bulgakova, G.T., Zhiber, A.V., Faidullin, T.A.: Non-equilibrium two-phase filtration. *Math. Model. RAS* **18**(10), 19–38 (2006)
3. Klizas, P., Gadeikis, S., Norkus, A., Zilioniene, D., Dundulis, K.: Investigation of geofiltration properties of clay soils. *Baltic J. Road Bridge Eng.* **9**(3), 235–240 (2014). <https://doi.org/10.3846/bjrbe.2014.29>
4. Ilyin, S.O., Strelets, L.A.: Basic fundamentals of petroleum rheology and their application for the investigation of crude oils of different natures. *Energy Fuels* **32**(1), 268–278 (2018). <https://doi.org/10.1021/acs.energyfuels.7b03058>
5. Huliienko, S.V., Korniienko, Y.M., Gatilov, K.O.: Modern trends in the mathematical simulation of pressure-driven membrane processes. *J. Eng. Sci.* **7**(1), F1–F21 (2020). [https://doi.org/10.21272/jes.2020.7\(1\).f1](https://doi.org/10.21272/jes.2020.7(1).f1)
6. Frigaard, I.A., Paso, K.G., de Souza Mendes, P.R.: Bingham's model in the oil and gas industry. *Rheol. Acta* **56**(3), 259–282 (2017). <https://doi.org/10.1007/s00397-017-0999-y>
7. Sklabinskyi, V., Liaposhchenko, O., Pavlenko, I., Lytvynenko, O., Demianenko, M.: Modelling of liquid's distribution and migration in the fibrous filter layer in the process of inertial-filtering separation. In: Ivanov, V., et al. (eds.) *DSMIE 2018*. LNME, pp. 489–497. Springer, Cham (2019). https://doi.org/10.1007/978-3-319-93587-4_51
8. Plyatsuk, L.D., Ablieieva, I., Vaskin, R.A., Yeskendirov, M., Hurets, L.L.: Mathematical modeling of gas-cleaning equipment with a highly developed phase contact surface. *J. Eng. Sci.* **5**(2), F19–F24 (2018). [https://doi.org/10.21272/jes.2018.5\(2\).f4](https://doi.org/10.21272/jes.2018.5(2).f4)
9. Xin, X., et al.: Non-newtonian flow characteristics of heavy oil in the Bohai bay oilfield: experimental and simulation studies. *Energies* **10**(11), 1698 (2017). <https://doi.org/10.3390/en10111698>
10. Dimitriou, C.J., McKinley, G.H.: A comprehensive constitutive law for waxy crude oil: a thixotropic yield stress fluid. *Soft Matter* **10**(35), 6619–6644 (2014). <https://doi.org/10.1039/c4sm00578c>
11. Khusainov, A.T., Strelalov, A.V.: Models hydraulic components productive formations. *Oil Gas Bus.* **5**, 119–123 (2014)

12. Cueto-Felgueroso, L., Juanes, R.: A phase field model of unsaturated flow. *Water Resour. Res.* **45**, W10409 (2009). <https://doi.org/10.1029/2009WR007945>
13. Coulibaly, K.M., Long, C.M., Borden, R.C.: Transport of edible oil emulsions in clayey sands: one-dimensional column results and model development. *J. Hydrol. Eng.* **11**(3), 230–237 (2006)
14. Pachepskya, Y., Timlinb, D., Rawlsc, W.: Generalized Richards' equation to simulate water transport in unsaturated soils. *J. Hydrol.* **272**, 3–13 (2003)
15. Rabbani, H.S., Joekar-Niasar, V., Pak, T., Shokri, N.: New insights on the complex dynamics of two-phase flow in porous media under intermediate-wet conditions. *Scientific Reports* **7**(1), 4584 (2017). 10.1038/s41598-017-04545-4.
16. Ravi, V., Williams, J.R.: Estimation of infiltration rate in the vadose zone: compilation of simple mathematical models, vol. I. U.S. EPA (1998)
17. Liaposhchenko, O., et al.: Improvement of parameters for the multi-functional oil-gas separator of 'heater-treater' type. In: 2019 IEEE 6th International Conference on Industrial Engineering and Applications (ICIEA), Tokyo, Japan, 2019, pp. 66–71 (2019). <https://doi.org/10.1109/IEA.2019.8715203>.
18. Ogden, F.L., Lai, W., Steinke, R.C., Zhu, J., Talbot, C.A., Wilson, J.L.: A new general 1-D vadose zone flow solution method. *Water Resour. Res.* **51**(6), 4282–4300 (2015). doi: <https://doi.org/10.1002/2015wr017126>
19. Kashchenko, N.M.: Moisture transfer processes in porous media. *Vestnik Immanuel Kant Baltic Federal Univ.* **10**, 56–58 (2010)
20. Flowers, T.C., Hunt, J.R.: Viscous and gravitational contributions to mixing during vertical brine transport in watersaturated porous media. *Water Resour. Res.* **43**(1), W01407 (2007). <https://doi.org/10.1029/2005WR004773>
21. Muller, K.A., Esfahani, S.G., Chapra, S.C., Ramsburg, C.A.: Transport and retention of concentrated oil-in-water emulsions in porous media. *Environ. Sci. Technol.* **52**, 4256–4264 (2018). <https://doi.org/10.1021/acs.est.7b06012>
22. Ansys, C.: User's Guide-14. ANSYS Inc., New York. (2020)



Analysis of the Effectiveness of the Thermopressor for Charge Air Cooling of Marine Engines

Dmytro Konovalov^(✉) , Mykola Radchenko ,
Halina Kobalava , Andrii Radchenko , and Oleg Savenkov 

Admiral Makarov National University of Shipbuilding,
9, Heroes of Ukraine Avenue, Mykolayiv 54025, Ukraine

Abstract. Circuit solutions of cooling systems by using thermopressors were developed and analyzed in the article. The efficiency of the thermopressor application for the charge air cooling system with single-stage compression was analyzed. A method of the fine water atomization into the charge air by a thermopressor was proposed for contact cooling of the charge air and ecological humidification of the charge air at the inlet to the engine cylinders. The use of a thermopressor makes it possible to realize the effect of thermo-gas-dynamic compression. This effect increases the pressure while simultaneously decreasing the temperature during the finely dispersed water evaporation injected into the airflow, moving near the sound speed. Moreover, contact cooling of the charge air by using thermopressors does not require complex mechanical spray systems. The reduction in the power consumed by the compressors was 7–12%, due to which, in turn, it was possible to increase the power of the internal combustion engine by 1–2%.

Keywords: Turbocharger · Contact cooling · Internal combustion engine

1 Introduction

The reserves for increasing the internal combustion engine (ICE) efficiency are largely associated with the improvement of external systems. These systems design to ensure the optimal initial parameters of the ICE operating cycle and the turbocharging system. Reduction of the power consumed by the turbocharger (TC) of the charge air provides the occurrence of the turbine power reserve, which could be transmitted to the engine shaft or used, for example, to drive an electric generator. Improving the turbocharging system is one of the promising areas for increasing the efficiency of modern internal combustion engines.

2 Literature Review

Charge air cooling is used to achieve two goals: increasing the power and reducing the thermal load of parts of the cylinder-piston group (CPG) of the engine [1–3].

Air cooling allows to increase air density and hence the air charge mass in the engine cylinder. Increasing the mass of the air charge in the cylinder allows burning more fuel and carrying out the main task of boosting – to increase engine power [4–6].

Along with an increase in engine power, air cooling allows improving the operating conditions of the CPG parts due to a decrease in the temperature of the piston, cylinder sleeve and cover, and gas exchange components [7, 8].

A diagram of the charge air cooling system with single-stage air compression is shown in Fig. 1. In modern marine diesel engines, the charge air cooler (CAC) is a heat exchanger with several heat-consuming circuits: a high-temperature circuit for producing low-pressure flow; a low-temperature circuit for heating feed water for steam boilers; a circuit for a hot water supply and heating system [9], which is cooled with seawater. Liquid separators (LS) are installed according to CAC.

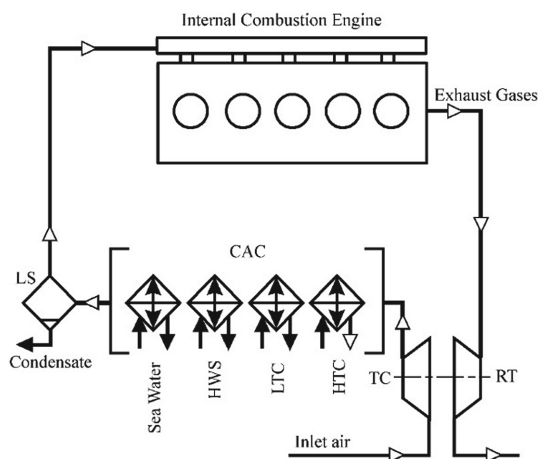


Fig. 1. Scheme of the charge air cooling system for the medium-speed marine diesel engine: LS – liquid separator; CAC – charge air cooler; TC – turbocharger; HWS – hot water supply system; LTC – low-temperature circuit; HTC – high-temperature circuit.

In modern internal combustion engines, charge air humidification reduces NO_x emissions into the atmosphere [10, 11]. The amount of water supplied to the ICE with forced air must be 3 times the amount of fuel burned. It can reduce nitrogen emissions by 70 to 80% [12, 13]. Due to its high heat capacity, water vapor takes away a significant amount of heat for vaporization, leading to a decrease in the temperature in the combustion chamber. Given that the rate of NO_x formation is directly dependent on the temperature, the more water vapor in the gas mixture in the cylinder, the lower the temperature is in the combustion zone, and less nitrogen oxides are formed [14, 15].

The use of a thermopressor (TP), which is installed behind the turbocharger, will partially or completely exclude the use of more structurally complex charge air humidification systems (HAE – Humid Air Engine).

Thereby, air cooling by using the thermopressor can allow, on the one hand, to provide intensive cooling of the air, and on the other hand, it will provide much more efficient atomization of water in a gas flow at speed near sonic.

A known method of using the energy of exhaust gases of the diesel ICE for a gas turbine drives the compressor for air pressure increase (more boost pressure). An air cooling system is used to decrease the temperature of the compressed air, first in the water charge air coolers, and then in the expansion process in a turbo expander to the required pressure engine boost [16, 17]. The feasibility of using excess energy of exhaust gases from diesel ICE in turboexpander refrigerating machines for preliminary cooling of the outside air at the turbocharger inlet has been proposed [18, 19].

The studies [20] showed that the complex use of intermediate surface cooling and additional contact cooling by water injection of charge air during compression in a second-stage compressor followed by expansion in an expander (air refrigeration machine) had provided deep cooling the charge air. Respectively, it contributed to the reduction compressor power of the second stage and, consequently, the receiving of additional power of the TC turbine.

The thermo-gas-dynamic compression (thermopression) effect makes it possible to combine two processes: contact cooling of charge air and pressure increase, which reduce the cost of compressor power [21]. Thermopression increases gas pressure in the process of instantaneous evaporation of water injected into a gas (air) flow, which is accelerated to a speed close to sound [22–24]. In this case, heat is removed from the charge air to evaporate water, due to which its temperature decreases. The thermopressor is a compact jet device that is significantly superior in size to other surface and contact-type cooling devices. It provides a slight increase in pressure. Efficient water atomization occurs due to the combined action of turbulization of the accelerated airflow and instantaneous evaporation [25].

The complex use of internal air cooling in the compressor (and at the compressor inlet) of a turbocharged unit was proposed using heat-using refrigerators for deep cooling of the charge air [26, 27]. Such an integrated system made it possible to provide optimal air parameters at the inlet to the engine cylinders and redistribute the components of the thermal and energy balance in the direction of increasing the internal combustion engine performance [28, 29]. Also, the comprehensive use of up-to-date technologies in designing energy-efficient technologies are presented in [30, 31].

3 Research Methodology

In technology, processes are widely used in which the movement of gas through channels occurs under various external influences. There are the following external influences: change in the cross-sectional area of the channel; energy exchange with the environment in the form of mechanical energy transfer or heat transfer; friction to the channel walls; change in gas flow character due to the liquid supply into the flow; processes of mechanical and thermal interaction of liquid droplets and gas flow, etc.

Intensive supply causes an increase in aerodynamic resistance, and heat removal causes a decrease. With intensive heat removal and appropriate organization of the working process, it is possible to significantly reduce the resistance and increase the

total pressure in the gas flow. Due to the thermal effect (heat removal), the gas flow is compressed. Due to the removal of heat from the gas flow, the device, an increase in the total gas pressure occurs, was called a thermopressor.

Heat removal can be carried out by contact heat exchange through the channel walls, and evaporative cooling of cooling water injected into the gas flow. The possibility of the process with an increase in the total pressure of the flow during evaporative cooling was first theoretically shown in 1946 by L.A. Vulis [32].

In the real thermopressor, the gas expansion process takes place in a well-profiled channel almost adiabatically. Finely atomized water is supplied in the confuser part of the thermopressor, where the gas flow moves at a speed of (0.5–0.9) *M*. The interaction of these flows occurs in the evaporation area. It is followed by the acceleration and fragmentation of droplets and a certain deceleration of the gas flow, heating and evaporation of droplets, and gas cooling. A two-phase flow is formed, moving at high speed, in which the processes of heat and mass transfer, changes in the composition of the vapor-gas-liquid mixture, and all flow parameters take place. These processes continue in the thermopressor diffuser, where general deceleration of the flow and an increase in static pressure occur.

It is possible to conclude that the thermopressor use in the charge air cooling system is advisable, while it is possible to ensure a high intensity of the cooling process (with smaller dimensions of the heat exchanger) and highly efficient water spraying.

The calculation methodology formed the basis of the developed software package was based on the theory of thermo-gas-dynamic compression (thermopression) [22, 24], design and experimental research of the thermopressor [25, 33]. Water flow is supplied to the confuser part of the thermopressor and finely sprayed by using special nozzles.

A comparative-calculation method of research was used in this work to determine the thermodynamic and energy efficiency of a thermopressor cooling system as part of a power plant. A proprietary software package was developed to use this method, and it allows:

1. to simulate working processes in a thermopressor;
2. to calculate the main structural elements of the thermopressor;
3. to calculate the energy efficiency and main indicators of the engine when using thermopressor cooling systems, taking into account changes in climatic and hydrometeorological conditions and particular operating modes of the power plant.

The results of experimental and theoretical studies [23, 24] allowed concluding that an increase in total pressure by 20% is quite achievable. Experiments carried out on small thermopressor models, and high inlet temperatures have shown that the relative effect of thermo-gas-dynamic compression may be up to 15%.

The calculation of thermo-gas-dynamic compression was carried out according to the methods [23, 33]. The total pressure increase in the thermopressor is determined by the equation [34]:

$$\frac{P_2}{P_1} = \left(\frac{T_2}{T_1}\right)^{-\frac{B M^2}{2}} - \frac{(\zeta_{loc} + \zeta_{tr} \frac{l}{D}) \rho \alpha_{tph}^2 M^2}{2P_1}, \tag{1}$$

where parameter B is determined from the dependence:

$$B = 1 - 2 \frac{C_p}{C_{inj}}, \tag{2}$$

where l/D is the ratio of the length to the diameter of the mixing chamber; α_{tph} is a two-phase flow sound speed; ζ_{loc} , ζ_{tr} – resistance coefficients: local and friction along the length.

The calculation of the processes of heat and mass transfer during the droplet evaporation in the thermopressor working chamber was carried out according to the classical equations by the well-known methods [34–36].

A schematic solution of the charge air cooling system with thermopressor cooling was developed and analyzed in this paper. A diagram with the thermopressor use as a CAC for the main turbocharger is shown in Fig. 2.

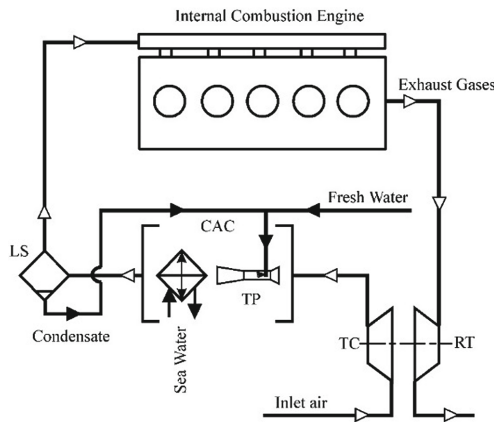


Fig. 2. Scheme of the charge air cooling system by using thermopressor: LS – liquid separator; CAC – charge air cooler; TC – turbocharger; TP – thermopressor; AI – air intercooler; RT – recovery turbine

The air is sucked by a single-stage turbocharger (TC) and compressed to a pressure less than the pressure at the inlet to the internal combustion engine cylinders. After that, air with high temperature and pressure enters the thermopressor (TP) for evaporative cooling. The air temperature is significantly reduced. At the same time, the pressure is increased due to the effect of thermo-gas-dynamic compression to the required value corresponding to the engine inlet. The additional air temperature decrease is carried out in the charge air coolers (CAC).

The scheme analysis was carried out about the standard classical schemes for cooling the charge air in single-stage turbochargers. The calculations were carried out for a medium-speed engine 5L21/31 from MAN B&W ($N_e = 1000 \text{ kW}$, $n = 1000 \text{ min}^{-1}$).

The research aims to analyze the thermodynamic efficiency increase of the internal combustion engine by cooling the charge air with a thermopressor. As a result of the thermopression effect, the air pressure is increased, the compressor power for compressing air is reduced, the air charge mass is increased, and correspondingly, the power in the internal combustion engine is increased.

4 Results

The pressure increase at the thermopressor outlet ΔP_{tp} significantly depends on the temperature decrease during cooling Δt_{tp} . Therefore, the air temperature at the inlet t_{tp1} is important. The air temperature at the inlet of the thermopressor corresponds to the discharge air temperature of the turbocharger. The air temperature at the inlet of the thermopressor is $t_{tc} = 150\text{--}240 \text{ }^\circ\text{C}$. The higher the temperature behind the turbocharger, the higher the temperature at the inlet, and the degree of pressure increase π_c in the turbocharger.

The minimum temperature at the outlet of the TP t_{tp2} was taken to be a temperature 2–3 $^\circ\text{C}$ higher than the dew point temperature. The air temperature in the thermopressor was $t_{tp2} = 60\text{--}92 \text{ }^\circ\text{C}$. The temperature difference in the thermopressor (cooling) is $\Delta t_{tp} = t_{tp1} - t_{tp2} = 90\text{--}170 \text{ }^\circ\text{C}$. However, it is advisable to estimate the temperature decrease by the temperature ratio $\Delta T_d = (T_{tp1}/T_{tp2}) = 1.27\text{--}1.47$.

The thermopression effect will be higher with increasing temperature ratio ΔT_d . The pressure increase was $\Delta P_{tp} = 15\text{--}22\%$ (Fig. 3a) for an “ideal” thermopressor (pressure losses to overcome hydraulic resistances are not taken into account), and the pressure increase was $\Delta P_{tp} = 9\text{--}17\%$ (Fig. 3b) for the “real” thermopressor. Higher pressures correspond to higher outlet temperatures (45–55 $^\circ\text{C}$). The increase in air pressure at the outlet of the thermopressor decreases the degree of pressure increase π_c of the turbocharger. For example, with a total degree of pressure increase $\pi_c = 4.6$, the degree of pressure increase for a turbocharger decreases to $\pi_c = 4.0\text{--}4.1$, and with a total degree of pressure increase, $\pi_c = 3.0$ to 2.7–2.8.

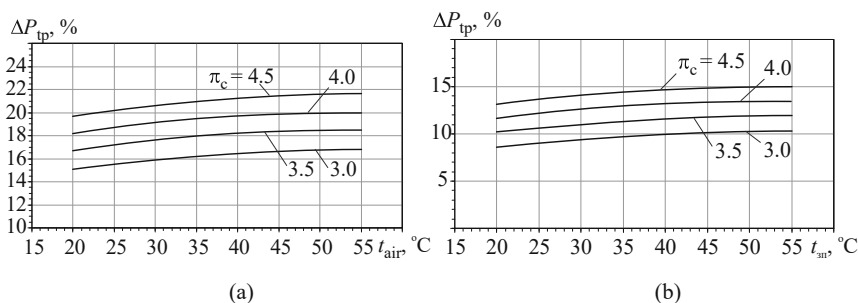


Fig. 3. Dependences of the total pressure relative increase in the “ideal” thermopressor $\Delta P_{tp} = P_{tp2}/P_{tp1}$ (a) and the “real” thermopressor (b) at different degrees of pressure increase π_c on the inlet air temperature t_{air} .

On the other hand, an increase in the inlet air temperature increases the compression work and, as a consequence, the turbocharger power is increased too. With one-stage compression, the decrease in power ΔN_{tc} increases from 12 to 28 kW (Fig. 4, a) or from 7 to 12% (Fig. 4, b) depending on the degree of pressure increase π_c , and from 1.2 to 3.0% (Fig. 5) relative to engine power.

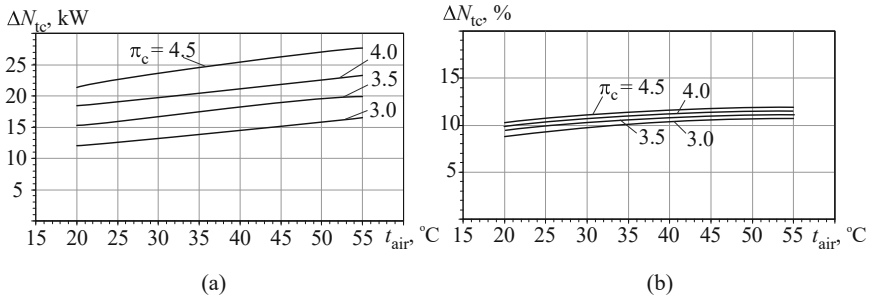


Fig. 4. Dependences of the turbocharger power decrease ΔN_{tc} (a), (b) at different degrees of pressure increase π_c on the inlet air temperature t_{air} .

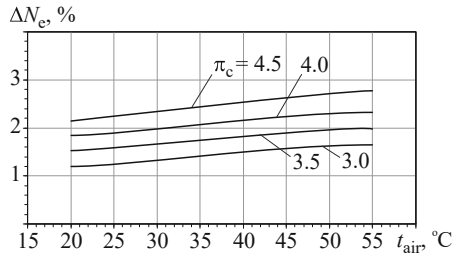


Fig. 5. Dependences of the relative increase in the ICE power ΔN_e at different degrees of pressure increase π_c on the inlet air temperature t_{air} .

The water consumption required for complete evaporation in the thermopressor G_w is 0.06–0.12 kg/s or 2–4% relative to the charge air consumption (Fig. 6).

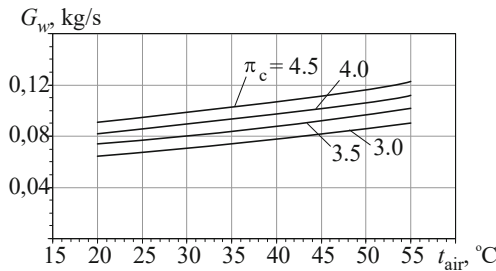


Fig. 6. Dependences of the water consumption G_w in the thermopressor at different degrees of pressure increase π_c on the inlet air temperature t_{air}

It can be concluded from the above analysis that it is advisable to use a thermopressor in the one-stage air compression scheme.

Condensate from the liquid separator (LS) should be used for injection into the thermopressor (Fig. 2).

5 Conclusions

A method of the fine water atomization in the charge air by using a thermopressor was proposed to contact cooling and ecological humidification (to reduce the emission of nitrogen oxides NO_x) of the charge air the inlet to the internal combustion engine cylinders. Moreover, contact cooling of the charge air by using thermopressors does not require complex mechanical spray systems.

The use of thermopressors in charge air cooling systems makes it possible to reduce the power consumed by the compressors N_{tc} for a single-stage boost system by 7–12%, due to which the engine power is increased by 1–2% depending on the inlet air temperature t_{air} and degree of pressure increase π_c . The effect of the charge air cooling by using thermopressor increases with an increase in the air temperature t_{air} at the turbocharger inlet: the value of the TC power N_{tc} is decreased with a corresponding increase in engine power.

The relative (referred to the airflow consumption) water mass flow consumption, which should be injected with its complete evaporation into the thermopressor, was determined, which amounted to 2–4%.

References



1. Steffens, D.: The diesel engine and the environment. Cole Engineering Conference Proceedings. Houston, Texas (2003)
2. Kiran, A.V.N.S., Ramanjaneyulu, B., Lokanath, M., Nagendra, S., Balachander, G.E.: Control of exhaust emissions using piston coating on two-stroke SI engines with gasoline blends. *J. Eng. Sci.* **8**(1), H16H20 (2021). [https://doi.org/10.21272/jes.2021.8\(1\).h3](https://doi.org/10.21272/jes.2021.8(1).h3)
3. Radchenko, A., Trushliakov, E., Kosowski, K., Mikielewicz, D., Radchenko, M.: Innovative turbine intake air cooling systems and their rational designing. *Energies* **13**(23), 6201 (2020). <https://doi.org/10.3390/en13236201>
4. Danilecki, K., Eliaz, J.: The Potential of Exhaust Waste Heat Use in a Turbocharged Diesel Engine for Charge Air Cooling. SAE Technical Paper 2020012089 (2020)
5. Cipollone, R., Di Battista, D., Vittorini, D.: Experimental assessment of engine charge air cooling by a refrigeration unit. *Energy Procedia*, 10671074 (2017)
6. Akimov, O.V., et al.: Computer engineering and design of cast parts for internal combustion engine crankcase. *J. Eng. Sci.* **6**(2), E24E30 (2019). [https://doi.org/10.21272/jes.2019.6\(2\).e4](https://doi.org/10.21272/jes.2019.6(2).e4)
7. Novella, R., Dolz, V., Martin, J., Royo-Pascual, L.: Thermodynamic analysis of an absorption refrigeration system used to cool down the intake air in an internal combustion engine. *Appl. Therm. Eng.* **111**, 257270 (2017)
8. Manzela, A.A., Hanriot, S.M., Gomez, L.C., Sodre, J.R.: Using engine exhaust gas as energy source for an absorption refrigeration system. *Appl. Energy* **8**, 11411148 (2010)

9. Liaposhchenko, O., et al.: Improvement of parameters for the multi-functional oil-gas separator of heater-treater type. In: 2019 IEEE 6th International Conference on Industrial Engineering and Applications (ICIEA), Tokyo, Japan, 2019, pp. 6671 (2019). <https://doi.org/10.1109/IEA.2019.8715203>
10. Takasaki, K., Fukuyoshi, T., Abe, S.: Improvement of Diesel Combustion with Stratified Fuel/Water Injection System. Shin-Nosuke Osafune Mitsubishi Heavy Ind. (1998)
11. Kornienko, V., Radchenko, M., Radchenko, R., Konovalov, D., Andreev, A., Pyryunko, M.: Improving the efficiency of heat recovery circuits of cogeneration plants with combustion of water-fuel emulsions. *Therm. Sci.* **25(1, Part B)**, 791800 (2021). <https://doi.org/10.2298/TSCI200116154K>
12. Arunachalam, P., Tuner, M., Tunestal, P., Thern, M.: Humid air motor: a novel concept to decrease the emissions using the exhaust heat. SAE Tech. Paper 2017012369 (2017)
13. Cai, Y., Wang, K., Kong, S., Bian, Z.: Effect of split injection and intake air humidification on combustion and emission characteristics of a marine diesel engine in partially premixed low-temperature combustion mode. SAE Technical Papers 2020010298 (2020)
14. Bartkowski, T., Eicheldinger, S., Prager, M., Wachtmeister, G.: Effects of ambient air humidity on emissions and efficiency of large-bore lean-burn otto gas engines in development and application. ASME, Power Division (2020)
15. Iyer, A.A., Rane, I.P., Upasani, K.S., Bhosale, Y.P., Gawande, S.H.: Experimental study on the effect of water injection in an internal combustion engine. *Int. Rev. Mech. Eng.* **11(6)**, 379386 (2017)
16. Trushliakov, E., Radchenko, A., Radchenko, M., Kantor, S., Zielikov, O.: The Efficiency of refrigeration capacity regulation in the ambient air conditioning systems. In: Ivanov, V., et al. (eds.) *Advances in Design, Simulation and Manufacturing III (DSMIE 2020)*. LNME, pp. 343353. Springer, Cham (2020)
17. Radchenko, M., Radchenko, R., Tkachenko, V., Kantor, S., Smolyanoy, E.: Increasing the operation efficiency of railway air conditioning system on the base of its simulation along the route line. In: Nechyporuk, M., et al. (eds.) *ICTME (ICTM 2019)*. AISC, vol. 1113, pp. 461467. Springer, Cham (2020)
18. Mostafavi, M., Agnew, B.: Thermodynamic analysis of combined diesel engine and absorption unit turbocharged engine with intercooling. *Appl. Therm. Eng.* **16(89)**, 733740 (1996)
19. Hufford, P.E.: Absorption chillers maximize cogeneration value. *ASHRAE Transactions*, 428433 (1991)
20. Urbach, H.B., et al.: Reduction of NOx emissions from marine power plants. In: *Proceedings of the Air and Waste Management Association s Annual Meeting and Exhibition* (1997)
21. Perel shtejn, B.K.: Entropy analysis of thermal resistance in the gas turbine engine combustion and effect of aerothermopression. *Aviat. Technol.* **1**, 7780 (2003)
22. Shapiro, A., Wadleigh, K.: The aerothermopressor a device for improving the performance of a gas-turbine power plant. In: *Proceedings of the Trans. ASME 1956*, pp.617653. Cambridge, USA (1956)
23. Fowle, A.: An experimental investigation of an aerothermopressor having a gas flow capacity of 25 pounds per second. Dissertation, Massachusetts Institute of Technology, USA (1972)
24. Erickson, J.: A theoretical and experimental investigation of the aerothermopressor process. Dissertation, Massachusetts Institute of Technology, USA (1958)
25. Konovalov, D., Kobalava, H., Maksymov, V., Radchenko, R., Avdeev, M.: Experimental research of the excessive water injection effect on resistances in the flow part of a low-flow aerothermopressor. In: Ivanov, V., Pavlenko, I., Liaposhchenko, O., Machado, J., Edl, M.

- (eds.) DSMIE 2020. LNME, pp. 292301. Springer, Cham (2020). https://doi.org/10.1007/978-3-030-50491-5_28
26. Vittorini, D., Bartolomeo, M.D., Battista, D.D., Cipollone, R.: Charge air subcooling in a diesel engine via refrigeration unit effects on the turbocharger equilibrium. *Energy Procedia* **148**, 822829 (2018)
 27. Khovanskyi, S., Pavlenko, I., Pitel, J., Mizakova, J., Ochowiak, M., Grechka, I.: Solving the coupled aerodynamic and thermal problem for modeling the air distribution devices with perforated plates. *Energies* **12**(18), 3488 (2019). <https://doi.org/10.3390/en12183488>
 28. Cipollone, R., Di Battista, D., Vittorini, D.: Experimental assessment of engine charge air cooling by a refrigeration unit. *Energy Procedia* **126**, 10671074 (2017)
 29. Cipollone, R., Di Battista, D., Gualtieri, A., Massimi, M.: Development of thermal modeling in support of engine cooling design. *SAE Technical Papers* 2013240090 (2013)
 30. Ivanov, V., Pavlenko, I., Trojanowska, J., Zuban, Y., Samokhvalov, D., Bun, P.: Using the augmented reality for training engineering students. In: 4th International Conference of the Virtual and Augmented Reality in Education, VARE 2018, pp. 5764 (2018)
 31. Bun, P., Trojanowska, J., Ivanov, V., Pavlenko, I.: The use of virtual reality training application to increase the effectiveness of workshops in the field of lean manufacturing. In: 4th International Conference of the Virtual and Augmented Reality in Education, VARE 2018, pp. 6571 (2018)
 32. Vulis, L.A.: *Gas Flow Thermodynamics*. Gosenergoizdat, Moscow (1950)
 33. Kobalava, H., Konovalov, D., Radchenko, R., Forduy, S., Maksymov, V.: Numerical simulation of an aerothermopressor with incomplete evaporation for intercooling of the gas turbine engine. In: Nechyporuk, M., Pavlikov, V., Kritskiy, D. (eds.) *ICTM 2020. LNNS*, vol. 188, pp. 519530. Springer, Cham (2021). https://doi.org/10.1007/978-3-030-66717-7_44
 34. Sirignano, W.A.: *Fluid Dynamics and Transport of Droplets and Sprays*, 2nd edn. Cambridge University Press, New York (2010)
 35. Chen, Z., Xie, Q., Chen, G., Yu, Y., Zhao, Z.: Numerical simulation of single-nozzle large scale spray cooling on drum wall. *Therm. Sci.* **22**(1A), 359370 (2018)
 36. Jafarmadar, S., Jahangirramini, A.: Numerical simulation of flash boiling effect in a 3-dimensional chamber using computational fluid dynamic Techniques. *Int. J. Eng.* **29**(5), 8795 (2016)



Kinematic Analysis of an Oscillatory System of a Shaking Conveyor-Separator

Vitaliy Korendiy[✉] , Oleksandr Kachur , and Petro Dmyterko 

Lviv Polytechnic National University,
12, S. Bandera Street, 79013 Lviv, Ukraine
vitalii.m.korendii@lpnu.ua

Abstract. The paper focuses on the estimation of kinematic parameters of the oscillatory system of the shaking conveyor-separator. Unlike the traditional shaking conveyors, the proposed machine is equipped with two working members. The upper one is designed as a shaking screen, below which there is installed a conveying tray. The mesh dimension of the screen can vary in a wide range and depends on the products to be separated. The angle of vibration of the working members and the ratio between the amplitudes of horizontal and vertical oscillations can be changed according to the technological requirements by changing the length of the pusher of the driving crank mechanism. The equations describing the motion of the oscillatory system of the shaking conveyor-separator are derived. Using the derived equations, the numerical modeling of the system's oscillations is carried out in MathCad software. Basic kinematic parameters of the screen and the tray, particularly their horizontal and vertical displacements, velocities, and accelerations, are analyzed. Using the solid model of the shaking conveyor-separator designed in SolidWorks software, the simulation of the oscillatory system's motion is performed. The results of the simulation are presented in the form of time dependencies of the corresponding kinematic parameters. The agreement of the results of numerical modeling and computer simulation is analyzed.

Keywords: Crank mechanism · Shaking screen · Vibrating conveyor · Numerical modelling · Simulation · Velocity · Acceleration

1 Introduction

The sustainable development of any industry cannot be provided without its automation. The latter ensures the improvement of manufacturing productivity and products quality, the increase of resource-use efficiency, the reduction of the total costs of the final products, etc. One of the most perspective directions of automation of manufacturing and technological processes is implementing vibratory equipment.

Vibratory machinery and technologies are fundamentally different from the traditional (non-vibratory) means of industrial automation. Using vibrational principles while designing new machinery and implementing new technologies allows for obtaining tangible results to improve their energy efficiency, productivity, reliability, etc. Further development of such prospective means of automation can solve the

significantly important problems of creating environmentally-friendly and energy-efficient technologies. The paper aims to develop and investigate a vibratory machine for simultaneous conveying and separating various loose and bulky products.

2 Literature Review

Among a great variety of vibratory machines, the shaking (reciprocating) conveyors with directed (rectilinear) oscillations of the working members are of the most structurally simple ones [1]. The paper [2] analyzes the influence of design and operational parameters on the dynamic behavior of a shaking conveyor with a centrifugal vibration exciter. Modeling the process of conveying various loose and bulky products has been carried out in [3]. In the paper [4], the author considered the possibilities of reducing the influence of the eccentric vibration exciter of the double-mass vibratory conveyor on the ground, ensuring optimal conveying conditions. The single-mass oscillatory system of a vibratory conveyor with the optimized set of springs is investigated in [5]. The problems of reducing energy losses during the operation of vibratory conveying and screening machines are thoroughly studied in [6]. In the paper [7], the authors analyzed the process of self-synchronization of inertial vibration exciters.

The paper [8] considers the design and operational peculiarities of the double-track reciprocating conveyor with straight-line oscillations of the working elements. The possibilities of the amplitude-frequency control of electromagnetically driven vibratory conveyors are studied in [9]. The mathematical model, computer simulation results, and experimental investigations of the operation of a linear resonant vibratory conveyor are presented in [10]. In the paper [11], the authors analyzed the operational efficiency and dynamic behavior of vibro-impact systems with pulsed electromagnetic excitation. The possibilities of modernization of single-frequency vibratory systems and the implementation of dual-frequency ones are considered [12]. The novel design of a vibratory conveyor and simulation results of its kinematics is presented in [13]. The single-mass oscillatory system of the shaking conveyor with crank-and-rod vibration exciter is investigated in [14]. The kinematics and the dynamic behavior of the shaking conveyor, as well as the stress-strain state of its elements, are considered in [15]. The research study [16] describes the kinetic-energy parameters of the elements of the shaking conveyor. The paper [17] considers the kinematic and dynamic analysis of the six-link oscillating mechanism of the shaking conveyor.

The design and operational peculiarities of the eccentric-pendulum-type vibrating table are analyzed in [18]. The simulation and experimental testing of the linear vibratory conveyor are carried out in research [19]. In the paper [20], the authors studied different operational conditions of a vibratory conveyor for bulky products. The paper [21] is dedicated to the kinematic and dynamic analysis of the three-mass vibratory system with crank excitation mechanism.

Although mathematical modeling and computer simulation of kinematics and dynamics of shaking (reciprocating) conveyors have already been thoroughly investigated in numerous publications, the novelty of the present paper consists in improving the general design, and analysis of operational peculiarities and kinematic characteristics of the single-degree-of-freedom shaking conveyor-separator equipped by two working members: the separating screen and the conveying tray.

3 Research Methodology

3.1 Design Diagram of the Conveyor-Separator

Let us consider the design and operational peculiarities of the proposed shaking conveyor-separator with eccentric drive (Fig. 1) constructed based on the single-mass oscillatory system with directed (rectilinear) vibrations of the working members (the screen 6 and tray 1). Unlike the traditional shaking conveyors, the proposed machine is equipped with two working members. The upper one is designed as a shaking screen 6, below which a vibrating conveyor is installed (conveying tray) 1.

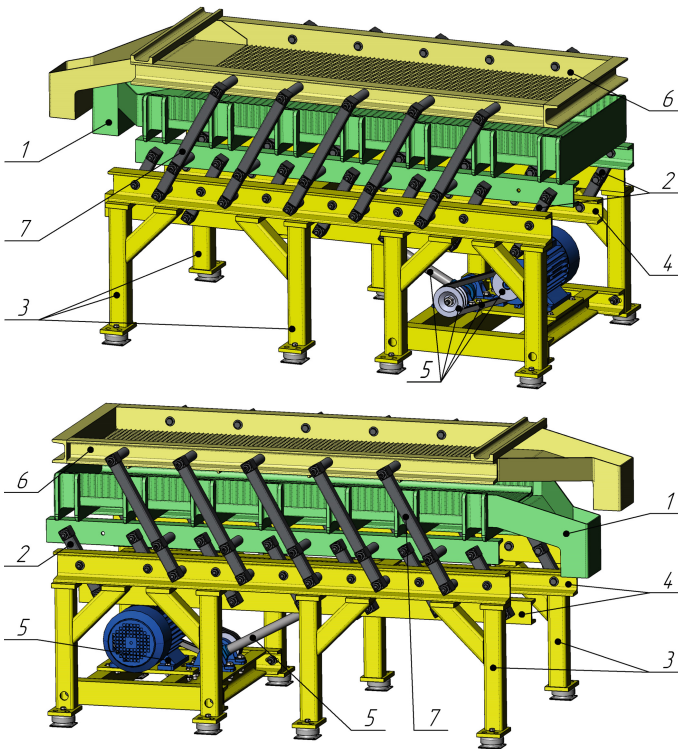


Fig. 1. The proposed design of the shaking conveyor-separator: 1 – conveying tray; 2, 7 – oscillating rods (rockers); 3 – machine’s body; 4 – movable frame; 5 – driving crank mechanism; 6 – separating screen.

The products of various types (piecewise, loose, bulky, etc.) are conveyed along with the shaking screen 6. Screen 6 and conveyor 1 are attached to the corresponding oscillating rods (rockers) 7 and 2 with the help of hinged-elastic elements (rubber-metal sleeves). The rockers 2 are hinged at their middle sections on the unmovable base (machine’s body) 3. The movable frame 4 of the driving crank mechanism 5 is hingedly joined with the lower ends of the oscillating rods (rockers) 2. The electric

motor and the eccentric shaft of the drive are mounted on the machine's body (unmovable base) 3. To transmit the torque from the motor shaft to the eccentric shaft (crank) of the vibration exciter, a belt transmission is used.

Considering the necessity of equipping the shaking conveyor by the additional separating system 6, there is proposed to use the system of intermediate oscillating rods (rockers) 7. The shaking screen (separator) 6 is hinged on the rockers 7 using the rubber-metal sleeves (hinged-elastic elements). The oscillating rods 7 are hinged on the machine's body 3 at their lower ends and are hingedly joined with the conveying tray 1 at their middle sections.

The operation of the proposed conveyor-separator is performed as follows. The rotating shaft of the electric motor sets into motion the eccentric shaft of the crank mechanism through the belt transmission. The crank is hingedly joined with the pushing rod of the vibration exciter 5. The pushing rod sets into oscillatory motion the frame 4, transmits the oscillations to the working member (conveying tray) 1 utilizing the rockers 2. Using the rockers 7, the oscillations are transmitted from the conveying tray 1 to the shaking screen (separator) 6. Taking into account the fact that the initial (neutral) position of the crank mechanism is characterized by the inclination angle β of the rockers 2 and 7 relative to the vertical axis, there are provided the directed (rectilinear) oscillations of the conveying tray 1 and the separating 6 at the same angle β relative to the horizontal axis.

The use of the shaking screen 6 ensures the possibility of separating the mixture of bulky, loose, or piecewise products into components of different sizes depending on the mesh dimension of the screen. The larger components are conveyed by separator 6, while the smaller ones are screened through separator 6 and are conveyed by the vibrating tray 1. Using changing the angular velocity of the driving motor's shaft, it is possible to control the frequency of forced oscillations of the working members (separating the screen and conveying tray). The kinematic parameters of the machine's oscillatory system influence the conveying regime – detached (lifted-off) or non-detached. It allows controlling the operation of the vibratory conveyor according to different technological requirements depending on the product type (loose, bulky, piecewise products etc.).

3.2 Kinematic Analysis of the Oscillatory System

The kinematic diagram of the eccentric drive of the shaking conveyor-separator with directed (rectilinear) oscillations of the working members is presented in Fig. 2. The driving (exciting) mechanism consists of the crank (eccentric shaft) 1. The crank is hinged on the machine's body 0 at its one end (point O), while the other end (point A) is hingedly joined with the pushing (connecting) rod 2. The latter is hingedly joined with lever 3 at point B . The levers 3, 6, and rockers 4, 5 form a parallelogram-type (parallel link, pantograph-type) mechanism. The links (rockers) 4 and 5 are set into rotary motion, while the other links (levers) 4 and 5 are set into the reciprocating motion. The crank (eccentric shaft) 1 rotates about the hinge O , setting into oscillatory motion the pushing (connecting) rod 2; the generalized coordinate φ characterizes the crank's rotation. Unlike the existent shaking conveyors, the proposed machine is equipped with the additional parallelogram-type (parallel link, pantograph-type)

mechanism $LNQRPM$, which is joined with the machine's body using the hinges L and M . The hinges N and O of the mechanism are joined with a lever 6 (attached to the conveying tray). The lever 9 (attached to the separating tray) is hingedly joined with the rockers 7 and 8 at the points Q and R .

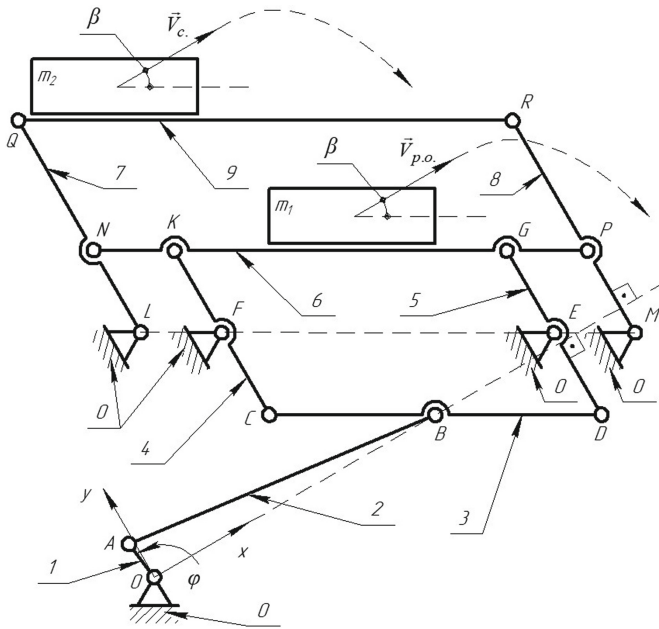


Fig. 2. Kinematic diagram of the oscillatory system of the shaking conveyor-separator

Analyzing the kinematic diagram of the oscillatory system (Fig. 2), it can be concluded that the system consists of ten links: fixed member (stationary base) 0 and nine movable links: crank 1, connecting rod 2, levers 3, 6, 9, rockers 4, 5, 7, 8. All the links are joined in pairs with the help of fifteen revolute kinematic pairs of the fifth class – cylindrical hinges $O, A, B, C, D, E, F, G, K, L, N, Q, R, P, M$. The degree of freedom of the considered oscillatory system is equal to one. Therefore, to describe the mechanism's motion, it is necessary to prescribe one generalized coordinate, e.g., the angle φ . For further kinematic analysis, let us adopt the coordinate system Oxy with the origin at point O (Fig. 2). The Ox axis is directed perpendicularly to the rockers 4, 5, 7, 8, i.e., at the angle β with the horizontal axis.

Taking into account the large length of the pushing (connecting) rod 2 relative to the eccentricity value (the length of the crank 1), we can neglect the displacement of the hinge B along the Oy axis (Fig. 2). In such a case, we can assume that point B and the working members of the conveyor-separator perform the directed (rectilinear) oscillations at the angle β with the horizontal axis due to the rotation of the eccentric shaft (crank 1). Using the method of closed vector loops, let us derive the equation of motion of the hinge B setting the angle φ as the angle of inclination of the crank OA relative to

the positive direction of the Ox axis. Constructing the closed vector loop in the form of the triangle ΔOAB and using the cosine law, we obtain:

$$AB^2 = OA^2 + OB^2 - 2 \cdot OA \cdot OB \cdot \cos \angle AOB = OA^2 + OB^2 - 2 \cdot OA \cdot OB \cdot \cos \varphi. \quad (1)$$

Using the Eq. (1), let us determine the length of the OB side of the triangle ΔOAB , which defines the x_B coordinate of the hinge B :

$$AB = x_B = OA \cdot \cos \varphi + \sqrt{AB^2 - OA^2 \cdot \sin^2 \varphi}. \quad (2)$$

Prescribing the law of changing the angular coordinate $\varphi = \varphi(t)$ and setting the ratio between the lengths KF (GE) and FC (ED), let us derive the law of oscillatory motion of the lower working member (conveying tray) caused by rotation of the eccentric shaft (crank):

$$A_{c.t.}(t) = -x_B(t) \cdot \frac{KF}{FC} = -\left(OA \cdot \cos \varphi(t) + \sqrt{AB^2 - OA^2 \cdot \sin^2 \varphi(t)}\right) \cdot \frac{KF}{FC}. \quad (3)$$

Taking into account the necessity of equipping the conveyor by the separating screen set into motion by the shaking tray with the help of parallelogram-type (parallel link, pantograph-type) mechanism, let us derive the law of oscillatory motion of the upper working member (separating screen):

$$A_{s.s.}(t) = -x_B(t) \cdot \frac{KF}{FC} \cdot \frac{QN}{NL} = -\left(OA \cdot \cos \varphi(t) + \sqrt{AB^2 - OA^2 \cdot \sin^2 \varphi(t)}\right) \cdot \frac{QN}{FC}, \quad (4)$$

where $KF = NL$ taking into account the structural peculiarities of the parallelogram-type (parallel link, pantograph-type) mechanism.

Differentiating the Eqs. (3) and (4) concerning time t , it is possible to determine the laws of changing the velocities and accelerations of the working members. It is useful to know the horizontal and vertical projections of the corresponding kinematic parameters in most cases. Taking into account the inclination angle β of the oscillating rods relative to the vertical axis (i.e., the vibration angle), let us derive the expressions for calculating the corresponding displacements:

$$A_{c.t.hor.}(t) = A_{c.t.}(t) \cdot \cos \beta; \quad A_{c.t.vert.}(t) = A_{c.t.}(t) \cdot \sin \beta; \quad (5)$$

$$A_{s.s.hor.}(t) = A_{s.s.}(t) \cdot \cos \beta; \quad A_{s.s.vert.}(t) = A_{s.s.}(t) \cdot \sin \beta. \quad (6)$$

4 Results

4.1 Results of Numerical Modeling

To carry out numerical modeling of the oscillatory system’s motion, let us set the following input data: the angle of inclination of the conveying tray and the shaking screen relative to the horizontal axis $\alpha = 0^\circ$; the working frequency $\nu = 8.33$ Hz (500 rpm); the lengths of the mechanism’s links $OA = 5.8$ mm, $B = 346$ mm, $NL = KF = GE = PM = FC = ED = 72.5$ mm, $QN = RP = 205$ mm; the vibration angle $\beta = 31^\circ$; the law of changing the angular position of the crank (eccentric shaft) $\varphi(t) = 2 \cdot \pi \cdot \nu \cdot t \approx 52.4 \cdot t$. Substituting the input data into Eqs. (5) and (6), let us plot the time dependencies of the kinematic parameters of the working members of the conveyor-separator using MathCad software (Fig. 3).

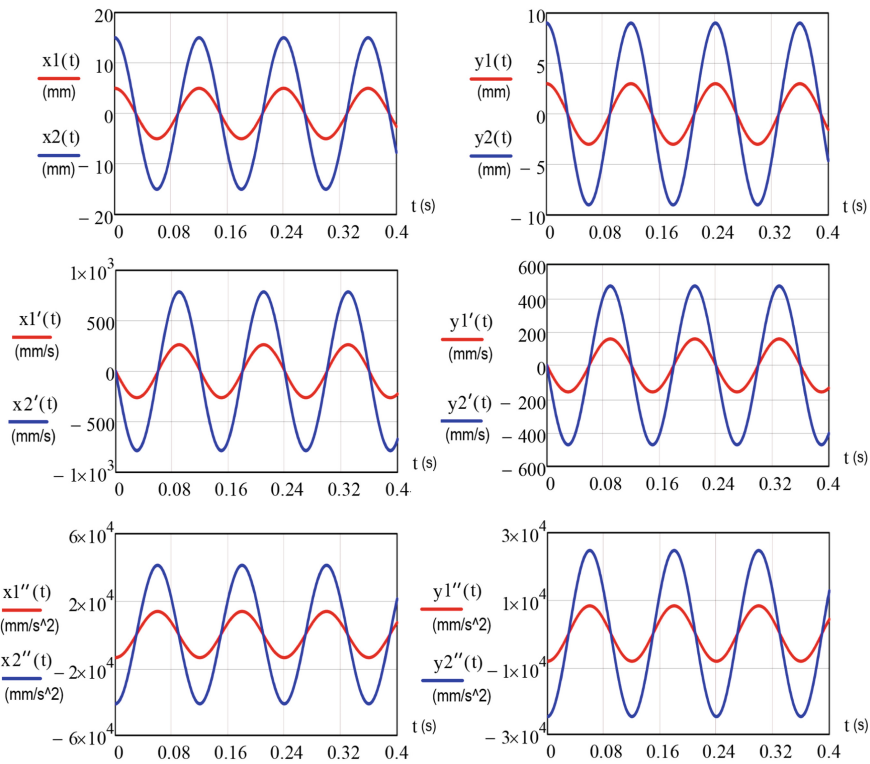


Fig. 3. Results of numerical modeling of the oscillatory system’s motion: x_1, y_1, x_2, y_2 – horizontal and vertical displacements of the tray (1) and the screen (2); x_1', y_1', x_2', y_2' – horizontal and vertical velocities of the tray (1) and the screen (2); $x_1'', y_1'', x_2'', y_2''$ – horizontal and vertical accelerations of the tray (1) and the screen (2)

4.2 Results of Computer Simulation

To analyze the correctness of the derived analytical expressions describing the motion of the oscillatory system of the shaking conveyor-separator, let us carry out the computer simulation of its operation using the corresponding solid model designed in SolidWorks software (see Fig. 1). The simulation results (Fig. 4) are presented in the form of time dependencies of the corresponding kinematic parameters (displacements, velocities, and accelerations) of the working members.

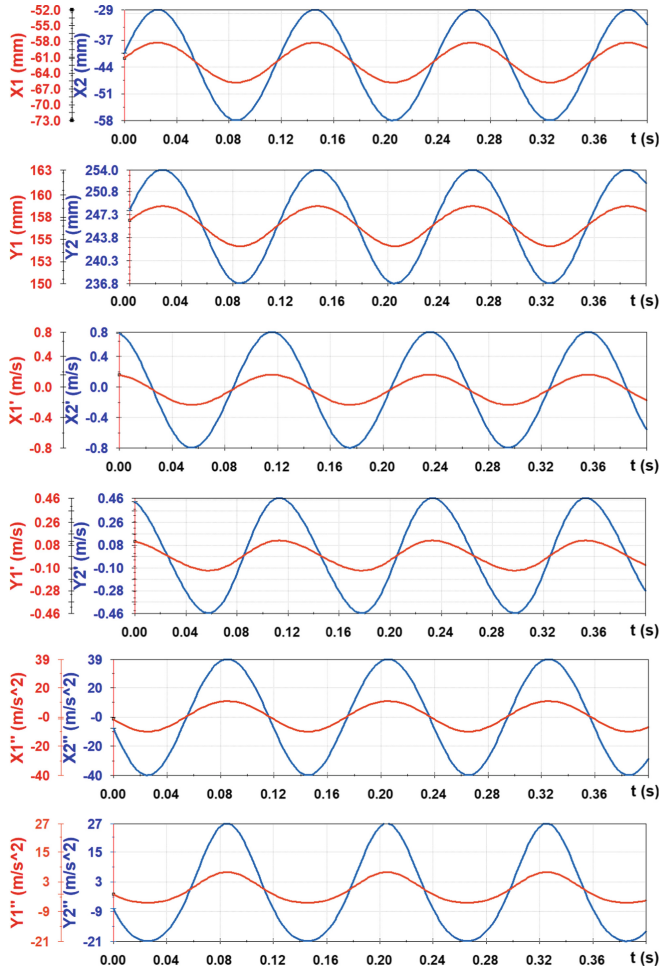


Fig. 4. Results of computer simulation of the oscillatory system's motion: X_1 , Y_1 , X_2 , Y_2 – horizontal and vertical displacements of the tray (1) and the screen (2); X_1' , Y_1' , X_2' , Y_2' – horizontal and vertical velocities of the tray (1) and the screen (2); X_1'' , Y_1'' , X_2'' , Y_2'' – horizontal and vertical accelerations of the tray (1) and the screen (2)

Analyzing the obtained time dependencies (Fig. 3 and Fig. 4), it can be concluded that the relations between the amplitudes, velocities, and accelerations of the working members (separating the screen and conveying tray) depend on the lengths of the corresponding oscillating rods. When the length of the link QN is larger than the length of the link NL , the amplitude values of the kinematic parameters of the separator exceed the ones of the conveying tray (Figs. 3 and 4). If the ratio $QN/NL < 1$, the amplitude values of the amplitudes, velocities, and accelerations of the separator are smaller than the ones of the conveying tray.

5 Conclusions

In the present paper, the improved design of the shaking conveyor is equipped with an additional separating screen. It ensures the possibility of separating the mixture of bulky, loose, or piecewise products into components of different sizes depending on the mesh dimension of the screen. The larger components are conveyed by the separator, while the smaller ones are screened through the separator sieve and are conveyed by the vibrating tray.

Based on the proposed design of the shaking conveyor-separator, the kinematic diagram of its oscillatory system is developed, and the equations of motion of the working members (separating the screen and conveying tray) are derived. Using the derived equation, the numerical modeling of the oscillatory system's motion is carried out in MathCad software. To substitute the correctness of the theoretical investigations, the computer simulation of the machine's operation is performed using its solid model designed in SolidWorks software. The results of numerical modeling and computer simulation are in satisfactory agreement. For the case of the crank length equal to 5.8 mm and the vibration angle $\beta = 31^\circ$, the amplitudes of horizontal oscillations of the working members are about 15 mm (for the separating screen) and 5 mm (for the conveying tray); the corresponding vertical amplitudes are about 9 mm and 3 mm. The maximal vertical acceleration of the shaking screen is about 27 m/s^2 , and of the conveyor – 9 m/s^2 . It ensures effective screening of loose and bulky products in detached (lifted-off) separating regimes and, at the same time, effective conveying of the separated (screened) products along with the tray under non-detached conditions.

Considering the simplifying assumptions applied during numerical modeling and computer simulation, in further investigations on the paper's subject, it is necessary to carry out experimental testing of the machine prototype.





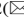

References

1. Parameswaran, M.A., Ganapathy, S.: Vibratory conveying – analysis and design: a review. *Mech. Mach. Theory* **14**(2), 89–97 (1979)
2. Alişverişi, F.: Computational dynamic analysis of single-mass freely shaking conveyors with centrifugal vibration exciter. In: İnan, E., Sengupta, D., Banerjee, M., Mukhopadhyay, B., Demiray, H. (eds.) *Vibration Problems ICOVP-2007*. Springer Proceedings in Physics, vol. 126, pp. 7–13. Springer, Dordrecht (2008). https://doi.org/10.1007/978-1-4020-9100-1_2

3. Bednarski, L., Michalczyk, J.: Modelling of the working process of vibratory conveyors applied in the metallurgical industry. *Arch. Metall. Mater.* **62**(2), 721–728 (2017)
4. Sturm, M.: Two-mass linear vibratory conveyor with reduced vibration transmission to the ground. *Vibroeng. Proc.* **13**, 20–23 (2017)
5. Sturm, M.: Modification of the motion characteristics of a one-mass linear vibratory conveyor. *Vibroeng. Proc.* **19**, 17–21 (2019)
6. Blekhman, I.I., Blekhman, L.I., Vaisberg, L.A., Vasilkov, V.B.: Energy consumption in vibrational transportation and process machines. *Obogashchenie Rud* **1**, 18–27 (2019)
7. Cieplok, G., Wójcik, K.: Conditions for self-synchronization of inertial vibrators of vibratory conveyors in general motion. *J. Theor. Appl. Mech. (Poland)* **58**(2), 513–524 (2020)
8. Tian, X., Li, Q., He, C., Cai, Y., Zhang, Y., Yang, Z.: Design and experiment of reciprocating double track straight line conveyor. *Acta Mech. Malays.* **2**(2), 01–04 (2018)
9. Despotović, Z.V., Lečić, M., Jović, M.R., Djuric, A.: Vibration control of resonant vibratory feeders with electromagnetic excitation. *FME Trans.* **4**(4), 281–289 (2014)
10. Despotović, Ž.V., Urukalo, D., Lečić, M.R., Čosić, A.: Mathematical modeling of resonant linear vibratory conveyor with electromagnetic excitation: simulations and experimental results. *Appl. Math. Model.* **41**, 1–24 (2017)
11. Gursky, V., Kuzio, I., Korendiy, V.: Optimal synthesis and implementation of resonant vibratory systems. *Univ. J. Mech. Eng.* **6**(2), 38–46 (2018)
12. Gursky, V.M., Kuzio, I.V., Lanets, O.S., Kisała, P., Tolegenova, A., Syzdykpayeva, A.: Implementation of dual-frequency resonant vibratory machines with pulsed electromagnetic drive. *Przegl. Elektrotech.* **95**(4), 41–46 (2019)
13. Hsieh, W.H., Tsai, C.H.: A Study on a novel vibrating conveyor. *Key Eng. Mater.* **419–420**, 45–48 (2009)
14. Alişverişi, G.F.: Nonlinear analysis of shaking conveyors with single-mass; crank-and-rod excitors. In: *AIP Conference Proceedings*, vol. 1400, no. 1, pp. 60–65 (2011)
15. Algazy, Z.: The substantiating of the dynamic parameters of the shaking conveyor mechanism. *Vibroeng. Proc.* **5**, 15–20 (2015)
16. Yeleukulov, Y., et al.: Mechanical analysis of vibratory conveyor mechanism. In: *MATEC Web of Conferences*, vol. 226, art. no. 01019 (2018)
17. Umbetkulov, Y., et al.: Dynamic force analysis of a six-link planar mechanism. In: *MATEC Web of Conferences*, vol. 251, art. no. 04028 (2018)
18. Lanets, O.S., Dmytriv, V.T., Borovets, V.M., Derevenko, I.A., Horodetsky, I.M.: Analytical model of the two-mass above resonance system of the eccentric-pendulum type vibration table. *Int. J. Appl. Mech. Eng.* **25**(4), 116–129 (2020)
19. Buzzoni, M., Battarra, M., Mucchi, E., Dalpiaz, G.: Motion analysis of a linear vibratory feeder: dynamic modeling and experimental verification. *Mech. Mach. Theory* **114**, 98–110 (2017)
20. Fanghella, P.: Multibody modelling of a linear feeder for bulk materials. *Mech. Mach. Sci.* **94**, 265–273 (2021)
21. Korendiy, V., Lanets, O., Kachur, O., Dmyterko, P., Kachmar, R.: Determination of inertia-stiffness parameters and motion modelling of three-mass vibratory system with crank excitation mechanism. *Vibroeng. Proc.* **36**, 7–12 (2021)



Cleaning of Parts with Detonating Gas Mixtures

Alexey Losev¹ , Igor Bychkov¹ , Anna Selezneva¹ ,
Vira Shendryk²  , and Sergii Shendryk² 

¹ National Aerospace University named after M. Y. Zhukovsky «Kharkiv Aviation Institute», 17, Chkalov Street, 61070 Kharkiv, Ukraine

² Sumy State University, 2, Rymyskogo-Korsakova Street, Sumy 40007, Ukraine
v. shendryk@cs.sumdu.edu.ua

Abstract. An overwhelming number of defects occur for production reasons due to technology deficiencies. The thermal-impulse method allows you to flexibly automate the cleaning operations from technological contaminants in particles, burrs and quickly wearing out part of the microrelief when obtaining a close to the absolute degree of cleaning surfaces and edges the listed liquids. The technological capabilities of thermal-impulse treatment, control parameters, and factors on which the rational choice of processing modes for machine parts and mechanisms depend are considered. The factors influencing the determination of the optimal modes of cleaning the edges and surfaces of the parts and the factors allowing to form the technical characteristics of the heat source and equipment as a whole, realizing the optimal modes with self-regulation properties, have been determined and systematized. Parts were analyzed after processing by thermal impulse method and for comparison with thermochemical. Therefore, detonating gas technologies are the most attractive because of their versatility and flexibility concerning parts with complex configurations of internal and external surfaces.

Keywords: Edge rounding · Thermal-impulse process · Temperature field · Thermophysical properties · Burrs

1 Introduction

An integrated approach to ensuring the quality of aerospace technology provides for technological support that excludes the negative impact of related phenomena on product quality. Negative accompanying phenomena of technological processes are the cause of hidden defects that appear in operation. These defects include primary technological pollution in the form of microparticles, a rapidly wearing part of the surface microrelief, burrs on the surfaces and edges of parts. The most massive contamination of hydraulic systems occurs at the beginning of the operation of products with particles less than 5 μm . According to statistical data, most aircraft hydraulic system failures associated with pump failure, jamming of distribution and control devices, and increased wear of critical parts occur due to technological pollution. Therefore, one of the most important measures to ensure aircraft units' reliability and the service life is to

fulfill the requirements for industrial cleanliness of unit parts and hydraulic systems during production and operation. A distinctive feature of the production of aircraft units is to ensure their minimum weight, the use of a variety, including high-strength materials: aluminum, steel, titanium alloys, alloys based on copper, plastics, and rubber, and high precision manufacturing of slide and plunger pairs, gears and other parts. The nomenclature of parts at one enterprise can amount to several tens of thousands for a small-scale type of production, and the nomenclature of used materials exceeds more than a hundred items. All this leads to the overwhelming number of defects occurring for production reasons due to technology deficiencies. So, according to statistics, 85% of removal from bench tests of GTE engines occurs due to poor performance of technologies for finishing and cleaning the surfaces of parts from technological pollution [1]. More than one hundred and twenty finishing and cleaning treatment methods are known, using mechanical, chemical, various physical processes. Detonating gas technologies are the most attractive because of their versatility and flexibility for parts with complex configurations of internal and external surfaces.

2 Literature Review

Mechanical treatment is not only a means of ensuring the accuracy of the dimensions of the product but is also a source of technological contamination in the form of burrs, microparticles, and a rapidly wearing part of the microrelief [2–4]. The paper [3] analyzed micro-milling's particular characteristics through a systematic series of experiments, including cutting forces, vibrations, burr formation, and surface quality. Burr formation mechanism in [4] was studied via 3D finite element simulation together with experimental observations. The paper [5] investigated the effect of vibration applied in the feed direction on the burr generation mechanism in vibration-assisted micro-milling. In [6] proved that the main purpose of the cutting parameters optimization of micro-milling is to avoid cutting parameters locating in the strong edge-size-effect zone. The study [7] aimed to identify the reasons and conditions behind the burr formation and investigate the effect of machining conditions, tool wear, and tool coating on the amount of burr formation. In [8], the burr values increase with the curvature for the top burrs because of the expanded plowing region due to the curvature effect. Thereby, it is impossible to avoid burr formation in cutting [5–8], and their complete removal with a razor tool is impossible because its use leads to the formation of smaller secondary burrs [4, 7, 9]. Withal the thermochemical method has become widespread. A combustible gas mixture with an excess of oxygen (up to 50%) is used as a heat source. This method allows you to remove burrs from parts of any shape, from small diameter holes, at the intersection of channels, i.e., where there is access to a combustible mixture. No additional burrs are formed during processing [2]. The advantages also include high productivity, versatility, flexibility [10], the ability to automate the process, the stability of processing results, a wide range of processed materials by changing the ratio of components and the mass of the combustible mixture [11, 12]. When using the thermochemical method, the burrs are melted simultaneously with oxidation. The release of combustion products from the working chamber is carried out after 3...10 s when changing the bottom with parts. Prolonged contact of

combustion products with the workpieces leads to their cooling and the condensation of oxides on the surfaces of the workpieces, tooling, and working chamber. Figure 1 shows a classic view of a steel part after thermochemical treatment. The gas detonation method differs from the thermochemical method in that detonating mixtures are used without an excess of oxidant. With this method, the burrs are melted simultaneously with partial oxidation [13]. On the surfaces of parts, in addition to oxides, melted liquids settle in the form of spherical drops, which are removed by a repeated cycle with detonating stoichiometric gas mixtures of lower pressure.

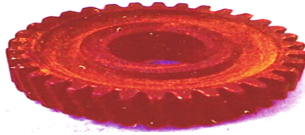


Fig. 1. Gear after thermochemical removal of burrs.

This negative phenomenon leads to additional heating of parts, an increase in the cost of processing, and a decrease in the service life of the seals of the replaceable bottoms of the working chamber. The thermal-impulse method differs from the thermochemical method in that thermophysical processes are dominant. At the same time, burrs and other technological contaminants are removed by melting, followed by controlled discharge of combustion products from the working chamber before they begin to condense on the surfaces of the workpieces. This method was developed for cleaning surfaces and edges after mechanical processing of high-precision parts of aircraft assemblies and instruments, which are characterized by high accuracy and the presence of microparticles [14], the use of high-strength materials, a complex configuration of internal and external surfaces, minimal weight and other features. Figure 2 shows a typical view of a part of an aircraft unit after thermal pulse treatment. The advantages of the method include flexibility, high productivity, a combination of cleaning and finishing operations on surfaces and edges, the ability to process complexly shaped high-precision parts, including parts of fuel equipment and parts of clockwork (Fig. 3).

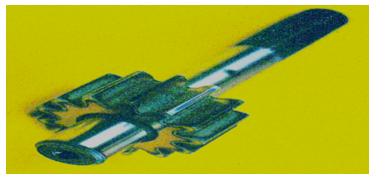


Fig. 2. Gear appearance after thermal-impulse treatment.

A feature of the thermal pulse method is removing contaminating particles and burrs of a given thickness by adjusting two technological parameters - heat flux density and heating time [15]. It makes it possible to eliminate damage to structural elements of parts by self-regulation of the reflow process.

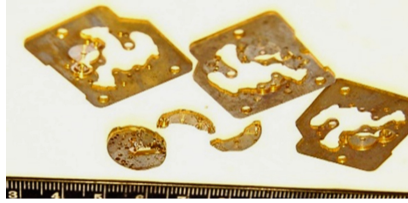


Fig. 3. Details of watch mechanisms after thermal-impulse treatment.

3 Research Methodology

Thermal-impulse treatment of parts of hydraulic and fuel systems makes it possible to reliably clean from primary technological contaminants, including the quickly wearing part of microroughness, which significantly increases the reliability and durability of aircraft hydro-fuel units in operation. The technological subsystem of thermal-impulse treatment includes processes of various nature that occur in the processed parts and equipment. Each of these processes is influenced to one degree or another by many circumstances, which are given in Table 1. When forming the optimal processing conditions for specific parts, it is necessary to solve a contradictory task – to melt liquid and removable parts and avoid negative consequences from exposure to high-temperature and aggressive gas combustion products. Such conditions can be met by coordinating the characteristics of the heating source and the part with the subsequent organization of the process of local removal of liquids. The thermal-impulse method allows avoiding or minimizing the negative consequences of the contact of combustion products with the processed parts due to a time-dosed heat impulse. The essence of impulse technologies is to create conditions under which the energy in the impulse source is exactly as necessary to perform useful work on the part. Ideally, the energy available to the equipment and the required for the technological process should be equal. Lack of energy excludes processing, and excess – leads to the melting of larger elements or damage to the part. The established regularities of the temperature variation of the part's elements are given depending on their thickness and thermophysical properties of materials at the optimal heating time [16, 17]. Such regular dependencies are individual for all materials. They consider the thermophysical features of materials and the geometric parameters of the elements of parts. The design features of parts are determined by the functional purpose and the corresponding requirements for surfaces and edges, which inevitably lead to the need to correct the calculated dependencies (modes) for materials. The calculated modes of processing parts are the initial data for setting up equipment.

4 Results

Considering the peculiarities of aircraft production and operation of equipment, subjective factors should be excluded when developing processes for thermal-impulse treatment. Therefore, the systematization and analysis of factors carried out based on

the fundamental laws of thermal physics, thermodynamics, the results of studies of detonation combustion of gas mixtures, supplemented by the necessary conditions for solving the set technological problems, made it possible to determine scientifically substantiated conditions for thermal-impulse treatment of specific parts.

Table 1. Factors affecting ensuring optimal quality of parts and determining treatment modes.

Part	Equipment
<ul style="list-style-type: none"> - the melting temperature; - specific heat of fusion; - thermal conductivity; - heat capacity; - material density; - dimensions of the edges rounding radius; - the presence of thin-walled elements; - the presence of different wall thicknesses; - the presence of intersecting channels; - the value of roughness; - requirements for the microrelief of surfaces; -requirements for the initial roughness of the surfaces forming the edges; -requirements for the quality of edge rounding; -requirements for the accuracy and cleanliness of surfaces; - overall dimensions; - mass; - surface area 	<ul style="list-style-type: none"> - overall dimensions of the combustion chamber and volume; - chemical composition of the combustible mixture; - gas mixture combustion mode; - parameters of combustion products; - chamber loading density; - the surface area of the combustion chamber, fixtures, and parts; -the volume of fixture and parts; -accuracy of dosing components of the gas mixture; - the pressure of the combustible mixture; - the calorific value of fuel; - the speed of the combustion products exhaust system; - combustion chamber surface temperature
Determine the optimal: treatment time, source power	Provide the optimal: treatment time, source power

Optimization of technological modes in the form of temperature fields is performed by calculation using physical and mathematical models of heating liquids, heat-stressed elements, and an array of parts. The heat supplied from the energy source to the part and the removed elements are determined by the following relationship:

$$F \int_{\tau_1}^{\tau_n} \int_{q_1}^{q_n} dqd\tau = Q,$$

where F – is the area of surfaces receiving heat, q – is the density of the heat flux, τ – is the processing time, Q – is the amount of heat used to heat the burrs (parts, working chamber, fixtures [18, 19]).

It was theoretically established that the optimal processing time implements the condition of the minimum heat flux density (heat consumption) and depends only on the thermal-physical properties of the material and the thickness of the removed element. The temperature of the part’s elements depends on the magnitude of the heat flux (power of the heating source) and the heating time. In research work [1], examples of

regular changes in the temperature of various materials from the thickness of the elements are given at the optimum processing time. These regular dependencies are individual characteristics of each material and allow you to set the modes of material processing and, accordingly, the technical characteristics of the equipment. But for high-quality processing of parts, the design features of the parts should be taken into account: the presence of different wall thickness, thin-walled elements, the requirements for the dimensions of the edge radii, the requirements for the cleanliness of surfaces and microrelief, which determine the conditions for the necessary correction of the modes, as a rule, in the direction of tightening in time and accuracy. To provide the required heat flux density and the optimal processing time, it is necessary to consider the total surface area in contact with the combustion products. The process of thermal-impulse treatment always occurs with excess thermal energy, proportional to the area of the surfaces that receive heat. Therefore, to discharge excess energy, the equipment for thermal-impulse treatment is equipped with a system for releasing combustion products with adjustable speed. Figure 4 shows a typical oscillogram of the thermal impulse treatment process, where the processes of combustion and discharge of exhaust gases are recorded in time and the temperature change of the prototype.

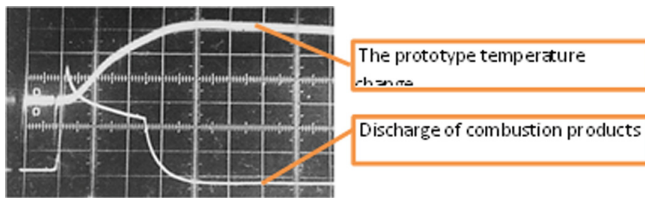


Fig. 4. The typical oscillogram of a thermal-impulse process.

Table 2 shows the thermophysical properties of pure metals used as bases for obtaining the corresponding groups of structural alloys and the relative energy consumption of their melting when removing burrs of the same volume. The energy costs for melting pure materials are threshold or maximum for alloys based on these metals. For example, the energy consumption of melting iron burrs and alloyed alloy based on it is given. These data make it possible to preliminarily estimate the level of energy costs for processing parts made of alloys of these metals and greatly simplify the experimental determination of the parameters of deburring on massive parts of low accuracy. But with a relatively similar energy consumption of the processes of reflowing burrs from different materials, the heat source characteristics can be radically different due to the thermophysical properties of the processed materials and the design features of parts. For example, the heat consumption for reflowing burrs of the same size for copper and titanium is practically equal, and the thermal conductivity coefficients of these materials differ by 20 times. Figure 5 shows the typical principle of operation of a pulsed heat source and the change in the temperature field of a copper burr over time. Figure 6 shows the difference in the temperature field with time for a titanium burr of the same size as a copper one. The time at which a titanium burr can

melt through its entire thickness is more than ten times slower than a copper one. For equipment that implements these technologies, the following conditions must be met - on the one hand, ensure the duration of the pulse sources, and on the other, the speed of the discharge of excess thermal energy (waste combustion products). If the removed element of the part has not warmed up and, accordingly, has not melted over the entire thickness, then removal will not occur. But if the time of intensive (impulse) heating is longer than the optimal one, then the part's elements of greater thickness will melt or be damaged, which, given the design features of the parts and the requirements for the reliability of aircraft units, is unacceptable. The use of an impulse heating source for reflowing the removable elements of the parts makes it possible to expand the scope of application of detonating gas mixtures both in terms of the nomenclature of parts and materials and in technological processes.

Table 2. Comparison of heat consumption for melting the most used bases for alloys.

Material	The melting temperature, T_m (°C)	Thickness, ρ (kg·dm ⁻²)	Thermal conductivity, λ (mean) (W·(m·deg) ⁻²)	Energy intensity, C (kJ·(kg·deg) ⁻²)	Relative heat consumption Q^*
Magnesium	650	1.70	131	1.060	1.00
Zinc	420	7.13	106	0.384	1.07
Aluminum	660	2.70	202	0.880	1.47
Titanium	1680	4.50	18	0.601	3.15
Copper	1083	8.96	366	0.451	3.18
Steel X18H10T	1425	7.9	(16.4)* 22	0.508 mean	3.8
Iron	1535	7.87	(76)* 33	0.427	4.10
Nickel	1453	8.90	74.5	0.450	4.73
Chromium	1900	7.19	75.7	0.482	4.80

* (16.4) (76) – thermal conductivity at 20 °C

When choosing the modes of thermal pulse processing, a contradictory task is solved - the melting of the removed element and preserving the part in its original state. To remove a burr or an element of a part of a given size and to heat the part to a minimum, it is necessary to know the time of their heating reflow. In works [15, 16], regular changes in the temperature of the part's elements are established depending on their thickness [17] and the thermophysical properties of materials at the optimal heating time. Such dependencies are calculated and built for each material individually. To determine the processing modes of specific parts, the condition is necessary but not sufficient. It is especially correct for parts of aerospace engineering units. Increased requirements for industrial cleanliness, reliability, the accuracy of parts, their minimum weight, and a complex configuration of external and internal surfaces of body parts obliges us to look for technological ways to improve the quality of products that exclude subjective factors. The thermophysical properties of materials and the size of liquids determine the energy consumption of the process of their reflow but do not guarantee a high quality of processing of surfaces and edges of parts.

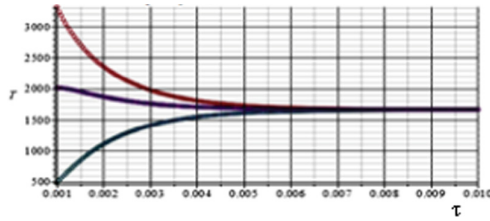


Fig. 5. Impulse heating of titanium burr.

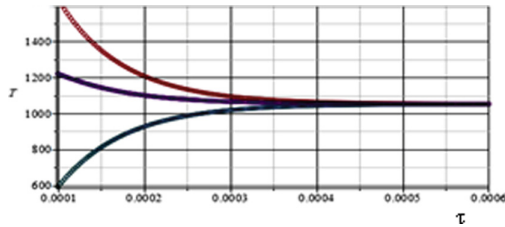


Fig. 6. Impulse heating of copper burr.

The need to create a high heat flux density in a pulsed mode uses a combustible mixture with a significant excess of thermal energy (proportional to the total surface area in contact with the combustion products). The impulse heat supply is 10–30% of the total amount of heat energy [16]. The next group of factors that characterize a part is requirements for accuracy, surface cleanliness, wall thickness, surface area and weight, requirements for rounding of sharp edges. This group of parameters tightens the range of process parameters, both in time and in the power of the heat source. Requirements for surface cleanliness limit the time of contact of combustion products with workpieces by cooling down to the condensation temperature of oxides. So, the accuracy of parts determines the requirements for the conditions of their fixation in the device, the requirements for the cleanliness of the surfaces - the conditions for the release of combustion products. The presence of thin-walled elements and mating elements of different thicknesses lead to clarification of the requirements for the accuracy of the controlled parameters of the equipment, the value of the pressure of the combustible mixture. In the presence of channels, including intersecting ones, it is necessary to consider the intensity of the heat supply by the pulsed source. When choosing modes, it is essential to consider the presence of thin partitions and walls in parts. This circumstance is especially important if the part's material has a high thermal conductivity. For parts made from aluminum and copper alloys, incorrectly selected modes can lead to so-called spall damage. If the factors characterizing the part dictate the processing modes, then the factors related to the heat sources determine the technological capabilities of the equipment. Processing of parts with a given quality is possible if the characteristics of the equipment match the conditions of the technological process. The composition of the combustible mixture, the metering accuracy, its parameters, the free volume of the working chamber, the combustion mode of the mixture, the surface area of the chamber, and the device, the degree of chamber loading determine the

composition amount of thermal energy. The chemical composition of the combustible mixture, the dimensions of the chamber, and the speed of the combustion products exhaust system are determined by controlling the time parameter [20]. As noted earlier, in the conditions of manufacturing aircraft units, it is advisable to use an impulse source of thermal energy, which corresponds to the period of damping of shock waves in the working chamber. It is known that the rate of detonation in gases is constant and depends on the chemical composition of the combustible mixture, and the decay period of subsequent shock waves depends on the size of the working chamber. To ensure the required heat flux density, the pressure of the combustible gas mixture is regulated. The strength of the equipment design limits the maximum pressures of the combustible mixture. Therefore, the degree of loading of the chamber volume, the area of heat-removing surfaces, the accuracy of their determination, and the accuracy of dosing the combustible mixture are important parameters affecting processing quality. The processing time is controlled by both the chemical composition of the combustible mixture and the dimensions of the working chamber. The speed of the combustion products exhaust system provides a mode of thermal effect on the part: impulse, mixed, or with a predominance of a constant power heat source. The mode of the exhaust of combustion products has a significant effect on the contamination of surfaces with oxides that condense from the gaseous environment. Table 2 shows the thermophysical properties of metals, which make it possible to demonstrate the need for two adjustable parameters in thermal-impulse treatment. The thermal-impulse method allows you to adjust the duration of the heat impulse, which makes it possible to limit the maximum thickness of the removed liquids without changing the initial state of the part. This expanded the field of application of detonating gas mixtures, both in terms of the nomenclature of parts and the number of technological processes implemented. Figure 7 shows a fragment of a body part made of aluminum alloy before and after rounding the edges at the intersection of threaded holes.

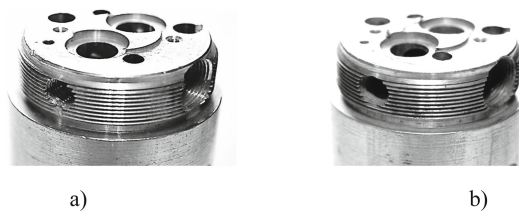


Fig. 7. Body part made of AL 9 alloy before (a) and after (b) removal of liquids and rounding of edges on threaded holes.

Using the factors characterizing the parts, it became possible to combine the operations of deburring, surface finishing, removing the quickly wearing part of the microrelief, and rounding the edges of parts made of materials with high thermal conductivity by optimizing processing modes to maintain the original quality of the material of the parts (Fig. 7). Comparative analysis of the cost of deburring from one part showed that the cost of deburring from one part by the thermal-impulse method is 2.2 times less than that of a foreign analogy.

5 Conclusions

The thermal-impulse method of cleaning parts from technological contaminants in the form of particles, burrs, and quickly wearing out part of the microrelief allows you to flexibly automate these operations when obtaining a close to the absolute degree of cleaning surfaces and edges from the listed liquids. The use of the impulse mode when treating parts in an environment of detonating gas mixtures has significantly improved the quality of cleaning the surfaces and edges of high-precision parts at all manufacturing stages, including finishing. Regulation of the processing time and power of the heat source makes it possible to increase the accuracy of dosing the energy used in technological processes, which ensures the minimum possible heating of parts. Detonating gas technologies are the most attractive because of their versatility and flexibility to parts with complex configurations of internal and external surfaces.

Acknowledgment. This research was partially supported by International Association for Technological Development and Innovations.






1. References

1. Niknam, S., Davoodi, B., Davim, J.P., Songmene, V.: Mechanical deburring and edge-finishing processes for aluminum parts—a review. *Int. J. Adv. Manuf. Technol.* **95**(1–4), 1101–25 (2018)
2. ALP De San Román, Chaves-Jacob, J., Linares, J.M., Arrazola, P.J.: Analytical-method for polishing-surface prediction considering tool flexibility and grain-material interaction. *J. Mater. Process. Technol.*, 117208 (2021)
3. Balázs, B.Z., Takács, M.: Experimental investigation and optimisation of the micro milling process of hardened hot-work tool steel. *Int. J. Adv. Manuf. Technol.* **106**(11–12), 5289–5305 (2020). <https://doi.org/10.1007/s00170-020-04991-x>
4. Chen, L., Deng, D., Pi, G., Huang, X., Zhou, W.: Burr formation and surface roughness characteristics in micro-milling of microchannels. *Int. J. Adv. Manuf. Technol.* **111**(5–6), 1277–1290 (2020). <https://doi.org/10.1007/s00170-020-06170-4>
5. Chen, W., Teng, X., Zheng, L., Xie, W., Huo, D.: Burr reduction mechanism in vibration-assisted micro milling. *Manuf. Lett.* **16**(2018), 6–9 (2018)
6. Chen, Y., Wang, T., Zhang, A.G.: Research on parameter optimization of micro-milling al7075 based on edge-size-effect. *Micromachines* **11**(2), 1–15 (2020)
7. Hanson, C., Hiwase, P., Chen, X., Jahan, M.P., Ma, J., Arbuckle, G.: Experimental investigation and numerical simulation of burr formation in micro-milling of polycarbonates. *Procedia Manuf.* **34**(2019), 293–304 (2019)
8. Khan, K., Varghese, A., Dixit, P., Joshi, S.S.: Effect of tool path complexity on top burrs in micromilling. *Procedia Manuf.* **34**(2019), 432–439 (2019)
9. Hajiahmadi, S.: Burr size investigation in micro milling of stainless steel 316L. *Int. J. Lightweight Mater. Manufacture* **2**(4), 296–304 (2019)
10. Ivanov, V., Vashchenko, S., Rong, Y.: Information support of the computer-aided fixture design system. In: *CEUR Workshop Proceedings*, vol. 1614, pp. 73–86 (2016)
11. Akimov, O.V., et al.: Computer engineering and design of cast parts for internal combustion engine crankcase. *J. Eng. Sci.* **6**(2), E24–E30 (2019). [https://doi.org/10.21272/jes.2019.6\(2\).e4](https://doi.org/10.21272/jes.2019.6(2).e4)

12. Kiran, A.V.N.S., Ramanjaneyulu, B., Lokanath, M., Nagendra, S., Balachander, G.E.: Control of exhaust emissions using piston coating on two-stroke SI engines with gasoline blends. *J. Eng. Sci.* **8**(1), H16–H20 (2021). [https://doi.org/10.21272/jes.2021.8\(1\).h3](https://doi.org/10.21272/jes.2021.8(1).h3)
13. Aurich, J.C., Dornfeld, D., Arrazola, P.J., Franke, V., Leitz, L., Min, S.: Burrs-Analysis, control and removal. *CIRP Ann. Manuf. Technol.* **58**, 519–542 (2009)
14. Rui, Z., Zi, Z., Minghui, H.: The art of laser ablation in aeroengine: the crown jewel of modern industry. *J. Appl. Phys.* **127**, 080902 (2020). <https://doi.org/10.1063/1.5134813>
15. Kumar, M., Bajpai, V.: Experimental investigation of top burr formation in high-speed micro-milling of Ti6Al4V alloy. *Proc. Inst. Mech. Eng. Part B: J. Eng. Manuf.* **234**(4), 730–738 (2019)
16. Loseva, O., Losev, A., Majorova, E.: Development of physical and mathematical models of impulse-periodic processes of heating the elements of the part. In: *Proceedings International Scientific and Practical Conference Public communication in science: philosophical, cultural, political, economic and IT context. Collection of scientific papers «ΛΟΓΟΣ»*, vol. 2, pp. 97–104. European Scientific Platform, Houston, USA (2020)
17. Jin, S.Y., Pramanik, A., Basak, A.K., Prakash, C., Shankar, S., Debnath, S.: Burr formation and its treatments—a review. *Int. J. Adv. Manuf. Technol.* **107**(5–6), 2189–2210 (2020). <https://doi.org/10.1007/s00170-020-05203-2>
18. Ivanov, V., Pavlenko, I., Liaposhchenko, O., Gusak, O., Pavlenko, V.: Determination of contact points between workpiece and fixture elements as a tool for augmented reality in fixture design. *Wireless Netw.* **27**(3), 1657–1664 (2019). <https://doi.org/10.1007/s11276-019-02026-2>
19. Pavlenko, I., et al.: Parameter identification of cutting forces in crankshaft grinding using artificial neural networks. *Materials* **13**(23), 5357 (2020). <https://doi.org/10.3390/ma13235357>
20. Abele, E., Schützer, K., Güth, S., Meinhard, A.: Deburring of cross-drilled holes with ball-end cutters—modeling the tool path. *Prod. Eng. Res. Devel.* **12**(1), 25–33 (2017). <https://doi.org/10.1007/s11740-017-0781-0>



Optimization of the Composition of High-Octane Gasoline with Bio-Components

Nina Merezhko¹ , Valentyna Tkachuk² ,
Volodymyr Komakha¹ , Oleksandr Povstyanoy² ,
and Taras Karavaiev¹ 

¹ Kyiv National University of Trade and Economics,
19, Kioto Street, Kyiv 02156, Ukraine

² Lutsk National Technical University, 75, Lvivska Street, Lutsk 43018, Ukraine
v. tkachuk@lntu.edu.ua

Abstract. The production of fuels of petroleum origin that would meet the increased requirements for environmental properties is constantly growing. The composition of the composition (catalytic reforming gasoline, hydrotreated catalytic cracking, benzene refined, petroleum solvent, straight-run gasoline, bioisobutyl alcohol, methyltertbutyl ether) on the performance properties of gasoline was studied. Mathematical models of the “composition - properties” type have been developed, which made it possible to optimize the ratio of the components of the composition of high-octane gasoline and bioadditives. The purpose of the article is to optimize the composition of high-octane gasoline compositions for spark-ignition engines using bioadditives. Mathematical models of the selected type were obtained using the central composite rotatable plan (CCRP) of the experiment, with the specified values of the initial factors in the studied range of values. As a result of the conducted research, optimal compositions of high-octane gasoline of various brands using bioadditives were obtained.

Keywords: Gasoline · Biocomponents · Mathematical modeling · Octane number · Bioisobutyl alcohol · Methyltertbutyl ether · Optimal composition

1 Introduction

The production of fuels of petroleum origin that would meet the increased requirements for environmental properties is constantly growing [1, 2]. This article is based on the results of previous studies [3], where it was established that the ratio of components of the composition of high-methane gasoline that would meet the requirements of SSTU 7687:2015 to Euro-5 gasoline [4–6] in terms of octane number, sulfur content, aromatic hydrocarbons and benzene, indicators of fractional composition, the concentration of actual resins is achieved by the optimal ratio of refined products and bioadditives. The purpose of the article is to optimize the composition of high-octane gasoline compositions for spark-ignition engines using bioadditives.

2 Literature Review

World's scientists are studying mixed fuels with different ratios of components to improve their operational properties [7]. Bioethanol-based fuel mixture compositions for internal combustion engines have been developed [8]. Simultaneously, the octane number increases only due to bioethanol, which is present in such a mixture. The bioethanol content in such gasoline is up to 79.9%, and the hydrocarbon components of the oil refinery are used only in the amount of 20%.

Another well-known composition of mixed gasoline [9] contains catalytic reforming gasoline, catalytic cracking gasoline; straight-run gasoline; butanes; oxygenates; alkylate. The disadvantage of this composition is the need to use expensive alkylates, isomerizates, butanes, which, in addition, are acute deficient. So, optimization of the composition of mixed high-octane gasoline with bio-additives, scientific justification of its composition is appropriate and relevant.

In studies [10, 11], the effect of oxygenates on increasing the detonation resistance of mixed fuels with their use is proved. The use of bio-components allows to improve the operational properties of fuels and ensure high requirements for their environmental friendliness [12, 13]. I also, in [14, 15], modern trades in designing technological equipment are proposed.

Fuel supply and demand for fuel will differ over the next 50 years due to a steady reduction in fossil fuels. Harmful contaminants released into the atmosphere have greatly degraded the ecosystem, and there is a strong need to reduce or preserve these emissions under safe limits [16, 17]. Most of the study has evaluated the best alternative fuel, which increases engine performance parameters and significantly reduces emission parameters [18–20]. Finally, in [21–23], critical issues concerning the development of multi-functional energy-efficient equipment have been proposed.

3 Researches Methodology

The object of research is gasoline with different content of hydrocarbon additives and bioadditives. The subject of the study is the properties of high-octane gasoline, taking into account changes in the ratio of components of the composition.

Mathematical models of the selected type were obtained using the central composite rotatable plan (CCRP) of the experiment, with the specified values of the initial factors in the studied range of values. Mixed factors that characterize the ratio of the main fuel components were chosen as such variables, namely: x_1 – gasoline content, mass %; x_2 – bioisobutyl alcohol content, mass %; x_3 – methyltertbutyl ether content, mass %. The response functions select indicators of the properties of the obtained mixtures: y_1 – octane number; y_2 – benzene content, % vol.; y_3 – sulfur content, mg/kg; y_4 – content of aromatic hydrocarbons, % vol. To obtain an array of data and further optimize the composition of high-octane gasoline, a complete factor experiment of type 2^3 was implemented, completed to a second-order rotatable Box-Hunter plan with six experimental points in the center of the plan and a star shoulder of 1.6818, and statistical analysis of mathematical models was carried out.

The octane number according to the engine method was determined according to GOST 511:2015 Engine fuel. Motor method for determining the octane number. The sulfur content was determined according to SSTU ISO 20846:2009 “Petroleum products. Determination of the sulfur content in automobile fuel by ultraviolet fluorescence” (ISO 20846:2004, IDT). The aromatic hydrocarbons content was determined according to SSTU 7686:2015 “Gasoline. Determination of individual components by high-resolution gas chromatography on a 100-m capillary column”. The benzene content was determined according to SSTU EN12177:2009 “Petroleum products. Unleaded gasoline. Determination of benzene content by gas chromatography”. Modeling of the “composition-property” process was carried out using a 2-order model.

The significance of regression coefficients was evaluated according to the student’s criterion. Given that the experimental data corresponded to a normal distribution law hypothesis, calculations were performed with a confidence probability of 0.95. Construction of the planning matrix, calculation of coefficients of regression models, verification of their significance and adequacy, and mathematical processing of experimental data were performed using the *STAT-SENS* and *STATISTICA 10* software.

4 Results

To determine the scope of the experiment, the effect of biocomponents on the change in the octane number of the base gasoline base was established. Basic bases of A-92 are gasoline (hydrotreated catalytic cracking gasoline – 53% vol.; catalytic reforming reformat – 35% vol.; refined benzene production – 12% vol.) and A-95 (hydrotreated catalytic cracking gasoline – 50% vol.; catalytic reforming reformat – 44% vol.; petroleum solvent – 6% vol.). It was obtained by mixing the corresponding petroleum components. The effect of biocomponents on the change in the octane number of the base gasoline base was determined. To do this, bio-components were added to the base bases in the amount of 5, 7, and 10% vol. everyone. Methyltretine butyl ether (MTBE) and bioisobutanol (BIBS) were used as biocomponents. The effect of biocomponents on the octane characteristics of the main base of gasoline A-92 and gasoline A-95 was established (Table 1).

Table 1. Effect of biocomponents on detonation resistance.

Main basis of applications	Octane number of the base for A-92	Octane number of basics for the A-95
100% vol. of main basics	90	94.3
95% vol. of base + 5% vol. MTBE	91.3	95.3
93% vol. of base + 7% vol. MTBE	92.9	95.8
90% vol. of base + 10% vol. MTBE	92.7	96.4
95% vol. of base + 5% vol. BIBS	90.5	94.8
93% vol. of base + 7% vol. BIBS	91.4	95.1
90% vol. of base + 10% vol. BIBS	91.8	95.7

From the above data, it can be seen that the greatest increase in the octane number is given by the addition of MTBE in the amount of 10% for gasoline a-92 and a-95, to a lesser extent bioisobutanol. The possibility of increasing the octane number through biocomponents makes it possible to reduce the content of components with a high proportion of aromatic carbohydrates, particularly catalytic cracking gasoline and catalytic reforming reformat, partially replace them with low-octane straight-run gasoline. Studies of the effect of bioadditives allowed us to establish the scope of the experiment.

According to the central composite rotatable plan of the experiment, 7 model compositions were developed, illustrated with examples of the ratio of components in Tables 2 and 3. To quantify the number of given factors, modeling of the compositions of experimental compositions was carried out taking into account that the factor x_1 (gasoline content) corresponds to the total content of gasoline catalytic reforming, catalytic cracking, and straight – run-in the ratio of 55:35:10, respectively, and the total content of components was adjusted to 100% using refined benzene production and petroleum solvent in the ratio of 55:45. To obtain mathematical dependencies of the form $y = f(x_i)$ for $i = 3$, the zero level of the selected factors and their variation interval are set. In this case, the center of the plan is located at a point with coordinates x_1, x_2, x_3 , respectively 72, 4, 8 and intervals of variation – 6, 2, 2 the results of the experiment on the central composite rotatable plan, taking into account the center of the plan and intervals of variation, are shown in Table 3.

Table 2. Compositions of experimental compositions of gasoline using bioadditives.

Component	Component content, mass % in the experimental composition						
	1	2	3	4	5	6	7
Catalytic reforming gasoline	36.3	42.9	36.3	42.9	36.3	42.9	36.3
Catalytic cracking gasoline	23.1	27.3	23.1	27.3	23.1	27.3	23.1
Straight-run gasoline	6.6	7.8	6.6	7.8	6.6	7.8	6.6
Bioisobutyl alcohol	2	2	6	6	2	2	6
Methyltert-butyl ether	6	6	6	6	10	10	10
Refined benzene production	14.3	7.7	12.1	5.5	12.1	5.5	9.9
Petroleum solvent	11.7	6.3	9.9	4.5	9.9	4.5	8.1

The results of computer calculations of the significance of the coefficients of the obtained regression equations with the gradual exclusion of insignificant components of the model made it possible to obtain mathematical models \hat{y}_1 – \hat{y}_4 :

$$\hat{y}_1 = 95.148 + 1.5956x_1 + 0.88267x_2 + 1.9777x_3 + 0.5375x_1x_2 + 0.5375x_1x_3 + 0.5375x_2x_3 + 0.03226x_2^2$$

$$\hat{y}_2 = 0.45867 + 0.03528x_1$$

$$\hat{y}_3 = 5.2729 + 1.9797x_1 - 0.13859x_1^2$$

$$\hat{y}_4 = 33.6 + 2.009x_1,$$

where \hat{y}_i – predicted values of the output variable using the j -th model.

Table 3. Compositions of experimental compositions of gasoline using bioadditives.

Component	Component content, mass % in the experimental composition								
	8	9	10	11	12	13	14	15	
Catalytic reforming gasoline	42.9	45.2	34.1	39.6	39.6	39.6	39.6	39.6	
Catalytic cracking gasoline	27.3	28.8	21.7	25.2	25.2	25.2	25.2	25.2	
Straight-run gasoline	7.8	8.2	6.2	7.2	7.2	7.2	7.2	7.2	
Bioisobutyl alcohol	6	4	4	7.35	0.7	4	4	4	
Methyltretbutyl ether	10	8	8	8	8	11.4	4.65	8	
Refined benzene production	3.3	3.3	14.4	6.95	10.7	6.9	10.7	8.8	
Petroleum solvent	2.7	2.65	11.8	5.7	8.7	5.7	8.7	7.2	

Figure 1 presents graphical reviews of the studied parameters for factors x_1 (gasoline content) and x_2 (bioisobutyl alcohol content) in the range of ± 2 encoded units with a fixed value of x_3 at the level of 0. From Fig. 2b–2d, it can be concluded that the content of benzene, sulfur, and aromatic hydrocarbons correlates exclusively with the content of gasoline in the studied mixtures since the additives used (bioisobutyl alcohol and methyltretbutyl ether) do not contain these compounds in their composition. At the same time, the influence of factors on the detonation resistance index (octane number) demonstrates a rather complex interaction with each other. Figure 1a shows that an increase in the content of bioisobutyl alcohol in the studied composition effectively increases the detonation resistance of fuel in the range from 93 to 96.

For a comprehensive study of the interaction of the studied factors on the detonation resistance indicator, diagrams of graphical responses of factors x_2 – x_3 are constructed at fixed values of factor x_1 with fixation at the levels of $-1, 0, +1$ (Fig. 2).

When determining the optimal content of components, it was taken into account that the content of aromatic hydrocarbons in the gasoline composition should not exceed 35 Vol.%, sulfur content – no more than 10 mg/kg, benzene content – no more than 1.0 Vol.%, and the octane number is in the ranges corresponding to the brand of gasoline: a – 92 (92–93), a-95 (95–96).

Table 4. Results of studies of gasoline quality indicators using bioadditives.

No. of composition	Experiment plan, unit code			Component content, WT. %			Property indicators			
	x_1	x_2	x_3	Gasoline	Bioisobutyl alcohol	Methyl tert-butyl ether	Octane number	Benzene content, % vol	Sulphur content, mg/kg	The content of aromatic hydrocarbons, % vol
1	-1	-1	-1	66,0	2,0	6,0	93,1	0,43	3,1	31,6
2	1	-1	-1	78,0	2,0	6,0	93,3	0,50	7,0	35,6
3	-1	1	-1	66,0	6,0	6,0	92,8	0,42	3,1	31,6
4	1	1	-1	78,0	6,0	6,0	96,3	0,49	7,0	35,6
5	-1	-1	1	66,0	2,0	10,0	94,1	0,42	3,1	31,6
6	1	-1	1	78,0	2,0	10,0	97,6	0,49	7,0	35,6
7	-1	1	1	66,0	6,0	10,0	97,1	0,42	3,1	31,6
8	1	1	1	78,0	6,0	10,0	101,6	0,49	7,0	35,6
9	1,6818	0	0	82,091	4,0	8,0	98,0	0,52	8,4	37
10	-1,6818	0	0	61,909	4,0	8,0	92,0	0,40	1,6	30,2
11	0	1,6818	0	72,0	7,4	8,0	97,4	0,46	5,2	33,6
12	0	-1,6818	0	72,0	0,6	8,0	96,0	0,46	5,2	33,6
13	0	0	1,6818	72,0	4,0	11,4	98,8	0,46	5,2	33,6
14	0	0	-1,6818	72,0	4,0	4,6	91,6	0,46	5,2	33,6
15	0	0	0	72,0	4,0	8,0	95,2	0,46	5,2	33,6

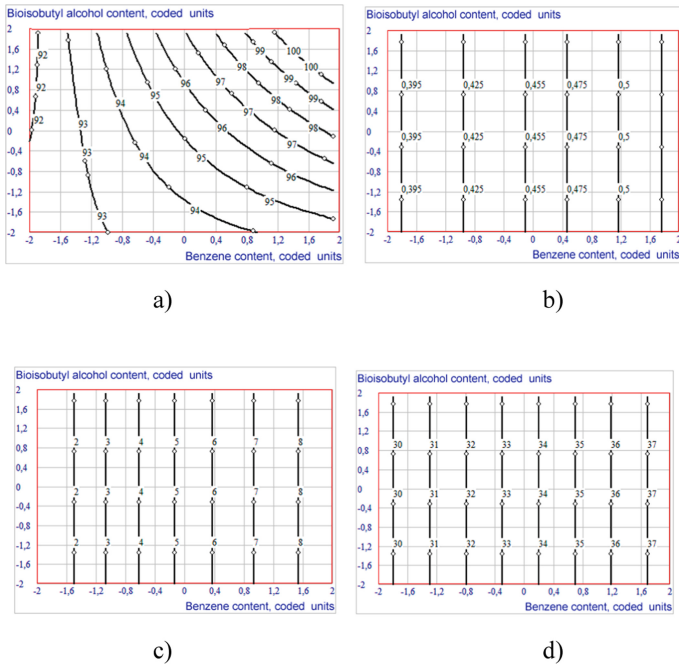


Fig. 1. Feedback diagrams for factors x_1 and x_2 at $x_3 = 0$ by parameters: a) octane number; b) benzene content, % vol.; c) sulfur content, mg/kg; d) content of aromatic hydrocarbons, % vol.

By using multi-criteria optimization of the data array based on the obtained mathematical models, the values of factors corresponding to the optimal compositions of high-octane gasoline with bioadditives are obtained in encoded units and natural values. The parameters and results of the search for the optimal composition are shown in Table 4. By stabilizing one factor at the optimal level, and the initial variables in the range of their technological values from minimum to maximum, a compromise plot can be obtained. So, if the gasoline content in the A-92 composition is stabilized at an optimal level (-1.12), then a compromise section is obtained (Fig. 3a) provides for the consumption of bioisobutyl alcohol and methyltertbutyl ether in the optimal mode. In this case, the control vector of the mixture composition is located at the point with the coordinates: $x_2 = +0.84$; $x_3 = -0.85$, which in natural terms corresponds to the consumption of these components of 5.68 mass % and 6.3 mass %, respectively. Therefore, if the gasoline content in the composition a-92 is stabilized at a certain optimal level (-1.12 code units; 65.28 mass %), then a compromise section is obtained (Fig. 3a) provides for the consumption of bioisobutyl alcohol and methyltertbutyl ether in the optimal mode. In this case, the vector of control of the composition of the mixture is located at the point with the coordinates: $x_2 = +0.84$; $x_3 = -0.85$, which in natural terms corresponds to the consumption of these components of 5.68 mass % and 6.3 mass %, respectively. Similarly, a compromise section of the composition of high-octane gasoline corresponding to the A-95 brand is determined (Fig. 3b).

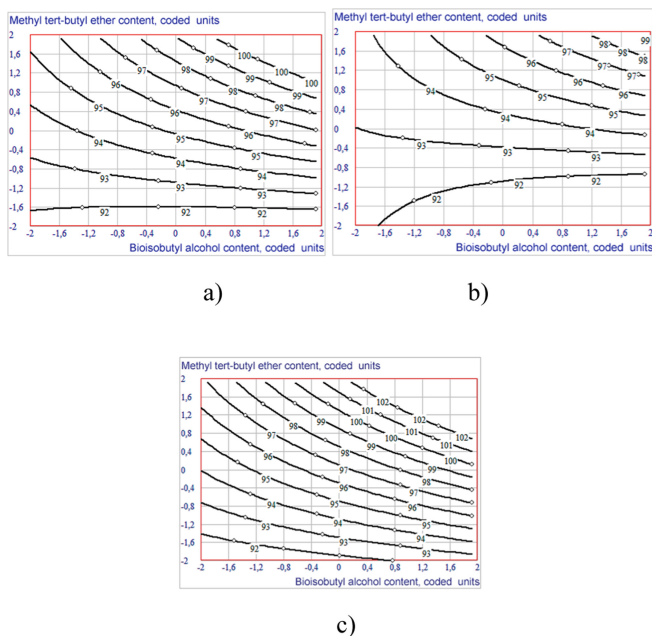


Fig. 2. Response diagrams for factors x_2 and x_3 by the octane number parameter at fixed values of factor x_1 at the level of: a) 0; b) -1; c) + 1.

Table 5. Warehouse optimization parameters and results high-octane gasoline using bioadditives.

Brand of gasoline	The desired parameter values are set				Obtained factor values					
					Coded			Natural		
	\hat{y}_1	\hat{y}_2	\hat{y}_3	\hat{y}_4	x_1	x_2	x_3	x_1 , mass %	x_2 , mass %	x_3 , mass %
A-92	92–93	0,0–1,0	0–10	30–35	-1,12	+0,84	-0,85	65,28	5,68	6,3
A-95	95–96	0,0–1,0	0–10	30–35	-0,96	+1,21	+0,81	66,24	6,42	9,62

Considering the obtained optimization results for factors $x_1 - x_3$, the following optimal compositions of high-octane gasoline for marks A-92, A-95 were determined (Table 6).

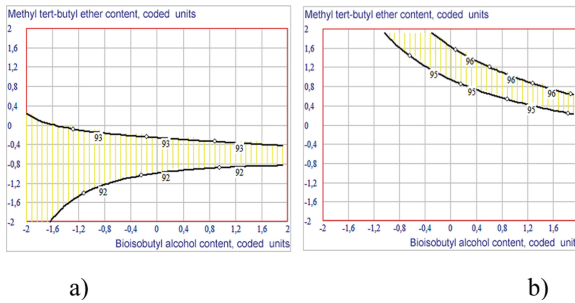


Fig. 3. Compromise area of the optimal composition of high-octane gasoline using bioadditives of the brand: a) A-92 at fixed values of x_1 at the level -1.12 ; b) A-95 at fixed values of x_1 at the level -0.96 .

Table 6. Optimal compositions of high-octane gasoline using bioadditives.

Name of component	Component content depending on the brand of high-octane gasoline, mass %	
	A-92	A-95
Catalytic reforming gasoline	35.90	36.43
Catalytic cracking gasoline	22.85	23.18
Straight-run gasoline	6.53	6.62
Bioisobutyl alcohol	5.68	6.42
Methyltertbutyl ether	6.30	9.62
Refined benzene production	12.51	9.75
Petroleum solvent	10.23	7.98
Total	100.00	100.00

5 Conclusions

As a result of the conducted research, optimal compositions of high-octane gasoline of various brands using bioadditives were obtained. The consumption of components in a mixture of high-octane gasoline with bioadditives of bioisobutyl alcohol and methyl-tertbutyl ether is: for the A-92 gasoline brand - 65.28; 5.68 and 6.3 mass %; for the brand of gasoline A-95 – 66.24; 6.42; 9.62 mass %. In addition, an optimal compromise area was established for the production of gasoline with the specified parameters with the ability to adjust the content of bioadditives in the studied compositions.






References

1. Zhang, Yu., et al.: Modeling, simulation, and optimization for producing ultra-low sulfur and high-octane number gasoline by separation and conversion of fluid catalytic cracking naphtha. *Fuel* 299, 120740 (2021)
2. Liaposhchenko, O., et al.: Modeling of technological processes for a rectification plant in second-generation bioethanol production. *Processes* 9(6), 944 (2021). <https://doi.org/10.3390/pr9060944>
3. Merezhko, N., Tkachuk, V., Rechun, O., Zahoruiko, V., Priadko, O.: Infrared spectroscopy of gasolines with addition of ethanol. In: Tonkonogyi, V. et al. (eds) *Advanced Manufacturing Processes. InterPartner 2019. Lecture Notes in Mechanical Engineering*, pp. 442–450. Springer, Cham (2020).
4. Gaidai, O.O., Zubenko, S.O., Polunkin, Ye.V., Pyliavskiy, V.S.: Ecological and operational characteristics of motor biofuel E-85. In: *Materials of the collection of articles of the III All-Ukrainian Congress of Ecologists*, pp. 308–310. Vinnutsya (2017).
5. Kiran, A.V.N.S., Ramanjaneyulu, B., Lokanath, M., Nagendra, S., Balachander, G.E.: Control of exhaust emissions using piston coating on two-stroke SI engines with gasoline blends. *Journal of Engineering Sciences* 8(1), H16–H20 (2021). [https://doi.org/10.21272/jes.2021.8\(1\).h3](https://doi.org/10.21272/jes.2021.8(1).h3)
6. Vaskina, I., Plyatsuk, L., Vaskin, R., Ablicieva, I., Sydorenko, S.: Patterns of pollutants distribution from vehicles to the roadside ecosystems. In: Ivanov, V., et al. (eds.) *DSMIE 2019. LNME*, pp. 893–902. Springer, Cham (2020). https://doi.org/10.1007/978-3-030-22365-6_89
7. Doğu, Y., Kantaroğlu, F.: Experimental investigation of effects of single and mixed alternative fuels (gasoline, CNG, LPG, acetone, naphthalene, and boron derivatives) on a commercial i-DSI engine. *Energy Sources, Part A: Recovery, Utilization, and Environmental Effects* (2020). <https://doi.org/10.1080/15567036.2020.1800864>
8. Onoichenko, S.N., Emelianov, V.E., Aleksandrova, E.V.: The use of isopropanol-based additives in the production of gasoline. *Oil Refining Petrochemistry* 2, 32–36 (2003)
9. Tsarev, A.V., Karpov, C.A.: Improving the environmental and operational characteristics of motor gasolines by introducing oxygenates. *Chem. Technol.* 8(7), 324–328 (2017)
10. Elfasakhany, A.: *Alcohols as Fuels in Spark Ignition Engines. Second Blended Generation*. Lambert Academic Publishing, Bahnhofstrabe (2017)
11. Thakur, F., Kaviti, A., Gehlot, R.: Modelling the performance and emissions of ethanol-gasoline blend on a gasoline engine using ANFIS. *Int. J. Ambient Energy* (2021). <https://doi.org/10.1080/01430750.2021.1873856>

12. Cay, Y., I. Korkmaz, A. Cicek, Kara, F.: Prediction of Engine Performance and Exhaust Emissions for Gasoline and Methanol Using Artificial Neural Network. *Energy*, 177–188 (2013)
13. Ivanov, V., Pavlenko, I., Trojanowska, J., Zuban, Y., Samokhvalov, D., Bun, P.: Using the augmented reality for training engineering students. In: 4th International Conference of the Virtual and Augmented Reality in Education, VARE 2018, pp. 57–64 (2018)
14. Bun, P., Trojanowska, J., Ivanov, V., Pavlenko, I.: The use of virtual reality training application to increase the effectiveness of workshops in the field of lean manufacturing. In: 4th International Conference of the Virtual and Augmented Reality in Education, VARE 2018, pp. 65–71 (2018)
15. Dagaut, P., Togbe, S.: Experimental and modeling study of the kinetics of oxidation of ethanol-gasoline surrogate mixtures (E85 surrogate) in a jet-stirred reactor. *Energy Fuels* **22** (5), 3499–3505 (2008)
16. Isin, O., Uzunsoy, E.: Predicting the exhaust emissions of a spark ignition engine using adaptive neuro-fuzzy inference system. *Arabian J. Sci. Eng.* **38**(12), 3485–3493 (2013). <https://doi.org/10.1007/s13369-013-0637-7>
17. Kapusuz, M., Ozcan, H., Yamin, J.A.: Research of performance on a spark ignition engine fueled by alcohol–gasoline blends using artificial neural networks. *Appl. Thermal Eng.* 525–534 (2015)
18. Kiani Deh Kiani, M., Ghobadian, B., Ommi, F., Najafi, G., Yusaf, T.: Artificial neural networks approach for the prediction of thermal balance of SI engine using ethanol-gasoline blends. In: Quirchmayr, G., Basl, J., You, I., Xu, L., Weippl, E. (eds.) CD-ARES 2012. LNCS, vol. 7465, pp. 31–43. Springer, Heidelberg (2012). https://doi.org/10.1007/978-3-642-32498-7_3
19. Akimov, O.V., et al.: Computer engineering and design of cast parts for internal combustion engine crankcase. *J. Eng. Sci.* **6**(2), E24–E30 (2019). [https://doi.org/10.21272/jes.2019.6\(2\).e4](https://doi.org/10.21272/jes.2019.6(2).e4)
20. Kiani, M.K.D., Ghobadian, B., Tavakoli, T., Nikbakht, A.M., Najafi, G.: Application of artificial neural networks for the prediction of performance and exhaust emissions in the SI engine using ethanol-gasoline blends. *Energy* **35**(1), 65–69 (2016)
21. Liaposhchenko, O., Pavlenko, I., Ivanov, V., Demianenko, M., Starynskiy, O., Kuric, I., Khukhryanskiy, O.: Improvement of parameters for the multi-functional oil-gas separator of ‘heater-treater’ type. In: 2019 IEEE 6th International Conference on Industrial Engineering and Applications (ICIEA), Tokyo, Japan, 2019, pp. 66–71 (2019). <https://doi.org/10.1109/IEA.2019.8715203>
22. Liaposhchenko, O., Pavlenko, I., Monkova, K., Demianenko, M., Starynskiy, O.: Numerical simulation of aeroelastic interaction between gas-liquid flow and deformable elements in modular separation devices. In: Ivanov, V., et al. (eds.) DSMIE 2019. LNME, pp. 765–774. Springer, Cham (2020). https://doi.org/10.1007/978-3-030-22365-6_76
23. Radchenko, R., Kornienko, V., Pyrysunko, M., Bogdanov, M., Andreev, A.: Enhancing the efficiency of marine diesel engine by deep waste heat recovery on the base of its simulation along the route line. In: Nechyporuk, M., Pavlikov, V., Kritskiy, D. (eds.) Integrated Computer Technologies in Mechanical Engineering. AISC, vol. 1113, pp. 337–350. Springer, Cham (2020). https://doi.org/10.1007/978-3-030-37618-5_29



Experimental Investigation of Gas-Liquid Layer Height in a Combined Contact Device

Viktor Moiseev¹ , Oleksandr Liaposhchenko² ,
Michal Hatala³ , Eugenia Manoilo¹ ,
and Oleg Khukhryanskiy^{2,4} 

¹ National Technical University “Kharkiv Polytechnic Institute”,
2, Kyrpychova Street, Kharkiv 61002, Ukraine
o.liaposhchenko@pohnp.sumdu.edu.ua

² Sumy State University, 2, Rymaskogo-Korsakova Street, Sumy 40007, Ukraine

³ Technical University of Kosice, 9, Letna Street, Kosice 04200,
Slovak Republic

⁴ UzLITI Engineering, 129 B, Amir Temur Avenue, Tashkent 100099,
Republic of Uzbekistan

Abstract. In the article are considered some hydrodynamic performances of a combined contact device. The experimental laboratory installation for studying hydrodynamics is shown in the article. The experiment conditions and the specificity of the installation of contact blocks inside the column are described. It was specified that a more homogeneous gas-liquid structure is obtained using a stabilizer, which is highly structured and turbulized. When installing two stabilizers, there is a significant reduction in the spray zone since the presence of a stabilizer due to its design and the input effects that are created in it at the end of each lamella distributes the captured spray over the entire geometric surface, thereby creating an additional mass transfer surface. The second stabilizer acts as a splash trap and holds back the foam layer. It was found that the best parameters of stabilizers for specified conditions. Determination of the factors that influence the height of the gas-liquid layer in a combined contact device has shown that the most characteristic parameters affecting the height of the gas-liquid layer are the gas velocity, the diameter of the plate holes, and the free cross-section of the device. As a result of the research and statistical data processing, an equation was obtained for determining the height of the gas-liquid layer in a combined contact device using small-hole and large-hole plates. Realization of the stabilization method of the gas-liquid layer extends the scope of foaming devices and opens up possibilities for intensifying technological processes.

Keywords: Hydrodynamics · Stabilization · Foam layer · Plate · Turbulization

1 Introduction

The mass transfer processes and the technological equipment are commonly used in various industries [1, 2] to multiphase flows purifying from impurities dangerous to the environment, increasing the target components concentration in solutions, and

separating gas-liquid mixtures into different fractions [3–5], associated with it the rapid technological development of multicomponent streams purification and separation. One of the main directions in designing intensive hydrodynamic modes of liquid and gas-phase motion [6, 7]. The intensity rising methods of the above processes can be both constructive using structured multi-profile packing in various combinations of their arrangement in the equipment. The technological methods are the phase motion speed, pressure, temperature increasing, the correlation of the operating parameters, the stable foam layers formation [8].

2 Literature Review

In the papers [9–12], the column apparatus efficiency increasing ways and methods are investigated and analyzed. At the same time, most articles paid attention to local flow parameters determining during the gas mixture absorption in packed columns, the liquid distribution over the packing surface [6, 7], the heat and mass transfer coefficients determination for phases [13–15]. The influence of the technological parameters, mixtures flow rates, flows temperature and pressure, components physical properties, flow non-uniformity, and constructive ones, such as packing type, packing inclination angle, perforation, the packing material microstructure, on the separation efficiency is investigated in some works as [16–22]. In [7, 12, 14, 18] research, the structured packing type and non-structured packing [6] were considered. The heat and mass transfer processes mathematical models, which make it possible to optimize packed column design, the separation components degree, and the mass transfer characteristics for each of the phases, are being developed [23–26].

One of the promising ways to intensify mass transfer is foam layer creation, which can significantly increase gas-liquid interaction. Much less attention has been paid to this phenomenon due to the complexity of the foaming layer structure. However, in [27], the effect of the inlet fluid velocity and the hydrophobic of dispersed particles on the stable foam layer height was considered, and in [28], the use of foam layer stabilizers was substantiated and confirmed. So, the industrial realization of the stabilization method of the gas-liquid layer greatly extends the scope of foaming devices and opens up new possibilities for intensifying technological processes with the simultaneous creation of low-waste technologies [28].

3 Research Methodology

The choices of methods for studying hydrodynamics and the choice of gas-liquid systems associated with experimental methods are essential since they largely depend on the successful solution of research problems. For hydraulic tests, the specified conditions are well-met by the gas-liquid “air-water” system, which explains the frequency of its use in studies of packed beds, nozzles, and poppet contact devices. Since this system can provide solutions to problems related to studying hydrodynamic characteristics of the combined vehicle under study, it was chosen as a working system. In this study, no additional reagents were introduced into the water, and, accordingly,

the surface tension and viscosity of the liquid phase were not changed. A schematic drawing of the experimental stand for studying hydrodynamics is shown in Fig. 1.

The combined laboratory apparatus is made by connecting three elements with an internal diameter of 240 mm. The experimental installation consists of the following main elements: a vertical column apparatus, a fan with a gas duct, a water supply system, a water distribution system, and a catchment system.

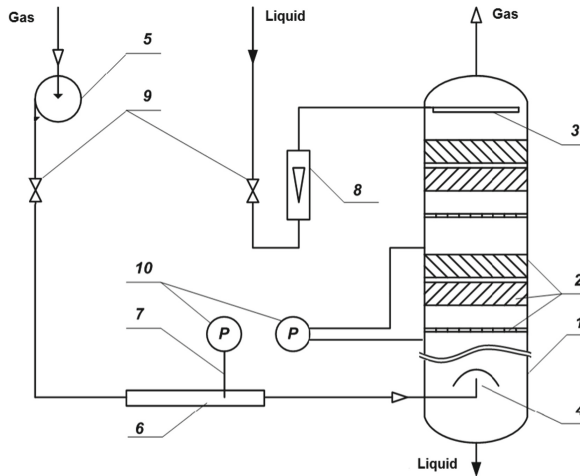


Fig. 1. Diagram of a laboratory installation for studying the hydraulic resistance of a combined contact device: 1 - column; 2 - block of a combined contact device; 3 - liquid distributor; 4 - gas distributor; 5 - gas blower; 6 - measuring tube; 7 - tube Pitot; 8 - rotameter; 9 - valves; 10 - differential pressure gauges.

The combined contact block is installed in the middle of the working section of the column, in the upper section of the column, there is a separator and a water distribution system, and the lower section is designed to enter the airflow through the hole for air supply and water collection located in it.

In the column, the countercurrent movement of phases is organized. Air from the gas fan is fed through the flue to the lower part of the device. Then it passes through the grid distributor, as a result of which a uniform speed profile is achieved at the entrance to the contact block. At the same time, the liquid phase from the pressure vessel is fed into the column for irrigation.

For a uniform initial distribution of the liquid phase over the cross-section of the apparatus, a distributor is installed on top. During passing through the device, the liquid is distributed over the surface of the contact devices, and the gas phase occupies the entire free volume of the device. Then the liquid enters the storage tank, and the gas is released into the atmosphere. Three combined contact blocks were installed in the column. The middle block was an operating element. When studying the combined contact block, the foam height and the hydraulic resistance of the contact block were measured. To measure pressure drops, selectors were used, which were placed inside

the column and connected to the differential micro manometer using hoses through fittings provided in the column for this purpose.

For determining the differential pressure above and below the block, pressure sensors were installed, which are tubes Pitot that allow recording the change in the dynamic influence of the ascending gas flow depending on its expenditure, liquid phase expenditure, and geometry contact device elements. The pressure sensors are connected to a differential pressure gauge, from which the differential pressure in the contact block layer is measured.

First of all, experimental studies of the hydraulic resistance of a dry contact block were carried out. The working medium in the experiments was air. Tests were carried out for several modifications of combined contact blocks, which differed from each other by the presence of one or two (contact elements) stabilizers installed at a distance from the failure plate and the distance between the stabilizers.

The hydraulic resistance of a dry combined contact device was determined as a function of air velocity. The hydraulic resistance was determined depending on the gas velocity and the liquid load for various modifications of the contact blocks.

Hydraulic resistance is one of the essential characteristics of apparatuses for carrying out gas purification and heat and mass transfer processes, making it possible to evaluate their effectiveness. All experiments to determine the height of the bubbling layer were accompanied by the measurement of hydraulic resistance.

Experimental detection of hydraulic resistance of combo unit was to the following: one or two packages stabilizers fit in a column over failure plate (second layer with rotation 90° to the first concerning the axis of the column, and with remote a gap against to the first one) then at various gas speeds, which modified using valves was purged air from gas blowers. The air velocity was calculated according to the readings of the micro manometer connected to the Pitot tube, and the corresponding hydraulic resistance of the dry device was recorded a micro manometer connected to the following devices: before and after the contact device with gas samplers.

For measuring the hydraulic resistance of the irrigated device, water was pumped into the column by a pump. The flow rate was regulated by a valve installed according to the rotameter readings. Water was distributed over the column's cross-section by a sprinkler. Then the air supply was turned on, and the hydraulic resistance of the irrigated area was reduced. The contact device was measured similarly to the hydraulic resistance of a dry contact device.

The choice of gas velocities was determined by the gas blower performance and the limits of the (operating) stable mode. First, the measurements were carried out from the lowest possible speed (limited by the micro manometer) to the maximum possible speed and then reverse again to the minimum speed. The gas velocity factor in columns equipped with bubble bed stabilizers for the air-water system is within the limits of $1,5 - 5 \text{ kg}^{0.5}/(\text{sm}^{0.5})$.

4 Results

Its mathematical model completely determines the hydrodynamics of the process. The form of the fundamental equations follows from the structure of liquid and gas flows in the contact device. When conduct research, hydrodynamic modes and visual observations installed the following areas gas-liquid layer the combined contact device: for the gas-liquid system without use stabilization the foam layer when working finely perforated plates gas-liquid the layer is not uniform, includes large gas bubbles, channels, bags and torches and there is rocking gas-liquid layer, leading to exposure leaf plates in some places particle gas without contact with liquid.

A more homogeneous gas-liquid structure is obtained when using a stabilizer, which is highly structured and turbulized. With the help of stabilizers, it is possible to achieve the direction of gas and liquid flows and evenly distribute them over the entire cross-sectional area of the device, level out the bypass and pumping of the gas-liquid layer, increase the height of the foam, reduce the spray zone and their number, and as a result, increase the mass transfer surface.

When installing two stabilizers, there is a significant reduction in the spray zone since the presence of a stabilizer due to its design and the input effects that are created in it at the end of each lamella distributes the captured spray over the entire geometric surface, thereby creating an additional mass transfer surface. The second stabilizer acts as a splash trap and holds back the foam layer.

To achieve the upper height of the gas-liquid layer and homogeneous foam, studies were carried out to determine the main design parameters of the combined contact device using stabilizers and a hole plate (Figs. 2, 3, 4 and 5).

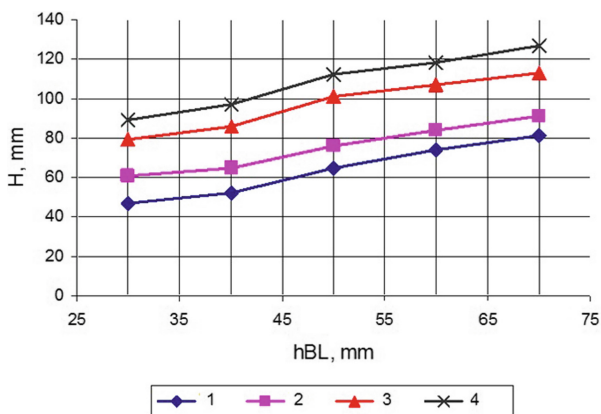


Fig. 2. Dependence of the height of the gas-liquid layer on the height of the stabilizer block (h_{BL}), mm: $S_o = 0,217 \text{ m}^2/\text{m}^2$, $d_o = 15 \text{ mm}$, $L_o = 5 \text{ m}^3/\text{m}^2 \text{ hour}$, 1 – $w_G = 2 \text{ m/s}$; 2 – $w_G = 2,5 \text{ m/s}$; 3 – $w_G = 3 \text{ m/s}$; 4 – $w_G = 3,5 \text{ m/s}$; 5 – $w_G = 4 \text{ m/s}$.

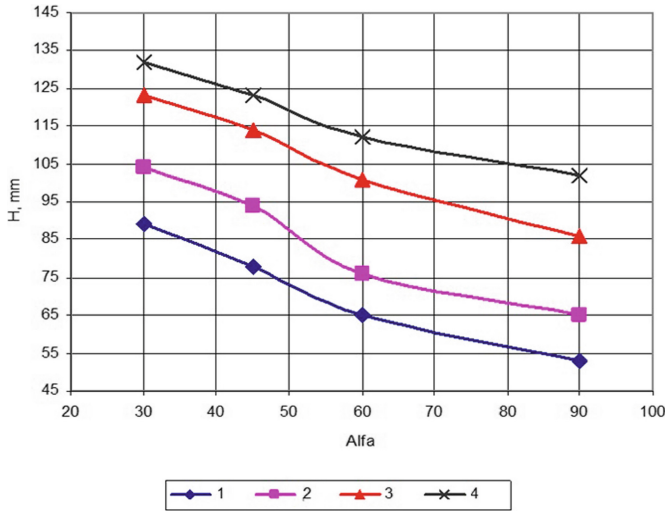


Fig. 3. Dependence of the height of the gas-liquid layer on the angle of inclination of the stabilizer corrugation (α), $S_o = 0,217 \text{ m}^2/\text{m}^2$, $d_o = 15 \text{ mm}$, $L_o = 5 \text{ m}^3/\text{m}^2 \text{ hour}$; 1 – $w_G = 2 \text{ m/s}$; 2 – $w_G = 2,5 \text{ m/s}$; 3 – $w_G = 3 \text{ m/s}$; 4 – $w_G = 4 \text{ m/s}$.

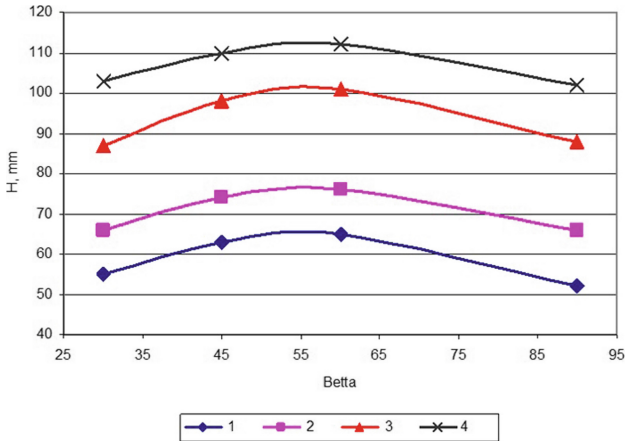


Fig. 4. Dependence of the height of the gas-liquid layer on the angle of corrugation of the block lamellae β : $S_o = 0,217 \text{ m}^2/\text{m}^2$, $d_o = 15 \text{ mm}$, $L_o = 5 \text{ m}^3/\text{m}^2 \text{ hour}$; 1 – $w_G = 2 \text{ m/s}$; 2 – $w_G = 2,5 \text{ m/s}$; 3 – $w_G = 3 \text{ m/s}$; 4 – $w_G = 4 \text{ m/s}$.

As a result of research, it was found that the best there are the following parameters of stabilizer: block height 50–60 mm, angle of inclination of the corrugation to the horizontal axis (α) 45–60°, the angle between the edges of the corrugation of the lamellae of the block (β) 45–60°, the height of the corrugation face 5–15 mm, the lamella can additionally be perforated with holes of 2–3 mm in increments of 5–10 mm, depending on the process conditions.

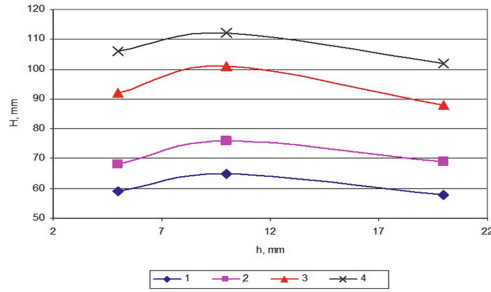


Fig. 5. Dependence of the gas-liquid layer height on the corrugation height h : $S_0 = 0,217 \text{ m}^2/\text{m}^2$, $d_o = 15 \text{ mm}$, $L_o = 5 \text{ m}^3/\text{m}^2\text{hour}$; 1 – $w_G = 2 \text{ m/s}$; 2 – $w_G = 2,5 \text{ m/s}$; 3 – $w_G = 3 \text{ m/s}$; 4 – $w_G = 4 \text{ m/s}$.

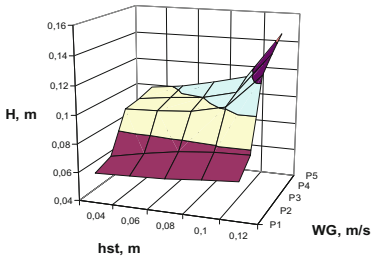


Fig. 6. Dependence of the height of the gas-liquid layer on the location of the stabilizer above the plate $S_0 = 0,137 \text{ m}^2/\text{m}^2$; $d_o = 0,012 \text{ m}$.

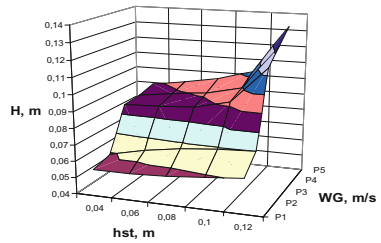


Fig. 7. Dependence of the height of the gas-liquid layer on the location of the stabilizer above the plate $S_0 = 0,217 \text{ m}^2/\text{m}^2$; $d_o = 0,015 \text{ m}$.

When studying the height of the gas-liquid layer, a pattern was found (Fig. 2). This shows that the height of the gas-liquid layer is increased with the stabilizer bar block height. When stabilization, the foam layer achieved uniform distribution the foam layer aligned concentration profiles, twists gas-liquid stream, and later significantly reduced large-scale ripple of the foam layer and decreases the passage gas without interaction with the liquid. Further increase in height and quantity stabilizers leads to a proportional increase in hydraulic resistance, and the increase in work efficiency slows down.

As the angle of inclination of the stabilizer corrugation increases (Fig. 3), the height of the gas-liquid foam layer gradually decreases. This is because there is a sharp change in the direction of movement of the gas-liquid system at right angles to the horizon and partial destruction of the swirling foam layer. When studying the corrugation angle block slats (Fig. 4) height of the foam layer H is peaked at $\beta = 45 \div 60^\circ$. The dependence of the height of the foam layer on the height of the corrugation face shows (Fig. 5) that h in which the contact device effectively operates is due to the stabilization effect of the foam layer. In this case, the side height is increased from 5 to 10 mm.

Experiments determine the effect of the height of the stabilizer position above the plate canvas on the foam layer height. Figures 6 and 7 show that installing the stabilizer

at the height of 100–120 mm above the plate surface and an increase in the gas velocity contribute to an increase in the height of the foam layer and operation at modes close to the upper limit the operating limits.

When determining the ratio between the free section of the plate S_0 and the free cross-section of the stabilizer ε , we assume that it should be $\varepsilon/S_0 > 1,5$, the stabilizer takes from 5–15% of the total free cross-section area of the device. Specified the ratio ε/S_0 is performed for all types of contact elements investigated and varies from 2,2 to 9.

The studies which determine the height of the stabilized gas-liquid foam layer for the air-water system are described by the following dependence for small-hole and large-hole plates

$$H = f(W_G, S_0, d_0, L_0)$$

where W_G is the gas velocity in the free cross-section of the device, m/s; S_0 - the free cross-section of the contact block, m^2/m^2 ; d_0 - the diameter of the hole on the plate, m; L_0 - irrigation density, m^3/m^2 hour.

As a result of the conducted research and statistical data processing, an equation was obtained for determining the height of the gas-liquid layer in a combined contact device using small-hole and large-hole plates

$$H = 1,68 W_G^{0,75} \cdot L_0^{0,25} \cdot S_0^{-1,65} \cdot d_0^{-0,14} \cdot \rho_L^{-1}$$

Deviations of the calculated values of the height of the gas-liquid layer from the experimental values do not exceed 10%.

5 Conclusions

Based on the conducted research, we choose the following design parameters of the contact block: diameter of the holes of the plate $d_0 = 0,015$ m, the height of the block stabilizer 50 mm; height side faces of the slats block 10 mm; angle bevel edge to the horizontal axis - 60–90°, the angle between the corrugation side faces is 45–60°.

The height of the foam layer is one of the main indicators of foaming, which allows asserting the development of the phase contact surface and the efficiency of the processes carried out in the foam layer.

Studies of the height of the gas-liquid layer have shown that its height depends on the gas speed in the free section. With the growth of W_G , there is also an increase in H . Moreover, an increase in the gas-liquid layer height was compared when working with a hole plate without a stabilizer and with installed stabilizers 1 and 2. The foam layer height depends on the hole diameter and the gas velocity. There is also a significant influence of the free cross-section of the contact device, which is mainly determined by the free cross-section of the hole plate. An increase in the free cross-section leads to a decrease in the observed gas-liquid layer height, which is due to a decrease in the retention capacity at low gas velocities.

So, determining the factors that influence the height of the gas-liquid layer in a combined contact device have shown that the most characteristic parameters affecting the height of the gas-liquid layer are the gas velocity, the diameter of the plate holes, and the diameter of the plate holes and the free cross-section of the device.

Realization of the stabilization method of the gas-liquid layer greatly extends the scope of foaming devices and opens up new possibilities for intensifying varied technological processes.

Acknowledgment. All the results of the research were achieved within the projects “Development and Implementation of Energy Efficient Modular Separation Devices for Oil and Gas Purification Equipment” (State reg. No. 0117U003931), and “Creation of new granular materials for nuclear fuel and catalysts in the active hydrodynamic environment” (State reg. No. 0120U102036) ordered by the Ministry of Education and Science of Ukraine. The main experimental and simulation results were obtained as a Ph.D. student Oleg Khukhryanskiy during the research internship “Hydrodynamic and heat and mass transfer characteristics of modular combined disk-packed contact sections” at the Faculty of Manufacturing Technologies of the Technical University of Kosice. This research was partially funded by International Association for Technological Development and Innovations.

References






1. Wang, S., Wu, B., Lu, Y., Zhang, K., Chen, H.: Effect of packing structure on anisotropic effective thermal conductivity of thin ceramic pebble bed. *Nucl. Eng. Technol.* **21**, 28–30 (2021)
2. Cheng, S., et al.: Investigation of flow regime in debris bed formation behavior with nonspherical particles. *Nucl. Eng. Technol.* **50**, 43–53 (2018)
3. Sklabinskyi, V., Liaposhchenko, O., Pavlenko, I., Lytvynenko, O., Demianenko, M.: Modelling of liquid’s distribution and migration in the fibrous filter layer in the process of inertial-filtering separation. In: Ivanov, V., et al. (eds.) *DSMIE 2018. LNME*, pp. 489–497. Springer, Cham (2019). https://doi.org/10.1007/978-3-319-93587-4_51
4. Liaposhchenko, O., Pavlenko, I., Ivanov, V., Demianenko, M., Starynskiy, O., Kuric, I., Khukhryanskiy, O.: Improvement of parameters for the multi-functional oil-gas separator of ‘heater-treater’ type. In: 2019 IEEE 6th International Conference on Industrial Engineering and Applications (ICIEA), Tokyo, Japan, pp. 66–71 (2019). <https://doi.org/10.1109/IEA.2019.8715203>
5. Liaposhchenko, O., Pavlenko, I., Monkova, K., Demianenko, M., Starynskiy, O.: Numerical simulation of aeroelastic interaction between gas-liquid flow and deformable elements in modular separation devices. In: Ivanov, V., et al. (eds.) *DSMIE 2019. LNME*, pp. 765–774. Springer, Cham (2020). https://doi.org/10.1007/978-3-030-22365-6_76
6. Fourati, M., Roig, V., Raynal, L.: Experimental study of liquid spreading in structured packings. *Chem. Eng. Sci.* **80**, 1–15 (2012)
7. Pavlenko, A.N., Pecherkin, N.I., Zhukov, V.E., Meski, G., Houghton, P.: Overview of methods to control the liquid distribution in distillation columns with structured packing: improving separation efficiency. *Renewable Sustainable Energy Rev.* **132**, 110092 (2020)
8. Liaposhchenko, O., Khukhryanskiy, O., Moiseev, V., Ochowiak, M., Manoilo, E.: Intensification of foam layered apparatus by foam stabilization. *J. Eng. Sci.* **5**(2), F13–F18 (2018). [https://doi.org/10.21272/jes.2018.5\(2\).f3](https://doi.org/10.21272/jes.2018.5(2).f3)

9. Zbytovský, J., Sommer, T., Zapletal, M., Trejbal, J.: Comparison of various column packing materials efficiency for hydrocarbons and aqueous mixtures. *Chem. Biochem. Eng. Q.* **33**(2), 183–190 (2019)
10. Sovilj, M., Nikolovski, B., Spasojevic, M., Mauhar, S.: Packed bed absorption column: hydrodynamics and mass transfer. *Acta Periodica Technologica* **50**, 260–269 (2019)
11. Qi, G., Wang, S.: Experimental study and rate-based modeling on combined CO₂ and SO₂ absorption using aqueous NH₃ in packed column. *Appl. Energy* **206**, 1532–1543 (2017)
12. Fu, K., Rongwong, W., Liang, Z., Na, Y., Idem, R., Tontiwachwuthikul, P.: Experimental analyses of mass transfer and heat transfer of post-combustion CO₂ absorption using hybrid solvent MEA-MeOH in an absorber. *Chem. Eng. J.* **260**, 11–19 (2015)
13. Sema, T.: Mass transfer of CO₂ absorption in hybrid MEA-methanol solvents in packed column. *Energy Procedia* **37**, 883–889 (2013)
14. Flagiello, D., Natale, F. D., Lancia, A., Erto, A.: Characterization of mass transfer coefficients and pressure drops for packed towers with Mellapak 250.X. *Chem. Eng. Res. Design* **161**, 340–356 (2020)
15. Kong, Q.J., Liu, D.Y., Wang, P., Xie, D.Q., Wu, Q., Zhao, X.Y.: Experimental study on the heat and mass transfer characteristics of a counter-flow wet cooling tower with foam ceramic packing. *Thermophys. Aeromech.* **26**(2), 267–279 (2019). <https://doi.org/10.1134/S0869864319020100>
16. Chen, R., Tian, M., Chen, S., Tian, W., Su, G.H., Qiu, S.: Three dimensional thermal hydraulic characteristic analysis of reactor core based on porous media method. *Ann. Nucl. Energy* **104**, 178–190 (2017)
17. Volf, M., Demianenko, M., Starynskiy, O., Liaposhchenko, O., Nejad, A.M.: Numerical simulation of the mass-transfer process between ammonia and water in the absorption chiller. In: Ivanov, V., Pavlenko, I., Liaposhchenko, O., Machado, J., Edl, M. (eds) *Advances in Design, Simulation and Manufacturing III. DSMIE 2020. Lecture Notes in Mechanical Engineering*, pp. 239–248. Springer, Cham (2020). doi: https://doi.org/10.1007/978-3-030-50491-5_23
18. Lu, Y.B., Tang, G.H.: Experimental investigation of fluid through porous media packed with single-diameter and multi-diameter spheres. *Transp. Porous Media* **110**, 449–459 (2015)
19. Plyatsuk, L.D., Ablicieva, I.Y., Vaskin, R.A., Yeskendirov, M., Hurets, L.L.: Mathematical modeling of gas-cleaning equipment with a highly developed phase contact surface. *J. Eng. Sci.* **5**(2), F19–F24 (2018). [https://doi.org/10.21272/jes.2018.5\(2\).f4](https://doi.org/10.21272/jes.2018.5(2).f4)
20. Kornienko, V., Radchenko, R., Konovalov, D., Andreev, A., Pyrysunko, M.: Characteristics of the rotary cup atomizer used as afterburning installation in exhaust gas boiler flue. In: Ivanov, V., Pavlenko, I., Liaposhchenko, O., Machado, J., Edl, M. (eds) *Advances in Design, Simulation and Manufacturing III. DSMIE 2020. Lecture Notes in Mechanical Engineering*, pp. 302–311. Springer, Cham (2020). https://doi.org/10.1007/978-3-030-50491-5_29
21. Plyatsuk, L., Chernysh, Y.: The removal of hydrogen sulfide in the biodesulfurization system using granulated phosphogypsum. *Eurasian Chem. Technol. J.* **18**(1), 47–54 (2016). <https://doi.org/10.18321/ectj395>
22. Liaposhchenko, O., Pavlenko, I., Demianenko, M., Starynskiy, O., Pitel, J.: The methodology of numerical simulations of separation process in SPR-separator. In: 2nd International Workshop on Computer Modeling and Intelligent Systems. CMIS 2019. *CEUR Workshop Proceedings*, vol. 2353, pp. 822–832 (2019)
23. Jacimovic, N., Genic, S., Jacimovic, B.: Sizing of packed deaeration columns. *Chem. Eng. Technol.* **42**(12), 2709–2716 (2019)
24. Ling, H., Liu, S., Wang, T., Gao, H., Liang, Z.: Characterization and correlations of CO₂ absorption performance into aqueous amine blended solution of monoethanola-mine

- (MEA) and N, N-Dimethylethanolamine (DMEA) in a packed column. *Energy Fuels* **33**(8), 7614–7625 (2019)
25. Poortalari, H., Sabet, J.K., Varaminian, F.: Separation performance investigation of packed distillation columns using simple NEQ approach based on packing multicomponent efficiencies and effective mass transfer coefficients. *Korean J. Chem. Eng.* **35**(5), 1151–1166 (2018)
 26. Rejl, F.J.: Liquid phase axial mixing in distillation column packed with structured packing: effect on column performance. *Chem. Eng. Res. Des.* **148**, 129–141 (2019)
 27. Clavier, R., Chikhi, N., Fichot, F., Quintard, M.: Modeling of inertial multi-phase flows through high permeability porous media: friction closure laws. *Multiphase Flow* **91**, 243–261 (2017)
 28. Moiseev, V., Liaposhchenko, O., Trebuna, P., Manoilo, E., Khukhryanskiy, O.: Properties of heat and mass transfer processes in the tubular grids with the heat exchanger as a stabilizer. In: Ivanov, V., et al. (eds.) *DSMIE 2019. LNME*, pp. 795–804. Springer, Cham (2020). https://doi.org/10.1007/978-3-030-22365-6_79



Rational Loading on Combined Waste Heat Recovery Cooling System

Andrii Radchenko¹ , Serhiy Forduy² , Serhiy Kantor² ,
Oleksii Zelikov¹ , and Viktor Khaldobin¹ 

¹ Admiral Makarov National University of Shipbuilding,
9, Heroes of Ukraine Ave., Mykolayiv, Ukraine
² LTD “Zavod”Ekvator”, Mykolayiv, Ukraine

Abstract. Combined cooling, heat and power (CCHP), or trigeneration, systems based on gas engines as driving engines, are among the main prosperous trends in energy-saving technologies. Addition reserves of enhancement of such integrated energy systems efficiency increase fuel efficiency of their basic gas engines by cyclic air cooling. The processing of the monitoring data on gas engine fuel efficiency has proved inefficient operation of traditional cooling all the engine room incoming air in the central conditioner fed by chilled water from absorption lithium-bromide chiller using engine exhaust heat. An advanced system of gas engine inlet air two-stage deep cooling by combined absorption-ejector chiller with absorption chiller as a high-temperature stage and ejector chiller as a low-temperature stage has been developed. The method of rational loading of the proposed engine inlet air cooling system proved annual fuel reduction by about 50 % higher than traditional cooling by absorption chillers in temperate climatic conditions.

Keywords: Combined cooling · Heat · Power · Combustion engine · Ejector · Absorption chiller

1 Introduction

The combined cooling, heat, and power (CCHP) gained widespread applications [1, 2]. Such trigeneration is considered as the main trend in energy-saving technologies [3, 4]. As driving engines in CCHP, gas engines (GE) are widely used [5, 6]. A large power augmentation is gained in gas turbines (GT) [7, 8]. The fuel efficiency of basic engines can be increased by cyclic air cooling [9, 10]. In a typical GE intake air cooling system, all the ambient air incoming engine room is cooled in a central conditioner fed by chilled water from absorption lithium-bromide chiller (ACh) using exhaust heat [11, 12]. Because of the large incoming air volume and heat influx to air in the engine room from where it is sucked into the engine turbocharger, the intake air temperature is considerably increased. It results in falling engine fuel efficiency.

In order to provide deeper engine cyclic air cooling in addition to ACh the refrigerant is to be used [13, 14]. To evaluate the cooling effect, GE fuel consumption and power output data at varying ambient air temperatures can be received by treating GE fuel efficiency monitoring [12, 15].

The study's goal is to improve the fuel efficiency of the gas engine of the CCHP plant by combined inlet air cooling in a two-stage absorption-ejector chiller utilizing exhaust heat and rationally designed to provide close to maximum annual fuel reduction.

2 Literature Review

An enhancement of fuel efficiency of combustion engines is possible by cooling cyclic air in waste heat recovery chillers [16, 17]. The ACh are the most widely used in CCHP plants and provide cooling air to about 15 °C with a high coefficient of performance (COP is 0.7 to 0.8) [18]. The refrigerant vapor-compression chillers consume electrical energy to drive compressors and provide cooling air practically to any low temperature [13]. The most simple in design refrigerant ejector chillers (ECh) can cool air to 5-10°C but with low COP of 0.2 to 0.3 [12, 13].

The efficiency of waste heat recovery cooling is especially high for the engines with the combustion of water-fuel emulsion [19, 20]. It is achieved due to the application of low temperature condensing surfaces [21, 22] providing deeper exhaust gas heat utilization that leads to additional heat converted in refrigeration. For cooling cyclic air of combustion engines, Jet technologies have a growing application [23]. They can be used for cooling scavenge air in internal combustion engines (ICE) [24, 25]. Jet cooling is especially effective in GT [26]. The high-efficiency heat exchangers should be applied to reduce cooling system sizes [28, 29].

3 Research Methodology

The efficiency of gas engine inlet air cooling was investigated for the CCHP plant of combined energy supply at the "Sandora"–"PepsiCo Ukraine" (Nikolaev, Ukraine). The CCHP plant is equipped with two cogenerative Jenbacher gas engines, JMS 420 GS-N.LC (rated electric power output $P_{eISO} = 1400$ kW, heat power $Q_h = 1500$ kW of each engine). The heat of exhaust gas, scavenge air-gas mixture, engine jacket cooling water, and lubricating oil is used for heating water to about 90 °C. The hot water is used in AR-D500L2 Century absorption Li-Br chiller to produce chilled water of 7 to 12 °C, which is spent for technological needs and feeding to the central air conditioner that provides cooling ambient air incoming the engine room, from where it is sucked into the engine turbocharger.

The cooling capacity Q_0 spending for ambient air cooling is calculated according to heat balance on coolant (chilled water from ACh):

$$Q_0 = c_w(t_{w1} - t_{w2})G_w, \quad (1)$$

where c_w – specific heat of water [kJ/(kg·K)]; t_{w1} and t_{w2} – measured temperature of water at the inlet and outlet of air cooler [°C]; G_w – water mass flow rate [kg/s].

The values of current volume fuel consumption $B_{e,v}$, m³/h, and electrical power output P_e , kW, of gas engine JMS 420 GS-N.LC was taken by treating corresponding

monitoring data on $B_{e,v}$ and P_e in dependence on the air temperature at the engine inlet t_{a2} . Specific volume fuel consumption is calculated as $b_{e,v} = B_e / P_e$, m^3 / kWh , and specific mass fuel consumption as $b_e = b_{e,v} \rho_g = \rho_g B_e / P_e$, kg / kWh , where ρ_g – density of fuel gas, kg / m^3 .

The results of monitoring data processing were used as a decrease in specific fuel consumption Δb_e due to engine intake air temperature drop Δt by 1°C , i.e., $\Delta b_e / \Delta t$.

The values of rational design cooling capacities needed for cooling air in ACh to $t_{a2} = 15^\circ\text{C}$ and in ECh to $t_{a2} = 7$ and 10°C were calculated according to the developed method [10] with taking into account current effect in fuel reduction ΔB , kg / h , due to cooling engine intake air at varying actual ambient air temperatures t_{amb} and relative humidities φ_{amb} .

The yearly varying real weather data collected in the weather datasets of the meteorological center were used by applying the “online” program “mundomanz.com”.

The current fuel-saving B , kg , for hour time duration τ , h , due to cooling engine intake air with temperature decrease Δt_a , $^\circ\text{C}$, is calculated according to correlation:

$$B = \Delta t_a \cdot \tau (\Delta b_e / \Delta t_a) \cdot P_e, \quad (2)$$

where $\Delta t_a = t_{amb} - t_{a2}$ – decrease in air temperature [$^\circ\text{C}$]; t_{amb} – ambient air temperature [$^\circ\text{C}$]; t_{a2} – air temperature at the air cooler outlet [$^\circ\text{C}$].

The annual fuel saving $\sum B$, kg , is calculated by summarizing current fuel reduction B on step by step (hour by hour) basis as $\sum B$:

$$\sum B = \sum [\Delta t_a \cdot \tau (\Delta b_e / \Delta t_a) \cdot P_e] \quad (3)$$

The annual fuel saving $\sum B$ in response to its consumption is used as a primary criterion for assessing engine intake air cooling system efficiency yearly operation.

The values of cooling capacities Q_0 spent for intake air cooling with temperature decrease Δt_a are calculated as

$$Q_0 = (c_a \xi \Delta t_a) G_a, \quad (4)$$

where: c_a – specific heat of moist air [$\text{kJ} / (\text{kg} \cdot \text{K})$]; ξ – specific heat ratio of total heat, including sensible and latent heat, to sensible heat rejected from the air during to its cooling; $\Delta t_a = t_a - t_{a2}$ – decrease in air temperature [$^\circ\text{C}$]; t_a – ambient air temperature [$^\circ\text{C}$]; t_{a2} – air temperature at the air cooler outlet [$^\circ\text{C}$]; G_a – air mass flow rate [kg / s].

A rational design cooling capacity $Q_{0,rat}$ is determined to exclude its unproductive expenses caused by overestimating (oversizing chiller) without obtaining a noticeable effect in increasing the annual fuel saving $\sum B$.

With this, the values of refrigeration capacity $Q_{0,15}$ for cooling ambient air from its current temperature t_{amb} to the temperature $t_{a2} = 15^\circ\text{C}$ and $Q_{0,10}$ for cooling ambient air $t_{a2} = 10^\circ\text{C}$ have been calculated for current site climatic conditions.

4 Results

The scheme of a typical gas engine inlet air cooling system with an absorption chiller is presented in Fig. 1.

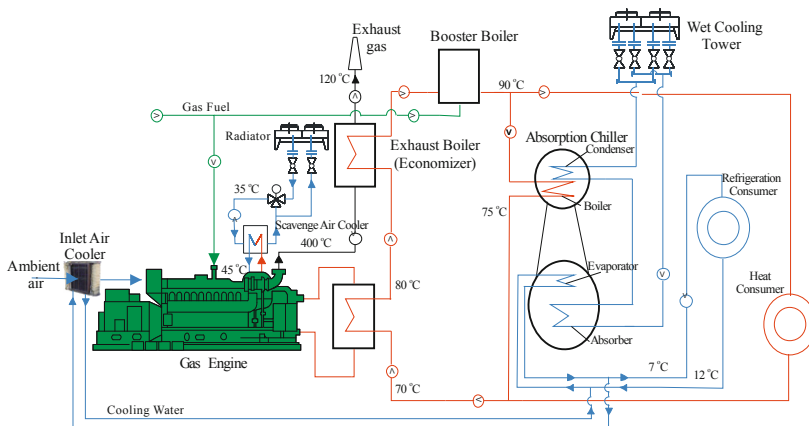


Fig. 1. The scheme of a typical gas engine inlet air cooling system with an absorption chiller.

In a typical gas engine inlet air cooling system, all the ambient air coming into the engine room is cooled in the inlet air cooler of the central conditioner fed by chilled water from the absorption chiller utilizing the exhaust heat of the engines. Because of much more increased volume of incoming ambient air (about twice higher than engine cyclic air mass flow) and heat influx to the cooled air from engine room surroundings the temperature of intake air t_{in} at the entrance of engine turbocharger suctioning it from engine room can be considerably higher than 20 or 25 °C in hot summer days. At the raised ambient air temperatures, the radiators (dry coolers) cannot cool the scavenge air to the required reliable level of its temperature at the outlet of the scavenging air cooler (of about 40 to 45 °C). It causes automatically decreasing the engine gas supply to maintain a charged gas-air mixture temperature at the inlet of engine combustion cylinders at the appropriate level.

Daily changes of specific gas consumption b_e received by treatment of monitoring data on the fuel efficiency of JMS 420 GS-N.LC is presented in Fig. 2.

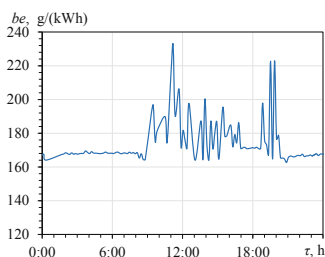


Fig. 2. Daily changes of specific gas consumption b_e of engine JMS 420 GS-N.LC.

A reduction of specific gas fuel consumption b_e is possible by addition decreasing temperature of engine cyclic air with mass flow rate G , fed to the turbocharger directly, as compared with typical cooling all the ambient air (of twice engine cyclic airflow G), coming into the engine room, to the temperature t_{in} of 20 to 25 °C and higher in hot summer days.

The scheme of the developed gas engine cyclic air cooling system with refrigerant ejector and absorption chillers is presented in Fig. 3.

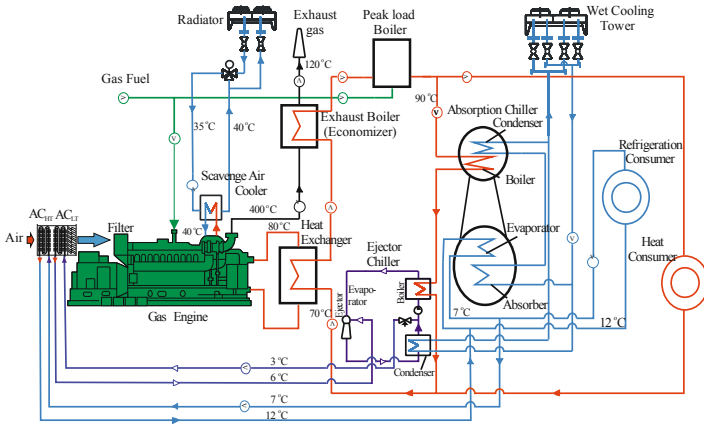


Fig. 3. The scheme of developed gas engine intake air cooling system with absorption and ejector chillers: AC_{HT} – high-temperature air cooler; AC_{LT} – low-temperature air cooler.

According to this scheme, chilled water from the absorption Li-Br chiller with a temperature of 7 °C is used as a coolant in high-temperature air cooler AC_{HT} as the first stage for cooling ambient air to 15 °C. The further subcooling air to 10 or 7 °C is conducted in low-temperature air cooler AC_{LT} by refrigerant boiling at the temperature of about 2 to 4 °C from ECh as the second stage of the combined two-stage AECh. The chilled air from a two-stage air cooler is directed through air ducting immediately to the suction of the engine turbocharger.

The values of cooling capacities $Q_{0,7,10,15}$ and heat $Q_{h,7,10,15}$ required for cooling engine inlet air to the temperatures 7, 10, and 15 °C are presented in Fig. 4 and Fig. 5.

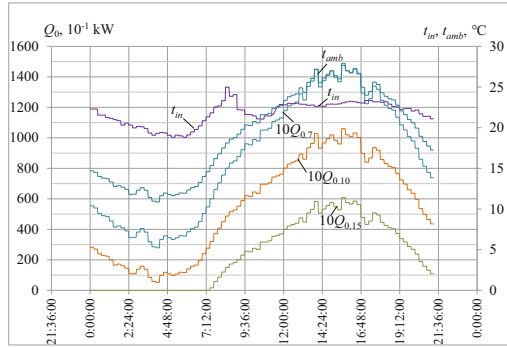


Fig. 4. Daily changes of cooling capacities $Q_{0,7,10,15}$, required for cooling engine inlet air to 7, 10, and 15 °C in the developed cooling system with varying ambient temperatures t_{amb} during time τ .

The values of available exhaust heat Q_h , the heat required $Q_{h,7,10,15}$ for cooling ambient air to $t_{a2} = 7, 10$ °C (in AECh) and 15 °C (in ACh) in developed engine intake air cooling system (in Fig. 3) and $Q_{h,ACh.in}$ in a typical existing system ($t_{a2} = t_{in}$) and corresponding remained heat $\Delta Q_{h,7,10,15}$ in developed and $\Delta Q_{h,ACh.in}$ in typical systems are presented in Fig. 5.

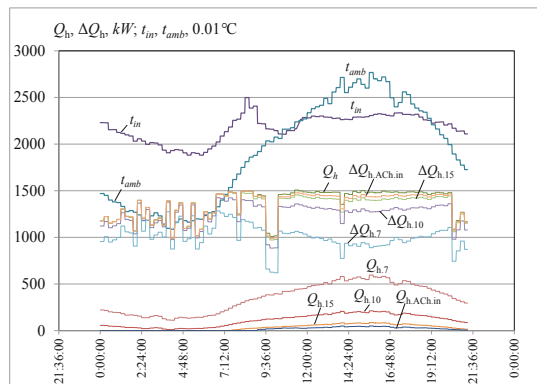


Fig. 5. Daily changes of available exhaust heat Q_h , the heat required $Q_{h,7,10,15}$ for cooling ambient air and remained heat $\Delta Q_{h,7,10,15}$ in developed engine inlet air cooling system (Fig. 3) and $\Delta Q_{h,ACh.in}$ in the typical system and the available heat Q_h .

The enhancement of gas engine fuel efficiency due to the application of developed intake air cooling system can be estimated by decreasing current specific mass fuel consumption Δb_e and summarized daily values of mass fuel reduction $\sum \Delta B_e$ due to engine inlet air cooling to the temperatures of 7, 10 and 15 °C (Fig. 6).

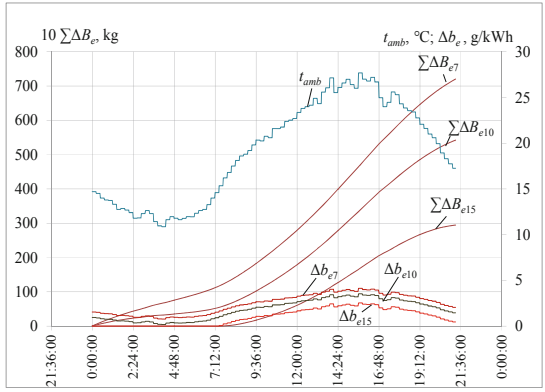


Fig. 6. Daily variation of decrease in current engine specific gas consumption Δb_e and summarized daily values of mass fuel reduction $\Sigma \Delta B_e$ due to engine inlet air cooling to 7, 10 and 15 °C with a variety of ambient temperatures t_{amb} during time τ .

As Fig. 6 shows, the application of developed engine cyclic air cooling system provides decreasing current specific fuel consumption Δb_e by the values of 2 to 3 g/kWh at increased ambient air temperatures t_{amb} , that leads to their summarized daily values ΣB_e of about 50 kg for gas engine JMS 420 GS-N.L of 1400 kW power output, i.e., practically twice larger than by typical cooling in ACh.

The efficiency of the engine intake air cooling system and a rational value of its design cooling capacity without system oversizing can be determined by a developed method based on annual fuel saving as a primary criterion. With this, the annual fuel saving ΣB is calculated by summarizing all the current fuel reductions B through step by step procedure along with the overall range of cooling capacities Q_0 for a considered temperature of cooled air t_{a2} (Fig. 7).

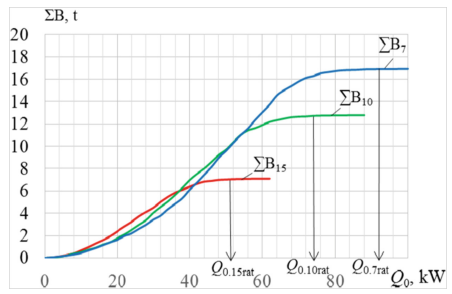


Fig. 7. Annual fuel-saving ΣB due to cooling ambient air at the inlet of a gas engine to $t_{a2} = 7, 10$ and 15 °C versus cooling capacities Q_0 needed: $Q_{0.7,10,15}$ – rational design values.

As Fig. 7 shows, a developed cooling system with combined AECh of design cooling capacity $Q_{0,10}$ about 70 kW, provides cooling ambient air to $t_{a2} = 10$ °C with annual fuel saving $\sum B_{10}$ about 12.3 t is closed to a maximum value.

It is seen, although a rate of increment of annual fuel saving $\sum B$ above this value is negligible, the range of cooling capacities Q_0 needed to provide a maximum value of $\sum B$, i.e., to cover the maximum current cooling duties Q_0 , is still wide. It approves a considerable oversizing of the cooling system, designed traditionally to cover the maximum current cooling needs Q_0 . So, the proper (rational) values of design cooling capacities Q_0 are determined for an appropriately sized cooling system.

As Fig. 7 shows, the application of the developed method of cooling system rational designing allows to reduce the sizes of the system by about 15 to 20% due to rational design cooling capacities Q_{0rat} decreased by $\Delta Q_0 = Q_{0max} - Q_{0rat}$ compared with their maximum values Q_{0max} calculated traditionally.

The method allows estimating the efficiency of applying the proposed advanced cooling system with combined AECh for deeper engine inlet air cooling to $t_{a2} = 7$ and 10 °C as compared with traditional cooling to $t_{a2} = 15$ °C in ACh. As Fig. 7 shows, applying a combined engine intake air cooling system to $t_{a2} = 10$ and 7 °C in AECh provides annual fuel saving $\sum B$ in 1.5 to 2.0 times higher than cooling to $t_{a2} = 15$ °C in ACh for temperate climatic conditions.

5 Conclusions

The results of processing the monitoring data on the fuel efficiency of driving gas engines in combined electricity, heat, and cooling generation plant have proved inefficient operation of traditional cooling. All the engine room incoming air in central conditioner fed by chilled water from absorption lithium-bromide chiller.

An advanced system of gas engine inlet air two-stage deep cooling by combined absorption-ejector chiller has been developed.

The method of rational loading of the proposed engine inlet air cooling system proved the increment of annual fuel reduction at raised ambient air temperatures by about 50% compared with traditional cooling by absorption chillers.

An advanced cooling system provides decreasing specific fuel consumption by 2.0 to 3.0 g/kWh due to stabilized low temperature of the air at the suction of engine turbocharger at increased ambient air temperatures.

The proposed system does not require considerable additional investments over the existing one, so the ejector chiller generally consists of heat exchangers and can use existing cooling towers to remove rejected heat (Fig. 4).

References

1. Canova, A., Cavallero, C., Freschi, F., Giaccone, L., Repetto, M., Tartaglia, M.: Optimal energy management. *IEEE Ind. Appl. Mag.* **15**, 62–65 (2009)

2. Rodriguez-Aumente, P.A., Rodriguez-Hidalgo, M.C., Nogueira, J.I., Lecuona, A., Vene-gas, M.C.: District heating and cooling for business buildings in Madrid. *Appl. Therm. Eng.* **50**, 1496–1503 (2013)
3. Chua, K.J., Yang, W.M., Wong, T.Z., et al.: Integrating renewable energy technologies to support building trigeneration – a multi-criteria analysis. *Renewable Energy* **41**, 358–367 (2012)
4. Carvalho, M., Serra, L.M., Lozano, M.A.: Geographic evaluation of trigeneration systems in the tertiary sector. Effect of climatic and electricity supply conditions. *Energy* **36**, 1931–1939 (2011)
5. Suamir, I.N., Tassou, S.A.: Performance evaluation of integrated trigeneration and CO₂ refrigeration systems. *Appl. Therm. Eng.* **50**, 1487–1495 (2013)
6. Freschi, F., Giaccone, L., Lazzeroni, P., Repetto, M.: Economic and environmental analysis of a trigeneration system for food-industry: a case study. *Appl. Energy* **107**, 157–172 (2013)
7. Komuro, T., Ito, E., Sonoda, T., Tomita, Y., Hidaka, K., Shibutani, S.: Power output augmentation of gas turbine combined cycle by inlet-air cooling system of chiller type under high ambient air temperature. *Mitsubishi Heavy Indust. Technical Rev.* **47**(4), 33–39 (2010)
8. Oktay, Z., Coskun, C., Dincer, I.: A new approach for predicting cooling degree-hours and energy requirements in buildings. *Energy* **36**(8), 4855–4863 (2011)
9. Günnür, Şen, G. et al.: The effect of ambient temperature on electric power generation in natural gas combined cycle power plant-A case study. *Energy Reports* **4**, 682–690 (2018)
10. Trushliakov, E., Radchenko, A., Forduy, S., Zubarev, A., Hrych, A.: Increasing the operation efficiency of air conditioning system for integrated power plant on the base of its monitoring. In: Nechyporuk, M., et al. (eds.) *Integrated Computer Technologies in Mechanical Engineering (ICTM 2019)*. *Advances in Intelligent Systems and Computing*, vol. 1113, pp. 351–360. Springer, Cham (2020). https://doi.org/10.1007/978-3-030-37618-5_30
11. Elsenbruch, T.: Jenbacher gas engines a variety of efficient applications. Bucureşti (2010)
12. Radchenko, R., Pyrysunko, M., Radchenko, A., Andreev, A., Kornienko, V.: Ship engine intake air cooling by ejector chiller using recirculation gas Heat. In: Tonkonogyi, V., et al. (eds.) *Advanced Manufacturing Processes II. InterPartner 2020. Lecture Notes in Mechanical Engineering*, pp. 734–743. Springer, Cham (2021). https://doi.org/10.1007/978-3-030-68014-5_71
13. Trushliakov, E., Radchenko, A., Radchenko, M., Kantor, S., Zielikov, O.: The Efficiency of refrigeration capacity regulation in the ambient air conditioning systems. In: Ivanov V., et al. (eds.) *Advances in Design, Simulation and Manufacturing III (DSMIE 2020)*. *Lecture Notes in Mechanical Engineering*, pp. 343–353. Springer, Cham (2020). https://doi.org/10.1007/978-3-030-50491-5_33
14. Radchenko, N.I.: On reducing the size of liquid separators for injector circulation plate freezers. *Int. J. Refrig* **8**(5), 267–269 (1985)
15. Radchenko, M., Mikielewicz, D., Tkachenko, V., Klugmann, M., Andreev, A.: Enhancement of the operation efficiency of the transport air conditioning system. In: Ivanov V., et al. (eds.) *Advances in Design, Simulation and Manufacturing III (DSMIE 2020)*. *Lecture Notes in Mechanical Engineering*, pp. 332–342. Springer, Cham (2020). https://doi.org/10.1007/978-3-030-50491-5_32
16. Forsyth, J.L.: Gas turbine inlet air chilling for LNG. In: *IGT International Liquefied Natural Gas Conference Proceedings*, vol. 3, pp. 1763–1778 (2013)
17. Kalhori, S.B., Rabiei, H., Mansoori, Z.: Mashad trigeneration potential – an opportunity for CO₂ abatement in Iran. *Energy Convers. Manage.* **60**, 106–114 (2012)
18. Ghaebi, H., Karimkashi, Sh., Saidi M.H.: Integration of an absorption chiller in a total CHP site for utilizing its cooling production potential based on R-curveconcept. *Int. J. Refrig.* **35** (2012)

19. Kornienko, V., Radchenko, R., Konovalov, D., Andreev, A., Pyrysunko, M.: Characteristics of the rotary cup atomizer used as afterburning installation in exhaust gas boiler flue. In: Ivanov, V., et al. (eds.) *Advances in Design, Simulation and Manufacturing III (DSMIE-2020)*. Lecture Notes in Mechanical Engineering, pp. 302–311. Springer, Cham (2020)
20. Radchenko, M., Radchenko, R., Kornienko, V., Pyrysunko, M.: Semi-empirical correlations of pollution processes on the condensation surfaces of exhaust gas boilers with water-fuel emulsion combustion. In: Ivanov V., et al. (eds.) *Advances in Design, Simulation and Manufacturing II (DSMIE 2019)*. Lecture Notes in Mechanical Engineering, pp. 853–862. Springer, Cham (2020). https://doi.org/10.1007/978-3-030-22365-6_85
21. Kornienko, V., Radchenko, M., Radchenko, R., Konovalov, D., Andreev, A., Pyrysunko, M.: Improving the efficiency of heat recovery circuits of cogeneration plants with combustion of water-fuel emulsions. *Therm. Sci.* **25**(1B), 791–800 (2021). <https://doi.org/10.2298/TSCI200116154K>
22. Kornienko, V., Radchenko, R., Mikielawicz, D., Pyrysunko, M., Andreev, A.: Improvement of characteristics of water-fuel rotary cup atomizer in a boiler. In: Tonkonogyi, V., et al. (eds.) *InterPartner 2020. LNME*, pp. 664–674. Springer, Cham (2021). https://doi.org/10.1007/978-3-030-68014-5_64
23. Radchenko, R., Pyrysunko, M., Kornienko, V., Scurtu, I.-C., Patyk, R.: Improving the ecological and energy efficiency of internal combustion engines by ejector chiller using recirculation gas heat. In: Nechyporuk M., et al. (eds.) *Integrated Computer Technologies in Mechanical Engineering. Advances in Intelligent Systems and Computing*, vol.188, 531–541. Springer, Cham (2021)
24. Radchenko, M., Radchenko, R., Tkachenko, V., Kantor, S., Smolyanoy, E.: Increasing the operation efficiency of railway air conditioning system on the base of its simulation along the route line. In: Nechyporuk M., et al. (eds.) *ICTME (ICTM 2019)*. AISC (2020), vol 1113, pp. 461–467. Springer, Cham (2020). https://doi.org/10.1007/978-3-030-37618-5_39
25. Konovalov, D., Kobalava, H., Maksymov, V., Radchenko, R., Avdeev, M.: experimental research of the excessive water injection effect on resistances in the flow part of a low-flow aerothermopressor. In: Ivanov, V., Pavlenko, I., Liaposhchenko, O., Machado, J., Edl, M. (eds.) *DSMIE 2020. LNME*, pp. 292–301. Springer, Cham (2020). https://doi.org/10.1007/978-3-030-50491-5_28
26. Konovalov, D., Kobalava, H., Radchenko, M., Scurtu, I.C., Radchenko, R.: Determination of hydraulic resistance of the aerothermopressor for gas turbine cyclic air cooling. In: *TE-RE-RD 2020, E3S Web of Conferences*, vol. 180, pp. 01012 (2020)
27. Günnur, Şen, G. et al.: The effect of ambient temperature on electric power generation in natural gas combined cycle power plant-A case study. *Energy Reports*, vol. 4, pp. 682–690 (2018)
28. Dąbrowski, P., Klugmann, M., Mikielawicz, D.: Channel blockage and flow maldistribution during unsteady flow in a model microchannel plate heat exchanger. *J. Appl. Fluid Mech.* **12**, 1023–1035 (2019)
29. Dąbrowski, P., Klugmann, M., Mikielawicz, D.: Selected studies of flow maldistribution in a minichannel plate heat exchanger. *Arch. Thermodyn.* **38**, 135–148 (2017)



Improvement of Environmental and Energy Efficiency of Marine Engines by Utilizing the Ecological Recirculation of Gas Heat in an Absorption Chiller

Roman Radchenko¹  , Maxim Pyrysunko² ,
Victoria Kornienko² , Andrii Andreev² , and Artem Hrych¹ 

¹ Admiral Makarov National University of Shipbuilding, 9, Heroes of Ukraine Ave., Mykolayiv 54025, Ukraine

² Kherson Branch of Admiral Makarov National University of Shipbuilding, 44, Ushakova Ave., Kherson 73000, Ukraine

Abstract. Technical regulation is carried out based on the real possibility of ensuring the required level of environmental friendliness of harmful emissions. Requirements for the environmental safety of ships are developed by the International Marine Organization (IMO). The requirements of IMO standards, applications, and protocols of the MARPOL 73/78 convention regulate technical, organizational, and legal environmental protection issues at sea. Their implementation often leads to a reduction of the economic and energy performance of marine diesel engines. However, the main difficulties in ensuring the environmental safety of internal combustion engines are associated with the selectivity of the components of the exhaust gases system. The innovative scheme of Exhaust Gas Recirculation (EGR) system with using the heat of recirculation gas by absorption chiller (ACh) for cooling the air at the intake of main ship engine is proposed. The effect of using the heat of recirculation gas for cooling engine intake air is analyzed considering the changing climatic conditions on the vessel's route line. The results of calculations have shown reducing the emissions of harmful substances (NO_x by 26 to 39%; SO_x by 9 to 14%) when the engine is running with recirculation of gas.

Keywords: Ecology · Exhaust gas recirculation · Absorption chiller · Harmful emissions

1 Introduction

The ships are the sources of air pollutions that account for about 60 to 80% of all pollutants. Among these substances, the most harmful to nature are emissions from the exhaust gases of internal combustion engines [1, 2]. Like all other types of transport, sea and river vessels are a source of an environmental hazard. Although, the overall balance the share of air pollution from ships is relatively small and does not exceed 3%. However, in places of intensive navigation and ports, a stable air and water pollution level is created, exceeding the concentration limit by 10–15 times. The main shipboard

source of environmental pollution is the main and auxiliary combustion engines of the power plants. Diesel engines dominating as the main marine engines and diesel generators are preferable in terms of fuel efficiency, service life, and the ability to operate on heavy fuel oil (HFO). The combustion of diesel fuel produces hydrocarbons (C_nH_m), sulfur oxides (SO_x), carbon oxides (CO and CO_2), soot, and nitrogen oxides (NO_x).

Reducing the number of harmful substances in exhaust gases is an effective method for the greening of ship engines. Exhaust gas recirculation (a method known as EGR - Exhaust Gas Recirculation) is carried out by bypassing exhaust gases from the manifold to the receiver. The EGR technology is one of the advanced methods for reducing NO_x and SO_x . But this method has a negative effect. The usage of EGR increases the specific fuel consumption (SFC) of the engines [3, 4].

It is justified to use the technologies of the utilization of recirculation exhaust gas heat for cooling engine intake air to improve the environmental and fuel efficiency of the marine diesel engine using EGR systems [5]. These technologies allow increasing fuel economy by cooling the cyclic air in waste heat using chillers (WHUCh) [6, 7].

2 Literature Review

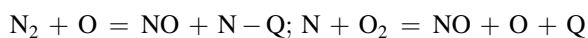
Nowadays, it is possible to speak about clean air only conditionally, especially in industrial zones. In most cases, the ambient air is polluted. Presenting in the atmospheric air and polluting it, harmful substances negatively affect human life.

Diesel exhaust gases are complex gas mixture containing more than 200 components. The four components nitrogen (N_2), oxygen (O_2), carbon dioxide (CO_2), and water (H_2O), make up $99 \div 99.9\%$ of the exhaust gas volume. For ecology, they are non-toxic. The remaining $0.1 \div 1\%$ of the volume of exhaust gases are components that pose an environmental hazard. Their danger is usually assessed by two characteristics: toxicity and smokiness [8].

The toxicity of exhaust gases is the number of gaseous components that harm wildlife and humans. Among the many toxic components, about $80 \div 95\%$ are accounted for by five of them. The degree of their harmfulness is different and in relative form can be expressed by the ratio:

$$CO : CH_x : SO_x : NO_x : RCHO = 1 : 2 : 16 : 40 : 40$$

Nitrogen oxides undoubtedly lead in the list of the main toxic components. The exhaust gases of diesel engines contain about 10 compounds of nitrogen with oxygen, but the dominant is NO . Its share is $95 \div 98\%$ of all oxides. The remaining $2 \div 5\%$ are higher nitrogen oxides: etc. Nitric oxide is formed in the combustion chamber of an engine during fuel combustion. Oxidation is carried out by two chain reactions:

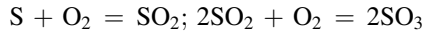


The first reaction is decisive and endothermic. It means: nitrogen oxidation can take place only when heat is expended at high temperatures (actually more than 2000 K);

NO output does not depend on the chemical composition of the fuel; the duration of the reaction, and, accordingly, the amount of formed nitrogen oxide depends on the temperature.

NO₂ is considered the main toxic component of exhaust gases. Its toxicity is 7 times higher than that of NO.

The formation of sulfur oxides in the combustion chamber of the engine is subject to the following chain reactions



The starting material for these reactions is the sulfur contained in the fuel. Consequently, the SO_x content in the exhaust gas is uniquely determined and controlled by the fuel quality. Sulfur oxides are undesirable components in exhaust gases.

Annex VI of MARPOL 73/78 regulates the emission of nitrogen oxides from the exhaust gases of marine diesel engines and the sulfur content of the fuel. Since 2016 the IMO Tier 3 standard has been introduced, which assumes the reduction in nitrogen oxide emissions by 80%. It is extremely difficult to meet such stringent requirements; revolutionary technical solutions must fulfill these requirements. The IMO Tier 3 requirements are valid only in certain water areas, the so-called “Emission Control Areas” (ECA). For sailing on the high seas, Tier 2 regulations remained in effect after 2016 [9].

The methods for reducing toxicity are differentiated concerning the harmful components of the exhaust gases. For example, measures aimed at reducing NO_x do not positively affect CO and CH_x, but in relation to soot emissions, they have the opposite effect. Therefore, the choice of one or another method for improving the environmental friendliness of an internal combustion engine is always accompanied by the search for the compromise between toxicity, smoke, fuel efficiency, and the cost of implementing the method.

In the meantime, MAN Diesel will continue to study EGR systems for reducing NO_x emissions in practice. It is shown that the introduction of exhaust gas recirculation in combination with the Miller cycle, two-stage high-pressure, and Common-Rail fuel system with electrically controlled injectors allows reducing NO_x emissions by up to 80% and bringing them to 2 g/ kWh). To avoid smoke, the fuel injection pressure is increased to 170 MPa. Thus, using the EGR system allows, in principle, to meet the Tier 3 requirements [10].

Today, the innovative approaches for designing technological equipment are proposed in [11, 12]. Notably, it is promising to use technologies to increase combustion engines’ fuel and energy efficiency with EGR systems [13]. It would combine high environmental efficiency [14] with engine fuel efficiency due to waste heat utilization [15–17] and engine cyclic air cooling by applying refrigeration [18, 19], trigeneration or integrated energy systems [20], and jet technologies, and statistical treatment of data of influence of actual climatic conditions [21, 22] on performance characteristics of cooling systems [23, 24]. To evaluate the effectiveness of technologies for reducing harmful emissions and saving fuel, methods and modeling [25, 26] of the influence of environmental parameters on the performance of waste heat recovery cooling systems are used, monitoring and experiments [27, 28] are carried out. Such technologies

provide engine cyclic air cooling by waste heat [29, 30] using ejector chillers (ECh) as the most simple in design and high efficient absorption chillers (ACh) with a coefficient of performance $\zeta = 0.6\text{--}0.7$. Using this efficient heat exchanger [31–33] with equalized flow distribution [34, 35] can be used for cooling [36, 37].

The study aims to assess the efficiency of the ship's main engines with an ecological EGR system through intake air precooling by the ACh using the heat of recirculation exhaust gas.

3 Research Methodology

The effectiveness of the application of the proposed technical solution was analyzed based on the EGR system typical for MAN low-speed two-stroke diesel engines under the Tier III environmental conditions. Recirculation is provided by bypassing part of the exhaust gases purified from harmful gases in the scrubber after cooling in the heat exchanger-gas cooler.

It provided a schematic solution using the heat-using circuit of the ACh for the two-stroke engine 6G50ME-C9.6 [38], responsible for Tier III environmental conditions. To analyze the system parameters and characteristics of the diesel engine, the CEAS software package was used. The next initial data were used for the calculation: power – $N_e = 9288$ kW; engine load – $N_{MCR} = 90\%$; SFC – $g_e = 166.0$ g/(kWh); speed – $n_e = 96.5$ rpm; EGR system.

The calculation of the engine characteristics was carried out on the operating mode during the voyage of the dry-cargo ship from Odessa to Shanghai. In Fig. 1, there are changes in the climatic conditions during the voyage (temperature of seawater t_w , ambient air temperature t_a , relative humidity φ_a , and absolute humidity d_a).

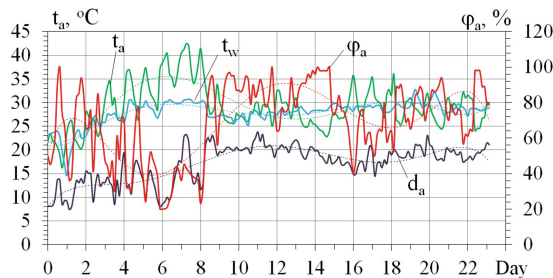


Fig. 1. The variation of climatic conditions (air temperature t_a , the temperature of seawater t_w , absolute humidity d_a , and relative humidity φ_a) during the vessel trade voyage Odessa-Shanghai.

The calculation of the operating parameters of the heat-recovery contour based on the absorption chillers was carried out according to the equations used in the software package developed at the Department of Conditioning and Refrigeration of admiral Makarov National University of Shipbuilding (Ukraine).

The calculation of the operating parameters of the heat-recovery contour based on the absorption chillers was carried out according to heat balances.

$$Q_0 = (c_a \xi \Delta t_a) G_a, \quad (1)$$

The refrigeration capacity is calculated as:

where $\Delta t_a = t_{amb} - t_{a2}$ – decrease in air temperature; t_a – air temperature at the inlet of engine turbocharger, °C; t_{a2} – temperature of cooled air at the air cooler outlet, °C; c_{ma} – specific heat of moist air, kJ/(kg·K); G_a – air mass flow rate, kg/s; ξ – specific heat ratio of the overall heat (latent and sensible heat) to the sensible heat removed from the air during cooling.

The heat coefficient ζ is the ratio of the cooling capacity Q_0 (the amount of heat removed from the cycle air) to the amount of heat expended Q_g supplied to the ACh from the exhaust gases or charge air:

$$\zeta = Q_0/Q_g \quad (2)$$

The values of the cooling capacity $Q_{0.15}$ required to cool the air at the engine inlet were calculated based on the decrease in its temperature from the current temperature in the engine room t_{a1} ($t_{a1} = t_{ch} + 10$ °C) to $t_{a2} = 15$ °C by the value Δt_{15} , available cooling capacity $Q_{0rg(0.7)}$ - taking into account the transformation of the available heat of exhaust gases $Q_{h.rg}$ into cold to the ACh:

$$Q_0 = Q_{h.rg} \zeta \quad (3)$$

Required heat consumption $Q_{0.15(0.7)}$ for cooling the air at the engine inlet device to the temperature $t_{a2} = 15$ °C on the ACh:

$$Q_{0.15(0.7)} = Q_{0.15}/\zeta \quad (4)$$

During the voyage, the available cooling capacity $Q_{0rg(0.7)}$ exceeds its value $Q_{0.15}$ required to cool the air at the engine inlet to the temperature $t_{a2} = 15$ °C, as the heat of exhaust gases $Q_{h.rg}$ is much higher than its required value $Q_{h.15(0.7)}$ for cooling the air at the engine inlet to $t_{a2} = 15$ °C.

The following characteristics of the ACh were selected: temperature of hilled water $t_{cw} = 7$ °C; coefficient of performance $\zeta = 0.7$.

4 Results

The solution using the ACh was developed and analyzed (Fig. 2). During the usage of the EGR system, some of the exhaust gases (10–40%) go into the scrubber recycling system (SRS). In it, they are purified by spraying water through nozzles [39]. Then the exhaust gases are cooled in the heat exchanger - gas cooler (heater [40] of water for refrigerant generator of ACh), condensed vapor from exhaust gases is drained through

condensate trap and cooled gases are fed by the fan to the scavenge air receiver, where gases are mixed with the scavenge air coming from the turbocharger.

It is suggested to use the heat of the recirculating gases for high-pressure liquid refrigerant evaporation in the generator of ACh with a generation of high-pressure refrigerant vapor as motive fluid for absorption to suck a low-pressure refrigerant vapor from refrigerant evaporator – air cooler (AC-RE) at the intake of the turbocharger. Thus, the cooling capacity of ACh is used for cooling air at the intake of the engine turbocharger.

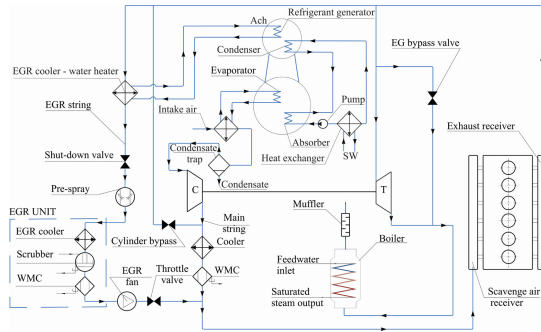


Fig. 2. Scheme of EGR-technology for the two-stroke diesel engine 6G50ME-C9.6 with ACh.

During the voyage of the vessel for the engine 6G50ME-C9.6, the SFC without EGR system is 165–167 g/(kWh) (Fig. 3). SFC with EGR system on the route is 168–170 g/(kWh). In this case, the RC is $K_r = 13\text{--}15\%$. The total mass of the exhaust gases flow rate $G_g = 18\text{--}20$ kg/s, and the flow of recirculating flue gases is $G_{g,r} = 2.8\text{--}2.9$ kg/s. The mass flow rate of “fresh” air to the engine turbocharger is $G_a = 16\text{--}17$ kg/s without EGR system and with EGR system $G_{a,egr} = 13\text{--}14$ kg/s.

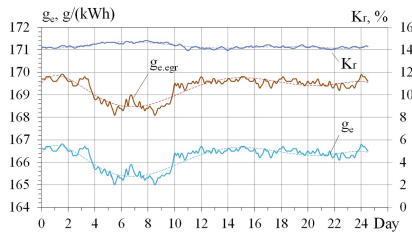


Fig. 3. Variation of specific fuel consumption g_e of the engine without EGR and $g_{e,egr}$ – with the EGR system, recirculation coefficient K_r during the vessel route Odessa-Shanghai.

For the engine 6G50ME-C9.6, according to the calculations using the CEAS software package, when cooling intake air for every 10 °C, a reduction in specific fuel consumption is 0.109 g/(kWh·K) for every 1 °C of the air temperature drop.

The results of analysing the operation efficiency of recirculation gas heat-recovery ACh with coefficient of performance $\zeta = 0.6, 0.7$ show the following cooling capacity received (Fig. 4): $Q_{0,rg(0.6)} = 595\text{--}640 \text{ kW}$ ($\zeta = 0.6$), $Q_{0,rg(0.7)} = 690\text{--}750 \text{ kW}$ ($\zeta = 0.7$).

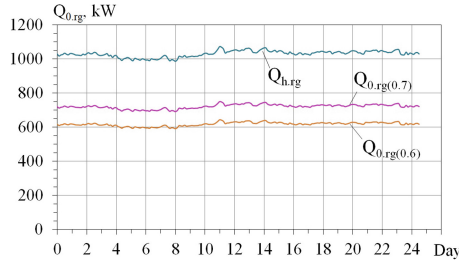


Fig. 4. Variation of available heat of exhaust recirculation gas (rg) $Q_{h,rg}$, cooling capacity $Q_{0,rg}$ (0.6), and $Q_{0,rg}$ (0.7) generated by ACh using the gas heat $Q_{h,rg}$ at the coefficient of performance ($\zeta = 0.6, 0.7$) during the vessel route Odessa-Shanghai.

The t_{hl} temperature has been selected, taking into account the risk of low-temperature corrosion. This method reduces the temperature of the air that enters the engine turbocharger: $\Delta t_{a(0.6)} = 7.4\text{--}17.2 \text{ }^\circ\text{C}$ ($\zeta = 0.6$) and $\Delta t_{a(0.7)} = 9.3\text{--}21.5 \text{ }^\circ\text{C}$ ($\zeta = 0.7$). In turn, this leads to a decrease in the specific fuel consumption SFC.

A decrease in the temperature of intake air due to its cooling by the chillers leads to decreased SFC and the total fuel economy $\sum B_f$.

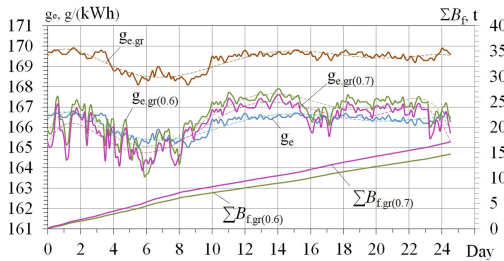


Fig. 5. Variation of SFC of the engine with EGR system without using its heat for engine intake air cooling $g_{e,gr}$, with using its heat for engine intake air cooling $g_{e,gr}$ at different coefficients of performance $\zeta = 0.6$ and 0.7 in ACh and SFC g_e – due to engine intake air cooling to $t_{c2} = 15 \text{ }^\circ\text{C}$ and $\sum B_{f,gr(0.6)}$, $\sum B_{f,gr(0.7)}$ summarized along the vessel route.

This happens during the vessel route due to decrease in the temperature of intake air at the turbocharger cooled by ACh using the heat of RG at different coefficients of performance is the following (Fig. 5): $\sum B_{f(0.6)} = 14.7 \text{ t}$ (for $\zeta = 0.6$), $\sum B_{f(0.7)} = 17.2 \text{ t}$ (for $\zeta = 0.7$) and $\sum B_{f(0.7)} = 16.5 \text{ t}$ (for $\zeta = 0.70$).

This technology allows to reduce harmful emissions more than 0.2–0.3% for SO_x and NO_x , but for EGR system $\zeta = 0.7$ is: $\Delta g_{\text{NO}_x(0.7)} = 26.3\text{--}39.1\%$ (4.7–6.7 g/(kWh)); $\Delta g_{\text{SO}_x(0.7)} = 9.6\text{--}14.3\%$ (1.1–1.5 g/(kWh)). Meanwhile, it should be emphasized that this enhances CO_2 emissions by $\Delta g_{\text{CO}_2(0.7)} = 1.5\text{--}1.7\%$ (6.3–9.4 g/(kWh)).

For the price [41] of heavy fuel oil IFO380 370 \$/t the savings in consumed fuel cost during the ship route Odessa-Shanghai are 5439 \$ ($\zeta = 0.60$) and 6364 \$ ($\zeta = 0.70$). A vessel on this route makes up to 12 voyages per year. Then the annual savings in fuel cost will be 65268 \$ ($\zeta = 0.6$) and 76368 \$ ($\zeta = 0.70$). The ONDA heat exchanger MPE 1350 [42] can be applied in the ejector chiller. Its cost is about 30000 \$ taking into account the cost of its mounting. Proceeding from this, the payback time of waste heat recovery installation will be about 1 year.

5 Conclusions

The developed novel systems achieve double effect due to using the waste heat of recirculation gas, traditionally removed aboard by sea water, for engine cyclic air cooling and, hence, decreasing the heat load on the scrubber recycling system and decreasing specific fuel consumption due to intake air cooling simultaneously.

The method of precooling intake air at the diesel engine turbocharger by ACh using the heat of recirculation exhaust gas is well actualized into ICE with an EGR system.

An analysis of the influence of changes in climatic conditions on the Odessa-Shanghai route on air cooling at the inlet to the turbocharger of the MAN 6G50ME-C9.6 diesel engine has been carried out.

It was determined that the use of ecological recirculation gas heat in ACh allows reducing the air temperature at the intake of the ship's main diesel engine by about 30° C and provides a reduction of the specific fuel consumption by about 3.5 g/(kW·h). Simultaneously, the harmful emissions are reduced due to EGR: of NO_x by about 35%; SO_x by 14%.

References

1. Pham, V.V.: Advanced technology solutions for treatment and control noxious emission of large marine diesel engines: a brief review. *J. Mech. Eng. Res. Dev.* **42**(5), 21–27 (2019)
2. Radchenko, R., Pyrysunko, M., Radchenko, A., Andreev, A., Kornienko, V.: Ship engine intake air cooling by ejector chiller using recirculation gas heat. In: Tonkonogyi, V., Ivanov, V., Trojanowska, J., Oborskyi, G., Grabchenko, A., Pavlenko, I., Edl, M., Kuric, I., Dasic, P. (eds.) *InterPartner 2020. LNME*, pp. 734–743. Springer, Cham (2021). https://doi.org/10.1007/978-3-030-68014-5_71
3. Thirumala Sai Kumar, J., Karthikeya Sharma, T., Madhu Murthy, K., Amba Prasad Rao, G.: Effect of reformed EGR on the performance and emissions of a diesel engine: A numerical study. *Alexandria Eng. J.* **57**, 517–525 (2018)
4. Trushliakov, E., Radchenko, M., Bohdal, T., Radchenko, R., Kantor, S.: An innovative air conditioning system for changeable heat loads. In: Tonkonogyi, V. et al. (eds.) *Advanced Manufacturing Processes. InterPartner-2019. Lecture Notes in Mechanical Engineering*, pp. 616–625. Springer, Cham (2020)






5. Thangaraja, J., Kannan, C.: Effect of exhaust gas recirculation on advanced diesel combustion and alternate fuels-a review. *Appl. Energy* **180**, 169–184 (2016)
6. Radchenko, N., Radchenko, A., Tsoy, A., Mikielewicz, D., Kantor, S., Tkachenko, V.: Improving the efficiency of railway conditioners in actual climatic conditions of operation. In: AIP Conference Proceedings 2285, no. 030072 (2020). <https://doi.org/10.1063/5.0026789020N>
7. Radchenko, A., Stachel, A., Forduy, S., Portnoi, B., Rizun, O.: Analysis of the efficiency of engine inlet air chilling unit with cooling towers. In: Ivanov, V., et al. (eds.) DSMIE 2020. LNME, pp. 322–331. Springer, Cham (2020). https://doi.org/10.1007/978-3-030-50491-5_31
8. Grünenwald, B., Knödler, W., Saumweber, C.: A methodology for evaluation of charge air coolers for low pressure EGR systems with respect to corrosion. *Veh. Therm. Manage. Syst. Conf. Exhib.* **10**, 57–67 (2011)
9. Hadjab, R., Kadja, M.: Computational fluid dynamics simulation of heat transfer performance of exhaust gas recirculation coolers for heavy-duty diesel engines. *Therm. Sci.* **22**(6B), 2733–2745 (2018)
10. MAN Diesel, Turbo. <http://marine.man.eu/docs/librariesprovider6/technical-papers/tier-iii-two-stroke-technology.pdf?sfvrsn=18>. Accessed 10 April 2020
11. Ivanov, V., Pavlenko, I., Trojanowska, J., Zuban, Y., Samokhvalov, D., Bun, P.: Using the augmented reality for training engineering students. In: 4th International Conference of the Virtual and Augmented Reality in Education, VARE 2018, pp. 57–64 (2018)
12. Bun, P., Trojanowska, J., Ivanov, V., Pavlenko, I.: The use of virtual reality training application to increase the effectiveness of workshops in the field of lean manufacturing. In: 4th International Conference of the Virtual and Augmented Reality in Education, VARE 2018, pp. 65–71 (2018)
13. Kumar, J. Thirumala, S., et al.: Effect of reformed EGR on the performance and emissions of a diesel engine: A numerical study. *Alexandria Eng. J.* **57**, 517–525 (2018)
14. Radchenko, A., Trushliakov, E., Kosowski, K., Mikielewicz, D., Radchenko, M.: Innovative turbine intake air cooling systems and their rational designing. *Energies* **13**(23), 6201 (2020). <https://doi.org/10.3390/en13236201>
15. Nagendra, S., Santosh Kumar, B., Kiran, A.V.N.S., Ramanjaneyalu, C., Nagamani, K.: Quantification of execution and emission efficiency of a fueled diesel engine. *J. Eng. Sci.* **7** (1), G15–G20 (2020). [https://doi.org/10.21272/jes.2020.7\(1\).g3](https://doi.org/10.21272/jes.2020.7(1).g3)
16. Cherednichenko, O., Mitienkova, V.: Analysis of the impact of thermochemical recuperation of waste heat on the energy efficiency of gas carriers marine. *Sci. Appl.* **19**, 72–82 (2020)
17. Trushliakov, E., Radchenko, A., Forduy, S., Zubarev, A., Hrych, A.: Increasing the operation efficiency of air conditioning system for integrated power plant on the base of its monitoring. In: Nechyporuk, M., Pavlikov, V., Kritskiy, D. (eds.) *Integrated Computer Technologies in Mechanical Engineering (ICTM 2019)*. Advances in Intelligent Systems and Computing, vol. 1113, pp. 351–360. Springer, Cham (2020)
18. Cherednichenko, O., Tkach, M., Dotsenko, S.: The usage of a waste heat recovery metal-hydride unit of continuous operation in the maritime energy. In: 2019 IEEE International Conference on Modern Electrical and Energy Systems (MEES). pp. 510–513 (2019)
19. Trushliakov, E., Radchenko, A., Radchenko, M., Kantor, S., Zielikov, O.: The efficiency of refrigeration capacity regulation in the ambient air conditioning systems. In: Ivanov, V., et al. (eds.) *Advances in Design, Simulation and Manufacturing III (DSMIE-2020)*. Lecture Notes in Mechanical Engineering, pp. 343–353. Springer, Cham (2020). https://doi.org/10.1007/978-3-030-50491-5_33
20. Radchenko, A., Mikielewicz, D., Forduy, S., Radchenko, M., Zubarev, A.: Monitoring the fuel efficiency of gas engine in integrated energy system. In: Nechyporuk, M., et al. (eds.)

- Integrated Computer Technologies in Mechanical Engineering (ICTM 2019). *Advances in Intelligent Systems and Computing*, vol. 1113, pp. 361–370. Springer, Cham (2020)
21. Cherednichenko, O., Serbin, S., Dzida, M.: Application of thermo-chemical technologies for converging of associated gas in diesel-gas turbine installations for oil and gas floating units. *Polish Maritime Res.* **26**(3), 181–187 (2019)
 22. Bohdal, L., Kukielka, L., Świłło, S., Radchenko, A., Kułakowska, A.: Modelling and experimental analysis of shear-slitting process of light metal alloys using FEM, SPH and vision-based methods. In: *AIP Conference Proceedings 2078*, no. 020060 (2019)
 23. Radchenko, M., Radchenko, R., Tkachenko, V., Kantor, S., Smolyanoy, E.: Increasing the operation efficiency of railway air conditioning system on the base of its simulation along the route line. In: Nechyporuk, M., et al. (eds.) *Integrated Computer Technologies in Mechanical Engineering*. AISC, vol. 1113, pp. 461–467. Springer, Cham (2020). https://doi.org/10.1007/978-3-030-37618-5_39
 24. Konovalov, D., Kobalava, H., Radchenko, M., Scurtu, I.C., Radchenko, R.: Determination of hydraulic resistance of the aerothermopressor for gas turbine cyclic air cooling. In: *TE-RE-RD 2020*, E3S Web of Conferences, vol. 180, p. 0101231 (2020). <https://doi.org/10.1051/e3sconf/202018001012>
 25. Shu, G., Liang, Y., Wei, H., Tian, H., Zhao, J., Liu, L.: A review of waste heat recovery on two-stroke IC engine aboard ships. *Renew. Sustain. Energy Rev.* **19**, 385–401 (2013)
 26. Bohdal, L., Kukielka, L., Radchenko, A., Patyk, R., Kułakowski, M., Chodór, J.: Modelling of guillotining process of grain oriented silicon steel using FEM. In: *AIP Conference Proceedings 2078*, no. 020080 (2019)
 27. Bohdal, L., Kukielka, L., Legutko, S., Patyk, R., Radchenko, A.M.: Modeling and experimental analysis of shear-slitting of AA6111-T4 aluminum alloy sheet. *Materials* **13** (14), 3175 (2020). <https://doi.org/10.3390/ma13143175>
 28. Radchenko, A., Scurtu, I.-C., Radchenko, M., Forduy, S., Zubarev, A.: Monitoring the efficiency of cooling air at the inlet of gas engine in integrated energy system. *Therm. Sci.* **00**, 344 (2020)
 29. De Serio, D., de Oliveira, A., Sodr e, J. R.: Application of an EGR system in a direct injection diesel engine to reduce NOx emissions. *J. Phys. Conf. Ser.* **745**(3) (2016)
 30. Kornienko, V., Radchenko, M., Radchenko, R., Konovalov, D., Andreev, A., Pyrysunko, M.: Improving the efficiency of heat recovery circuits of cogeneration plants with combustion of water-fuel emulsions. *Therm. Sci.* **25**(1 Part B), 791–800 (2021). <https://doi.org/10.2298/TSCI200116154K>
 31. Dąbrowski, P., Klugmann, M., Mikielewicz, D.: Selected studies of flow maldistribution in a minichannel plate heat exchanger. *Arch. Thermodyn.* **38**, 135–148 (2017)
 32. Nogueira, E.: Thermal performance in heat exchangers by the irreversibility, effectiveness, and efficiency concepts using nanofluids. *J. Eng. Sci.* **7**(2), F1–F7 (2020). [https://doi.org/10.21272/jes.2020.7\(2\).f1](https://doi.org/10.21272/jes.2020.7(2).f1)
 33. Radchenko, A., Trushliakov, E., Tkachenko, V., Portnoi, B., Prjadko, O.: Improvement of the refrigeration capacity utilizing for the ambient air conditioning system. In: Tonkonogyi, V., et al. (eds.) *InterPartner 2020*. LNME, pp. 714–723. Springer, Cham (2021). https://doi.org/10.1007/978-3-030-68014-5_69
 34. Kumar, R., Singh, G., Mikielewicz, D.: Numerical study on mitigation of flow maldistribution in parallel microchannel heat sink: channels variable width versus variable height approach. *J. Electron. Packag.* **141**, 21009–21011 (2019)
 35. Dąbrowski, P., Klugmann, M., Mikielewicz, D.: Channel blockage and flow maldistribution during unsteady flow in a model microchannel plate heat exchanger. *J. Appl. Fluid Mech.* **12**, 1023–1035 (2019)

36. Radchenko, M., Mikielewicz, D., Tkachenko, V., Klugmann, M., Andreev, A.: Enhancement of the operation efficiency of the transport air conditioning system. In: Ivanov, V., et al. (eds.) DSMIE 2020. LNME, pp. 332–342. Springer, Cham (2020). https://doi.org/10.1007/978-3-030-50491-5_32
37. Butrymowicz, D., Gagan, J., Śmierciew, K., Łukaszuk, M., Dudar, A., Pawluczuk, A., Łapiński, A., Kuryłowicz, A.: Investigations of prototype ejection refrigeration system driven by low grade heat. In: HTRSE-2018, E3S Web of Conferences 70, 03002 (2018)
38. MAN Diesel Turbo.: CEAS Engine Calculations. <https://marine.man-es.com/two-stroke/ceas>. Accessed 22 June 2019
39. Ochowiak, M., Włodarczyk, S., Pavlenko, I., Janecki, D., Krupinska, A., Markowska, M.: Study on interfacial surface in modified spray tower. processes 7(8), 532 (2019). <https://doi.org/10.3390/pr7080532>
40. Liaposhchenko, O., Pavlenko, I., Ivanov, V., Demianenko, M., Starynskiy, O., Kuric, I., Khukhryanskiy, O.: Improvement of parameters for the multi-functional oil-gas separator of ‘heater-treater’ type. In: 2019 IEEE 6th International Conference on Industrial Engineering and Applications (ICIEA), Tokyo, Japan, 2019, pp. 66–71 (2019). <https://doi.org/10.1109/IEA.2019.8715203>
41. Ship, B.: <https://shipandbunker.com/prices#VLSFO>. Accessed 10 April 2020
42. Onda, S.p.A.: <https://www.onda-it.com/eng/products/shell-and-tube-heat-exchangers/dry-expansions-evaporators-mpe>. Accessed 10 April 2020



Relaxation Shock Absorbers with Additional Mechanical Control Circuit

Ihor Sydorenko^(✉) , Vladimir Semenyuk , Valeriy Lingur ,
Liubov Bovnegra , and Kateryna Kirkopulo 

Odessa National Polytechnic University,
1, Shevchenko Ave., Odessa 65044, Ukraine

Abstract. In modern mechanical engineering, there are a large number of shock absorber designs with the ability to adjust the damping characteristics, which are called relaxation. At present, hydraulic piston shock absorbers with the translational motion of the movable element relative to the body are used as dissipation devices in suspensions. These shock absorbers realize the performance of the throttle-valve type only, which is associated with the functionality of these devices, depending on design constraints. In this work, the synthesis of fundamentally new relaxation dampers was carried out, the performance of which is not related to the pressure in the working cavity. Their essential difference is the presence of a mechanical control loop in the structure, which determines a close relationship between the operating characteristics of the shock absorber and the amount of movement of its moving element relative to the body. In the synthesis process, the approbation of the corresponding methodology was carried out, built based on modeling technical systems with modified kinematic graphs. The synthesis results are presented in the form of two constructive implemented samples. A comparative analysis of the obtained samples was carried out, and their main operational characteristics were determined.

Keywords: Graph theory · Kinematic graphs · Shock absorber · Performance characteristics · Mechanical control

1 Introduction

One of the most effective methods of dealing with vibrations is using devices for their damping as part of a technical system by converting mechanical energy into heat. Such devices, called shock absorbers, are used in conjunction with elastic elements in springs and torsion bars. To damp-free the vibrations of large masses and prevent high relative speeds of smaller masses, masses are connected by elastic elements.

Currently, the most widespread is hydraulic shock absorbers (shock absorbers of viscous friction). Among them are shock absorbers with a friction force proportional to the speed of movement of the working body (the vast majority of modern hydraulic shock absorbers) and shock absorbers with a friction force on the working body that depends on movement (relaxation) [1]. In relaxation shock absorbers, the friction force

on the working body can be either proportional to the displacement or have a nonlinear dependence. The relationship between the friction force on the working body of the shock absorber and its speed (displacement) is called the operating characteristic of the shock absorber [2].

Due to increased requirements for the protection of technical systems from oscillations associated with expanding the spectrum of amplitudes and frequencies of their external disturbance, the existing shock absorbers with their operating characteristics in some cases are not effective. Alternative relaxation shock absorbers with adjustable operating characteristics do not always have the functionality to realize the required performance [3]. In this regard, the synthesis of new designs of relaxation shock absorbers with extended functionality to implement the required (target) characteristics is relevant.

2 Literature Review

For existing designs of relaxation shock absorbers, there are four ways to control their performance. These ways include: mechanical, hydromechanical, electromechanical, and electromagnetic [4, 5]. The first and second of the indicated ways are the most common and are inherent in the vast majority of existing shock absorbers, which are passive mechanical systems [6].

The mechanical regulation method is realized by overlapping the throttling holes, which are formed depending on the specific geometry of the piston and housing during their joint movement [7]. In the case of a hydromechanical control method, the throttling hole in the piston completely or partially overlaps a single or packet membrane (elastic washer or a set of them) [4]. It is the magnitude of the membrane deformation under the action of pressure in the shock absorber cavity that determines the corresponding size of the throttled hole [8, 9]. Electromechanical and electromagnetic methods of regulating performance characteristics are characteristic of shock absorbers, an external energy source, and active mechanical systems [10, 11].

Studies in which the analysis of passive dissipative suspension elements have been carried out show that adjusting their characteristics more important than the design of the shock absorber itself is the constructive implementation and geometric parameters of throttling holes and elements used to cover them [12]. This is because, in the hydraulic shock absorber consisting of housing 1 of the piston 2 and the element covering the throttle hole 3, damping is carried out due to the hydraulic resistance of the liquid working fluid, which flows through narrow channels (Fig. 1). Creating such channels 4 is used as a parameter that allows one to select hydraulic shock absorbers of the throttle or throttle-valve type [13].

However, the development and intensification of technical and technological processes require other performance characteristics that cannot be implemented using existing structures of relaxation shock absorbers due to their low functionality.

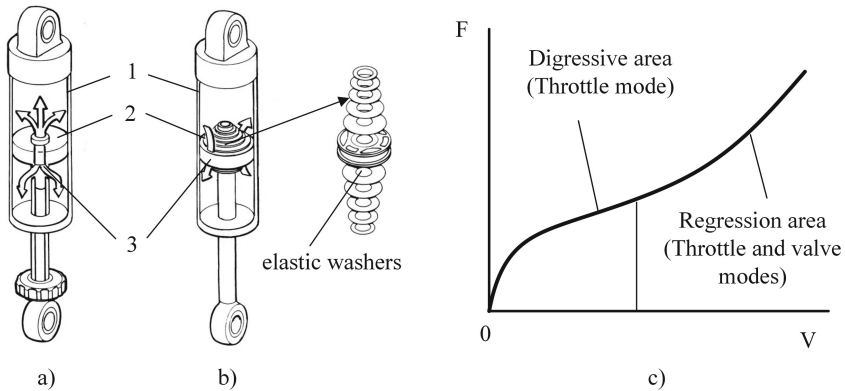


Fig. 1. Hydraulic shock absorbers: throttle type (a); throttle - valve type (b); operating characteristic of the shock absorber in the form of the dependence of the force on its piston on the speed of movement (c).

The alternative using shock absorbers, representing active systems, due to their relatively high cost and additional energy consumption, is selective and is justified only for unique or expensive equipment [14]. Therefore, the synthesis of new structures of passive shock absorbers with extended functionality, which can implement the required (target) performance, is an urgent scientific and applied problem.

3 Research Methodology

At present, a sufficiently large number of techniques have been developed that allow performing the structural synthesis of mechanical devices based on their required parameters [10, 15]. However, it is impossible to single out the methods directly related to the synthesis of structures of controlled shock absorbers.

A technique based on the axiomatic theory of modified kinematic graphs is used successfully for the structural analysis and synthesis of controlled mechanical devices [15, 16]. The essence of the technique lies in the fact that the structure of a certain uncontrolled device, taken as the basic one, can be expanded with additional mechanical structures to organize a specific mechanical control. When synthesizing a mechanical device using this method, a device model is used in the form of a modified kinematic graph, which, unlike a conventional kinematic graph, where only kinematic connections between device elements are considered, non-kinematic connections are added (Fig. 2).

In this case, these connections of a non-kinematic nature are modeled by adding a “marked” edge to the kinematic graph (edge b, Fig. 2, d). In this case, an idealized representation of the structure of any plane passive device, with one or several parameters that are subject to controlled change, is a modified kinematic graph (not two-pole),

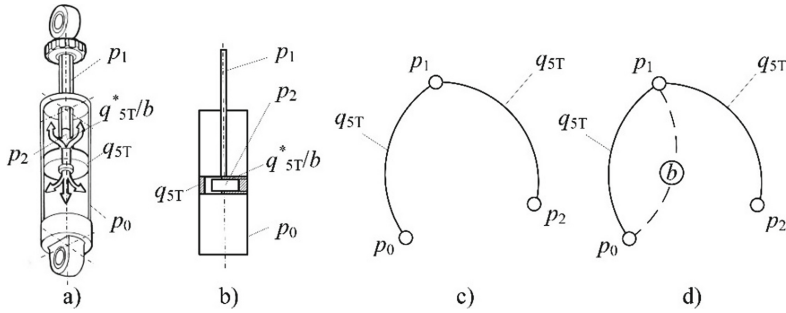


Fig. 2. Modeling a device using a modified kinematic graph: device (a); kinematic diagram of the device (b); model in the form of a kinematic graph (c); model in the form of a modified kinematic graph (d).

which characterizes the negative mobility of the device under consideration by the following expression.

$$W = 3(p_{\Sigma} - 1) - 2q_5 - q_4 - q_b \geq 0 \tag{1}$$

where p_{Σ} – the total number of graph vertices corresponding to the number of hard parts of the device; q_i – the number of ribs of the graph equal to the number of kinematic pairs of the i -th class; q_b – the number of ribs of the graph, equal to the number of non-kinematic bonds (elastic and dissipative) between the hard parts of the device, while this component does not affect the kinematic characteristics of the device and can be considered as a virtual kinematic pair of the 4-th class.

The possibility of kinematic control of one or another parameter of the device, which is subject to controlled change, can be judged by using the indicator for the modified kinematic graph used in the form of a cyclomatic number

$$\sigma = q - p_{\Sigma} + 1 \geq z \tag{2}$$

where q is the number of ribs of the graph that determine both kinematic and non-kinematic interactions; p_{Σ} is the total number of vertices of the graph, z - an indicator of monitored parameters.

Indicator of controlled parameters, the dependence of which on their number (the number of marked ribs), defined by the expression

$$z = q_b + 1.$$

It is easy to see that according to indicators (2) and (3), the device taken as an example for modeling with a modified kinematic graph is not independently controlled (Fig. 2). The presence of an element p_2 in its design, which defines the corresponding model as a graph with a hanging vertex, allows us to speak only of manual control of the performance characteristics of this device. Changing its operating characteristics can be carried out by radially displacing element p_2 in the grooves of element p_1 to change the area of the throttling hole. It is not difficult to notice that the device must be removed from the working position and disassembled for this purpose.

The studies were theoretically substantiated and experimentally confirmed that a device with a mechanical control system must meet three primary conditions [16, 17]. The first condition (1), which defines the mechanism under consideration as a mechanism with excess mobility, corresponds to the modification of the model in the form of a kinematic graph by introducing non-kinematic elements into it. Condition (2) determines the presence in the graph of at least two cycles corresponding to two types: the main cycle associated with the functional interaction of the device elements that determine its performance and the cycle that determines the change in the conditions of such interaction - control cycles. The third condition, which determines the presence of mechanical control, is determined by the presence of one or more cycles, provided that the marked edge e^* is an element of the set of edges $G(E)$ of this cycle

$$e^* \in G(E) \quad (3)$$

These conditions are accepted by the main conditions in the synthesis of mechanisms with a mechanical control system based on their model in the form of a modified kinematic graph.

4 Results

When synthesizing structures of relaxation shock absorbers with a mechanical control system, it is necessary to determine how it is supposed to control the dissipation of the future device.

At present, a new version of the shock absorber dissipation control is proposed, based on a controlled change in the properties of its working fluid in the form of a magnetoelectric fluid. However, the simplest and most common control method is to change the throttle hole in the shock absorber piston. This is done using bypass valves in some existing shock absorber designs. The synthesized design provides the connection of the performance characteristics of the shock absorber, not with the pressure. However, with the piston movement, the use of valves in the proposed design is not provided. However, an element that covers the throttle hole in the shock absorber's piston according to some kinematic law may be a necessary and sufficient condition for its synthesis. Justifying the need for an additional movable element in the form of an overlapping plate for the throttle hole in the shock absorber's piston, it is easy to conclude that it interacts with the piston in some contact. This contact interaction can be realized in the form of a kinematic pair of the 5th class, for example, translational (p_{5T}).

Thus, the previously presented shock absorber model can be used as the initial data for the synthesis of a new device, using it as the basic structure of synthesis (Fig. 3, a).

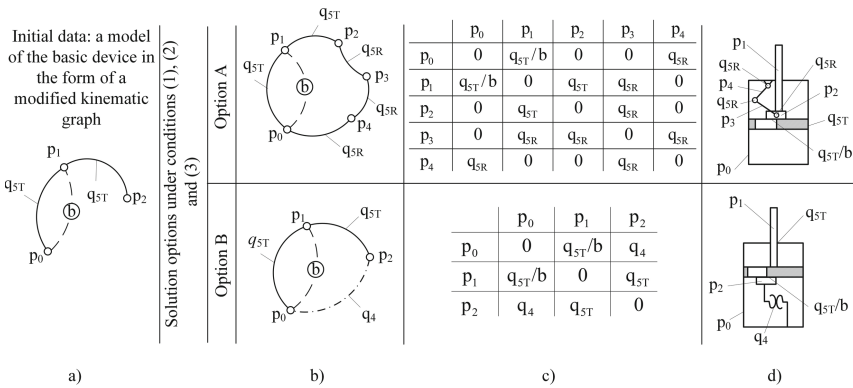


Fig. 3. Synthesis of relaxation shock absorbers with a mechanical control system: initial data (a), device models in the form of modified kinematic graphs satisfying three synthesis conditions (b); assembly matrices for synthesized devices (c); kinematic diagrams of synthesized devices (d).

The synthesis task is to expand the basic structure by introducing into the model an additional number of poles and edges and the order of their placement when the accepted synthesis conditions are met. In this case, it is necessary to obtain an increase in the cyclomatic number, taking into account the fulfillment of condition (3).

Based on the condition of minimizing the number of additional elements of the model in the form of a graph, the following options for expanding the basic structure are possible (Fig. 3, b):

- option A, in which the original basic structure can be extended with poles p_3 , p_4 , and three additional ribs that correspond to rotational kinematic pairs of the 5th class;
- option B, in which an additional edge corresponding can extend the original basic structure to the kinematic pair of the 4th class. The calculations based on the indicators of the synthesis conditions indicate their exact implementation for the two presented options.

Table 1. Correspondence of models to the conditions of synthesis of a passive device with a mechanical control system.

Model	Condition			Fulfillment of conditions
	(1)	(2)	(3)	
Basic	$W = 1$	$\sigma = 1$	–	No
Option A	$W = 1$	$\sigma = 2$	$p_0 - \mathbf{b} - p_1 - q_{ST} - p_2 - q_{ST} - p_3 - q_{SR} - p_4 - q_{SR} - p_0$	Yes
Option B	$W = 0$	$\sigma = 2$	$p_0 - \mathbf{b} - p_1 - q_{ST} - p_2 - q_4 - p_0$	Yes

The correspondence of the basic model and the obtained variants to the conditions of synthesis of a passive device with a mechanical control system are shown in Table 1.

Further work with assembly matrices obtained based on models in the form of modified kinematic graphs (Fig. 3, c) allows you to develop kinematic diagrams of synthesized devices (Fig. 3, d).

The design implementation of the obtained kinematic diagrams in the form of 3D device models was performed using the CAD package Autodesk Inventor Series (Fig. 4).

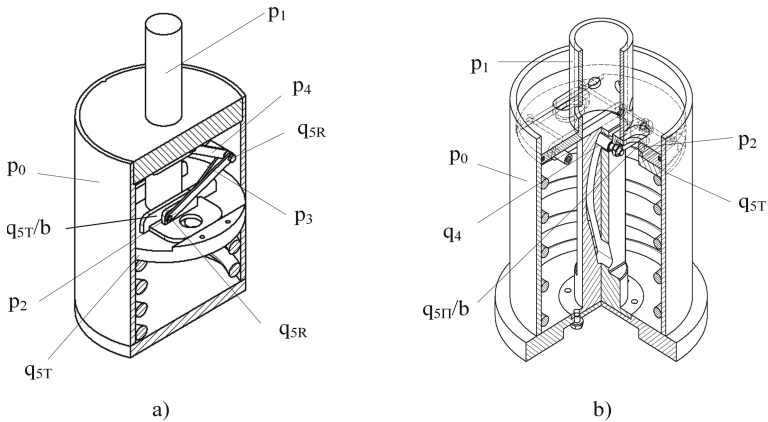


Fig. 4. Design implementation of synthesized devices: option A (a); option B (b) (the designation of the device elements corresponds to the designations adopted in their modeling by modified kinematic graphs).

Checking the kinematics and strength of the main elements of the synthesized relaxation shock absorbers with a mechanical control system, carried out using the applied CAD package, fully confirms their operability, which was the basis for patenting the synthesized devices. In addition, the studies carried out show that the percentage of unification of rubber, fasteners, and body parts in the proposed design solutions is relatively high and amounts to 65%. This is because the design of the shock absorber, adopted as the basic device in the synthesis, is quite widespread. All this allows us to assert a slight increase in the cost of production of such shock absorbers at specialized enterprises since this does not require a serious change in the technological process.

5 Conclusions

Simulation of the kinematics of the synthesized devices showed a close relationship between the change in the area of the throttling holes and the geometric parameters of the additional mechanical circuit added to the basic device.

A comparative analysis of the synthesized devices showed that the realized piston movement in sample A is less than in sample B, which is associated with a lever system in the working cavity of the latter. In addition, this lever system (which occupies a certain volume of one of the parts of the working cavity of sample A) also determines the different dissipation coefficients, depending on the movement direction of the piston. In sample B, large displacements of the piston can be realized, while the volumes of the working cavity with the middle position of the piston are the same for this device. In this regard, the direction of movement of the piston does not have a particular effect on the damping factor. From a technological point of view, the manufacture of sample B looks somewhat more complicated than sample A. However, in terms of the functional capabilities—the cost of manufacturing, both synthesized samples can be considered quite effective.

The obtained results of kinematic modeling suggest that the presented designs will make it possible to implement the operating characteristics of various forms of non-linearity. For sample A, this can be achieved by using asymmetric throttling holes, and for sample B, using a different shape of the cam mechanism determines the kinematic pair of the 4th class.

It is advisable to evaluate the efficiency of the synthesized samples according to the criterion of compliance of the realized working characteristics with some target ones, which are implemented using shock absorbers with other (electromechanical or electromagnetic) types of control.

References

1. Dixon, C.J.: *The Shock Absorber Handbook*. John Wiley & Sons Ltd, England (2007)
2. Shirladze, A., Ivanov, V., Kireev, V.: *Hydraulic and pneumatic systems*. 2nd ed. IC MGТУ “Stankin”, “Yanys”, Moscow (2013). [in Russian]
3. Nikitin, O.: *Hydraulics and hydropneumatic drive*. MGТУ Bauman, Moscow (2012). [in Russian]
4. Fuentes, R., Mineo, C., Pierce, S.G., Worden, K., Cross, E.J.: A probabilistic compressive sensing framework with applications to ultrasound signal processing. *Mech. Syst. Signal Process.* **117**, 383–402 (2019)
5. Ryabov, I.M., Kovalev, A.M., Chernyshov, K.V.: Effect of types of road surface and the speed of the moving car on the oscillation amplitude its inertia mass of a dynamic vibration absorber of wheel. *Automobile Industry* **7**, 18–19 (2013)
6. Emelyanov, R.: Modeling of the hydraulic drive working process with throttle regulation. *Constr. Road Mach.* **11**, 62–64 (2010)
7. Lu, Y.J., Li, N.C.: Research on damping characteristics of shock absorber for heavy vehicle. *J. Appl. Sci. Eng. Technol.* **5**(3), 842–849 (2013)
8. Green, P.L., Worden, K.: Modelling friction in a nonlinear dynamic system via Bayesian inference. In: *Conference Proceedings of the Society for Experimental Mechanics Series*, vol. 6, pp. 543–553 (2013)
9. Sharma, P., Nittin, S., Dimple, S., Parveen, S.: Analysis of automotive passive suspension system with matlab program generation. *Int. J. Adv. Technol.* **4**, 115–119 (2016)
10. Duym, S., Randy, S., Koenraad, R.: Evaluation of shock absorber models. *Veh. Syst. Dyn.* **27**(2), 109–127 (2007)

11. Siczek, K., Kuhar, M.: Researches on the amount of recuperated energy by electromagnetic shock absorber in small car. *J. KONES Powertrain Transp.* **20**(3), 367–374 (2013)
12. Jolly, M., Margolis, D.: Regenerative system for vibration control. *J. Vibr. Acoustic* **119**(2), 208–205 (1997)
13. Gysen, B., Tom, P., Paulides, J.: Efficiency of a regenerative direct drive active suspension. *IEEE Trans. Veh. Technol.* **60**(4), 123–135 (2011)
14. Chiu, T.: An improved algorithm for the construction of generalized kinematic chains. *Mech. Mach. Theor.* **78**, 229–247 (2014)
15. Simoni, R., Carboni, A.P., Martins, D.: Enumeration of kinematic chains and mechanisms. *Proc. Inst. Mech. Eng. C J. Mech. Eng. Sci.* **223**(4), 1017–1024 (2009)
16. Sydorenko, I.: Analysis of the structure of the relaxation shock absorbers and modified the traditional kinematic graph. *ASB Mech. Mach. Tools Mater.* **1**(26), 88–91 (2014)
17. Sydorenko, I.: Synthesis of pressure reducing valve with enhanced functionality. *Odes'kyi Politechnichnyi Universytet, Pratsi* **1**, 14–20 (2017)



Method of Electrohydraulic Activation of Water-Lime Suspension in Sugar Production

Volodymyr Vasyliv¹ , Mikhailo Mushtruk¹ ,
Marija Zheplinska¹ , Roman Mukoid², and Serhii Tkachenko³ 

¹ National University of Life and Environmental Sciences of Ukraine,
15, Heroes of Defense St., Kyiv 03041, Ukraine

mixej.1984@ukr.net

² National University of Food Technology, 68, Volodymyrska St.,
Kyiv 01601, Ukraine

³ Institute of Food Resources of the National Academy of Agrarian Sciences
of Ukraine, 4a, E. Sverstiuk St., Kyiv 02002, Ukraine

Abstract. In the modern technology of beet-sugar production for purification of diffusion juices, the primary reagent use lime is given in juice as water-lime suspension (water-lime suspension). The cost of lime for purification of diffusion juice is 2–3% by weight of beets, while the effect of purification from non-sugars does not exceed 30%, often falling to 25%. It is known that freshly prepared water-lime suspension contains up to 30% of impurities, which contain 80–85% of potentially active lime, which is discharged into the dump, making irreversible losses of lime for beet-sugar production. Disposal of these impurities by activating free but inactive and bound lime would reduce its losses during the purification of the aqueous-lime suspension. In this regard, and in order to economically use exhaustive deposits of limestone, increase the degree of utilization of potentially active lime, which is excreted with impurities, increase the effect of purification of beet-sugar production juices and reduce sugar costs, there is a need to find new ways. Today, the technologies of many industries use various electrophysical methods to increase the activity of chemical reagents, particularly a method of creating an electric discharge in a liquid, which results in an electrohydraulic effect. This work is devoted to developing a method of electrohydraulic treatment of water-lime suspension in beet-sugar production to increase its activity and reduce losses of active lime with impurities, which will reduce lime costs for juice purification and increase the effect of purification and sugar yield.

Keywords: Lime · Water-lime suspension · Electrohydraulic effect · Lime activity · Clinker materials

1 Introduction

Lime in the sugar industry is obtained by firing limestone in mine kilns. The chemical and fractional composition of limestone must meet the technical conditions of “Limestone for the sugar industry” [1]. The content of calcium carbonate in limestone

should be not less than 93% by weight of dry limestone, so impurities in limestone should be no more than 7% [2]. Lime unloaded from the kiln is divided into free lime, consisting of active and inactive calcium oxide and bound. Only active calcium oxide is used in the technological process - lime, which reacts with water during quenching, turning into calcium hydroxide [3]. Anything that does not react with water during quenching must be removed by cleaning the aqueous-lime suspension from impurities [4].

Thus, the inactive lime as a part of the free lime is the sum of coarse-grained low-activity calcium oxide, which is slugged with films of bound lime [5]. Inactive lime can be converted to active by grinding. But the typical technological scheme of preparation of water-lime suspension in sugar factories does not provide grinding, so inactive lime and bound lime is removed from the water-lime suspension during purification from impurities, making irreversible losses of CaO for sugar production [6]. It should be noted that fine fractions of lime react especially actively with limestone impurities [7].

Coarse-grained recrystallized lime and bound lime are commonly referred to as calcination. It is clear that the burn, which reacts extremely slowly with water even at a temperature of 80–90 °C, is removed by cleaning the aqueous-lime suspension, taking with it most of the potentially active CaO. The amount of this lime at a firing temperature greater than 1350 °C can reach 20% of the mass of total lime [8].

2 Literature Review

The physicochemical properties of the water-lime suspension can be influenced in such ways as using various additives in the preparation of water-lime suspension, devices - dispersants and others [9]. In sugar production, a separate direction of improving the quality of water-lime suspension - activation of water-lime suspension, ie technical measures (or a set of technical measures) used in the preparation of water-lime suspension to improve its technological value [10].

Under the activity of the aqueous-lime suspension means the percentage of lime in the form of calcium hydroxide in the entire lime-containing component of the aqueous-lime suspension [11]. It is believed that the higher the content of Ca(OH)₂ in the entire lime-containing component of the water-lime suspension, the greater its ability to chemically interact with sugars of diffusion juice during preliminary and main defecation and carbon dioxide during saturation [12].

The most well-known methods of activation are:

- mechanical - mechanical dispersion of particles of the extinguishing mass or ready water-lime suspension;
- chemical (reagent) - addition of certain chemicals - dispersants, suspension stabilizers, substances that accelerate quenching, increase the solubility of calcium hydroxide - during quenching of lime or in slaked lime.

The disadvantages of such activation methods are that it is impossible to dispose of potentially active lime contained in impurities [13]. This indicates the feasibility of finding a fundamentally new way to improve the quality of the water-lime suspension, the use of which would eliminate the existing shortcomings [14].

One of the modern directions of development and research of a fundamentally new way to improve the quality of water-lime suspension is the electrohydraulic treatment of water-lime suspension [15].

The electrohydraulic effect is a high-voltage electric discharge in a liquid medium. During the formation of an electric discharge in a liquid, energy is released over a relatively short time [16]. A powerful high-voltage electric pulse with a steep leading edge causes various physical phenomena [17]. In particular - the appearance of ultra-high pulsed hydraulic pressures, electromagnetic radiation in a wide range of frequencies - sometimes to X-ray, cavitation phenomena [18].

The study of the influence of the electrohydraulic effect on the quality of the water-lime suspension will increase its activity, which will lead to an improvement in the effect of purification of juices and savings of limestone and fuel on its firing.

The aim of the work is to develop an electrohydraulic method of activating the water-lime suspension to intensify the processes of purification of beet-sugar production juices. To achieve this goal, it is necessary to solve the following tasks:

- to investigate the effect of electrohydraulic effect on the activity of water-lime suspension;
- to investigate the change in the dispersion of the water-lime suspension at different parameters of electrohydraulic treatment;
- to investigate the influence of the electrohydraulic effect on the activation of bound lime.

3 Research Methodology

Modern generally accepted and special methods of research and analysis of suspensions of water-lime suspension, lime water, distilled and tap water, cement are used in work. The main parameters of the electrohydraulic effect, which we varied in the study, were the discharge voltage and the number of electric discharges [19].

The developed experimental electrohydraulic installation (Fig. 1) consists of the electric discharge chamber 1 and the generator of pulse currents 7.

The cylindrical case of the electric discharge chamber 1 made of stainless steel is established on risers of bed 2 using two lugs 3, on one axis welded to an external surface of electric discharge chamber 1. This allows you to move discharge chamber 1 from a vertical position to a horizontal position without removing it from the risers of frame 2. This design solution provides convenience if necessary, to drain the processed product remaining in the discharge chamber 1 and to wash it. The tightness of the electric discharge chamber 1 is provided by a cover 4 attached to the chamber using a flange connection. In cover 4 is mounted electrically isolated from it, the positive electrode 5. The negative electrode 10 is mounted at the bottom of discharge chamber 1. The interelectrode distance is regulated by the vertical movement of the leg of the negative electrode 10 using a threaded connection. Both electrodes are connected to the pulse current generator 7 using high-voltage cables 6. Pipes 8, 9 are intended for the input and output of the processed product.

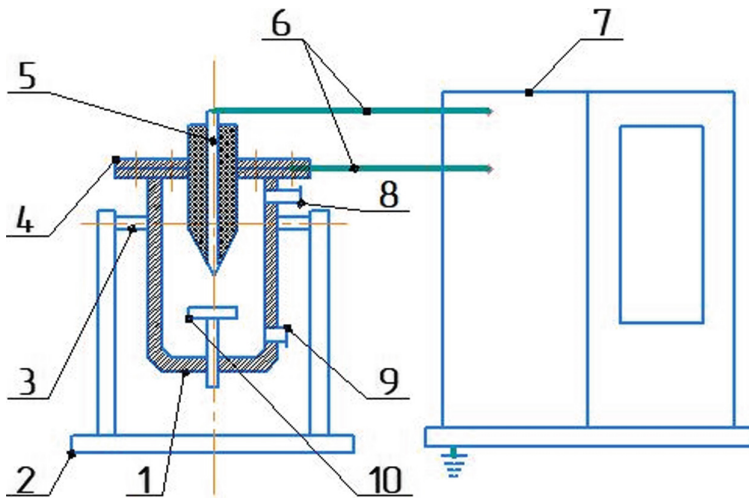


Fig. 1. Schematic diagram of an experimental electrohydraulic installation.

The work uses generally accepted and special methods of research and analysis. In the water-lime suspension before and after electrohydraulic treatment were determined: activity, specific conductivity of the conductometer OK-102/1 company Radelkis, stratification rate and volume of sediment $\text{Ca}(\text{OH})_2$, the solubility of lime in lime water, dispersion and specific surface area Mastersizer, the duration of the activation effect, studied the effect of the electrohydraulic effect on bound lime.

4 Results

For establishing a rational regime of electrohydraulic treatment of water-lime suspension, a broad series of microscopy of preparations of water-lime suspension was treated in different modes. As a result, a rational mode was determined: the discharge voltage in the range of 30 – 45 kV, and the number of discharges with increasing voltage decreases from 15 discharges at 30 kV to 10 discharges at 45 kV.

Figure 2 presents two photographs of the untreated original aqueous-lime suspension. Large and medium-sized calcium hydroxide micelles, as well as single hydrated particles of $\text{Ca}(\text{OH})_2$, are observed on them.

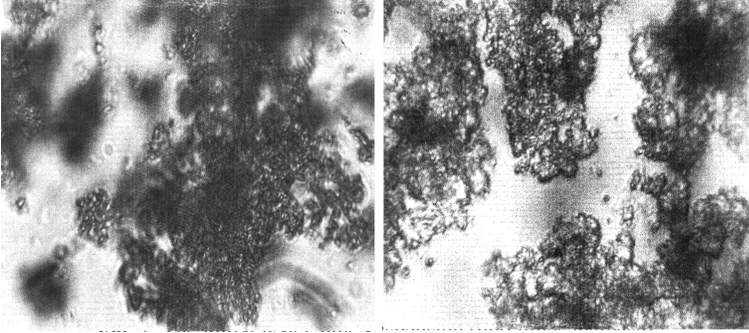


Fig. 2. The initial water-lime suspension (660 times increase).

After electrohydraulic treatment of the water-lime suspension at a voltage of 30 kV with 10 discharges, the micelles are disaggregated, but a number of medium-sized micelles can still be traced (Fig. 3). During electrohydraulic treatment with 15 discharges at the same voltage, the number of single hydrated particles of calcium hydroxide increases, and the micelles that remain intact have a small size (Fig. 4). The disaggregation of agglomerates of calcium hydroxide micelles looks more vivid during electrohydraulic treatment of water-lime suspension with 10 discharges at a voltage of 45 kV (Figs. 5, 6).

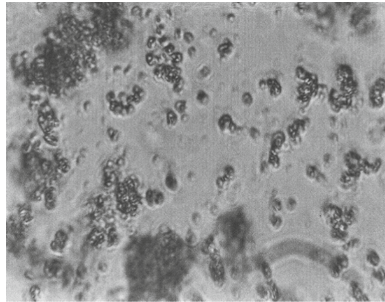


Fig. 3. Lime milk, treated with 10 discharges at a voltage of 30 kV (660 times increase).

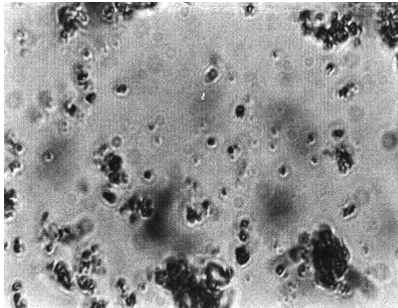


Fig. 4. Lime milk, treated with 15 discharges at a voltage of 30 kV (660 times increase).

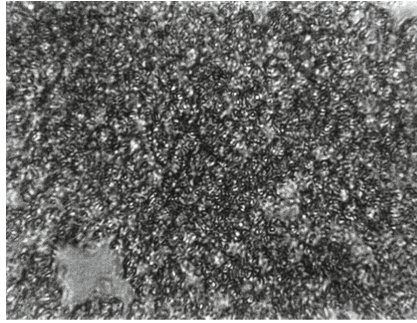


Fig. 5. Final lime milk (660 times increase).

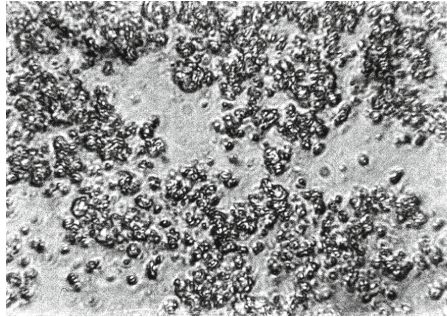


Fig. 6. Lime milk, treated with 10 discharges at a voltage of 45 kV (660 times increase).

Thus, due to the electrohydraulic treatment of the water-lime suspension in the range of specific modes is almost complete disaggregation of agglomerates of micelles of calcium hydroxide.

It is established that in a particular mode of electrohydraulic treatment, the activity of the water-lime suspension increases by 12–14% compared with the activity of the untreated suspension (Table 1).

The increase in the activity of the aqueous-lime suspension can be explained by the fact that there is intense destruction of both lime particles that did not react with water during quenching and the electrohydraulic effect agglomerates of calcium hydroxide micelles to monparticles that react quickly and entirely with acid.

To be sure that in the process of electrohydraulic treatment of water-lime suspension, there is an increase in the dispersion of the solid phase, samples of the suspension were examined for dispersion and specific surface of the solid phase using the device of the German company “Mastersizer μ ” [20].

The water-lime suspension was treated with electrohydraulic discharges in 15 discharges at a voltage of 30 kV and 10 discharges at a voltage of 45 kV.

The obtained graphs of the particle size distribution of the solid phase of the water-lime suspension untreated and treated with electrohydraulic discharges are presented in Fig. 7.

Table 1. Influence of electrohydraulic effect on the activity of water-lime suspension.

	Before processing			After processing					
	CaO _{act} , % suspension mass	CaO _{sum} , % suspension mass	Activity, %	High voltage, kV	Number of discharges	CaO _{act} , % suspension mass	CaO _{sum} , % suspension mass	Activity, %	Activity increase, %
1	15.2	18.2	83.5	30	10	17.4	18.2	95.6	12.1
2	15.0	18.3	82.0	30	10	17.2	18.3	94.0	12.0
3	15.3	18.6	82.2	30	15	17.7	18.6	95.2	13.0
4	15.3	18.5	82.7	45	10	17.9	18.5	96.7	14.0
5	15.1	18.6	81.2	45	15	17.7	18.6	95.2	14.0

According to the obtained data (Fig. 7), the untreated polydisperse water-lime suspension (1) is dominated by particles with a size of 20 μm . The percentage of the fraction of this size in the total volume of the suspension is 67. (2) the percentage of this fraction increases to 77. And when treating aqueous-lime suspension with 10 discharges at a voltage of 45 kV in the entire volume of the suspension is dominated by particles of 14.2 μm , accounting for 80% of the total solid phase (3). This significantly affects the specific surface area of the solid phase, which in the untreated water-lime suspension was 0.311 m^2/g , after treatment with 15 discharges at 30 kV - 0.350 m^2/g , and after treatment with 10 discharges at 45kV - 0.69 m^2/g , i.e., increased compared to the untreated suspension by 2.2 times.

As already mentioned, one of the components of the water-lime suspension is bound lime. Bound lime includes calcium carbonate (CaCO_3), calcium sulfate (CaCO_4), and complex lime compounds with limestone and solid fuel admixtures. These compounds are called clinker minerals and are the products of the high-temperature reaction of CaO with SiO_2 , Al_2O_3 , and Fe_2O_3 . They are always present in lime, but in violation of the firing temperature, their number increases significantly, and the amount of active lime, which binds to complex compounds - clinker minerals, can reach 20 – 25% by weight of the total kiln lime [21]. Clinker minerals react very slowly with water during quenching and are removed with impurities during the purification of water-lime suspension, so the lime, which is part of clinker minerals, is a non-recoverable loss for sugar production. The presence of clinker minerals in lime milk is undesirable from a technological point of view. Therefore, of great interest is the possibility of isolating lime from them during the preparation of water-lime suspension.

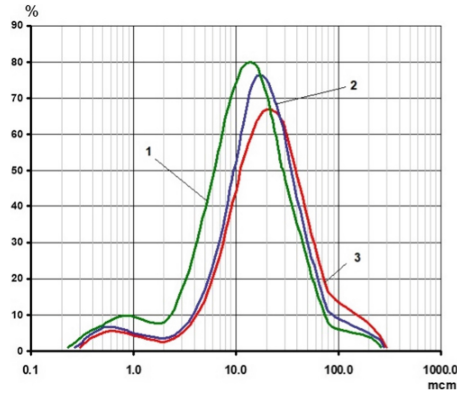


Fig. 7. Changing the dispersion of the solid phase of the water-lime suspension during electrohydraulic treatment depending on the discharge voltage and the number of discharges: 1– untreated water-lime suspension; 2– treated at a voltage of 30 kV and the number of discharges 15; 3– treated at a voltage of 45kV and the number of discharges 10.

It is not possible to obtain bound lime that does not contain free lime in the laboratory. The temperature of formation of clinker minerals: silicates, aluminates, and ferrites of calcium oxide is 1250 – 1500 °C, and they can be obtained only in industrial conditions. An ideal example of a mixture of clinker minerals that do not contain free lime is cement.

We have experimentally determined that the treatment of an aqueous suspension of cement with electrohydraulic discharges accelerates its reaction with water, thereby increasing the content of dissolved lime in water, pH, and specific conductivity of cement water. It was found that the activity of the water-cement suspension immediately after electrohydraulic treatment increases sharply from 21.2% to 29.6%, and then, for another two hours, continues to increase to 34.9%.

The increase in the suspension activity is accompanied by an increase in the pH of the solution from 12.15 to 12.45. The increase in activity is also facilitated by increasing the solubility of lime in water for two hours – from 0.036% to 0.103% of CaO (to the mass of the solution). Consequently, an increase in specific conductivity from 0.415 Cm/m to 0.835 Cm/m This is a consequence of the grinding of particles of cement slurry and the destruction of molecules of complex compounds of clinker minerals with the release of lime in the free state during electrohydraulic treatment.

Externally treated with electrohydraulic discharges, the water-cement suspension had an increased number of gem-like formations, and its solid phase resembles clay silt.

This action of electro-hydraulic discharges makes it possible to release a specific part of the lime, which was in a bound state, thereby disposing of the burn according to the typical technological scheme of preparation of the water-lime suspension is discarded into the dump.

5 Conclusions

The influence of electrohydraulic effect on the properties of water-lime suspension is investigated, and the expediency of its application for activation of water-lime suspension is substantiated. The rational processing mode, which lies within the voltage of 30–45 kV at the number of discharges of 15–10, is determined.

The effect of increasing the activity of the water-lime suspension treated with electrohydraulic discharges in the experimentally determined mode by 12–14% compared with the activity of the untreated suspension was established.

Increasing the dispersion of the solid phase of the aqueous-lime suspension after its treatment increases the specific surface area of the solid phase $\text{Ca}(\text{OH})_2$ in 2.2 times compared to the untreated suspension.

The destructive effect of electrohydraulic discharges on bound lime, which is present in the water-lime suspension, allows to utilize quicklime by 15–20% by weight of total CaO, which is obtained in the lime department of the sugar factory, and this is for sugar production with a capacity of 3000 tons of sugar beet processing per day is 15 - 21 tons of CaO per day.

References

1. Zheplinska, M., Mushtruk, M., Kos, T., et al.: The influence of cavitation effects on the purification processes of beet sugar production juices. *Potravinarstvo Slovak J. Food Sci.* **14**, 451–457 (2020)
2. Marangu, J.M.: Effects of sulfuric acid attack on hydrated calcined clay–limestone cement mortars. *J. Sustain. Cement-Based Mater.* **1**, 1–15 (2020)
3. Rajeswari, M., Seenivasagan, R., Prabhakaran, P., Rajakumar, S., Ayyasamy, P.M.: Lab scale process on the removal of nitrate in ground water enriched with denitrifying bacterium and starch as a sole carbon source. *J. Water Process Eng.* **13**, 189–195 (2016)
4. Machado, P., Steiner, F., Zuffo, A., Machado, R.: Could the supply of boron and zinc improve resistance of potato to early blight? *Potato Res.* **61**(2), 169–182 (2018)
5. Xu, J., Wang, X., Liu, X., Xia, J., Zhang, T., Xiong, P.: Enzymatic in situ saccharification of lignocellulosic biomass in ionic liquids using an ionic liquid-tolerant cellulases. *Biomass Bioenerg.* **93**, 180–186 (2016)
6. Howlader, M., French, W., Shields-Menard, S., Amirsadeghi, M., Green, M., Rai, N.: Microbial cell disruption for improving lipid recovery using pressurized CO₂: role of CO₂ solubility in cell suspension, sugar broth, and spent media. *Biotechnol. Prog.* **33**(3), 737–748 (2017)
7. Carter, C., Saitone, T.L., Schaefer, K.: Managed trade: The US–Mexico sugar suspension agreements. *Canadian J. Econ./Revue Canadienne d'économique* **52**(3), 1195–1222 (2019)
8. Ilyas, R., Sapuan, S., Ibrahim, R., et al.: Effect of sugar palm nanofibrillated cellulose concentrations on morphological, mechanical and physical properties of biodegradable films based on agro-waste sugar palm (*Arenga pinnata* (Wurmb.) Merr) starch. *J. Mater. Res. Technol.* **8**(5), 4819–4830 (2019)
9. Kucher, L.: Forecasting of the impact of acidity on the content of mobile forms of potassium in the soils of forest-steppes of Ukraine. *Polish J. Soil Sci.* **52**(2), 269 (2019)

10. Fernandes, M., Ferro, M., Paulino, A., et al.: Comparative study on hydrolysis and bioethanol production from cardoon and rockrose pretreated by dilute acid hydrolysis. *Ind. Crops Prod.* **111**, 633–641 (2018)
11. Palamarchuk, I., Mushtuk, M., Sukhenko, V., et al.: Modelling of the process of vibromechanical activation of plant raw material hydrolysis for pectin extraction. *Potravinarstvo Slovak J. Food Sci.* **14**, 239–246 (2020)
12. Jung, J.W., Kim, N.S., Jang, S.H., et al.: Production and characterization of recombinant human acid α -glucosidase in transgenic rice cell suspension culture. *J. Biotechnol.* **226**, 44–53 (2016)
13. Langenaeken, N., De Schepper, C., De Schutter, D., Courtin, C.: Different gelatinization characteristics of small and large barley starch granules impact their enzymatic hydrolysis and sugar production during mashing. *Food Chem.* **295**, 138–146 (2019)
14. Corbin, J.M., Kailemia, M.J., Cadieux, C.L., et al.: Purification, characterization, and N-glycosylation of recombinant butyrylcholinesterase from transgenic rice cell suspension cultures. *Biotechnol. Bioeng.* **115**(5), 1301–1310 (2018)
15. Hamouda, R.A., Sherif, S.A., Ghareeb, M.M.: Bioethanol production by various hydrolysis and fermentation processes with micro and macro green algae. *Waste and Biomass Valorization* **9**(9), 1495–1501 (2018)
16. Maslova, O., Stepanov, N., Senko, O., Efremenko, E.: Production of various organic acids from different renewable sources by immobilized cells in the regimes of separate hydrolysis and fermentation (SHF) and simultaneous saccharification and fermentation (SFF). *Biores. Technol.* **272**, 1–9 (2019)
17. Duke, S., Henson, C., Bockelman, H.: Comparisons of Modern US and Canadian Malting Barley Cultivars with Those from Pre-Prohibition: III. Wort Sugar Production during Mashing. *J. Am. Soc. Brewing Chem.* **76**(2), 96–111 (2018).
18. Fox, G.P., Staunton, M., Agnew, E., D'Arcy, B.: Effect of varying starch properties and mashing conditions on wort sugar profiles. *J. Inst. Brew.* **125**(4), 412–421 (2019)
19. Evans, D.E., Fox, G.P.: Comparison of diastatic power enzyme release and persistence during modified institute of brewing 65° C and congress programmed mashes. *J. Am. Soc. Brew. Chem.* **75**(4), 302–311 (2017)
20. Felix, O.E.: Production of malt-based sugar syrup from enzymatic hydrolysis of malted sorghum and millet grains. *Asian Food Sci. J.*, 1–17 (2020)
21. Cheng, M., Huang, H., Dien, B., Singh, V.: The costs of sugar production from different feedstocks and processing technologies. *Biofuels, Bioprod. Biorefin.* **13**(3), 723–739 (2019)

Engineering Education



Implementation of Digital Twins for Industry 4.0 in the Engineering Study Program

Peter Arras¹  and Galyna Tabunshchuk² 

¹ KU Leuven, 5, J. Denayerlaan St., 2860 Sint-Katelijne-Waver, Belgium
peter.arras@kuleuven.be

² National University “Zaporizhzhia Polytechnic”, 64, Zhukovskogo 69063,
Zaporizhzhia, Ukraine

Abstract. In a fast-changing digital era – the characteristic of Industry 4.0, the impact of new technology on mechanical design is tremendous. The use of virtual prototypes to get closer to a first-time-right design is extended to become a real digital twin with the introduction and embedding of IoT from the design stage. Simulations are typically used for design, and in certain cases, offline optimization. Digital twins are used for the entire design-execute-change-decommission lifecycle in real-time. It is the task of engineering education to introduce this technology to students. Due to a combination of many technologies, the challenge is to find an appropriate model for diversity. As a model to cope with the multi-disciplinary character of digital twins from the design stage on, a movable photovoltaic installation with a solar tracker is used. This twin contains the different stages from virtual prototype to digital twin in a setup that can be implemented in a project-based education methodology.

Keywords: Virtual prototype · Digital twin · Solar panel · Solar tracker

1 Introduction

Digitalization in every field of technology is speeding up continuously. The product design and development in the past relied primarily on experience and engineering judgment in producing concept designs. Next physical prototypes were then constructed and tested in order to evaluate the characteristics and compliance to requirements. Without methodologies to evaluate the performance of design in advance, the prototypes were unlikely to meet expectations, so usually, the initial concept had to be re-designed several times to address weaker performance revealed in prototype testing.

Today, manufacturers are under pressure to reduce time to market and optimize products to higher levels of performance and reliability. Methods for easier, quicker, and cheaper design processes like CAD/CAE became common practice. The use of virtual prototypes (VP) – in which engineering simulation software is used to predict product behavior before constructing physical prototypes - allows engineers to explore the performance of multiple design alternatives without investing the time and money required to build physical prototypes.

The next step to better designs is not only using simulation to improve designs, but also by using data generated during the lifespan of a design. Using Internet of Things

(IoT) to collect data from smart products and transmitting in real-time to analyze using big data technology. The introduction and embedding of IoT from the design stage on to make the virtual prototype behave (even) more as the real object converts the VP into a digital twin (DT). DTs are used for the entire design-execute-change-decommission lifecycle in real-time and lead to design optimization based on measured data.

A teaching-by-project approach seems to be the most appropriate method to have engineering students implement the technologies and experience all aspects of the web around the digital twin. Already Confucius (450BC) observed and stated “Tell me and I Will Forget; Show Me and I May Remember; Involve Me and I Will Understand”. These old words have been formalized and proven by pedagogical research and noted down in Dale’s cone of experience [6].

The challenge for education is to incorporate all these new techniques in the study curriculum of engineers. As – from its nature – DT is a multidisciplinary approach combining different technologies and processes, a traditional approach in separate subjects would not be appropriate. Secondly, the study of cases only without implementation by students is also doomed to underestimation or oversimplification of DT technology.

In the literature review, a definition of virtual prototype and digital twin is presented. Next, a model/case study is presented, which is used to teach engineering students in electro-mechanics on the subject of DT.

2 Literature Review

2.1 Virtual Prototype (VP)

In mechanical design, virtual prototypes had become standard practices over the last decades, when after the 1990s design moved away from drawing-centered to model-centered.

Virtual prototyping (VP) is a method in the process of product design. VP involves using computer-aided design (CAD) and computer-aided engineering (CAE) software to validate a design before committing to making a physical prototype. In electro-mechanical design, this is done by creating 3D-computer generated geometrical shapes (parts) and combining them into an “assembly” and subsequent testing different mechanical motions, fit and function, and strength to analyze and optimize (Fig. 1).

A VP contains shape (like in technical drawings or 3D CAD models) and all attributes and properties necessary in the model to become a virtual prototype. This means the system’s material properties and dynamical response are embedded in the model, so it “behaves” like the actual physical system.

After analyzing and optimizing, the design is further detailed and build (development).

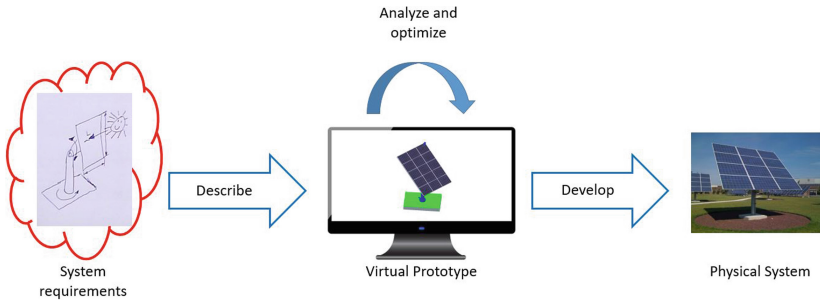


Fig. 1. Virtual prototype.

2.2 Digital Twin (DT)

For the digital twin, there are many definitions. A DT is a digital replica of a living or non-living physical entity [1]. DT refers to a digital replica of potential and actual physical assets (physical twin), processes, people, places, systems, and devices used for various purposes [2]. The digital representation provides both the elements and the dynamics of how an Internet of things (IoT) device operates and lives throughout its life cycle [3]. Digital representations are fully integrated with real-time data exchange between an existing physical object and a digital object in both directions. One might refer to it as Digital Twin [4].

Definitions of DT technology all contain two important characteristics (Fig. 2). Firstly, the connection between the physical model and the corresponding virtual prototype. Secondly, this connection is established by generating and transferring in both directions real-time data using sensors and actuators. The digital twin is a core enabler of autonomy and, therefore, the key to achieving a new level of flexibility in automation systems [5].

DTs integrate IoT, artificial intelligence, machine learning, and software analytics to create dynamic digital simulation models that update and change similar to their physical counterparts. A digital twin continuously learns and updates itself from multiple sources to represent its near real-time status, working condition, or position. A DT also integrates historical data from past usage to update its digital model.

This monitoring and updating of the VP and after design iteration the physical model is called the digital thread of the DT. The digital thread is the whole of IT-related objects and processes that connect the design to the physical model. It contains the sensors and physical connections for the monitoring and measuring of the physical behavior of the model, the control software and algorithms to drive modifications, and the actuators/controlling hardware that can change the state of the physical model.

DT technology is considered a key technology for Industry 4.0. Most of the described examples in the literature deal with process monitoring, with very few with the complete design cycle. DTs are used for different tasks, such as fault diagnosis in photovoltaic installations both on the rooftop and building integrated photovoltaic systems [7], manufacturing assembly systems [8], or autonomous electrical charging stations [9], and entire cities for policy support [10].

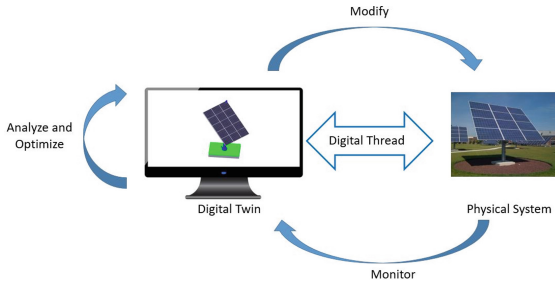


Fig. 2. Digital twin.

DTs are becoming an integral part of the digital transformation that impacts all aspects of life and has a significant impact on the educational system [11]. Students (and teachers) are the future generation of users and responsible for the roll-out of digitalization. It means they need to be trained to conceive, build and maintain digital twins too.

Implementing a DT concept for industrial equipment can also partially solve problems related to hardware unavailability for the remote learning process, which is now very actual with the pandemic situation and improve the professional training quality when the pandemic is over [12].

3 Research Methodology

The challenges on introducing the DT technology from design thinking to a working model and optimization of it into the teaching of engineers are big.

On the one hand, the boundary conditions of teaching students limit a number of key properties and foreseen benefits of the DT-technology: DT technology aims to improve the next generation of the design through the feedback of data generated during the operation of the operation the current design. This is very difficult to achieve in a student environment as students do not have the time nor means to iterate their design. So the challenge is finding a setup that can mimic this optimization.

On the other hand, we want the DT to be part of the total concept in the design life cycle span, so we do not want separate design cases, VP, and DT. Dale [6] showed that the best way to teach students is to experience the methodology themselves.

The model's objectives are that students can design, build, and optimize a virtual prototype and use it as a basis for their own digital twin, in which the feedback and integration of real-time (measuring) data are implemented. Simultaneously, we want to integrate as much as possible from the recognized technologies which enable the making and implementation of a DT (Fig. 3). Integrated technology in this model is circled in Fig. 3 in green and future integration in orange. It shows that the model/case offers all necessary technologies and is still comprehensive enough for students.

The proposed methodology is to implement a course with the theoretical background of the digital twin technology in electro-mechanical systems with case studies and examples of existing digital twins, combined with the design and construction of a

digital twin. Besides the technology, professional skills are integrated into the assignment. Students will work in multi-disciplinary teams of students (mechanical engineers, automation engineers, software engineers), which need much communication and will also need to take care of the information and documentation of the model for the users.

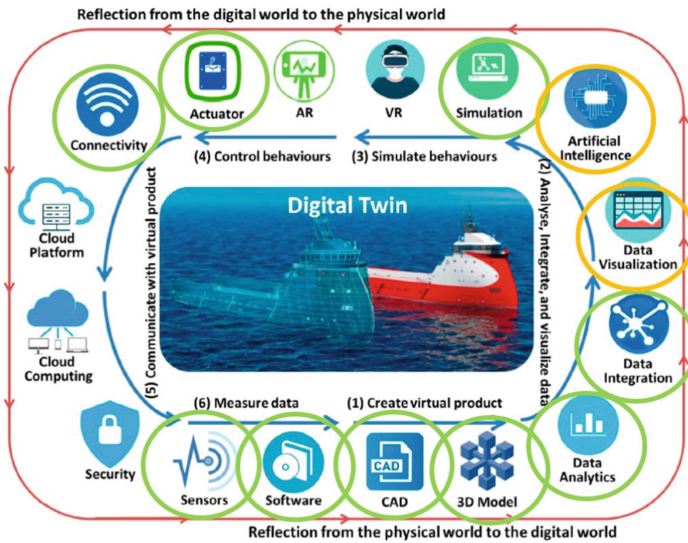


Fig. 3. Enabling technology of digital twin, adapted from [1].

As a case for the student project, we use a moveable solar panel with a control and sensor system (Fig. 4) as this is a comprehensive model, which is also scalable from lab-size to full-blown life-size models. It is also a system for renewable energy, it can serve as a case for courses on sustainability.

In this model, we integrate the following steps and show the course interaction with other courses of the curriculum:

- The making of a virtual prototype as the base for the digital model of the system. It consists of three major parts
 - Make 3D CAD model: interaction with courses on design, mechanical machine components, electrical drives (Fig. 4, arrow 1)
 - Introduce properties and requirements in the CAD model to make it a virtual prototype: interaction with material sciences, mechanics, dynamics (Fig. 4, arrow 1)
 - Optimize the model through calculated simulations to have the best possible design: interaction with mechanics, numerical methods as FEA (Finite Elements Analysis), MBA (Multi-body analysis for mechanisms), CFD (Computational Fluid Dynamics). (Fig. 4, arrow 2)

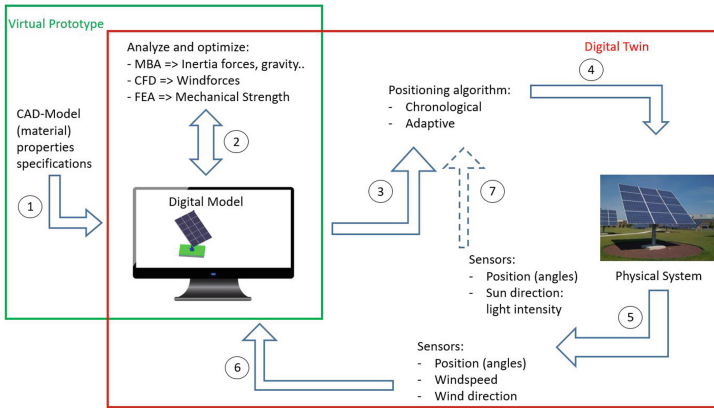


Fig. 4. Digital twin setup.

- Adding control for the positioning of the system:
 - Control position of the real physical system through a control algorithm. The algorithm can be chronological (in which the solar panel is oriented according to its physical position on earth in combination with the calendar) or adaptive (in which the sun is constantly tracked and the panel's orientation is adjusted to be perpendicular to the sun-vector). (Fig. 4, arrow 3, 4). The control algorithm is also fed by the virtual prototype, which could detect dangerous situations from the point of view of structural strength or adjustments and instruct the control to go into safe mode.
 - This part has interaction with courses on control theory, automation technology, and computational methods for the algorithms.
- Making of the digital twin:
 - Instrumentation of the physical system by adding sensors and feedback network (Fig. 4, arrow 5, 6):
 - Sensors for: orientation angles, solar/light intensity detectors, wind speed (anemometer), wind direction (wind vane), temperature, delivered power, deflection of the installation/mechanical loading of the structure (strain gauges), snow detection (optical sensor)
 - Network: wired or wireless connection
- This digital twin incorporates/offers the following possibilities:
 - Feedback from the physical system via the solar/light intensity detectors for adjusting/adapting the orientation control.
 - Data acquisition and analogue/digital conversion on sensor-information.
 - Visualization of data: accumulated power in time.
 - Real-time updates the virtual prototype and recalculate mechanical forces and strength to detect possible dangerous situations (e.g., extreme wind load versus panel orientation).

- Use of big (accumulated) data and possible (future) integration of AI (artificial intelligence)/machine learning: from the interaction between temperature/cooling/cooling energy and delivered power and the accumulated power efficiency, studies can be conducted, and future design improvements can be studied/simulated.

4 Results

At the first stage, the virtual prototype of the solar panel installation has been built in CREO6.0 (PTC). The model consists of the 3D-CAD representation of the installation, including the material properties and requirements.

The model has been calculated to optimize the design towards strength, in which discrete/worst-case scenarios for loads have been implemented. For this, an MBA (Multi-Body Analysis) and FEA (Finite Elements Analysis) have been integrated.

For the digital twin, a feedback loop has been implemented so that the real-time position/orientation of the physical model updates the virtual prototype, i.e., the model reacts on sensor measurements for the orientation, and the CAD model is updated accordingly.

First feedback sensors are the position of the panel (used for the digital twin angles ANGLE_PYLON and ANGLE_PANEL), the wind direction (ANGLE_WIND), and WIND_SPEED (Fig. 5). Feedback information is stored in a CSV-formatted file in which each line contains a time-stamp and the values of each sensor data:

```
Set Name;SENSORS/ANGLE1_GP;SENSORS/ANGLE2_PSP;
SENSORS/ANGLE3_WIND;SENSORS/WIND_SPEED
2020-09-27T07:00:30.126Z;0;0;0;0
2020-09-27T07:00:31.126Z;10;0;0;5
...
2020-09-27T07:00:38.126Z;90;45;40;20
```

The values are next coupled to internal parameters in the digital twin through using an object of the “sensor”-type in the software. These resulting parameters drive the digital twin for positioning using the angles for calculations using the wind speed and angles.

Wind speed results in wind pressure acting on the panel:

$$P = 0.613 \cdot v^2, \quad (1)$$

where v – wind speed, m/s; P – wind pressure, Pa

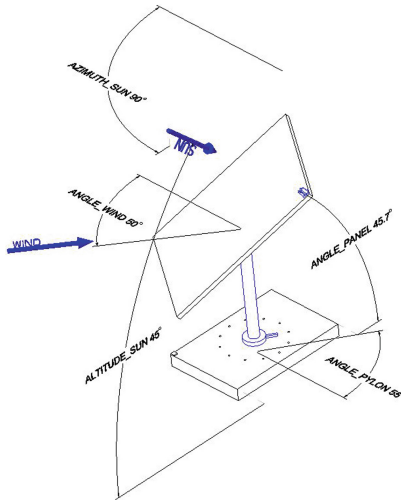


Fig. 5. VP, indicating the angles and current sensor values for the positioning in the figure.

During the design stage, wind speeds are taken from the references. In the feedback stage, wind speed is the measured WIND_SPEED. Generally, wind speed ranges from 0 m/s (no wind) to over 32.6 m/s (in a hurricane). The mentioned wind speeds are mean speeds, averaged over 10 min by convention.

The wind pressure is converted to a wind force to serve as a load in the FEA-strength analysis of the structure:

$$F = A \cdot P \cdot C_d, \tag{2}$$

where A – projected surface (m^2) of the solar panel; P is the wind pressure; C_d – drag coefficient (dimensionless). The projected surface is the surface of the solar panel perpendicular to the wind vector and depends on the wind vector and actual position (PYLON_ANGLE and PANEL_ANGLE).

The drag coefficient is dependent on the actual shape of the element which is hit by the wind. For ease of calculation, we use standard drag coefficients for a cylinder (pylon) of 1,2 and the panel’s flat surface a coefficient of 2,0.

The adaption of the digital twin to the sensor data and the (re)calculations according to the actual data can be seen in Fig. 6.

We have a dual-axis tip-tilt configuration [13], with a vertical and horizontal rotation axis.

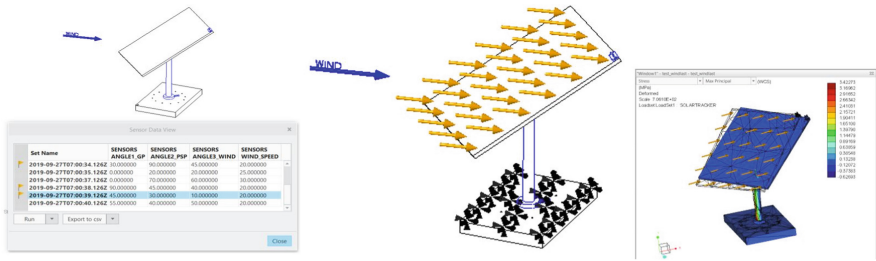


Fig. 6. Update of the positioning of the VT and FEA model and results with the positioning.

The position can also be generated by the control algorithm towards the virtual prototype. Several approaches to the tracking algorithm exist [13–15]. The positioning algorithm functions on a chronological base in the current setup, meaning date, time, and position on the world map determine the panel's orientation. The algorithm is clock-based and does not adapt to solar conditions at each moment. Every day there is a reset towards the predicted ideal orientation. This chronological algorithm is a good and easy basis to start from and be adapted and elaborated in the student project.

5 Conclusions

The proposed model and case study for integrating the digital twin concept from design to the monitoring stage of a real-life construction into engineering studies has proven feasible.

The challenge of making a comprehensive case that is at the same time compact to fit in the available timing of students' curriculum while still containing all technologies enabling digital twins has been realized. The model makes it possible to use a step-by-step introduction from virtual prototype to digital twin and encourages a multi-disciplinary approach between mechanical engineers, automation/electronics engineers, and software engineers.

For future work, there are ample possibilities left in the digital twin of the solar panel towards data visualization and the use of AI (artificial intelligence) to optimize the efficiency of power generation and integration in a cloud-based platform.

Acknowledgment. This work is carried out partly with the support of Erasmus + KA2 project 619034-EPP-1-2020-1-UA-EPPKA2-CBHE-JP “Cross-domain competences for healthy and safe work in the 21st century” (WORK4CE).





References

1. Tao, F., et al.: Digital twin-driven product design framework. *Int. J. Prod. Res.* **57**(12), 3935–3953 (2019). <https://doi.org/10.1080/00207543.2018.1443229>

2. Assawaarakul, C., Srisawat, W., Ayuthaya, S.D.N., Wattanasirichaigoon S.: Integrate digital twin to exist production system for industry 4.0. In: 2019 4th Technology Innovation Management and Engineering Science International Conference (TIMES-iCON). Bangkok, Thailand, pp. 1–5 (2019). <https://doi.org/10.1109/TIMES-iCON47539.2019.9024430>
3. Pires, F., Cachada, A., Barbosa, J., Moreira, A. P., Leitão P.: Digital twin in industry 4.0: technologies, applications and challenges. In: IEEE 17th International Conference on Industrial Informatics (INDIN). Helsinki, Finland, pp. 721–726 (2019). <https://doi.org/10.1109/INDIN41052.2019.8972134>
4. Kritzinger, W., Karner, M., Traar, G., Henjes, J., Sihl, W.: Digital twin in manufacturing: a categorical literature review and classification. *IFAC-PapersOnLine* **51**(11), 1016–1022 (2018)
5. Rosen, R., et al.: About the importance of the autonomy and digital twins for the future of manufacturing. *IFAC-PapersOnLine* **48–3**, 567–572 (2015)
6. Dale, E.: *Audio-Visual Methods in Teaching*. Dryden Press, New York (1969)
7. Jain, P., Poon, J., Singh, J.P., Spanos, C., Sanders, S.R., Panda S.K.: A digital twin approach for fault diagnosis in distributed photovoltaic systems. *IEEE Trans. Power Electron.* **35**(1), 940–956 (2020). <https://doi.org/10.1109/TPEL.2019.2911594>
8. Arras, P., Tabunshchik, G., Korotunov, S., Okhmak, V.: Modeling and simulation of the services for vehicle charging infrastructure interaction. In: 10th IEEE International Conference on Intelligent Data Acquisition and Advanced Computing Systems: Technology and Applications (IDAACS). Metz, France, pp. 330–333 (2019). <https://doi.org/10.1109/IDAACS.2019.8924449>
9. Židek, K., Piteř, J., Adámek, M., Lazorík, P., Hořovský, A.: Digital twin of experimental smart manufacturing assembly system for industry 4.0 concept. *Sustainability* **12**(9), 3658 (2020). <https://doi.org/10.3390/su12093658>
10. Dembski, F., Wössner, U., Letzgus, M., Ruddat, M., Yamu, C.: Urban digital twins for smart cities and citizens. *Sustainability* **12**, 2307 (2020). <https://doi.org/10.3390/su12062307>
11. Saracco, R.: Digital twins: bridging physical space and cyberspace. *Computer* **52**(12), 58–64 (2019). <https://doi.org/10.1109/MC.2019.2942803>
12. Rassudov, L., Korunets, A.: COVID-19 pandemic challenges for engineering education. In: 2020 XI International Conference on Electrical Power Drive Systems (ICEPDS). Saint Petersburg, Russia, pp. 1–3 (2020). <https://doi.org/10.1109/ICEPDS47235.2020.9249285>
13. Hafez, A.Z., Yousef, A.M., Harag, N.M.: Solar tracking systems: technologies and trackers drive types – a review. *Renew. Sustain. Energy Rev.* **91**, 754–782 (2018). <https://doi.org/10.1016/j.rser.2018.03.094>
14. Tharamuttam, J.K., Ng, A.K.: Design and development of an automatic solar tracker. *Energy Procedia* **143**, 629–634 (2017). <https://doi.org/10.1016/j.egypro.2017.12.738>
15. Mane, S.G., Korachagaon, I., Hans, M.R., Sawant, A.S.: Simulation of dual axis solar tracking system. In: International Conference on Information, Communication, Engineering and Technology (ICICET). Pune, pp. 1–5 (2018). <https://doi.org/10.1109/ICICET.2018.8533760>



The Technology of the Learning Outcomes Test Development

Petro Luzan¹ , Oleksandr Koshuk¹ , Olena Titova² ,
and Iryna Mosia¹ 

¹ Institute of Vocational Education of the National Academy of Pedagogical Sciences of Ukraine, 98a, Vito-Lithuanian Lane, Kyiv 03045, Ukraine

² Dmytro Motornyi Tavria State Agrotechnological University,
18, B. Khmelnitsky Ave., Melitopol 72310, Ukraine
olena.titova@tsatu.edu.ua

Abstract. The paper presents the technology for developing a test of learning outcomes applied to engineering students. Considering the evidence, which reflected the practice of learning outcomes testing and tests development, the need to study the problem was revealed. There was a lack of scientifically based recommendations that allow designing valid and reliable assessment tools for the learning outcomes diagnostics under competency-based education. The finding of the current research was formed as a technology of the test development. The substantiated technology included four phases: organization and preparation, design and expertize reflection and diagnostics, and final technological phase. Each phase involved certain stages. The proposed diagnostic procedures made it possible to design valid tests that met the quality criteria in examining the level of learning outcomes for engineering students. When the test developer adheres strictly to the reasonable testing phases, they obtain an algorithm for creating a valid test item, which could be accumulated in a test database and then used to design tests. Following the technology stages, an educator/examiner/test developer could design, justify and evaluate the test item according to a scientific basis rather than their intuition. That enables objective and reliable results of student's achievements testing.

Keywords: Learning outcomes · Test · Engineering students · Assessment · Evaluation · Validity · Test items

1 Introduction

Testing and evaluating in higher engineering education are the most important means of motivating and stimulating students' cognitive learning activities. The objects of testing in competency-based learning are knowledge, skills, attitudes, and beliefs, the relationships between things, ability and skills to apply the acquired knowledge in practice, experience of creative activity, values, etc. The results of the analysis of the scientific sources gave grounds to assert that in the available scientific papers. There was no unity in scientists' opinions on the approaches to developing objective, valid, reliable methods, forms, and technologies for assessing students' competence.

Teaching practice also needed thorough methodological developments as usual methods and forms of knowledge testing that have been used for years to appear to be extremely limited for assessing students' competence and achievements.

This situation required changes in the system of monitoring student's achievements, designing and applying objective diagnostic techniques, and studying didactic problems related to various aspects in the development and application of methods for learning outcomes assessment. Investigating the methodological aspects of skills and abilities testing for engineering students is significantly important and expedient. They were considered while designing test development technology to guarantee the possibility for the educator/examiner to perform objective and reliable results of student's achievements.

2 Literature Review

The analysis of the published research on test design and application enabled the investigation of those issues, which are being investigated recently. The researchers have studied the aspects of different methods of student achievement assessment and test effectiveness [1, 2], the opportunities and obstacles of the process of test development and application [3, 4], as well as the questions of suitable assessments of such skills as professional knowledge, critical thinking, and problem-solving [5, 6]. The problem of a test and testing results validation has been considered and the analysis of existing approaches [7, 8].

Despite the obvious effect of the scientific approach to assessing learning outcomes in higher education [9], nowadays, there is a lack of methodological recommendations for the test development procedure to create valid assessment tools. There is also a need to develop a scientific base for conducting and evaluating test results under the conditions of educational digitalization [10] and forced-choice of distance learning as feasible during quarantine periods.

In addition, there are noticeable differences in the views of scientists on the principles and approaches to creating test items of different levels and tests in general. Other aspects under consideration were the technology of test creating and differentiation of test items by degree of complexity. These issues prevent the effective use of a test as a method of objective measurement of student's learning outcomes and actualize the study of the problem connected with educational test designing.

The purpose of the study was to substantiate the technology of testing as a valid method of assessment and evaluation of students' learning outcomes. Some advanced theories of didactic measurements became the base for the substantiation. To achieve the goal, the following tasks were planned: to substantiate some characteristics of the students' learning outcomes testing, describe the phases and stages of the test development technology, present the method of designing different test items, summarize the results in the form of a structural and logical diagram.

3 Research Methodology

To solve the research goals, a set of theoretical and empirical methods was used. Theoretical approaches included analysis of scientific sources (dissertations, conference proceedings, periodicals, philosophical, psychological, pedagogical, methodological literature) and regulations (laws, standards, acts, concepts) to study the state of the problem and analyze existing solutions. The comparison was used to compare approaches and identify the leading ideas and directions of scientific solutions. Synthesis was applied at the stage of substantiation of the theoretical base for the technology. Generalization enabled the formulation of conclusions. Empirical methods included questionnaires, observation of participants in the pedagogical process, interviews of students and teachers to reveal any difficulties and limitations connected with an objective and reliable assessment of student's learning achievements.

We would note the advantages of testing compared to empirical (traditional customary) ways to monitor student's learning outcomes. Firstly, properly organized testing allows checking a much larger amount of knowledge than traditional methods of control. In some cases, the test enables checking the entire amount of educational results provided by the curriculum. Secondly, a teacher can test the learning outcomes at a certain stage of the course. For this purpose, the test includes items of a certain type. They allow using a scientific basis to check the mastery of educational material in a certain period rather than perform it intuitively [11]. Thirdly, tests do not have established shortcomings inherent in traditional methods of control (subjectivity of assessment, inability to restore results, relatively small amount of verification of the content of educational material, different complexity of tasks given to students to determine their level of mastering, different number, and volume of additional questions, etc.).

It should be emphasized that during testing, we have the opportunity to deal simultaneously with a significant number of students. Online testing immediately provides a score for the student after completing the test. There is a possibility to repeat the test conditions several times to find out changes in the level of students' mastering. Considering the results of the scientific works analysis [11], we assume that the testing technology is a model of pedagogical activity that reflects the procedure for implementing and formulating assessment goals, creating sets of test items, testing itself, and evaluating testing results. When certain requirements are met, they provide scientifically based and objective results in determining the student's achievements. The technology presented could be applied to design tests in all the engineering subjects, e.g., Farm Machines, Mechatronic Systems, Hydraulic Drive, etc.

4 Results

After that, we directly described each phase and stage in designing testing methods, verifying and evaluating learning outcomes.

The I Phase (Organization and Preparation)

Stage 1. Definition of the testing purpose and objectives. The purpose and objectives of testing depend primarily on the type of control. In particular, the preliminary examination (diagnostic testing) assesses the level and structure of students' readiness to master a new discipline. During ongoing monitoring (formative testing), tests are used to gauge student learning and obtain operational data on the level of students' knowledge to organize effective management of the educational process. The control at the end of the learning module (benchmark testing) involves identifying and evaluating the results of learning a particular module as a completed part of the curriculum. Summative testing aims to identify the system and structure of students' knowledge for a long period of study (semester, academic year, etc.).

Stage 2. Structuring the content of learning materials or compiling a register of knowledge elements. When structuring the content of learning materials, it is advisable to use the educational and professional programs and the curriculum. Firstly, it is necessary to single out the most important educational outcomes from the list of ones that students should master according to the standard. Then they need to be structured into groups [12]. The group C (concept) includes categories, terms, concepts, designations, P (phenomena) has properties, phenomena, facts, observations, descriptions of technical objects, mechanisms, etc., R (relations) are made up with relations, theorems, laws, rules, theories, models, structures, etc., A (algorithms) consists of algorithms of activity (problem-solving, proof of theorems, etc.), sequence of actions, procedures, rules of decision-making, etc. Sometimes it is advisable to determine the structure of the learning content and use such structuring of the material to identify typical groups of learning components. If the content of learning material is difficult to structure, it is recommended to compile a register of learning elements [11, 13].

Stage 3. Choosing the type of test items. There are main requirements for designing test items. Firstly, a student can perceive the task content immediately after the first reading. Secondly, the content of the task should be limited to 7 ± 2 portions of information because a person can keep in short-term memory just that number of elements. Thirdly, the test item should be based on a true statement (it is not recommended to ask questions about the things which are not used, do not work, do not exist, etc.). Fourthly, in the content of the task, there should be no contradictory opinions or statements. Finally, it is desirable to provide, if necessary, only mental arithmetic. There are two types of items in pedagogical tests: tasks with free answers (open); tasks with given alternatives (closed). Open items include a completion type (a fill-in-the-blank). The fill-in-the-blank item offers the student to enter a word, a number, or formula using the keyboard (or writing it down on paper). There are some examples.

1. A kind of valve at a certain current rapidly reduces the resistance and passes the current further (from the collector to the emitter) is

The key is a transistor.

Another variant of the item includes listing when the student is offered to list components, properties, characteristics of the object required in the task. The example is:

2. Name three main elements of the simplest electrical circuit:

1 _____; 2 _____; 3 _____.

The key is the source of electric energy, electric energy receiver, connecting wires.

Closed items consist of instructions and a list of possible answers or the elements used by the student to choose or compose the correct answer. Items with given variants of answers are divided into single-alphabetic, double- and multi-alphabetic. One-alphabetic tasks (multiple choice) contain questions or conditions of the problem and one list of possible answers or their elements used to choose the correct answer (Fig. 1).

The diagram shows a test item structure with four numbered components:

- 1**: Choose the correct option(s). More than one option can be chosen.
- 2**: Which devices can be used to measure electrical resistance:
- 3**: A list of options:
 - 1 Ammeter
 - 2 Voltmeter
 - 3 Wattmeter
 - 4 Ohmmeter
 - 5 Webermeter
 - 6 Megohmmeter
 - 7 Faradometer
 - 8 Frequency meter
- 4**: Correct answer: 4, 6.

Fig. 1. The main elements of a single-alphabetic (multiple choice) test item 1 is instructions, 2 is a task, 3 is options, 4 is a key (may be given after the student’s choice)

The peculiarity of a single-alphabetic (multiple choice) test item is that it contains both correct and incorrect answers. The incorrect answers (distractors) must be homogeneous to show the same properties and belong to the same category as the correct answer. Tasks for restoring the sequence of answers include a question or a condition of the problem and a list of answer options that the student must arrange in a clearly defined sequence, for example:

Establish the correct sequence of stages for the metallurgical process:

- 1 Steel smelting
- 2 Cast iron smelting
- 3 Ingots getting
- 4 Preparation of iron ore
- 5 Production of rolled metal

The key is 4, 2, 3, 1, 5.

A variety of the items above are selective and organizational tasks, which offer the student to choose the correct answers and arrange them in a clearly defined sequence. Matching type of the items is used when there is a clear pairwise correspondence between the elements of two alphabets (lists) such as names of the elements and their

designations in drawings or diagrams, names of objects in different languages, words, and their synonyms, etc.

In addition to the methodology for selecting the test items, it is needed to note that the test should contain items of all types and meet the basic requirement: the test should represent the amount of learning outcomes that must be checked.

The II Phase (Design and Expertize)

Stage 4. Development of items sets and test construction. The length of the test (the number of the items) should be enough to cover all the important issues of the learning subject (concepts, laws, patterns, hypotheses, facts, structural components of the theory, methods of practice, etc.). According to this indicator, there are short tests (10–20 test items), medium tests (20–500 items), and long ones (500 and more items). During the experimental work, we proved the validity of the opinions [12, 13], that the optimal number of tasks in testing, which lasts 30 min, should be 30–60 items.

At this stage of substantiation of testing technology for assessing engineering students' learning achievements, it is expedient to consider the difficulty of test items. Scientific and methodological sources give various recommendations for solving this problem. In particular, V. Avanesov [13] offers the following component layout: half of the items in the set should be the lowest level of difficulty (familiarization and orientation level: awareness about elements, including categories, terms, concepts, names, properties, phenomena, facts, description of objects, mechanisms, etc.); a third of testing tasks are designed to check the awareness of a higher conceptual and analytical level (knowledge of basic relations, theorems, laws, concepts, rules, hypotheses, theories, models, analytical, graphical, logical dependencies, structures); the rest of the tasks in the set are to be of the highest level of difficulty (a productive and synthetic level which shows the ability to use in practice algorithms of activity, in particular, algorithms for solving problems, proving theorems, procedures, rules of decision making, behavior, etc.).

Stage 5. Expert assessment of tests by teachers. During the experimental research, the evaluation of the qualitative characteristics, the correctness of the formulation of the conditions of test items, the accuracy of formulation of the test, in general, involves teachers (experts) who have teaching experience in certain disciplines. The experts are given reminders of defects, which could occur in test items. The defects include semantic difficulty, grammatical and logical hints, long (noticeable) correct answers, repetition of words, the tendency to convergence, etc. The stage is planned to eliminate errors and inaccuracies of wording. In addition, teachers passing the tests must time their work. The experts' answers are compared with the etalon. Some adjustments to the content of the test are made according to the recommendations of the experts.

Stage 6. Checking the test on a control sample of students. To obtain statistically significant results in control testing, the following conditions must be met [13]: control testing should be conducted in several parallel groups, at least twice, on different days and with varying options of the test, there must be at least 20 people in each group, the same conditions of control testing should be provided in all groups (time, place, duration of inspection), all respondents should receive approximately the same difficulty test items, it is advisable to perform the testing using special software.

Stage 7. Analysis of the control testing results. To properly evaluate the results of the control testing, it is necessary to determine the evaluation methodology. There are several approaches to the evaluation of testing results. They are described in detail in the works [6, 13, 14]. The technology of assessment of the test items is based on the following requirements [13]: if the task is solved correctly, the student receives 1 point, if at least one of all the correct options is not marked, or, in addition to the correct ones, at least one incorrect option is added, 0 points are scored.

Phase III (Reflection and Diagnostics).

Stage 8. Selection of valid test items for the basic set. The validity of a test is considered to be a complex concept [14]. It includes the validity of the toolkit (validity of a test item, the validity of the test), the validity of the method (content validity, validity of compliance), the validity of testing and evaluation procedures. The test validity indicates the test measures and how well they do that [14, 15]. Considering this, the validity of test items is determined based on such characteristics as difficulty (level of information assimilation, according to B. Bloom's taxonomy [16, 17]), distributiveness (ability to distinguish students with different levels of knowledge with sufficient accuracy).

Stage 9. Compilation of the final test. To complete a test of 30–60 items, which make up the test length, are selected from the base of test items. Together they reflect the content of the discipline, module, rubric, etc. The tasks are arranged to meet the requirements. Firstly, inhomogeneous tests constructed for a separate discipline or a module, the difficulty must increase. Secondly, in heterogeneous tests, made up of several disciplines, the items are placed in a spiral; when the test is first completed with the easiest tasks, then the next level of difficulty goes. When compiling the summative test, it is important to agree on two conditions: to cover the content of learning material with a set of multi-level tasks entirely and to adhere to the terms of testing.

Stage 10. Preliminary test quality control. To pre-check the quality of the test, it is necessary to involve students (80–100 people) who have already mastered the discipline. Students' actions are timed, and the time required for testing is determined. In addition, the resolution of the tasks is checked again, in particular, the tasks answered by less than 5% of students. We recommend using the Powell optimization method. Alternative methods by Polak Ribière and Fletcher Reeves were also tested. The conclusion about a greater error was made.

Stage 11. Evaluation of the validity and reliability of the test. The validity of the test is assessed experimentally. To do this, a group of students (at least 50 people) consistently passes two types of testing: test items and written testing on the issues that reflect the test items' content. If the distribution of the students' scores after those two control measures coincides with the significance level of 0.05, the test is considered to be valid. The reliability of the test is related to the accuracy of measuring the level of student achievements. Among the variety of ways to determine this indicator, the simplest, in our opinion, is to calculate the Pearson correlation coefficient between the results of repeated trials of the same test in the same group (at least 50 people). If the correlation coefficient value is more than 0.7, the reliability of the test is considered sufficient.

The IV Phase (Final Technological)

Stage 12. Testing. The testing procedure also affects the validity of the method for objective assessment of learning outcomes. It should be noted that testing involves compliance with certain psychological requirements [18]. It is also important to follow the rules: the student must be sure that the exam with test items is more objective than an oral examination or a written test, the student must be warned that he can perform the tasks in any sequence convenient for him, when testing, students should be alerted about the limited time, it is necessary to adhere to confidentiality of testing, before the testing, students should be informed about the low probability of random guessing, it is essential to reduce terms of the score calculations as much as possible [7, 19].

Stage 13. Evaluation of testing results. According to B. Bloom's Taxonomy of Educational Objectives [16, 17], the level of knowledge is the lowest level of the cognitive domain. At this level, the quality of assimilation of concepts, facts, principles, methods, design features, technical characteristics, etc., is checked through the test. At the level of comprehension (the second level of the taxonomy), the possession of knowledge is tested, and the ability to explain facts, approaches, principles, interpret the material in a certain way, and carry out its transformation. To test the results on these levels, it is advisable to use multiple choice and matching test items types. The tasks for restoring the sequence are used to assess the levels of analysis and synthesis.

Such levels of knowledge as evaluation and creation are extremely difficult to assess using a test. There can be no single answer, so the problem should be solved in different ways. Therefore, the test method should be combined with other methods, such as a written (essay), calculation and graphic tasks, projects, or creativity tests [20].

5 Conclusions

The proposed technology of test development makes it possible to carry out valid test items that meet the quality criteria in determining the levels of student's learning outcomes and achievements. Thus, when test developers use a scientific approach, they have an opportunity to create a database of diverse test items, construct a valid test, conduct testing and evaluation procedures, and obtain objective, reliable results while testing engineering students. The technology for test development includes four phases (organization and preparation, design and expertize reflection and diagnostics, and final technological phase) realized in thirteen stages that describe the whole procedure starting from the definition of the testing purpose and objectives students' testing results.

Further scientific research on valid test development could be devoted to developing a system and instruments for assessing the quality of professional engineering education. Moreover, such issues as the objectivity of the student's outcomes assessment and the influence of the number of questions, their complexity, response time, etc., on the objectivity of testing require additional study.






References

1. Baird, J.A., Andrich, D., Hopfenbeck, T.N., Stobart, G.: Assessment and learning: fields apart? *Assess. Educ. Principles Policy Pract.* **24**(3), 317–350 (2017). <https://doi.org/10.1080/0969594X.2017.1319337>
2. Brown, G.T.L.: *Assessment of Student Achievement*. Routledge (2018)
3. Spiel, C., Schober, B.: Challenges for evaluation in higher education: entrance examinations and beyond: the sample case of medical education. In: Zlatkin-Troitschanskaia, O., Toepper, M., Pant, H., Lautenbach, C., Kuhn, C. (eds.) *Assessment of learning outcomes in higher education. Cross-national comparisons and perspectives*, pp. 59–71. Springer, Cham (2018). https://doi.org/10.1007/978-3-319-74338-7_4
4. Walstad, W.B., Wagner, J.: The disaggregation of value-added test scores to assess learning outcomes in economics courses. *J. Econ. Educ.* **47**(2), 121–131 (2016)
5. Sosnytska, N., Titova, O., Symonenko, S., Kravets, O.: Examining the creative potential of engineering students. In: Nadykto, V. (ed.) *Modern Development Paths of Agricultural Production*, pp. 299–306. Springer, Cham (2019). https://doi.org/10.1007/978-3-030-14918-5_31
6. Nagel, M.T., Zlatkin-Troitschanskaia, O., Schmidt, S., Beck, K.: Performance assessment of generic and domain-specific skills in higher education economics. In: Zlatkin-Troitschanskaia, O., Pant, H., Toepper, M., Lautenbach, C. (eds.) *Student Learning in German Higher Education*, pp. 281–299. Springer, Wiesbaden (2020). https://doi.org/10.1007/978-3-658-27886-1_14
7. Kadriye, E., Pellegrino, J.W.: *Validation of Score Meaning for the Next Generation of Assessments: The Use of Response Processes*. Taylor & Francis (2017)
8. Butler, A.: Repeated testing produces superior transfer of learning relative to repeated studying. *J. Exp. Psychol. Learn. Mem. Cogn.* **36**, 1118–1133 (2010)
9. Firman, F., Baedhowi, B., Murtini, W.: The effectiveness of the scientific approach to improve student learning outcomes. *Int. J. Active Learn.* **3**(2), 86–91 (2018)
10. Mahalanabis, A.: *Theory and Application of Digital Control*. Elsevier Science (2014)
11. Wasilev, I.: On the possibility of using multirange scales in the process of professional training of future workers. *Challenges Eng. Pedagogical Educ.* **6**, 86–93 (2004)
12. Gierl, M., Bulut, O., Zhang, X.: Using computerized formative testing to support personalized learning in higher education: an application of two assessment technologies. In: Zheng, R. (eds.) *Digital Technologies and Instructional Design for Personalized Learning*, pp. 99–119. IGI Global (2018). <https://doi.org/10.4018/978-1-5225-3940-7.ch005>
13. Avanesov, V.: *Composition of Test Tasks*. Testing Center, Moscow (2002)
14. McLean, S., Kramer, B., Beglar, D.: The creation and validation of a listening vocabulary levels test. *Lang. Teach. Res.* **19**(6), 741–760 (2015). <https://doi.org/10.1177/1362168814567889>
15. Cranney, J., Ahn, M., McKinnon, R., Morris, S., Watts, K.: The testing effect, collaborative learning, and retrieval-induced facilitation in a classroom setting. *Eur. J. Cogn. Psychol.* **21**(6), 919–940 (2009). <https://doi.org/10.1080/09541440802413505>
16. Bloom, B.S., Engelhart, M.D., Furst, E.J., Hill, W.H., Krathwohl, D.R.: *Taxonomy of Educational Objectives: The Classification of Educational Goals. Handbook I: Cognitive Domain*. David McKay Company (1956)
17. Anderson, L.W., Krathwohl, D.: *A taxonomy for learning, teaching, and assessing: a revision of Bloom’s taxonomy of educational objectives*. Longman (2001)

18. Sorrel, M.A., Barrada, J.R., de la Torre, J., Abad, F.J.: Adapting cognitive diagnosis computerized adaptive testing item selection rules to traditional item response theory. *PLoS ONE* **15**(1), e0227196 (2020). <https://doi.org/10.1371/journal.pone.0227196>
19. Gierl, M.J., Lai, H., Turner, S.R.: Using automatic item generation to create multiple-choice test items. *Med. Educ.* **46**, 757–765 (2012). <https://doi.org/10.1111/j.1365-2923.2012.04289.x>
20. Titova, O., Sosnytska, N.: The engineer’s creative potential scales. In: 2020 IEEE Problems of Automated Electrodrive. Theory and Practice (PAEP), pp. 1–4. Kremenchuk, Ukraine (2020). <https://doi.org/10.1109/PAEP49887.2020.9240882>



Administrative Fundamentals of Ecological Competence Forming in Agricultural Engineering Students Under Conditions of Their Professional Training

Viktor Nagayev¹  , Iryna Danchenko¹ ,
Tetiana Mitiashkina¹ , and Vecheslav Kyrepin² 

¹ Kharkiv Petro Vasylenko National Technical University of Agriculture,
44, Alchevskih St, Kharkiv 61002, Ukraine
² Mykolayiv National Agrarian University,
9, Georgy Gongadze St., Mykolaiv 54020, Ukraine

Abstract. The purpose of the article is to study the problem of the formation of ecological competence of future agricultural engineers based on modeling the content of professional training as a holistic pedagogical process of managing students' learning activities. Theoretical and empirical methods (monographic analysis, synthesis, modeling, forecasting) were used in the research. The model for ecological competence forming of future agricultural engineers was presented as a semantic network. The requirements of educational qualification descriptors were the initial points for the model. The finishing point was an aggregate of criteria of professional competence. Experimental research was conducted based on the Kharkiv Petro Vasylenko National Technical University of Agriculture on the example of educational disciplines that formed future specialists' professional competence at a bachelor and master levels in Agricultural Engineering. Research results confirmed the adequacy of the model for the process of ecological competence forming in agricultural engineering students during their professional education. Realization of the model for the process of ecological competence forming in future engineers of agrarian sphere provided visualization of pedagogical conditions for didactic processes activation and organizational and technological algorithms under the conditions of management, co-management, and self-management of students' learning. As a result, the quality of professional training has increased. The practical significance of the obtained results lies in the possibility of applying the proposed management model in the educational process of higher education institutions in the process of forming the environmental competence of future engineers in the agricultural sector.

Keywords: Ecological competence · Engineering education · Professional training · Agricultural engineers · Model · Management model

1 Introduction

Today ecological education is defined as one of the basic world civilization priorities in the system of factors for ecologization of all types of human activity. It is considered an independent and urgent problem and an important instrument for ecological processes management, the main lever of improvement in production and consumption, taking into account the possibilities of the biosphere. Ecological competence forming in agricultural engineering students is an obligatory learning outcome in the process of their professional education. The functional providing of engineering processes is closely related to the environment. Agricultural engineers are expected to possess fundamental knowledge both in mechanization and automation of production processes and also in the field of ecological technologies of agroengineering. The necessity of priority change in engineering education is becoming more obvious. The priorities should focus on forming and developing students' ecological thinking and abilities to apply ecological technologies and improve existing ecosystems [1]. We consider the specific functioning of agrarian industry and the necessity of ecological problems solving to enhance environmental quality. In this context, ecological competence forming in agricultural engineering students is one of the actual and near-term tasks for education development [2].

Unfortunately, today, the contradiction between the growing amount of engineering work in the agricultural industry and insufficient engineer ecological competence level is obvious. That requires substantial modernization of the pedagogical system based on the development of innovative didactics methods, forms, and facilities for forming and developing ecological competence of future engineers of the agrarian sphere. At these terms, the pedagogical system of innovative level of education needs the substantial reflection of the newest administrative tendencies in the process of engineering education at the level of technological process of students' ecological competence forming. These aspects require planning organizational and administrative models for engineering education. The models would provide technological achievement of the assured level of ecological competence (EC) of future specialists [3].

2 Literature Review

According to the Determination and Selection of Competencies international project (DeSeCo), the definition of educational competencies is suggested. It considers a general global view of the future, including the most advanced ideas of democratical values and targets connected with balanced development of humanity based on ecology development of a technical process, an environment defense, and economical stability [4].

An ecological competence allows a specialist to solve the ecological safety and safety of labor in production surroundings without harming the environment. Nowadays, an ecological problem refers to the list of global problems of humanity, enthralling after the scales and meaningfulness of all spheres of activity, including agriculture. As a strategic decision of this problem in the 1980s, the International Commission on Environment and Development, which was created by the decision of

the United Nations, offered a conception of sustainable development [5]. The leading role in realizing sustainable development concept is the development of ecological culture by the higher school. It influences significantly on final forming and outlining of the fundamental components of future specialist's world view. It is the period of active formation of the value-semantic sphere of personality and possession of practical methods and requirements of ecological imperative.

The latest positions of the national strategy of education development in Ukraine state that under the conditions of ecological competence forming the educational process must organically connect the professional training with modern technologies of development of ecological thinking by researches in industry of ecological safety and revival of biosphere according to modern terms of digital pedagogics (SMART educational complexes, information, and communication technologies, digital resources, and facilities of activation of cognitive activity of students) [6]. The need to regulate environmental processes on a global and regional scale necessitates the modernization of the content of engineering education and upbringing, which cannot overcome the contradictions between the existing and appropriate level of environmental knowledge.

The solution to this pedagogical problem is possible only if the competence characteristics of the future agricultural engineer will be based on scientifically grounded goals, integration of scientific knowledge, and public demand. Acquisition of ecological competence by prospective engineering personnel of the agrarian branch aims to complete the formation of the ecological culture of specialists. The starting point of higher environmental education is the formation of applicants for high environmental culture, deep environmental knowledge and biosphere worldview, training of bachelors and masters in all areas of environmental, practical, managerial, educational, and scientific activities.

Analysis of recent publications on the topic of the study [7] allows us to identify some general approaches to ensuring the organizational and pedagogical conditions of the process of environmental competence forming in future engineering personnel of the agricultural sector:

- formation of the motivation and value mechanism of assimilation by students of competence characteristics of educational result;
- development of ecological culture and system thinking in future specialists;
- development of models for managing the content of education based on a holistic pedagogical process;
- introduction of computer-oriented systems and information technologies;
- application of innovative learning technologies in the conditions of the distance form of the educational process;
- introduction of student research projects in the field of environmental education;
- intensification of practical training of future engineers in terms of production.

Thus, the analysis of the level of elaboration of the problem of ecological competence forming in future engineers of the agricultural sphere is an actual component of complex research for obtaining high-quality engineering education.

The purpose of the article is to substantiate the model of environmental competence of future agricultural engineers and design an appropriate pedagogical model of

managing the process of environmental competence forming in terms of engineering education.

3 Research Methodology

The study is based on a set of methodological approaches to the formation and development of environmental competence of engineering personnel in the agricultural sector. First of all: competence, system, activity, technological, managerial, personality-oriented, culturological, axiological, and other approaches.

The methodology of the competence approach in the ecological competence formation is connected with the idea of comprehensive development of the future agricultural engineer, training him as an expert and as a person able to solve environmental problems, implement environmental safety measures, and ensure the development of ecological culture. The competence approach is humanitarian in its basis. It aims to form humanistic values, the development of worldview qualities of future professionals, their creativity, and their ability to self-educational activities. The concept of *the competence approach* is interpreted as the focus of the educational process on the formation of competencies (crucial, subject, general professional, special professional) personality. That provides formed general professional competence of the specialist [8, 9].

A high level of achievement of ecological competence requires the use of innovative technologies and didactic models of pedagogical process management. This article proposes introducing a pedagogical model of managing the educational activities of students in the process of ecological competence forming in engineering personnel of the agricultural sector.

The following research methods were used to solve the set tasks: theoretical (aspectual and conceptual-terminological analysis of literature sources, comparative analysis, generalization and systematization of scientific directions and educational programs of engineering specialists); empirical (functional analysis of research results, statistical processing, and data interpretation). The use of a set of methodological approaches and methods allowed to form a didactic management system for the formation of environmental competence of future agricultural engineers, taking into account modern organizational forms and pedagogical technologies to achieve educational results.

4 Results

To determine the component structure of environmental competence of future engineers in the agricultural sector, we consider the integral characteristic of the content of pedagogical activities, professional competence. Competence is an objective category that captures a socially recognized set of a certain level of knowledge, skills, abilities, experience, etc., which can be applied in a wide range of human activities [10]. The professional competence of an agricultural engineer includes such qualities as: technological culture, ecological culture, organizational and managerial culture, the culture

of scientific activity, experience in organizing engineering activities, etc. Each of these groups is based on very specific content primary qualities.

The ecological orientation of society is designed to adapt the theoretical justification of the essence of the transformation of general norms and principles of engineering to the specific conditions of environmental competence forming in specialists. A review of the definitions of the environmental competence concept of [11, 12] allowed us to conclude that this definition does not have a single point of view. The generally accepted point of view is that the essence of environmental competence is based on knowledge, values, inclinations, and acquired experience, which determine a person's ability to solve environmental problems. This concept is considered a higher level of tasks that specialists need to be able to solve, regardless of the profile of training, both from the standpoint of reducing the negative impact on nature and improving the environment.

Studying the cultural aspect of engineering allowed us to conclude that the EC can be considered an independent cultural phenomenon, a form of intercultural interaction, used as a model of moral behavior concerning the biosphere and society [13]. Consideration of the psychological aspect of engineering helped to identify the features of the content of environmental competence as a motivationally conditioned value characteristic of the personality of the agricultural engineer to characterize its phased organization [14]. Based on the analysis of the production aspect, the features of the application of environmental competence in the professional activity of the engineer, forms, and types of its implementation are determined [15]. Taking into account these aspects allowed us to conclude that for effective environmental competence forming, the specialist must have a purposeful system of knowledge, skills, and abilities to use safe technologies in agricultural engineering, experience in using environmentally friendly technologies, high level of environmental culture, motivational and value orientation, demonstrate the ability to self-develop environmental competence.

The previous provisions prove that environmental competence must correspond to specific areas of professional activity of the engineer and have a structural and functional design in the form of a model for the competence of a specialist in terms of training. Based on the aspect analysis, the ecological competence of the future agricultural engineer is defined as the ability of a specialist to successfully implement environmental measures in professional activities, based on systematic knowledge of environmental support of technological processes and methods of implementation, skills, planning experience, organization, motivation, and control over the functioning of the ecological system. It also includes a set of personal qualities that cover the motivation, value, moral and ethical standards of environmental goals. The component structure of the EC is determined based on the philosophical category of *experience*. According to a category, in the process of purposeful assimilation of knowledge about the object and its subsequent transformation, new connections, properties, patterns are opened, new methods and tools are tested, certain value orientations are acquired in the field of organization of ecological activity.

Analysis of the competence approach [16, 17] allowed to determine the components of environmental competence of the future engineer of the agricultural sector and, on this basis, to develop an appropriate model based on the criterion of the formation of environmental experience (Fig. 1).

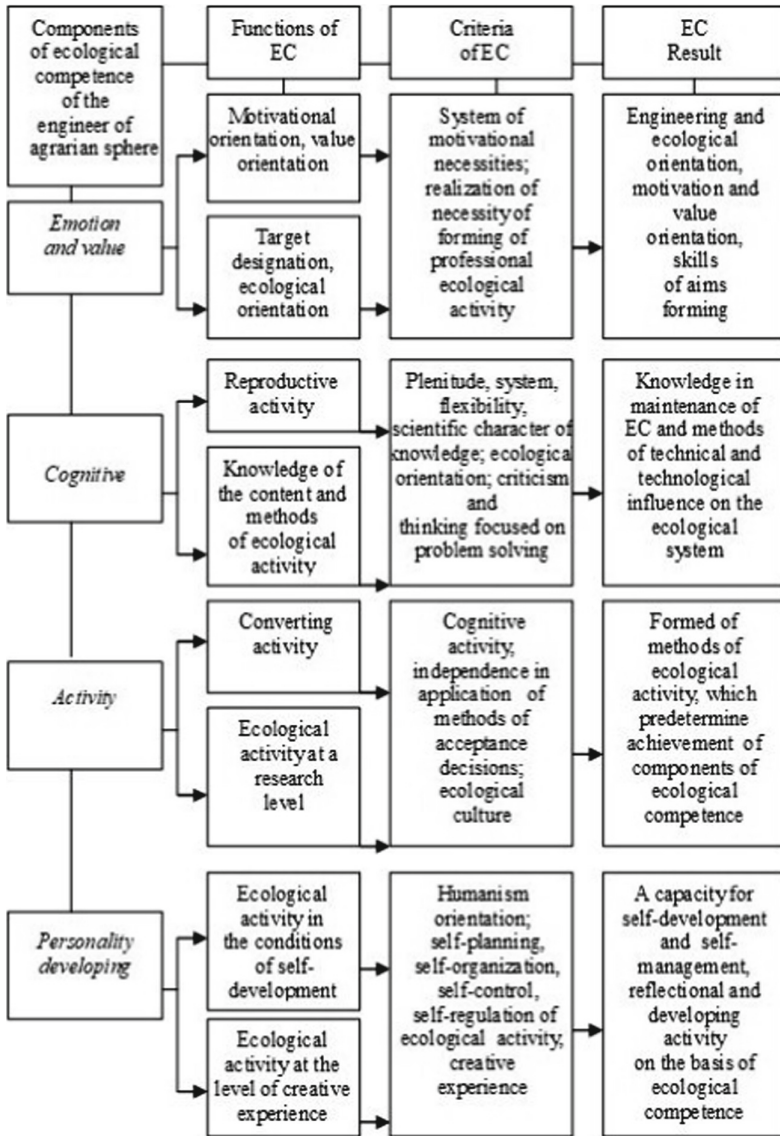


Fig. 1. The model of ecological competence of an agricultural engineer.

We understand the model of ecological competence of the future engineer of the agricultural branch as an integrative structure with the following components: emotional and value (motivational needs, interests, goals, and values of ecological activity); cognitive (completeness, system, flexibility of knowledge, their scientific nature, ethical orientation of knowledge); activity (cognitive activity, creative ecological activity, abilities and skills to apply ecologically safe technologies, to implement innovative projects in the field of ecological safety); personal development (ability to self-

development, skills and abilities to improve the existing ecological system, to design new algorithms for achieving environmental goals in terms of engineering).

The presented model of ecological competence of an agricultural engineer is based on the classical ideals of rationalism, recognition of the omnipotence of the human mind, and scientific comprehensiveness. The model organizes the educational process to achieve the goal through purposeful knowledge of environmental reality within the educational process. It is achieved through knowledge of the laws of nature and society because the determining cause of the ecological crisis is the mismatch between the paths of socio-technical development and the laws of evolution of the biosphere. This model defines the goals and content of environmental activities in the system of engineering training. Considering the state requirements for the professional competence of agricultural engineers, it is possible to offer adequate functional models of agricultural engineers at the level of formation of their environmental competence. The analysis of modern paradigms (knowledge, cultural, humanistic) allowed determining the theoretical, methodological, and axiological guidelines for implementing this model in forming the EC of future agricultural engineers [18].

The expediency of applying the concept of student-centered learning as a theoretical basis for the formation of EC is substantiated. To implement this concept, taking into account the results of scientific and pedagogical research [19], we have proposed a pedagogical technology for managing the process of formation of the EC of future agricultural engineers. Regarding the technological process of environmental competence forming in future professionals, the pedagogical system should be provided with didactic mechanisms for managing students' learning and creative activities at all stages of the educational program [20]. This technology aims to increase the efficiency of the formation of environmental competence of the future engineer of agricultural profile based on systematic management of the pedagogical process.

We present a model of managing the process of EC forming in future agricultural engineers in the form of a semantic network, the initial peaks of which are the requirements of educational and qualification characteristics and educational and professional training programs. The final peak is a set of educational components of the environmental competence of agricultural engineers. Achieving educational results is based on the pedagogical influence of functional didactic units, the tops of which are management functions: planning, organization, motivation, control, and analysis.

The general dependence of the level of ecological competence (EC) forming in future agricultural engineers at the level of criteria achievement for educational activities (x_1, x_2, \dots, x_n) in terms of management of the set of functions for planning, organization, motivation, control and regulation $\Sigma (P, O, M, K, P)$ can be represented by the function of achieving the initial, intermediate and final goals:

$$EC = f\{\Sigma P(X_n) + \Sigma O(X_n) + \Sigma M(X_n) + \Sigma C(X_n) + \Sigma A(X_n)\} \quad (1)$$

where: $\Sigma (P, O, M, C, A)$ are the intermediate goal functions (planning, organization, motivation, control, regulation); (x_p) is criteria for didactic goals (indicators of the level of environmental competence formation in the relevant management function).

The development function of the individual determines the components of environmental competence based on its continuous development under the influence of educational processes. Let's consider ecological competence as a constantly growing characteristic of the professional competence of the future agricultural engineer. We can offer a general mathematical model for the process of achieving the level of ecological competence formation in the form of a mathematical power function:

$$EC = A * (x_1^a + x_2^b + \dots x_n^c) \quad (2)$$

where: EC is a conditional definition of the achieved level of ecological competence in the process of managing student activities; A is a constant coefficient that reflects the dependence of the level of formation of environmental competence on the factor characteristics (pedagogical conditions) and the organizational level of management of students' educational activities; $X_1 \dots X_n$ are the conditional definition of factor features that are taken into account as criteria of ecological competence in determining this function; a, b, c are indicators of degree at numerical values of factor signs.

The results of research on the nature of the process of achieving students' learning goals give reason to believe that the management model of the process of acquiring the formation of environmental competence can be represented as a nonlinear parabolic dependence.

5 Conclusions

Environmental competence is an integral attribute of the professional engineering activity of agricultural specialists. Ecological competence of agricultural engineers is a system of acquired environmental and engineering knowledge, skills, experience in professional engineering, mastery of methods for effective solution and prevention of environmental problems, the ability to choose optimal technologies and technical means in terms of production activities taking into account possible environmental consequences and moral and ethical imperatives.

Based on the analysis of the content of engineering activities, the structural components of the model of ecological competence of future engineers of the agricultural sector were determined: emotion and value, cognitive, activity, personal developing. Ecological competence forming in agricultural engineering students is carried out based on the pedagogical influence of functional didactic knots, which tops are administrative functions: planning, organization, motivation, control, regulation.

The new results concerning the visualization of the process of formation of environmental competence of future engineers in the agricultural sector were obtained. It is represented by a management model in the form of a mathematical power function. In this case, the productivity of achieving educational results is determined by the level of pedagogical influence on educational activities by the teacher and the level of co-management and self-management by the student.

Due to the application of the functional management system, the controllability of the pedagogical process is ensured. That determines the high level of formation of ecological competence. The results showed that experimental groups' students were by 25% better in professional skills during internships at enterprises.

The obtained results allowed to determine the ways of further scientific and pedagogical research in this direction: development of information electronic methodical systems of educational and methodical support in the conditions of ecological competence forming in future engineers of the agricultural profile; introduction of pedagogical SMART technologies of management of educational and creative activity of students during the period of their engineering education.






References

1. Nathan, R., et al.: A movement ecology paradigm for unifying organismal movement research. *Proc. Natl. Acad. Sci. U. S. A.* **105**(49), 19052–19059 (2008). <https://doi.org/10.1073/pnas.0800375105>
2. National strategy of development of education in Ukraine on 2012–2021: Accepted by Cabinet of Ministers of Ukraine a 11 heather. <http://www.kmu.gov.ua/control/uk/publish/article>. Accessed 16 Feb 2021
3. Hadgraft, R.G., Kolmos, A.: Emerging learning environments in engineering education. *Australas. J. Eng. Educ.* **25**(1), 3–16 (2020). <https://doi.org/10.1080/22054952.2020.1713522>
4. Rychen, D.S., Salganik, L.H.: *Defining and Selecting Key Competencies*. Hogrefe & Huber Publishers, Göttingen (2001)
5. United Nations World Commission on Environment and Development: *Report of the World Commission on Environment and Development: Our Common Future*. Oxford University Press, Oxford (1987)
6. Klochko, O.V., Nagaev, V.M., Kljchko, V.I., Pradivliannyi, M.G., Didukh, L.I.: Computer oriented systems as a means of empowerment approach implementation to training managers in the economic sphere. *Inf. Technol. Learn. Tools* **68**(6), 33–46 (2018)
7. Symonenko, S., Zaitseva, N., Titova, O., Vynogradova, M.: Development of communicative competence as a precondition of competitive software engineer formation. In: Nadykto, V. (ed.) *Modern Development Paths of Agricultural Production*, pp. 307–315. Springer, Cham (2019). https://doi.org/10.1007/978-3-030-14918-5_32
8. Winterton, J., Delamare, F.: *Typology of knowledge, skills and competences: clarification of the concept and prototype*. Cedefop Reference serie 64. Office for Official Publications of the European Communities, Luxembourg (2006)
9. Huit, W.: *Motivation to Learn: An Overview*. Educational Psychology Interactive. Valdosta State University, Valdosta (2001)
10. Boon, J., Klink, M.: Competencies: the triumph of fuzzy concept. *Proc. Acad. Hum. Resour. Dev. Annu. Conf.* **1**, 327–334 (2002)
11. Tomakov, V.Y.: *Conception of Forming of Ecological Competence of Future Engineer*: Monograph. Kursk HTU, Kursk (2009)
12. Biriukova, N.A.: The formation of an ecological consciousness. *Russ. Educ. Soc.* **12**, 34–45 (2014). <https://doi.org/10.1080/10609393.2005.11056938>
13. Yashnik, S.: Ethno-culture varieties of management culture and socio-normative prerequisites of its development. *Educ. Technol. Inform.* **5**, 264–272 (2014). [in Czech]
14. Mansfield, B.: Competence in transition. *J. Eur. Ind. Training* **28**(2/3/4), 327–324 (2004)

15. Koshuk, O.B.: Perspective directions of modernization to vocational training of future mechanical engineers agricultural industry. *Sci. J. Innov. Solutions Mod. Sci.* **8**(17), 24–36 (2017)
16. Lushchyk, Y.: Training future agrarians: specifics of academic programmes of bachelor's degrees in Great Britain. *Central Eur. J. Sci. Res.* **5**(41), 42–52 (2017). [in Czech]
17. Cropley, D.H., Cropley, A.J.: Engineering creativity: A systems concept of functional creativity. *Creativity Across Domains Faces Muse* **1**(15), 169–185 (2005)
18. Gjugh, H.: Environmental education, narrative complexity and postmodern science fiction. *Int. J. Sci. Educ.* **15**, 607–625 (1993)
19. Klochko, O., Nagayev V., Kovaleko, O., Fedorets, V.: Forming of professionally creative competence of prospective agrarian managers by facilities of digital technologies. In: *Proceedings of the International Scientific Conference. Society. Integration. Education*, vol. IV(11), pp. 460–474 (2020). <https://doi.org/10.17770/sie2020vol4.4847>
20. Leal Filho, W., Nesbit, S. (eds.): *New Developments in Engineering Education for Sustainable Development*. WSS, Springer, Cham (2016). <https://doi.org/10.1007/978-3-319-32933-8>



Electronic Textbooks as Means for Developing Professional Competencies of Engineering Students

Vitalii Svyrydiuk¹ , Petro Luzan² , Olha Svyrydiuk¹ ,
Olena Titova³ , and Oksana Popova⁴ 

¹ Pavlo Tychyna Uman State Pedagogical University, 28, Sadova St.,
Uman 20300, Ukraine

Vetal-79@i.ua

² Department Institute of Vocational Education and Training of NAES, 98,
Chapaievskhe Ave., Kyiv 03045, Ukraine

³ Tavria State Agrotechnological University, 18, B. Khmelnitsky Ave.,
Melitopol 72310, Ukraine

⁴ Republican Institute For Vocational Education, 32, K. Liebkhneht St.,
220004 Minsk, Belarus

Abstract. The article is devoted to the problem of electronic textbooks (e-textbooks) introduction into the practice of engineering education. This study focused on applying electronic textbooks to improve students' professional competence development during their acquisition of Electrical Engineering disciplines. The approach of purposeful development of students' knowledge and skills in the electrical engineering field was used. The *Electrical Engineering* electronic textbook was developed using the open Internet universal system of information management (CMS) Joomla 3.5. The e-textbook included 20 topics supported by theoretical information, illustrations, and electrical processes simulations with the opportunity to manage the simulations. The electronic textbook was equipped with the tests to provide systematic, incremental and purposeful acquisition of the learning content. The test also enabled to assess of students' learning outcomes of the *Electrical Engineering* course. The electronic textbook was tested under the conditions of five Ukrainian vocational schools. The experiment results provided evidence of the electronic textbook efficiency in developing the professional competence of engineering students with a probability of 95%. The conclusion about the positive impact of the electronic textbook application on the students' learning outcomes, development of their needs, motives, and goals was not accidental. Some directions of further research have been outlined.

Keywords: E-textbook · Professional competence · Engineering education · Electrical Engineering · Visual information · Pedagogical experiment

1 Introduction

Nowadays, engineering productions need a competent engineer, a flexible, mobile, purposeful personality with an active civil position, who has successfully acquired educational and professional competencies, can solve problems, and is ready to lifelong learning developing his professional career. Therefore, the successful adaptation of a graduate of vocational (technical) educational institutes (hereinafter – V (VT) EI) to the real conditions of production increasingly depends on students' thorough mastery of the advanced engineering knowledge combined with their practical application skills. Developing professional competence of engineering students requires improvement of their information and digital literacy, design skills, analysis, and decision-making skills with a high level of reflection.

In the digital society, where intelligent mobile devices are becoming more and more popular, the information and communication technologies allow easy, fast global access to educational, scientific, and other information at any time. It is also possible to apply digital technologies in self-education when a student can find the answer to any question through discussion on forums, qualified consultations, video instructions, training tests, etc.

2 Literature Review

In V (VT) EI, engineering students' competence-oriented training is the systematic mastering by students a set of fundamental professional and key competencies. In general, competence is interpreted as the person's ability to perform a certain type of activity, which is expressed through knowledge, skills, moral and ethical values, and other personal qualities.

It should be noted that general professional competencies are knowledge and skills that are common to the profession. For example, according to the educational standard [1, 2], an electrician who will repair and maintain electrical equipment must know principles of energy conservation, rational operation of electrical equipment, safety regulations, and the basics of labor law, a market economy, and entrepreneurship. Recent research showed that engineering students should be focused on using electricity, operating electrical equipment and power tools effectively, processing information to solve problems, and performing professional duties successfully. Necessary knowledge and skills complete the content of general professional competencies of the future graduate [3].

Analyzing the factors that affect the quality of engineering education, scientists emphasize that in the structure of electrical professional competencies, the central core is knowledge and skills in electrical engineering, a discipline that covers electrical and magnetic phenomena, electricity production, transmission, distribution, among consumers and its conversion into other types of energy [4]. The point, in this case, is that the results of mastering the *Electrical Engineering* discipline form the subject of electrical competence of future experts in electrical engineering. In the current study, that phenomenon was considered the dominant professional competence of the prospective electrician. It determines the electrician's readiness to carry out qualified

installation, repair, adjustment, and maintenance of electrical equipment, lighting, and routine work due to a balanced combination of electrical knowledge, skills, needs, and motives for mastering innovative experience in the field of electrical engineering.

To increase the efficiency of mastering the learning content in electrical competence by engineering students, a teacher should use a set of teaching aids which include material and ideal objects, intermediaries, and tools to activate the students' educational and cognitive activities, optimize the educational process, improve its quality. The newly declared provisions are confirmed by scientists [5], highlighting some functions of teaching aids. Firstly, it's compensatory (facilitating the process of acquiring knowledge, reducing the time and effort for studying). Secondly, they mean informativeness (transmission, deepening, concretization of learning content). Thirdly, integrativeness (study of an educational object, process, or phenomenon both in parts and as a whole) is included. Fourthly, instrumentality (safe and rational provision of educational and cognitive activities of students and mentoring activities of the teacher) has been emphasized. Finally, communicativeness (the quality of being willing, eager, or able to talk or impart information in teacher-student or student-student groups) [6].

There is no doubt that the mentioned functions of electronic educational resources (EER) fully perform teaching aids based on digital media of any type, placed on the Internet, reproduced by electronic digital technical means, and used in the educational process [7, 8]. Since the subject of our research is related to the use of e-textbooks, we consider it is important to cover the characteristics and requirements of that e-learning tool.

Scientists note that an e-textbook is interpreted as an electronic educational publication with a systematic presentation of educational material that corresponds to the syllabus [7, 8], contains digital objects of various formats, and provides interaction between a student and a teacher fostering engineering student's creativity [9, 10]. Regulatory requirements for the content, organization of material, interface, design, etc., are set for this type of e-learning resources. Summarizing the existing requirements, we can state that an e-textbook should be designed with a high level of artistic design, clearly structured and logically organized learning content as well as productive methodological tools [11, 12]. An e-textbook should be designed on the principles of clarity, accessibility, activity and consciousness, and consistency. There is one more vital idea that learning with an e-textbook should be organized to consider the students' individual characteristics [13]. That should be the dominant vector [14].

The scientists emphasize that an e-textbook has significant advantages if requirements are met compared with the conventional hard copy of a textbook [15, 16]. Obviously, the positive effect of an e-textbook could be achieved due to the use of hyperlinks, audio and video files, computer animation, provision of a high level of visibility of learning content. All those tools exceed the static representation of diagrams, graphs, charts, and photos used in a printed textbook. Another relevant quality of an e-textbook is mentioned in the publications [12, 13, 16]. It can be quickly updated compared with a printed textbook. Moreover, when using the e-textbook, it is possible to consider students' individual abilities through text, hypertext or frame structure, hints, multi-level test tasks, etc. The application of an e-textbook for distance learning enables feedback and interaction and simplicity and convenience while using various gadgets (smartphones, tablets, and laptops) [9].

Despite the extensive publications on the problem of electronic textbooks designing and application, some issues still require to be studied. The fact is that the acquisition of subject competencies takes place in stages according to the following logic: a) setting and understanding the cognitive task, creation of students' learning incentives, b) students' perception of new material from different sources, c) comprehension and generalization of new knowledge, d) consolidation and improvement of new knowledge, e) application of knowledge in practice, the formation of skills and abilities, f) verification and analysis of students' competence achievements. Naturally, each stage of that competence-oriented study has its own learning goal, the achievement of which is aimed at students' mastering the competencies of a particular discipline. The development of the methodological basis to meet the requirements of every stage was one of the goals of the current research [5].

In this regard, the research was aimed at the approaches to provide the requirements for the development of electronic educational resources. As the problem principle includes appropriate forms, methods, and means of learning based on the logic of students' search activities, we set the goal to study the question of the content of an e-textbook and the ways of its organization so that it includes concepts and methods for a sufficiently high level of generalization, synthesis of inductive and deductive activities, the emergence of problem situations in the students' minds.

3 Research Methodology


The system of work methods with an e-textbook should determine the choice of methods for students' theoretical and practical activities and provide the optimal combination of word and clarity, inductive and deductive, sensory and rational, knowledge and practical action, etc. We used theoretical, comparison, synthesis, and abstraction, empirical and statistical methods to achieve this goal. Theoretical methods allowed to analyze published resources on the research problem to clarify the content of basic concepts and findings, justify the application of theoretical principles for development and application of an e-textbook to develop students' engineering competence, study teaching practice at V (VT) E institutions, available software as well as normative sources to trace the development of pedagogical thought on the problem. That enabled us to determine the directions of the current research. Comparison, synthesis, and abstraction methods were used to justify applying Joomla 3.5 open universal control system for publishing information on the Internet (CMS). It was used for the development of the *Electrical Engineering* e-textbook. Empirical methods (observation, questionnaire, pedagogical experiment) were employed to study and prove the effectiveness of the *Electrical Engineering* e-textbook for shaping electrical and technical competence in engineering students. The statistical method enabled gathering and processing experiment data and determining the statistical significance of the results obtained in the experimental part of the study.

4 Results

During the e-textbook development process, the designers should consider the mentioned requirements for the content, organization of learning information, interface, design of e-textbooks, theoretical provisions on the laws of visual perception of data, the selectivity of students' attention in acquiring new knowledge. The *Electrical Engineering* e-textbook employs the content and structure designed according to the logic of the educational process [17, 18].

Structurally, the e-textbook includes 20 topics and a laboratory workshop on the Electrical Engineering subject. Each topic of the e-textbook is presented in the following order: diagrams with reference signals; theoretical material using a comprehensive (both reproductive and problem) presentation of the material, a combination of verbal and visual (photo, presentation, video, gif-animation, etc.) presentation of information (Fig. 1).

Закон Ома для ділянки електричного кола




$$U = I \cdot R$$

$$I = \frac{U}{R}$$

$$R = \frac{U}{I}$$

Сила струму в ділянці кола прямо пропорційна напрузі на кінцях цієї ділянки й обернено пропорційна її опорю

Закон Ома для повного кола, струму в електричному колі дозволяє визначити за певних умов, поділивши напругу всього кола — суму внутрішнього і зовнішнього опору.



Робота електричного струму дозволяє дізнатися величину сили струму, напруги і часу протікання струму. Потужність — це добутки сили струму на напругу. Роботу електричного струму вираховують у джоулах (Дж), а потужність — у ваттах (Вт).

$$A = I \cdot U \cdot t \quad P = UI = I^2 R = \frac{U^2}{R}$$

Подивись відео

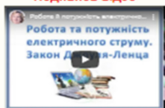


Fig. 1. A fragment of the presentation of theoretical material in the *Electrical Engineering* e-textbook on the topic *Alternating current and alternating current circuits* [19].

The e-textbook also includes virtual simulators (programs for simulation of electrotechnical equipment working processes, visualization of experiments with the ability to manage some parameters) presented in Fig. 2.



Fig. 2 Virtual simulator *Capacitor Laboratory* (fundamentals of electrostatics) [19].

The homework is provided as, for example, implementing visual diagrams for coding the content of learning material with the application of reference signals, practical tasks, exercises to consolidate new material, etc. (Fig. 3), tests for self-assessment of students' achievements, virtual laboratory work.



Fig. 3 A fragment of homework in the *Electrical Engineering* e-textbook on the topic *Electric machines of direct current* [19].

As a teacher should play the dominant role in the learning process which employs an e-textbook, we have defined the main teachers' functions. They include motivation of students, fostering educational and cognitive activities in mastering the material of an e-textbook, organization, regulation of the processes of mastering new knowledge and skills, coordination of education (frontal, group, pair, individual) forms, diagnostics, assessment of students' competence achievements to set promising educational tasks.

To provide productive students' activity while mastering electrical competence, students need to develop the skills of self-assessment, self-analysis, self-motivation, and self-organization. To respond to the current requirements of the graduates, e-textbook realizes the idea of equipping engineering students with a set of knowledge and developing their ability of self-development and self-study of technical phenomena, processes, and equipment. For this purpose, a complex of test items for self-control, which combines the verbal and visual representation of the information, uses possibilities of game and video to foster students' self-estimation of educational achievements. They have been developed and introduced in the e-textbook (Fig. 4). One more powerful stimulus was added to activate the cognitive activity of engineering students. It was a possibility to check the test answers immediately.



Fig. 4 An example of a test item using game forms [19].

A pedagogical experiment was conducted to determine the effectiveness of the *Electrical Engineering* e-textbook for the development of electrical competence of engineering students. The experimental study involved 29 teachers and 547 students from Bila Tserkva Vocational Lyceum state vocational school, Higher Vocational School № 34 Vynohradiv, Korsun-Shevchenko Vocational Lyceum state educational institution, Ovruch Vocational Lyceum, Uman Vocational Agricultural Lyceum state educational institution in 2018 and 2019. According to the parallel forming experiment program, control (293 students) and experimental (256 students) groups were chosen at the vocational schools.

The hypothesis, which was tested, stated that the development of electrical competence of engineering students would be more effective if students of the experimental

groups use an e-textbook (along with the usual teaching aids), which structurally and functionally corresponds to the logic of the educational process and takes into account the laws of visual perception of information. It is noteworthy that students used conventional textbooks while mastering the Electrical Engineering course in the control groups. The method of expert assessment was used to determine the levels (high, sufficient, medium, low) of students' competence.

The analysis of the pedagogical experiment results showed a certain advantage in the levels of electrical competence of the students who studied in the experimental groups compared with the control ones. In particular, about 74% of students in the experimental groups showed high and sufficient levels of electrical knowledge and skills formation at the end of the experiment. The share of students with high and adequate levels in the control groups was approximately 11% lower.

Experts also revealed unity because electrical competence's motivational and value component is better shaped in experimental groups' students. Compared to the results shown by students of the control groups, the share of respondents with a high level of needs and motives of electrical activity is higher by 5.94%, with sufficient, higher by 9.35%; with the average, lower by 12.16%; with low, lower by 3.13% (Fig. 5).

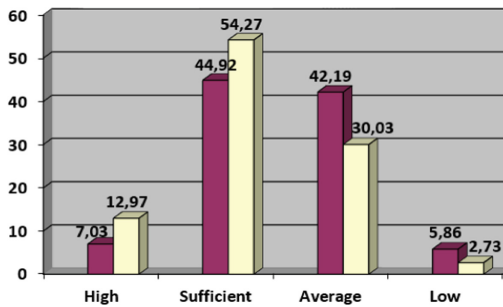


Fig. 5 The levels of electrical competence in students of control (■) and experimental (■) groups, %.

At the same time, it was noted that the learning method with an e-textbook influenced the reflexive ability of the students. It gave new information for additional research on the problem of forming personal qualities and students' reflective skills, which are considered to be quite painstaking tasks and require systematic efforts of the vocational schools teaching staff.

To compare the distributions of students in control and experimental groups, Statistics in Pedagogy application [20] was used after the expert assessment of the respondent's electrical competence levels. Since the results were measured on an ordinal scale and the number of gradations was 4 (four levels), the sample size was quite large ($n > 50$), the program automatically performed calculations according to the Pearson's test (c_2). The results of statistical calculations proved the efficiency of the e-textbook with a probability of 95%. It gave evidence that the conclusions about the

positive impact of the e-textbook on the students' outcomes, their motivation to master the Electrical Engineering course were not accidental.

5 Conclusions

The analysis of the theory and practice of engineering education showed that nowadays, advanced production needs a competent, flexible, mobile, and efficient engineer who can successfully solve problems and is ready for lifelong learning. Searching for ways to improve engineering students' information and digital literacy, design skills, analysis, and decision-making skills with a high level of reflection, we accepted and supported the overall opinion that digital technologies used for self-education help students find and process information effectively. To increase the efficiency of mastering the learning content by engineering students, we studied how the application of different teaching aids based on information and communication technologies influenced students' educational and cognitive abilities, optimized the educational process, and improved its quality. In this context, the subject of the current research was related to the use of e-textbooks. The *Electrical Engineering* e-textbook under consideration covered 20 topics and included a laboratory workshop on the subject, diagrams with reference signals, theoretical material with reproductive and problem presentation, a combination of verbal and visual aids. The e-textbook also included virtual simulators, home tasks, and control tests. The survey revealed that the learning process that employed an e-textbook enabled a teacher to play the dominant role in motivating students, fostering their educational and cognitive activities, regulating knowledge and skills mastering, diagnostics, and assessing students' achievements. To determine the effectiveness of the *Electrical Engineering* e-textbook for the development of electrical competence of engineering students, a pedagogical experiment was conducted. It involved 29 teachers and 547 students from 5 Ukrainian state vocational schools. The results showed significant differences in students' levels of electrical competence in experimental groups compared with control ones.

It has been stated that the development of engineering students' personal and professional qualities, their reflexive abilities is not currently intensive enough. That requires additional scientific and pedagogical research. Moreover, further research could be devoted to the justification of the didactic conditions for the extensive introduction of e-textbooks into the engineering educational process, designing and applying the criteria for learning outcomes assessment.

References

1. Electrician for repair and maintenance: Ukrainian Professional Standard for Engineering Education. <http://www.nmc.od.ua/wp-content/uploads/2019/03/F.pdf>. Accessed 14 Oct 2019
2. Becker, M.: Competence matrix for the sector electronics / electrical engineering. VQTS II Vocational Qualification Transfer System Leonardo da Vinci, LLP-LdV-TOI-2007-AT0017, Flensburg. http://www.biat.uni-flensburg.de/biat/Projekte/VQTS-II/WP2-VQTSCompetence-Matrix-Electrician-II_EN.pdf. Accessed 23 Aug 2019

3. Modlo, Ye., Semerikov, S.: Modernization of professional training of electromechanics bachelors. ICT-based Competence Approach (2018)
4. Loyalka, P., Carnoy, M., Froumin, I., Dossani, R., Tilak, J.B., Yang, P.: Factors affecting the quality of engineering education in the four largest emerging economies. *High. Educ.* **68**(6), 977–1004 (2014). <https://doi.org/10.1007/s10734-014-9755-8>
5. Fan, L.P.: Engineering education oriented teaching material construction for electrical and electronic technology. In: Lin, S., Huang, X. (eds.) CSEE 2011. CCIS, vol. 217, pp. 319–323. Springer, Heidelberg (2011). https://doi.org/10.1007/978-3-642-23339-5_58
6. Symonenko, S., Zaitseva, N., Titova, O., Vynogradova, M.: Development of communicative competence as a precondition of competitive software engineer formation. In: Nadykto, V. (ed.) *Modern Development Paths of Agricultural Production*, pp. 307–315. Springer, Cham (2019). https://doi.org/10.1007/978-3-030-14918-5_32
7. Hernandez-de-Menendez, M., Morales-Menendez, R.: Technological innovations and practices in engineering education: a review. *Int. J. Interact. Design Manuf. (IJIDeM)* **13** (2), 713–728 (2019). <https://doi.org/10.1007/s12008-019-00550-1>
8. Abdulla, M., Motamedi, Z., Majeed, A.: Redesigning Telecommunication Engineering Courses with CDIO geared for Polytechnic Education. In: *10th Conference on Canadian Engineering Education Association Proceedings* (2019). <https://doi.org/10.24908/PCEEA.V10.13855>
9. Hadgraft, R.G., Kolmos, A.: Emerging learning environments in engineering education. *Australas. J. Eng. Educ.* **25**(1), 3–16 (2020). <https://doi.org/10.1080/22054952.2020.1713522>
10. Haldorai, A., Murugan, S., Ramu, A.: Evolution, challenges, and application of intelligent ICT education: An overview. In: *Computer Applications in Engineering Education* (2020). <https://doi.org/10.1002/cae.22217>
11. Laketa, S., Drakulic, D.: Quality of lessons in traditional and electronic textbooks. In: *Interdisciplinary Description of Complex Systems, INDECS*, vol. 13, pp. 117–127 (2015). <https://doi.org/10.7906/indecs.13.1.12>
12. , Yc., Liu, TC., Kinshuk, R.: Research on teachers’ needs when using e-textbooks in teaching. *Smart Learn. Environ.* **2**(1) (2015). <https://doi.org/10.1186/s40561-014-0008-1>
13. Chiu, T.K.F.: Introducing electronic textbooks as daily-use technology in schools: a top-down adoption process. *Br. J. Edu. Technol.* **48**, 524–537 (2017). <https://doi.org/10.1111/bjjet.12432>
14. Bin, E., Islam, A., Gu, X., Spector, J.M., Wang, F.L.: A study of Chinese technical and vocational college teacher’ adoption and gratification in new technologies. *Br. J. Edu. Technol.* **51**(6), 2359–2375 (2020). <https://doi.org/10.1111/bjjet.12915>
15. Gerhart, N., Peak, D., Prybutok, V.R.: Encouraging e-textbook adoption: merging two models. *Decis. Sci. J. Innov. Educ.* **15**, 191–218 (2017). <https://doi.org/10.1111/dsji.12126>
16. Engbrecht, J.R.: Digital textbooks versus print textbooks. In: *Culminating Projects in Teacher Development*, vol. 35 (2018). https://repository.stcloudstate.edu/ed_etds/35. Accessed 12 Sept 2020
17. EDUCAUSE Homepage. <https://www.educause.edu/ecar>. Accessed 15 Oct 2020
18. All about Circuits: Lessons in Electric Circuit. <https://www.allaboutcircuits.com/textbook/>. Accessed 27 Dec 2019
19. Svyrydiuk V.: E-book electric engineering (2018). <http://upal-eltech.pto.org.ua/>. Accessed 24 Nov 2019
20. Statistics in Pedagogy: Computer application. <http://www.mtas.ru/uploads/stat.zip>. Accessed 12 July 2012

Author Index

A

Ablieieva, Iryna, 571
Acho Zuppa, Leonardo, 546
Akimov, Oleg, 292
Alnusirat, Walid, 313
Andreev, Andrii, 644
Arhat, Roman, 479
Arras, Peter, 677
Avdieieva, Olena, 499

B

Babenko, Yevgen, 151
Babov, Konstantin, 424
Badir, Karim Kashash, 383
Balalayeva, Elena, 489
Balaniuk, Anna, 98
Basova, Yevheniia, 127
Belhadi, Salim, 219
Berestovoi, Ivan, 489
Berladir, Kristina, 282
Berlizeva, Tatyana, 241
Bershak, Svetlana, 250
Bezpalova, Ala, 141
Bezverkhniuk, Tatiana, 424
Boiko, Andrii, 13
Boltianska, Nataliia, 22
Boltyansky, Oleg, 53
Bondar, Oleksandr, 13
Bondarenko, Tetiana, 415
Bovnegra, Liubov, 655
Bozhko, Tetiana, 455
Burdiak, Mykhailo, 119
Burla, Oksana, 571
Bychkov, Igor, 602

C

Cagáňová, Dagmar, 323
Chekh, Oleh, 571
Chmyr, Oksana, 119
Chukurna, Olena, 445
Chumachenko, Tatiana, 141, 180

D

Danchenko, Iryna, 697
Dichev, Dimitar, 415
Dmyterko, Petro, 592
Dobrovolskyi, Vitalii, 445
Dyadyura, Kostiantyn, 260
Dzhemalyadinov, Ruslan, 302
Dzhemelinskyi, Vitaliy, 313
Dzhemilov, Eshreb, 219, 302
Dziuba, Lidiia, 119

E

Emiroglu, Uğur, 219
Enrich-Prast, Alex, 571

F

Fedorovich, Vladimir, 151
Fomin, Oleksandr, 13
Forduy, Serhiy, 634
Frolenkova, Olga, 141, 180

G

Garashchenko, Yaroslav, 67
Glavchev, Maxim, 33
Gondlyakh, Aleksandr, 272
Grabovskiy, Andrey, 509
Grimzin, Igor, 67, 241

Gusak, Oleksandr, 282
Gushcha, Sergey, 424

H

Hatala, Michal, 623
Hovorun, Tetiana, 282
Hrebenyk, Liudmyla, 260
Hrechka, Iryna, 509
Hrych, Artem, 644
Hryshchenko, Iryna, 535
Hulchuk, Yurii, 323

I

Ilchuk, Nataliia, 323
Ivakhniuk, Tatyana, 260
Ivanov, Vitalii, 98, 521
Ivanova, Maryna, 127

J

Jiang, Xiaohong, 373

K

Kachur, Oleksandr, 592
Kaidash, Oksana, 343
Kalchenko, Vitaliy, 160
Kalchenko, Volodymyr, 160
Kamchatna-Stepanova, Kateryna, 292
Kantor, Serhiy, 634
Karavaiev, Taras, 613
Kassien, Oleg, 445
Khaldobin, Viktor, 634
Khlietova, Olha, 489
Khukhryanskiy, Oleg, 623
Kirkopulo, Kateryna, 655
Kishnevsky, Victor, 466
Klymenko, Nataliya, 141, 180
Kobalava, Halina, 582
Kolosov, Aleksandr, 272
Komakha, Volodymyr, 613
Konovalov, Dmytro, 582
Kopei, Volodymyr, 395
Korendiy, Vitaliy, 592
Kornienko, Victoria, 644
Koshuk, Oleksandr, 687
Kosmachevskiy, Volodymyr, 88
Kostina, Maryna, 43
Kostyk, Kateryna, 292
Kostyk, Viktoriia, 292
Kovalevska, Olena, 78
Kovalevskyy, Sergiy, 78
Kozakova, Natalia, 151
Kozhevnikov, Georgii, 33
Krol, Oleg, 3

Kukhar, Volodymyr, 489
Kukhareenko, Svitlana, 343
Kulesh, Ekaterina, 373
Kunitsyn, Maksym, 405
Kupriyanov, Oleksandr, 415
Kurgan, Victor, 250
Kuzhelnyi, Yaroslav, 160
Kyrepin, Vecheslav, 697
Kyrylenko, Nelya, 546
Kysylevska, Alona, 424

L

Lapuzin, Alexandr, 499
Larshin, Vasily, 170, 188
Lebedev, Vladimir, 141, 180
Lebedev, Vladimir, 302
Lesyk, Dmytro, 313
Levchenko, Roman, 479
Levinskyi, Oleksandr, 250
Liaposhchenko, Oleksandr, 623
Lingur, Valeriy, 655
Lishchenko, Natalia, 170, 188
Liu, Yiming, 373
Lopakov, Oleksii, 88
Losev, Alexey, 602
Luzan, Petro, 687, 707
Lysenko, Tatiana, 241
Lysyi, Oleksandr, 170

M

Machado, José, 455
Mahopets, Sergii, 353
Mamchur, Oleksandr, 272
Manoilo, Eugenia, 623
Martinez, Silvia, 313
Masharsky, Alexander, 435
Merezhko, Nina, 613
Migranov, Mars, 363
Mirzak, Volodimir, 353
Mitiashkina, Tetiana, 697
Moiseev, Viktor, 623
Mordyuk, Bohdan, 313
Mosia, Iryna, 687
Mukoid, Roman, 664
Mushtruk, Mikhailo, 664

N

Nagayev, Viktor, 697
Naidenko, Elena, 13
Nemyrovskiy, Yakiv, 353
Nesvidomin, Victor, 557

O

Oborskyi, Gennadii, 98, 466
 Onysko, Oleh, 395
 Orgjyan, Alexandr, 98
 Ostroverkh, Yevgeniy, 151

P

Panchenko, Anatolii, 22, 53
 Panchuk, Vitalii, 395
 Pashchenko, Eugen, 343
 Pashchenko, Viktor, 22
 Pasternak, Viktoriya, 323
 Pavlenko, Ivan, 521
 Pedun, Oleksandr, 479
 Permyakov, Alexander, 127
 Petrakov, Yuri, 199
 Pihnastyi, Oleh, 33
 Piliptsov, Dzmityr, 373
 Pitel, Jan, 521
 Pituley, Lolita, 395
 Plyatsuk, Leonid, 571
 Ponomarenko, Olga, 241
 Popova, Oksana, 707
 Povstyanoy, Oleksandr, 613
 Predrag, Dasic, 43
 Primova, Liudmyla, 260
 Prokopovych, Ihor, 43, 424
 Protasenko, Tatyana, 334
 Prydalnyi, Borys, 109
 Pujol Vazquez, Gisela, 546
 Puzyr, Ruslan, 479
 Puzyrov, Volodymyr, 546
 Pylypaka, Serhii, 535, 557
 Pylypchuk, Mariya, 119
 Pypysunko, Maxim, 644
 Pyzhov, Ivan, 151

R

Radchenko, Andrii, 582, 634
 Radchenko, Mykola, 582
 Radchenko, Roman, 644
 Rebezniuk, Ihor, 119
 Riabchenko, Serhii, 343
 Riaboshtan, Valentyn, 334
 Rogachev, Aliaksandr, 373
 Ruban, Anatolii, 521
 Rybenko, Iryna, 557

S

Savchenko, Denys, 343
 Savchenko, Ievgen, 521
 Savchenko, Nina, 546
 Savenkov, Oleg, 582
 Scherbina, Valeriy, 272

Schuliar, Iryna, 395
 Selezneva, Anna, 602
 Semenyuk, Vladimir, 655
 Semirnenko, Svetlana, 535
 Senyshyn, Anatolii, 229
 Shchetynin, Viktor, 479
 Shelkovyi, Oleksandr, 209
 Shendryk, Sergii, 602
 Shendryk, Vira, 602
 Shepelenko, Ihor, 353
 Shepeliev, Dmitry, 127
 Shilovich, Yaroslav, 272
 Shymchuk, Sergii, 383
 Shymchuk, Yurii, 383
 Shyrokyi, Yurii, 292
 Sierykh, Larysa, 557
 Sierykov, Volodymyr, 509
 Sikailo, Maksim, 199
 Sikirash, Yulia, 405
 Sira, Nataliia, 160
 Sklyar, Vasyl, 160
 Skvortsov, Ivan, 435
 Sokolov, Volodymyr, 3
 Strelchuk, Roman, 209
 Strumnikova, Natalia, 445
 Subotovich, Valery, 499
 Svirzhevskiy, Kostiantyn, 229
 Svyyrydiuk, Olha, 707
 Svyyrydiuk, Vitalii, 707
 Sydorenko, Ihor, 250, 655

T

Tabunshchuk, Galyna, 677
 Tigariiev, Volodymyr, 88
 Tikhenko, Valentin, 466
 Tikhomirov, Anatoly, 466
 Titova, Olena, 687, 707
 Tkachenko, Serhii, 664
 Tkachev, Aleksey, 43
 Tkachev, Anatolii, 43
 Tkachuk, Anatolii, 229, 383
 Tkachuk, Mykola, 509
 Tkachuk, Valentyna, 613
 Tonkonogyi, Volodymyr, 88, 98
 Touggui, Youssef, 219
 Trishch, Roman, 415
 Trokhymchuk, Ivanna, 229
 Tsekhanov, Yuri, 353
 Turmanidze, Raul, 13

U

Uminsky, Sergey, 170, 188
 Usov, Anatoly, 405
 Uysal, Alper, 219

V

Vasylevskyi, Oleg, [489](#)
Vasyliv, Volodymyr, [664](#)
Vaysman, Vladyslav, [445](#)
Vereschaka, Alexey, [363](#)
Verkholantseva, Valentyna, [53](#)
Vitiaziev, Jurii, [67](#)
Volina, Tatiana, [535](#), [557](#)
Volkov, Sergii, [22](#)
Voloshina, Angela, [22](#), [53](#)
Vyshegorodtseva, Maria, [260](#)

Y

Yakovenko, Ihor, [127](#)
Yakubovskaya, Svetlana, [302](#)
Yarmoliuk, Serhii, [455](#)

Yeputatov, Yuriy, [250](#)
Yevtushenko, Nataliia, [241](#)
Yudin, Yuriy, [499](#)

Z

Zablotskyi, Valentyn, [229](#)
Zabolotnyi, Oleg, [323](#), [455](#)
Zaichuk, Natalia, [383](#)
Zaitsev, Sergey, [466](#)
Zaleta, Olha, [455](#)
Zalevska, Olha, [535](#)
Zasiadko, Andrii, [53](#)
Zelikov, Oleksii, [634](#)
Zhadko, Maria, [334](#)
Zheplinska, Marija, [664](#)
Zubkov, Anatoly, [334](#)